
HANDBOOK OF THERMAL ANALYSIS AND CALORIMETRY

SERIES EDITOR: PATRICK K. GALLAGHER

VOLUME 3

**APPLICATIONS
TO POLYMERS AND PLASTICS**

EDITOR

STEPHEN Z.D. CHENG



ELSEVIER

HANDBOOK OF THERMAL ANALYSIS AND CALORIMETRY

SERIES EDITOR

PATRICK K. GALLAGHER

DEPARTMENT OF CHEMISTRY
OHIO STATE UNIVERSITY
USA



ELSEVIER

AMSTERDAM – BOSTON – LONDON – NEW YORK – OXFORD – PARIS
SAN DIEGO – SAN FRANCISCO – SINGAPORE – SYDNEY – TOKYO

This Page Intentionally Left Blank

HANDBOOK OF THERMAL ANALYSIS AND CALORIMETRY

VOLUME 3
APPLICATIONS TO POLYMERS AND PLASTICS

EDITED BY

STEPHEN Z.D. CHENG

DEPARTMENT OF POLYMER SCIENCE
UNIVERSITY OF AKRON
AKRON, OH 44325-3909
USA



2002

ELSEVIER

AMSTERDAM – BOSTON – LONDON – NEW YORK – OXFORD – PARIS
SAN DIEGO – SAN FRANCISCO – SINGAPORE – SYDNEY – TOKYO

ELSEVIER SCIENCE B.V.
Sara Burgerhartstraat 25
P.O. Box 211, 1000 AE Amsterdam, The Netherlands

© 2002 Elsevier Science B.V. All rights reserved.

This work is protected under copyright by Elsevier Science, and the following terms and conditions apply to its use:

Photocopying

Single photocopies of single chapters may be made for personal use as allowed by national copyright laws. Permission of the Publisher and payment of a fee is required for all other photocopying, including multiple or systematic copying, copying for advertising or promotional purposes, resale, and all forms of document delivery. Special rates are available for educational institutions that wish to make photocopies for non-profit educational classroom use.

Permissions may be sought directly from Elsevier Science via their homepage (<http://www.elsevier.com>) by selecting 'Customer support' and then 'Permissions'. Alternatively you can send an e-mail to: permissions@elsevier.co.uk, or fax to: (+44) 1865 853333.

In the USA, users may clear permissions and make payments through the Copyright Clearance Center, Inc., 222 Rosewood Drive, Danvers, MA 01923, USA; phone: (+1) 978 7508400, fax: (+1) 978 7504744, and in the UK through the Copyright Licensing Agency Rapid Clearance Service (CLARCS), 90 Tottenham Court Road, London W1P 0LP, UK; phone: (+44) 207 631 5555, fax: (+44) 207 631 5500. Other countries may have a local reprographic rights agency for payments.

Derivative Works

Tables of contents may be reproduced for internal circulation, but permission of Elsevier Science is required for resale or distribution of such material.

Permission of the Publisher is required for all other derivative works, including compilations and translations.

Electronic Storage or Usage

Permission of the Publisher is required to store or use electronically any material contained in this work, including any chapter or part of a chapter.

Except as outlined above, no part of this work may be reproduced, stored in a retrieval system or transmitted in any form or by any means, electronic, mechanical, photocopying, recording or otherwise, without prior written permission of the Publisher.

Address permissions requests to: Elsevier Science Global Rights Department, at the fax and e-mail addresses noted above.

Notice

No responsibility is assumed by the Publisher for any injury and/or damage to persons or property as a matter of products liability, negligence or otherwise, or from any use or operation of any methods, products, instructions or ideas contained in the material herein. Because of rapid advances in the medical sciences, in particular, independent verification of diagnoses and drugs dosages should be made.

First edition 2002

Library of Congress Cataloging in Publication Data

A catalog record from the Library of Congress has been applied for.

British Library Cataloguing in Publication Data

A catalogue record from the British Library has been applied for.

ISBN: 0-444-51286-1

⊗ The paper used in this publication meets the requirements of ANSI/NISO Z39.48-1992 (Permanence of Paper).
Printed in The Netherlands.

FOREWORD

The applications and interest in thermal analysis and calorimetry have grown enormously during the last half of the 20th century and the beginning of the 21st. The renaissance in these methods has been fuelled by several influences. Certainly the revolution in instrumentation brought on by the computer and automation has been a key factor. Our imagination and outlooks have also expanded to recognize the tremendous versatility of these techniques. They have long been used to characterize materials, decompositions and transitions. We now appreciate the fact that these techniques have greatly expanded their utility to studying many processes such as catalysis, hazards evaluation, etc. or to measuring important physical properties quickly, conveniently, and with markedly improved accuracy over that in the past.

Consequently, thermal analysis and calorimetry have grown in stature and more scientist and engineers have become, at least part time, practitioners. It is very desirable that these people new to the field can have a source of information describing the basic principles and current state of the art. Examples of the current applications of these methods are also essential to spur recognition of the potential for further uses. The application of these methods is highly interdisciplinary and any adequate description must encompass a range of topics well beyond the interests and capabilities of any single investigator. To this end, we have produced a convenient four-volume compendium of such information (a handbook) prepared by recognized experts.

Volume 1 describes the basic background information common to the broad subject in general. Thermodynamic and kinetic principles are discussed along with the instrumentation and methodology associated with thermoanalytical and calorimetric techniques. The purpose is to collect the discussion of these general principles and minimize redundancies in the subsequent volumes that are concerned with the applications of these principles and methods. More unique methods which pertain to specific processes or materials are covered in later volumes.

The three subsequent volumes primarily describe applications and are divided on the basis of general categories of materials. Volume 2 concerns the wide range of inorganic materials, e.g., chemicals, metals, etc. It covers the synthesis, characterization, and reactivity of such materials. Similarly, Volume 3 pertains to polymers and describes applications to these materials in an appropriate manner. Lastly the many important biological applications are described in Volume 4.

Each of these 4 Volumes has an Editor, who has been active in the field for many years and is an established expert in the material covered by that specific volume. This team of Editors has chosen authors with great care in an effort to produce a readable, informative handbook on this broad topic. The chapters are

not intended to be a comprehensive review of the specific subject. The intent is that they enable the reader to glean the essence of the subject and form the basis for further critical reading or actual involvement in the topic. Our goal is to spur your imagination to recognize the potential application of these methods to your specific goals and efforts. In addition, we hope to anticipate and answer your questions, to guide you in the selection of appropriate techniques, and to help you to apply them in a proper and meaningful manner.

P.K. GALLAGHER
Series Editor

PREFACE TO VOLUME 3

This volume focuses on the principles and techniques of thermal analysis and calorimetry of polymeric materials. Although there are several excellent reference books that I have cited, I find myself constantly checking each of them on my bookshelf. It is my intention that this volume will provide a unique addition to the literature in combining scientific concepts with technological aspects for a deeper understanding of their principles and practices.

Polymeric materials are the newest addition to the materials community. A very exciting new field of interdisciplinary macromolecular science and engineering is rapidly emerging: a field where materials science/polymer science, engineering disciplines, chemistry, physics and biology all intersect. This field will have a profound presence in 21st century chemical, pharmaceutical, biomedical, manufacturing, infrastructure, electronic, optical and information technologies. The origin of this field derives from an area of polymer science and engineering encompassing plastic technologies. This field is rapidly expanding to new interdisciplinary research areas such as biomaterials, macromolecular biology, novel macromolecular structures, environmental macromolecular science and engineering, innovative and nano-fabrications of products, and it is translating discoveries into technologies.

This volume comprises sixteen chapters that cover principles of materials' thermodynamic and thermal behaviors such as heat capacity of polymer solids and liquids, relaxation processes, molecular dynamics, polymer crystallization and melting, liquid crystalline polymers, copolymer and polymer blends, polymer films, fibers, thermosets, elastomers, composites and polymer degradation. Various methodologies of thermal analysis and calorimetry appear in all of these chapters. In particular, the stimulating current method and modulated differential scanning calorimetry, which are the most practical and actively discussed topics, are introduced.

The contributors to this volume include three generations of scientists: some of the most well-known pioneering scientists in their own polymer research areas; currently active researchers in different topics of thermal analysis and calorimetry; some of a new generation of scientists who will make substantial progress in the future. These invited contributors reflect my most sincere hope and firm confidence for the future of this research area.

I am extremely grateful to my major Professor, Dr. Bernhard Wunderlich, for his mentorship and guidance. This volume I dedicate to him with my thanks and best wishes to him and his family. I would like to thank my wife, Susan, and my daughter, Wendy. Without their complete selfless support, care, and love, I would not be where I am today. My thanks also go to Dr. Edith Turi for her continuous encouragement and to my students for their valuable help in putting these chapters into the right computer format. Finally, I would like to

acknowledge the various support I have received from the College of Polymer Science and Polymer Engineering at the University of Akron and the Division of Materials Research, and the National Science Foundation (DMR-9617030 and 0203994).

STEPHEN Z. D. CHENG
Volume Editor

Robert C. Musson & Trustees Professor
Chairman, Department of Polymer Science,
The University of Akron

CONTENTS

Foreword - P.K. Gallagher.....	v
Preface - S.Z.D. Cheng.....	vii
Contributors	xxvii
CHAPTER 1. HEAT CAPACITY OF POLYMERS (B. Wunderlich)	
1. MEASUREMENT OF HEAT CAPACITY.....	1
2. THERMODYNAMIC THEORY.....	5
3. QUANTUM MECHANICAL DESCRIPTION.....	5
4. THE HEAT CAPACITY OF SOLIDS.....	10
5. COMPLEX HEAT CAPACITY.....	14
6. THE ADVANCED THERMAL ANALYSIS SYSTEM, ATHAS	16
6.1. The crystallinity dependence of heat capacity.....	16
6.2. Heat capacities of solids	18
6.3. Polyoxide heat capacities	25
6.4. Heat capacities of liquids	27
7. EXAMPLES OF THE APPLICATION OF ATHAS.....	28
7.1. Poly(tetrafluoroethylene)	28
7.2. Poly(oxybenzoate-co-oxynaphthoate)	29
7.3. Large-amplitude motion of polyethylene	30
7.4. Polymethionine	31
7.5. MBPE-9	31
7.6. Liquid selenium	32
7.7. Poly(styrene-co-butadiene)	33
8. TEMPERATURE-MODULATED CALORIMETRY.....	34
8.1. Heat capacity and glass transition	36
8.2. First-order transitions and chemical reactions	40
9. CONCLUDING REMARKS.....	45
ACKNOWLEDGMENTS	46
REFERENCES.....	46

CHAPTER 2. THE GLASS TRANSITION: ITS MEASUREMENT AND UNDERLYING PHYSICS

(Gregory B. McKenna and Sindee L. Simon)

1. INTRODUCTION	49
2. THE APPARENT THERMODYNAMIC BEHAVIOR.....	50
2.1. Some thermodynamic definitions	50
2.2. Time or rate effects	52
2.3. Path dependence of the PVT surface	54
2.4. Isobaric (constant pressure) glass formation vs isochoric (constant volume) glass formation	55
3. KINETICS OF GLASS FORMATION.....	58
3.1. Preliminary comments	58
3.2. Phenomenology of structural recovery	59
3.2.1. The asymmetry of approach experiment	60
3.2.2. The memory or cross-over experiment	61
3.3. The Tool-Narayanaswamy-Moynihan-Kovacs-Aklonis-Hutchinson Ramos (TNM-KAHR) description of structural recovery	62
3.3.1. Strengths and weaknesses of the models	65
3.4. The thermoviscoelastic model	67
3.4.1. Model predictions for volume recovery: comparison with Kovacs' data.....	70
3.4.2. Strengths and weaknesses of the thermoviscoelastic model	72
3.5. Viscosity and segmental relaxation behavior above the glass transition temperature.....	73
4. MICROSCOPIC THEORIES RELATED TO THE GLASS TRANSITION.....	76
4.1. General comments	76
4.2. Free volume models	76
4.3. The Gibbs-DiMarzio configurational entropy model	78
4.4. Comparison of the free volume and configurational entropy models with experiments.....	81
5. MEASUREMENT OF T_g	81
5.1. General comments	81
5.2. Dilatometric methods	82
5.2.1. Fluid confinement dilatometry	82
5.2.2. Length change dilatometry.....	84
5.3. Calorimetric techniques	85

5.3.1. Differential scanning calorimetry (DSC)	86
5.3.2. Temperature-modulated differential scanning calorimetry (TMDSC).....	92
5.3.3. Dynamic heat spectroscopy (DHS)	94
6. PHYSICAL AGING EFFECTS	95
6.1. Linear viscoelastic regime	96
6.2. Nonlinear viscoelastic regime	99
6.3. Engineering properties	100
6.3.1. Yield strength	101
6.3.2. Failure related properties	101
6.3.3. Residual stresses	103
7. CONCLUDING REMARKS	104
ACKNOWLEDGMENTS	104
REFERENCES	104
CHAPTER 3. MECHANICAL RELAXATION PROCESSES IN POLYMERS (S. Matsuoka)	
1. WHAT DO WE MEAN BY THE RELAXATION PROCESS	111
1.1. On the experimental scale	111
1.2. On the molecular scale	116
2. INTERMOLECULAR COOPERATIVITY.....	119
2.1. Free volume and excess enthalpy in the condensed state	121
2.2. Excess enthalpy that drops faster than the conformational entropy	123
3. CHEMICAL STRUCTURE AND T_g	124
4. VISCOELASTICITY DATA ANALYSIS	127
4.1. Viscoelasticity data analysis near but above T_g	127
4.2. Viscoelasticity data analysis of polymer melt	131
4.2.1. Polymers in solution	131
4.2.2. Polymers in bulks	137
5. BEYOND LINEAR VISCOELASTICITY	143
REFERENCES	145

CHAPTER 4. DIELECTRIC ANALYSIS OF POLYMERS

(Peter Avakian, Howard W. Starkweather, Jr. and William G. Kampert)

1. INTRODUCTION	147
2. POLAR AMORPHOUS POLYMERS	150
2.1. Polymethyl methacrylate (PMMA)	150
2.2. Polycarbonate	152
2.3. Polyamides	154
3. NONPOLAR POLYMERS	157
3.1. Hydrocarbon polymers	157
3.2. Fluoropolymers	158
4. MISCIBILITY OF POLYMER BLENDS	159
5. COLD CRYSTALLIZATION OF AMORPHOUS POLYMERS ABOVE T_g	161
6. FREQUENCY-TEMPERATURE RELATIONSHIPS	163
ACKNOWLEDGMENTS	164
REFERENCES	164

CHAPTER 5. CRYSTALLIZATION AND MELTING OF METASTABLE CRYSTALLINE POLYMERS

(Stephen Z. D. Cheng and Shi Jin)

1. INTRODUCTION	167
2. THERMODYNAMIC DEFINITIONS OF THE PHASE AND PHASE TRANSITIONS	167
2.1. Description of phases	167
2.2. Definitions of phase transitions	169
2.3. Phase equilibrium and stability	172
2.4. Concepts of classical metastable states	173
2.5. Metastable states in polymers	174
3. POLYMER CRYSTALLIZATION AND MORPHOLOGY	175
3.1. Isothermal crystallization	176
3.2. Overall crystallization rates	178
3.3. Linear crystal growth rates	180

3.4. Non-isothermal crystallization	181
3.5. Crystalline morphology	182
4. POLYMER CRYSTAL MELTING	183
4.1. Extrapolations to obtain equilibrium melting properties	184
4.2. Metastability changes in polymer crystal melting	187
4.3. Interfaces between crystalline and amorphous regions	189
5. CONCLUDING REMARKS	191
ACKNOWLEDGMENTS	192
REFERENCES	192
CHAPTER 6. CRYSTALLIZATION, MELTING AND MORPHOLOGY OF HOMOGENEOUS ETHYLENE COPOLYMERS (Vincent B. F. Mathot and Harry Reynaers)	
1. INTRODUCTION	197
2. ETHYLENE-PROPYLENE COPOLYMERS	200
2.1. Influence of comonomer content on crystallization and melting	200
2.2. Heat capacity, enthalpy, crystallinity, baseline and excess heat capacity	204
2.3. Illustrating the use of the 'extrapolation method' for calculating crystallinities as applied to 'pseudo heat capacity' measurements on characteristic samples.....	212
2.4. Remarks on the use of the extrapolation method for crystallinity determination	212
2.5. Morphology	213
3. ETHYLENE-1-BUTENE COPOLYMERS	219
3.1. Influence of comonomer content	219
3.2. Metastability: influence of cooling rate	221
3.3. Morphology	222
3.3.1. Metastability: measurements as in temperature modulated calorimetry	224
4. ETHYLENE-1-OCTENE COPOLYMERS	225
4.1. Influence of comonomer content for copolymers with densities above about 870 kg/m ³	225
4.2. Copolymers having a density of about 870 kg/m ³	228
4.2.1. Micro chain structure	228

4.2.2. Crystallization and melting	229
4.2.3. Morphology	233
4.3. Characteristic copolymers with densities below about 870 kg/m ³	236
5. OVERVIEW	239
ACKNOWLEDGMENTS	240
REFERENCES	240
CHAPTER 7. RECENT ADVANCES IN THERMAL ANALYSIS OF THERMOTROPIC MAIN-CHAIN LIQUID CRYSTALLINE POLYMERS (Christopher Y. Li)	
1. INTRODUCTION	245
2. LIQUID CRYSTALS AND LIQUID CRYSTALLINE POLYMERS .	247
3. THERMODYNAMIC TRANSITION BEHAVIORS	253
4. ENANTIOTROPIC AND MONOTROPIC BEHAVIORS	259
5. EFFECTS OF MESOGENIC GROUPS AND SPACERS ON THE LIQUID CRYSTALLINE ORDERS AND STABILITY	263
6. CONCLUDING REMARKS	268
REFERENCES	268
CHAPTER 8. POLYMER BLENDS AND COPOLYMERS (James Runt and Jiang Huang)	
1. INTRODUCTION	273
2. BACKGROUND	273
2.1. Copolymers	273
2.2. Polymer blends	274
3. POLYMER BLENDS	274
3.1. Phase behavior – transitional analysis	274
3.1.1. Background	274

3.1.2. DSC	276
3.1.3. Dynamic mechanical and dielectric measurements	276
3.1.4. Crystalline blends	279
3.2. Crystalline polymer blends and copolymers	281
3.2.1. Co-crystallization	281
3.2.2. Crystalline homopolymer-copolymer blends	281
3.2.2.1. Poly(butylenes terephthalate)/poly(ester-ether) copolymers	281
3.2.2.2. Polytetrafluoroethylene blends	286
3.2.3. Melting point depression and the interaction parameter.....	287
3.2.3.1. Background	287
3.2.3.2. Determination of equilibrium melting points	288
3.2.3.3. Experimental melting points – true melting points	290
3.2.3.4. Ramifications for estimation of χ	291
ACKNOWLEDGMENTS	291
REFERENCES	292
 CHAPTER 9. THERMOSETS (Arturo Hale)	
1. INTRODUCTION	295
2. GENERAL CONCEPTS	296
3. CHEMISTRY AND APPLICATIONS OF THERMOSETTING POLYMERS	301
3.1. Phenolic resins	301
3.2. Melamines	301
3.3. Unsaturated polyester and vinyl esters	302
3.4. Epoxy resins	303
3.5. Thermoset polyurethanes	305
3.6. Bismaleimides	305
3.7. Cyanate ester resins	306
3.8. Polyimides	306
3.9. Benzoxazine resins	307
3.10 Silicon-based polymers	308
4. DETERMINATION OF EXTENT OF CURE	308
4.1. Sample preparation	309
4.2. DSC experimental parameters	310

4.2.1. Initial temperature	310
4.2.2. Final temperature	311
4.2.3. Heating rate	311
4.3. Determination of normalized extent of reaction	311
4.4. Determination of absolute extent of reaction	312
4.5. Heats of reaction of selected groups	315
5. GLASS TRANSITION TEMPERATURE	315
5.1. Generalities	315
5.2. Dependence of T_g on network and chemical structure	318
5.3. Change in specific heat (ΔC_p)	323
5.4. Physical aging	325
6. REACTION KINETICS	330
6.1. General principles	330
6.2. Kinetic parameters determination	334
6.3. Time-temperature superposition kinetics	336
6.4. Diffusion-controlled regime	337
7. PHOTO-INITIATED POLYMERIZATION	338
7.1. Free radical photo-polymerization	339
7.2. Cationic photo-polymerization	342
7.3. Photo-calorimetry	342
8. MODULATED TEMPERATURE DSC	348
9. CONCLUDING REMARKS	350
ACKNOWLEDGMENTS	351
REFERENCES	351
CHAPTER 10. THERMAL ANALYSIS OF POLYMER FILMS (Lei Zhu)	
1. INTRODUCTION	355
1.1. Film preparation and production	355
1.2. Multicomponent films	359
2. GENERAL EXPERIMENTAL CONSIDERATIONS IN THERMAL ANALYSIS OF POLYMER FILMS	360
2.1. Differential scanning calorimetry (DSC)	360

2.2. Thermomechanical analysis (TMA)	360
2.3. Thermogravimetric analysis (TGA)	363
2.4. Dynamic mechanical analysis (DMA)	364
2.5. Dielectric analysis (DEA)	366
2.6. Thermally stimulated current (TSC)	367
2.7. Thermally stimulated creep	368
3. THERMAL ANALYSIS OF SPECIFIC POLYMER FILMS	369
3.1. Polyimides	369
3.2. Polyolefins	381
3.2.1. Polyethylene (PE)	381
3.2.2. Polypropylene (PP)	387
3.3. Poly(ethylene terephthalate) (PET)	392
3.4. Polyamides (nylons)	399
3.4.1. Nylon 6	399
3.4.2. Nylon 66	403
4. CONCLUDING REMARKS	404
REFERENCES	404

CHAPTER 11. THERMAL ANALYSIS OF POLYMER FIBERS

(Alexander J. Jing, Anqiu Zhang and Zongquan Wu)

1. INTRODUCTION	409
1.1. Dimensions	409
1.2. Production of fibers	410
1.3. Mechanical properties	412
1.3.1. Terminology	412
1.3.2. Fiber stress-strain diagrams	413
1.3.3. Elastic recovery	415
1.4. Heat-resistance and thermal stability	415
1.5. Water absorption, regain and moisture content	416
2. FIBER STRUCTURE AND ITS DETERMINATION	417
2.1. Two-phase model	417
2.2. Intermediate state model	417
2.3. Crystallinity	419
2.3.1. Wide angle X-ray diffraction (WAXD)	419
2.3.1.1. Modified classic method	420
2.3.1.2. Mathematical simulation peak separation method	421
2.3.2. Small angle X-ray scattering (SAXS)	421

2.3.2.1. Invariant power	421
2.3.2.2. Correlation functional length	422
2.4. Orientation and molecular chain conformation.....	423
2.4.1. Birefringence	423
2.4.2. Sound speed method for orientation measurement	424
2.4.3. Dichroism	424
2.4.4. WAXD measurement of the degree of orientation in crystalline region	425
2.4.5. Orientation of amorphous region	425
3. THERMAL ANALYSIS OF FIBER	426
3.1. Differential scanning calorimetry (DSC)	428
3.1.1. Fiber sample preparation	428
3.1.2. Sample processing history	431
3.1.3. Heating rate effects on oriented fibers	431
3.2. Swelling differential scanning calorimetry (SDSC)	431
3.3. Thermo-mechanical analysis (TMA)	432
3.4. Dynamic mechanical analysis (DMA)	434
3.5. Thermogravimetric analyzer (TGA)	435
3.6. Thermal wide angle X-ray diffraction (TWAXD)	436
3.7. Thermal small angle X-ray scattering (TSAXS)	437
3.8. Summary of TA methods	438
4. CONVENTIONAL FIBERS AND THEIR MODIFICATIONS	439
4.1. Conventional fibers	439
4.1.1. Nylon fibers	439
4.1.1.1. Nylon 6	441
4.1.1.2. Nylon 66	443
4.1.2. Polyolefin fibers	443
4.1.2.1. Polyethylene (PE) fibers	444
4.1.2.2. Polypropylene (<i>I</i> -PP)	446
4.1.3. Polyacrylonitrile (PAN)	448
4.1.4. Polyesters	453
4.1.4.1. Poly(ethylene terephthalate) (PET)	453
4.1.4.2. Poly(butylenes terephthalate) (PBT)	460
4.1.5. Poly(vinyl alcohol) (PVA)	462
5. HIGH PERFORMANCE FIBERS	463
5.1. Aromatic polyamide fibers	464
5.2. Aromatic polyester fibers	469
5.3. Poly(phenylene sulfide) (PPS)	473
5.4. Poly[2,2'-(<i>m</i> -phenylene)-5,5'-bibenzimidazole] (PBI)	474

5.5. Aromatic polyimides	476
5.6. Poly(ether ether ketone) (PEEK)	478
5.7. Aromatic heterocyclic fibers	479
5.8. Carbon fiber	480
6. CONCLUDING REMARKS	482
REFERENCES	482

CHAPTER 12. THERMAL PROPERTIES OF HIGH TEMPERATURE POLYMER MATRIX FIBROUS COMPOSITES

(Roger J. Morgan, E. Eugene Shin and Jason E. Lincoln)

1. INTRODUCTION	491
2. RESULTS AND DISCUSSION	495
2.1. Bismaleimide composite matrices	495
2.1.1. Background and cure characterization	495
2.1.2. Composite microcracking formation and prevention	499
2.2. Polyimide composites	503
2.2.1. Background	503
2.2.2. Hydrothermal spike damage	504
2.2.3. Hydrolytic degradation	508
3. CONCLUDING REMARKS	516
REFERENCES	517

CHAPTER 13. THERMAL ANALYSIS AND CALORIMETRY OF ELASTOMERS

(Donald J. Burlett and Mark B. Altman)

1. INTRODUCTION	519
1.1. Viscoelasticity	520
1.2. Glass-to-rubber transition	521
1.3. Crystallinity	521
1.4. Chemical composition	522
1.5. Additives	522
1.6. Stability	523
1.7. Calorimetry and thermal analysis techniques	523

2. CLASSES OF ELASTOMER	526
2.1. Diene rubber (homopolymers)	526
2.2. Diene rubbers (copolymers)	526
2.3. Halogenated rubbers	527
2.4. Vinyl rubber	528
2.5. Miscellaneous rubber	528
3. SINGLE ELASTOMERS	529
3.1. Glass transition temperature	529
3.2. Crystalline melts	534
3.3. Stretching and deformation calorimetry	535
3.4. Thermal and oxidative stability	536
4. BLENDS	538
4.1. Glass transition temperature	539
4.2. Composition analysis	541
5. ADDITIVES	544
5.1. Fillers and reinforcing agents	545
5.2. Oils, plasticizers	553
5.3. Other additives and components	555
5.4. Compositional analysis/formula reconstruction	556
6. CURING	556
6.1. Peroxide cures	557
6.2. Sulfur-based	559
6.3. Miscellaneous	564
7. STABILITY	566
7.1. Oxidative stability	567
7.2. Thermal	572
7.3. Other	574
8. QUALITY CONTROL	576
9. FUTURE OPPORTUNITIES	578
9.1. Instrumentation	578
REFERENCES	580

CHAPTER 14. POLYMER DEGRADATION

(Joseph H. Flynn)

1. INTRODUCTION	587
2. GENERAL PHYSICAL, STRUCTURAL AND THERMODYNAMIC CONSIDERATIONS	589
2.1. Effect of physical state on degradation	589
2.2. Energetics-bond energies	590
2.3. Thermodynamics-ceiling temperatures	590
3. GENERAL THERMAL DEGRADATION MECHANISMS	593
3.1. Types of degradation reactions	593
3.2. Free radical chain reaction theory	594
3.3. Random scission	601
3.3.1. General theory	601
3.3.1.1. Closed system	602
3.3.1.2. Open systems	603
4. GENERAL THERMO-OXIDATIVE MECHANISMS	608
4.1. Introduction and scope	608
4.2. Oxidation mechanisms	609
5. GENERAL HYDROLYSIS MECHANISMS	613
5.1. Introduction	613
5.2. Hydrolysis mechanisms	614
6. LIFETIME PREDICTION OF POLYMERS BY THERMAL ANALYSIS	614
7. SOME SPECIFIC EXAMPLES OF DEGRADATION	616
7.1. Special cases for the degradation of vinyl type polymers	616
7.1.1. End initiation, complete zip: [(poly(methylmethacrylate))]	616
7.1.2. Random initiation, complete zip: [poly(alpha-methylstyrene)] ...	616
7.1.3. Poly(tetrafluoroethylene)	617
7.1.4. Polystyrene	617
7.1.5. Other special cases	619
7.2. Degradation of some other vinyl-type polymers	619
7.2.1. Poly(vinyl chloride) (PVC)	619
7.2.2. Poly(methylacrylic acid) (PMAA)	622
7.2.3. Polyvinyl acetate (PVA)	622
7.2.4. Polyvinyl (isopropenylacetate) (PVIPA)	622
7.2.5. Polyvinyl alcohol (PVAL)	623

7.3. Degradation of some heterochain polymers	623
7.3.1. Polyacetal and related polyethers	623
7.3.2. Nylon 6	624
7.3.3. Poly(ethylene adipate)	624
7.3.4. Polyurethanes	625
7.3.5. Polyethylene terephthalate (PET)	625
7.3.6. Polysiloxanes	626
7.3.7. Cellulose	626
7.4. Pryolytic reactions and aromatic and temperature-resistant thermo-setting polymers	627
7.4.1. Poly(phenylenes)	627
7.4.2. Phenolformaldehyde resin	628
7.4.3. Epoxy resins	629
7.4.4. Polycarbonates	629
7.4.5. Poly(pyromellitimide) H film	629
7.4.6. Polyacrylonitrile (PAN)	630
8. COPOLYMERS, BLENDS, MIXTURES	631
8.1. Introduction	631
8.2. Simple degradation theory and early investigations	632
8.3. More recent investigations	635
8.3.1. Thermal degradation of some alternating copolymers	635
8.3.2. Thermal degradation of block copolymers	637
8.3.3. Thermal degradation of some random copolymers	637
8.3.4. Thermal degradation of some blends and mixtures	639
9. CONCLUDING REMARKS	641
10. BIBLIOGRAPHY	641
11. REFERENCES	645

CHAPTER 15. THERMALLY STIMULATED CURRENTS: RECENT DEVELOPMENTS IN CHARACTERIZATION AND ANALYSIS OF POLYMERS

(Bryan B. Sauer)

1. INTRODUCTION	653
2. EXPERIMENTAL SECTION	657
2.1. TSC instrument	657
2.2. Sample preparation and geometry	658
2.3. Polarization/Depolarization sequences	659

3. ANALYSIS OF TSC-TS DATA	660
3.1. Bucci-Fieschi-Guidi and related analysis methods	660
3.2. TSC-TS curve fitting methods.....	662
3.3. Compensation	664
4. INTERPRETATION OF GLOBAL TSC RESULTS	667
4.1. Comparison of global TSC with a.c. dielectric and other techniques	667
4.2. Global TSC studies of glass transitions and $T > T_g$ transitions, comparisons with other techniques	668
4.3. Interpretation of the $T > T_g$ or ρ transition at higher temperatures	673
5. INTERPRETATION OF TSC-THERMAL SAMPLING (TSC-TS) RESULTS	674
5.1. Comparison of fitting routines for TSC-TS spectra applied to experimental data	675
5.2. Comparison of TSC-TS apparent activation energies with standard relaxation methods	681
5.3. The zero entropy prediction and a description of methods for distinguishing cooperative and non-cooperative relaxations	686
5.4. Explanation of high sensitivity of TSC-TS for cooperative motions	688
5.5. Selections from TSC-TS literature and comparison with the zero entropy prediction	691
5.6. Comparison with new analysis of derivatives of a.c. dielectric data to obtain activated parameters	694
6. TSC APPLICATIONS	697
6.1. Examples of TSC and TSC-TS studies of amorphous polymers	697
6.2. Amorphous and semi-crystalline liquid crystalline polymers	698
6.2.1. Side-chain LCPs	698
6.2.2. Copolyester main-chain LCPs with broad glass transitions	701
6.3. High crystallinity flexible polymers and fluoropolymers	703
7. CONCLUDING REMARKS	706
ACKNOWLEDGMENTS	708
REFERENCES	708

CHAPTER 16. TEMPERATURE MODULATED DIFFERENTIAL
SCANNING CALORIMETRY (TMDSC) –BASICS AND
APPLICATIONS TO POLYMERS

(C. Schick)

1. INTRODUCTION	713
2. DIFFERENTIAL SCANNING CALORIMETRY (DSC) – BASIC CONSIDERATIONS	717
2.1. Heat-flux DSC	717
2.2. Tian-Calvet type DSC	719
2.3. Power compensation DSC	720
2.4. Combination of heat-flow DSC and power compensation	721
3. TEMPERATURE MODULATED DIFFERENTIAL SCANNING CALORIMETRY (TMDSC)	722
3.1. Complex heat capacity and reversing and non-reversing heat capacity .	723
3.1.1. Determination of reversing and non-reversing heat capacity ...	724
3.1.1.1. Temperature modulated DSC (TMDSC)	724
3.1.1.2. StepScan™ DSC (SSDSC)	727
3.1.2. Determination of complex heat capacity	731
3.2. Data treatment algorithms	732
3.3. Frequency dependent heat capacity	737
3.3.1. Periodic perturbations – frequency domain	738
3.3.1.1. Single frequency measurements	738
3.3.1.2. Multi frequency measurements	738
3.3.2. Non-periodic perturbations – step response in time domain	741
3.4. Calibration	744
3.4.1. Heat capacity calibration	744
3.4.2. Temperature calibration	748
3.4.3. Heat capacity calibration examples	749
3.4.3.1. Results from “first-order” calibration	750
3.4.3.2. Results from “second-order” calibration	752
3.4.3.3. “Third-order” calibration	755
3.4.3.4. Remark concerning small samples	758
3.4.4. Conclusions regarding calibration	758
3.5. Thermal conductivity	760
3.5.1. Data treatment	761
3.5.1.1. The idea	761
3.5.1.2. The algorithm	761
3.5.2. Experimental results	765
3.5.3. Discussion of thermal conductivity determination	767

3.5.4. Conclusion regarding thermal conductivity	768
4. APPLICATIONS	768
4.1. Precise heat capacity	768
4.2. Glass transition	770
4.2.1. Vitrification and dynamic glass transition	770
4.2.2. Non-reversing heat capacity at glass transition	774
4.2.2.1. General criticism	774
4.2.2.2. Enthalpy retardation	775
4.2.3. Modeling the results from TMDSC at glass transition	777
4.2.4. Glass transitions superimposed by latent heats	778
4.2.4.1. Basic considerations	778
4.2.4.2. Glass transition superimposed by melting	780
4.2.4.3. Glass transition superimposed by crystallization	781
4.2.4.4. Glass transition superimposed by chemical reactions	784
4.2.4.5. Glass transition superimposed by evaporation	784
4.2.5. Conclusions regarding glass transition	785
4.3. Phase transitions	786
4.3.1. First-order phase transitions	787
4.3.1.1. Calibration related problems	787
4.3.1.2. Reorganization – The influence of the temperature time profile	789
4.3.1.3. Crystallization and melting kinetics	792
4.4. Reversing melting and crystallization	793
4.5. Other processes	800
5. CONCLUDING REMARKS	801
ACKNOWLEDGMENTS	802
REFERENCES	802
INDEX.....	811

This Page Intentionally Left Blank

CONTRIBUTORS

- Altman, Mark B.** Goodyear Tire & Rubber Company, 142 Goodyear Blvd., Akron, OH 44305, USA
- Avakian, Peter** E.I. du Pont de Nemours and Company, Central Research and Development, Experimental Station, P.O. Box 80356, Wilmington, DE 19880-0356, USA
- Burlett, Donald J.** Goodyear Tire & Rubber Company, 142 Goodyear Blvd., Akron, OH 44305, USA
- Cheng, Stephen Z. D.** Maurice Morton Institute and Department of Polymer Science, The University of Akron, Akron, OH 44325-3909, USA
- Flynn, Joseph H.** Scientific Thermal Research & Data Analysis (STRDA), 5309 Iroquois Rd., Bethesda, MD 20816, USA
- Hale, Arturo** AT&T Bell Laboratories, Room #7E-217, 600 Mountain Ave., Murray Hill, NJ 07974, USA
- Huang, Jiang** Polymer Science Program, Department of Materials Science and Engineering, The Pennsylvania State University, 320 Steidle Building, University Park, PA 16802-5007, USA
- Jin, Shi** Maurice Morton Institute and Department of Polymer Science, The University of Akron, Akron, OH 44325-3909, USA
- Jing, Alexander J.** Maurice Morton Institute and Department of Polymer Science, The University of Akron, Akron, OH 44325-3909, USA
- Kampert, William G.** E.I. du Pont de Nemours and Company, Central Research and Development, Experimental Station, P.O. Box 80356, Wilmington, DE 19880-0356, USA

- Li, Christopher Y.** Department of Materials Engineering, Drexel University Philadelphia, PA 19104, USA
- Lincoln, Jason E.** Polymer Matrix Composites Research Team, Materials and Manufacturing Directorate, Air Force Research Laboratory/MLBC, 2941 P Street, Room 136, Wright-Patterson Air Force Base, OH 45433, USA
- Mathot, Vincent B. F.** DSM Research, P.O. Box 18, 6160 MD Geleen, The Netherlands
- Matsuoka, Shiro** Polymer Research Institute, Polytechnic University, Six Metrotech Center, Brooklyn, NY 11201, USA
- McKenna, Gregory B.** Department of Chemical Engineering, Texas Technology University, Lubbock, Texas 79409-3121, USA
- Morgan, Roger J.** Department of Mechanical Engineering, Texas A&M University, College Station, Texas 77843-3123, USA
- Reynaers, Harry** Katholieke Universiteit Leuven, Celestijnenlaan 200F, B-3001 Leuven-Heverlee, Belgium
- Runt, James P.** Polymer Science Program, Department of Materials Science and Engineering, The Pennsylvania State University, 320 Steidle Building, University Park, PA 16802-5007, USA
- Sauer, Bryan B.** E.I. du Pont de Nemours and Company, Central Research and Development, Experimental Station, Wilmington, DE 19880-0356, USA
- Schick, Christoph E. G.** Department of Physics, University of Rostock, Universitätsplatz 3, 18051 Rostock, Germany
- Shin, E. Eugene** NASA Glenn Research Center at Lewis Field, Mail Stop 49-1 21000 Brookpark Rd., Cleveland, OH 44135, USA

- Simon, Sindee L.** Department of Chemical Engineering, Texas
Technology University, Lubbock, Texas 79409-3121,
USA
- Starkweather, Howard W. Jr.** E.I. du Pont de Nemours and Company,
Central Research and Development, Experimental
Station, P.O. Box 80356, Wilmington, DE 19880-
0356, USA
- Wu, Zongquan** Maurice Morton Institute of Polymer Science, The
University of Akron, Akron, OH 44325-3909, USA
- Wunderlich, Bernhard** Department of Chemistry, University of Tennessee,
Knoxville, TN 37996-1600, USA
- Zhu, Lei** Institute of Materials Science and Department of
Chemical Engineering, University of Connecticut,
Storrs, CT 06269-3222, USA
- Zhang, Anqiu** Maurice Morton Institute of Polymer Science, The
University of Akron, Akron, Ohio 44325-3909, USA

This Page Intentionally Left Blank

Chapter 1

Heat capacity of polymers*

B. Wunderlich

Department of Chemistry, The University of Tennessee, Knoxville, TN 37996-1600, USA; and the Chemical and Analytical Sciences Division, Oak Ridge National Laboratory, Oak Ridge, TN 37831-6197, USA

Heat capacity is the basic quantity derived from calorimetric measurements and is used in the description of its thermodynamics. For a full description of a system, heat capacity information is combined with heats of transition, reaction, *etc.* In the present Chapter the measurement and theory of heat capacity are discussed which leads to a description of the Advanced THERMAL ANALYSIS SYSTEM, ATHAS [1]. This system was developed over the last 30 years to increase the precision of thermal analysis of linear macromolecules and related small molecules.

1. MEASUREMENT OF HEAT CAPACITY

In a measurement of heat capacity one measures the heat, dQ , required to increase the temperature of the sample by dT :

$$C_p \equiv \frac{dQ}{dT} = \left(\frac{\partial H}{\partial T} \right)_{p,n}, \quad (1)$$

where H represents the enthalpy and p and n , are pressure and composition, which are kept constant. Classically, the measurement is done with an adiabatic calorimeter [2]. Even today, adiabatic calorimetry is the most precise method of measurement in the temperature range from 10 to 150 K.

* The submitted manuscript has been authored by a contractor of the U.S. Government under the contract No. DOE-AC05-00OR22725. Accordingly, the U.S. Government retains a non-exclusive, royalty-free license to publish, or reproduce the published form of this contribution, or allow others to do so, for U.S. Government purposes.

In an adiabatic calorimeter an attempt is made to follow step-wise temperature changes of an internally heated calorimeter in a well-controlled, adiabatic enclosure. Due to loss of heat caused by deviations from the adiabatic condition, corrections must be made to the heat added to the calorimeter, ΔQ . Similarly, the measured increase of temperature, ΔT , must be corrected for the temperature drifts of the calorimeter. The calculations are then given by:

$$c_p = \frac{\Delta Q_{corrected} - C'\Delta T_{corrected}}{m\Delta T_{corrected}}, \quad (2)$$

where the specific heat capacity c_p (in $\text{J K}^{-1} \text{g}^{-1}$) is calculated by subtracting the heat capacity of the empty calorimeter, its “water value” C' , and dividing by the mass of the sample, m . The evaluation of the corrections is time consuming, but at the heart of good calorimetry.

Modern control and measurement technology permitted some 30–40 years ago to miniaturize the calorimeter to measure down to milligram quantities in a differential scanning mode (DSC) [3]. In a symmetric setup, the difference in extraneous heat flux can be minimized and the remaining imbalance corrected for. Under the usual condition where sample and reference calorimeters (often aluminum pans) are identical and the reference pan is empty, one finds the heat capacity as:

$$mc_p = K\frac{\Delta T}{\beta} + \left(K\frac{\Delta T}{\beta} + C_p' \right) \left(\frac{d\Delta T/dT_r}{1 - (d\Delta T/dT_r)} \right) \approx K\frac{\Delta T}{\beta}, \quad (3)$$

where K is the Newton’s law constant, ΔT is the temperature difference between reference and sample ($T_r - T_s$), and β is the constant heating rate (in K min^{-1}). The left equation is exact, the right approximation neglects the difference in heating rates between reference and sample due to a slowly changing heat capacity of the sample. This limits the precision to $\pm 3\%$ or less.

In the more recently developed temperature-modulated DSC (TMDSC) [4], a sinusoidal or other periodic change in temperature is superimposed on the underlying heating rate. The heat capacity is now given by:

$$mc_p = \frac{A_\Delta}{A} \sqrt{\left(\frac{K}{\omega} \right)^2 + C_p'^2}, \quad (4)$$

where A_{Δ} and A are the maximum amplitudes of the modulation found in the temperature difference and sample temperature, respectively, and ω is the modulation frequency $2\pi/p$ (p = modulation period in seconds). The equation represents the reversing heat capacity. In case there is a difference between the result of the last two equations, this is called a nonreversing heat capacity, and is connected to processes within the sample that cannot be modulated properly, such as the change of temperature in the glass transition region, irreversible crystallization or reorganization, or heat losses.

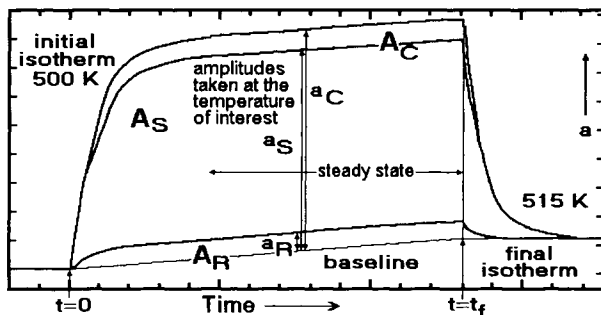


Fig. 1. Measurement and calibration by DSC.

Fig. 1 illustrates a heat-capacity measurement with a DSC. Central is the evaluation of the calibration constant at each temperature of measurement. Three consecutive runs must be made. The sample run (S) is made on the unknown, enclosed in the customary aluminum pan and an empty, closely-matched aluminum reference pan. The width of the temperature interval is dictated by the quality of the isothermal base line. In the example of Fig. 1 the initial isotherm is at 500 K and the final isotherm, at 515 K. Typical modern instrumentation may permit intervals as wide as 100 K. Measurements can also be made on cooling instead of heating. The cooling mode is particularly advantageous in the glass transition region since it avoids hysteresis. When measurements are made on cooling, all calibrations must necessarily also be made on cooling, using liquid-crystal transitions which do not supercool, for example, for temperature calibration [5]. As the heating is started, the DSC recording changes from the initial isotherm at 500 K in an exponential fashion to the steady-state amplitude on heating at constant rate β . After completion of the run, at time t_f , there is an exponential approach to the final isotherm at 515 K. The area between base line and the DSC run, called A_S , is the integral over the amplitude, a_S . A reference run (R) with a matched, second, empty aluminum-pan, instead of the sample, yields the small correction area A_R which may be positive or negative. Finally, a calibration run (C) with sapphire crystals (Al_2O_3) completes the experiment (area A_C). The difference between the

two areas, $A_S - A_R$, is a measure of the uncalibrated integral of the sample heat capacity:

$$K'/\beta = \frac{W(C) \overline{c_p(C)} \Delta T}{A_C - A_R} . \quad (5)$$

For a small temperature interval at constant heating rate β in the region of steady state in Fig. 1, it is sufficient to define an average heat capacity over the temperature range of interest to simplify the integral, as indicated. The uncalibrated heat capacity of Al_2O_3 is similarly evaluated using $A_C - A_R$. The proportionality constant, K' , can now be evaluated as:

$$\int_0^{t_f} C_p(S) \beta dt = \overline{C_p(S)} \Delta T = K' [A_S - A_R] / \beta . \quad (6)$$

The specific heat capacity of sapphire, $c_p(\text{Al}_2\text{O}_3)$, is well known, and the weight of sapphire used, $W(C) = W(\text{Al}_2\text{O}_3)$, must be determined with sufficient precision ($\pm 0.1\%$) so as not to affect the accuracy of the measurement ($\pm 1\%$ or better).

The initial and final exponential changes to steady state are sufficiently similar in area so that one may compute the heat capacities as a function of temperature directly from the amplitudes $a_S(T)$, $a_R(T)$, and $a_C(T)$ in the region of steady state. Eq. (7) and Eq. (8) outline the computations involved in the calibration:

$$\int_0^{t_f} C_p(S) \beta dt = C_p(S) \Delta T = K' [a_S - a_R] / \beta \quad \text{and} \quad (7)$$

$$K'/\beta = \frac{W(C) \overline{c_p(C)} \Delta T}{a_C - a_R} . \quad (8)$$

In a typical DSC experiment, a sample may weigh 20 mg and show a heat capacity of about 50 mJ K⁻¹. For a heating rate of 10 K min⁻¹ there would be, under steady-state conditions, a lag between the measured temperature and the actual temperature of about 0.4 K. This is an acceptable value for heat capacity that changes slowly with temperature. If necessary, lag corrections can be included in the computation. The typical instrument precision is reported to be ± 0.04 mJ s⁻¹ at 700 K. Heat capacities can thus be measured to a precision of $\pm 0.25\%$, respectable for such fast measurements. For TMDSC, sample mass and modulation parameters are chosen to modulate the whole sample with the same amplitude,

checked by measuring with varying sample masses [6], or calibration as a function of frequency is necessary.

2. THERMODYNAMIC THEORY

The importance of heat capacity becomes obvious when one realizes that by integration it is linked to the three basic quantities of thermodynamics, namely the enthalpy or energy (H , U), the Gibbs energy or free energy (G , F), and the entropy (S). Naturally, in cases where there are transitions in the temperature range of interest, their heats and entropies need to be added to the integration. The enthalpy or energy of a system can be linked to the total amount of thermal motion and interaction on a microscopic scale. The entropy of a system can be connected to the degree of order, and finally, the Gibbs energy (free enthalpy) or the Helmholtz free energy is related to the stability of the chosen system.

All experimental techniques lead to heat capacities at constant pressure, C_p . In terms of microscopic quantities, however, heat capacity at constant volume, C_v , is the more accessible quantity. The thermodynamic relationship between C_p and C_v is:

$$C_p - C_v = TV\alpha^2/\gamma \quad , \quad (9)$$

where α represents the expansivity and γ , the compressibility. Frequently, however, experimental data for the expansivity and compressibility are not available over the whole temperature range, so that one knows C_p , but has difficulties evaluating C_v . At moderate temperatures, as usually encountered below the melting point of linear macromolecules, one can assume that the expansivity is proportional to C_p . In addition, it was found that volume divided by compressibility does not change much with temperature. With these two empirical observations, one can derive the Nernst-Lindemann approximation for macromolecules [7]:

$$C_p - C_v = 3R A_o C_p T/T_m^o \quad , \quad (10)$$

with T_m^o representing the equilibrium melting temperature and $A_o = 3.9 \times 10^{-3} \text{ J}^{-1} \text{ K mol}$, an approximately universal constant.

3. QUANTUM MECHANICAL DESCRIPTION

In this section the link of C_v of solids to the microscopic properties will be derived. The system in question must, of necessity, be treated as a quantum-

mechanical system. Every microscopic system is assumed to be able to assume only certain states. The labels attached to these different states are 1, 2, 3, *etc.*, and their energies are $\epsilon_1, \epsilon_2, \epsilon_3, \text{etc.}$ Any given energy may, however, refer to more than one state so that the number of states that correspond to the same energy ϵ_i is designated g_i and is called the degeneracy of the energy level. Similarly, degeneracy g_2 refers to ϵ_2 , and g_3 to ϵ_3 . It is then assumed that many such microscopic systems make up the overall matter, the macroscopic system. At least initially, one can assume that all of the quantum-mechanical systems are equivalent. Furthermore, they should all be in thermal contact, but otherwise be independent. The number of microscopic systems that are occupying level 1 with energy level ϵ_1 is n_1 ; the number with ϵ_2 is n_2 ; the number with ϵ_3 is n_3 ; *etc.*

The number of microscopic systems is, for simplicity, assumed to be the number of molecules, N . It is given by the sum over all n_i . The value of N is directly known from the macroscopic description of the material through the chemical composition, mass, and Avogadro's number. Another easily evaluated macroscopic quantity is the total energy U . It must be the sum of the energies of all the microscopic, quantum-mechanical systems.

For complete evaluation of N and U , one needs, however, to know the distribution of the molecules over the different energy levels, something that is rarely available. To solve this problem, more assumptions must be made. The most important one is that one can take all possible distributions and replace them with the most probable distribution, the Boltzmann distribution. It turns out that this most probable distribution is so popular that the error due to this simplification is small, as long as the number of energy levels and atoms is large. The Boltzmann distribution is written as:

$$n_i/N = g_i \exp[-\epsilon_i / (kT)] / Q \quad , \quad \text{where} \quad (11)$$

$$Q = \sum g_i \exp[-\epsilon_i / (kT)] \quad . \quad (12)$$

Eq. (11) indicates that the fraction of the total number of molecules in state i , n_i/N , is equal to the number of energy levels of the state i , which is given by its degeneracy g_i , multiplied by some exponential factor and divided by the partition function, Q . The partition function Q is the sum over all the degeneracies for all the levels i , each multiplied by the same exponential factor as found in the numerator.

The meaning of the partition function becomes clearer when one looks at some limiting cases. At high temperature, when thermal energy is present in abundance,

$\exp[-\epsilon_i/(kT)]$ is close to one because the exponent is very small. Then Q is just the sum over all the possible energy levels of the quantum mechanical system. Under such conditions the Boltzmann distribution, Eq. (11), indicates that the fraction of molecules in level i , is the number of energy levels g_i , divided by the total number of available energy levels for the quantum-mechanical system. In other words, there is equipartition of the system over all available energy levels. The other limiting case occurs when kT is very much smaller than ϵ_i . In this case, temperature is relatively low. This makes the exponent large and negative; the weighting factor $\exp[-\epsilon_i/(kT)]$ is close to zero. One may then conclude that the energy levels of high energy (relative to kT) are not counted in the partition function. At low temperature, the system can occupy only levels of low energy.

$$U = N \sum g_i \epsilon_i \exp[-\epsilon_i/(kT)]/Q = NkT^2 (\partial \ln Q / \partial T)_{V,N} , \quad (13)$$

With this discussion, the most difficult part of the endeavor to connect the macroscopic energies to their microscopic origin is completed. The rest is mathematical drudgery that has largely been carried out in the literature. In order to get an equation for the total energy U , the Boltzmann distribution, Eq. (11), is inserted into the sum for the total energy. This process results in the final equation: where the correctness of the right equation can be seen by just carrying out the differentiation and comparing the result to the center equation. Now, that U is expressed in microscopic terms, one can also find the heat capacity at constant volume by differentiating Eq. (13) [see also Eq. (1)]:

$$C_v = (\partial U / \partial T)_{V,N} . \quad (14)$$

The partition function Q , the temperature T , and the total number of molecules N , need to be known for the computation of C_v . Next C_v can be converted to C_p using Eqs. (9) or (10), which, in turn, allows computation of H , S , and G .

For a simple example, one assumes to have only two energy levels for each atom or molecule, *i.e.*, there are only the levels ϵ_1 and ϵ_2 . A diagram of the energy levels is shown in Fig. 2. This situation may arise for computation of the contribution to C_v from molecules with two rotational isomers of different energies. For convenience, one sets the energy ϵ_1 equal to zero. Energy ϵ_2 lies then higher by $\Delta\epsilon$. Or, if one wants to express the energies in molar amounts, one multiplies $\Delta\epsilon$ by Avogadro's number N_A and comes up with the molar energy difference ΔE in J mol^{-1} . A similar change is necessary for kT ; per mole, it becomes RT . The partition function, Q , is given in Fig. 2. The next step involves insertion of Q into

$$Q = g_1 + g_2 \exp[-\Delta E/(RT)]$$

$$U = \frac{\Delta E}{1 + (g_1/g_2)e^{\Delta E/(RT)}} \quad \begin{array}{l} \epsilon_2 \\ \hline N_A \Delta \epsilon = \Delta E \\ \hline \epsilon_1 \end{array}$$

$$C_v = R \frac{(g_1/g_2)[\Delta E/(RT)]^2 e^{\Delta E/(RT)}}{[1 + (g_1/g_2)e^{\Delta E/(RT)}]^2}$$

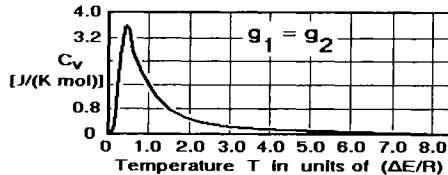


Fig. 2. Heat capacity for a molecule with two energy levels.

Eq. (13) and carrying out the differentiations. The graph in Fig. 2 shows the change in C_v for a system with equal degeneracies ($g_1 = g_2$). The abscissa is a reduced temperature—*i.e.*, the temperature is multiplied by R , the gas constant, and divided by ΔE . In this way the curve applies to all systems with two energy levels of equal degeneracy. The curve shows a relatively sharp peak at the reduced temperature of approximately 0.5. In this temperature region many molecules go from the lower to the higher energy level on increasing the temperature, causing the high heat capacity. At higher temperature, the heat capacity decreases exponentially over a fairly large temperature range. Finally, above about 5 in the reduced temperature scale, equipartition between the two levels is reached. This means that just as many systems are in the upper levels as are in the lower. No contribution to the heat capacity can arise any more. In dynamic equilibrium as many systems decrease in n_1 as increase.

The second example is that of the harmonic oscillator in Fig. 3. The harmonic oscillator is basic to understanding the heat capacity of solids since for many solids

v_i	ϵ_i	
5	5 $h\nu$	$\epsilon_i = v_i h\nu$
4	4 $h\nu$	$Q = 1 + e^{-h\nu/(kT)} + e^{-2h\nu/(kT)} + \dots$
3	3 $h\nu$	$Q = \frac{1}{1 - e^{-h\nu/(kT)}}$
2	2 $h\nu$	
1	$h\nu$	$\ln Q = -\ln[1 - e^{-h\nu/(kT)}]$
0	0	$v_i = \text{quantum number}$
		$h = \text{Planck's constant}$
		$\nu = \text{frequency in Hz}$

for one mole of vibrators:

$$C_v = \frac{R [h\nu/(kT)]^2 e^{h\nu/(kT)}}{[e^{h\nu/(kT)} - 1]^2}$$

Fig. 3. Energy levels and heat capacity for the harmonic oscillator.

vibrations are the only type of molecular motion. The harmonic oscillator is characterized by an unlimited set of energy levels of equal distances, the first few are shown in Fig. 3. The quantum numbers, ν , run from zero to infinity. The energies are written on the right-hand side of the levels. The difference in energy between any two successive energy levels is given by the quantity $h\nu$, where h is Planck's constant and ν is the frequency of the oscillator (in hertz). If one chooses the lowest energy level as the zero of energy, then all energies can be expressed as shown in Fig. 3. There is no degeneracy of energy levels in harmonic oscillators ($g_i = 1$). The partition function can then be written as shown. It is an infinite, convergent, geometrical series, a series that can easily be summed. Now it is a simple task to take the logarithm and carry out the differentiations necessary to reach the heat capacity. Note that for large exponents—*i.e.*, for a relatively low temperature—the heat capacity of Fig. 3 is identical to the one in Fig. 2 which was derived for the case of two energy levels only. This is reasonable, because at sufficiently low temperature most molecules will be in the lowest possible energy levels. As long as only very few of the molecules are excited to a higher energy level, it makes very little difference if there are more levels above the first excited energy level or not. All of these higher-energy levels are empty at low temperature and do not contribute to the energy and heat capacity. The heat capacity curve at relatively low temperature is thus identical for the two-level and the multilevel cases.

The heat capacity of the harmonic oscillator is used so frequently that it is abbreviated in Fig. 4 as $RE(\Theta/T)$, where R is the gas constant, and E is the Einstein function. The shape of the Einstein function is indicated in the graphs of Fig. 4. The fraction Θ/T stands for $h\nu/kT$, and $h\nu/k$ has the dimension of a temperature. This temperature is called the Einstein temperature, Θ_E , or theta temperature. A frequency expressed in Hz can easily be converted into the Einstein temperature by multiplication by 4.80×10^{-11} s K, a frequency expressed in wave numbers, cm^{-1} , must be multiplied by 1.4388 cm K. At temperature Θ , the heat capacity has reached 92% of its final value, R per mole of vibrations, or k per single vibrator. The heat capacity $3R$ per mole of atoms is also the classical value of the Dulong–Petit rule. Low-frequency vibrators reach their limiting value at low temperature, high-frequency vibrators at much higher temperature.

Up to now the calculations were carried out for one vibration frequency at a time. In reality, there is, however, a full spectrum of vibrations. Each vibration has a heat capacity contribution characteristic of its frequency. One finds, that because of vibrational coupling and anharmonicity of the vibrations, the separation into normal modes is questionable. The actual energy levels are actually not equally spaced, as needed for Fig. 3, nor are they temperature-independent. There is hope, however,

that supercomputers will ultimately permit more precise evaluation of temperature dependent vibrational spectra and heat capacities. In the meantime, approximations exist to help one to better understand C_v for solids.

4. THE HEAT CAPACITY OF SOLIDS

To overcome the need to compute the full frequency spectrum of solids, a series of approximations have been developed over the years. The simplest is the Einstein approximation [8]. In it, one characterizes all vibrations of the solid by a single,

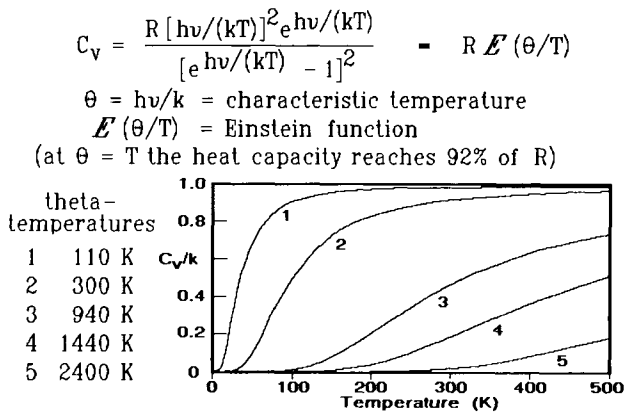


Fig. 4. Einstein function E and C_v for harmonic oscillators.

average frequency, and then one uses the Einstein function of Fig. 4 with its single frequency to calculate the heat capacity. The Einstein frequency, ν_E , is in calorimetry usually expressed by its temperature θ_E . The whole spectrum, thus, is represented by a single frequency. Looking at actual measurements, one finds that at temperatures above about 20 K, heat capacities of monatomic solids can, indeed, be represented by a single frequency. Typical values for the Einstein temperatures θ_E for Na, Al, B and C (diamond) are 150, 385, 1220, and 1450 K, respectively. These θ -values correspond approximately to the heat capacity represented by curves 1 to 4 in Fig. 4. Elements with strong bonds are known as hard solids and have high θ -temperatures; elements with weaker bonds are softer and have lower θ -temperatures. Somewhat less obvious from the examples is that heavy atoms have lower θ -temperatures than lighter ones. These correlations are easily proven by the standard calculations of frequencies of vibrators of different force constants and masses. The frequency is proportional to $(f/m)^{1/2}$, where f is the force constant and m is the appropriate mass.

The problem that the Einstein function does not seem to give a sufficiently accurate heat capacity at low temperature was resolved by Debye by summing the Einstein functions for a classical distributions of vibrators for an isotropic continuum in one, two, or three dimensions [9], as shown in Fig. 5. To agree with the quantum mechanical number of possible vibrators, these distributions were cut-off at the appropriate frequencies ν_1 , ν_2 , and ν_3 , respectively. The three functions: D_1 , D_2 , and D_3 , are given by:

$$C_v/NR = D_1(\Theta_1/T) = (T/\Theta_1) \int_0^{(\Theta_1/T)} \frac{(\Theta/T)^2 \exp(\Theta/T)}{[\exp(\Theta/T) - 1]^2} d(\Theta/T) \quad , \quad (15)$$

$$C_v/NR = D_2(\Theta_2/T) = 2(T/\Theta_2)^2 \int_0^{(\Theta_2/T)} \frac{(\Theta/T)^3 \exp(\Theta/T)}{[\exp(\Theta/T) - 1]^2} d(\Theta/T) \quad , \quad (16)$$

$$C_v/NR = D_3(\Theta_3/T) = 3(T/\Theta_3)^3 \int_0^{(\Theta_3/T)} \frac{(\Theta/T)^4 \exp(\Theta/T)}{[\exp(\Theta/T) - 1]^2} d(\Theta/T) \quad . \quad (17)$$

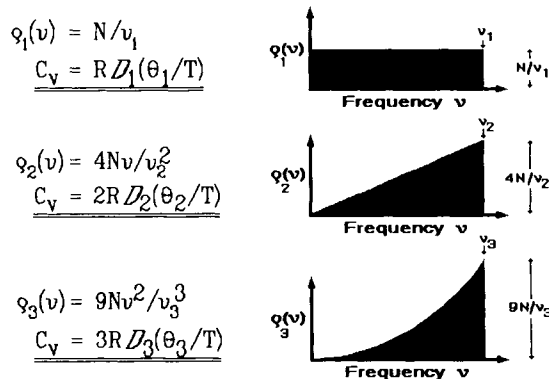


Fig. 5. Frequency distributions [densities of states, $\rho(\nu)$] for the one-, two-, and three-dimensional Debye functions D .

In Table 1 a listing of the Θ -temperatures is given which permits the calculation of actual heat capacities for almost 100 elements and compounds [10].

To see the correspondence of the approximate frequency spectra, the calculated full frequency distribution for diamond is drawn in Fig.6. It does not agree too well with the Einstein Θ -value of 1450 K (3×10^{13} Hz), nor does it fit the smooth, quadratic increase in $\rho(\nu)$ expected from a Debye Θ -value of 2050 K (4.3×10^{13} Hz)

Table 1 Debye Temperatures of crystals in K at $T \approx \Theta_3/2$.

Element	Element	Element	Element	Element
Ar 90	Cr 430	Hg 100	Ne 60	Si 630
Ag 220	Cs 45	I ₂ 105	Ni 440	Sn(fcc) 240
Al 385	Cu 310	In 140	O ₂ 90	Sn(tetr) 140
As 275	Dy 155	Ir 290	Os 250	Sr 170
Au 180	Er 165	K 100	Pa 150	Ta 230
B 1220	Fe 460	Kr 60	Pb 85	Tb 175
Be 940	Ga(trig) 240	La 130	Pd 275	Te 130
Bi 120	Ga(tetr) 125	Li 420	Pr 120	Th 140
C(dia) 2050	Gd 160	Mg 330	Pt 225	Tl 355
C(graph) 760	Ge 370	Mn 420	Rb 60	Tl 90
Cs 230	H ₂ (para) 115	Mo 375	Re 300	V 280
Cd(hcp) 280	H ₂ (ortho) 105	N ₂ 70	Rh 350	W 315
Ce 110	D ₂ 95	Na 150	Rn 400	Y 230
Cl ₂ 115	He 30	Nb 265	Sb 140	Zn 250
Co 440	Hf 195	Nd 150	Se 150	Zr 240
Compound	Compound	Compound	Compound	Compound
AgBr 140	AuCu ₃ (ordered) 200	CrCl ₃ 100	KI 195	
AgCl 180	AuCu ₃ (disord.) 180	Cr ₂ O ₃ 360	LiF 680	
Alums 80	BN 600	FeS ₂ 630	MgO 800	
As ₂ O ₃ 140	CaF ₂ 470	KBr 180	MoS ₂ 290	
As ₂ O ₅ 240	CrCl ₂ 80	KCl 230	NaCl 280	

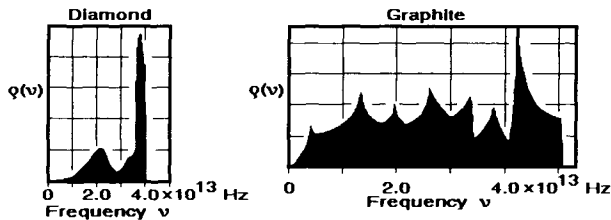


Fig. 6. Frequency distributions for diamond and graphite.

of Fig. 5. Because of the averaging nature of the Debye function, it still reproduces the heat capacity, but the vibrational spectrum shows that the quadratic frequency dependence reaches only to 2×10^{13} Hz, which corresponds to 1000 K. Then, there is a gap, followed by a sharp peak, terminating at 4×10^{13} Hz which is equal to 1920 K.

The frequency spectrum of graphite is also shown in Fig. 6. It has a layer-like crystal structure. Its frequency spectrum is also not at all related to a three-dimensional Debye function with a Θ -value of 760 K. The quadratic frequency increase at low frequencies stops already at 5×10^{12} Hz, or 240 K. The rest of the spectrum is rather complicated, but fits perhaps better to a two-dimensional Debye function with a Θ_2 value of 1370 K [11]. The last maximum in the spectrum comes at about 4.5×10^{13} Hz (2160 K), somewhat higher than the diamond frequencies. This is reasonable, since the in-plane vibrations in graphite involve C=C-double bonds, which are stronger than the single bonds in diamond. A more extensive discussion of the heat capacities of various allotropes of carbon including fullerene, C₆₀, is given in reference [12].

Table 2 Examples of two- and three-dimensional Debye temperature of group IV chalcogenides.

Substance	Crystal Structure	3-D Θ	2-D Θ_l	2-D Θ_t
GeS	orthorhombic layer	-	505	200
GeSe	orthorhombic layer	(270)	345	185
GeTe	trigonal, distorted NaCl	205	-	-
SnS	orthorhombic layer	300	400	160
SnSe	orthorhombic layer	(230)	-	-
SnTe	cubic NaCl	175	-	-
PbS	cubic NaCl	225	-	-
PbSe	cubic NaCl	150	-	-
PbTe	cubic NaCl	130	-	-
GeS ₂	orthorhombic layer	-	705	175
GeSe ₂	hexagonal layer	-	480	100
SnS ₂	hexagonal layer	-	570	265

$$C_{V3-D}(AB) = 6R\mathcal{D}_3(\Theta_3/T)$$

$$C_{V2-D}(AB) = 4R\mathcal{D}_2(\Theta_l/T) + 2R\mathcal{D}_2(\Theta_t/T)$$

$$C_{V2-D}(AB_2) = 6R\mathcal{D}_2(\Theta_l/T) + 3R\mathcal{D}_2(\Theta_t/T)$$

In Table 2 results from the ATHAS laboratory on group IV chalcogenides are listed [13]. The crystals of these compounds form a link between strict layer structures whose heat capacities should be approximated with a two-dimensional Debye function, and crystals of NaCl structure that have equally strong bonds in all three directions of space and, thus, should be approximated by a three-dimensional Debye function. As expected, the heat capacities correspond to the structures. The dashes in Table 2 indicate that no reasonable fit could be obtained for the experimental data to the given Debye function. For GeSe both approaches were possible, but the two-dimensional Debye function represents the heat capacity with a somewhat smaller error. For SnS and SnSe, the temperature range for data fit was too narrow to yield a clear answer.

As mentioned in the discussion of the two-dimensional Debye function, one needs to distinguish between the two longitudinal vibrations per atom or ion within the layer planes and the one transverse vibration per atom or ion directed at right angles to the layer plane. As expected, the longitudinal Θ -temperatures, Θ_l , are higher than the transverse ones, Θ_t . The bottom three equations in Table 2 illustrate the calculation of heat capacity for all compounds listed. The experimental heat capacities can be represented by the listed Θ -temperatures to better than $\pm 3\%$. The temperature range of fit is from 50 K to room temperature. Above room temperature, the heat capacities of these compounds of rather heavy elements are almost fully excited, *i.e.*, their heat capacity is not far from $3R$ per atom. In this temperature range, precise values of the $C_p - C_v$ correction are more important for the match of calculation and experiment than the actual frequency distribution. Furthermore, as the temperature increases, one expects that the actual vibrations deviate more and more from those calculated with the harmonic oscillator model. Little is known, however, about the influence of anharmonicity of vibrations on heat capacity. For the calculation of the thermodynamic functions, one needs, thus, to use actually measured heat capacities. Fortunately, today these can be gathered easily by differential scanning calorimetry.

5. COMPLEX HEAT CAPACITY

In general, one can represent a complex number $z = a + ib$, with $i = \sqrt{-1}$, as:

$$z = |z|e^{i\theta} = |z|(\cos\theta + i\sin\theta), \quad \text{with} \quad (18)$$

$$|z| = \sqrt{a^2 + b^2}; \quad \cos\theta = \frac{a}{|z|}; \quad \text{and} \quad \sin\theta = \frac{b}{|z|}. \quad (19)$$

For the description of periodic changes, as in modulated-temperature differential scanning calorimetry, TMDSC, or Fourier analyses, the introduction of complex quantities is convenient and lucid, but brings no new physical insight over the representation in real numbers. The complex heat capacity has proven useful in the interpretation of thermal conductivity of gases of molecules with slowly responding internal degrees of freedom and may be of use representing the slow response in the glass transition. For the specific complex heat capacity measured at frequency ω , $C_p(\omega)$, with its reactive (real) part $C_p'(\omega)$ and the imaginary part $iC_p''(\omega)$, one must use the following equation to make the dissipative part, $C_p''(\omega)$, positive:

$$C_p(\omega) = C_p'(\omega) - iC_p''(\omega). \quad (20)$$

The real quantities of Eq. (20) are then written as:

$$C_p'(\omega) = C_p^e - \frac{\omega^2(\tau_{T,p}^e)^2\Delta^e C_p}{1 + \omega^2(\tau_{T,p}^e)^2} \quad \text{and} \quad (21)$$

$$C_p''(\omega) = \frac{\omega\tau_{T,p}^e\Delta^e C_p}{1 + \omega^2(\tau_{T,p}^e)^2}, \quad (22)$$

where $\tau_{T,p}^e$ is the Debye relaxation time of the system. The reactive part $C_p'(\omega)$ of $C_p(\omega)$ is the dynamic analog of C_p^e , the C_p at equilibrium. Accordingly, the limiting cases of a system in internal equilibrium and a system in arrested equilibrium are, respectively:

$$\omega\tau_{T,p}^e \ll 1; \quad C_p(\omega) = C_p'(\omega) = C_p^e, \quad \text{and} \quad (23)$$

$$\omega \tau_{T,p}^e \gg 1 ; \quad C_p(\omega) = C_p'(\omega) = C_{p,\zeta^e} . \quad (24)$$

The internal degree of freedom, ζ , contributes $\Delta^e C_p$ at low frequencies to the equilibrium specific heat capacity. With increasing ω , this contribution decreases, and finally disappears.

The limiting dissipative parts, $C_p''(\omega)$, without analogs in equilibrium thermodynamics, are:

$$\omega \tau_{T,p}^e \ll 1 ; \quad C_p''(\omega) = \omega \tau_{T,p}^e \Delta^e C_p , \text{ and} \quad (25)$$

$$\omega \tau_{T,p}^e \gg 1 \quad C_p''(\omega) = \Delta^e C_p / \omega \tau_{T,p}^e , \quad (26)$$

so that the dissipative part disappears in internal equilibrium ($\tau_{T,p}^e \rightarrow 0$) as well as in arrested equilibrium ($\tau_{T,p}^e \rightarrow \infty$). Fig. 7 illustrates the changes of $C_p'(\omega)$ and $C_p''(\omega)$ with $\omega \tau_{T,p}^e$.

The dissipative heat capacity $C_p''(\omega)$ is a measure of Δ_s , the entropy produced in non-equilibrium per half-period of the oscillation $T(t) - T^e$:

$$C_p''(\omega) = (1/\pi) (T^e/A_T)^2 \Delta_s . \quad (27)$$

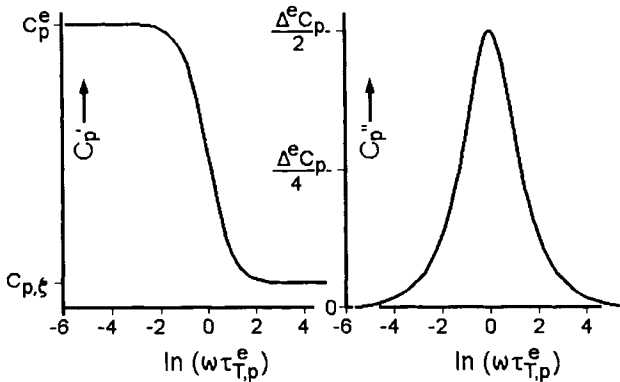


Fig. 7. Reactive and dissipative parts of complex heat capacity.

6. THE ADVANCED THERMAL ANALYSIS SYSTEM, ATHAS

In order to describe the heat capacities of linear macromolecules, the Advanced Thermal Analysis System was developed [1]. It consists of the link of the heat capacity of the solids to an approximate frequency spectrum and the comparison of the heat capacity of liquids to the contributions from its constituent groups.

6.1. The crystallinity dependence of heat capacity

Several steps are necessary before the heat capacity can be linked to its various contributions. First, one finds that linear macromolecules do not normally crystallize completely; they are semicrystalline. The restriction to crystallization is caused by kinetic hindrance to full extension of the molecular chains which, in the amorphous phase, are randomly coiled and entangled. Furthermore, in cases where the molecular structure is not sufficiently regular, the crystallinity may be further reduced, or even completely absent, so that the molecules remain amorphous at all temperatures. Many copolymers are examples of polymers that do not crystallize.

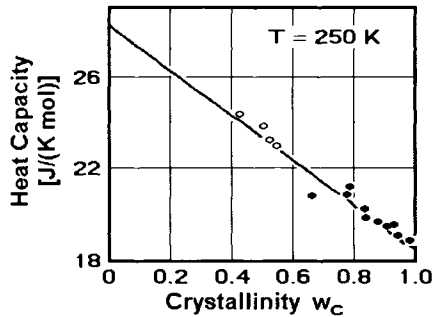


Fig. 8. Heat capacity of polyethylene as function of crystallinity at 250 K [14].

The first step in the analysis must thus be to establish the crystallinity-dependence of the heat capacity. In Fig. 8 the heat capacity of polyethylene, the most analyzed polymer [14], is plotted as a function of crystallinity at 250 K, close to the glass transition temperature ($T_g = 237$ K). The fact that polyethylene, $[(CH_2)_x]$, is semicrystalline implies that the sample is metastable, *i.e.*, not in equilibrium. Thermodynamics requires that a one-component system, such as polyethylene, can have two phases in equilibrium only at the melting temperature (phase rule, at constant pressure).

One way to establish the weight-fraction crystallinity, w_c , is from density measurement, others are X-ray diffraction or infrared spectroscopy [15]. Plotting the measured heat capacities of samples with different crystallinity often results in a linear relationship. Such plots allow the extrapolation to crystallinity zero to find

the heat capacity of the amorphous sample, and to crystallinity 1.0, to find the heat capacity of the completely crystalline sample. This is possible even if the limiting cases are not experimentally available.

The graphs of Fig. 9 summarize the dependence of the heat capacity of polyethylene on crystallinity at high and low temperatures. All curves on the left have a linear crystallinity dependence. At low temperature, the fully crystalline sample ($w_c = 1.0$) has a T^3 temperature dependence of the heat capacity up to 10 K (single point in the graph), as is required for the low-temperature limit of the three-dimensional Debye function of Eq. (17). One concludes that the beginning of the frequency spectrum is, as documented for diamond and graphite in Fig. 6, quadratic in its dependence on frequency of the density of vibrational states, $\rho(\nu)$ (see also Fig. 5). This ν^2 -dependence does not extend to higher temperatures. At 15 K, the T^3 -dependence is lost, and more details are needed to describe the heat capacity of amorphous polyethylene.

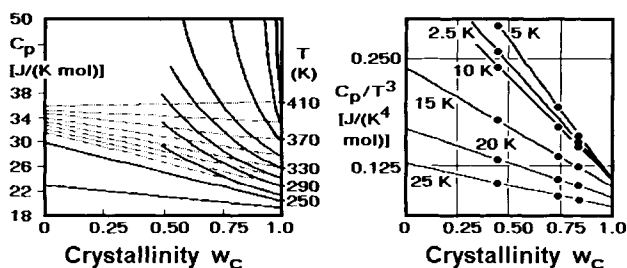


Fig. 9. Heat capacity of polyethylene as function of crystallinity at various temperatures [14].

The amorphous polyethylene ($w_c = 0$) seems, in contrast, never to reach a T^3 dependence on temperature of the heat capacity. Note that the curves of the figure do not even change monotonously with temperature in the C_p/T^3 plot.

As the temperature is raised, the dependence on crystallinity of the heat capacity becomes less; it is only a few percent between 50 to 200 K. In this temperature range, heat capacity is largely independent of the physical structure. Glass and crystal have almost the same heat capacity. This is followed again by a steeper increase in the heat capacity of the amorphous polymer as it undergoes the glass transition at about 240 K. It is of interest to note that the fully amorphous value from this graph agrees well with the heat capacity of the liquid, extrapolated from above the melting temperature (414.6 K) which leads to a value of $28.3 \text{ J K mol}^{-1}$ at 240 K [1].

Finally, the left curves of Fig. 9 show that above about 260 K, melting of small, metastable crystals causes abnormal, nonlinear deviations in the heat capacity versus crystallinity plots. The measured data are indicated by the heavy lines in the figure. The thin lines indicate how continued additivity would look. The points for

amorphous polyethylene on the ordinate of the left figure represent the heat capacity of the melt and agree with the extrapolation from experiments with the equilibrium melt at high temperature. All heat capacity contributions above the thin lines are, thus, assigned to nonequilibrium melting.

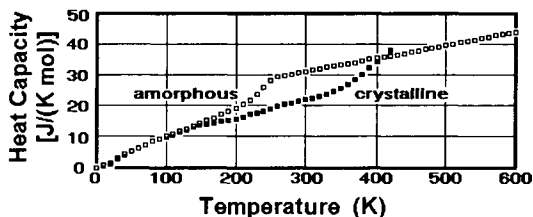


Fig. 10. Extrapolated heat capacities of polyethylene [14].

Fig. 10 illustrates the completed analysis. A number of other polymers are also described in the ATHAS Data Bank [1], but most information is available for the discussion of polyethylene. The heat capacity of the crystalline polyethylene is characterized by the T^3 dependence to 10 K. This is followed by a change to a linear temperature dependence up to about 200 K. The latter temperature dependence of the heat capacity fits a one-dimensional Debye function given by Eq. (15). Then, one notices a slowing of the increase of the crystalline heat capacity with temperature, at about 200 to 250 K, to show a renewed increase above 300 K, to reach values equal to and higher than the heat capacity of melted polyethylene (close to the melting temperature). At low temperatures the heat capacity of the glassy polyethylene shows large deviations from the heat capacity of the crystal (see Fig. 9). At these temperatures the absolute value of the heat capacity is, however, so small that it is not discernable in Fig. 10, and also does not contribute significantly to the integral quantities H , S , and G at room temperature. After a long range of almost equal heat capacities of crystal and glass, the glass transition is obvious at about 240 K. In the melt, the heat capacity is linear over a very wide range of temperature.

6.2. Heat capacities of solids

The quite complicated temperature dependence of the macroscopic heat capacity of polyethylene and other polymers must now be explained by a microscopic model of thermal motion. Neither a single Einstein function nor any of the Debye functions have any resemblance of the experimental data for the solid state, while the heat capacity of the liquid seems to be a simple straight line, not only for polyethylene, but also for many other polymers (but not for all!). Based on the ATHAS Data Bank of experimental heat capacities [1] the analysis system for solids and liquids was derived as is summarized in the schematic of Fig. 11.

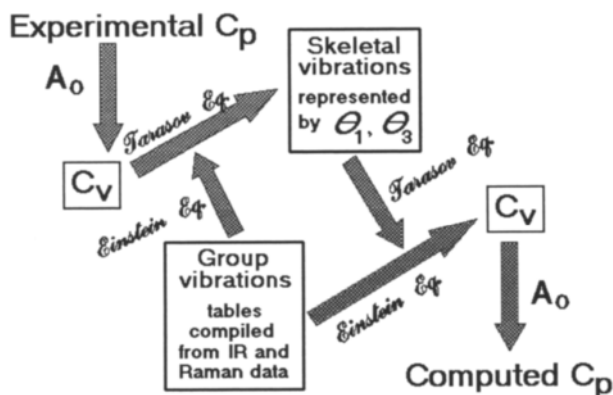


Fig. 11. Scheme of ATHAS [1].

The most detailed analysis is possible for solid polymers. Fig. 11 illustrates how first the experimental data are linked to an approximate frequency spectrum (left half of Fig. 11). Once this is accomplished, a “heat capacity due to vibrations only” can be calculated (right half of Fig. 11). The computed heat capacity agrees at low temperatures with the experiment and can be used to extend the temperature range of vibrational heat capacity by extrapolation. At high temperature, one can identify deviations from the vibrational heat capacity, largely due to the beginning large-amplitude motion. For the heat capacities of the liquids, and also for solids at higher temperatures, it was found empirically that the group contributions of the chain units which make-up the molecules can approximate the changes in heat capacity. This empirical observation was used to derive an addition scheme for the heat capacities of polymers [16].

After the crystallinity dependence has been established, the heat capacity of the solid at constant pressure, C_p , must be changed to the heat capacity at constant volume C_v , as indicated by Eqs. (9) or (10) and indicated in the first step of Fig. 11. For most polymers, use is made of the Lindemann approximation since compress-

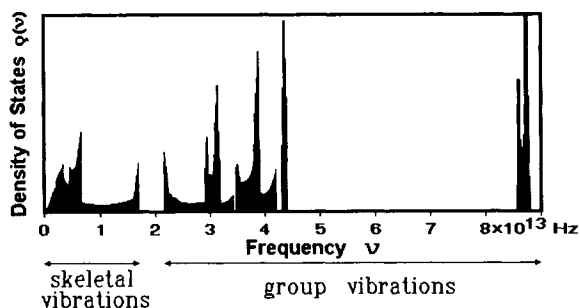


Fig. 12. Frequency spectrum of polyethylene from normal mode calculations [17].

All motions of higher frequency will now be called group vibrations, because these vibrations involve oscillations of relatively isolated groupings of atoms along the backbone chain. Fig. 13 illustrates that the C-C-stretching vibration is not a skeletal vibration because of the special geometry of the backbone chain. In the

Table 3 Group vibrations of polyethylene

Vibration Type	$\Theta_E, \Theta_L, \Theta_U$ (K)	N
CH ₂ sym. stretch	4097.7	1.00
CH ₂ asym. stretch	4148.1	1.00
CH ₂ bending	2074.7	1.00
CH ₂ wagging	1699.3-1976.6	0.65
	1976.6	0.35
CH ₂ twisting +	1689.6-1874.3	0.48
CH ₂ rocking	1874.3	0.52
C-C stretching	1377.6-1637.5	0.34
	1377.6-1525.4	0.35
	1525.4	0.31
CH ₂ twisting +	1494.1	0.04
CH ₂ rocking	1038.0-1494.1	0.59
	1079.1	0.37

first set of group vibrations, between 2 and 5×10^{13} Hz, one finds five degrees of freedom. These oscillations involve mainly the bending of the C-H bond and the C-C stretching vibration. The sketches 3-6 in Fig. 13 illustrate the approximate C-H motions of the bending vibrations. The first type of motion involves the symmetrical bending of the hydrogens (3). The bending motion is indicated by the arrows. The next type of oscillation is the rocking motion (4). In this case both hydrogens move in the same direction and rock the chain back and forth. The third type of motion in this group, listed as number 5, is the wagging motion. One can think of it as a motion in which the two hydrogens come out of the plane of the paper and then go back behind the plane of the paper. The twisting motion (6), finally, is the asymmetric counterpart of the wagging motions—*i.e.*, one hydrogen atom moves out of the plane of the paper while the other goes back behind the plane of the paper. In addition to these bending motions of C-H, there is a motion in the same frequency region that is involved with the stretching of the bond between two adjacent carbon atoms (sketch 9). This stretching of a C-C bond has a much higher frequency than the torsion and bending involved in the skeletal modes. These five vibrations are the ones responsible for the renewed increase of the heat capacity starting at about 300 K. Below 200 K their contributions to the heat capacity are small.

Finally, the CH₂ groups have two more degrees of freedom, the ones that contribute to the very high frequencies above 8×10^{13} Hz. These are the C-H stretching vibrations. There is a symmetric and an asymmetric one, as shown in sketches 7 and 8 of Fig. 13. These frequencies are so high that at 400 K their contribution to the heat capacity is still small. Summing all these contributions to the heat capacity of polyethylene, one finds that up to about 300 K mainly the skeletal vibrations contribute to the heat capacity; above 300 K, increasing contributions come from the group vibrations in the region of $2-5 \times 10^{13}$ Hz, and if at 700-800 K solid polyethylene could exist, one would get the additional

contributions from the C-H stretching vibrations, but polyethylene crystals melt before these vibrations are excited significantly. When fully excited, the total of nine vibrations, possible for the three atoms of the CH₂ unit, would lead to a heat capacity of 75 J K⁻¹ mol⁻¹. At the melting temperature, only half of these vibrations are excited since C_v is only about 38 J K⁻¹ mol⁻¹.

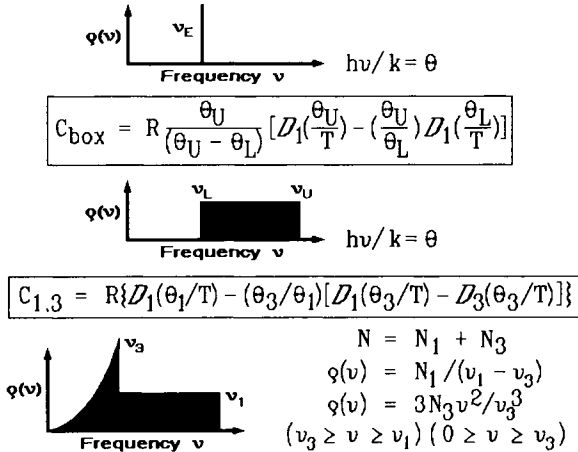


Fig. 14. Vibrational heat capacity contributions for solids.

The next step in the analysis is to find an approximation for the skeletal vibration spectrum since the lowest skeletal vibrations are, as mentioned above, not well-enough known, and often even the higher skeletal vibrations have not been established. To obtain an experimental, skeletal heat capacity, the contributions of the group vibrations to the heat capacity are subtracted from C_v, as indicated in Fig. 11. Table 3 contains a list of the group vibration frequencies derived from the normal mode analysis of Fig. 12. If such a table is not available for the given polymer, results for the same group in other polymers or small-molecule model compounds can be used as an approximation. The computations for the group-vibration table are illustrated by the two top entries in Fig. 14. The narrow frequency ranges are treated as single Einstein functions (see Fig. 4), the wider distributions are broken into single frequencies and box distributions as, for example for the C-C-stretching mode in Table 3. The lower frequency limit of the box distribution is given by θ_L , the upper one by θ_U and the one-dimensional Debye functions are given by Eq. (15).

The next step in the ATHAS analysis of Fig. 11 is to assess the skeletal heat capacity. The skeletal vibrations are coupled so extensively that their distributions stretch to zero frequency and are often called acoustical vibrations (although the acoustic vibrations reach only to about 20,000 Hz). In the lowest-frequency region one must consider that the vibrations couple intermolecularly because the

wavelengths of the vibrations become larger than the anisotropy caused by the molecular chain structure and the detailed arrangement is of little consequence at the lowest frequencies. In this frequency region the three-dimensional Debye function of Eq. (17) should apply, as derived for an isotropic solid. To approximate the skeletal vibrations of linear macromolecules, one starts at low frequency with a three-dimensional Debye function, and then switches to a one-dimensional Debye function, as shown at the bottom of Fig. 14.

Such an approach was suggested first by Tarasov [18]. The skeletal vibration frequencies are separated into two groups, the intermolecular, acoustic group, characterized by a three-dimensional Θ -temperature, Θ_3 (with frequencies between zero and ν_3), and an intramolecular group with frequencies between ν_3 and ν_1 , characterized by a one-dimensional Θ -temperature, Θ_1 . The boxed Tarasov equation in Fig. 14 shows the needed computation. By assuming the number of vibrators in the intermolecular part is Θ_3/Θ_1 , one has reduced the adjustable parameters in the equation from three (N_3 , Θ_3 , and Θ_1) to only two (Θ_3 and Θ_1). The Tarasov equation is then fitted to the experimental skeletal heat capacities at low temperatures to get Θ_3 , and at higher temperatures to get Θ_1 . Computer programs for fitting over the whole temperature region are available [19]. For crystalline polyethylene, a good fit was achieved for $\Theta_3 = 158$ K and $\Theta_1 = 519$ K and for amorphous polyethylene $\Theta_3 = 80$ K and $\Theta_1 = 519$ K. Efforts to fit with the three parameters N_3 , Θ_3 , and Θ_1 , or with the four parameters of separate longitudinal and transverse Tarasov equations has shown no advantages.

With the Tarasov theta-parameters and Table 3 of group-vibration frequencies, the heat capacity due to vibrations can be calculated over the full temperature range, completing the ATHAS analysis of Fig. 11. Fig. 15 shows the result for crystalline polyethylene. Up to 250 K the analysis is in full agreement with the experimental data, and at higher temperatures valuable information can be extracted from the deviations of the experiment, as will be shown below. A detailed understanding of the origin of the heat capacity of polyethylene is, thus, possible. The link between the macroscopic heat capacity and the microscopic molecular

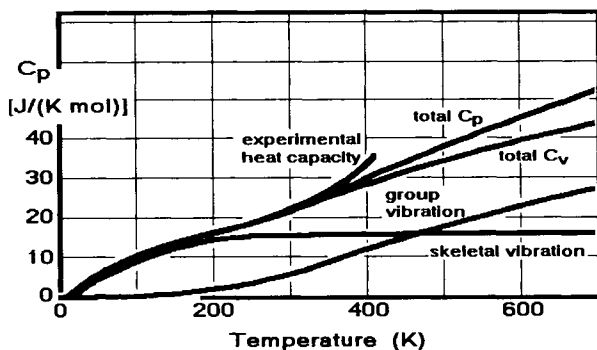


Fig. 15. Heat capacities of crystalline polyethylene.

motion is established.

A newer fitting procedure is shown in Fig. 16 and Fig. 17 [19], an example of one of the most complicated linear macromolecules, a solid, water-free protein. The protein chosen is bovine α -chymotrypsinogen, type 2. Its degree of polymerization is 245, containing all 20 naturally occurring amino acids in known amounts and in an established sequence. The molar mass is 25,646 Da. All group vibration contributions were calculated using the data accumulated for synthetic poly(amino acids) in the ATHAS data bank, and then subtracted from the experimental C_v (see Fig. 11). The remaining experimental skeletal heat capacity up to 300 K was then fitted to a Tarasov expression for 3005 vibrators (N_s), as shown in Fig. 16. A 20×20 mesh with Θ_3 values between 10 and 200 K and Θ_1 between 200 and 900 K is evaluated point by point, and fitted to the experimental C_p . It is obvious that a

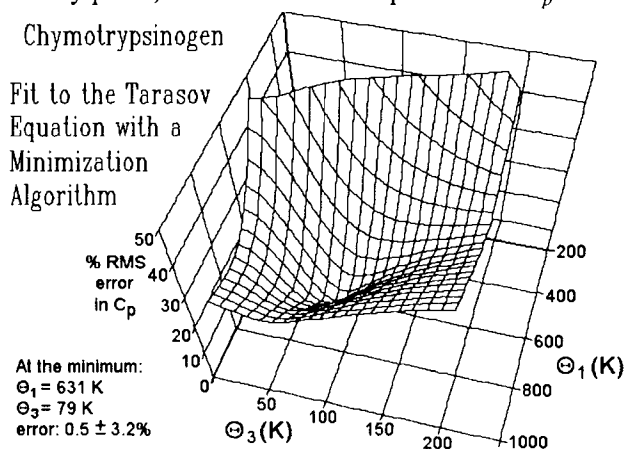


Fig. 16. Tarasov fit for bovine α -chymotrypsinogen.

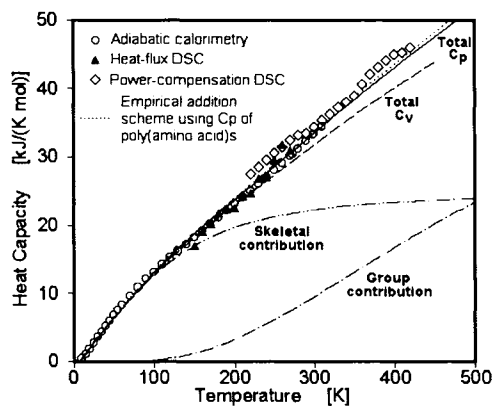


Fig. 17. Heat capacities of chymotrypsinogen.

unique minimum in error is present in Fig. 16, proving also the relevance of the ATHAS for the evaluation of the vibrational C_p of proteins. An interpolation method was used to fix the minimum between the mesh points. Fig. 17 illustrates the fit between calculation from the vibrational contributions and the experiments from various laboratories. Within the experimental error, which is particularly large for proteins which are difficult to obtain free of water, the measured and calculated data agree. Glass transition and possible segmental melting occur above the temperature range measured. Also indicated are the results of an empirical addition scheme [16], using the appropriate proportions of C_p from all poly(amino acid)s available in the ATHAS data bank [1].

6.3. Polyoxide heat capacities

Besides providing heat capacities of single polymers, the ATHAS data bank permits also to correlate data of homologous series of polymers. The aliphatic series of polyoxides is an example to be analyzed next [20]. An approximate spectrum of the group vibrations poly(oxymethylene). POM, $[(\text{CH}_2-\text{O}-)_x]$, the simplest polyoxide, is listed in Table 4. The CH_2 -bending and -stretching vibrations are similar to the data for polyethylene in Table 3. The fitted theta-temperatures are $\Theta_3 = 117$ K and $\Theta_l = 232$ K. Note that they are calculated for only two modes of vibration instead of the expected four for the two backbone atoms in the repeating unit. The missing two skeletal vibrations, contributed by the added O^- group, are included (arbitrarily) in the list of group vibrations since they are reasonably well established.

Table 4 Group vibrations of poly(oxymethylene)

Vibration Type	$\Theta_E, \Theta_L, \Theta_U$ (K)	N
CH ₂ symm. stretch	4284.7	1.00
CH ₂ asym. stretch	4168.2	1.00
CH ₂ bending	2104.5	1.00
CH ₂ wagging	2018.6	1.00
CH ₂ twisting	1921.9	1.00
CH ₂ rocking	1524.7	0.20
	1707.2	0.24
	1524.7-1707.2	0.56
C-O stretching	1385.1	0.22
	1632.1	0.11
	1385.1-1632.1	0.57
	1304.6	1.00
chain bending	889.7	1.00
	655.0	0.23
	359.7-440.2	0.29
	359.7-655.0	0.48

The table of group vibration frequencies with their Θ -temperatures and the number of skeletal vibrators, N_s , with their two Θ -temperatures permits now to calculate the total C_v and, with help of the expressions for $C_p - C_v$, also C_p . Fig. 18 show the results of such calculations, not only for POM, but also for polyethylene (PE, bottom curve) and a whole series of homologous, aliphatic polyoxides. The calculations are based on the proper number of group vibrations for the number of O^- and CH_2^- in the repeating units:

PO8M	= Poly(oxyoctamethylene) $[O-(CH_2)_8]_x$
POMO4M	= Poly(oxymethyleneoxytetramethylene) $[O-CH_2-O-(CH_2)_4]_x$
PO4M	= Poly(oxytetramethylene) $[O-(CH_2)_4]_x$
PO3M	= Poly(oxytrimethylene) $[O-(CH_2)_3]_x$
POMOE	= Poly(oxymethyleneoxyethylene) $[O-CH_2-O-(CH_2)_2]_x$
POE	= Poly(oxyethylene) $[O-(CH_2)_2]_x$
POM	= Poly(oxymethylene) $[O-CH_2]_x$
PE	= Polyethylene [poly(methylene)] $[CH_2]_x$

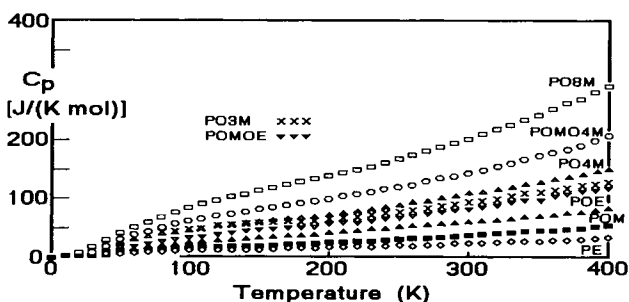


Fig. 18. Heat capacities of a series of polyoxides [20].

The more detailed analysis of the heat capacities of the solid, aliphatic polyoxides is summarized in Fig. 19. It displays the changes of θ_1 and θ_3 with chemical composition. It is thus possible to also estimate θ_1 and θ_3 values for intermediate compositions, and to compute heat capacities of unknown polyoxides or copolymers of different monomers without new measurements. An interesting observation is that the values of θ_1 are not very dependent on the crystallinity (see also the polyethylene data, above). The values for θ_3 , in contrast, are as much as double as high for the crystalline polymers than for the glassy ones. Since the θ_3 values are,

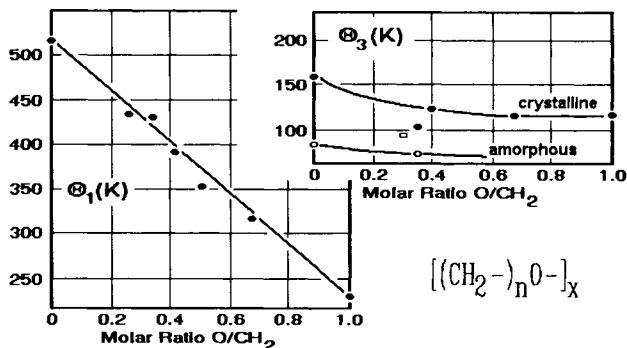


Fig. 19. Theta temperatures for a series of polyoxides.

however, relatively small, the skeletal contributions are usually close to fully excited above room temperature.

Similar analyses were accomplished for more than 150 macromolecules. The data on N , Θ_1 , and Θ_3 together with the ranges of experimental C_p data, are collected in the ATHAS data bank together with detailed data tables [1]. The precision of these computed heat capacities is in general better than $\pm 5\%$, close to the common experimental accuracy.

The strict additivity of the heat capacity contributions of the group vibrations, and the continuous change in Θ_1 with chemical composition, led to the development of addition schemes for heat capacities [16]. As long as the contributions of the backbone groupings that constitute the polymers are known empirically, it is possible to estimate the heat capacity of unknown polymers and copolymer from these contributions. The just completed discussion of the Tarasov analysis indicates that, indeed, the group vibrations are additive, but that at lower temperatures deviations are to be expected as long as the intermolecular skeletal vibrations are not sufficiently excited. In this case it may, however, also be possible to estimate Θ_3 from a list of similar polymers and calculate an improved estimate of the heat capacity.

6.4. Heat capacities of liquids

The heat capacities of liquids are much more difficult to understand. The motion in the liquid state involves in addition to vibrational motion also large-amplitude rotations and possibly also translations. Since, however, in the liquid state polymers are usually in equilibrium, measurements are more reproducible than for the semicrystalline samples.

The addition scheme helps to connect larger bodies of data for liquid polymers [16]. In the liquid state one is always at sufficiently high temperature so that the

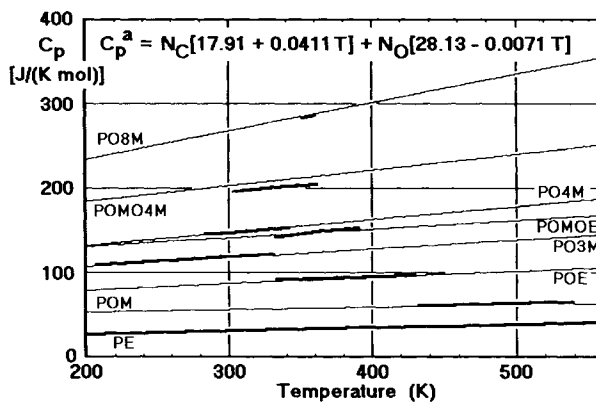


Fig. 20. Heat capacity of liquid polyoxides.

intermolecular skeletal vibrations are fully excited so that additivity holds for both the intramolecular skeletal vibrations and the group vibrations. Fig. 20 shows the experimental data for the liquids for the same series of polyoxides as analyzed for the solid state. The equation in the top of the graph represents all the thin lines, while the thick lines represent the experimental data. The equation for C_p^a was arrived at by least-squares fitting of all experiments and seems more precise than any of the separate experiments.

Another example of the heat capacities of a homologous series of liquid polymers is given in Fig. 21. Data are presented for the aliphatic nylons, labeled by their number of carbon atoms in the repeating units. Again, a single equation represents all data.

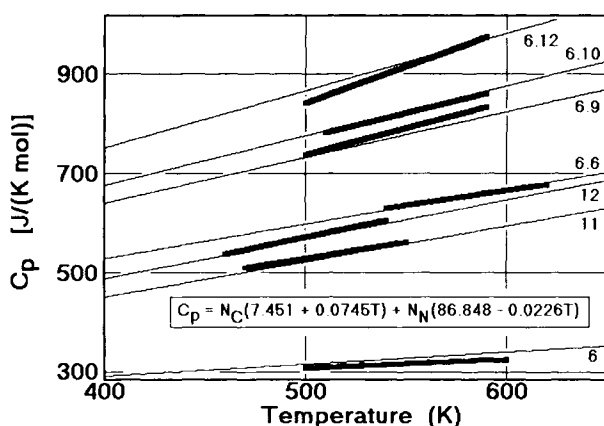


Fig. 21. Heat capacities of liquid nylons.

7. EXAMPLES OF THE APPLICATION OF ATHAS

The application of the ATHAS has produced a large volume of critically reviewed and interpreted heat capacity data on solid and liquid homopolymers. This knowledge is helpful in the determination of the integral thermodynamic functions which are also part of the data bank [1]. Even of greater importance is the help these basic data give in the separation of nonequilibrium enthalpy and heat capacity effects, as will be illustrated in a number of examples.

7.1. Poly(tetrafluoroethylene)

Fig. 22 shows the analysis of the heat capacity of crystalline polytetrafluoroethylene (PTFE). The comparison between calculation and measurement is given in Fig. 23. As in the case of the polyoxides, it is also possible to predict heat capacities of all less fluorinated polyethylenes. The measured sample was almost completely

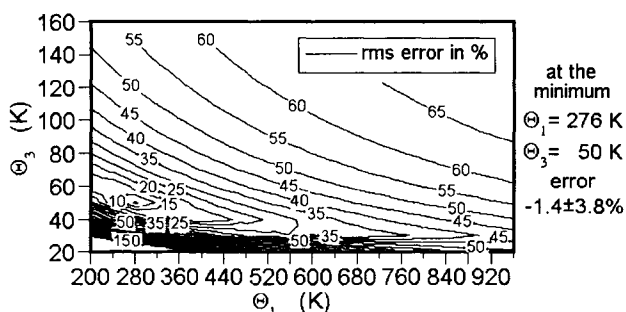


Fig. 22. Fit of crystalline polytetrafluoroethylene heat capacity data to the Tarasov equation [19].

crystalline. It is obvious from the graph that there are two rather broad endotherms superimposed on the heat capacity curves. The room temperature transition is particularly broad. It represents a crystal-to-condis-crystal transition. Without the computed heat capacity as a base line, it is impossible to separate the heat of transition quantitatively from the heat capacity. Based on these data it was possible to show that the entropies of transition, when added for the two transitions, give a similar value ($9.6 \text{ J K}^{-1} \text{ mol}^{-1}$) as the entropy of fusion of polyethylene ($9.9 \text{ J K}^{-1} \text{ mol}^{-1}$). The high temperature of the appearance of liquid PTFE, thus, is due to the disorder in the crystal, not to a lesser entropy in the melt.

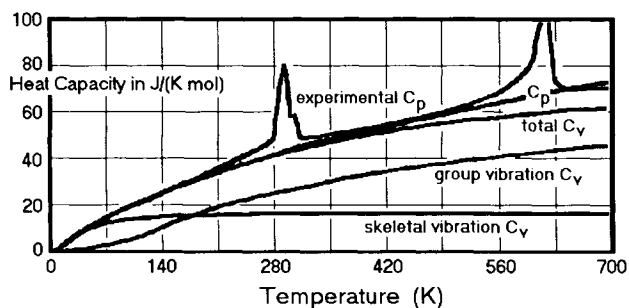


Fig. 23. Heat capacity of polytetrafluoroethylene [21].

7.2. Poly(oxybenzoate-co-oxynaphthoate)

Fig. 24 represents an even more complicated polymer system. In this case the macromolecule is the random copolymer poly(oxybenzoate-co-oxynaphthoate), a high-strength material (Vectra™). The graph shows a rather small endotherm and a rather broad, possibly two-stage glass transition that stretches over more than 100 K. Without precise computation of the liquid and solid heat capacities, it would not have been possible to identify the glass transition and provide important characteristics for the practical application of the polymer. The broad glass transition is

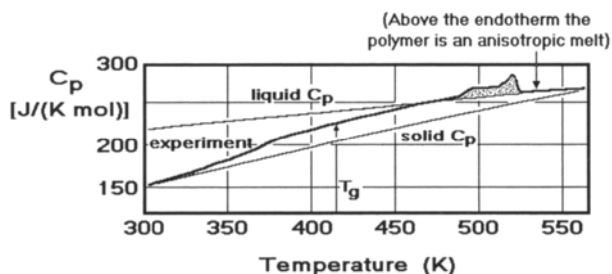


Fig. 24. Heat capacity of poly(oxybenzoate-co-oxynaphthoate) with 58 mol-% oxybenzoate [22].

caused by the small amount of ordering in the copolymer that produced a nanophase-separated structure with each molecule traversing many different nanophases.

7.3. Large-amplitude motion of polyethylene

The increasing deviation from the glassy or crystalline vibrational heat capacity of polyethylene with temperature was already noted in Figs. 10 and 15. In Fig. 25 they are once more compared. The glassy polyethylene shows local *gauche-trans* conformation-exchanges to almost 100 K. With mechanical measurements, this temperature range has been identified as the γ -transition. The small increase in heat capacity between 100 and 230 K has also been mistaken for the glass transition, which, however, is clearly seen at 237 K. A similar increase in heat capacity occurs for the crystalline polyethylene below the melting transition. It could also be linked to local formation of dynamic *gauche*-defects in the crystals [23]. One expects that these small increases in heat capacity are of importance for the understanding of plastic deformation. Many other polymers have similar gradual beginnings of the increase in heat capacity at the glass transition and also before melting.

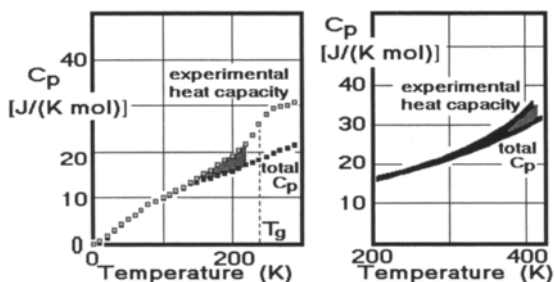


Fig. 25. Deviation of glassy (left) and crystalline (right) C_p .

7.4. Polymethionine

Fig. 26 and Fig. 27 illustrate the analysis of the heat capacity of anhydrous, solid polymethionine, a synthetic poly(amino acid) $[\text{CH}(\text{CH}_2-\text{CH}_2-\text{S}-\text{CH}_3)-\text{CO}-\text{NH}-]_x$. This is one of the 20 poly(amino acid)s that can be made out of the naturally occurring amino acids. All were analyzed for C_p [24]. These data form the basis for the addition scheme of protein heat capacities. Of interest is the positive deviation starting at room temperature or may be even earlier. It was suggested that this increase is connected with a glass transition involving the side groups of the polymer. Confirmation of this possibility is still needed.

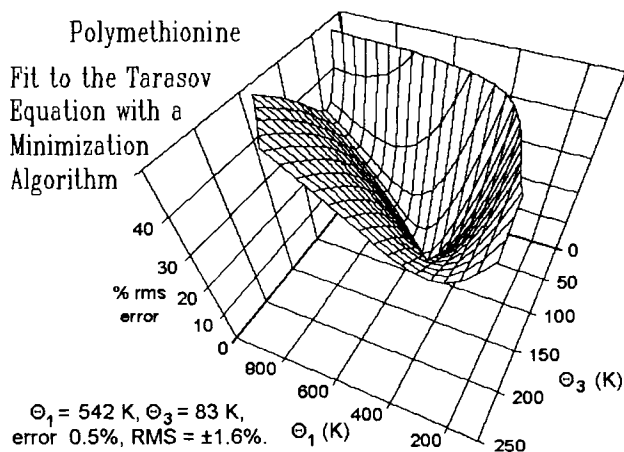


Fig. 26. Tarasov fit for a poly(amino acid).

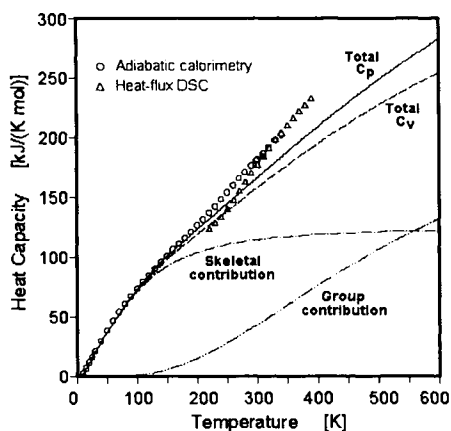


Fig. 27. Heat capacity of polymethionine

7.5. MBPE-9

Macromolecules that contain aliphatic and aromatic sequences in their backbone

structure have special possibilities to exist as liquid crystals or as condisc crystals. The thermal analysis of a polyether based on the semiflexible mesogen 1-(4-hydroxyphenyl)-2-(2-methyl-4-hydroxyphenyl)ethane is copied in Fig. 28. The computed vibration-only heat capacity is reached somewhat below the glass transition, but above the glass transition the heat capacity does not reach the computed value expected from the crystallinity derived from the heat of fusion ($w_c = 0.43$). One assumes that there is some rigid-amorphous fraction present. Furthermore, the entropy of fusion indicates considerable conformational disorder in the crystal that freezes in its own “glass transition,” indicated by the cross-hatched area.

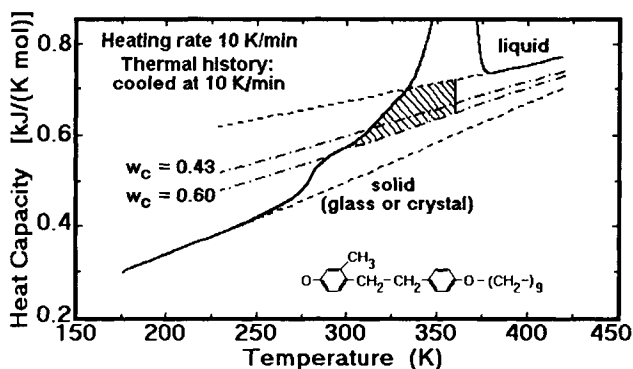


Fig. 28. Heat capacity of MBPE-9.

7.6. Liquid selenium

The heat capacity of liquid selenium, which is also a linear macromolecule illustrates the effect of chemical equilibria. The heat capacity for many liquid, linear macromolecules increases linearly with temperature, despite the fact that one expects an exponential increase in C_v from the vibrational contributions of the C-H-bending and -stretching vibrations. To understand this observation, one has to remember that from the changes of the heat capacity from vibrational motion (R) to rotational motion ($R/2$) a decreasing heat capacity contribution results with increasing temperature. Also, the hole-theory of liquids includes a decrease in the hole contribution to the heat capacity since it is calculated similar to the case of two energy states shown in Fig. 2. The maximum in heat capacity occurs close to the glass transition temperature. The subsequent decrease seems to be able to compensate the vibrational increase in heat capacity for a considerable temperature range. Looking at the heat capacity of the liquid selenium, one finds that there are no group vibrations to produce the exponential increase in C_p and, indeed, the heat capacity of liquid Se decreases with temperature starting from the glass-transition temperature. The decrease in C_p is nonlinear. At high temperature, C_p increases

again.

These changes in heat capacity with temperature are specific to Se, and an explanation is given in Fig. 29. Curve 1 represents the experimental data; curve 2, the vibrational contributions as derived from the crystalline vibrational spectrum. The difference between curves 1 and 3 represent the special contribution to the heat capacity that arises from the ring-chain equilibrium, *i.e.*, from a chemical reaction. The melt of selenium consists of very long macromolecules $(\text{Se-})_x$ and rings (mainly Se_8). The two components are in a temperature-dependent chemical equilibrium, and the differences between curves 1 and 3 are estimates of the heat of reaction per kelvin of temperature-increase for this process. Finally, the difference between curves 3 and 4 are estimates of the heat capacity due to the hole equilibrium. It decreases with temperature, as expected. The agreement between curves 4 and 2 are, finally, a measure of the quality of the model that was chosen for the interpretation of the change of heat capacity with temperature. Selenium represents, thus, a case where a chemical heat of reaction is included in the measurement of heat capacity.

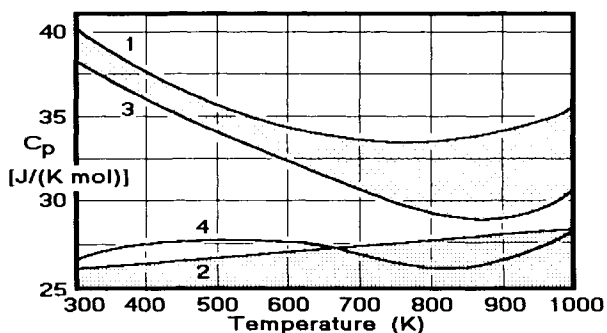


Fig. 29. Heat capacity of liquid selenium (curve 1).

From the addition scheme of heat capacities, it is possible to deduce the heat capacity of another, hypothetical, monatomic polymeric chain, namely $(\text{O-})_x$. Its heat capacity is estimated by subtracting the $(\text{CH}_2)_c$ contribution to the heat capacity from the total heat capacities of the polyoxides which are shown in Fig. 20. As in the Se heat capacities, the heat capacity of $(\text{O-})_x$ decreases with temperature.

7.7. Poly(styrene-co-butadiene)

To describe heat capacities of copolymers, it is naturally impossible to measure each and every composition. But since the heat capacities in the solid state at temperatures above, perhaps 100 K, are additive with respect to composition, and the same is true for the liquid states, estimates can be made of the heat capacities of all copolymers. Fig. 30 shows the additivity of the heat capacities of

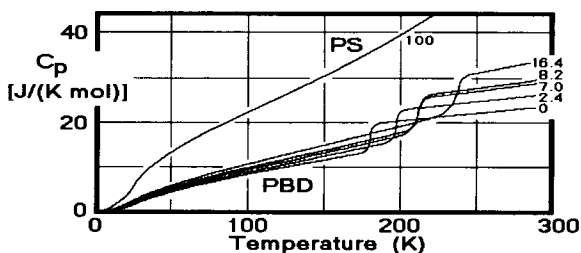


Fig. 30. Heat capacities of poly(styrene-*co*-butadiene) of the given concentrations in mole-% styrene.

poly(styrene-*co*-butadiene). These measurements were done many years ago by adiabatic calorimetry [25], and it was possible later to derive the heat capacity of the copolymers from their molar composition and the heat capacities of the constituent homopolymers. A notable feature of the polybutadiene (PBD) and copolymer heat capacities is the increase in temperature of the glass transition with styrene composition. The glass transition of pure polystyrene (PS) occurs at 373 K.. Comparing now the heat capacity measured by calorimetry with the heat capacity calculated from the addition scheme, one finds an error between 0 and 4% from 10 K to the beginning of the glass-transition region. But even above the glass-transition temperature, the additivity works well. The errors are less than 5%. Note that for the addition scheme the contributions of both components, the butadiene as well as the styrene, must be taken as their liquid heat capacities as soon as the copolymer glass-transition temperature has been exceeded. Position and breadth of the glass transition has to be predicted from other considerations.

8. TEMPERATURE-MODULATED CALORIMETRY

Temperature-modulated differential scanning calorimetry, TMDSC, opened a new vista to thermal analysis. While in the past careful extrapolation of data from non-equilibrium states to true equilibrium (crystal) and frozen equilibrium (glass) was necessary, it may now become possible to test for the state of a sample directly. In the following sections a first analysis of some of the interesting applications of TMDSC is given. Most of the examples are taken from the files of the ATHAS laboratory. For a full, up-to-date listing see our web site, given also for the information on the data bank [1].

Three types of measurements can be carried out with a typical TMDSC: 1). Standard DSC measurements in which the sample is heated continually at a fixed rate, achieved by turning off the modulation [see Eq. (3)]; 2). Quasi-isothermal TMDSC where the base-temperature of measurement is kept constant at T_o ($\langle\beta\rangle = 0$), and modulation occurs about this T_o , and a wider temperature range is covered by separate, successive runs at increasing or decreasing T_o ; 3). Standard TMDSC,

where the base temperature changes with an underlying rate $\langle\beta\rangle$ while a continuous temperature modulation is superimposed (see also Sect. 1).

The basic equations needed to follow temperature and heat capacity are shown in Fig. 31 [compare to Eqs. (3) and (4)]. In modulation experiments the angular brackets, $\langle \rangle$, indicate that the quantity is to be averaged over one modulation period, p , from time $t - p/2$ to time $t + p/2$. This averaging procedure eliminates the sinusoidal changes of the modulation frequency ω .

Standard DSC is based on the difference in lags $\Delta T = T_r - T_s$, as illustrated in the top sketch of Fig. 31. The equation for C_p indicates greater precision at faster heating rate and greater sample mass. The upper limits are set by the need to maintain a negligible temperature gradient within the sample [3]. As mass and heating rate increase, the measured C_p applies to increasingly lower average temperatures, a rather small effect for samples with small changes of C_p with temperature.

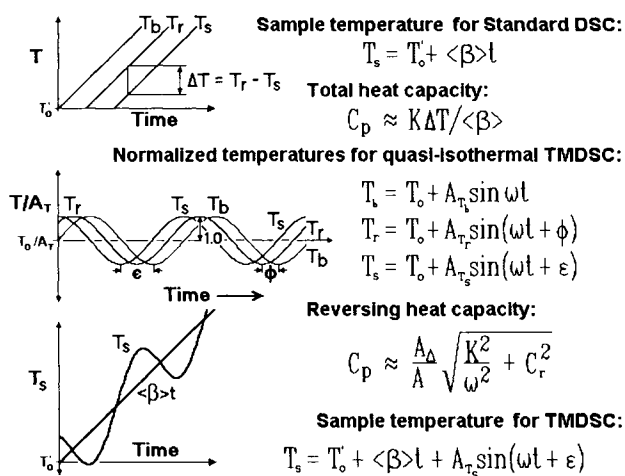


Fig. 31. Response and equations for TMDSC modes.

The quasi-isothermal TMDSC relies for measurement on the modulation. One can await steady state before beginning data collection and extracts only the contribution that is sinusoidally modulated with the proper frequency [6]. The heat capacity of Fig. 31 is thus only the reversing part of the measurement. Most of the inadvertent losses are eliminated. The sketch in Fig. 31 shows the ideal response. At steady state, the phase shifts ϕ and ϵ and the modulation amplitudes are linked to the reversing heat capacities. The limits of precision are set in this case by the requirement that the sample is fully modulated and shows a linear heat-flow rate response. As the sample size increases, the measured amplitude and phase lag may

not be identical throughout the sample. Special calibration methods have been developed and need to be checked by repeat measurements with different sample masses [6]. Longer times required to cover temperature ranges in steps, using perhaps 10–20 min per point, can be compensated partially by measuring in larger temperature steps (≈ 10 K).

The normal TMDSC, displayed at the bottom of Fig. 31 uses the underlying heating rate $\langle \beta \rangle \neq 0$. Two time scales, that of frequency ω and that of $\langle \beta \rangle$ are to be considered in case of time-dependent measurements. It is also possible to deconvolute the effect of the underlying heating rate, which is often similar to the standard DSC, and the reversing heat capacity. For a sample that responds reversibly, the two measurements are identical. A sample that does not respond reversibly on heating and cooling can be analyzed in detail to measure its non-reversing behavior. The reversing heat capacity can be extracted with the expression for quasi-isothermal analysis, indicated in Fig. 31. One performs then a pseudo-isothermal analyses by subtracting the averages $\langle \Delta T \rangle$ and $\langle T_s \rangle$ from the instantaneous responses $\Delta T(t)$ and $T_s(t)$. This is only precise, if steady state is approximately maintained during the modulation, and the response is linear. Measurements at different frequency ω can be used to overcome some of these difficulties.

8.1. Heat capacity and glass transition

Polydioxanone (PPDX) with a repeating unit of $(\text{CH}_2-\text{CH}_2-\text{O}-\text{CH}_2-\text{COO}-)_x$ can serve as an example of a comparative study of heat capacity using three methods of calorimetry. The results are shown in Fig. 32. The adiabatic calorimetry was done on a semicrystalline sample, the DSC and quasi-isothermal TMDSC, on an initially amorphous samples. All methods of measurement give the same result below the glass transition temperature and the calculated contributions of skeletal and group vibrations can easily be recognized. The difference between quenched

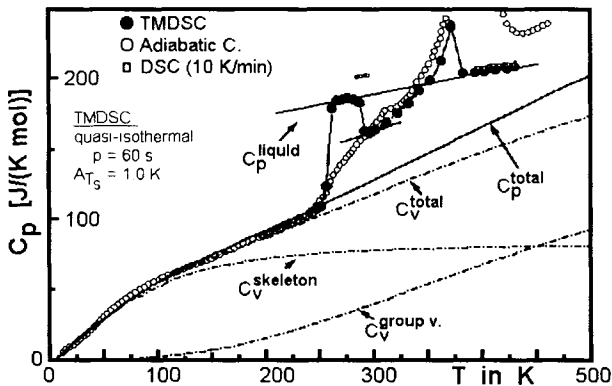


Fig. 32. Heat Capacity of polydioxanone (PPDX).

(●) and semicrystalline samples (○) are obvious. The approach of the amorphous sample to the semicrystalline one signifies cold crystallization and its kinetics can be followed with TMDSC. The approach to the melting region is initially similar, but the reversing C_p (●) shows only little melting, most of the melting is irreversible.

The application of TMDSC to the study of glass transitions is demonstrated in Fig. 33. The instantaneous heat flow $HF(t)$ (proportional to $\Delta T = T_r - T_s$) is shown in the glass transition region for a slowly cooled sample of polystyrene [27]. In this case the modulation remains close to sinusoidal and the reversing heat capacity, shown expanded on the right side of the figure, can be separated from the total heat flow which is close to the standard DSC trace. The reversing C_p is a clean representation of the frequency-dependent heat capacity of the sample. It can be analyzed quantitatively, and then it gives the kinetic parameters of the glass transition. The difference between the total and the reversing heat capacity shows the hysteresis, *i.e.*, the enthalpy relaxation due to the slower cooling of the sample than applied on heating. This enthalpy relaxation characterizes the sample's thermal history and can also be evaluated quantitatively.

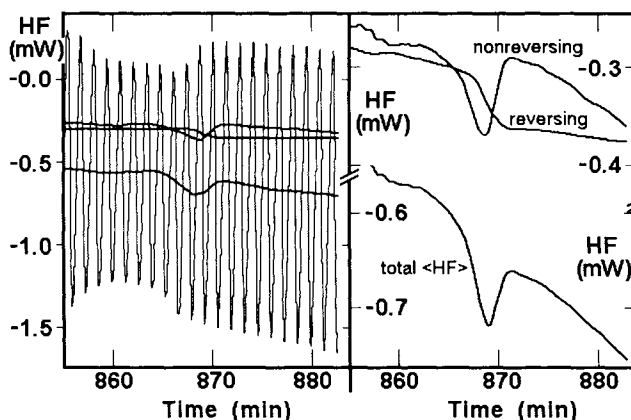


Fig. 33. Direct recording of $HF(t)$ (left) and the derived reversing, nonreversing and total heat flows (right) for polystyrene in the glass transition region [27].

Fig. 34 illustrates for an amorphous poly(ethylene terephthalate) (PET) how the reversing heat capacity can be calculated as a function of modulation frequency after evaluation of the kinetic parameters from a limited number of measurements [28]. The same kinetic parameters can be used in the “hole model of the glass transition” [29]. The number of holes ζ is then the internal variable. The hole model allows the calculation of the kinetics of the change of ζ as a function of time at constant pressure:

$$\frac{d\zeta}{dt} = \frac{1}{\tau} (\zeta^e - \zeta) , \tag{28}$$

with τ representing a relaxation time linked to an activation energy of hole formation derived from the time-dependence of the liquid heat capacity.

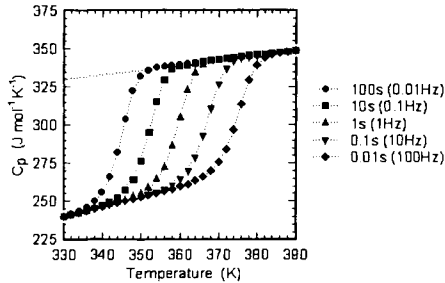
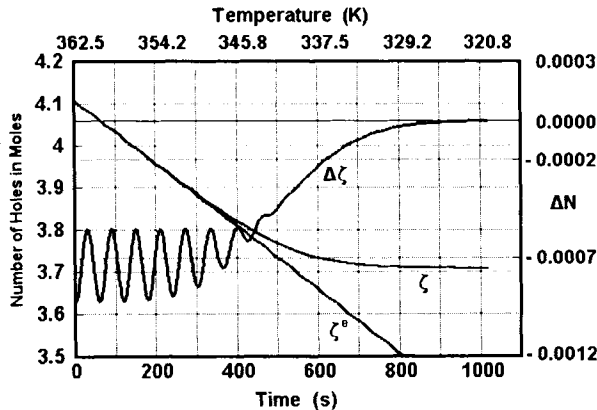


Fig. 34. Reversing C_p of PET at various frequencies. Extrapolated from experiments with p values from 30–90 s [28].

Eq. (28) can be linked to the irreversible thermodynamics. These conditions are, however, not fulfilled for the glass transition. Eq. (28) has, thus, been solved numerically for typical TMDSC parameters using an Arrhenius expression [30], and also, with similar results, using a single-parameter version of the KAHR model commonly applied to analyze DMA data in the glass transition [31].



$\langle q \rangle = -2.5 \text{ K/min}$, $A = 0.1 \text{ K}$, $p = 60 \text{ s}$, $\text{time } 0 - 1020 \text{ s} = 362.5 - 320 \text{ K}$, $\text{fictive temp} = 340.34 \text{ K}$

Fig. 35. Change of number of “holes” on cooling through the glass transition, modeled on experiments with PET [30].

Fig. 35 illustrates the numerical solution of the non-linear Eq. (28). The change

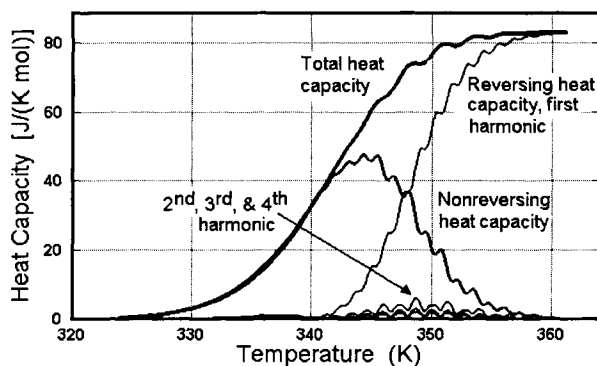


Fig. 36. Computed heat capacities at the glass transition.

of ζ as a function of time and temperature on cooling is shown for PET. The initial number of holes is the equilibrium value at T_o , the starting temperature, ζ^e . The decrease in number of holes and the decrease in oscillation amplitude in the glass transition is clearly shown. With hole energies and equilibrium numbers of holes calculated from the heat capacities of the liquid and glass, the total and reversing apparent heat capacities in the glass transition region can be calculated, as shown in Fig. 36. The calculations were done as with the typical software used for TMDSC, but leaving out smoothing to better assess smaller effects. The remaining oscillations in the total heat capacity could be linked to the interference of the underlying heating rate with the modulation, which leads to a small change in oscillation frequency (Doppler effect). The reversing heat capacity is the first harmonic only. It could be shown by partial solution of the heat-flow equations that small, but not negligible contributions come from the second harmonic, not evaluated. This contribution is due to the exponential change of relaxation time which gives on modulation a larger effect on heating than on cooling. Finally, there is for the same reason also a constant increase of the base-line of the oscillating heat flow. This contribution is, naturally, included in the total heat capacity. Furthermore, the third and fourth harmonic contributions which are mainly due to the change in modulation frequency which cause errors in the analysis. Overall, it seems thus that the glass transition can be studied by TMDSC, but it is necessary to develop more transparent software for the detailed analysis of the kinetics. One needs to know to what degree the temperature control may compensate the frequency shift and have a more detailed temperature profile within the sample. It may not be enough to assume a negligible temperature gradient within the sample. All these special effects are, however, small, and until recently were less than the error limit.

8.2. First-order transitions and chemical reactions

The TMDSC in temperature ranges of absorption or evolution of latent heats is also of interest since it may allow to identify heat capacity changes in the presence of larger heat effects. The early discovery of the practically complete exclusion of irreversible, exponential processes from the reversing heat capacity is a typical example ([4], see also Fig. 32). Under such circumstances the reversing heat capacity can be measured with good precision in the presence of rather large heat effects. Care must be taken, however, that the latent heat effects are not temperature dependent and do not disturb the steady state of the modulated portion of the heat-flow rate. If the latent-heat effect is reversible it will also have a components of frequency ω and the true heat capacity must be extrapolated from outside the transition region.

Besides the crystallization shown in Fig. 32, evaporation, sublimation, and chemical reactions (such as oxidation, pyrolysis, and curing) are examples that make heat capacity measurements by standard DSC impossible. The heat capacity measured under these conditions needs to be analyzed after it has been ascertained that the latent heat does not affect the reversing heat capacity. As long as the measured substance is liquid or solid, the dissipative contribution to the complex heat capacity should be negligible. In case the heat capacities changes due to the change of state, the kinetics of the reaction can be followed by TMDSC. A specially successful example has been the detection of the changes of the glass transition temperature during curing of thermosetting polymers as shown in Fig. 37 [32]. The progress of the exothermic, irreversible cure reaction indicated by the nonreversing heat-flow rate causes the gradual vitrification of the sample, documented by the simultaneously measured reversing specific heat capacity.

The case of a sharp equilibrium transition is illustrated in Fig. 38. The figure represents a plot of the sample (sensor) temperature and the heat-flow rate $HF(t)$ [33]. Clearly, enormous melting peaks are added to the relatively small modulated heat-flow rate due to heat capacity (seen below 5 and above 15 s). As indicated in

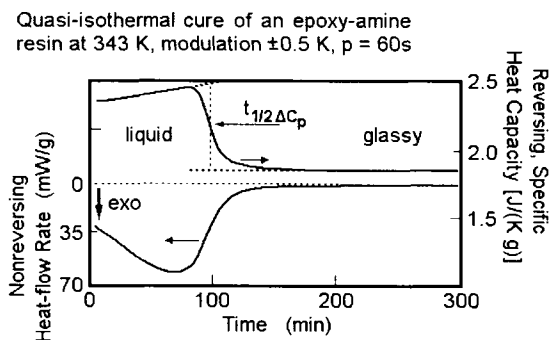


Fig. 37. Change of specific heat capacity during cure [32].

the figure, after the first few melting and crystallization peaks almost full melting and crystallization is possible during each cycle. The quantitative analysis of this trace can only be done in the time domain, *i.e.*, analogous to a standard DSC trace with a wavy baseline. One must assume that the sample temperature is constant between the beginning and peak of melting (at the equilibrium melting temperature

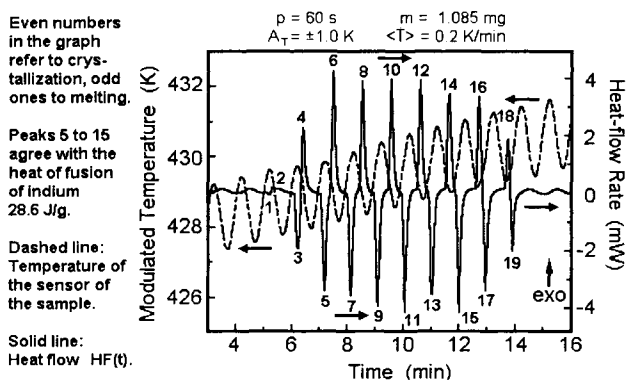


Fig. 38. Heat flow and temperature in TMDSC of indium.

T_m). The sensor temperature is, however, driven to higher temperature by the heat-flow rate required by the modulation program that attempts to reach amplitude A . A modulation of the reference temperature would not change the modulation of the heater temperature and record a more constant sample temperature. A trace as in Fig. 38 is useful for calibration of the TMDSC. Of interest is also the retention of nuclei up to melting peak 5 which avoids supercooling in the immediate vicinity of the melting temperature and permits calibration of the heating as well as cooling cycle. For indium, the melting and crystallization rates are sufficiently fast that there is little chance to study time effects.

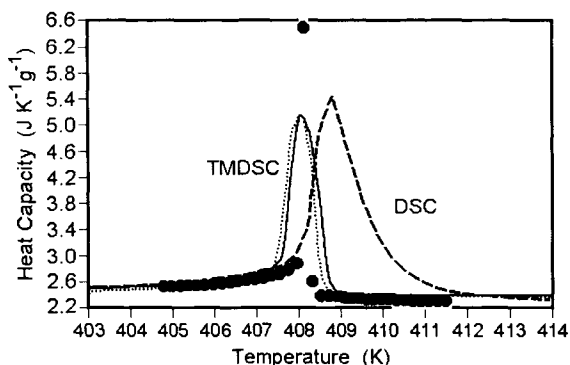


Fig. 39. Comparison of TMDSC on heating and cooling with quasi-isothermal TMDSC (●) and standard DSC (---) for the isotropization transition of 4,4'-azoxyanisole [34].

An example of the reversible isotropization and ordering of a liquid crystal is shown in Fig. 39 [34]. Good agreement is seen for the extrapolated onset temperature of the DSC trace taken at 10 K min^{-1} and the sharp maximum in quasi-isothermal TMDSC ($A = 0.1 \text{ K}$, successive points every 0.2 K). The broadening of the TMDSC trace is caused by the modulation amplitude that was chosen to be 0.5 K and the breadth of the time window used for the data analysis (1.5 p , corresponding to $\langle\beta\rangle = 0.2 \text{ K min}^{-1}$ to 0.3 K for $p = 60 \text{ s}$). The main problem is, however, that the areas for the enthalpies of the transitions do not agree at all. As seen already in the case of indium in the transition region of Fig. 38, the response to modulation is deviating from sinusoidal, *i.e.*, the reversing heat capacity is not assessing the transition fully as seen in Fig. 40.

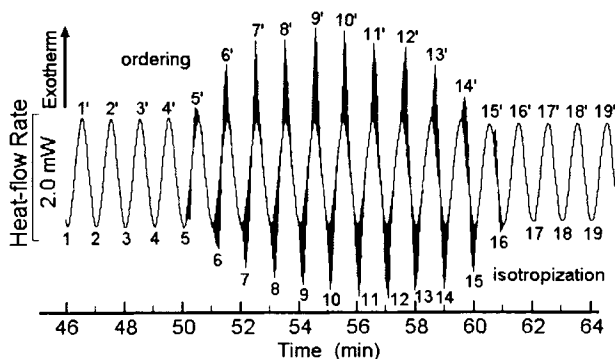


Fig. 40. Heat flow in the time domain on TMDSC of a liquid crystal similar as in Fig. 39 ($A = 1 \text{ K}$, $p = 60 \text{ s}$, $\langle\beta\rangle = +0.1 \text{ K}$).

The change in behavior, when going to a liquid-crystalline polymer is shown in Fig. 41 for a main-chain, macromolecule that was synthesized by coupling 4,4'-

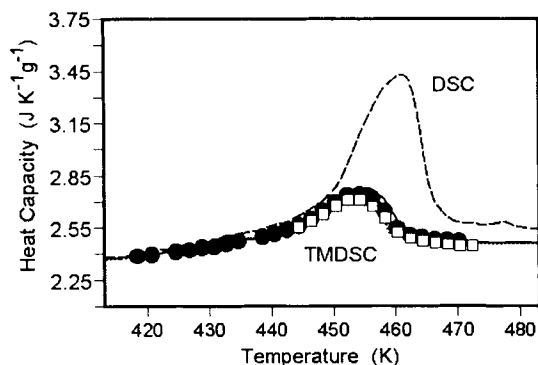


Fig. 41. Isotropization of DHMS-7,9 by DSC (10 K min^{-1}), TMDSC ($A = 0.5 \text{ K}$, $\langle\beta\rangle = \pm 0.2 \text{ K}$, $p = 60 \text{ s}$) and quasi-isothermal TMDSC (\bullet) at ($A = 0.1 \text{ K}$, 15 and 30 min per run).

dihydroxy- α -methylstilbene (DHMS) with a 1:1 molar mixture of 1,7-dibromoheptane and 1,9-dibromononane (DHMS-7,9). Now quasi-isothermal and standard TMDSC agree because of the much broader transition, but the areas are still not related to the heat of transition.

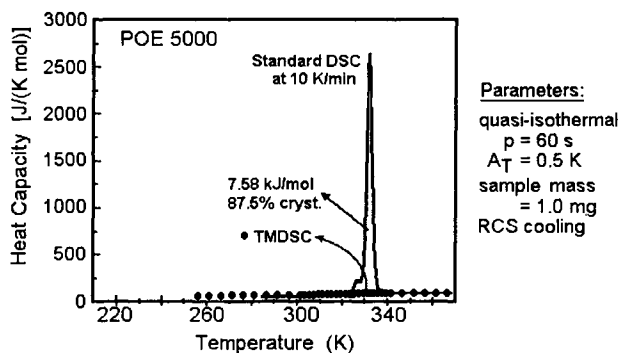


Fig. 42. Melting of POE by DSC (10 K min^{-1}) and quasi-isothermal TMDSC (\circ) ($A = 0.5 \text{ K}$, $p = 60 \text{ s}$, 20 min) [36].

Turning to the melting transition of polymers, it is well known that such materials do not melt and crystallize reversibly [35]. The irreversible nature is illustrated in Fig. 42 with a well-crystallized poly(oxyethylene), POE, of a molar mass of 4540 Da. The quasi-isothermal TMDSC shows practically no effect of melting, while the standard DSC indicates the melting peak.

The broad melting range that is common for many macromolecules may be analyzed in the same fashion, as shown in Fig. 42 with the assurance that well grown polymer crystals do not contribute to the reversing heat capacity of quasi-isothermal TMDSC. The quasi-isothermal mode is preferred in these experiments in order to assure the attainment of steady state after the initial increase of temperature which causes the corresponding irreversible melting.

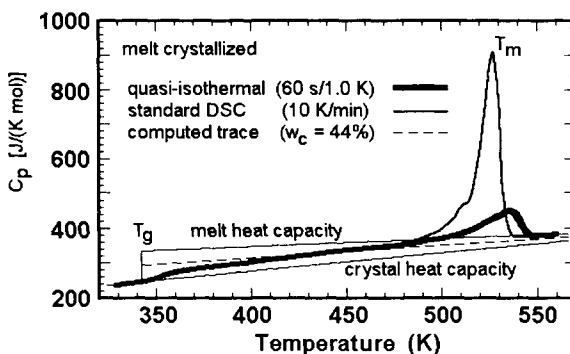


Fig. 43. Melting of PET by standard DSC (10 K min^{-1}) and quasi-isothermal TMDSC (\blacksquare) ($A = 1 \text{ K}$, $p = 60 \text{ s}$) [37].

A surprising result is the curve of Fig. 43 taken for poly(ethylene terephthalate) (PET). It shows a rather broad increase in the reversing heat capacity in the melting range. The maximum level attained is much lower than found in a standard DSC trace which reveals the full heat of fusion with a peak height of about $900 \text{ J K}^{-1} \text{ mol}^{-1}$. Less than 10% of the heat of fusion is found underneath the endothermic, reversing heat capacity. A detailed analysis suggests that a local melting and crystallization equilibrium exists on a molecular scale in these poorly crystallized materials [37]. This local equilibrium changes with time and the reversing heat capacity drifts over many hours towards the expected heat capacity level of the semicrystalline material, but without ever reaching it, as shown in Fig. 44 [38].

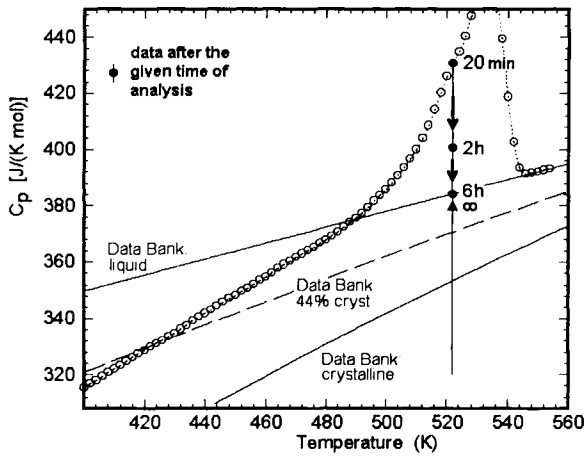


Fig. 44. Quasi-isothermal TMDSC of PET as in Fig. 43, but extension of the measuring time as shown in the Fig.. The value for time ∞ was extrapolated exponentially [38].

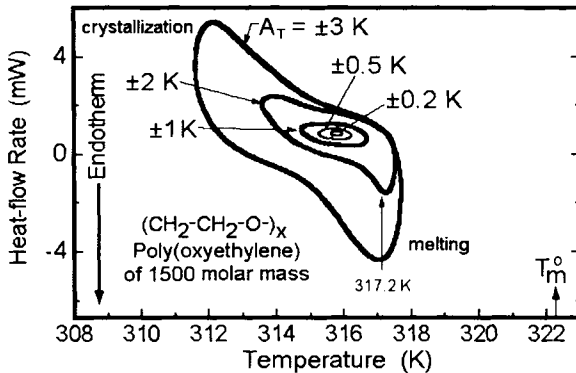


Fig. 45. Lissajous figure of PEO in the melting region showing a some poorly crystallized low molar mass material melting and crystallize at sufficiently large modulation amplitude [39].

Additional observations were made on lower molar mass POE (1500 Da), shown in Fig. 45 [39]. In this case the range of metastability of the polymer melt could be bridged for a small fraction of the polymer by temperature modulation with a sufficiently large amplitude. The Lissajous figures reveals the well-separated crystallization and melting domains. Again, the long-time experiment indicates that the produced crystal fractions are not constant with time. In this case they increase with time, probably due to diffusion limited access to crystallization sites.

These experiments with TMDSC in regions of latent heat evolution and absorption show a rich field of study of irreversible effects that has barely been touched. The examples indicate that as soon as larger amounts of latent heat are involved, great care must be taken to assess the steady state and determine the limits of sample mass and modulation parameters for quantitative experiments. In most cases the analysis of heats of transition is best done in the time domain. For reversible heats of transition, the heat flow is usually not sinusoidal, leading to limited information with analyses using the first harmonic only. In case the heat capacity of the material in the transition region can be assessed, the same methods as described in Sects. 8 and 8.1 can be used. The benefit of a complex heat capacity seems limited, although one can imagine that transitions with low latent heats and a suitably simple transition rate may fall into the range of validity. An extensive update of “Reversible Crystallization and the Rigid Amorphous Phase in Semicrystalline Macromolecules” is being submitted for publication and extends the literature to the end of the year 2001 [40].

9. CONCLUDING REMARKS

Heat capacity is one of the few macroscopic quantities that is closely linked to the microscopic, molecular motion. By establishing the baseline of vibrations-only heat capacities from the analysis of solids at low temperatures, the changes in the types of motion can be found and with the help of the DSC, fast quantitative analyses can be made. Based on the complete accumulation of data it is possible to predict the heat capacities before samples become available. Calorimetry, and the new temperature-modulated calorimetry, have enabled a much more detailed analysis of polymeric materials. The adiabatic calorimetry still dominates in the area of low-temperature measurement of heat capacities and is vital for derivation of the Tarasov parameters for the skeletal contribution to the heat capacity. Standard DSC has become a valuable tool in extending measurements from 150 to 1000 K. It also is the basic tool for measurements of heats of transitions and quick characterization of polymers. Once this characterization is complete, TMDSC with its slower underlying heating rate or step-wise heating can be applied for a detailed check of overlapping effects with different degrees of reversibility and long-time changes in reversing processes, for the study of the quantitative thermal properties

in the transition regions, and links between morphology and transition behavior. Any high-quality thermal analysis laboratory should have a TMDSC capability. Central to the quantitative interpretation is the ATHAS for identifying the vibration-only heat capacity and estimating the liquid heat capacity so that the region between glass transition and melting can be assessed quantitatively.

ACKNOWLEDGMENTS

This work was supported by the Division of Materials Research, National Science Foundation, Polymers Program, Grant # DMR-9703692 and the Division of Materials Sciences and Engineering, Office of Basic Energy Sciences, U.S. Department of Energy at Oak Ridge National Laboratory, managed and operated by UT-Battelle, LLC, for the U.S. Department of Energy, under contract number DOE-AC05-00OR22725.

REFERENCES

1. B. Wunderlich, "The Athas Data Base on Heat Capacities of Polymers." *Pure Applied Chem.*, 67 (1995) 1919; U. Gaur, H.-C. Shu, A. Mehta, S.-F. Lau, B. B. Wunderlich, M. Varma-Nair, and B. Wunderlich, *J. Phys. Chem. Ref. Data*, 10 (1981) 89, 119, 1001, 1051; 11 (1982) 313, 1065; 12 (1983) 29, 65, 91; and 20 (1991) 349; for updates of publications and the data bank check: <http://web.utk.edu/~athas>.
2. W. Nernst, *Ann. Physik*, 36 (1911) 395.
3. B. Wunderlich, "Thermal Analysis." Academic Press, Boston, 1990.
4. M. Reading, D. Elliot, and V. L. Hill, *J. Thermal Anal.*, 40 (1993) 949; P. S. Gill, S. R. Sauerbrunn and M. Reading, *J. Thermal Anal.*, 40 (1993) 931; M. Reading, *Trends in Polymer Sci.*, 8 (1993) 248.
5. J. D. Menczel and T. M. Leslie, *Thermochim. Acta*, 166 (1990) 309; G. W. H. Höhne, H. K. Cammenga, W. Eysel, E. Gmelin and W. Hemminger, *Thermochim. Acta*, 160 (1990) 1.
6. A. Boller, Y. Jin and B. Wunderlich, *J. Thermal Analysis* 42 (1994) 307.
7. R. Pan, M. Varma, and B. Wunderlich, *J. Thermal Anal.*, 35 (1989) 955.
8. A. Einstein, *Ann. Physik*, 22 (1907) 180, 800.
9. P. Debye, *Ann. Phys*, 39 (1912) 789.
10. E. Schrödinger, in H. Geiger, and K. Scheel, eds., "Handbuch der Physik." Springer Verlag, Berlin, Vol. 10, p.275, 1926.
11. B. Wunderlich and H. Baur, *Heat Capacities of Linear High Polymers* (transl. into Russian by Yu. Godovsky, Publishing House "Mir", Moscow, 1972). *Fortschr. Hochpolymeren Forsch. (Adv. Polymer Sci.)*, 7 (1970) 151.
12. B. Wunderlich and Y. Jin, *Thermochim. Acta*, 226 (1993) 169.
13. U. Gaur, G. Pultz, H. Wiedemeier, and B. Wunderlich, *J. Thermal Anal.*, 21 (1981) 309.
14. U. Gaur and B. Wunderlich, *J. Phys. Chem., Ref. Data*, 10, (1981) 119.
15. B. Wunderlich, "Macromolecular Physics, Vol. 1, Crystal Structure, Morphology, Defects." Academic Press, New York, London, 1973.
16. U. Gaur, M.-Y. Cao, R. Pan and B. Wunderlich, *J. Thermal Anal.*, 31 (1986) 421; R. Pan,

- M.-Y. Cao and B. Wunderlich, *J. Thermal Anal.*, 31 (1986) 1319.
17. J. Barnes and B. Fanconi, *J. Phys. Chem. Ref. Data*, 7 (1978) 309.
 18. V. V. Tarasov, *Zh. Fiz. Khim.*, 24 (1950) 111.
 19. Yu. V. Cheban, S. F. Lau and B. Wunderlich, *Colloid Polymer Sci.*, 260 (1982) 9; F. Lau and B. Wunderlich, *J. Thermal Anal.*, 28 (1983) 59; M. Pyda, M. Bartkowiak, and B. Wunderlich, *J. Thermal Analysis and Calorimetry*, 52 (1998) 631; G. Zhang and B. Wunderlich, *J. Thermal Analysis*, 47 (1996) 899.
 20. J. Grebowicz, H. Suzuki, and B. Wunderlich, *Polymer*, 26 (1985) 561.
 21. S.-F. Lau, H. Suzuki, and B. Wunderlich, *J. Polymer Sci., Polymer Phys. Ed.*, 22 (1984) 379.
 22. M.-Y. Cao, M. Varma-Nair, and B. Wunderlich, *Polymers for Advanced Technology*, 1 (1990) 151.
 23. B. G. Sumpter, D. W. Noid, G. L. Liang and B. Wunderlich, "Atomistic Dynamics of Macromolecular Crystals." *Adv. Polymer Sci.*, 116 (1994) 27.
 24. K. Roles and B. Wunderlich, *Biopolymers*, 31 (1991) 477; K. A. Roles, A. Xenopoulos and B. Wunderlich, *Biopolymers*, 33 (1993) 753.
 25. L. A. Wood and N. Bekkedahl, *Polymer Letters*, 5 (1967) 169.
 26. K. Ishikiriyama, M. Pyda, G. Zhang, T. Forschner, J. Grebowicz, and B. Wunderlich, *J. Macromol. Sci.-Phys.*, B37 (1997) 27.
 27. A. Boller, C. Schick, and B. Wunderlich, *Thermochim. Acta*, 266 (1995) 97.
 28. B. Wunderlich and I. Okazaki, *J. Thermal Analysis*, 49 (1997) 57.
 29. N. Hirai and H. Eyring, *J. Appl. Phys.*, 29 (1958) 810; *J. Polymer Sci.* 37 (1959) 51.
 30. B. Wunderlich, A. Boller, I Okazaki, and S. Kreitmeier, *J. Thermal Analysis*, 47 (1996) 1013.
 31. J. M. Hutchinson and S. Montserrat, *Thermochim. Acta*, 286 (1996) 263.
 32. G. Van Assche, A. Van Hemelrijck, H. Rahier, and B. Van Mele, *Thermochim. Acta*, 268 (1995) 121; 286 (1996) 209.
 33. K. Ishikiriyama, A. Boller, and B. Wunderlich, *J. Thermal Analysis*, 50 (1997) 547.
 34. W. Chen, M. Dadmun, G. Zhang, A. Boller, and B. Wunderlich, *Thermochim. Acta.*, 324 (1998) 87.
 35. B. Wunderlich, "Macromolecular Physics, Vol. 3, Crystal Melting." Academic Press, New York, London, 1980.
 36. K. Ishikiriyama and B. Wunderlich, *Macromolecules*, 30 (1997) 4126.
 37. K. Ishikiriyama and B. Wunderlich, *J. Polymer Sci., Part B, Polymer Phys.*, 35 (1997) 1877.
 38. I. Okazaki and B. Wunderlich, *Macromolecules*, 30 (1997) 1758.
 39. I. Okazaki and B. Wunderlich, *Macromol. Chem. Phys. Rapid Comm.*, 18 (1997) 313.
 40. B. Wunderlich, *Macromolecular Science*, to be submitted for publication in 2002.

This Page Intentionally Left Blank

Chapter 2

The glass transition: its measurement and underlying physics

Gregory B. McKenna and Sindee L. Simon

Department of Chemical Engineering, Texas Tech University, Lubbock, TX 79409-3121, *greg.mckenna@coe.ttu.edu* and *sindee.simon@coe.ttu.edu*

The glass transition is an important phenomenon in the practical world, where it determines the use temperature and processing temperature for many materials, particularly polymers. In addition, the underlying physics of glassy materials, while extensively studied, is still rich in phenomena that are not fully understood and still lead to conflict within the scientific community. Here, we describe both the thermodynamic and kinetic aspects of the glass transition event and discuss some of the underlying physics of glass forming materials as well as how we currently describe the phenomenology. We then, briefly, discuss some of the techniques used to measure the glass transition temperature. Our review ends with a brief discussion of the effects of structural recovery on viscoelastic properties and the engineering properties of polymers--a process that has come to be known as physical aging.

1. INTRODUCTION

The glass transition temperature T_g is a very important parameter that is used to characterize, and often specify, a material. Yet, if we were to walk into a typical thermal analysis or polymer characterization laboratory today, there would be a range of instruments available to 'measure' the glass transition temperature T_g of a given material and, were we to compare the measurements from the different methods, we would likely find significant differences [1]--perhaps by as much as 10°C to 15°C. Are such differences important? The simplistic answer is sometimes yes and sometimes no. In fact, the range of differences for such apparently 'simple' measurements is a reflection of the great complexity and richness of the glass transition phenomenon itself. Such measurements can be more profitably used if one better understands the physics underlying the glass transition and how the physics is reflected in the measurements themselves. It is the purpose

of the current chapter to survey the physics of glassy and glass forming materials to provide the reader with a better understanding of the phenomenology of glasses and how this can affect measurements of the glass transition.

It is important to realize that the physics of glasses and glass formation is not completely understood. In fact, there has been much [2] made of a recent comment by Nobel Laureate P.W. Anderson [3] in *Science* that “The deepest and most interesting unsolved problem in solid state theory is probably the theory of the nature of glass and the glass transition.” But this should not discourage the reader. We do have a great deal of knowledge about the glass transition event--and its richness is fascinating. Furthermore, by examining this richness and incorporating it into how we think about our measurements on glasses, we will be able to make better interpretations of our data and, conceivably, improve our measurements and the processes that we use in creating products from glass-forming systems.

The chapter is broken into sections that consider first the thermodynamic and kinetic phenomena associated with the glass transition: we describe the thermodynamic surface of glass-formers and the underlying kinetic phenomena of glasses that give rise to a path dependence of the thermodynamic surface. We then consider the common microscopic models related to the glass transition: free volume and configurational entropy. These set the stage to examine how we measure T_g and what the measurements mean. Finally, we devote a section to the so-called physical aging process, which tells us how the ‘rich phenomenology’ of the glass transition itself affects material performance. Hopefully, the reader will come away with a sense of the beauty of glass formation as a natural wonder in addition to a better understanding of how to apply this appreciation to the interpretation of measurements and evaluation of material performance.

2. THE APPARENT THERMODYNAMIC BEHAVIOR

2.1. Some thermodynamic definitions

Before defining the glass transition we go back to some basic concepts from thermodynamics and remind the reader of the definitions of thermodynamic transitions. According to Ehrenfest [4], a *first-order* phase transition is defined for a free energy function which is continuous in any given state variable (*e.g.*, pressure P , temperature T , volume V), but is discontinuous in the first partial derivatives with respect to the relevant state variables. Thus, if we speak of the Gibbs Free energy, then at the transition G is continuous and $[\partial G/\partial T]_P$ and $[\partial G/\partial P]_T$ are discontinuous. At a typical first-order transition point, such as fusion or vaporization, there is a discontinuity [5] in entropy S , volume V and enthalpy H :

$$\left[\frac{\partial G}{\partial T} \right]_P = -S \quad (1)$$

$$\left[\frac{\partial G}{\partial P} \right]_T = V \quad (2)$$

$$\left[\frac{\partial(G/T)}{\partial(1/T)} \right]_P = H \quad (3)$$

In a similar way, we can define [5-7] a *second-order transition* through the observation of discontinuity in the second partial derivatives of the free energy function with respect to the relevant state variables. In this case both the free energy function and its first partial derivatives would be continuous functions of the state variables. Thus, there is no discontinuity in S , V or H at the transition but there is in the heat capacity C_p , the compressibility κ , and the coefficient of thermal expansion α :

$$-\left[\frac{\partial^2 G}{\partial T^2} \right]_P = \left[\frac{\partial S}{\partial T} \right]_P = \frac{C_p}{T} \quad (4)$$

$$\left[\frac{\partial^2 G}{\partial P^2} \right]_T = \left[\frac{\partial V}{\partial P} \right]_T = -\kappa V \quad (5)$$

$$\frac{\partial}{\partial T} \left[\left[\frac{\partial(G/T)}{\partial(1/T)} \right]_P \right] = \left[\frac{\partial H}{\partial T} \right]_P = C_p \quad (6)$$

$$\left[\frac{\partial}{\partial T} \left[\frac{\partial G}{\partial P} \right]_T \right]_P = \left[\frac{\partial V}{\partial T} \right]_P = \alpha V \quad (7)$$

The glass transition is often considered to be a second-order phase transition. Fig. 1 presents a schematic of the differences in thermodynamic parameters as functions of temperature for first and second-order transitions and for the glass transition [8]. It is important conceptually to understand the differences among these thermodynamic transitions. However, there is still disagreement as to whether the glass transition is purely kinetic or if it is a kinetic manifestation of an underlying thermodynamic transition. What is clear is that the measurements we make in the laboratory are influenced by the kinetics which are manifested as a *path*

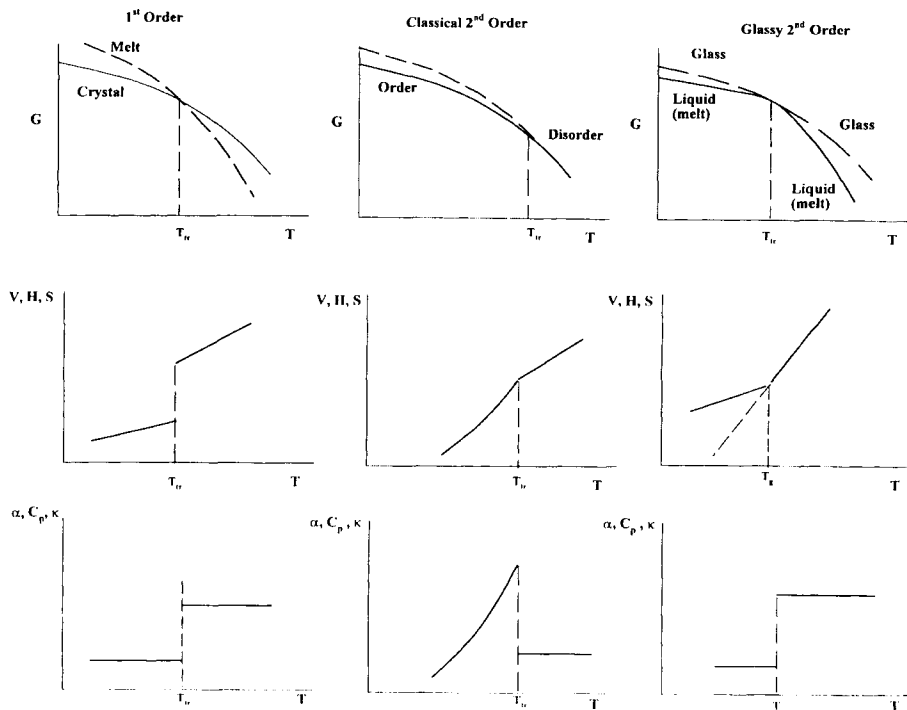


Fig.1. Schematic representation of the thermodynamic responses relevant to first and second-order transitions in the Ehrenfest sense and the glass transition.

dependence of the measured T_g . We now turn to the various aspects of the kinetics of the glass transition event and how these might influence measurements related to the glass transition temperature.

2.2. Time or rate effects

There is a now classic figure of the one atmosphere volume-temperature (V - T) surface of a polymer glass obtained by A. J. Kovacs [9] that illustrates one of the difficulties of dealing with the glass transition. The data were obtained in simple, but time-consuming, experiments. The sample was equilibrated volumetrically at a high temperature. Then the temperature was stepped to a lower temperature and the volume was measured at a specified time after the temperature change. The procedure was repeated for successively lower temperatures using the same waiting time (isochronal condition). What we show in Fig. 2 is that the appearance of the glass transition depends upon the time at which the measurement was taken. Thus, if 0.02 h was used as the “step” time, the point, call it the glass

transition temperature T_g at which the V - T behavior of the material begins to fall off of the equilibrium liquid line is higher than that obtained when the time for the step is 100 h. In Fig. 2 we see, in fact, that the apparent transition from liquid-like behavior to glass-like behavior changes by approximately 10°C for a time difference of about three logarithmic decades. If one considers these data as equivalent to those taken at different cooling rates, then it is clear that the apparent glass transition temperature decreases as the cooling rate decreases. This is illustrative of one aspect of the behavior of glass-forming systems: the volume-temperature behavior (and the apparent transition temperature T_g) depends on the rate (or time scale) of the measurement. Here we looked at the cooling rate. It is well known that the heating rate has similar effects, that are complicated by additional aspects of the kinetics of glassy behavior and are discussed in Section 3. At this point, though, we can see that the apparent V - T surface in simple cooling experiments depends upon how fast we make the measurement.

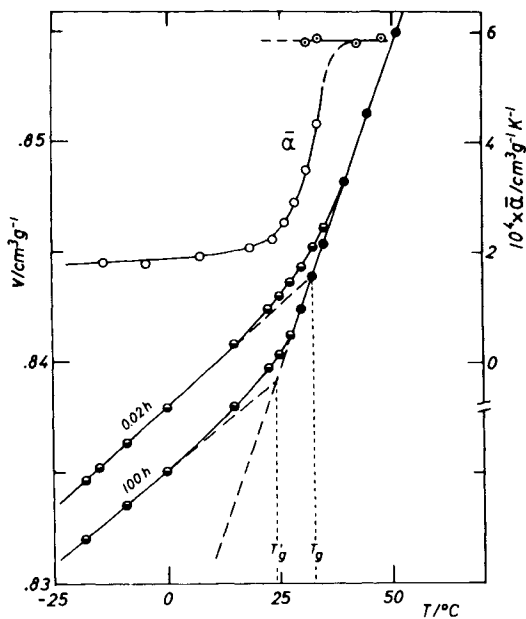


Fig. 2. Volume vs. temperature plot for poly(vinyl acetate) showing effects of experimental time on the apparent glass transition. Also shown is the change in the coefficient of thermal expansion at the glass transition. (After Reference 9. Figure courtesy of A.J. Kovacs).

2.3. Path dependence of the PVT Surface

In addition to rate effects, the PVT surface for a glass depends upon the path of glass formation. This is readily illustrated by reviewing the very elegant set of P - V - T experiments performed by McKinney and Goldstein [10] in the 1970's on a poly(vinyl acetate) (PVAc) glass forming system. In their experiments the PVT surface of the PVAc was measured in two different ways. In what they referred to as a constant formation history glass, the sample was prepared at a single pressure in the liquid state and cooled at a fixed rate to far below the glass transition. Changing pressure and temperature in the glassy state and measuring the volume resulted in data such as those depicted in Fig. 3. These data show, first, that the glass transition is pressure dependent. However, more information is obtained when we compare the data for the constant formation history glass with those for what McKinney and Goldstein referred to as a variable formation history glass--what we would, today, refer to as isobaric glass formation. For the variable history glasses, the PVT surface was created by running experiments in which the liquid was pressurized above the glass transition temperature and cooled at the pressure of interest at a constant rate. The volume-temperature behavior was recorded for that particular pressure. Then the sample was heated to above the glass transition, brought to another pressure and another isobaric V - T curve was obtained upon cooling. The results for this procedure are shown in Fig. 4. Again we note that the T_g is pressure dependent. However, upon comparison with Fig. 3 we see differences in the PVT surfaces for the glassy state. Of course, in the equilibrium liquid state the surfaces are the same. For the constant formation history glass, the

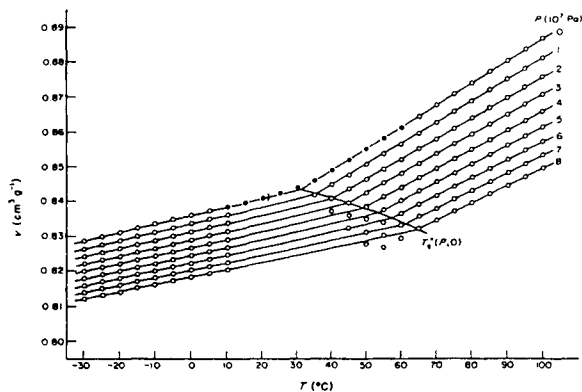


Fig. 3. Volume-temperature plot for poly(vinyl acetate) at different pressures for a "constant formation history" glass. See text for discussion. (After McKinney and Goldstein, Reference 10).

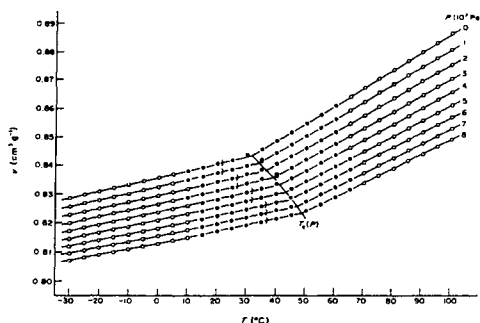


Fig. 4. Volume-temperature plot for poly(vinyl acetate) for isobaric glass formation. See text for discussion. (After McKinney and Goldstein, Reference 10).

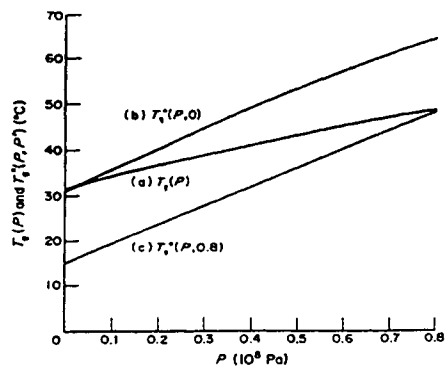


Fig. 5. Pressure dependence of the glass transition of poly(vinyl acetate) for different glass formation histories. a) isobaric glass formation; b) "constant formation history" at atmospheric pressure; c) "constant formation history" at 0.8×10^8 Pa. See text for discussion. (After McKinney and Goldstein, Reference 10).

specific volumes in the glassy state are generally greater than for the isobaric glasses at the same pressure. Perhaps more importantly, one observes that the pressure dependence of the glass transition temperature is greater for the constant formation history glass than for the isobaric glass. This is illustrated in Fig. 5 where the center curve is for the isobaric glass, the upper curve is for a constant formation history of one atmosphere (0.1 MPa) and the lower curve is for a constant formation history glass formed at 800 atmospheres (80 MPa). The difference in the pressure dependence of the glass transition temperature dT_g/dP values for the two types of formation history is nearly a factor of two. What is happening is that the bulk modulus of the glass is greater than that of the liquid. Hence when the glass is pressurized its specific volume changes less than it would in the melt. This leads to a difference in the glassy state PVT surface between the two formation histories and a consequent difference in the glass transition temperature. The T_g differs because it is estimated from the intersection of the equilibrium surface with two different glassy surfaces. Another important point here is that the glass transition is itself pressure dependent--an important point to consider in polymer processing where high pressures are often used.

2.4. Isobaric (constant pressure) glass formation vs isochoric (constant volume) glass formation

In the previous section we showed that the PVT surface of the glass can be path dependent and that the magnitude of the glass transition and its pressure

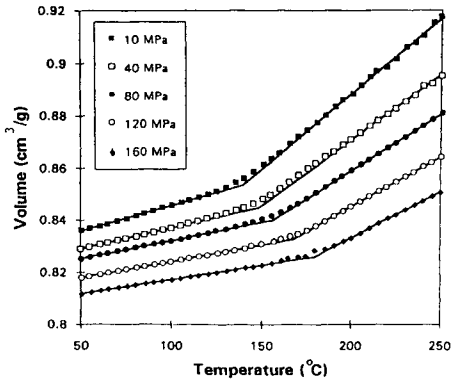


Fig. 6. Volume-temperature plot for isobaric glass formation of polycarbonate at pressures shown. (After Colucci, *et al*, Reference 11).

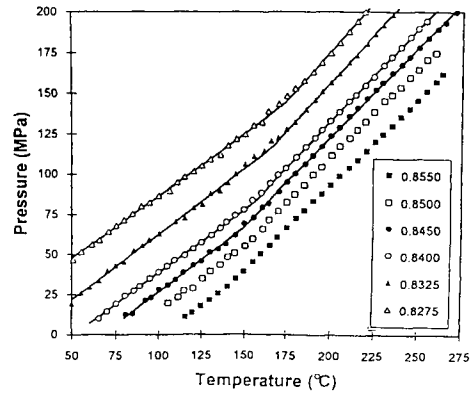


Fig. 7. Pressure-temperature plot for isochoric glass formation of polycarbonate at volumes shown. (After Colucci, *et al*, Reference 11).

dependence were functions of whether the glassy surface was obtained isobarically (at constant pressure) by pressurizing the liquid and cooling from above the T_g or if it was obtained for a glass formed at a single formation pressure with the pressure being varied in the glassy state. It seems natural to ask how the glass transition or glass itself might change for other formation histories. In a recent study, Colucci, *et al* [11] performed experiments in which a polycarbonate material was pressurized in the liquid state and then the liquid volume was maintained constant (isochoric) by varying the pressure while temperature was reduced at a constant rate. The results were compared with those obtained for the sample cooled at the same rate but at constant pressure, rather than constant volume. Fig. 6 and Fig. 7 show the results for both the isobaric and the isochoric glass formation paths. Examination of the two figures shows that the glass transition is much more abrupt for the isobaric path than for the isochoric path. Also, the glass formed isochorically has a smaller volume than that formed isobarically. The glass formation points are the same within the experimental uncertainties. Fig. 8 shows a 3-D representation of the isochoric and isobaric PVT surfaces. It is clear that the glass formed isochorically is more dense than that formed isobarically. As found for the two pressure histories described above, then, the glassy state thermodynamic parameters depend on whether one creates the glass via a constant pressure history or a constant volume history. However, in this case, it does seem that the glass formation points are the same. As shown in Table 1 the isochoric glass has a greater compressibility β and greater coefficient of thermal expansion α than does the isobarically formed glass. Yet the glass formation points are the same. In addition, as discussed later, the material properties depend on the density of the glass and this implies that performance as well as measurement of glassy properties can depend on the glass formation path or history.

In summary, the thermodynamic properties of materials in the glassy state are path dependent. In the next section we examine some aspects of glassy kinetics that provide a potential means of modeling the path dependence of the thermodynamic properties of materials in the glassy state.

Table 1

Comparison of thermodynamic parameters for polycarbonate. P_{gf} is the glass formation pressure, V_{gf} is the glass formation volume, T_{gf} is the glass formation temperature, α_r and α_g are the coefficients of thermal expansion (volumetric) in the rubbery and glassy states, respectively. β_r and β_g are the compressibilities in the rubbery and glassy states respectively. The data are from Colucci, *et al* [11].

P_{gf} (MPa)	V_{gf} (cm ³ /g)	T_{gf} (°C)	$\alpha_r \times 10^4$ (K ⁻¹)	$\alpha_g \times 10^4$ (K ⁻¹)	$\beta_r \times 10^4$ (MPa ⁻¹)	$\beta_g \times 10^4$ (MPa ⁻¹)
80	0.8400	155	5.54±0.18	Isobaric: 1.70±0.08	4.11±0.25	Isobaric: 2.49±0.08
				Isochoric: 2.70±0.08		Isochoric: 3.61±0.10
120	0.8325	167	4.40 ±0.05	Isobaric: 1.47±0.10	4.12±0.04	Isobaric: 2.54±0.15
				Isochoric: 2.52±0.13		Isochoric: 3.71±0.13

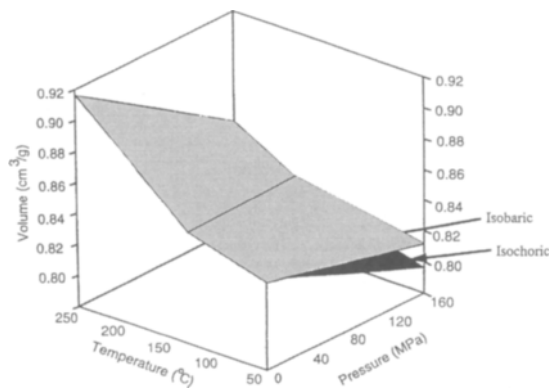


Fig. 8. Three dimensional representation of the PVT surfaces for isochoric and isobaric glass formation of polycarbonate. (After Colucci, *et al*, Reference 11).

3. KINETICS of GLASS FORMATION

3.1. Preliminary comments

The kinetic response of a glassy material is generally referred to as structural recovery [6,9,12-14]. Ready illustrations are given by recalling Fig. 2 or looking at the schematic in Fig. 9. When one cools from the liquid state into the glass to some temperature below T_g (say temperature A in Fig. 9) then the inherently non-equilibrium state of the glass spontaneously evolves towards equilibrium (as indicated by the arrow in the figure). The time evolution of the glassy structure after the temperature is changed from near T_g to below it in a *down-jump* is shown in Fig. 10 from classic data by Kovacs[9] for volume recovery experiments. In the figure, the volume departure from equilibrium is defined as $\delta = (v - v_\infty)/v_\infty$ where v is the specific volume and v_∞ is its value in equilibrium (infinite time). The family of curves obtained in such *down-jump* experiments to different temperatures is referred to as the family of *intrinsic isotherms*. As seen in Fig. 10, the rate of volume recovery (for the intrinsic isotherms) is a strong function of temperature, *i.e.*, the time to reach equilibrium ($\delta = 0$) increases as the temperature decreases.

Another important definition in studying glasses was initially developed by Tool [15,16] and is used frequently in the description of glassy kinetics, as discussed subsequently. This is the fictive temperature T_f . Referring again to Fig. 9, T_f is defined as the point of intersection of a line extrapolated from a point (B) in volume (or enthalpy) space to the equilibrium (liquid) line along a line parallel to the glassy line. Hence, along the glass line in Fig. 9, $T_f = T_g$ and along the equilibrium line, $T_f = T$. T_f and δ both define the state or structure of the glass and

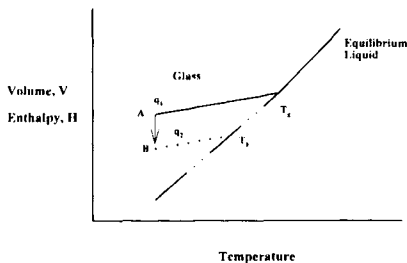


Fig. 9. Schematic of enthalpy or volume vs temperature for glass forming materials. See text for discussion.

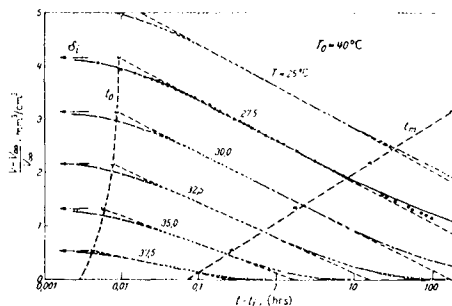


Fig. 10. Intrinsic isotherms for poly(vinyl acetate) in down-jump experiments from $T_0 = 40^\circ\text{C}$ to temperatures indicated in figure. (Data from Reference 9. Figure courtesy of A. J. Kovacs).

they are related through the differences in the liquid and glassy slopes of Fig. 9. However, they have subtly different meanings when one thinks of the structural state of the glass. However, the formalisms developed to describe the kinetics of glasses using one or the other definition are mathematically equivalent and give the same results.

The volume and enthalpy responses of glasses are important from a practical view because the changing ‘thermodynamic state’ of the non-equilibrium glass impacts the mechanical response of the polymer in a process referred to as physical aging [17,18]. In this instance, it is observed that after a down-jump from above T_g to below it, the mechanical properties evolve in such a way that, for example, the yield strength, relaxation modulus and material brittleness increase. In addition, the thermal properties are affected by the structural recovery and the nonlinearities of structural recovery can even have an influence on the way in which one should interpret thermal measurements [19,20]. Hence, an understanding of structural recovery and physical aging phenomena is important [21]. In this section we review the phenomenology of structural recovery and the equations used to describe, not only the cooling rate effects on T_g and the intrinsic isotherms, but also the asymmetry of approach and memory (or cross-over) effects. In addition, we show how the equations successfully describe non-isothermal behaviors in thermal measurements typical of a classical differential scanning calorimeter. The importance of these behaviors to the measurement of T_g is discussed in a subsequent section.

3.2. Phenomenology of structural recovery

As noted above, there is a significant impact of thermal history, even simple thermal histories, on the measured properties of glass forming materials, including polymers. While the rate effects on the glass transition temperature and the observation that the volume evolves after a down-jump in temperature (*intrinsic isotherms*, Fig. 10) are well documented, the behavior of glasses is more complex and richer than evidenced in these experiments. The general richness of behaviors is seen in the classic volume dilatometry experiments performed by Kovacs [9] on a poly(vinyl acetate) polymer. His findings are widely recognized as general for both polymers and other glass forming materials [22]. Here we discuss two types of experiment: *asymmetry of approach* and *memory (cross-over)* experiments. From these we define some ‘essential ingredients’ for the description of the general phenomenology of the kinetics of glasses and write the equations that were developed through a series of advances beginning in the 1940's. The strengths and limitations of the equations are discussed and one practical example of the power of the models is presented for differential scanning calorimetry (DSC) of a polymer glass.

3.2.1. The asymmetry of approach experiment

The asymmetry of approach experiment is important to understand because it demonstrates the highly nonlinear nature of structural recovery in glass forming materials. While we describe it in terms of the volume recovery here, we note that the same sort of response would be seen if one were to measure the enthalpy recovery. The experiment involves equilibrating the glass at temperatures above or below the final temperature of measurement and then performing *down-jump* and *up-jump* experiments to the same final temperature. If the magnitude of the temperature-jump is the same for both conditions, a linear response would show that the up-jump is the mirror image of the down-jump. On the other hand, as shown in Fig. 11, the Kovacs results for experiments with 5°C T -jumps demonstrate that the responses are far from mirror images and, in fact, the up-jump response is observed to begin at very large volume departures δ from equilibrium and exhibits an apparent equilibration time that appears significantly longer than that obtained in the down-jump experiment. An explanation for this observation was first discussed by Tool [15,16]. The essential argument is that the molecular mobility depends on both the temperature and the thermodynamic state or structure of the glass. Hence, in the down-jump experiment the structure shows a positive departure from equilibrium which decreases with time giving rise to a progressively slowing process--what Kovacs [9] referred to as 'autoretarded'. On the other hand, in the up-jump experiment one begins with large negative departures from equilibrium and the mobility increases with increasing time. Hence, one sees an apparently 'autocatalytic' response on the logarithmic time scale used in these experiments. As presented subsequently, inclusion of a material time that depends on the departure from equilibrium leads to the strong non-linearity seen in Fig. 11.

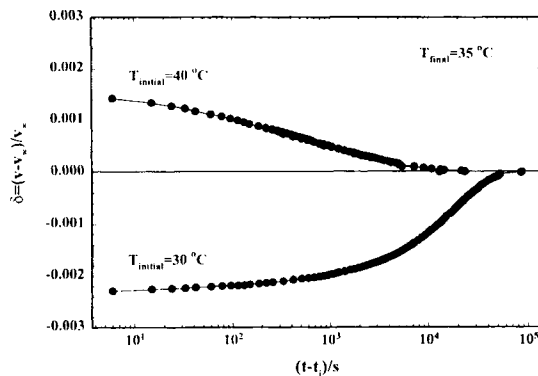


Fig. 11. Results from an asymmetry of approach experiment for poly(vinyl acetate) at a final temperature of $T = 35^\circ\text{C}$ for initial temperatures of 30°C and 40°C as indicated in figure. (Data from Reference 9.)

It is worthwhile to note here that the non-linearity is strong even though the volume strain (departure from equilibrium δ) is small, being on the order of 1 to 2 $\times 10^{-3}$. Hence, our first essential ingredient is a ‘material clock’ or time scale that depends on the instantaneous structure of the glass. It will also depend on temperature as indicated by the temperature dependence of the intrinsic isotherms in Fig. 10.

3.2.2. The memory or cross-over experiment

The other experiment that provides important information concerning the nature of the structural recovery response of glass forming materials is the memory or cross-over experiment. The experiment involves a *two-step* thermal history. First, one does a down-jump to some temperature below the glass transition and allows the structure to recovery partially towards equilibrium. After the partial annealing, the temperature is then increased to T_o and the volume recovery is measured. In the Kovacs[9] experiments, the conditions of annealing were chosen such that upon performing the up-jump to the final test temperature, the volume departure from equilibrium was close to zero (this implies that the partial recovery was performed until the fictive temperature T_f reached the temperature T_o after the second T -jump.) As shown in Fig. 12, the value of δ starts close to zero (or

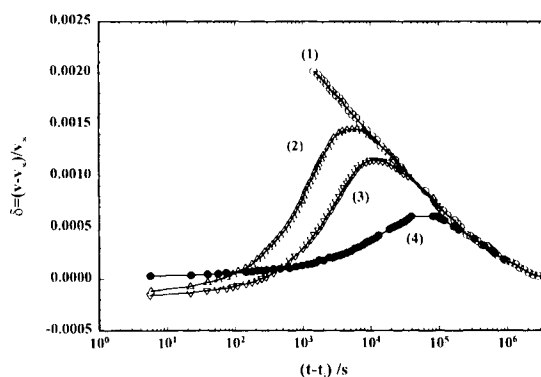


Fig. 12. Results from Kovacs' memory experiments on a poly(vinyl acetate) glass. The experiments are performed by treating the samples such that there are two temperature steps. First, one quenches the glass from 40°C to an annealing temperature T_a and the material is allowed to anneal (recover) partially towards equilibrium for an annealing (aging) time t_a before being up-quenched to the final test temperature $T = 30^\circ\text{C}$. In the figure the curve numbers correspond to different thermal treatments: 1). $T_a = 30^\circ\text{C}$; $t_a = 0$; 2). $T_a = 10^\circ\text{C}$; $t_a = 160$ h; 3). $T_a = 15^\circ\text{C}$; $t_a = 140$ h; 4) $T_a = 25^\circ\text{C}$; $t_a = 90$ h. (Data from Reference 9).

slightly below) and then increases (crosses over zero) and goes through a maximum before merging with the structural recovery result obtained for a single-step history to T_o . From the time when Tool [15,16] originally observed the cross-over phenomenon and until the 1970's the description of structural recovery was largely considered within the framework of single relaxation time models. Although the asymmetry of approach experiments can be treated qualitatively by a single relaxation time that changes due to the changing structure of the material, the memory experiment demonstrates conclusively that one needs to have multiple (at least two) relaxation times to describe structural recovery. Hence, the second 'essential ingredient' needed for the description of the structural recovery process is a non-exponential decay function which is often considered either in terms of a sum of exponentials or as a stretched exponential function as discussed subsequently.

3.3. The Tool [15,16] -Narayanaswamy [23] -Moynihan [12] -Kovacs [24] -Aklonis-Hutchinson-Ramos (TNM- KAHR) description of structural recovery

The final piece that has been put in to complete the puzzle and allow one to reasonably well describe the major features of structural recovery is a set of equations that relates the stimulus, *i.e.*, temperature history, to the response, *i.e.*, the volume or enthalpy recovery. The TNM-KAHR models do this by postulating that the behavior can be described using a viscoelastic constitutive equation that looks like linear viscoelasticity in *reduced time*. The equations developed by TNM and KAHR are slightly different in conception, but are mathematically equivalent. Here we follow the development according to KAHR and point out the TNM equivalencies and differences. We also note that, in addition to the 'essential ingredients' discussed above, the commonly used forms of the TNM and KAHR models assume that the viscoelastic response follows thermo-rheological simplicity in both temperature and structure; *i.e.*, the molecular mobility depends on both temperature and structure simply by a shifting of the time scale. The shape of the response function is unaltered.

The essence of the KAHR model is the following equation:

$$\delta(z) = -\Delta\alpha \int_0^t R(z-z') \frac{dT}{dz'} dz' \quad (8)$$

where, for volume recovery experiments, $\Delta\alpha$ is the change in coefficient of thermal expansion at the glass transition (the difference between the liquid and glassy coefficients $\alpha_l - \alpha_g$), T is temperature, $\delta(z)$ is the departure from equilibrium, $R(z)$ is the viscoelastic response function (a retardation function, but common usage has

come to use the term relaxation to describe the structural recovery or relaxation response), and z is the reduced time:

$$z = \int_0^t \frac{d\xi}{a_T a_\delta} \quad (9)$$

and the parameters a_T and a_δ are shift factors that describe how the temperature and the volume departure from equilibrium affect the characteristic relaxation times. The viscoelastic response function is given by:

$$R(z) = \sum_{i=1}^N g_i e^{-z/\tau_i} \quad (10)$$

The nonlinearity of the material response in the KAHR model comes from the fact that δ depends on itself in Eq. (8) through the reduced time of Eq. (9). If there were no structure dependence of z ($a_\delta = 1$) the equations would be identical to those of linear thermo-viscoelasticity.

In the case of the TNM version of the model, the viscoelastic response function is given in terms of the stretched exponential or Kohlrausch [25] - Williams-Watts [26] (KWW) function:

$$R(z) = e^{-(z/\tau_0)^\beta} \quad (11)$$

Furthermore, in the TNM equations, the reduced time is now defined in terms of a temperature shift factor a_T and a structure shift factor a_{T_f} which depends on the fictive temperature T_f rather than on the departure from equilibrium:

$$z = \int_0^t \frac{d\xi}{a_T a_{T_f}} \quad (12)$$

The two formalisms are equivalent, but there may be subtle differences between the physical interpretations of the parameters. If one speaks of the structure as δ , then the iso-structural state is a line approximately parallel to the equilibrium volume or enthalpy (recall Fig. 9). If one assumes that the fictive temperature T_f defines structure, the iso-structural state is defined along lines with a slope equal to the glassy coefficient of thermal expansion. We do not elaborate further on this point.

In the KAHR model the shift factors a_T and a_δ were originally considered to be the following functions of T and δ :

$$\frac{\tau_i(T, \delta)}{\tau_{i,r}} = a_T a_\delta = e^{-\theta(T-T_r)} e^{-\frac{(1-x)\theta\delta}{\Delta\alpha}} \quad (13)$$

where the first exponential term is a_T and the second is a_δ . $\tau_i(T, \delta)$ is the relaxation time at the relevant values of temperature and structure and the $\tau_{i,r}$ refers to the relaxation time at the reference state, generally taken for $T_r = T_g$ and $\delta = 0$. The parameter x is a partition parameter $0 \leq x \leq 1$ that determines the relative importance of temperature and structure on the relaxation times. The parameter θ is a material constant that characterizes the temperature dependence of the relaxation times in equilibrium. KAHR used $\theta \approx E_a/RT_g^2$ where E_a is an activation energy and R is the gas constant.

In the case of the TNM model the shift factors a_T and a_{T_f} were originally assumed to follow the following function of T and T_f :

$$\frac{\tau_0(T, T_f)}{\tau_{0,r}} = a_T a_{T_f} = e^{\frac{x\Delta h}{R}(\frac{1}{T} - \frac{1}{T_r})} e^{\frac{(1-x)\Delta h}{R}(\frac{1}{T_f} - \frac{1}{T_r})} \quad (14)$$

where now τ_0 is the characteristic time in the KWW expression (Eq. (11)), the arguments T and T_f are the temperature and fictive temperature respectively. $\tau_{0,r}$ refers to the relaxation time at the reference state, generally taken for $T_r = T_f = T_g$. Δh is an activation energy. Clearly the parameters in equations 13 and 14 can be related, yet have subtly different meanings. In addition to the original references, the reader is referred to the review by Hodge [14] for further discussion of the interrelationships between the material parameters for the two approaches. We also note that other relationships from those presented in Equations 13 and 14 can be used in the models without changing the underlying physical concepts outlined in the discussion of the “essential ingredients” that form the basis of the models.

An important aspect of the models discussed above is that the equations apply to both volume and enthalpy experiments. For enthalpy one substitutes ΔC_p for $\Delta\alpha$ in equations 8 and 13. It is worth noting, as well, that the response function $R(z)$ has been reported as both being and not being the same for enthalpy and volume recovery [27-30]. In addition, we note that the solution of the equations in differential form may be easier for many histories. Then, in terms of the fictive temperature based TNM model, we write:

$$\frac{dT_F}{dT} = 1 - \exp\left[-\left(\int_0^t \frac{dt}{\tau_0}\right)^\beta\right] \quad (15)$$

and, for any arbitrary thermal history starting in equilibrium at $T = T_r$, we can solve equations 14 and 15 simultaneously using numerical procedures:

$$T_{F,n} = T_r + \sum_{i=1}^n \Delta T_i \left[1 - \exp\left(-\sum_{j=1}^n \left(\frac{\Delta t_j}{\tau_{0,j}}\right)^\beta\right) \right] \quad (16)$$

where $T_{F,n}$ is the fictive temperature after the n^{th} temperature step, Δt_i is the time step, ΔT_i is the temperature step associated with the i^{th} time step and $\tau_{0,j}$ is calculated from Eq. (14) using known material parameters. Some typical TNM parameters are presented in Table 2 for polymers.

3.3.1. Strengths and Weaknesses of the Models

The TNM-KAHR frameworks are very powerful and reasonably straightforward to use. A good example of the success of the models is seen in Figs. 13 and 14 in which the asymmetry of approach [31] and memory experiments [32] are calculated from the KAHR model. In Fig. 13, the asymmetry data for jumps to 140°C for a polycarbonate material are compared with KAHR model calculations. The model parameters were determined [31] from an optimization to data from experiments at 130°C, 135°C and 140°C. It is readily seen that the asymmetry of approach is in reasonable quantitative agreement with the data. Fig. 14 compares Kovacs' original memory data for PVAc at 30°C with the calculations [32] based on the KAHR model in which the parameters were obtained from experiments at 30°C, 35°C and 40°C. Although the agreement between theory and experiment is not perfect, it can be seen that the model does a reasonable job of reproducing the

Table 2

Tool-Narayanaswamy-Moynihan Model parameters for some typical glass forming systems.

Material	T_g (K)	$\Delta h/R$ (K)	x	β	$\ln(A/s)$	C_{pk} (J/g/K) { α_k (K ⁻¹)}	C_{pl} (J/g/K) { α_l (K ⁻¹)}	Reference
Poly(vinyl acetate)	310	39,900	0.35	0.57	-81	0.92	1.97	129
Polystyrene	373.2	80,000	0.46	0.71	-216	1.52	1.77	20
	370.2	145,000	0.15	0.48	-384.9	{2.1 x 10 ⁻⁴ }	{5.5 x 10 ⁻⁴ }	30
Poly(vinyl chloride)	353	225,000	0.10	0.23	-622	1.12	1.43	20

memory effects.

Particularly relevant to this paper, because structural recovery can effect the measurement of the glass transition, is the fact that much work has been performed to compare the above models with results from differential scanning calorimetry (DSC)--perhaps the most common method of estimating the glass transition

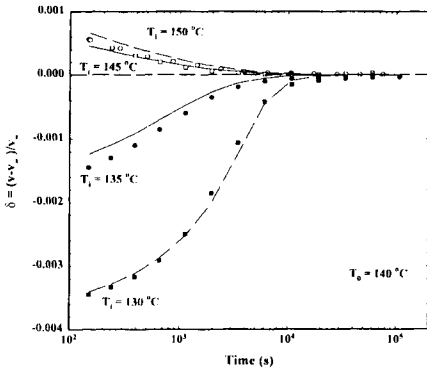


Fig. 13. Plot of asymmetry of approach experiments in a polycarbonate material aged into equilibrium at temperatures T_i and then jumped to a final test temperature of $T_0=140^\circ\text{C}$. Points are for experimental data and lines represent Kahr model calculations. (Data after reference 31).

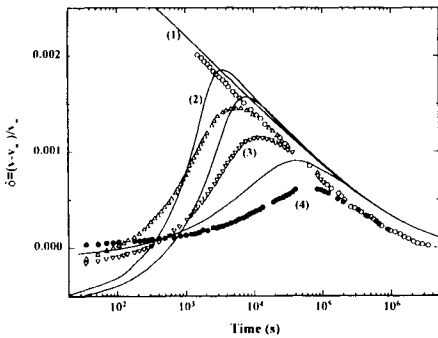


Fig. 14. Comparison of Kahr model calculations (lines) with the Kovacs' memory experiment data depicted in Fig. 12. Note that the time axis is for time after the beginning of the quench rather than the end as in Fig. 12. Curve numbers have the same meaning as in Fig. 12. (Calculations courtesy of C.R. Schultheisz, Reference 32).

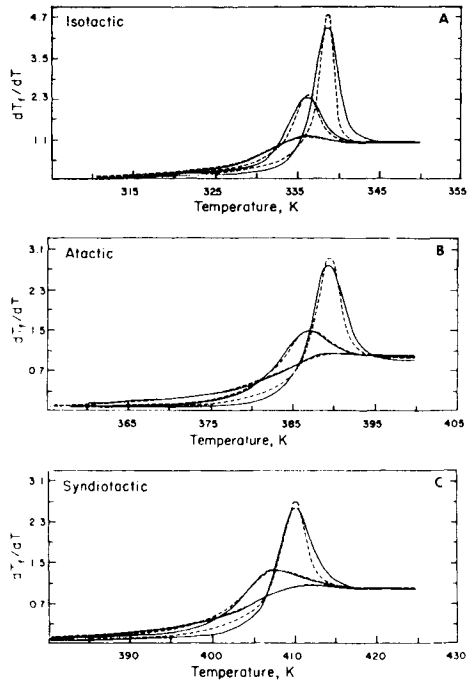


Fig. 15. Comparison of experimental (solid) and calculated (dashed) enthalpy recovery curves for a) isotactic PMMA; b) atactic PMMA; c) syndiotactic PMMA. The annealing was performed approximately 15°C below T_g . The curves represent aging times of 0 s, 6×10^3 s and 60×10^3 s, with the peak height increasing as the annealing time increases. See text for discussion. (Reprinted with permission of the American Chemical Society, ©1986, Tribone, J.J., O'Reilly, J.M., and Greener, J. "Analysis of Enthalpy Relaxation in Poly(methyl Methacrylate) - Effects of Tacticity, Deuteration, and Thermal History," *Macromolecules*, Reference 33).

temperature. At this point, we simply show that when one performs enthalpy recovery experiments followed by a heating scan, as is typically done in DSC measurements, we find that the models adequately describe the data. A comparison [33] of model predictions with typical DSC data is shown in Fig. 15. The scans themselves are interesting because, for certain thermal treatments, they show both a sub-glass transition peak and a large excess enthalpy peak near to T_g . The models reproduce both features.

As an additional point, we note that similar kinetics as those described above might be expected for experiments in which one changes pressure at constant temperature. This is the case and an appropriate version of the KAHR model has been used to describe the experimental results [34] reasonably well. Furthermore, in a recent development, we have shown that the models extend successfully to the aging behavior of glass-forming liquids confined in nano-porous matrixes [35].

To a very good first approximation, it is clear that the TNM-KAHR models can reproduce the major phenomena that are observed for the kinetics of structural recovery in glassy materials. However, there is much work that has been performed over the past two decades that shows that the TNM-KAHR models are somewhat deficient and require further refinement. What are the weaknesses? First, it is now reasonably well accepted that the models are not capable of describing experiments outside of a narrow range of temperatures without changing the material parameters [36]. This fact has led to discussion of the possible problems with the models. One suggestion is that the assumption of thermo-rheological-structural simplicity is incorrect because there seems to be a systematic trend in the value of the KWW β -parameter with changing thermal history [37,38]. There has also been considerable effort expended to develop models based on different physical assumptions. We discuss one such model in the next section.

Another weakness of the models is their inability to describe deep quenches or long aging times [36]. Furthermore, the so-called τ -effective paradox [9] and expansion gap [9] are not predicted by the current models [6,39]. These weaknesses need further research, and are often controversial in and of themselves [40,41]. Hence, while the weaknesses of the models are reasonably well understood, the successful development of the next generation of models that overcome these weaknesses is yet to occur. At this point, it can only be said that we have a good first-order handle on the problem of structural recovery in glass forming systems, including polymers, and the TNM-KAHR approaches have been very successful. Their successors have yet to be accepted. One alternative approach is presented in the next section.

3.4. The thermoviscoelastic model

A conceptual difficulty of the TNM-KAHR-type models is that they begin with a construction in which it is assumed that the first derivative thermodynamic

property, *e.g.*, the volume, depends on the second derivative, *e.g.*, the coefficient of thermal expansion change at the glass transition, plus a response function that depends on reduced time. While this is operationally reasonable because it describes a departure from equilibrium and how that departure changes with time, it is not so satisfying at a fundamental level because it does not tell us the response from the fundamental thermodynamic level of the free energy of the system. We recognize that non-equilibrium thermodynamics is a very difficult subject and, in fact, there is currently no single model that is accepted. However, in the past several years there has been a serious effort at the Purdue University School of Chemical Engineering under the direction of J. M. Caruthers [42-46] to adapt one such formalism to the problem of glassy materials. The formalism is that of Rational Mechanics [47,48] or Rational Thermodynamics and we examine, albeit too briefly, the Caruthers group's contributions in this area.

The thermoviscoelastic model is an extension of the original ideas of Coleman [47,48] and Noll [49] for a non-equilibrium thermodynamics referred to in the literature as rational mechanics or rational thermodynamics. Historically this approach has been controversial for a range of reasons beyond the scope of this article. However, one very important issue in the development and uses of the rational mechanics framework has been the need to deal with multiple integral expansions of the relevant response functions and the inherent complexity that arrives in dealing with such representations. The important contribution by Lustig, Shay and Caruthers [46] (LSG) was the ability to truncate the multiple integrals and arrive at single integral representations of the material behavior. This leads to a very attractive and tractable set of equations for describing the material response. Because the single integral forms are of themselves insufficient to describe the observed nonlinear response of a glass forming materials, LSG introduced a reduced time, much as used in the models presented above, that depends on the configurational entropy. Hence, one starts with the assumption that there exists a free energy potential functional that is time-dependent. Appropriate differentiation of the functional results in volume, enthalpy and mechanical responses that contain sufficient information to predict strongly non-linear behavior from laboratory determined linear viscoelastic response functions.

The detailed development followed by LSG is beyond the scope of this paper. In the fluid form of the so-called "KGAC" version of the model, through single integral terms, is given by the following equations for the stress and entropy. Significantly, we note that an important aspect of the model is that all of the material parameters are related to response functions obtained from linear viscoelastic measurements, *PVT* measurements and heat capacity measurements:

Stress:

$$\begin{aligned}
 T(t) = & -P^{(\infty)}I + \frac{\rho}{\rho_R} \int_{-\infty}^t G_{\Delta}(I_3(t), \theta(t), t^* - \xi^*) \left[\frac{dC_i(\xi)}{d\xi} - \frac{1}{3}I \frac{dI_{ii}(\xi)}{d\xi} \right] d\xi \\
 & + \frac{\rho}{\rho_R} I \int_{-\infty}^t \frac{1}{2} K_{\Delta}(I_3(t), \theta(t), t^* - \xi^*) \frac{dI_{ii}(\xi)}{d\xi} d\xi \\
 & + \frac{\rho}{\rho_R} I \int_{-\infty}^t 2\rho_R A_{\Delta}(I_3(t), \theta(t), t^* - \xi^*) \frac{d\theta(\xi)}{d\xi} d\xi
 \end{aligned} \tag{17}$$

Entropy:

$$\begin{aligned}
 \eta(t) = & \eta^{(\infty)}(I_3(t), \theta(t)) - \int_{-\infty}^t A_{\Delta}(I_3(t), \theta(t), t^* - \xi^*) \frac{dI_{ii}(\xi)}{d\xi} d\xi \\
 & - \int_{-\infty}^t 2C_{\Delta}(I_3(t), \theta(t), t^* - \xi^*) \frac{d\theta(\xi)}{d\xi} d\xi
 \end{aligned} \tag{18}$$

where P is the pressure and η is the entropy. The superscript (∞) implies the equilibrium value. ρ is the density and ρ_R is its value in the undeformed, reference state. I is the identity tensor, I_3 is the third absolute strain invariant of the deformation tensor (related to the volume change), $C_i(\tau)$ is the relative right Cauchy-Green strain tensor and $I_{ii}(\tau)$ is the first relative strain invariant of $C_i(\tau)$. We note that in the Caruthers' Group the notation is that θ is the absolute temperature and not to be confused with the definition of θ in the KAHN model. The important material response functions in the equations give the model its acronym of KGAC. The K_{Δ} term is the relaxation function for the bulk modulus, G_{Δ} is the shear modulus relaxation function, A_{Δ} is a constant volume thermal stress function and C_{Δ} is the constant volume heat capacity divided by temperature. Finally, the reduced time t^* is defined by:

$$t^* = \int_0^t \frac{d\xi}{a(\xi)} \tag{19}$$

where $a(\xi)$ is a generalized shift factor that is taken to depend on the configurational entropy following the Adam-Gibbs [50] relationship:

$$\log a = M \left[\frac{1}{\eta_c \theta} - \frac{1}{\eta_{cr} \theta_r} \right] \quad (20)$$

where M is a constant, η_c and η_{cr} are the configurational entropy in the current and reference states respectively, θ and θ_r are the temperature and reference temperature respectively. The configurational entropy can be calculated from the experimental heat capacity data assuming that it is approximately equal to the total. The reader is referred to McWilliams[45] for further discussion. Also, we note that Hodge [14] discussed this form of shift factor in the TNM equations for enthalpy recovery.

3.4.1. Model Predictions for Volume Recovery: Comparison with Kovacs' data

One major issue in the use of the KGAC model is a relative lack of complete sets of the material parameters needed in equations 17-19. This is in spite of the fact that the parameters are, in principle, obtainable from linear viscoelastic and thermodynamic measurements. As one might surmise from the prior sections, there is a considerable amount of relevant data available for poly(vinyl acetate). Although the data is for different samples and was obtained in different laboratories, it is sufficient to make comparisons with the volume recovery data of Kovacs [9] that we cited previously. Such comparisons using the KGAC form of the thermoviscoelastic model have been made for different types of thermal and mechanical histories by several Ph.D. students at Purdue [42-45]. Here we summarize the results reported by McWilliams [45] in his thesis for the KGAC model comparisons to the Kovacs asymmetry of approach and memory experiments.

McWilliams [45] took the simplifications suggested by LSG for the material parameters and assumed that K_Δ , G_Δ , A_Δ , and C_Δ could be written as functions that factor into a part that depends on the instantaneous temperature and volume and a part that depends on the reduced time t^* :

$$\begin{aligned} K_\Delta(\theta(t), \nu(t), t^*) &= \Delta_K(\theta(t), \nu(t)) k_\Delta(t^*) \\ G_\Delta(\theta(t), \nu(t), t^*) &= \Delta_G(\theta(t), \nu(t)) g_\Delta(t^*) \\ A_\Delta(\theta(t), \nu(t), t^*) &= \Delta_A(\theta(t), \nu(t)) a_\Delta(t^*) \\ C_\Delta(\theta(t), \nu(t), t^*) &= \Delta_C(\theta(t), \nu(t)) c_\Delta(t^*) \end{aligned} \quad (21)$$

McWilliams also assumed that the functions Δ_K , Δ_G , Δ_A are constants, Δ_C is a linear function of temperature θ and the temperature of glass formation θ_{gf} and the functions k_Δ , g_Δ , a_Δ , k_Δ were given by stretched exponential relaxation functions:

$$\begin{aligned} K_\Delta &= \Delta K; & G_\Delta &= \Delta G; \\ A_\Delta &= \Delta A; & C_\Delta &= \Delta C = C_0 + C_\theta(\theta - \theta_{gf}) \\ K_\Delta &= e^{-(t^*/\tau_K)^{\beta_K}}; & G_\Delta &= e^{-(t^*/\tau_G)^{\beta_G}}; \\ A_\Delta &= e^{-(t^*/\tau_A)^{\beta_A}}; & C_\Delta &= e^{-(t^*/\tau_C)^{\beta_C}} \end{aligned} \quad (22)$$

The values for the different parameters used by McWilliams are given in Table 3.

Importantly, this framework is logically a direct extension of a non-equilibrium thermodynamics and, once material parameters are determined, gives reasonable approximations to the observed experimental data. The agreement between the model calculations of McWilliams for the Kovacs [9] data for the asymmetry of approach and the memory experiments discussed earlier are shown in Figures 16 and 17 respectively. Clearly, the thermoviscoelastic model provides a very reasonable description of these data. Furthermore, the model has the

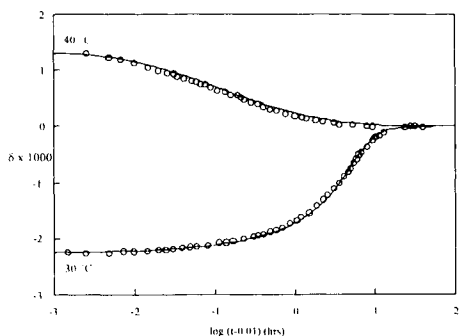


Fig. 16. Data (symbols) for asymmetry of approach experiments in poly(vinyl acetate) compared with calculations from KGAC model (lines). Data are same as those in Fig. 11. (Reprinted with permission of D.S. McWilliams, Reference 45).

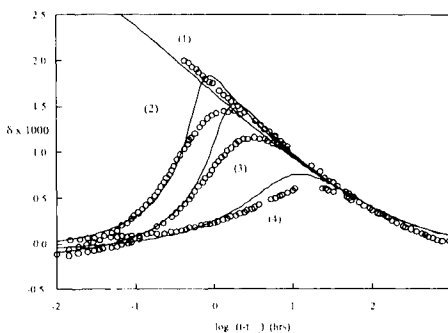


Fig. 17. Data (symbols) for memory experiments in poly(vinyl acetate) compared with calculations from KGAC model (lines). Data are same as those in Fig. 12. (Reprinted with permission of D.S. McWilliams, Reference 45).

Table 3.

Thermoviscoelastic parameters used by McWilliams [45] in his simulations of structural recovery for poly(vinyl acetate).

Parameter	Value
ΔA	2.22 bar cm ³ / gK
ΔK	14,700 bar
$\Delta C = C_0 + C_\theta(\theta - \theta_{g\theta})$	-
C_0	0.00278 bar cm ³ /gK ²
C_θ	-1.51x10 ⁻⁵ bar cm ³ /gK ³
B	2200 g/bar cm ³
$\theta_0 \eta_\infty$	80.3 bar cm ³ /g
Δ	0.232 bar cm ³ /gK
θ_2	5.95°C
$\log(\tau_a)$	3.41 s
$\log(\tau_t)$	2.86 s
$\log(\tau_c)$	3.20 s
β	0.381
$\theta_{g\theta}$	30.6°C
$v_{g\theta}$	0.8340 cm ³ /g

potential to predict other responses such as the non-linear viscoelastic and yield responses of glassy polymers over the range of temperatures from above to below the glass transition temperature.

3.4.2. Strengths and weaknesses of the thermoviscoelastic model

The thermoviscoelastic model is obviously more difficult to implement than are the TNM-KAHR types of model and there is a bigger array of experimental data needed to obtain all of the material functions in the model if one wants to describe only, for example, the volume recovery behavior of the glass forming system. In addition, the model has similar problems with the description of deep quenches and long aging times as do the TNM-KAHR models. The strength of the model is that it is, in principle, general. Hence, more than the structural recovery response can be described, and in fact, the model has been used with some success to look at

physical aging [51] and nonlinear viscoelastic [43-45] responses of polymers. Furthermore, the current KGAC model is a simplification and further developments of the model might well prove to be in better agreement with data. Finally, it is worth noting that this model is one of the first advances in the development of equations to describe structural recovery to appear in about 20 years. It points towards new ways of looking at material response and, if not fully successful, may yet pave the way towards a more complete picture of structural recovery and the glass transition.

3.5. Viscosity and segmental relaxation behavior above the glass transition temperature

Prior to moving on to outline the microscopic models that are commonly used to describe the glass transition, it is worth reminding the reader that part of the phenomenology of glass forming materials is related to the observation that the molecular mobility above the glass transition, that is in the equilibrium state, is characterized by strongly non-Arrhenius temperature behavior. There are several ways in which to look at such behavior and here we briefly present the Vogel [52]-Fulcher [53] expression and that of Williams, Landel and Ferry [54,55] (WLF). In addition, we introduce the concept of liquid fragility proposed by Angell [56] in his extensive work on small molecule glass forming liquids.

The first point to examine is the observation that the viscosity of glass forming liquids, including polymers, is strongly non-Arrhenius. Such behavior is shown in Fig. 18 for a polymer melt [57]. The common means of describing such non-Arrhenius temperature dependence is through the Vogel-Fulcher equation:

$$\eta = \eta_0 e^{-\left[\frac{B'}{T-T_\infty}\right]} \quad (23)$$

$$\log \eta = \log \eta_0 - \frac{B'}{T-T_\infty}$$

where η is the viscosity, η_0 is an empirical prefactor, B' is a material parameter (it would be the activation energy if T_∞ were equal to zero, T is temperature and T_∞ is the temperature at which the viscosity becomes singular. T_∞ is often referred to as the Vogel temperature and is generally found to be approximately 50°C below the conventional glass transition temperature. The Vogel equation (Eq. (23)) is readily

related to the WLF equation: related to the WLF equation:

$$\log a_T = \log \frac{\eta}{\eta_{ref}} + \log \frac{T_0 \rho_0}{T \rho} \quad (24)$$

$$\log a_T = \frac{-C_1^0 (T - T_0)}{C_2^0 + T - T_0}$$

where η_{ref} is the viscosity at an appropriate reference temperature T_0 , T is the temperature of interest and ρ and ρ_0 are the density at the T and T_0 respectively. Often the ratio $T_0 \rho_0 / T \rho$ is small and can be ignored. The parameters in equations 24 and 23 can be related:

$$B' = C_1^0 (T_0 - T_\infty) \quad (25)$$

$$T_\infty = T_0 - C_2^0$$

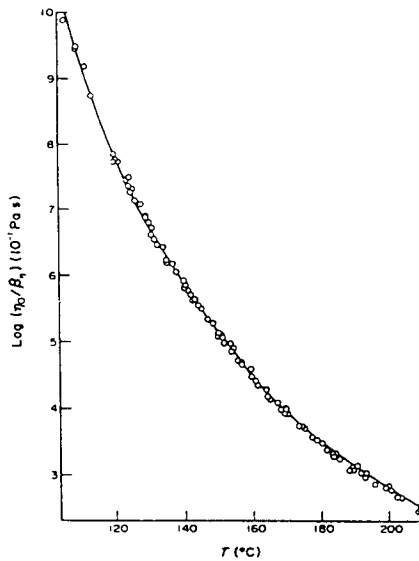


Fig. 18. Logarithm of reduced viscosity vs temperature for melts of cyclic polystyrene molecules showing rapid increase as T_g is approached. The line represents the fit to the data of Eq. (23). (After Reference 57).

Finally, we introduce a concept made popular by Angell for classifying the thermal behavior of glass forming liquids: fragility. This concept was originally introduced in an attempt to establish some link between the observed thermodynamic behaviors of glass forming systems and the temperature dependence of the viscosity. The idea was that the tendency of materials to form glasses would be determined by their ‘strength’ in the liquid state. Then, strong liquids would have stable structures (local to intermediate range order) and properties that do not change dramatically in going from the liquid to the glass. On the other hand, ‘fragile’ liquids would have less stable structures and the property changes in going from the liquid to the glassy state would be more evident. For the thermodynamic properties, such as heat capacity, the change in going from the liquid to the glass (ΔC_p or $C_{p,l}/C_{p,g}$) would be measures of the liquid fragility. For the viscosity, the strong liquids would exhibit nearly Arrhenius temperature behavior and the fragile liquids would show strongly Vogel-Fulcher or WLF-types of behavior. Fig. 19 depicts the classic “Angell” plot as a normalized Arrhenius plot of viscosity vs T_g/T and an insert of the heat capacity changes at the glass transition. Although this approach to describing glasses is becoming widely used because it provides a means of classifying the ‘glass-forming’ tendency of materials based on chemical structure, its applicability to polymers is currently a subject of

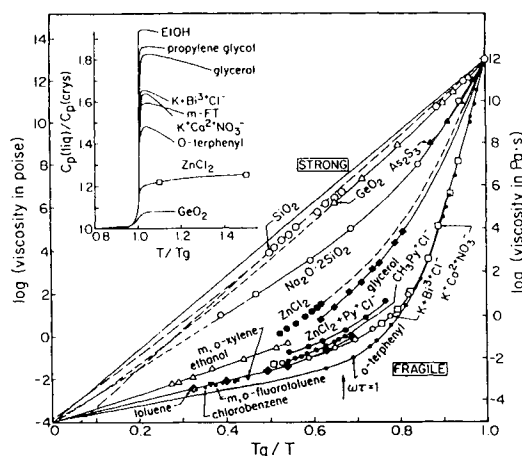


Fig. 19. Viscosity-reduced temperature (fragility or Angell) plot for glass forming liquids. Insert shows heat capacity change at the glass transition. (Reprinted with permission of C.A. Angell. From Angell, C.A. (1985) “Strong and Fragile Liquids,” in *Relaxations in Complex Systems*, ed. By K.L. Ngai and G.B. Wright, National Technical Information Service, U.S. Department of Commerce, Springfield, VA 22161, p. 3-11. Reference 56).

continued contention in the literature [27,58-62]. The future will determine its ultimate utility beyond the standard Vogel-Fulcher and WLF sorts of descriptions.

4. MICROSCOPIC THEORIES RELATED TO THE GLASS TRANSITION

4.1. General Comments

Thus far, we have described the apparent thermodynamic response of glass forming systems and noted its path dependence. In addition, we have rather extensively described the kinetic phenomenology of structural recovery and we have presented several models that are very powerful in their description of the observed behavior. Clearly, the kinetics of glass forming systems is of great importance to an understanding of the glass transition and its measurement. We also presented some information about the temperature dependence of the viscosity of glass forming liquids. In spite of the large amount of data and observation on the behavior of glasses and glass forming liquids, there is still a question of the exact nature of the glass transition. In a simplistic way, the question boils down to a controversy that on one side the glass transition is viewed as a purely kinetic phenomenon, while on the other side, the glass transition is thought of as a kinetic manifestation of an underlying thermodynamic transition. Resolution of the conflict is very hard because of the fact that the experimental measurements are greatly affected by kinetics and the long times required to reach equilibrium makes equilibrium experiments nearly impossible except relatively close to or above the generally observed (nominal) T_g . Furthermore, simply proving that one theory or model of the glass transition does not describe all of the available data and observed phenomena doesn't truly tell us whether the actual transition is thermodynamic or kinetic. This being said, there are two major types of model that have historically been used in the description of the T_g and these are still useful--at least for providing estimates of changes in T_g with, for example, composition, pressure and molecular weight. These are the free volume models and the configurational entropy models. In what follows we present a brief overview of both.

4.2. Free volume models

There are many different models of the glass transition that depend on the concept of free volume. While not identical, these models all have in common the idea that there exists some unoccupied volume in materials that consists of holes of molecular size or imperfections in the packing order of molecules which arise from their random arrangement in either the liquid or the glass. In fact, free volume was originally invoked to account for fluidity and non-Arrhenius temperature dependence of liquids introduced briefly above. Perhaps the best known of the free volume formulations comes from Doolittle [63] who wrote an equation for the

viscosity of simple liquids:

$$\ln \eta = \ln A + \frac{B(v - v_f)}{v_f} \quad (26)$$

where η is the viscosity, v_f is the specific ‘free’ space or volume and v is the global specific volume and B is an arbitrary parameter. Although Eq. (26) gives a reasonable representation of the viscosity of many simple liquids, Doolittle recognized early on that the definition of the “free” and “occupied” spaces was difficult although these could be related by $v_f = v - v_o$, where v_o is the limiting or occupied volume.

The free-volume concept was exploited to describe the viscosity behavior of polymers in the work of Fox and Flory [64] and that of Williams, Landel and Ferry [55]. When the free volume is defined to vary linearly with temperature, the WLF equation (Eq. (24)) can be derived from the Doolittle equation (Eq. (26)). Following the development provided by Ferry [54] we first examine Fig. 20 to define the free volume v , fractional free volume f , and occupied volume v_o , keeping

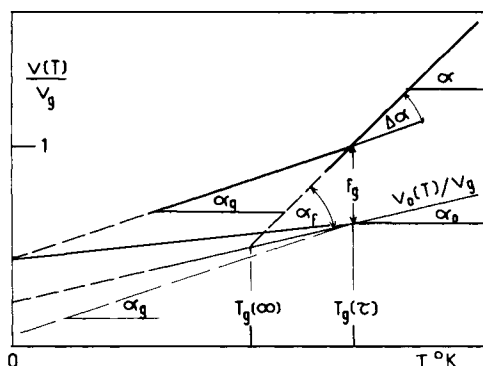


Fig. 20. Schematic of the variation of the total specific volume $V(T)/V_g$, occupied volume $V_o(T)$ and free volume at $T_g(f_g)$ with temperature T for a supercooled liquid. α_g is the coefficient of expansion (total) of the glass, α is the coefficient of expansion of the liquid, α_o is the coefficient of expansion of the occupied volume. $\Delta\alpha = \alpha - \alpha_g$ is the difference in slope between the liquid and glassy states. $T_g(\tau)$ is the glass transition temperature at some time τ (or equivalent cooling rate) and $T_g(\infty)$ is the glass transition temperature at infinite time. (After Reference 9. Figure Courtesy of A.J. Kovacs).

in mind that the free volume is the excess over the occupied volume:

$$f = \frac{v_f}{v} = f_0 + \alpha_f(T - T_0) \quad (27)$$

where α_f is the coefficient of thermal expansion of the free volume. T_0 is the reference temperature described above. Then, the WLF equation can be rewritten in terms of the free volume:

$$\log a_T = \frac{-(B/2.303/f_0)(T - T_0)}{f_0/\alpha_f + T - T_0} \quad (28)$$

and we note that B is the arbitrary parameter of Eq. (26). Obviously the parameters in Eq. (28) can be identified with those in Eq. (24). We also note that if we identify the reference temperature T_0 with the glass transition temperature T_g , the free volume fraction at T_g is:

$$f_g = \frac{B}{2.303 C_1^g} \quad (29)$$

When one takes B to be unity, the free volume fraction can be obtained and its value at T_g for polymers falls between 0.01 and 0.04. Originally WLF had found a value of $f_g = 0.025$. As noted above, Doolittle struggled with the definition of the free volume and its true value is difficult to determine. However, when the development is consistent, the description of the viscosity-temperature dependence is readily deduced and there is a physical insight gained that the molecular mobility decreases as the space available decreases and this leads to non-Arrhenius temperature dependence. In addition, the free volume model provides an adequate empirical framework for describing the pressure [54] dependence of the viscosity as well as its temperature dependence. We do not discuss this further here.

4.3. The Gibbs-DiMarzio [65,66] configurational entropy model

The Gibbs-DiMarzio [65,66] theory of the glass transition results from an application of the Flory [67]-Huggins [68] lattice model of a system of macromolecules. This limits its applicability in terms of small molecule systems, but it has been argued by DiMarzio [69] that the approach is powerful specifically because polymers can form glasses from systems that have no underlying crystalline phase, which makes arguments about the existence of metastable glasses

(which are strongly dependent on kinetic questions) irrelevant to the equilibrium thermodynamic state described by the lattice model.

The parameters relevant to the lattice model are obtained from examination of Fig. 21 [70]. The polymer chains of degree of polymerization X have many configurations which fit onto the lattice of coordination number Z . Each chain has a lowest energy shape and, the more the shape deviates from it, the greater the internal energy of the molecule. Gibbs and DiMarzio assumed a simple form for the energy in terms of the fraction f of bonds 'flexed' out of the lowest energy state and the energy associated with the flexed and unflexed potential wells ϵ_2 and ϵ_1 . They also allowed for n_θ vacant sites on the lattice. This latter results in a hole energy that is proportional to the number of intermolecular or van der Waals bonds (bond energy α) broken by introduction of the vacancies into the lattice. The model is minimal in that it has just two energies, $\Delta\epsilon = \epsilon_2 - \epsilon_1$ and α , and two parameters, f and n_θ . The latter two parameters are controlled by the energies.

The calculation of the partition function can be done by the standard Flory-Huggins lattice method. The Gibbs-DiMarzio calculations for the lattice model gave a true second-order transition at a temperature T_2 . Fig. 22 shows a schematic of the entropy-pressure-temperature surface predicted by Gibbs and DiMarzio. The transition that occurs at a critical value of entropy (zero configurational entropy) is interpreted to be the thermodynamic glass transition. Because kinetics intervenes, Gibbs and DiMarzio argue that the measured glass transition reflects the

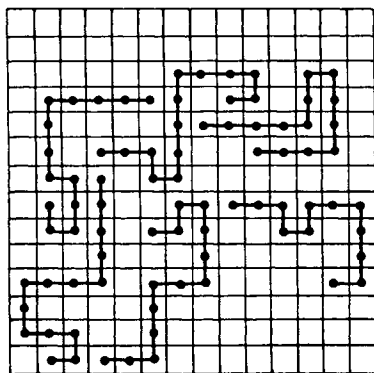


Fig. 21. Representation of the Gibbs-DiMarzio model. A lattice of coordination number Z is used to calculate the number of complexions for a system of n_x molecules each of length X . Energy α is associated with holes and energy $\Delta\epsilon$ is associated with flexing of a bond from its low energy shape. (After Reference 70).

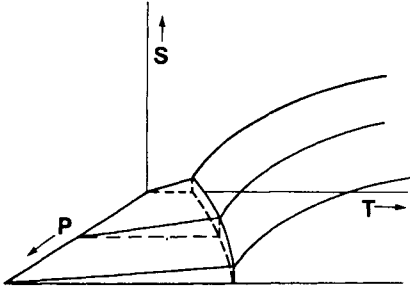


Fig. 22. Schematic representation of the *SPT* surface calculated from the Gibbs-DiMarzio lattice model. The mean-field calculation on the lattice model results in a second-order transition in the Ehrenfest sense. (After Reference 70).

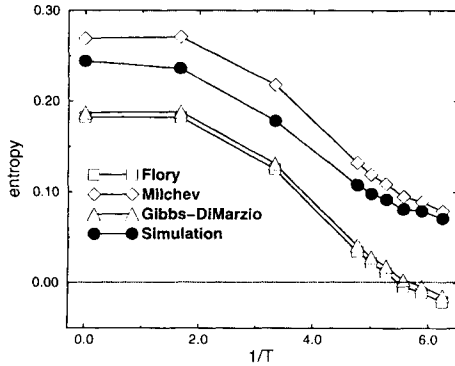


Fig. 23. Entropy vs inverse temperature for several models and by computer simulation showing transition-like behavior. (With permission of J. Baschnagel, Baschnagel, J., Wolfgardt, M., Paul, W., and Binder, K., Reference 71).

underlying transition that occurs at T_2 .

The configurational entropy model for the glass transition gives a physical insight into the transition at T_2 . When the system is cooled isobarically, the number of allowed arrangements for the molecules decreases for two reasons. First, the number of holes decreases (a volume decrease) and the configurational entropy due to permuting holes and chains decreases. Second, the configurational entropy of the molecules decreases because the chains favor low energy states (shapes) at lower temperatures. The $T(P)$ line where the total configurational entropy first becomes zero defines the temperature at which the thermodynamic transition takes place.

An important point about the configurational entropy model is that it is often criticized because computer simulations seem to indicate that the transition is not a 'true' transition, but is rounded. However, this does not change the argument that the entropy controls the underlying change in properties in going through what we refer to as the glass transition temperature. It does imply that the transition is not a true transition in the Ehrenfest sense discussed previously, *i.e.*, there are no discontinuities in the second derivatives of the relevant thermodynamic properties at T_2 . This is a minor point and does not change the contention that the entropy models of the glass transition provide a thermodynamic explanation in contrast to the free volume models which are based on kinetic arguments. Fig. 23 shows computer calculations [71] for the entropy vs temperature for different variations of the lattice model. The reader is referred to a special symposium proceedings [72] on entropy and the glass transition for an extensive discussion of the entropy concept and glassy behavior.

4.4. Comparison of the free volume and configurational entropy models with experiments

A quantitative model that would allow the *ab initio* calculation of the glass transition is far from available. However, both the free volume and configurational entropy models allow for the prediction of changes in the glass transition temperature with, *e.g.*, composition, pressure, and molecular weight, independent of how it might be measured. There is an extensive body of literature describing how the models behave and what their limitations are and it is beyond the scope of the current article to discuss them. It is important that the reader be aware that both free volume models and the entropy models are relatively successful in describing the observed behaviors. The one exception is that free volume models are not very good at describing the entropy part of the thermodynamics of glasses, *i.e.*, the heat capacities and the heat capacity change at T_g are not very well predicted [6]. In addition, as discussed earlier, when one cools a glass forming liquid at constant volume, one still observes [11] a glass transition--an observation that was quantitatively at odds with the Fox and Flory [63] free volume model [11]. The current authors prefer the entropy approach to glassy behavior, but recognize that much of the literature data has been analyzed in terms of free volume and that the concept provides a useful framework for describing data and obtaining insights into the glassy behavior and how it changes with different experimental variables. The reader is referred to reference 6 for more detail.

5. MEASUREMENT OF T_g

5.1. General Comments

From the above discussions it is clear that the glass transition is affected by many parameters and that the way in which we measure it will also affect the value of the reported glass transition. Therefore, if one wants to report a change of the glass transition with some other parameter, *e.g.*, pressure or composition, it is of great importance to be very careful in describing the measurement procedure used to obtain the glass transition temperature. If one is not specific about such things as heating and cooling rates, method, sample size and so forth, it becomes very difficult to compare results between laboratories.

In addition to these points of specifying adequately the exact experimental techniques used, the reader needs to be aware that many measurements are performed by scanning in temperature either up or down. In either case, thermal lag effects can be present and influence the apparent T_g . In the case of heating of glassy materials, there are special problems that arise due to the structural recovery events described above and we recommend performing experiments upon cooling whenever the experiment is sensitive enough to do this. Upon heating, one should report a fictive temperature rather than a glass temperature and this will be

discussed below when calorimetric techniques are discussed. Unfortunately, there is not complete agreement among practitioners on the preferred method of measurement, but it is of primal importance to specify the experiment as completely as is possible.

In the following sections we describe some typical techniques for measuring the glass transition temperature and attempt to indicate the strengths and weaknesses of each. We also indicate the ability of such techniques to measure kinetic properties associated with the glassy structure. We do not look at methods such as dynamic mechanical or dielectric measurements as they have been widely described elsewhere and their interpretation is, in fact, more difficult than the methods presented here that provide a transition in “thermodynamic” properties.

5.2. Dilatometric methods

Dilatometry is a method for measuring volume. Although dilatometry is not the most common method of measurement in glass forming systems, we discuss it first here because the data first presented in the prior sections was obtained in very elegant experiments performed by A. J. Kovacs using fluid confinement dilatometry methods for a poly(vinyl acetate) polymer. Generally, dilatometric measurements can be made either in a confining fluid to obtain the volume change of the sample or through length change measurements.

It is common, particularly in fluid confinement dilatometry experiments, to report the first derivative of the free energy state variable, the volume. The data can then, if appropriate, be analyzed in terms of the coefficient of thermal expansion. Hence, in Fig. 2, we see a volume-temperature plot and the T_g is estimated from the intersection of the slopes of lines drawn through the points at high temperature and low temperature (above and below the apparent transition). In addition, dilatometric techniques, including the length change methods, are often continuous or semi-continuous measurements in which volume (or its change relative to a reference) can be measured as functions of time, temperature or pressure. This can lead to very good accuracy in both the change and in the derivative of the change with time, temperature or pressure. (See, for example, references 9, 10, 11, 39, 40, 41).

5.2.1. Fluid confinement dilatometry

The methods used by Kovacs in his studies were based on the Bekkedahl [73] dilatometer depicted schematically in Fig. 24. The apparatus is essentially a quartz tube in which a sample is placed and then surrounded by an appropriate fluid. The tube is attached to a capillary of known (calibrated) diameter and volume changes are observed by measuring the height change of the fluid column in the capillary. However, despite the simplicity, the method is somewhat cumbersome and few people carry out such dilatometric measurements today because they are

not as convenient as other techniques. Perhaps the biggest disadvantages of the method lie in the need to evacuate the system in order to fill it with the confining fluid and the fact that, for polymers, the fluid should not interact with the polymer, which leads, commonly, to the use of mercury, a material whose physical properties are well known, as the confining fluid. Mercury has the advantage of excellent thermal conductivity there minimizes temperature gradients in the sample cell. Also, the temperature range over which mercury can be used is fairly broad (melting point is -39°C and the one atmosphere boiling point is 357°C) [74]. Toxicity of the vapors, however, reduce the upper limit somewhat. An advantage of mercury confinement dilatometry is that the system can be immersed in a liquid bath, which lends itself to relatively easy temperature control and stability when high precision in the measurements is required. Typical estimates [40,41] for the accuracy of the Kovacs measurements, for example, are that the long time volume stability was approximately $2 \times 10^{-5} \text{ cm}^3/\text{cm}^3$. This limitation is related to the fact that liquid mercury has a relatively high coefficient of thermal expansion and generally makes up 50% or more of the total sample cell volume. Finally, the fluid confinement dilatometer has a significant advantage over linear measurements. Because the material is under very small hydrostatic stresses there is little tendency to change dimensions due to creep. Therefore, measurements are readily made through the glass transition where the material might flow. The reader is referred

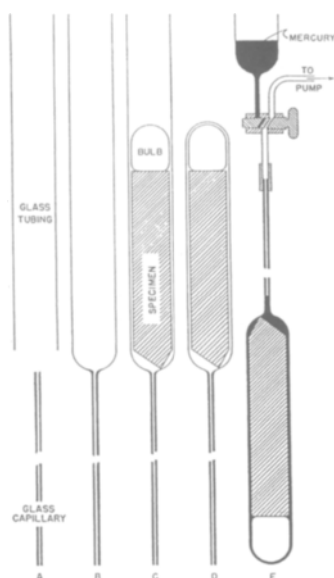


Fig. 24. Schematic of the Bekkedahl fluid confinement dilatometer. (After Reference 73).

to Figures 2-4, 6-8, 10-14 for typical data taken using fluid confinement dilatometers. From the Figures 3, 4, 6 showing volume-temperature plots at different pressures, it is clear that the confinement technique also lends itself well to measurements under hydrostatic pressure.

The actual measurement of the glass transition is made by taking the point of intersection of the liquid state v - T line with that of the glassy state v - T line. Typical errors in the estimates of T_g from isobaric measurements are reported to be of the order of $\pm(1 \text{ to } 2^\circ\text{C})$, due primarily to the uncertainty of the estimates of the slopes in the v - T behavior and corresponding extrapolation of the uncertain lines to a point of intersection (See reference 11 for a discussion of the statistical methods used to make the error estimates). An advantage of the fluid confinement measurement is that it can be made on cooling, which reduces some of the difficulties which occur due to structural recovery in heating experiments. It is important, as in all T_g measurements, to fully specify the thermal history applied to the sample. For example, recalling Fig. 2, the T_g depends on the time-scale of the experiment.

We also note that special, deformation dilatometers have been built for fundamental studies [75-78] of the effects of deformation on volume changes and could, conceivably, be used to examine the influence of deformation on the glass transition temperature.

5.2.2. Length change dilatometry

The most straight forward means of measuring the change in volume of an isotropic sample is to measure the change in length with temperature. This is evidently a popular method as reflected by three different standard test methods published by the ASTM [79-81]. Furthermore, when sample flow (creep) is not a potential problem, length change measurements can be more accurate than the fluid confinement techniques discussed above. [The reason for this is that, in the confinement method, the fluid volume changes make up a significant part of the measured volume change and these need to be taken into account.] The problem of sample flow is normally not a big effect far below the glass transition, but when the T_g is approached it becomes an issue. Most of the standard length change methods all require some sort of mass be applied to the sample. Furthermore, the mass of the sample itself can lead to flow when the viscosity of the sample becomes small enough. When flow becomes a problem, the fluid confinement methods are the best techniques because they measure the volume of the sample.

The accuracy of the length change methods is determined by the ability to measure the absolute length, L , and the magnitude of the length change. If one is interested in the coefficient of thermal expansion, the interferometric methods lead to an estimated expanded uncertainty of 40 nm/m/K. Comparing this with a typical coefficient of thermal expansion of 3×10^{-5} m/m/K, the relative expanded

uncertainty of the measurement is then approximately 1.3×10^{-3} . This would assume, of course, that the sample did not flow and that the sample temperature is known perfectly. Additional errors in the measurement would result from fluctuations or gradients in temperature. A typical uncertainty, which is valid for all of the methods of measurement, can be estimated based on the coefficient of thermal expansion of the material and the sample length. Additionally, errors of measurement can be due to other factors, such as the actual temperature fluctuations, thermal expansion of the apparatus supports and, perhaps most importantly near to the glass transition, flow of the sample under the sample weight and weights of any instrument parts, such as mirrors in the interferometric method.

In the case of less sophisticated methods [79,80] in which the length change is measured with a micrometer or a linear variable differential transformer (LVDT) displacement transducer, one needs to be concerned with flow and with the sample geometry. For example, a resolution of the sample length change of $1 \mu\text{m}$ would correspond to a 3°C temperature change for the above material if the sample length were approximately 1 cm. On the other hand, measurements with thin films by such a technique would require temperature accuracy of approximately $3 \times 10^{-5}\text{C}$ if the film had a thickness of $100 \mu\text{m}$. Clearly, such “push rod” methods are not made for measuring the change of coefficient of thermal expansion of thin films in the thickness direction.

On the other hand, for research purposes, the expansion of films of thickness of hundreds of nm can be measured using X-ray [82,83] or neutron [84] reflectivity or ellipsometry [85]. Such techniques are clearly not for routine use. In the case of measurement of the thermal expansion coefficients of films having thicknesses between several μm and 100's of μm , there are interferometric methods [86] which are reasonably sophisticated. In addition, current research at NIST [87] and elsewhere [88] also suggests that very careful capacitance methods may be possible for measurement of the coefficient of thermal expansion in the thickness direction of thin films.

Also, for kinetic studies of structural recovery, dilatometry is the only method for which it is relatively easy to obtain more or less continuous data. When structural recovery is measured in, for example, differential scanning calorimetry (described below), one is required to make a separate measurement for each data point in time. This can be very cumbersome and time consuming.

5.3. Calorimetric techniques

Absolute calorimetry to measure the enthalpy is extremely difficult to carry out and it is much more common to measure the constant pressure heat capacity. Since the C_p is a second derivative (of the free energy) parameter, what is observed experimentally is a “jump” in going from the liquid to the glass. Modern scanning calorimetric apparatuses exist that make such measurements easy. In addition,

there are now methods available in which the temperature scan can be accompanied by a superimposed sinusoidal temperature fluctuation. In this case the measurement is referred to as temperature modulated differential scanning calorimetry or TMDSC. An analogous method in the time domain has also been developed recently that is referred to as step-scan DSC. Finally, a relatively new technique referred to as third harmonic dynamic heat spectroscopy (DHS) has been developed to measure apparent dynamic heat capacity and its changes to measure the glass transition. These techniques are discussed briefly below.

5.3.1. Differential scanning calorimetry (DSC)

Differential scanning calorimetry (DSC) is the most common method of measuring T_g (or T_f) due to its simplicity, speed, and use of small samples [89]. Currently on the market are both power-compensated and heat-flux DSCs. In the first, the differential heat flow is measured between a sample encapsulated in a pan and a reference pan. The sample and reference are in placed in separate furnaces and each is maintained at the program temperature. In heat flux DSC, the sample and reference are located in the same furnace and sit on a metal plate which is heated from the sides according to the temperature program; the differential temperature between the sample and reference is measured and, based on this, the differential heat flow needed to maintain them at the program temperature is calculated and reported. In any case for the scanning calorimetry methods, the apparent heat capacity of the sample C_{app} is related to the differential heat flow (HF) by the underlying heating rate (dT/dt):

$$HF = C_{app} \frac{dT}{dt} \quad (30)$$

assuming that the weight of the sample pan and reference pan are identical. In Eq. (30) we use the term apparent heat capacity because C_{app} contains both sensible heat effects (due to the true heat capacity C_p) as well as heat effects due to processes such as crystallization, chemical reaction, and structural recovery.

This brings us to the most important point for measuring T_g from DSC: to obtain an accurate measure of T_g , the effects of the annealing peaks and/or undershoots caused by structural recovery (see Section III) must be separated from the step change in the heat capacity that occurs at the glass transition. Before reviewing the procedures used to accomplish this, it is instructive to review how the annealing peak and undershoot arise. Fig. 25 shows a schematic of enthalpy versus temperature and C_{app} versus temperature. The solid line shows the ideal behavior during cooling at a given rate and during heating at the same rate. In this

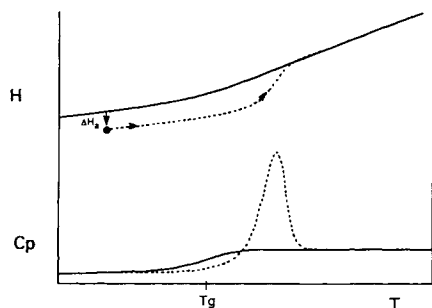


Fig. 25. Schematic of enthalpy and heat capacity as a function of temperature. The solid lines shows ideal behavior. The dashed line shows the behavior of an aged glass which displays an enthalpy overshoot at T_g .

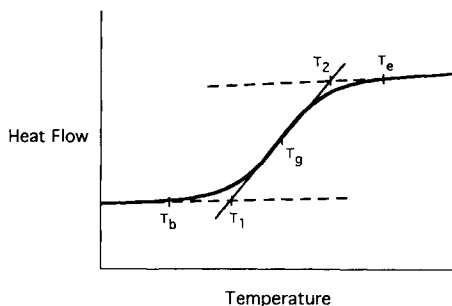


Fig. 26. Schematic of measurement of T_g from the step change in the heat capacity in DSC.

ideal case, there is no hysteresis between the cooling and heating curves, and the enthalpy curve shows simply a change in slope at T_g . The corresponding C_{app} curve (solid line) shows only the step change at T_g since C_{app} is simply the temperature derivative of the enthalpy (see Eq. (6)). From this step change, T_g is often defined as the temperature at which the heat capacity is mid-way between the extrapolated glass and liquid heat capacities, as shown in Fig. 26. Other relevant parameters that characterize the glass transition are ΔC_p , the difference between the extrapolated liquid (C_{pl}) and glassy (C_{pg}) heat capacities at T_g , and some measure of the breadth of the transition, such as T_b and T_e , the temperatures of the beginning and end of the transition. Wunderlich [89] also suggests reporting the intersections of the tangent at T_g with the extrapolated liquid and glass heat capacities. (These are T_1 and T_2 in Fig. 26, respectively).

In contrast to this ideal case, the dashed line in Fig. 25 shows the behavior of a glass on heating after having been aged isothermally. (Comparable behavior would be observed if the aged glass were obtained by cooling slowly relative to the heating rate.) As shown in the enthalpy schematic, the aged glass cannot follow the equilibrium line during heating but overshoots it before recovering back to equilibrium at a higher temperature. This phenomenon can be explained by the longer relaxation time of the aged glass (due to the fact that it is closer to equilibrium, see equations 13 and 14) and can be fit by the models of structural recovery, as was shown in Fig. 15. Since the apparent heat capacity is the derivative of the enthalpy curve, the enthalpic response of the aged glass results in an annealing peak in the DSC trace. The peak temperature does not correspond to T_g , but, for example, increases as the aging time and aging temperature increase for isothermal aging [90]. The annealing peak may even occur below T_g if the material is aged at a low enough temperature [6].

It is important that the endothermic annealing peak not be present when determining T_g . To a lesser extent, it is also important that exothermic undershoots not be present. These occur in rapidly quenched samples that then relax during the heating scan in the DSC. When an undershoot is present, the apparent value of ΔC_p at T_g is larger than the true value, and the value of T_g will generally be incorrect due not only to the fact that ΔC_p is not correct but also because undershoots are often followed by annealing peaks that occur because the material has aged during heating.

Annealing peaks and undershoots compromise one's ability to obtain T_g . Since these arise during heating for aged or rapidly quenched glasses, the most straightforward method of obtaining T_g by DSC is on cooling from the equilibrium state to below T_g . Such experiments have not been routinely performed in the past because temperature calibration of DSC instruments could not be performed on cooling because of supercooling that occurred in the crystalline standards traditionally used for calibration. Recently, however, a procedure for calibrating the DSC using liquid crystalline materials that do not supercool has been developed [91,92]. Hence, cooling experiments in the DSC are now possible provided that the user has adequate cooling capacity in their DSC. It is our opinion that cooling experiments are the experiment of choice for obtaining T_g from the DSC measurements when it is possible. It is also important to remark that the cooling rates that can be programmed on a commercial instrument are often not physically attainable because of the thermal mass and conductivity of the samples and apparatus. Hence, care should be taken when reporting high cooling rate data.

On the other hand, when one does perform heating experiments, the fictive temperature T_f , rather than T_g , can be obtained. Similar to T_g , T_f depends only on the cooling rate for a simple thermal history of cooling followed by heating in the DSC. When no annealing peak is present, T_f and T_g are comparable, as indicated in Fig. 25 for an ideal material in which there is no hysteresis between the cooling and heating scans. We designate T_f of the unaged glass, T_f' , following the convention introduced by Moynihan [93] to indicate that it can be used to define the glass transition temperature. (Instrument manufacturers, for the most part, do not currently make this distinction, calling T_f' the glass transition temperature T_g .)

On the other hand, when an annealing peak is present, the value of T_f is not comparable to T_g but is a measure of the structure (or departure from equilibrium) of the aged glass. The simplest way of obtaining T_f' for an aged glass is to use a procedure that involves two temperature scans: the first heating of the aged sample shows the annealing peak; immediately after completion the heating scan, the sample is cooled in the DSC and a second heating scan should not show the annealing peak and T_f' can be obtained. This procedure is somewhat cumbersome since the user needs to be present during the first scan to quench the sample at the proper time to insure that higher temperature processes (such as chemical reaction

or degradation) do not occur.

There are several methods for obtaining the fictive temperature T_f of an aged glass from DSC heating scans. The most common procedure involves integrating the heat capacity curve to obtain enthalpy versus temperature. T_f is then obtained simply by extrapolating the liquid and glassy lines to the point of intersection. This technique gives good results if the curvature of the baseline does not change over the temperature range of the measurement and if the glass line is readily extrapolated from deep in the glassy state. Errors on the order of several degrees can occur when an undershoot occurs during the heating scan and the glass line is extrapolated from the curved portion of the enthalpy curve rather than from lower temperatures. Moynihan [94] published the equation governing the procedure for obtaining the fictive temperature in aged glasses:

$$\int_{T_f}^{T > T_g} (C_{pl} - C_{pg}) dT = \int_{T < T_g}^{T > T_g} (C_{app} - C_{pg}) dT \quad (31)$$

On the heat capacity trace, the procedure for obtaining T_f from Eq. (31) is analogous to equating areas 1 and 2 in Fig. 27 [94,95]. A graphical procedure was recently proposed by Plazek and Frund [96], but it is not exactly equivalent to Moynihan's method. However, they reported agreement with the more exact method to within approximately 1.5°C for the thermal histories that they examined. This is probably due to compensating errors in the approximate method. In any event, because of the ease with which the integration can now be performed using computers, and the fact that DSC commercial software packages often perform the

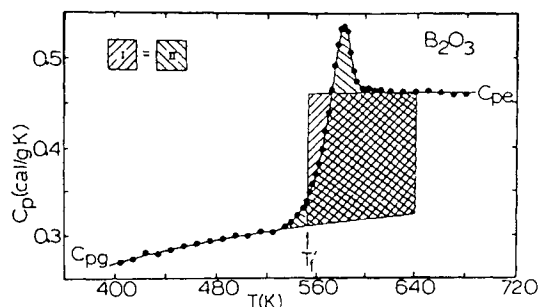


Fig. 27. Determination of the fictive temperature T_f from a DSC scan in which there is an annealing peak present. (Reprinted with permission of C.T. Moynihan. From Moynihan, C.T., Lee, S.-K., Tatsumisago, M. and Minami, T. (1996), Reference 93).

integration, the more exact procedures should be used. Here, though, care should be taken as the commercial software does not generally use Eq. (31).

Another method [1] for determining T_f for the aged glass requires both aged and unaged temperature scans to be obtained using the same heating rate. From the unaged scan, one obtains a value of $T_f(T_f')$ comparable to T_g . The difference in areas between the two curves gives the enthalpy difference between the aged glass and the unaged glass (ΔH_a in Fig. 25). From ΔH_a , T_f is calculated from:

$$\Delta H_a = \int_{T_f}^{T_f'} \Delta C_p(T) dT \tag{32}$$

Or, if one can assume that ΔC_p is constant over the temperature range from T_f to T_g :

$$T_f = T_f' - \frac{\Delta H}{\Delta C_p} \tag{33}$$

This method is shown graphically in Fig. 28. The disadvantage of this method is that two temperature scans must be performed. The advantage is that both T_f of the unaged glass (comparable to T_g) and T_f of the aged glass are obtained.

The absolute error in values of T_g obtained by DSC arise from thermal gradients in the sample itself, instrument calibration errors, uncertainty arising from the repeatability of the experiments, and baseline stability. The largest of these errors is often that due to the thermal gradients in the DSC sample. Thermal gradients arise from the relative low thermal conductivity of polymeric samples, and have been estimated by various researchers [14,98-102] to be on the order of

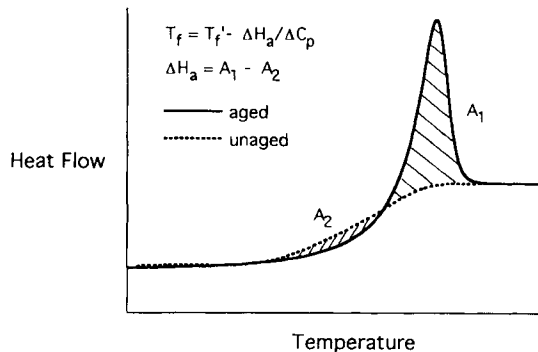


Fig. 28. Determination of fictive temperature T_f in a DSC measurement by using "aged" and "unaged" scans.

1°C for heating rates of 10°C/min. The average temperature in the sample on cooling will then be approximately 0.7°C higher than the program temperature, and on heating, approximately 0.7°C lower, resulting in systematic errors of this magnitude for the value of T_g or T_f (low for cooling scans, high for heating scans). The gradients in the sample can be minimized by using thinner samples and lower rates of heating or cooling when possible. Flynn [95] suggests correcting for thermal lag by heating (or cooling) the sample at various rates and extrapolating the value of T_f (or T_g) to zero heating rate and reporting the zero heating rate value. Obviously, use of Flynn's method would also require calibrating the instrument at the various heating (or cooling) rates used.

Errors due to the temperature calibration of the DSC are generally small, approximately 0.1°C at the point of calibration. Substantial errors (on the order of several degrees) may result, however, away from the point of calibration, and it is wise to run calibration standards close to and/or bracketing the expected T_g of the sample. The calibration standards should be run again after the calibration is performed in order to insure the accuracy of the temperature calibration.

Besides the systematic errors due to thermal gradients and temperature calibration, both of which can be accounted for, there are random errors associated with measuring T_g (or T_f). The experimental repeatability has been measured to be about 1°C for heating rates ranging from 1 to 100°C/min, being somewhat lower at higher heating rates [103]. The lack of repeatability may be attributed in part to differences in sample placement within the DSC [101], differences in thermal contact [14], and errors due to the repeatability of the data analysis. The error due to off-center sample placement was measured to be 0.1°C at 15°C/min [101]. The error in T_g due to poor thermal contact may be minimized by using a highly conductive grease between the sample pan and the furnace and by insuring that the bottom of the sample pan is flat [14]. The random errors due to the repeatability of the data analysis are generally at least 0.1°C. These latter errors arise from the fact that small changes in the slopes of the extrapolated liquid and glass lines change the value of T_g obtained; the latter problem is exacerbated for broad transitions and curved baselines. These errors may become systematic when the analysis is performed by a computer code always using the same algorithm.

The error in T_f for unaged glasses (those that were simply cooled from above T_g before the heating scan is performed) is similar to that for T_g . For aged glasses, the measurement of T_f by DSC is more dependent than T_g on baseline stability. In both Moynihan's method and the analogous method where the heat capacity curves are integrated to give enthalpy, the glass line should be extrapolated from deep in the glassy state, resulting in errors if the baseline is curved. The method utilizing an aged and unaged scan is less sensitive to baseline stability due to the fact that the scans can be run one after another resulting in less time for changes in the baseline to occur.

5.3.2. Temperature-Modulated Differential Scanning Calorimetry (TMDSC)

Temperature-modulated differential scanning calorimetry (TMDSC) is a relatively new thermal analysis technique in which the normal temperature scan used in DSC is generally overlaid by a low-frequency sinusoidal perturbation ranging from approximately 0.001 to 0.1 Hz [104]. A typical temperature history used in TMDSC is depicted schematically in Fig. 29. In the TMDSC method the sinusoidal heat flow required to maintain the desired sinusoidal temperature history is measured. The purported advantages of TMDSC include improved resolution and sensitivity, in addition to being able to separate overlapping phenomena [104].

The analysis of the TMDSC is currently the subject of debate [104-107]. However, the approach suggested by Reading [105] and used by both Wunderlich [108] and some commercial instrument manufacturers involves separating the heat flow into reversing and non-reversing components. A typical TMDSC scan with total, reversing, and non-reversing heat flows, is shown in Fig. 30.

The reversing component is obtained from the amplitude of the first harmonic of the heat flow using a Fourier transform of the data (or an approximation thereof), whereas the non-reversing heat flow is the difference between the average heat flow and the reversing heat flow [105]. The reversing heat flow is assumed to contain only information about the sensible heat, *i.e.*, that arising from the term $C_p dT/dt$. Consequently, at the glass transition, it has been suggested that the step change that would be observed if the glass were not aged will be obtained from the reversing heat flow, whereas the non-reversing heat flow will give the enthalpy difference between the aged glass and an unaged glass. If these assumptions were correct, one could obtain the same information from one TMDSC scan as from the two scan method described above (*i.e.*, where the first DSC scan is performed on the aged sample to give the annealing peak, and the second is performed on heating after cooling the sample immediately after the

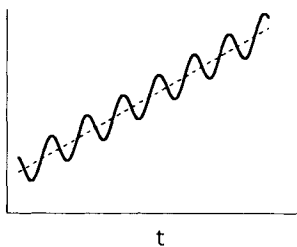


Fig. 29. Schematic of temperature as a function of time in a typical TMDSC heating ramp.

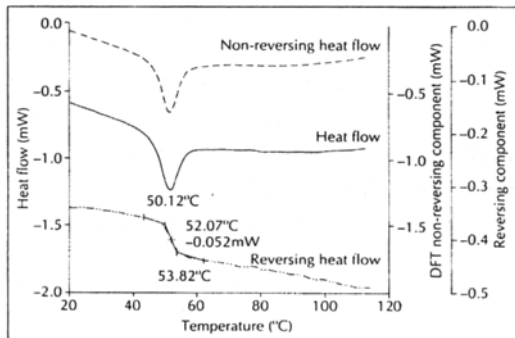


Fig. 30. Typical TMDSC results for an aged epoxy showing the total, reversing, and non-reversing heat flows. (Reprinted with permission of M. Reading. From Reference 104).

annealing peak is completed). Consequently one would obtain both T_f' of the unaged glass and T_f of the aged glass from this type of analysis of the TMDSC data. T_f' is obtained from the reversing heat flow; T_f is obtained from the area ΔH of the non-reversing heat flow, coupled with Eq. (33). The connection of the reversing heat flow to the step change at the glass transition implies that the glass transition for an unaged glass is a linear process and that it will only contribute to the first harmonic term in the sinusoidal heat flow signal. It also implicitly assumes that the recovery leading to the annealing peak will make no contribution to the first harmonic. There is no theoretical basis for these assumptions, but there is empirical evidence that they are good approximations in some cases.

We [109] have recently used the TNM model to simulate TMDSC experiments and showed that, in fact, the values of T_f' (or T_g) obtained from the reversing heat flow are within 1°C of expected values for TMDSC experiments in which there are at least four cycles through the transition. In the same work, we found that the values of ΔH predicted by the nonreversing heat flow could significantly differ from the expected values. Our findings are consistent with the experimental work of Montserrat [110], Hutchinson and Montserrat [111] and Reading and Luyt [112], both of whom found that particularly at long aging times, ΔH measured by TMDSC differed significantly from that measured by DSC. The errors in equating ΔH to the nonreversing heat flow arise from three sources: enthalpy undershoots, contributions of structural recovery to the first harmonic and/or contributions of the step change at T_g to higher harmonics, and interactions between the dynamic response of a low frequency probe to a high scanning rate. The latter source of error can be eliminated by insuring the conditions of linearity and stationarity [113] are met by having enough cycles through the transition. The first source of error can be minimized by insuring that undershoots are not present; this can be accomplished by insuring that the ΔC_p from the total and reversing heat flows are identical since undershoots result in an apparent increase in ΔC_p in the total heat flow. The second source of error, however, cannot be controlled and it can only be accounted for by using the nonlinear models of structural recovery to extract the data. Hence, it is concluded, that although T_f' or T_g can be obtained accurately from the reversing heat flow in TMDSC, T_f and ΔH of aged glasses cannot be obtained reliably.

In addition to being subject to errors introduced by the method of data analysis, the values of T_f' and T_f obtained from TMDSC, are also subject to the same errors (due to thermal gradients, temperature calibration, repeatability, and baseline stability) as measurements made using conventional DSC. Finally, it is important to be aware that the TMDSC may require even more care in the calibration of the instrument than is the conventional DSC because problems of phase lag introduced by thermal contact between the sample and pan, pan and

surface and within the instrument can lead to significant variability between samples [114].

5.3.3. Dynamic Heat Spectroscopy (DHS)

Dynamic heat spectroscopy (DHS) is both a calorimetric and a dynamic technique. It is, for a thermal measurement technique, a high-frequency (approximately 0.02 to 4000 Hz) technique. DHS was pioneered by Nagel and co-workers [115-120] and has also been used by Donth and co-workers [121,122] and others [123,124]. No commercial instruments are currently available, yet it appears to the current authors to offer great promise in the future as a measurement technique.

In DHS experiments, a resistive heater is surrounded by the sample fluid. The resistive heater is typically a thin wire or a thin metallic film deposited on a glass substrate. By applying a sinusoidally varying current to the resistive heater, the sample temperature at the heater surface oscillates sinusoidally but out-of-phase with the input current and at double the frequency. The third harmonic of the oscillating voltage in the heater is measured to obtain the temperature oscillations. Through solution of the initial boundary value problem for heat diffusion, the temperature at the heater surface is related to the product of an apparently complex quantity (C_p^* , κ^* , ρ^*), where the units of the heat capacity are $\text{J g}^{-1} \text{K}^{-1}$, κ is the thermal conductivity ($\text{W cm}^{-1} \text{K}^{-1}$) and ρ is the density (g cm^{-3}). It is unclear which of the three parameters should be complex, but Birge and Nagel, among others, have generally assumed that the complex quantity is C_p^* .

Birge and Nagel obtained specific heat spectroscopy data for glycerol in a temperature range from -54.2°C to -69.3°C and found that the apparent heat capacity is frequency dependent. They further analyzed the data in a fashion analogous to linear (viscoelastic) response theory to give an in-phase component $\kappa C_p'$ and a loss (out-of-phase) component $\kappa C_p''$. Some typical results from their measurements are shown in Fig. 31 where it can be seen that the point of the decrease or drop in the storage component and the peak in the loss component shift to higher frequencies as the measurement temperature increases.

Although several interpretations of the DHS experiments have been made in terms of various fluctuating quantities [115,125-128], such as enthalpy, temperature, entropy and thermal conductivity, we [129] have claimed that, in spite of the fact that ac calorimetry is performed above the nominal glass transition temperature, the high frequency of the measurements puts the experiments in the vicinity of the frequency-dependent T_g . In other words, in high-frequency ac calorimetry measurements, we are dealing not with equilibrium liquids but with non-equilibrium, high fictive temperature glasses where the response is dominated by structural recovery. In fact we have [129] successfully modeled the Birge and Nagel data, as shown in Fig. 31, using the TNM model of structural recovery

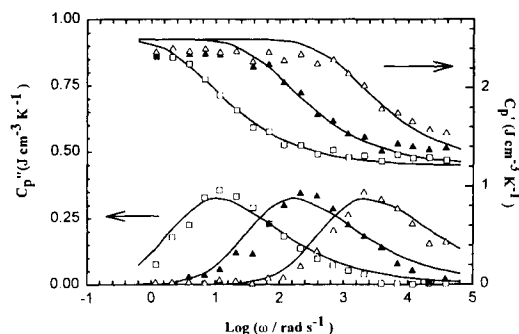


Fig. 31. Dynamic heat spectroscopy data for glycerol at temperatures of -54.2 , -68.1 , and -69.3°C (from left to right) obtained by Birge and Nagel¹⁰⁰. Lines are fits to the data using the TNM model¹¹⁴. (After Reference 129).

discussed earlier in this paper. Thus, T_g can be obtained from the DHS data in Fig. 29 as a function of frequency. Using the same definition as is often used in DSC, the frequency at which the transition occurs for a given measurement temperature would be taken to be the frequency at which the heat capacity is mid-way between the liquid and glassy values of C_p' . Alternatively, the transition can be defined as the maximum in C_p'' (or analogously at the inflection point of C_p'). The two definitions give similar results. For the glycerol data shown in Fig. 31: $T_g = -69.3^\circ\text{C}$ at 10 rad s^{-1} , -68.1°C at 200 rad s^{-1} , and -54.2°C at 1000 rad s^{-1} .

6. PHYSICAL AGING EFFECTS

In the above sections we have outlined the basics of structural recovery in polymers and have indicated how some of the effects observed are important in defining or assigning the glass transition temperature. In addition to this fundamental issue, it is also true that structural recovery actually has a large effect on the performance of materials for different applications. As a result of changes in the thermodynamic state variables, other properties also change in a process that has come to be known as physical aging—a term initially coined by Struik [17] in his landmark book on the subject. The field of physical aging has progressed beyond the work of Struik, yet remains very much grounded in his original findings. In the following sections we survey the important phenomenology of physical aging and its impact on material mechanical properties. We first examine the effect of structural recovery on the linear viscoelastic response of polymers. This is followed by a discussion of the response in the large stress or deformation regime (nonlinear viscoelastic response) and a presentation of the impact of aging on some engineering properties.

6.1. Linear viscoelastic regime

Referring to Fig. 9, we recall that after cooling a glass-forming liquid quickly through the glass transition, the volume and enthalpy responses of the non-equilibrium glass evolve with time in a process referred to as structural recovery. Fig. 10 is recalled to the reader to show the time evolution of the volume recovery. Associated with the changes in volume or enthalpy are changes in the linear viscoelastic properties that we refer to as physical aging. Struik [17] showed that the linear viscoelastic properties of a material during physical aging could be well described by a reduced time concept that we can refer to as time-aging time superposition. This is akin to the time-structure superposition discussed previously in describing the TNM-KAHR models of structural recovery.

The experimental evidence for time-aging time superposition comes from straight-forward experiments in creep, stress relaxation or dynamic mechanical measurements. The important point is to imagine that the experiment of interest looks like a ‘probe’ of the structural state of the aging glass. Then, it becomes an obvious requirement that the duration of the probe be such that the changes in glassy structure are negligible during the period of the probing experiment; *i.e.*, the measured response is unaffected by the underlying structural recovery. Interaction effects can arise in two ways. First, the probe is very long and the viscoelastic response function itself is altered by the structural recovery. Second, the probes themselves, if too close together interact as the longer probe remembers the earlier probe. To avoid these effects, Struik [17] proposed two protocols that, in the linear viscoelastic regime are equivalent. In the first, depicted schematically in Fig. 32, the material is quenched at time $t = 0$. A first probe is applied at an aging time $t_{e,1}$ and the sample is loaded or deformed for a time t_1 . In order to keep the structure changes negligible during the aging experiment, it is important that the time t_i be less than approximately one tenth of $t_{e,i}$. The second probe is then applied at $t_{e,2} \approx 2 t_{e,1}$, the third probe at $t_{e,3} \approx 2 t_{e,2}$, and so on. The result is that the time between probes is large compared to the loading time, hence the interactions between the succeeding probes is small as well.

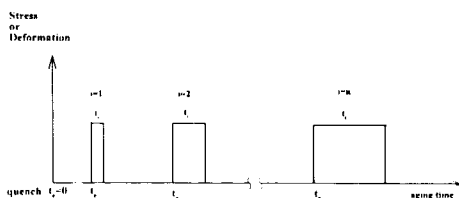


Fig. 32. Schematic of sequential loading history applied to samples after a quench for physical aging experiments. Note that the $t_{e,i}$ represent increasing aging times where $t_{e,i+1} \approx 2 t_{e,i}$. The t_i are the loading times and $t_i/t_{e,i} < 0.10$.

The second sort of protocol suggested by Struik [17] requires the material response at each aging time to be measured in a separate experiment. In the linear viscoelastic regime, this method and that described above are equivalent. However, in the nonlinear regime, it seems that it is very difficult to get the long probes to not be affected by the shorter probes and the two methods are not equivalent [17,130], although they give qualitatively similar results. The non-linear regime is discussed subsequently.

The results for an experiment using the sequential probe technique and for stress relaxation conditions are depicted in Fig. 33. As can be seen, as the time after the quench gets longer, the relaxation modulus increases. The increase is well described by considering that the response has shifted to longer relaxation times through the time-aging time superposition principle. This can be understood by considering a relaxation function $G(t)$:

$$G(z) = G_0 e^{-(z/\tau)^\beta} \quad \text{or} \quad G(z) = \sum_{i=0}^N G_i e^{-z/\tau_i} \quad (34)$$

where, as previously, z is the reduced time, now defined in terms of the aging time shift factor a_{te} required to superimpose the viscoelastic data:

$$z = \int_0^t \frac{d\zeta}{a_{te}} \quad (35)$$

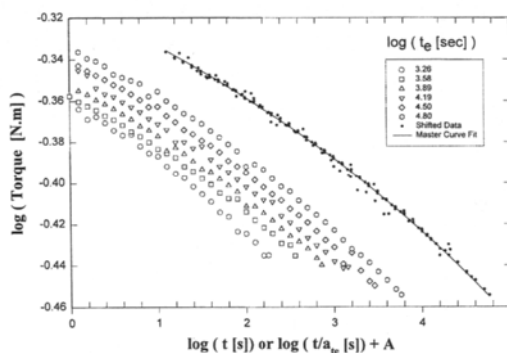


Fig. 33. Typical aging behavior for a polycarbonate quenched from above the glass transition to a temperature of 70°C where aging begins. The logarithms of the aging times t_e are depicted in the legend. The reduced or master curve is shifted one decade for clarity. (After Reference 130).

A very interesting result from the data of Struik [17] and others is that the aging time shift factor is readily represented as a simple power law in the elapsed aging time t_e :

$$a_{te} = a_o t_e^\mu \tag{36}$$

where a_o is a fitting parameter and μ is the double logarithmic shift rate determined from the slope of a plot of $\log a_{te}$ vs $\log t_e$:

$$\mu = \frac{d \log a_{te}}{d \log t_e} \tag{37}$$

Fig. 34 depicts a double logarithmic plot of the shift factor vs the aging time for polycarbonate aged at different temperatures. It is seen that the shift rate can depend on temperature. Also, we note, that for most materials, $\mu \leq 1$, although Struik [17] reported a value for polycarbonate of 1.2. Other researchers [130,131] have found that μ for polycarbonate is less than unity, which is more in line with values found for other polymers.

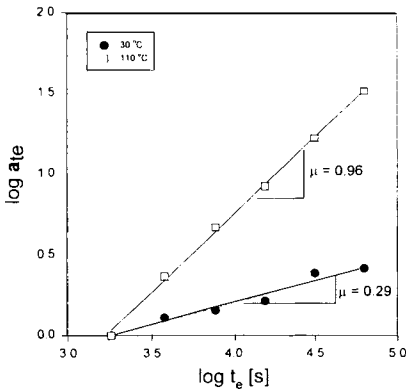


Fig. 34. Typical behavior for the aging time shift factor vs aging time for a polycarbonate glass showing that shift rate can depend on temperature.. Temperatures are as indicated in plot. (After Reference 130)

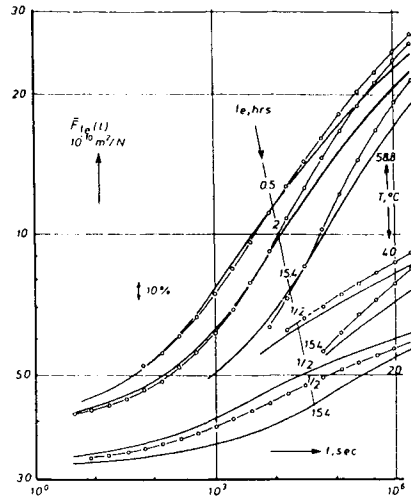


Fig. 35. Comparison of long term predictions from short term tests using reduced time concepts. (Reprinted with permission of L.C.E. Struik. From Struik, L.C. E. Reference 17).

The time-aging time superposition scheme has been widely used to describe the behavior of polymers during physical aging. It has been less widely used to actually make long term predictions of material behavior, although this issue was addressed by Struik [17] in his initial work. In Fig. 35 we see the predictions for long time behavior in creep for a poly(vinyl chloride) (PVC) glassy polymer. It can be seen that the agreement between prediction and experiment are reasonable. There has been significant recent work to use these principles to estimate the long term creep behavior of polymers and composites [132-136].

Finally, we note that the principles of time-aging time superposition are not readily applicable for materials in which there may be multiple relaxations. McKenna and Kovacs [137] found that the large β relaxation in poly(methyl methacrylate) led to violations of time-aging time superposition. However, recent work by Read and Tomlins [138,139] showed that one could treat several glassy polymers that have two relaxations by assigning different aging behaviors to the glassy α -dispersion and to the sub-glass β -dispersion. In their studies, the peaks were fairly broadly separated and they observed that the β -dispersion was essentially unchanged during aging and that the α -dispersion followed normal time-aging time superposition. In recent work one of us [140-142] was able to extend the approach of Read and Tomlins to both amorphous and semi-crystalline poly(ethylene naphthalate) (PEN) for which the β -relaxation is very strong and overlaps with the α -relaxation. This area of research requires further elaboration in the future to determine how such relaxations and their description with time aging time-superposition works for long term performance predictions. Finally, we also note that aging time superposition generally requires vertical shifting of the data. The fundamental physical reasons for such shifts is currently unknown.

6.2. Nonlinear viscoelastic regime

The picture of physical aging put forth above applies to the linear viscoelastic or small stress and deformation regime. However, upon increasing the magnitude of the 'probe' stress or deformation, the behavior changes. The observed phenomena are widely agreed upon, however, their interpretation is still controversial. There are several types of observation that have been made in examining the impact of structural recovery on the nonlinear viscoelastic response, the most common being an early one by Struik [17] that the shift rate μ decreases as the stress increases. Fig. 36 indicates schematically what this implies: at small stresses the change in the material response upon aging is greater than for large stresses at similar aging times. Fig. 37 shows data for the shift factor vs aging time for different applied 'probe' stress magnitudes for an epoxy glass [143]. Without considering the interpretation of this observation, it is clear that the impact of structural recovery on the aging response decreases as the applied stress increases.

The range of issues involved in establishing the cause of the decreased aging

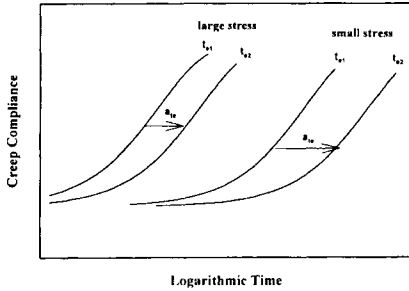


Fig. 36. Schematic of impact of structural recovery on small stress response compared to that for large stresses.

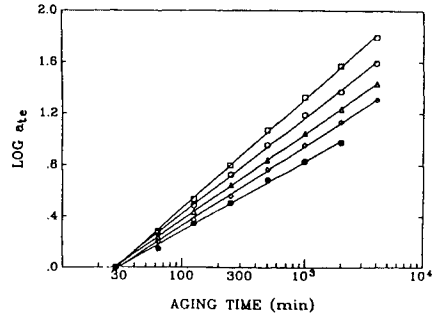


Fig. 37. Double logarithmic representation of the aging time shift factor a_{te} vs aging time t_c for an epoxy glass aged at T_k -13.2 K. Symbols represent results from tests in which aging response was “probed” at different levels of applied stress: (□) 1 M Pa; (○) 5 M Pa; (Δ) 10 M Pa; (◇) 15 M Pa; (●) 20 M Pa. (After Reference 143).

rate is rather large and the reader is referred to the original research for the continuing [143-154] discussion of the effects of structural recovery on large stress or deformation responses and vice-versa. Suffice it to say that the original interpretation was that erasure or rejuvenation of the material caused a decrease in the aging rate. The current debate revolves around the observation that, in spite of the reduced shift rates, mechanical equilibration times and volume recovery times seem to be unaffected by the magnitude of the applied stress [143,150,151,153,155]. Also, we note that some experiments have also been interpreted to imply acceleration [156,157] of aging due to the applied stress. Next, we, briefly, report some of the effects that structural recovery or physical aging have on the engineering properties of materials.

6.3. Engineering properties

It is evident that the time-dependent properties of polymers can vary considerably due to changes in the underlying structural state. In fact, the notion of ‘aging’ of the material, may not be a very good one. As seen above, the ‘physical aging’ of the viscoelastic properties actually leads to enhanced resistance to either stress (lower creep compliance or longer retardation times) or deformation (higher modulus or longer relaxation times). As we show below, one needs to consider the application, and sometimes the specific polymer, to know if the structural recovery or ‘aging’ is going to enhance or diminish the performance of the polymer.

6.3.1. Yield Strength

In his pioneering work on physical aging, Struik [17], observed that the yield strength is affected by the structural recovery. Clearly, because aging can cause an increase in the yield strength, the 'aging' effect is not necessarily detrimental to the performance of the polymeric resin. Struik reported his findings for thermoplastics, as has Bauwens [158] and others [159]. Not surprisingly, thermosets show similar effects as depicted in Fig. 38 from data by G'Sell and McKenna [160] for an epoxy glass. Clearly, the impact of aging is to improve the yield strength.

6.3.2. Failure related properties

The failure response of polymeric materials is, typically, time- or rate-dependent and consequently exhibits many of the same sort of changes as do the viscoelastic or yield strength due to structural recovery or during physical aging. For example, creep rupture lifetimes have been shown to vary with aging time in PMMA [161,162] and polystyrene [163]. Creep rupture lifetime is the time for failure under a constant (normally tensile) load and is a measure of the long term durability of a polymer. Fig. 39 shows the lifetime in creep rupture experiments for

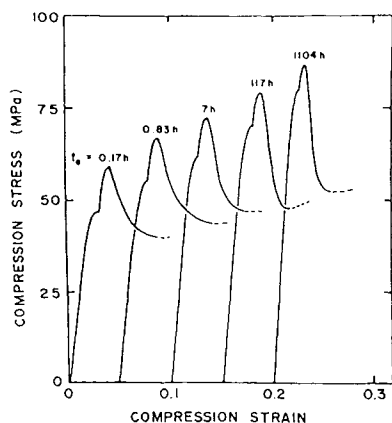


Fig. 38. Typical compression stress-strain curves obtained at $T_g - 10^\circ\text{C}$ for an epoxy and for different aging times as indicated. Each successive curve is offset arbitrarily for clarity. The tests were performed by loading at a slow rate until the yield maximum was reached and then the strain rate was increased by a factor of 10 to obtain full yield. (After Reference 160).

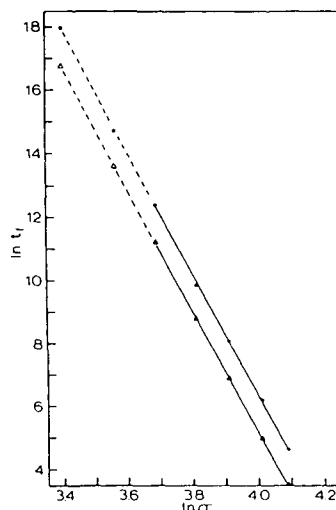


Fig. 39. Double logarithmic representation of the creep rupture time t_r vs applied stress for poly(methyl methacrylate) tested at 22.5°C . Triangles represent data obtained for freshly quenched samples. Circles are for samples aged at room temperature for 5 years. (After Reference 161).

PMMA that was either freshly quenched or aged at ambient temperature for 5 years. In this set of experiments it is clear that aging increases the lifetime of the material by a factor of about 2 to 3. However, the reader is cautioned about the beneficial effects of aging on the durability because failure mechanisms for different polymers may vary with resultingly different effects of aging on the failure response. In fact, Arnold [163] observed a decrease in lifetime for polystyrene in creep experiments upon aging.

To illustrate further the complexity that might be involved in the failure response of polymers in physical aging experiments, it is useful to examine the impact of aging on craze initiation and growth. Crazes are generally perceived to be precursors to the rupture of polymers as they precede crack growth across a sample (or object in service) [164-166]. In recent work, Gusler and McKenna [167] examined the impact of structural recovery on the craze initiation in both polystyrene and a styrene-acrylonitrile copolymer. As shown in Fig. 40 the craze initiation event depends on physical aging. Furthermore, subsequent to initiation, the craze must grow to cause ultimate failure. Fig. 41 shows a transition in the craze growth rate from rapid to slow for a styrene-acrylonitrile copolymer observed by Delin and McKenna [168]. Without attempting to explain these events because the observations themselves are relatively recent, it is clear that structural recovery or physical aging has an important impact on the craze behavior of polymeric glasses. Finally, we note that there are reports in the literature of increasing brittleness [17] and reduced fracture toughness [169] during physical aging. The

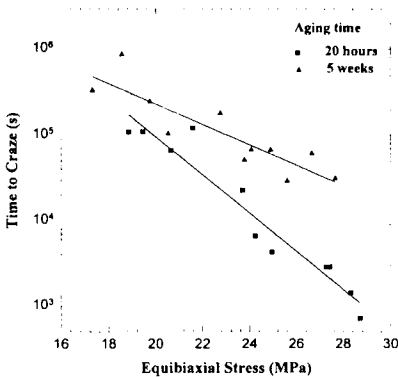


Fig. 40. Time to craze vs equibiaxial stress for a styrene-acrylonitrile copolymer at 22°C and at different aging times, as indicated. Solid lines are linear regressions to data and the dotted lines represent the 95 % confidence limit on the regression. (After Reference 167).

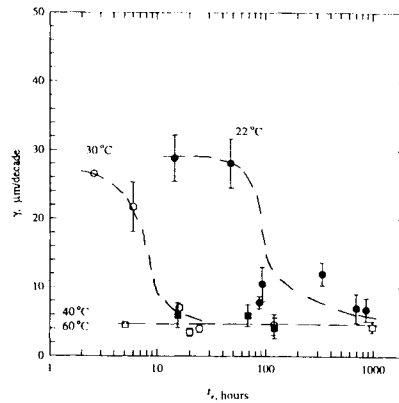


Fig. 41. Logarithmic craze growth rate vs logarithm of aging time for a styrene-acrylonitrile copolymer at different aging temperatures, as indicated. Plot shows transition from rapid growth to slower growth with aging at the two lower temperatures. (After Reference 168).

impact of aging on failure properties has yet to be fully elucidated and is a field that requires further work. The point for the reader to keep in mind, then, is that performance of polymeric materials can vary dramatically depending on the thermal history and the understanding of the phenomenology is linked to both the physics of structural recovery and the specific mechanisms involved in the failure event itself.

6.3.3. Residual stresses

As a final remark, the full structural recovery/physical aging process can be important in the development of residual stresses in materials. In fact, the original Narayanaswamy developments of the TNM model discussed in the early sections of this chapter were motivated by the issue of residual stresses in flat plate glass used in automotive windshields. In a very important continuation of the original developments of Narayanaswamy [23], Chambers and co-workers [170] implemented the TNM model to resolve a problem at the Department of Energy in which glass-to-metal seals were failing during manufacture. In this instance, it is desirable that an inner metallic core be hermetically sealed by a glass matrix. To prevent long term stress rupture (cracking, and see above) of the glass seal it is desirable that it be under compression. To place the glass seal under compression a surrounding metal jacket of higher thermal expansion is placed around the glass and the differential expansion was expected to result in a compression. However, it was observed that the seals cracked. Chambers and co-workers found, upon implementing the TNM model in a finite element code, that the residual stresses

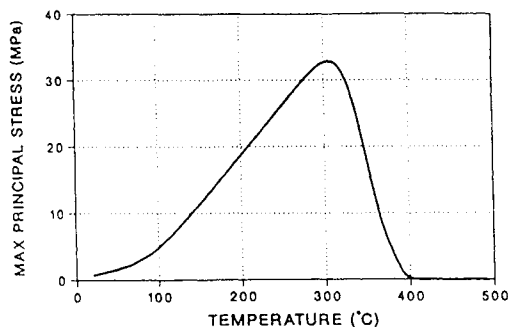


Fig. 42. Finite element model predictions of stress history upon cooling in a glass-metal seal. Tensile stress arises due to structural recovery effects. Thermo-elastic analysis resulted in an ambient temperature compressive stress of - 6.7 M Pa. (Reprinted with permission of The American Ceramic Society, From Chambers, R.S. , Gerstle, F.D. and Monroe, S.L., Reference 170).

during cooling actually went through a maximum in tension at about 100°C below the T_g and remained in tension until ambient temperatures. This counter-intuitive result is shown in Fig. 42. The model was subsequently run to choose cooling parameters such that the tensile maximum in the cooling stress was reduced and the final ambient residual stress in the glass was compressive. Clearly, an understanding of the structural recovery process in this instance led to a resolution of a very practical manufacturing problem. How this would impact, *e.g.*, composite material or any “bi-material” structures performance is a point that needs to be considered in design [171].

7. CONCLUDING REMARKS

In this chapter we have attempted to give the reader an understanding of the phenomena that surround the glass transition. We discuss both thermodynamic and kinetic aspects of glassy materials. In addition, it is hoped that the reader comes away with an appreciation both of the richness of the physics underlying the glass transition and the importance of understanding some of this physics when measuring the glass transition temperature and when measuring the properties of polymers upon traversing through the glass transition as well as at normal use temperatures. In polymers, this latter temperature is often relatively close to the glass transition (<125°C) and the material can undergo dramatic “physical aging” which impacts long term durability and the measurement of engineering properties. The chapter also attempts to indicate where the research needs are to make further advances in some of the underlying fundamentals of the glass transition (TNM, KAHR and KGAC phenomenological models) and the impact on engineering properties (yield, failure, residual stresses).

ACKNOWLEDGEMENTS

For GBM, parts of this work were completed at the Polymers Division, National Institute of Standards and Technology. For SLS, parts of the work were completed at the Department of Chemical and Petroleum Engineering at the University of Pittsburgh. The authors also gratefully acknowledge the support of Texas Tech University [GBM, SLS] and the J.R. Bradford Endowment in the College of Engineering [GBM].

REFERENCES

1. Assignment of the Glass Transition, Ed. by R. J. Seyler, ASTM STP 1249, American Society of Testing and Materials, Philadelphia, PA. (1994).
2. S. C. Glotzer, *Comp. Mater. Sci.*, 4 (1995) 283.

3. P. W. Anderson, *Science*, 267 (1995) 1616.
4. P. Ehrenfest, *Proceedings of the Koninklijke Nederlandse Akademie van Wetenschappen*, 36 (1933) 153.
5. R. A. Swalin, *Thermodynamics of Solids*, 2nd edition, Wiley, New York, 1972.
6. G. B. McKenna, *Comprehensive Polymer Science*. Vol. 2, *Polymer Properties*, (Eds By C. Booth and C. Price), Pergamon, Oxford, 1989.
7. J. J. Aklonis and W. J. MacKnight, *Introduction to Polymer Viscoelasticity*, Wiley, New York, 1983.
8. R. N. Haward, *The Physics of Glassy Polymers*, Wiley, New York, 1973.
9. A. J. Kovacs, *Fortschritte der Hochpolymeren-Forschung*, 3 (1963) 394.
10. J. E. McKinney and M. Goldstein, *J. Res. Natl. Inst. Stan.*, 78A (1974) 331.
11. D. M. Colucci, G. B. McKenna, J. J. Filliben, A. Lee, D. B. Curtiss, K. B. Bowman, J. D. Russell, *J. Polym. Sci., Phys. Ed.*, 35 (1997) 1561.
12. C. T. Moynihan, P. B. Macedo, C. J. Montrose, P. K. Gupta, M. A. DeBolt, J. F. Dill, B. E. Dom, P. W. Drake, A. J. Esteal, P. B. Elterman, R. P. Moeller, H. Sasabe, J. A. Wilder, *Ann. NY. Acad. Sci.*, 279 (1976) 15.
13. G. W. Scherer, *Relaxation in Glass and Composites*, Wiley, New York, 1986.
14. I. M. Hodge, *J. Non-cryst. Solids*, 169 (1994) 211.
15. A. Q. Tool, *J. Res. Natl. Inst. Stan.*, 37 (1946) 73.
16. A. Q. Tool, *J. Am. Ceram. Soc.*, 29 (1946) 240.
17. L. C. E. Struik, *Physical Aging in Polymers and Other Amorphous Materials*, Elsevier, Amsterdam, 1978.
18. J. M. Hutchinson, *Prog. Polym. Sci.*, 20 (1995) 703.
19. S. L. Simon and G. B. McKenna, *Proceedings of the North American Thermal Analysis Society*, (1997) 358.
20. S. L. Simon and G. B. McKenna, *Thermochim. Acta*, 307 (1997) 1.
21. G. B. McKenna, *J. Res. Natl. Inst. Stan.*, 99 (1994) 169.
22. G. B. McKenna, *J. Polym. Sci. Part B: Polym. Phys.*, 34 (1996) 2463.
23. O. S. Narayanaswamy, *J. Am. Ceram. Soc.*, 54 (1971) 491.
24. A. J. Kovacs, J. J. Aklonis, J. M. Hutchinson and A. R. Ramos, *J. Polym. Sci. Part B: Polym. Phys.*, 17 (1979) 1097.
25. R. Kohlrausch, *Annalen der Physik und Chemie von J. C. Poggendorff*, 91 (1854) 179.
26. G. Williams and D. C. Watts, *Trans. Faraday Soc.*, 66 (1970) 80.
27. S. L. Simon, D. J. Plazek, J. W. Sobieski, E. T. McGregor, *J. Polym. Sci. Part B: Polym. Phys.*, 35 (1997) 929.
28. A. Weitz and B. Wunderlich, *J. Polym. Sci. Part B: Polym. Phys.*, 12 (1974) 2473.
29. J. M. G. Cowie, S. Harris, I. J. McEwen, *Macromolecules*, 31 (1998) 2611.
30. S. L. Simon, J. W. Sobieski and D. J. Plazek, *Polymer*, 42 (2001) 2555.
31. C. R. Schultheisz, and G. B. McKenna, *Proc. NATAS 25th Annual Conference*, (1997) 366.
32. C. R. Schultheisz, NIST, Gaithersburg, MD 20899, (unpublished data).
33. J. J. Tribone, J. M. O'Reilly and J. Greener, *Macromolecules*, 19 (1986) 1732.
34. J. J. Tribone, J. M. O'Reilly, J. Greener, *J. Polym. Sci. Part B: Polym. Phys.*, 27 (1989) 837.
35. S. L. Simon, J.-Y. Park and G. B. McKenna, *Proceedings of the 29th Annual Conference of the North American Thermal Analysis Society*, Omnipress, Madison, WI, 2001, 435.

36. G. B. McKenna, C. A. Angell, R. W. Rendell, C. T. Moynihan, A. J. Kovacs, J. M. Hutchinson, M. Oguni, J. Oreilly, L. Struik, I. M. Hodge, J. C. Bauwens, E. Oleynick, S. Rekhson, G. Williams, S. Matsuoka, *J. Non-cryst. Solids*, 131 (1991) 528.
37. J. M. O'Reilly, *CRC Critical Reviews in Solid State and Materials Sciences*, 13 (1987) 259.
38. S. L. Simon, *Macromolecules*, 30 (1997) 4056.
39. A. J. Kovacs, J. M. Hutchinson and J. J. Aklonis, *The Structure of Non-Crystalline Materials*, New York, 1977.
40. L. C. E. Struik, *Polymer*, 38 (1997) 4677.
41. G. B. McKenna, M. R. Vangel, A. L. Rukhin, S. D. Leigh, B. Lotz, C. Straupe, *Polymer*, 40 (1999) 5183.
42. J. M. Caruthers, School of Chemical Engineering, Purdue University, Lafayette, IN. The work is primarily published in Ph.D. thesis referenced below. There is one publication with Lustig, Shay and Caruthers also referenced below.
43. S. R. Lustig, Ph.D. Thesis, Purdue University, Lafayette, IN, 1989.
44. D. M. Colucci, Ph.D. Thesis, School of Chemical Engineering, Purdue University, Lafayette, IN, 1995.
45. D. S. McWilliams, Ph.D. Thesis, Purdue University, Lafayette, IN, 1996.
46. S. R. Lustig, R. M. Shay, J. M. Caruthers, *J. Rheol.*, 40 (1996) 69.
47. B. D. Coleman, *Archives of Rational Mechanics and Analysis*, 17 (1964a) 1.
48. B. D. Coleman, *Archives of Rational Mechanics and Analysis*, 17 (1964b) 230.
49. W. Noll, *Archives of Rational Mechanics and Analysis*, 2 (1958) 197.
50. G. Adam and J. H. Gibbs, *J. Chem. Phys.*, 43 (1965) 139.
51. C. R. Schultheisz, D. M. Colucci, G. B. McKenna and J. M. Caruthers, *Mechanics of Plastics and Plastic Composites*, American Society of Mechanical Engineers, MD-68 and AMD-215 (1995) 251.
52. H. Vogel, *Phys. Z.*, 22 (1921) 645.
53. G. S. Fulcher, *J. Am. Ceram. Soc.*, 8 (1925) 339.
54. J. D. Ferry, *Viscoelastic Properties of Polymers*, 3rd. Edition, J. Wiley and Sons, New York, 1980.
55. M. L. Williams, R. F. Landel and J. D. Ferry, *J. Am. Chem. Soc.*, 77 (1955) 3701.
56. C. A. Angell, *Relaxations in Complex Systems* (Ed. By K.L. Ngai and G.B. Wright), National Technical Information Service, U.S. Department of Commerce, Springfield, VA 22161, 1985.
57. G. B. McKenna, G. Hadziioannou, P. Lutz, G. Hild, C. Strazielle, C. Straupe, P. Rempp and A. J. Kovacs, *Macromolecules*, 20 (1987) 498.
58. D. Huang and G. B. McKenna, *J. Chem. Phys.*, 114, (2001) 5621.
59. C. M. Roland, P. G. Santangelo and K. L. Ngai, *J. Chem. Phys.*, 111 (1999) 5593.
60. D. M. Colucci and G. B. McKenna, *Mater. Res. Soc. Symp. Proc.*, 455 (1997) 171.
61. K. L. Ngai and O. Yamamuro, *J. Chem. Phys.*, 111 (1999) 10403.
62. G. P. Johari, *J. Chem. Phys.*, 112 (2000) 8958.
63. A. K. Doolittle, *J. Appl. Phys.*, 22 (1951) 1471.
64. T. G. Fox Jr. and P. J. Flory, *J. Appl. Phys.*, 21 (1950) 581.
65. J. H. Gibbs and E. A. DiMarzio, *J. Chem. Phys.*, 28 (1958) 373.
66. E. A. DiMarzio and J. H. Gibbs, *J. Chem. Phys.*, 28 (1958) 807.
67. P. J. Flory, *Principles of Polymer Chemistry*, Cornell University Press, Ithaca, NY, 1953.
68. M. L. Huggins, *Ann. NY Acad. Sci.*, 43 (1942) 1.

69. E. A. DiMarzio, *Comp. Mater. Sci.*, 4 (1995) 317.
70. E. A. DiMarzio, *Ann. NY Acad. Sci.*, 371 (1981) 1.
71. J. Baschnagel, M. Wolfgardt, W. Paul and K. Binder, *J. Res. Natl. Inst. Stan.*, 102, 159.
72. G. B. McKenna and S.C. Glotzer, *J. Res. Natl. Inst. Stan.*, 102(2) (1997)
73. N. Bekkedahl, *Journal of Research, National Bureau of Standards*, 42 (1949) 145.
74. *Handbook of Chemistry and Physics*, 48th edition, The Chemical and Rubber Company, Cleveland, OH, 1967.
75. S. I. Naqui and I. M. Robinson, *J. Mater. Sci.*, 28 (1993) 1421.
76. F. Ramsteiner, *Polymer Testing*, 15 (1996) 401.
77. R. Pixa, V. Ledu and C. Wippler, *Colloid Polym. Sci.*, 266 (1988) 913.
78. R. S. Duran and G. B. McKenna, *J. Rheol.*, 34 (1990) 813.
79. American Society for Testing and Materials (ASTM) (1994), E-289-94, 1994 Annual Book of Standards, Volume 14.02, ASTM, Philadelphia, PA, 168.
80. American Society for Testing and Materials (ASTM) (1994), E-228-85, 1994 Annual Book of Standards, Volume 14.02, ASTM, Philadelphia, PA, 133.
81. American Society for Testing and Materials (ASTM) (1994), E-831-95, 1994 Annual Book of Standards, Volume 14.02, ASTM, Philadelphia, PA, 544.
82. G. Reiter, *Macromolecules*, 27 (1994) 3046.
83. W. E. Wallace, J. H. VanZanten, W. L. Wu, *Phys. Rev. E*, 52 (1995) R3329 Part A.
84. W. L. Wu, S. K. Satija, C. F. Majkrzak, *Polym. Commun.*, 32 (1991) 363.
85. J. L. Keddie, R. A. L. Jones, R. A. Cory, *Europhys. Lett.*, 27 (1994) 59.
86. N. Shimizu, J. Yuguchi, H. Takahashi, *Proceedings of the SPIE, The International Society for Optical Engineering*, 2873, 1996, 123.
87. M. Schen, F. I. Mopsik, W. Wu, W. E. Wallace, N. C. B. Tan, G. T. Davis, W. Guthrie, *Polym. Preprints*, 211 (1996) 218.
88. H. M. Tong, H. K. D. Hsuen, K. L. Saenger and G. W. Su, *Rev. Sci. Instrum.*, 62 (1991) 422.
89. B. Wunderlich, *Assignment of the Glass Transition*, ASTM STP 1249, 17, American Society for Testing and Materials, Philadelphia, PA, 1994.
90. I. M. Hodge and A. R. Berens, *Macromolecules*, 18 (1985) 1980.
91. J. D. Menczel and T. M. Leslie, *Thermochim. Acta*, 166 (1990) 309.
92. J. D. Menczel and T. M. Leslie, *J. Therm. Anal.*, 40 (1993) 957.
93. C. T. Moynihan, S.-K. Lee, M. Tatsumisago and T. Minami, *Thermochim. Acta*, 280/281 (1996) 153.
94. C. T. Moynihan, A. J. Esteal, M. A. DeBolt and J. Tucker, *J. Am. Ceram. Soc.*, 59 (1976) 12.
95. J. H. Flynn, *Thermochim. Acta*, 8 (1974) 69.
96. D. J. Plazek and Z. N. Frund Jr., *J. Polym. Sci. Part B: Polym. Phys.*, 28 (1990) 431.
97. S. E. B., *J. Polym. Sci. Part A-2*, 10 (1972) 1255.
98. J. M. Hutchinson, M. Ruddy, M. R. Wilson, *Polymer*, 29 (1988) 152.
99. M. J. Richardson, P. J. Burrington, *J. Therm. Anal.*, 6 (1974) 345.
100. M. A. Debolt, Ph.D. Thesis, Catholic University of America, Washington, D.C. 1976.
101. E. Donoghue, T. S. Ellis, R. E. Darasz, *Analytical Calorimetry*, Volume 5 (Ed. By, P. Gioll), Plenum, New York, 1984.
102. H. E. Bair, *Assignment of the Glass Transition*, ASTM STP 1249, 50, American Society for Testing and Materials, Philadelphia, PA, 1994.
103. J. R. Saffell, *Assignment of the Glass Transition*, ASTM STP 1249, 137, American Society for Testing and Materials, Philadelphia, PA, 1994.

104. S. L. Simon, *Thermochim. Acta*, 374 (2001) 55.
105. M. Reading, *TRIP*, 1 (1993) 248.
106. J. E. K. Schawe, *Thermochim. Acta*, 260 (1995) 1.
107. S. L. Simon, and G. B. McKenna, *Proceedings of the North American Thermal Analysis Society* (1998 In Press).
108. B. Wunderlich, Y. Jin and A. Boller, *Thermochim. Acta*, 238 (1994) 277.
109. S. L. Simon and G. B. McKenna, *Thermochim. Acta*, 348 (2000) 77.
110. S. Montserrat, *J. Polym. Sci., Polym. Phys. Ed.*, 38 (2000) 2272.
111. J. M. Hutchinson and S. Montserrat, *Thermochim. Acta*, 305 (1997) 257.
112. M. Reading and R. Luyt, *J. Thermal Anal. Calorim.*, 54 (1998) 535.
113. M. Merzlyakov and C. Schick, *Thermochim. Acta*, 330 (1999), 55.
114. S. Weyer, A. Hensel and C. Schick, *Thermochim. Acta*, 304/305 (1997) 267.
115. N. O. Birge and S. R. Nagel, *Phys. Rev. Lett.*, 54 (1985) 2674.
116. N. O. Birge, *Phys. Rev. B*, 34 (1986) 1631.
117. N. O. Birge and S. R. Nagel, *Rev. Sci. Instrum.*, 58 (1987) 1464.
118. S. R. Nagel, *Phase Transitions and Relaxation in Systems with Competing Energy Scales*, (Eds T. Riste and D. Sherrington), Kluwer Academic Publishers, Netherlands, 1993.
119. P. K. Dixon and S. R. Nagel, *Phys. Rev. Lett.*, 61 (1988) 341.
120. P. K. Dixon, *Phys. Rev. B*, 42 (1990) 8179.
121. M. Beiner, J. Korus, H. Lockwenz, K. Schroter and E. Donth, *Macromolecules*, 29 (1996) 5183.
122. E. Donth, M. Beiner, S. Reissig, J. Korus, F. Garwe, S. Vieweg, S. Kahle, E. Hempel and K. Schroter, *Macromolecules*, 29 (1996) 6589.
123. N. Menon, *J. Chem. Phys.*, 105 (1996) 5246.
124. H. Leyser, A. Schulte, W. Doster and W. Petry, *Phys. Rev. E*, 51 (1995) 5899.
125. W. Götze and A. Latz, *J. Phys-Condens. Mat.*, 1 (1989) 4169.
126. J. Jackle, *Physica A*, 162 (1990) 377.
127. J. K. Nielsen and J. C. Dyre, *Phys. Rev. B*, 54 (1996) 15754.
128. D. W. Oxtoby, *J. Chem. Phys.*, 85 (1986) 1549.
129. S. L. Simon and G. B. McKenna, *J. Chem. Phys.*, 107 (1997), 8678.
130. P. A. O'Connell and G. B. McKenna, *Polym. Eng. Sci.*, 37 (1997) 1485.
131. J. L. Sullivan, *Composite Science and Technology*, 39 (1990) 207.
132. R. D. Bradshaw and L.C. Brinson, *Composite Science and Technology*, submitted (1998).
133. R. D. Bradshaw and L. C. Brinson, *Polym. Eng. Sci.*, 37 (1997) 31.
134. T. S. Gates and M. Feldman, *NASA Langley Research Center TM 109114* (1994).
135. P. E. Tomlins and B. E. Read, *Polymer*, 39 (1998) 355.
136. P. E. Tomlins, *Polymer*, 37 (1996) 3907.
137. G. B. McKenna and A. J. Kovacs, *Polym. Eng. Sci.*, 24 (1984) 1131.
138. B. E. Read, G. D. Dean and P. E. Tomlins, *Polymer*, 29 (1988) 2159.
139. G. D. Dean, B. E. Read and G. D. Small, *Plast. Rub. Proc. Appl.*, 9 (1988) 173.
140. M. L. Cerrada and G. B. McKenna, *Time Dependent and Nonlinear Effects in Polymers and Composites*, (Ed. R.A. Schapery), American Society of Testing and Materials, Special Technical Publication, STP 1357 (1998 submitted).
141. M. L. Cerrada, G.B. McKenna, J. M. O'Reilly, J. Greener and J. R. Gillmor, *Society of Plastics Engineers, ANTEC 98, II* (1998) 2198.
142. M. L. Cerrada and G. B. McKenna, *Macromolecules*, 33 (2000) 3065.

143. A. Lee and G. B. McKenna, *Polymer*, 31 (1990) 423.
144. L. C. E. Struik, *Polymer*, 38 (1997) 4053.
145. O. A. Hasan and M. C. Boyce, *Polymer*, 34 (1993) 5085.
146. M. Aboulfaraj, C. G'Sell, D. Mangelinck and G. B. McKenna, *J. Non-Cryst. Solids*, 172-174 (1994) 615.
147. T. Ricco and T. L. Smith, *Polymer*, 26 (1985) 1979.
148. T. L. Smith, G. Levita and W.K. Moonan, *J. Polym. Sci., Polym. Phys. Ed.*, 26 (1988) 875.
149. A. F. Yee, R. J. Bankert, K. L. Ngai and R.W. Rendell, *J. Polym. Sci., Polym. Phys. Ed.*, 26 (1988) 2463.
150. M. M. Santore, R. S. Duran and G. B. McKenna, *Polymer*, 32 (1991) 2377.
151. G. B. McKenna, *J. Non-Cryst. Solids*, 172-174 (1994) 756.
152. G. B. McKenna and L. J. Zapas, *Polym. Eng. Sci.*, 26 (1986) 725.
153. W. K. Waldron Jr., G. B. McKenna and M. M. Santore, *J. Rheol.*, 39 (1995) 471.
154. G. B. McKenna and L. J. Zapas, *J. Polym. Sci., Polym. Phys. Ed.*, 23 (1985) 1647.
155. G. B. McKenna, Y. Leterrier and C. R. Schultheisz, *Polym. Eng. Sci.*, 35 (1995) 403.
156. F. A. Myers, F. C. Cama and S. S. Sternstein, *Ann. NY Acad. Sci.*, 279 (1976) 94.
157. D. M. Colucci, P. A. O'Connell and G. B. McKenna, *Polym. Eng. Sci.*, 37 (1997) 1469.
158. J. C. Bauwens, *Plast. Rub. Proc. Appl.*, 7 (1987) 143.
159. O. A. Hasan, M. C. Boyce, X. S. Li, S. Berko, *J. Polym. Sci. Part B: Polym. Phys.*, 31 (1993) 185.
160. C. G'Sell and G. B. McKenna, *Polymer*, 33 (1992) 2103.
161. J. M. Crissman and G. B. McKenna, *J. Polym. Sci., Polym. Phys. Ed.*, 25 (1987) 1667.
162. J. M. Crissman and G. B. McKenna, *J. Polym. Sci., Polym. Phys. Ed.*, 28 (1990) 1463.
163. J. C. Arnold, *J. Polym. Sci., Polym. Phys. Ed.*, 31 (1993) 1451.
164. R. P. Kambour, *Encyclopedia of Polymer Science and Engineering*, Vol. 4, 2nd Edition, John Wiley and Sons, New York, 1986, 299.
165. E.J. Kramer and L. L. Berger, *Adv. Polym. Sci.*, 91/92 (1990) 1.
166. A. S. Argon and M. M. Salama, *Philosophical Magazine*, 36 (1977) 1217.
167. G. M. Gusler and G. B. McKenna, *Polym. Eng. Sci.*, 37 (1997) 1442.
168. M. Delin and G. B. McKenna, *SPE ANTEC*, (1998) 1668.
169. T. D. Chang and J. O. Brittain, *Polym. Eng. Sci.*, 22 (1982) 1228.
170. R. S. Chambers, F. D. Gerstle and S. L. Monroe, *J. Am. Ceram. Soc.*, 72 (1989) 929.
171. G. B. McKenna, *J. Res. Natl. Inst. Stan.*, 99 (1994) 169.

This Page Intentionally Left Blank

Chapter 3

Mechanical relaxation processes in polymers

S. Matsuoka

Polymer Research Institute, Six Metrotech Center
Brooklyn, New York 11201*

1. WHAT DO WE MEAN BY THE RELAXATION PROCESS

The thermodynamic equilibrium is described by the minimum Gibbs free energy, $H-TS$. If a force is applied, the free energy will rise. When it is released, it will return to the original minimum free energy. The process involves a change in the shape, volume, and entropy. A typical solid material, such as a metal or a glass, is considered elastic, because it responds by almost instantaneous deformation, with the speed of sound. On the other extreme from the elastic material is a liquid such as water and oil. Its viscosity is the measure of resistance to the force by the internal friction. The rate of deformation or the flow rate, increases with a greater force. The steadily flowing liquid is in a dynamic equilibrium from the thermodynamic viewpoint.

A viscoelastic material exhibits some attributes of solid and liquid materials. It exhibits both 'instantaneous' and delayed response. To reach an equilibrium, it takes time. The time constant for this process is the relaxation time. In thermodynamic terms, the relaxation process is the process which takes time for a perturbed state with higher energy to return to the equilibrium state.

1.1. On the experimental scale

A stress relaxation experiment follows the above definition of relaxation closely. The sample is subjected to an initial strain and held when the stress is measured. The strain is a deformation per unit dimension in the sample, such as cm/cm. The stress, or the force per unit area, initially rises, with the speed of the

* 161 Thackeray Drive, Basking Ridge, NJ 07920

sound. The instantaneous stress divided by the strain is the *unrelaxed* modulus, E_0 for tension, and G_0 for shear. As the strain is maintained, the liquid-like behavior begins to manifest and a local relaxation of mechanical energy begins. The stress begins to decrease. The rate of mechanical relaxation is measured by the time dependent stress divided by the fixed strain, called the relaxation modulus, $E(t)$ or $G(t)$. When the modulus in this case is independent of the strain magnitude, it is a material characterization parameter. The response is termed linear viscoelasticity.

The relaxation process can be analyzed as a rate process, with the relaxation time as the time constant, *i.e.*,

$$\frac{dG}{dt} = -\frac{G}{\tau} \quad (1)$$

where τ is the relaxation time. The solution of the above differential equation is given by the equation:

$$G(t) = G_0 \exp(-t/\tau) \quad (2)$$

Eq. (1) is a linear differential equation and thus both G_0 and τ in Eq. (2) are constant.

When this viscoelastic material is subjected to a constant rate of deforming, as in the steady flow of a liquid, the shear stress σ will increase initially fast, but later reaches a plateau, according to the following equation:

$$\sigma = \dot{\gamma} G_0 \tau [1 - \exp(-t/\tau)] \quad (3)$$

which can be obtained by integrating the incremental stresses with the use of $G(t)$ from Eq. (2). $\dot{\gamma}$ is the strain rate, $d\gamma/dt$. The linear viscoelastic steady state viscosity η_{ss} is obtained from Eq. (3) at $t \rightarrow \infty$, and

$$\eta_{ss} = G_0 \tau \quad (4)$$

which equals the area under the curve of the relaxation modulus $G(t)$.

When the viscoelastic material is subjected to a constant force, the strain increases with time. The ratio of the increasing strain over the constant stress is the creep compliance. The equilibrium steady state in creep experiment is in the state of the steady state flow, with the rate of the stress/viscosity. Thus the creep compliance $J(t)$ is described by the equation:

$$J(t) = J_0 + \Delta J \left[1 - \exp\left(-\frac{t}{\tau}\right) \right] + \frac{t}{\eta_{ss}} \quad (5)$$

where J_0 is the initial elastic compliance, and ΔJ is the total amplitude of relaxation.

Eq. (5) is derived from a rate process equation, $dJ/dt = -J/\tau$, comparable to Eq. (1) for the relaxation modulus, but Eqs. 3 and 5 are mathematically incompatible, *i.e.*, one and the same material cannot exhibit behavior that follow both. This will be explained later in more detail.

Most real materials exhibit multiple relaxation modes. The relaxation modulus of a real material must be described as a sum of many relaxation moduli, *i.e.*,

$$G(t) = \sum_i G_i \exp\left(-\frac{t}{\tau_i}\right) \quad (6)$$

G_i is the intensity of the i -th mode. G_i as function of τ_i and is called the relaxation spectrum, often in the integral form rather than the discrete form illustrated here. Similarly, ΔJ_i is called a retardation spectrum. ΔJ_i can be derived from G_i , and vice versa without assuming a functional form. A distribution in relaxation times arises for many reasons. Copolymers, blends, and composites manifest a viscoelastic response that is the sum of the components. Homopolymers themselves also exhibit multiple modes of relaxation, owing to their molecular weight distribution. Even purely monodisperse homopolymers exhibit multiple modes, as different lengths of molecular strands exhibit different relaxation times.

A viscoelastic experiment can be performed with a periodic cycle of stress and strain. With the strain cycle, $\gamma(t) = \gamma_a \sin \omega t$, the stress must also be a sinusoidal form with the same frequency, but the strain lags the stress in phase angle due to the delayed (viscous) component of the behavior. By integrating the product of the modulus with respect to the sinusoidal strain, the stress after reaching the steady state is obtained, *i.e.*,

$$\sigma(t) = \frac{G_0 \omega^2 \tau^2}{1 + \omega^2 \tau^2} \gamma_a \sin \omega t + \frac{G_0 \omega \tau}{1 + \omega^2 \tau^2} \gamma_a \cos \omega t \quad (7)$$

where ω is the circular frequency in radians / s. The first and second modulus terms are called the in-phase (storage) modulus and the loss modulus, G' and G'' , respectively. The in-phase modulus G' is,

$$G' = \frac{G_0 \omega^2 \tau^2}{1 + \omega^2 \tau^2} \tag{8}$$

and the loss modulus, G'' is,

$$G'' = \frac{G_0 \omega \tau}{1 + \omega^2 \tau^2} \tag{9}$$

As can be seen from the two equations above, at very low frequency relative to the relaxation time, *i.e.*, $\omega \ll 1/\tau$, the plot of $\log G'$ versus $\log \omega$ will have the slope of 2, while $\log G''$ versus $\log \omega$ will have the slope of 1. This corresponds to the regime of the longest relaxation time called the *terminal relaxation zone*. It is an important parameter in the melt viscoelasticity.

If there are multiple relaxation times, the plot of in-phase modulus G' versus ω takes an appearance of the mirror image of the relaxation modulus versus time, over the most time range except at the terminal zone where the slope of the log-log plot for the latter is not -2 but $-t/\tau$ and bends down. The loss modulus versus ω is about the same as G_i versus $1/\tau_i$, the relaxation spectrum, and as such, G'' is often used to analyze the distribution of relaxation times. When analyzing experimental data, the discrete spectrum assigned at every half decade interval in ω proves practical and useful.

The complex dynamic modulus $G^* = G' + j G''$, where $j = \sqrt{-1}$, is by definition the reciprocal of the complex compliance, $J^* = J' - jJ''$, obtained from the same raw data. From this, a theoretical relationship between the relaxation modulus and the creep compliance can be derived:

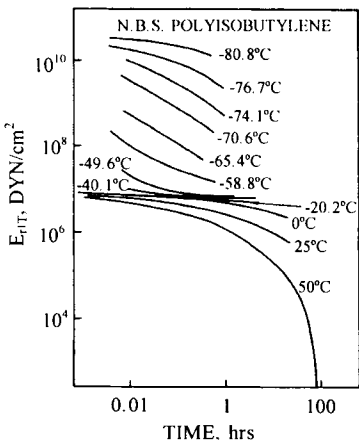


Fig. 1. Relaxation data for poly-isobutylene taken at various temp.

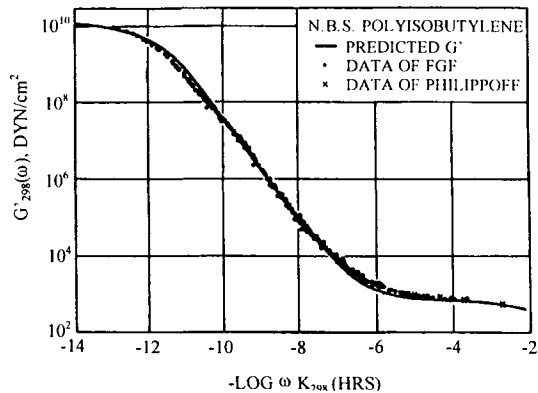


Fig. 2. Master Curve from Fig. 1 created by T-t superposition.

$$\int_0^t G(t-x)J(x)dx = t \quad (10)$$

By substituting $G(t)$ in Eq. (2) and $J(t)$ in Eq. (5), one finds that ΔJ must be 0 in order for Eq. (10) to hold. It simply means that Eq. (2), the Maxwell model, would behave as a Newtonian fluid under a constant stress. The real source of this inconsistency is in the assumption that the compliance is the sum of the instantaneous strain, the time dependent strain, and the steady flow strain. The time-dependent mechanical strains are not additive, but levels of energy are.

However, the electrical equivalent of the compliance is physically realistic. The dielectric permittivity (dielectric constant) is based on the capacitive and resistive energy components arising from the dipole displacement current. $\Delta\epsilon$ for dielectric relaxation is the equivalent of ΔJ , and it is used as the basis of analysis for the dynamics of relaxation processes.

The relaxation spectrum of a typical amorphous polymer can span over more than 14 decades of time. This entire range is practically impossible for experiment, even the span in time scale from the highest frequency of 100 Hz in dynamic test to the longest time of 1 year in the relaxation test is less than 10 decades. The dielectric data of up to 10 MHz would add another 4 decades to bring it to 4 decades. A plot of relaxation function data over the entire span in time or frequency to include all significant relaxation modes at a reference temperature is called a master curve.

In the past, the master curves, such as shown in Fig. 2 above, have been constructed by combining the data obtained over a short time span at various temperatures, as shown in Fig. 1, both from Catsiff and Tobolsky [1]. The time-temperature superposition is possible because each relaxation mode has the same temperature dependence, and the entire spectrum could be shifted with temperature without changing the distribution. In other words, observing a database taken at a given temperature is to be looking through a window of time, a portion of a master curve that shifts in its entirety with a choice of temperature. The 'shift factor' tells how much in log time (or frequency) to shift from the reference temperature to the temperature of interest, defined by $\log a_T$. The shift factor a_T is the ratio of the corresponding relaxation time τ_i at T over the same τ_i at the reference temperature for the master curve, *i.e.*, $\log a_T = \log (\tau_T / \tau_{ref})$.

There are three well-known empirical equations that describe the shift factors. They are all two parameter equations and are, as expected, exactly equivalent and interconvertible. They are the WLF (Williams-Landel-Ferry) equation [2], Doolittle's free volume equation [3], and the Vogel-Fulcher equation [4] as shown below:

Williams-Landel-Ferry (WLF) Formula:

$$\log a_T = \frac{c_1(T - T_{ref})}{c_2 + T - T_{ref}} \quad (11)$$

where c_1 , and c_2 are parameters, T_{ref} is the reference temperature. If T_g is chosen as T_{ref} , then $c_1 \cong 17$ and $c_2 \cong 50\text{K}$.

Doolittle Free Volume Equation:

$$\log a_T = \frac{1}{\alpha_f(T - T_0)} - \frac{1}{\alpha_f(T_{ref} - T_0)} \quad (12)$$

where α_f is the thermal expansion coefficient of the free volume fraction, and T_0 is the extrapolated temperature toward zero free volume.

Vogel Formula (of Vogel-Fulcher Formula):

$$\log a_T = \frac{\Delta\mu}{2.3R} \left[\frac{1}{T - T_0} - \frac{1}{T_{ref} - T_0} \right] \quad (13)$$

where c is a constant, $\Delta\mu$ is an energy parameter (~ 3.3 kcal) and R is the gas constant. T_0 is the zero rate glass temperature and is about 50K below T_g of a quenched glassy state. The significance of the values of these parameters will be discussed in molecular terms in section 1.2.

In contrast to these formulas, the conventional rate process will result in the shift factor with the constant activation energy ΔE .

Arrhenius (constant activation energy) formula:

$$\log a_T = \frac{\Delta E}{2.3R} \left[\frac{1}{T} - \frac{1}{T_{ref}} \right] \quad (14)$$

which has been found to apply to the β -relaxation, the crystalline α_c -relaxation, and for the main α -relaxation below T_g in the glassy state.

1.2. On the molecular scale

The molecular analysis of viscoelasticity assumes that the intensity of each mode of relaxation reflects the population of the related molecular motion. The unrelaxed modulus G_i for the i^{th} mode is proportional to the concentration (g/cm^3) divided by the molecular weight of the segmental species related to that mode of relaxation with τ_i . We prefer to think of the relaxation modulus as the

instantaneous elastic strain energy (erg/cm^3) raised per unit strain (cm/cm), which equals the dimension of the modulus, dynes/cm^2 . If we consider the distribution of stress tensors as the distribution of the (scalar) strain energy, then the additivity of the moduli or the viscosity in proportion to the relative amount of each component make sense. Certainly, one does not expect the stress nor strain to be uniform in a heterogeneous structure. The G_i as normalized strain energy is a material dependent linear coefficient, and it is expected to be proportional to the local concentration of related species. The same can be said of the dielectric intensity $\Delta\epsilon$, but for the compliance ΔJ it is less clear.

For a polymer molecule, the highest elastic modulus is exhibited with the bending of the angle between the consecutive main chain bonds. This is the hardest degree of freedom, in comparison to the softer degrees of freedom such as their rotation. The highest possible modulus in polymers should be nearly equal to the modulus of diamond, $5.5 \times 10^{12} \text{ dynes/cm}^2$. The high pressure extruded polyethylene by Porter [5] is presumably of a structure in which no rotation of bonds is allowed, and the modulus is of the order of near $10^{12} \text{ dynes/cm}^2$. In terms of per mol of bonds, this energy is 1.4×10^{13} ergs per unit strain per mol of bonds. For the diamond, the bending of C-C bonds, locked in four ways, is expected to increase the stiffness. The computer modeling by Suter [6] reveals that the much of the deformation comes from the rotation of bonds, and as such,, the modulus is expected to be perhaps an order of magnitude softer. One can estimate the rotational stiffness of the main chain bond in a glassy polymer, *e.g.* polystyrene, from the fact that at yield point, the rotation will go over the energy barrier for the conformational change, 3.3 kcal, or 1.4×10^{11} ergs per yield strain per mol of conformer. Assuming the yield strain of 4% for polystyrene (in compression) and the conformer size to be 54, G_0 of $6.4 \times 10^{10} \text{ dynes/cm}^2$ is obtained. This is probably the upper limit for the unrelated modulus in amorphous polymers.

At the longer extreme of time, the polymer viscoelasticity involves an entire molecule or even many molecules in entanglement. The elastic energy arises from the tendency for rubber like molecules to assume the random conformations. The molecular conformations are changing constantly, with the speed of brownian motion, in pico seconds, and we shall consider this to be the instantaneous time scale. (Actually, what we consider the unrelated modulus for entanglement is much slower than this.) When the molecule is stretched, the number of conformations is reduced from Ω_u to Ω , and the entropy from S_u to S . Therefore,

$$S - S_u = k \ln (\Omega_u / \Omega) \quad (14)$$

which is evaluated by any of the several methods involving the statistical mechanics of the rubber like elasticity. The following equation is obtained for the change in Helmholtz free energy under the tensile strain ε :

$$T(S - S_u) = -\frac{1}{2}k[(1 + \varepsilon)^2 + 2(1 + \varepsilon) - 3] \quad (15)$$

for one mole of random coils. Notice the molecular weight of the polymer chain does not enter here. k is Boltzmann constant.

To obtain the stress, or the free energy change per unit strain, we differentiate above, $dT\Delta S/d\varepsilon$, to obtain

$$\frac{dT(S - S_u)}{d\varepsilon} = RT[(1 + \varepsilon) + 1] \quad (16)$$

The modulus is the stress at unit strain, $\varepsilon = 1$, but to convert it from per mol of molecule to the unit volume, it must be multiplied by (density ρ /molecular weight M); hence, for the tensile modulus E_0 is obtained by the equation:

$$E_0 = \frac{3\rho RT}{M} \quad (17)$$

Now, utilizing the relationship $E = 2(1 + \nu)G$ between the tensile and shear moduli, where ν is the Poisson ratio, the shear modulus G_0 in dynes/cm² is obtained:

$$G_0 = \frac{\rho RT}{M} \quad (18)$$

This elastic shear modulus is an entropic spring constant and is a very weak force constant. If we substitute the conformer molecular weight 54 of polystyrene, in an attempt to obtain the highest value by substituting one bead instead of a polymer molecule, G_0 of 4.7×10^8 dynes/cm² is obtained, that is 100 times smaller than the elasticity estimated from the rotation of polystyrene conformers. In the condensed state, at higher frequencies, the rubber-like elasticity gradually gives way to the elasticity of solids in which the potential energy becomes the predominant factor. The viscoelasticity at high frequency in polymers is not unlike for nonpolymeric liquids, and a model for the glass transition, observed both in polymers and nonpolymers, must not be specific only to polymers.

2. INTERMOLECULAR COOPERATIVITY

In polymers, the shape change is interpreted as the conformational change of the polymer molecules. In the high frequency regime where the rubber like spring is no longer an adequate model for the unrelaxed modulus, the conformational change involving the rotation of conformers is used as the measure of a change in shapes. The free energy of deformation cannot be estimated from the statistics of long chains, but the free energy of local conformational changes becomes relevant.

The smallest unit of a conformational change is the bond rotation in the main chain. It is the softest degree of freedom. The conformers would be rocking in the minimum free energy well, but once in a while it gains enough kinetic energy to jump over the energy barrier to another conformation. In the presence of a force field, there will be more jumps of these conformers into the direction favoring the strain energy relief, *i.e.* the stress relaxation. In the linear viscoelasticity range, the strain energy is not nearly comparable to the energy barrier for the conformational change. As compared to the barrier of 3300 cal/mol of bond, the unrelaxed energy for the strain of 1% is 2.4 cal/cm³. If we choose the molecular weight of 54 again, it is only 130 cal/mol, so these two levels of energy are out of range of each other and the strain energy does not affect the free energy of conformational change. The thermodynamic probability, determined by the population of the fluctuations that reach the free energy level of the barrier that separates the gauche from the trans conformation determines the relaxation time. According to the Boltzmann rule, the probability for the conformer to be in the free energy level $\Delta\mu$ higher than the initial state is $\phi_0 \exp(-\Delta\mu/kT)$, where ϕ_0 is the population of the initial state, in our case the gauche conformation, at temperature T .

The relaxation timer τ at T , in comparison with τ^* at a reference temperature T^* , is evaluated according to this model which follows the Arrhenius equation:

$$\ln(\tau/\tau^*) = \frac{\Delta\mu}{k} \left(\frac{1}{T} - \frac{1}{T^*} \right) \quad (19)$$

This equation does not fit the experimental data, whereas a good fit is obtained with Vogel-Fulcher equation, Eq. (13) with the *right* value of $\Delta\mu$ of 3.3 kcal. The predicted τ by Eq. (19) is too short. However, it fits NMR data on the methyl group rotation in polyethylene [7].

The Arrhenius model obviously needs modification to account for a much higher apparent activation energy that depends on temperature. Liquids are

actually closer to solids than to a gas. The heat of vaporization for most liquids is much greater than the heat of fusion, which indicates that the cohesive energy of liquids is not much different from that of solids. The specific volume changes only by 10% at fusion. All this means that there are strong intermolecular forces in the liquids. Such forces must make it more difficult to complete a successful rotation of a bond for local conformational relaxation. This is viewed as an act of interference by other conformers around it, and requires intermolecular cooperation. In case of nonpolymers, there are apparently different degrees of interference for different kinds of liquid molecules. A complex molecule such as cc-glucose is capable of different configurations such as the boat and the chair configurations. The temperature dependence of the dielectric relaxation is nearly the same as that of polyvinyl acetate, including undergoing the glass transition and physical aging at nearly the same time-temperature condition [8]. The liquids capable of conformational changes are called "Kneser" liquids. Herzfeld and Litovitz [9] have shown that these liquids exhibit excessive degree of energy loss in sound wave propagation, and which they explain is the exchange of energy between the external and internal degrees of freedom. The external degrees of freedom are translations and rotations, whereas the internal degrees of freedom are vibrations and oscillations, *etc.* To us, the external degrees of freedom are the successful jumps and the internal degrees of freedom are those unsuccessful ones against the barrier. In these liquids that is capable of internal configurational changes, many cycles of vibrations are wasted because of the interference as the configurations of the neighbors must be right for the successful relaxation. The unsuccessful oscillation by a conformer might be called a collision with a neighbor preventing from gaining the external degrees of freedom. Such interference among neighbor conformers increases with the density, as the temperature is decreased.

The degree of interference can be quantified by the number, z , of conformers that are interfering with each other. Each such group is called a domain of cooperativity. Within a domain, all conformers can relax only simultaneously. This occurs when the randomly oscillating conformers happened to attain the barrier energy simultaneously. This is a small probability as compared to the frequency of oscillatory rotation of individual conformers. The relaxation time of each conformer, τ , is now coupled with others within the domain so that, if there are z conformers in the domain, the cooperative relaxation time is $\tilde{\tau}$. The free energy barrier is now $\Delta\mu z$, and we thus modify Eq. (19):

$$\ln(\tau/\tau^*) = \frac{\Delta\mu}{k} \left[\frac{z}{T} - \frac{1}{T^*} \right] \quad (20)$$

The domain size is related to the space available between the conformers, and is proportional to the density. The smaller the extra space, the larger the number z . As the temperature is lowered, z increases. The relaxation time τ increases by orders of magnitude until it becomes excessively slow to be able to respond to equilibrate with outside the system (external force) and the glass transition intervenes. Then at the other extreme at high temperature, T^* , the space is large enough that conformers can relax free of interference from neighbors. In this case z is 1 and Eq. (20) becomes identical to Eq. (19). This is what is expected of the methyl group rotation mentioned earlier, which is expected to be free of intermolecular interference. Its activation energy is ~ 3 kcal and is constant to the room temperature.

2.1. Free volume and excess enthalpy in the condensed state

The thermal expansion coefficient α_l of many liquids is about $7 \times 10^{-4} \text{ K}^{-1}$, and that of the glassy state (as well as the crystalline state), α_s for polymers is about $2 \times 10^{-4} \text{ K}^{-1}$. The thermal expansion coefficient of the free volume is, therefore, $\Delta\alpha = 5 \times 10^{-4} \text{ K}^{-1}$. Assuming $\Delta\alpha$ to be constant in the range between T_g and T^* , the number of domain N_A/z is proportional to the temperature. Theoretically it is possible to extend the equilibrium condition to below T_g by following the proportionality of $1/z$ down to the temperature T_0 at which $1/z = 0$ or $z \rightarrow \infty$. At T_0 , then, it is in equilibrium but τ becomes infinity. Later we will identify T_0 with Kauzman's zero entropy temperature [10]. Now, we formulate z versus T :

$$z = \frac{T^* - T_0}{T^*} \frac{T}{T - T_0} \quad (21)$$

Defining a new $\Delta\mu' = \Delta\mu (T^* - T_0)/T^*$, for Eq. (20),

$$\ln(\tau/\tau^*) = \frac{\Delta\mu'}{k} \left[\frac{1}{T - T_0} - \frac{1}{T^* - T_0} \right] \quad (22)$$

which is the Vogel-Fulcher equation, Eq. (13). (Actually this $\Delta\mu'$, rather than $\Delta\mu$, is the actual activation energy 3.3 kcal. The latter is greater than this value because it includes the cohesive energy from the neighbors). The free volume is usually considered to be Van der Waal's excess volume, *i.e.*, the difference

between the liquid and the crystalline specific volumes. It should extrapolate to zero at 0 K. The free volume is 40% of the total volume at 800 K, which later will be shown to be our T^* , the temperature at which $z = 1$. Most polymers actually degrade well below 800 K, as this is the temperature that the kinetic energy is almost half of the barrier energy.

Doolittle's free volume in Eq. (12) is different from the physical free volume. It is made to vanish at T_0 , where the domain size reaches infinity. This is an *ad hoc* formula, and it is difficult to define it using physically tractable variables other than the implied parameters that fit the relaxation shift factor.

Looking at the WLF equation, Eq. (11), the coefficient c_2 equals 50 K when T_g is taken as the reference temperature. Since both c_1^g and c_2^g seem to be nearly universal when T_g is chosen as T_{ref} , it is called the 'universal WLF equation'. That $c_2^g \sim 50$ means that T_0 for most polymers is 50 K below T_g . This value $T_0 = T_g - 50$, is used in Eq. (22). Experimentally, this T_g is for the quenched glassy state that is measured by DSC at -10 K/min., or by taking the temperature the E'' peak in DMA at 10 rad/s.

The excess enthalpy is a familiar term to thermal analysts. It is the integral with T of the excess specific heat ΔC_p above T_g , and refers to that portion of enthalpy in excess of the vibrational heat of a solid. ΔC_p is measured in terms of energy per g per K. We have been discussing the thermodynamics, however, in terms per mole of conformer. We will continue to discuss on this basis, and later compare with data by converting to per gram basis.

The conformational entropy is the logarithm of the probability of mixing all rotational isomeric states such as the trans and two gauche states of the conformer. The molar concentration ϕ of the gauche state is obtained from the formula:

$$\phi = 2 \exp(-\Delta\Gamma / kT) / [1 + 2 \exp(-\Delta\Gamma / kT)] \quad (23)$$

where $\Delta\Gamma$ is the energy difference between the gauche and trans conformations, ca. 500 cal. The factor 2 is placed because there are three possible angles per bond. The entropy of mixing, *i.e.* the conformational entropy, S_c , for the trans and gauche conformations is obtained through an approximation:

$$S_c = -3k [\phi \ln\phi + (1-\phi) \ln(1-\phi)] \quad (24)$$

The factor 3 is placed in the equation because each conformer (trans or gauche) has a choice of three bond angles.

This entropy does not vanish at T_0 ; it reaches zero at 0 K. So what is the Kauzmann's zero entropy temperature? In order to explain, we revisit the domain

model. In that model, the degree of freedom (for rotation) within a domain is no more than the degree of freedom for one conformer, since all z conformers had to relax together. The entropy per mole of domain is equal to S_c in Eq. (24), but the entropy per mole of conformer now has to be divided by z , or S_c/z . (Remember, a mole of domains is z times greater in mass than a mole of conformer.) We call this entropy the excess entropy, S_x . Similarly, the excess enthalpy $H_x = H_c/z$. The measured ΔC_p per mole of conformer is dH_x/dT , not dH_c/dT , and from the temperature dependence of z , the following is true:

$$\Delta C_p = \frac{T^*}{T^* - T_0} \frac{dH_c}{dT} \quad (25)$$

Adam and Gibbs [11] termed S_x the cooperative entropy, and set $z = S_c/S_x$ and obtained the celebrated Adam-Gibbs equation,

$$\ln(\tau/\tau^*) = \frac{\Delta\mu}{k} \left[\frac{S_c}{S_z} \frac{1}{T} - \frac{1}{T^*} \right] \quad (26)$$

where S_z is the same as S_x . Eq. (26) can be converted to the Vogel-Fulcher equation by substituting $S_c/S_z = z$, and z as a function of the temperature as shown before.

2.2. Excess enthalpy that drops faster than the conformational entropy

Both S_x and H_x vanish at T_0 . If the specific heat of a liquid is measured, and the entropy is calculated from the formula $dS/dT = C_p/T$, it would be found to drop much faster than the conformational entropy itself. The measured entropy seems to vanish at T_0 rather than at 0 K. Thus T_0 has been called the zero entropy temperature. Actually, the conformational entropy, which persists as long as the amorphous disorder persists, is far from nearing zero at T_g , as Monerie *et al.* have shown [12]. There is a Flory temperature [13] where the stiffness gained at low temperature will bring a certain order and rigidity, but this is related to the energy difference between the rotational isomers, Γ , and has nothing to do with the glass.

Recalling Eq. (25), the ratio for ΔC_p per mole of conformer over $T \cdot dS_c/dT$ thus scales with z , and is also equal to $T^*/(T^* - T_0)$. Thus ΔC_p , per gram of conformer is obtained by dividing it by the conformer molecular weight M :

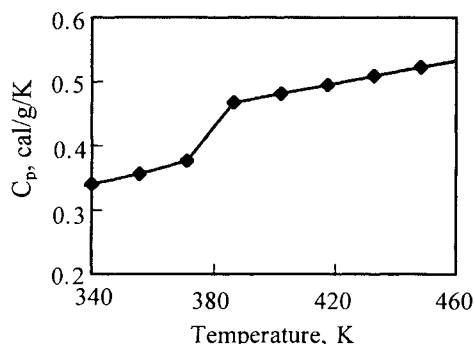


Fig. 3. Calculated C_p from Eq. (27) for $T_0 = 370\text{K}$

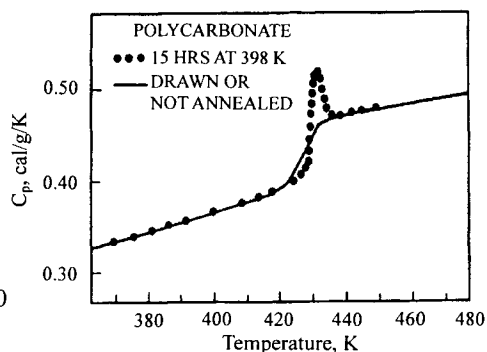


Fig. 4. Experimental C_p for polycarbonate

$$\Delta C_p \text{ per gram} = \frac{1}{M} \frac{T^*}{T^* - T_0} T \frac{dS_c}{dT} \quad (27)$$

and dS_c/dT can be evaluated from Eqs. 23 and 24. In Fig. 3, Eq. (27) was used to calculate actual ΔC_p for a polymer with $T_0 = 100^\circ\text{C}$ or T_g of 150°C . How to calculate M from T_g will be shown in the next section. For polycarbonate, $M = 77$.

The ratio $T^*/(T^* - T_0)$ is the coefficient that changes the thermodynamic quantities into the physics that involves cooperativity.

3. CHEMICAL STRUCTURE AND T_g

All thermodynamic arguments in the preceding sections have been based on the basis of mole of conformers. As such, everything was scaled by the number of conformers, and a kind of universal picture has emerged that applies to all polymers. But if everything is scaleable per mole of conformers, then the relaxation time scaled from τ^* at T^* would be the same, and all polymer would exhibit the same T_g . Clearly, T_0 is different from polymer to polymer. We will explore now the structural factor that makes a difference in T_0 from polymer to polymer.

For polymers with different conformer sizes, what is different is the absolute free volume. The contribution of the free volume to entropy can be estimated in the same way the configurational entropy of the ideal gas is calculated. The ideal gas molecule is a point mass with no occupied volume. Its configurational entropy arises from the spatial arrangement of these point masses, and it is equal to $-k \ln V$. We think of our free volume as the portion of

the volume after subtracting the occupied volume, with no mass, but with the same number as there are conformers. The configurational entropy of these 'points', S_v , equals $-k \ln V_f$, where V_f is the van der Waals free volume. If we

Table 1
Conformer Size and T_g

	Polymer	M	$T_g, ^\circ\text{C}$	T^*-T_0	$\ln M$	c_3
1	polyethylene (linear)	14/1	-110	660	2.64	1742
2	polyethylene (branch)	41/2	-30	580	3.02	1751
3	1,4-poly(butadiene)	54/3	-55	605	2.85	1750
4	1,2-poly(butadiene)	54/2	20	530	3.30	1749
5	polyisobutylene 56/3.5	-74	624	2.77	1728	
6	polypropylene 42/2	-30	580	3.04	1765	
7	gutta percha	68/3	-10	560	3.12	1748
8	cis-polyisoprene 68/4	-69	619	2.83	1753	
9	poly(4-methyl pentene)	85/3	29	521	3.34	1742
10	polyvinyl chloride	62/2	90	460	3.43	1577
11	polystyrene	108/2	100	450	3.93	1769
12	poly((α methyl styrene)	119/1	180	370	4.78	1768
13	poly(trifluoro-chloroethylene)	118/3	79	471	3.67	1728
14	polyvinyl acetate	86/3	29	521	3.36	1748
15	polyoxymethyl ether	30/1.8	-73	623	2.80	1752
16	polyoxyethylene 44/2.6	-67	617	2.83	1745	
17	polyoxypropylene	58/3.5	-75	625	2.81	1754
18	polyoxybutylene 72/4.5	-88	638	2.77	1768	
19	polyvinyl methylether	58/2.7	-22	572	3.07	1754
20	polyvinylisopropyl ether	86/3.8	-12	562	3.12	1753
21	polyvinylbutyl ether	100/5.8	-56	606	2.85	1725
22	polyvinylhexyl ether	128/7.8	-74	624	2.80	1746
23	polymethyl methacrylate	100/2	105	445	3.91	1741
24	isotactic polymethyl methacrylate	100/3	46	504	3.51	1767
33	polyethyl methacrylate	114/3	65	485	3.64	1764
34	polymethyl acrylate	86/3.5	9	541	3.20	1732
35	poly(t-butyl acrylate)	132/4.5	31	519	3.38	1753
40	polyphenylene sulfide	108/2	110	440	3.99	1755
41	polyphenylene oxide	92/2	90	460	3.83	1761
42	polyethylene terephthalate	182/5	64	486	3.59	1746
43	polycarbonate	254/3.3	147	403	4.34	1750
44	polyether etherketone	288/3.3	158	392	4.47	1752
45	polysulfone	444/3.5	187	363	4.84	1758
46	polyether imide	596/4	200	350	5.00	1750
47	polyimide (PNMA)	207/1	222	328	5.33	1749
48	poly(tri-methyl phenylene ether)	172/1	210	340	5.15	1750
49	Kevlar®	242/1	235	315	5.49	1729
48	polyether sulfone	232/1	225	325	5.45	1770

imagine an equilibrium state slightly above T_0 (even if it might take a million years to get there), the excess entropy per mole of conformers for the conformational probability is the same for all polymers, but the difference exists only in S_v . But this entropy also must reach zero at its T_0 . This entropy, S_v , also, must be multiplied by $(T^* - T_0)/T^*$, because we are dealing with a mole of conformer and not a mole of domain. S_v is different depending on the conformer size, as it depends on the absolute amount of free volume. In order to establish the equivalence of molar entropy for different conformer size and T_0 , $S_v(T^* - T_0)/T^*$ must be equal for different polymers. Since the molar free volume is proportional to the molecular size, if we ignore the density variation among polymers ($\sim 1 \text{ g/cm}^3$), we can obtain the following equation:

$$(T^* - T_0) \ln M = C_3 \quad (28)$$

In Table 1, the conformer sizes of polymers were estimated, generally (but not always) by dividing the repeat unit by the number of rotatable links. By substituting this M in Eq. (28), T_0 is obtained, and $T_g = T_0 + 50$ was compared with the experimental T_g , obtained either from DSC or dynamic mechanical test with E'' peak at 100 rad/s. When in agreement, C_3 equals 1750. Not all of the estimates follow a simple procedure. For the -O- linkage, $\Delta\mu$ is only a third of $\Delta\mu$ for the c-c bond. This was compensated by assigning a third for a linkage as in polycarbonate. For branches, the first addition of a conformer to the main chain does not contribute to the conformational change, so the average M increases and T_g increases, but further additions of conformers to the branch will add to the number of conformers per repeat unit and if the added monomer is smaller than the existing average size, then its T_g decreases.

One can use Eq. (28) backwards. When T_g is known, but unsure of the conformer size because of a complicated structure with branches, ether links, crosslinks, *etc.*, the average M can be estimated from T_g with the use of Eq. (28). There is another way of independently checking the estimates of conformers per repeat unit. The number of conformers per repeat unit is usually the number of cooperative units in the β transition. The β transition occurs within the restricted environment in which the largest conformer in the repeat unit is pinned, but the rest can still rotate cooperatively. The cooperativity this time is not between conformers of different molecular chains but among the consecutively lined conformers in the same chain. The crank shaft model of polyethylene provides a visual model. The number of cooperative units is the same as the number of conformers in the repeat unit. Thus, for polycarbonate z_β

is 3.3, with which $\Delta\mu_{\beta}$ of 10.9 kcal is obtained. The experimental apparent activation energy for the β relaxation in polycarbonate is 10.5 kcal.

4. VISCOELASTICITY DATA ANALYSIS

There are actually two distinctly different regimes of molecular relaxation in polymers. We have alluded earlier to this when we calculated the two different kinds of unrelaxed moduli, G_0 . One was for the solid like behavior in which the conformers were packed tightly, and the unrelaxed modulus corresponded to the state before that tightly associated structure could be relaxed. The order of magnitude for G_0 was 10^{10} dynes/cm². The other was for the relaxation of a whole polymer molecule or a large part of it, where the elastic modulus arises from the tendency of a molecule to return to random conformations. The value of G_0 for the latter was typically 10^6 dynes/cm². The magnitudes of the relaxation time for the two regimes are even further apart, typically by 10 orders of magnitude. Both processes exhibit a broad distribution of relaxation times, as a result of coupled relaxation processes. An example was already given for the cooperative relaxation where the relaxation time of each conformer rotation was coupled to the neighbors in the same domain to obtain τ . Coupling of the relaxation modes also exist in the rubbery molecules. Here different parts of a molecule move in translation in different directions. In the small-strain dynamic mechanical test, the amplitude is small and linear viscoelasticity is observed. The conformation of molecules or even parts of molecules are statistically isotropic, so a steady flow process in the background does not exist and does not have to be invoked as part of the model. When a coordinated motion shifts a center of mass of a strand in the direction of reducing the mechanical energy, the molecule is in the process of relaxation. A coordinated motion means two motions working together to move the center of mass of the whole molecule. Only the odd harmonics ($p = 1, 3, 5, \text{etc.}$) contributes toward moving the mass center. In the condensed state, the molecules are packed like spaghetti, and conformers touch each other. For those polymers to move in that environment, each segment must move against the energy barrier of cooperatively interfering conformers. The temperature dependence of all modes of relaxation in a polymer, from the fast conformational relaxation to the slow relaxation of the whole molecular chain is controlled by the same conformational barrier. Thus the entire master relaxation curve is shifted with the same T - τ shift factor described by the Vogel-Fulcher (WLF) equation.

4.1. Viscoelasticity data analysis near but above T_g

Fig. 5 is a master curve for the relaxation modulus of a typical amorphous polymer. The two regimes mentioned earlier are (1) the liquid to-glass like

regime from $\log G(t)$ of 10 to 8, and (2) the rubbery regime extending to the entanglement from 8 to 4 or even lower (in dynes/cm³). In this section, the liquid/glass regime (1) will be discussed.

This regime of relaxation is the cooperative relaxation of conformers already discussed in 2. It is observed both in polymers and nonpolymers. The relaxation modulus and the dielectric data are suitable data. The dielectric analysis is capable of measuring at high frequency, and is useful in observation of near glassy dynamics in the equilibrium above T_g . In Fig. 5, a line was drawn with the notation KWW. This stands for the well-known Kohlrausch-Williams-Watts equation [14],

$$G(t) = G_0 \exp\left[-(t/\tau)^\beta\right] \quad (29)$$

which is also known by the name 'stretched exponential function'. It takes care of the distribution of relaxation times particularly in the time region shorter than the characteristic relaxation time τ . The loss maximum will be located at $\omega = \tau$, and at the higher frequency side of the maximum, $\log G''$ versus $\log \omega$ will be a straight line with a slope of $-\beta$. The slope would have been 1 instead of $\beta < 1$, if there was only a single relaxation time τ .

The origin of the distribution of relaxation times in this case is the distribution of domain size. In the equilibrium state, the density fluctuations will cause a certain distribution in free volume, which can be calculated as the distribution of z at a temperature above T_g

Eq. (20) describes not only the temperature dependence of τ but also the

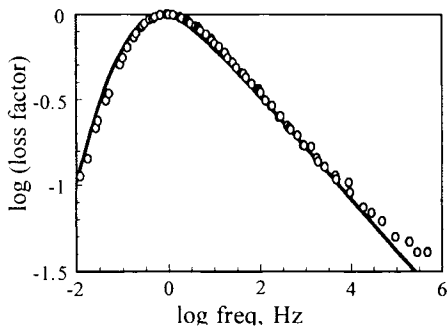


Fig. 5. Master Curve for Relaxation Modulus at T_g , Factor normalized by ϵ'' max.

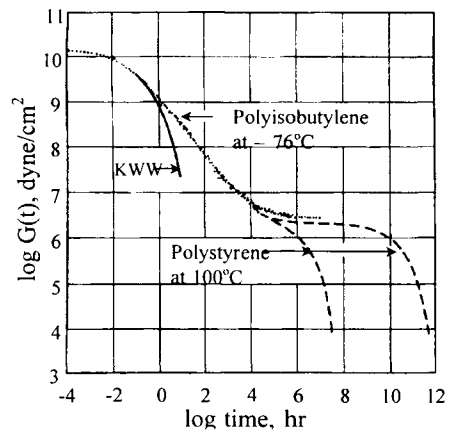


Fig. 6. Dielectric Loss

dependence on z . If we now assume the distribution of z to be Gaussian, the intensity for z_i is obtained:

$$G_i = G_0 \exp[-\Delta\mu z_i/kT] \quad (30)$$

Substituting z_i into Eq. (20) will obtain the relaxation spectrum $G_i(\tau_i)$:

$$\ln(\tau_i/\tau) = \Delta\mu/kT \ln(G_i/G_0) \quad (31)$$

and the slope β equals $RT/\Delta\mu$, which at 400 K is about 0.24. The experimental value from Fig. 6 is between 2.3 to 2.8, depending where the slope is taken. This is only true for $T > T_g$. Below T_g , the domain sizes are 'frozen' and each τ_i will shift with temperature with activation energy $\Delta\mu z_i$, *i.e.*, for the same $-\Delta T$, the larger domains will increase the relaxation time much faster than the smaller domains. As a result, the value β will decrease precipitously below T_g . This β_g below T_g can be calculated by the formula:

$$\frac{1}{\beta_g} = \frac{1}{\beta_f} + \frac{\Delta\mu}{R} \left[\frac{T_f}{T(T_f - T_0)} - \frac{1}{T} \right] \quad (32)$$

where β_f is the equilibrium value at the fictive temperature T_f of the given glassy state of interest. (T_f is lower for the aged glassy state.) In practice any β slightly above T_g is close enough to β_f . This β_g can be used to predict the creep/relaxation behavior as well as the scaling of viscoplastic stress/strain curves at different temperatures and strain rates, even up to the impact regime [15], such as the stress at constant rates of strain:

$$\sigma = \gamma G_0 \left(\frac{\dot{\gamma}}{\dot{\gamma}_0} \right)^\beta \exp \left[-\frac{\gamma}{\gamma^*} \left(\frac{\dot{\gamma}}{\dot{\gamma}_0} \right)^\beta \right] \quad (33)$$

and this β is actually β_g of Eq. (32). It is typically 0.02 as compared to the equilibrium value an order of magnitude greater. In Fig. 7, Eq. (33) is tested with actual stress strain data for polycarbonate. A good agreement is obtained when necking of the sample could be avoided. By thermally insulating the sample and adiabatically run, the sample *cools* and the sample deforms uniformly [15]. Viscoplasticity is an important nonlinear property of polymers

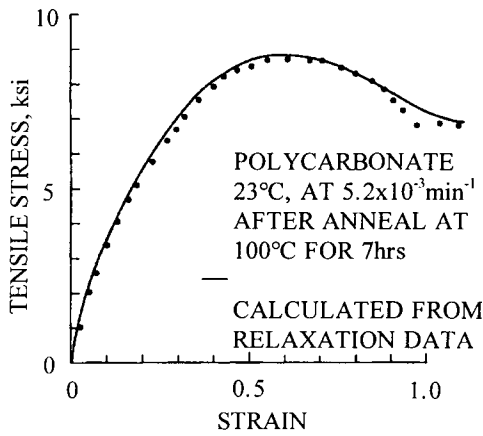


Fig. 7. The stress Strain using Eq. (33) for viscoplasticity.

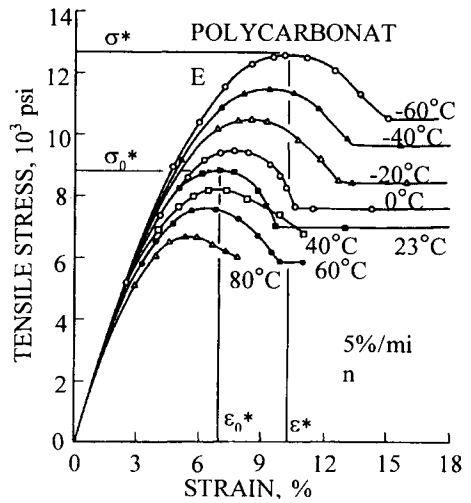


Fig. 8. Stress-strain data at different temperatures at constant strain rate

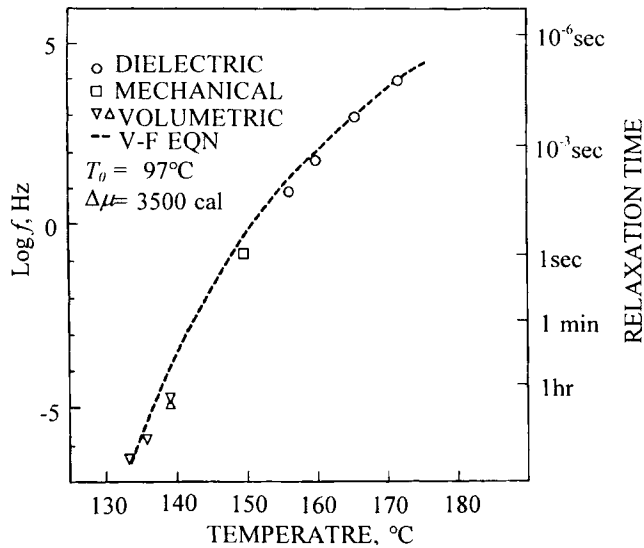


Fig. 9. The characteristic frequency corresponding to τ for polycarbonate plotted against temperature. The dotted curve is the Vogel-Fulcher (or WLF) calculation.

both in the solid and molten states. More will be discussed toward the end of the chapter.

The temperature dependence of the relaxation time above T_g in equilibrium follows the Vogel-Fulcher equation. The transition map in which log frequency for the loss maximum is plotted against T is shown in Fig. 9. The data are a collection from all sorts of thermal and dynamic techniques, and even include the relaxation time extracted from.

4.2. Viscoelasticity data analysis of polymer melt

4.2.1. Polymers in Solution

The motion of a solute molecule suspended in a flowing solvent is dragged by the frictional force from the surrounding solvent. The molecular frictional coefficient is, according to the Einstein velocity relation,

$$\frac{\eta - \eta_0}{\eta_0} = 2.5n_{solute}V \quad (34)$$

where, η is the viscosity of the solution and η_0 , the viscosity of the solvent. The ratio, $(\eta - \eta_0)/\eta_0$ is called the *specific viscosity*. n_{solute} is the number of solute molecules per unit volume, and V_e is the volume of one solute molecule, termed *hydrodynamic volume*. If the particle is approximately spherical, it the effective hydrodynamic volume $V_e = 4\pi R_e^3/3$, where R_e is the effective radius of one molecule. The number of solute molecules per unit volume, n_{solute} , is equal to the concentration divided by the molecular weight. Accordingly, Eq. (34) is written in molecular terms as below:

$$\frac{\eta - \eta_0}{\eta_0} = 2.5 \frac{cN_A}{M} V_e = 10.5 \frac{cN_A R_e^3}{M} \quad (35)$$

where N_A is Avogadro's number; c , the concentration in g/cm^3 ; and M , the relative molecular weight.

The *reduced viscosity* is obtained by dividing the specific viscosity by the concentration, c . The *intrinsic viscosity*, denoted by $[\eta]$, is obtained from the reduced viscosity extrapolated to zero concentration, therefore it is equal to the right hand side of Eq. (35) without c , or it is equal to the hydrodynamic volume of the molecule divided by its molecular weight.

Suspended free in the solvent, a polymer chain will attain a random conformation, the state of highest disorder being the most probable state, as briefly discussed in 1.2. The conformation of a molecule is described in terms of the position of one end of the chain relative to the other end. In a simple

model in which a bond between the consecutive “beads” can rotate freely, or the *freely jointed* bonds, the statistics of conformations can be worked out by the statistics of N random space walks (in three dimensions) with each step of distance l . The polymer chain is represented by the chain with N beads, bonded by the bond length l . A bead plus a bond is perhaps close to our definition of a conformer. From the calculation, the mean square of the end-to-end distance, $\langle r^2 \rangle$, is equal to Nl^2 , (actually $2Nl^2$ if a freely rotating tetrahedral chain is considered, but here we mean the effective or equivalent chains, so l can be $\sqrt{2}$ bond length); the root-mean-square $\langle r^2 \rangle^{1/2}$ is equal to $\sqrt{N}l$. If we assume it to be the equivalent of the diameter of a sphere, its volume is $0.52N^{3/2}l^3$. Substituting this for V_e in Eq. (35) and dividing by c , the intrinsic viscosity is obtained:

$$[\eta] = 3.1 \times 10^{23} \frac{N^{3/2}l^3}{M} \quad (36)$$

The empirical value of the coefficient above is $2 \sim 2.5 \times 10^{23}$ in cgs units. (It is the Flory [16] coefficient, ϕ . If we use the radius of gyration $\langle s^2 \rangle^{1/2}$, the distance from the center to the end of the molecule, as R_e , instead of the above calculation, the coefficient of 1.70×10^{23} is obtained, using the relationship: $\langle r^2 \rangle = 6 \langle s^2 \rangle$. These three values for ϕ demonstrate that the hydrodynamic volume and the thermodynamic volume of chain statistics are fairly close. It means that the sphere of a random coil of a chain holds solvent molecules within it and flows with it, and that that volume is nearly the same as the volume described by either the end-to-end distance or by the radius of gyration.

As evident from the formula $N^{1/2}l$ for the radius, the density of the ball of a polymer chain is not uniform, but decreases outward from the center. This is the most stable state that results in the highest overall entropy and the lowest free energy. Further away from the center of the ball, more solvent molecules are found.

Even though the hydrodynamic volume is in good agreement with the mean volume of a coil, its molecular weight dependence for the real polymers needs some modification. Constraints in conformations tend to increase the mean radius. With the increase in molecular weight, the volume for a real chain grows faster than the volume of a freely jointed chain, so instead of being proportional to $\langle r^2 \rangle^{3/2}$ or $M^{3/2}$, it is set to be proportional to $M^{3\nu}$, where the value of ν is typically about 0.58, or $3\nu = 1.7$ (The Flory number for ν is 3/5). The need for this modification arises from the fact that polymer chain segments cannot occupy the same space at the same time, thus slightly limiting the conformational probability, resulting in a slightly increased expansion. It is

called the excluded volume effect. The intrinsic viscosity is described by an empirical form:

$$[\eta] = KM^{\nu-1} \quad (37)$$

The value of the constant K depends on the molecular weight of the conformer, or the 'bead' in the string of the polymer chain. For a number of polymers, in the θ solvents, the values of K are near 10^{-3} for a number of polymers (dl/g is used for $[\eta]$ by the polymer chemists) [17].

By assuming the free bond rotation, we have neglected the energy difference between different rotational bond angles, *e.g.* the *gauche* versus *trans* conformations, but this is not much of a problem at a high enough temperature. Its value being about 500 to 800 cal/mol of bond, the calculated concentration of each conformation is fairly constant at room temperature and above. At -100°C , however, there are significantly high concentration of *trans* conformation [16]. On the other hand, if the energy difference is much greater because of intramolecular hydrogen bonding, *etc.*, then the chain can stiffen and the minimum chain length for the Gaussian statistics to hold will increase substantially.

The relaxation of polymer molecules in dilute solution is one of the most important aspects of polymer dynamics. In the dilute solutions, molecules are isolated from each other so the relaxation time is not affected from the intermolecular interaction. Debye's [18] treatment on the dielectric relaxation of liquid molecules was also based on the Stokes' formula, and is given by:

$$\tau = \zeta / 2kT = 4\pi \eta_0 R_e^3 / 2kT = 3\eta_0 V_e / 2kT \quad (38)$$

where ζ is the molecular friction coefficient and η_0 the viscosity (of the solvent). This equation has been found to hold fairly well for large spherical molecules in solvents with appreciably smaller molecules, *e.g.*, Gammexane (γ isomer of $\text{C}_6\text{H}_6\text{Cl}_6$) in benzene [19].

In the early part of this chapter, we have shown that the steady state viscosity for a viscoelastic body is equal to the product of the elastic (unrelaxed) modulus G_0 and the relaxation time τ . Now this viscosity is in fact derived from the friction due to the differential flow of the solvent and the polymer molecules, *i.e.* $(\eta - \eta_0)$ in Eqs. (34) and (35). The modulus is equal to RT multiplied by the number of molecules per cm^3 , or cRT/M . The relaxation time τ of the solution is:

$$\tau = \frac{(\eta - \eta_0)}{cRT} M = \frac{[\eta]M}{RT} \eta_0 = KM^{3\nu-1} \frac{M}{RT} \eta_0 = \frac{\eta_0}{RT} KM^{3\nu} \quad (39)$$

which is expectedly very similar to Eq. (38). Thus the relaxation time is proportional to the hydrodynamic volume of the solute.

The dielectric relaxation time of polyisoprene in the dilute solution of an alkane solvent known as Isopar-G by Patel and Takahashi [20,15]. The relaxation time extrapolated to zero concentration has been empirically described by the formula:

$$\tau_{M,0} = 1.03 \times 10^{-14} M^{1.69} \quad (40)$$

The intrinsic viscosity has been empirically formulated by the expression:

$$[\eta] = 1.94 \times 10^{-2} M^{0.70} \text{ cm}^3 / \text{g} \quad (41)$$

for the polyisoprene dissolved in the above-mentioned alkane. With Eq. (41) and the measured value of 1 cp for η_0 , the coefficient for Eq. (40) of 0.77×10^{-14} instead of 1.03×10^{-14} obtains. The discrepancy may be closed if we modify Eq. (39) by adding the factor of 1.5 from the Debye formula, Eq. (38); then 1.16×10^{-13} is obtained as compared to the experimental value of 1.03×10^{-13} .

When the concentration is increased to a “semi-dilute solution”, the molecular balls come closer to each other and, helped by the dynamic fluctuations, they begin to touch their neighbors. This can happen at very low concentrations. Again referring to the dielectric work by Patel and Takahashi, the fundamental relaxation time of the isolated sphere depends on the molecular weight through the following formula:

$$\log \tau_{m,c} = \log \tau_{m,0} + 2.1 \times 10^{-2} cM^{0.57} \quad (42)$$

where the subscript ‘0’ refers to the extrapolation to $c = 0$. We have theorized that the term $cM^{0.57}$ is the product of the concentration c and the radius $\sim M^\nu$, and it is a parameter for the degrees of contact between neighboring molecules. It enters the formula for the logarithm of hydrodynamic volume ($\sim \log \tau$) because the volume differential is normalized, *i.e.* $\Delta \tau / \tau = \Delta \ln \tau$. Detailed discussion is found in reference [15]. It is the onset of intermolecular coupling, or entanglement, at a very dilute stage. M^ν is like the diameter of the molecular ball, whereas $cM^{3\nu-1}$ is the total volume of balls per cm^3 of solution. This term $c[\eta] \sim cM^{3\nu-1}$, named after Simha [21], is used as a measure of the intermolecular proximity.

The relaxation time of a ball of chain molecule is thus proportional to its volume. It is possible to have a relaxation of part of a whole chain, as a higher mode than the fundamental slowest mode. The diameter of a ball of a part of the molecule is smaller in proportion to $N^{1/2}$. There are many modes of relaxation in a polymer molecule. Each mode may be compared with a vibrational mode of a piano wire; the fundamental mode is for the whole length of wire vibrating with two ends as nodes, and the second harmonic being the additional node added in the center so the frequency of vibration is doubled, and the third, the fourth and so on. The longest relaxation time is for the dominant fundamental mode, and it involves the whole molecule. The hydrodynamic ball is a three dimensionally symmetrical sphere having three degrees of freedom. As we saw it, the longest relaxation time involves the (radius)³ or $M^3\nu$, and is proportional to the hydrodynamic volume in the dilute solution, in which the polymer balls are far enough apart that they do not touch each other.

Fig. 10 is the plot of the dielectric loss versus frequency for the polyisoprene solution with various molecular weights, shifted so they overlap at the respective loss maximum. The slope is 1 for the low frequency side of the spectrum for all samples, indicating that the frequency for the loss maximum indeed corresponds to the longest (terminal) relaxation time. The slope on the high frequency side starts at 0.58 at the lowest concentration. This value for the slope is equal to $1/3\nu$, and 3ν is the separation between τ_1 and τ_p as it is the ratio of the volume of the large and the small balls between the first and the p -th modes. The slope decreases with increasing concentration, meaning the rise of intensity at the higher modes, presumably because more segments have entered

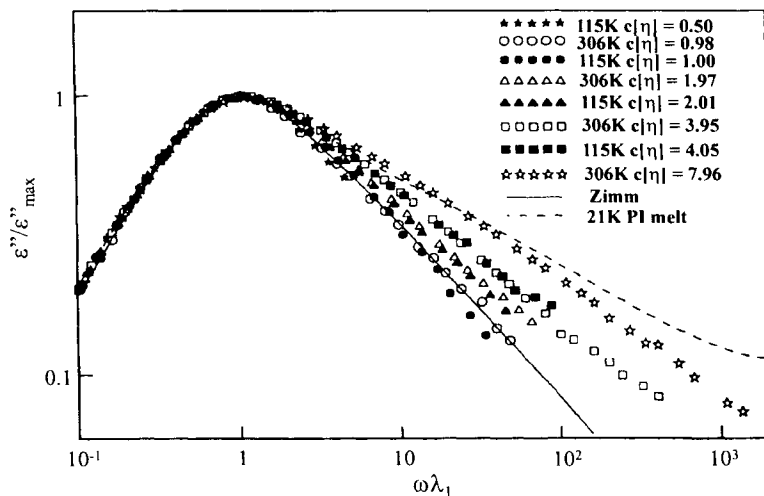


Fig. 10. Dielectric loss vs. frequency adjusted (horizontally) for the peaks to overlap. The shift factor is as described by Eq. (40).

into the once isolated sphere, and the penetration starts with the shorter lengths of the strands. Eventually, these higher modes become very intense as the intermolecular coupling becomes complete when polymer molecules are fully meshed. Such a state is achieved when the local density becomes uniform throughout the solution. The entanglement becomes fully developed at this stage. Although such a state is obviously attained in the polymer melt, it can be realized in solutions as well. In the case of hyaluronan, there are all kinds indications for a fully developed entanglement system at 1% (10mg/cm³) concentration [22].

There should be a minimum molecular weight to form a non-draining ball. A polymer chain has a natural radius of curvature as specified by $\langle r^2 \rangle$ or $\langle s^2 \rangle$. If the length of a chain is less than the contour of sphere with natural radius, then the ball is not completely formed to hold the solvent within. This is a free-draining conformation. The critical size for the smallest possible ball is formed can be calculated by comparing the free energy of squeezing out the excluded volume against the free energy of the loss of entropy. This "smallest ball" is essentially the same as de Gennes's "blob". We define M_e the critical molecular weight for the minimum ball-forming. Polymer chains of molecular weight less than M_e are worm-like molecules.

The worm-like chains will behave differently than the ball-like chains. The effective hydrodynamic volume is no longer described by a sphere of random coil that carries many solvent molecules trapped in it. Rather, the solvent molecules flow past these worm-like polymer chains. The effective hydrodynamic volume of a long rod-like rigid polymer would have to be estimated by another model, such as the cylinder of certain dimensions and rigidity, *e.g.*, the molecular mass per unit length and the persistence length, respectively [23].

As for the worm-like, free-draining molecules, the viscosity is proportional to M and the relaxation time is proportional to M^2 , so here again the viscosity is equal to the relaxation time divided by M . The shear modulus of the worm-like molecules must also be considered the entropic spring, as it is implied to be proportional to cRT/M for $M < M_e$, and it satisfies the relationship $\eta = G\tau$ [24-26]. The dynamics of the worm-like molecules in suspension has been modeled by Rouse [27] and Bueche [28]. The flexible chain is considered a series of "entropy springs" arising from its tendency to return to the most probable conformation when perturbed. The viscosity arises from the friction from the fluid flowing past the chain segments, resulting in the proportionality with the chain length. The doubly logarithmic plot of the intrinsic viscosity versus the molecular weight results in the slope of 1 for worm-like molecules, instead of $3\nu-1$ or 0.7 for the ball-like molecules (This is what Staudinger said!). Many polymer solutions, including hyaluronan solutions, exhibit this very behavior when the chains are short, as shown in Fig. 11, whereas above the critical

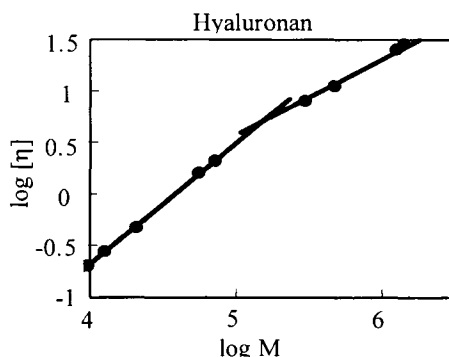


Fig. 11. log intrinsic viscosity versus

molecular weight the slope is the familiar $0.7, 3 \nu - 1$ [From Shimada *et al*, 29]. The critical molecular weight that divides the worm-like behavior from the ball-like behavior, depends on the flexibility of the chain.

For hyaluronan in dilute solution with pH near 7, the critical molecular weight has been shown to be about 1.7×10^5 by these authors, and the slope of $\log[\eta]$ versus $\log M$ were 0.76 above M_c , and 1.2 below M_c . Wik *et al* [30] found the values of 0.78 above M_c , and between 0.9 to 1.2 below M_c . Yanaki *et al* [31] found that the intrinsic viscosity value is sensitive to the flow rate of measurement, even though the concentration is extrapolated to 0, and obtained the value of 0.83 for the zero flow rate $[\eta]\dot{\gamma} = 0$ even above M_c . This means that a ball can hold more solvent if flowing very slowly.

4.2.2. Polymers in bulks

Mechanical properties are measured with unit dimensions such as cm, and cm^2 . While the molecular scaling is done with the number of conformers, *i.e.* per mole. The stress or the modulus, for example, are in the unit of dynes/cm^2 , not force per number of conformers squared. Polymers with larger size beads are more rigid per the same unit length (nm) than those with smaller beads per nm, but the number of conformers to form a radius *in numbers of conformers* may not be different. The critical *molecular weight* for changing the behavior from the worm to the ball depends on the stiffness of the chain, and they differ from polymer to polymer. The critical *number* N_e of conformers may not be so different. In fact N_e turns out to be about 500 [15], as will be discussed. The closeness of this value among many polymers implies that the chain stiffness can be scaled by the conformer size, as the glass transition temperature has been shown to be closely related to the conformer size [15].

N_e can be estimated by comparing the volume of a ball, which depends on $N^{3/2}$, with the volume of the polymer chain without the solvent, which depends

on N . The volume of a ball of a chain with N conformers, V_N , is described by the formula:

$$V_N = \frac{4\pi}{3} \langle s^2 \rangle^{\frac{3}{2}} = 0.28N^{\frac{3}{2}}l^3 \quad (43)$$

by utilizing the fact $\langle s^2 \rangle = Nl^2/6$. V_N cannot be smaller than the packed polymer volume NV_c , where V_c is the average volume of one conformer in the condensed state. The ratio l^3/V_c is crucial in determining the value of the critical length, N_e , *i.e.*, the volume of a ball must be greater than the packed polymer volume. Taking $l = 15.4$ nm from ethane, and assuming 14 cm³ for 1 mol of polyethylene conformer $-\text{CH}_2-$, we obtained l^3/V_c of 0.157. Using this value in Eq. (43), we obtained $V_N = NV_c$ when $N = 500$, and $V_N > NV_c$, when $N > 500$. When the molecular weight of a conformer is larger than the polyethylene unit, then l^3 is expected to be proportionately larger, as the bulk density of polymers do not vary by much (at least nothing like the molecular weight of their conformers), so the quantity l^3/V_c is possibly insensitive to the kind of polymers. These model calculations do not mean that inside this ball is assumed packed with polymer segments. It only means the thermodynamic impossibility for a chain of lesser length to form a hydrodynamic volume, and we maintain that the term chain rigidity merely means the size of conformers. The concentration inside is more than the overall concentration, but how much depends on whether a poor or good solvent is used. The radius of part of a chain inside the ball is no less than the radius of gyration for the contour length N_e , so it is a worm within the ball, even though it is part of a longer chain that makes up a larger ball.

The physics of the entanglement phenomena still remains incompletely understood in spite of decades of work and a wealth of ideas. We list here some phenomenological observations that are accepted as universal:

1. The melt viscosity is proportional to $M^{3.4}$, and so is the terminal (longest) relaxation time.
2. There is the critical molecular weight M_v , for the onset of a proportionality to $M^{3.4}$ for the melt viscosity. At lower molecular weight the viscosity is proportional to $\sim M$.
3. The elastic modulus for the entangled state is independent of the whole molecular weight, *i.e.*, $G_e \sim \rho RT/M_e$, where ρ is the density. In a semi-dilute solution where molecules might touch but the local concentration is much higher than the overall concentration, it will have to be multiplied by the number of molecules per unit volume, c/M , or c^2 .
4. The critical molecular weight M_e varies widely from polymer to polymer, but when divided by the average molecular weight of the conformers (the beads), the number N_e comes to about 500 for many polymers.

5. The flow viscosity (at increasingly large strain) decreases with shear rate, but its shear rate dependence is very close to the frequency dependence of the magnitude of the complex dynamic viscosity, $|\eta^*|$ measured at a very small strain amplitude. [Cox-Merz Rule 32].

A traditional view [33,34] of entanglement has been to consider a network of polymer molecules similar to the crosslinked network except that the entangled network becomes disentangled under the stress with the relaxation time that is proportional to $M^{3.4}$. Bueche introduced a “slippage factor” for the train of molecules being pulled by one molecule to increase the relaxation time, and with the “efficiency” of about 50%, he obtained the value of 3.5 for the exponent 3.4. A more recent model by de Gennes [35] and Doi and Edwards [36] take polymer molecules to snake through; the relaxation time is a result of coupling three modes: to produce a tunnel, then for the molecule to move into the tunnel, and finally close the space left behind. Each mode is considered to be proportional to the molecular weight, and coupling the three τ , produces M^3 dependence for both viscosity η and the relaxation time τ .

Both theories bank on the conformations of polymer molecules under large strains for the entangled coupling to show the effect. On the other hand, any linear viscoelastic theory for the entanglement must be applicable to extremely small perturbations, so one cannot invoke a state of flow as the condition for the entanglement to take effect. Molecules must retain their spherically symmetrical conformations and the entanglement still has to work. In fact the entanglement phenomenon is being observed in no flowing, non-invasive experiments, such as the dielectric measurement by Kremer [37] and Watanabe and coworkers [38]. The molecular conformations in this case can safely be assumed as unperturbed.

Our model [15] views the key factor in the condensed state to be interpenetrating polymer chains, which are the basis of the entangled coupling. We do subscribe to de Gennes’s idea of the “blob” as the smallest hydrodynamic

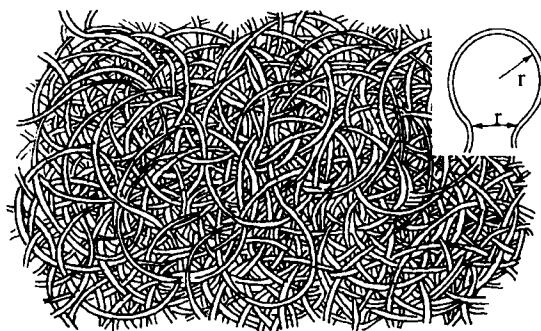


Fig. 12. A heuristic picture of molecules

ball with modulus $\rho RT/M_e$. His blobs, however, are connected in a train, so the whole polymer molecule is a string of connected blobs to form a superblob with its own super random conformation. Our molecules are “onions”, with the core ball the same as the “blob”. The layer of onion skins, each radius corresponding to the radius of gyration of the p -th mode for the loop length of (total length)/ p , with $p = 1$ being the fundamental mode of the whole molecule that includes the outermost onion skin. A big departure of this onion from a real onion is that parts of other molecules have invaded into those layers of onion skins such that the local density has become uniform throughout the whole melt and is equal to the density of the conformer. When this body of intermingled polymer chains is slightly deformed, the centers of mass of two adjacent polymer molecules are displaced by a small distance, *e.g.*, by 0.1% of the original distance. The stress initially rises but immediately begins to relax with the coupled relaxation time of the two molecules, or the product of the individual relaxation times. We have earlier shown that the relaxation time of an isolated molecule with the molecular weight greater than M_e to be proportional to $M^{1.7}$ and the coupled relaxation time means squaring each τ , which will obtain $M^{3.4}$. As for the modulus, there are c/M_e number of strands throughout the solution or the melt. The modulus would be $G_e = cRT/M_e$ or $c = \rho$ for the melt.

A useful aspect of this simple model is in the prediction of the higher modes. The higher modes are produced from parts of molecules such that the relaxation time for the p -th mode corresponds to the molecular length M/p , for $M/P > M_e$. The relaxation time of the p -th mode without coupling is proportional $\tau_1/p^{1.7}$ (which gave the slope of $-1/1.7 = -0.58$ on the high frequency side of the dielectric loss for the dilute solution, shown in Fig. 10), and with the coupling it $\tau_1/p^{3.4}$. Since the smaller number of conformers per molecule are involved in the higher modes, the ‘concentration’ of the p -th mode is one p -th the number of conformers involved in the fundamental mode. Only the odd terms, $p = 1, 3, 5, \text{etc.}$ can be effective in moving the center of mass of the strand. Putting this all together, one obtains the relaxation spectrum from $\rho RT/pM_e$, for the intensity. The relaxation modulus of the entanglement coupling is given below, for the storage modulus:

$$G'(\omega) = \frac{\rho RT}{M_e} \sum_{p, \text{ odd}} \frac{1}{p} \frac{\omega^2 (\tau_1 / p^{3.4})^2}{1 + \omega^2 (\tau_1 / p^{3.4})^2} \quad (44a)$$

and for the loss modulus:

$$G''(\omega) = \frac{\rho RT}{M_e} \sum_{p, \text{odd}} \frac{1}{p} \frac{\omega(\tau_1/p^{3.4})}{1 + \omega^2(\tau_1/p^{3.4})^2} \quad (44b)$$

where τ_1 is the terminal (longest) relaxation time, and it is the fundamental mode. Again, for the solution, c should be used instead of ρ .

In Fig. 13, the dynamic moduli are constructed using Eq. (44) for the polystyrene melt at 160°C, illustrating a good agreement for the calculated lines with Graessley's data shown by points. If the coils were isolated, the high frequency side of the loss G'' maximum would have been a straight line with the slope of $-(1/3\nu-1) = -0.57$, as for the dielectric data for polyisoprene solution. As it is for the melt, the intermolecular coupling boosts the higher modes, and the slope for the monodisperse polymer should be $\{1/(3.4+1)\} = 0.227$ for G' , and -0.227 for G'' . In our analysis, three molecular weight species with $\tau_1 = 50s$, $5s$, and $0.5s$, with the intensity of $H = 1 \times 10^6$, 5×10^5 , and 2×10^5 dynes/cm², respectively, for $T = 160^\circ\text{C}$, were chosen through iterations to give a good fit. (H is the value of the delta function at each τ_1 .) This means that this polymer sample was *equivalent* to a mixture of three molecular weight species, weighted by the respective magnitude of H s. The true elastic modulus G_e is the sum of the dirac deltas for the fundamental modes only, $G_e = \sum H$, and is equal to 1.7×10^6 dynes/cm², which will obtain $M_e = 2.14 \times 10^4$. The value of G_{exp} obtained by extrapolating the quantity $[|G^*|^2/G']$ to infinite frequency can be twice as great as $G_e = \sum H$, because the higher modes for the same molecule is included in

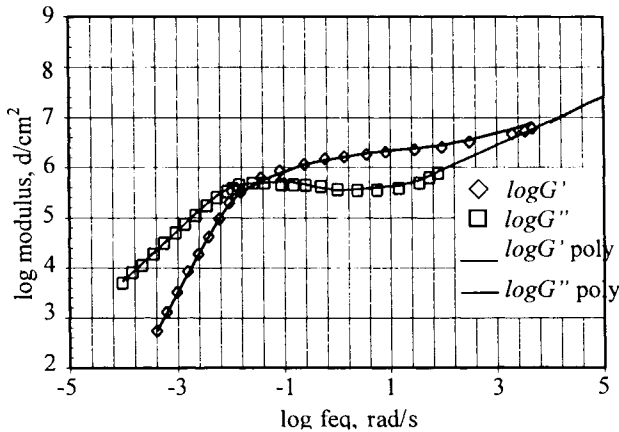


Fig. 13. Dynamic Mechanical Moduli G' and G'' constructed for a polystyrene melt at 160°C by using the model described in Eqs. (44)a and b.

G_{exp} , i.e., $G_{exp} = (1+1/3+1/5+1/7+...)G_e$. The critical molecular weight M_v for the viscosity should not be calculated from G_{exp} , or it would be *smaller* than M_e . The measured viscosity also is a sum of all modes and as such, $M_v = (1+1/3+1/5+1/7+...)M_e$. If up to the seventh mode is added, M_v of 3.59×10^4 is obtained. These values are in close agreement with the observations made for the critical molecular weight from the viscosity slope change. Thus G_e and M_e represent the smallest ball size, or de Gennes's blob. The value of M_e depends on the chain stiffness, and the chain is stiffer when the size of conformer is larger. From the spectrum, the molecular weight distribution of the polymer sample has been calculated: $M_w = 3.9 \times 10^5$ and $M_n = 3.5 \times 10^5$ with M_w/M_n of 1.1. This procedure was repeated for other molecular weight species, although the results are not shown here, and a satisfactory agreement was obtained for the entire range of entanglement forming molecular weight [15].

The blob is not purely elastic, but it too is viscoelastic. Its relaxation time is the shortest for the entanglement network, since it is the smallest, and corresponds to the highest mode for all balls. The relaxation time for this blob is 1.6×10^{-3} s for polystyrene at 160°C. At the same time, M_e is the *highest* molecular weight for the free-draining worms.

The worm-like behavior has been modeled by a string of beads connected by springs suspended in a fluid. The model is known as the Rouse/Bueche model. The relaxation time τ_p for the p-th mode is proportional to $(M/p)^2$, whereas the spring constant is the same for all modes. Hence, the dynamic moduli G' and G'' for the worm-like chains are described by the formulas

$$G'(\omega) = \frac{\rho RT}{M_e} \sum_p \frac{\omega^2 (\tau_1 / p^2)^2}{1 + \omega^2 (\tau_1 / p^2)^2} \quad (45a)$$

and

$$G''(\omega) = \frac{\rho RT}{M_e} \sum_p \frac{\omega (\tau_1 / p^2)}{1 + \omega^2 (\tau_1 / p^2)^2} \quad (45b)$$

to be compared with Eqs. (44)a and (44)b for the ball-like behavior. In this range of frequency, $\log G'$ and $\log G''$ overlap on top of each other, with the slope of 1/2. The viscosity, being the product $\{c/M\}G\tau$, or $\propto (1/M) \times M^2$, is proportional to M for the worm-like behavior.

Finally, Fig. 14 is the result of all of the discussions in this section put together. A master curve was produced versus frequency first for the entanglement regime using Eq. (44), the transition regime using Eq. (45), and the glassy area using the spectrum shown in Fig. 6 and Eq. (29). Then transforming that master curve into an isochronal plot, versus temperature at a

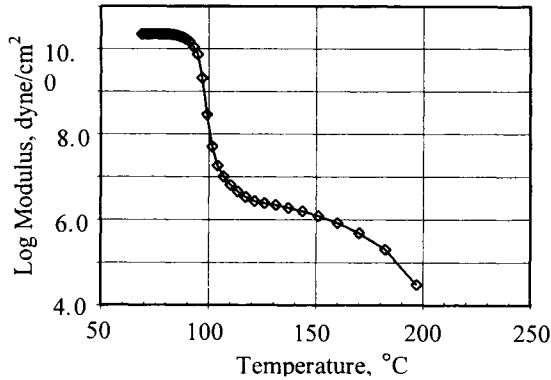


Fig. 14. A Master Isochronal Relaxation Modulus for Polystyrene. against temperature; it compares well with the data published by Tobolsky and Yu (Ref. p 76).

fixed frequency of 0, 1 rad/s. This curve compares very well with the “10 seconds” modulus plotted.

5. BEYOND LINEAR VISCOELASTICITY

First, continuing on the linear viscoelastic behavior, let us consider the case for subjecting a single relaxation time linear viscoelastic material to a constant rate of strain, $\dot{\gamma}$. The shear stress σ rises as described by the following equation:

$$\sigma = \dot{\gamma} \int_0^t G_0 \exp\left(-\frac{t-x}{\tau}\right) dx = \dot{\gamma} G_0 \tau \left[1 - \exp\left(-\frac{t}{\tau}\right)\right] \quad (46)$$

where G_0 is the elastic constant and is equal to the entropic spring constant $\rho RT/M_e$.

After a long time as compared to τ , the flowing polymer molecules come to the steady state, and the stress reaches the steady state stress $\sigma_{ss} = \dot{\gamma} G_0 \tau$, hence the steady state viscosity is $G_0 \tau$, and it is independent of the rate of strain $\dot{\gamma}$. Linear viscoelastic behavior means the steady state stress σ_{ss} to be proportional to the strain rate, and increases without a theoretical limit in proportion to the strain rate. On the other hand, a real material will reach a limiting value for the stress. This maximum stress it can sustain can be the yield stress in a classical plastic body. The yield criterion is the maximum strain energy (a type of mechanical free energy). The energy criterion is known by the name of its

author, von Mises. A viscoelastic body could also reach a stress limit also. If it is deformed too fast, *i.e.* $\dot{\gamma} \gg 1/\tau$, the entangled isotropic structure can break up and the ball will undergo a *plastic deformation*, in which case the stress is independent of flow rate. The apparent viscosity is now inversely proportional to the flow rate, instead of being constant as in linear viscoelastic flow. A plot of log viscosity versus log shear rate would be -1.

Because polymers exhibit multiple relaxation times, at a given rate of strain rate, the plastic yield stress will depend on the shear rate, as briefly presented in 3.3, and explained in detail below. There is a cut-off point in the strain rate for the linear viscoelasticity, beyond which the plasticity takes over as the stress being the critical factor. A mode with short relaxation time stays linear viscoelastic up to a considerably high rate of flow, while a mode with long relaxation time will reach the yield stress at much slower shear rate. All these modes with $\tau_p < \dot{\gamma}$ will behave according to linear viscoelasticity, and the rest will behave according to plasticity. At a faster rate of strain, there will be less number of those modes which remain linear viscoelastic, and more would act as plastic. Thus, at faster rates of strain, the apparent viscosity decreases. The slope β of log viscosity versus log shear rate can never reach -1, but the steepest slope would be $(1/(3.4+1+1)-1) = -0.815$, since $\eta_p = \tau_p/M_p$. The value for β can be obtained from the slope of $\log G'/\omega$ versus ω . Other ways of finding the value for β are very complicated, and involve certain assumptions on the constitutive equations [39,40].

To formulate the viscoplastic flow stress, the steady state stress σ_{ss} is introduced as the viscoplastic stress:

$$\sigma_{ss} = \dot{\gamma} \sum_p G_p \tau_p \left[1 - \exp\left(\frac{\gamma^*}{\dot{\gamma} \tau_p}\right) \right] \cong \dot{\gamma} \sum_p G_p \tau_p \left[1 + \left(\frac{\dot{\gamma} \tau_p}{\gamma^*}\right)^2 \right]^{1/2} \quad (47)$$

where γ^* is the yield stress divided by the unrelaxed modulus, and is called the yield strain here.

The last term in the above equation would be exactly the magnitude of the complex dynamic viscosity if $\omega = \dot{\gamma}/\gamma^*$. If the yield strain γ^* is 1, then the frequency ω in the complex modulus can be substituted by the flow rate to obtain the exact identity between the two kinds of entirely different viscosity terms, one the nonNewtonian flow viscosity and the other the linear viscoelastic complex viscosity calculated from G' and G'' . This identity of η and $|\eta^*|$ is known as the Cox-Merz empirical rule.

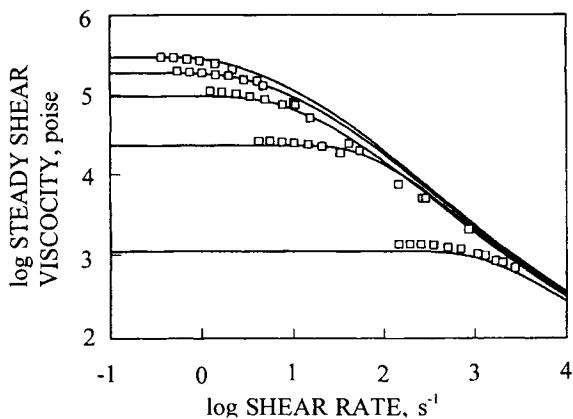


Fig.15. Steady flow viscosity constructed from viscoplasticity

The yield strain γ^* is not always equal to 1 in real polymers and as such, some shifting is required. There is also a stress overshoot, going over a maximum before settling to σ_{ss} as observed by Maxwell and Nguyen [41]. In a shear thinning environment, this is as though slowing down the apparent strain rate temporarily, and when plotted against the real strain rate, the viscosity will reach a maximum between the slow and a fast rates. The steady state viscosity is calculated for the polystyrene samples we studied. The result is shown in Fig. 15, and compared with the data of Stratton.

REFERENCES:

1. E. Catsiff, and A. V. Tobolsky, *J. Colloid Sci.*, 10 (1955) 375.
2. M. L. Williams, R. F. Landel, and J. D. Ferry, *J. Am. Chem. Soc.*, 77 (1955) 3701.
3. A. K. Doolittle, *J. Appl. Phys.*, 22 (1951)1471.
4. H. Vogel, *Physik. Z.*, 22 (1921) 645.
5. R. S. Porter, ed., *Strength and Stiffness of Polymers*, Dekker, NY. 1983.
6. D. N. Theodorou, and U. W. Suter, *Macromolecules*,18 (1985) 35.
7. D. W. McCall, U. S. Nat. Bur. Stand. Publication, (1968) 301, Washington, DC.
8. S. Matsuoka, *J. Res. Natl. Inst. Stand. Technol.*, 102 (1997) 213.
9. K. F. Herzfeld, and T. A. Litovitz, *Absorption and Dispersion of Ultrasonic Waves*, Academic Press, New York and London, 1959.
10. W. Kauzman, *Chem. Rev.*, 43 (1948) 219.
11. G. Adam and J. H. Gibbs, *J. Chem. Phys.*, 43 (1965) 139.
12. M. Theodorou, B.Jasse, L. Monnerie, *J. Polym Sci. Phys.* 23 (1985) 445.
13. P. J. Flory, *Proc. Roy. Acad. Sci.*, A234 (1956) 73.
14. G. Williams and D. C. Watts, *Trans. Faraday Soc.*, 67 (1971) 1323.
15. S. Matsuoka, *S. Relaxation, Phenomena in Polymers*, Hanser, Munich, New York, 1992.
16. P. J. Flory and T. G. Fox Jr., *J. Am. Chem. Soc.* 73 (1951) 1904.

17. F. Billmeyer Jr., *Textbook of Polymer Science*, Wiley, NY, 1962, 82.
18. P. Debye, *Polar Molecules Chemical Catalog Co.* 1929 Dover Publications.
19. R. J. Meakins, *Trans Faraday Soc.* 54 (1958) 1160.
20. S. S. Patel and K. N. Takahashi, *Macromolecules*, 26 (1993) 1043.
21. R. Simha and L. Utracki, *J. Polym. Sci.*, A-25 (1967) 853.
22. T. Yanaki and T. Yamaguchi, *Biopolymers*, 30 (1990) 415.
23. H. Yamakawa, *Macromolecules*, 10 (1977) 692.
24. G. C. Berry, *J. Rheol.* 40 (1996) 1129.
25. T. Kotaka and K. Osaki, *J. Polym. Sci.*, 15C (1966) 453.
26. T. Norisue, *Prog. Polym. Sci.*, 18 (1993) 543.
27. P. E. Rouse and K. Sittel, *J. Appl. Phys.*, 24 (1953) 690.
28. F. Bueche, *J. Chem. Phys.*, 22 (1954) 1570.
29. E. Shimada and G. Matsumura, *J. Biochem.*, 78 (1975) 513.
30. H. Bothner, T. Waaler and O. Wik, *Int. J. Biol. Macromol.*, 10 (1988) 287.
31. T. Yanaki and M. Yamaguchi, *Chem. Pharm. Bull.*, 42 (1994) 1651.
32. W. P. Cox and E. H. Merz, *J. Polym. Sci.*, 28 (1958) 619.
33. Green, M. S. and A. V. Tobolsky, *J. Chem. Phys.*, 14 (1946) 80.
34. J. D. Ferry, *Viscoelastic Properties of Polymers*, Wiley, NY, 1978.
35. P.-G. de Gennes, *Scaling Concepts in Polymer Physics*, Cornell U. Press, Ithaca, 1979.
36. M. Doi and S. Edwards, *J. Chem. Soc., Faraday Trans.*, 74 (1978) 1802.
37. F. Kremer, *Macromolecules*, 23 (1990) 829.
38. H. Watanabe, K. Adachi and T. Kotaka, *Macromolecules*, 24 (1991) 2981.
39. W. W. Graessley, *J. Chem. Phys.*, 47 (1967) 1942.
40. R. A. Stratton, *J. Colloid Interf. Sci.*, 22 (1966) 517.
41. B. Maxwell and M. Nguyen, *Polym. Eng. Sci.*, 19 (1979) 1140.

Chapter 4

Dielectric analysis of polymers

Peter Avakian, Howard W. Starkweather, Jr. and William G. Kampert

DuPont Central Research and Development, Experimental Station, Wilmington, Delaware 19880-0356

1. INTRODUCTION

Dielectric analysis is used along with dynamic mechanical analysis (DMA) to study viscoelastic relaxations. In addition to its relevance to electrical applications of materials, it is a probe for molecular motions and for certain aspects of morphology and structure. Dielectric analysis is sensitive only to internal motions, which involve the reorientation of electrical dipoles.

Fig. 1 shows the introduction of a symbolic dielectric (containing permanent dipoles) into the space between the electrodes of a capacitor. Initially, the dielectric material is unpolarized and the dipoles are oriented at random. The electric field between the electrodes due to the applied voltage tends to rotate the dipoles so that the material becomes either partially or fully polarized. Generally only a partial polarization occurs in practice. When a dielectric is present in a capacitor, the charges within the material tend to approach the electrode of opposite charge, thereby inducing the flow of additional charges onto the capacitor plates from the voltage source (battery). Thus, the presence of the dielectric increases the charge storing ability or capacitance of the capacitor. The ratio of the capacitances with and without the dielectric is called the dielectric constant or permittivity, ϵ' .

Actually, the permittivity is not a constant but depends on the temperature and frequency or time. The complex dielectric permittivity may be expressed by

$$\epsilon^* = \epsilon' - i\epsilon'' \quad (1)$$

where ϵ' is the real part, and ϵ'' is the imaginary part. The latter is also known as the dielectric loss factor. The dielectric loss tangent or dissipation factor is given by

$$\tan \delta = \epsilon''/\epsilon' \quad (2)$$

The permittivity is equivalent to the compliance, the reciprocal of the modulus, in a mechanical experiment. When a sinusoidal voltage is applied to the plates of a capacitor containing a dielectric, the resulting sinusoidal charge lags the voltage by the phase angle (or loss angle), δ .

The way in which ϵ' and ϵ'' vary is summarized in Fig. 2. When the temperature is low or the frequency is high, the relaxation time for internal motions is long compared to the reciprocal of the instrumental alternating voltage frequency. The amplitude of the electric field induced dipolar motions is small. The permittivity is low, and there is little energy loss. At high temperatures and low frequencies, the internal motions easily keep up with the alternating voltage. Under these conditions, the permittivity is high and, due to the low "internal friction", the energy loss is low. At intermediate temperatures,

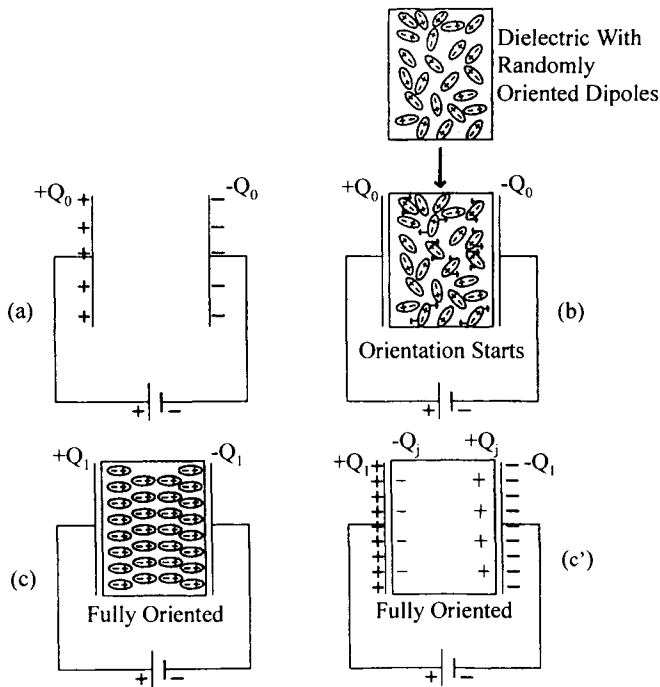


Fig. 1. Polarization of a dielectric in a parallel plate capacitor

Starting with an empty parallel plate capacitor connected to a battery (a), a dielectric polymeric sample containing randomly oriented dipoles is inserted between the plates of the capacitor (b). The electric field between the plates of the capacitor causes the orientation of the dipoles in the sample resulting in a sheet of bound negative charges and bound positive charges at the opposite faces of the sample (c), and this leads to accumulation of additional charges on the capacitor plates (c').

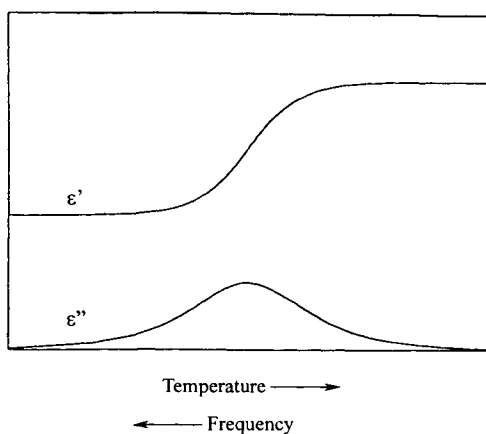


Fig. 2. Dependence of the dielectric parameters on temperature and frequency

when the experimental frequency is comparable to the rate of the internal motions, the permittivity goes through intermediate values, and there is a maximum in the loss. The higher loss arises from the combined effect of appreciable amplitude for the field induced dipolar motions and appreciable magnitude for the “internal friction”. The dependence of the dissipation factor on temperature and frequency is similar to that for ε'' .

Many polymers exhibit multiple relaxations, and the loss and dissipation factors have several maxima. These are generally designated by the Greek letters, α , β , γ , etc., in the order of decreasing temperature. The α -relaxation is frequently the glass transition (T_g) which is associated with the onset of the motion of relatively long chain segments in the amorphous regions. Secondary relaxations at lower temperatures are attributed to more local internal motions.

The most widely used frequencies in dielectric analysis are from 10^2 to 10^5 Hz (cycles per second). All relaxations occur at higher temperatures as the frequency of measurement is increased. The location of the loss maxima may be determined from either isochronal (constant frequency) temperature scans or isothermal frequency scans. While the former are more widely used, the latter may be preferred for scientific analysis because of the changes of volume with temperature. The relationship between temperature and frequency is expressed in terms of the Arrhenius relationship where E_a is the activation energy, A the preexponential factor, and R the gas constant.

$$f = A \exp(-E_a/RT) \quad (3)$$

$$E_a = -R \, d(\ln f)/d(1/T) \quad (4)$$

For a more detailed introduction to dielectric spectroscopy of polymers, including the experimental methodology, the reader could examine references 1-5 and references cited therein.

2. POLAR AMORPHOUS POLYMERS

2.1. Polymethyl methacrylate (PMMA)

The dielectric properties of a sample of PMMA, which had been polymerized by casting to form a cylinder for optical studies, were measured at frequencies from 10 to 10^5 Hz. The dissipation factor at the even decade frequencies is plotted against temperature in Fig. 3. The most prominent feature is the β -relaxation which occurs at a temperature which varies with frequency from 30°C at 10Hz to 145°C at 10^5 Hz, corresponding to an Arrhenius activation energy (from Eq. (4)) of about 85 kJ/mol.

The α -relaxation which corresponds to the glass transition was resolved as a peak only at frequencies from 10 to 200 Hz. At higher temperatures and frequencies, it merges with the β -relaxation.

When two peaks overlap, they appear to be shifted toward each other. Thus, the temperature of the α -relaxation appears to be almost independent of frequency at about 127°C. On the other hand, the temperature of the β -relaxation appears to increase more rapidly with frequency under conditions where it overlaps the α -relaxation. These features are shown in Fig. 4, which is a so-called relaxation map, a plot of log frequency vs. the reciprocal of the absolute temperature.

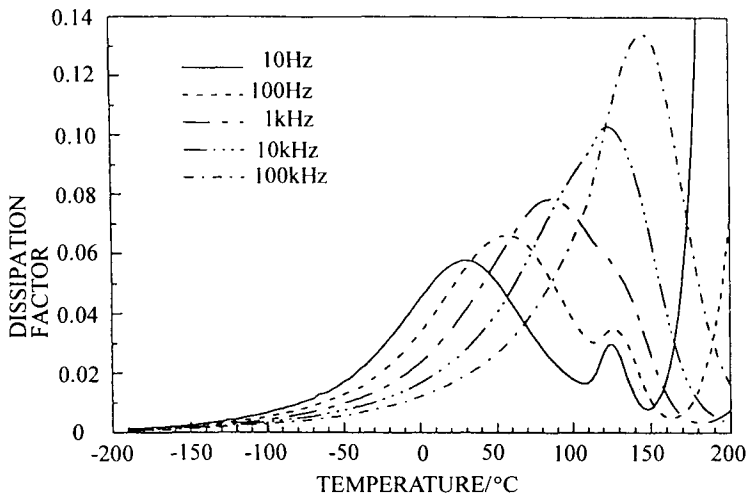


Fig. 3. Dissipation factor of polymethyl methacrylate

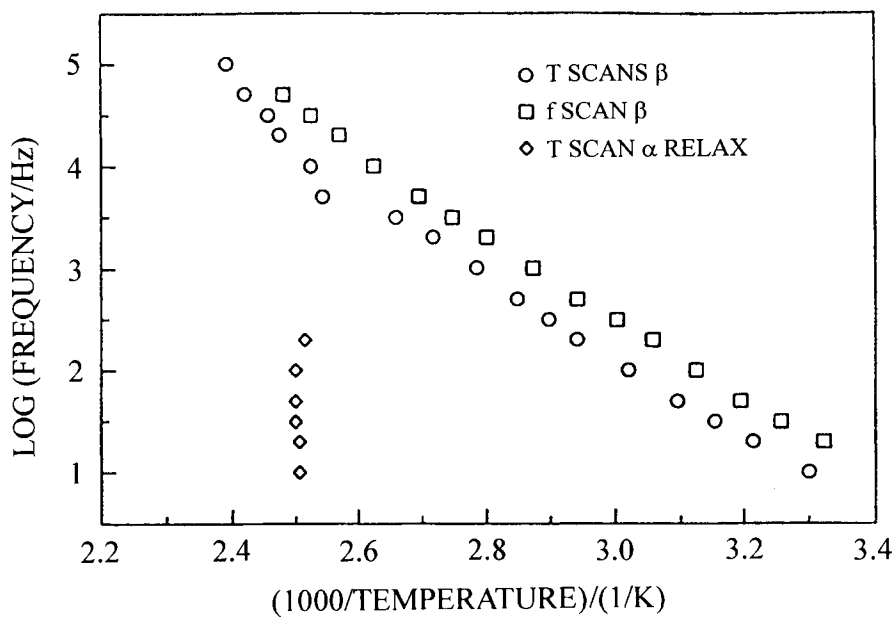


Fig. 4. Relaxation map for polymethyl methacrylate

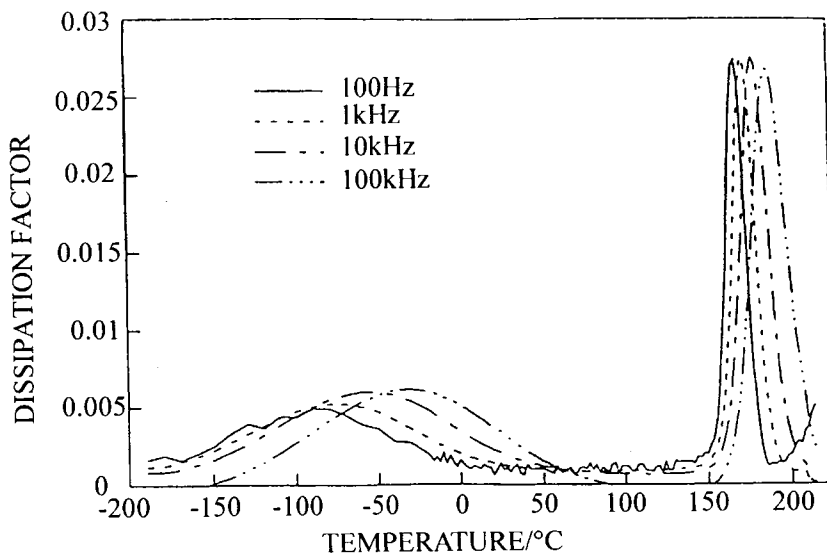


Fig. 5. Dissipation factor of polycarbonate

2.2. Polycarbonate

The analysis of the viscoelastic behavior of the polycarbonate based on bis phenol-A is simplified by the fact that the principal relaxations are well separated. At a frequency of 1 kHz, the peak for the β -relaxation occurs at -75°C and that for the α -relaxation at 174°C . As shown in Fig. 5, the β peak is broader when plotted against temperature, and the temperature of its maximum increases more rapidly with increasing frequency. In other words, its activation energy is smaller. On the other hand, the peak height is much greater for the α -relaxation or glass transition. The relaxation map for polycarbonate is shown in Fig. 6. The activation energies are 636 kJ/mol for the α -relaxation and 38 kJ/mol for the β -relaxation.

The variations of ϵ' and ϵ'' with temperature and frequency are shown in Figures 7 and 8. A Plot of ϵ'' vs. ϵ' is known as a complex plane or Cole-Cole plot. The intercepts with the ϵ' axis are the unrelaxed and relaxed permittivities, ϵ_u and ϵ_R , respectively. The unrelaxed permittivity is the limiting value at low temperatures and high frequencies, while ϵ_R is the limiting value at high temperatures and low frequencies.

For the β -relaxation in polycarbonate and most secondary relaxations, the points of the complex plane plot can be fitted by an arc of a circle whose origin lies below the ϵ' axis. This relationship is known as the Cole-Cole equation. For this relaxation as shown in Fig. 9, ϵ_u is 2.77 and ϵ_R is 2.96.

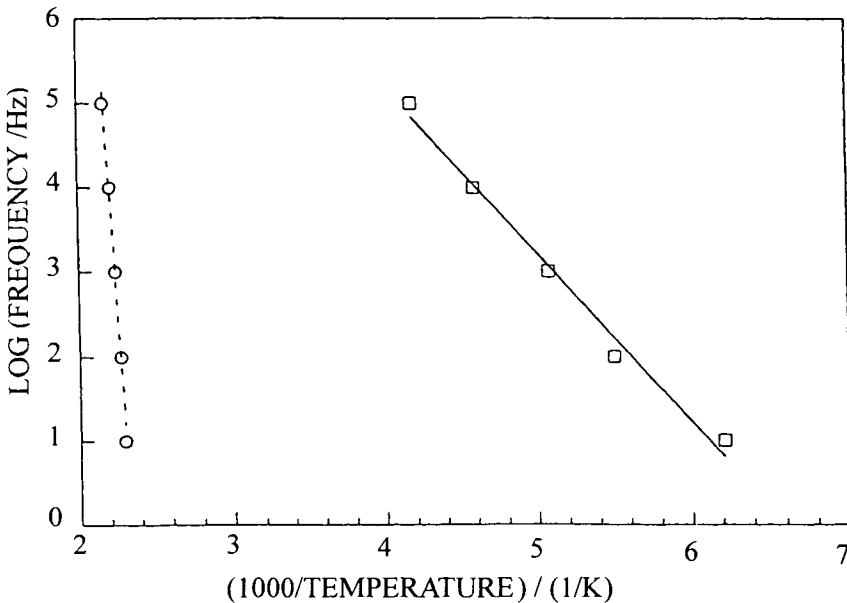


Fig. 6. Relaxation map for polycarbonate.

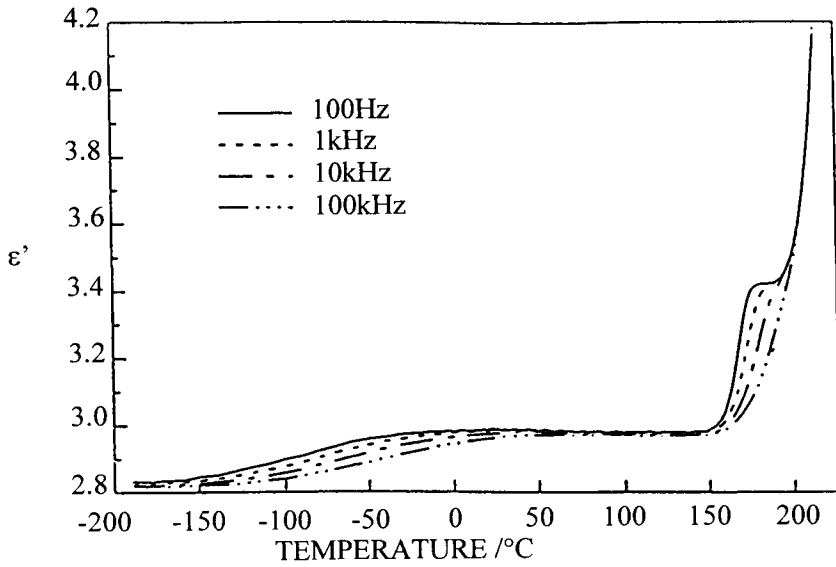


Fig. 7. Permittivity of polycarbonate

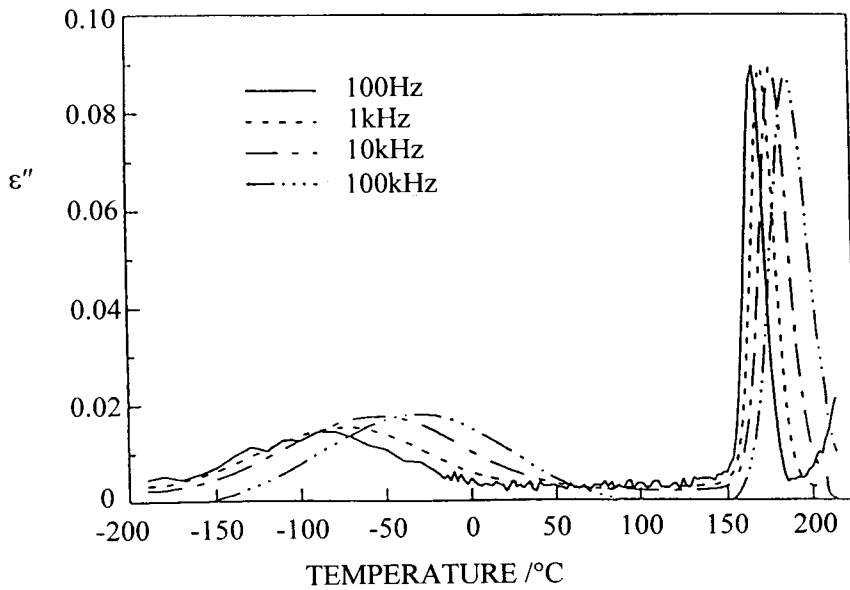


Fig. 8. Loss factor of polycarbonate

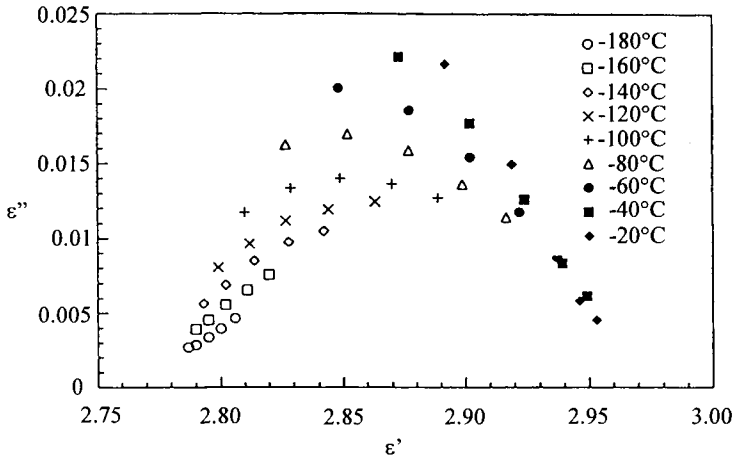


Fig. 9. Complex plane plot for the β -relaxation of polycarbonate

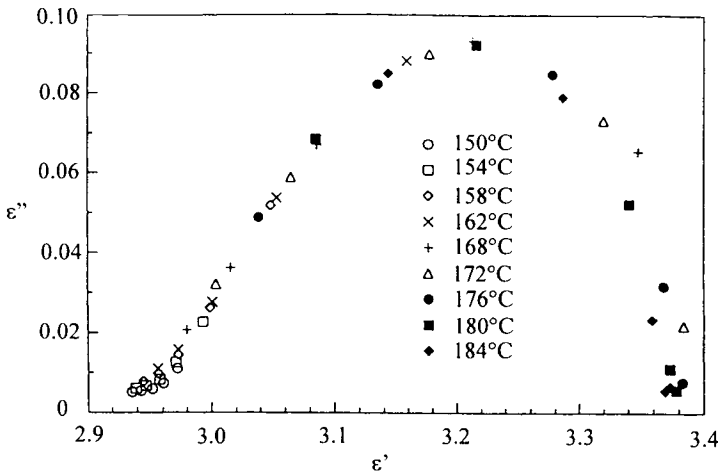


Fig. 10. Complex plane plot for the α -relaxation in polycarbonate

For the α -relaxation in polycarbonate and glass transitions in general, the complex plane plot is asymmetric, being stretched on the low temperature, high frequency, or low ϵ' side to approximate a straight line. As is shown in Fig. 10, the points from various temperatures and frequencies in the region of the α -relaxation point to values of 2.94 for ϵ_u and 3.38 for ϵ_R .

2.3. Polyamides

Dynamic Mechanical measurements on aliphatic polyamides at frequencies near 1 Hz have revealed γ , β , and α -relaxations at about -123, -23, and -77°C,

respectively. All of these relaxations have been assigned to internal motions in the amorphous regions of the semicrystalline polymers.

While these relaxations are reflected in both the dielectric and mechanical properties, the former are complicated by the effect of conductivity at high temperatures [6]. This is shown by the tendency of the dielectric loss factor, ε'' , to become inversely proportional to the frequency at low frequencies and high temperatures. This problem can be addressed by presenting the data in the form of the electric modulus, M , which is the reciprocal of the permittivity.

$$M' + iM'' = (\varepsilon' - i\varepsilon'')^{-1} \quad (5)$$

$$M' = \varepsilon' / (\varepsilon'^2 + \varepsilon''^2), \quad M'' = \varepsilon'' / (\varepsilon'^2 + \varepsilon''^2) \quad (6)$$

The three functions, ε'' , $\tan \delta$, and M'' , for Nylon 6 measured at 1 kHz, are plotted against temperature in Fig. 11 [6]. The γ and β -relaxations appear as shoulders at about -90 and -20°C , respectively. The α -relaxation also forms a shoulder for ε'' and $\tan \delta$ but appears as a peak in M'' at about 70°C .

There is a second peak in M'' at 125°C which has been called the "conductivity relaxation". It is a result of the algebraic relationships among the permittivity, the electric modulus, and the conductivity. For the conductivity relaxation, the relationships among M'' , M' and the frequency at a given temperature correspond to a Debye relaxation having a single relaxation time [6].

The apparent activation energies for conductivity in Nylons 6 and 66 are about 105 kJ/mol. The dielectric behavior of polyamides can be clarified by

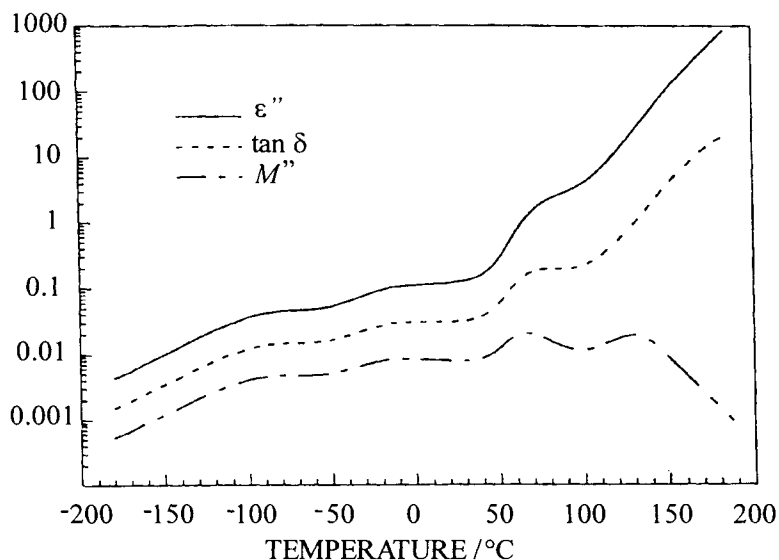


Fig. 11. Loss functions for Nylon 6. (Adapted with permission from reference 6; copyright 1992, John Wiley & Sons, Inc.)

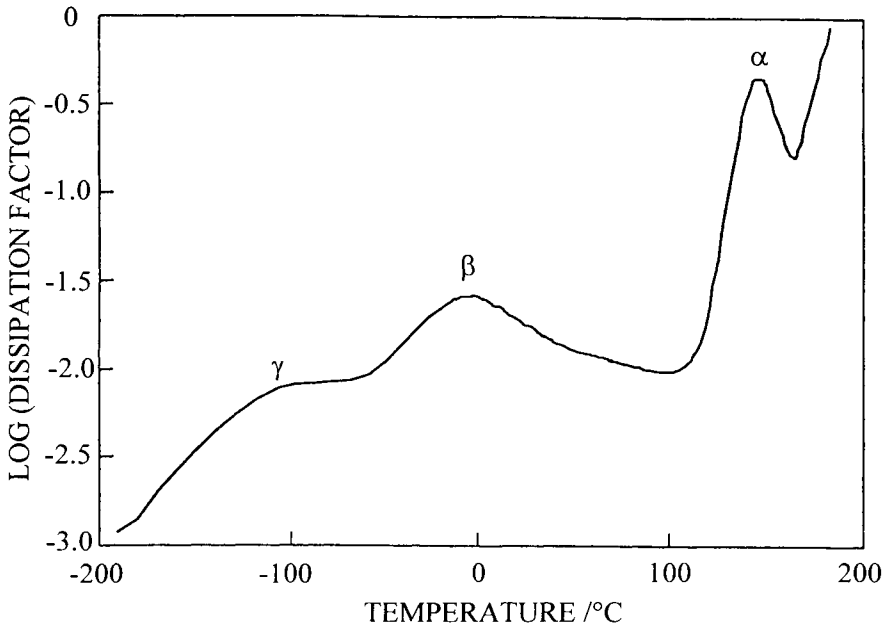


Fig. 12. Dissipation factor at 1 kHz for Nylon 6-I/T(70/30) (Adapted with permission from reference 7; copyright 1991, American Chemical Society.)

considering a partially aromatic polymer such as Nylon 6-I/T(70/30), the polyamide derived from hexamethylene diamine and a 70/30 mixture of isophthalic and terephthalic acids [7]. The dissipation factor measured at 1kHz on a sample of this polymer which had been conditioned to 11.3% relative humidity (RH) is plotted against temperature in Fig. 12. The positions of the γ and β -relaxations are not far from those which were observed for Nylon 6, but the α -relaxation has been moved to about 140°C. Thus, an effect of introducing the aromatic structure has been to greatly increase the temperature of the α -relaxation or glass transition and separate it clearly from the β -relaxation.

Measurements on a series of samples conditioned to various relative humidities showed that the temperature of the α -relaxation varies linearly with humidity from 154°C at 0% RH to 60°C at 100% RH. In both aliphatic and partially aromatic polyamides, the temperature of the α -relaxation decreases by almost 100°C between dryness and saturation and depends linearly on relative humidity. However, while in aliphatic polyamides the relaxation passes through room temperature in the midrange of humidity, in Nylon 6-I/T(70/30), it is always well above room temperature.

The effect of low levels of humidity on the γ and β -relaxations in Nylon 6-I/T(70/30) is shown in Fig. 13. As the humidity was increased between dryness and 22.5%, the strength of the β -relaxation increased, and the γ -relaxation faded

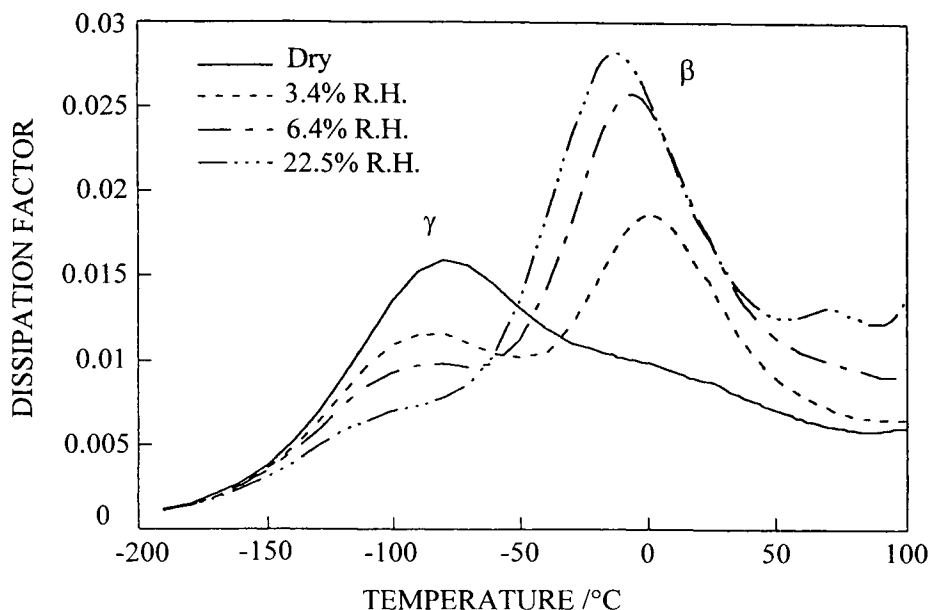


Fig. 13. Effect of humidity on the γ and β -relaxations in Nylon 6-I/T (70/30). (Adapted with permission from reference 7; copyright 1991, American Chemical Society.)

away. Additional changes in strength at higher humidities were minor, but the temperature of the β -relaxation decreased throughout the humidity range.

The γ -relaxation has been attributed to local motions of sequences of methylene units. The fact that it is dielectrically active indicates that there must be some involvement of the polar amide groups. Mechanical studies have found a similar suppression of the γ -relaxation when nylon absorbs water accompanied by an increase in the modulus at low temperatures. This is an example of antiplasticization. It is suggested that at low temperatures, water can form a mechanically stable complex with the amide groups in nylon. The β -relaxation is attributed to motions of labile amide-water complexes.

3. NONPOLAR POLYMERS

3.1. Hydrocarbon polymers

Dielectric loss peaks reflect internal motions, which involve the reorientation of electric dipoles. If there is no dipole moment, such a motion will be dielectrically silent even though it produces strong effects when studied by dynamic mechanical analysis (DMA) or nuclear magnetic resonance (NMR). This is generally the case with hydrocarbon molecules unless they have been

decorated with dipoles through chlorination or oxidation to form carbonyl or hydroxyl groups [8]. Since polyolefins, such as polyethylene and polypropylene, are extremely susceptible to oxidation, they may well show dielectric relaxations unless great care is taken. An additional complication is the fact that certain widely-used stabilizers contain polar phenolic groups.

A feature of polyolefins of special interest is a relaxation at temperatures very close to absolute zero [9-11]. The frequency of this relaxation is proportional to the absolute temperature with a slope of 1 kHz/K. It has been attributed to quantum mechanical tunneling and probably reflects the reorientation of hydroxyl groups on either the polymer *per se* or stabilizer molecules. Since this process would require only the motion of a proton, the suggestion of tunneling seems reasonable.

3.2. Fluoropolymers

Carbon-fluorine bonds are highly polar. Nevertheless, if the chemical bond angles in a perfluoroalkane were tetrahedral, the dipole vectors would cancel each other, and the overall molecule would have a dipole moment of zero. Therefore, any dielectric activity is evidence for conformations having

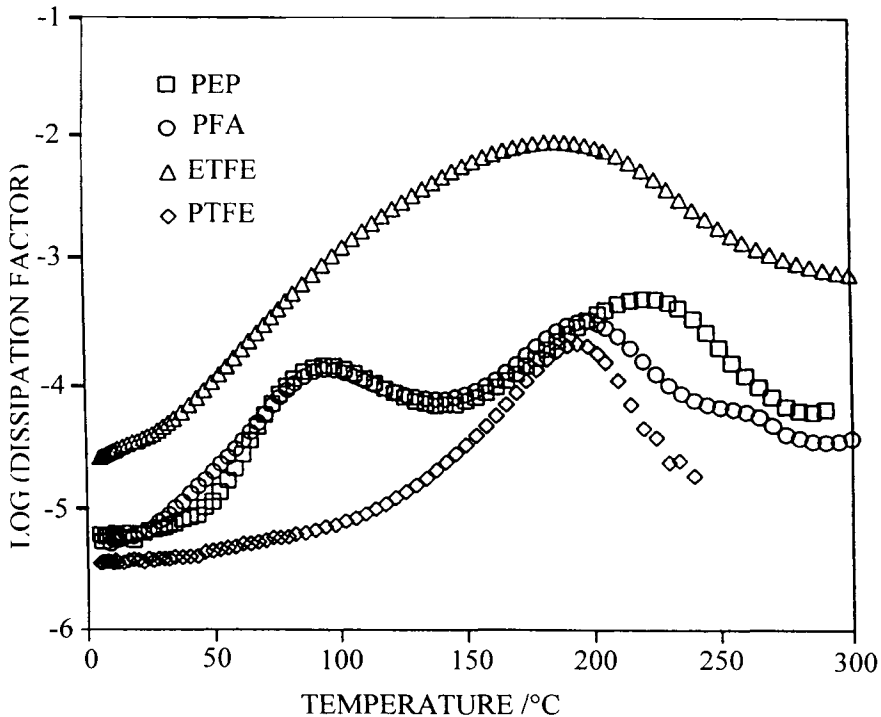


Fig. 14. Dissipation factor of PTFE and copolymers of TFE (Adapted with permission from reference 16; copyright 1991, American Chemical Society)

nontetrahedral bond angles. The presence of such angles is not unexpected in view of the known molecular conformation in crystals of polytetrafluoroethylene (PTFE). Unlike the planar zigzag in polyethylene, the repulsion between the fluorine atoms attached to next nearest neighboring carbon atoms in PTFE produces a helical conformation.

It is well known that three mechanical relaxations are observed in PTFE [12]. The γ -relaxation which is seen at about -98°C at a frequency of 1 Hz, is attributed to the motion of short chain segments in the amorphous regions. The β -relaxation is associated with the transitions at 19 and 30°C in the crystalline phase. Finally, the α -relaxation at about 127°C is attributed to motions of longer chain segments in the amorphous regions. In early work, it was reported that each of these relaxations was dielectrically active [13,14]. However, it now appears that the samples in those studies contained extraneous dipoles.

In more recent studies, it has been found that only the γ -relaxation produces a dielectric loss peak in PTFE [15,16]. This is shown in Fig. 14 for PTFE and certain copolymers of tetrafluoro-ethylene (TFE). At 1 kHz, the peak occurs at -79°C for PTFE, at -53°C for FEP, the copolymer of TFE with hexafluoropropylene, at -75°C for PFA, the copolymer of TFE with perfluoro vinyl propyl ether, and at -87°C for E/TFE, a largely alternating copolymer of TFE with ethylene. The activation energies for these relaxations are 45 kJ/mol for and about 67 kJ/mol for E/TFE the other polymers.

Both FEP and PFA exhibit an additional relaxation at -179°C with an activation energy of 15.5 kJ/mol which is attributed to motions of the side groups which are not present in PTFE or E/TFE [16,17]. There is a small dielectric loss associated with the α -relaxation in FEP [15] and a more substantial one for the α -relaxation in E/TFE [18].

PTFE is able to absorb small amounts of certain compounds of relatively low cohesive energy density, e.g. 2% carbon tetrachloride and 1.4% chloroform. While both of these additives have been shown to affect the dynamic mechanical properties [19], only chloroform has a dipole moment. The presence of absorbed chloroform increases the peak height for the γ -relaxation and introduces a new relaxation at -206°C with an activation energy of 12 kJ/mol in isochronal frequency scans and -224°C with an activation energy of 9.4 kJ/mol in isothermal frequency scans [20]. This relaxation which is stronger than the γ -relaxation is attributed to the reorientation of individual molecules of absorbed chloroform.

4. MISCIBILITY OF POLYMER BLENDS

It is widely agreed that the behavior of the glass transition provides the best evidence of whether or not polymers in a blend are miscible on a molecularly intimate level. If they are miscible, a single T_g should be observed at a

temperature intermediate between those for the component polymers. Otherwise, there will be two T_g 's at temperatures close to those for the component polymers. It has been found that dynamic mechanical analysis can reveal features which are hard to see by DSC. While the same kind of information can be obtained by dielectric analysis, there have been relatively few studies in which this approach has been used.

Fijimoto and Yoshimiya [21] studied blends of cis-1,4-polybutadiene (BR) with natural rubber (NR) and styrene butadiene rubber (SBR), respectively. The dielectric frequency was 100 kHz, and the compositions were varied at intervals of 20%. As shown in Fig. 15, the SBR-BR blends exhibited a single loss peak. However, separate peaks were found in the NR-BR blends. This indicates that the former are miscible, and the latter are not. In a subsequent study [22], it was shown that SBR containing up to 30% styrene is miscible in BR, but those with 40% or more styrene are not.

MacKnight and coworkers [23] conducted dielectric studies of blends of poly(2,6-dimethyl-1,4-phenylene oxide) (PPO) with polystyrene at intervals of 25% in composition using five frequencies from 10^2 to 10^5 Hz. They reported a sigmoidal dependence of T_g on composition and that miscibility was incomplete with a combination of PPO-rich and polystyrene-rich regions. However, in subsequent work by Shultz and Beach [24], it was concluded that PPO and polystyrene are miscible when adequately blended.

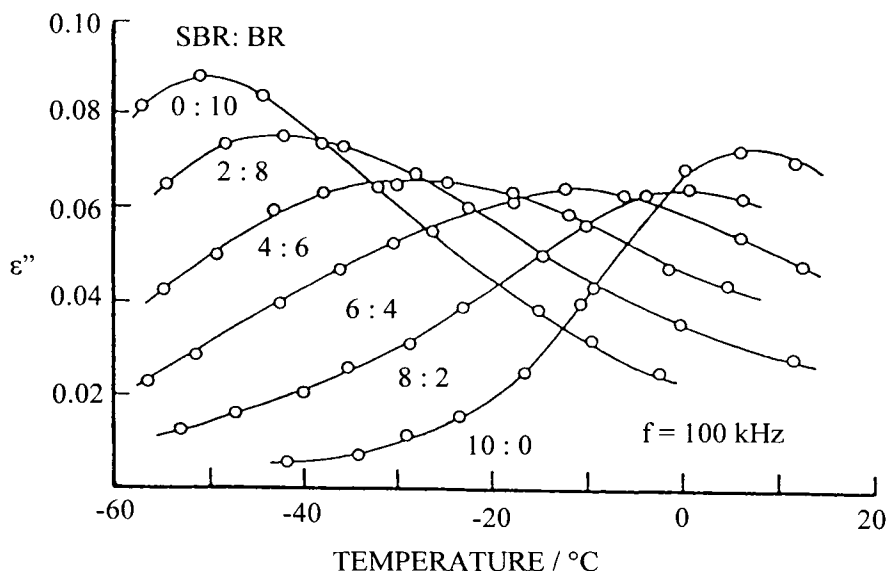


Fig. 15. Blends of rubbers. (Adapted with permission from reference 21; copyright 1968, American Chemical Society.)

Feldman and Rusu [25] reported dielectric measurements on blends of polyvinyl chloride (PVC) and a copolymer of ethylene and vinyl acetate (EVA), a polymeric plasticizer containing 45% vinyl acetate. The T_g 's were 98 - 100°C for PVC, -3°C for EVA, and 46°C for a 50/50 blend. While T_g varied linearly with composition, the maximum value of $\tan \delta$ showed a positive deviation from linearity. This was attributed to dipolar interactions between the components.

Naito and coworkers [26] studied blends of polymethyl methacrylate (PMMA) with a styrene/acrylonitrile copolymer (PSAN) containing 28% acrylonitrile at composition intervals of 25%. They used a Fourier transform dielectric spectrometer, which gave an effective range of log frequency from -0.5 to +4. These blends exhibited a single α -relaxation peak at a temperature which varied linearly with composition.

While the α -relaxation gives the primary evidence for miscibility, some of these studies contain comments on changes in secondary relaxations which are attributed to local motions in one of the components.

5. COLD CRYSTALLIZATION OF AMORPHOUS POLYMERS ABOVE T_g

A number of crystallizable polymers can be made essentially amorphous by cooling rapidly from the melt. A DSC scan on such a sample will exhibit a glass transition followed by a crystallization exotherm and eventually a melting endotherm. In a comparable dielectric scan, the permittivity will increase at the glass transition and decrease at the crystallization temperature. There will be a maxima in the dissipation factor at both temperatures corresponding to an increase and a decrease in the internal motions, respectively.

The situation is complicated by the fact that the observed temperature of the α -relaxation or glass transition depends on the frequency of the dielectric measurement while the crystallization temperature depends on the rate of heating. The equivalent frequency of a DSC measurement is very low. Thus, in dielectric measurements, the separation between the glass transition and the crystallization temperature is reduced and may even disappear.

This is illustrated for poly(ether ether ketone) (PEEK). In a DSC scan, T_g appears at 140°C followed by a crystallization exotherm at 160°C and a melting endotherm at 345°C. The corresponding dielectric data taken at 10^2 - 10^5 Hz are shown in Figs. 16 and 17. The real part of the permittivity, ϵ' , exhibits a maximum at 167 - 170°C followed by a minimum at about 175°C. As expected for phenomena related to cold crystallization, these temperatures are essentially independent of the dielectric frequency.

Maxima in the dissipation factor appear at 162, 166, 167.5, and 169°C at 10^2 , 10^3 , 10^4 , and 10^5 Hz, respectively. At the two lower frequencies, the peaks

are large and sharp as expected for a glass transition. However, at 10^4 and 10^5 Hz, the peak height decreased markedly. This is followed by a second, broader maximum in the dissipation factor at 187°C for 10^4 Hz and 197°C for 10^5 Hz. It

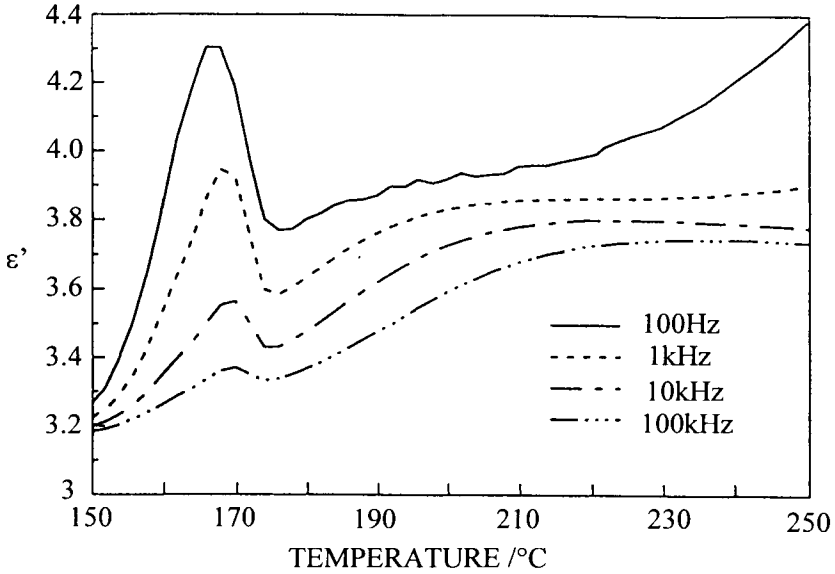


Fig. 16. Changes in ϵ' during cold crystallization in PEEK

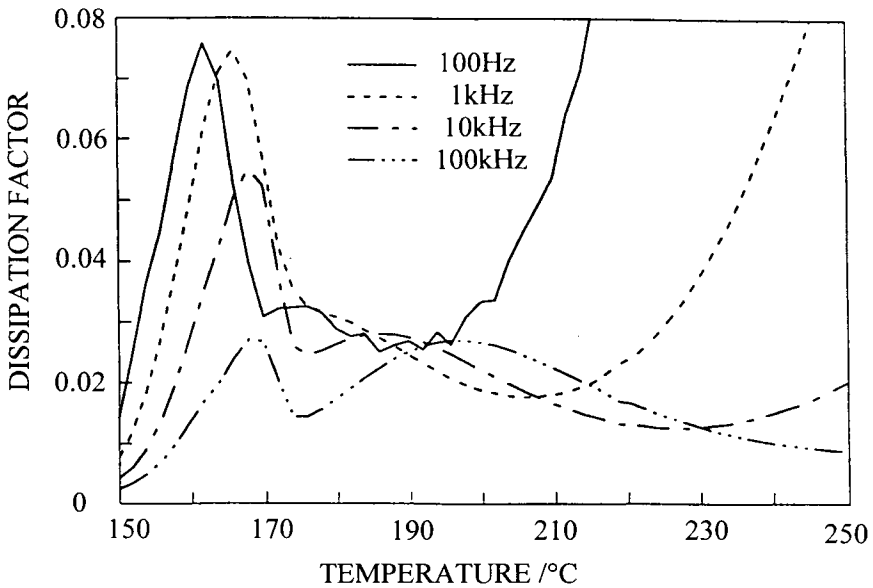


Fig. 17. Changes in dissipation factor during cold crystallization in PEEK

is characteristic for many polymers that after crystallization, the glass transition is shifted to higher temperatures and broadened. It is concluded that cold crystallization occurs before the glass transition is fully resolved at the higher frequencies.

It is clear that cold crystallization is more clearly recognized by DSC and that dielectric data on these systems must be interpreted with caution. In these situations, it may be helpful in trying to separate the effects of the glass transition and cold crystallization to repeat the experiment at various heating rates.

6. FREQUENCY-TEMPERATURE RELATIONSHIPS

The frequency-temperature relationships for viscoelastic relaxations are generally derived from similar equations for chemical kinetics with the angular velocity ($2\pi f$) taking the place of the reaction rate constant. The oldest of these is the Arrhenius equation (Eq. (3)). An alternative is derived from Eyring [27-29]

$$f = (kT/2\pi h) \exp(-\Delta H^\ddagger/RT) \exp(\Delta S^\ddagger/R) \quad (7)$$

where k is the Boltzmann constant, h is the Planck constant, and ΔH^\ddagger and ΔS^\ddagger are the activation enthalpy and entropy, respectively.

$$\Delta H^\ddagger = -R \, d \ln(f/T) / d(1/T) \quad (8)$$

It is easily shown from Equations 4 and 8 that

$$\Delta H^\ddagger = E_a - RT \quad (9)$$

Eq. (7) can be rearranged on terms of the activation free energy.

$$\Delta F^\ddagger = \Delta H^\ddagger - T\Delta S^\ddagger = RT[\ln(k/2\pi h) + \ln(T/f)] \quad (10)$$

For many secondary relaxations, ΔS^\ddagger is close to zero and ΔF^\ddagger is essentially independent of temperature. These processes are known as simple, noncooperative relaxations. On the other hand, for glass transitions, the activation energy, enthalpy, and entropy have large positive values. However, in the limit of high temperature and frequency, the activation energy of the glass transition declines and the activation entropy tends towards zero [30].

As the temperature is decreased, the internal motion requires the cooperative motion of increasingly large amounts of material. Thus, the nature of the relaxation changes, and the values of the apparent activation parameters

become very large. In a relaxation map, this is seen as a curved relationship for the glass transition which frequently follows the empirical WLF equation [31]. It should be noted, however, that the activation free energy is always less than the strength of a primary chemical bond.

ACKNOWLEDGMENTS

John R. Dowell collected a great deal of the dielectric data and Lucille Turnauer-Avakian prepared Fig. 1.

REFERENCES

1. J. M. Pochan, J. J. Fitzgerald and G. Williams, Determination of Electronic and Optical Properties, edited by B.W. Rossiter and R.C. Baetzold, Physical Methods of Chemistry Series, 2nd ed., Vol. VIII, John Wiley & Sons, Inc., New York, 1993, p. 391.
2. N. G. McCrum, B. E. Read and G. Williams, Anelastic and Dielectric Effects in Polymeric Solids, John Wiley & Sons Ltd., London, 1967; Dover Publications, Inc., New York, 1991.
3. R. H. Boyd, Methods of Experimental Physics, Vol. 16, Part C, Academic Press, New York, 1980, p. 379.
4. A. R. Blythe, Electrical Properties of Polymers, Cambridge University Press, Cambridge, 1979.
5. P. Hedvig, Dielectric Spectroscopy of Polymers, John Wiley & Sons, New York, 1977.
6. H.W. Starkweather and P. Avakian, J. Polym. Sci., Part B, Polym. Phys. Ed., 30 (1992) 637.
7. P. Avakian, R. R. Matheson and H. W. Starkweather, Macromolecules, 24 (1991) 4698.
8. C. Ashcroft and R. H. Boyd, J. Polym. Sci., Polym. Phys. Ed., 14 (1976) 2153.
9. P. S. Vincet, Brit. J. Appl. Phys. (J. Phys. D), Ser. 2, 2 (1969) 699.
10. W. A. Phillips, Proc. Roy. Soc. London A, 319 (1970) 565.
11. H. W. Starkweather, P. Avakian, R. R. Matheson, J. J. Fontanella and M. C. Wintersgill, Macromolecules, 25 (1992) 6871.
12. N. G. McCrum, J. Polym. Sci., 34 (1959) 355.
13. S. P. Kabin, Sov. Phys.-Tech. Phys., 1 (1956) 2542.
14. F. Krum and F. H. Müller, Kolloid Z., 164 (1959) 81.
15. E. Sacher, J. Macromol. Sci., B19 (1981) 109.
16. H. W. Starkweather, P. Avakian, R. R. Matheson, J. J. Fontanella and M. C. Wintersgill, Macromolecules, 24 (1991) 3853.
17. R. K. Eby and F. C. Wilson, J. Appl. Phys., 33 (1962) 2951.
18. H. W. Starkweather, J. Polym. Sci., Polym. Phys. Ed., 11 (1973) 587.
19. H. W. Starkweather, Macromolecules, 17 (1984) 1178.
20. H. W. Starkweather, P. Avakian, R. R. Matheson, J. J. Fontanella and M. C. Wintersgill, Macromolecules, 25 (1992) 1475.
21. K. Fujimoto and N. Yoshimura, Rubber Chem. Tech. 41 (1968) 669.
22. K. Fujimoto and N. Yoshimura, Rubber Chem. Tech. 41 (1968) 1109.
23. W. J. MacKnight, J. Stoelting and F. E. Karasz, Adv. Chem. Ser., 99 (1971) 29.
24. A. R. Shultz and B. M. Beach, Macromolecules, 7 (1974) 902.
25. D. Feldman and M. Rusu, Eur. Polym. J., 10 (1974) 41.

26. K. Naito, G. E. Johnson, D.L. Allara and T. K. Kwei, *Macromolecules*, 11 (1978) 1260.
27. H. W. Starkweather, *Macromolecules*, 14 (1981) 1277.
28. H. W. Starkweather, *Macromolecules*, 21 (1988) 1798.
29. H. W. Starkweather, *Polymer*, 32 (1991) 2443.
30. H. W. Starkweather, *Macromolecules*, 26 (1993) 4805.
31. M. L. Williams, R. F. Landel and J. D. Ferry, *J. Am. Chem. Soc.*, 77 (1955) 3701.

This Page Intentionally Left Blank

Chapter 5

Crystallization and melting of metastable crystalline polymers

Stephen Z. D. Cheng and Shi Jin

Maurice Morton Institute and Department of Polymer Science,
The University Akron, Akron, Ohio 44325-3909

1. INTRODUCTION

Crystalline polymers constitute a class of important engineering plastic materials in industrial applications and human daily lives. Some of the largest quantities produced each year in polymer industries are polyethylene and copolymers, polypropylene, polyesters and nylons. All of these materials are crystalline polymers. Different from small molecular materials such as metals and organics, fully crystalline polymers are impossible to obtain using common processing conditions. A more precise characterization of crystalline polymers should be “semicrystalline polymers.” Therefore, more than one phase exists, namely, crystalline and amorphous phases in semicrystalline polymers. The concept of crystallinity has been established based on this two-phase model assumption. There are many experimental methods to determine crystallinity. In principle, three classes of methods are commonly used based on: 1) thermodynamics, 2) diffraction, and 3) spectroscopy. Among them, thermal analyses to measure thermodynamic properties in determining crystallinity remains the most common method in both academic and industrial research. In this chapter, we will first introduce general definitions of phases and phase transitions followed by metastability concepts in polymer crystals. Polymer crystallization, morphology and crystal melting are the main topics that will be discussed.

2. THERMODYNAMIC DEFINITIONS OF THE PHASE AND PHASE TRANSITIONS

2.1. Descriptions of phases

States of matter and transformations between these states are not only the subject of condensed matter physics, they are also important in materials science and engineering because of their close correlation to material performance. It is

known that solids, liquids and gases are the three basic states of matter, and they exhibit completely different material properties for a single compound in the macroscopic world. However, in order to describe detailed structures in each phase, one needs to investigate the symmetry of the phase to distinguish microscopic arrangements. A group of arbitrary translation, rotation and reflection operations is defined as the Euclidean group (both point and space groups). Since a fluid phase (liquid or gas) is invariant under all of these operations, its symmetry group is the Euclidean group. Fluids thus have the highest possible symmetry, *i.e.*, they have the largest number of symmetry operations. This implies that fluids have the lowest order: they possess short-range order but no long-range order. However, it should be noted that liquids and gases cannot be distinguished by symmetry. We now understand that through continuously changing a system's thermodynamic functions, it is possible to achieve an evolution from a liquid to a gas phase by going around a critical point.

Other states of matter are invariant only under some subgroups of the Euclidean group. They possess lower symmetry than the fluid phases due to the existence of certain long-range ordered structures in other phases. For example, crystalline solids possess average structures that are invariant only with respect to fixed and discrete lattice translations. Another class of materials that possesses order and symmetry in between homogeneous, isotropic liquids and crystalline solids are mesophases which have certain positional and/or rotational long-range orders introduced.

When we describe a phase from a structural point of view, a concept of structure function representing the average relative molecular positions is used. This task can usually be fulfilled via a number density operator [1]. This specifies the number of molecules per unit volume at $\mathbf{r}(x,y,z)$ as $n(\mathbf{r})$ in a three-dimensional space. The ensemble average of the density operator is the average density $\langle n(\mathbf{r}) \rangle$ at \mathbf{r} . In homogeneous isotropic fluids, this average density is the ratio between the overall number of molecules and the corresponding volume of the system. Therefore, the $\langle n(\mathbf{r}) \rangle$ is independent of both the magnitude and direction of \mathbf{r} in these systems, *i.e.*, the fluids are rotationally and translationally invariant. The full Euclidean symmetry, however, no longer exists in mesophases and crystalline solids. In a perfect crystalline solid, *e.g.*, the number density operator becomes periodic, and the molecule density is invariant only with respect to a translational lattice vector.

A correlation between two-point density operators at \mathbf{r}_1 and \mathbf{r}_2 is called the correlation function. Note that correlation functions of the density are ensemble averages of products of the density operator at different positions in space. A Fourier transform of the correlation function of the molecule density is defined as a structural function. Scattering experimental methods can be used to measure these functions. A commonly used density-density correlation function is one of

the Ursell functions which incorporates the difference between $\langle n(\mathbf{r}_1)n(\mathbf{r}_2) \rangle$ and $\langle n(\mathbf{r}_1) \rangle \langle n(\mathbf{r}_2) \rangle$. When the correlation function does not depend on the difference in position in three-dimensional space, as in homogeneous fluids, a correlation function can be reconstructed from a structure function. Since periodic ordered solids do not meet this criterion, correlation functions have to be obtained via diffraction methods.

The structural symmetry of a system is traditionally described by molecular positions in three-dimensional space with molecular motions and interactions. Classical mechanics are useful to describe motion through analytical solutions of a series of differential equations. Nevertheless, it can only solve problems considering interactions among a few molecules (a few body problem). For a system which contains a large numbers of molecules (*e.g.*, on the order of 10^{27} molecules, such as a liter of water), this precise calculation quickly goes beyond its capability to yield analytical solutions. On the other hand, another approach exists in which a system can be described using macroscopic material parameters, such as temperature (T), pressure (P), volume (V), internal energy (E), entropy (S), enthalpy (H) and others based on thermodynamics. This thermodynamic description is based on a few empirical laws (three laws of classical thermodynamics), such as: 1) the conservation of energy (energy cannot be created or eliminated), 2) heat cannot be spontaneously transferred from a low temperature body to a high temperature body, and 3) one never reaches absolute zero Kelvin, *etc.* The attempt to connect microscopic motion and macroscopic properties can be achieved through an understanding that the properties of a system are attributed to an average of individual contribution of the molecules. Statistical mechanics provides a link which connects both worlds.

2.2. Definitions of phase transitions

In 1933, Ehrenfest first proposed a classification for phase transitions based on classical thermodynamics [2]. This classification made use of the continuity of the thermodynamic Gibbs free energy (G) and its derivatives. It states that a first-order transition, defined based on G , is continuous. However, the first derivative of the G is discontinuous. This implies that at the first-order transition temperature, all of the thermodynamic functions except for Gibbs free energy exhibit discontinuous changes in a temperature-pressure ensemble. Fig. 1a shows a relationship between G and T at a constant P for a first-order transition. One can also construct a similar relationship between G and P at a constant T . When we consider the first derivatives of the G , their physical quantities are familiar thermodynamic functions such as H , S and V . If we establish relationships between these thermodynamic functions and T as shown in Fig. 1b, all of them exhibit discontinuous changes at the transition temperature representing first-order transitions. When we plot the second derivatives of the G , which are expansivity (α), compressibility (β), and heat capacity (c_p), *etc.*

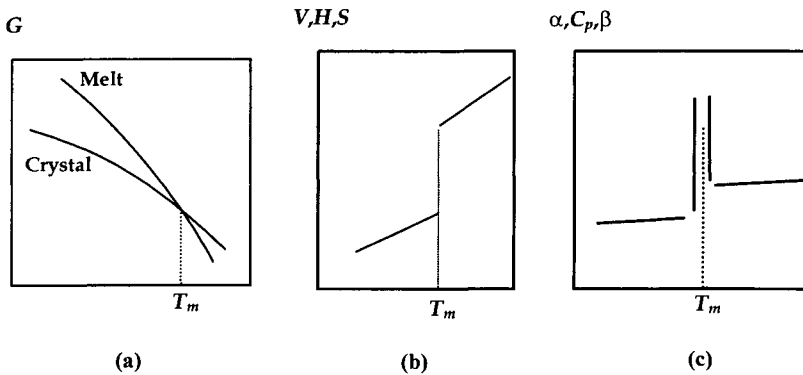


Fig. 1. Schematic relationship between Gibbs free energy and temperature at a constant pressure (a); the first derivatives of the Gibbs free energy with respect to temperature to describe the first-order transitions (b); and the second derivatives of the Gibbs free energy with respect to temperature to describe the first-order transitions (c).

versus T at the transition temperature, a sharp peak with an infinite height (in these quantities) and infinitely narrow (in T) can be observed (Fig. 1c).

For a second-order transition, the G - T diagram can be seen in Fig. 2a. It is interesting that one phase always possesses a lower G compared with another before and after the second-order transition. The thermodynamic functions that are expressed by the first derivatives of G now show a continuous function with respect to T , but their derivatives cannot be taken at the transition temperature (Fig. 2b). Therefore, their second derivatives exhibit a discontinuous change when they are plotted with respect to T (Fig. 2c). As we can see, all these thermodynamic quantities can be measured in thermal analysis.

In general, the Ehrenfest type phase transition states that a K^{th} -order transition can be defined as one in which all of the $(K-1)$ derivatives of the free

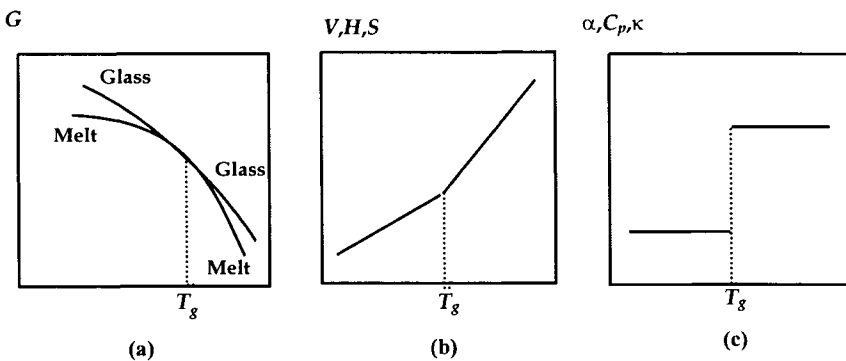


Fig. 2. Schematic relationship between Gibbs free energy and temperature at a constant pressure (a); the first derivatives of the Gibbs free energy with respect to temperature to describe the first-order transitions (b); and the second derivatives of the Gibbs free energy with respect to temperature to describe the second-order transitions (c).

energy are continuous and the K^{th} derivative is discontinuous [2]. We can experimentally observe first-order (crystallization and melting, most of liquid crystal transitions *etc.*) and second-order transitions (the critical point of a transformation between liquid and gas phases, super-fluid and super-conductive transitions without an external magnetic field, several ferromagnetic phase transitions such as the Curie point, *etc.*). In multiple component mixtures, a few specific two-dimensional systems and theoretical predictions (such as the Bose-Einstein condensation in an ideal Bose gas, *etc.*), transitions with higher than the second-order are found. For simplicity, a first-order transition can be recognized as a discontinuous transition, and second- or higher-order transitions may be classified as a continuous transition or critical phenomena.

When a material exhibits a transformation from one phase to another, the degree of order and the corresponding symmetry change at the transition point. Generally speaking, a high-temperature phase usually possesses a relatively low degree of order with a relatively high symmetry, while a low-temperature phase shows the opposite trend. The order parameter (Φ) is used in the mean-field theory to describe these phase transitions [3]. At high temperatures, the order parameter can be defined to be zero. At a transition temperature, some types of order set in and below this temperature Φ are non-zero. If Φ rises continuously from zero, the transition is second-order. When Φ jumps discontinuously to a non-zero value just below the transition temperature, the transition is first-order.

From a macroscopic point of view, thermodynamics dictates whether a phase transition is intrinsically possible at a given T , P in a single component system or additional composition if in a multiple component system. A complete understanding of the phase behavior is described by a phase diagram. Another issue, which is equally important, is how fast the phase transformation can be completed and the new phase can form. This is kinetics. Experimentally, we can observe the evolution of structural or property parameters with time and correlate these quantities with phase transformation kinetics. However, molecular models are needed to link macroscopic experimental observations and illustrate specific characteristics in each kinetic process.

Polymers exhibit profound phase transformation behaviors. One way to understand the phase transformations in polymers is to classify the phase transitions into two categories: those involving collections of macromolecules (bulks) and involving an isolated macromolecule [4]. Phase transitions in collections of macromolecules include *e.g.*, crystallization and melting (first-order), liquid crystal/plastic crystal transformations (first- or second-order), glass transitions (second-order-like), sol-gel transitions (first-order), liquid-liquid separations in two component systems (first-order, second-order at critical point), solid-solid transitions (first-order), block copolymers, membranes, soaps micelles and vesicles (first- or second-order). On the other hand, the basic approach for transitions in an isolated macromolecule is to find a partition

function of an isolated chain molecule using statistical mechanics and then, obtain its equilibrium thermodynamic properties. Under certain restrictions, the transitions can be found based on the discontinuity of the derivatives of the G . These transitions also belong to the Ehrenfest type. Examples include helix-random coil transitions in triple-stranded DNAs (first-order) double-stranded deoxyribonucleic acid (second-order) or single-stranded polypeptides (diffuse order), polymer threading a membrane (first-order), adsorption onto a surface (second-order) and collapse transitions (second- or first-order, depending upon the solvent) [4].

2.3. Phase equilibrium and stability

Two different thermodynamic concepts are important: equilibrium and stability. To describe the difference between the two, one can use analogs of classical mechanics as shown in Fig. 3. A state in equilibrium means that the summation of the forces and toques on that system are zero. However, the stability of a system reflects how a system responds to an outside perturbation. When a system reduces and finally diminishes the perturbation, the system becomes stable. On the other hand, if a system enlarges this perturbation, the system remains unstable. As shown in Fig. 3, case (a) demonstrates an unstable equilibrium, case (b) shows a stable equilibrium, while case (c) displays random equilibrium [5].

These concepts can also be applied in the case of thermodynamics. In a case similar to Fig. 3, if we consider a plot between G and Φ , a phase in thermodynamic equilibrium would require that $dG/d\Phi = 0$. However, for a stable phase it is also necessary that $d^2G/d\Phi^2 > 0$. The first violation of these criteria occurs at $d^2G/d\Phi^2 = 0$ indicating the limit of (thermodynamic) stability. In order to have a stability equal to the limit of stability, it is required that $d^3G/d\Phi^3 = 0$ and $d^4G/d\Phi^4 > 0$. This is necessary and sufficient for the stability criteria. Therefore, the phase stability criterion, in general, can be stated as a system where the lowest-order non-vanishing even derivative is positive and all lower-order derivatives are zero.

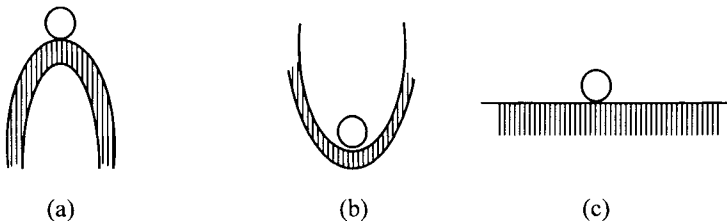


Fig. 3. Schematic diagram of the concept of stability based on analog of mechanics (a) unstable equilibrium; (b) stable equilibrium; and (c) random equilibrium.

2.4. Concepts of classical metastable states

The metastable state is an important concept in terms of both scientific understanding and practical material applications. For a single component, the definition of the metastable state is that, in a T - P ensemble, a state may exist even though it is thermodynamically less stable than its ultimate equilibrium state. This state is stable with respect to infinitesimal fluctuations but is not at the global G minimum where the equilibrium state of the system is located [5,6]. It is interesting that at the end of the nineteenth century, Ostwald formulated his “stage rule” which clearly reflected this understanding [7]. According to this rule, a transformation from one stable state to another will proceed via metastable states whenever such states exist, and follow a stage of increasing stability. One of the most important tasks of thermal analysis is to recognize the role of metastable states in various phases and phase transitions.

Theoretically, a plot of G and Φ of a metastable state, $dG/d\Phi = 0$ and $d^2G/d\Phi^2 > 0$. This is analogous to the ultimate equilibrium state. Therefore, $G(\Phi)$ is the essential function for judging the stability or metastability of a system and for describing its phase and phase transition behaviors. Many approaches for obtaining $G(\Phi)$ have been proposed such as the mean-field and other field theories. Detailed descriptions of these theories can be found in textbooks of condensed matter physics such as in reference [1], which has been largely followed in this chapter.

Although the metastable state will eventually enter the ultimate equilibrium state, the question remains: how will the relaxation process take (making this a typical kinetic issue). In other words, the lifetime (τ) of the metastable state must be longer than the experimental observation time scale (τ_{obs}) while the molecular relaxation time (τ_{rel}) of a specific measurable property must be shorter than the lifetime of the metastable state ($\tau > \tau_{obs} \gg \tau_{rel}$). However, a relaxation of the metastable state towards the equilibrium state requires overcoming a Gibbs free energy barrier. The height of this activated barrier depends on the depth of penetration into the metastable state (undercooling, ΔT at constant P). This process is called nucleation (both homogeneous and heterogeneous). The kinetic rate at which the nucleus critical size is reached depends entirely upon the height of the Gibbs free energy barrier. In this process, fluctuations are localized, but are large in amplitude. Based on the classical nucleation theory, the barrier never vanishes and therefore, no unstable state exists. On the other hand, relaxation from an unstable state towards equilibrium is spontaneous and known as a spinodal decomposition. This process is free from an energy barrier and the equilibrium phase growth is characterized by long-wavelength fluctuations with small amplitude [8,9].

It needs to be pointed out that in the phase diagram of a crystal-liquid transition, which is different from the known liquid-gas phase relationship, no

critical point exists. The phase boundary lines extend towards infinity or meet with other phases. Superheated crystals and undercooled liquids are metastable states. A similar delineation between the crystalline solid phases (polymorphs) may also exist. In this case, it is essential to realize that unless we are at the cross over of the G lines as shown in Fig. 1a, all but one of the possible polymorphs correspond to metastable states. In this case, G lines in the metastable states shown in Fig. 1a cannot extend infinitely with respect to T but must end at the limit of metastability. Presently, we know little about the singular properties of the limit of metastability in crystal-liquid and crystal-crystal transitions.

The absolute limit of metastability is determined by thermodynamics. Nevertheless, in many phase transitions, kinetics is the practical determining factor of the limit of metastability. The microscopic origin of the existence of metastable states is puzzling with regard to the Ostwald stage rule. One may ask how the molecules can be “trapped” into a local G minimum. One generalized explanation is that there is a higher probability that molecules will chose a pathway which possesses a lower G barrier due to a limited fluctuation amplitude, regardless of the phase stability formed after molecules overcome the barrier. In other words, the molecules are “blind” and they cannot predict the thermodynamic outcome on the other side of this barrier. A macroscopic, metastable state forms which can be detected as long as the time and size scales of this state are compatible with those of the experimental observations when enough molecules are in the G local minimum. Therefore, One may propose based on a phenomenological argument that during a transformation process, a metastable state can exist due to its fast kinetic pathway (lower G barrier) even though this state is thermodynamically less stable than the ultimate equilibrium state.

2.5. Metastable states in polymers

When the classical metastable states are discussed, we consider these states to be of infinite size. There is a broad class of metastable states in polymers where their metastability is dictated by the microscopic phase size on different length scales (usually, at least one of the three-dimensional sizes is less than one micrometer). This source of this metastability can be from one of many things such as exhaustion of available materials, geometric restrictions (*i.e.*, thin films or cavities), molecular mobility (*i.e.*, vitrification), and phase formation kinetics (*i.e.*, polymer lamellar crystals) *etc.* The term circumstantial is used to categorize metastability through different phase formation mechanisms. Common features of both classical and circumstantial metastable states show that they are both in a local G minimum, and they strive towards the state of absolute stability. In other words, they have the tendency to change with time,

transform, and/or “age”, slowly or quickly, depending on the circumstances which result from their intended use.

Polymers exhibit profound examples of classical and circumstantial metastable states. In many cases, these two kinds of metastable states may be interlinked causing complicated experimental observations. For example, when liquid-liquid phase separation occurs in solutions or blends, the system does not proceed to a state of ultimate stability. An example of this is a phase separated mixture of water and oil. This system provides a variety of microscopic phase morphologies, and the formation mechanisms of these phase morphologies are determined by nucleation or by spinodal mechanisms. If the phase separated polymer blends reached their ultimate stable states quickly, these metastable phase morphologies would disappear and this research field might not be as interesting and rewarding as it is today. A more complicated case is where one of the components is crystallizable after the phase separation. Additional crystal morphologies may form within one of the phase morphologies formed by the liquid-liquid phase separation. On the other hand, when a vitrification is introduced into a system that has undergone the liquid-liquid phase separation, this process may interrupt the phase separation resulting in the phase morphology being “locked in”. This can happen in either liquid-liquid phase separation or crystallization, and the microscopic phase and/or crystal morphologies may be frozen. Therefore, there is a hierarchy of morphologies, each with a corresponding hierarchy of metastabilities.

For homopolymers, a fully crystalline state with extended chain crystals has not been reached under normal crystallization conditions. In reality, crystalline polymers have been shown to possess an amorphous-crystalline ratio that is always less than 100% (crystallinity < 100%). The reasons preventing complete crystallization from occurring come from a range of factors, all of which are associated with the long chain nature of the polymers and are kinetic in origin. However, the amorphous content in these semicrystalline polymers comprises a range of states from localized fully amorphous domains to the surface regions of the crystals. Also, intermediate stages may be present that can be characterized as strained amorphous or rigid amorphous states between crystalline and amorphous regions.

3. POLYMER CRYSTALLIZATION AND MORPHOLOGY

Crystallization is a process of crystal formation from the mobile, isotropic liquid state. It took considerable time and effort to understand crystallization in polymers. The key issues in polymer crystallization are the molecular size and the flexibility and chemical regularity of the chains. Each of these factors can lead to metastable states in the crystals. The chain-folding principle during the crystallization of polymers was proposed in the 1950s due to the experimental

observations of single lamellar crystals grown in solution [10-12]. This principle states that mobile, flexible, linear chain molecules of sufficient length take on chain-folding conformations in initial crystallization. As a result, lamellar crystals having a thickness ranging from 5 to 50 nm are a typical morphology found in polymer crystals grown from the melt [13,14] or solution [10-12]. Within polymer crystals, three-dimensional positional, bond, and chain orientational long-range orders exist with chain conformations in the crystals having the lowest rotational energies. However, due to the chain folding, polymer lamellar crystals possess two large folded basal surfaces (top and bottom lamellar surfaces) with positive surface free energy. From a thermodynamic point of view, if the material is below the melting temperature (T_m), ordering of molecules and packing into an ordered array must occur to produce the most stable crystals. However, this is not possible in a limited time for a long chain molecule. Therefore, a compromise is found in chain folding, and the folded chains in polymer crystals (in most cases) do not extend substantially once they are produced. This feature of the polymer crystallization process thus exhibits kinetic influences.

3.1. Isothermal crystallization

The formation of a crystal occurs in at least two stages: nucleation and growth. Heterogeneous nucleation requires crystal nuclei in the melt or solution before the initiation of crystallization. Homogeneous nucleation occurs when the nuclei are generated spontaneously. Two nucleation types normally observed are athermal (constant number of nuclei) and thermal (nuclei changing in number with time). Most often, the nucleation that occurs in polymer crystallization is in between these two limiting cases [15].

Detailed kinetics for polymer crystal growth is based on the absolute-reaction-rate theory [16]. The nucleation barriers are caused by the surface free energies of the nucleus, the decrease of S , and increase the interactions (enthalpy, H) among the chain molecules. These factors become major terms in the G nucleation barrier that is dominant when T is close to the T_m . On the other hand, when T approaches the glass transition temperature (T_g), segmental motion across the phase boundary becomes more restricted. This phenomenon is critically associated with the temperature dependence of the viscosity in the undercooled melt. The nucleation rate (I^*) can be described as

$$I^* = (NK/T)\exp\{-(\Delta G^* + \Delta G_\eta)/kT\} \quad (1)$$

where ΔG^* is the G free energy of a nucleus of critical size. ΔG_η stands the free energy of activation energy which governs the short distance diffusion of the crystallizing element across the phase boundary.

If one uses a thermodynamic description to illustrate the primary nucleation barrier of ΔG^* , two competing terms need to be considered when the crystal size is small: bulk free energy which is negative and surface free energy ($\Sigma A \sigma$, where A is the overall surface areas and σ is the specific surface free energy) which is positive. For the simplest model, one can write a relationship of

$$\Delta G_i = -\alpha^2 l \Delta g_f + 4a l \sigma + 2a^2 \sigma_e \quad (2)$$

where ΔG_i is the free energy barrier of the i th crystallizable element, Δg_f is the bulk free energy change in fusion, a and l are the width and thickness of the nucleus, and σ and σ_e are the specific lateral and folded surface free energies, respectively. The term of ΔG^* can be obtained from the maximum value of the ΔG_i through an exercise of the first derivatives with respect to a and l equal to zero, and they are

$$a^* = 4\sigma/\Delta g_f \quad \text{and} \quad l^* = 4\sigma_e/\Delta g_f \quad (3)$$

and

$$\Delta G^* = 32\sigma^2\sigma_e T_m^2 / (\Delta h_f \Delta T \rho_c)^2 \quad (4)$$

where T_m is the melting temperature, Δh_f is the transition enthalpy, ΔT is undercooling defined by $(T_m - T_c)$, and ρ_c is the crystal density. Here, the term of Δg_f has been replaced by Δh_f using an approximation of $\Delta g_f = \Delta h_f T_c \Delta T / T_m$.

Following the nucleation, the crystal growth rate can usually be measured through microscopic techniques. The final crystal morphology is determined by the slowest crystal growth front along the crystal planes (directions). A constant (linear) crystal growth rate with size is a good indication that the crystallization is nucleation-controlled [17,18]. In fact, the linear crystal growth can also be viewed as a surface nucleation event: a secondary nucleation on a pre-existed crystal surface (heterogeneous nucleation) [15] whose thermodynamic description is only slightly different from the primary nucleation. Similar to eqs.(1) - (3), one can write a free energy barrier for a surface nucleation

$$\Delta G_i = -ab_0 l \Delta g_f + 2 b_0 l \sigma + 2a b_0 \sigma_e \quad (5)$$

where the dimension b is assumed to be the molecular dimension b_0 . Therefore, the critical nucleation sizes are

$$a^* = 2\sigma/\Delta g_f \quad \text{and} \quad l^* = 2\sigma_e/\Delta g_f \quad (6)$$

and the critical nucleation barrier is

$$\Delta G^* = 4\sigma\sigma_e T_m / (\Delta h_f \Delta T \rho_c) \quad (7)$$

Note that nucleation and crystal growth can only occur somewhere between the T_m and the T_g .

3.2. Overall crystallization rates

The overall crystallization is a combination of nucleation and crystal growth kinetics, and it is accessible through differential scanning calorimetry (DSC) and other thermal analysis (such as dilatometry) and structure sensitive (such as wide-angle X-ray diffraction) techniques. If one assumes a three-dimensional crystal growth in the free growth approximation, the total crystal volume (V_f^c) formed at a constant temperature (isothermal crystallization) can be calculated:

$$V_f^c = \frac{4}{3} N \pi G_R^3 t^3 \quad (8)$$

where N represents the number of heterogeneous athermal nuclei per unit volume, G_R is the linear crystal growth rate, and t is the crystallization time. If the impingement effect, which slows down the overall crystallization, is taken into account, the Avrami equation can be used [19-21]

$$V_f^c = 1 - \exp\{-Kt^n\} \quad (9)$$

or using its easier double logarithm form:

$$\log[-\ln(1 - V_f^c)] = \log K + n \log t \quad (10)$$

where K is a temperature-dependent parameter that contains nucleation, linear growth rate, and crystal geometrical information. For example, in the case of athermal nucleation in three-dimensional spherulitic growth, this parameter is expressed as:

$$K = \frac{4}{3} N \pi G_R^3 \quad (11)$$

Therefore, one can indirectly calculate G_R through the parameter K if the nucleation density is known. The exponent of t^n term is most easily extracted from experimental data and is the so-called dimensionality parameter that indicates the dimension of crystal growth. Unfortunately, the exponents do not uniquely correspond to the crystal dimension (type of morphology). It is evident that more than just the macroscopic observation of the crystallinity increase in DSC is necessary to draw definite conclusions about the microscopic mechanism

of crystallization. Without morphological information, the Avrami analysis provides little more than a convenient representation of the experimental data.

Additional complications in the Avrami treatment such as volume changes during crystallization, incomplete crystallization, slowing of the growth rate with time, annealing and perfection effects during and after crystallization, *etc.*, are not taken into account in this kinetic treatment. Eq. (10) may be modified to resolve some of these concerns, but relatively complicated mathematical treatments are involved [22]. Detailed discussion of the Avrami equation in polymer crystallization can be found in reference 15.

Experimentally, isothermal crystallization can be carried out in DSC and other thermal analysis and structural characterization methods when only the time scale is changed while keeping the temperature constant. Fig. 4 shows the schematic DSC traces at different temperatures for isothermal crystallization. After a sample is quenched from the isotropic melt to a preset crystallization temperature, an exothermic process can be observed with respect to time. This can be used to analyze isothermal crystallization kinetics since at each time, the amount of the crystallinity (a ratio between the heat of fusion at this time and the equilibrium heat of fusion) can be determined. However, this method can only be used in a relatively narrow crystallization temperature region because the exothermic process cannot be directly observed due to the prolonged transformation process when the crystallization temperature becomes relatively high. Therefore, a second method has to be used to observe the isothermal crystallization kinetics. The sample is again quenched from the isotropic melt to the preset isothermal crystallization temperature. After a fixed time at this crystallization temperature, the samples are directly heated to the isotropic melt.

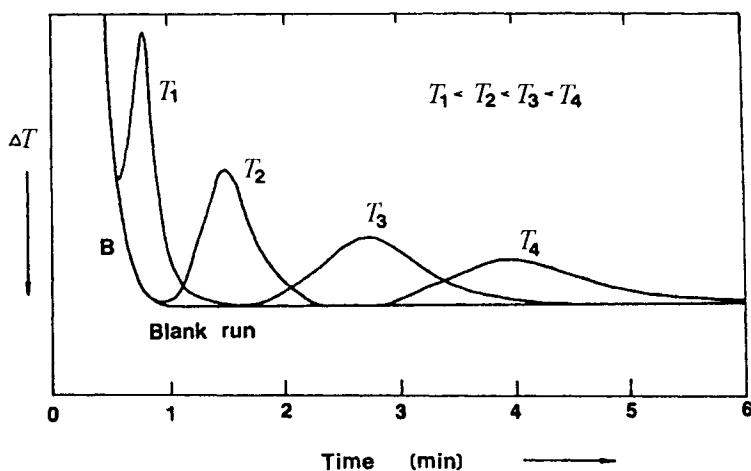


Fig. 4. Schematic drawing of a set of DSC traces at different temperatures in isothermal crystallization experiments.

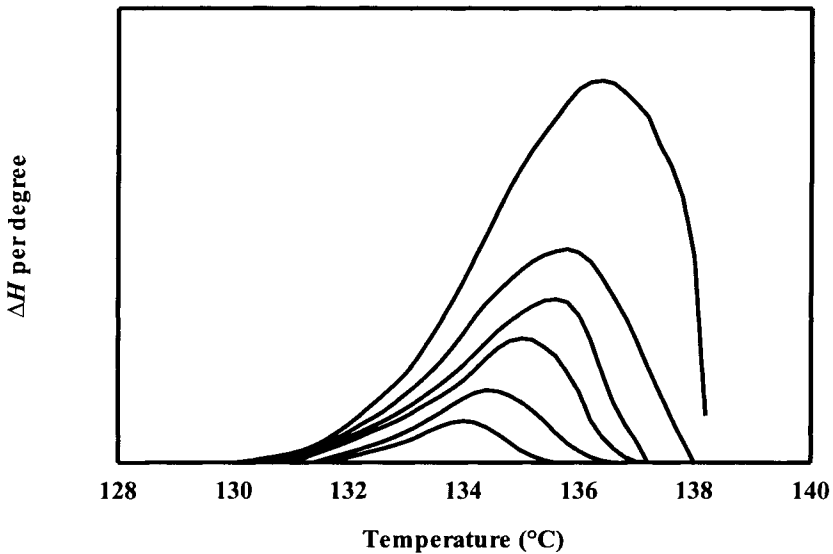


Fig. 5. Set of DSC heating curves after PE was crystallized at 128°C at different times ranging from 5 min to 69 min in the presence of extended chain crystals as seeds [15].

Fig. 5 shows a set of DSC heating curves for PE after being isothermally crystallized at different times [15]. In this method, the endothermic processes recorded during heating represent the portions of the crystals that had been formed during this period of time at the crystallization temperature. Therefore, this portion can be used to calculate the crystallinity.

A survey of over sixty melt crystallized polymeric materials has shown that the Avrami dimensionality parameter n of each is above two and independent of chain flexibility. The polymers include flexible polyethylene (PE) [23-26], poly(ethylene oxide) (PEO) [27-30], isotactic polypropylene (it-PP) [31-34], poly(ethylene terephthalate) (PET) [35-37], poly(aryl ether ether ketone)s (PEEKs) [38,39], poly(thio-1,4-phenylene) (PPS) [40], and polyimides [41]. Polymer crystallization may also occur from liquid crystalline (LC) phases or more generally, from mesophases. The Avrami equation has also been used to treat transition kinetics. For example, crystallization from a LC phase in copolyesters leads to very low exponents using the Avrami treatment [22]. However, other examples have shown dimensionality parameters greater than one and even as high as three [42-48].

3.3. Linear crystal growth rates

One measures the crystal growth rates along the interface between the crystal and the melt using light microscopy techniques for crystal aggregates

such as spherulites. The observations of growing crystal spherulites are called spherulitic growth rates. In a few special cases, single crystal growth rates can also be measured. Two issues are involved: first, are the crystal growth rates linear? Second, what relationship can be established for polymer crystal growth rates measured along a radius direction of crystal aggregates and along a single crystal plane normal? For the first issue, if the crystal growth rates are linear before spherulite impingement occurs, the crystal formation mechanism must be nucleation controlled. However, if the crystal growth rates are non-linear, then quantitative relationships must be studied. For example, when the growth rate is dependent upon time in a relationship of $t^{1/2}$, the growth mechanism can be thought of as being diffusion controlled. The second issue is closely associated with the crystal morphology. Using experiments to determine the crystal structural orientation in the aggregates, one can estimate the relationship between the radius growth direction of the crystal aggregates and crystallographic planes along which the crystal growth takes place.

Generally speaking, traditional thermal analysis techniques cannot directly detect crystal growth rates. Most of the reported works have used the Avrami treatment to obtain $\log K$, and then converted K to the growth rates using Eq. (11) under the condition that the crystal morphology is known.

3.4. Non-isothermal crystallization

Non-isothermal crystallization of polymers is easier to carry out experimentally using different cooling rates. Nevertheless, theoretical treatment of the non-isothermal crystallization is relatively difficult. Several examples such as PET [49], and PEEK [38] have been reported. With increasing cooling rates, the width of the exothermic crystallization peak increases, accompanied by a lowering of the peak temperature. All of the efforts to treat non-isothermal crystallization data are performed under the assumption that the Avrami treatment is still applicable. Three kinetic treatments have been proposed: those of Ozawa [49], Kissinger [50], and Marseglia [51]. The first treatment was based on the crystallization behavior of polymers, while the later two were based on small molecules:

$$1 - V_f^c = \frac{K(T)}{q^m} \quad (12)$$

$$\ln \frac{q}{T_p^2} = \text{Constant} - \frac{E_\alpha}{nkT_p} \quad (13)$$

and

$$\ln \frac{q}{T_p} = \text{Constant} - \frac{E_\alpha}{nkT_p} \quad (14)$$

where q is the heating or cooling rate (dT/dt), T_p represents the peak temperature in non-isothermal crystallization process, and E_a is an activation energy for the crystallization. Again, the annealing effects and second crystallization process may complicate these treatments.

The importance of understanding the crystallization behavior of polymeric materials with respect to engineering applications lies in the need to know how fast the polymer crystallizes and how broad its crystallization temperature range is. The ability of a polymer to crystallize is determined by both T_g and T_m . The difference between these two temperatures is usually called the “crystallization temperature window” [52]. Most of the polymers exhibit windows of over 140°C to 180°C as in PE, *it*-PP, PEEK, PET, PPS, *etc.* On the other hand, some of the high-temperature polyimides show a crystallization window that can be as 100°C or less. This narrow crystallization temperature window substantially affects the crystalline morphology [53].

3.5. Crystalline morphology

There are several structural hierarchies from the crystal unit cell to polymer bulk sample properties. This fact leads to complicated structure-property relationships in polymeric materials since each structure hierarchy effects the bulk properties differently [54]. The macroscopic properties are not a simple summation of all the effects from these hierarchies. Therefore, crystalline morphology has become a broad research area to specifically deal with these problems.

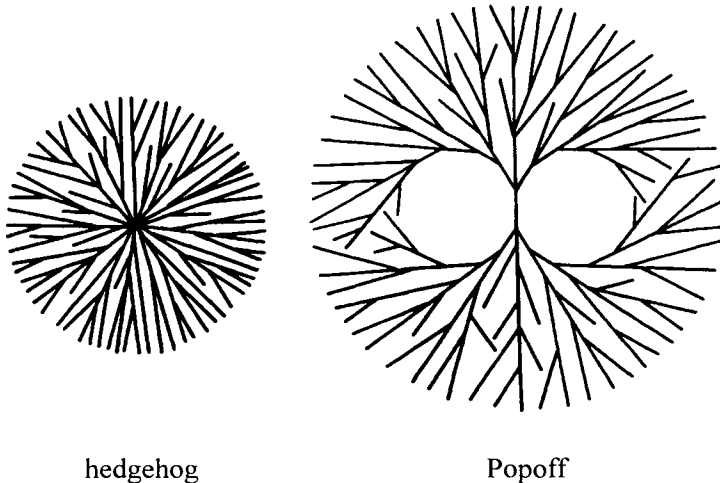


Fig. 6. Two types of spherulites: (a) hedgehog type and (b) Popoff type [15]

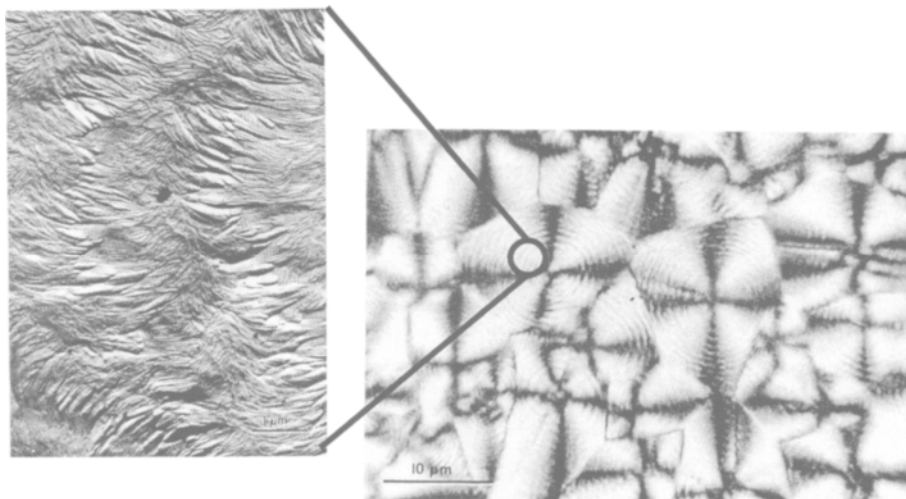


Fig. 7. Spherulitic morphology observed in polarized light microscopy and transmission electron microscopy [15]

The basic morphological building block in polymer crystals is lamellar crystals, which are one length scale above the crystal unit cell. It is surprising to note that, disregarding the chain rigidity, a wide range of crystalline polymers form lamellar crystals through chain folding in both solution and melt crystallization [55,56]. The nature of these lamellar crystals can be clearly identified through microscopic techniques (both light and electron microscopes) and small angle X-ray scattering experiments. Furthermore, the thickness of these lamellae is proportional to the reciprocal of ΔT in crystallization. This implies that these lamellar crystals having different thickness possess different degrees of metastability [5,6,57].

The formation of crystal aggregates, which is another length scale of the morphology, is critically dependent upon how the lamellae cooperatively pack together [55]. In crystallization from the melt, a common observation of crystal morphology in this length scale is spherulites. Phenomenologically, the spherulitic structures formed from lamellae can be thought of as following one of two types: the hedgehog or the Popoff types (Fig. 6a and 6b [15]). Experimental observations have proven that spherulites found in polarized light microscopy consist of stacked lamellar crystals as shown in Fig. 7. However, the detailed spherulitic formation mechanism is still beyond our current understanding.

4. POLYMER CRYSTAL MELTING

For a single component system in a crystalline phase with 100% crystallinity (a single completely crystallized phase), equilibrium thermodynamics teaches us

that crystal melting is a first-order transition. It also states the relationship between the melting temperature and changes in H and S holds and is given as follows:

$$T_m^\circ = \frac{\Delta H_f}{\Delta S_f} \quad (15)$$

Unfortunately, almost all the experimental results indicate that the melting of polymer crystals is metastable in nature due to small crystal sizes (lamellar or fibrillar morphology) and crystal defects. Only part of the material is crystalline meaning the polymer possesses less than 100% crystallinity [54]. Simple methods such as annealing the crystals at a temperature close to the T_m and heating the sample at very slow rates are often utilized in small molecule crystals. However, these methods are not successful in obtaining equilibrium, extended chain polymer crystals. Usually, broad melting transition peaks with a fraction of the equilibrium heat of fusion are observed. As a result, two aspects of crystal melting in polymeric materials need to be addressed: how to determine the equilibrium melting data, and how to precisely study the melting of metastable crystals?

4.1. Extrapolations to obtain equilibrium melting properties

For polymer crystals, the equilibrium thermodynamic data can only be obtained through proper extrapolation methods. Three extrapolation methods are generally used to determine the equilibrium T_m and heat of fusion (ΔH_f): (1) Extrapolation from the equilibrium melting data of monomers and oligomers to polymers, (2) Extrapolation from the melting data of small crystals to the large crystals, and (3) Extrapolation of the melting data obtained from isothermal crystallization or annealing with respect to the crystallization or annealing temperature [57]. In each of these extrapolations, many experimental methods are involved. For example, the crystal size (lamellar thickness) may be measured using small angle X-ray scattering, transmission electron microscopy, and infrared and Raman spectroscopy. Crystallinity can be measured using wide angle X-ray diffraction, density, and DSC experiments. Among these methods, thermal analysis techniques are the most essential for equilibrium melting data determination.

In the first method, the extrapolation procedure involves measuring the T_m s of monomer and oligomer homologues of the polymer in question. These homologues must be able to grow equilibrium crystals (extended chain crystals) so that extrapolation of their T_m s to the infinite molecular weight is possible. A classical example come from the equilibrium melting temperature of PE extrapolated from n -paraffins with 11 to 140 carbon atoms. The extrapolated T_m^0

ranges between 141.1°C and 146.5°C [58-61] compared to the measured T_m of PE extended chain crystals of 141.4°C [62]. Other examples can be seen with PEO [63,64], it-PP [65-67] and poly(tetramethyl-p-silphenylene siloxane) [68,69].

The second extrapolation method in evaluating the T_m^0 involves measuring the T_m of well-defined, small crystals and extrapolating to the infinite size using the Thomson-Gibbs equation [57]. This method is especially useful since the prominent crystal morphology is lamellar crystals. In the case of laterally large lamellae, only the top and bottom surfaces contribute significantly to the G of the crystal so the Thomson-Gibbs equation can be simplified to give:

$$T_m = T_m^0 \left(1 - \frac{2\sigma_e}{\ell \Delta H_f} \right) \quad (16)$$

where σ_e is the top and bottom specific surface free energy as defined previously, ΔH_f is the equilibrium heat of fusion, and ℓ is the lamellar thickness. Since the T_m in Eq. (16) refers to metastable small crystals, a precise determination of T_m requires eliminating all effects of annealing and recrystallization during heating (see below). Equilibrium melting data have been obtained using this kind of extrapolation for semicrystalline polymer systems such as very flexible PE [59,70-72], it-PP [65] PEO to semiflexible PEEK and other semicrystalline polymers [73-76]. For example, Fig. 8 illustrates the relationship between T_m and reciprocal lamellar thickness for PE crystals [4].

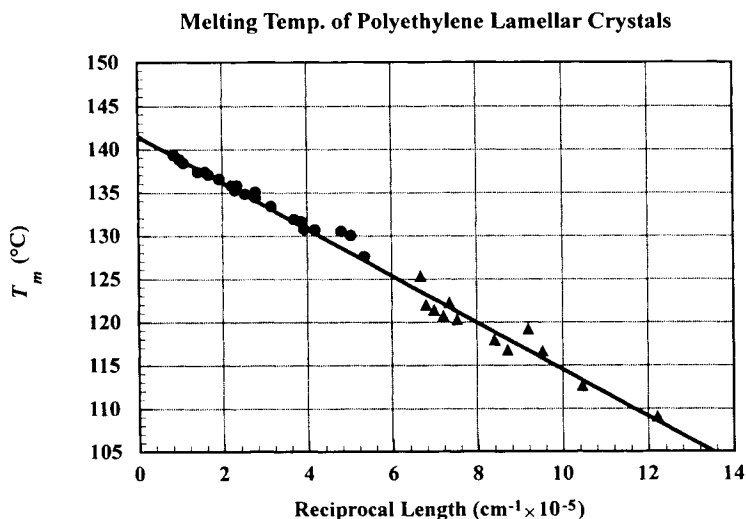


Fig. 8. Relationship between T_m and lamellar thickness of PE crystals having different thicknesses (metastability) [57]

The third method involves plotting the relationship between crystallization temperature (T_c) and T_m (in this case isothermal crystallization is performed). This method only relies on DSC measurements. Commonly, this extrapolation is called a Hoffman-Weeks extrapolation [77]. From eq. (16), one can derive the expression of

$$T_m = \frac{T_m^\circ(2\beta - 1) + T_c}{2\beta} \quad (17)$$

under an assumption that on isothermal crystallization, the fold length is fixed at a value proportional to the reciprocal of the ΔT . Here, β indicates the fold length in multiples of the primary, homogeneous nucleus. This equation describes a family of straight lines for different β 's which all intersect when $T_m = T_c = T_m^\circ$. Since this extrapolation method can be performed relatively easily, many polymer systems have been investigated in this way [for a review see reference 57]. Fig. 9 shows an example of such a relationship for it-PP fractions with different isotacticities [65]. Recently, there has been a discussion regarding the validity of this linear extrapolation and proposals put forth for a new non-linear extrapolation method [78]. However, if the T_m is carefully determined for metastable crystals with different lamellar thickness, this method should yield data close to the other two extrapolations.

A practical way to determine the equilibrium heat of fusion (100% crystallinity), is to combine two or more experimental methods to obtain percentage of crystals (crystallinity) in a semicrystalline material and then

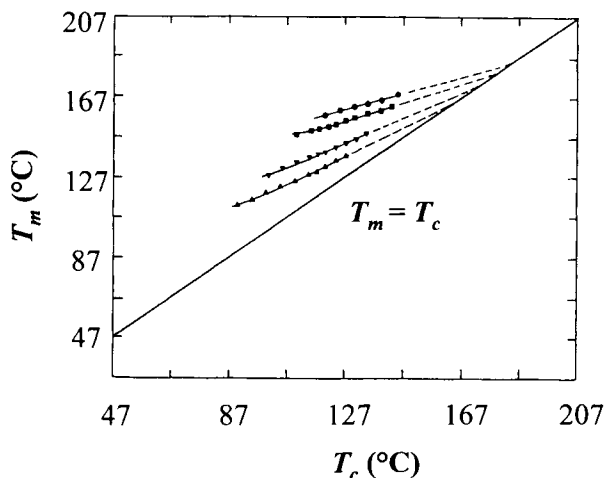


Fig. 9. Relationship between isothermal crystallization temperatures and melting temperatures for it-PP having different isotacticities [65]

extrapolate the heat of fusion observed to 100% crystallinity. Commonly used experimental methods include DSC measurements combined with wide angle X-ray diffraction and/or density measurements. One polymer in which this method has been applied to is poly(ethylene terephthalate) [79]. Diluent and copolymer effects may also permit an estimation of the equilibrium heat of fusion based on the Flory-Huggins equation [80-82]. An extrapolation between the heat of fusion of oligomer homologues can also be made to obtain the equilibrium heat of fusion. Such an extrapolation was carried out in PPS oligomers and found that, for up to seven repeat units, the equilibrium heat of fusion was extrapolated to be 11.4 kJ/mol [83]. This value fits very well with other extrapolation methods [84].

4.2. Metastability changes in polymer crystal melting

Since polymer crystals are metastable and have limited sizes, they can be annealed and recrystallized during heating even though their equilibrium form of the crystals cannot be obtained. The less stable the crystal is, the easier it can be annealed. In other words, the crystal metastability changes during heating. As a result, the observed T_m from the thermal diagram may not represent the true T_m of the crystal which originally existed prior to heating. In order to keep the crystal metastability from changing during heating, one needs to use a heating rate that is faster (or at least equal to) the previous cooling rate the sample was subjected to in non-isothermal experiments. This issue is the main cause of argument over how to precisely obtain extrapolated T_m^0 s and ΔH_f s as described previously. This issue becomes even more complicated when a polymorphous material is involved. However, various methods have been developed to avoid such changes of metastability: (1) Using very fast heating so that the crystals do not have enough time to reorganize; (2) Chemically cross-linking the molecules in the amorphous region of the semicrystalline polymer so that annealing by increasing lamellar thickness is not possible; and (3) Etching the fold surface so that the molecules are trapped as oligomers which prevents thickening of the lamellar crystals. Detailed descriptions of each method have appeared in a number of publications and are summarized in reference 57.

A more broad issue concerning metastable crystal melting is recognizing reorganization and recrystallization of crystals during heating. This is important because the observed crystal melting behavior may not represent the true crystal melting of the original metastability formed in the previous thermal history. One the example involves the double melting endotherms observed during heating in DSC after isothermal crystallization experiments which exists in almost all semicrystalline polymers: a major endotherm is at a high temperature and a minor endotherm about 10 to 30°C above the T_c . For many years, people tried to explain this observation by utilizing two different assumptions [73-76,85-94]. First, only the low-melting temperature crystals were formed during the isothermal crystallization. Secondly, the high-temperature-melting endotherm

was associated with reorganization and/or recrystallization during heating to a higher temperature than the T_c . However, if the heating rate is fast enough, one would expect the reorganization and recrystallization processes could no longer take place. In this case, only one, low-melting-temperature-endotherm should be observed corresponding to one type of crystal morphology with single metastability. However, people argue that if one extrapolates the heating rate to completely diminish the high-temperature-melting endotherm, the heating rate would have to be extremely fast. Therefore, two morphological features must coexist in these samples. Although many structural and morphological models have been proposed to explain these experimental observations, these two features in general, are identified as crystallization that has taken place under non-confined and confined environments. These crystallization conditions lead to different metastabilities of these two crystal populations and thus, two different T_m s. The detailed features of these models are currently subject to discussions and arguments.

Another example of metastability changes in thermal analysis can be seen in the measurement of the T_m of stretched semicrystalline polymer samples such as fibers and highly oriented films. It is known that stretching a semicrystalline sample helps to develop crystals due to the orientation of chain molecules

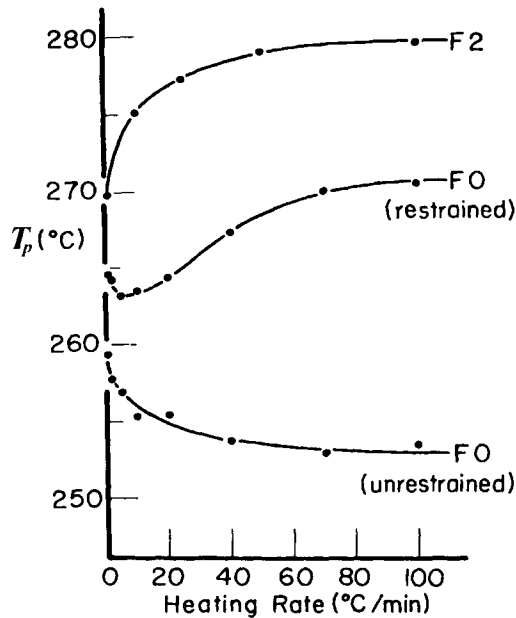


Fig. 10. Melting temperatures for drawn poly(ethylene terephthalate) fibers. F2 sample was annealed fibers at 250°C for 24 hours. The fibers had free ends when they were analyzed. FO sample was as-received and the fiber ends were with and without restraints during the analysis [96].

introduced by a one-dimensional mechanical force field along the stretched direction. However, a practical method to precisely measure T_m of deformed polymer samples is difficult since internal stresses remain in the polymer samples after applying the mechanical force [95]. The effect of these internal stresses on the T_m of stretched samples is complicated and varies with the region these stresses are frozen in. If the stress is concentrated in the crystalline region, the crystal sizes can decrease due to the introduction of defects and the increase of grains resulting in a decrease of the T_m . On the other hand, if the internal stress is frozen into the amorphous region of the samples, the T_m may increase due to the crystals being held tightly by the stretched molecules in the rigid amorphous region.

Many research reports have shown that the measured melting temperatures of stretched samples can be significantly different when the samples were prepared with or without restraining the fiber ends. Fig. 10 shows examples of PET drawn tire cord fibers [96]. In this figure, it is evident that unstrained PET fibers exhibit T_m s as much as 20°C lower compared with strained ones. However, unstrained PET fibers annealed at 250°C for 24 hours show a much higher T_m than even the strained PET fibers. This clearly indicates that the metastability of these PET crystals (in the fibers) is critically dependent upon their respective thermal histories and testing conditions.

4.3. Interfaces between crystalline and amorphous regions

Thermodynamic approaches can also provide information on identifying interfaces between crystalline and amorphous regions in semicrystalline polymers. The most commonly used method involves measuring the Δh_f via DSC. By knowing the equilibrium ΔH_f , the crystallinity of a sample can be easily calculated:

$$w^c = 1 - \frac{\Delta h_f(m)}{\Delta H_f} \quad (18)$$

where $\Delta h_f(m)$ is the measured heat of fusion of a specific polymer crystal. Again, the ΔH_f can only be obtained using proper extrapolation methods, corrected procedures, and necessary data treatments. Over 100 equilibrium heats of fusion data have been listed in reference 97, which has been critically reviewed.

If the two-phase model was strictly a precise description of a semicrystalline polymer whose crystalline and amorphous parts were devoid of sharp boundaries and connections, its macroscopic mechanical response towards outside forces would be very weak. There must be some proportion of material between these

two parts that would create interfaces. The thermal analysis characterization of the interfacial structures in semicrystalline polymers: identifying so-called “rigid amorphous fractions” to precisely determine crystallinity and the mobile amorphous portion of a semicrystalline sample. This concept can be traced back as far as thirty years ago. However, extensive studies have been carried out only in the past ten to fifteen years [85-94]. Research on the interface between the crystalline and amorphous regions in bulk polymers have also been carried out using different experimental methods such as small angle X-ray scattering, carbon-13 solid state NMR, Raman spectroscopy and TEM [98-104].

In order to examine the validity of the two-phase (crystallinity) model, one needs to first establish the heat capacity data in solid and liquid states of the polymers. With these data, one could predict that for a semicrystalline polymer

$$w^c = 1 - \frac{\Delta c_p(m)}{\Delta c_p(a)} \quad (19)$$

where w^c is the weight-fraction crystallinity that is usually obtained by DSC measurements, density determination, and/or wide angle X-ray diffraction experiments. The terms $\Delta c_p(m)$ and $\Delta c_p(a)$ are the heat capacity increases at T_g for the semicrystalline sample and the amorphous sample, respectively. Surprisingly, a wide variety of behaviors that deviate from the ideal two-phase model exist. A positive heat capacity deviation is observed for practically all polymers long before the fusion endotherm begins. This observation has been linked to pre-melting and/or defect formation. For PE and PTFE, these positive deviations close to the melting temperatures are well-analyzed [97,105]. On the other hand, the heat capacities of polyoxymethylene (POM) show a negative deviation at somewhat lower temperatures relative to the melting temperature [87,88]. This reveals an extra fraction in the polymer that contributes to neither the $\Delta c_p(m)$ at T_g nor to the $\Delta h_f(m)$ at T_m , which is so-called the “rigid amorphous fraction”. In POM this rigid amorphous fraction does not show any sign of softening up to the polymer melting point. Similar measurements in *it*-PP exhibit a rigid amorphous fraction that gradually unfreezes leading to the occasionally observed “double glass transition” [106]. As a result, if a rigid amorphous fraction exists in a semicrystalline polymer, the two-phase model cannot be used to describe that system, and

$$w^c < 1 - \frac{\Delta c_p(m)}{\Delta c_p(a)} = f_r \quad (20)$$

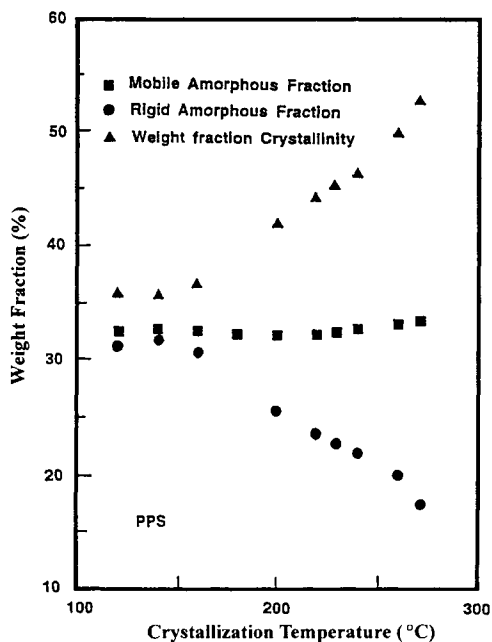


Fig. 11. Three portions of rigid amorphous, mobile amorphous, and crystallinity changes in PPS with crystallization temperatures [108].

The resulting difference between equations (10) and (11) is the rigid amorphous fraction in a polymer, $f_r - w^c$. Most of the thermoplastic engineering polymers such as PEEK [89], PPS [90], PPO [91], PET [107], PEN [92], PBT [93] and polyimides [94] show this kind of behavior which is critically dependent upon the samples thermal history. Fig. 11 shows three fractions in a high molecular weight linear PPS sample in which the non-mobile amorphous fraction above T_g represents the rigid amorphous fraction [54]. More complicated situations may also be observed by combining both positive and negative deviations of heat capacities in a semicrystalline polymer. However, other structural characterization methods are necessary to distinguish these deviations and to separate the two effects.

5. CONCLUDING REMARKS

In summary, the basic theory and technique of thermal analysis has been developed extensively during the past forty years. The macroscopic thermal characterization in the area of polymer materials and in particular, polymer phase and phase transitions, is based on thermodynamics and kinetics. The link between macroscopic thermal behaviors and microscopic origins has been

established in many cases. This research has elucidated a detailed understanding of composition, structure, and history of polymeric materials. However, thermal analysis techniques will continue to play an important role as we enter the twenty-first century in predicting the performance of polymeric materials for applications in advanced science and technology. It is also clear that the current application of thermal analysis techniques to polymeric materials has not reached a level where all the information has been precisely recognized and analyzed. Further efforts need to be made to make more precise measurements using thermal analysis techniques. For example, time-dependent irreversible transition behaviors in polymers can be combined with in-situ temperature-controlled experiments for the study of structures and dynamics of polymer phase transitions that are traditionally studied by diffraction, scattering, spectroscopy, and microscopy. Another important part of developing thermal analysis techniques will involve performing on-line thermal measurements during production. Overall, we expect that thermal analysis techniques can bring and stimulate a broad inquiry of scientific knowledge and technical innovation.

ACKNOWLEDGEMENT

This review was supported by National Science Foundation (DMR 0203994).

REFERENCES:

1. P. M. Chaikin, T. C. Lubersky, Principles of Condensed Matter Physics, Cambridge University Press, New York, 1995.
2. P. Ehrenfest, Proc. Acad. Sci., Amsterdam, 1933;36,153; Sppl. 75b, Mitt. Kammerlingh Onnes Inst., Leiden.
3. L. D. Landau, Phys. Z. Sowjetunion 1937;11,26; repinted In Collected Papers of L. D. Lanau, ed. D ter Haar, New York, Pergamon, 1965.
4. E. A. Dimarzio, Prog. Polym. Sci., 24 (1999) 329.
5. S. Z. D. Cheng, A. Keller, Annu. Rev. Mater. Sci., 28 (1998), 533.
6. A. Keller, S. Z. D. Cheng, Polymer, 39 (1998) 4461.
7. W. Z. Ostwald, Phys. Chem., 22 (1897) 286.
8. V. P. Skripov, Metastable Liquids, John Wiley & Sons, New York, 1974.
9. P. G. Debenedetti, Metastable Liquids, Concepts and Principles, Princeton University Press, New Jersey, 1996.
10. R. Jaccodine, Nature, 176 (1955) 305.
11. A. Keller, Phil. Mag., 2 (1957) 1171.
12. P. H. Till Jr., J. Polym. Sci., 24 (1957) 301.
13. E. W. Fischer, Z. Naturforsch., 12A (1957) 753.
14. K. Kobayashi, Kagaku(Chem.), 8 (1962) 203.
15. B. Wunderlich, Macromolecular Physics, Vol. II, Crystal Nucleation, Growth, Annealing, Academic Press, New York, 1976.
16. D. Turnbull, J. C. Fisher, J. Chem. Phys., 17 (1949) 71.
17. J. I. Lauritzen Jr, J. D. Hoffman, J. Appl. Phys., 44 (1973) 4340.

18. J. D. Hoffman, G. T. Davis, J. I. Lauritzen Jr., in "Treatise on Solid State Chemistry", N. B. Hannay Ed., Plenum, New York, 1976, Vol. III, Chapt. 7.
19. M. Avrami, *J. Chem. Phys.*, 7 (1939) 1103.
20. M. Avrami, *J. Chem. Phys.*, 8 (1940) 212.
21. M. Avrami, *J. Chem. Phys.*, 9 (1940) 177.
22. S. Z. D. Cheng, *Macromolecules*, 21 (1988) 2475; 3327.
23. E. Ergoz, J. G. Fatou, L. Mandelkern, *Macromolecules*, 5 (1972) 147.
24. J. G. Fatou, C. Marco, L. Mandelkern, *Polymer*, 31 (1990) 890.
25. J. G. Fatou, C. Marco, L. Mandelkern, *Polymer*, 31 (1990) 1685.
26. L. Mandelkern, F. A. Quinn, P. J. Flory, *J. Appl. Phys.*, 25 (1954) 830.
27. G. Vidotto, D. Levy, A. J. Kovacs, *Z. Kolloid, Z. Polym.*, 230 (1969) 289.
28. D. R. Beech, C. Booth, *J. Polym. Sci. Part A-2*, 10 (1972) 1555.
29. S. Z. D. Cheng, B. Wunderlich, *J. Polym. Sci. Polym. Phys. Ed.*, 24 (1986) 595.
30. Y. K. Godovsky, G. L. Slonimsky, *Polym. Sci. USSR*, 8 (1966) 441.
31. Y. K. Godovsky, *Polym. Sci. USSR*, 11 (1969) 2423.
32. C. F. Pratt, S. Y. Hobbs, *Polymer*, 17 (1976) 12.
33. E. Martuscelli, M. Pracella, G. D. Volpe, P. Greco, *Polymer*, 24 (1983) 693; *Makromol. Chem.*, 185 (1984) 1041.
34. J. J. Janimak, S. Z. D. Cheng, A. Q. Zhang, E. T. Hsieh, *Polymer*, 33 (1992) 728.
35. F. D. Hartley, F. W. Lord, L. B. Morgan, *Phil. Trans. Roy. Soc.*, A247 (1954) 23.
36. F. Rybnikar, *Coll. Czech. Chem. Commun.*, 25 (1960) 1529.
37. F. van Antwerpen, D. W. van Krevelen, *J. Polym. Sci. Polym. Phys. Ed.*, 10 (1972) 2423.
38. P. Cebe, S. D. Hong, *Polymer*, 27 (1986) 1183.
39. M. Day, Y. Deslandes, J. Roovers, T. Suprunchuk, *Polymer*, 32 (1991) 1258.
40. L. C. Lopez, G. L. Wilkes, *Polymer*, 29 (1988) 106.
41. D. P. Heberer, S. Z. D. Cheng, J. S. Barley, S. H. S. Lien, R. G. Bryant, F. W. Harris, *Macromolecules*, 24 (1991) 1890.
42. X. Liu, S. Hu, M. Shi, M. Xu, Q. Zhou, D. Xu, *Polymer*, 30 (1989) 273.
43. S. K. Bhattacharya, A. Misra, R. S. Stein, R. W. Lenz, P. E. Hahn, *Polym. Bull.*, 16 (1986) 465.
44. S. Z. D. Cheng, J. J. Janimak, T. M. Lipinski, K. Sridhar, X. Y. Hung, F. W. Harris, *Polymer*, 31 (1990) 1122.
45. R. J. Ciora, J. H. Magill, *Macromolecules*, 23 (1990) 2350; 2359.
46. S. Z. D. Cheng, A. Q. Zhang, R. L. Johnson, Z. Wu, H. H. Wu, *Macromolecules*, 23 (1990) 1196.
47. H. Jonsson, E. Wallgren, A. Hult, U. W. Gedde, *Macromolecules*, 23 (1991) 1041.
48. I. Campoy, C. Marco, M. A. Gomez, J. G. Fatou, *Macromolecules*, 25 (1992) 4392.
49. T. Ozawa, *J. Thermal Analysis*, 2 (1970) 301.
50. H. Kissinger, *Anal. Chem.*, 29 (1957) 1702.
51. E. A. Marseglia, *J. Non-Cryst. Solids*, 41 (1980) 31.
52. S. Z. D. Cheng, *J. Appl. Polym. Sci. Appl. Polym. Symp.*, 43 (1989) 315.
53. S. Z. D. Cheng, M. C. Mittleman, D. X. Shen, T. M. Chalmers, S. H. S. Lien, C. C. Tso, P. A. Gabori, F. W. Harris, *Polym. Internl.*, 29 (1992) 201.
54. C. Y. Li, S. Z. D. Cheng, *Semicrystalline polymers*, in *Encyclopedia of Polymer Science and Technology*, Wiley & Son, 2002.
55. B. Wunderlich, *Macromolecular Physics*, Vol. I, Crystal Structure, Morphology, Defects, Academic Press, New York, 1973.

56. S. Z. D. Cheng, C. Y. Li, Single crystals: formations and structures. In *Encyclopedia of Materials: Science and Technology*, pp. 7487-7491, Third edition, John Wiley & Sons, New York, 2001.
57. B. Wunderlich, *Macromolecular Physics*, Vol. III, Crystal Melting, Academic Press, New York, 1980.
58. M. G. Broadhurst, *J. Chem. Phys.*, 36 (1962) 2578; *J. Res. Nat. Bur. Std.*, 70A (1967) 481.
59. P. J. Flory, A. Vrij, *J. Am. Chem. Soc.*, 85 (1963) 2548.
60. J. D. Hoffman, L. J. Frolen, G. S. Ross, J. I. Lauritzen Jr., *J. Res. Nat. Bur. Std.*, 79A (1975) 671.
61. B. Wunderlich, G. Czornyj, *Macromolecules*, 10 (1977) 906.
62. T. Arakawa, B. Wunderlich, *J. Polym. Sci. Polym. Symp.*, 16 (1967) 653.
63. C. P. Buckley, A. J. Kovacs, *Prog. Colloid Polym. Sci.*, 58 (1975) 44.
64. S. Z. D. Cheng, B. Wunderlich, *J. Polym. Sci. Polym. Phys. Ed.*, 24 (1986) 577.
65. S. Z. D. Cheng, J. J. Janimak, A. Zhang, E. T. Hsieh, *Polymer*, 32 (1991) 648.
66. K. Mezghani, P. J. Phillips, *Macromolecules*, 27 (1994) 6145.
67. J. N. Xu, S. Srinivas, H. Marand, P. Agarwal, *Macromolecules*, 31 (1998) 8230.
68. J. H. Magill, *J. Appl. Phys.*, 35 (1964) 3249.
69. J. H. Magill, *J. Polym. Sci. Part A-2*, 7 (1969) 1187.
70. K. H. Illers, H. Hendus, *Makromol. Chem.*, 113 (1968) 1.
71. R. G. Brown, R. K. Eby, *J. Appl. Phys.*, 35 (1964) 1151.
72. B. Wunderlich, P. Sullivan, T. Arakawa, A. B. DiCyan, J. F. Flood, *J. Polym. Sci. Part A*, 1 (1963) 3581.
73. C. P. Buckley, A. J. Kovacs, *Colloid Polym. Sci.*, 58 (1975) 44.
74. D. J. Blundell, B. N. Osborn, *Polymer*, 24 (1983) 953.
75. Y. C. Lee, R. S. Porter, *Macromolecules*, 20 (1987) 1336.
76. B. S. Hsiao and K. Gardner, *Polymer in press*.
77. J. D. Hoffman, J. J. Weeks, *J. Res. Natl. Bur. Std.*, 66A (1962) 13.
78. H. Marand, J. Xu, S. Srinivas, *Macromolecules*, 31 (1998) 8219.
79. A. Mehta, U. Gaur, B. Wunderlich, *J. Polym. Sci. Polym. Phys. Ed.*, 16 (1978) 289.
80. P. J. Flory, *J. Chem. Phys.*, 9 (1941) 660; 10 (1942) 51.
81. M. L. Huggins, *J. Phys. Chem.*, 46 (1942) 151.
82. L. Mandelkern, *Crystallization of Polymers*, McGraw-Hill, New York, 1964.
83. Unpublished data at Phillips Petroleum Company.
84. P. Huo, P. Cebe, *Colloid Polym. Sci.*, 270 (1992) 840.
85. P. Cebe, S. D. Hong, *Polymer*, 27 (1986) 1183.
86. D. C. Bassett, R. H. Olley, T. A. M. Al Raheil, *Polymer*, 29 (1988) 1745.
87. H. Suzuki, J. Grebowicz, B. Wunderlich, *Makromol. Chem.*, 189 (1985) 1109.
88. H. Suzuki, J. Grebowicz, B. Wunderlich, *Brit. Polym. J.*, 17 (1985) 1.
89. S. Z. D. Cheng, M. Y. Cao, B. Wunderlich, *Macromolecules*, 19 (1986) 1868.
90. S. Z. D. Cheng, B. Wunderlich, *Macromolecules*, 20 (1987) 1630.
91. S. Z. D. Cheng, Z. Wu, B. Wunderlich, *Macromolecules*, 20 (1987) 2802.
92. S. Z. D. Cheng, B. Wunderlich, *Macromolecules*, 21 (1988) 789.
93. S. Z. D. Cheng, R. Pan, B. Wunderlich, *Makromol. Chem.*, 189 (1988) 2243.
94. S. Z. D. Cheng, D. P. Heberer, H. S. Lien, F. W. Harris, *J. Polym. Sci. Polym. Phys. Ed.*, 28 (1990) 655.
95. M. Jaffe, *Thermal Characterization in Polymeric Materials*, Turi, E. Ed. Second Ed. 1997.
96. A. Mayagi, B. Wunderlich. *J. Polym. Sci. Polym. Phys. Ed.*, 10 (1972) 1401.

97. B. Wunderlich, *Thermal Analysis*, Academic Press, New York, 1991.
98. G. R. Strobl, W. J. K. Hagedorn, *J. Polym. Sci. Polym. Phys. Ed.*, 16 (1978) 1181.
99. I. G. Voigt-Martin, G. M. Stack, A. J. Peacock, L. Mandelkern, *J. Polym. Sci. Polym. Phys. Ed.*, 27 (1989) 957.
100. I. G. Voigt-Martin, L. Mandelkern, *J. Polym. Sci. Polym. Phys. Ed.*, 27 (1989) 987.
101. L. Mandelkern, R. G. Alamo, M. A. Kennedy, *Macromolecules*, 23 (1990) 4721.
102. R. G. Alamo, B. D. Viers, L. Mandelkern, *Macromolecules*, 26 (1993) 5740.
103. N. Striberk, R. G. Alamo, L. Mandelkern, H. G. Zachmann, *Macromolecules*, 28 (1995) 5029.
104. R. Kitamaru, T. Nakaoki, R. G. Alamo, L. Mandelkern, *Macromolecules*, 29 (1996) 6847.
105. S. F. Lau, H. Suzuki, B. Wunderlich, *J. Polym. Sci. Polym. Phys. Ed.*, 22 (1984) 379.
106. J. Grebowicz, S. F. Lau, B. Wunderlich, *J. Polym. Sci. Polym. Symp.*, 71 (1984) 19.
107. J. Menzel, B. Wunderlich, *J. Polym. Sci. Polym. Lett. Ed.*, 19 (1981) 261.
108. C. Y. Li and S. Z. D. Cheng, *Semicrystalline Polymers in Encyclopedia of Polymer Science and Technology*, Wiley & Son, 2002.

This Page Intentionally Left Blank

Chapter 6

Crystallization, melting and morphology of homogeneous ethylene copolymers

Vincent B. F. Mathot^{@*} and Harry Reynaers*

[@]DSM Research, P.O. Box 18, 6160 MD Geleen, The Netherlands

*Katholieke Universiteit Leuven, Celestijnenlaan 200F, B-3001 Leuven-Heverlee, Belgium

1. INTRODUCTION

Ever since their introduction, more than 65 years ago, polyethylenes have been extensively studied [1,2,3,4,5,6,7]. The first polyethylene to be commercialized was LDPE, followed by such products as HDPE, EPDM, and UHMWPE. In the early eighties heterogeneous LLDPE copolymers were introduced in the market, followed by VLDPEs a few years later. These polymers have recently been described in great detail in an overview [8]. Today, research is focused mainly on homogeneous copolymers polymerized with the aid of metallocene catalysts [9,10]. In this chapter we shall therefore concentrate on homogeneous copolymers [8,11,12].

The most effective control parameters in determining the properties of polyethylene end products are the molar mass distribution and the amount and distribution of short chain branching [6,8,13,14,15,16,17,18,19,20], because these parameters strongly influence crystallization. Short chain branching may or may not be caused by copolymerization or terpolymerization.

When is a copolymer homogeneous and when is it heterogeneous [8,18,21,22]? We will consider an ethylene copolymer to be *homogeneous if the statistics of ethylene and comonomer addition can be characterized by a single set of reactivity values, independent of the chain length*. In the case of such polymers, changes in the ethylene-to-comonomer ratio at the catalyst site can lead to changes in comonomer addition during polymerization. The definition of homogeneity implies that in a homogeneous copolymer the addition statistics is the same regardless of whether the chains have the same or different lengths (molar masses). Since the (co)monomer addition (that is, polymerization)

[@] To whom correspondence should be addressed. E-mail: vincent.mathot@dsm-group.com

process considered here is a statistical process, *very* short chains may well differ from the rest in terms of composition, for example comonomer content or sequence length distribution. However, the molar mass distribution of the polymer will normally be such that even the shortest chains have so many monomer units that their composition does not differ significantly from that of the longer chains.

A copolymer that does not meet these criteria is considered to be heterogeneous. For example, in LLDPE and VLDPE products manufactured with the aid of Ziegler-Natta catalysts the molar mass usually decreases with increasing comonomer content because the comonomer acts as a chain stopper. This is the case even in one and the same product: if the comonomer content is measured as a function of the molar mass it is found that the shortest chains are generally the most heavily branched. But there is more. Fractionation studies have revealed that even chains of the same length differ greatly in comonomer content and sequence length distribution. The extreme heterogeneity of comonomer addition makes these copolymers extremely complex [21,22,23, 24,25,26,27]. However, at the same time they are very interesting because their morphology and properties are to a large extent influenced by the heterogeneity [28,29,30]. The heterogeneity is to be attributed to the presence of at least two active catalyst sites. It is not easy to clarify the chain microstructure because the ethylene and comonomer sequence length distributions cannot be measured by any method. Not even by ^{13}C -NMR, because this technique can measure no methylene sequence lengths longer than 5.

Even in the case of homogeneous copolymers, measuring the chain microstructure is no easy task, although the presence of only one active catalyst site makes evaluation much simpler. DSC can give a first indication of heterogeneity because, as we shall discuss in detail later, there are relationships between chain microstructure, crystallization, crystallite size distribution and melting behavior. A DSC curve can sometimes function as a fingerprint of the molecular structure, provided the analyst knows the system well. If a DSC curve is multi-peaked, it should be investigated whether this is due to reorganization, in particular recrystallization (obviously, the polymer's thermal history should be taken into consideration in this analysis). If the peaks are far apart, the chances are that the multiple peaks are due to heterogeneity of the chain microstructure.

If the DSC curve is single-peaked, this does not necessarily indicate a homogeneous copolymer. Several peaks may merge because they are close together or as a result of nucleation or co-crystallization. Examples of this can also be found in non-copolymers, for example in heterogeneously branched polyethylenes such as HDPE and LDPE [31,32]. So even in the case of copolymers with single-peaked DSC curves a ^{13}C -NMR analysis of the chain microstructure can give meaningful results only if it has first been established beyond doubt by fractionation that the copolymer is not heterogeneous.

Fractionation, which is here understood to be the physical separation (for the purpose of further fractionation and/or characterization) of fractions which differ in structure, can be very laborious. The interest in fractionation research has been revived since the introduction of LLDPE. Various fractionation techniques and methods are available. A fractionation on the basis of molar mass is always successful and can be carried out by means of size exclusion chromatography (SEC), direct extraction (DE), liquid-liquid separation, *etc.* Fractionation on the basis of crystallizability can also be effected in various ways. Well-known techniques are temperature rising elution chromatography (TREF) (see references in [8]), crystallization analysis fractionation (CRYSTAF) [33], *etc.* Combinations - cross fractionations - are possible, for example DE - TREF, P(reparative)SEC - TREF, TREF - SEC, *etc.*, see [8]. Various techniques are available for evaluating the fractions obtained, for example viscosity measurements, IR, DSC and light scattering. Since a crystallization fractionation is based on crystallization in solution followed by dissolution (melting), the researcher should be aware that crystallization and dissolution mechanisms play a major role. In fractionation in solution, too, the comonomer content and the comonomer distribution are important parameters and a crystallization fractionation in particular can be highly effective. However, few people are aware that reorganization can play an important role even when the cooling process is very slow, as in the case of TREF [34]. The molar mass is also a parameter in crystallization [6,8,31,35,36,37,38,39,40,41,42,43], especially when the comonomer content is a function of the molar mass, as is the case in many HDPEs, LDPE, LLDPE, VLDPE [40]. For these polymers, the best approach is to first fractionate on the basis of molar mass and subsequently on the basis of crystallizability, rather than the other way round [38]. Unfortunately, in practice usually the reverse order is applied because this makes it possible to use SEC in the second step. SEC is a well-established, readily usable technique that requires little material. However, in case of a molar-mass dependency of the comonomer content the results of the first fractionation may be almost uninterpretable, which means that the results of subsequent fractionations can only get worse.

Even in homogeneous copolymers the chain length may influence the crystallization process. Therefore, one should preferably first carry out a fractionation on the basis of chain length (*i.e.* molar mass). It is generally assumed that only short chains influence the melting behaviour, but this is not always true. In crystallization from the melt the crystallization behaviour is clearly affected by entanglements and the diffusion problems associated with these, while in subsequent melting the melting temperature is seemingly independent of the chain length due to reorganization processes [44], while the crystallinity drastically decreases with increasing chain length. In crystallization in solution the diffusion problem is smaller, but in subsequent dissolution reorganization plays a greater role, as mentioned earlier. In such a case the

degree to which reorganization can be prevented depends in part on the chain microstructure (nature and number of branches) because this microstructure greatly influences the mobility of chains inside crystals and the recrystallization possibilities.

2. ETHYLENE-PROPYLENE COPOLYMERS

2.1. Influence of comonomer content on crystallization and melting

Fig. 1 shows the results of DSC measurements [45] on a series of homogeneous ethylene-propylene copolymers [46,47] whose propylene content ranges from 4.4 to 35.3 (mol)%. The measurements show the extremely large influence of the propylene content on crystallization and melting. Two effects can be observed: as the propylene content increases, the crystallization and melting processes shift to lower temperatures and the areas under the peaks become smaller. Obviously, propylene interferes with the crystallization process in a major way.

Nucleation [7] plays an important role in the crystallization process for all samples, see Fig. 1a, as can be seen from the large change in dq/dT at the onset of crystallization in cooling. The nucleation barrier is highest at a low degree of supercooling, so its effect is greatest in the samples with the lowest comonomer contents. As the comonomer content increases, the barrier becomes lower and the curves become less pronounced. In the most heavily copolymerized samples the DSC curve has no peak at all. Therefore, for these samples it is difficult to describe the DSC curves in terms of characteristic temperatures. When the temperature is decreased further after the onset of crystallization, further crystallization takes place (as a result of nucleation and growth).

In the case of the least copolymerized samples, such as EP 208 (4.4 (mol)% propylene) and EP 207 (10.6 (mol)% propylene) the DSC curves do not show when crystallization stops. This is because in a copolymer the heat capacities of the crystalline and amorphous phases are temperature-dependent, which means that even at a constant crystallinity dq/dT will never be constant and this effect will need to be corrected for. Such a correction is possible, as will be demonstrated later for EP 207 and the ethylene-1-octene copolymer EO V. In the case of EP 207 it is clear from the excess heat capacity curve, see below, that the crystallization region spans about 100 degrees, namely from about 80 to -20°C. As the comonomer content increases, crystallization increasingly interferes with the glass transition. In the case of the more heavily copolymerized samples, for example EP 198 (30.8 (mol)% propylene), even an ordinary DSC curve shows this, because for these samples the glass transition is clearly recognizable by the stepwise change in dq/dT at the lowest temperatures. In the case of the samples with the highest comonomer contents, see the DSC heating curves in Fig. 1b, it is clearly visible that the melting process starts immediately

after devitrification. For the copolymers shown here, the glass transition temperature (taken as, for example, the point where the DSC curve shows an inflection, or determined using the enthalpy method) decreases from about -35 to about -60°C as the propylene content increases.

The temperature range of the crystallization process and the specific shape of the DSC curve are determined by the degree to which the crystallizable units in the copolymer chain, in this case the ethylene units, are able to crystallize. In the case of the copolymers discussed here the polymerization process is a

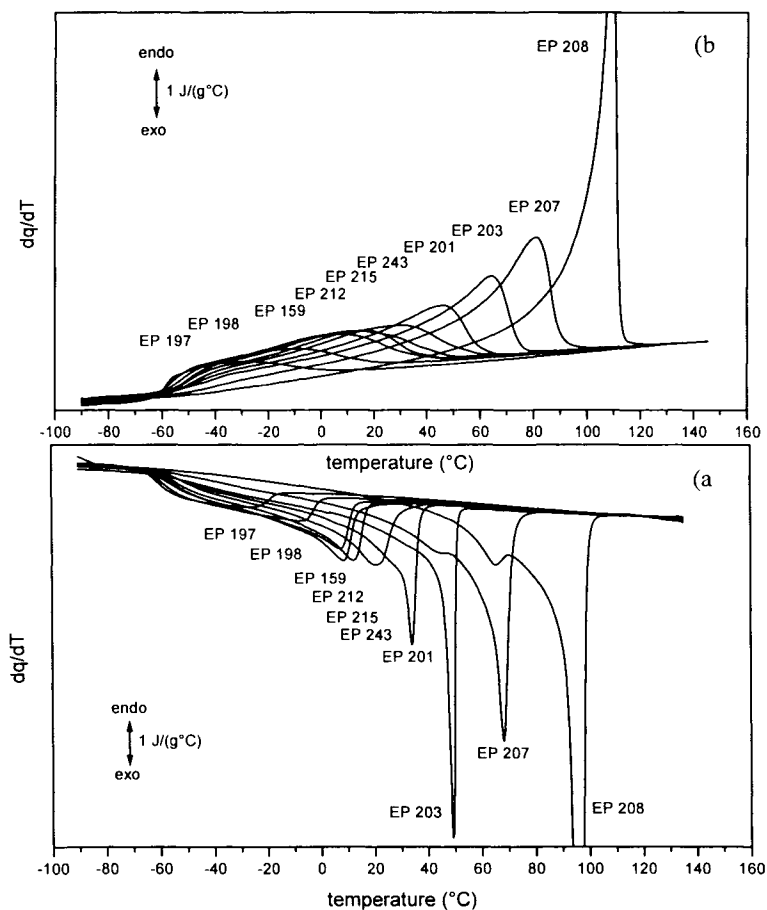


Fig. 1. DSC-2920 (TA Instruments) pseudo- c_p cooling (a) and subsequent heating (b) curves at $10^{\circ}\text{C}/\text{min}$ in between -100 and 150°C for homogeneous ethylene-propylene copolymers with varying propylene content ((mol)%): 4.4 (EP 208); 10.6 (EP 207); 17.4 (EP 203); 19.0 (EP 201); 22.2 (EP 215); 22.4 (EP 243); 24.7 (EP 212); 26.4 (EP 159); 30.8 (EP 198); 35.3 (EP 197). The curves were fixed at the same value at 120°C (a) and 130°C (b).

statistical process [46,47] which can readily be described with the aid of Markovian statistics (see later). This means that in the polymer chain there is a certain distribution of uninterrupted ethylene sequence lengths. These ethylene sequences are separated by non-crystallizable propylene units, which may occur in isolation or in sequences. Since longer ethylene sequences will more readily form large and hence stable nuclei, these will be the first to try to nucleate and form crystallites. Thus, for thermodynamic reasons [13,14,15,48] it is to be expected that during crystallization a fractionation according to ethylene sequence length takes place, and this is confirmed by the research carried out so far. Since there is an *ethylene sequence length distribution*, upon crystallization a corresponding *crystallization temperature distribution* will arise which in its turn will give rise to a *crystallite size distribution*, which (for thermodynamic reasons) will result in a *melting temperature distribution*. Since nucleation plays such an important role in crystallization and the associated kinetics cannot (yet) be described in a theoretical model, many researchers opt for modeling the melting process. In this way they aim to describe relationships between the ethylene sequence length distribution and the melting temperature distribution. In the case of the samples with the highest comonomer contents this is probably correct, but in the case of samples such as EP 208 reorganization is likely to occur during heating. One may assume that during this process the crystallites will be perfected and their dimensions will increase; this explains the metastability [44] of macromolecular crystallites. Obviously, the exact relationship between the distributions mentioned is not simple, neither for crystallization nor for melting, because all kinds of kinetic effects play a role: nucleation, reorganization during the measurement, *etc.* So although the DSC cooling and heating curves are reflections of crystallizing and melting ethylene sequences, respectively, this does not mean that the relations are straightforward and simple.

At low comonomer contents, the ethylene sequences will be folded in the crystallites. An important reason for this is that due to all kinds of hindering effects relating to the nature of the macromolecular chains (entanglements; the need for molecular nucleation [4], *etc.*) the high nucleation barriers cannot be overcome at low degrees of supercooling. As a result, long sequences do not crystallize into crystallites of comparable dimensions. Crystallization takes place at higher degrees of supercooling, at which the critical dimensions for nucleation are smaller. The resulting longitudinal crystallite dimension (more or less in the direction of the chain) can then be much smaller than the ethylene sequence length and such a sequence will have to fold in order to be maximally incorporated into the crystallite. Folding is moreover a highly effective way of avoiding crowding [1,49,50] at the crystallite surface, and for the same reason only part of the sequences are able to cross over to other crystallites as so-called 'tie molecules'. In the case of polyethylene, crowding would lead to the unlikely

situation where the density of the amorphous phase would exceed that of the crystalline phase.

The higher the comonomer content, the shorter the average ethylene sequence length. In copolymers with a very high comonomer content the average ethylene sequence length may come close to the crystallite dimension in the chain direction. This is because the increased hindrance from side chains due to incorporated comonomers leads to a lowering of the crystallization temperature, in other words an increase in the degree of supercooling. As a result, the driving force of crystallization increases and the nucleation barrier decreases, so that the critical dimension may become of the same order of magnitude as the ethylene sequence length. However, at a lower crystallization temperature the mobility of the chains and hence their diffusability decreases, so that the matching will never be perfect [51,52]. At the same time, the lateral crystallite dimensions (more or less perpendicular to the chain direction) will become smaller. This effectively prevents crowding; extreme examples are fringed micelle crystallites, whose lateral dimensions are assumed to be very small, especially in combination with a highly curved interface [1].

Clearly, propylene strongly hinders the crystallization process when it is used as a comonomer in ethylene-dominated chains. So the hindering effects of the comonomers to be discussed below (butene and octene) can only be stronger. It is a well-known fact that comparatively longer side chains (such as those resulting from octene incorporation) interfere more strongly with the crystallization process. This second-order effect is due to the mechanism by which the crystallization process is hindered. It is generally assumed that up to a certain extent propylene can be incorporated into a crystallite as a defect (inclusion) [6,53,54,55,56,57,58,59], without disturbing the order of the unit cell too much. In the case of octene, however, inclusion is unlikely and one must assume that octene units are excluded from the crystallites [54,56,60,61,62]. As a consequence, for this comonomer the relationships between ethylene sequence length distribution \Leftrightarrow crystallization temperature distribution \Leftrightarrow crystallite dimension distribution \Leftrightarrow and melting temperature distribution will be more straightforward.

In the cooling curves of the least copolymerized samples another, small peak can be observed, see for example EP 208 and EP 207 at about 66°C and about 45°C, respectively, in Fig. 1. These peaks, for which no explanation has been provided until now, occur in all ethylene-based polymers [63], and even in linear polyethylene [64]. There is a relationship between the position of the peak and the ethylene content: the higher the ethylene content, the higher the temperature at which the peak occurs. Since there is never a corresponding peak in the heating curve, we assume that the peak is due to some form of homogeneous nucleation: a nucleation without any external surface, which means that the nucleation barrier is very high so that nucleation takes place at

much lower temperatures than in the case of heterogeneous nucleation (the most common mechanism). After homogeneous nucleation, melting takes place at much higher temperatures because the melting temperature is representative of the dimensions of the crystalline structure after growth. This ultimate crystalline structure will in any case, upon growth and possible reorganization during cooling and heating, be much larger than the nucleus at the crystallization temperature, so the melting temperature will probably be situated on the low-temperature side of the main peak and will therefore no longer be visible. However, all this is speculation and needs to be specifically investigated.

2.2. Heat capacity, enthalpy, crystallinity, baseline and excess heat capacity

The measurements shown in Fig. 1 are so-called ‘pseudo- c_p ’ measurements [63]. This means that one and the same empty-pan measurement was subtracted from all pan + sample measurements in order to obtain a first-order correction for instrumental curvature of the DSC curves. This is necessary because measurements with instrumental curvature are useless for determining a heat of transition or crystallinity. In pseudo- c_p measurements no absolute c_p scale is aimed at. If the energy calibration is not (very) temperature-dependent, for some calorimeters it suffices to carry out a single sapphire calibration or even an indium calibration. This means the measurements are easier to carry out than a true c_p measurement. It has been found in practice that such measurements nevertheless yield acceptable results which provide satisfactory answers to most questions.

Before discussing results obtained by this method we shall first discuss the possibilities offered by true c_p measurements with reference to the ethylene-propylene copolymer EP 207 [11], see Fig. 2. The cooling and heating curves in Fig. 2a were measured using the ‘continuous measuring method’, which means that a single measuring run was carried out which covered the entire temperature range of interest [63]. In the case of polymers this measuring method is to be preferred because - in the classical, ‘stepwise measuring method’ - every isothermal step can give rise to further crystallization or melting as well as to reorganization processes, such as annealing, recrystallization *etc.* If such processes occur during an isothermal step, the measuring results are meaningless. Fig. 5.6 in [63] shows an example of a case where no measurement was possible in the crystallization and melting peak of a linear polyethylene (LPE). Obviously, the ‘continuous measuring method’ imposes high demands on the stability of the calorimeter (prevention of drift!) because there are only two calibration points (isotherms) left. In Fig. 2b cooling and heating curves for EP 207 obtained via the ‘continuous measuring method’ are compared with those obtained according to the classical ‘stepwise method’. Differences can be observed on the high-temperature side, from about 40°C upwards. The step size was 25°C, except between 60 and 100°C, where a step of 35°C was required to

obtain an acceptable signal or to be able to introduce an isothermal stay. On the low-temperature side the results are in good agreement, especially if we take into account that the measurements were carried out on two different DSC-7

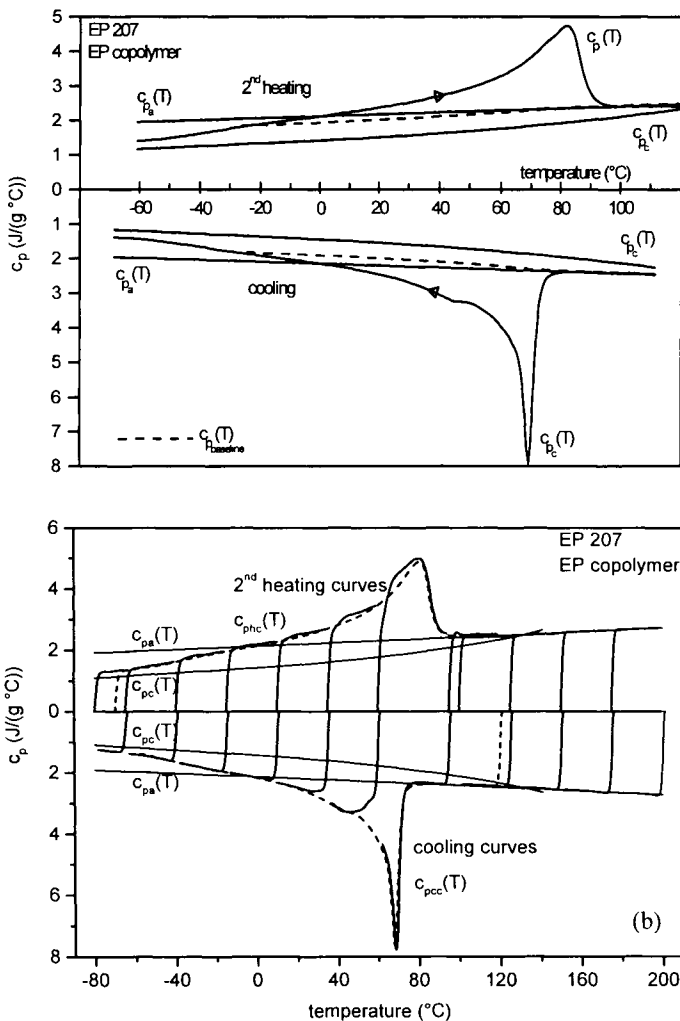


Fig. 2. DSC-7 (Perkin-Elmer) specific heat capacity curves, $c_p(T)$, at 10°C/min for EP 207 obtained in cooling (downwards) and subsequent heating (upwards); the reference curves for the amorphous phase, $c_{pa}(T)$, and for the crystalline phase, $c_{pc}(T)$; and the baseline curves, $c_{pb}(T)$

a. continuous specific heat capacity curves in between -70 and 120°C;

b. continuous and step-wise specific heat capacity curves in between -70 and 120°C resp. in between -80 and 200°C.

instruments. Clearly, stepwise measurements are not suitable for polyethylenes if there is a substantial dq/dT , but we are interested only in processes in which there is such a dq/dT . The 'continuous measuring method' has yet another advantage in that it enables the use of high scan rates [65,66], for example to avoid recrystallization and in general to be able to study the kinetics of processes in a quantitative way.

Fig. 2a successively shows crystallization and vitrification in cooling (downward curve) and subsequent devitrification and melting in heating (upward curve). In both cases (positive) c_p values are obtained. The characteristic small peak during cooling is also present. Now how do we decide where crystallization stops during the cooling run and where melting begins during the heating run? Likewise, one may wonder whether the heats of crystallization and melting and the crystallinity can be determined and if so, how. In the case of polymers these questions can be answered [63] and the procedure is in fact straightforward, provided the two-phase model is applicable. Even when three phases are present (e.g. when an additional rigid amorphous phase is present [63,67,68]) there are possibilities for determining the heats of crystallization and melting and the crystallinity, but in that case a suitable (morphological) model needs to be postulated. For the ethylene copolymers under review here the two-phase model

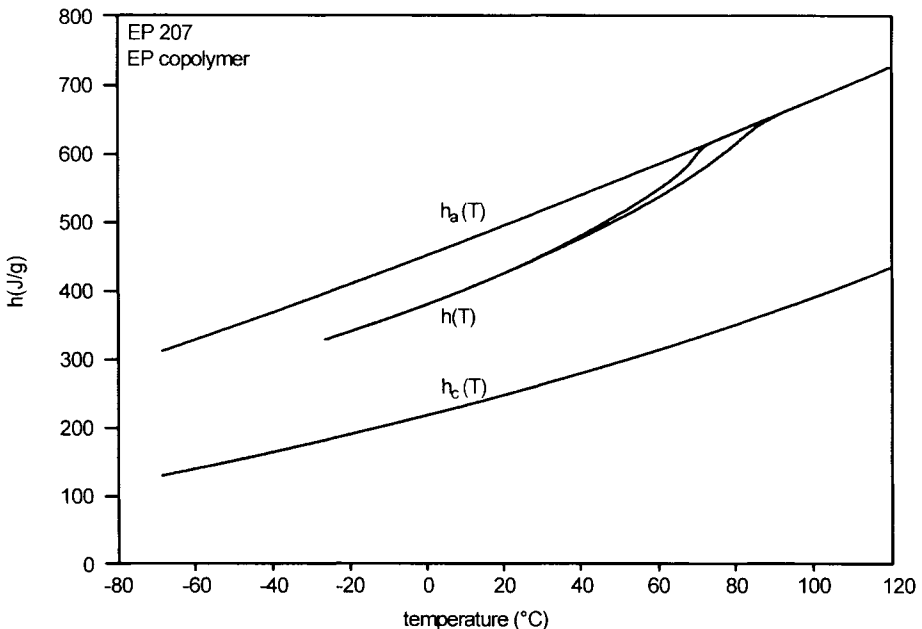


Fig. 3. Specific enthalpy cooling curve, subsequent heating curve and reference curves $h_a(T)$ and $h_c(T)$ for EP 207, based on the specific heat capacity curves shown in Fig. 2a.

has been found to be adequate. This model is based on the assumption that the sample can be divided into 100% crystalline and 100% amorphous regions; for a detailed discussion see [63]. Another assumption is that the enthalpies of these regions are additive according to mass fraction. For a large number of polymers the heat capacity reference functions for the 100% crystalline and 100% amorphous regions, $c_{pc}(T)$ and $c_{pa}(T)$, respectively, are known [69].

Fig. 2 shows not only the experimental heat capacity curves but also the c_p reference curves for polyethylenes [11,70]. In the melt part of both the cooling curve and the heating curve $c_p(T)$ and $c_{pa}(T)$ coincide, which illustrates that $c_{pa}(T)$ provides meaningful information. The figure also shows that in this region the experimental curves are symmetrical with respect to the temperature axis. These similarities are important and sensitive quality criteria for c_p measurements.

Fig. 3 shows the enthalpy reference functions, $h_a(T)$ and $h_c(T)$ respectively [70]. These enthalpy curves can be calculated from $c_{pc}(T)$ and $c_{pa}(T)$, respectively, by simple integration, together with the heat of melting at the equilibrium melting temperature, $\Delta h(T_m^*)$. In this figure, the cooling and heating curves coincide at low temperatures (in other words, they form a closed cycle), which is an indicator of the quality of the measurement. It is important to realize that all reference curves are temperature-dependent, and hence also the heat of melting $\Delta h(T) = h_a(T) - h_c(T)$, which is sometimes called the enthalpy reference differential function. Depending on the polymer, the value of the heat of melting at room temperature or at the glass transition temperature may be as low as 50% of the heat of melting at the equilibrium melting temperature.

We shall now discuss the calculation of the crystallinity as a function of the temperature [63]. Assuming, as mentioned above, that the two-phase model is valid for EP 207, we may assume additivity of the enthalpy contributions for the two phases -- amorphous and crystalline [63]:

$$h(T) = w^c(T)h_c(T) + w^a(T)h_a(T) \quad (1)$$

where

$$w^c(T) + w^a(T) = 1 \quad (2)$$

With the aid of these two expressions we can define the (temperature dependent) enthalpy-based mass fraction crystallinity, $w^c(T)$, below T_m^* , the equilibrium crystal-melt transition temperature:

$$w^c(T) = \frac{h_a(T) - h(T)}{h_a(T) - h_c(T)} \quad (3)$$

For EP 207 the maximum crystallinity at -20°C is about 32%, see Fig. 4. Fig. 4 also includes the mass crystallinities calculated from real-time WAXD

measurements [11]. For this particular copolymer the results obtained with the two techniques are still in good agreement and any discrepancies are probably due to thermal lag problems with the synchrotron measuring set-up. Later we shall see that the discrepancy between DSC and WAXD results increases as the comonomer content increases. In this figure, as in Fig. 3, the DSC crystallinity curves form a closed cycle. Such a perfect agreement is the exception rather than the rule because on account of the method used for calculating the crystallinity the value obtained is very sensitive not only to crystallization and melting but also to any experimental imperfections such as curvature, drift, *etc.* The curve once again shows that the crystallinity at room temperature is a rather arbitrary point, which is meaningful only in the case of applications at room temperature or if a comparison is made with a measurement carried out at room temperature, for example a crystallinity value based on density, an X-ray measurement, *etc.* However, the only way to obtain real insight is to carry out a measurement as a function of temperature, and it is in such cases that DSC has proved to be one of the few techniques available for quick and quantitative determination of temperature-dependent crystallinities. According to our experience it is possible, using the 'continuous measuring method', to determine the mass crystallinity

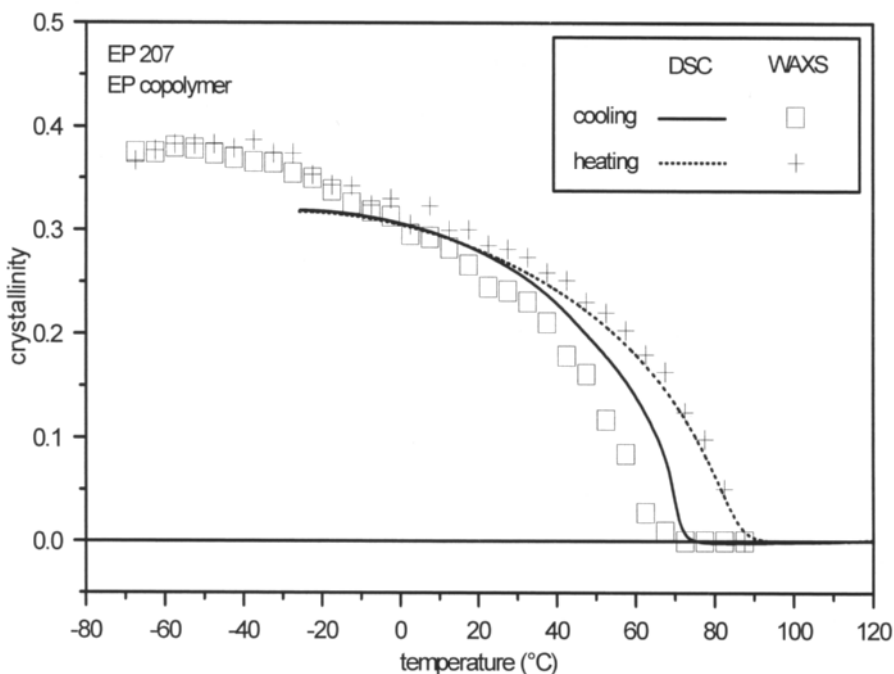


Fig. 4. Enthalpy-based mass crystallinity curves based on DSC (as calculated from curves shown in Fig. 3), and mass crystallinity curves from WAXD, for cooling and subsequent heating at 10°C/min for EP 207.

with an absolute accuracy of $\pm 2\%$. Below we shall discuss an alternative DSC method for determining crystallinities, which is based on the ‘pseudo- c_p ’ measurements mentioned earlier. Finally, it should be noted that for the samples we have studied we have always found a good agreement (typically better than 3% absolute) between mass crystallinities calculated from c_p measurements and from density measurements.

Especially in crystallinity calculations, the temperature dependence of enthalpies should be taken into account. So it is incorrect to assume a fixed value, for example the value at T_m° which is often used, because the crystallinities thus obtained may well be too low. In the case of polyethylenes, the deviation may well be more than 10%, and with other polymers deviations of up to 30% are possible. In such cases a comparison with the crystallinities obtained using other methods is meaningless and the data cannot be used as a basis for determining whether or not an interphase or third phase is present.

It is also clear that the measurements of Figs. 1 and 2 alone are not sufficient for determining the heats of crystallization and melting. For such determinations the so-called excess-heat capacity curves need to be determined. This can be done by subtracting the so-called baseline heat capacity curves from the curves measured. The procedure has been described and applied earlier [63,71]; we shall only give a brief overview here.

Differentiation of $h(T)$ in (1) with respect to temperature

$$c_p(T) = (dh/dT)_p \quad (4)$$

yields

$$c_p(T) = w^c(T)c_{pc}(T) + h_c(T)dw^c(T)/dT + w^a(T)c_{pa}(T) + h_a(T)dw^a(T)/dT \quad (5)$$

$$= w^c(T)c_{pc}(T) + [1 - w^c(T)]c_{pa}(T) - [h_a(T) - h_c(T)]dw^c(T)/dT \quad (6)$$

The $w(T)$ terms are regarded as belonging to the ‘baseline’ heat capacity and the $dw(T)/dT$ terms as belonging to the ‘excess’ heat capacity:

$$C_{pb}(T) = w^c(T)c_{pc}(T) + [1 - w^c(T)]c_{pa}(T) \quad (7)$$

$$c_{pe}(T) = [h_a(T) - h_c(T)]dw^c(T)/dT \quad (8)$$

and

$$c_p(T) = C_{pb}(T) + c_{pe}(T) \quad (9)$$

The baseline heat capacity reflects the contributions of the temperature-dependent c_{pa} and c_{pc} to the experimental $c_p(T)$ via the crystallinity. In Fig. 2a the resulting baseline heat capacity curves are plotted for EP 207. These differ not only from each other but (of course) also from the reference curves. The points where they intersect with the measured curves indicate the temperatures where,

in a cooling run, crystallization ends (because vitrification interferes with the crystallization process) and, in a heating run, melting begins (because the mobility of the chain segments increases due to devitrification).

The excess heat capacity reflects contributions such as (re)crystallization, annealing and melting) processes by which the crystallinity is changed) to the experimental heat capacity. The first part of the right-hand member of (8), the enthalpy reference differential function $h_a(T) - h_c(T) = \Delta h(T)$, is known for many polymers, see for example the ATHAS databank [69]. The second part, the change in crystallinity with temperature $dw^c(T)/dT$, can be numerically calculated from $w^c(T)$, which function is given by (3).

Fig. 5 shows the excess heat capacity curves for EP 207. It is clear that crystallization and melting take place above about -25°C . By determining (partial) areas under the cooling and heating curves at a specific temperature we can obtain *the* heats of crystallization and melting, respectively, at that temperature for EP 207 at the given history. Of course, this determination method is equivalent to the determination in Fig. 2a of the (partial) areas enclosed by the baseline curves and the measured curves. The excess curves are actually the most interesting ones because these are by definition related to changes in crystallinity. Therefore, theoretical models should be able to predict or describe these curves.

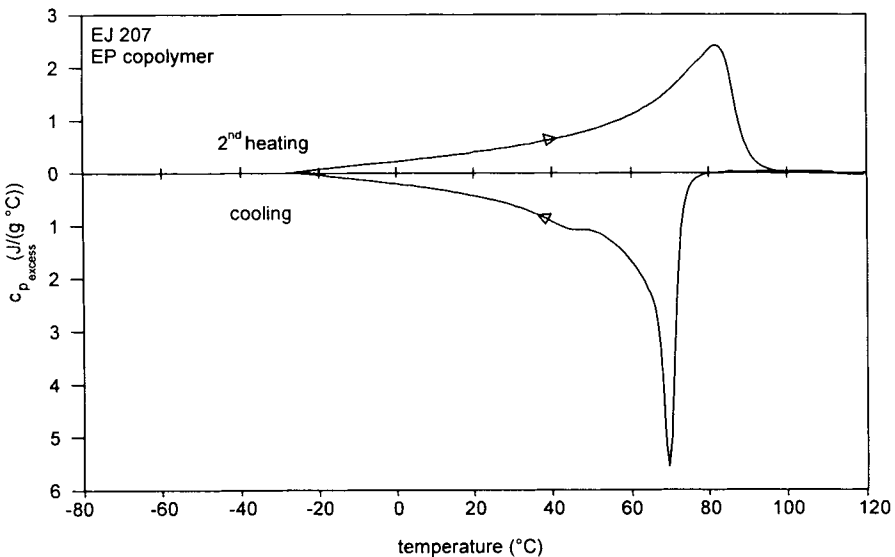


Fig. 5. Specific excess-heat capacity curves for EP 207 for cooling and subsequent heating at $10^\circ\text{C}/\text{min}$, as calculated from measurements shown in the preceding figures.

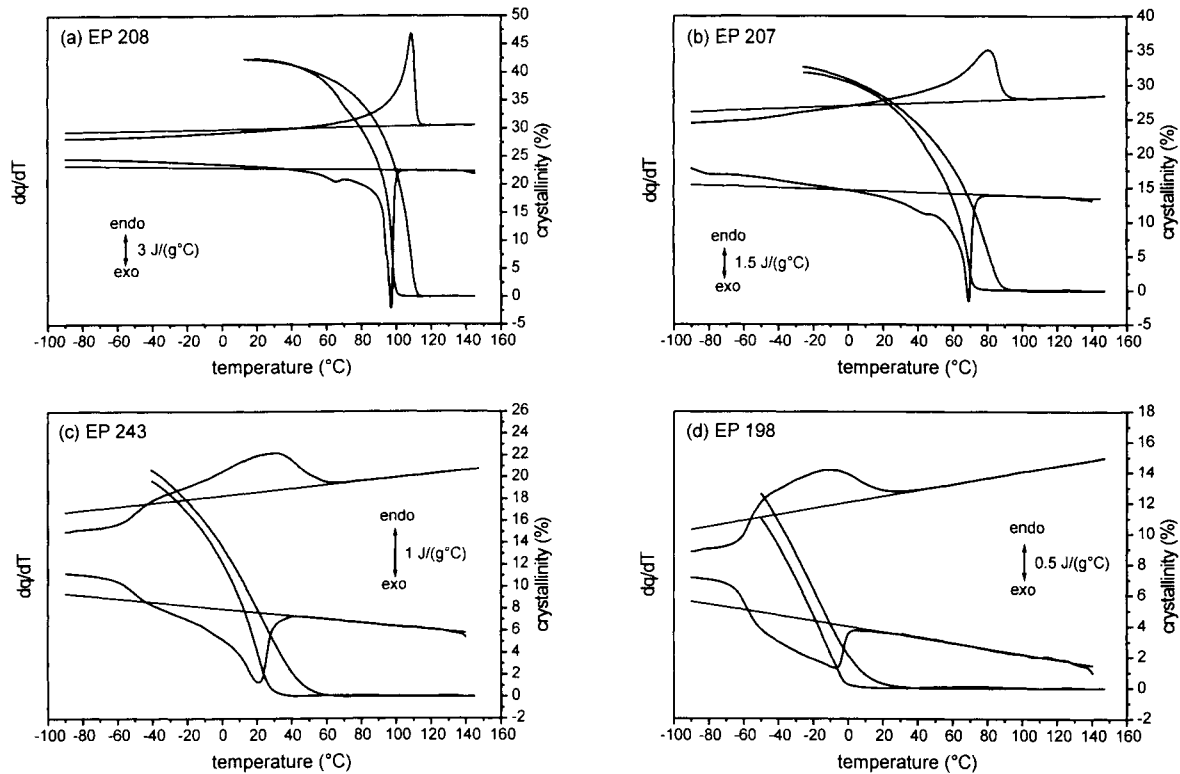


Fig. 6. DSC-2920 pseudo- c_p cooling (downwards) and subsequent heating (upwards) curves at 10°C/min in between -100 and 150°C for homogeneous ethylene-propylene copolymers with varying propylene content (mole%). (a): EP 208 (4.4%); (b): EP 207 (10.6%); (c): EP 243 (22.4%); (d): EP 198 (30.8%). The curves are located vertically arbitrarily. Also shown the crystallinity curves for cooling and subsequent heating, as based on the pseudo- c_p measurements, according to the 'extrapolation method'.

2.3. Illustrating the use of the ‘extrapolation method’ for calculating crystallinities as applied to ‘pseudo heat capacity’ measurements on characteristic samples

In Figs. 6a-d a number of characteristic samples are shown on which measurements were carried out according to the above-mentioned ‘pseudo- c_p ’ method. Some samples have been extensively discussed above (EP 207, 10.6 (mol)% propylene) and elsewhere (EP 243, 22.4 (mol)% propylene, in [12]; EP 198, 30.8 (mol)% propylene, in [11]) on the basis of c_p measurements. The crystallinity curves included in the figures were determined according to the ‘extrapolation method’. This method, which is extensively discussed and illustrated in [63] and can be universally applied using a recently developed software package [72], uses extrapolation from the melt to estimate the contribution to the DSC signal of the (100%) amorphous phase. Such an extrapolation can be applied to c_p measurements, ‘pseudo- c_p ’ measurements and even ordinary DSC measurements provided there is no instrumental curvature, or not any more. If we combine this with the temperature dependent enthalpy reference differential function $\Delta h(T) = h_a(T) - h_c(T)$, which, as stated earlier, is known for many polymers and in any case for polyethylene, we can calculate the crystallinity as a function of the temperature. A comparison of the values found here with those obtained via the ‘ c_p method’ shows that they are in good agreement.

2.4. Remarks on the use of the extrapolation method for crystallinity determination

It is expected that the ‘extrapolation method’ described above will rapidly increase in popularity, for two reasons. In the first place the demand for quantitative DSC measurements will increase because, as observed before, DSC is the only technique enabling rapid and quantitative determination of crystallinities as a function of the temperature. Moreover, other advanced techniques are also increasingly becoming available, for example real-time X-ray analysis with the aid of synchrotron facilities, so that results can be compared. Secondly, the above-mentioned software package can make the method suitable for any DSC user, regardless of the type of instrument used.

Given this development, there is all the more reason to critically review the advantages and drawbacks of the method. In using the extrapolation method, several points need to be given attention:

- a crucial step in the method is effective correction for ‘instrumental curvature’. It has been found in practice that subtracting an empty-pan measurement, though necessary, may not be sufficient; it is essential that the DSC performs optimally and that ambient influences are stabilized, in particular with regard to the cooling unit, temperature fluctuations in the laboratory, *etc.*;

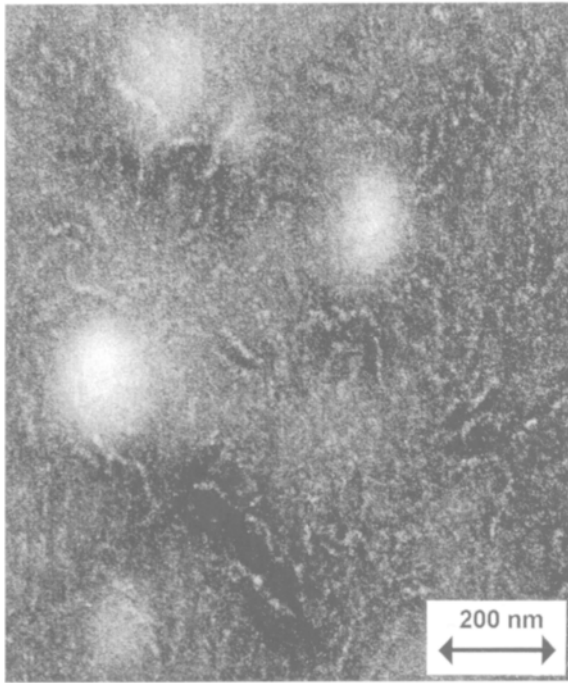
- in order for the extrapolation method to be applicable, extrapolation should be possible of course, in other words, the temperature range of the melt part of the DSC curve should be sufficiently wide;
- analysts should take into account the possibility of chemical reactions occurring (such as transesterification, transamidation, *etc.*);
- if possible, the lowest measuring temperature should be such that a state of constant crystallinity is reached; this will enable a simple check on the crystallinity curve at low temperatures.

It should be noted that abandoning the absolute scale (because it is not necessary for the extrapolation method) has certain disadvantages. For one thing, it is no longer possible to compare the measured heat flow and enthalpy differences with values reported in the literature [69]. This would otherwise be possible particularly in the melt and below the glass transition. Other simple and effective checks are also no longer available. To give an example: it can no longer be checked whether the heat capacities of the melt parts of cooling and heating curves are equal and have a positive temperature coefficient (which they must virtually always have).

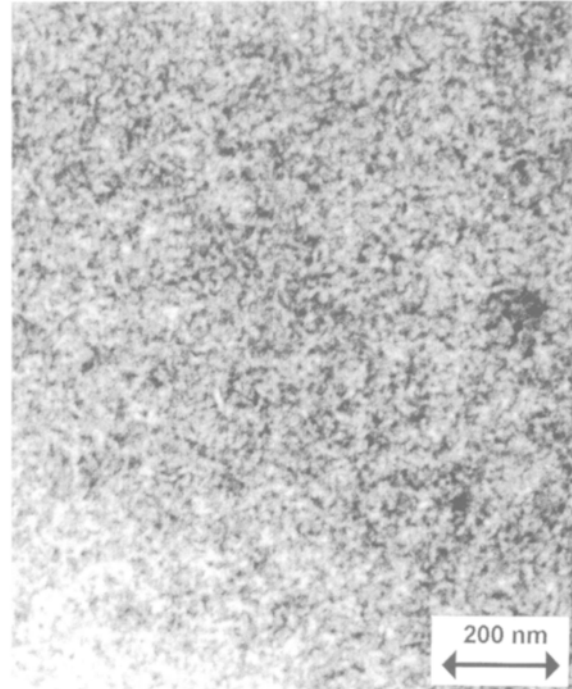
In conclusion, the 'extrapolation method' sketched above enables an analyst-independent determination of the crystallinity as a function of temperature in both cooling and heating. It is not necessary to perform heat capacity measurements, although it is of crucial importance that instrumental curvature of DSC curves has been removed via an empty sample pan correction. Experience has shown that due to the nature of the extrapolation (often across wide temperature ranges) and the nature of the calculation, see (3), this determination is extremely sensitive - not only to small differences in crystallization and melting but also to experimental imperfections. The best method is still a heat capacity measurement combined with an evaluation of the internal consistency of heat capacity and enthalpy data and a check with literature data (if available).

2.5. Morphology

We shall now turn our attention to the morphology of some ethylene-propylene copolymers. As the comonomer content increases the crystallization and melting processes shift to lower temperatures, see Fig. 1. This means that the copolymers with the highest propylene contents, such as EP 198, are amorphous at room temperature whereas in the case of a copolymer such as EP 212 (24.7 (mol)% propylene) the amount of crystallinity depends on whether room temperature is reached via cooling (sample is amorphous) or in heating after crystallization (sample is partially crystalline), see Fig. 1. So in this case, too, it is important to carry out measurements as a function of temperature or at least provide an adequate thermal history. In the case of a TEM micrograph this implies that the choice of staining temperature is very important. In the case of



A



B

Fig. 7. TEM micrographs of two homogeneous ethylene-propylene copolymers after staining at room temperature (A) lamellar base morphology for EP 207 and additional granular structures (B) granular base morphology in the case of EP 203.

EP 207 and EP 203, for example, a staining temperature of 60°C, which is fairly common for chlorosulphonic acid staining, would reveal only a limited part of the semi-crystalline morphology. In EP 203 no crystallinity would be seen if the sample were stained immediately after cooling to 60°C. For this reason, we opted for staining at room temperature after cooling as in a DSC measurement and subsequently trimming at -120°C. As the activity of the staining agents used decreases with decreasing temperature, staining at temperatures lower than 0°C is hardly ever practiced because the staining times would be prohibitively long. At present, staining at room temperature, let alone at 0°C, is only just feasible.

Fig. 7 shows the resulting TEM micrographs for the EPs 203 and 207 [12]. The base morphology of EP 207 is lamellar, while there are also granular structures present. These are structures, whose lateral and longitudinal dimensions are of the same order of magnitude [10,12,73,74]. So we are confronted with different morphologies in one and the same sample [75]. This is in agreement with the existence of a crystallite dimension distribution in these

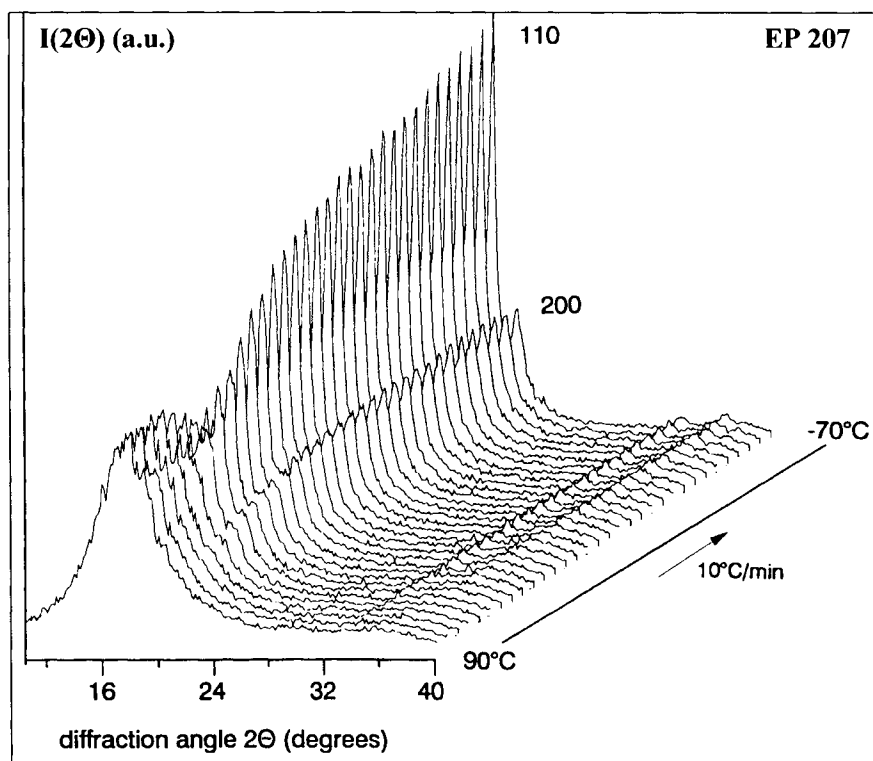


Fig. 8. WAXD curves for EP 207, after 1 min. waiting time at about 90°C, during cooling to about -70°C at 10°C/min.

samples as mentioned earlier. Unfortunately, it is not (yet) possible to establish exactly what this distribution is, so for the time being we have to describe it in qualitative terms. The longest and thickest lamellae are formed at the highest crystallization temperatures and no doubt are made up of the longest ethylene sequences. In EP 207 the average thickness of the lamellae is about 9 nm. The lengths are difficult to determine because, due to the nature of the staining technique used, only edge-on lamellae are readily visible and flat-on lamellae cannot be discerned. So twisting of edge-on lamellae would make them invisible. Nevertheless, lengths of about 250 nm are visible. This points to a considerable degree of crystallization of the longest ethylene sequences. Unfortunately, the volume fraction of lamellae is difficult to estimate. This means it is difficult to even qualitatively estimate the corresponding fraction of the ethylene sequence length distribution. The polymerization statistics show that the longest ethylene sequences contain 40-60 ethylene units. So the extended lengths of these sequences will vary between about 10 and 15 nm. So it seems that such sequences are present in the lamellae in extended form and at an angle to avoid crowding problems. We may also assume that, again in order to avoid crowding problems, a considerable portion of the chains will re-enter the crystallites. This re-entry is facilitated by the possible inclusion of propylene in the crystal lattice as a defect. All the same, it is remarkable that in such a copolymer lamellae with such large lateral dimensions occur. In EP 203 no lamellae are to be seen; the base morphology is granular, with dimensions of 2 - 12 nm.

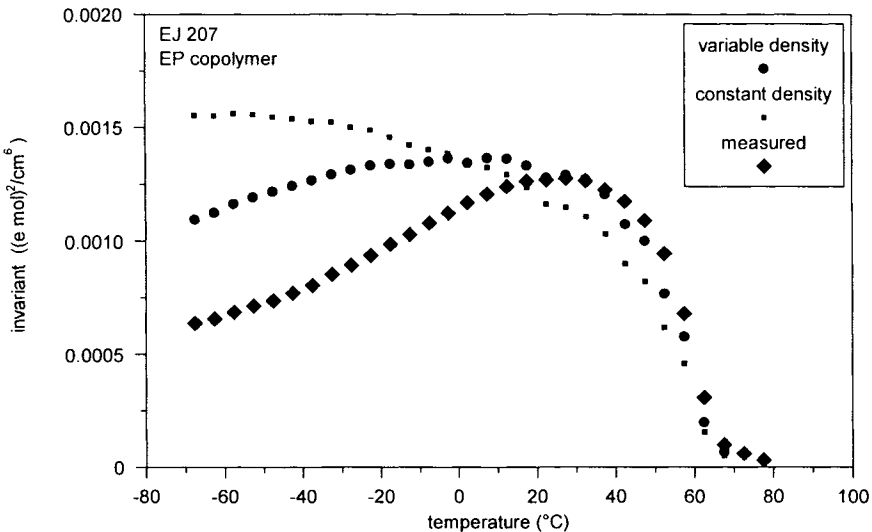


Fig. 9. SAXS measured and calculated invariant curves for EP 207 during cooling from about 90 to about -70°C at 10°C/min, see text for explanation of variable and constant density curves.

In Fig. 4 it was already shown that for EP 207 the mass crystallinities determined with the aid of DSC and WAXD are in agreement. Fig. 8 shows the WAXD real-time cooling curves [11]. During cooling at 10°C/min, 110 and 200 reflections are formed which correspond to the orthorhombic unit cell. The 110 reflection served as a basis for the calculation of the crystallinity. A 3-band analysis [45], using the Pearson functions for the 110 and 200 reflections and the amorphous band, of a static WAXD measurement at room temperature after cooling from the melt at the same scan rate gave a similar crystallinity of about 25%.

Fig. 9 shows the scattering invariant as a function of temperature as derived from real-time SAXS curves [11] due to crystallization during cooling for EP 207. The onset of crystallization is in good agreement with the DSC and WAXD results, cf. Figs. 2 and 8 respectively, although during the WAXD and SAXS measurements the sample was cooled from 90°C, at which temperature according to DSC a portion of the material is still melting. For a two-phase system the invariant is described by

$$Q(T) = C v^c(T) [1 - v^c(T)] [d_c(T) - d_a(T)]^2 \quad (10)$$

where the constant C depends on the equipment used and represents the conversion factor from electron density (e mol/cm^3) to mass density (g/cm^3). The (volume) crystallinity $v^c(T)$ represents the fraction of crystalline phase with mass density $d_c(T)$; $1 - v^c(T)$ represents the fraction of amorphous phase with mass density $d_a(T)$. The maximum in the curve is caused by a combination of two effects: an increase in the product of $v^c(T)$ and $[1 - v^c(T)]$ and a decrease in $[d_c(T) - d_a(T)]^2$ with decreasing temperature. However, attempts to describe the temperature dependency of the invariant with the aid of the temperature-dependent volume crystallinity according to WAXD and densities according to Swan and Wilksi [76,77,78] have been only partially successful, see ‘variable density’ in the Figure. For the high-temperature side agreement was reached, and a maximum was also found, but the low-temperature side could not be fitted. The ‘constant density’ curve shows that when the temperature dependency is not taken into account there is not even a maximum. The deviation at low temperatures may be due to overestimation of the density of the crystalline phase. Monte Carlo simulations [79] have shown that when crystallization takes place at lower and lower temperatures, the crystallites are increasingly ‘frustrated’. By this we mean that there are fewer and fewer crystallites with an orthorhombic lattice in which a crystallized ethylene unit is surrounded by four other ethylene units in directions perpendicular to the chain direction. A lower coordination number (in the simulation the coordination number was found to be about 3) and consequently a lower density of the crystalline phase might explain the above-mentioned deviation at low temperatures.

We shall now discuss in more detail the ‘frustrated’ crystallization that occurs when the comonomer content increases even further. EP 243 is a good example [12]. In Fig. 6 this copolymer displays a normal crystallization and melting pattern. Nothing in the DSC curves points to a deviant behavior, and the same is true of the heat capacity curves, enthalpies and crystallinity curves shown in reference [11]. However, in the WAXD curves hardly any recognizable orthorhombic reflections can be distinguished. This indicates that the crystalline structures - which are definitely present according to the DSC results - do not produce any constructive interference. This is probably due to a combination of the small dimensions and the imperfect nature of the crystallites. This has been found to be the general pattern, and we shall return to it when discussing the ethylene-1-octene copolymers.

SAXS measurements, too, show that crystallization and melting take place in EP 243. In Fig. 10 the intensity of the correlation maximum increases during heating, then goes through a maximum and finally decreases. The invariant shows a similar pattern with increasing temperature. Again, the signal on the high-temperature side corresponds to the point where melting ends in the DSC heating curve. It is interesting that for all copolymers a correlation maximum is found, although the intensity of this maximum decreases as the comonomer content increases. Apparently, there are always electron-density fluctuations

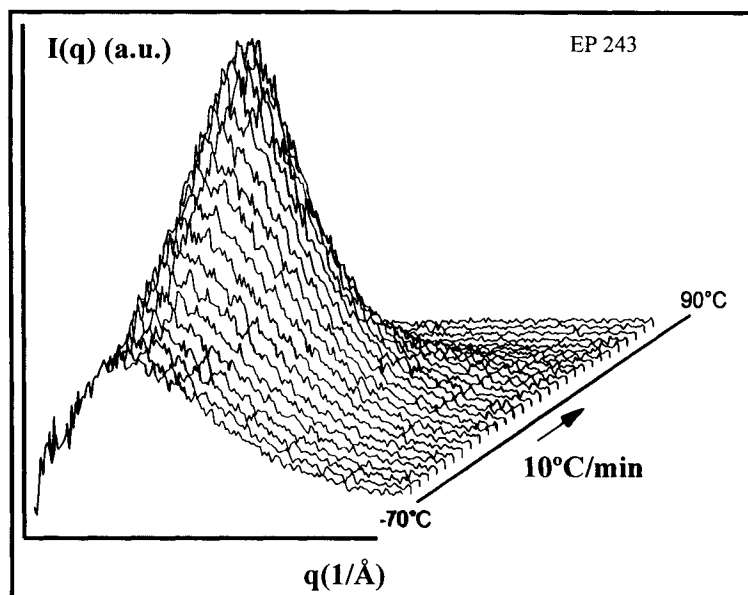


Fig. 10. Dynamic SAXS curves of the homogeneous ethylene-propylene copolymer EP 243 measured during heating at 10°C/min from approx. -70 to approx. 90°C. 1 Frame corresponds to a temperature interval of 5°C.

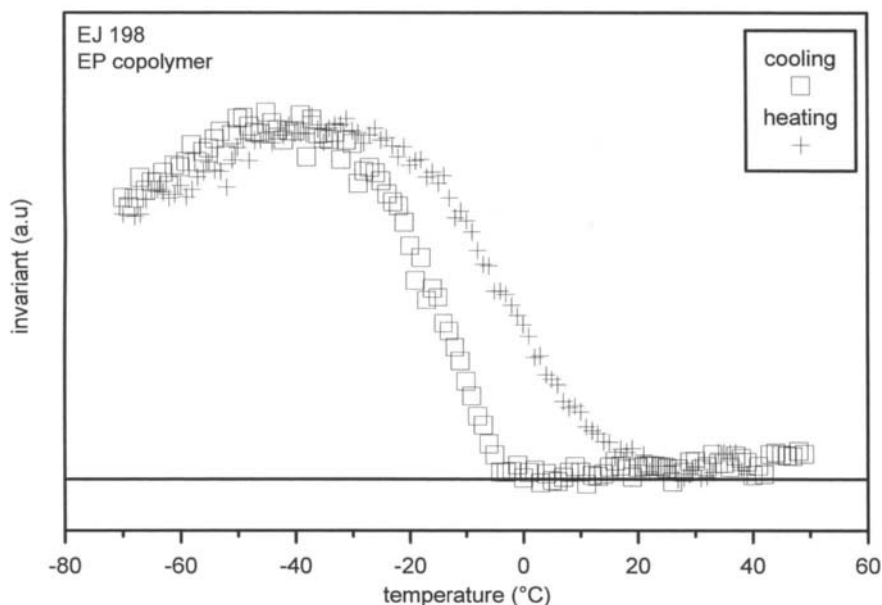


Fig. 11. SAXS invariant curves for cooling and subsequent heating at $20^{\circ}\text{C}/\text{min}$ in between approx. -70°C and approx. 50°C for the homogeneous ethylene-propylene copolymer EP 198.

generating a correlation maximum.

An extreme example of the pattern described here is EP 198. In Fig. 6 the DSC and crystallinity curves for this copolymer are given. The c_p measurements are reported in [12]. WAXD measurements show no reflection whatsoever. Again, crystallization and melting can be measured with the aid of SAXS invariant curves, see Fig. 11, and again the results are in agreement with the DSC results as far as the onset of crystallization and the end of melting are concerned. And once again there is a weak correlation maximum in the $I(q, T)$ curves.

3. ETHYLENE-1-BUTENE COPOLYMERS

3.1. Influence of comonomer content

Fig. 12 gives an overview of DSC curves [45] representing the crystallization and melting of ethylene-1-butene copolymers EB 1, 2, 3 and 5, whose butene content is 4.0, 6.4, 10.7 and 12.0 (mol)%, respectively. The density of the compression-molded specimen plates was 910, 901, 884 and 878 kg/m^3 , respectively. The corresponding crystallinity curves can be found in reference [12]. Compared with the ethylene-propylene copolymers, the EBs have considerably lower T_c and T_m values [80]. Although this may be due in part to a

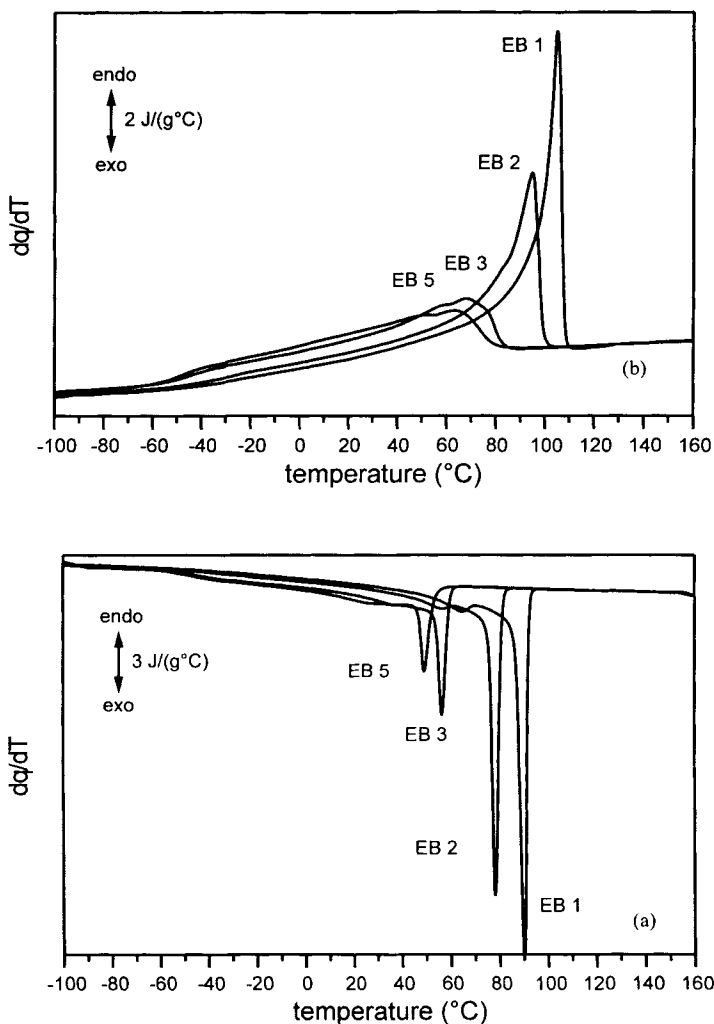


Fig. 12. DSC-2920 pseudo- c_p cooling (a) and subsequent heating (b) curves at $10^{\circ}\text{C}/\text{min}$ in between -110 and 170°C for homogeneous ethylene-1-butene copolymers with varying butene content ((mol)%): 4.0 (EB 1); 6.4 (EB 2); 10.7 (EB 3); 12.0 (EB 5). The curves were fixed at the same value at 120°C (a) and 130°C (b).

difference in ethylene sequence length distribution resulting from a difference in polymerization conditions (catalyst, reaction conditions, *etc.*) there is a more general reason, namely that butene is less likely to be included in the crystal lattice than propylene. Upon cooling we again see small crystallization peaks, which are most pronounced in the case of EB 1 and EB 2.

3.2. Metastability: influence of cooling rate

The metastability of crystallization and melting [81,44] of EBs is illustrated in Fig. 13 with the help of EB 2. Even the limited variation in cooling rate, from 0.5 to 25°C/min, has a major influence on the temperature corresponding to the peak in the DSC cooling curve (which we shall here call the crystallization temperature). The temperature corresponding to the DSC heating curve (which we shall here call the melting temperature) is independent of the cooling rate, which points to a considerable degree of reorganization during heating. Although this phenomenon is known to occur in linear polyethylenes [8], it is remarkable that it should occur in copolymers as well. Remarkable, because an important mechanism in reorganization is sliding diffusion of chain (parts) [82,83], which is facilitated when the mobility of the chain is enhanced *e.g.* at a sufficiently high temperature (*e.g.* when a sample is cooled or heated during a DSC or X-ray measurement), during which process the chain segments in the crystallites are able to assume a more optimum conformation. When the comonomer content increases, we may assume that sliding diffusion is increasingly hindered by the side chains. Apparently, sliding diffusion is still possible in EB 2, perhaps because the long ethylene sequences are folded and therefore have room to rearrange themselves. Be this as it may, Fig. 13 shows that it is important to record the crystallization process as well and not just focus

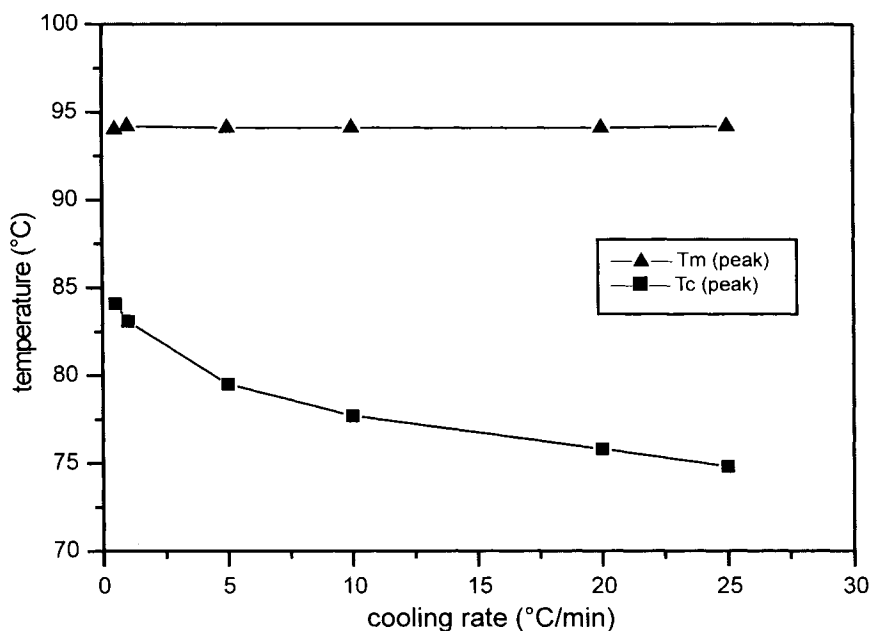


Fig. 13. DSC-2920 peak temperatures in cooling (T_c) at various rates and subsequent heating (T_m) at 10°C/min for EB 2 (6.4 (mol)% butene).

on the melting process. Many researchers assume that the melting process is to a much lesser degree kinetically determined and that it therefore lends itself to a theoretical (thermodynamic) interpretation. However, this is a wrong assumption, which is based on the constancy of the melting temperature. The fact that the melting temperature is constant only shows that a heating rate of $10^{\circ}\text{C}/\text{min}$ is by no means sufficient to avoid reorganization.

So it is wrong to assume that the melting process is to a much lesser degree kinetically determined: Fig. 13 shows that even for the copolymer discussed here crystallization and melting are to a large extent kinetically determined. This is in line with previously reported research [8,38,44] on the crystallization and melting behavior of linear polyethylenes. It is very well known that in LPEs the melting temperature increases with increasing molar mass; after an initial strong increase, T_m approaches an asymptotic value. The above-mentioned research showed that this asymptotic value - just as the constancy of T_m mentioned above - must be due to considerable reorganization during heating, and probably even during cooling. Of course, it is to be expected that this reorganization influences morphological parameters such as the lamellar dimensions, in particular the lamellar thickness. An approximate simulation showed that the lamellar thickness can increase during both cooling and heating, depending on the temperature at which nucleation starts, the cooling rate and the heating rate. This implies among other things that the relationship between the morphology at room temperature on the one hand and the temperature of crystallization and the temperature of melting on the other is much less straightforward than many researchers think. The same holds for the relationship between T_c and T_m . The latter conclusion has often been reported in the literature; the so-called Hoffman-Weeks plot [7,84] often shows an unexpected pattern of T_m versus T_c due to reorganization during cooling and heating. Likewise, Gibbs-Thomson plots [85] should be interpreted with great caution [95,86]. All this goes to show that real-time morphological analysis is very important. Therefore, the development of real-time X-ray measuring techniques using synchrotron facilities is a major leap forward. When combined with DSC [87], these measuring techniques provide a lot more insight into the kinetics of crystallization and melting and the reorganization processes associated with these [86]. In the (near?) future we may expect scanning probe microscopy in combination with techniques such as thermal analysis, spectroscopy, NMR, pyrolysis-GC-MS, *etc.*, to provide detailed, spatial-resolved information about physical processes of specific chemical structures - and this as a function of temperature and time.

3.3. Morphology

The TEM micrographs, Fig. 14, of EB 1, EB 2 and EB 5 show that these copolymers have a lamellar base morphology [12]. The thickness of the lamellae

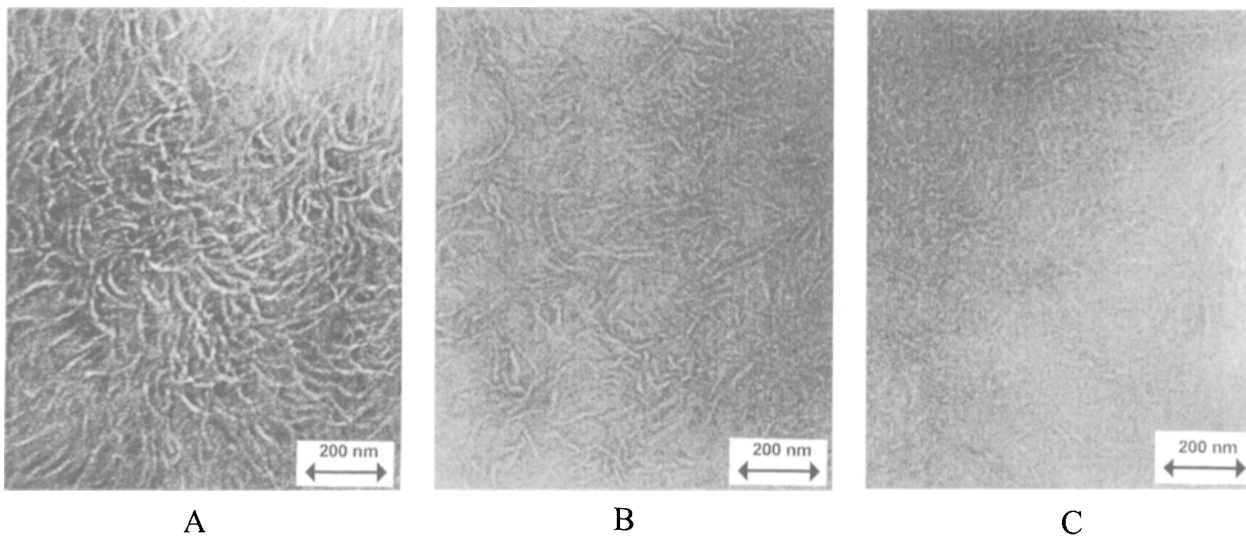


Fig. 14. TEM micrographs of three homogeneous ethylene-1-butene copolymers after staining at room temperature. Lamellar base morphologies for EB 1 (A), EB 2 (B) and EB 5 (C).

decreases with increasing butene content: from about 8.4 via 7.4 to 5.7 nm. The lateral dimensions seem to decrease as well. Only EB 1 and EB 2 show spherulitic superstructures with diameters of 15 to 20 μm . In copolymers the spherulitic superstructures generally disappear as the comonomer content increases. Of course, the transition from a lamellar structure to a granular structure is related to this.

3.3.1. Metastability: measurements as in temperature modulated calorimetry

Recently [45], melting experiments have been performed that are interesting for several reasons. SAXS measurements were performed during a scan-iso temperature-time program as customarily applied in some types of temperature modulated DSC (TMDSC) experiments. Other modulations used in TMDSC experiments include sinus, scan-scan, *etc.* Temperature modulated calorimetry (TMC) [88,89,90], as it is generally called, is increasingly being used for the study of crystallization, melting and reorganization processes [91,92]. It is hoped that TMC will be able to probe the differences in time scale of these processes and will thus give information about individual processes.

It is crucial to obtain morphological information as well, and to obtain it using the same thermal history [93]. Measurements on EB 2 show that the invariant from SAXS is heavily influenced by the time-temperature program and also reflects a superposition. On the one hand, the *maximum* in the curve is caused by a combination of two effects associated with an increase in temperature, see equation (10): a *decrease* in the product of $v^c(T)$ and $[1 - v^c(T)]$ (lowering of the crystallinity by melting at absolute values for the crystallinity of below 50%, see [12] for a crystallinity curve for EB 2) and an *increase* in $[d_c(T) - d_a(T)]^2$ (as caused by the temperature dependencies of the densities of the amorphous and crystalline phases). This is analogous to the behavior shown in Fig. 9. However, on the other hand, on top of this melting process fast reorganization takes place [86], as was also concluded from the measurements shown in Fig. 13. Possibly, also reversible crystallization (without nucleation) and melting occur, as reported in the literature [91,92,93].

The time-temperature program too heavily influences the long period and the thickness of the amorphous layer. The increase in the long period appears to be fully attributable to the increase in the amorphous layer thickness: the lamellar thickness is nearly constant.

An important implication, which follows from the discussion above, is that in EB 2 a considerable degree of reorganization occurs during static (isothermal) measurements within a few minutes. Therefore, in this temperature range static WAXD and SAXS measurements are meaningless and even in dynamic measurements a considerable degree of reorganization is to be expected. This is also consistent with the fact that in c_p measurements with DSC the 'continuous

measuring method' has to be used rather than the classical 'stepwise method', because the isotherms in this temperature range are not reliable.

4. ETHYLENE-1-OCTENE COPOLYMERS

4.1. Influence of comonomer content for copolymers with densities above about 870 kg/m^3

On the analogy of Figs. 1 and 12 we shall now first give an overview of the first series of ethylene-1-octene copolymers to be discussed, see Fig. 15. The

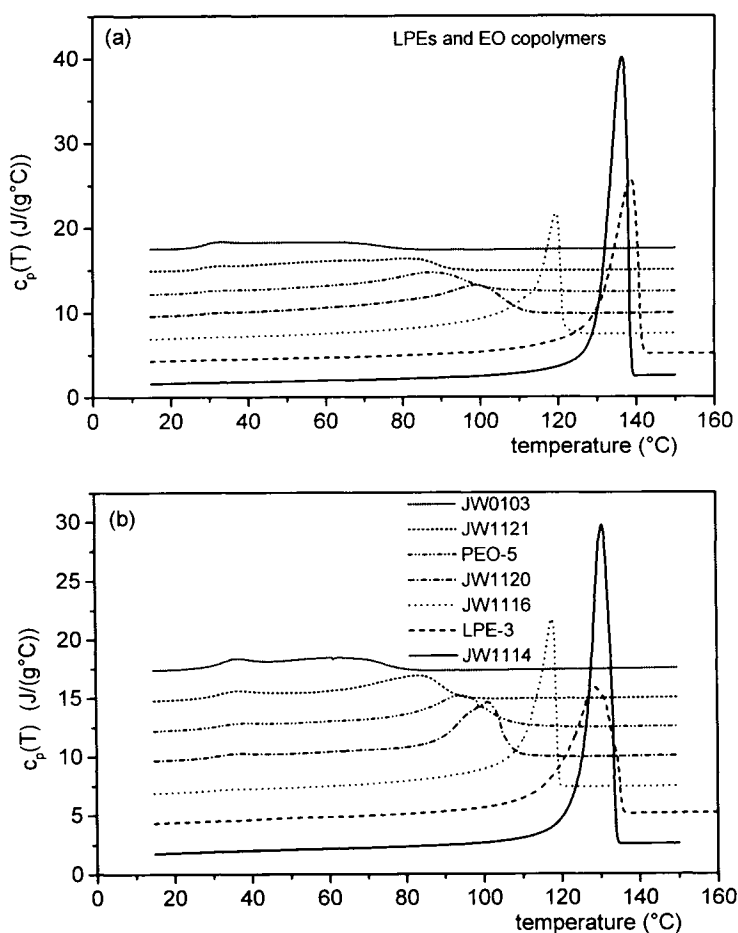


Fig. 15. DSC-7 heat capacity curves for two LPEs (JW1114 and LPE-3) and some homogeneous ethylene-1-octene copolymers obtained in heating at $5^\circ\text{C}/\text{min}$ after cooling at $0.1^\circ\text{C}/\text{min}$ (a) and after quenching in liquid nitrogen (b). The curves have been shifted upwards by steps of $2.5 \text{ J}/(\text{g}^\circ\text{C})$ with respect to JW1114.

results shown here were obtained in c_p measurements on the copolymers JW1116, JW1120, PEO-5, JW1121 and JW0103 [94, 95]. Their octene contents (in (mol)%), and weight-average molar masses (in kg/mol according to SEC) are: 2.1 and 47 (JW1116); 5.2 and 31 (JW1120); 5.5 and 345 (PEO-5); 8.0 and 34 (JW1121); 11.8 and 46 (JW0103), plus two LPEs, JW1114 ($M_w = 52$ kg/mol) and LPE-3 ($M_w = 119.6$ kg/mol, this sample is NBS SRM 1484). Their densities

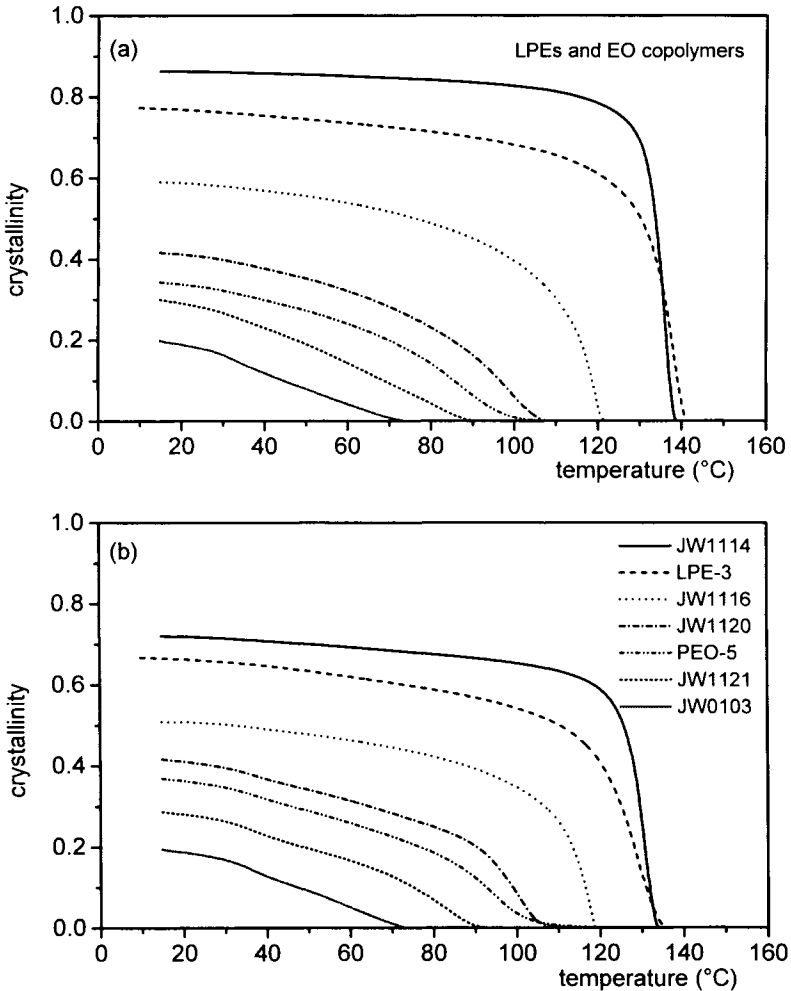


Fig. 16. Enthalpy-based mass crystallinity curves for two LPEs (JW1114 and LPE-3) and some homogeneous ethylene-1-octene copolymers based on the DSC heat capacity measurements, see Fig. 15, in heating at 5°C/min after cooling at 0.1°C/min (a) and after quenching in liquid nitrogen (b).

after compression molding are above 870 kg/m^3 . Since the curves shown are heating curves obtained at scan rates of $5^\circ\text{C}/\text{min}$, after quenching and slowly cooling at $0.1^\circ\text{C}/\text{min}$, we may expect that as far as the melting temperatures are concerned part of the thermal history has been erased due to reorganization. A remarkable feature of the copolymers is that in the heating curves after quenching the peak on the high-temperature side is more pronounced and narrower. Due to extensive cocrystallization during quenching, fast melting and recrystallization during subsequent heating occur, while superposition of the related endothermic and exothermic signals result in an overall shift of the endotherm to slightly higher temperatures [86,86,95], although the final melting temperature does not change much. An important effect of variations in the cooling rate is that the crystallinities of the LPEs and the least copolymerized samples change considerably, see Fig. 16. In LPE the crystallinity at room temperature after quenching is about 10-15% (absolute) lower than after slow cooling. In the copolymer JW1116 the difference is about 5%, while in copolymers with higher octene contents there is no longer any difference.

These results show that in view of the possible occurrence of reorganization processes it is necessary to systematically study the influence of the cooling and heating rate on both crystallization and melting. Although such studies are very time-consuming, they are very useful because they greatly improve the quality of the interpretation. In day-to-day industrial practice often only heating curves are recorded at a standard heating rate after cooling at (usually) the same rate. Since reorganization is a combination of the influences of the molecular structure and of the thermal history (which may or may not have been imposed by the analyst), the degree of reorganization will in principle be different for samples that are molecularly different. If analysts ignore this, their databases will to a large extent be contaminated with results that give more information about reorganization during melting than about the melting of crystalline structures in direct relation to the thermal history. This does not mean that no useful correlations can be obtained after a standard treatment, but it does mean that the significance of the results can be greatly improved. Moreover, given the possibilities currently offered by robotization and software for imposing various combinations of cooling and heating rates, attention needs to be paid to ways of improving the quality of the results rather than increasing the quantity or production capacity. In other words, the analyst increasingly has to choose between contenting himself with correlations or striving to establish relations.

The c_p measurements shown in Fig. 15 were carried out from 10°C . For the copolymers with the highest octene contents this means that at this temperature the crystallinity is not maximum; it would be maximum at lower temperatures. Thus, ongoing crystallization partly explains why around room temperature one can still observe an influence of the storage at room

temperature, see the step in the DSC curves. This phenomenon is also partly due to annealing during storage of the crystalline structures formed during cooling. The latter cause plays a role in isothermal stays at any temperature [95]. This is readily observable if the sample is subsequently cooled over a small temperature range and then heated. The heat capacity derived from the heating curve will then be smaller below the annealing temperature and higher above the annealing temperature; around the annealing temperature the $c_p(T)$ curve assumes the shape of a rotated S , while the heating curve without annealing has the usual shape (no S).

4.2. Copolymers having a density of about 870 kg/m³

The reason why we should pay special attention to ethylene-1-octene copolymers with a density after compression molding at room temperature of about 870 kg/m³ is that for copolymers with lower densities, see below, WAXD shows only vague crystal reflections or no reflections at all at temperatures up to the glass transition. The fairly arbitrary point where the reflections disappear corresponds to a room-temperature DSC mass crystallinity (within the two-phase model) of about 15% and an octene content of about 13 (mol)%. These figures of course depend on the microstructure (for more blocky copolymers they will be different) and are only indicative.

4.2.1. Micro chain structure

Since the ethylene sequence length distribution of the copolymers discussed here plays such a crucial role in crystallization, we shall show some aspects of the microstructure with reference to EO J, which copolymer also has been referred to as EO V(anadium) [11,12]. With the aid of ¹³C-NMR measurements and a model specifically developed for this purpose [96], which takes into account the possibility of inversion of octene in the chain (depending on the catalyst system 'normal' and 'inverted' octene will occur [96,97,98], also when metallocene catalysts are used), the copolymer statistics of ethylene and octene addition was determined. This statistics is characterized by the probabilities of addition of the monomers, or alternatively, by the reactivity values. By fitting the ¹³C-NMR spectrum of EO V with the model we concluded that the octene content was 12.7 (mol)%, the inversion percentage 19.2% and the product of the copolymer reactivity values 0.41. This value of r_{er_o} corresponds to polymerization statistics, intermediate between alternating and random. We shall here give a 'copolymer presentation' in which only ethylenes and octenes are pictured (so no distinction is made between normal and inverted octene), see Fig. 17 [12]. A characteristic part of the chain has been simulated via a Monte Carlo procedure. The ethylene sequences are clearly distinguishable and it is clear that they are formed as a result of interruptions due to the incorporation of octene into the chain. Most of the octenes occur in isolation. Obviously, since the

EO-copolymer		EO V-based			
Monomer	Symbol	mole(%)	r ($r_e r_o = .41$)	P	s_n
ethylene	□	87.3	24.661	.863	7.3
octene	■		.017	.061	1.1

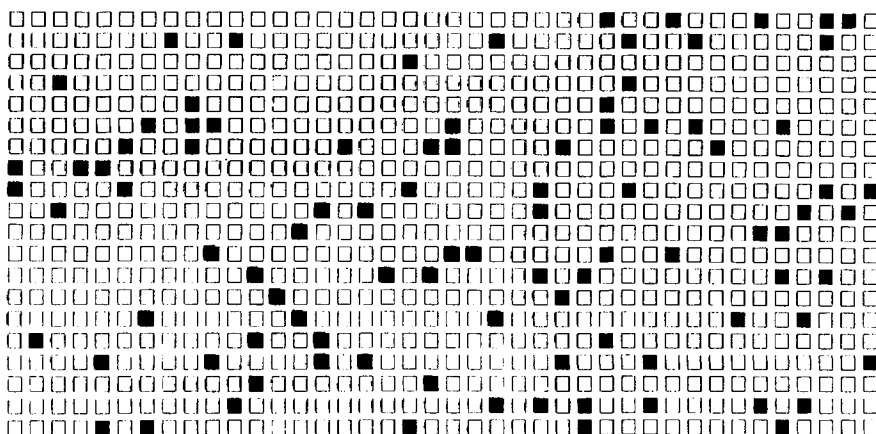


Fig. 17. Simulation (via the 'common r set' for a series of copolymers) of the chain structure of the vanadium based homogeneous ethylene-1-octene copolymer with $X_e = 88.5\%$. The chain is constructed by linking the end of each line to the beginning of the next line. Copolymer presentation of the succession of ethylene and 1-octene units. $P_{ee} = 0.863$ and $P_{oo} = 0.061$ are chain propagation probabilities; s_n is the number-average sequence length.

octenes cannot be incorporated into the crystal lattice, they will greatly hinder the crystallization process. Of course, the statistics is not correct because the part of the chain shown is much too small. A simulation of tens of thousands of units would be necessary to make sure that the associated statistics is close to the analytically calculated one (based on the calculated propagation probabilities or reactivity values). The result of such an analytical calculation is shown in Fig. 18. It includes the ethylene and propylene sequence length distributions. The largest sequence contains about 50 ethylene units, the number-average ethylene sequence length is 7.3.

4.2.2. Crystallization and melting

At this point it is illustrative to look at the differences between the ethylene-propylene copolymer EP 207 and the ethylene-1-octene copolymer EO V discussed here. The ethylene contents do not differ much; they amount to 89.4 and 88.5, respectively and do not explain the extremely large differences between the compression-molded densities at room temperature (896 and 872

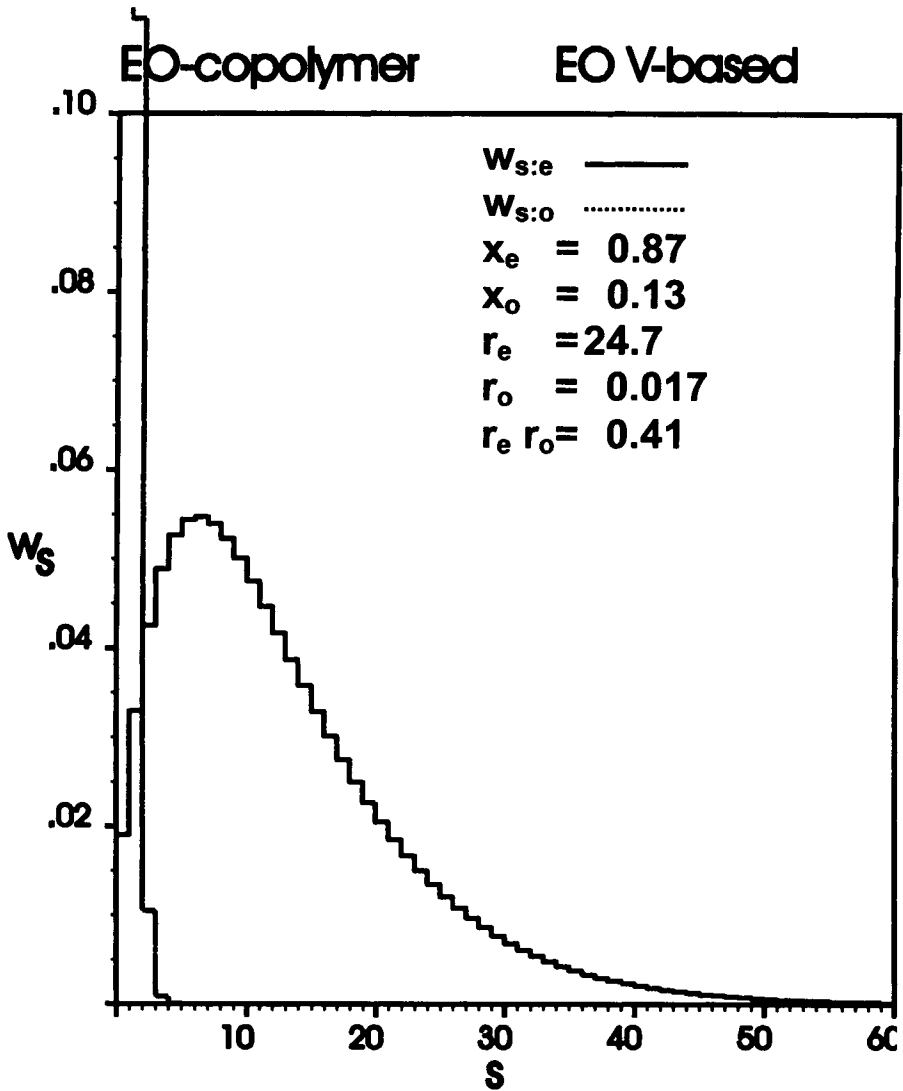


Fig. 18. Ethylene, $w_{s:e}$, and 1-octene, $w_{s:o}$, sequence length distributions for the vanadium-based homogeneous ethylene-1-octene copolymer.

kg/m³, respectively); between the crystallization peak temperatures (slightly below 70°C and around 40°C, respectively); between the melting peak temperatures (just above 80°C and around 60°C, respectively), and between the maximum crystallinities (about 32% and about 24%, respectively). As discussed earlier, the differences are directly related to differences in crystallization behavior: partial inclusion of propylene in the crystal lattice and virtually

complete exclusion of octene from the crystal lattice. Butene copolymers are intermediate in this respect; see for example the values measured for EB 5.

Another interesting comparison is that between homogeneous copolymers polymerized with different catalysts. In recent years, metallocene catalysts in particular have enjoyed a great interest [9,10,11,12,75,99,100,101,102,103,104,105]. They offer advantages with respect to the control of the polymerization process in that they make it possible to control molar mass and comonomer addition independently of each other. In metallocene-catalyzed copolymers, too, (co)monomer addition is a statistical process and the same considerations apply as in the previous section. This also holds for the crystallization and melting behavior.

We shall illustrate this with reference to EO V(anadium) and a metallocene-catalyzed copolymer, EO M(etallocene) [11]. EO V and EO M have (NMR) octene contents of 11.5 and 12.5%, respectively and compression molded densities at room temperature of 872 and 870 kg/m³, respectively. Since the octene contents are not exactly the same, we may expect differences in the parameters that characterize the crystallization and melting behavior: T_c , T_m , crystallinity, *etc.* What we want to know here is whether there are substantial differences in 'overall' behavior as expressed in the DSC cooling and heating curves.

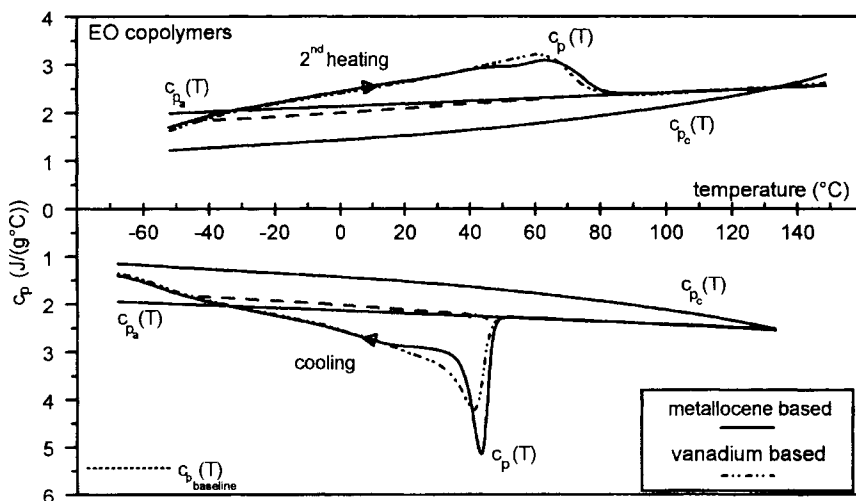


Fig. 19. DSC-7 continuous specific heat capacity curves, $c_p(T)$, at 20°C/min; the reference curves, $c_{pa}(T)$ and $c_{pc}(T)$, and the baseline curves, $c_{pb}(T)$ (---), for two homogeneous ethylene-1-octene copolymers produced with the aid of different catalyst systems. Cooling curves (downwards) and subsequent heating curves (upwards).

Fig. 19 shows that these specific copolymers display much the same behavior: the same wide temperature range of crystallization and melting; vitrification in the same range and also the same heat effects. There are only

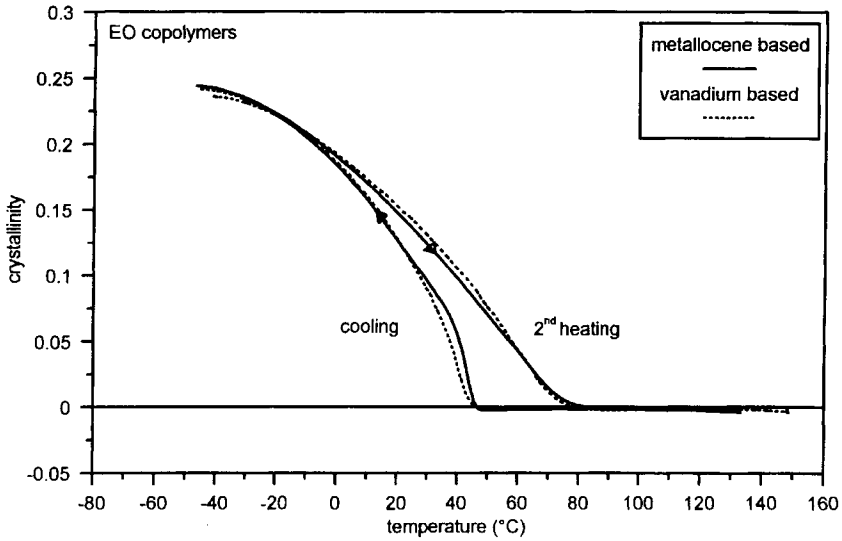


Fig. 20. Enthalpy-based mass crystallinity curves for cooling and heating as obtained from Fig. 19.

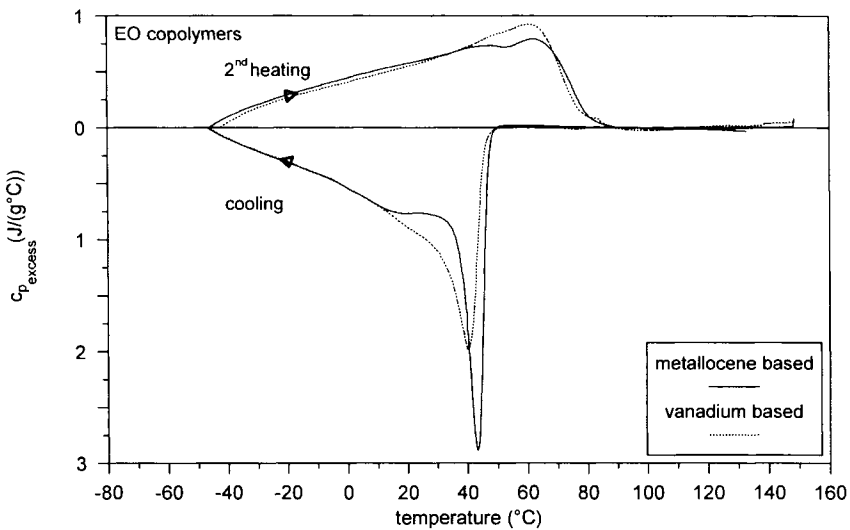


Fig. 21. Specific excess-heat capacity curves for cooling and subsequent heating at 20°C/min for two EO copolymers produced with the aid of different catalyst systems.

differences in crystallization, but these are probably attributable to a difference in nucleation (density) because they are hardly reflected in the melting curve due to reorganization. The crystallinity curves confirm the similarity in crystallization and melting behavior, see Fig. 20. The resulting excess heat capacity curves provide a detailed insight into the above-mentioned similarities and subtle differences, see Fig. 21.

All this implies that the crystallite dimension distributions and hence the ethylene sequence distributions of the two copolymers cannot be very different. Since their octene contents do differ, this could mean that the sets of reactivity values are slightly different, resulting in similar chain statistics. However, this conclusion cannot be verified because the octene contents, too, are subject to measurement errors. In this respect it is of importance that for EO V, as mentioned before, see Fig. 17, fitting of the ^{13}C -NMR spectrum with the model used yielded an octene content of 12.7 (mol)% which is in line with the octene contents of 12.5 and 13.6 (mol)% for EO M, as found via NMR and IR, respectively. A difference of 1 (mol)% would cause a difference of about 4°C in T_c and T_m (peak temperatures) measured via DSC. This indicates that accurate determination of the comonomer content is very important. Since it is difficult to improve the accuracy of the measurements, a better approach would be to establish relationships between the comonomer content and T_c , T_m and the crystallinity, compare these and then draw conclusions. In doing this we assume, of course, that the NMR spectra allow a comparable interpretation. There is clearly a need for a study in which metallocene-catalyzed and vanadium-catalyzed ethylene-1-octene copolymers are compared. On the basis of the results reported here, we assume for the time being that the two samples compared here do not differ substantially, although this is of course not a general conclusion.

4.2.3. Morphology

The TEM micrographs in Fig. 22 show that the copolymers have a granular base morphology with additional lamellar structures [12]. It should be noted, though, that in transition situations it is difficult to indicate what is the 'base morphology'. The granular dimensions are about 4 - 10 nm. In addition, thin, short and irregularly shaped lamellae with a thickness of about 6 nm are visible. The extended length of the longest ethylene sequences with about 30-40 units, see Fig. 18, varies from about 7.5 to 10 nm, which means the sequences may be included in the crystallites in extended form at an angle. We may also assume there is no perfect matching of ethylene sequences according to length, because a perfect fractionation of ethylene sequences is unlikely at the crystallization temperatures of these copolymers (which are below 50°C for both EO V and EO M).

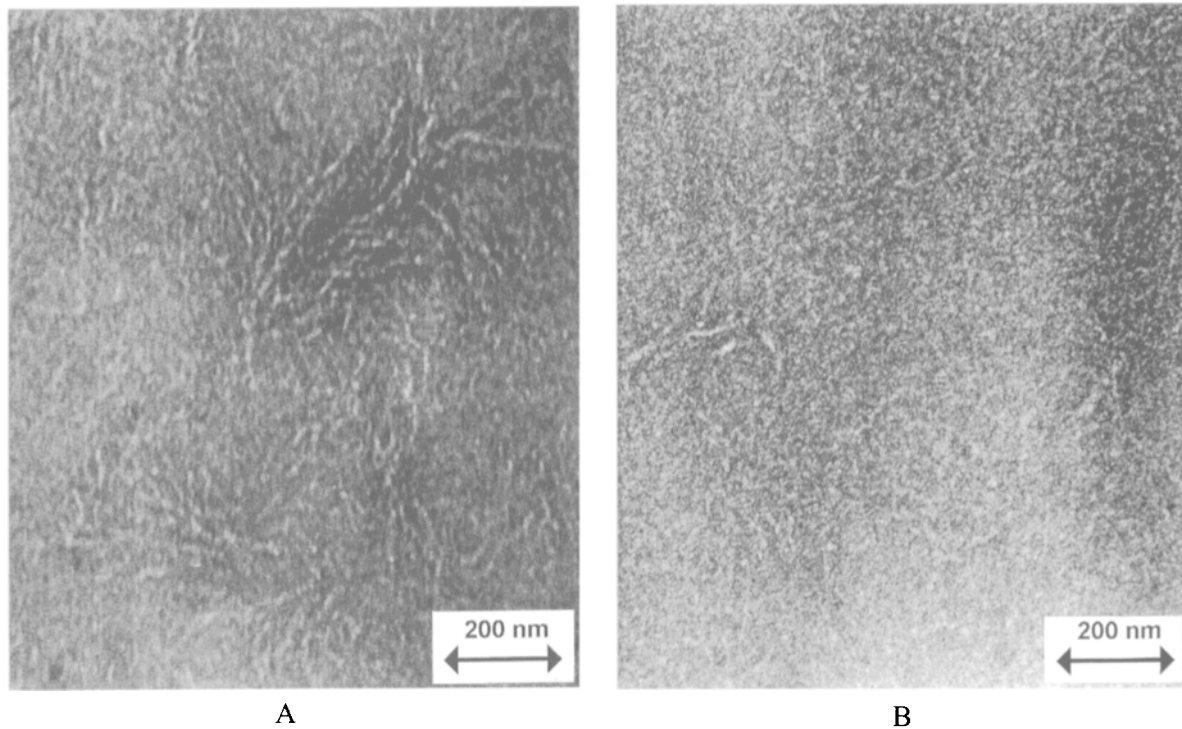


Fig. 22. TEM micrographs of two homogeneous ethylene -1-octene copolymers after staining with chlorosulphonic acid at room temperature. Granular base morphology and additional lamellar structures (A) the metallocene-based EO copolymer (B) the vanadium-based EO copolymer.

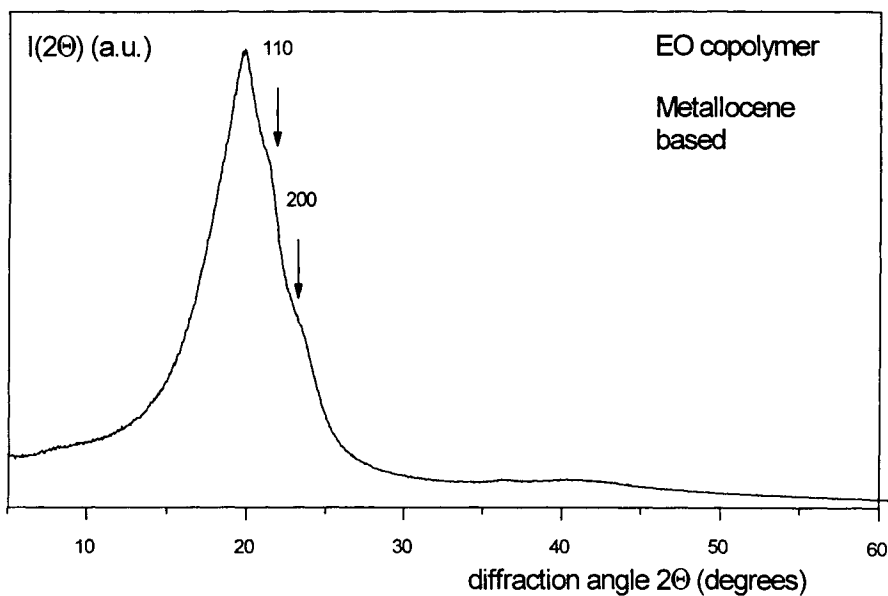


Fig. 23. WAXD curve for the metallocene-based homogeneous ethylene-1-octene copolymer after cooling from 150°C to room temperature at 20°C/min.

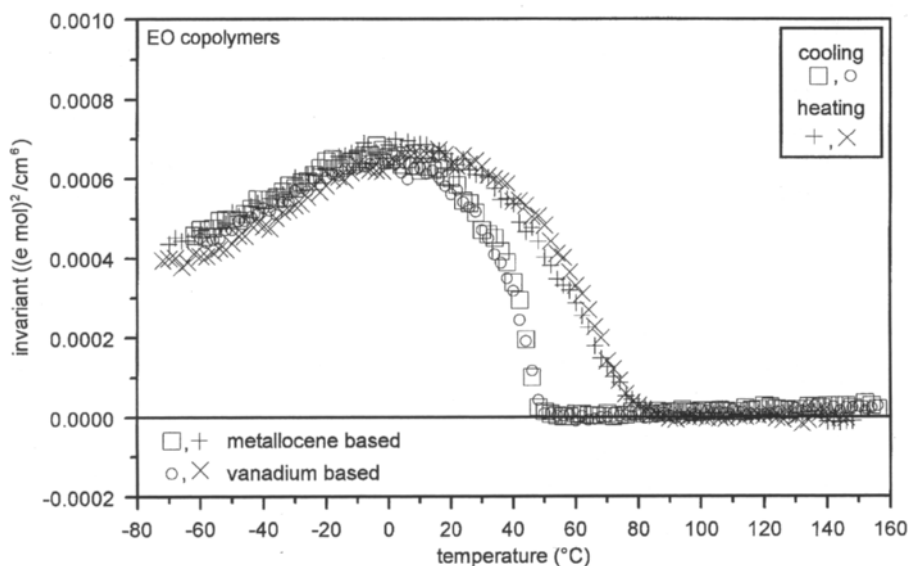


Fig. 24. SAXS invariant curves for cooling and subsequent heating at 20°C/min for two homogeneous ethylene-1-octene copolymers, produced with the aid of different catalyst systems.

It will be clear that a morphology like the one shown in Fig. 22 will produce hardly any constructive interference in WAXD. As a consequence, a WAXD picture taken at room temperature will show only vague orthorhombic 110 and 200 reflections, see Fig. 23, even though at this temperature the most perfectly formed crystallites -- including lamellae -- are already present. This does not change much when the measuring temperature is lowered, so the conclusion must be that granular structures, possible fringed micelles structures and in particular 'clusters of crystallized ethylenes' [79] do contribute to a less extent to these reflections. The WAXD peak is not entirely void of information, though; see for example the well-defined maximum [91,106].

SAXS, on the other hand, yields readily measurable invariants, as in the case of ethylene-propylene copolymers, see Fig. 24. Again, the results are in good agreement with the DSC results as far as the onset of crystallization and the end of melting are concerned.

4.3. Characteristic copolymers with densities below about 870 kg/m³

Fig. 25 shows DSC curves and the corresponding crystallinity curves (obtained via the extrapolation method) for several characteristic ethylene-1-octene copolymers from a second series [45], this time with octene contents ranging from 14.2 to 44 (mol)% and compression molded densities below 870 kg/m³. The copolymers were produced using the same single site catalyst as used for the first series, see Figs. 16 and 17. The results shown in Fig. 25 illustrate once again that it is important to extend the temperature range of the measurement to include the glass transition, because in a cooling run crystallization continues until vitrification renders further crystallization impossible and because in a heating run melting already starts during devitrification. In EO I (14.2 (mol)% octene) the crystallinity at the glass transition temperature is about three times as high as the value at room temperature, whereas in EO H (20.8 (mol)% octene) crystallization does not start until 10°C and only in the heating run some crystallinity is present at room temperature due to hysteresis. Finally, EO A (44.0 (mol)% octene) shows no crystallization at all, just vitrification in cooling and devitrification with enthalpy recovery in heating. The copolymers with the highest octene contents show no crystalline reflections whatsoever in WAXD.

Fig. 26 shows the SAXS invariant curves for this series of copolymers as measured at DESY, HASYLAB (Hamburg, Germany). As far as their shape is concerned, the curves for EO V (= EO J) are in good agreement with those in Fig. 24, which were measured at SRS, SERC Daresbury Laboratory (Warrington, UK). The scale in Fig. 26 is relative (but comparable, see scale factors) whereas in Fig. 24 it is absolute. A remarkable finding is that even EO A gives invariant curves for cooling and heating which point to crystallization and melting, whereas the DSC curves (see Fig. 25) show nothing of the kind.

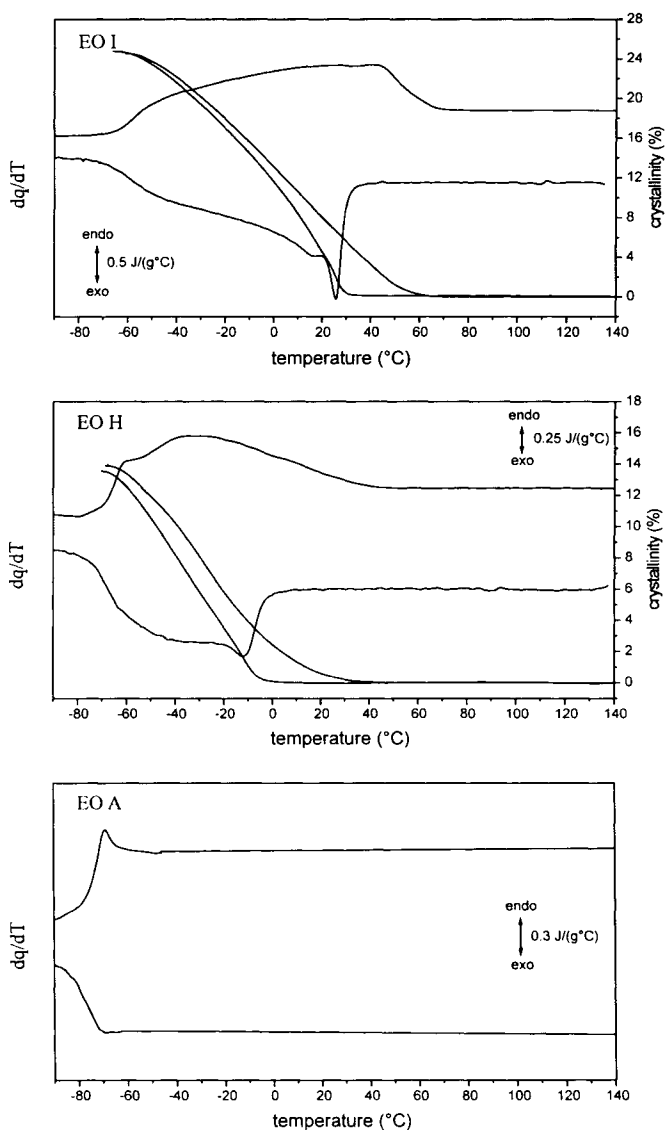


Fig. 25. DSC-2920 pseudo- c_p cooling (downwards) and subsequent heating (upwards) curves at 10 $^{\circ}\text{C}/\text{min}$ in between -100 and 150 $^{\circ}\text{C}$ for homogeneous ethylene-1-octene copolymers with varying octene content ((mol)%). (a): EO I (14.2%); (b): EO H (20.8%); (c): EO A (44.0%). The curves are located vertically arbitrarily. Also shown the crystallinity curves for cooling and subsequent heating, as based on the pseudo- c_p measurements, according to the 'extrapolation method'.

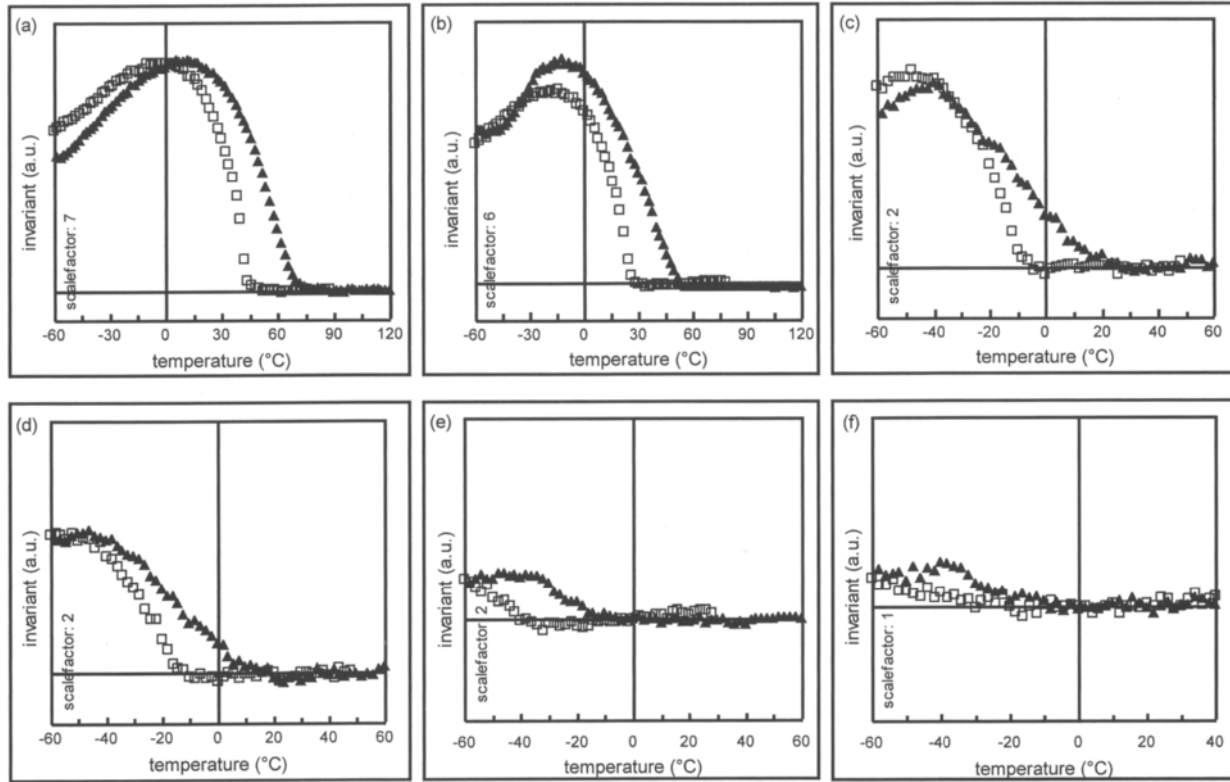


Fig. 26. SAXS invariant curves for cooling at 5°C/min (\square) and subsequent heating at 10°C/min (\blacktriangle) for homogeneous ethylene-1-octene copolymers with varying octene content (mole%). (a): EO J = EO V (11.5%); (b): EO I (14.2%); (c): EO H (20.8%); (d): EO D (24.0%); (e): EO C (31.1%); (f): EO A (44%). Invariants have indicated (arbitrary) scales.

5. OVERVIEW

Finally, we shall make some comments, which relate to all of the copolymers discussed here. The first concerns the split between copolymers with compression-molded densities higher than 870 kg/m^3 and those with densities below this value. It should be stressed that we only wish to indicate that below this density it is increasingly difficult to determine crystalline reflections with the aid of WAXD for the ethylene-1-octene copolymers reported here and that 870 kg/m^3 is an interesting density to consider. The fact that there are hardly any WAXD reflections indicates that the crystallites have become too small and/or too imperfect to produce significant constructive interference in WAXD. However, DSC and SAXS measurements have shown that also below this density (which for the present copolymers roughly corresponds to a DSC mass crystallinity of 15% and an octene content of 13 (mol)%) crystallization and melting still occur. In the DSC and SAXS results no discontinuity is observable as the comonomer content increases.

The techniques discussed here show that, as we move from LPE to a copolymer which is no longer crystallizable by increasing the comonomer content, the morphology gradually changes as follows: from lamellar crystallites that are organized into superstructures such as axialites or spherulites in the case of LPE; via isolated lamellae that decrease in number, whose average longitudinal dimension (thickness) and lateral dimension decrease and which are no longer organized into superstructures; to granular structures that can barely be made visible even with the aid of TEM. When the crystallization process is 'frustrated' even more, 'fringed-micelle crystallites' and 'clusters of loosely packed crystallized ethylene sequences' might ultimately be formed. In the limit of crystallization at the glass transition, crystallization might be limited even further to pure 'nearest neighbor crystallization' as in the 'cold crystallization' model [107]. However, these structures are generally speculations, certainly in the case of ethylene copolymers, and have never been directly observed. This is not surprising, given the problems encountered in TEM studies of these copolymers. In this respect, it is to be expected that Scanning Probe Microscopy techniques, like temperature-dependent AFM imaging, will become of help.

Clearly, compared with extremely heterogeneous copolymers such as LLDPE and VLDPE, homogeneous copolymers like the ones discussed here are much simpler in terms of structure, crystallization and melting behaviour and morphology. This is because during the polymerization of homogeneous copolymers there is only one reactive site, resulting in a statistical distribution of the ethylene and comonomer units over the chains. The corresponding ethylene and comonomer sequence length distributions are single-peaked. The statistical distribution applies to all chains, and in this sense the homogeneous copolymers are intra- and intermolecularly homogeneous. Since the process involved is a

statistical one, there may be statistical differences between the chains (in particular in the case of short chains and/or chains containing only small quantities of comonomer). However, these differences are one order of magnitude smaller than those occurring in LLDPE and VLDPE chains and cannot be confused with these, at least not with the current types; in the next few years hybrid types are expected to be developed [108].

Even in homogeneous copolymers several morphological entities can exist in one and the same sample, which is because a copolymer always contains a whole range of ethylene sequence lengths on account of the chain growth statistics. So, at certain comonomer contents, ethylene sequences can be so long that they can still form lamellae while there are also smaller ones which can only form granular structures. As a result, in homogeneous copolymers several morphologies can be present. In extremely heterogeneous copolymers like VLDPE, nearly all possible morphologies are present.

ACKNOWLEDGEMENTS

The authors would like to thank J. van den Bosch, G. Evens, the late R. Graff, J. Pijpers, J. van Ruiten, P. Verweij and J. van Welzen for providing the copolymers. S. Coolen, B. Goderis, M. Pijpers, R. Scherrenberg and M. Walet are thanked for the DSC, TEM and X-ray measurements they performed and for discussions. Special thanks are due to S. Vanden Eynde, who provided recent DSC and X-ray results obtained as part of her Ph.D. work at the Katholieke Universiteit Leuven (Belgium).

REFERENCES

1. Proceedings of the 'Golden Jubilee Conference' Polyethylenes 1933-1983: Past, Present and Future, 8-10 June 1983, The Plastics and Rubber Institute, Chameleon Press Ltd, London (1983) 1.
2. L. Mandelkern, 'Crystallization of Polymers', McGraw-Hill, New York (1964).
3. B. Wunderlich, 'Macromolecular Physics, Vol. 1: Crystal Structure, Morphology, Defects', Academic Press, New York (1973).
4. B. Wunderlich, 'Macromolecular Physics, Vol. 2: Crystal Nucleation, Growth, Annealing', Academic Press, New York (1976).
5. B. Wunderlich, 'Macromolecular Physics, Vol. 3: Crystal Melting', Academic Press, New York (1980).
6. R.G. Alamo and L. Mandelkern, in 'Thermal Analysis and Calorimetry in Polymer Physics' (Ed. V.B.F. Mathot), Special issue *Thermochimica Acta*, 238 (1994) 155.
7. J.D. Hoffman and R.L. Miller, *Polymer*, 38(13) (1997) 3151.
8. Mathot, V.B.F. 'The Crystallization and Melting Region' in 'Calorimetry and Thermal Analysis of Polymers' (Ed. V.B.F. Mathot), Hanser Publishers, Munich Vienna New York (1994) Ch. 9, 231.
9. S. Hosoda, A. Uemura, Y. Shigematsu, I. Yamamoto and K. Kojima, *Stud. Surf. Sci. Catal.*, 89 (1994) 365.

10. Y-C. Hwang, S. Chum, R. Guerra and K. Sehanobish, Antec '94 SPE Conference Proceedings, Vol. III (1994) 3414.
11. V.B.F. Mathot, R.L. Scherrenberg, T.F.J. Pijpers and W. Bras, in 'Special issue in honour of Prof. Bernhard Wunderlich's 65th birthday', Journal of Thermal Analysis, (Ed. E.A. Turi) 46(3-4) (1996) 681.
12. V.B.F. Mathot, R.L. Scherrenberg, M.F.J. Pijpers and Y.M.T. Engelen, 'Structure, Crystallisation and Morphology of Homogeneous Ethylene-Propylene, Ethylene-1-Butene and Ethylene-1-Octene Copolymers with High Comonomer Contents' in 'Trends In Polyolefin Science and Technology' (Ed. S. Hosoda), Research Signpost, Trivandrum (India) (1997) 71.
13. P.J. Flory, J. Chem. Phys., 15(9) (1947) 684.
14. P. J. Flory, Trans. Faraday Soc., 51 (1955) 848.
15. P.J. Flory and L. J. Mandelkern, J. Polym. Sci., 21 (1956) 345.
16. K Casey, C.T. Elston and M.K. Phibbs, Polym. Letters, 2 (1964) 1053.
17. I.J. Bastien, R.W. Ford and H.D. Mak, Polym. Letters, 4 (1966) 147.
18. C.T. Elston, Can. Pat. No. 984 (1967) 213.
19. S.-D. Clas, K.E. McFaddin, K.E. Russell, M.V. Scammel-Bullock and I.R. Peat, J. Polym. Sci.: Part A: Polym. Chem., 25 (1987) 3105.
20. K.K. Dohrer, L.G. Hazlitt and N.F. Whiteman, J. Plast. Film Sheeting, 4(3) (1988) 214.
21. V. Mathot, in 'Polycon '84 LLDPE', The Plastics and Rubber Institute, London (1984) 1.
22. V.B.F. Mathot, H.M. Schoffeleers, A.M.G. Brands and M.F.J. Pijpers in 'Morphology of Polymers' (Ed. B. Sedláček), Walter de Gruyter & Co., Berlin - New York (1986) 363.
23. S. Hosoda, Polym. J., 20(5) (1988) 383.
24. P. Schouterden, G. Groeninckx, B. Van der Heyden and F. Jansen, Polymer, 28 (1987) 2099.
25. P. Schouterden, M. Vandermarliere, C. Riekel, M. Koch, G. Groeninckx and H. Reynaers, Macromolecules, 22 (1989) 237.
26. V.B.F. Mathot and M.F.J. Pijpers, J. Appl. Polym. Sci., 39(4) (1990) 979.
27. F. Defoor, G. Groeninckx, P. Schouterden and B. van der Heyden, Polymer, 33 (1992) 3878.
28. R.A.C. Deblieck and V.B.F. Mathot, J. Mater. Sci. Lett., 7 (1988) 1276.
29. F. Defoor, G. Groeninckx, P. Schouterden and B. van der Heyden, Polymer, 33 (1992) 5186.
30. F. Defoor, G. Groeninckx, H. Reynaers, P. Schouterden and B. van der Heyden, Macromolecules, 26 (1993) 2575.
31. V.B.F. Mathot, 'Crystallization and Melting of Linear, Branched and Copolymerized Polyethylenes as Revealed by Fractionation Methods and DSC' in 'New Advances in Polyolefins' (Ed. T.C. Chung), Plenum Press (1994) 121.
32. H.N.A.M. Steenbakkers-Menting, 'Chlorination of Ultrahigh Molecular Weight Polyethylene', Ph.D. Thesis, Technical University of Eindhoven, The Netherlands (1995).
33. B. Monrabal, 'Chemical composition distribution analysis in polyolefins. Introduction to crystallization analysis fractionation.CRYSTAF' in 'Trends In Polyolefin Science and Technology' (Ed. S. Hosoda), Research Signpost, Trivandrum (India) (1997) 119.
34. H. Phuong-Nguyen and G. Delmas, in 'Thermal Analysis and Calorimetry in Polymer Physics' (Ed. V.B.F. Mathot), Special issue Thermochemica Acta, 238 (1994) 257.
35. K. Murata and S. Kobayashi, Kobunshi Kagaku, 26 (1969) 536.
36. J.M. Barrales-Rienda and J.M.G. Fatou, Polymer, 13 (1972) 407.
37. J.-H. Hser and S.H. Carr, Polym. Eng. Sci., 19 (1979) 436.

38. V.B.F. Mathot and M.F.J. Pijpers, *Polymer Bulletin*, 11 (1984) 297.
39. J.H. Magill, in 'Polymer Handbook' 3rd ed. (Eds J. Brandrup and E.H. Immergut), Wiley, (1989) VI/279.
40. V. Mathot, T. Pijpers and W. Bunge, in 'Polym. Prepr. of the Am. Chem. Soc., Div. Polym. Chem., ACS Meeting Recent Advances in Polyolefin Polymers' 67, Fall Meeting, Washington (1992) 143.
41. R.G. Alamo, E.K.M. Chan, L. Mandelkern and I.G. Voigt-Martin, *Macromolecules*, 25(24) (1992) 6381.
42. R.G. Alamo, B.D. Viers and L. Mandelkern, *Macromolecules*, 26 (1993) 5740.
43. V.B.F. Mathot, in 'Crystallization of Polymers', (Ed. M. Dosière), NATO ASI-C Series Mathematical and Physical Sciences (1993) 102.
44. V.B.F. Mathot, R.L. Scherrenberg and T.F.J. Pijpers, *Polymer*, 39(19) (1998) 4541.
45. S. Vanden Eynde, V.B.F. Mathot, M.H.J. Koch and H. Reynaers, to be published in *Polymer*.
46. V. Mathot, M. Pijpers, J. Beulen, R. Graff and G. van der Velden, in 'Proceedings of the Second European Symposium on Thermal Analysis 1981 (ESTA-2)' (Ed. D. Dollimore), Heyden, London (1981) 264.
47. B.K. Hunter, K.E. Russell, M.V. Scammell and S.L. Thompson, *J. Polym. Sci.: Part A: Polym. Chem.*, 22 (1984) 1383.
48. J.E. Wagner, S. Abu-Iqyas, K. Monar and P.J. Phillips, *Antec '98 SPE Conference Proceedings*, 56th(Vol. 2) (1998) 1516.
49. P.J. Flory, *J. Amer. Chem. Soc.*, 84 (1962) 2857.
50. C.G. Vonk, in 'Integration of Fundamental Polymer Science and Technology', (Eds. L.A. Kleintjens and P.J. Lemstra), Elsevier Applied Science Publishers Ltd, Essex, England (1986) 471.
51. H.G. Kilian, in 'Thermal Analysis and Calorimetry in Polymer Physics' (Ed. V.B.F. Mathot), *Special issue Thermochimica Acta*, 238 (1994) 113.
52. P.J. Phillips, M-H. Kim and K. Monar, *Annu. Tech. Conf. - Soc. Plast. Eng.*, 53(2) (1995) 1481.
53. R.B. Richards, *J. Appl. Chem.*, 1 (1951) 370.
54. C.H. Baker and L. Mandelkern, *Polymer*, 7 (1966) 71.
55. C.G. Vonk, in *Proceedings of the 'Golden Jubilee Conference' Polyethylenes 1933-1983: Past, Present and Future*, 8-10 June 1983, The Plastics and Rubber Institute, Chameleon Press Ltd, London (1983) D2.1.
56. R. Alamo, R. Domszy and L. Mandelkern, *J. Phys. Chem.*, 88 (1984) 6587.
57. F.J. Baltá Calleja and C.G. Vonk, 'X-ray Scattering of Synthetic Polymers', *Polymer Science Library* 8, Elsevier, Amsterdam (1989).
58. C.G. Vonk and H. Reynaers, *Polym. Commun.*, 31 (1990) 190.
59. S. Hosoda, H. Nomura, Y. Gotoh and H. Kihara, *Polymer*, 31 (1990) 1999.
60. J. Martinez de Salazar and F.J. Baltá Calleja, *J. Cryst. Growth*, 48 (1979) 283.
61. C. France, P.J. Hendra, W.F. Maddams and H.A. Willis, *Polymer*, 28 (1987) 710.
62. J. Martinez de Salazar, M. Sánchez Cuesta and F.J. Baltá Calleja, *Colloid & Polymer Sci.*, 265 (1987) 239.
63. V.B.F. Mathot, 'Thermal Characterization of States of Matter' in 'Calorimetry and Thermal Analysis of Polymers', (Ed. V.B.F. Mathot), Hanser Publishers, Munich Vienna New York (1994) Ch. 5, 105.
64. V.B.F. Mathot and M.F.J. Pijpers, *J. Therm. Anal.*, 28 (1983) 349.
65. R. Domszy, in *Proceedings of 'Metallocenes 96'*, Düsseldorf (1996) 251.

- 66 M.F.J. Pijpers, V.B.F. Mathot, B. Goderis, R. Scherrenberg and E. van der Vegte, to be published.
67. S.Z.D. Cheng and B. Wunderlich, *Macromolecules*, 21 (1988) 789.
68. S.Z.D. Cheng, R. Pan and B. Wunderlich, *Makromol. Chem.*, 189 (1988) 2443.
69. ATHAS data bank. For a recent description see: B. Wunderlich, *Pure and Appl. Chem.*, 67 (1995) 1019. The ATHAS data bank 1980: U. Gaur, S.-F. Lau, H.-C. Shu, B.B. Wunderlich, A. Mehta and B. Wunderlich, *J. Phys. Chem. Ref. Data*, 10 (1981) 89; 119; 1001; 1051/ 11(1982) 313; 1065/ 12 (1983) 29; 65; 91. Update: M. Varma-Nair and B. J. Wunderlich, *Phys. Chem. Ref. Data*, 20(2) (1991) 349; 404. For detailed information see WWW address on the Internet: <http://funnelweb.utcc.edu/~athas>.
70. V.B.F. Mathot, *Polymer*, 25 (1984) 579. Errata: V.B.F. Mathot, *Polymer*, 27 (1986) 969.
71. V.B.F. Mathot and M.F.J. Pijpers, *Thermochim. Acta*, 151 (1989) 241.
72. V. Mathot, T. Pijpers, M. Steinmetz and G. van der Plaats, in 'Proceedings of the 25th North American Thermal Analysis Society Conference', (Ed. R.J. Morgan) September 7-9, 1997, McLean, Virginia (1997) 64. The 'Temperature Dependent Crystallinity software program' which runs under Windows 95/NT has been developed by DSM Research BV and Anatech BV jointly, which program is available through Perkin-Elmer.
73. S. Bensason, J. Minick, A. Moet, S. Chum, A. Hiltner and E. J. Baer, *J. Polym. Sci.: Part B: Polym. Phys.*, 34 (1996) 1301.
74. P.J. Phillips and K. Monar, *Antec '96 SPE Conference Proceedings*, 54th(Vol. 2) (1996) 1624.
75. J. Minick, A. Moet, A. Hiltner, E. Baer, and S.P. Chum, *J. Appl. Polym. Sci.*, 58 (1995) 1371.
76. P.R. Swan, *J. Polym. Sci.*, 56 (1962) 403.
77. H. Wilski, *Kunststoffe*, 54 (1964)10.
78. H. Wilski, *Kunststoffe*, 54 (1964) 90.
79. J. van Ruiten, F. van Dieren and V.B.F. Mathot, in 'Crystallization of Polymers' (Ed. M. Dosière); NATO ASI-C Series Mathematical and Physical Sciences (1993) 481.
80. R.G. Alamo, L. Mandelkern, in 'Thermal Analysis and Calorimetry in Polymer Physics' (Ed. V.B.F. Mathot), Special issue *Thermochimica Acta*, 238 (1994) 155.
81. A. Keller, *Macromol. Symp.*, 98 (1995) 1.
82. M. Hikosaka, *Polymer*, 28 (1987) 1257.
83. M. Hikosaka, *Polymer*, 31 (1990) 458.
84. J.D. Hoffman and J.J. Weeks, *J. Res. Nat. Bur. Std.*, 66A (1962) 13.
85. B. Wunderlich, 'Macromolecular Physics, Vol. 3: Crystal Melting', Academic Press, New York (1980).
86. B. Goderis, M. Peeters, V.B.F. Mathot, M.H.J. Koch, W. Bras, A.J. Ryan and H. Reynaers, to be published in *J. Polym. Sci.: Part B: Polym. Phys.*
87. J.T. Koberstein and T.P Russell, *Polym. Mater. Sci. Eng.*, 51 (1984) 141.
88. 'Thermal Analysis and Calorimetry in Polymer Physics' (Ed. V.B.F. Mathot), Special issue *Thermochimica Acta*, 238 (1994).
89. 'Temperature Modulated Calorimetry' (Eds. C. Schick, G.W.H. Höhne), Special issue *Thermochimica Acta*, 304/305 (1997).
90. R. Scherrenberg, V. Mathot and P. Steeman, in 'Temperature Modulated DSC' (Eds. L.H. Judovits, J.D. Menczel), Special issue *Journal of Thermal Analysis*, 54 (1998) 477.
91. R. Androsch, *Polymer*, 40 (1999) 2805.
92. R. Scherrenberg, V. Mathot and A. Van Hemelrijck, 'Lahnwitz seminar on temperature modulated DSC 1998' (Eds. C. Schick, G.W.H. Höhne), Special issue *Thermochimica*

- Acta, 330 (1999) 3.
93. B. Goderis, H. Reynaers, R.L. Scherrenberg, V.B.F. Mathot and M.H.J. Koch, to be published in *Macromolecules*.
 94. M. Peeters, B. Goderis, C. Vonk, H. Reynaers and V. Mathot, *J. Polym. Sci.: Part B: Polym. Phys.*, 35 (1997) 2689.
 95. M. Peeters, B. Goderis, H. Reynaers and V. Mathot, *J. Polym. Sci.: Part B: Polym. Phys.*, 37 (1999) 83.
 96. V.B.F. Mathot, Ch.C.M. Fabrie, G.P.J.M. Tiemersma-Thoone and G.P.M. van der Velden, in 'Proceedings Int. Rubber Conf. (IRC)', October 15-18, 1985, Kyoto (1985) 334.
 97. V.B.F. Mathot and Ch.C.M. Fabrie, *J. Polym. Sci.: Part B: Polym. Phys.*, 28 (1990) 2487.
 98. V.B.F. Mathot, Ch.C.M. Fabrie, G.P.J.M. Tiemersma-Thoone and G.P.M. van der Velden, *J. Polym. Sci.: Part B: Polym. Phys.*, 28 (1990) 2509.
 99. H. Sinn and W. Kaminsky, *Angewandte Chemie, International Edition, Engl.*, 19 (1980) 390.
 100. C.S. Speed, B.C. Trudell, A.K. Mehta and F.C. Stehling, *SPE Polyolefins* (1991) VII 45.
 101. K.W. Swogger, *Second International Business Forum on Specialty Polyolefins, SPO '92*, Sept., (1992) 155.
 102. Childress, B.C. 1994. *Worldwide Metallocene Conference MetCon '94*, Houston, USA
 103. M.J. Schneider and R. Mülhaupt, *J. Molec. Catalysis A: Chemical*, 101 (1995) 11.
 104. V.B.F. Mathot, R.L. Scherrenberg, M.F.J. Pijpers and W. Bras, in *Polym. Prepr. of the Am. Chem. Soc., Div. Polym. Chem.* 36(1), ACS Meeting Advances in Crystalline Polymers, California Meeting, Anaheim (1995) 302.
 105. M. Arnold, S. Bornemann, F. Köller, T. Menke and J. Kressler, *Macromol. Chem. Phys.*, 199(12) (1998) 2647.
 106. D.C. McFaddin, K.E. Russell, W. Gang and R.D. Heyding, *J. Polym. Sci.: Part B: Polym. Phys.*, 31 (1993) 175.
 107. B. J. Wunderlich, *Chem. Phys.*, 29(6) (1958) 1395.
 108. H.S. Cho, J.S. Chung, J.H. Han, Y.G. Ko and W.Y. Lee, *J. Appl. Polym. Sci.*, 70(9) (1998) 1707.

Chapter 7

Recent advances in thermal analysis of thermotropic main-chain liquid crystalline polymers

Christopher Y. Li

Department of Materials Engineering, Drexel University, 3141 Chestnut Street, Philadelphia, PA, 19104

Thermal analysis has been one of the major methods to identify thermotropic phase transition behaviors of liquid crystalline polymers and study their thermodynamic properties. In this review, thermotropic liquid crystalline polymers phase structures will be briefly summarized, followed by three different research aspects related to their thermodynamic properties that can be measured by thermal characterization methods. The first aspect is an understanding of thermodynamic transition behaviors. It is known that liquid crystalline transition parameters (such as transition temperatures and heats of the transitions) show little cooling and heating rate dependence, which indicates that these transitions are close to equilibrium and is one of the major characteristics used in the identification of liquid crystalline phases. The second aspect is focused on the enantiotropic and monotropic liquid crystalline behaviors. The enantiotropic phase possesses a *stable* liquid crystalline state in a temperature region between crystal melting and isotropization, while the monotropic phase is always *metastable* over the entire temperature region. Monotropic liquid crystalline transitions provide an opportunity to study kinetics of crystallization from the isotropic melt and the liquid crystalline state. In particular, when the liquid crystalline transition and crystallization rates are close to each other, it is predicted that a possible competition between the formations of these two phases may exist. The third aspect of this review is dedicated to a quantitative method in investigating the contributions to the liquid crystalline orders from both mesogenic groups and aliphatic spacers, which leads to a further understanding of the molecular origins of the liquid crystalline phase stability.

1. INTRODUCTION

The term liquid crystal signifies a state of molecular aggregation that is intermediate between the crystalline solid and the amorphous liquid. Studies

show that an essential requirement for this mesomorphism to occur is that the molecule possesses a geometrically anisotropic shape, like a rod or a disc as shown in Fig. 1, in addition to specific interactions [1,2]. Phase transitions related to the liquid crystalline states may be brought about by purely thermal processes or by influence of solvents, giving rise to thermotropic or lyotropic liquid crystals, respectively [1,2]. The first small molecule liquid crystal was discovered in 1888 [3] and since then, more than 700,000 liquid crystalline molecules have been synthesized and numerous liquid crystalline phases have been identified [4]. The foundation of liquid crystal physics was laid as early as in the 1920's. However, interest in these substances died down over the next three decades. There has been a resurgence of activity in this field beginning in the 1970's, partly due to the realization that liquid crystals have important uses in the flat-panel display technology [4]. From then on, research in this field has grown almost exponentially. According to a recent estimate by Vill, the current number of publications related to liquid crystals is about 65,000 papers and patents [4].

From the structural point of view, liquid crystalline phases are a series of mesophases that possess order and symmetry between that of three-dimensionally long range ordered crystals and three-dimensionally short range ordered liquids [1,5]. Determination of different phases is not only based on their equilibrium thermodynamic properties, but also their structural order and symmetry. General speaking, three orders can be distinguished, namely molecular orientational order, bond orientational order and positional order. Fig. 2 shows a schematic diagram of these three types of orders. Liquid crystals are considered to possess at least one of these orders in one dimension as shown in Fig. 3. The liquid crystalline order is also explained as one kind of "soft order" recently proposed by de Gennes in his Nobel Lecture [6]. Liquid crystalline structure and phase behaviors have been reviewed in a number of excellent papers [1,2,4,7-12]. The author would attempt to briefly summarize the essential background of thermotropic liquid crystalline polymers before review several recent advances in thermal characterization of thermotropic main-chain liquid crystalline polymers. Important aspects include equilibrium thermodynamic transitions, enantiotropic and monotropic transition behavior and their transition

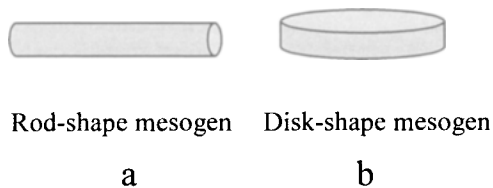


Fig. 1. Two typical shapes of liquid crystalline mesogenic groups: (a) rod and (b) disc

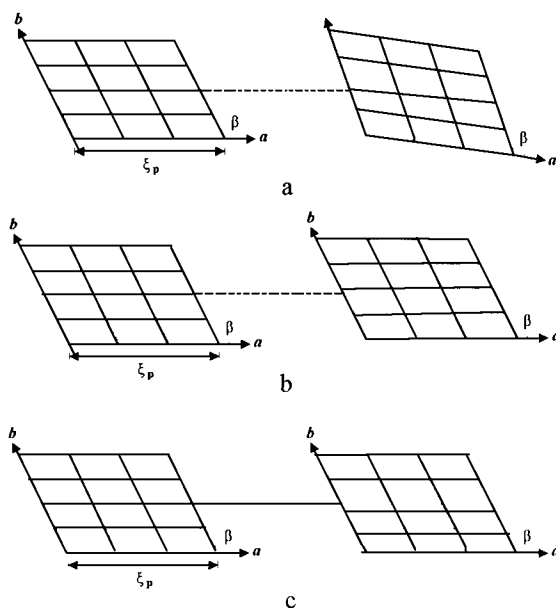


Fig. 2. Schematic illustrations of three types of orders: molecular orientational (a), bond orientational (b) and positional orders (c). Note that in this figure, the molecular orientation is perpendicular to the a - and b -axes

kinetics. In addition, the determination of liquid crystalline stability based on chemical structures in the mesogenic groups and flexible spacers as well as the identification of highly ordered smectic phases will be discussed.

2. LIQUID CRYSTALS AND LIQUID CRYSTALLINE POLYMERS

Numerous liquid crystalline phases have been identified up to today and there are two major categories of liquid crystalline phases: calamitic and discotic, which are determined by the shape of the mesogenic groups [7,8]. Fig. 3 shows a chart summarizing the typical calamitic liquid crystalline phases with their corresponding structural orders and Fig. 4 shows the schematic structures of three liquid crystalline phases: nematic (N), smectic A (S_A), and smectic C (S_C). As shown in Fig. 3, the least ordered liquid crystalline phase is the N phase that only possesses molecular orientational order due to the anisotropy of the molecular geometric shape (Fig. 4a). The next ordering level introduced is the so-called layer structure, which is represented by a S_A or a S_C phase (Fig. 4b and 4c). The structural difference between S_A and S_C is that in S_A phase, the mesogenic groups are perpendicular to the layer structure while in S_C phases; the mesogenic groups are tilted away from the layer normal. Following the S_A phase,

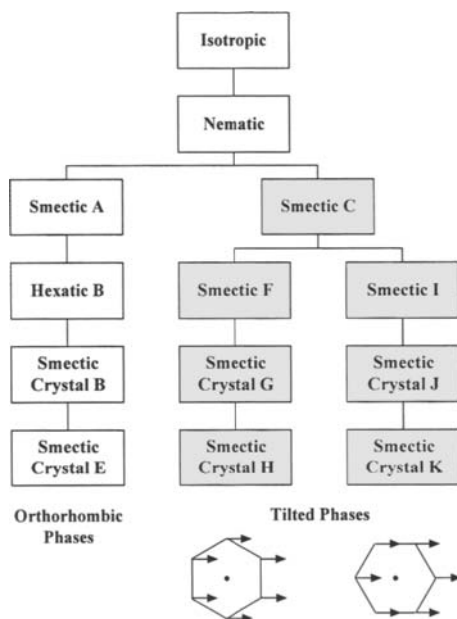


Fig. 3. Classification of calamitic liquid crystalline phases and their corresponding structural orders

the hexatic B (H_B), smectic crystal B (S_B) and smectic crystal E (S_E) phases are observed. In this series, the long axis of the molecules is oriented perpendicular to the layer surface, while order is increasingly developed from positional order normal to the layer in S_A , bond orientational order in H_B , positional order within the layers in S_B and finally, asymmetric axial site symmetry in S_E [9,10]. Two separated, highly ordered smectic phases are recognized after the S_C phase. Both of these phases possess long molecular axes that are tilted with respect to the layer surface normal. The development of order in both cases is correspondingly identical as in the first series progressed from S_A to S_E . The difference between these two series lies in the tilt directions: the smectic F (S_F), smectic crystal G (S_G), and smectic crystal H (S_H) possess a long axis tilted towards one side while the long axis directions in the smectic I (S_I), smectic crystal J (S_J) and smectic crystal K (S_K) are tilted towards an apex (Fig. 3). Furthermore, the S_F , S_G , S_I and S_J phases exhibit hexagonal (or pseudo-hexagonal) packing when viewed parallel to the long axis. The packing of the tilted long axis gives rise to a monoclinic lattice (for S_F and S_G phases $a > b$ while in S_I and S_J phases $a < b$). On the other hand, the packing becomes an orthorhombic, herringbone type in the S_H and S_K phases [9,10]. The main experimental methods used to identify these highly ordered smectic phases in small molecule liquid crystals are wide

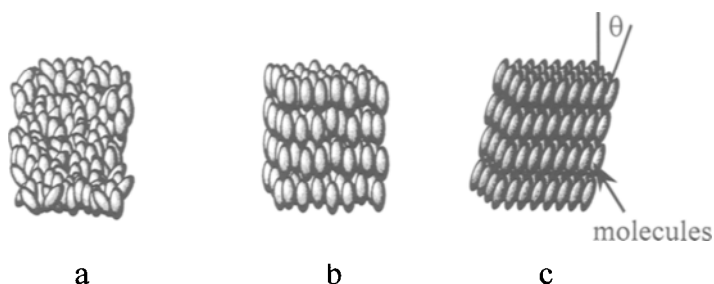


Fig. 4. Schematic representation of liquid crystalline nematic (a) smectic A (b) and smectic C (c) states

angle X-ray diffraction (WAXD), calorimetry, polarized light microscopy (PLM) and phase mixing experiments [9]. The structural identification in small molecule liquid crystals is convincing since, in many cases, monodomains of small molecule liquid crystals can be obtained *via* external force fields. Therefore, sharp reflections can be observed to determine the structural order and symmetry.

Even though the chemistry establishment was slow to accept Staudinger's advocacy of the long chain concept for polymer molecules, Vorlander began to study the effect of increasing the molecular weight of liquid crystalline materials as early as 1923 [13]. He synthesized a rigid-rod polymer by linking benzene rings through ester groups. The resulting polymer, poly(*p*-benzamide), was in a birefringent powder form which charred without softening. The concept of liquid crystalline polymers was then proved [14,15]. Although synthetic lyotropic liquid crystalline polymers as fiber spinning solutions were investigated by Dupont through the 1960s for the development of aromatic amid fibers [16], the infusibility problem of thermotropic main-chain liquid crystalline polymers was not solved until the 1970s (see below). An enormous amount of effort has been made during the last twenty years on the synthesis and understanding of the transition behavior of liquid crystalline polymers [16-22].

Liquid crystalline polymers possess a unique combination of the characteristics peculiar to liquid crystals with those typical of polymers, namely, molecular architectures, dimensional stability, mechanical orientability, durability, ease of processability and moldability [14, 15]. The structure of liquid crystalline polymers depends on how the mesogenic groups are introduced and connected to form polymer chains. From an architectural point of view, there are three major types of liquid crystalline polymers: side-chain liquid crystalline polymers main-chain liquid crystalline polymers (MCLCPs), and combined liquid crystalline polymers as illustrated in Fig. 5. Detailed architectures of liquid crystalline polymers are reviewed in some excellent articles [16-18]. There

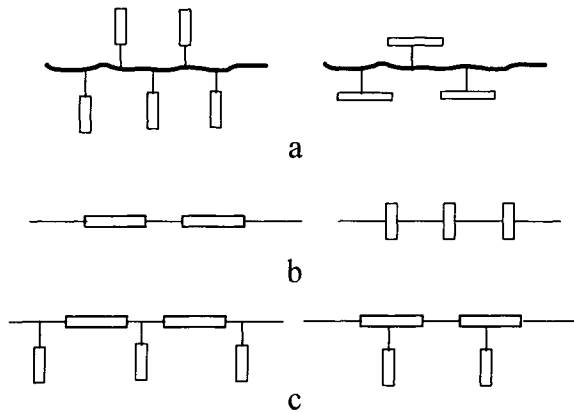


Fig. 5. Schematic drawing of different liquid crystalline polymer architectures: a) side chain liquid crystalline polymer; b) main-chain liquid crystalline polymer; and c) combined liquid crystalline polymer

are seemingly unlimited numbers of systems of liquid crystalline polymers since one can vary the main chains, the spacers, the mesogens, the degree of polymerization, *etc.*, to tune the final structure. We will focus on MCLCPs in the following discussion.

MCLCPs consist of consecutive connections of mesogen groups, and therefore, the mesogen groups are included in the polymer backbones [15]. A main problem for MCLCPs is that transition temperatures of these polymers are usually too high, typically above the degradation point. Structural modifications of MCLCPs are concentrated either on decreasing of the transition enthalpy

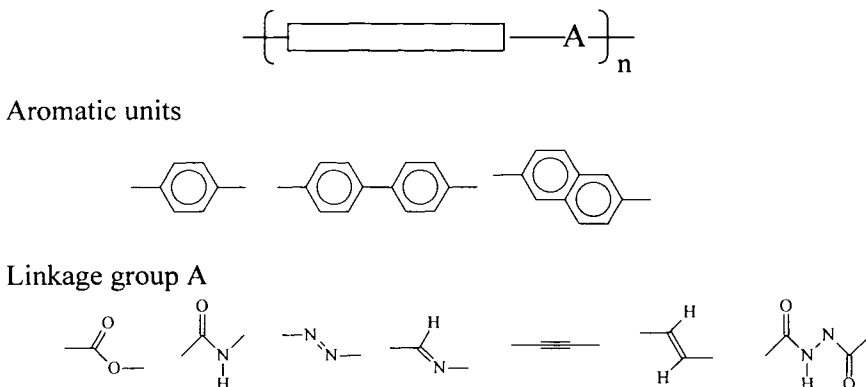


Fig. 6. Typical aromatic units and linkage groups in aromatic MCLCPs [15]

and/or increasing the transition entropy in order to lower the melting point. This can be accomplished by using different types of linkage groups and ways they link the aromatic moieties together.

Based on connecting groups, two types of MCLCPs can be defined: aromatic MCLCPs and semi-flexible MCLCPs [15]. In aromatic MCLCPs, a sequence of aromatic moieties is linked by an even number of atoms or heterocyclic units. Typical linkage groups as well as aromatic moieties are shown in Fig. 6 and the various structural modifications are schematically illustrated in Fig. 7. The strategies used to achieve aromatic main-chain liquid crystalline phases can be summarized as the following: incorporation of monomer units of different length, such as the *p*-phenyl, *p*-biphenyl, or *p*-triphenyl moieties shown in Fig. 7a and incorporation of kinked and/or double kinked comonomers (Fig. 7b and c); and a step-wise shift along the polymer backbone induced by introducing a so-called 'crankshaft' monomers (Fig. 7d), particularly 2,6-disubstituted naphthalene derivatives. The intermolecular interactions can also be lowered substantially by lateral substituents, which can be either flexible (Fig. 7e) or bulky and stiff (Fig. 7f). Monomers with noncoplanar conformation are, for example, 2,2'-substituted bi-phenylenes or binaphthyl derivatives (Fig. 7g). This reduces the intermolecular interactions between the chains very effectively. These monomers reduce the chain stiffness far less than the bulky substituents. Combinations of these different structural modifications can be used and have been utilized in numerous examples to modify liquid crystalline polymers' properties.

Another important concept for the modification of MCLCPs is the incorporation of flexible spacers between mesogenic units, and thus this type of modifications is called semi-flexible MCLCPs. The flexible spacers are capable of a variety of different configurations at accessible energy levels. The regularly alternating arrangement of flexible spacers and rigid anisotropic groups gives rise to thermotropic MCLCPs. Most semi-flexible MCLCPs are synthesized based on conventional step-growth polymerization reactions between appropriate monomers. Following this approach, a wide variety of MCLCPs with highly differentiated structures have been prepared, including polyesters, polyethers, polyurethanes, polyamides, polysiloxanes, poly(β -aminoester)s, and poly(β -thioester)s. Among them, polyesters represent the majority of the studied liquid-crystalline polymers.

Liquid crystalline transition from the isotropic melt (I) in polymers usually exhibits a thermodynamic first-order transition and is a near equilibrium process, which is confirmed by the cooling and heating rate independence of the transition parameters. Such behaviors can be easily determined through differential scanning calorimetry (DSC) at different cooling and heating rates. PLM methods find relatively limited used in polymer liquid crystals since the

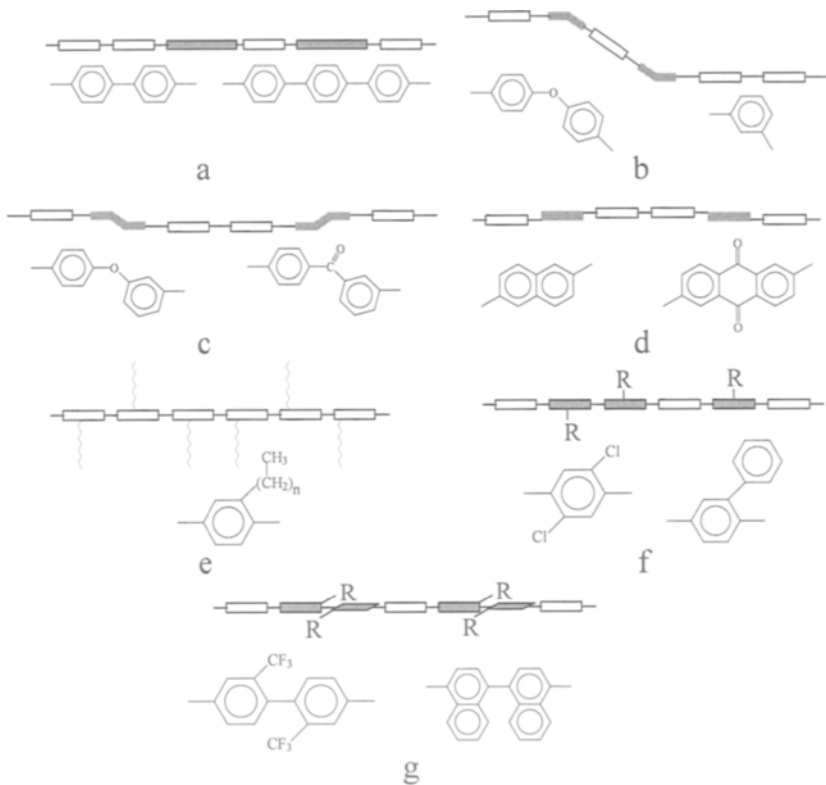


Fig. 7. Modification for para-linked aromatic polymers including typical monomer structures: monomer units of different length (a), kinked conomers (b) double kinked conomers (c) "crankshaft" conomers (d), flexible lateral substituents (e), bulky and stiff lateral substituents (f), monomers with non-coplanar conformation (g) [15]

average domain size of polymer liquid crystals is much smaller than that in their small molecular counterparts. On the other hand, structural changes during the transition can be characterized *via* WAXD powder experiments. During the $I \rightarrow N$ liquid crystal transition, a shift of the d -spacing in the broad halo towards a higher reflection angle can be seen. This shift represents a decrease of the average lateral distance between chain molecules. In addition, for the $I \rightarrow S_A$ and $I \rightarrow S_C$ transitions directly from the isotropic melt, an additional sharp diffraction peak in the low-angle region appears and represents the layer spacing in the smectic phase. For highly ordered smectic phases, WAXD diffraction peak(s) can also be observed in the high-angle region. WAXD fiber patterns obtained from oriented samples are essential for distinguishing three-dimensional crystal packing from highly ordered smectic phases. They also provide further detailed

information about the lateral chain packing, layer structure and order correlation. Small angle light scattering is also used to study liquid crystalline morphologies. For semi-crystalline polymers having a liquid crystalline state, the “lamellar decoration” method using transmission electron microscopy (TEM) has been developed to establish relationships between molecular characteristics, such as chain rigidity, molecular weight, and Frank defect constants. Molecular motions in the liquid crystalline states have also been investigated *via* ^{13}C -solid state nuclear magnetic resonance. During the last two decades, thermodynamic properties and morphological identifications of thermotropic main-chain liquid crystalline polymers have been progressively understood. The nematic state has been the most commonly reported phase in main-chain liquid crystalline polymers. Recently, some studies have shown that S_A and S_C phases may also be possible in these polymers [23-27]. It should be noted that the difference between polymers and small molecule liquid crystals is the connectivity that exists in the polymer case. Despite this difference, it has been shown that the classification of the liquid crystalline phases illustrated in Fig. 3 may also be found in main-chain liquid crystalline polymers based on careful thermodynamic, structural and morphological studies.

3. THERMODYNAMIC TRANSITION BEHAVIORS

Thermodynamically, a first-order transition is defined as the transition temperature at which the first derivatives of Gibbs free energy G with respect to temperature (H , S , V) are discontinuous [28]. This can be understood through a diagram of the G versus temperature as shown in Fig. 8 [29]. Since polymers do not enter the gas phase (degradation occurs prior to the temperature for polymer to transfer to gas state), only condensed phases are represented in the figure. For a hypothetical equilibrium polymer crystal, crystal melting occurs at the equilibrium melting temperature at which

$$\Delta G = G_{liq.} - G_{cryst.} = 0 \quad (1)$$

Complications in this plot are that polymer crystals are usually not perfect and do not show a single-phase behavior; rather, they possess limited crystal sizes, different types of defects, and also coexist with amorphous and/or other phases. This leads to different thermodynamic metastabilities in the crystals that are not at the equilibrium condition. Therefore, their Gibbs free energy levels are higher than that of the equilibrium crystal (Fig. 8). A similar case can also be discussed in polymer melts. Different Gibbs free energy levels exist due to deformation of the melt and the corresponding increase in pressure. As a result, a discussion of a metastable phase transition using equilibrium thermodynamics is extremely

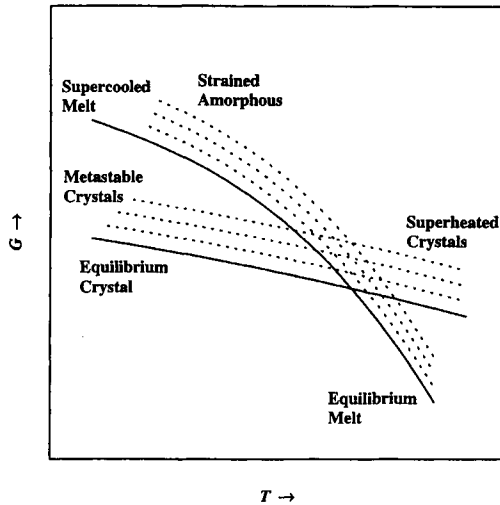


Fig. 8. Gibbs free energy diagram with respect to temperature for crystal and isotropic melt at different metastabilities [29]

difficult and caution must be taken unless the metastability of the crystal does not change during the study. Furthermore, almost all of the processes involving the crystal and mesophase transitions in polymers show first-order behavior [29].

Crystallization is also a nucleation-controlled process. Since classical nucleation theory is solely based on a critical nucleation size that is a balance between the volume Gibbs free energy change (which is negative) during the crystallization and the surface free energies (which are positive). The nucleation barrier is thus proportional to the reciprocal of the square of the undercooling for primary nucleation, or the reciprocal of the undercooling for surface nucleation. As a result, the crystallization rate decreases when the temperature approaches the melting point due to the drastic increasing of the critical nucleation size and therefore, the nucleation barrier. The crystallization rate also decreases when the glass transition temperature is approached since molecular motion ceases at that temperature.

When a crystalline polymer sample is cooled from its isotropic melt, the crystallization kinetics depends upon the cooling rate. In DSC experiments, a slower cooling rate will lead to a crystallization process occurring at a higher temperature with a narrower exothermic crystallization peak. The crystal formed is thermodynamically more stable compared with those in the samples cooled at a faster rate. This illustrates the cooling rate dependence of crystallization due to the nucleation process. Generally speaking, a change in cooling rate from $2.5^{\circ}\text{C}/\text{min}$ to $40^{\circ}\text{C}/\text{min}$ will cause a difference of several tens of degrees in peak

temperatures for the crystallization exotherm, while the percentage of crystals (crystallinity) may also decrease. This is particularly true when polymers having slow crystallization behaviors are studied. For example, a study of non-isothermal crystallization in poly(ether ether ketone) indicates that the exotherm peak temperature decreases by almost 30°C when the cooling rate changes from 2.5°C/min to 40°C/min and the peak width becomes increasingly broad (the width at half-height is almost doubled), while the crystallinity also decreases [30]. Using the models of non-isothermal crystallization kinetics based on the assumption that the Avrami type of crystallization is valid, the nucleation parameters can be deduced [31].

The cooling rate dependence is, however, much less drastic when one studies liquid crystalline phase transitions. In general, the transitions involving liquid crystalline polymers are close to equilibrium as long as molecular mobility is not hampered. It is well known that in a wide cooling rate range, the low order liquid crystalline phase (such as N, S_A and S_C) transitions from the isotropic melt are cooling rate independent [32-36]. Very recently, a series of highly ordered smectic and smectic crystal phases (S_F, S_G and S_H) have been identified in a series of main-chain liquid crystalline polyethers synthesized from 1-(4-hydroxy-4'-biphenyl)-2-(4-hydroxyphenyl) propane and α,ω -dibromoalkanes [TPP(n)] [37-39]. This series of polyethers shows complicated phase behavior. Their phase diagrams are shown in Figs. 9 and 10 for both odd- and even-TPP(n)s with respect to the number of methylene units [37-39]. These phase transitions can be

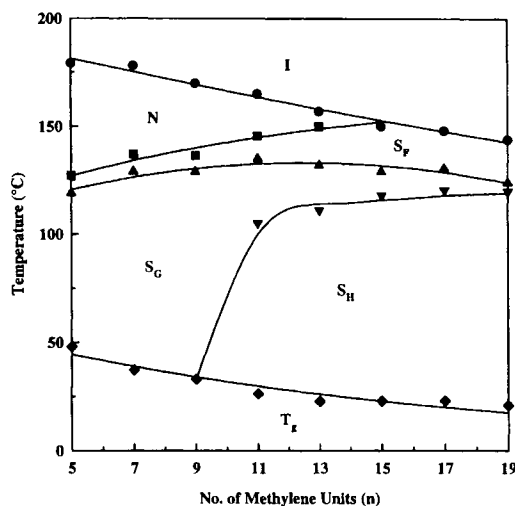


Fig. 9. Phase diagrams for TPP(n = odd)s with respect to the number of methylene units [38]

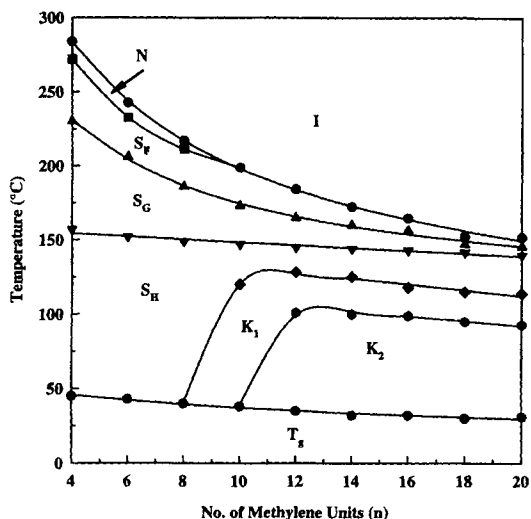


Fig. 10. Phase diagrams for TPP($n = \text{even}$)s with respect to the number of methylene units [39]

detected using DSC in a wide cooling and heating rate range between $2.5^\circ\text{C}/\text{min}$ and $40^\circ\text{C}/\text{min}$, and the transition temperatures and heats of transition show little cooling and heating rate dependence. Therefore, phase transitions associated not only with the liquid crystalline phases involving low levels of order but also with highly ordered smectic and smectic crystal phases exhibit cooling and heating rate independence. This is perhaps one of the most important characteristics in liquid a crystalline transition that distinguishes it from a crystallization process.

It should also be noted that when a liquid crystalline transition is close to the glass transition temperature, the transition might possess cooling rate dependence. This is due to the fact that molecular mobility decreases substantially when the temperature approaches the glass transition. An example is one polymer in a series of poly(ester imide)s synthesized from N-[4-(chloroformyl)phenyl]-4-(chloroformyl)phthalimide and the respective diols [PEIM(n)] [35]. This polymer possesses a methylene unit number of seven [PEIM($n = 7$)]. The liquid crystalline transition temperature in PEIM($n = 7$) and its glass transition temperature are only eleven degree apart. Only under a very slow cooling rate (say $< 1^\circ\text{C}/\text{min}$), can the exothermic $I \rightarrow S_A$ transition be observed [26]. However, this behavior can easily be distinguished from a crystallization process *via* structural characterization such as *in-situ* WAXD experiments at temperatures near the transition.

Another unique feature of MCLCPs is that the transition behaviors are molecular weight dependent. However, it is a difficult task to study the

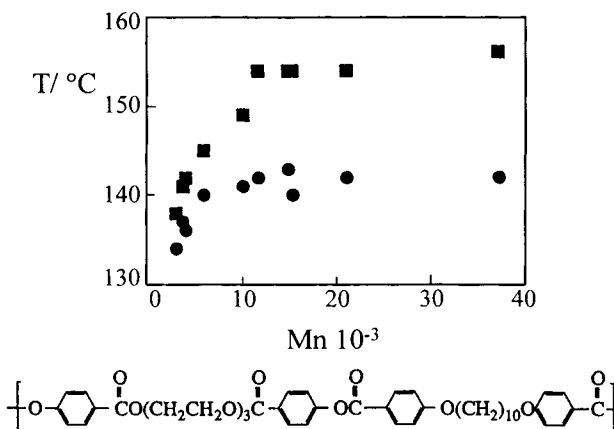


Fig. 11. The melting (■) and N-I transition (●) temperatures as functions of molecular weight [15]

molecular weight dependence for MCLCP since that the narrow molecular weight samples are not readily available. One tedious means is to use the time-consuming fractionation techniques. Fig. 11 shows the strong polymer molecular weight dependence of the N phase temperature range of a main chain polyester (structure is shown in the figure) [15,39-43]. Both T_i and T_m increase steeply as first and then more gradually with increasing molecular weight of the polymer. There appears to be a critical value of about $M_n = 10,000$ g/mol after which the transition temperatures T_i and T_m remain constant with further increasing molecular weight. The increase in T_i with molecular weight is more pronounced than for T_m and therefore the N phase range widens with increasing molecular weight. Also of interest is that the entropy change ΔS_i also increases from 17.5 J/(K mol) to a saturation value of 17.5 J/(K mol) with increasing temperature. Such an increase in the thermodynamic phase transition temperatures and entropies with molecular weight is ascribed to an increased cooperativity between distant units belonging to the same polymer chain, as mediated by the orientational field of the N phase. The cooperative ordering of the rigid groups enhances the overall rigidity of the polymer chain and consequently imparts an increasing first-order character to the isotropization transition.

The transition temperature dependence of the molecular weight may lead to the failure of the observation of possible phases due to the molecular weight distribution. Fig. 12 shows the DSC cooling curve of a chiral liquid crystalline polyesters synthesized from (R)-(-)-4'- ω -[2-(*p*-hydroxy-*o*-nitrophenyloxy)-1-propyloxy]-1-nonyloxy}-4-biphenyl carboxylic acid with $M_n = 16,000$ g/mol and PDI = 2 (abbreviated as PET(R*-9)) [44-46]. At scanning rate of 5°C/min to

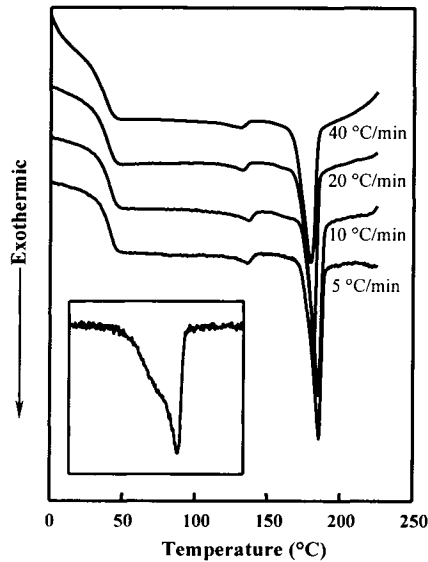


Fig. 12. DSC cooling curve of PET(R*-9) at different cooling rate from 5 to 40°C/min. The in-set of cooling curve of 1°C/min shows the “shoulder” of the high temperature transition peak, indicate that there are three phases involved in this temperature region (S_A^* , twist grain boundary A, and I) [46].

40°C/min, Two transition peaks can be identifies as proved also by WAXD as well as PLM experiments. However, if we decrease the scanning rate to as low as 1°C/min, a “shoulder” of the original peak can be identified for the high temperature transition peak, which indicate that at temperature region from 165°C to 190°C, two transition behaviors can be identified, namely Twist Grain boundary A phase to chiral smectic A phase (S_A^*) and S_A^* to chiral smectic C phase (S_C^*). It is believed that for monodispersed sample, each of the transition peaks would be sharper and therefore, such phenomenon would be less likely to occur. Broadening of transition temperatures of polydispersed MCLCPs would also lead to possible bi-phase behavior at the N-I transition. Of interest is the molecular weight dependence. According to references 45-47, samples with high molecular weight ($M_n = 20,000$ g/mol) and narrow molecular weight distribution ($PDI < 1.5$) and samples with low molecular weight ($M_n = 6,000$ g/mol) and narrow or relatively wide molecular weight distribution ($PDI < 1.6$) do not show N-I biphasic separation. However, samples with intermediate molecular weight ($M_n = 8,000 - 15,000$ g/mol) and relatively narrow or wide molecular weight distributions ($PDI = 1.7-2.4$) show N-isotropic bi-phase separation. Therefore, the phase segregation behavior appears to be due to the effects of the molecular weight and the molecular weight distribution of the polymer.

Since the liquid crystalline transitions are close to thermodynamic equilibrium, it is possible to deduce the entropy contribution at each transition temperature through the equation

$$T = \frac{\Delta H}{\Delta S} \quad (2)$$

Since the thermodynamic parameters T and ΔH can be measured using the calorimetric methods, the entropy change ΔS at the transition temperature can thus be calculated. It is understood that this term is attributed to the different orders as illustrated in Fig. 2. Roughly speaking, the ΔS term can be separated by

$$\Delta S = \Delta S_{mol.orient.} + \Delta S_{bond orient.} + \Delta S_{posit.} \quad (3)$$

For example, the N phase possesses the least molecular ordering having only quasi-long range or long range orientational order introduced compared to the isotropic melt. As a result, the ΔS term for the I \rightarrow N phase transition is only attributed to the first term on the right side of equation 3. With increasing degrees of order, the second and third terms on the right side of equation 3 are gradually involved [50].

4. ENANTIOTROPIC AND MONOTROPIC BEHAVIORS

Two classes of mesophase transition behaviors can be identified: enantiotropic and monotropic. Enantiotropic liquid crystalline phases are thermodynamically stable in a temperature region between the crystal melting temperature and the isotropization temperature. Monotropic phases, however, are metastable throughout the entire temperature range. Experimentally, monotropic phases can only be observed on cooling providing the crystallization process is bypassed by undercooling due to the nucleation process. The recognition of monotropic phases can be traced as far back as 1877 [51]. From a thermodynamic point of view, one can readily understand the monotropic phase through a diagram of the Gibbs free energy of the different phases *versus* temperature as shown in Fig. 13. The mesophase can only be observed when the cooling rate is fast enough to prevent the crystallization process from occurring until below the mesophase transition temperature [52]. In small molecule liquid crystals, a few examples have been reported to show the monotropic liquid crystalline behavior [53,54]. When the mesogenic groups of these liquid crystals were used to synthesize polymers and methylene units were adopted to connect these mesogenic groups, the monotropic liquid crystalline behavior remains. One example is 1-(4-alkylphenyl)-2-(4-cyanophenyl)ethane [55] and its polymer analog, synthesized

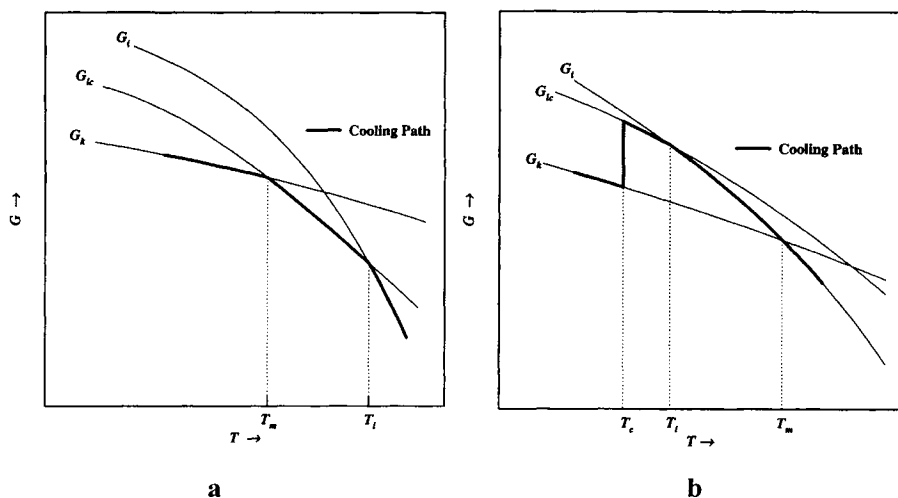


Fig. 13. Gibbs free energy diagram with respect to temperature for (a) enantiotropic and (b) monotropic liquid crystalline behavior

from the coupling of 1-(4-hydroxyphenyl)-2-(2-methyl-4-hydroxyphenyl)ethane and odd-numbered α,ω -dibromoalkanes (MBPE) [32,34], which both show monotropic behavior.

From DSC experiments, enantiotropic and monotropic behaviors can be readily distinguished as shown in Fig. 14. An enantiotropic liquid crystalline state possesses a thermodynamically stable phase in a temperature range between T_m and T_i as shown in Fig. 14a. The liquid crystalline transition always occurs above the crystal melting temperature and can be observed during both cooling and heating experiments. However, the monotropic liquid crystalline phase appears due to the bypassing of the crystallization process using a fast cooling rate (Fig. 14b). As a result, the liquid crystalline transition may be seen only upon during cooling but not on heating. Note that the monotropic phase transition is a broad definition of phase behavior and is not only limited to cases of the liquid crystalline state such as N and smectic phases (including highly ordered smectic phases) with respect to the isotropic melt, but also may occur between liquid crystalline phases and even with crystalline phases. Some examples of monotropic liquid crystalline transitions which have been identified during cooling are given in references 34-39, 56. The reason for the appearance of monotropic behavior is most likely due to the decrease in rigidity, linearity, symmetry and aspect ratio of the mesogenic groups, which lead to a reduction of the liquid crystalline phase stability and therefore, a decrease in the transition temperature which is most likely due to the large ΔS term at the transition.

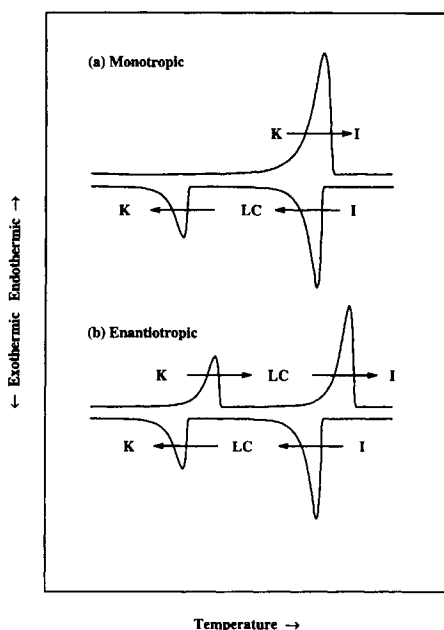


Fig. 14. DSC observations of (a) monotropic and (b) enantiotropic liquid crystalline transitions during cooling and subsequent heating

Monotropic liquid crystalline behavior provides a unique opportunity for a study of crystallization kinetics from both the isotropic melt and the liquid crystalline states. One must consider three phase transition rates: a crystallization rate (crystallized from isotropic melt), a liquid crystalline formation rate (formed from the isotropic melt) and a crystallization rate (crystallized from the liquid crystalline state). Three kinetic regions for these phase transformation rates can be identified as shown in Fig. 15 [56]: crystallization directly from the isotropic melt (region I), crystallization from the liquid crystalline phase in which the liquid crystalline formation rate is much faster than that of crystallization (region III) and a crystallization rate which has the same order of magnitude as that of the liquid crystalline phase (region II). Crystallization from the isotropic melt in region I is a nucleation-controlled process [57,58]. On the other hand, liquid crystalline transformations from the isotropic melt are near equilibrium transitions and therefore, the transition kinetics are fast and difficult to determine experimentally [59-63].

In Fig. 15, both the phase formation rates of crystallization and the liquid crystalline phase formation from the isotropic melt are illustrated [55]. Under the condition that the crystal structures formed from the liquid crystalline phase and crystallized directly from the melt are the same, it can be understood that in

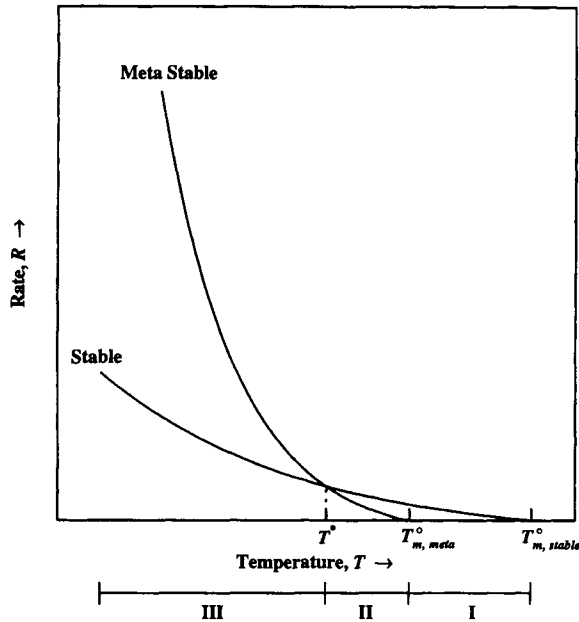


Fig. 15. Phase transformation rates for a monotropic liquid crystalline polymer including three regions: crystallization from the isotropic melt, liquid crystalline formation from the isotropic melt, and crystallization from the liquid crystalline state [55]

region III, crystallization from the liquid crystalline state is actually a two-step phase transformation process from the isotropic melt to the crystalline state. This process consists of the $I \rightarrow N$ phase transition followed by the $N \rightarrow K$ (K : crystal) transition. Therefore, the liquid crystalline state is a metastable phase with respect to the ultimate crystal and it is an intermediate state in the crystallization process. One may predict that the crystallization rate from the liquid crystalline state should be faster than the rate of crystallization rate from the melt. This is indeed the case for a series of PEIM(n)s [63]. Fig. 16 shows the overall crystallization rates over the whole temperature range for PEIM ($n = 11$) as an example. The existence of a pre-ordered phase (here, the liquid crystalline phase) enhances the crystallization rate below T .

Region II in Fig. 15 is of particular interest and deserves further discussion since in this region both crystallization and liquid crystalline formation rates from the melt have the same order of magnitude. As a result, two possibilities may exist. The transitions may enhance or hamper one other. If the latter case is true, one may expect that the crystallization rate in this region should exhibit a

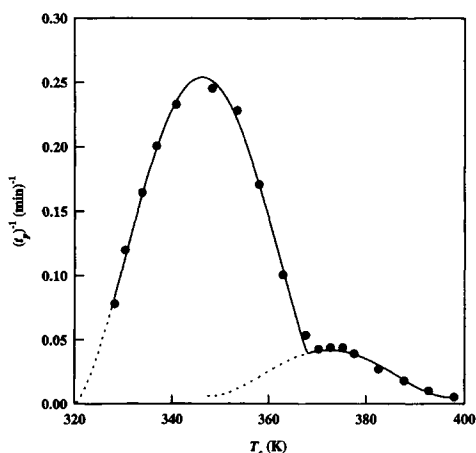


Fig. 16. Overall crystallization rate changes at different isothermal temperatures for PEIM ($n = 11$) [63]

minimum due to the competition between these two structural formations. However, this expectation must be proven by experimental observations.

5. EFFECTS OF MESOGENIC GROUPS AND SPACERS ON THE LIQUID CRYSTALLINE ORDERS AND STABILITY

In thermotropic main-chain liquid crystalline polymers consisting of both mesogenic groups and methylene units (spacers), it is of interest to find that the spacers may also partially contribute to the changes of enthalpy and entropy during liquid crystalline transitions with an even-odd alternation [64-68]. This may be due to the fact that even-numbered methylene units in spacers preserve certain structural orders when the majority of C-C bonds in the spacer possess *trans* conformations. Experimentally, this phenomenon has been reported since the early 1980s. Conformational calculations were also carried out to support these experimental findings. On the other hand, ethylene oxide and siloxane spacers do not have such a contribution [66] due to the flexible nature of the spacers. A series of poly(azomethine ether)s with different numbers of ethylene oxide spacers showed that the enthalpy and entropy changes at the I \rightarrow N transitions are nearly independent of the number of spacers [32]. This conclusion can also be reached by comparing the changes of enthalpy and entropy of a polymer and its corresponding mesogenic model compound. If the spacers do not contribute to the changes, the changes of enthalpy and entropy in both systems

should be similar. Otherwise, those of the polymer should possess greater enthalpy and entropy changes compared to those of the model compound.

Detailed analyses in the contribution of the transition thermodynamic properties from both mesogenic groups and methylene spacers can be achieved *via* plots between these properties and the number of methylene spacers. This plot was first proposed by Blumstein and Blumstein in a series of (4,4'-dihydroxy-2,2'-dimethyl-azoxybenzene)alkanedioic acid (ME9-Sn) [69-71]. In a range of less than thirteen methylene units in the spacers, these plots yield linear relationships. The slopes of these relationships represent the contribution of each mole of methylene unit to the enthalpy and entropy changes at the transition temperature, while the intercept gives the contribution of the molar mesogenic groups to these properties. If the mesogenic groups are not able to provide enough stability to the liquid crystalline phase the methylene units may have to provide an increased contributions. Sometimes, the liquid crystalline transition behavior may even change from enantiotropic to monotropic type before the liquid crystalline phase is completely destabilized. This case has been found in polyethers MBPE [32,34] and PEIM(n)s [35,36], both of which only exhibit monotropic liquid crystalline behavior. The enthalpy and entropy changes of these two polymers as well as ME9-Sns are listed in Table I for comparison.

A very recent investigation on a series of liquid crystalline polyethers, TPP (n = 4-20), has indicated that this series of polyethers exhibits complicated

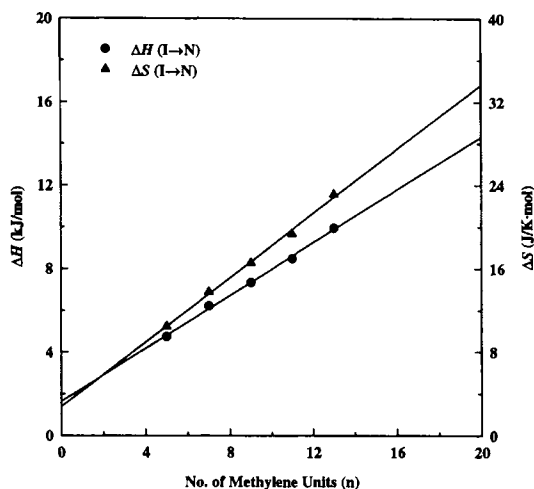


Fig. 17. Relationships of the I \rightarrow N enthalpy and entropy changes with respect to the number of methylene units in odd-TPP (n \leq 13)s [38]

Table 1

The transition enthalpy and entropy changes for methylene units and mesogenic groups for the liquid crystalline transitions in BMPE ($n = \text{odd}$)s, ME9-Sn and PEIM(n)s

Sample	Transition	ΔH (kJ/mol)		ΔS (J/K mol)	
		Mesogen	Methylene	Mesogen	Methylene
Odd-BPME	I \rightarrow N	0.11	0.64	1.30	1.90
Odd-PEIM	I \rightarrow S _A	0.58	0.40	1.35	1.07
Odd-ME9-Sn	I \rightarrow N	0.94	0.19	1.41	0.57
Even-PEIM	I \rightarrow S _A	0.58	0.80	1.35	2.30
Even-ME9-Sn	I \rightarrow N	4.70	0.16	7.55	0.87

phase behavior and has been carefully studied *via* WAXD, PLM and TEM and electron diffraction experiments. These phases have been assigned as shown in Fig. 9 and 10 for both series of TPP($n = \text{odd}$)s and TPP($n = \text{even}$)s [37-39]. The changes of thermodynamic properties of the mesogenic groups with methylene units at each transition temperature obtained from DSC experiments also indirectly supports the identification of the phase structures in the liquid crystalline state.

In TPP($n = \text{odd}$)s, the enthalpy and entropy changes of the I \rightarrow N transition for TPP($n \leq 13$)s can be plotted against the number of methylene units as shown in Fig. 17, and the corresponding slopes and intercepts are listed in Table II. It is interesting to note that when increasing the number of methylene units, the enthalpy change at the transition increases linearly and has a slope of 0.63 kJ/(mol of methylene units). This clearly reveals that the methylene units also join the ordering process during this I \rightarrow N transition and the slope roughly represents the contribution to the nematic order for each methylene unit. The entropy change of each methylene units at the transition is 1.54 J/(K mol) obtained from a similar plot (Fig. 17). An extrapolation to zero methylene unit in Fig. 17 yields the enthalpy change of this transition for a pure mesogenic group at the transition that is 1.64 kJ/mol. The entropy change of the mesogenic group alone at the transition obtained from the extrapolation is 2.80 J/(K mol). The absolute values of the enthalpy and entropy changes of this nematic liquid crystalline transition in TPP($n = \text{odd}$)s are higher than those commonly found in enantiotropic liquid crystalline polymers such as in the case of ME9-Sn (Table I).

The enthalpy and entropy changes of the N \rightarrow S_F transition for odd-TPP($n \leq 13$)s indicate that the methylene units still take part in the ordering process, and involve a contribution to the enthalpy change of transition of 0.43 kJ/mol and an

entropy change of 0.96 J/(K mol) for each methylene unit. The extrapolated intercept values for the enthalpy and entropy changes during this transition for the mesogenic groups are 0.50 kJ/mol and 1.78 J/(K mol), respectively. For odd-TPP($n \geq 15$)s, the S_F phase appears directly after passing through the highest transition temperature (Fig. 17). The relationship between the enthalpy and entropy changes of the $I \rightarrow S_F$ transition and the number of the methylene units can also be used to obtain the slopes and intercepts (Table II).

Furthermore, one expects that the summation of the thermodynamic parameters in odd-TPP($n \leq 13$)s where two consecutive transitions are taking place ($I \rightarrow N$ and $N \rightarrow S_F$) should fit the same relationships as those of the single-step $I \rightarrow S_F$ transitions for odd-TPP($n \geq 15$)s. It is indeed true that both sets of enthalpy and entropy changes for all TPP($n = \text{odd}$)s fit very well in the same linear relationships as shown in Fig. 18 and in Table II. The same observations can also be made in TPP($n = \text{even}$)s [39]. This indicates that the additivity assumption proposed is held. As a result, the N phase can be recognized as an intermediate phase in the $I \rightarrow S_F$ transition, which obeys Ostwald's law of successive states which dictates that a phase will occur step-by-step through successively more stable polymorphs [72].

When one discusses the transitions of $S_F \rightarrow S_G$ and $S_G \rightarrow S_{II}$ for all TPP($n = \text{odd}$)s, the relationships of the enthalpy and entropy changes with the number of methylene units also yield slopes which represents their contributions per mole of methylene units. However, it is surprising that the changes for the

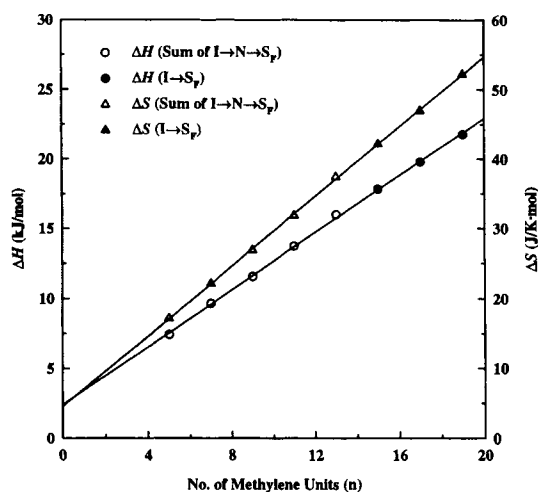


Fig. 18. Relationships of the $I \rightarrow N$ and $N \rightarrow S_F$ enthalpy and entropy changes for odd-TPP($n \leq 13$)s and $I \rightarrow S_F$ enthalpy and entropy changes for odd-TPP($n \geq 15$)s with respect to the number of methylene units [38]

Table 2

The transition enthalpy and entropy changes for methylene units and mesogenic groups for the liquid crystalline transitions in TPP(n)s.

Transition	ΔH (kJ/mol)		ΔS (J/K mol)		
	Mesogen	Methylene	Mesogen	Methylene	
Odd	I \rightarrow N	1.64	0.63	2.80	1.54
	N \rightarrow S _F	0.50	0.43	1.78	0.96
	I \rightarrow S _F	2.14	1.06	4.58	2.50
	S _F \rightarrow S _G	~0	0.42	~0	1.04
	S _G \rightarrow S _H	~0	0.92	~0	2.35
Even	I \rightarrow N	5.01	0.40	7.56	1.12
	N \rightarrow S _F	7.15	0.16	11.43	0.73
	I \rightarrow S _F	12.16	0.56	19.14	1.81
	S _F \rightarrow S _G	2.45	0.32	3.85	0.89
	S _G \rightarrow S _H	~0	0.95	~0	2.25

mesogenic groups are close to zero (the intercepts at $n = 0$ are approximately equal to zero). This implies that during these transitions, the ordering process is solely occurring in the methylene units. A similar analysis can be carried out in TPP($n = \text{even}$)s and all of the enthalpy and entropy changes at those transition temperatures are listed in Table II for the purpose of comparison and discussion. Furthermore, the discussion can be followed by comparing the contributions from the mesogenic groups and methylene units in TPP($n = \text{odd}$)s and TPP($n = \text{even}$)s. For example, it is evident from Table II that the enthalpy and entropy changes of the I \rightarrow N transition for the TPP($n = \text{odd}$)s are relatively small compared with those in TPP($n = \text{even}$)s. This may be due to the odd-even alternation which affects the mesogenic group packing and orientation correlation due to different methylene unit conformations. Both of these changes illustrate that the nematic structure in TPP($n = \text{even}$)s retains better order than those in TPP($n = \text{odd}$)s. Moreover, in the I \rightarrow N transition the major differences of the enthalpy and entropy changes are attributed to the mesogenic groups in TPP($n = \text{even}$)s which are much greater than those in TPP($n = \text{odd}$)s, while those changes of the methylene units in TPP($n = \text{even}$)s are slightly smaller than those in TPP($n = \text{odd}$)s.

It is particularly interesting to note that in the S_F \rightarrow S_G transition in all TPP($n = \text{odd}$)s, the extrapolations of both the relationships to zero methylene

unit (intercepts) are close to zero. This indicates that the ordering process of these transitions is basically attributed to the methylene units and the mesogenic groups do not contribute. However, for the $S_G \rightarrow S_H$ transitions in TPP($n = \text{even}$)s, both the changes of enthalpy and entropy are not equal to zero [73]. This reveals that the formation mechanism of these phase in TPP($n = \text{even}$)s is intrinsically different from that of those transitions in TPP($n = \text{odd}$)s. Quantitative analyses for the thermodynamic properties of liquid crystalline transitions can thus be conducted to obtain detailed information regarding the molecular interactions (the change of enthalpy) and disorder (the change of entropy) as summarized in reference 71.

6. CONCLUDING REMARKS

In summary, this review has discussed three aspects of calorimetric characterization in thermotropic main-chain liquid crystalline polymers. Many research aspects in this area are equally important and yet have not been covered here. Our purpose is to convey to the readers that in liquid crystalline polymers, highly ordered smectic phases may exist. To identify these phases, however, it is necessary to combine the studies of thermodynamic transition properties with structural order and symmetry. The most important difference between these highly ordered smectic phases and polymer lamellar crystals, from a thermodynamic point of view, lies in the fact that these smectic phase transitions possess little undercooling dependence, while for the crystallization process a clear undercooling dependence may be seen at different cooling rates. The recognition of enantiotropic and monotropic liquid crystalline behaviors is critical to the understanding of the competition between transition thermodynamics and kinetics. Specially, monotropic liquid crystalline behavior provides an opportunity to investigate the crystallization kinetics from both the melt and liquid crystalline state. A prediction of the rate competition between the crystallization and liquid crystalline formation from the melt may lead to new experimental observations. The thermodynamic stability of a liquid crystalline state in main-chain liquid crystalline polymers is attributed to contributions of both mesogenic groups and methylene units. The relationships between the enthalpy and entropy changes and the number of methylene units separate these two contributions *via* their slopes and intercepts. This method has provided indirect evidence for the identification of the formation of structural order in liquid crystalline phases.

REFERENCES

1. P. G. de Gennes, J. Prost, *The Physics of Liquid Crystals* 2nd ed. Clarendon: Oxford, 1993.

2. S. Chandrasekhar, "Liquid Crystal", 2nd Ed., Cambridge University Press, New York, 1992.
3. F. Reinitzer, *Monatsch.*, 9 (1888) 421.
4. D. Demus, J. Goodby, G. W. Gray, H-W. Spiess and V. Vill, (eds.) *Handbook of Liquid Crystals*, Wiley-VCH: New York, Vol. 1, 1998.
5. G. Friedel, *Ann. Physique*, 18 (1922) 273.
6. P. G. de Gennes, in *Soft Matter (Nobel Lecture)*, *Angew.-Chem. Int. Ed. Engl.*, 31 (1992) 842.
7. D. Demus, J. Goodby, G. W. Gray, H-W. Spiess and V. Vill, (eds.) *Handbook of Liquid Crystals*, Wiley-VCH: New York, Vol. 2a, 1998.
8. D. Demus, J. Goodby, G. W. Gray, H-W. Spiess and V. Vill, (eds.) *Handbook of Liquid Crystals*, Wiley-VCH: New York, Vol. 2b, 1998.
9. G. W. Gray and J. W. G. Goodby, *Smectic Liquid Crystals*, Leonard Hill, London, 1984.
10. P. S. Pershan *Structure of Liquid Crystal Phases*, World Scientific Publishing, Singapore, 1988.
11. B. Wunderlich and J. Grebowicz, *Adv. Polym. Sci.*, 60/61 (1984) 1.
12. W. Chen, A. Toda, I. K. Moon and B. Wunderlich, *J. Polym. Sci., Polym. Phys.*, 37 (1999) 1539.
13. D. Z. Vorlander, *Phys. Chem.*, 105 (1923) 211.
14. A. Blumstein, (eds.) *Polymeric Liquid Crystals* Plenum: NY, 1992.
15. D. Demus, J. Goodby, G. W. Gray, H-W. Spiess and V. Vill, (eds.) *Handbook of Liquid Crystals*, Wiley-VCH: New York, Vol. 3, 1998.
16. C. B. McArdle, *Side Chain Liquid Crystalline Polymers* Blackies: Glasgow, 1989.
17. A. M. Donald and A. H. Windle, *Liquid Crystalline Polymers* Cambridge Univ: Cambridge, 1992.
18. C. Neol and P. Navard, *Prog. Polym. Sci.*, 16 (1991) 55.
19. S. L. Kwolek, P. W. Morgan, J. R. Schaeffgen and L. W. Gulrich, *Macromolecules*, 10 (1977) 1390.
20. A. Ciferri, (eds.) *Liquid Crystallinity in Polymers, Principles and Fundamental Properties*, VCH: New York, 1991.
21. A. M. Donald and A. H. Windle, *Liquid Crystalline Polymers*, Cambridge Univ. Press, 1992.
22. V. Percec and D. Tomazos, in *Comprehensive Polymer Science*, G. Allen, S. L. Aggarwal and S. Russo Eds. Pergamon: Oxford, 1992. First Supplement, pp. 300-356. In this review, over four hundred references were collected.
23. A. Thierry, A. Skoulios, G. Lang and S. Forestier, *Mol. Cryst. Liq., Cryst. Lett. Sect.*, 41 (1978) 125.
24. A. Roviello and A. Sirigu, *Gass. Chim. Ital.*, 110 (1980) 403.
25. P. Frosini and A. Marchetti, *Makromol. Rapid Commun.*, 3 (1982) 795.
26. C. K. Ober, J. I. Jin, R. W. Lenz *Makromol. Rapid Commun.*, 4 (1983) 49.
27. C. Noel, in *Polymeric Liquid Crystals*, Blumstein A. Ed.; Plenum: New York, 1985; pp. 21-63.
28. P. Ehrenfest, *Proc. Acad. Sci. Amsterdam*, 36 (1933) 153.
29. B. Wunderlich, *Macromolecular Physics*, Vol. 3, *Crystal Melting*, Academic Press: New York, 1980.
30. S. Z. D. Cheng, *J. Appl. Polym. Sci. Appl. Polym. Symp.*, 43 (1989) 315.
31. T. J. Ozawa, *Thermal Analysis*, 2 (1970) 301.
32. S. Z. D. Cheng, J. Janimak, K. Sridhar and F. W. Harris, *Polymer*, 30 (1989) 494.
33. S. Z. D. Cheng, M. A. Yandrasits and V. Percec, *Polymer*, 32 (1991) 1284.

34. M. A. Yandrasits, S. Z. D. Cheng, A. Zhang, J.-L. Cheng, B. Wunderlich and V. Percec, *Macromolecules*, 25 (1992) 2112.
35. R. Pardey, F. W. Harris, S. Z. D. Cheng, J. Aducci, J. V. Facinelli and R. W. Lenz, *Macromolecules*, 25 (1992) 5060.
36. R. Pardey, F. W. Harris, S. Z. D. Cheng, J. Aducci, J. V. Facinelli, R. W. Lenz, *Macromolecules*, 26 (1993) 3687.
37. S. Z. D. Cheng, Y. Yoon, A. Zhang, E. P. Savitski, J.-Y. Park, P. Percec and P. Chu, *Macromol. Rapid Commun.*, 16 (1995) 533.
38. Y. Yoon, A. Zhang, R.-M. Ho, S. Z. D. Cheng, V. Percec and P. Chu, *Macromolecules*, 29 (1996) 294.
39. Y. Yoon, R.-M. Ho, F.-M. Li, S. Z. D. Cheng, V. Percec and P. Chu, *Macromolecules*, 29 (1996) 4528.
40. W. R. Krigbaum, T. Ishikawa, J. Watanabe, H. Toriumi, K. Kubota and J. Preston, *J. Polym. Sci. Polym. Phys. Ed.*, 21 (1983) 1851.
41. R. B. Blumstein, E. M. Stickles, M. M. Gauthier, A. Blumstein, and F. Volino, *Macromolecules*, 22 (1984) 177.
42. G. Galli, E. Chiellini, A. S. Angeloni and M. Laus, *Macromolecules*, 22 (1989) 1120.
43. M. Laus, A. S. Angeloni, G. Galli, and E. Chiellini, *Makromol. Chem*, 191 (1990) 147.
44. C. Y. Li, S. Z. D. Cheng, J. J. Ge, F. Bai, J. Z. Zhang, I. K. Mann, F. W. Harris, L-C Chien and B. Lotz, *Phys. Rev. Lett.*, 83 (1999) 4558.
45. C. Y. Li, S. Z. D. Cheng, J. J. Ge, F. Bai, J. Z. Zhang, I. K. Mann, L-C Chien, F. W. Harris and B. Lotz, *J. Am. Chem. Soc.*, 122 (2000) 72.
46. C. Y. Li, J. J. Ge, F. Bai, J. Z. Zhang, B. H. Calhoun, L-C Chien, F. W. Harris and S. Z. D. Cheng, *Polymer*, 41 (2000) 8953.
47. J. F. D'Alles, P. P. Wu, A. Blumstein, R. B. Blumstein *Mol. Cryst. Liq. Cryst. Lett.*, 3 (1986) 103.
48. J. F. D'Allest, P. Sixou, A. Blumstein, R. B. Blumstein, *Mol. Cryst. Liq. Cryst.*, 157 (1988) 229.
49. M. Laus, D. Caretti, A. S. Angeloni, G. Galli and E. Chiellini, *Macromolecules*, 24 (1991) 1459.
50. Y. Jing, B. Wunderlich, S. Z. D. Cheng, M. A. Yandrasits and A. Zhang, *Polymers in Advanced Technology*, 5 (1994) 785.
51. O. Lehmann, *Uber Physikalische Isomerie*; from Keller, H., 1877. *History of Liquid Crystals. Mol. Cryst. Liq. Cryst.*, 21 (1973) 1.
52. V. Percec and A. Keller, *Macromolecules*, 23 (1990) 4347.
53. N. Carr and G. W. Gray *Mol. Cryst. Liq. Cryst.*, 124 (1985) 27.
54. B. M. Andrews and G. W. Gray, *Mol. Cryst. Liq. Cryst.*, 123 (1985) 257.
55. A. Keller, in *Crystallization of Polymers*, Dosiere, M. Ed., NATO ASI Series C, Vol. 405, p. 13.
56. A. J. Jing, O. Taikum, C. Y. Li, F. W. Harris, and S. Z. D. Cheng, *Polymer*, 43 (2002) 3431.
57. J. D. Hoffman, G. T. Davis, J. I. Lauritzen Jr., In *Treatise on Solid State Chemistry*, Hannay, N. B., (eds.), Plenum: New York, 1976; Vol. 3, Chapter 7, pp. 497-614.
58. B. Wunderlich, *Macromolecular Physics*, Vol. 2, *Crystal Nucleation, Growth, Annealing*, Academic Press: New York, 1976.
59. S. Z. D. Cheng, *Macromolecules*, 21 (1988) 2475.
60. S. Z. D. Cheng, J. J. Janimak, T. M. Lipinski, K. Sridhar, X.-Y. Huang and F. W. Harris, *Polymer*, 31 (1990) 1122.
61. H. Jonsson, E. Wallgren, A. Hult and Geedde, U. W. *Macromolecules*, 23 (1990) 1041.

62. I. Campoy, C. Marco, M. A. Gomez and J. G. Fatou, *Macromolecules*, 25 (1995) 4392.
63. R. Pardey, W. W. Wu, J-H Chen, F. W. Harris, S. Z. D. Cheng, A. Keller, J. Aducci, J. V. Facinelli and R. W. Lenz, *Macromolecules*, 27 (1994) 5794.
64. P. G. de Gennes, *Mol. Cryst. Liq. Cryst. Lett. Sect.*, 102 (1984) 95.
65. A. Roviello and A. Sirigu, *Makromol. Chem.*, 183 (1982) 904.
66. C. K. Ober, J. Jin, R. W. Lenz, *Adv. Polym. Sci.*, 59 (1984) 103.
67. A. Abe, *Macromolecules*, 17 (1984) 2280.
68. D. Y. Yoon and S. Bruckner, *Macromolecules*, 18 (1985) 651.
69. A. Blumstein and O. Thomas, *Macromolecules*, 15, (1982) 1264.
70. R. B. Blumstein, E. M. Stickles and A. Blumstein, *Mol. Cryst. Liq. Cryst. Lett. Sect.*, 82 (1982) 205.
71. R. B. Blumstein and A. Blumstein, *Mol. Cryst. Liq. Cryst.*, 165 (1988) 361.
72. W. Z. Ostwalds, *Phys. Chem.*, 22 (1897) 286.
73. Y. Yoon, R.-M. Ho, F.-M. Li, S. Z. D. Cheng, V. Percec and P. Chu, *J. Thermal Analys.*, 47 (1996) 957.

This Page Intentionally Left Blank

Chapter 8

Polymer blends and copolymers

James Runt and Jiang Huang*

Department of Materials Science and Engineering and the Materials Research Institute, The Pennsylvania State University, University Park, PA 16802

1. INTRODUCTION

Thermal analysis techniques have played, and continue to play, a prominent role in the characterization and development of polymer blends and copolymers of various architectures. Our goal in this chapter is not to present a comprehensive literature review of the subject but to provide background material and several examples of the utility of thermal analysis methods in understanding phase behavior, crystallization and melting behavior, etc. in these complex polymer systems. As the authors have had a particular interest in crystalline materials, and these constitute an important fraction of the polymers in use today, many of the examples cited below involve crystalline polymers.

2. BACKGROUND

2.1. Copolymers

Copolymers are macromolecules that are synthesized from two or more different monomer units. The principle architectures or arrangements of the building blocks are determined by relative monomer reactivities and the synthetic procedures used. The different chemical units can be arranged in random, blocky (block or graft copolymers) or alternating fashion. The most common block copolymers are: diblocks, where relatively long segments of monomers A and B are connected at one end (A-A-A- ... -A-B-B-B- ... -B); triblock copolymers, which are frequently of the $A_n-B_m-A_n$ type; and multiblock copolymers [(A-A-... -A-B-B- ... -B)_x]. While random and alternating copolymers generally exhibit a single phase structure, relatively high molecular weight block and graft copolymers often exhibit a phase separated morphology. However, due to the interconnectivity of the species, one observes microphase

* Present address: Rippey Corp., El Dorado Hills, CA 95662

separation as opposed to the larger scale segregation found for the great majority of polymer blends.

Thermoplastic elastomers are an important class of materials that are frequently derived from tri- or multiblock architectures. These polymers are composed of a relatively high concentration of 'soft' blocks (blocks that are amorphous and have low glass transition temperatures, T_g) and two or more 'hard' blocks/molecule. The 'hard' segments provide physical crosslinks and reinforcement and are either amorphous with $T_g >$ room temperature or crystalline with a melting point above room temperature. Styrene-butadiene-styrene triblock copolymers are a typical example - the glassy, phase separated polystyrene domains provide the multifunctional physical crosslinks. Poly(ester-ether) and polyurethane thermoplastic elastomers are based on multiblock architectures. The interested reader should see references 1 and 2 for further reading related to block copolymers and thermoplastic elastomers.

We have not provided a separate section on the application of thermal analysis techniques to copolymers but have incorporated this discussion into the sections on polymer blends. Reference 3 contains a number examples of the uses of thermal analysis in the characterization of block and graft copolymers.

2.2. Polymer blends

Polymer blends are physical mixtures of two or more polymers (these could be homopolymers or copolymers) and are of great technological significance - it has been estimated that $\sim 30\%$ of all polymers are sold in mixed form [4]. Interest in these materials has arisen principally from the ability to modify mechanical properties (*e.g.* rubber toughening) and to tailor properties for particular applications. There have been many advances in the science and engineering of polymer blends in the past two decades and the interested reader is referred to references 4 - 7.

We will focus in the next sections on binary mixtures. The phase behavior of such systems is well known to be a function of temperature, pressure and concentration. The great majority of polymer blends ($\sim 90\%$) have been found to be multiphase - either completely immiscible or multiphase with some limited mixing. This is primarily the result of the small combinatorial entropy of mixing of the dissimilar polymer chains. The remaining portion are single phase, melt-miscible mixtures. The terms 'compatibility' and 'incompatibility' will be avoided as they have been used in a number of different contexts in the literature.

3. POLYMER BLENDS

3.1. Phase behavior - transitional analysis

3.1.1. Background

Many techniques have been used to characterize single *vs.* multiphase character in polymer blends. Optical clarity is often used as a first indication: in

the absence of crystallinity, a single-phase material is expected to be optically clear whereas a multiphase mixture (in which the average dispersed phase size is on the order of the wavelength of visible light or larger) should be opaque. Although useful, there are a number of potential problems including similar refractive indices of the phases, anomalies created as a result of sample preparation, etc. Electron and optical microscopy techniques are used frequently in an attempt to resolve phase structure in polymer blends and block copolymers. Optical microscopy is useful when phase sizes are greater than ca. 1 μm and there is sufficient contrast. Phase contrast is obviously required for transmission electron microscopy as well and this is generally accomplished by using a high electron density staining agent (usually osmium tetroxide or ruthenium tetroxide). The introduction of atomic force microscopy, particularly in the tapping mode, has facilitated characterization of the phase-separated structure of phase separated blends and copolymers.

Measurement of the number and location of glass transition temperatures by thermal analysis techniques is by far the most common approach of assessing phase behavior in a particular temperature range in polymer blends. In a binary mixture, if two T_g s are observed at the same temperatures as those of the component polymers, implying that the polymers are completely immiscible. A single T_g between those of the components indicates miscibility. T_g intervals for miscible polymers are frequently broadened compared to those of the components, as a result of a distribution of local environments. One may also see two T_g s but shifted 'inwards' from the components. This is usually taken to indicate multiphase behavior with some mixing between the components and one sometimes hears such mixtures referred to as being 'partially miscible'. However, as discussed in more detail below, one must take great care when drawing conclusions in the case of multiple T_g s.

A number of expressions have been used to model or predict the T_g of miscible mixtures [8-11]. The Fox-Flory Eq. (11), originally derived for random copolymers, is probably the most widely used:

$$1/T_g = w_1/T_{g1} + w_2/T_{g2} \quad (1)$$

where the w 's represent the weight fractions of components 1 and 2. A more general expression has been proposed by Couchman [10]:

$$\ln T_g = \frac{w_1 \Delta C_{p1} \ln T_{g1} + w_2 \Delta C_{p2} \ln T_{g2}}{w_1 \Delta C_{p1} + w_2 \Delta C_{p2}} \quad (2)$$

where the ΔC_p 's are the heat capacity changes at T_g for the component polymers, as measured by DSC. Eq. (2) reduces to the Fox-Flory expression when $T_{g1} \approx$

T_{g2} and $\Delta C_{p1}T_{g1} \approx \Delta C_{p2}T_{g2}$. Attempts have also been made to connect the experimentally derived T_{gs} of miscible blends to intermolecular interactions (*i.e.*, the polymer-polymer interaction parameter, χ) [12,13]. Some of these approaches use the Gordon-Taylor expression [8] and an additional term related to the interactions. More recently, Painter, *et al.* have proposed an equation for the composition dependence of T_g of miscible mixtures (and random copolymers) involving strong intermolecular interactions like hydrogen bonding [14].

In the case where multiple glass transitions are observed (by DSC or other techniques), one can easily estimate the compositions and amount of each phase, employing a mixing rule such as the Fox-Flory expression. Let ω_1 and ω_2 be the weight fractions of the lower and upper temperature transition phases, respectively. The weight fractions of the two components in the blend are given by $\bar{\omega}_{ij}$ and ω_{ij} . The former notation represents the weight fraction of the i^{th} component (either polymer 1 or 2) in the j^{th} phase (either the lower or upper temperature transition phase), referred to one gram of each phase. The various ω_{ij} are the weight fractions referred to one gram of total sample. A series of algebraic equations can be constructed based on the relationships between the weight fractions defined above as well as the known weight fractions of the polymers in the mixture [15]. (For a crystalline blend, these weight fractions refer to the amorphous phases only.) Choice of a mixing rule is required and allows one to calculate the various $\bar{\omega}_{ij}$ from the experimental transition temperatures.

3.1.2. DSC

Measurement of glass transition temperatures by DSC is rapid, requires only small sample sizes and instruments are widely available. However, the heat capacity change can sometimes be difficult to resolve, particularly for blends containing crystalline polymers, where the transition is relatively broad due to restrictions on the mobility of the amorphous segments by the crystals. There is also difficulty when the T_{gs} of the components are in close proximity. In this case, it may be possible to use the enthalpy relaxation method to resolve the closely spaced transitions [16,17]. This approach involves quenching the blends (and neat polymers) from the melt and physically aging at a temperature below T_g for a given time. The enthalpy relaxation that occurs during this time is recovered during subsequent heating and is characterized by an endothermic peak(s) in the region of the glass transition. The location and magnitude of this peak are a function of the thermal treatment and polymer structure. Comparison of the enthalpy recovery of the blends in question with that of the component polymers can expedite resolution of closely occurring T_{gs} .

DSC has also been used in the characterization of phase separation of miscible polymer blends on heating (*i.e.*, characterization of lower critical solution temperature behavior) [18,19]. Generally, the heat of demixing is relatively small and demixing occurs over a relatively wide temperature range. Therefore the ‘demixing peak’ is not generally observed.

3.1.3. Dynamic mechanical and dielectric measurements

Transitions associated with segmental motion (T_g -like motion) are readily characterized by dynamic mechanical (DMA) and dielectric methods and these techniques have also been routinely used to characterize polymer blends. Analysis is often performed in the temperature ramping mode but a more careful evaluation of the relaxation behavior requires isothermal, frequency-plane measurements. The reader is referred to Chapters 3 and 4 for a complete discussion of mechanical and dielectric analysis, respectively.

Figs. 1a and b give examples of the use of DMA in the characterization of the transitional behavior of miscible and multiphase blends, respectively. Fig. 1a shows the variation of the shear storage modulus (G') and mechanical damping ($\tan\delta$) as a function of temperature at a relatively low frequency for poly(vinylchloride) [PVC], an ethylene/ethyl acrylate/carbon monoxide

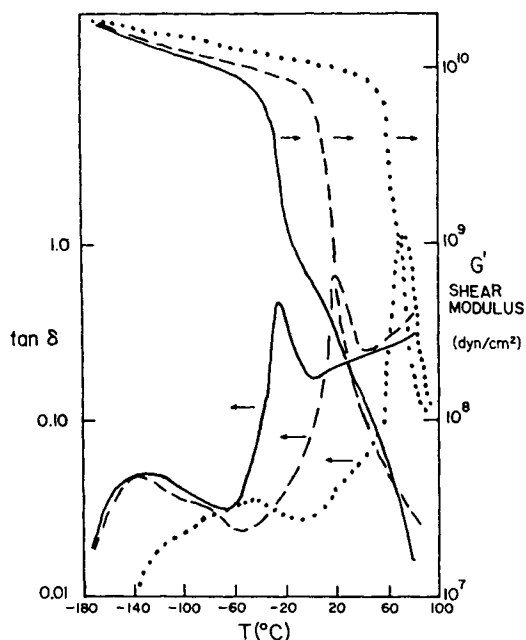


Fig. 1a. Storage shear modulus and $\tan\delta$ vs. temperature for: poly(vinyl chloride); — an ethylene/ethyl acrylate/carbon monoxide terpolymer and; ---- a 50/50 blend of the polymers. Reprinted with permission from reference 20.

terpolymer and a 50/50 blend of the polymers [20]. The blend exhibits a single transition associated with segmental motion (this will be referred to as the α -transition), intermediate in temperature to those of the neat polymers. [The α -transition is that seen near 80°C for PVC and near -20°C for the terpolymer in Fig. 1a]. Thus, these polymers are miscible in this temperature range. The second example is a blend of polystyrene with a relatively small amount of styrene-butadiene random copolymer (the copolymer having a relatively high butadiene content and hence a low T_g) [21]. The storage shear modulus and damping (the logarithmic decrement, proportional to $\tan\delta$) as a function of temperature is shown for one such blend in Fig. 1b. Note that two α -transitions are observed and these are very near those of the component polymers. Electron microscopy on similar blends shows clear evidence of phase separation and thus it is concluded that the multiple α -transitions in Fig. 1b arise from the multiphase structure.

In polymer blends and copolymers with permanent dipole moments, dielectric relaxation measurements have proven to be particularly valuable due to the wide range of frequencies readily available. Dielectric measurements have been used extensively to characterize phase behavior and dynamics in polymer blends and this has been reviewed in a recent publication [22]. In particular, analysis of relaxation spectra associated with T_g of miscible blends has received considerable attention in recent years [23,24]. For multiphase blends and copolymers, care must be exercised in the interpretation of the

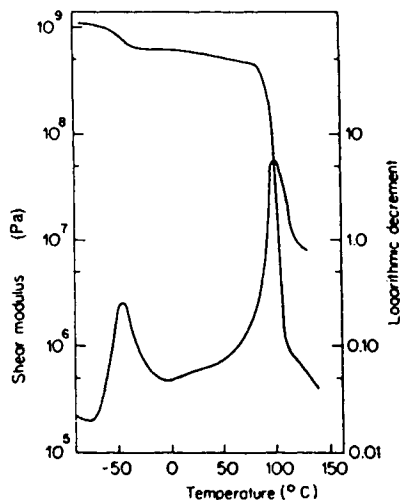


Fig. 1b. Storage shear modulus and logarithmic decrement vs. temperature for a blend of poly(styrene) and a styrene - butadiene random copolymer. Reprinted with permission from reference 21.

dielectric relaxation behavior due to the possibility of Maxwell-Wagner-Sillars (MWS) interfacial polarization. This phenomenon occurs in multiphase systems with non-identical dielectric properties as a result of accumulation of charge at the interfaces and gives rise to relaxation behavior that can be difficult to distinguish from that arising from dipole relaxation. The position, strength and shape of an MWS relaxation depend on the volume fraction, geometry and conductivity of the dispersed phase and the permittivity of the phases. Various theoretical expressions for different dispersed phase geometries and volume fractions have been derived [25], but the morphology of multiphase polymer mixtures is often complex or not well defined, making modeling difficult.

3.1.4. Crystalline blends

In the case where one or both of the components in the blend are crystalline, the interpretation of transitional behavior may not be as straightforward.

For the case of a melt-miscible polymer blend of a semi-crystalline and an amorphous polymer, the length scale over which the diluent diffuses during crystallization is determined by the relationship between the diffusion coefficient of the amorphous polymer and the crystallization rate [26-29]. The diluent polymer can reside in interlamellar regions, interfibrillar regions, between spherulites or some combination of these, as shown in Fig. 2 [27]. Multiple locations for the amorphous polymer would in general be expected to lead to amorphous regions with different compositions and hence different T_g s. Thus, it is natural for a semi-crystalline blend, even though melt-miscible above the melting point, to exhibit multiple T_g s.

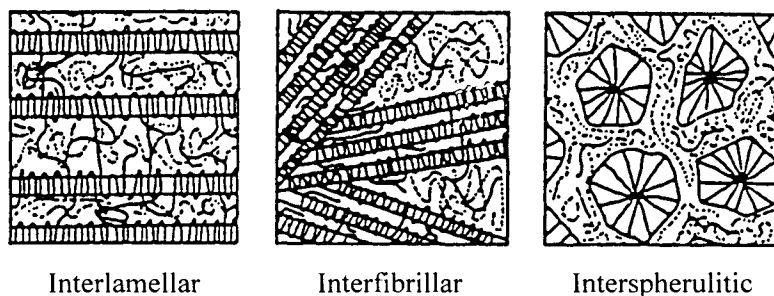


Fig. 2. Schematic drawing of possible modes of diluent segregation on crystallization of a melt-miscible blend of a semi-crystalline and amorphous polymer: (a) interlamellar; (b) interfibrillar; (c) interspherulitic. Note that the magnification increases from right to left in the above drawings. Legend: — semi-crystalline polymer; ···· amorphous polymer. Reprinted with permission from reference 27.

Some rather interesting relaxation behavior (almost exclusively from dielectric measurements) has been reported for melt-miscible, semi-crystalline blends [30-33]. For example, consider the case of blends of poly(methyl methacrylate) [PMMA] and poly(vinylidene fluoride) [PVF₂]. These polymers are well known to be miscible in the melt and PVF₂ crystallizes on cooling from the melt when its composition in the blend is significant. Fig. 3 shows the dielectric loss factor as a function of temperature for PVF₂ and selected PVF₂/PMMA blends [33].

The relaxation near 0°C at this frequency in spectrum of neat PVF₂ has been associated with segmental (T_g -like) motion in the amorphous phase (this is referred to as the β -transition since PVF₂ is semi-crystalline). A mixed phase relaxation is indicated at relatively high temperatures (not shown in Fig. 3). However, note that a relaxation persists in blends that are crystalline at the same temperature as the PVF₂ β process: the relaxation strength decreases with PVF₂ content and the relaxation seems to disappear when the blends are no longer crystalline.

Given the preceding discussion of microstructure and amorphous environment, one might initially speculate that there are amorphous regions with different compositions. However, for materials crystallized under similar conditions, small-angle X-ray scattering experiments have indicated that all PMMA is contained in interlamellar regions. It has been proposed that crystal - amorphous interphases are the microstructural regions responsible for the relaxation in the blends in Fig. 3. Thirty-five years ago, Flory predicted the

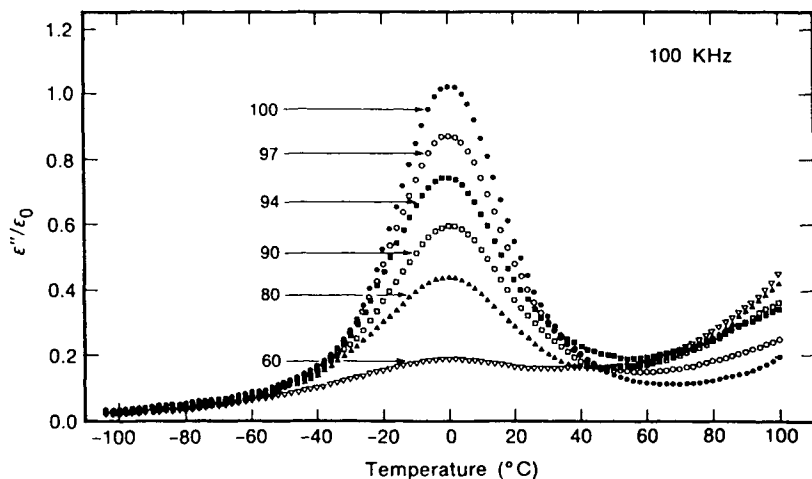


Fig. 3. Dielectric loss factor vs. temperature at 100 kHz for PVF₂ / PMMA blends. The weight percentages of PVF₂ in the blends are noted in the figure. Reprinted with permission from reference 33.

existence of transition regions in semi-crystalline polymers between the crystalline lamella and the isotropic amorphous phase [34]. In the intervening years, the results of many experimental methods have demonstrated the existence of such interphase regions, and sizes have been measured to be on the order of 1 - 3 nm [*e.g.*, 35,36]. Considering that typical polymer lamellae and amorphous regions are ~ 5 - 20 nm thick, these interfacial regions can constitute an appreciable portion of the microstructure and exhibit an important influence on properties. Likewise, the existence of crystal-amorphous interphases has been predicted for the case of melt-miscible blends where one of the components crystallizes, and the interphases are predicted to contain only the crystalline component for blends which do not exhibit strong intermolecular interactions [37].

An alternative explanation for the behavior seen in Fig. 3 arises from a more general phenomenon (*i.e.*, not restricted to crystalline systems) - concentration fluctuations. Concentration fluctuations are intrinsic to miscible blends: there exists a myriad of local environments that fluctuate about the average blend composition [38]. A theoretical model predicts that macroscopically miscible blends with relatively weak intermolecular interactions and large differences in T_g exhibit two 'dynamic microenvironments': one with a mobility close to that of the average blend mobility and another near that of the lower T_g component [39]. Distinct relaxations have been observed in a number of cases for miscible blends [40-42] and it has been proposed as an alternative explanation for the origin of behavior in Fig. 3 [39].

3.2. Crystalline polymer blends and copolymers

The authors have had a continuing interest in blends of two crystalline polymers, where one of the components is a copolymer (either random or blocky). A segment of this work has focused on co-crystal formation and provides a good example of the methodology used to characterize co-crystallization by DSC. The utility of DSC in investigating nucleation by the homopolymer in such mixtures is also demonstrated in this work. We first present some background on the phenomenon of co-crystallization and follow this with some selected examples.

3.2.1. Co-crystallization

The term 'co-crystallization' refers to crystallization of both components in the same lamellar crystals. For co-crystallization to occur the component polymers must exhibit a measure of melt miscibility, their repeat unit chemistry must be similar and their crystal unit cells must exhibit similar lattice parameters.

As a result of these rather restrictive criteria, co-crystallization is a rare phenomenon: there are only a handful of polymer blends in which co-crystal formation has been reasonably well established and in each of these the chemistry of the components is very similar: mixtures of poly(aryl ether ketones) [43], vinylidene fluoride-trifluoroethylene copolymer blends [44] and blends of different polyethylenes (*e.g.* high density and linear low) [45,46].

A variety of experimental techniques have been used to probe for co-crystallization including wide-angle X-ray diffraction (to determine any composition dependent change in lattice parameters) and temperature rising elution fractionation (simultaneous or separate elution of the polymers) [47]. However, the classic approach is to characterize the number of melting points and their location by DSC. Co-crystallization is indicated if one melting endotherm is observed, implying one crystal population containing both polymers. However, lamellar reorganization frequently occurs during heating and, coupled with low polymer thermal conductivity, complicates the melting behavior. Characterization of the crystallization behavior via DSC is also very useful in helping to resolve whether there are one or multiple crystal populations. This is illustrated in the following section.

3.2.2. Crystalline homopolymer - copolymer blends

3.2.2.1. Poly(butylene terephthalate)/poly(ester-ether) copolymers

The first examples are for blends of poly(butylene terephthalate) [PBT] with poly(ester-ether) multiblock copolymers [PEE] containing various 'hard' segment concentrations [48,49]. The hard, crystallizable blocks of the copolymer are chemically identical to the repeating unit structure of PBT, as are the crystal structure and lattice parameters of the hard segment crystals [50]. In addition, PEE copolymers containing ≥ 80 wt % hard segments were found to be miscible with PBT. Thus the stringent requirements for possible co-crystallization are met in blends containing copolymers with high hard segment concentrations.

The melting behavior of completely immiscible blends (PBT/PEE copolymers containing 51 wt% hard segments [PEE-51]) is what would be expected from the melting of two separate crystal populations. This is not the case for melt-miscible blends. Fig. 4 shows the melting behavior of PBT, a PEE copolymer containing 80 wt% hard segments (PEE-80) and a 50/50 blend of the two, crystallized on cooling at 2.5°C/min.

The multiple endotherms result from melting and recrystallization during the DSC experiment and the lower temperature endotherm is closely related to the melting of crystals that existed prior to heating. Thus, the conclusion is reached that the 50/50 blend contains only one crystal population when crystallized in this way. The melting behavior of PBT/PEE-80 blends of different composition crystallized under various conditions exhibit evidence of

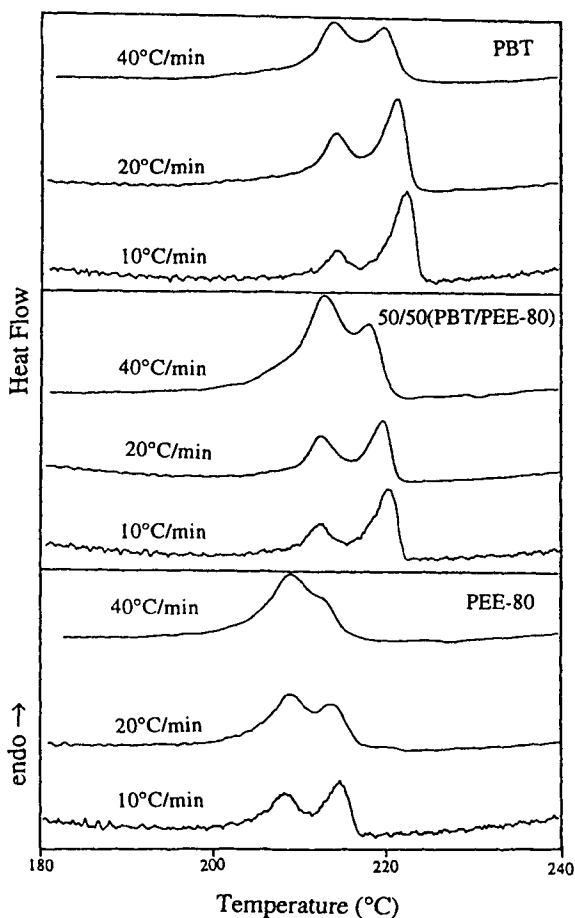


Fig. 4. DSC melting behavior at various heating rates of PBT, PEE-80 and a 50/50 PBT/PEE-80 blend, crystallized on cooling from the melt at 2.5°C/min. Reprinted from reference 48.

only a single crystal population. However, when isothermally crystallized, the melting points of the component polymers are nearly the same and the melting behavior cannot be used to distinguish between separate and co-crystal formation.

The crystallization behavior proves to be particularly insightful in this case. One would generally expect completely immiscible blends like PBT/PEE-51 to exhibit separate crystallization behavior, and this was found to be the case. However, the melt-miscible PBT/PEE-80 blends crystallize very differently, as demonstrated in Figs. 5 and 6. Fig. 5 shows the crystallization behavior (at a cooling rate of 40°C/min) of several PBT/PEE-80 blends, the neat polymers and

a physically mixed sample ("PBT & PEE-80") used to represent the case where the components crystallize separately.

Only one exotherm is observed for the blends and the heats of

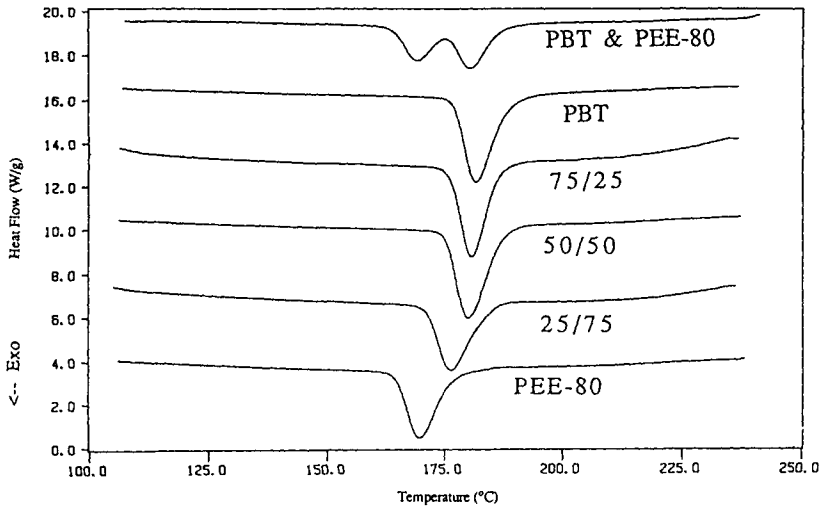


Fig. 5. Crystallization of PBT, PEE-80, three PBT/PEE-80 blends and a physical mixture of PBT and PEE-80 ("PBT & PEE-80") upon cooling from the melt at $40^{\circ}\text{C}/\text{min}$. Reprinted from reference 48.

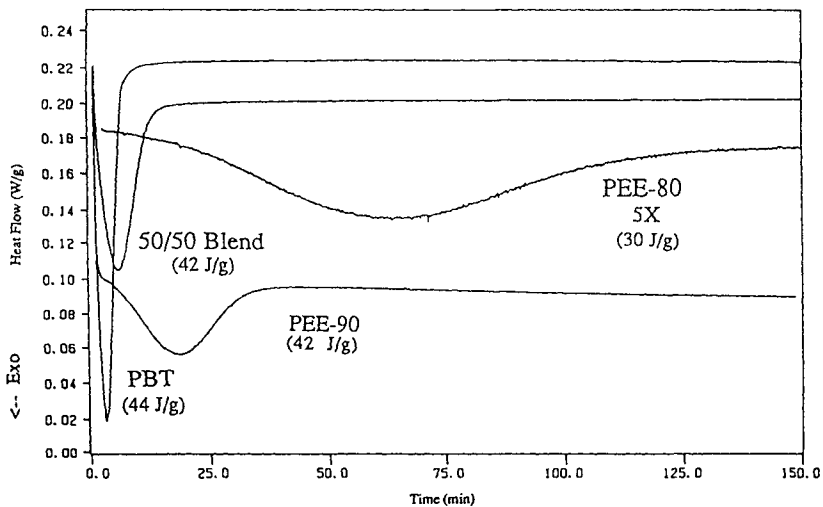


Fig. 6. Isothermal crystallization at 205°C of PBT, PEE copolymers containing 80 and 90 wt% hard segments and a 50/50 blend of PBT and PEE-80. Measured heats of crystallization appear in parentheses under each legend. The PEE-80 curve is magnified by a factor of five. Reprinted from reference 48.

crystallization are between those of the neat polymers. This strongly suggests that PBT and PEE-80 crystallize simultaneously. Such behavior was found at all crystallization conditions explored.

Fig. 6 illustrates typical behavior for the PBT/PEE-80 blends when crystallized under isothermal conditions. Only a single crystallization exotherm is observed for the blends (the 50/50 mixture is shown in Fig. 6). The blends crystallize much faster than a simple average of the component polymers; the crystallization rate for the 50/50 blend is only slightly slower than that of PBT. It is envisioned that, since PBT is more readily crystallizable than the miscible copolymer, a small portion of PBT crystallizes first and acts to nucleate the further crystallization of PBT and PEE-80. All evidence (including that from small angle X-ray scattering) points to co-crystallization between PBT and PEE copolymers that are miscible with PBT, under *all* crystallization conditions. This is distinct from other cases described in the literature where co-crystallization is favored by relatively rapid crystallization conditions, with separate crystallization occurring when crystallization is conducted more slowly.

Homopolymer nucleation is not observed in completely immiscible PBT/PEE blends but is found when there is some limited miscibility. PBT/PEE-65 blends are multiphase in the melt but dielectric measurements indicate that a relatively small amount of the copolymer resides in the PBT-rich phase. The isothermal crystallization (at 195°C) of a 50/50 mixture of PBT and PEE-65 can be seen in Fig. 7. The crystallization of the copolymer itself is found to take about 40 min. at this temperature while neat PBT crystallizes in about 2 min.

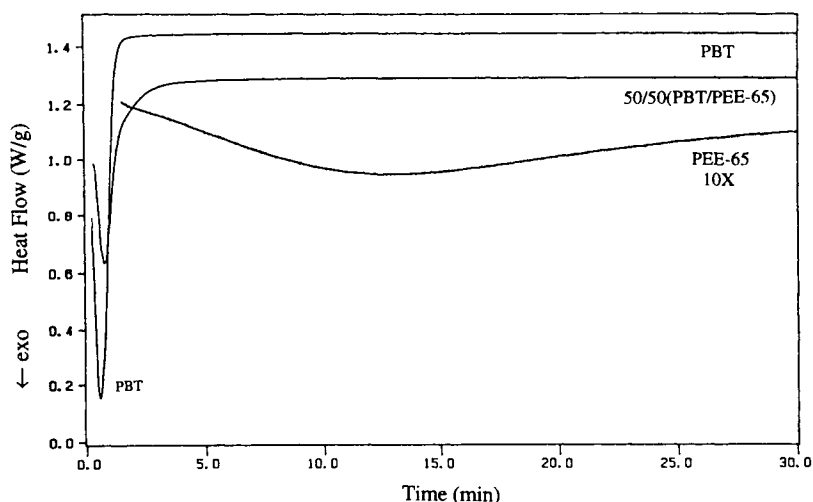


Fig. 7. Isothermal crystallization of PBT, PEE-65 and a 50/50 blend of PBT and PEE-65 at 195°C. The neat copolymer curve is magnified by a factor of ten. Reprinted from reference 48.

The 50/50 PBT/PEE-65 blend exhibits a single crystallization exotherm and crystallization is complete within ~ 5 min., much more like that of PBT. However, on melting, PBT/PEE-65 blends crystallized under isothermal and other conditions exhibit melting behavior indicative of both components. Therefore, although some limited co-crystal formation cannot be ruled out, the most plausible explanation for the observed behavior is that PBT crystals at the phase boundaries serve as nucleation sites for copolymer chains in adjacent phases.

3.2.2.2. *Polytetrafluoroethylene blends*

The second example of the utility of thermal analysis techniques (particularly DSC) in study of crystalline blends are mixtures of poly(tetrafluoroethylene) [PTFE] and poly[tetrafluoroethylene-co-perfluoro(alkylvinyl ether)] (PFA) [51]. PFA is a random copolymer of tetrafluoroethylene and a small amount ($\sim 1 - 2$ mole %) of perfluoropropylvinyl ether. Dynamic mechanical measurements indicate additive behavior of the characteristic crystal - crystal transitions suggesting separate PTFE and PFA crystalline regions when crystallized at moderate rates from the melt. Although the amorphous phase behavior is difficult to assess in these blends due to the uncertain origin of the α transition [52,53], if the α relaxation is associated with segmental motion, the experimental results indicate a single amorphous environment.

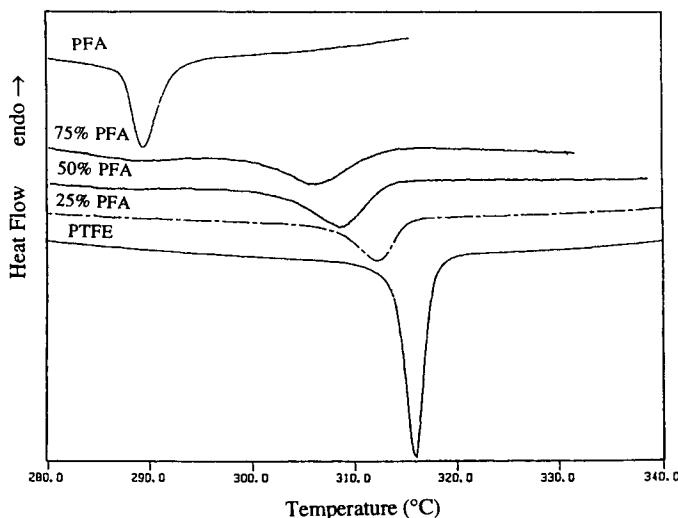


Fig. 8. DSC crystallization behavior (on cooling at $2^{\circ}\text{C}/\text{min}$) after 1 minute in the melt at 400°C . Heating rate = 20°C . Reprinted from reference 51.

As seen in Fig. 8, PTFE has an important influence on the crystallization (nucleation) of PFA. Much (but not all) of the PFA in the blends has concluded crystallization (the blends have intermediate heats of crystallization) at a temperature higher than the onset of crystallization for neat PFA.

Clearly, crystallization of the PTFE and PFA are not separate. Under usual crystallization conditions, blends exhibit multiple crystal disordering transitions (see Fig. 9) indicating that there are sufficiently large spatial regions of crystalline PTFE and PFA. However, a single, intermediate temperature is observed after very rapid crystallization from the melt. It was speculated that co-crystallization was the origin of this behavior [51]. This behavior also lends support to the idea that the polymers are well mixed in the melt.

3.2.3. Melting point depression and the interaction parameter

3.2.3.1. Background

Melting point depression is one of the most popular methods used in attempting to characterize the strength of the intermolecular interactions in binary, miscible polymer blends that contain crystalline polymers. Essentially, one is concerned with comparing the (equilibrium) melting point of a neat crystalline polymer with that of the same polymer in the blend. For two relatively high molecular weight polymers (*i.e.* where the entropy of mixing can be neglected), using the thermodynamics of Scott [54], Nishi and Wang [55] showed:

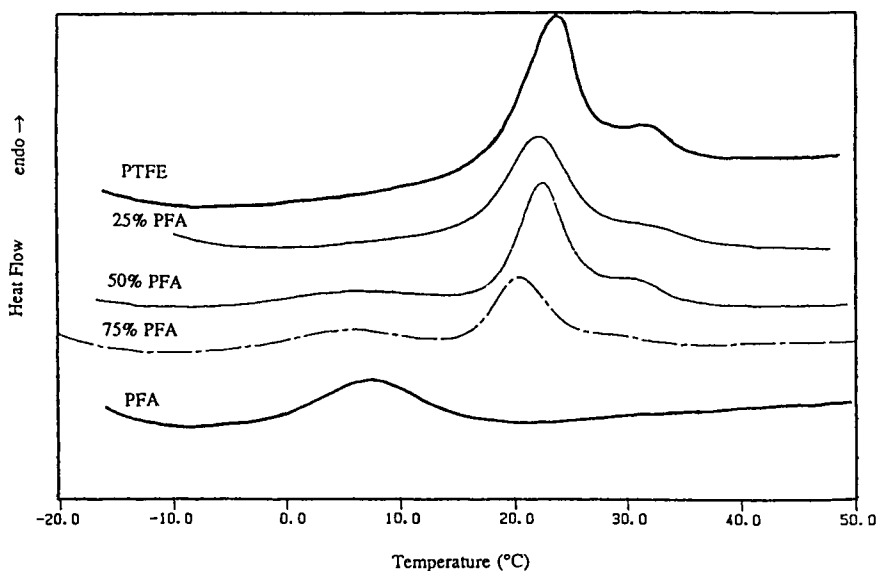


Fig. 9. DSC thermograms of neat PTFE, PFA and selected blends (after hot pressing at 400°C) in the region of the crystal - crystal transitions (heating rate = 20°C/min). Reprinted from reference 51.

$$\frac{1}{T_m^0} - \frac{1}{T_m} = \frac{-R\bar{V}_c}{\Delta H_f^0 \bar{V}_a} (\chi V_a^2) \quad (3)$$

where \bar{V} is the molar volume, V the volume fraction of the component in the mixture, ΔH_f^0 the perfect crystal heat of fusion, R the gas constant, T_m^0 the equilibrium melting point of the neat crystallizable component, $T_m^{0'}$ the equilibrium melting point of the crystalline polymer in the blend and χ the polymer - polymer interaction parameter. The subscripts a and c denote the amorphous and crystalline components, respectively.

Although quite popular, there are several practical difficulties that are sometimes neglected when using this method. A number of earlier papers used experimental melting points from DSC or optical microscopy rather than equilibrium values in Eq. (3), leading to erroneous values of χ . The experimental T_m in a miscible mixture will be related to the thermodynamic depression that arises from the 'solvent' as well the increase in crystal thickness at a given T_c that results from the reduction in degree of supercooling.* Although the thermodynamic term should dominate [56], the depression of the experimental melting point would in general underestimate the equilibrium depression [57,58].

3.2.3.2. *Determination of equilibrium melting points*

One of two extrapolation methods is generally employed for estimation of T_m^0 (or $T_m^{0'}$). The Gibbs-Thomson approach utilizes the relationship between crystal thickness and crystal stability for thin lamellar crystals [59]:

$$T_m = T_m^0 \left[1 - \frac{2\sigma_e}{\Delta H_f^0(l_c)} \right] \quad (4)$$

where T_m is the observed melting point for a crystal of thickness l_c and σ_e the end (fold) surface free energy. T_m^0 and σ_e can be determined from the intercept and slope respectively of a plot of experimental melting points vs. $1/l_c$. Surprisingly, this approach has been rarely used for polymer blends, presumably because it requires determination of l_c , a non-trivial issue. Small-angle X-ray scattering (SAXS) is normally used to determine crystal thicknesses [60], although the Raman longitudinal acoustic mode is a possibility for some polymers as well [e.g. 61,62]. When it is known that the system is completely filled by lamellar stacks, l_c can be obtained from the measured SAXS long

* In fact, the lamellar thickness of the crystalline polymer in a strongly-interacting mixture has been found to increase by as much as a factor of two, when the materials are crystallized at the same T_c [29].

period and *bulk* crystallinity (which in this case is the same as the SAXS crystallinity normal to the lamellar stacks, the so-called linear crystallinity). However, particularly for systems with lower degrees of bulk crystallinity, the bulk and linear crystallinities need not be the same and l_c may be determined from the calculated correlation or interface distribution functions [63]. Even then, one cannot immediately distinguish l_c from the amorphous layer thickness - this requires additional information.

A more popular method is to utilize the Hoffman-Weeks expression, derived from Eq. (4) and several simplifying assumptions [59]:

$$T_m = T_m^0(1 - 1/\gamma) + T_c/\gamma \quad (5)$$

where γ is the factor by which the crystals thicken at T_c . The apparent equilibrium melting point is then obtained from a plot of T_m vs. T_c as the intercept of the extrapolated data with the line $T_m = T_c$ (see for example reference 64).

The popularity of this approach stems from the need to measure only the experimental melting points and the (apparent) ease with which this can be done (see below). However, Hoffman-Weeks plots are sometimes curved making unambiguous estimation of T_m^0 difficult. Moreover, recent papers call into question the general utility of the Hoffman-Weeks expression for determining T_m^0 's [e.g. 65].

A third method has been proposed in which T_m^0 (or $T_m^{0'}$) can be estimated from the statistical fit of spherulitic growth rate data to the Lauritzen-Hoffman (LH) kinetic model [66]. In brief, this procedure is as follows. A seed value for the equilibrium melting point is chosen and a linear regression of the following function conducted using the seed value:

$$\ln G + \frac{U^*}{R(T_c - T_\infty)} \text{ vs. } \frac{1}{T_c(\Delta T)f} \quad (6)$$

where G is the spherulitic growth rate, U^* the activation energy for transport of segments across the melt-crystal interface, T_∞ the temperature below which all viscous flow ceases (often taken as $T_g - 30$ K), ΔT the degree of supercooling ($= T_m^0 - T_c$) and f a function which accounts for the temperature dependence of the heat of fusion. From the linear regression, values of the slope ($= K_g$, the nucleation constant) and intercept (G_0 , the pre-exponential value) are obtained. From the LH kinetic theory:

$$\ln G_0 - \frac{K_g}{T_c(\Delta T)f} = \ln G + \frac{U^*}{R(T_c - T_\infty)} \quad (7)$$

The values of the left hand side of this expression, calculated with the initial K_g and G_0 , are compared to those of the right hand side, which are calculated based on the experimentally measured growth rates. The statistical variance of the fit is determined. The process is continued with different trial T_m^0 values and the value that results in the minimum variance is chosen as the equilibrium melting temperature of the polymer or blend in question. This method has been used successfully on several semi-crystalline polymers including poly(pivalolactone), isotactic poly(styrene) and poly(L-lactide) [PLLA] [66-68]. See reference 66 for further discussion and precautions for utilizing this approach.

As an illustration of the utility of this methodology let us examine the case of PLLA and several random poly(L-lactide-*co*-meso lactide) copolymers. In a recent publication, we explored the lamellar microstructure and crystallization kinetics of four poly(L-lactide-*co*-meso lactide) copolymers having meso concentrations ranging from 0 to 12% [68]. Lamellar thicknesses were derived from SAXS and the Gibbs-Thomson approach was used to determine the equilibrium melting temperatures. There is very good agreement between T_m^0 found for PLLA and values reported in the literature [69,70]. T_m^0 decreases dramatically with increasing meso-lactide concentration in the copolymer as expected: from 214°C for PLLA to about 165°C for the copolymer containing 12% meso-lactide defects, a decrease of ~ 50°C. T_m^0 s derived from the data-fitting procedure of Huang, *et al.* using spherulitic growth rates result in values that are in excellent agreement with those from the classic Gibbs-Thomson approach for PLLA. Since the glass transition temperatures of the copolymers are the same (~ 57°C), the crystallization window narrows significantly with increasing meso-lactide concentration.

3.2.3.3. Experimental melting points - true melting points

Apparent melting points are obviously quite easy to measure with techniques like DSC or optical microscopy. But what are these representative of? What we desire is the 'true' melting point - that associated with melting of crystals of mean thickness l_c that were formed from the crystallization process. However, determining the true T_m is not necessarily a simple matter. It is well known that crystalline lamellae are prone to reorganization during heating in DSC or optical microscopy experiments, particularly at slow heating rates. This can lead to multiple melting peaks or, if there is insufficient resolution (due, for example, to 'large' specimen sizes), a broad endotherm with a T_m higher than the true value. In addition, polymers generally have low thermal conductivity that leads to thermal inhomogeneity during heating and cooling cycles and artificially high melting points, broadened endotherms and lack of resolution between multiple endotherms. This is a strong function of specimen size and geometry and one must minimize specimen size to facilitate heat transfer [71].

If one is only concerned with obtaining a ballpark figure for the melting point of a blend or neat crystalline polymer, then the above issues are of little significance. However, if a detailed analysis is to be undertaken (like determination of T_m^0), these factors are critical and can lead to serious errors in T_m^0 if ignored, regardless of which method is chosen to perform the analysis. As an example, let us take the case of the equilibrium melting point of PBT [72]. An analysis was conducted on melting points determined from hot stage optical microscopy experiments and an apparent T_m^0 of $\sim 260^\circ\text{C}$ was found upon extrapolation, about 25°C higher than T_m^0 reported from melting of PBT oligomers [73]. However, T_m is generally defined as the disappearance of the last traces of birefringence in optical microscopy experiments and heating rates are often on the order of $10^\circ\text{C}/\text{min.}$, frequently too low to inhibit lamellar reorganization during the course of the experiment. Thus, as in the current example, the T_m 's reflect the melting of reorganized crystals and one would expect to arrive at an extrapolated T_m^0 that is significantly higher than the true value. This was confirmed in a parallel set of DSC experiments. Samples sizes of ~ 0.5 mg were used: the location of the apparent melting point was about 2°C higher for samples ~ 4 mg in size. Below 0.5 mg, T_m was independent of size and the same within experimental error as the (extrapolated) T_m at zero sample weight.

3.2.3.4. *Ramifications for estimation of χ*

Clearly, measured T_m s which do not reflect the true melting points of semi-crystalline blends will lead to unreliable $T_m^{0'}$ values and, hence, unreliable χ 's. Even in the case where true T_m s are measured and $T_m^{0'}$ determined carefully, one must take care before treating χ derived in this way with confidence. Reported equilibrium melting point depressions are frequently on the order of ca. 5°C and rarely above 10°C , even at the highest diluent concentrations. Uncertainties in extrapolated $T_m^{0'}$, although infrequently reported, are estimated to be in the range of a few to 5 degree Celsius or more, depending on the quantity and quality of the experimental data. Therefore, relatively small measured melting point depressions are likely to be within experimental error. A careful analysis of the statistical significance of any melting point depression should be conducted prior to attempting to estimate χ using Eq. (3).

ACKNOWLEDGMENTS

The authors would like to express their appreciation to the National Science Foundation (DMR - 9900638) for support of this research.

REFERENCES

1. A. Noshay and J. E. McGrath, *Block Polymers*, Academic Press, New York, 1977.
2. N. R. Legge, G. Holden and H. E. Schroeder (Eds.), *Thermoplastic Elastomers*, A Comprehensive Review, Hanser, New York, 1989.
3. S. W. Shalaby and H. E. Bair, in *Thermal Characterization of Polymeric Materials*, E. A. Turi (ed.), Academic Press, New York, Ch. 4, 1981.
4. L. A. Utracki, *Polymer Alloys and Blends, Thermodynamics and Rheology*, Oxford University Press, Hanser, New York, 1990.
5. D. R. Paul and S. Newman (Eds.), *Polymer Blends*, Vols 1 & 2, Academic Press, New York, 1978.
6. O. Olabisi, L. M. Robeson, M. T. Shaw, *Polymer-Polymer Miscibility*, Academic Press, New York, 1979.
7. M. M. Coleman, J.F. Graf and P.C. Painter, *Specific Interactions and the Miscibility of Polymer Blends*, Technomic Publishing, Lancaster, PA, 1991.
8. H. A. Schneider, *Polymer*, 30 (1989) 771.
9. J. M. Pochan, C. L. Beatty and D. F. Pochan, *Polymer*, 20 (1979) 879.
10. P. R. Couchman, *Phys. Lett.*, 70A (1979) 155.
11. T.G. Fox, *Bull. Am. Phys. Soc.*, 1 (1956) 123.
12. T. K. Kwei, E. M. Pearce, J. R. Pennacchia and M. Charton, *Macromolecules*, 20 (1987) 1174.
13. X. Lu and R. A. Weiss, *Macromolecules*, 25 (1992) 3242.
14. P. C. Painter, J. F. Graf and M. M. Coleman, *Macromolecules*, 24 (1991) 5630.
15. G. S. Rellick and J. Runt, *J. Polym. Sci. Polym. Phys. Ed.*, 24 (1986) 279.
16. M. Bosma, G. ten Brinke and T. S. Ellis, *Macromolecules*, 21 (1988) 1465.
17. A. A. C. M. Oudhuis and G. ten Brinke, *Macromolecules*, 25 (1992) 698.
18. M. Ebert, R. W. Garbella and J. H. Wendorff, *Makromol. Chem. Rapid Commun.*, 7 (1986) 65.
19. J. M. Rodriguez-Parada and V. Percec, *J. Polym. Sci. Polym. Chem. Ed.*, 24 (1986) 579.
20. L. M. Robeson and J. E. McGrath, *Polym. Eng. Sci.*, 17 (1977) 300.
21. L. E. Nielsen, *Mechanical Properties of Polymers*, Van Nostrand Reinhold, New York, 1962.
22. J. Runt, in *Dielectric Spectroscopy of Polymeric Materials: Fundamentals and Applications*, J. Runt and J. J. Fitzgerald (Eds.), ACS Books, Ch. 10, 1997.
23. A. Zetsche and E.W. Fischer, *Acta. Polymer*, 45 (1994) 168.
24. C.M. Roland and K.L. Ngai, *Macromolecules*, 25 (1992) 363.
25. A.M. North, R.A. Pethrick and A.D. Wilson, *Polymer*, 19 (1978) 913.
26. H. D. Keith and F. J. Padden, *J. Appl. Phys.*, 34 (1963) 2409.
27. G. Crevecoeur and G. Goeninx, *Macromolecules*, 24 (1991) 1190.
28. S. D. Hudson, D. D. Davis and A. J. Lovinger, *Macromolecules*, 25 (1992) 1759.
29. S. Talibuddin, L. Wu, J. Runt and J. S. Lin, *Macromolecules*, 29 (1996) 7527.
30. B. Hahn, J. Wendorff and D. Y. Yoon, *Macromolecules*, 18 (1985) 718.
31. D. Y. Yoon, Y. Ando, S. Rozstaczer, S. K. Kumar and G. C. Alfonso, *Macromol. Chem. Macromol. Symp.*, 50 (1991) 183.
32. J. Runt, C. A. Barron, X. Zhang and S. K. Kumar, *Macromolecules*, 24 (1991) 3466.
33. Y. Ando and D. Y. Yoon, *Polym. Preprints*, (Am. Chem. Soc.; Div. Polym. Chem.) 28(1) (1987) 26.
34. P. J. Flory, *J. Am. Chem. Soc.*, 84 (1962) 2857.
35. H. Muira, J. Hirschenger and A. D. English, *Macromolecules*, 23 (1990) 2169.

36. L. Mandelkern, R. G. Alamo and M. A. Kennedy, *Macromolecules*, 23 (1990) 4721.
37. S. K. Kumar and D. Y. Yoon, *Macromolecules*, 22 (1991) 5414.
38. G. Katana, E. W. Fischer, T. Hack, V. Abetz and F. Kremer, *Macromolecules*, 28 (1995) 2714.
39. S. K. Kumar, R. H. Colby, S. H. Anastasiadis and G. Fytas, *J. Chem. Phys.*, 105 (1996) 3777.
40. X. Quan, G. E. Johnson, E. W. Anderson and H. S. Lee, *Macromolecules*, 24 (1991) 6500.
41. G. C. Chung, J. A. Kornfield and S. D. Smith, *Macromolecules*, 27 (1994) 964.
42. A. Alegria, J. Colmenaro, K. L. Ngai and C. M. Roland, *Macromolecules*, 27 (1994) 4486.
43. C. K. Sham, G. Guerra, F. E. Karasz and W.J. MacKnight, *Polymer*, 29 (1988) 1016.
44. H. Tanaka, A. J. Lovinger, D. D. Davis, *J. Polym. Sci. Polym. Phys. Ed.*, 28 (1990) 2183.
45. S. Hu, T. Kyu and R. S. Stein, *J. Polym. Sci. Polym. Phys. Ed.*, 25 (1987) 71.
46. D. R. Norton and A. Kellar, *J. Mater. Sci.*, 19 (1984) 447.
47. M. Farr, Ph. D. Thesis, The Pennsylvania State University, 1990.
48. K. P. Gallagher, X. Zhang, J. P. Runt, G. Hunyh-ba and J. S. Lin, *Macromolecules*, 26 (1993) 588.
49. J. Runt, L. Du, L. M. Martynowicz, D. M. Brezny, M. Mayo, M. E. Hancock, *Macromolecules*, 22 (1989) 3908.
50. R. M. Briber and E. L. Thomas, *Polymer*, 26 (1985) 8.
51. J. Runt, L. Jin, S. Talibuddin and C. R. Davis, *Macromolecules*, 28 (1995) 2781.
52. H.W. Starkweather, *J. Polym. Sci. Polym. Phys Ed.*, 20 (1982) 751.
53. S. F. Lau, J. P. Wesson and B. Wunderlich, *Macromolecules*, 17 (1984) 1102.
54. R. L. Scott, *J. Chem. Phys.*, 17 (1949) 279.
55. T. Nishi and T. T. Wang, *Macromolecules*, 8 (1975) 909.
56. J. Runt, P. B. Rim and S. E. Howe, *Polymer Bulletin*, 11(1984) 517.
57. P. B. Rim and J. Runt, *Macromolecules*, 17 (1984) 1520.
58. K. P. Gallagher and J. Runt, *Polym. Comm.*, 32 (1991) 180.
59. J. D. Hoffman, G. T. Davis and J. I. Lauritzen, Jr. in *Treatise on Solid State Chemistry*, N. B. Hannay (ed.), Vol. 3 (Ch. 7), Plenum Press, New York, 1976.
60. E. Balta Calleja and C. G. Vonk, *X-ray Scattering of Synthetic Polymers*, Elsevier, Amsterdam, 1989.
61. L. Mandelkern, R. G. Alamo and M.A. Kennedy, *Macromolecules*, 23 (1990) 4721.
62. J. Runt, R. Wagner and M. Zimmer, *Macromolecules*, 20 (1987) 2531.
63. G. R. Strobl, M. Schneider and I. Voigt-Martin, *J. Polym. Sci. Polym. Phys. Ed.*, 19 (1980) 1361.
64. A. Eshuis, E. Roerdink and G. Challa, *Polymer*, 23 (1982) 735.
65. H. Marand, J. Xu, J. and S. Srinivas, *Macromolecules*, 31 (1998) 8219.
66. J. Huang, A. Prasad and H. Marand, *Polymer*, 35 (1994) 1896.
67. J. Huang and H. Marand, *Macromolecules*, 30 (1997) 1069.
68. J. Huang, J. Runt, E. Hall, R. Kean, N. Buehler and J. S. Lin, *Macromolecules*, 31 (1998) 2593.
69. R. Vasanthakumar and A. J. Pennings, *Polymer*, 24 (1983) 175.
70. H. Tsuji and Y. Ikada, *Polymer*, 36 (1995) 2709.
71. J. Runt and I. R. Harrison in, *Methods of Experimental Physics*, R. Fava (ed.), Academic Press, New York, Vol. 16B (Ch. 9), 1980.
72. J. Runt, D. M. Miley, X. Zhang, K. P. Gallagher, K. McFeaters and J. Fishburn, *Macromolecules*, 25 (1992) 1929.

73. M. Ebert, R. W. Garbella and J. H. Wendorff, *Makromol. Chem. Rapid Commun.*, 7 (1986) 65.

Chapter 9

Thermosets

Arturo Hale

OFS Laboratories, 600 Mountain Ave., Murray Hill, NJ 07974, U.S.A.

1. INTRODUCTION

The Toltec and Mayan cultures in ancient Mexico used natural rubber to produce balls employed in a “sport” (“*juego de pelota*”, or ball-game) that had deep ritual significance. This material was the basis of the first artificially crosslinked polymer (the first “thermoset”), when MacIntosh and Hancock in England and Goodyear in the United States discovered in 1839 that mixing natural rubber with sulfur gave a moldable composition that could be set by heating (vulcanization) and converted into a useful, non-tacky material [1]. The first all-synthetic thermoset polymer is commonly attributed to Leo Baekland, who in 1907 patented a polymer resulting from the reaction of phenol and formaldehyde (“Bakelite”) [2]. Baekland was the first to successfully commercialize this polymer, but he was not the original inventor. Adolph Bayer had inadvertently obtained this polymer in 1872, and Blumer introduced a commercial phenol-formaldehyde thermoplastic resin in 1902 [3,4]. The field of thermosetting polymers has expanded dramatically since Baekland’s times.

Although the consumption of thermosetting polymers on a weight basis is small compared to the total consumption of synthetic polymers, the importance of thermosetting polymers is far greater than that inferred from sheer tonnage, since these materials are key to a number of different industries, such as aerospace, automotive, electronic, telecommunications, and medical industries, finding applications as high performance composites, adhesives, coatings, insulators, electronic encapsulants, dental materials, body implants, *etc.* Some of the attributes of thermosets include high temperature stability, dimensional stability and resistance to creep, and solvent resistance.

The purpose of this chapter is to describe how calorimetry can be used to study thermosetting polymers. It is intended as a concise guide to teach basic principles and techniques, and it provides practical suggestions for the experimentalist. This work is not meant to be a comprehensive literature survey. For an extensive literature review the reader can consult the excellent

contribution by R. B. Prime [5], which, though “only” a chapter, is actually a thorough treatise on thermosetting polymers.

2. GENERAL CONCEPTS

The term “thermosetting polymer” was originally introduced to describe resins that start out as fluids and solidify or “set” upon heating, in contrast to “thermoplastic polymers,” which become fluid upon heating. The designation “thermosetting polymer,” or “thermoset,” has been expanded to include the general case of resins or monomers that solidify or set *irreversibly*, by any of several mechanisms. Although heating is still the most common way to set off solidification of a thermoset, there are some resins that can set by the action of light, or simply by mixing two components together at room temperature. Even though the last two cases are not thermosets in the semantic sense of the word (since it is not necessary to apply heat in order to solidify the resins), these materials are commonly accepted as thermosets because the solidification process involves an irreversible crosslinking reaction.

The main characteristic that distinguishes thermosets is the irreversibility of the solidification process that takes place as a result of chemical reaction. This chemical reaction is typically a polymerization reaction that leads to a macroscopic network molecule (some exceptions will be described in section 3). The starting point is a group of small molecules in the liquid state. These small molecules start reacting with each other step by step, forming increasingly larger molecules that branch out like a tree. Eventually the branches of different “trees” start merging with each other, forming a network or “crosslinked” structure. Ultimately, all the “trees” end up linked into one giant network. The polymer thus formed will have a permanent shape defined by the shape of the container at the time the network was formed. This polymer is insoluble and infusible as a result of its three-dimensional network structure.

If the viscosity of the resin is monitored as a function of conversion (at a constant temperature), one will observe a behavior that looks qualitatively like the curve shown in Fig. 1a. The viscosity increases gradually at the beginning of the reaction, but its growth accelerates continuously, until its value diverges (becomes infinity) at a certain critical point called the gel point. The gel point is a threshold at which enough “trees” throughout the reacting sample link together to form an incipient network. Before reaching the gel point the sample is a fluid; it cannot support a load without deforming continuously. After reaching the gel point, the sample has some mechanical integrity; it does not flow, and it is capable of supporting a load. This is illustrated in Fig. 1b, which shows how the elastic modulus changes with conversion. Initially the elastic modulus is zero, which means that the sample is a fluid incapable of supporting a load; at the gel

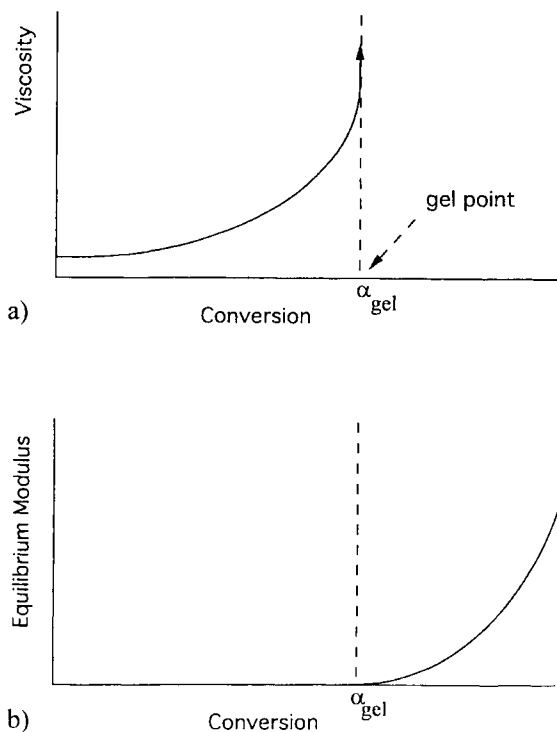


Fig. 1. Qualitative behavior of a thermoset cure. a) Viscosity versus conversion; b) equilibrium modulus versus conversion

point the modulus starts growing. As more and more “trees” get incorporated into the network, this network is capable of bearing larger loads.

It is important to understand that not all the molecules are incorporated into the network at the gel point. In fact, the weight fraction of the molecules that are attached to the network at the gel point is vanishingly small. Up to the gel point, the whole reacting mass is soluble. As the molecules become incorporated to the network, they become insoluble; however, there are still molecules and “trees” that are not incorporated into the network and therefore can be extracted with a solvent. The amount of soluble material as the reaction progresses can be described qualitatively as follows: At any point in time during a thermosetting polymerization there is a mixture of molecules and “trees” of different sizes. After the gel point, the system consists of a macroscopic network embedded in a “sea” of smaller molecules and “trees,” much like a choral reef. As the reaction progresses, these small molecules and “trees” react with each

other and with the macroscopic network, until ultimately they all come to form part of it. Thus the soluble fraction equals one from the beginning of the reaction until the gel point, whereupon it suffers a sharp decrease, reaching zero at full conversion.

From the processing point of view, it is very important to know when the gel point will occur, because after the material gels it will not flow; therefore one has to ensure that, for example, in a molding operation the mold is filled before the polymer gels.

The architecture of the polymer being formed depends on the functionality of the components. The functionality of a molecule is defined as the number of reactive sites present in that molecule. If the components are bifunctional (functionality = 2), a linear polymer chain will be formed. In order to form a network or crosslinked structure, it is necessary to have at least some molecules with a functionality of three or higher.

The extent of reaction at which the polymer gels depends on the functionalities of the components and their stoichiometric ratio. In the case of a step polymerization in which a monomer containing f reactive groups A reacts with a monomer containing g reactive groups B , the extent of reaction α at which gelation occurs is given by [6]

$$r\alpha^2 = 1/[(f-1)(g-1)] \quad (1)$$

where α is the conversion of A groups, and r , the stoichiometric imbalance, is defined as the ratio of A groups to B groups. This equation assumes that the reactivity of all groups is the same.

For example, if the sample consists of a molecule containing four A groups reacting with a molecule containing two B groups, and the mixture is stoichiometrically balanced ($r=1$), the conversion at gelation is $1/[(4-1)(2-1)]^{1/2} = 0.577$.

In the cases where the reactivity of the groups is not the same, or when the reactivity changes as the reaction takes place, Eq. (1) is not valid. These cases have been discussed by Miller and Macosko in a series of papers [7-9].

The discussion so far has focused on one kind of polymerization mechanism: the step mechanism, also known as condensation. This mechanism consists of reactive groups that react with each other one at a time, step by step. Each reaction is an independent event. Examples of step reactions include epoxy-amine reactions, isocyanate-hydroxyl reactions (urethane formation), hydrosilylation reactions, phenol-formaldehyde condensation, *etc.* These reactions will be described in more detail in section 3. There is another kind of reaction mechanism that is very important but is often overlooked in the study of thermosetting polymers: the chain mechanism, also known as addition. In this scheme, a monomer molecule is first activated or "initiated;" this activated

species is very reactive and it can very quickly “sprout” a chain by adding a series of monomers. Two monomers cannot react with one another unless one of them has been “activated.” The chain mechanism leads to different reaction kinetics and a different network buildup than the step mechanism. Chain reactions achieve gelation at a much lower conversion than step reactions. At any given moment, the molecular size distribution is very different in both cases. The molecular weight buildup in a step reaction is more gradual, leading to a broad unimodal molecular weight distribution, whereas a chain reaction builds large molecules very quickly, but has a bimodal molecular weight distribution comprising high molecular weight polymer and unreacted monomer. Examples of materials that polymerize by a chain mechanism include acrylates and methacrylates, vinyls, and cationically-initiated epoxies and vinyl ethers.

Eq. (1) cannot be used to predict the gel point in chain reactions, because the architecture of the network is completely different. Williams and Vallo [10] have published a “recursive fragment approach” to predict network properties of chain polymerized systems.

Once formed, a thermosetting polymer is insoluble and infusible and it has a permanent shape; therefore, any part or artifact made of a thermosetting polymer requires that the polymerization be carried *in situ*. As with any chemical reaction, there is a change in the energetic state of the molecules during polymerization. Some chemical bonds are broken, and new chemical bonds are formed. The net difference between the bond dissociation and bond formation energies will be released or absorbed as heat. The change in Gibbs free energy determines whether a reaction is thermodynamically favored or not. The change in Gibbs free energy is given by

$$\Delta G = \Delta H - T\Delta S \quad (2)$$

where ΔH is the change in enthalpy, T is the absolute temperature, and ΔS is the change in entropy. Since a polymeric structure has a higher degree of order than the original monomers, the change in entropy upon polymerization is negative. This means that $-T\Delta S$ is positive, implying that the change in enthalpy upon polymerization must be negative (and larger in absolute value than $T\Delta S$) in order for the reaction to be thermodynamically favored. This change in enthalpy is released as heat, and is commonly known as the heat of polymerization or heat of reaction. Much of this chapter will be devoted to the measurement of the heat of polymerization and its use to determine extent of reaction and reaction kinetics.

Another important issue with many thermosets is the onset of vitrification during the polymerization reaction. In some systems, as the network crosslinks more and more, a point is reached at which the network is so tight that the molecular segments do not have enough energy to overcome the rotational barriers to motion, and mobility is severely limited. This point, known as

vitrification, is characterized by a sudden stiffening of the material, and a sudden drop in the rate of reaction. This topic will be treated in more detail in section 5.

The interplay between gelation and vitrification can be better understood with the help of a “time-temperature-transformation” (TTT) diagram [11-14], such as the one shown in Fig. 2. This diagram shows the physical state of a thermosetting polymer after a certain reaction time. For example, a system at a temperature between $_{gel}T_g$ and $T_{g\infty}$ starts as a liquid. After reacting for a certain time at this temperature it gels as it crosses the “gelation” line on Fig. 2. It continues reacting in the gel state, until it vitrifies when it crosses the “vitrification” line. At this point the reaction becomes extremely sluggish. If the reaction is carried out at a higher temperature (but still lower than $T_{g\infty}$), both gelation and vitrification will take place sooner because of the faster reaction kinetics. If the reaction temperature is high enough (greater than $T_{g\infty}$), the reaction will proceed without vitrification. For this particular polymer, even if it is fully reacted, the thermal energy available at temperatures greater than $T_{g\infty}$ is enough for the molecular segments to overcome the rotational barriers. Section 5 will deal with this issue in some depth. It is important to note that a TTT diagram is meaningful only if it is read horizontally, that is, it only describes isothermal cures. To build an actual TTT diagram for a real thermosetting system involves measuring experimentally the time to gelation and the time to vitrification at different reaction temperatures. This has been done for a variety

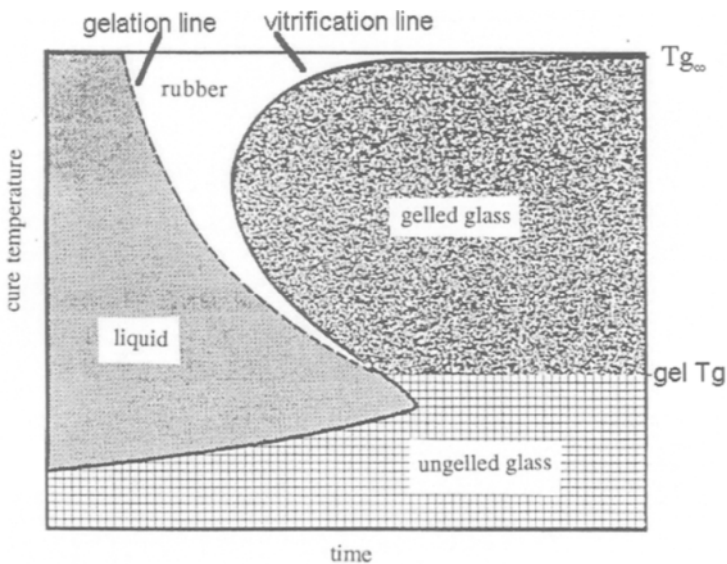


Fig. 2. Time temperature transformation (TTT) cure diagram, after Gillham and coworkers [11-14]

of thermosetting systems by John Gillham's group at Princeton University as well as by researchers elsewhere [11-17].

As discussed in section 8, modulated-temperature DSC can also be used to construct the vitrification curve of the TTT diagram.

3. CHEMISTRY AND APPLICATIONS OF THERMOSETTING POLYMERS

3.1. Phenolic resins

As discussed in section 1, phenolic resins carry the distinction of being the first fully synthetic polymer. These resins are the product of the acid or base catalyzed reaction between phenol and formaldehyde. In the case of acid catalysis, most of the reaction consists of a condensation between phenol and formaldehyde to yield methylene-linked phenols and water as a by-product [3]. In the case of base catalysis, addition of formaldehyde to phenol to form methylolphenols is more common [3]. It is evident that the release of water as a reaction by-product represented a challenge in the manufacturing processes using this resin; indeed it limits the usefulness of employing DSC as an analytical tool unless high pressure capsules or cells are utilized. Baekland's "heat and pressure" patent in 1907 solved this problem and enabled the full commercialization of these resins.

The main attributes of phenolic resins are excellent rigidity, dimensional stability and creep resistance, as well as good electrical properties at elevated temperatures. Phenolic molding compounds always contain fillers; otherwise they would be too brittle.

Phenolic resins are used in the manufacture of plywood and particle board, as well as in molding compounds for electrical applications, brake linings, industrial laminates, and decorative laminates such as "Formica" [3].

3.2. Melamines

Urea resins, the ancestors of melamine resins, were first introduced in the 1920s as molding compounds and as adhesives in the early 1930s. The curing chemistry of these resins consists of a base-catalyzed addition of formaldehyde to urea, forming methylol urea, followed by acid-catalyzed condensation of the methylol groups to form methylol ether bridges and ultimately methylene bridges. The introduction of melamine by Ciba A. G. in 1936 provided a monomer that yielded products that were harder and more resistant to chemicals and water than urea resins [18]. Melamine, also known as 2,4,6-triamino-1,3,5-triazine, reacts with formaldehyde in a similar way as ureas, except that the reaction with melamine occurs more readily and more completely [18].

Melamine molding compounds are best known for their hardness, excellent and permanent colorability, arc-resistant nontracking characteristics, and self-

extinguishing flame resistance. Plates, dinnerware, household goods, kitchen cabinet finishes and some electrical uses constitute the major markets for melamines [18, 19].

3.3. Unsaturated polyesters and vinyl esters

Unsaturated polyester resins are formed by the condensation reaction of a difunctional alcohol with a difunctional carboxylic acid. One of these components, typically the acid, has olefinic unsaturation. The linear polymer thus formed, often called an “alkyd”, can then form a thermoset polymer by crosslinking the double bonds with monomers such as styrene or methacrylates. This crosslinking reaction proceeds by a free-radical mechanism and does not yield by-products. The free radicals to initiate the crosslinking reaction can be generated by the decomposition of peroxides, azo compounds, photo-initiators, or directly by electron beams.

The properties of the final polymer such as rigidity, toughness, flexibility and cost can be tailored to suit the end user's needs by selecting the right combination of acid, alcohol, and monomer raw materials. Commonly used alcohols include propylene glycol, ethylene glycol, dipropylene glycol, diethylene glycol, neopentyl glycol, trimethylolpentanediol, cyclohexane dimethanol, propoxylated bisphenol-A, hydrogenated bisphenol-A, and dibromoneopentyl glycol; acids include phthalic anhydride, maleic anhydride, adipic acid, isophthalic acid, terephthalic acid, fumaric acid, glutaric acid, *etc.*; monomers include styrene, methyl methacrylate, butyl acrylate, butyl methacrylate, alpha-methyl styrene, vinyl toluene, *p*-methyl styrene, diallyl phthalate, diallyl isophthalate, octyl acrylamide, trimethylol propane triacrylate, triallyl cyanurate, triallyl isocyanurate, diallyl maleate, *etc.* [20].

Vinyl esters are the reaction products of epoxy resins with ethylenically unsaturated carboxylic acids. The terminal unsaturation groups of these products are most commonly methacrylates or acrylates. These groups can react with themselves or with added monomers such as styrene to form crosslinked structures. As in the case of unsaturated polyesters, the crosslinking reaction involves a free radical mechanism.

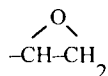
Liquid polyester resins lend themselves very well to casting operations. Some applications include cultured marble and onyx, polymer concrete, and monolithic flooring [20]. Polymer concretes are used to patch highways and bridges because of their fast cure [19].

Unsaturated polyesters and vinyl esters are mostly used in glass-reinforced composites; they are very well suited for processes such as pultrusion, filament winding, injection, compression, and resin transfer molding. Common applications comprise boat hulls, automotive body parts, building panels, housings, bathroom components, pipes and pressure vessels, *etc.* [19].

3.4. Epoxy resins

Epoxy resins are among the most versatile thermosets. Perhaps their best known application is as adhesives, but they have a wide variety of other uses, such as high performance composites for the aerospace and automotive industries, matrix materials for electronic printed circuit boards, encapsulants for integrated circuits, potting compounds, insulators for filament winding and transformers, corrosion- and temperature- resistant coatings, construction materials, *etc.* The literature abounds in monographs about epoxy resins. One of the best is the handbook by Lee and Neville [21]. Although this book is several decades old, it is an excellent reference and most of the information there is still true. A newer comprehensive handbook was published by May and Tanaka [22]. This comprehensive handbook has thousands of references.

The basis of epoxy resins is the epoxide group, also known as oxirane ring:



There are many commercial compounds containing epoxy groups. The most common synthetic routes are oxidation of carbon-carbon double bonds or condensation of hydroxyl groups with epichlorohydrin. These are straightforward, one-step reactions that use readily available reagents; thus, many epoxies are relatively cheap. Epoxy resins were originally developed in the 1930s, but large scale production did not take off until the late 1940s or early 1950s [21]. In the early 1990s, the major producers of epoxy resins sold in the United States were Dow Chemical, Shell, Union Carbide, and Ciba. The last few years of the millennium have been very turbulent for the chemical industry, resulting in a multitude of consolidation and spin-off operations. For example, the epoxy business that used to be part of Shell (the well-known “Epon” family of resins, as well as “Epikote”, “Epirez” and “Epikure” resins) is now Resolution Performance Products (<http://www.resins-versatics.com>); Union Carbide has merged with Dow, and Ciba’s epoxy products are now handled by Vantico. Dow’s epoxy products include the D.E.R. and D.E.N. resins, and Vantico markets the Araldite family of resins.

Probably the most ubiquitous epoxy resin is diglycidyl ether of bisphenol-A (DGEBA). It is widely used for adhesives, coatings and composites. Other important epoxies used for high temperature applications include epoxy novolacs (polyglycidyl ethers of phenol-formaldehyde novolacs) and tetraglycidyl ether of diamino diphenyl methane (TGDDM). These aromatic-based epoxies provide rigid, high T_g thermoset polymers. They can be flexibilized by using reactive aliphatic diluents such as butyl glycidyl ether or polypropylene glycol diglycidyl ether. Cycloaliphatic epoxies such as 3,4-epoxycyclohexylmethyl 3,4-epoxycyclohexanecarboxylate are used as electrical insulators because their

manufacturing process does not introduce ionic impurities; they are also used in UV-curable formulations.

Because epoxy rings are susceptible both to electrophilic attack on its oxygen atom or to nucleophilic attack on its terminal carbon, they can react with either acidic or basic compounds. Epoxies typically react without releasing by-products; the reaction usually proceeds by opening the epoxide ring, with the electron-rich atom of the curing agent (typically nitrogen, oxygen or sulfur) forming a covalent bond with the terminal epoxy carbon, while the epoxide oxygen remains attached to the tertiary carbon and captures a hydrogen from the curing agent to become a pendant hydroxyl. Under some circumstances, this pendant epoxy may react further with remaining epoxy groups (etherification reaction).

Probably the most commonly used curing reaction with epoxies is that with amines. Primary amines are more reactive than secondary amines, and aliphatic amines are more reactive than aromatic amines. Aromatic amines require heating to at least 100°C to initiate the reaction, whereas aliphatic amines start reacting at room temperature. Hydroxyl groups and especially phenolic hydroxyls can accelerate the epoxy-amine cure. Since the reaction of an epoxide with an amine generates a pendant hydroxyl group, this group can itself accelerate the reaction of other epoxy groups, and thus the reaction is autocatalytic. Cycloaliphatic epoxies are not as reactive towards amines as glycidyl ether epoxies. Amine-cured epoxies are widely used as adhesives and as high performance composites for example in aircraft.

Epoxies can also be cured with carboxylic acid or carboxylic acid anhydrides; cycloaliphatic epoxies are more reactive towards these curing agents than glycidyl ether epoxies. Some anhydride-cured epoxies are well known for their outstanding high temperature stability.

Mercaptans can react very quickly with epoxies even at sub-ambient temperatures when the proper catalyst is used (*e.g.* 2,4,6-tris (dimethyl-amino-methyl) phenol).

Phenolic curing agents, catalyzed with imidazoles or tertiary amines, are commonly employed for high-temperature curing epoxies, especially as encapsulants of microelectronic circuits.

Amides and polyamides are also commonly employed as curing agents.

Epoxies can also be homopolymerized either cationically or anionically. These reactions are chain reactions as opposed to the step reactions discussed previously. Cationic polymerization can be initiated by Lewis acids such as BF_3 complexes, or by photogenerated Bronsted acids such as onium salts. The latter will be discussed further in section 7.2. Anionic polymerization of epoxies can be initiated by tertiary amines or imidazoles.

This variety of curing reactions provides the formulator with a multitude of choices of curing agents to tailor the properties of the thermosetting system.

The primary factors affecting the choice of a chemical system for a given application are processing constraints and performance requirements. From the processing point of view, the important parameters are cure temperature, gel time, and viscosity. Some of the important properties of the reacted or cured product include modulus (stiffness), strength, temperature resistance, and chemical resistance. One of the most important properties of a thermosetting polymer is its glass transition temperature, the temperature at which the rigid glass softens and becomes a rubber. Since thermosetting materials are crosslinked, they do not melt and flow upon heating. At a high enough temperature there will be enough energy for the molecular segments to rearrange and relax, but since they are all tied together by the crosslinks, they will not flow. This phenomenon, known as the glass transition temperature, will be discussed in more detail in section 5.

3.5. Thermoset polyurethanes

Polyurethanes are the reaction products of molecules containing isocyanate groups (-N=C=O) with molecules containing hydroxyl groups. The step-addition reaction can be catalyzed with tertiary amines or with tin compounds (*e.g.* dibutyltin dilaurate), and it proceeds without evolution of by-products to produce a urethane linkage $[\text{-NH-C(=O)-O-}]$. Polyurethanes were invented by Otto Bayer in 1937 [23]. The wide variety of hydroxyl-containing molecules (polyols), and, to a lesser extent, of isocyanate-containing molecules available, leads to incredible versatility to formulate polyurethanes, from soft rubbers to hard coatings. They are used as adhesives, sealants, coatings, flexible and rigid foams, on automotive parts, *etc.* They are tough, abrasion-resistant materials thanks to high inter-chain cohesion provided by strong hydrogen bonding. In addition, many formulations are engineered to phase-separate during polymerization, generating rubbery domains in hard matrices or hard, reinforcing domains in rubbery matrices, both cases contributing to improved toughness.

Formation of polyurethanes can proceed extremely fast even at room temperature. This feature is exploited in reaction injection molding (RIM), a process in which two liquid reagents are mixed as they are injected into a mold; the polymerization reaction proceeds very swiftly, and a solid part can be taken out of the mold seconds to a few minutes after injection [24].

3.6. Bismaleimides

Bismaleimides are synthesized by the condensation reaction of maleic anhydride with a diamine such as methylene dianiline. They undergo crosslinking at high temperatures through the C=C residual unsaturation. Bismaleimides are used in applications where the heat resistance of epoxies is not sufficient, having the capability of performing at continuous use

temperatures of 200°C – 230°C [19]. Bismaleimides are used as heat resistant coatings, as well as in the manufacture of printed circuit boards and composites for military aircraft and aerospace applications.

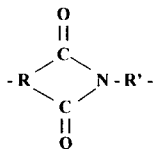
3.7. Cyanate ester resins

Cyanate ester resins contain the $-O-C\equiv N$ reactive group attached to a phenyl ring. They cure through a cyclo-trimerization reaction in which three $-O-C\equiv N$ groups form a cyanurate ring. A practical synthetic route to manufacturing stable cyanate esters was developed by Bayer in the 1960s[25], but these resins did not become commercially available until 1976 [26]. The consolidations and divestitures suffered by the chemical industry also affected cyanate ester resins, which are now marketed by Vantico under the “AroCy” brand name. An excellent monograph on cyanate ester resins has been published [27].

Cyanate esters have very good processing characteristics, high temperature stability, and very low water absorption as compared to epoxies and bismaleimides. They can be employed as composites for aircraft, encapsulants for microelectronics, printed circuit boards, *etc.* Their low dielectric loss and low water absorption are probably the main advantages with respect to epoxies, although these features come at a price.

3.8. Polyimides

Polyimides are widely known for their outstanding high temperature resistance. Polyimides are polymers that contain the following imide structure in the polymer backbone:



This structure has exceptional thermo-oxidative stability. The *R* groups are usually aromatic moieties. The most commonly used polyimides are regarded as thermosetting polymers because they are processed like thermosets, but they are actually linear, non-crosslinked polymers. During the processing procedure, one starts with a somewhat dilute solution of a polyimide precursor (typically a polyamic acid or an amic ester intermediate), which is coated or processed in the desired way. The solvent is then evaporated, and the precursor is cured at high temperatures, causing a cyclodehydration reaction (imidization) to occur. This reaction stiffens the backbone considerably, leading to a thermo-oxidatively stable, high T_g linear polymer. The T_g is so high that the fully cured polymer cannot be processed without thermal degradation – thus these polymers

are regarded as thermosets. The imidization reaction requires temperatures greater than 140°C, and usually as high as 300°C to ensure cyclization [28]. Some popular polyimides are based on pyromellitic anhydride and di-(4-aminophenyl)ether, for example DuPont's Kapton[®] (supplied as film) and Vespel[®] (supplied as sintered parts) [28].

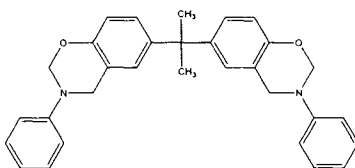
In addition there are true thermoplastic polyimides, in which flexible linkages have been introduced into the backbone to provide melt processability. An example of this family of polyimides is General Electric's Ultem[®].

Another class of polyimides is exemplified by PMR-15, originally developed by NASA and now available commercially from HyComp Inc. as HyComp[®]-100 resin. These resins are based on low molecular weight precursors that can be processed as concentrated solutions or as powders; the resulting polymers are rated for 230°C - 290°C use temperatures.

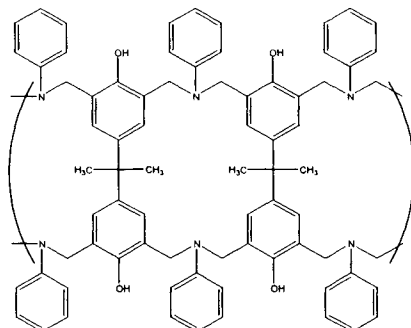
Polyimides in general have high impact and tensile strength on top of their outstanding high temperature resistance. Applications include aerospace, (engine components, insulation for wire and cable, bearings), chip carrier for integrated circuits, printed wiring boards, coatings, and films for electric motors [19].

3.9. Benzoxazine resins

An exciting recent development in the thermoset field is the introduction of thermosetting polymers based on benzoxazine groups. The following monomer



undergoes polymerization starting at 150°C to yield the following polymer[29]:



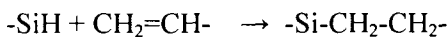
The polymerization takes place without releasing by-products. Benzoxazine resins, marketed by HyComp (HyComp[®]500) and by Shikoku Chemicals corporation, are claimed to withstand continuous use temperatures of up to 230°C, have good dielectric properties, and near zero cure-shrinkage. These resins can reportedly be co-cured with epoxies and with phenolics.

3.10. Silicon-based polymers

Crosslinked polymers based on poly(dimethylsiloxane) (PDMS), commonly called silicones, are widely used as adhesives, encapsulants and sealants. These polymers are usually very soft and compliant, and have very low T_g s. In addition they exhibit very high thermal stability. PDMS can easily be functionalized not only at the ends of the chain but also as pendant groups throughout the chain. Probably the most commonly used reactive groups are SiOH and acetoxy groups, which in the presence of atmospheric moisture will condense to form Si-O-Si linkages, yielding acetic acid as a by-product (hence the vinegar odor released by many “RTV” (room temperature vulcanization) silicone sealants). SiOH groups can also condense with alkoxy groups to form SiOSi linkages, with the release of the corresponding alcohol; they can also condense among themselves with the release of water.

PDMS can also be functionalized with epoxy groups, amine groups, isocyanate groups, *etc.*, and then the crosslinking reaction will proceed as discussed in previous sections.

A very useful curing reaction employed with silicones is the hydrosilylation reaction, also known as hydrosilation reaction. This reaction consists in the addition of silicon hydride (SiH) to a vinyl bond:



This reaction is catalyzed by platinum. By using different platinum complexes, the reaction can be tailored to occur quickly or slowly at either room temperature or higher temperatures. It is very attractive because there is no release of by-products.

4. DETERMINATION OF EXTENT OF CURE

The physical properties of a thermosetting polymer depend strongly on the extent of cure. An improperly cured polymer will have lower solvent resistance, lower modulus and lower heat resistance than a fully cured material. Many instances of underperforming products can be traced to an incomplete cure.

Differential scanning calorimetry (DSC) provides a simple yet powerful way to analyze thermosetting polymers for extent of cure. As mentioned in section 2, thermosetting polymerizations are accompanied by a release of heat.

The amount of heat released is proportional to the number of groups that have reacted. Each chemical reaction has a characteristic heat of reaction per mole of reacting unit. Since DSC can measure directly the heat evolved by a reaction, it can be used to quantify the number of reactive groups that have reacted. If one does not know off-hand (from the literature or from previous experience) the molar heat of reaction of the chemical system one is studying and the concentration of reactive groups, then the first step needed when DSC is used for determining extent of cure is to measure the total heat of reaction of a sample that starts out completely unreacted. This is most conveniently done by a “dynamic scan,” an experiment in which the temperature is ramped linearly. The heat of reaction appears as an exothermic peak in the DSC scan; integration of this peak provides a quantitative measure of the heat of reaction. An example is shown in Fig. 3. The following experimental procedure is recommended:

4.1. Sample preparation

It is very important to ensure that the sample is in intimate contact with the bottom of the crucible that holds it. Liquid samples pose no problem in this regard, but if a sample is solid, one should try to maximize this contact. The ideal sample is a flat, thin film. If the sample is a powder, it is advisable to pelletize it provided a suitable press is available; otherwise one can compact the

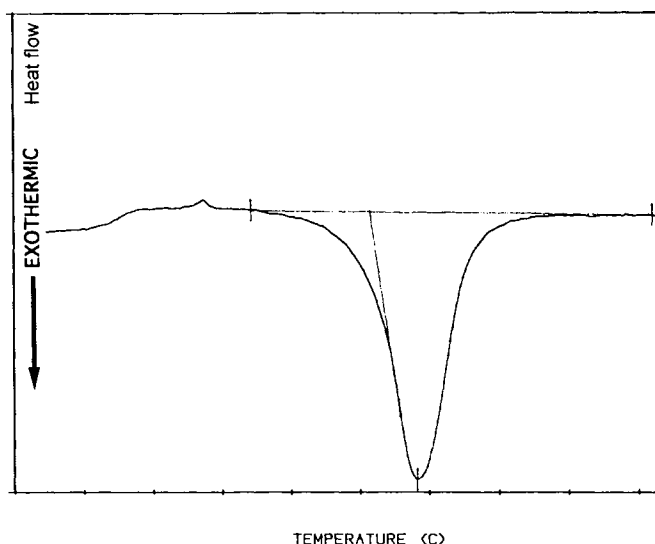


Fig. 3. Typical DSC scan of a thermosetting resin, showing first the glass transition temperature of the unreacted resin, followed by a very small melting peak of a mold-release additive, and then by the large exothermic peak corresponding to the heat of reaction.

powder inside the crucible by lightly hammering down using a flat-headed rod. Some DSC crucibles come with a lid that presses down against the sample when it is crimped. It is important to have an accurate measure of the sample weight. The accuracy of the heat of reaction measurement is only as good as the weight measurement. The recommended sample weight is a tradeoff between sensitivity and thermal conductivity-related delays. A large sample weight will give a stronger signal, but the heat conduction through a thick sample will cause a somewhat delayed reading. Recommended sample weights are between 5 and 20 mg.

Some samples may evolve volatiles as a result either of residual solvent evaporation or as a reaction by-product in the case of condensation reactions. In these cases, the enthalpy of vaporization and the loss of mass will cause the baseline to shift, leading to erroneous results. This problem can be mitigated by employing high-pressure DSC pans. The draw-back of this solution is that these pans usually made of steel, are heavy and have lower thermal conductivity, thus adversely affecting the sensitivity and response time of the instrument. Some manufacturers offer high pressure DSC cells. In the case of residual solvent, attempts should be made to remove the solvent before the DSC run, if at all possible. Although drying the sample in vacuum at room temperature may help somewhat, it usually is not enough, since a good portion of the solvent may remain associated with the sample if the latter is solid. The only way to completely remove solvent in solid samples is to heat them above their glass transition temperatures to allow the solvent to escape, although of course this might lead to some advancement of the chemical reaction in some systems.

4.2. DSC experimental parameters

The next question is what values to choose for the initial temperature, final temperature, and heating rate of the DSC experiment.

4.2.1. Initial temperature

The selection of the initial temperature obviously depends on the temperature at which the thermoset starts reacting. If the system reacts at room temperature, then some information will be lost during the time that the sample is mixed and weighed, since some reaction will take place unrecorded. Because the DSC usually shows some transient behavior at the beginning of a heating ramp, it is advisable to start the run at least 20°C below the expected onset of the reaction. It is preferable, if at all possible, to start at an even lower temperature, for example 40°C below the expected start of the reaction. This will provide a more reliable baseline for subsequent integration. If any cooling below room temperature is involved, one should be on the lookout for the possibility of phase separation in the sample.

4.2.2. Final temperature

The final temperature should be high enough to allow the reaction to go to completion, yet low enough to prevent thermal decomposition. Epoxies can typically be scanned up to 250 - 275°C. At around 300°C one may see some indications of thermal degradation, which reveals itself as the onset of a new exotherm. Urethanes and esters may show indication of thermal degradation at lower temperatures. Other materials such as polyimides, on the other hand, can withstand much higher temperatures. Ideally one wants a final temperature that will allow full development of the exotherm curve and a flat baseline at the end of the run. Some times this may not be possible because thermal decomposition may begin almost immediately after the reaction is completed. In such cases one should try to optimize the heating rate.

4.2.3. Heating rate

The optimum heating rate is a tradeoff between instrumental sensitivity and allowing enough time for the reaction to be completed. The signal detected by the DSC is directly proportional to the heating rate. Thus, the signal in an experiment run at 20°C/min is twice as strong as that of an experiment carried out at 10°C/min. On the other hand, within a given temperature interval, a faster heating rate implies that the sample has a shorter residence time; a longer heating rate provides the sample with more time to react. It is common to employ heating rates between 5 and 20°C/min. In order to select the appropriate heating rate, one should select the fastest rate that still allows enough time for the reaction to be completed, as indicated by a fully developed exotherm peak with straight baselines on either side of the peak. The most accurate way to select the appropriate heating rate is to run several samples at different heating rates, integrate the area under the peak, and select the heating rate that provides the largest value of heat of reaction. Ideally the heat of reaction should be independent of heating rate, but the measured heat of reaction could be lower than expected for several reasons: a) If the heating rate is too fast, there may not be enough time for the reaction to proceed to completion; b) if the heating rate is too slow, the signal may be too low for the instrument to detect all of the heat being evolved. The effect of heating rate on the measure heat of reaction has been studied by Fava [30].

4.3. Determination of normalized extent of reaction

The simplest way to measure the extent of cure of a partially reacted sample involves scanning it in the DSC to measure any residual exotherm, and comparing this residual exotherm to the heat of reaction measured on a completely unreacted sample. The conversion or extent of reaction can be calculated from

$$\alpha = 1 - \Delta H_{\text{res}}/\Delta H_{\text{dyn}} \quad (3)$$

where ΔH_{res} is the residual heat of reaction measured from the sample in question, and ΔH_{dyn} is the heat of reaction measured from a dynamic scan of a “fresh” unreacted sample of the same thermosetting material.

It is very important to keep in mind that this procedure only provides relative numbers for conversion that are normalized. Thus if one observes no residual heat of reaction, the implication is that the sample is fully reacted, *i.e.* $\alpha=1$. In most cases this is not quite true, although it may be enough for practical purposes.

4.4. Determination of absolute extent of reaction

The absolute extent of reaction is defined as the fraction of reactive groups that are actually reacted. The procedure described in the previous paragraph only provides a relative number; it only gives the fraction of reacted groups out of reactive groups that could react within the topological and time constraints of the experiment. In reality there may be more groups that are left unreacted but cannot react because of topological limitations. These topological limitations are caused by the crosslinked structure of the polymer. A number of reactive groups are constrained by the network from moving too far, thus preventing them from reacting with other constrained groups. Thus it is impossible to achieve true 100% conversion in a thermosetting polymer formed by the polymerization of multifunctional monomers [31,32]. Since these topologically restricted groups will not react during the DSC measurements, ΔH_{dyn} does not represent the true full heat of reaction. The method described in the previous paragraph is still useful because, even though it does not provide the true extent of reaction, it does give a relative extent of reaction that indicates how many of the groups that can realistically be expected to react within the given experimental conditions have actually reacted.

In order to determine the absolute extent of reaction, one needs to measure the *total* heat of reaction of a sample in which *all* the reactive groups are allowed to react. The best way to achieve this is to measure the heat of reaction of monofunctional model compounds that have the same reactive groups as the sample of interest. The reaction of monofunctional compounds is not hampered by topological limitations, and the heat of reaction per mole of reactive group is the same for the monofunctional or the polyfunctional compounds. For example, a stoichiometric mixture of a polyfunctional epoxy cresol novolac and a cresol novolac hardener, shown in Fig. 4, does not react to completion because of topological limitations. Solid state NMR reveals the presence of unreacted epoxide groups even after the mixture has been “fully” cured. In order to measure the total heat of reaction, one can employ phenyl glycidyl ether and *o*-cresol as model compounds (Fig. 5). Using these model compounds, the

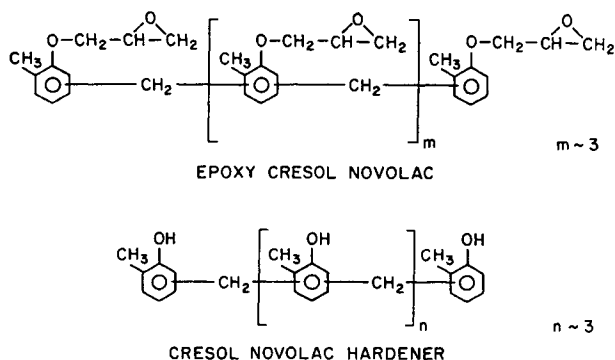


Fig. 4. Molecular structures of epoxy cresol novolac and cresol novolac hardener resins.

enthalpy of reaction of an epoxide with a phenolic hydroxyl has been measured to be -20.7 kcal/mol (-86.7 kJ/mol) [33]. Another option is to use theoretical or experimental ΔH values from the literature. Some values for common reactions are summarized in section 4.5.

Once one has the true total heat of reaction ΔH_{tot} , the absolute conversion is given by

$$\alpha = [\Delta H_{\text{dyn}} - \Delta H_{\text{res}}] / \Delta H_{\text{tot}} + \alpha_0 \quad (4)$$

where α_0 accounts for any small amount of reaction that may take place between the time that the sample is mixed together and the time ΔH_{dyn} is measured. α_0 could be significant if the components are mixed at elevated temperatures. In general it must be measured independently, for example by titration (in the case of epoxies, a titration procedure is described in ASTM-D1652). The use of Eqs. (3) and (4) can be better understood by looking at the following examples.

Example 1: A customer complains that parts made using an epoxy made by Company X are not meeting adhesion strength specifications. The customer mails Company X some of these parts. The first step Company X takes is to determine whether the epoxy has been properly cured. To do this some epoxy is removed from the part, and a dynamic DSC test is run on it. The DSC shows a small exothermic peak (residual heat of reaction) whose integral indicates an exotherm $\Delta H_{\text{res}} = -60$ J/g. A DSC scan of a fresh, unreacted sample of the same epoxy yields an exotherm $\Delta H_{\text{dyn}} = -300$ J/g. This scan shows the “total” heat of reaction. As discussed above, this may not be the true total heat of reaction, but for practical purposes it is a measure of the total number of reactive groups that can realistically react for this epoxy. Thus, the (normalized) extent of reaction of the tested sample is given by Eq. (3):

$$\alpha = 1 - \Delta H_{\text{res}}/\Delta H_{\text{dyn}} = 1 - 60/300 = 0.8$$

In other words, the sample is only 80% reacted, and therefore it does not possess the full adhesive strength it is capable of. This result seems to indicate an improper cure schedule by the customer.

Example 2. Determination of the “true” conversion of a partially reacted sample. Sample A is a partially cured sample consisting of an epoxy novolac cured with a phenolic novolac (Fig. 4). This partially cured sample is placed in the DSC for a dynamic scan, obtaining a small exotherm which upon integration yields $\Delta H_{\text{res}} = -75$ J/g. A dynamic scan of a fresh, unreacted sample of this material produces an exotherm of $\Delta H_{\text{dyn}} = -198.2$ J/g. Thus, the normalized conversion is given by

$$\alpha = 1 - \Delta H_{\text{res}}/\Delta H_{\text{dyn}} = 1 - 75/198.2 = 0.62$$

However, the high functionality of the monomers of this composition leads to a very highly crosslinked network. At some point, some reactive groups will be “pinned” down in place by its reacted neighbors, and the only other groups available for reaction may be pinned down at a different, unreachable location on the network. At this stage, the network may be “fully” reacted for most practical purposes in the sense that the available unreacted groups cannot react with each other because they are topologically limited. The reaction has gone as far as it can go. However, there are still unreacted groups that can be detected spectroscopically. One can also use thermal analysis to determine how many of these unreacted groups remain. To this end, one must determine the true total heat of reaction for this sample assuming all the reactive groups can find each other. One way to do this is to measure the heat of reaction of model *monofunctional* monomers containing the same reactive groups as the ones under study. As these monofunctional monomers react, they form dimers. There is no network formation to hinder the mobility or accessibility of the reaction groups. Thus one can measure the full heat of reaction per mole of reactive group. Appropriate model compounds for this example are *o*-cresyl glycidyl ether and *o*-cresol, shown in Fig. 5. The heat of reaction of these compounds is measured

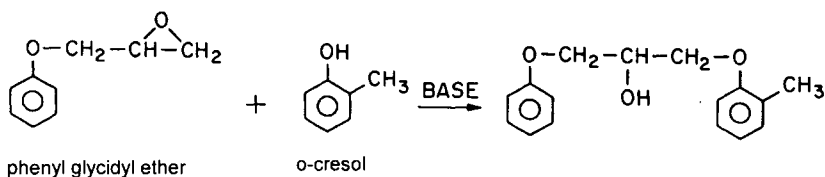


Fig. 5. Model compounds used to study the reaction between epoxies and phenolic hydroxyls.

by the DSC in J/g units. This number is converted to heat per *mole* of epoxy, obtaining $\Delta H_{\text{tot}} = -86.7$ kJ/mol. The multifunctional epoxy-novolac in Fig. 4 should have the same heat of reaction per mole epoxy if all the epoxies could react. From the chemical formula and the original mixing ratio of the components one can determine that the equivalent weight per mole of epoxy in this resin is 341 g/mol. If all the epoxy groups could react, the reaction exotherm would be $(-86,700 \text{ J/mol}) / (341 \text{ g/mol}) = -254 \text{ J/g}$. This is the total heat of reaction ΔH_{tot} . Therefore, using Eq. (4), the “true” conversion of Sample A is:

$$\alpha = [\Delta H_{\text{dyn}} - \Delta H_{\text{res}}] / \Delta H_{\text{tot}} = [198.2 - 75] / 254 = 0.485$$

In this example we have not taken into account the term α_0 . This term accounts for any reaction that may have taken place during the mixing process of the epoxy and the curing agent. In most cases this value is small, but if one suspects it plays a role it should be determined independently, for example by titration.

It is important to note that in order to obtain a meaningful conversion value, the upper temperature of the DSC scan must exceed the glass transition temperature of the fully cured material (see next section).

4.5. Heats of reaction of selected groups

Prime [5] has compiled values of heats of reaction obtained from several literature sources. Some of these values are summarized here:

Epoxy-amine: from -102 to -110 kJ/mol.

Epoxy-phenol: -86.7 kJ/mol

Cyanate ester cyclotrimerization: from -92 to -115 kJ/mol

C=C polymerization (styrene/vinyl esters): -69 kJ/mol

Acrylate photo-polymerization: from -78 to -86 kJ/mol

In addition, Macosko [24] has summarized polymerization reactions measured for polyurethanes and polyureas:

Aromatic isocyanate – hydroxyl: -84 kJ/mol

Aromatic isocyanate – amine: from -93 to -112 kJ/mol

5. GLASS TRANSITION TEMPERATURE

5.1. Generalities

The glass transition temperature (T_g) is a key parameter in thermosetting polymers, not only from the product performance point of view, but also from the processing point of view, since it may strongly affect the reaction kinetics. The glass transition temperature marks the boundary between the glassy, rigid

state of a polymer and the soft, flexible (or fluid) state of the polymer. Below the glass transition temperature, the available energy is insufficient to allow the molecules coordinated mobility (although there may be some localized motion), so the material is rigid; above the glass transition, the molecules can cooperatively relax. In the case of a linear polymer, the molecules can flow past each other above the glass transition temperature – the polymer is a “melt.” In the case of thermoset polymers above the glass transition temperature, the chemical crosslinks prevent the molecules from flowing, but there is enough mobility for molecules to cooperatively relax, and the polymer becomes flexible and “rubbery.” The concept of cooperative motion that characterizes T_g can be more readily understood by making an analogy to the crowds that pack a subway car in New York City during rush hour. If somebody wants to scratch his head, he may find that there is not enough room for his arm to move up to his head. However, if someone else about 10 feet away moves around a little, and the person next to her shifts slightly, and so on, eventually there may be a slight opening that will allow our friend to stretch his arm and scratch his head. This cooperative motion involving several people is akin to the cooperative motion that different segments of the polymer undergo at the glass transition temperature. It should be kept in mind, though, that even after softening, the polymer will tend to retain its shape. It will not flow because the chemical crosslinks hold the structure together.

The importance of T_g is obvious from the performance standpoint. If the polymer is used as a load-bearing structural element, T_g defines an upper bound for its use temperature. For example, if certain polymer is used as part of the body of an airplane, one needs to ensure that the polymer will not be exposed to a temperature higher than its glass transition to keep it in its rigid state, since above T_g the polymer will soften. On the other hand, if the polymer is being employed as a flexible rubber, then T_g represents a lower bound on its use temperature. Failure to recognize this has led to tragic consequences; for example, a few years ago an o-ring in the space shuttle lost its flexibility by being cooled below its T_g , leading to a fuel leak that caused a catastrophic explosion.

As a polymer is heated through its glass transition temperature, several changes take place. Quantitatively, the change from “rigid” to “rubbery” means that the elastic modulus drops by several orders of magnitude. The modulus of practically all neat (no inorganic filler) glassy polymers is on the order of a single digit multiple of 10^9 Pa. As the polymer is heated through its glass transition temperature, the modulus can drop several orders of magnitude depending on the crosslink density. For very lightly crosslinked systems, the modulus above T_g is on the order of 10^5 Pa; whereas for very highly crosslinked systems the modulus above T_g could be as high as 10^8 Pa.

Other changes also take place at the glass transition temperature. The specific volume increases relatively linearly below T_g , but around T_g the slope of this increase changes, achieving a larger slope above T_g . This is a reflection of the thermal expansion coefficient's increasing by a factor of about 3 at the glass transition temperature. One way to rationalize this behavior is using free volume arguments. Below T_g , the free volume stays relatively constant or "frozen-in." The thermal expansion is associated with an increased amplitude in the chemical bond thermal vibrations. Above the glass transition temperature, there is an additional expansion from the free volume itself increasing with temperature.

The enthalpy of a polymer changes with temperature in an analogous manner to the specific volume. The specific heat C_p , like the expansion coefficient, undergoes a step change at the glass transition temperature. This step change is exploited by calorimetric equipment to detect and measure the glass transition temperature of materials. The glass transition phenomenon does not take place at a sharply defined temperature; actually it occurs within a range of temperatures. Therefore it is important to define a consistent way of reporting T_g . This issue has been discussed at length by Bair [34]. Fig. 6 illustrates the DSC output showing the glass transition of an uncured acrylate adhesive [34]. By convention, T_g is taken as the temperature at which the step increment in C_p reaches half of the total ΔC_p value (ΔC_p is the difference in specific heat between the glassy and the rubbery states). As a polymer is heated through its glass transition temperature, it undergoes a *positive* step-change in its specific heat, *i.e.*, the direction of the step change is endothermic. A larger specific heat means that it takes more energy to heat a given mass of the sample from temperature A

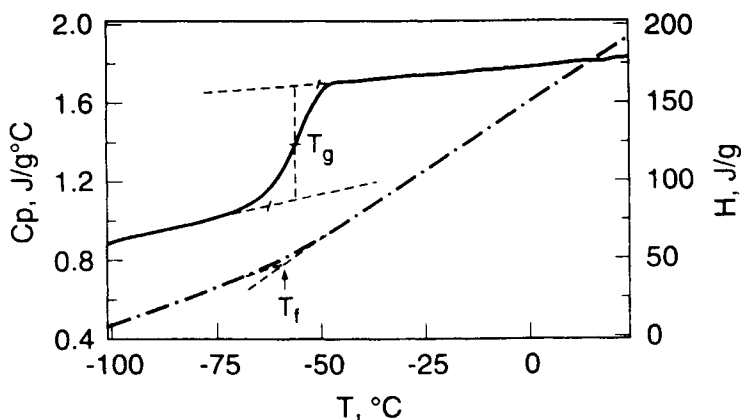


Fig. 6. Specific heat (continuous line) and enthalpy (dashed line) for an uncured acrylate adhesive. The specific heat curve shows how the mid-point T_g is determined. The change in slope of the enthalpy curve determines the fictive temperature T_f . (After Bair [34]).

to temperature B. A very interesting and counterintuitive phenomenon occurs when a sample is cooled through its glass transition temperature. A DSC scan of this experiment will show a step-change in the *endothermic* direction. This is opposite to what happens with, for example, the melting transition of a crystalline sample. Upon heating a solid crystalline sample through its melting point, the DSC will show an endothermic melting peak. Cooling the melt will generate an exothermic crystallization peak. A glass transition will appear as an endothermic step both upon heating and upon cooling. This phenomenon can be used sometimes to verify whether a suspected transition is a glass transition temperature and not some other thermal event. The endothermic character of the glass transition on a DSC cooling experiment seems counterintuitive because the specific heat *drops* as a sample is cooled through T_g (*i.e.* one would expect an exothermic shift). The reason the transition appears as an endothermic transition is that upon cooling the DSC is really reporting a measure of $-C_p$. This is not always evident because most DSCs display a *relative* scale in the ordinate. The absolute value of C_p indeed decreases as the polymer is cooled through T_g , but this change is reported by the DSC as an increase in $-C_p$. For example, if a given sample has a C_p of $2.0 \text{ J g}^{-1} \text{ K}^{-1}$ in the glassy region and $2.5 \text{ J g}^{-1} \text{ K}^{-1}$ in the rubbery region, a heating DSC experiment will obviously show an endothermic transition corresponding to the step from 2.0 to 2.5, whereas a cooling DSC experiment will show a step from -2.5 to -2.0 , which, while also in the endothermic direction, corresponds to a drop in absolute value of C_p .

5.2. Dependence of T_g on network and chemical structure

The glass transition temperature of a thermosetting polymer depends on the crosslink density, the number of free chain-ends, and the rigidity of the polymeric segments. The crosslink density is perhaps the most studied variable affecting the T_g of thermosets, but it must be kept in mind that other factors are important too. Fox and Loshaek [35] first proposed that the glass transition temperature in crosslinked systems increases linearly with the concentration of crosslinks, and rationalized this by proposing that each crosslink restricts the free volume by a certain amount. An alternate theory has been proposed by Gibbs and DiMarzio [36,37], who propose that the glass transition temperature is related to a true thermodynamic transition at which the configurational entropy vanishes. According to DiMarzio [38], the crosslinks affect T_g by reducing the configurational entropy. DiMarzio's theory leads to a linear dependence of $1/T_g$ versus crosslink density. Both the Fox-Loshaek and the DiMarzio equations do a reasonable job describing T_g in lightly crosslinked systems, although a constant predicted by DiMarzio to be universal is not truly universal.

Systems with moderate and high crosslink densities show upward curvatures in their T_g versus crosslink density dependencies that cannot be fitted

by the Fox-Loshaek or DiMarzio equations. Probably the most popular equation to model the T_g in thermosets is the DiBenedetto equation [39]:

$$\frac{T_g - T_{g0}}{T_{g0}} = \frac{(\varepsilon_\infty / \varepsilon_0 - c_\infty / c_0)x}{1 - (1 - c_\infty / c_0)x} \quad (5)$$

where x is the crosslink density defined as “the fraction of all segments that are crosslinked [39], ε is the lattice energy, c is the segmental mobility, and the subindices 0 and ∞ refer to the uncrosslinked and the fully crosslinked polymers, respectively. There has been considerable interest in the literature to model the change in the glass transition of a thermosetting polymer as it is being formed, *i.e.* to model T_g as a function of conversion. During this process, the crosslink density increases, but it is not the only T_g – determining variable. At the same time, the amount of free monomer decreases, as well as the number of free chain-ends. All these factors combined influence the evolution of T_g . The DiBenedetto equation has been widely used as an empirical relation to fit T_g versus conversion data, simply by using conversion instead of crosslink density in Eq. (5) and using the lattice energy and segmental mobility as adjustable parameters [12,40,41]. Even though this is not strictly correct (in a later publication [42], DiBenedetto pointed out that the applicability of the principle of corresponding states he used to derive his equation is open to serious question when applied to highly crosslinked systems), it works very well as an empirical equation.

Pascault and Williams [43] have used Couchman’s thermodynamic arguments [44] to obtain a similar equation in which there are no fitting parameters; all the parameters can be obtained if one knows the T_g and the change of C_p at the glass transition (ΔC_p) both of the unreacted monomer and of the fully reacted polymer:

$$\frac{T_g - T_{g0}}{T_{g\infty} - T_{g0}} = \frac{\lambda\alpha}{1 - (1 - \lambda)\alpha} \quad (6)$$

where $\lambda = \Delta C_{p\infty} / \Delta C_{p0}$, the subindex 0 represents the unreacted system, and the subindex ∞ represents the fully reacted network.

There have been other attempts to methodically describe T_g versus conversion in thermosets as a combination of the effect of chain ends and of crosslinks [45,46]. Stutz and coworkers [45] adapted DiBenedetto’s equation (Eq. (5)) by using the Fox-Flory equation [47,48] to describe the influence of

chain ends on T_g , using the number of junction points as the crosslinks, and assuming that c_{∞}/c_0 is zero. The equation they obtained is

$$T_g = [T_{gl\infty} - k_1 (1-\alpha)] \left[1 + k_2 \frac{X_c}{1-X_c} \right] \quad (7)$$

where $T_{gl\infty}$ is the “reference true backbone glass temperature”, that is, the hypothetical glass transition temperature of an infinite *linear* polymer with the same chemical structure as the thermoset under study, k_1 is a constant characterizing the influence of end-groups on T_g , k_2 is another constant characterizing the influence of crosslinks, α is the conversion of reactive groups, and X_c is the crosslink density; any junction with a functionality of three or higher is considered to be a crosslink, and the higher-functionality crosslinks are weighted more heavily than the lower-functionality crosslinks.

Eqs. (5-7) work very well for many thermosetting systems. However, they fail to fit some systems that have a very sharp upswing of T_g with conversion in the later stages of cure. Hale, Macosko and Bair [46] have proposed an additional contribution from non idealities at very high crosslink densities to model these systems:

$$T_g = \frac{\left(\frac{1}{1/T_{g0} - k\alpha} \right)}{\left(1 - \frac{K_2 X}{1 - \Psi X^2} \right)} \quad (8)$$

where T_{g0} is the glass transition temperature of the unreacted system, α is the extent of reaction, k is a constant that incorporates the effect of chain ends, K_2 is DiMarzio’s constant originally thought to be “universal” [38], X is a measure of the crosslink density defined as the moles of chains per mole of segments, and Ψ is an empirical constant that lumps together the effects of nonidealities such as non-Gaussian behavior and steric effects on the chain configurations of highly crosslinked systems. The constant k can be evaluated independently from experiments using a non-branching system [46]. Eq. (8) has been used successfully used to model T_g versus conversion in very highly crosslinked systems that could not be fitted by other equations, albeit at the expense of introducing an extra parameter.

Fig. 7 shows T_g data as a function of conversion obtained by partial isothermal cures of an epoxy novolac system [46]. The samples were cured isothermally in the DSC for a specified amount of time, then quenched, and then scanned dynamically in the DSC. T_g values were obtained from the dynamic

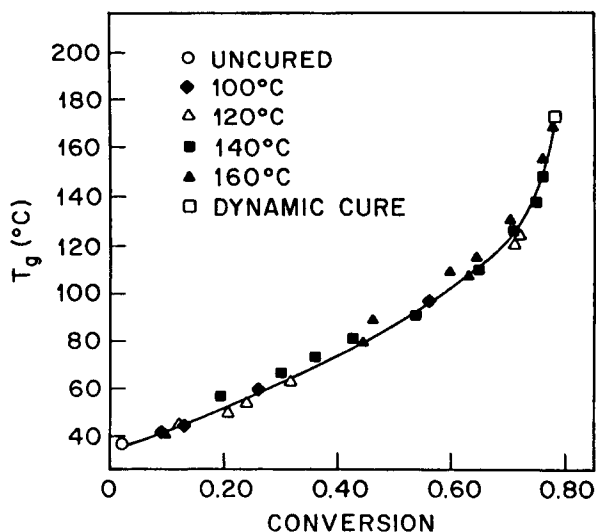


Fig. 7. Glass transition temperature as a function of conversion for an epoxy-novolac system cured with a phenolic novolac. The different symbols represent the temperatures at which the resin was cured (after Hale *et al.* [46]).

scan, as well as the residual heat of reaction, which was used to calculate conversion as outlined in section 4. It is evident that T_g is a unique function of conversion regardless of the cure temperature. This phenomenon has been widely observed in thermosetting systems such as epoxies [49]. In order for this behavior to take place, one of the following conditions must be met: a) there is only one chemical reaction taking place; b) if there is more than one reaction taking place, their activation energies are similar; c) if there are two or more reactions with different activation energies taking place, their kinetics are such that they occur sequentially. The one-to-one relationship between T_g and conversion, together with the steep dependence of T_g on conversion at high conversions, suggests that T_g can be used as a more sensitive monitor of extent of reaction than the measurement of residual heat [50].

The evolution of T_g with conversion is important from a practical standpoint because it is intimately related to reaction kinetics and to the final degree of cure obtained on a sample. Fig. 8 shows isothermal data of conversion as a function of reaction time at different reaction temperatures [46]. At long times, the conversions level off at values well short of 100%. In fact, the lower the reaction temperature, the lower the ultimate conversion value achieved. The relevance of this phenomenon is obvious: *if the material is not cured at a high enough temperature, it will not be fully reacted, even though the reaction may appear to have stopped.* Fig. 9 provides some information that helps explain the

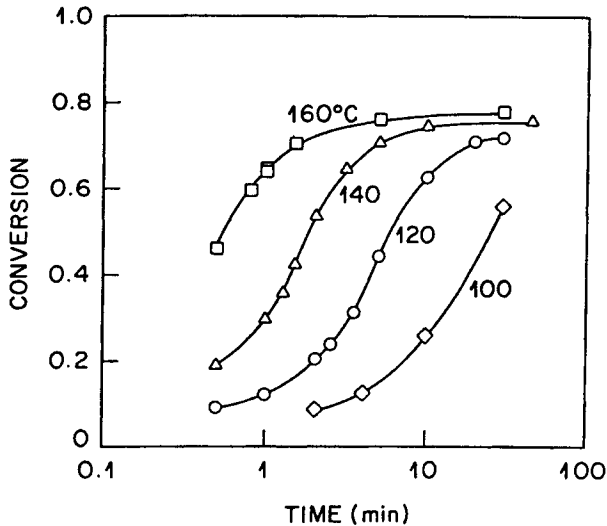


Fig. 8. Conversion as a function of time at different reaction temperatures for an epoxy novolac cured with a phenolic novolac (after Hale *et al.* [46]).

reason for the apparent limiting ultimate conversion at a given temperature. This figure shows curves of conversion as a function of time for an epoxy sample cured isothermally at three different temperatures: 26°C, 60°C and 105°C [51]. In addition, the glass transition temperatures of the partially reacted samples at different times are shown in the figure next to each data point. One can see that the slope of the conversion curve drops drastically when T_g becomes comparable to the reaction temperature. This is the point when the reaction vitrifies: the sample suffers a transformation from rubbery to glassy by virtue of the glass transition temperature surpassing the reaction temperature as a result of the crosslinking reaction. As the sample becomes glassy, the mobility is drastically reduced, so the reactive groups cannot find each other within a reasonable time frame, and the reaction slows down considerably. Although some investigators claim that the reaction is “quenched” at this point [11-13], in reality the reaction proceeds extremely slowly under a diffusion-controlled (or more correctly, a relaxation-controlled) regime. Fig. 9 also illustrates this point: after the conversion levels off, it still keeps on increasing, but at a very reduced rate; the increasing glass transition temperature is also an indication of further reaction. For example, the epoxy of Fig. 9 achieved a T_g of 41°C after reacting for a few hours at 23°C. Even though at this point some would claim that the reaction would have been “quenched” because the reaction temperature is below T_g [11-13], Fig. 9 clearly shows that the reaction proceeds slowly but steadily, causing T_g to increase to 71°C after a few months. This system was monitored by H. E.

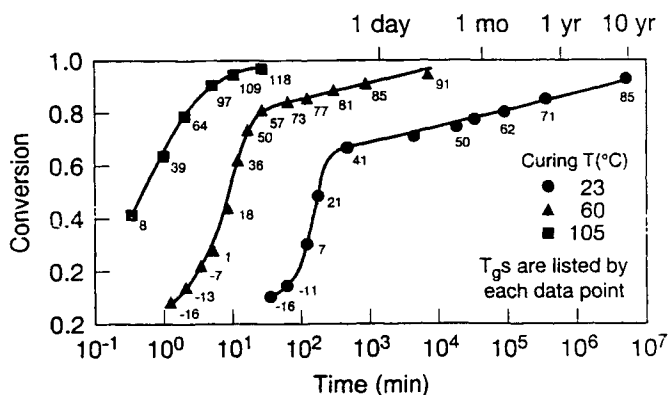


Fig. 9. Conversion as a function of time for an epoxy adhesive cured at three different temperatures. The number next to each experimental point represents the glass transition temperature of that sample (after Bair [51]; the 10 year point was measured after reference 51 was published).

Bair after reference (51) was published; after 10 years at room temperature, the epoxy T_g had increased to 85°C.

For any given chemical composition of a thermosetting polymer, there is a maximum T_g obtainable if all the reactive groups that can potentially react are allowed to react (although, as explained earlier, it may be impossible to fully-crosslink highly-functional densely crosslinked polymers because of topological limitations). This maximum obtainable T_g is often referred to as $T_{g\infty}$. In order to cure a thermosetting polymer as completely as possible, the reaction temperature at some point should at least equal to or preferably exceed $T_{g\infty}$, in order to ensure that there is enough mobility for the reactive groups to find each other. It is not necessary to carry out all the reaction at $T > T_{g\infty}$; in fact sometimes this could lead to increased internal stresses. In some applications where a different material is encapsulated by or bonded to a thermoset, it may be desirable to either slowly ramp up the cure temperature or to perform the cure by starting at a low or moderate temperature, and then increasing the temperature in steps. Eventually, the highest temperature to which the sample is exposed should be higher than $T_{g\infty}$ in order to ensure full cure.

5.3. Change in specific heat (ΔC_p)

A polymer heated or cooled through its T_g experiences a step change in its specific heat. This step change is known as ΔC_p : $\Delta C_p = C_{p(\text{rubber})} - C_{p(\text{glass})}$. To calculate this quantity from a DSC scan, one first draws a baseline through the glassy region and another baseline through the rubbery region. Then one determines the difference between the values of the ordinates of these two baselines at T_g (Δy). ΔC_p is given by:

$$\Delta C_p = \Delta y / (m \beta) \quad (9)$$

where m is the mass of the sample and β is the heating rate.

In section 4.2.3 it was mentioned that the sensitivity of the DSC is directly proportional to the heating rate. This is obvious from Eq. (9): ΔC_p is a material parameter, so for a given material, the DSC output is

$$\Delta y = \Delta C_p \cdot m \cdot \beta \quad (10)$$

Therefore if one is having difficulties to detect a “weak” T_g , one can try running the experiment at a faster heating rate, or using a larger sample, or both. It should be kept in mind that the temperature calibration of a DSC is for a specific heating rate. If a different heating rate is employed from that employed for calibration, a correction is needed. This will be discussed in section 6.

The error bars in the measurement of ΔC_p are usually large, so it is recommended to repeat the measurement several times and report the average.

Knowing the ΔC_p of a polymer can be very useful, for example, to quantify the amount of polymer in a multiphase system, because the observed Δy is a function of the amount of material that is undergoing the transition. For instance, if one has a polymer that is filled with silica and has a T_g of 150°C, the observed Δy is caused by the polymer only; the silica does not contribute. Thus, if the ΔC_p of the neat polymer is known, the amount of polymer in the composite sample is simply

$$m_{\text{neat polymer}} = \Delta y_{\text{composite}} / [\Delta C_{p \text{ neat}} \cdot \beta] \quad (11)$$

Most versions of DSC software automatically *calculate* ΔC_p rather than Δy when a T_g is calculated. In the case of a composite material, the value *measured* by the DSC is

$$\Delta y_{\text{composite}} = \Delta C_{p \text{ neat polymer}} \cdot m_{\text{neat polymer}} \cdot \beta \quad (12)$$

because only the polymer contributes to the step in C_p . However, the ΔC_p that the software calculates uses the total weight of the composite sample:

$$\Delta C_{p \text{ composite}} = \Delta y_{\text{composite}} / (m_{\text{composite}} \beta) \quad (13)$$

Rearranging and dividing these two expressions we obtain

$$m_{\text{neat polymer}} / m_{\text{composite}} = \Delta C_{p \text{ composite}} / \Delta C_{p \text{ neat polymer}} \quad (14)$$

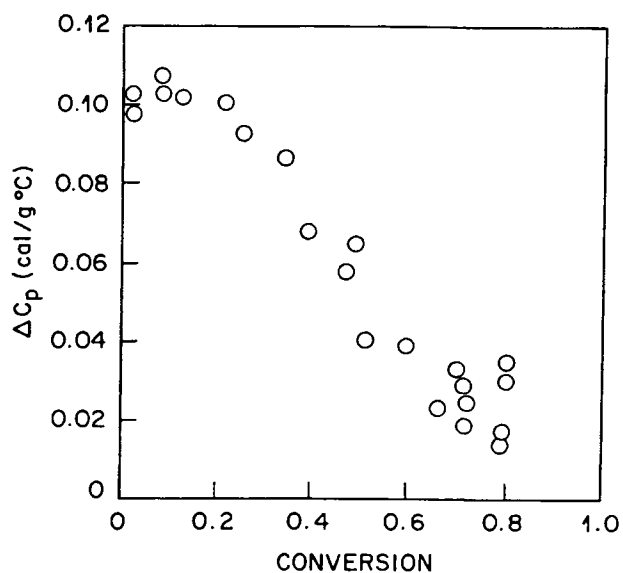


Fig. 10. Change in specific heat at the glass transition as a function of conversion for an epoxy novolac cured with a phenolic novolac (after Hale *et al.* [46]).

ΔC_p is related to the mobility and configurational entropy of the network [52]. As the crosslink density of a polymer increases, the mobility decreases, and ΔC_p decreases too. Fig. 10 shows ΔC_p versus conversion values measured for the epoxy-novolac system of Fig. 4. One can observe the significant drop in ΔC_p values as a function of conversion. The low values of ΔC_p at high crosslink densities sometimes make T_g difficult to detect. This difficulty has led many people to erroneously conclude that a certain polymer “has no T_g ,” or that it “cannot be measured.” There are several tricks one can play to detect this “undetectable” T_g . As discussed previously, one can use larger samples sizes and/or faster heating rates to improve the instrument sensitivity. Another possibility is to exploit the phenomenon of physical aging, as explained in the next section.

5.4. Physical aging

The glassy state is not in thermodynamic equilibrium. The experimentally observed glass transition has a kinetic character as evidenced by its dependence on heating or cooling rate. A polymer in the glassy state gradually contracts or shrinks towards the equilibrium “liquidus” line (Fig. 11). A polymer in the rubbery state (above T_g) is in thermodynamic equilibrium, since there is enough mobility for the molecules to achieve their most favored thermodynamic state.

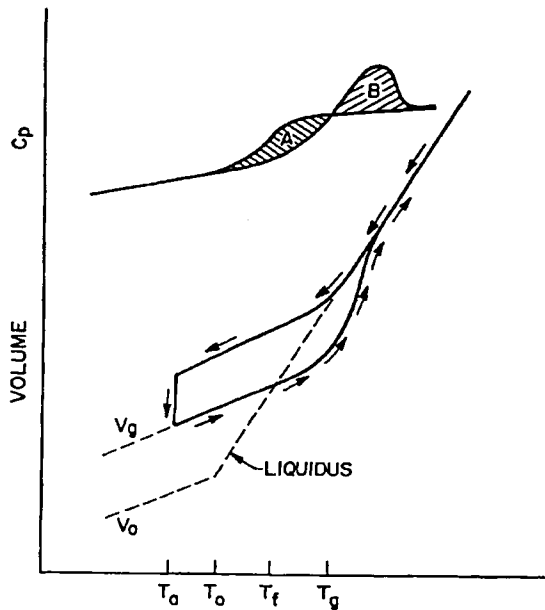


Fig. 11. Specific volume as a function of temperature (lower graph) and specific heat as a function of temperature (upper graph) for an amorphous material. The arrows show a cooling trajectory from the rubbery state to the glassy state, followed by isothermal densification at T_a , followed by subsequent heating back to the rubbery state. The B curve on the upper graph represents the enthalpy recovery peak.

On the other hand, a polymer in the glassy state (below T_g) does not have enough mobility to reach its thermodynamic equilibrium. The molecules “want” to relax to their equilibrium state, but the lack of mobility prevents them from doing so in a reasonable time frame. The theoretical equilibrium state at a given temperature is denser (lower specific volume) than the glassy state; thus, a glassy polymer tends to shrink or contract in order to achieve its equilibrium state. This shrinking process may be very slow. Its rate obviously depends on mobility; therefore, the closer one gets to the glass transition temperature, the faster the shrinking process. At the same time, as the polymer shrinks, the shrinkage rate continuously decreases, because the shrinkage process eliminates “free volume,” therefore reducing mobility. This isothermal shrinking of a glassy material is known as physical aging. This topic is covered in more detail in the chapters by McKenna and by Matsuoka in this volume. An excellent monograph that covers this area has been published by Struik [53]. Haward [54] and Matsuoka [55] also deal with this subject.

The phenomenon of physical aging is responsible for endothermic peaks that sometimes are observed at the glass transition temperature such as the ones seen in Fig. 12 [34]. Typically, if a glassy polymer is kept at a temperature of,

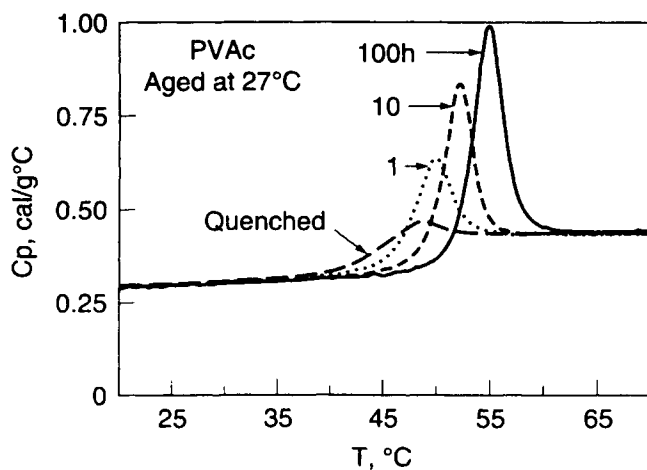


Fig. 12. Specific heat as a function of temperature for a poly(vinyl acetate) polymer aged at 27°C for different amounts of time (after Bair [34]).

for example, 10 or 15°C below T_g for a few hours or longer, a subsequent DSC scan will reveal a peak such as the ones shown in Fig. 12. Once this sample is heated above T_g , a subsequent fast cooling and re-scan schedule will produce the “quenched” curve shown in Fig. 12. The annealing peak has been “erased.” Fig. 11 provides a qualitative understanding of the reason for this peak. The bottom part of this qualitative figure represents either the enthalpy or the specific volume as a function of temperature. Let us start with a polymer in its equilibrium rubbery state at a temperature above the glass transition temperature. As this material is cooled down below its glass transition temperature at a given cooling rate, it follows the path shown in the figure. If the material is held isothermally at temperature T_a , it will undergo physical aging as explained in the previous paragraph. The material will therefore shrink isothermally. If the material is then heated back to a temperature above T_g , it will get back to its equilibrium state. However, in order to achieve this it has to follow the lower trajectory shown in Fig. 11. In order to come back to its equilibrium state above T_g , the material must “recover” the enthalpy it “lost” during the aging process at T_a . This recovery is seen as an increased slope in the lower trajectory in Fig. 11. The output of the DSC is actually dH/dT , the slope of the H versus T curve. Plotting the dH/dT for the lower trajectory results in the characteristic “annealing peak” seen when a physically aged sample is scanned in the DSC; the peak maximum corresponds to the maximum slope in the H versus T plot (upper graph “B” in Fig. 11).

The existence of this “annealing peak” can be exploited for analytical purposes, but at the same time one must be aware that its presence may affect

other measurements. Samples aged for different amounts of time and subsequently scanned in the DSC will show annealing peaks of different heights. The height of this peak depends on the aging temperature and on the aging time; the longer the time at a given temperature, the higher the annealing peak. The rate of aging depends on temperature as well as on aging time itself. If the sample temperature is far below T_g , there is not much mobility to allow for volume and enthalpy relaxation, so there will not be much physical aging. On the other hand, at temperatures close to T_g , the enhanced mobility will allow relaxations to occur faster, so the sample will age more quickly. As the sample ages and densifies, the amount of “free volume” decreases, making subsequent relaxations more difficult. Therefore isothermal physical aging is an ever decelerating process. Similar conclusions can be drawn from using entropy arguments instead of free volume arguments.

The presence of an annealing peak in an unknown sample can be used to shed some light on its thermal history. A practical application of this phenomenon is using it to resolve or detect weak glass transitions. There are several cases when a glass transition temperature may be difficult to detect. For example if the sample is too small, or if it is a highly filled composite, or a very highly crosslinked polymer, the signal may be too weak to be easily detected. One trick one can play to reveal this glass transition, if one has a rough idea of where to expect it, is to age the sample at 15°C below its expected value for about 15 hours or longer. After aging, the sample should be cooled rapidly by about 20 to 50°C and then scanned in the DSC. The physical aging process will very likely cause an endothermic annealing peak in the glass transition region that should be easily detected. This technique has also been successfully used to resolve overlapping T_g s in polymer blends [56-58].

In some cases an annealing peak resulting from physical aging can be mistaken for a melting peak. However, a second scan following a fast cooling from the rubbery state will show a glass transition without signs of the annealing peak.

If a sample is cured isothermally at a temperature below its ultimate glass transition temperature, the sample will eventually vitrify as T_g catches up with the reaction temperature (section 5.2). As the reaction proceeds in the “diffusion controlled” mode, T_g keeps on rising because of the increasing crosslink density. We then have a glassy sample below its T_g , so physical aging will take place concurrently with the diffusion-controlled reaction. In fact, the reaction kinetics becomes controlled by the ongoing relaxation time as in the physical aging of the glassy polymer [55,59]. If a sample that has been cured for a long time under these diffusion-controlled conditions is cooled in the DSC and then scanned dynamically, an endothermic annealing peak (related to the physical aging process) will appear followed by an exothermic peak related to the residual cure of the unreacted groups that had not reacted due to the sluggishness of the

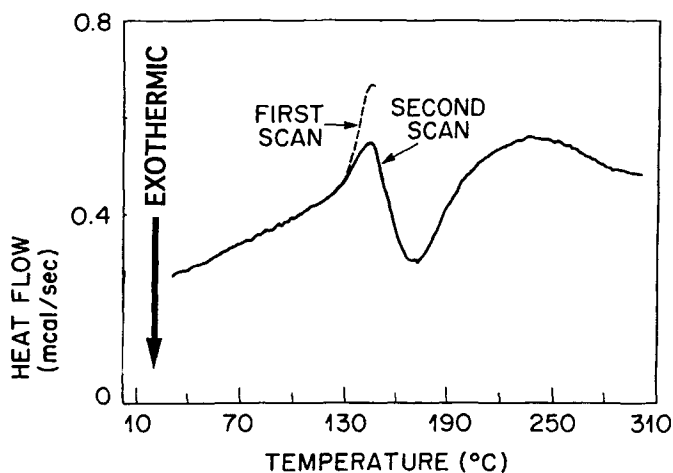


Fig. 13. Residual heat of reaction of an epoxy resin that had been cured for one hour at 120°C. The annealing peak has been erased in the second scan [46].

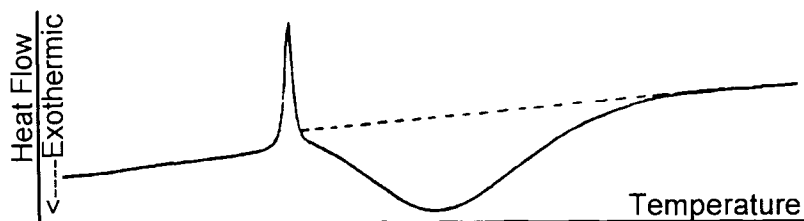


Fig. 14. Residual heat of reaction of an epoxy resin that underwent extensive physical aging during cure. The dashed line indicates the baseline used for integration (after Bair [51]).

diffusion-controlled reaction mode. It is important to be aware of this phenomenon, because otherwise one could reach erroneous results if one intends to use the residual heat of reaction to calculate the extent of reaction of such a sample. This is illustrated in Fig. 13. This figure represents the residual heat of reaction of an epoxy sample that had been cured for one hour at 120°C [46]. The first scan shows an endothermic process associated both with the glass transition and with the relaxation of physical aging. The DSC run was stopped immediately after the highest point of the endothermic process, the sample was quenched, and a second scan was obtained. If one had carried out only one full scan, an unsuspecting subject might have been tempted to calculate the residual heat using the highest point of the endothermic process as one of the limits for integration of the exothermic peak. This would lead to incorrect results, because

on the left side of the peak there is an endothermic component caused by physical aging. One would thus calculate an artificially high residual heat, leading to an artificially low extent of reaction. In order to perform the correct calculation in this example, there are three choices:

a) One can closely monitor the DSC experiment, and quench the sample immediately after it reaches the maximum of the annealing peak. At this point the aging behavior has been “erased,” but not enough time has elapsed to allow the residual cure to take place. A subsequent scan will show the residual exothermic peak without the annealing peak, eliminating the uncertainty of the integration limits to determine the residual heat of reaction (Fig. 13).

b) If there is a flat, straight baseline on the high temperature side of the exothermic peak, one can simply extrapolate this baseline to the left and use the area under the curve (Fig. 14).

c) If one knows from independent measurements what the ΔC_p should be (recall that ΔC_p may itself be a function of conversion), then one can draw a baseline from the end of the exotherm to a point at the beginning of the exotherm determined by ΔC_p [51].

6. REACTION KINETICS

6.1. General principles

The key factor that distinguishes thermosetting polymers from thermoplastic polymers is the fact that the processing of the material into its final form involves a chemical reaction. Understanding the speed at which this reaction takes place as well as its dependence on variables such as temperature is of paramount importance to determine the proper processing conditions. Calorimetry, especially DSC, is ideally suited for this endeavor, because the output of the DSC is directly proportional to the rate of reaction. The rate of reaction is related to the DSC ordinate by the following expression:

$$\text{rate} \equiv da/dt = - [y - y_b]/[m \Delta H] \quad (15)$$

where a is the conversion of reactive groups, y is the ordinate of the DSC output (mW), y_b is the ordinate of the baseline, m is the sample mass (mg), and ΔH is the enthalpy of reaction in (J/g)(=mJ/mg). Fig. 15 illustrates a typical isothermal DSC run.

It is a unique feature of the DSC that it provides a direct measurement of the *rate* of reaction. Just about every other analytical technique measures concentration of reactive groups, which must be differentiated to obtain rate of reaction. Although obtaining a derivative is not a problem when one has an analytical equation, differentiating experimental data creates other problems. There is always some error or uncertainty associated with experimental data. If

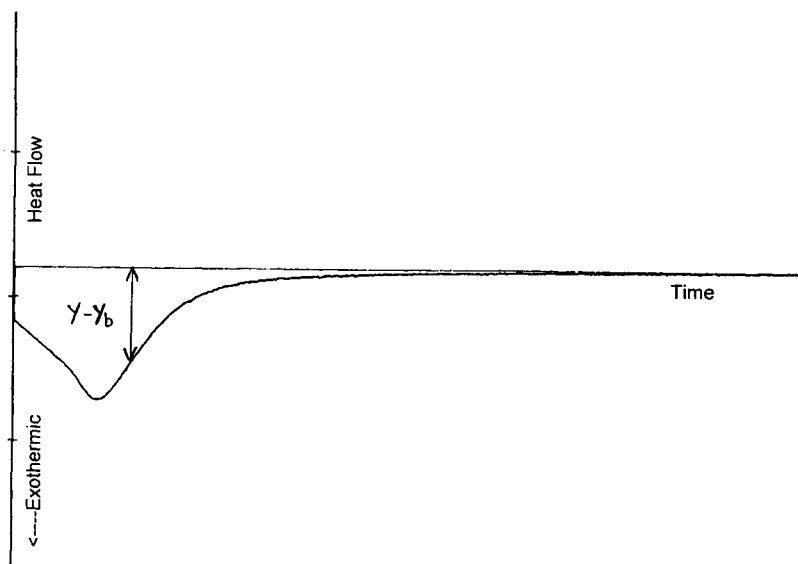


Fig. 15. Isothermal DSC run of an epoxy cured at 130°C. The ordinate $y-y_b$ is a direct measure of the rate of reaction.

each experimental data point has a certain error, the line that connects them is jagged, not smooth. This implies that the local slope of this jagged curve varies from point to point, so obtaining the derivative by discrete differentiation will lead to large errors. Therefore it is very important to smooth the data before obtaining the derivative. DSC avoids this problem because it provides a direct reading of the reaction rate.

The rate of reaction is a function of temperature and of the concentration of reactive groups (which in turn depends on the conversion α):

$$d\alpha/dt = k(T) F(\alpha) \quad (16)$$

Higher concentrations of reactive groups mean that the probability of two reactive groups finding each other is higher, and therefore the reaction rate is higher. At higher temperatures, the average kinetic energy of the molecules is higher, increasing the chances that a given collision between two reactive molecules will overcome the activation energy barrier and result in a chemical reaction. This accounts for the faster reaction rates at higher temperatures.

The functionality of reaction rate on temperature is given by the Arrhenius equation:

$$k(T) = A e^{-E_a/(RT)} \quad (17)$$

where A is a constant known as the frequency factor or pre-exponential factor, E_a is the activation energy of the reaction, and R is the gas constant.

The functionality of reaction rate on conversion $F(\alpha)$ can be very simple or very complicated depending on the reaction mechanism. In many reactions, this functionality is simply a power function. The exponent n is known as the *order* of the reaction:

$$F(\alpha) = (1 - \alpha)^n \quad (18)$$

In an n^{th} order reaction, the rate of reaction at a given temperature decreases monotonically as the reactants get consumed. There are several reactions of great importance in thermosetting systems that do not follow n^{th} order kinetics. Epoxy resins and cyanate esters are two examples of reactions that follow an *autocatalytic* mechanism, in which a product of the reaction catalyzes the reaction. During the initial stages of the reaction, the reaction rate actually increases with conversion, because of the formation of a catalytic species that accelerates the reaction. Eventually the starting reagents get depleted, and the reaction rate drops again. Thus a plot of reaction rate versus time at a given temperature will go through a maximum. A simple phenomenological equation that can describe this type of mechanism is

$$F(\alpha) = \alpha^m (1 - \alpha)^n \quad (19)$$

The α^m factor accounts for the initial increase in reaction rate, while the $(1 - \alpha)^n$ factor is responsible for the eventual decrease of reaction rate. Combining Eqs. (16), (17) and (19) we obtain

$$d\alpha/dt = A e^{-E_a/(RT)} \alpha^m (1 - \alpha)^n \quad (20)$$

Since autocatalytic reactions involve at least two separate reactions, sometimes the above equation cannot adequately describe the temperature dependence, because it uses only one activation energy to lump together the temperature effects of different reactions. A more accurate equation is the following [60-62]:

$$d\alpha/dt = (k_1 + k_2 \alpha^m) (1 - \alpha)^n \quad (21)$$

where $k_i = A_i e^{-E_{a_i}/(RT)}$

Figs. 15 and 16 show isothermal DSC scans of an epoxy resin at 130°C and 150°C, respectively. Both curves show the typical shape of an autocatalytic

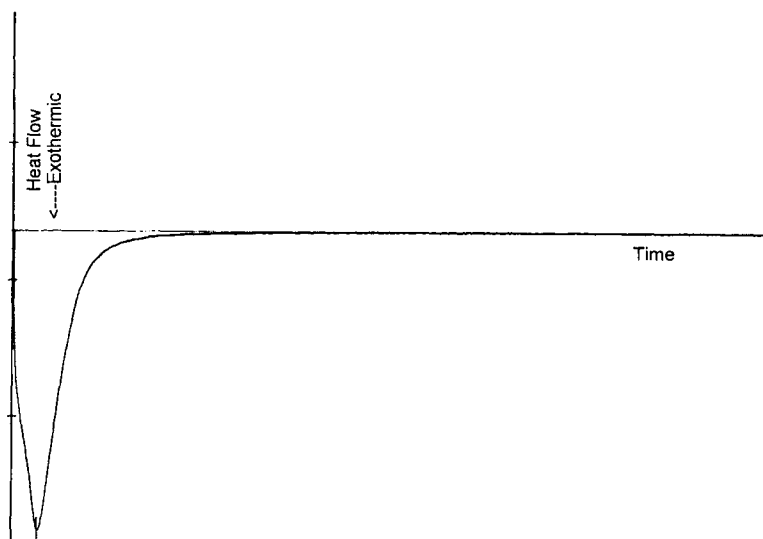


Fig. 16. Isothermal DSC run of an epoxy cured at 150°C. This graph, drawn on the same scale as Fig. 15, shows the faster reaction rate obtained at a higher cure temperature.

reaction. As expected, the reaction at higher temperature is faster than the one at lower temperature.

In order to obtain accurate isothermal kinetic data, it is important to verify that the DSC is calibrated for isothermal conditions. This issue is often

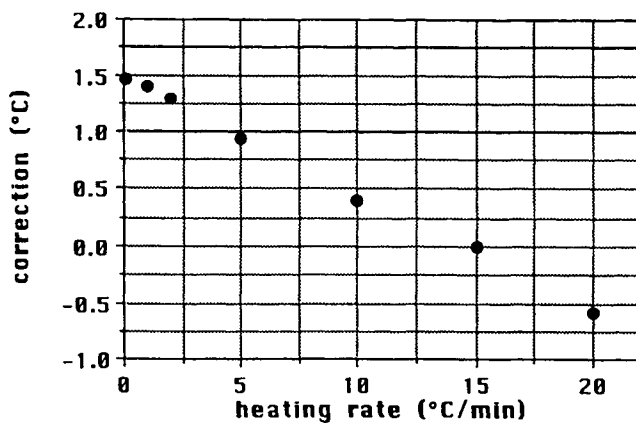


Fig. 17. Temperature correction needed for a DSC calibrated at 15°C/min when a different scanning rate is used, based on the melting point of an indium standard. This calibration curve is specific to each individual instrument.

overlooked, but most DSCs are usually calibrated under dynamic (linear heating programs) conditions. Fig. 17 shows a typical curve that shows the temperature correction needed on a DSC calibrated at a heating rate of 15°C/min if a different heating rate is used. This curve can be obtained simply by running a standard (for example pure indium) at different heating rates and comparing the measured melting point to the theoretical value. By extrapolating to zero heating rate, one can see that a correction of 1.5°C is needed for isothermal experiments. The curve shown in Fig. 17 was obtained for a specific DSC instrument. It is not intended to be a universal curve; a separate curve should be obtained for each individual instrument.

6.2. Kinetic parameters determination

Most commercially available thermal analysis equipment come with software that can automatically fit kinetic equations. This is very convenient, but one must always be aware of the dangers of using “canned” software. Once one obtains kinetic parameters using either “canned” software or one’s own equations, it is important to test these parameters by comparing experimental results with predicted results under conditions *different* from those used to obtain the parameters. For example, if the kinetic parameters were obtained from isothermal runs at different temperatures, one should test them on a dynamic run (*i.e.* using a linear temperature ramp). Similarly, if the parameters were obtained from dynamic runs, they should be tested either on isothermal experiments or on dynamic runs at rates different from those used to obtain the fitting parameters.

The simplest case to handle is if we simply have an n^{th} order reaction. This is described by

$$d\alpha/dt = k(T) (1 - \alpha)^n \quad (22)$$

Taking the logarithm on both sides of this equation yields

$$\log (d\alpha/dt) = n \log (1 - \alpha) + \log [k(T)] \quad (23)$$

Thus, a plot of $\log(\text{rate})$ versus $\log (1 - \alpha)$ will produce a straight line with a slope of n and an intercept of $\log[k(T)]$. To generate this plot, one must obtain the rate from Eq. (15); the conversion can be calculated by integrating the area under the DSC curve from the beginning of the reaction up to the time at which the corresponding rate is being recorded.

This procedure is repeated at different temperatures. If the reaction truly is n^{th} order, the slope of all these curves should be about the same (n). In order to obtain the activation energy and pre-exponential factor (Eq. (17)), one simply needs to plot $\ln[k(T)]$ versus $1/T$ (making sure that the temperature is in Kelvin). The slope of this straight line is $-E_a/R$, and the intercept is $\ln(A)$.

A logical experimental question is how to bring the sample up to the desired temperature for the isothermal cure. One possibility involves pre-programming the DSC to achieve the desired temperature, and then introducing the sample, and the other possibility is introducing the sample at room temperature and then heating it in the DSC to the desired temperature. The first possibility is not recommendable because it is not very reproducible: after the DSC is opened to deposit the sample, it will not be properly equilibrated, and the transient time to reach an equilibrium condition will vary from run to run according to how long it took to deposit the sample in the DSC. The second possibility may introduce some uncertainty, but it can be remedied. This procedure consists of introducing the sample into the DSC at room temperature, and then programming the DSC to heat the sample as fast as possible to the desired temperature (for example at 200°C/min). There is a clear possibility that the sample will partially react during this heating ramp. In addition, once the sample reaches the desired temperature, the DSC typically shows a transient behavior for a few seconds until it stabilizes. Some reaction can also occur during this period. Therefore, it is necessary to estimate how much reaction takes place during these stages and include it in the conversion calculation. One way to do this is to keep undisturbed in the DSC the same sample used to obtain the isothermal run, and re-run it using exactly the same program. Before this, though, one should ensure that the sample is fully cured, for example by heating it in the DSC to finalize the cure (for instance, carrying out a dynamic run up to 275°C). After the fully cured sample is run in the DSC using exactly the same program that was used to obtain the isothermal kinetic data, this run can be used as a baseline, and the conversion can be calculated by taking the area under the *difference* of these two curves (the original isothermal run including the heating ramp to get there and the same run on the cured sample). Another way to estimate this correction is to take a fresh sample, run a full dynamic scan, then take another fresh sample, heat it up to the isothermal reaction temperature and quench it immediately, and then run a full dynamic scan. The difference in reaction heats between these two full dynamic scans will give an indication of whether there is a significant amount of reaction taking place during the initial fast heating ramp. This difference will slightly overestimate the correction needed on an isothermal run, because it includes reaction that takes place during the fast heating and the fast cooling ramps, whereas the isothermal run includes reaction only during the heating ramp. As a first order approximation, one can use half of this value as a correction to be added to the isothermal heat of reaction.

It is also possible to obtain kinetic parameters of n^{th} order reactions from dynamic runs. This procedure is simpler from the experimental standpoint, but it may lead to errors because of mathematical artifacts, as discussed below. Combining Eqs. (22) and (17) we obtain

$$d\alpha/dt = A e^{-E_a/(RT)}(1-\alpha)^n \quad (24)$$

Taking the logarithm on both sides of the above equation yields

$$\ln(d\alpha/dt) = \ln(A) - E_a/R(1/T) + n \ln(1-\alpha) \quad (25)$$

Thus, if one has a set of data of da/dt as a function of the two variables $(1/T)$ and $(1-\alpha)$ one can perform a multilinear regression to obtain the parameters $\ln(A)$, $(-E_a/R)$ and n . This kind of regression is typically performed on data obtained from several dynamic DSC runs employing different heating rates. In practice, even if such a regression produces a good fit to the experimental data, one should be cautious about using the fitted parameters to predict kinetics under different conditions than those used to obtain the experimental data (e.g. at a different heating rate, or to predict isothermal data). In many instances these fitted parameters provide poor predictions for different heating rates. After obtaining the fitting parameters, one should always check the equation by comparing the prediction to experimental results obtained under different conditions than those used to obtain the fit.

A common problem when one has only dynamic scans is that it is not evident whether the reaction mechanism is autocatalytic. In fact, if one is using canned software, one may obtain a reasonable fit to dynamic runs using n^{th} order kinetics, even if the mechanism is autocatalytic. The parameters are forced to fit the equation, but because it is the wrong equation, large errors will be incurred when the equation is used for other conditions. An isothermal run can be very revealing, because if the mechanism is autocatalytic the result will be obvious: an n^{th} order kinetics isothermal run will yield a monotonic curve (continuously decreasing reaction rate), whereas an autocatalytic isothermal run will go through a reaction rate maximum.

Fitting the parameters of an autocatalytic reaction is not as simple as the case of n^{th} order kinetics, because Eq. (21) is not easily linearized. In this case it is suggested that one obtain isothermal data at different temperatures. Then a nonlinear optimization method must be used to fit the parameters m , n , $k_1(T)$ and $k_2(T)$ at each temperature. For this optimization, it is suggested to use $\log[k_1(T)]$ instead of $k_1(T)$ as a fitting parameter; this change of variable makes it easier for the optimization algorithm to converge to a solution. A convenient optimization algorithm has been proposed by Marquardt [63].

6.3. Time-temperature superposition kinetics

In some cases one can obtain a phenomenological approximation of the activation energy by using time-temperature superposition of data obtained for a certain physical variable. For example, if one has data of glass transition

temperature as a function of curing time at a given temperature, then one can plot T_g versus $\log(\text{time})$ for that given temperature. The procedure is repeated for different curing temperatures. The data are plotted together as separate isotherms, and each isotherm curve is then shifted horizontally to superimpose all the curves. The shift factor is recorded and plotted versus $1/T$, and the resulting slope is $-E_a/R$. This approach has been used by several authors (14,64), who show that it works in the regime where the reaction rate is controlled by chemical kinetics. When the reaction becomes diffusion-controlled, the curves do not superimpose, rendering this approach inadequate for this regime.

6.4. Diffusion-controlled regime

During a thermosetting polymerization, molecular mobility decreases as the reaction proceeds, because of the restrictions imposed by the crosslinked structure. In the case of highly crosslinked systems, if the chemical moieties are rigid enough, a stage is reached at which the glass transition temperature of the polymer reaches and then exceeds the reaction temperature. At this point, the drastic reduction in mobility leads in a change of the chemical reaction mechanism from chemical kinetic control to diffusion-control. In the diffusion control regime, the time it takes for the reactive groups to “diffuse” and find each other is much longer than the intrinsic chemical reaction time. The discussion presented in the following paragraphs pertains to step-wise reaction thermosets. The case of chain reactions, such as those initiated by free radicals, is much more complicated; it will be briefly discussed in section 7.

Despite the wide use of the term “diffusion control,” the actual phenomenon governing this regime is the relaxation of polymer chains rather than true diffusion. Matsuoka and coworkers [55,59] have shown that the so-called diffusion control reaction in thermosetting system can be quantitatively described by the same equations used to model polymer relaxation. Matsuoka has provided the listing of a computer program to carry out these calculations [55].

One approach to deal with diffusion control is to use Eq. (16) with a general kinetic term that encompasses both chemical control and diffusion control:

$$k = \frac{1}{1/k_c + 1/k_d} \quad (26)$$

where k_c is the chemical-control kinetic constant (Eq. (17)) and k_d is the diffusion-control kinetic constant. Since k_d is related to molecular mobility, it usually involves a term $(T - T_g)$: k_d becomes more important as T_g approaches

and eventually surpasses T . Using free volume arguments, the following equation has been derived to model k_d [65]:

$$k_d = K_0 \exp \left(B \left[1 - \frac{1}{f_g + \alpha_f (T - T_g)} \right] \right) \quad (27)$$

where K_0 and B are adjustable constants, f_g is the fractional free volume at T_g , considered to be equal to 0.025 [66], and α_f is the thermal expansion coefficient of the free volume. For amorphous polymers at temperatures between T_g and $T_g + 100^\circ\text{C}$, $\alpha_f = 4.8 \times 10^{-4} \text{ K}^{-1}$ [65]. Below T_g , a value of 4.8×10^{-5} has been suggested [67].

Another approach to model the evolution of reaction rate throughout both the chemical and the diffusion control regime has been proposed by other authors [68-70]. This approach consists in multiplying the chemical-control rate of reaction by a correction factor that accounts for diffusion control:

$$d\alpha/dt = (d\alpha/dt)_c DF(\alpha, T) \quad (28)$$

where the subscript c denotes chemical control, and $DF(\alpha, T)$ is the diffusion factor correcting the chemical rate in conditions where mobility is constrained. DF varies from 1 in the undisturbed state to 0 in the case of a "frozen" glass.

van Assche *et al.* [68] have proposed a new mobility factor DF^* based on specific heats:

$$DF^*(t, T) = \frac{C_p(t, T) - C_{p_g}(T)}{C_{p_l}(t, T) - C_{p_g}(T)} \quad (29)$$

where $C_p(t, T)$ is the instantaneous specific heat at a given cure time and reaction temperature, $C_{p_g}(T)$ is the specific heat of the glassy state at temperature T , and $C_{p_l}(t, T)$ is the specific heat in conditions where no mobility restrictions exist. In the initial stages of the reaction, $C_{p_l}(t, T)$ is the same as $C_p(t, T)$; as the sample starts to vitrify and $C_p(t, T)$ drops, $C_{p_l}(t, T)$ is calculated simply by a linear extrapolation of the initial part of the curve. This topic will be revisited in the discussion of modulated DSC (section 8).

7. PHOTO-INITIATED POLYMERIZATION

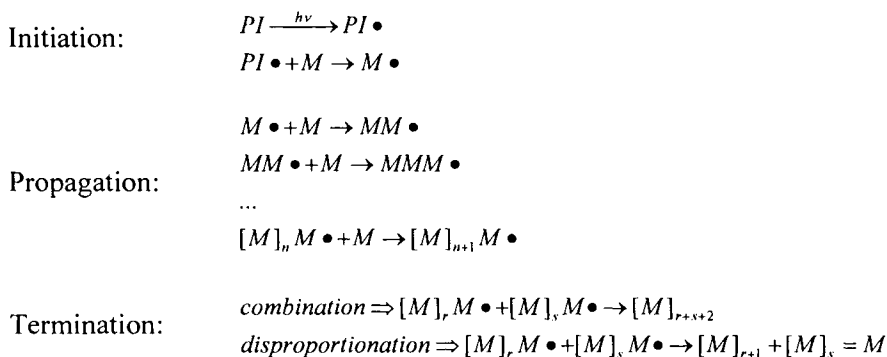
Photo-initiated polymerization refers to a polymerization process initiated by the action of light. This area has seen tremendous growth over the last decade, both

from the applications and from the fundamental understanding point of view. Although, semantically speaking, photo-initiated polymers are not thermosets in the sense that they don't cure by the action of heat, if one follows the "spirit" of the concept of thermosets then photo-initiated polymers can be included in the same family of thermosets. For all practical purposes, photo-initiated polymerization is used to form crosslinked polymers, although in principle one could also use it to form linear polymers.

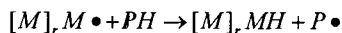
There are several features that make photo-initiated polymerization very attractive for applications such as coatings: very fast, room-temperature, on-demand cure. The two main avenues to form photo-initiated polymers consist of free-radical mechanisms and cationic mechanisms.

7.1. Free radical photo-polymerization

The majority of commercial photo-polymerization systems is based on free radical chemistry. These systems typically consist of blends of ethylenically unsaturated compounds such as acrylates or methacrylates, and a small amount (0.5 to 6%) of a photo-initiator. The photo-initiator (*PI*) absorbs light in a given range of wavelengths (usually in the UV region, but there are several visible-light photo-initiators available), and splits into free-radical fragments (*PI*•). In some cases the free radicals thus formed can initiate a polymerization by reacting directly with the double bond of a monomer; in other cases the free radicals abstract hydrogen atoms from other species, which in turn become the initiating species. The reaction then proceeds as in any traditional free radical polymerization: monomers add to the initiated species (propagation), and the chains keep on growing until two growing chains find each other and terminate either by combination or by disproportionation. This process is represented below:



In addition, a growing chain can terminate by abstracting a hydrogen from another molecule (solvent, monomer or polymer), which in turn becomes a free radical and can propagate the reaction). This process is known as chain transfer:



In many reactions, chain transfer determines the ultimate crosslink density achieved during cure.

Both the reaction kinetics and the network formation in free-radical systems are very different from the step reactions described earlier in this chapter. In an ideal system where diffusion control is not an issue, the rate of polymerization is given by:

$$R_p = \frac{k_p}{\sqrt{k_t}} \sqrt{R_i} [M] \quad (30)$$

where k_p and k_t are the kinetic constants for propagation and termination, respectively, R_i is the rate of initiation, and $[M]$ is the monomer concentration. The initiation rate in turn is given by:

$$R_i = \phi I [PI] \quad (31)$$

where ϕ is a factor called photo-initiator efficiency which varies from 0 to 1, I is the intensity of the irradiation, and $[PI]$ is the photo-initiator concentration.

One of the main differences between the kinetics of traditional step-reaction thermosets and photo-initiated free radical polymerization is the temperature dependence. It is well known that higher temperatures will accelerate the cure of thermosets such as epoxies, silicones and urethanes. However, this is not the case in photo-initiated free radical systems. The rate of photo-initiation itself (R_i) is fairly independent of temperature, since the activation energy for this reaction comes directly from light absorption and not from thermal motions. From Eqs. (30) and (17) one can easily see that the temperature dependence of R_p is given by the factor $\exp\{-[1/RT][E_p - E_t/2]\}$, where E_p and E_t are the activation energies for propagation and termination, respectively. Thus, if $E_t/2 > E_p$, the overall reaction rate will actually slow down if the temperature is increased. This is actually the case in many practical systems, in particular where molecular mobility is limited, since an increase in temperature will facilitate termination to a greater extent than propagation.

Free radical systems also behave very differently from step-polymerization systems in the diffusion-control regime. In the case of step polymers, discussed in section 6.4, the onset of the diffusion control regime causes a drastic reduction in the rate of polymerization. On the contrary, free-radical systems can experience an *acceleration* of the rate of reaction when diffusion control becomes important. This phenomenon, commonly known as

the “gel effect” or the “Trommsdorff effect”, is caused by the fact that as mobility becomes limited, termination reactions (which involve long polymer chains) are more severely affected than propagation reactions. This leads to an increase in the overall rate of polymerization.

The kinetics of realistic photo-polymerization systems can differ markedly from the idealized Eq. (30). There are many phenomena that cause photo-polymerization to be much more complex. One example is the phenomenon known as “reaction diffusion” mechanism [71-73]. This mechanism occurs when relatively immobile free radicals, instead of terminating by diffusing and reacting directly with each other, propagate through a matrix of unreacted functional groups and monomer, until a second radical is encountered for termination. Instead of requiring diffusion of two large molecular species to find each other and terminate, this mechanism relies on the free radical itself “jumping” from a relatively immobile species, propagating (and polymerizing) through adjacent functional groups, thus changing the physical location of the free radical without the original molecule traveling. Eventually this “jumping” free radical encounters another free radical and terminates. The “reaction diffusion” mechanism is evidenced by k_t being proportional to k_p in this regime. Other complexities in free radical polymerization involve chain length-dependent termination [74,75] and primary radical termination [76].

Most photo-polymerizations of crosslinked systems of commercial interest are carried out using high intensity UV sources. It has been experimentally observed that k_p and k_t are actually not constant throughout the reaction. During the exposure process, the reaction goes through three stages [77]:

Stage I: the reaction rate increases rapidly with time because of the Trommsdorff effect described previously, until a maximum reaction rate is reached.

Stage II: the reaction rate remains constant for a period corresponding to about 30% conversion. During this stage the reaction is in the “reaction diffusion” control mode.

Stage III: propagation becomes diffusion controlled, and the reaction rate drops.

In addition, it has been found that, at high light intensities, the polymerization rate does not follow a square root dependence on light intensity as expected from Eqs. (30) and (31). In fact, at very high intensities a saturation effect is reached – polymerization rate becomes independent of light intensity [77]. The proposed explanation is that under these conditions the concentration of primary free radicals (those generated directly by illumination before propagation takes place) is much larger than that of the macroradicals (the radicals on the propagating growing chains), and therefore termination is dominated not by bi-molecular termination between macroradicals, but by termination with primary radicals [76]. A comprehensive kinetic model for free

radical photo-polymerization systems has been published recently by Goodner and Bowman [78].

7.2. Cationic photo-polymerization

Several classes of molecules can undergo polymerization initiated by an acid species (cationic polymerization). Examples of these molecules include epoxies, vinyl ethers, oxetanes, *etc.* Although the existence of the cationic polymerization mechanism has been known for many decades, it was not till the invention of iodonium and sulfonium salts photo-initiators by Crivello in the late 1970s that cationic *photo-polymerization* became practical [79-82].

Considerable attention has been devoted to the study of the mechanism of cationic photo-initiation, which is somewhat complex. Upon irradiation and after several steps involving radical ions, a Bronsted acid is generated. This acid species can initiate a chain polymerization of a suitable monomer such as an epoxy. The polymerization is typically terminated by chain transfer to impurities or other species such as alcohols. There is no equivalent to the bi-molecular termination mechanism common with free radical systems.

One of the most significant differences between cationic and free radical photo-polymerizations is that the cationic mechanism is a "living" polymerization - once the acid species is generated, it remains active even after irradiation stops. In fact, even after the monomer is depleted, further polymerization is possible by the addition of more monomer. On the contrary, free radicals "die" soon after irradiation stops, usually by reacting with each other or by oxygen quenching. The polymerization that takes place after irradiation stops is called "dark reaction." In the case of cationic systems, the dark reaction is extremely important to obtain full cure; in fact, manufacturers of commercial cationic photopolymers usually recommend a thermal (dark) post-cure after the photoirradiation process. The importance of the dark reaction to achieve full properties will be discussed in the next section. Though the dark reaction in free radical systems is not as important from the end-user point of view, it has been reported that a significant fraction of the polymerization in some very fast free radical systems occurs as a dark reaction a few seconds after illumination has stopped [77].

Cationic polymerization of epoxies and of vinyl ethers has been described in detail in the literature. Crivello has published a number of overviews [83,84]. Decker and coworkers have published experimental kinetic studies of epoxies [85] and vinyl ethers [86].

7.3. Photo-calorimetry

DSC is a very useful tool in the study of photo-initiated polymerization, but it also has important limitations. There are several "photo-DSC"s available commercially. They are also known as "DPC," differential photo-calorimeter.

Such systems can also be easily custom-built starting with a traditional DSC. The main idea consists in allowing light to hit the sample and reference pans while maintaining thermal insulation. This is commonly achieved by employing quartz windows, since quartz is both transparent and a good thermal insulator. It is advisable to filter the infrared out of the light beams to prevent the light itself from heating the sample. Even if the IR is filtered out, the DSC will register a response when intense light hits the sample holder. Therefore, it is important to ensure that the light beam also hits the reference pan, and that the intensity of the light hitting the reference and the sample containers is the same. In many cases, even after carefully balancing the beam to ensure equal energy densities in sample and reference, one frequently observes a shift in the baseline when illumination is turned on, even if one has an inert sample. It is therefore advisable to always re-run the experiment after the reaction is over, and use the second run as a baseline to be subtracted from the initial experimental run (Fig. 18).

A convenient way to balance the beam to ensure that the intensity of the light hitting the sample is the same as that hitting the reference is to place a black carbon disk in each of the DSC containers (sample and reference), and irradiate both sample and reference. Some photo-DSCs have built-in optics with mirrors that allow the adjustment of the relative intensity of the two beams. If this is not available, one can use neutral density filters, making adjustments until the net output of the DSC is 0 mW (no change between lamp off and lamp on), indicating that both the sample and the reference are receiving the same amount of energy. It should be noted that there is always a transient change in the baseline during startup of the illumination period, but after a few seconds it stabilizes to its steady state. Once the beam is balanced, one can use the carbon disks to measure the actual intensity of the beam hitting the sample. The procedure consists in monitoring the DSC output while blocking the light hitting the reference side. When light hits the black carbon disk on the sample side, it is converted into heat, which is recorded by the DSC as a shift in the baseline. Dividing the shift in the baseline (mW) by the cross sectional area of the carbon disks provides a measure of the light intensity.

Photo DSC is commonly used to measure kinetics of photopolymerizing systems. As in the case of other thermosetting reactions, the output of the DSC is directly proportional to the rate of reaction. Reproducibility, however, is much more difficult to achieve in photo-calorimetry than in standard calorimetry; thus, appropriate sample preparation is critical. Because the sample must be exposed to light, it is obvious that one cannot use standard aluminum sealed pans. In some cases one can just use an open pan, but in general it is necessary to cover the sample with a transparent material to prevent evaporation of volatile components. Sample thickness plays more of a critical role in photo-calorimetry than in standard calorimetry. The reason is that, as light gets absorbed from top

to bottom, less light penetrates through the thickness of the sample. Therefore, at any given instant, the reaction rate on top of the sample is larger than that at the bottom of the sample. Ideally one wants a sample as thin as practically possible, but in any event, the most important issue is to ensure that all samples in a series of comparative experiments have the same thickness. One way to achieve this in the case of samples with high viscosity is to weigh a droplet very accurately on a flat DSC pan (for example 0.600 mg), and to deposit on top of it a circular film of a transparent material such as a quartz disk or a polyvinylidene fluoride (PVDF) film. The transparent material will spread out the liquid to form a flat liquid film; the thickness is controlled by the amount of material used. There are specially designed photo-DSC pans that consist of a “well” area where the liquid is held, and an upper ledge or landing that holds a quartz window. Although these pans are in principle very convenient, a common problem with them is that the liquid tends to form a concave meniscus as it wets the aluminum pan, climbing up the walls, so the thickness of the liquid film is never uniform. We have found that this problem can be circumvented by pre-treating the aluminum pan with a low-surface energy coating, preferably a fluorinated coating, such as NovecTM EGC-1700 (a dilute solution of a fluoropolymer), available from 3M. Organic liquids do not wet the pans treated with this procedure, so it is possible to get nice and flat films without meniscus problems. In some cases we have found that the intensity of the beam is not uniform throughout the cross-sectional area of the sample. This problem makes itself evident if the reaction has an induction time: the regions where the light intensity is the highest start reacting before regions with lower light intensity, giving rise to apparent multiple reaction peaks. In these cases it is better to

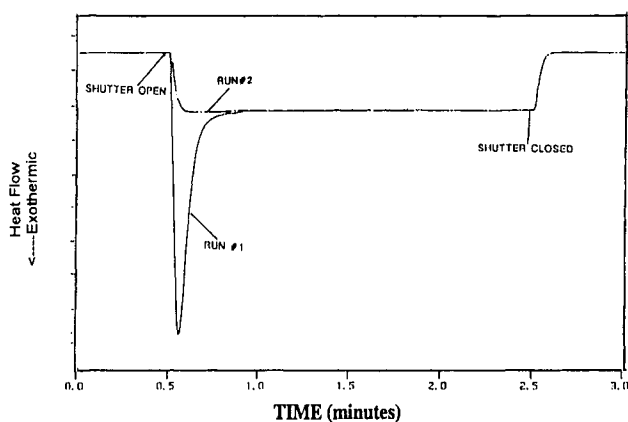


Fig. 18. Example of a photo-DSC run on a UV curable resin

employ a sample consisting of a very small droplet in the center of the sample holder, rather than a sample that spreads throughout the whole sample holder surface.

Once one learns to deal with the special sample preparation techniques needed in photo-calorimetry, the actual DSC runs and data analysis can be carried out in a manner analogous to that of other thermosetting systems. Because the light itself will usually cause a shift in the baseline, it is recommended that sample illumination not be started immediately at the beginning of the DSC run, but to wait, for example, 30 seconds before starting irradiation, and to continue the DSC run for 30 to 60 seconds after the irradiation has terminated. This way it will be easy to observe the shift in the baseline caused by illumination. Upon conclusion of the experiment, an identical run should be performed again without disturbing the sample. Assuming that the sample reacted completely during the first run, the second run will provide an indication of the thermal effect of illumination on the baseline, and can be used to correct the first run simply by performing a subtraction operation (Fig. 18).

As is the case with thermally cured thermosets, isothermal photopolymerization does not necessarily lead to a fully cured polymer if vitrification occurs during polymerization (see section 5.2). In order to achieve full conversion it is necessary to carry out the reaction above the ultimate glass transition temperature of the polymer. This should be kept in mind when one uses photo-calorimetry to determine extent of reaction.

Photo-DSC does not lend itself to the study of very fast photopolymerizations because of its relatively slow response time. Many photopolymerizations occur in fractions of a second, but the response of the photo-DSC is on the order of seconds. A technique known as RT-IR ("real time infrared spectroscopy") is recommended to study ultrafast photo-polymerizations [77,87].

With lower light intensities, when the reaction takes place in a time scale of minutes, photo-DSC can be very useful [88,89]. Anseth and coworkers demonstrated the use of photo-DSC to study the polymerization kinetics of multifunctional acrylates and methacrylates [89]. Using Eqs. (30) and (31) and the methodology outlined in section 6, one can obtain the lumped parameter $k_p/k_t^{1/2}$. The termination constant can be determined independently from the dark reaction: once the shutter for the light source is closed, generation of new radicals stops, and the concentration of free radicals is governed by the termination reaction. The dark reaction can be followed with the DSC; assuming that k_t is approximately constant over a small time interval, one can obtain [89]:

$$k_t^{1/2} = \frac{K}{2(t_1 - t_0)} \left[\frac{[M]_{t=t_1}}{R_{p,t=t_1}} - \frac{[M]_{t=t_0}}{R_{p,t=t_0}} \right] \quad (32)$$

where K is defined as the ratio $k_p/k_t^{1/2}$ determined from the steady state analysis, $[M]$ is the monomer concentration, R_p is the rate of polymerization measured directly from the DSC output as outlined in section 6.1 (Eq. (15)), and t_0 is referenced to the beginning of the dark period. It has been pointed out earlier that the values of k_p and k_t actually change during the course of the polymerization.

As mentioned in the previous section, the temperature dependence of kinetics in free radical photo-polymerizations can be different from that in thermally activated systems. In many situations the termination reaction may be more sensitive to temperature than the propagation reaction, causing the overall rate of reaction to drop with temperature; this behavior may be counterintuitive to those used to dealing with simple reaction kinetics. For example, Fig. 19 shows the conversion as a function of time at different temperatures for a photo-polymerized urethane acrylate [90]. It is evident that the photo-polymerization proceeds more slowly at higher temperatures.

In addition to the reaction rate, the cure temperature can also influence the properties of the fully cured system. It has been shown that the elastic modulus of *fully cured* rubbery urethane acrylates is lower for samples cured at high

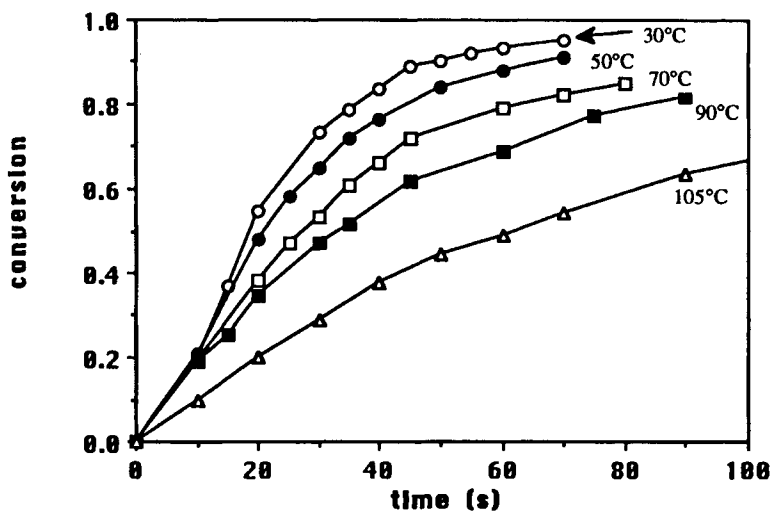


Fig. 19. Conversion versus time for a UV-cured urethane acrylate [90]

temperatures than for samples cured at lower temperatures, as shown in Fig. 20 [90]. This behavior has been attributed to an increased importance of chain transfer reactions at higher temperatures that lead to more imperfect networks.

In the case of cationically photocured systems, one typically observes the “traditional” increase of reaction rate at higher temperatures. In fact, in many cases elevated temperatures are needed in order to carry the reaction to completion in short time frames. The dark reaction in cationic photo-polymerizations can play a very significant role. Olsson and coworkers [91] have shown that room temperature photo-polymerization of a cycloaliphatic epoxy proceeds to a very limited extent during the irradiation period. An isothermal DSC run performed under irradiation at 30°C in a photo-calorimeter shows what appears to be a full exothermic peak; however, integration of this peak reveals a heat of reaction of -46 J/g, which is only 7% of the full heat of reaction expected for this epoxy resin. The glass transition temperature of a sample measured fifteen minutes after room temperature photo-polymerization was -20°C, well below the polymerization temperature. This demonstrates that diffusion control is not the reason behind the low conversion. The dark reaction, which proceeds steadily at room temperature, manifests itself as an increase in modulus and glass transition temperature. For example, in the aforementioned cycloaliphatic epoxy, the storage modulus increases from 0.2 GPa (measured 15 minutes after UV exposure) to an asymptotic value of 2.8 GPa after 1,500 minutes at room temperature. Photo-polymerization can immediately lead to

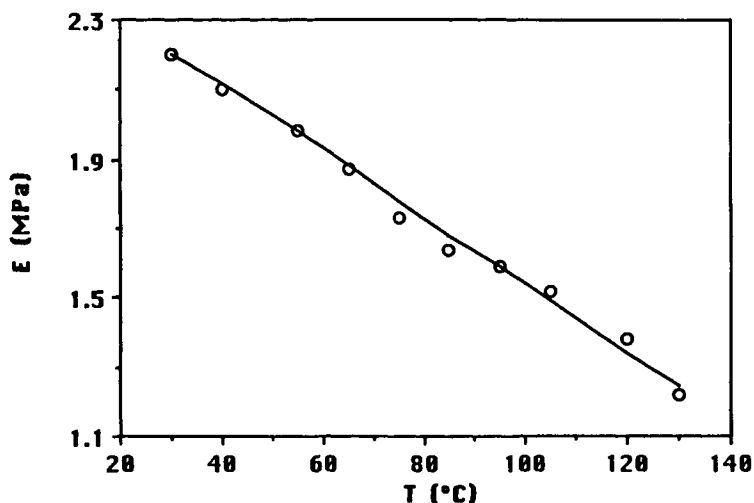


Fig. 20. Room-temperature elastic modulus of a fully reacted urethane acrylate cured at different temperatures

high levels of conversion if the irradiation is carried out at higher temperatures. For example, the reaction exotherm on the cycloaliphatic epoxy discussed above photopolymerized at 100°C is -560 J/g, which corresponds to an extent of reaction of 84% (as compared to the 7% reaction obtained with a photopolymerization carried out at room temperature) [91]. This example illustrates the importance of understanding the possible role of polymerization temperature on the overall extent of reaction, and the value of understanding qualitatively and quantitatively what results one should expect.

8. MODULATED TEMPERATURE DSC

The last decade has seen the commercialization of a powerful new calorimetric technique: modulated temperature differential scanning calorimetry (MT-DSC). This technique can be employed to deconvolute certain overlapping transitions by superimposing some kind of small amplitude temperature modulation on the underlying heating rate [92,93]. Several modulation schemes can in principle be employed: sinusoidal, saw-tooth, “ladder”, *etc.* For the sake of simplicity we shall initiate this discussion assuming a sinusoidal modulation scheme.

When a small-amplitude sine wave is superimposed on an isothermal or a linearly changing temperature program, the temperature modulation gives rise to a modulated heat flow response. One component of the heat flow signal, known as the “reversing” component, contains information from processes which are able to follow the alternating heating and cooling; this component consists of phenomena that are reversible within the time scale of the temperature oscillation. The part of the heat flow signal that, once initiated, cannot be reversed by the cyclic heating/cooling, is known as the “non-reversing” component. In order to extract the reversing and non-reversing components out of the raw signal, the latter undergoes mathematical manipulations including continuous integration, averaging and smoothing over more than one modulation period, and using a discrete Fourier transform algorithm [68,94,95]. A linear approximation is involved that requires a small amplitude of the temperature modulation and a sufficiently small underlying heating rate.

The heat capacity of the sample can be extracted directly from the reversing component of the heat flow signal; thus, transitions associated directly with the heat capacity, such as the glass transition temperature, can be considered “reversing transitions.” On the other hand, examples of non-reversing transitions include chemical reactions, molecular relaxations, cold crystallizations, evaporations, *etc.* Some transitions, such as polymer melting, contain both reversing and non-reversing characteristics.

MT-DSC can be used to separate a reversing from a non-reversing transition that would overlap in a standard DSC run. The classical example is a sample that contains polyethylene terephthalate (PET) and polycarbonate (PC).

PET shows a cold crystallization phenomenon between 130°C and 150°C that masks the glass transition of PC. However, a run employing the MT-DSC method allows to separate these transitions: a curve displaying the reversing component shows only the PC glass transition, while a curve representing the non-reversing component exhibits only the PET crystallization [92].

Differential scanning calorimeters equipped with sinusoidal modulation capabilities have been commercialized by TA Instruments under the trade name of Modulated Differential Scanning Calorimetry (MDSC). It is possible to obtain similar results by using different temperature modulation schemes such as saw-tooth or ladder wave shapes. Perkin-Elmer supplies instruments equipped with Step-Scan technology, which enables the deconvolution of reversing and non-reversing transitions by employing a “ladder” temperature profile – a program in which the DSC run is broken down into many small isothermal and linear ramping components.

The features of MT-DSC make it a very useful tool in the analysis of thermosetting systems. van Mele and coworkers [68,96] have demonstrated how this technique can be used to determine the vitrification time during the isothermal cure of thermosets. These investigators actually performed “quasi-isothermal” experiments, in which the temperature was sinusoidally modulated with an amplitude of 0.5°C and a period of 60 s. The chemical systems studied included amine-cured epoxies and anhydride-cured epoxies. van Assche and coworkers demonstrated that the heat capacity data extracted from the reversing component of the heat flow shows a transition during the quasi-isothermal run. As the cure proceeds, the heat capacity increases linearly. However, at a certain point the heat capacity undergoes a sudden step-decrease, much like the one that would be expected when a rubber transforms into a glass at the glass transition temperature. Independent measurements of T_g as a function of conversion confirm that this step decrease in C_p observed using MT-DSC techniques is indeed associated with the vitrification of the material. Conventional DSC is not capable of detecting this transition directly in one run. In order to obtain this information with a conventional DSC, it would be necessary to perform a number of experiments in which the run is stopped by quenching after partially reacting the sample, followed by a dynamic scan to measure the glass transition temperature and the residual heat of cure. After performing several of these experiments, one can generate a T_g versus conversion graph. Then, for a given isothermal cure, one can determine at what degree of conversion a T_g will be achieved that is equal to the reaction temperature – this constitutes the vitrification point. MT-DSC permits the determination of vitrification in a single run. van Hemelrijck, van Mele and coworkers [68,96] have shown how to employ this technique to generate a temperature-time-transformation (TTT) diagram.

As discussed in sections 5.2 and 6.4, when vitrification occurs during an isothermal cure of a thermosetting polymer the reaction slows down dramatically, becoming controlled by molecular mobility (“diffusion control”). van Assche and coworkers proposed a mobility factor DF^* to quantify the reaction kinetics in the diffusion control regime (section 6.4). This mobility factor can be evaluated directly using C_p data obtained with the MT-DSC. In order to verify the validity of this mobility factor DF^* , van Assche and collaborators compared it to the diffusion factor DF obtained by dividing the observed rate of reaction by the calculated reaction rate assuming that the reaction is kinetically controlled (Eqs. 21 and 28). Excellent agreement was observed.

Another application of MT-DSC for thermosetting systems is to separate the “annealing peak” due to physical aging and molecular relaxation from a glass transition. As discussed in section 5.4, an “annealing peak” on top of a glass transition can sometimes be mistaken for a melting endotherm. MT-DSC can be used to separate these phenomena, since the annealing peak is a non-reversing transition, whereas the glass transition is a reversing transition.

In the case of partially reacted samples where the residual reaction exotherm appears immediately after the glass transition temperature, the glass transition step may be masked by the reaction exotherm. MT-DSC can be used in this instance to reveal the presence of the glass transition temperature, since it is a reversing phenomenon, as opposed to the non-reversing nature of the reaction exotherm. Olsson, Bair and coworkers [91] have demonstrated how MT-DSC can be used to detect the glass transition temperature of a partially reacted epoxy resin that is partially masked by the residual reaction exotherm. The “reversing” portion of the MT-DSC scan reveals both the T_g of the sample before thermal cure *and* the T_g of the fully-cured epoxy after the end of the reaction exotherm. These results were obtained using the “step-scan” methodology of MT-DSC. The signal was generated from a series of 118 repetitive temperature steps of 2.5°C at a rate of 5°C/min with an isothermal hold of 30 seconds between each heating step.

9. CONCLUDING REMARKS

Thermosetting polymers are characterized by the fact that their processing into a finished product involves an irreversible chemical reaction. Calorimetry is uniquely positioned among analytical techniques to study thermosetting polymers, because, by measuring the heat evolved by the chemical reaction, one can directly access the progress of the reaction. Thus calorimetry is very attractive to measure extent of cure and reaction kinetics. The glass transition temperature is probably the most commonly used property to characterize a thermosetting polymer. In addition to being intricately related to reaction

kinetics, the glass transition temperature provides a measure of what the appropriate usage temperature of the product may be. Calorimetry provides a simple and efficient way of measuring glass transition temperatures. The advent of Modulated Temperature DSC in recent years has made it possible to determine vitrification times in a single experiment, thus enabling the process designer to select appropriate cure schedules more efficiently.

ACKNOWLEDGEMENTS

The author thanks the editor of this volume, Professor Stephen Cheng, for his continuing encouragement and support and for his infinite patience. The many years of collaboration with Harvey Bair, as well as his friendship and mentorship, are most gratefully appreciated. The author also expresses his warmest thanks to Dr. Edith Turi, his teacher and colleague in the area of thermal analysis education. The author's present and past management at OFS Laboratories and at Bell Laboratories are kindly acknowledged for their support and understanding, especially Lee Blyler, Xina Quan and Shiro Matusoka.

REFERENCES

1. F. Rodriguez, Principles of Polymer Systems, 3rd Edition, Hemisphere Publishing Corporation, New York, 1989.
2. L. H. Baekland, U.S. Patent 942,699; July 13, 1907.
3. A. L. Wooten, in Handbook of Thermoset Plastics, S. H. Goodman (Ed.), Noyes Publications, Park Ridge, NJ, 1986, p. 18.
4. Knopf and W. Sheib, Chemistry and Applications of Phenolic Resins, Springer-Verlag, New York, 1979.
5. R. B. Prime, in Thermal Characterization of Polymeric Materials, 2nd Edition, E. A. Turi (Ed.), Academic Press, San Diego, 1997, Volume 2, p. 1379.
6. W. Macosko and D. R. Miller, *Macromolecules*, 9 (1976) 199.
7. R. Miller and C. W. Macosko, *Macromolecules*, 11 (1978) 656.
8. R. Miller and C. W. Macosko, *Macromolecules*, 13 (1980) 1063.
9. R. Miller and C. W. Macosko, *J. Polym. Sci.*, 26 (1988) 1.
10. R. J. J. Williams and C. I. Vallo, *Macromolecules*, 21 (1988) 2571.
11. J. K. Gillham, in Developments in Polymer Characterization – 3, J. V. Dawkins (Ed.), Applied Science, London, 1982, p. 159.
12. J. B. Enns and J. K. Gillham, *J. Appl. Polym. Sci.*, 28 (1983) 2567.
13. J. K. Gillham, *Poly. Eng. Sci.*, 26 (1986) 1429.
14. W. X. Zukas, *J. Appl. Polym. Sci.*, 53 (1994) 429.
15. Wisanrakkit and J. K. Gillham, *J. Appl. Polym. Sci.*, 41 (1990) 2885.
16. S. L. Simon and J. K. Gillham, *J. Appl. Polym. Sci.*, 53 (1994) 709.
17. M. T. DeMeuse, J. K. Gillham and F. Parodi, *J. Appl. Polym. Sci.*, 64 (1997) 15.
18. A. L. Wooten, in Handbook of Thermoset Plastics, S. H. Goodman (Ed.), Noyes Publications, Park Ridge, NJ, 1986, p. 45.
19. M. L. Berins (Ed.), *Plastics Engineering Handbook of the Society of the Plastics Industry*, Fifth Edition, van Nostrand Reinhold, New York, 1991.

20. O. C. Zasko, in *Handbook of Thermoset Plastics*, S. H. Goodman (Ed.), Noyes Publications, Park Ridge, NJ, 1986, p. 59.
21. Lee and K. Neville, *Handbook of Epoxy Resins*, McGraw-Hill, New York, 1967.
22. C. A. May and Y. Tanaka (eds.), *Epoxy Resins: Chemistry and Technology*, Marcel Dekker, New York, 1973.
23. M. Szycher, *Szycher's Handbook of Polyurethanes*, CRC Press, Boca Raton, Florida, 1999.
24. C. W. Macosko, *RIM Fundamentals of Reaction Injection Molding*, Hanser Publishers, Munich, 1989.
25. E. Crigat, R. Püter, *Angew. Chem. Int. Edit.*, 6 (1967) 206.
26. K. K. Weirauch, P. G. Gemeinhardt and A. L. Baron, *Soc. Plast. Eng. Tech. Papers*, 22 (1976) 317.
27. Hamerton, *Chemistry and Technology of Cyanate Ester Resins*, Blackie Academic and Professional, Glasgow, 1994.
28. A. L. Landis, in *Handbook of Thermoset Plastics*, S. H. Goodman (Ed.) Noyes Publications, Park Ridge, NJ, 1986, p. 266.
29. Website www.shikoku.co.jp/eng/product/labo/benzo/main.html
30. R. A. Fava, *Polymer*, 9 (1968) 137.
31. E. F. Oleinik, *Pure Appl. Chem.*, 53 (1981) 1567.
32. E. F. Oleinik, *Adv. Polym. Sci.*, 80 (1986) 49.
33. A. Hale, C. W. Macosko and H. E. Bair, *J. Appl. Polym. Sci.*, 38 (1989) 1253.
34. E. Bair, ASTM STP 1249, R. J. Seyler, Ed., American Society for Testing and Materials, Philadelphia, 1994, p. 50.
35. T. G. Fox and S. Loshaek, *J. Polym. Sci.*, 15 (1955) 371.
36. H. Gibbs and E. A. DiMarzio, *J. Chem. Phys.*, 28 (1958) 373.
37. E. A. DiMarzio and J. H. Gibbs, *J. Chem. Phys.*, 28 (1958) 807.
38. E. A. DiMarzio, *J. Res. Natl. Bur. Std., Sect. A*, 68A (1964) 611.
39. A. T. DiBenedetto, "unpublished results", as cited by L. E. Nielsen, *J. Macromol. Sci., Rev. Macromol. Chem.*, C3 (1969) 69.
40. H. E. Adabbo and R. J. J. Williams, *J. Appl. Polym. Sci.*, 27 (1982) 1327.
41. C. Feger and W. J. MacKnight, *Macromolecules*, 18 (1985) 280.
42. A. T. DiBenedetto, *J. Polym. Sci., Part B: Polym. Phys.*, 25 (1987) 1949.
43. P. Pascault and R. J. J. Williams, *J. Polym. Sci., Part B: Polym. Phys.*, 28 (1990) 85.
44. P. R. Couchman, *Macromolecules*, 13 (1980) 1272.
45. H. Stutz, K. H. Illers, and J. Mertes, *J. Polym. Sci., Part B: Polym. Phys.* 28 (1990) 1483.
46. A. Hale, C. W. Macosko, and H. E. Bair, *Macromolecules*, 24 (1991) 2610.
47. T. G. Fox and P. J. Flory, *J. Appl. Phys.*, 21 (1950) 581.
48. T. G. Fox and P. J. Flory, *J. Polym. Sci.*, 14 (1954) 315.
49. S. Lunak, J. Vladyka, and K. Dusek, *Polymer*, 19 (1978) 931.
50. G. Wisanrakkit and J. K. Gillham, *J. Coat. Tech.*, 62 (1990) 35.
51. H. E. Bair, *Polym. Prepr.*, 26 (1985) 10.
52. E. A. DiMarzio and F. Dowell, *J. Appl. Phys.*, 50 (1979) 6061.
53. C. E. Struik, *Physical Aging in Amorphous Polymers and Other Materials*, Elsevier, New York, 1978.
54. R. N. Haward (Ed.), *The Physics of Glassy Polymers*, John Wiley and Sons, New York, 1973.
55. S. Matsuoka, *Relaxation Phenomena in Polymers*, Hanser Publishers, Munich, 1992.

56. A. Hale and H. E. Bair, in *Thermal Characterization of Polymeric Materials*, 2nd Edition, E. A. Turi (Ed.), Academic Press, San Diego, 1997, Volume 1, p. 745.
57. R. Grooten and G. ten Brinke, *Macromolecules*, 22 (1989) 1761.
58. G. ten Brinke, L. Oudhuis, and T. S. Ellis, *Thermochim. Acta*, 238 (1994) 75.
59. S. Matsuoka, X. Quan, H. E. Bair, and D. J. Boyle, *Macromolecules*, 22 (1989) 4093.
60. S. Sourour and M. R. Kamal, *Thermochimica Acta*, 14 (1976) 41.
61. E. Ryan and A. Dutta, *Polymer*, 20 (1979) 203.
62. A. Hale, M. García, C. W. Macosko, and L. T. Manzione, *Soc. Plat. Eng. Tech. Papers*, 35 (1989) 796.
63. D. W. Marquardt, *J. Soc. Ind. Appl. Math.*, 11(1963) 431.
64. R. B. Prime, in *Thermal Characterization of Polymeric Materials*, E. A. Turi (Ed.), Academic Press, New York, 1981, p. 435.
65. F. G. A. E. Huguenin and M. T. Klein, *Ind. Eng. Chem. Prod. Res. Dev.*, 24 (1985) 166.
66. L. Williams, R. F. Landel, and J. D. Ferry, *J. Am. Chem. Soc.*, 77 (1955) 3701.
67. L. D. Bravenec, Ph.D. Thesis, University of Delaware, 1983.
68. G. van Assche, A. van Hemelrijck, H. Rahier, and B. van Mele, *Thermochimica Acta*, 268 (1995) 121.
69. H. Stutz, J. Mertes, and K. Nuebecker, *J. Polym. Sci. Part A: Polym. Chem.*, 31 (1993) 1879.
70. H. Stutz and J. Mertes, *J. Polym. Sci. Part A: Polym. Chem.*, 31 (1993) 2031.
71. K. S. Anseth, C. M. Wang, and C. N. Bowman, *Macromolecules*, 27 (1994) 650.
72. M. D. Goodner, H. R. Lee, and C. N. Bowman, *Ind. Eng. Chem. Res.*, 36 (1997) 1247.
73. J. S. Young and C. W. Bowman, *Macromolecules*, 32 (1999) 6073.
74. K. A. Berchtold, L. G. Lovell, J. Nie, B. Hacıoglu, and C. N. Bowman, *Polymer*, 42 (2001) 4925.
75. K. A. Berchtold, B. Hacıoglu, L. Lovell, J. Nie, and C. N. Bowman, *Macromolecules*, 34 (2001) 5103.
76. M. D. Goodner and C. N. Bowman, *Macromolecules*, 32 (1999) 6552.
77. C. Decker, B. Elzaouk, and D. Decker, *J. Macromol. Sci.- Pure Appl. Chem.*, A33 (1996) 173.
78. M. D. Goodner and C. N. Bowman, *Chem. Eng. Sci.*, 57 (2002) 887.
79. J. V. Crivello, and J. H. W. Lam, *Macromolecules*, 10 (1977) 1307.
80. J. V. Crivello, U. S. Patent 4,058,401.
81. J. V. Crivello and J. H. W. Lam, *J. Polym. Sci., Polym. Chem. Ed.*, 17 (1979) 977.
82. J. V. Crivello, *J. Polym. Sci. Part A – Polym. Chem.*, 37 (1999) 4241.
83. J. V. Crivello, *Adv. Polym. Sci.*, 62 (1984) 1.
84. J. V. Crivello, in *Radiation Curing in Polymer Science and Technology – Volume II*, J. P. Fouassier and J. F. Rabek, Elsevier Applied Science, New York, 1993, p. 435.
85. C. Decker, T. T. N. Viet, and H. P. Thi, *Polym. International*, 50 (2001) 986.
86. C. Decker, C. Bianchi, D. Decker, and F. Morel, *Prog. Org. Coat.*, 42 (2001) 253.
87. C. Decker and K. Moussa, *Makromol. Chem.*, 189 (1988) 2381.
88. C. Hoyle, in *Radiation Curing Science and Technology*, S. P. Pappas (Ed.), Plenum Press, New York, 1992, p. 57.
89. K. S. Anseth, C. N. Bowman, and N. A. Peppas, *J. Polym. Sci.: Part A: Polym. Chem.*, 32 (1994) 139.
90. R. Levin, A. Hale, A. L. Harris, N. J. Levinos, and F. C. Schilling, *Polym. Mat. Sci. Eng.*, 72 (1995) 524.

91. R. T. Olsson, H. E. Bair, V. Kuck, and A. Hale, ACS Symp. Ser., in press.
92. S. Gill, S. R. Sauerbrunn, and M. Reading, *J. Therm. Anal.*, 40 (1993) 931.
93. M. Reading, D. Elliott, and V. L. Hill, *J. Therm. Anal.*, 40 (1993) 949.
94. G. van Assche, A. van Hemelrijck, and B. van Mele, *J. Therm. Anal.*, 49 (1997) 443.
95. J. Schawe, *Thermochimica Acta*, 261 (1995) 183.
96. A. van Hemelrijck and B. van Mele, *J. Therm. Anal.*, 49 (1997) 437.

Chapter 10

Thermal analysis of polymer films

Lei Zhu

Institute of Materials Science and Department of Chemical Engineering,
University of Connecticut, Storrs, CT 06269-3222

1. INTRODUCTION

Polymer films may be considered as polymer layers or plates, where the length and width of the layer are much greater than its thickness. Generally, the thickness of a polymer film could range from a few tens of nanometers to about 0.3 millimeters. Thicker films tend to be stiffer and are usually termed as sheets. The principal applications of films are packaging and substrates for a variety of media (*e.g.*, recording tape).

1.1. Film preparation and production

Solution-casting, spin-coating, and Langmuir-Blodgett (LB) techniques are among many methods to fabricate polymer thin films. To obtain a cast film, a polymer solution is deposited onto an extremely smooth substrate surface (*e.g.*, silicon wafer, glass slide, *etc.*). After solvent evaporation, the films can be stripped from the substrate. The film thickness can be generally tuned by changing the concentration of the polymer solution and the spreading area. In order to obtain uniform films, the substrate has to be extremely leveled, *e.g.*, on a suspension table. The lower limit of the surface roughness can reach 1 nm by this method.

Spin coating was developed by microelectronic industry for making resists and protective layers. In this method, the polymer solution is rapidly spun onto a flat, smooth substrate. Spreading film and promoting solvent evaporation happen in fractions of second. The film thickness, which varies from ~ 50 nm to microns, is controlled by the concentration of the solution and the spin speed. For films less than 50 nm thick, pinholes could occur due to flow instabilities. Polymer films obtained by spin coating are more uniform than solution cast films. The surface roughness can reach as low as 0.3 - 0.5 nm for amorphous polymers.

As monolayer materials (usually amphiphilic molecules) spread on the water surface, they will undergo several phase transformations upon the

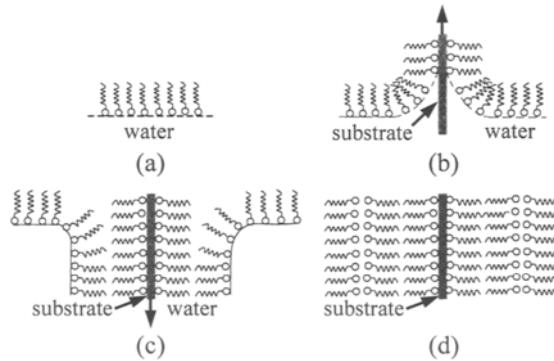


Fig. 1. (a) Self-assembled monolayer on water surface. (b) and (c) successive depositions of monolayers onto a substrate. (d) Y-type Langmuir-Blodgett film deposition

application of surface compression. This is the two-dimensional equivalent of the pressure versus volume isotherm for gas/liquid/solid transitions. The LB technique involves the vertical movement of a solid substrate through the monolayers/air interface [1-2]. Fig. 1 shows the most common form of the LB film deposition. As shown, these stack in a head-to-head and tail-to-tail pattern; this deposition mode is called Y-type. Although this is the most frequently encountered situation, instances in which the floating monolayer is only transferred to the substrate as it is being inserted into the subphase, or only as it is being removed, are often observed. Mixed deposition modes are sometimes encountered and, for some materials, the deposition type can change as the LB film is built up. It is also possible to build up films containing more than one type of monomolecular layer. In the simplest case, alternate-layer films may be produced by raising the substrate through a monolayer of one material (consisting of molecules of compound A) and then lowering the substrate through a monolayer of a second substrate (compound B). A multilayer structure consisting of ABABAB... layers is produced.

Films used in industries can be extruded from either the melt or solution. The basic steps for film fabrication are (1) polymer delivery, including liquefying, feeding, filtering, and metering, (2) extrusion/film formation, (3) solidification; (4) orientation; and (5) annealing. The films are formed by extrusion casting the molten polymer, followed by biaxial stretching and heat setting. This process is almost exclusively carried out with linear slot dies combined with a system of cooling and heating, as well as guiding rolls and tenter frames.

The standard flat-film process for a typical polyester, poly(ethylene terephthalate) (PET), is shown in Fig. 2 [3]. Funnel-type, belt-type, fluidized bed, or vacuum dryers are used to remove moisture (0.2 - 0.5%) in the polymer

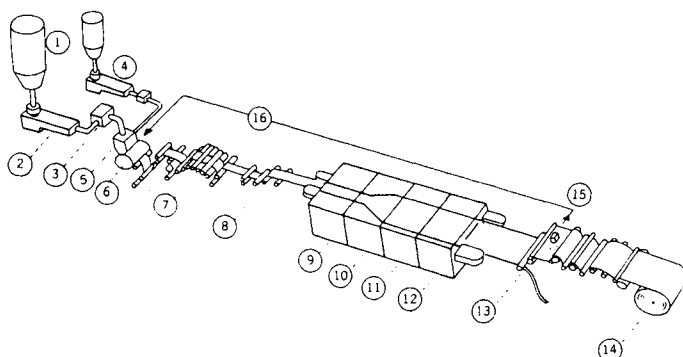


Fig. 2. Standard polyester flat-film manufacturing process: (1) Dryer, (2) extruder, (3) filter, (4) coextruder, (5) die, (6) casting, (7) longitudinal stretching, (8) in-line coating, (9) preheating zone (tenter), (10) transverse stretching, (11) heat-set zone, (12) cooling zone, (13) edge trimming, (14) windup, (15) thickness gauge, (16) automatic die gap control. Reprinted with permission from John Wiley & Sons, Inc. [3]

chips (Fig. 2-1). The dried chips (0.01% water) are fed directly to the extruder (Fig. 2-2) in an inert atmosphere. Before entering the die, the melt is filtered through packs (Fig. 2-3) of sintered or non-woven metal disks with average pore sizes of 5 - 30 μm , depending on market requirements. Coextrusion is feasible with polyester films and is carried out using multimanifold dies or confining block equipment. Compatibility of the layers is necessary for casting as well as for biaxial stretching and heat-setting processes.

The extrusion die gap and width are designed according to the final film dimensions and draw ratios desired (Fig. 2-5). The thickness profile is adjusted during production by manual or electrical control of die bolts and their corresponding influence on the die gap. The melt is extruded onto a highly polished casting drum (Fig. 2-6). Contact to the drum is assisted by electrostatic spinning, where a high voltage field forces the charged melt onto the drum. This eliminates air entrapment between the web and the drum, and ensures high surface quality.

Molecular orientation of the cast sheet is achieved by stretching the continuous web longitudinally (MD) and transversely (TD), either in sequence or simultaneously. In the sequential process, MD stretching normally takes place in one or more gaps between parallel rolls (Fig. 2-7) of defined and controlled temperatures with incremental circumferential speed. Crystallinity and orientation created by stretching depend on draw ratio (roll speed ratio) and film temperature. Some manufacturers employ an in-line coating process (Fig. 2-8) before the tenter to apply thin coatings of organic polymers to alter the surface characteristics of the film.

The largest tenter frames (Figs. 2-9 through 2-12) operate in an ultraclean environment with critically controlled heat transfer throughout the process. In

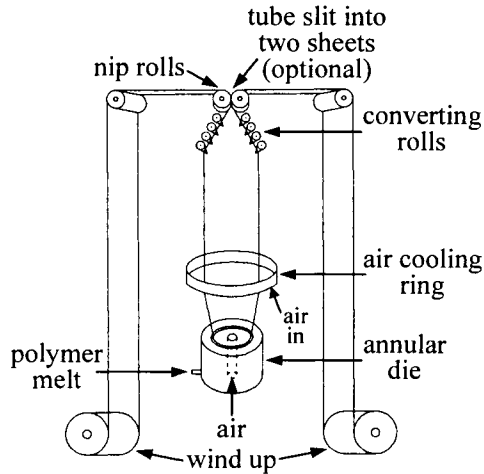


Fig. 3. Schematic of film-blowing process

the tenter the film edges are gripped by rows of clips mounted on endless chains. In the next tenter section the interchain distance is increased, stretching the film transversely.

Simultaneous biaxial stretching is performed in special tenter frames where the clips are not interconnected and stretching can therefore be carried out by accelerating the individual clips in the machine direction within the diverging TD draw section by the action of screws with a progressive pitch or a pantograph. Biaxial orientation, regardless of methods used, is followed by a heat-setting or annealing step (Fig. 2-11). The film is cooled (Fig. 2-12) in the last section of the tenter, released from the lips, trimmed, monitored for thickness (by traversing a radioactive source and sensor), and wound to form a master roll (Fig. 2-14).

If the extrusion die is annular, the process is called film blowing (Fig. 3). Air and/or other gases are pumped inside the emerging tube. A small, positive air pressure “blows up” and stretches the film laterally. A pair of nip or pinch rollers pulls the film away from the die. These rolls serve a dual function. They collapse the tube, trapping the gas and maintaining the inflation pressure. They also run faster than the polymer passes through the die; thus, the film is also stretched axially. Film blowing provides biaxial stretching in a single step. However, only low levels of orientation can be obtained before the molten film ruptures. Air is usually blown on the outside of the tube to cool the polymer and limit the expansion, although cooling is not as rapid as in the flat film process. After they are nipped, the edges of the collapsed tube may be trimmed to produce two flat films. Alternatively, the film can be cut laterally to produce plastic bags.

The major advantages of the flat film process are thickness uniformity, clarity or lack of haze, and the ability to orient and anneal the films. The major advantages of the blowing process are that it can produce wide films from relatively small dies and that simultaneous biaxial stretching makes it easier to produce “balanced” films. Note that blown films, like spun fibers, have a low level of orientation.

The “zone drawing-zone annealing” method is another special technique to prepare high-modulus, high-strength films [4-6]. This method consists of two steps: zone drawing and zone annealing, since it is difficult to directly convert the original unoriented film into a highly oriented and highly crystalline film. Zone drawing is done on the original unoriented film in order to extend and align the molecular chains, whereas zone annealing is subsequently carried out on the zone-drawn film with the intention of breaking up the original lamellar crystals and forming extended-chain crystals under high tension. During processing, the film is zone drawn by moving a slit-shaped heater from the lower part of the film to the upper part. Subsequently, the zone-drawn film is zone-annealed at the most suitable temperature for crystallization under high tension. The temperature and tension for zone annealing are much higher than those for zone drawing. Zone drawing can produce a drawn film with a much more homogeneous structure and a constant width, compared with conventional hot drawing in an oven.

Films can also be produced from solid polymers via calendering. In the calendering process, polymer chips or a thick film is passed between closely spaced, highly polished, heated rolls. The combination of heat and pressure produces a thin film. In this process, the manufacturer has little control of orientation. Chips with different colors can be calendered together to generate marble effects, for example, for floor tiles.

1.2. Multicomponent films

While simple polymer films are important, coated and multilayer or laminated films are quite common, such as coated polyester films for holographic films and for recording tapes, and most food-packaging films. Coatings are thin ($< 25 \mu\text{m}$) layers of usually polymeric material deposited onto a plastic film. Coatings are generally applied to films to enhance surface characteristics, barrier properties, and eating sealability.

Laminated films differ from coatings in that the components are films before they are combined. Typically two or more rolls of film are unwound, plied, bonded together, and rewound as a laminate. Using laminates, fabricators can often achieve specific combinations of properties at lower film thickness and cost than single-layer films. In fact, some property combinations may be impossible to obtain with known single-polymer systems. For example, a polyethylene (PE)/PET laminate provides improved barrier properties for both

oxygen and moisture. It is also common to coat or laminate polymers onto non-polymeric substrates such as paper or metal foil.

2. GENERAL EXPERIMENTAL CONSIDERATIONS IN THERMAL ANALYSIS OF POLYMER FILMS

A film is a particularly convenient form for most thermal analysis methods, because it is straightforward to cut a film into suitable shapes for general tests. For thin films, desired sample weights can be achieved by simple stacking of the film samples. Care must be taken not to deform the film during sample preparation and handling. Such deformation will significantly and irreproducibly alter the thermal response, especially those responses that are related to the processing history. The thermal response of films reflects the entire processing history of the sample, including any history induced during uses such as heating, abrasion, deformation, *etc.* Multilayer films consist of layers of different polymers or coated films will reflect both the processing history and the chemistry of each component in their thermal response.

2.1. Differential scanning calorimetry (DSC)

Films can be divided into two categories: unoriented films and oriented films. For the unoriented films, the thermal analysis results are the same as those of polymeric powders, chips and pieces cut from granules, or as-spun (unoriented) fibers. The melting, crystallization, and glass transition characteristics of these systems are not complicated by orientation effects.

The case of oriented films is more complex. Orientation and double orientation will change the characteristic temperatures, as well as the heats of transitions. Thus, the DSC curves of these oriented systems are more complicated, but they also contain more information. In addition to the effects of orientation, the DSC response will vary depending on the temperature of drawing, the draw rate, the draw ratio (DR), whether the measurement was carried out at a fixed length (constrained state measurement), whether shrinkage was allowed to take place during the heating (unconstrained state or free-to-shrink measurement), *etc.* Most DSC measurements on oriented films have been carried out in an unconstrained state other than the constrained state (*i.e.*, more difficult technically). In these cases, it should be noted that the shrinkage of semicrystalline oriented film samples leads to melting points that are lower than those in the constrained state or fixed length measurements. Therefore, shrinkage of oriented films plays a crucial role during DSC heating.

2.2. Thermomechanical analysis (TMA)

Care should be taken to minimize the edge effects in TMA experiments. In contrast to fibers, the position of the cut strip with respect to the geometry of

the original film is of paramount importance, because the local molecular chain and crystalline orientation is a very strong function of the position in the film where the particular sample is cut.

TMA can be easily used to determine the coefficient of thermal expansion (CTE) in both in-plane and out-of-plane directions ($\alpha_{//}$ and α_{\perp} , respectively). For the in-plane CTE measurement, the linear CTE values can be obtained by extrapolating the apparent CTEs under different tensions to zero stress.

For the out-of-plane CTE measurement, several methods have been carefully examined. Saraf and co-workers [7] reported the set of the “capacitance change technique” to determine the α_{\perp} . In this technique, a square area is cut out from the polymer film, and the remaining U-shaped film is placed between two parallel plate electrodes (Fig. 4). This cut-out area is considerably larger than the surface area of the electrodes, so the capacitance of the capacitor measured through the air gap will not be affected by the dielectric properties of the polymeric film. Then, the α_{\perp} is calculated on the changes in the capacitance of the capacitor, so essentially the polymer film is used as a spacer to set the distance between the electrodes.

The α_{\perp} can also be obtained by means of the Fabry-Perot laser interferometric technique [8,9]. In this method, a disk from a polymer film with a hole in its center is placed between a beam splitter and a reflective substrate. Then, a laser beam from a low-power He-Ne source is directed onto the air gap formed by the polymer opening at an incidence angle close to normal, and the change in the thickness of the film during heating (or cooling) is calculated by measuring the changing phase difference between the interfering reflections. The Fabry-Perot laser interferometric technique has larger errors due to uncertainty in the initial film thickness (because the films are not perfectly flat), and this leads to an overestimation of the calculated α_{\perp} values. These errors were largely eliminated in the phase shift technique [10], where the changes in the film thickness were calculated from the phase shift taking place between

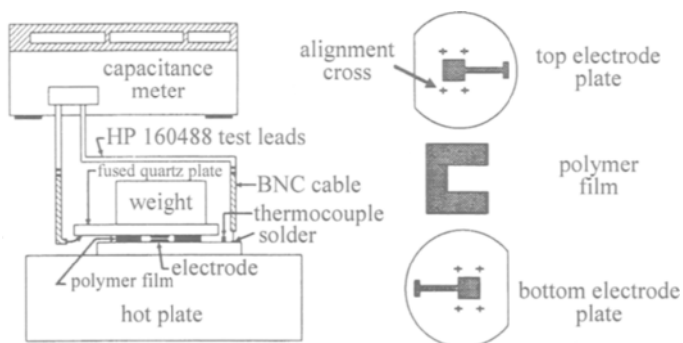


Fig. 4. Measurement of thin polymer film's CTE in the thickness direction using the capacitance technique. Reprinted with permission from John Wiley & Sons, Inc. [7]

laser beams reflected from the polymer surface at the edge of the film and beams reflected from the neighboring substrate.

The α_{\perp} may also be calculated from the volumetric expansion coefficient (CVE) and the in-plane CTE, provided that there is no in-plane anisotropy for the polymer thin films (*i.e.*, $\text{CVE} = \alpha_{//}^2 \times \alpha_{\perp}$). Pottiger *et al.* reported results on the effect of orientation on the anisotropy of thermal expansion of several polyimide films [11]. The CVE was measured using a PVT technique based on Bridgeman bellows by a pressure-volume-temperature apparatus operating with mercury as a confining fluid, as described by Zoller *et al.* [12,13]. The results showed that CVE was essentially constant, independent of molecular orientation and sample thickness. The α_{\perp} was always higher than the $\alpha_{//}$, and the $\alpha_{//}$ was shown to decrease at the expense of the increase of the α_{\perp} .

The α_{\perp} and T_g can also be determined by several other methods, such as ellipsometry, X-ray reflectivity (XR), and local thermal analysis. Beaucage *et al.* [14] used ellipsometry to determine the temperature dependence of the refractive index, and thus the thickness of thin polystyrene films. In this technique the non-invasive determination of the refractive index and the thickness of the polymer film cast on a reflective substrate can be carried out. Thus, this technique allows the determination of the α_{\perp} and T_g of the polymer films.

The thickness, roughness of both the top and bottom interfaces, and electron density distribution can be determined by XR for the polymer films. This technique involves experimentally determining the reflected intensity as a function of the scattering vector, $q = 4\pi\sin\theta/\lambda$ (λ is the wavelength and θ is the specular reflection angle), and then determining the properties by fitting to a model electron density profile. The thickness was determined with a standard

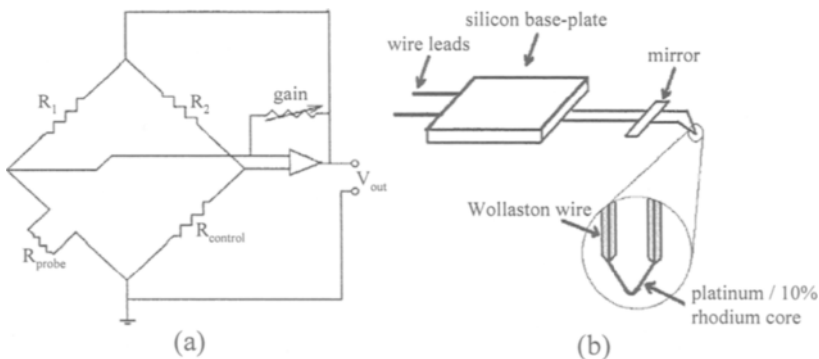


Fig. 5. (a) Schematic of the Wheatstone bridge circuit used to heat the resistive probe and record heat flows from the probe into the sample. (b) Schematic of the thermal probe that forms the probe resistance of the Wheatstone bridge. The Wollaston process wire is silver; the wire is attached to a silicon die for mounting on the scanning probe microscope head. Reprinted with permission from American Chemical Society. [15]

uncertainty of 0.2 nm.

In the local thermal analysis proposed by de Pablo *et al.* [15] resistive thermal probes connected to a thermal control unit were mounted in a scanning probe microscope equipped with a scanning head to measure the T_g for polymer films. The thermal probe was placed in contact with the sample surface and heated. The thermal control unit is a device that sets the resistance of the probe by changing the current through it with 0.05 Ω precision resistors connected to a Wheatstone bridge (Fig. 5a). The probe was a platinum/10% rhodium thermistor material that has a known dependence of temperature on resistance (Fig. 5b). The increase in power associated with the T_g event was best observed by plotting the derivative of power supplied to the probe as a function of temperature. The onset of the increase in the derivative signal as the set point of the temperature of the probe was ramped upward was identified as the T_g of the polymer film.

Ellipsometry, XR, and local thermal analysis are well-established techniques for measuring the properties of ultrathin films. Using ellipsometry and XR, T_g is determined by measuring changes in the thermal expansion of the film. In ellipsometry, the thickness data can be gathered with relative ease for a large number of points over the temperature range of interest, and the change in slope indicative of T_g is easily detected. The CTE determined by ellipsometry, however, rarely if ever matches the bulk values, even though the ratio of the measured glassy CTE to rubbery CTE is consistent with the ratio of the bulk values. For XR, the thickness of the film at each temperature is determined from fitting the reflected intensity of a single wavelength over an angular range to an electron density model. It is experimentally impractical to make a large number of thickness measurements using XR, so the temperature resolution of the XR experiments is poorer than that of the ellipsometry experiments. Using XR, it is difficult to obtain a precise T_g value. The CTE values determined by XR, however, are in good agreement with the bulk values both below and above T_g . Using local thermal analysis, on the other hand, T_g is determined by measuring changes in the heat capacity and thermal conductivity of the film and the area of contact between the probe and the polymer surface. Local thermal analysis is extremely useful for determining T_g , but yields no information on the CTE.

2.3. Thermogravimetric analysis (TGA)

Film is particularly suitable for TGA evaluation in the form of punched-out disks. Orientation effects will play little role on final results. The chemistry and stability of each component in coated and multilayer films are of special interest. Combining TGA with other analytical techniques, such as mass spectroscopy, gas chromatography, size exclusion chromatography, *etc.*, to allow identification of decomposing species adds to the sophistication and utility of these experiments.

2.4. Dynamic mechanical analysis (DMA)

DMA sometimes is referred as mechanical spectroscopy. It can easily be used on films, but the film quality must be good; otherwise, it may easily break during the test. Most commercial DMA instruments apply a sinusoidal tensile strain to one end of the film and measure the resultant stress at its other end. Thus, the complex tensile modulus of the sample (E^*) and its components (the real part, E' - the storage modulus, and the imaginary part, E'' - the loss modulus), as well as $\tan\delta = E''/E'$, can be calculated. The storage modulus generally decreases with increasing temperature, although increases are possible, e.g., during cold crystallization of amorphous films of crystallizable polymers. The transitions are displayed as peaks on the loss modulus or $\tan\delta$ versus temperature curves.

The transitions recorded in a dynamic relaxation experiment are generally designated α , β , γ , etc. Following the most accepted terminology, the highest temperature transition is called the α relaxation, and then the transitions are called β , γ , δ , etc., in the order of decreasing temperature [16]. The following are the major transitions recorded by dynamic mechanical analysis:

1. The highest-temperature (α) relaxation can be a crystalline relaxation, or it may correspond to the onset of large-scale segmental motion such as glass transition. A crystalline relaxation (often designated as α_c or α'), which takes place between the T_g and the melting temperature (T_m), is attributed to molecular motion within the crystals. Many polymers possess this dispersion, and the existence of this relaxation may be extremely important for film-stretching purposes. For example, the stretching has to be carried out at temperatures beyond α_c , i.e., between T_{α_c} and T_m , at which there is sufficient segmental mobility even in the crystalline phase.

2. Not all polymers exhibit a crystalline relaxation. Then, the α relaxation corresponds to the glass transition, which is the onset of cooperative motion of the polymeric chain segments. The temperature at which this transition takes place is higher than that measured by DSC because of the time scale of the experiment (the frequency effect). Also, the peak in $\tan\delta$ will occur at a higher temperature than the corresponding peak in the loss modulus (E''), which is considered to be more accurate.

3. Often, cold crystallization is recorded for amorphous but crystallizable films during heating. Since the cold crystallization takes place somewhat above the glass transition, the modulus first decreases considerably (because of the glass transition) and then suddenly increases to an even greater extent, because the storage modulus of a semicrystalline film is usually higher than that of the amorphous film.

4. Additional relaxations (β , γ , δ , *etc.*) may be found at lower temperatures, and they correspond to motion of side groups or onset of certain localized motion or hindered sites in the chain backbone.

The interpretation of the transitions recorded by DMA is not always straightforward. The origin of many well-known polymeric transitions is still debated in the literature. The α -relaxation peak is generally the easiest to identify with the help of other thermal analysis techniques such as DSC. At the glass transition temperature (T_g), E' decreases drastically; the magnitude of this decrease is much higher for amorphous than for semicrystalline polymers (three orders of magnitude for amorphous polymers versus less than one for semicrystalline ones). The magnitude of secondary transitions such as β , γ , δ , *etc.* is smaller than the magnitude of the α -dispersion peak. The transition next below the glass transition is usually designated as the β transition, and it often takes place at $0.75T_g$. This transition usually means amorphous phase relaxation. A γ transition may take place below the β transition. Often it is related to side-group motions in the amorphous and crystalline phases, end-group rotation, crystalline defects, or backbone-chain motions of short segments or groups. Sometimes, the γ -relaxation is attributed to a restricted motion of the main chain if at least four $-\text{CH}_2-$ groups are linked together on a linear part of the polymer chain [17]. This mechanism is known as the "crankshaft" mechanism [18,19], and may explain the γ -relaxation in PE, poly(propylene oxide), polyoxymethylene, and polyamides.

Thin films cannot support compressive stress in the DMA measurements. If the static stress is absent, or not large enough, sample buckling will occur, and part of the stress signal will be truncated [20]. The magnitude of the static tensile stress applied to the sample will have an effect on the DMA results, especially on the storage modulus [21]. Too little tensile stress is undesirable because of sample buckling, as mentioned. However, too much tensile stress is also undesirable, as it may result in a considerable amount of sample creep, and irreversible changes will occur in the structure of the samples. This is especially important at high temperatures. Since DMA measurements are mostly carried out in a wide temperature range, shrinkage, thermal expansion, and sample softening or creep will change the static stress in the sample. As a consequence, it is necessary to have a mechanism that can adjust the sample tension as the temperature is changed (autotension). Most commercial instruments do have some automated system to control the static force on the sample. This static force can be constant or change with temperature.

In addition to dynamic mechanical analysis, the most important of these measurements are determination of stress-strain curves, creep, and stress relaxation measurements. Measurement of the stress-strain curves is necessary because the pretension and the strain level for tensile DMA measurements of

thin films have to be determined before proper DMA measurements. Thus, the film is deformed at a constant rate, and the stress necessary for this deformation is measured and displayed as a $\sigma = f(\varepsilon)$ curve.

The dynamic mechanical properties of films can be tested as a function of morphology or structure (crystallinity, orientation, *etc.*), and as a function of the external variables (frequency, humidity, *etc.*). As a rule, the $\sigma = f(\varepsilon)$ curves shift toward higher temperatures as the frequency is increased in accordance with kinetic considerations (time-temperature superposition). Since the transition temperatures are strongly frequency dependent, they should always be considered together with the frequency.

Anisotropy is an inherent property of films, *i.e.*, they have different physical properties in different directions. DMA is one of the best techniques to measure this anisotropy directly. In principle, all oriented systems have several different moduli depending upon the symmetry of the system [22]. Thus, the anisotropy of polymer films can be easily studied using specimens cut in directions with certain angles to the stretch direction.

2.5. Dielectric analysis (DEA)

DEA is also referred as dielectric spectroscopy or dielectric relaxation spectroscopy. In a DEA experiment, poorer-quality films are more adequate than in a DMA experiment, since the sample is not brought into mechanical oscillation, and thus the film integrity is not endangered during the measurement. In a DEA test, one monitors the orientation or oscillation imparted to mobile molecular dipoles within sample as a function of an applied frequency and temperature. The frequency range can be very broad if combinations of several instruments are used (from 10^{-4} Hz to 10^{10} Hz). Polymers having polar bonds are obviously necessary for this technique, since dipolar reorientation is involved, but the commercial instruments are usually sensitive enough to record dielectric spectra of small concentrations of polar units or small resultant dipole moments. Thus, a special problem of this technique is the case of polymers having no polar groups, such as PE or PTFE. In these cases, the effect of the dielectric relaxation may be enhanced by introducing a few polar groups, *e.g.*, using slight oxidation or adding a small amount of polar impurities.

Of special interest in dielectric analysis of polymers is the determination of the number of dipoles participating in a given transition, scaled to the total concentration of such dipoles in the sample. Thus, the structural transitions in polymers are accompanied by changes in their dielectric properties (dielectric constant and dielectric loss corresponding to the storage compliance and loss modulus of the DMA experiments). Therefore, the changes in the dielectric properties reflect the transitions taking place in polymers.

The relaxations in dielectric spectra are labeled similarly to those in DMA traces, *i.e.*, α , β , and γ transitions, starting at the highest-temperature (α)

relaxation, which is the onset of large-scale molecular motion (the glass transition) for an amorphous polymer or a crystal melting for a semicrystalline polymer. Local-mode motions, pendent-group rotations, and crystalline relaxations appear as moderate dispersions at lower temperatures. Therefore, in most cases, the relaxations may be parallel in both DMA and DEA experiments.

2.6. Thermally stimulated current (TSC)

A special area of dielectric analysis is TSC or thermally stimulated depolarization (TSD). TSC is based on the thermally activated decay of a polymer "electret." The development of an adequate theory of this behavior that includes polymers allows this thermally activated discharge to be used as a probe in the analysis of energetics of dipole relaxations [23]. In thermally stimulated current experiments on polymeric materials, a high-voltage, stabilized DC power supply is used to polarize a film sample between two electrodes at a temperature above the transition temperature of the process of interest (*e.g.*, T_g). While the sample is held at this temperature, an electric field on the order of $10^5 - 10^6$ V/m is applied. The sample is held at this temperature for a specified time, after which the temperature is lowered well below T_g . At this latter temperature, the nonequilibrium orientation of dipoles is fixed when the field is removed. A sensitive electrometer is used to short-circuit current while the sample is heated at a constant rate. Current is generated at temperatures where sufficient mobility is induced in the dipole sites. At these temperatures, the polarized sites can change their nonequilibrium, polarized orientation to an unoriented state that is closer to thermal equilibrium. Once relaxed, the unoriented dipole no longer contributes to the depolarization current. This technique, called "global TSC," produces results that are similar to DMA or DEA operating at very low frequencies ($10^{-3} - 10^{-4}$ Hz). Its advantage compared with other relaxation techniques is that it has high resolution, *i.e.*, the relaxations that overlap in higher-frequency relaxation techniques can be separated. Finally, one should keep in mind that this method is sensitive only to dielectric phenomena, *i.e.*, relaxations of polar groups.

A popular TSC method is the windowing polarization or relaxation map analysis (RMA), often also called the thermal sampling or thermal peak cleaning technique. This technique was developed by several research groups, such as Lacabanne and co-workers [24-27], and Ronarc'h and co-workers [28,29], Fischer and Roehl [30], and Sauer and co-workers [31-33]. In this technique the sample is brought to a polarization temperature T_p and the polarization voltage is applied. Then, the sample is held at temperature T_p for a period of time, which allows the orientation of all the dipoles that have mobility at or below this temperature. The temperature is then lowered 2 - 5°C below the polarization temperature and held at this temperature, T_{dp} , with voltage off for a period of time, which allows those dipoles that are mobile at or below T_{dp} to depolarize.

This leaves only those dipoles oriented that had mobility in the temperature window between T_p and T_{dp} . At the end of the polarization period, the temperature is lowered to T_o , where no dipole mobility is possible. From this temperature the sample is heated with a linear program. The depolarization current that is observed results only from those dipoles that have remained oriented in the temperature window. Thus, this polarization can be repeated using several polarization temperatures and several depolarization temperatures.

The described thermal peak cleaning technique can be utilized to determine the activation energies at any temperature regardless of whether a specific transition is present.

2.7. Thermally stimulated creep

Lacabanne *et al.* [34] developed a new technique for studying molecular motion in solid polymers, called thermally stimulated creep (TSCr). The principle of this method is as follows. At temperature T_o the sample is subjected to a stress of magnitude σ , for a period of time t_o . T_o and t_o are chosen so that a complete orientation of the mobile units is achieved. Then, the temperature is lowered to a temperature T_o ($T_o \ll T_o$), so that the molecular motion of interest is completely frozen. Finally, the stress is removed, and the sample is heated at a constant rate (Fig. 6). During heating, the mobile units can reorient. What is recorded are the strain γ , its time derivative $|\dot{\gamma}|$, and the temperature T versus time t . Using the so-called fractional loading program, one can differentiate between a discrete and a continuous distribution of retardation times. In such a program, the sample is subjected to the stress in discrete steps, *i.e.*, during a slow

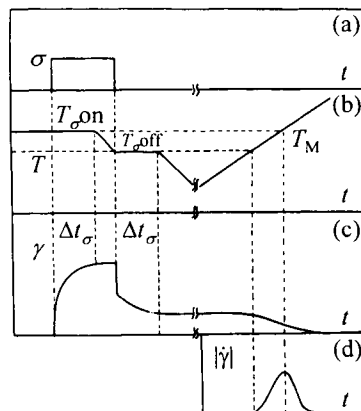


Fig. 6. A diagram showing the principle of TSCr: (a) stress σ as a function of time t ; (b) the temperature T of the sample as a function of time t ; (c) thermally stimulated creep γ as a function of time t ; and (d) the time derivative $|\dot{\gamma}|$ of thermally stimulated creep as a function of time t . Reprinted with permission from Marcel Dekker, Inc. [34]

cooling process, the stress is applied and then discontinued, then applied again, *etc.* When a discrete distribution of a finite number of retardation times exists, the temperature of the TSCr peak maximum (in the $|\dot{\gamma}|$ versus T curve) can take place only at temperature values corresponding to one of the retardation times. In contrast, when a continuous distribution of retardation times exists, a TSCr peak can be obtained with its maximum at any temperature in the temperature range where thermally stimulated creep can be found, by adjusting T_{σ} .

3. THERMAL ANALYSES OF SPECIFIC POLYMER FILMS

3.1. Polyimides

Aromatic polyimides have many useful properties such as high transition temperatures, excellent dimensional stability, and outstanding thermal and thermo-oxidative stability. They have been widely used in industry as integrated insulators due to their low CTEs and low dielectric constants. Linear optical anisotropy in the directions, which are parallel (in-plane) and perpendicular (out-of-plane) to the film surface, has been found in polyimide films. This optical anisotropy in the films has been utilized to design negative birefringent compensators for twist nematic (TN) or supertwist nematic (STN) liquid crystal displays (LCDs) to improve display's viewing angles. Soluble polyimides have therefore been sought to allow processing in the imide form in order to avoid many problems associated with handling poly(amic acid) (PAA) precursors.

Harris *et al.* developed two successful approaches to obtain solubility and thermal stability without sacrificing backbone rigidity and linearity using condensation polymerization of 4,4'-diamino-2,2'-disubstitutedbiphenyls with aromatic dianhydrides and 2,2'-disubstituted-4,4'-5,5'-biphenyltetracarboxylic dianhydrides with aromatic diamines [35-37]. The 4,4'-diamino-2,2'-disubstitutedbiphenyls include 4,4'-diamino-2,2'-dichlorobiphenyl (DCB), 4,4'-diamino-2,2'-dibromobiphenyl (DBB), 4,4'-diamino-2,2'-diiodobiphenyl (DIB), 4,4'-diamino-2,2'-dimethylbiphenyl (DMB), 4,4'-diamino-2,2'-dicyanobiphenyl (DCN), 4,4'-diamino-2,2'-bis(trifluoromethyl)biphenyl (PFMB), 4,4'-diamino-2,2'-bis(*p*-methylphenyl)biphenyl (MPPBZ), 4,4'-diamino-2,2'-bis(4-phenylphenyl)biphenyl (3PBZ), 4,4'-diamino-2,2'-bis(*p*-trifluoromethylphenyl)biphenyl (P6FDPBZ), 4,4'-diamino-3,3'-dimethylbiphenyl (OTOL), 4,4'-diamino-2,2'-bis(*o*-trifluoromethylphenyl)biphenyl (O6FDPBZ), 4,4'-diamino-2,2'-bis(*m*-trifluoromethylphenyl)biphenyl (M6FDPBZ), and 4,4'-diamino-2,2'-bis[3,5-bis(trifluoromethyl)phenyl]biphenyl (M12FDPBZ). The 2,2'-disubstituted-4,4'-5,5'-biphenyltetracarboxylic dianhydrides include 4,4',5,5'-biphenyltetracarboxylic dianhydride (BPDA), 2,2'-dibromo-4,4'-5,5'-biphenyltetracarboxylic dianhydride (DBBPDA), 2,2'-bis(trifluoromethyl)-4,4',5,5'-biphenyltetracarboxylic dianhydride (HFBPDA), 2,2'-diphenyl-4,4'-5,5'-biphenyltetracarboxylic dianhydride (DPBPDA), 2,2'-bis[*o*-(trifluoro-

methyl)phenyl]-4,4',5,5'-biphenyltetracarboxylic dianhydride (O6FDPBPDA), 2,2'-bis[*m*-(trifluoromethyl)phenyl]-4,4',5,5'-biphenyltetracarboxylic dianhydride (M6FDPBPDA), 2,2'-bis[*p*-(trifluoromethyl)phenyl]-4,4',5,5'-biphenyltetracarboxylic dianhydride (P6FDPBPDA), 2,2'-bis[3,5-bis(trifluoromethyl)phenyl]-4,4',5,5'-biphenyltetracarboxylic dianhydride (M12FDPBPDA), 2,2'-bis(3,4-dicarboxyphenyl)hexafluoropropane dianhydride (6FDA), and 2,2'-bis[4-(3,4-dicarboxyphenoxy)phenyl]propane dianhydride (BISADA).

Based on these diamines and dianhydrides, two series of polyimide samples have been studied. The first series consisted of polyimides synthesized from 6FDA dianhydride with different 4,4'-diamino-2,2'-disubstitutedbiphenyls, and are listed in Fig. 7 with corresponding chemical structures [38].

The second series consisted of polyimides synthesized from a fixed diamine structure with different 2,2'-disubstituted-4,4'-5,5'-biphenyltetracarboxylic dianhydrides. Two sets of polyimides were synthesized, PFMB-based and DMB-based polyimides. These polyimides are listed in Figs. 8 and 9 with their corresponding chemical structures [39].

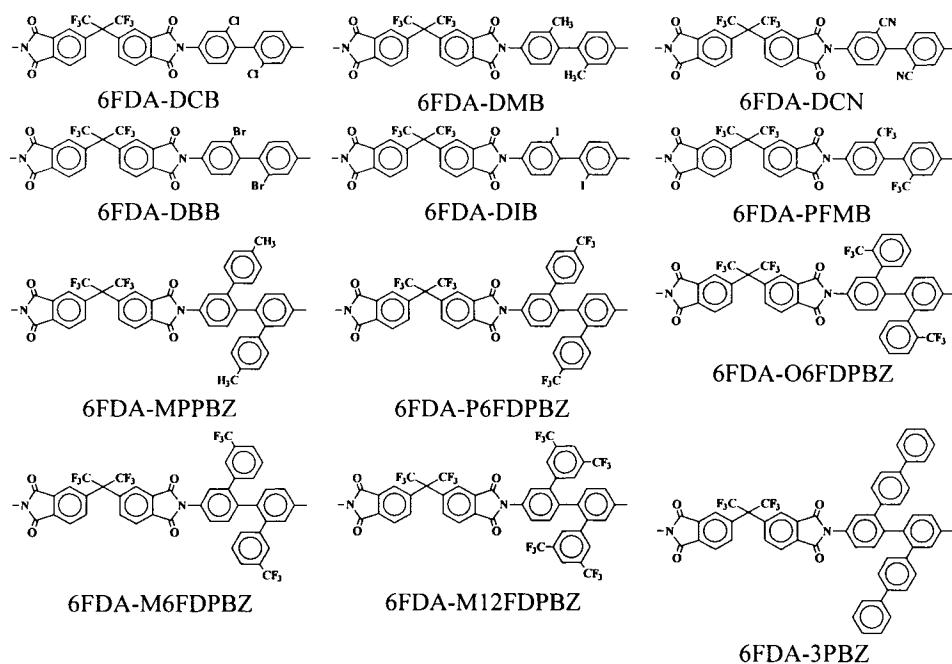


Fig. 7. A set of 6FDA-based aromatic polyimides synthesized from 6FDA dianhydride with different 4,4'-diamino-2,2'-disubstitutedbiphenyls. Reprinted with permission from Elsevier Science Ltd. [38]

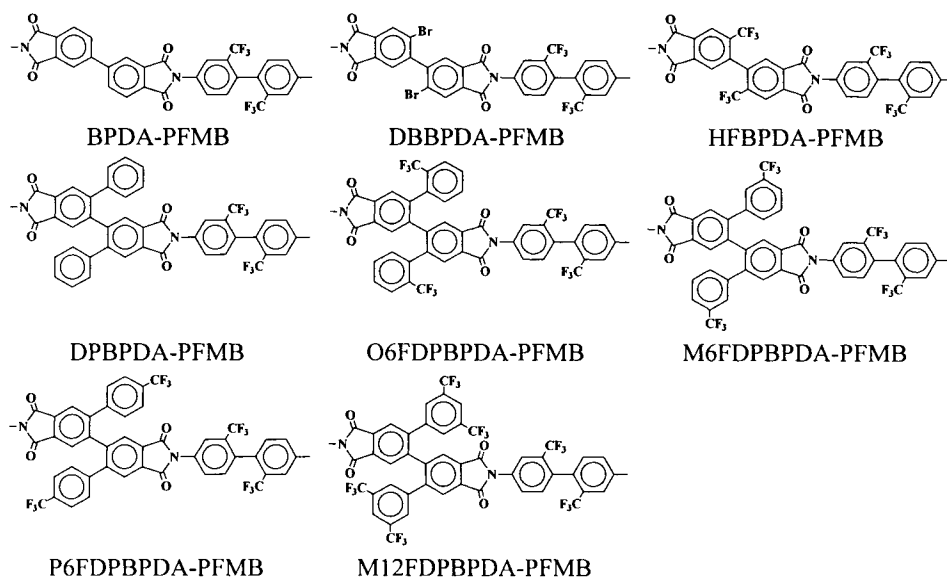


Fig. 8. A set of PFMB-based aromatic polyimides synthesized from PFMB diamine with different 2,2'-disubstituted-4,4'-5,5'-biphenyltetracarboxylic dianhydrides. Reprinted with permission from Elsevier Science Ltd. [39]

For the above structures, the steric repulsion of the substituents in the 2- and 2'-positions of the biphenyl moieties twist the rings dramatically out-of-plane. This twisted conformation inhibits chain packing and crystallization and thus improves the solubility, and it also breaks up the conjugation along the backbone and hinders the formation of intermolecular charge transfer complexes. Both of these effects contribute to a dramatic reduction in color. The films obtained from these polyimides can be utilized to design uniaxial negative birefringence (UNB) compensators in TN or STN-LCDs for improving viewing angles.

The optical refractive indices of the polyimide films were measured using a prism coupling wave-guide technique [40]. The in-plane CTEs ($\alpha_{//}$) and T_g s were measured by TMA tests on $\sim 20 \mu\text{m}$ polyimide films by extrapolation to zero stress. Two relaxation processes were observed above room temperature for all of the polyimide film samples studied. As an example in Figs. 10a and 10b, the low temperature relaxation is defined as a β relaxation process and the high temperature relaxation is an α relaxation process for 6FDA-PFMB film. The α relaxation corresponds to the glass transition while the β relaxation is a sub-glass transition. It was found that the β relaxation was more sensitive to

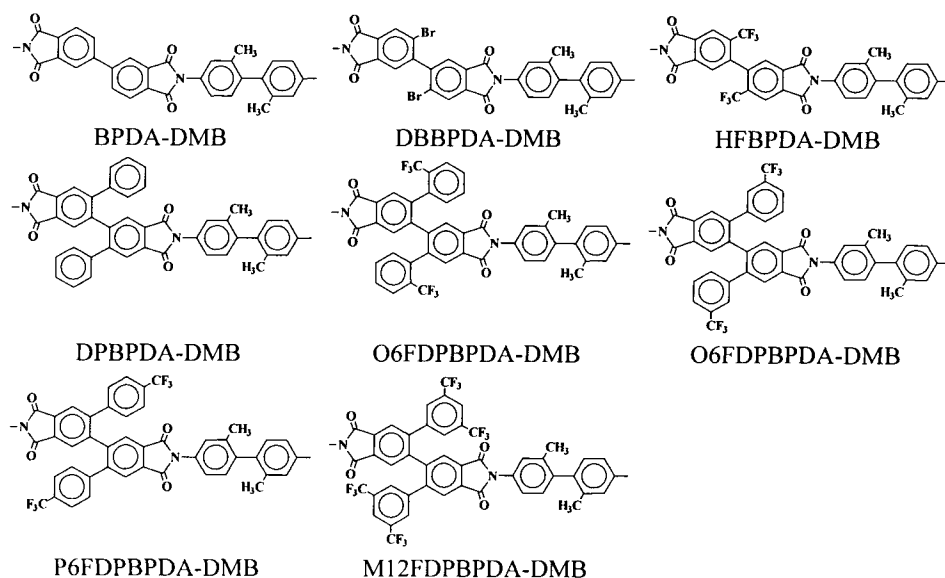


Fig. 9. A set of DMB-based aromatic polyimides synthesized from DMB diamine with different 2,2'-disubstituted-4,4'-5,5'-biphenyltetracarboxylic dianhydrides. Reprinted from Elsevier Science Ltd. [39]

frequency changes compared to the α relaxation. This indicates that the β relaxation has relatively low activation energy.

Increasing the size of disubstituted groups results in a decrease of the α relaxation temperature (from 373°C to 282°C), but an increase in the β relaxation temperature (from 112°C to 261°C) as shown in Fig. 11. This may be

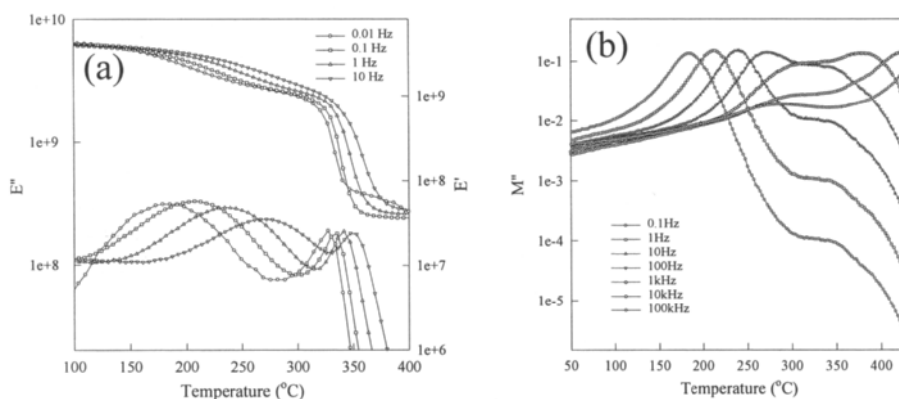


Fig. 10. (a) DMA and (b) DEA results for 6FDA-PFMB films. Reprinted with permission from Elsevier Science Ltd. [38]

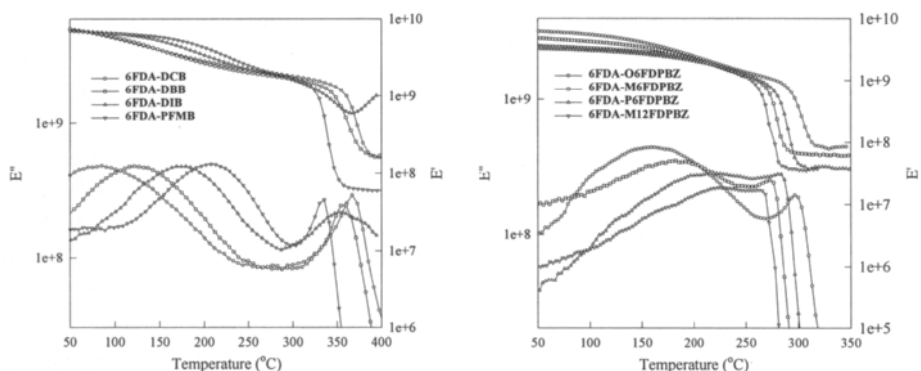


Fig. 11. DMA results at 0.1 Hz for various 6FDA-based polyimide films. Reprinted with permission from Elsevier Science Ltd. [38]

an indication that the size and anisotropic shape of the disubstituted groups affect these two relaxation processes differently. For the β relaxation process, the substituted groups mainly introduce stereo hindrance to hamper the local subgroup motion, while for the α relaxation process, it is the source of loosening molecular chain packing and thus, eliminating the segmental motion.

For 6FDA-based polyimides, the $\alpha_{//}$, T_g , UNB, and packing density data are summarized in Table 1 [41]. The packing density is defined by the film density divided by the repeating unit molecular weight of the polyimide.

Generally, the packing density decreases with increasing the side group

Table 1

The $\alpha_{//}$, T_g , UNB, packing density, and apparent activation energies for both α and β relaxations for 6FDA-based polyimides [41]

Diamine	$\alpha_{//}$ (ppm/°C)	T_g (°C) (TMA)	T_g (°C) (DSC)	UNB (Δn)	Packing density ($\times 10^{-3}$ mol/cm ³)	E_a (β) (kJ/mol)	E_a (α) (kJ/mol)
DCB	35.3	336	362	0.0563	2.252	97	656
DMB	39.1	325	355	0.0534	2.239	97	635
DCN	38.3	331	357	0.0521	2.227	116	702
DBB	37.5	329	353	0.0498	2.138	128	650
DIB	39.0	319	350	0.0431	2.001	146	713
PFMB	42.2	315	341	0.0426	2.027	157	963
MPPBZ	49.3	286	299	0.0352	1.693	180	947
O6FDPBZ	50.3	289	307	0.0330	1.633	158	731
M6FDPBZ	52.2	278	288	0.0355	1.630	217	801
P6FDPBZ	51.0	283	292	0.0328	1.612	255	1130
3PBZ	53.2	285	287	0.0312	1.488	—*	1085
M12FDPBZ	54.1	263	282	0.0271	1.471	270	933

* The data overlap with α relaxation, and thus not available.

sizes (see Fig. 7). The $\alpha_{//}$ increases, and the T_g and UNB decrease with decreasing the packing density. Therefore, the physical properties of these 6FDA-based polyimides can be predicted based on different packing densities (or different sizes and shapes of the disubstituted side groups).

The Arrhenius equation is used to obtain the apparent activation energies for these two relaxation processes, and the data for all 6FDA-based polyimides are listed in Table 1. Based on these experimental activation energies, the E_a for the β relaxation process increases from 97 kJ/mol for 6FDA-DCB to 270 kJ/mol for 6FDA-M12FDPBZ with increasing the size and anisotropic shape of the disubstituted groups. The apparent E_a s of α relaxation listed in Table 1 seem to show a trend that with increasing the size and anisotropy of the disubstituted groups, the E_a value also increases. This α process is associated with cooperative segmental motion at an even larger structural level as compared to that of the β relaxation. However, these activation energies are only apparent, and are obtained over a narrow frequency region.

If the approach proposed by Starkweather is used [42], the activation energy can thus be written:

$$E_a = RT\{1 + \ln[k/(2\pi h)]\} + \ln(T/f) + T\Delta S \tag{1}$$

where ΔS is activation entropy, f is frequency, h and k are the Plank and Boltzman constants, respectively. Starkweather proposed that for many relaxations, in particular, those involving small sub-chemical repeating unit groups which possess independent motion, the activation entropy ΔS should be

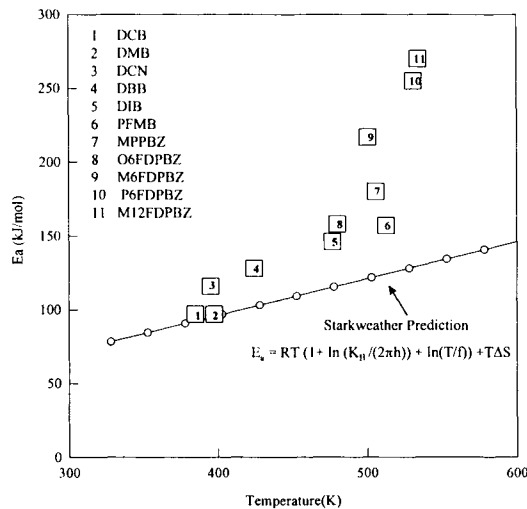


Fig. 12. Non-cooperative versus cooperative motion of β relaxation in 6FDA-based polyimide films. Reprinted with permission from Elsevier Science Ltd. [38]

close to zero [43]. Under this assumption for a relaxation at a frequency of 1 Hz, E_a follows a simple and almost linear dependence on temperature:

$$E_a = RT^{\circ} \{1 + \ln[k/(2\pi h)] + \ln(T^{\circ})\} \quad (2)$$

The extent to which the E_a exceeds this value is equal to $T^{\circ}\Delta S$. Eq. (2), therefore provides an effective lower limit for the E_a of a viscoelastic response.

Fig. 12 shows relationships between the activation energies of these aromatic polyimide films and temperature. The solid line in this figure is the calculated data based on Eq. (1). It is evident that the activation energies experimentally observed for the disubstituted groups which are smaller than CF_3 group (volumes less than 0.03 nm^3) fall on this calculated line. This indicates that the origin of these β relaxations is mainly attributed to a non-cooperative motion of diamines in the solid state. However, the experimental E_a starts to deviate from the Starkweather's line when the disubstituted groups increase their size and anisotropy, revealing that the molecular motion of these β relaxation processes is no longer non-cooperative, and rather, the cooperativity gradually increases.

The PFMB-based polyimide films have a fixed diamine (PFMB). A constant β_1 relaxation temperature (around 180°C at 0.01 Hz) can be observed for all of PFMB-based films (Fig. 13). In fact, the β_1 relaxation temperatures at all frequencies (from 0.01 to 10 Hz) are identical in these PFMB-based polyimide films. These results indicate that the β_1 relaxation is related to local motion of the diamine in polyimides. Therefore, polyimide films having the fixed diamine exhibit the same β_1 relaxation behavior. This conclusion is further supported by the experimental results of the DMB-based polyimide films. The

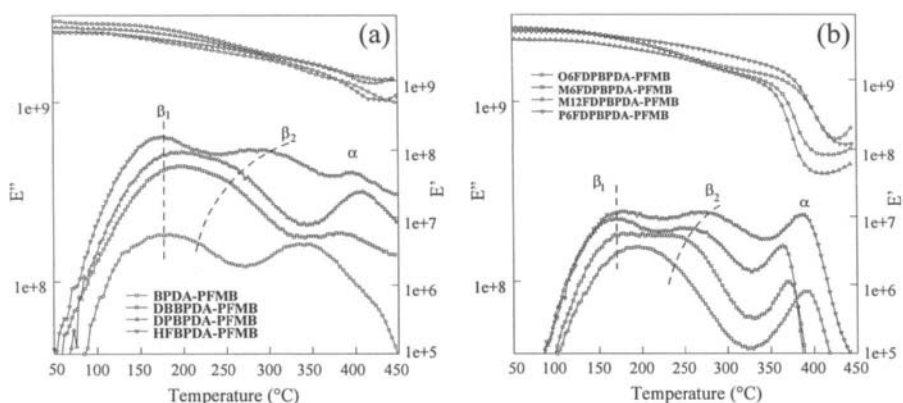


Fig. 13. DMA results at 0.01 Hz for various PFMB-based polyimide films. Reprinted with permission from Elsevier Science Ltd. [39]

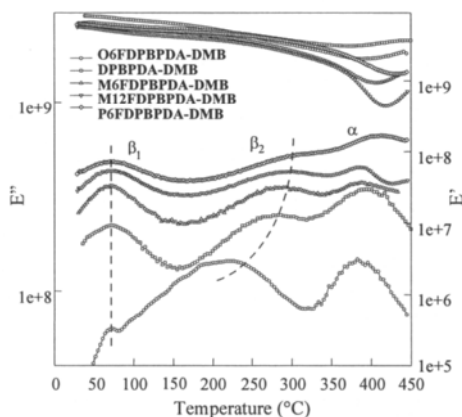


Fig. 14. DMA results at 0.01 Hz for various DMB-based polyimide films. Reprinted with permission from Elsevier Science, Ltd. [39]

DMB-based samples also have a fixed diamine (DMB). An identical β_1 relaxation temperature (around 58°C at 0.01 Hz) can be observed in all DMB-based films (Fig. 14). This β_1 relaxation also possesses the same frequency dependence (from 0.01 to 10 Hz) in these DMB-based samples.

In Fig. 13, the β_2 relaxation temperature at 0.01 Hz increases from 200°C to 300°C with increasing the size and anisotropic shape of disubstituted groups at 2,2'-positions of 2,2'-disubstituted-4,4',5,5'-biphenyltetracarboxylic dianhydrides. The same tendency of changes can also be observed in DMB-based films (Fig. 14). Thus, the β_2 relaxation is associated with the size and anisotropic shape of the disubstituted groups on 2,2'-positions of these dianhydrides.

The $\alpha_{//}$, T_g , UNB, and packing density data for PFMB- and DMB-based polyimides are summarized in Tables 2 and 3, respectively [41]. For both series,

Table 2

The $\alpha_{//}$, T_g , UNB, packing density, and apparent activation energies for both β_1 , β_2 , and α relaxations for PFMB-based polyimides [41]

Dianhydride	$\alpha_{//}$ (ppm/°C)	T_g (°C)	UNB (Δn)	Packing density ($\times 10^{-3}$ mol/cm ³)	$E_a(\beta_1)$ (kJ/mol)	$E_a(\beta_2)$ (kJ/mol)	$E_a(\alpha)$ (kJ/mol)
BPDA	7.06	304	0.1023	2.49	—*	—*	—*
DBBPDA	13.4	330	0.0752	2.30	—*	—*	—*
HFBPDA	23.2	332	0.0666	2.15	153	189	—*
DPBPDA	25.8	346	0.0635	2.08	—*	—*	—*
O6FDPBPDA	32.0	372	0.0577	1.71	—*	—*	731
M6FDPBPDA	32.7	342	0.0587	1.73	143	—*	967
P6FDPBPDA	34.5	356	0.0573	1.81	157	—*	1015
M12FDPBPDA	38.3	339	0.0501	1.61	150	—*	1115

* The data overlap with other relaxations, and thus not available.

Table 3

The α_{ij} , T_g , UNB, packing density, and apparent activation energies for both β_1 , β_2 , and α relaxations for DMB-based polyimides [41]

Dianhydride	α_{ij} (ppm/°C)	T_g (°C)	UNB (Δn)	Packing density ($\times 10^{-3}$ mol/cm ³)	$E_a(\beta_1)$ (kJ/mol)	$E_a(\beta_2)$ (kJ/mol)	$E_a(\alpha)$ (kJ/mol)
BPDA	1.26	334	0.1770	2.85	—*	—*	865
DBBPDA	10.5	337	0.0888	2.62	—*	—*	—*
HFBPDA	18.5	345	0.0734	2.49	106	—*	—*
DPBPDA	24.9	364	0.0706	2.11	106	—*	—*
O6FDPBPDA	26.5	369	0.0642	1.83	—*	168	754
M6FDPBPDA	30.6	346	0.0626	1.84	105	196	958
P6FDPBPDA	33.3	367	0.0624	1.96	101	—*	1105
M12FDPBPDA	36.9	342	0.0548	1.55	112	200	1031

* The data overlap with other relaxations, and thus not available.

the α_{ij} values gradually increase and the UNB values decrease with decreasing the packing density (or increasing the size and shape of the disubstituted side groups). The α_{ij} for each DMB-based polyimide film is smaller than that of the counterpart of PFMB-based polyimide film. This is because there is a smaller substituted group (methyl) on DMB compared to a larger one (trifluoromethyl) in PFMB.

The CTE values for both PFMB-based and DMB-based polyimide films are much lower than that of 6FDA-based polyimide films. Therefore, a 4,4',5,5'-biphenyltetracarboxylic dianhydride with the disubstituted groups on 2,2'-positions can result in a lower CTE comparing to 6FDA with an asymmetric linkage in the backbone.

It is interesting that both BPDA-PFMB and BPDA-DMB show the lowest T_g among the DMB-based polyimide films. The dependence of T_g on the size of disubstituted groups in dianhydrides for these two series of samples is different from that for 6FDA-based polyimide films. This has been explained by the existence of the *cis*-conformation in BPDA-PFMB and BPDA-DMB films. As the size of the disubstituted groups on dianhydrides increases, the looser packing may be the dominant factor and the T_g decreases with further increasing of the size of the disubstituted groups.

The T_g for each of the DMB-based polyimide films is several degrees higher than that of the corresponding one for the PFMB-based polyimide films. This is the size effect from diamine parts due to a smaller substituted group (methyl) on DMB compared to a larger one (trifluoromethyl) on PFMB.

The activation energies of the β_1 relaxation for these samples are all 150 ± 5 kJ/mol, independent of the dianhydride structure. This indicates that the origin of these β_1 relaxations is attributed to the diamine motion (PFMB). However, the α relaxation temperatures shift with changing the size of disubstituted groups

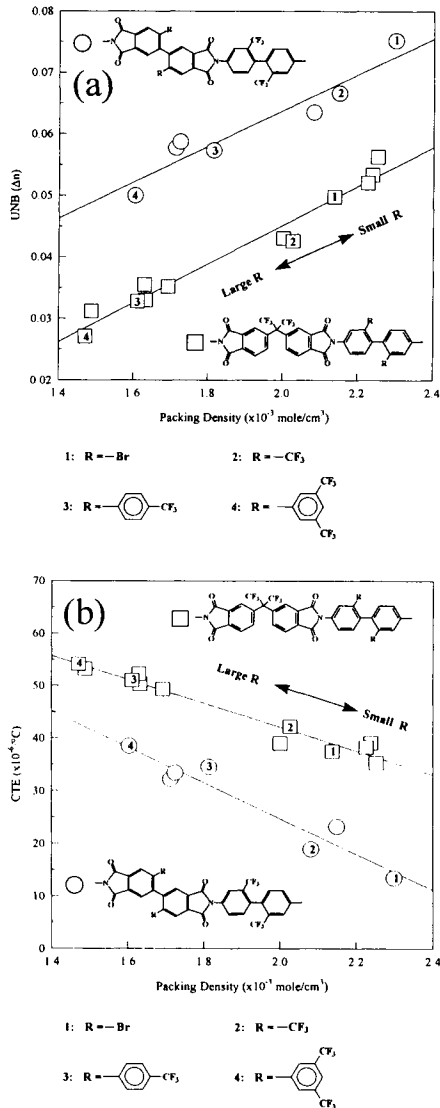


Fig. 15. (a) UNB and (b) $\alpha_{||}$ dependences on the packing density for 6FDA- and PFMB-based polyimide films [41]

on 2,2'-positions and the apparent activation energy ranges from 731 kJ/mol for O6FDPBPDA-PFMB to 1115 kJ/mol for M12FDPBPDA-PFMB (Table 2).

In Figs. 15a and 15b, the UNB and $\alpha_{||}$ versus packing density are plotted [41]. The UNB increases linearly and the $\alpha_{||}$ decreases linearly with the packing density. The slopes of the curves depend on the size and shape of the pendent

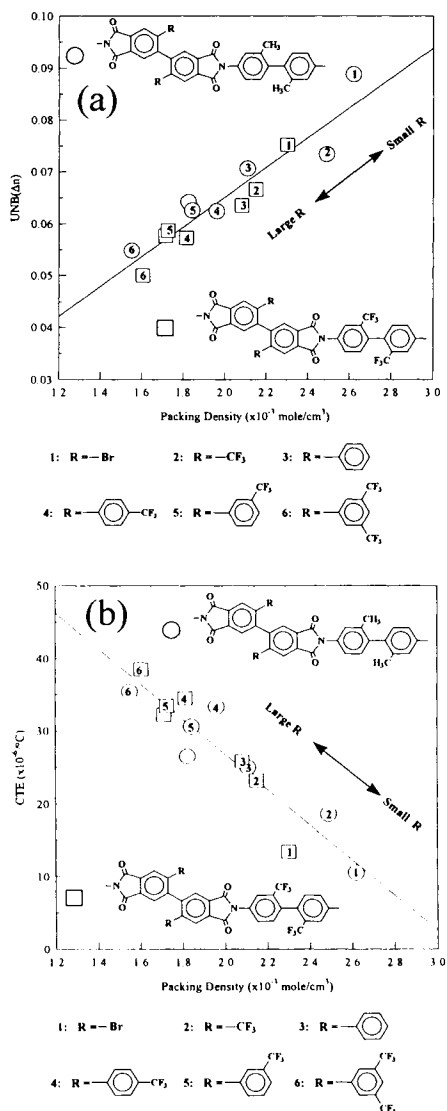


Fig. 16. (a) UNB and (b) $\alpha_{||}$ dependences on the packing density for PFMB- and DMB-based polyimide films [41]

groups: increasing the size of the pendent groups will decrease the UNB and decrease the $\alpha_{||}$ values. However, comparing the 6FDA- and PFMB-based polyimide films, the curves are shifted in the vertical direction. This is due to the different backbone structures. On the other hand, PFMB- and DMB-based polyimide films show interesting results, and the results are plotted in Fig. 16

[41]. The UNB and α_{ij} versus packing density fall on master curves due to the fact that the two series polyimides have basically the same backbone.

The capacitance technique for measuring the out-of-plane CTE has been applied to several polyimide films from pyromellitic dianhydride (PMDA)-oxydianiline (ODA), BPDA-ODA, and BPDA-*p*-phenylenediamine (PDA) [8,9]. The obtained α_{\perp} values were much higher than the CTE in-plane (*e.g.*, 81 ppm/°C as against 34 ppm/°C for Kapton H), and this difference was attributed to the in-plane orientation of the polyimide macromolecules. Coburn *et al.* [44] also found the CTE values of three different polyimides measured in the thickness direction to be an order of magnitude higher than the in-plane values. They used parallel measurements of volume expansivities from pressure-volume-temperature (PVT) data and TMA measurements in order to calculate the out-of-plane CTE. Ree *et al.* [45] reported results on anisotropic dielectric and thermal expansion behavior of poly(*p*-phenylene biphenyl tetracarboximide) multilayer and single-layer films. The same dynamic mechanical properties and the same glass transition were found for these two films. X-ray measurements indicated high in-plane orientation of the macromolecules. The α_{\perp} (74 ppm/°C) was considerably higher than the α_{ij} (2.6 - 5 ppm/°C).

Crystalline polyimides are also of interest. McHerron and Wilkes [46] described detailed DSC work performed on an electron beam-irradiated crystallizable polyimide (LARC-CPI) developed by the NASA Langley Research Center. This type of polyimide has an advantage over the traditional amorphous polyimides, since it has higher solvent resistance and improved mechanical properties (*e.g.*, modulus). Since this polyimide may be important for spacecraft applications, its response to ionizing radiation is of practical interest. The quenched, largely amorphous polymer has a T_g at 220°C, followed by a cold crystallization at $T_{cp} = 306^\circ\text{C}$, and finally a melting at $T_{mp} = 369^\circ\text{C}$. Pratt and co-workers [47] prepared a polyimide film from 4,4'-isophthaloyldiphthalic anhydride and 1,3-bis(4-aminophenoxy-4'-benzoyl)benzene. They cured the poly(amic acid) film in air at 100°C, then at 200°C. The polyimide film, when run in DSC, exhibited an endotherm at 286°C, then a cold crystallization at 317°C, followed by another endotherm at 350°C. The lower-temperature endotherm was attributed to melting of crystals formed by solvent-induced crystallization. The T_g was 216°C. Polarization optical microscopy revealed the presence of polyimide spherulites. Friler and Cebe [48] used DSC and hot-stage microscopy to follow crystallization in new types of polyimide films, described as NEW-TPI. In these polyimides, meta-linkages were introduced into the backbone, which lower the transition temperatures and make crystallization possible. The as-received amorphous film had a T_g at 251°C. Crystallization was not observed when the polyimide film was cooled from the melt, probably for very slow kinetics. If the as-received amorphous film was held at 300°C, two endothermic peaks were observed in the DSC trace recorded

during a subsequent heating at 320°C and 370°C. A shallow cold crystallization peak and a small melting peak were observed during heating of the amorphous films. The polyimide powder crystallized more easily during heating, and also during isothermal crystallization at 260°C. Hsiao and co-workers [49] also carried out a thermal characterization of New-TPI using TSC, DSC, and polarization optical microscopy. They determined the T_g as 250°C, and the equilibrium melting point (T_m°) as 406°C by the Hoffman-Weeks method; the heat of fusion of 100% crystalline polyimide was estimated to be 6.38 kJ/mol using polyimide films of 5- to 125- μm thickness. The evaluation of isothermal crystallization gave an Avrami exponent of 4, indicating three-dimensional (spherulitic) growth with thermal nucleation.

3.2. Polyolefins

3.2.1. Polyethylene (PE)

The equilibrium melting parameters of PE were directly measured on macroscopic extended-chain crystals [50]. T_m° is 141.4°C; the heat of fusion of 100% crystalline PE is $\Delta H_f^\circ = 293$ J/g. For the T_g of PE, one group accepts -36°C [51], while others favor -128°C [52]. TSC measurements indicated that both of these transitions have the characteristic of the glass transition [53]. This indicates that PE possesses a T_g having a very broad temperature region. PE films exhibit several relaxations. Its α relaxation (at *ca.* 60°C) is composed of at least two sub-relaxations, one of which corresponds to onset of the intra-crystalline motion, and the other to an inter-lamellar grain boundary slip. The β relaxation is between -30°C and -60°C; the origin of this dispersion is still in discussion. Finally, the relaxation at -120°C is assigned to local molecular motion.

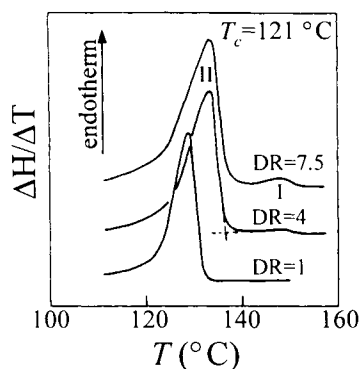


Fig. 17. Melting endotherms of lightly crosslinked PE films crystallized at 121°C at various elongations after irradiation with an electron beam of 10 Mrad. Perkin-Elmer DSC-1B, 10°C/min heating rate. Reprinted with permission from Marcel Dekker, Inc. [54]

Isothermal crystallization of lightly cross-linked PE films under constrained state was studied by Clough [54-56]. A small endothermic peak at temperatures above the major melting peak, which was attributed to melting of fibrillar crystals consisting partially of extended-chain crystals. This peak became detectable at draw ratios higher than $3.5\times$ with a melting point (end temperature of melting) of $150 - 152^\circ\text{C}$, thus at values comparable to the Illers [57] results, as shown in Fig. 17. This melting point did not depend on the crystallization temperature, and beyond the $3.5\times$ draw ratio it did not change considerably with the draw ratio. The heat of transition of this peak increased with draw ratio, reaching a maximum of *ca.* 5% crystallinity. Furthermore, the melting point increased linearly with the crystallization temperature in the unoriented sample, as expected (T_c was changed between 121.5°C and 127.5°C). Crystallization of highly oriented PE film samples in the DSC was also carried out between 132°C and 146°C . No exotherm could be observed in these experiments (probably because of instrument sensitivity problems), but the subsequent reheatings indicated the presence of the small, high temperature endotherm. In these experiments the major (lower temperature) peak was assigned to the melting of lamellar crystals, while the higher-temperature endotherm corresponds to the melting of fibrillar crystals consisting of partially extended chains. Wide-angle X-ray diffraction (WAXD) experiments of drawn PE films stress-crystallized near the melting point were also conducted [55,56]. Below $140^\circ\text{C} - 144^\circ\text{C}$, the (110) and the (200) peaks of the orthorhombic crystal forms of PE were observed. Then, a single additional peak was overlayed on the original WAXD pattern at $20.0 - 20.5^\circ$. At 150°C , the (110) and (200) peaks of PE disappeared,

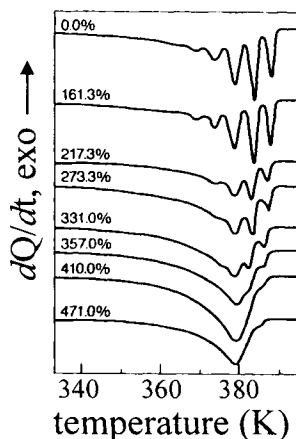


Fig. 18. Melting curves of LDPE film prepared by stepwise isothermal crystallization and stepwise heat treatment, and then drawn to various degrees indicated at each curve (samples taken from the neck portions). Data recorded by a Perkin-Elmer DSC-2 at a heating rate of $5^\circ\text{C}/\text{min}$. Reprinted with permission from John Wiley & Sons, Ltd. [60]

indicating essentially complete melting of the PE, but the new diffraction peak was preserved up to 177°C. However, no additional melting peak was observed in parallel DSC experiments. This WAXD peak was attributed to the hexagonal packing of PE chains caused by the high strain, suggesting that hexagonal chain packing (mesophase formation) was possible beyond T_m . The experiments of Illers [57] and Clough [54-56] proved the presence of extended-chain crystals in highly strained PE films. However, the melting behavior of these films (and generally of all highly deformed systems) was not determined by the crystalline phase alone; the amorphous phase also played a role. In the early studies, Peterlin and Meinel [58] came to a conclusion by studying DSC behavior of drawn PE that the tie molecules formed during the drawing were highly strained, and this helped to reduce the intra- and interchain energy of the amorphous phase (*trans* instead of *gauche* configurations), as well as the entropy of the amorphous regions. Later, Samuels [59] suggested that the melting point of drawn polypropylene samples was primarily determined by the orientation function of the amorphous regions.

Varga and co-workers [60] used stepwise isothermal crystallization and stepwise heat treatment to prepare low-density PE films having multiple melting peaks. It was shown that these melting curves truly reflect the thermal history of the samples, and a distinct “memory effect” was observed during the melting. It was suggested that the stepwise heat treatment led to formation of individually and independently melting crystallites. As indicated by the fact that the melting properties of drawn films originally had stepwise melting peaks, these individually melting crystallites had remarkable mechanical stability: the melting curves of the films did not change if the deformation level remained below *ca.* 200% stretching (see Fig. 18), far beyond the neck formation level (which is *ca.* 15 - 20%). At higher stretching, the individual melting peaks

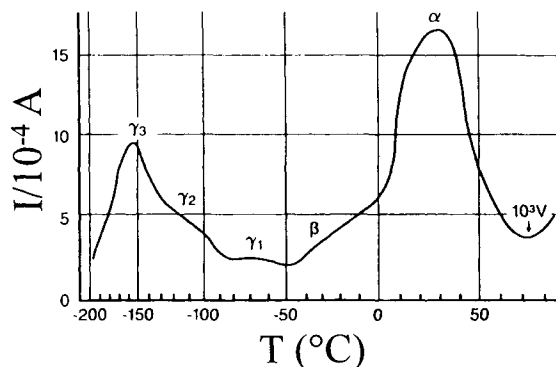


Fig. 19. Thermally stimulated current (TSC) spectrum of low-density PE. The arrow indicates the temperature of polarization. Reprinted with permission from John Wiley & Sons, Inc. [62]

gradually overlapped, the blurring starting with the low temperature peaks. Heating-rate-dependent experiments proved that this multiple melting behavior had nothing to do with reorganization during melting, and it was also shown that the crystallites having the individual melting peaks were thermally stable below the temperature of the heat treatment, which produced the crystallites. This "thermal memory effect" was attributed to the presence of irregularities (mainly branching or cross-linking) in the molecular chains.

After critically reviewed the different mechanical relaxation processes in PE, Boyd [61] suggested that there were three relaxations (α , β , and γ in the order of decreasing temperature), and all these had their origin in the amorphous phase. He considered the γ relaxation (with peak temperature at *ca.* -120°C) as having its origin in relatively localized molecular motion. The β relaxation was associated with the glass transition of PE (the peak was between -60°C and -30°C). The origin of the α relaxation (at *ca.* 60°C) was more complicated, because it required the presence of the crystalline phase. On a molecular scale, it related to the onset of translational, rotational motion in the crystals or shift of the chains by half a unit cell along the *c*-axis in the crystals, meaning a *c*-axis mobility. This elementary step changed the constraints on the amorphous segments attached to the crystals, and thus the amorphous regions might be able to further deform. Nevertheless, the α relaxation itself occurred in the amorphous phase. Berticat and coworkers [62] studied the thermally stimulated current spectra of low-density PE (Fig. 19). They showed that the α , β , and γ relaxations individually were consisted of sub-relaxation processes. Partial poling followed by calculation of the tangent of the dielectric loss angle for frequencies from 10^{-3} to 10^5 Hz resulted in seven sub-processes for the α relaxation, four sub-processes for the β relaxation, and three sub-processes for the γ relaxation. Classical DEA measurements indicated only the three relaxations at lower frequencies (0.09 to 1 kHz), and these relaxations could not be observed at higher frequencies (10 kHz). The lowest-temperature γ relaxation (γ_1 with *ca.* -160°C peak temperature at a frequency of 10^{-3} Hz) as considered by Boyer [19,63] as the glass transition of PE. The middle γ -relaxation peak (γ_2 at -120°C) was attributed to local mode relaxation [64-66], while the origin of the highest temperature γ process (γ_3 at -70°C), which had been found by Kakizaki and Hideshima [65], was unsolved. According to Berticat *et al.* [62], this last relaxation involved the crystalline regions, because this was the only γ relaxation that could be observed in linear PE. The β relaxation arised from branching in the polymer chains, because the intensity of this relaxation was directly proportional to the branch content [67,68]. Tanaka and co-workers [68] employed dynamic X-ray diffraction and dynamic birefringence in addition to DMA in studying the α relaxation of low-density PE. They concluded that this relaxation could be subdivided into a higher-temperature process (α_2), which

corresponded to intracrystalline motion with an activation energy of 130 - 250 kJ/mol, and a lower-temperature process (α_1) which involved an “inter-lamellar grain boundary slip” process with an E_a of 105 - 126 kJ/mol [65].

Stachurski and Ward [70] used the aggregate model to explain viscoelastic properties of low-density PE. The aggregate model was based on the relationship between the elastic properties of single crystals and polycrystalline aggregates consisting of a large number of small crystallites. The authors showed that the aggregate model predicted the anisotropy of the mechanical α relaxation in cold-drawn low density PE films. This anisotropy was related to the orientation of the PE crystallites. Therefore, it was concluded that this α relaxation was activated by shear of the crystallites. Owen and Ward [71] characterized the mechanical anisotropy of high-density PE films of different lamellar textures by measuring the temperature dependence of the extensional modulus under different angles to the stretch direction (0° parallel, 45° , and 90° perpendicular). The draw ratio was $8\times$. For the cold-drawn film, the small angle X-ray scattering (SAXS) and WAXS results are shown at the top of Fig. 20. It was clear that the cold-drawn, annealed PE films had double orientations with majority of the crystal lamellae oriented 45° to the draw direction, while the crystal lamellae were preferentially parallel to the drawn direction in 117°C -drawn, annealed PE films. The modulus measured parallel to the stretch

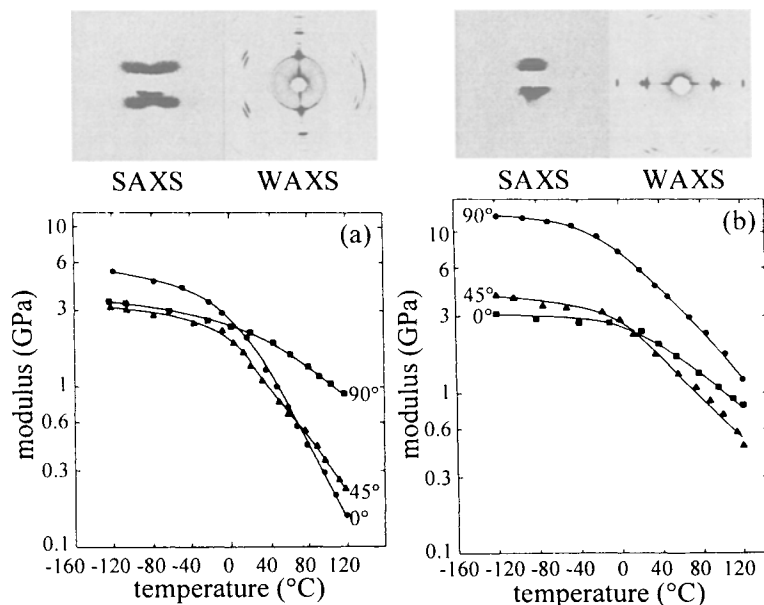


Fig. 20. Modulus data for (a) cold-drawn, annealed PE and (b) PE drawn at 117°C , annealed at 129.5°C . The top shows both SAXS and WAXS results for both cold-drawn and hot-drawn PE films. Reprinted with permission from Marcel Dekker, Inc. [71]

direction was always higher than that measured in the perpendicular direction, and the modulus measured at an angle of 45° was the lowest. However, the parallel modulus fell much more rapidly with temperature than the other two cases. Different results were obtained for hot-drawn films: the parallel modulus was always higher than the other two moduli at temperatures below 120°C . $E_{45} > E_{90}$ at low temperatures, and these two curves intercepted at 20°C to give $E_{45} < E_{90}$ at higher temperatures. It should be mentioned that in the cold-drawn and then annealed film, $E_{45} < E_{90}$ was always observed at all temperatures. At low temperatures $E_0 > E_{90} > E_{45}$, and E_0 intercepted with E_{90} at $\sim 10^\circ\text{C}$; finally, intercepted with E_{45} at $\sim 70^\circ\text{C}$. The interception of E_0 and E_{90} was explained on the basis of an inter-lamellar shear process. The decrease of E_0 was attributed to a reduction in the constraints to shear, and also to the decrease in the number of tie molecules or to the clarification of the lamellar texture. Therefore, it might be justified to assign the α relaxation to an inter-lamellar shear process, and it seemed to be proven that the existence of inter-lamellar tie molecules played an important role in determining the elastic modulus.

The dynamic mechanical and melting properties of ultradrawn high-modulus PE films produced by gelation/crystallization from decalin solution were also investigated by Sawatari and Matsuo [72]. Draw ratios of up to $300\times$ were used, and the drawing temperature was 135°C . Two methods were used to prepare the samples: quenching to room temperature (A-type) and annealing at 100°C for 60 min before cooling to room temperature (B-type). As expected, the melting peak shifted to higher temperatures, and the melting point approached a constant value of 155°C beyond draw ratios of $100\times$. Since this value was much higher than the equilibrium melting temperature of PE, it was assumed that the PE chains in the melt partially retained the extended-chain arrangement, meaning that the entropy of fusion must be smaller than the value that was obtained when fully crystalline extended-chain PE was transformed into the random coil conformation (superheating in a metastable melt). Although the melting point did not change beyond the draw ratio of $100\times$, the crystallinity of the samples continued to increase: it was 90.0% for the draw ratio of $100\times$, and 95.4% for the draw ratio of $300\times$. The dynamic storage modulus of the film also increased with the draw ratio. For the A-type samples with a draw ratio of $300\times$, the storage modulus at room temperature was 160 - 170 GPa, and it increased with temperature and reached a maximum of 180 - 190 GPa at 80°C (Fig. 21). This effect was attributed to annealing of the crystals during heating by decreasing lattice defects in the crystallites and further crystallizing the amorphous regions. The storage modulus of B-type samples decreased with increasing temperature, but even at 140°C (1.4°C below the equilibrium melting point of PE) the

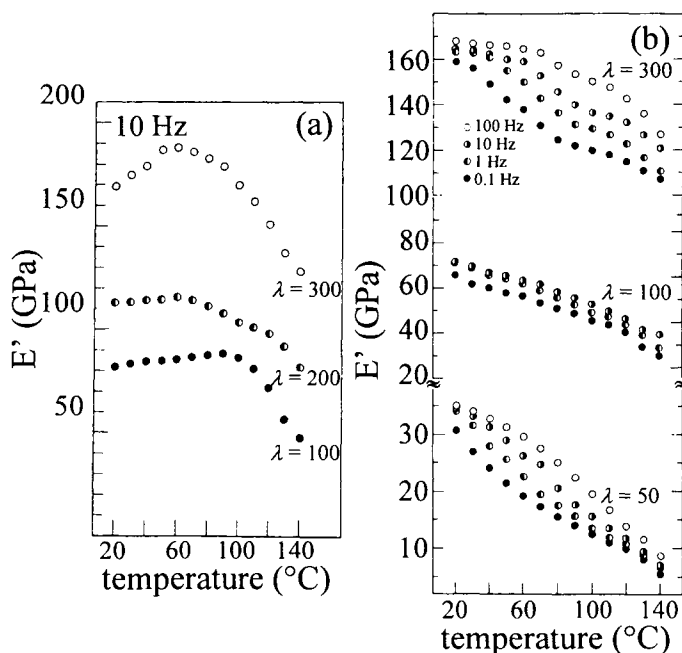


Fig. 21. Storage modulus E' versus temperature at different frequencies for (a) A-type and (b) B-type PE specimens with various draw ratios. Reprinted with permission from Springer-Verlag Heidelberg. [72]

modulus was still 120 GPa (Fig. 21). An additional attempt was made to improve the mechanical properties of the A-type drawn films by electron beam irradiation. However, the melting point of all the irradiated films decreased, and the mechanical properties became weaker. The crystallinity of the samples did exhibit slight increase up to the irradiation dose of 100 Mrad. This was assumed to be an annealing effect creating an increase of the sample temperature during the irradiation. Beyond 100 Mrad, the crystallinity decreased.

3.2.2. Polypropylene (PP)

The T_g of isotactic polypropylene (iPP) is -14°C [73,74], and its T_m° is somewhat uncertain. T_m° values from 187.5 to 220°C have been reported [50,74-77]. The heat of fusion of 100% crystalline polymer was estimated to be 165 J/g [50]. Atactic PP will not be considered here because, as in PP film production, only iPP is used for film production.

Samuels [78] provided a quantitative structural characterization of the deformation and shrinkage of iPP films. The parameters included the crystallinity x_c , the average orientation of the molecular chain axes in the crystal,

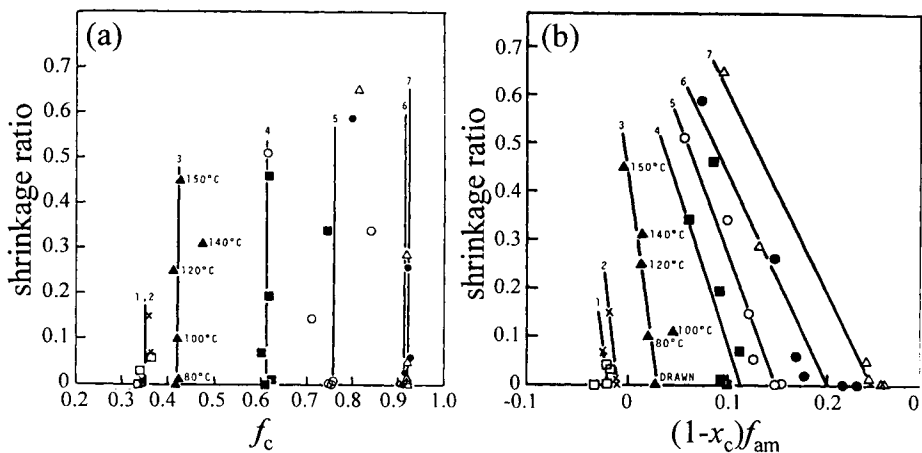


Fig. 22. Relationships between the shrinkage ratio and (a) f_c and (b) $(1-x_c)f_{am}$ of the shrunk film for oriented iPP films drawn at 110°C and shrunk at different temperatures. (\square) $f_{av} = 0.207$; (\times) $f_{av} = 0.240$; (\blacktriangle) $f_{av} = 0.294$; (\blacksquare) $f_{av} = 0.494$; (\circ) $f_{av} = 0.585$; (\bullet) $f_{av} = 0.746$; (\triangle) $f_{av} = 0.792$. Reprinted with permission from Marcel Dekker, Inc. [78]

f_c [Hermans orientation function defined as $f = (\langle 3\cos^2\theta \rangle - 1)/2$]; and the average orientation of the molecular chain axes of molecules in the noncrystalline region, f_{am} . Therefore, the average orientation state of the films was defined as $f_{av} = x_c f_c + (1-x_c)f_{am}$. In the plot of the shrinkage ratio versus f_c for iPP films with different f_{av} s (Fig. 22a), the crystal orientation function didn't change with thermal treatment. The slight change in crystal orientation was attributed to the changes in x_c (60 - 70%) under different thermal treatments. On the other hand, the amorphous orientations changed with thermal treatments (Fig. 22b): the amorphous orientation decreased as the temperature increased and the sample shrank. Therefore, it was proved that this shrinkage was controlled by the noncrystalline regions of iPP.

There is an extensive literature of dynamic mechanical analysis of iPP films. Inamura *et al.* [79] reported their study on the effect of swelling and annealing on the dynamic mechanical behavior of melt-crystallized and solution-crystallized iPP films. The highest-temperature α dispersion, which was considered a crystalline relaxation, of the melt-crystallized samples shifted to higher temperatures with annealing, but was not influenced by swelling. The β relaxation of the melt-crystallized sample exhibited a linear decrease in temperature after swelling with the amount of the absorbed solvent. No β dispersion was recorded for the solution-crystallized samples, but the α relaxation was more intense and broader than those of the melt-crystallized ones. In the swollen and annealed solution-crystallized films, new dispersion peaks were found at -55°C and at 0°C, respectively. For these films, the intensity of

the low-temperature α -relaxation component decreased after annealing, while the high-temperature α -relaxation peak component shifted to higher temperatures. Therefore, it was suggested that in the case of the solution-crystallized films, the segmental motion in the amorphous regions was highly constrained by the surrounding crystallites when compared to the melt-crystallized case. Both annealing and swelling helped to release these constraints. The intensity of the γ -relaxation peak of the melt-crystallized film decreased with swelling, while the γ peak of the solution-crystallized films was split into two peaks by swelling. Thus, the possibility was raised that the γ relaxation might take place simultaneously in both the amorphous and crystalline phases, which does not agree with the theoretical suggestions of Seferis and co-workers [80-83].

A DSC and DMA study of ultradrawn iPP films prepared by gelation/crystallization was reported by Matsuo and coworkers [84]. The main melting peak was observed to shift to higher temperature with increasing draw ratio (Fig. 23), and a new higher-temperature melting peak was found, with intensity that increased with increasing draw ratio. No superheating was observed unlike for ultradrawn PE (see the earlier discussion of PE). The dynamic storage modulus increased with increasing draw ratio, reaching 42 - 43 GPa at low temperatures for the draw ratio of 100 \times (Fig. 24a). Three relaxations

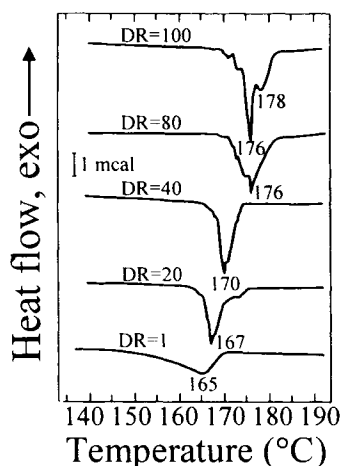


Fig. 23. The melting curves of iPP gel films drawn to different draw ratios (DRs). The draw ratios are indicated at each curve. Heating rate is 10°C/min. The measurements were performed in the unconstrained state using a Rigaku Denki 8089 TG-DSC instrument. Reprinted with permission from Society of Polymer Science of Japan, Nikon Kobunshi Gakkai. [84]

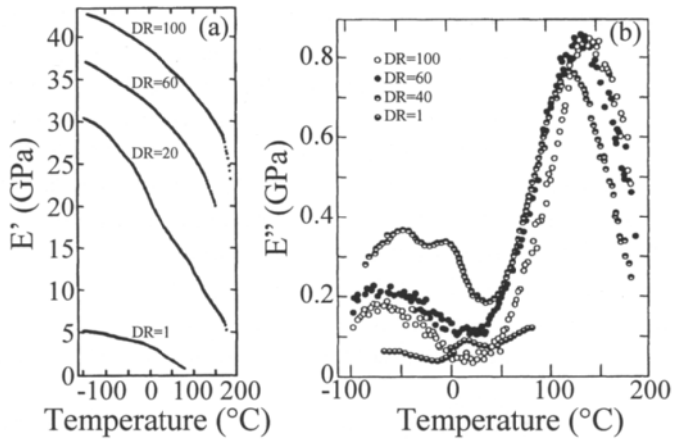


Fig. 24. The dynamic storage modulus (a) and loss modulus (b) of iPP gel films drawn to different draw ratios as a function of temperature. The draw ratios are indicated at each curve. Data generated with an Iwamoto Machine VES-P viscoelastic spectrometer at a frequency of 1 Hz. Reprinted by permission of Society of Polymer Science of Japan, Nikon Kobunshi Gakkai. [84]

were observed. The highest-temperature one (the α relaxation), which was attributed to a crystalline relaxation, shifted to higher temperatures with increasing draw ratio. This was explained by a decrease of the number of crystal defects. The β process corresponds to the glass transition. This relaxation was observed at 20°C for the undrawn film and shifted to -5°C at higher draw ratios (Fig. 24b). This indicated a more pronounced segmental motion in the amorphous phase with increasing draw ratio because, with increasing draw ratio, the crystallinity of the films increased. The behavior of the amorphous regions was speculated to become somewhat paracrystalline. The β peak disappeared at and beyond the draw ratio of 60 \times . The intensity of the γ -relaxation peak increased with increasing draw ratio, which was attributed mainly to a crystalline dispersion due to the high crystallinity of these samples. Dynamic mechanical properties of ultradrawn iPP films prepared by gelation/crystallization from solution were also reported by Sawatari and Matsuo [85]. The gel films were oriented at 165°C - 170°C up to draw ratios of 100 \times . The measured storage modulus of the films decreased with increasing temperature, although the measured crystal lattice modulus was independent of temperature. This was explained by an increase of the amorphous content of the films with increasing temperature, a process that became dominant beyond 130°C. The crystallinity of the 100 \times -drawn sample at room temperature was 86%. The relaxation mechanism of iPP was discussed as a function of draw ratio using master curves obtained by horizontal, then vertical shifting. Therefore, it was proven that two mechanical relaxations (α and β) exist. The activation energies of the α and β

relaxations decrease with increasing draw ratio. E_a values of 129 and 82 kJ/mol were obtained for the α and β processes, respectively, of the undrawn films.

An interpretation of the extensional modulus using the aggregate and fiber composite models was reported by Unwin and coworkers [86]. Roy and coworkers [87] reported DSC and DMA results on ultradrawn iPP films made of gel films of high-molecular-weight iPP prepared by gelation/crystallization from 1% decalin solution. The films were obtained by uniaxial drawing of the dry gel films. The crystallinity and the melting point of the drawn films increased with increasing draw ratio, reaching a maximum at 30 \times . Also, the dynamic storage modulus exhibited an increase with the draw ratio. The γ relaxation peak in the DMA measurements was absent or at least was very weak. The intensity of the β -relaxation peak (the glass transition) decreased and shifted to lower temperatures with increasing draw ratio. Increasing draw ratios resulted in shifting the crystalline α -relaxation peak toward higher temperatures and increasing its intensity.

Zhou and Cheng *et al.* studied sectorization with different thicknesses in the (100) and (010) sectors in syndiotactic polypropylene (sPP) lamellar single crystals [88]. It was found that both sectors possess the same crystal structure of form III based on the ED results. *In-situ* single-crystal growth can be observed using an AFM coupled with a hot stage. At $T_c = 120^\circ\text{C}$, the growth rate $G_{(010)}$ was about 1 order of magnitude faster than $G_{(100)}$, leading to a large aspect ratio R of the single crystals. The sectorization occurred at the beginning of the single-crystal growth, which was associated with different lamellar thickness. The thickness of both sectors increased during the isothermal crystallization. After the (100) thickness [$l_{(100)}$] stopped thickening, the (010) thickness [$l_{(010)}$] continued to increase. This led to a decrease of the thickness difference ratio from $\sim 35\%$ in the initial stage to $\sim 15\%$ in the later stage of crystallization. The growth rate data along the (010) and (100) normal in both the sectors, the lamellar thicknesses in both sectors, the aspect ratios and the thickness difference ratios at different t_c are listed in Table 4 for this single crystal. Stepwise cooling experiments for crystallization exhibited multiple lamellar thicknesses of the single crystals, revealing the thickness dependence on T_c (or, more precisely,

Table 4

Growth Rates [$G_{(010)}$ and $G_{(100)}$], lamellar thicknesses [$l_{(100)}$ and $l_{(010)}$], aspect ratios (α), and ratio of the thickness difference compared with the thickness of the (100) sectors (β) of an sPP single lamellar crystals for different t_c s at $T_c = 120^\circ\text{C}$. Reprinted with permission from American Chemical Society. [88]

t_c (min)	$G_{(010)}$	$G_{(100)}$	$l_{(100)}$	$l_{(010)}$	α	β
7	0.18	0.018	18.5	12.1	10.0	35%
21	0.18	0.017	20.0	13.2	10.3	35%
35	0.14	0.013	20.0	16.7	10.3	16%

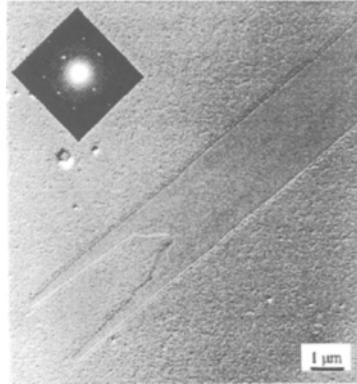


Fig. 25. Partially molten (010) sector of an sPP lamellar single crystal ($T_c = 130^\circ\text{C}$) observed in TEM using the temperature-gradient melting method. Note that the thicker crystal grown along the crystal/melting boundary in the (010) sector stops further melting of the crystals in the (010) sector. Reprinted with permission from American Chemical Society. [88]

the undercooling). The thermodynamic stabilities of these two sectors were found to be different for the perfectly annealed crystals: the (010) thin sectors apparently melted at a lower temperature compared with the (100) thick sectors observed in TEM (see Fig. 25). Superheated thinner crystals in the (010) sectors could be observed as soon as they were confined by the thicker lamellar crystals surrounding them. However, in the AFM observations of *in-situ* crystal melting, after heating the single crystals to only 5°C above the T_c (120°C), the (100) thick sectors started to melt along the free edges at the domains where defects had accumulated and served as melting nuclei. These molten domains could be repaired via a recrystallization process while annealing at this high temperature for an extended period of time. Further heating the single crystals led to a melting of both sectors along different melting pathways. For the thick (100) sectors the melting again took place via melting domains, while in the thin (010) sectors, the melting process started on the (010) free edges and progresses toward the inside of the sectors.

3.3. Poly(ethylene terephthalate) (PET)

The glass transition temperature of PET is 79°C , and its heat capacity increase at the glass transition is $77.8 \text{ J}/(\text{C}\cdot\text{mol})$ [89,90]. The T_m° of PET has been determined by various extrapolations to be 280°C [91,92]. The heat of fusion of the 100% crystalline polymer is around 140 J/g [93,94]. The nonequilibrium melting point of PET samples at a heating rate of $10^\circ\text{C}/\text{min}$ is usually $250^\circ\text{C} - 260^\circ\text{C}$. PET has two major relaxations. The α relaxation between 80°C and 125°C is essentially the glass transition, which depends on

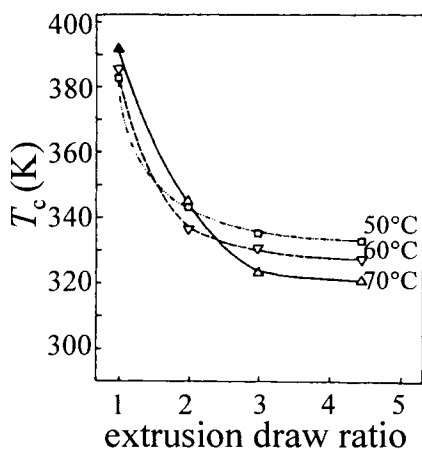


Fig. 26. Cold-crystallization temperature as a function of extrusion draw ratio EDR at various extrusion temperatures. Reprinted with permission from John Wiley & Sons, Inc. [100]

crystallinity and draw ratio [16,95]. The β relaxation (with the $\tan\delta$ peak temperature of *ca.* -40°C) is composed of at least two sub-relaxations. One is attributed to the hindered rotation of the methylene groups, and the other to the motion of the carbonyl groups associate with the *gauche* and *trans* configurations of the polymer chains [16,96-99].

A series of uniaxially drawn PET films by solid-state coextrusion below the T_g using extrusion draw ratios (EDR) between 1 (isotropic film) and 4.4 were prepared by Sun and co-workers [100]. The drawing was carried out at 67°C , and no neck formation was observed. The onset of the cold crystallization process depended on EDR at all extrusion temperatures (Fig. 26). The starting temperature of cold crystallization (T_{cco}) decreased with EDR up to EDR = 3. At higher EDR values, T_{cco} still decreased, but much more gently. Sun *et al.* concluded that more extended amorphous chains contained *trans* conformational isomer with increasing EDR, and they would be packed more easily into the crystal lattice than the amorphous segments of the undrawn samples, which contained more *gauche* conformational isomer. When the isotropic, undrawn films were annealed below 50°C , their cold crystallization parameters did not change. However, annealing beyond 50°C did lead to a decrease in T_{cco} , which was attributed to some chain rearrangement during the annealing process. If the extrusion temperature increased, this resulted in lower orientation of the coextrudates, and thus, T_{cco} increased. From nonisothermal cold crystallization experiments, the rate constant and the activation energy of cold crystallization were calculated. Note that the activation energy of cold crystallization is the minimum energy that the amorphous segments need to possess for a cold

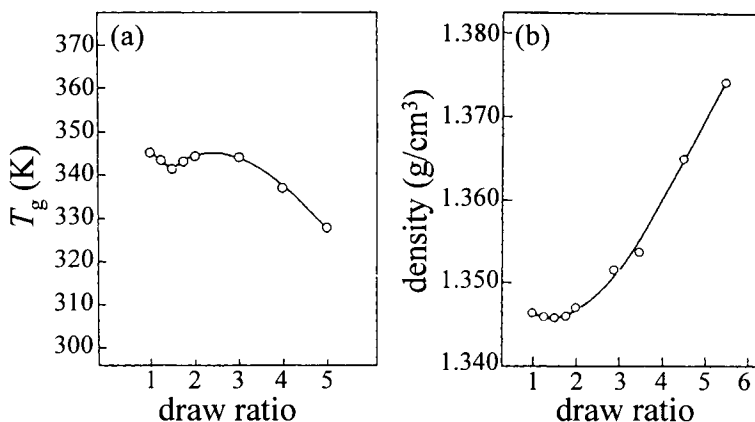


Fig. 27. (a) Change of T_g with draw ratio at heating rate of $16^\circ\text{C}/\text{min}$. (b) Change of density with draw ratio. Reprinted with permission from John Wiley & Sons, Inc. [103]

crystallization process. A first-order mechanism was obtained for cold crystallization of PET, supporting the earlier assumption of Mayhan *et al.* [101] and Miller [102]. The rate constant of cold crystallization increased rapidly with increasing EDR since cold crystallization was faster for more oriented or extended amorphous chains. T_{cc0} could also be influenced by annealing below T_g . In addition, it was concluded that the activation energy decreased rapidly with EDR, and the drop in E_a at higher extrusion temperatures was reduced.

The T_g of amorphous PET films was studied by Ito and Hatakeyama [103]. As the draw ratio increased (Fig. 27a), T_g initially decreased, reaching a minimum at DR = 1.5 ($T_g = 67^\circ\text{C}$). Further increasing draw ratios, T_g increased and reached a maximum at DR = 2.5 ($T_g = 70^\circ\text{C}$). At still higher draw ratios, T_g again decreased to 54°C at DR = 5. Correspondingly, the density of the film reached a minimum at DR = 1.5, then increased with the draw ratio (Fig. 27b). The birefringence increased with draw ratio, and the *trans* configuration content, as measured by infrared absorption, also had a minimum at DR = 1.5. The decrease of T_g when the draw ratio increased from 1 to 1.5 was explained by an increase in the configurational entropy. The decrease of T_g above DR = 2 was attributed to the increase of entropy associated with intermolecular interaction. Finally, it was suggested that from the point of view of molecular motion, local oscillations taking place in the amorphous regions of the PET films might determine the change of the T_g with the draw ratio.

The α transition of PET at first increased from 80°C to 125°C with increasing crystallinity, and then decreased with further increases of the crystallinity [16,95,96,104,105]. Illers and Breuer [16] attributed this phenomenon to changes in crystal sizes while the crystallinity was changing; on the other hand, Dumbleton and Murayama [95] explained this phenomenon by

changes in the number of crystallites. The temperature of relaxation also depended on the orientation of the film, but this dependence was rather complex, because the crystallinity dependence was superimposed on it [106]. However, when T_g 's of hot-drawn and undrawn PET films of similar crystallinity were compared, T_g of the unoriented film was 100°C, while T_g of the drawn fiber was 132°C (the crystallinity of both fibers was 42%). Since the long axes of the polymer molecules in the amorphous regions in the stretched state were preferentially aligned in the draw direction, the free volume was really reduced. Therefore, increasing orientation of the amorphous regions led to an increase in the T_g .

Coburn and Boyd [107] measured the dielectric properties of PET samples of different crystallinities (0 to 62%; the samples of higher crystallinities were crystallized under elevated pressures). It was shown that both the α and the β relaxations extrapolated to zero strength at 0% crystallinity, indicating an

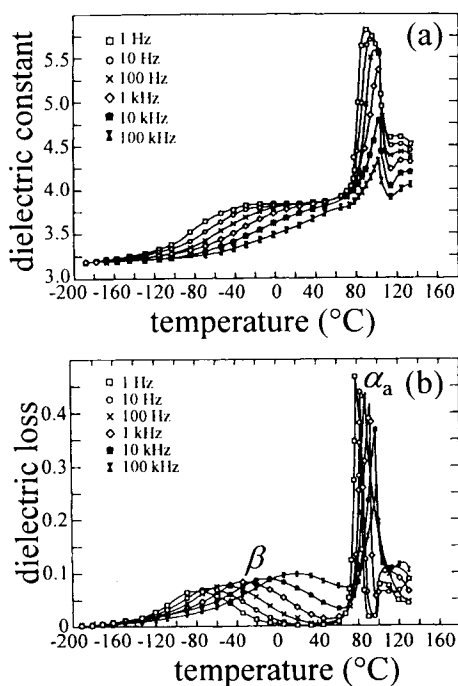


Figure 28. The dielectric constant (a) and dielectric loss (b) of a close-to-amorphous PET film at different frequencies. Home-made semi-automated dielectric instrument consisting of a transform arm ratio bridge (General Radio 1616 precision capacitance bridge), a microprocessor-controlled oscillator, and a two-phase detector (RG&G 5206 lock-in analyzer). The measurements were made in isothermal mode, and the temperature was increased in a stepwise manner. Reprinted with permission from American Chemical Society. [107]

amorphous-phase origin for both relaxations. The change of the dielectric constant and dielectric loss with temperature for a PET film of low crystallinity (4%) recorded at different frequencies is shown in Fig. 28. The α_a (α amorphous) and β relaxations of PET can be seen on these traces. The onset of cold crystallization was manifested as a drop in the dielectric constant. In addition, a new loss peak was observed at higher temperatures (Fig. 28b) due to the displacement of the loss process in the crystalline film.

Nowak and co-workers [108] also applied dielectric measurements to investigate cold crystallization of unfilled and filled (with 30% glass fiber or 10% aramid pulp) PET films after they were quenched from the melt. Isothermal and nonisothermal crystallization was performed. Their nonisothermal results were similar to those reported by Coburn and Boyd [107]: beyond the T_g , the dielectric constant dropped substantially because of cold crystallization. In the isothermal mode at low frequencies, Nowak *et al.* [108] observed two $\tan\delta$ peaks corresponding to the glass transition of PET: the lower-temperature relaxation corresponded to the glass transition of the “pure” amorphous phase, while the higher-temperature relaxation was assigned to the glass transition of the “constrained” amorphous phase in the developed spherulites. The Avrami evaluation of crystallization indicated an $n = 2.9$ value of the Avrami exponent for unfilled PET; this value corresponded to a three-dimensional growth (with heterogeneous nucleation). $n = 2.3$ was obtained for the filled PET, indicating that the geometry of growing entities changed: in this case, mainly two-dimensional crystallites grew, although the fractional value of the Avrami exponent indicated a mixed form of crystallization.

Dielectric measurements on biaxially oriented PET films were used by Sacher to understand the dynamic relaxation behavior [99]. In accordance with the DMA results by Illers and Breuer [16], the β relaxation of PET film was composed of at least two processes (Fig. 29). The activation energies of these processes could be determined by a curve resolution of the β relaxation: $E_{a1} = 109$ kJ/mol was obtained for the higher-temperature process, while $E_{a2} = 100$ kJ/mol for the lower-temperature β process. Sacher [109] developed a model that the local mode relaxation in PET films involved overlapping distributions of normal modes of field-induced cooperative motions. These cooperative motions extended over several repeating units, involve *trans* and *gauche* isomers of glycol linkages (wagging and rocking vibrations), and took place in both the crystalline and amorphous phases.

Davies and Ward [110] investigated the anisotropy of the α and β relaxations in oriented PET films using DMA and DEA experiments. The α relaxation exhibited strong mechanical anisotropy, but it turned out to be an isotropic dielectric process. In contrast, the β relaxation had a pronounced dielectric anisotropy, but hardly any mechanical anisotropy. It was found that

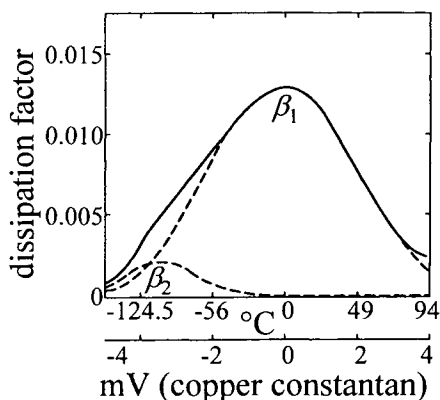


Fig. 29. The dielectric β relaxation of a commercial biaxially oriented PET film resolved into two peaks. The β_1 peak has been assigned by Illers and Breuer [16] to motion of carboxylate groups, and the β_2 peak to that of ethylenic linkages. The measurements have been made at a frequency of 100 kHz. Reprinted with permission from John Wiley & Sons, Ltd. [99]

the mechanical anisotropy of the α relaxation was not a consequence of orientation in the amorphous regions, but was related to the lamellar orientation. This transition was similar to the β relaxation in PE, and an inter-lamellar shear process was suggested. It was also suggested that all or some part of the β process took place in the crystalline phase.

Armeniades and Baer [97] studied the effect of crystallinity and orientation on the mechanical relaxations in PET between -269°C and 27°C . Two new low-temperature relaxations in PET were found (γ and δ at -227°C and -247°C , respectively, see Fig. 30), which were absent in the amorphous polymer. Note that the glass transition relaxation is taken as the α relaxation. Isotropic and uniaxially drawn PET films were studied using DMA experiments at various angles with respect to the orientation direction. In the isotropic film, $T_\beta = -64^\circ\text{C}$, and it was a very pronounced process. The intensity of the β relaxation decreased with increasing crystallinity in the isotropic film. The oriented but amorphous film (drawing temperature, T_d , below 40°C) exhibited a 5°C increase for the β relaxation from -64°C to -59°C . The β relaxation of the oriented films showed an increase in the intensity on the high-temperature side, and thus, the β dispersion could be resolved into three sub-relaxations (with peak temperatures at -163°C , -117°C , and 67°C). The existence of a fourth sub-relaxation was also possible at -38°C , which would be responsible for the broadening of the β relaxation with orientation. The β relaxation was related to motions of the methylene groups, and also to the motion of the carboxylene groups near *gauche* or *trans* chain segments, as suggested earlier by Illers and Breuer [16]. The

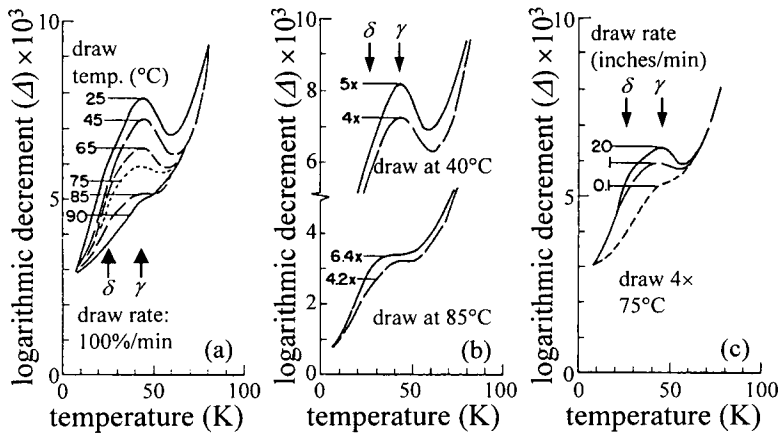


Fig. 30. Effects of draw temperature, extension, and draw rate on the γ and δ relaxations of PET films: (a) samples drawn 4 \times at 100%/min at different temperatures; (b) samples drawn to different extensions at 40 and 85°C; (c) samples drawn 4 \times at 75°C at different rates. Reprinted with permission from John Wiley & Sons, Inc. [97]

intensity of this relaxation decreased with increasing crystallinity. Also, it shifted to higher temperatures and broadened with increasing orientation. This shift was attributed to a relative increased in the population of *trans* chain segments (these increase the β_3 loss intensity) due to orientation. The γ and δ relaxations were absent in the amorphous films, but were intense in the crystalline and oriented samples. The γ relaxation was found in crystalline samples, and its intensity increased with crystal perfection. The γ relaxation was mostly affected by orientation, and it had the highest strength in samples having a large portion of oriented taut chain segments. Both of these relaxations had an activation energy of *ca.* 17 kJ/mol; thus, they might relate to the same mechanism. These relaxations were suggested to relate to defects in the supramolecular structure of PET. Therefore, the δ -loss was the strongest in samples annealed at high temperatures, and these samples were known to have high dislocation densities. The γ loss was the strongest in samples stretched below T_g (having a large void content); its intensity decreased with increasing T_d (because the void concentration decreases with increasing draw temperature).

Overall, the following single coherent view may be drawn to describe the relaxations in PET. The α relaxation of PET (with $\tan\delta$ peak temperature between 80°C and 125°C) corresponds to its glass transition. The β relaxation of PET ($\tan\delta$ peak temperature between -65°C and -40°C) seems to be mainly an amorphous relaxation, because its intensity decreases with increasing crystallinity, and it is found to be zero after extrapolation. The β relaxation may be resolved into three, possibly four, sub-relaxations, one of which may originate

from the crystalline phase. The remaining sub-relaxations seem to correspond to hindered rotation of the methylene groups and the *gauche-trans* configurations of the chains. PET also has two low-temperature crystalline relaxations related to crystal imperfections.

3.4. Polyamides (nylons)

The word *nylon* was originally a commercial registration by DuPont and now, it has been used as a generic term for linear aliphatic polyamides. These macromolecules have -NHCO- structural units in the main chain. The moisture regain of nylons is several percent, depending on the type of nylon and the relative humidity of air. The hydrogen bonding of water with the amide linkage can have a profound influence on the measured properties (moisture acts as a plasticizer, and thus lowers T_g). All nylons seem to have three major relaxation processes. The α relaxation, corresponding to the glass transition, takes place between room temperature and 80°C, depending on the water content and the type of nylon. The β relaxation takes place at *ca.* -50°C. Although there are various interpretations for this relaxation in the literature, the existence of this dispersion seems to be related to the presence of water or some other plasticizers. Finally, the γ relaxation, which is found at -150°C, has been assigned to the onset of rotation of the methylene groups in the backbone.

3.4.1. Nylon 6

The T_g of dry nylon 6 is 47°C [111]. The polymer is known to have several crystal forms [112]; the T_m of the α -crystal form is 270°C, and the heat of fusion of 100% crystalline nylon 6 is 230 J/g [93].

Partially dried nylon 6 gel films drawn by coextrusion with polyoxymethylene up to a maximum draw ratio of 5.7 \times were used in DSC test by Chuah and Porter [113]. The drawn gel film exhibited double orientation: some crystals oriented with the chain axis in the direction of the draw and originated from the drawn fibrous morphology; and other crystals oriented with the chain axis perpendicular to the direction of the draw, which were the initial fibrillar crystals. Two DSC endotherms were obtained on the nylon 6 gel film. The lower-temperature endotherm was identified as the melting of the lamellar crystals, while the higher-temperature endotherm mainly represented the melting of the fibrillar crystals. With increasing draw ratio, the intensity of the lower melting temperature peak decreased, and it was finally disappeared at a draw ratio of higher than 4.6 (Fig. 31). This was attributed to the destruction of the lamellar crystals during drawing. For example, at a draw ratio of 5.4 \times , only a single endotherm was found, which represented the melting of the fibrillar crystals. Furthermore, with increasing the draw-ratio, the crystallinity of the films was monotonically decreased from 55% (the undrawn film) to 45.5% (the

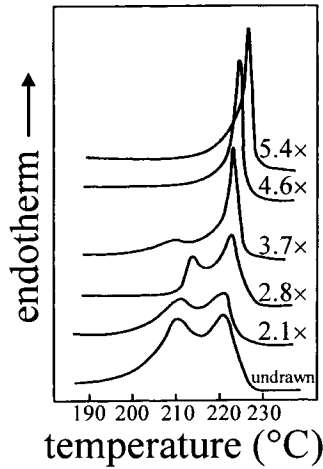


Fig. 31. The melting curves of undrawn and drawn by solid state coextrusion nylon 6 gel films. The draw ratio is indicated at the curves. The measurements were carried out in the unconstrained state on a Perkin-Elmer DSC-2 at a heating rate of $10^{\circ}\text{C}/\text{min}$. Reprinted with permission from Elsevier Science Ltd. [113]

film with a draw ratio of $5.7\times$). This might be due to the fact that a severe drawing process might destroy the original crystals.

The role of water on changing the thermal properties of polyamides is generally not fully understood. The intermolecular hydrogen bonds existed in nylons may be reduced by introducing water. On the other hand, water may help to build hydrogen bonds. A detailed description of the mechanical relaxation behavior of oriented nylon 6 film with changing moisture content was provided by Papir and co-workers [114]. The oriented films were produced by cold rolling at room temperature, which produced uniaxial-planar symmetry, and the chains were oriented along the direction of rolling. In those films, the hydrogen bonds were preferentially aligned in the transverse direction. The film samples for torsion pendulum were cut at 0° and 90° angles to the direction of rolling (called RD and TD samples, respectively). The samples were dried under special conditions (one week at 50°C and one week at room temperature in vacuum). Then, they were set at desired moisture level in an environmental chamber. The effect of gradual increase of moisture content (0, 0.5, 1.4 and 8% water) on the dynamic mechanical damping is shown in Fig. 32. The three relaxations, which had been known before ($T_{\alpha} = 80^{\circ}\text{C}$, $T_{\beta} = -43^{\circ}\text{C}$, and $T_{\gamma} = -127^{\circ}\text{C}$), were all affected by changes in the percentage of the amorphous phase and the water content in the polymer. The γ -relaxation peak shifted from -127°C for the dry sample to -148°C for the sample with 8% water content. The intensity of the γ peak decreased with increasing moisture content. At 8% water

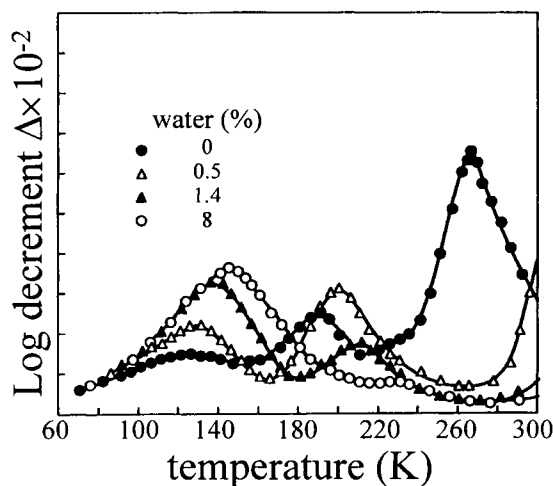


Fig. 32. The dynamic mechanical loss spectra in the high-temperature region (α , β , γ relaxations) of nylon 6 films as a function of moisture content. The isotropic nylon 6 film was oriented at room temperature by rolling with a 3-in.-diameter mill. The sample film was cut at 90° to the direction of rolling. Reprinted with permission from John Wiley & Sons, Inc. [114]

content, only 50% of the γ -relaxation intensity was seen. The β relaxation peak decreased with increasing moisture content from -43°C to -83°C as the water content increased from 0 to 8%. The intensity of the β -relaxation peak at first increased with increasing the water content of the sample from 0% to 1.4%, it then decreased as the moisture content increased to 8%. The α peak, which was above 27°C for most samples, and thus, did not appear in Fig. 32, also shifted continuously toward lower temperatures as the amount of absorbed water increased. A more drastic effect was seen with the α relaxation peak: its peak temperature decreased to -8°C as an effect of 8% water content (an 80°C - 90°C decrease), and the relaxation strength also decreased. The presence of water not only changed the characteristics of the α , β , and γ relaxations, but also affected the newly formed low-temperature δ and ε -relaxations. Furthermore, under the influence of water, the ε -relaxation (below -269°C) disappeared, and a new relaxation (ζ) appeared at -253°C . The tensile modulus of the films decreased by up to 20% under the influence of only 2% water. It was concluded that, as suggested by Puffr and Sabenda [115], two types of water might exist in nylon 6. Up to 2% water content, mainly tightly bound water existed, which formed bridges between pairs of CO- groups. The rest of the water content, beyond 2%, was loosely bound water and seemed to form aggregates connecting the CO- and NH-groups. The molecular structure changes by introducing water were also identified to affect the major relaxations. The α relaxation was caused by the

breakup of the hydrogen bonds due to motion of long chain segments in the amorphous region of nylon 6. The β relaxation seemed to correspond to movement of polar groups not hydrogen bonded and of polymer-water complex units. The γ relaxation had a complex nature: it probably involved the motion of the polar groups of nylon 6 together with the methylene sequences. The δ relaxation at -220°C was thought to originate in the amorphous phase, and the ϵ relaxation might correspond to the interactions between the hydrogen bonds in the amorphous phase. The δ relaxation was noticeable only at high water contents, and thus, it might be related to motion of aggregated ice in the amorphous regions. It was also shown that nylon 6 might be viscoelastically active below the temperature of the γ relaxation. Rele and Papir [116] showed that the relaxation strength of all three, α , β , and γ , relaxations of nylon 6 initially increased rapidly with the time of annealing at 170°C and 210°C , then suddenly decreased, and a minimum in the relaxation strength was at 65 - 75 min annealing. Later, the relaxation strength had another maximum at *ca.* 3 hrs annealing. The connection of these changes with the morphological changes (crystallization, crystal perfection, and the γ - α transition) in nylon 6 was speculated. Since the ordered domains of nylon 6 might also have their contributions to the principal relaxations, two distinct, simultaneous annealing mechanisms might be responsible for the above-described changes of the strength of the relaxations: crystallization of the amorphous polymer into poorly organized ordered regions and growth/perfection of the existing crystallites. It was speculated that the concentration of the crystal defects temporarily increased and then decreased to explain the increase and decrease of the relaxation strength. On the basis of TSC measurements, Frank and co-workers [117] suggested that three different ranges of water content in nylon 6 could be distinguished (firmly bound water, loosely bound water, and clustered water, depending on the water content), and that the critical contents were identified at 1.5 and 6.0%.

Hoashi and Andrews [118] studied the dynamic mechanical properties of nylon 6 films after different heat treatments and swelling. The crystallites in the original film were hexagonal, and they were changed completely into unoriented and oriented α -crystal form by heat treatment and phenol treatment, respectively (Fig. 33a). A treatment by I_2/KI solution, on the other hand, led to development of oriented γ crystallites. The heat treatment was done at 160°C , 200°C , and 212°C . The low-temperature side of the α_a peak was found to be frequency independent, and thus, it was attributed to melting of imperfect crystallites (Fig. 33b). When the shift factor ($\log a_T$) was calculated from the frequency dependence of position of the high-temperature side of the α_a -relaxation peak and plotted against $1/T$ for the heat-treated films, two intercepting straight lines were obtained. The temperature of interception increased with increasing heat-

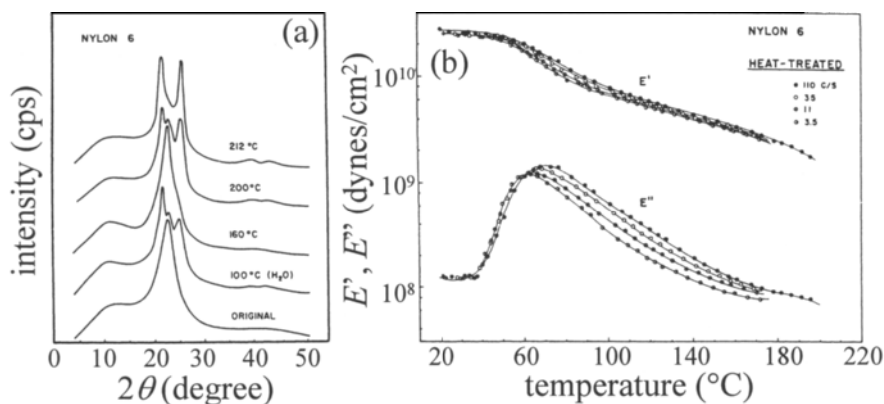


Fig. 33. (a) X-ray diffraction curves of nylon 6 heat-treated at different temperatures. (b) Tensile storage modulus E' and loss modulus E'' versus temperature at different frequencies for nylon 6 heat-treated at 212°C for 30 min. Reprinted with permission from John Wiley & Sons, Inc. [118]

treatment temperature. For the highest annealing temperature of 212°C, only one straight line was obtained, whose slope corresponded to the slope of the low-temperature lines of the other curves. Therefore, it was concluded that the α_a relaxation was likely to indicate dispersion for two phases. The α_{a1} peak, the lower-temperature relaxation, seemed to correspond to completely amorphous phase, since its temperature decreased with the amount of absorbed phenol (the plasticizing effect on an amorphous polymer). The position of the α_{a2} peak, the higher-temperature α_a relaxation, did not depend on the amount of the absorbed phenol, and thus, it must be attributed to a more highly ordered phase ("strained" amorphous or hexagonal crystal phase) in which phenol was not absorbed.

3.4.2. Nylon 66

The T_g of nylon 66 is 48°C [119]. Its T_m° is estimated to be *ca.* 280°C [93,120]; the heat of fusion of the 100% crystalline polymer is 190 J/g.

The effect of drawing and annealing on the dynamic mechanical properties of nylon 66 films were investigated by Dumbleton and Murayama [121]. The dynamic storage modulus was found to increase with increasing draw ratio. The position of the α relaxation taking place at 80°C - 90°C was only slightly affected by annealing treatments, but the transition moved to higher temperatures with increasing draw ratio (and thus, increasing the degree of orientation). The moduli measured parallel and perpendicular to the draw direction of a cold-drawn nylon 66 film appeared to be parallel to each other without interception. However, they intercepted in the region of primary relaxation (glass transition) for the film drawn at 200°C to 4.5 \times .

Murayama and Silverman [122] showed that the α relaxation of nylon 66 films shifted to higher temperatures with increasing the molecular weight.

4. CONCLUDING REMARKS

In this chapter, general experimental considerations for polymer thin film thermal analysis, such as DSC, TMA, DMA, DEA, *etc.*, have been introduced. On the basis of these experimental considerations, the thermal properties of some polymer films (*e.g.*, polyimides, PE, PP, PET, and nylons) with complex orientation patterns have been discussed. Generally, polymer films can be considered as the two-dimensional analogues of fibers, characterized by biaxial orientation in the plane of the film. Therefore, the thermal property along different directions with respect to the orientation direction can be different. Meanwhile, characterization of the *z*-direction properties of films is also important. Although these properties may often be inferred by indirect measurements, direct measurements are preferred.

Generally speaking, film thermal analysis is much more useful as a diagnostic tool than as a quality control tool, because many measurements should be taken in order to detect the property of a film web and this may not be always realistic. The flat geometry of films makes them easier to utilize in most thermal analysis equipment, and allows some straightforward measurements of *z*-direction properties, most notably the CTE and modulus. Also, the geometry of films allows the use of powerful dielectric loss spectroscopy and related techniques to gain large amounts of information quickly and conveniently.

In summary, this chapter gives a brief description of the thermal analysis of some industrially important polymer films. More comprehensive discussion should refer to Menczel *et al.* [123].

REFERENCES

1. (a) K. B. Blodgett, *J. Am. Chem. Soc.*, 56 (1934) 495; (b) K. B. Blodgett, *J. Am. Chem. Soc.*, 57 (1935) 1007.
2. I. Langmuir, *Trans. Faraday Soc.*, 15 (1920) 62.
3. E. Werner, M. J. Hopper, *Polyester Films*, in H. F. Mark *et al.* eds., *Encyclopedia of Polymer Science and Engineering*, Vol. 12, John Wiley & Sons, New York, 1988.
4. T. Kunugi, C. Ichenose, A. Suzuki, *J. Appl. Polym. Sci.*, 31 (1986) 429.
5. T. Kunugi, A. Mizushima, T. Hayakawa, *Polym. Commun.*, 27 (1986) 175.
6. T. Kunugi, T. Hayakawa, A. Mizushima, *Polymer*, 32 (1991) 808.
7. R. F. Saraf, H.-M. Tong, T.-W. Poon, B. D. Silverman, P. S. Ho, A. R. Rossi, *J. Appl. Polym. Sci.*, 46 (1992) 1329.
8. H. M. Tong, H. K. D. Hsuen, K. L. Saenger, G. W. Su, *Rev. Sci. Instrum.*, 62(2) (1991) 422.
9. H. M. Tong, G. W. Su, K. L. Saenger, *Annu. Tech. Conf.-Soc. Plast. Eng.*, 49 (1991) 1727.

10. G. Elsner, J. Kempf, J. W. Bartha, H. H. Wagner, *Thin Solid Films*, 185 (1990) 189.
11. M. T. Pottiger, J. C. Coburn, J. R. Edman, *J. Polym. Sci., Part B: Polym. Phys.*, 32 (1994) 825.
12. P. Zoller, P. Bolli, V. Pahud, H. Ackermann, *Rev. Sci. Instrum.*, 47 (1976) 948.
13. Y. A. Fakhreddine, P. Zoller, *Proc. 49th Annu. Tech. Conf., Soc. Plast. Eng.*, (1991) 1642.
14. G. Beaucage, R. Composto, R. S. Stein, *J. Polym. Sci., Part B: Polym. Phys.*, 31 (1993) 319.
15. D. S. Fryer, P. F. Nealey, J. J. de Pablo, *Macromolecules*, 33 (2000) 6439.
16. K. H. Illers, H. Breuer, *J. Colloid Sci.*, 18 (1963) 1.
17. A. H. Willbourn, *Trans. Faraday Soc.*, 54 (1958) 717.
18. T. F. Shatzki, *J. Polym. Sci.*, 57 (1962) 496.
19. R. F. Boyer, *Rubber Chem. Technol.*, 36 (1963) 1303.
20. M. Grehlinger, M. Kraft, *J. Plast. Film Sheeting*, 4 (1988) 318.
21. Y. P. Khanna, W. M. Wenner, R. Kumar, S. Kavesh, *J. Appl. Polym. Sci.*, 38(3) (1989) 571.
22. I. M. Ward, *Mechanical Properties of Solid Polymers*, Wiley (Interscience), New York, 1971.
23. J. van Turnhout, *Polym. J.* 2(2) (1971) 173.
24. A. Bernes, R. F. Boyer, D. Chatain, C. Lacabanne, J. P. Ibar, *Thermally Stimulated Current Studies of Transitions in Amorphous Polymers*, in S. E. Keinath, R. L. Miller, and J. K. Rieke, eds. *Order in the Amorphous State of Polymers*, Plenum, New York, 1987.
25. J. J. del Val, A. Alegria, J. Colmenero, C. Lacabanne, *J. Appl. Phys.*, 59(11) (1986) 3829.
26. H. Sharif Faruque, C. Lacabanne, *J. Mater. Sci.*, 25 (1990) 1977.
27. D. Chatain, P. Aautier, C. Lacabanne, *J. Polym. Sci., Polym. Phys. Ed.*, 11 (1973) 1631.
28. D. Ronarc'h, P. Audren, J. L. Moura, *J. Appl. Phys.*, 58 (1985) 466.
29. D. Ronarc'h, P. Audren, J. L. Moura, *J. Appl. Phys.*, 58 (1985) 474.
30. P. Fischer, P. Roehl, *J. Polym. Sci., Polym. Phys. Ed.*, 14 (1976) 531.
31. B. B. Sauer, P. Avakian, H. W. Starkweather, Jr., B. S. Hsiao, *Macromolecules*, 23 (1990) 5119.
32. B. B. Sauer, P. Avakian, *Polymer*, 33 (1992) 5128.
33. B. B. Sauer, P. Avakian, H. W. Starkweather, Jr., *J. Polym. Sci., Part B, Polym. Phys.*, 34 (1996) 517.
34. C. Lacabanne, D. G. Chatain, J. C. Monpagens, *J. Macromol. Sci., Phys.*, B13(4) (1977) 537.
35. F. W. Harris, S. L.-C. Hsu, *High Perform. Polym.*, 1 (1989) 1.
36. F. W. Harris, S.-H. Lin, F. Li, S. Z. D. Cheng, *Polymer*, 37 (1996) 5321.
37. S.-H. Lin, F. Li, S. Z. D. Cheng, F. W. Harris, *Macromolecules*, 31 (1998) 2080.
38. F. Li, S. Fang, J. J. Ge, P. S. Honigfort, J.-C. Chen, F. W. Harris, S. Z. D. Cheng, *Polymer*, 40 (1999) 4571.
39. F. Li, J. J. Ge, P. S. Honigfort, S. Fang, J.-C. Chen, F. W. Harris, S. Z. D. Cheng, *Polymer*, 40 (1999) 4987.
40. F. Li, K.-H. Kim, E. P. Savitski, J.-C. Chen, F. W. Harris, S. Z. D. Cheng, *Polymer*, 38 (1997) 3223.
41. F. Li, Ph.D. Dissertation, Department of Polymer Science, The University of Akron, Akron, OH, 1998.
42. H. W. Starkweather, Jr., *Macromolecules*, 23 (1990) 328.

43. H. W. Starkweather, Jr., *Polymer*, 32 (1991) 2443.
44. J. C. Coburn, M. T. Pottiger, A. E. Nader, C. A. Pryde, *Mater. Res. Soc. Symp. Proc.*, 264 (1992) 107.
45. M. Ree, K. J. Chen, D. P. Kirby, N. Katzenellenbogen, D. Grischkowsky, *J. Appl. Phys.*, 72 (1992) 2014.
46. D. C. McHerron, G. L. Wilkes, *J. Appl. Polym. Sci.*, 46 (1992) 1313.
47. J. R. Pratt, T. L. Clair, M. K. Gerber, C. R. Gautreaux, *NASA Tech. Memo. NASA-TM-101526, NAS 1.15:101526*, 1988.
48. J. B. Friler, P. Cebe, *Polym. Eng. Sci.*, 33(10) (1993) 587.
49. B. S. Hsiao, B. B. Sauer, A. Biswas, *J. Polym. Sci., Part B: Polym. Phys.*, 32 (1994) 737.
50. B. Wunderlich, G. Czornyj, *Macromolecules*, 10 (1977) 906.
51. U. Gaur, B. Wunderlich, *Macromolecules*, 13 (1980) 445.
52. C. L. Beatty, F. E. Karasz, *J. Macromol. Sci., Rev. Macromol. Chem.*, C17, (1979) 37.
53. E. Laredo, N. Suarez, A. Bello, L. Marquez, *J. Appl. Polym. Sci.*, 34 (1996) 641.
54. S. B. Clough, *J. Macromol. Sci., Phys.*, B4(1) (1970) 199.
55. S. B. Clough, *Polym. Lett.*, 8 (1970) 519.
56. S. B. Clough, *J. Appl. Polym. Sci.*, 15 (1971) 2141.
57. K. H. Illers, *Angew. Makromol. Chem.*, 12 (1970) 89.
58. A. Peterlin, J. Meinel, *J. Appl. Phys.*, 36 (1965) 3028.
59. R. J. Samuels, *J. Polym. Sci., Polym. Phys. Ed.*, 17 (1979) 535.
60. J. Varga, J. D. Menczel, A. Solti, *J. Therm. Anal.*, 17 (1979) 333.
61. R. H. Boyd, *Macromolecules*, 17 (1984) 903.
62. P. Berticat, B. Ai, H. T. Giam, D. Chatain, C. Lacabanne, *Makromol. Chem.*, 177 (1976) 1583.
63. R. F. Boyer, *Macromolecules*, 6 (1973) 288.
64. J. D. Hoffman, G. Williams, E. Passaglia, *J. Polym. Sci., Part C*, 14 (1966) 173.
65. M. Kakizaki, T. Hideshima, *J. Macromol. Sci., Phys.*, B8 (1973) 367.
66. R. F. Boyer, *J. Macromol. Sci., Phys.*, B9 (1974) 187.
67. R. F. Boyer, eds., *Transitions and Relaxations in Polymers*, Wiley (Interscience), New York, 1966.
68. K. M. Sinnott, *J. Polym. Sci., Part C*, 14 (1966) 141.
69. A. Tanaka, E. P. Chang, B. Delf, I. Kimura, R. S. Stein, *J. Polym. Sci., Polym. Phys. Ed.*, 11 (1973) 1891.
70. Z. H. Stachurski, I. M. Ward, *J. Macromol. Sci., Phys.*, B3(3) (1969) 427.
71. A. J. Owen, I. M. Ward, *J. Macromol. Sci., Phys.*, B19(1) (1981) 35.
72. C. Sawatari, M. Matsuo, *Colloid Polym. Sci.*, 263 (1985) 783.
73. E. Passaglia, H. K. Kevorkian, *J. Appl. Sci.*, 34 (1963) 90.
74. U. Gaur, B. Wunderlich, *J. Phys. Chem. Ref. Data*, 10 (1981) 1051.
75. W. W. Cox, A. A. Duswalt, *Polym. Eng. Sci.*, 7 (1967) 309.
76. J. G. Fatou, *Eur. Polym. J.*, 7 (1971) 1057.
77. R. J. Samuels, *J. Polym. Sci., Polym. Phys. Ed.*, 13 (1975) 1417.
78. R. J. Samuels, *J. Macromol. Sci., Phys.*, B8(1-2) (1973) 41.
79. I. Inamura, H. Ochiai, H. Yamamura, *J. Polym. Sci., Polym. Phys. Ed.*, 12 (1974) 2267.
80. J. C. Seferis, R. L. McCullough, R. J. Samuels, *Org. Coat. Plast. Chem.*, 35(2) (1975) 210.
81. J. C. Seferis, R. L. McCullough, R. J. Samuels, *Appl. Polym. Symp.*, 27 (1975) 205.
82. J. C. Seferis, R. L. McCullough, R. J. Samuels, *Polym. Eng. Sci.*, 16(5) (1976) 334.
83. J. C. Seferis, R. L. McCullough, R. J. Samuels, *J. Macromol. Sci., Phys.*, B13(3) (1977) 357.

84. M. Matsuo, C. Sawatari, T. Nakano, *Polym. J.*, 18 (1986) 759.
85. C. Sawatari, M. Matsuo, *Macromolecules*, 22 (1989) 2968.
86. A. P. Unwin, D. I. Bower, I. M. Ward, *Polymer*, 31 (1990) 882.
87. S. K. Roy, T. Kyu, R. St. John Manley, *Macromolecules*, 21 (1988) 499.
88. W. Zhou, S. Z. D. Cheng, S. Putthanarat, R. K. Eby, D. H. Reneker, B. Lotz, S. Magonov, E. T. Hsieh, R. G. Geerts, S. J. Palackal, G. R. Hawley, M. B. Welch, *Macromolecules*, 33 (2000) 6861.
89. J. D. Menczel, B. Wunderlich, *J. Polym. Sci., Polym. Lett. Ed.*, 19 (1981) 261.
90. U. Gaur, S.-F. Lau, B. Wunderlich, *J. Phys. Chem. Ref. Data*, 12 (1983) 65.
91. A. Wlochowicz, W. Przygocki, *J. Appl. Polym. Sci.*, 17 (1973) 1197.
92. M. Droescher, G. Wegner, *Polymer*, 19 (1978) 43.
93. B. Wunderlich, *Macromolular Physics*, Vol. 3, Academic Press, New York, 1980.
94. H. W. Starkweather Jr., P. Zoller, G. A. Jones, *J. Polym. Sci., Polym. Phys. Ed.*, 21 (1983) 295.
95. J. H. Dumbleton, T. Murayama, *Kolloid-Z. Z. Polym.*, 220 (1967) 41.
96. M. Takayanagi, M. Yoshino, S. Minami, *J. Polym. Sci.*, 61 (1962) S7.
97. C. D. Armeniades, E. Baer, *J. Polym. Sci., Part A-2*, 9 (1971) 1345.
98. H. K. Yip, H. L. Williams, *J. Appl. Polym. Sci.*, 20 (1976) 1217.
99. E. Sacher, *J. Polym. Sci., Part A-2*, 6 (1968) 1935.
100. T. Sun, J. Pereira, R. S. Porter, *J. Polym. Sci., Polym. Phys. Ed.*, 22 (1984) 1163.
101. K. G. Mayhan, W. J. James, W. Bosch, *J. Appl. Polym. Sci.*, 9 (1965) 3605.
102. B. J. Miller, *J. Appl. Polym. Sci.*, 11 (1967) 2343.
103. E. Ito, T. Hatakeyama, *J. Polym. Sci., Polym. Phys. Ed.*, 12 (1974) 1477.
104. A. B. Thompson, D. W. Woods, *Trans. Faraday Soc.*, 52 (1956) 1383.
105. T. Kawaguchi, *J. Polym. Sci.*, 32 (1958) 417.
106. J. H. Dumbleton, T. Murayama, J. P. Bell, *Kolloid-Z. Z. Polym.*, 228 (1968) 54.
107. J. C. Coburn, R. H. Boyd, *Macromolecules*, 19 (1986) 2238.
108. H. Nowak, G. Kalinka, G. Hinrichsen, *Acta Polym.*, 44 (1993) 25.
109. E. Sacher, *J. Macromol. Sci., Phys.*, B5(4) (1971) 739.
110. G. R. Davies, I. M. Ward, *J. Polym. Sci., Part A-2*, 10 (1971) 1153.
111. K. H. Illers, *Polymer*, 18 (1977) 551.
112. K. H. Illers, *Makromol. Chem.*, 179 (1978) 497.
113. H. H. Chuah, R. S. Porter, *Polymer*, 27 (1986) 1022.
114. Y. S. Papir, S. Kapur, C. E. Rogers, E. Baer, *J. Polym. Sci., Part A-2*, 10 (1972) 1305.
115. R. Puffr, J. Sabenda, *J. Polym. Sci., Part C*, 16 (1967) 79.
116. V. B. Vele, Y. S. Papir, *J. Macromol. Sci., Phys.*, B13(3) (1977) 405.
117. B. Frank, P. Fruebing, P. Pissis, *J. Appl. Polym. Sci.*, 34 (1996) 1853.
118. K. Hoashi, R. D. Andrews, *J. Polym. Sci., Part C*, 38 (1972) 387.
119. H. Mark, *Kolloid-Z. Z. Polym.*, 21(6/7) (1967) 126.
120. H. W. Starkweather Jr., P. Zoller, G. A. Jones, *J. Polym. Sci., Polym. Phys. Ed.*, 22 (1984) 1615.
121. J. H. Dumbleton, T. Murayama, *Kolloid-Z. Z. Polym.*, 238(1-2) (1970) 410.
122. T. Murayama, B. Silverman, *J. Polym. Sci., Polym. Phys. Ed.*, 11(10) (1973) 1873.
123. J. D. Menczel, J. Jaffe, W. E. Bessey, *Films*, in E. A. Turi (eds.), *Thermal Characterization of Polymeric Materials*, Vol. 2, 2nd ed., Academic Press, San Diego, 1997.

This Page Intentionally Left Blank

Chapter 11

Thermal analysis of polymer fibers

Alexander J. Jing, Anqiu Zhang and Zongquan Wu

Maurice Morton Institute and Department of Polymer Science,
The University Akron, Akron, Ohio 44325-3909

1. INTRODUCTION

Fibers may be defined as a type of material whose length is much greater than its cross-sectional dimensions. Usually, a ratio of the length to diameter for fibers is larger than 1000. Because of this anisotropy on geometry, fibers almost always show anisotropic micro-structure as well as anisotropic physical properties. All these anisotropic properties are attributed to the orientation of molecules along the fiber axes. Therefore, the thermal analysis on fibers is actually dealing with the thermal properties of oriented materials.

Due to a large amount of research activities on polymeric materials, thermal analysis is one of the most efficient, direct and convenient methods in monitoring the change of polymer structures and properties responding to variations of temperature, pressure and external fields, *etc.* For our case, thermal analysis can provide information which is useful in fiber processing, establishing structure and property, and probing interaction between fibers and matrix when the fibers are used as reinforcing parts in plastics. Before we carry out our discussion on the thermal analysis in fibers, some fundamental knowledge of the fiber materials should be introduced.

1.1. Dimensions

There are two important factors to describe the dimensions of fibers: the length and the diameter. According to the length, fibers can be classified as continuous filaments with infinite length or staples which are much shorter. Natural fibers, with the exception of silk, are obtained only in the staple form. A typical diameter for a textile fiber is between 1 μm and 30 μm .

In the textile industry, fiber size is characterized in units of linear density. In the international system (SI), the unit of this density is tex, which is defined as the weight in grams of 1,000 meters of fiber. Actually, the decitex, dtex, equals the weight in grams of 10,000 meters of a fiber, and it is most frequently used

because of similarities to the historically used unit, denier, defined as the weight in grams of 9,000 meters of fiber. Another unit is so-called cotton count, which represents the number of hanks (840 yard length per hank) which weighs one pound.

1.2. Production of fibers

The detailed properties of a given fiber are determined by the chemical structure of this fiber material and the conditions under which it is produced. In fact, dependence on processing conditions is as important as it is in the polymer chemical structure. Therefore, a brief description of the principle in fiber production processes is necessary. The processes of reshaping synthetic polymers into filaments and converting staple fibers into fibers are both termed spinning. In this section, the spinning is discussed as a fiber formation process.

Melt spinning is preferred in a polymer, which can be melted under reasonable temperature and pressure. When melt spinning is impossible due to the extreme melting conditions of the polymer, spinning with a polymer dissolved in certain kinds of solvent is used to form filaments. There are two kind of processing in solution spinning: one in which solvent is removed by evaporation (dry spinning) or one in which the solvent is leached out by another liquid which is miscible with the spinning solvent but is not a solvent for the polymer (wet spinning). Fig. 1 illustrates the fiber formation procedures using these three principal spinning methods [1].

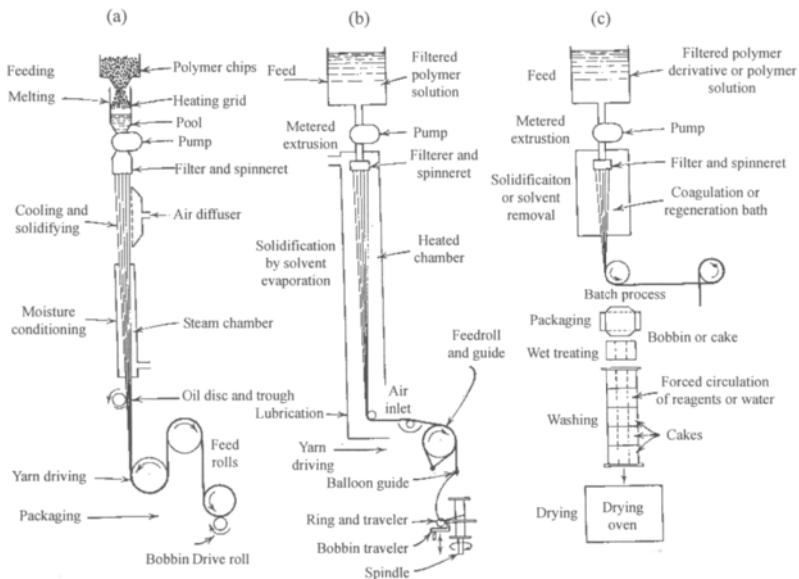


Fig. 1. Schematic diagrams of the three principal methods of spinning fibers (a) melt spinning (b) dry spinning (c) wet spinning [1]

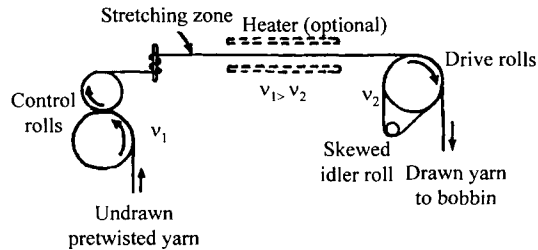


Fig. 2. Schematic diagram of a typical drawing process [1]

Immediately after spun out from the spinneret, the fibers usually possess only low levels of axial chain orientation. Further drawing must be carried out to achieve good chain orientation. The higher the draw ratio, the higher the molecular orientation in the fiber, and, therefore, the stronger and stiffer the fiber is along the fiber direction. A typical drawing process is illustrated in Fig. 2 [1]. The draw ratio is defined as the ratio of the initial to the final cross-section areas. In practice, the draw ratio is often specified as the ratio between output and input speeds.

Melting spinning is used for polyolefin, polyester and nylon fibers, which are the majority of synthetic fiber products. Drying spinning has been used for many years for spinning cellulose acetate from acetone solution, and is now employed for spinning polyacrylonitrile and the aramid fibers from solutions in

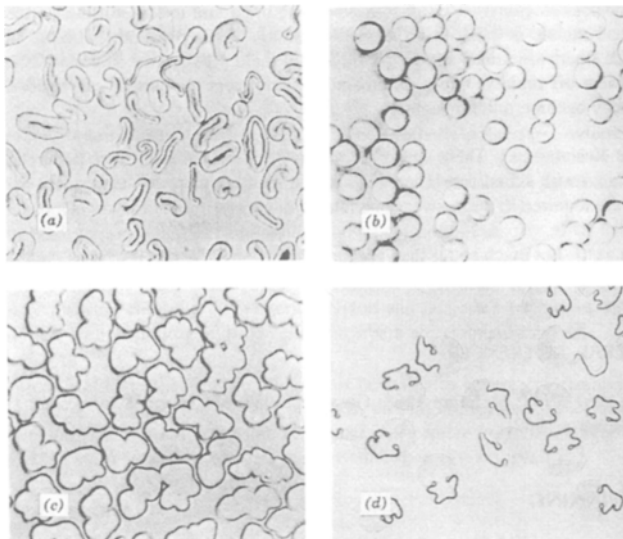


Fig. 3. Photographs (x250) of cross-section shapes of fibers (a) cotton (b) melt-spun polyester (c) dry-spun acetate (d) wet-spun conjugate viscose fiber [1,2]

dimethyl formamide or dimethyl acetamide. Wet spinning is commonly used for viscose cellulose, and some synthetic fibers, such as polyacrylonitrile spun from salt solutions.

The conversion of the spun polymer fibers in the melt or solution to a solid state involves cooling, solvent evaporation, and/or coagulation, depending on the type of spinning method used. Cooling of a fine filament is normally very rapid and can be controlled within relatively narrow processing parameter limits. Solvent evaporation involves simultaneous outward mass transfer and inward heat transfer, the rate-controlling step invariably being an outward diffusion of solvent. Coagulation involves two-way mass transfer; the coagulation agent diffusing inward and the products of coagulation diffusing out. As a consequence, it is relatively easy to obtain a melt-spun fiber that possesses uniform properties throughout its cross section, but it is difficult to do so with solution-spun or coagulated fibers. In addition, the rapid cooling of melt-spun fibers tend to produce an almost circular cross section, whereas in solution-spun fibers the cross sections are elliptical, and with coagulated fibers (because of the absence of strong surface-tension effects) the cross sections are highly convoluted [1,2], as shown in Fig. 3.

There are essential steps that must be taken between spinning and weaving. All natural and some synthetic fibers must be washed or scoured to free them of natural oils, dirt, chemicals and other foreign impurities. They must be lubricated and/or sized to reduce their friction against themselves or elements of the processing machinery. After this process, the fibers are ready for weaving.

1.3. Mechanical properties

The mechanical properties of fibers are quite anisotropic and have been the subject of much experimental work and theoretical investigation.

1.3.1. Terminology

The fiber stress-strain curves can be obtained by continuously increasing tensile force on a fiber until it breaks. There are many definitions regarding fiber strengths. The maximum force (unit: grams or Newtons) is called the absolute strength of the fiber. The ratio of a fiber's absolute strength to its density is called relative strength. Its units can be g/dtex (grams per dtex), g/d (grams per denier), N/m² (Newton per square meter, which is equal to "One" Pa, or "a" Pascal). For high performance fiber and composite materials, units of GPa (Giga Pascal or 10⁹ Pascal) or MPa (10⁶ Pascal) are commonly used. Table 1 shows the unit conversion of strength and modulus.

On the other hand, under a load, the fiber elongates and its cross-section area decreases continuously. If the original area is A , the break strength is σ , the final area upon breaking is A' , the real break strength $\sigma' = \sigma (A / A')$. Suppose

Table 1
Unit conversion of strength and modulus

unit	g/d	g/tex	kg/mm ²	dynes/cm ²	Pa	lb/in ²
g/d	1	9	9ρ	$8.818 \times 10^8 \rho$	$8.818 \times 10^7 \rho$	$1.028 \times 10^4 \rho$
g/tex	0.111	1	ρ	$9.798 \times 10^7 \rho$	$9.798 \times 10^6 \rho$	$1.421 \times 10^3 \rho$
kg/mm ²	$0.111/\rho$	$1/\rho$	$\rho/1$	9.798×10^7	9.798×10^6	1.421×10^3
dynes/cm ²	$1.134 \times 10^{-9}/\rho$	1.021×10^{-10}	1.021×10^{-8}	1	0.1	1.450×10^{-5}
Pa	$1.134 \times 10^{-8}/\rho$	1.021×10^{-9}	1.021×10^{-7}	10	1	1.450×10^{-4}
lb/in ²	$7.819 \times 10^{-5}/\rho$	$7.037 \times 10^{-4}/\rho$	7.037×10^{-4}	6.896×10^4	6.896×10^3	1

that the original and final length are L and L' , $A/A' = L'/L$, and therefore, $\sigma' = \sigma (L'/L) = \sigma (1 + \epsilon)$, where, $\epsilon = dL/L$, is called strain. This represents that the real strength is $(1 + \epsilon)$ times the imparted strength.

The fiber break length is another term to indicate the strength of a filament. If a filament is long enough, it could be broken by its own weight. The filament length that corresponds to the weight which equals to the filament absolute strength is called break strength (unit, 1000 m).

The tensile strength, which is one of the important parameters in applications, is measured by means of an instrument which supplies increasing load on the filament up to its breaking point. This breaking mechanism differs from the real breaking mechanism in cloth wearing, in which case, the loads on fabrics are multi-cycle, mild and directionally variant. That is why the strength of wool is weaker than that of cotton, though wool fabrics are more durable than cotton fabrics. The elongation necessary to break a fiber is a useful quantity and it is called the breaking extension. It may be expressed by the actual, the fractional, or the percentage increment in length and is termed the breaking extension.

1.3.2. Fiber stress-strain diagrams

Combining both of the stress (strength) and strain (elongation) of fibers, stress-strain diagrams can be obtained. These stress-strain diagrams of fibers are obviously obtained by using a strength test machine of the auto-graphic type. Two kinds of instruments that are used are operating at a constant rate of loading or are operating at a constant rate of extension. If the fiber obeys Hooke's Law, the stress-strain line is linear with a constant slope, and the fiber is elastic. Usually, after a few percent of extension, the elongation of the fiber becomes greater than that indicated by the straight-line curve (see Fig. 4). This generally indicates that plastic flow in the fibers has set in, and the fiber is no longer truly elastic, but is actually viscoelastic.

The initial modulus is equal to the slope of the stress-strain diagram at the origin part of the curve (after removal of any crimp). This slope usually remains

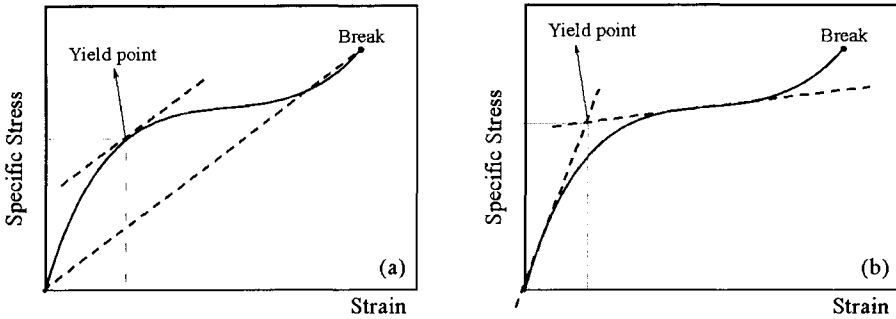


Fig. 4. Different definition of yield point on stress-strain diagrams for fiber samples: (a) Meredith's construction (b) Coplan's construction

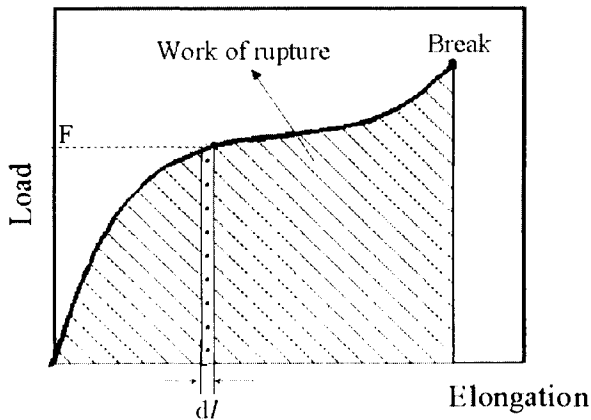


Fig. 5. Definition of work of rupture

constant over the initial portion of the diagram, shown in Fig. 4. The unit of modulus measured is identical as those of stress or specific stress.

In a stress-strain diagram, the spot corresponding to the departure from a straight line is called the yielding point, after which the modulus decreases. For conventional fibers, this turning takes place in a very early stage of elongation. High performance fibers, however, usually have higher yield points. Meredith and Coplan suggested using two slightly different ways to obtain the yield point as shown in Fig. 4 [3,4].

The area under the stress-strain diagram, $\int_0^y F \cdot dl$, is called the work of rupture. Here, the y is the elongation at break, F is the corresponding force, and dl represents the differential length between 0 and y . This indicates the total work that the external force can load on the fiber up to its break. On the other hand, the relative work of rupture is presented as a ratio between the work of rupture and the $N/\text{tex} \times \text{fiber length (cm)}$. This means the work of rupture

needed for 1 cm length fiber with 1 tex density, and it represents the toughness of a fiber product. The higher the relative work of rupture, the longer the lifetime of the fiber product.

1.3.3. Elastic recovery

Under load, the fiber simultaneously undergoes elastic, high elastic and plastic deformation. After the load is released, elastic and a fast response of highly elastic deformation will recover. The remaining of the deformation consists of the slow high elastic deformation (needs a longer relaxation time) and the plastic deformation. The elastic recovery is defined as $\varepsilon_E / \varepsilon_T \times 100 = (\varepsilon_T - \varepsilon_P) / \varepsilon_T \times 100$, where ε_T is the total strain during stretch, ε_E is the elastic strain and ε_P is the plastic strain.

1.4. Heat-resistance and thermal stability [5]

Fibers are subjected to certain high temperature environments not only in processing (dyeing, drying, *etc.*), but also in use (washing and ironing). For industrial applications, the conditions are more severe at higher temperatures (even at 400 - 500°C) and for a prolonged period of time. For example, maintaining the mechanical performance of the tire cores in a high-temperature environment during driving is important. It is also important for fibers to be used as electrical insulate materials.

The high temperature effect on the fiber materials is reflected in three aspects. First, the changes of mechanical properties of the fibers, especially, the changes in strength and extension on temperature. Secondly, the chemical reaction of the fibers (dehydration, thermal degradation, thermal oxidation). And thirdly, the physical changes of the fibers (such as shape deformation, plastic flow, softening, tacking, *etc.*) with varying temperatures. These changes depend on the original characteristics of polymers. Only thermally stable polymers can make a fiber with practical utility in high-temperature environments. The chemical changes in high-temperature environments are more complicated, and vary with the media used. If heat treatment is carried out under vacuum or in inert gas environments, only thermal degradation takes place. In the presence of oxygen in air, oxidation, thermo-scission of chain molecules may also take place, and new functional groups, such as aldehydes, carboxyl and ozonides may form. Accompanied with thermal degradation and oxy-degradation, the color of fibers changes into yellow or brown. Conjugate double bonds, especially those connecting with the aldehyde groups form color easily. The main reason for decreases of the fiber tensile properties, *i.e.* strength and initial modulus with temperature is the reduction of intermolecular interaction and degradation of chain molecules.

As a factor, thermal stability usually also illustrates the fiber stability during high temperature treatment. It is defined by the melting point and how high is the decomposition temperature.

1.5. Water absorption, regain and moisture content [6]

Water absorption changes the properties of fibers, of which in particular, are hydrophilic in nature. It causes swelling, which alters the dimensions of fibers, and causes changes in size, shape, and stiffness. The mechanical properties and the frictional properties change as well. There are three kinds of water types existing in these fibers: liquid, solid and molecular compound type. Liquid water on the fiber surface performs a wet feeling corresponding to wet fibers. "Water ambition" is adopted to describe the total content of this water type. Fibers or fabrics containing water with solid and molecular compound types perform a dry feeling and appearance. "Regain and moisture content" are used to describe such types of the water content. The moisture content of the material is one of the most important issues in determining a fiber's electrical properties including the static electric phenomenon.

There is also a commercial importance of moisture absorption in fibers. There may be more than 100 kg of water in 1 ton of viscous rayon. On the other hand, the amount of water gained after the dry fibers being exposed to a wet-environment is also called regain or moisture content. There are two parameters which are essential: regain (R), which represents the weight percentage of absorbed water in fibers relative to the weight of the dry fibers; and moisture content (M), which is the weight percentage of absorbed water in fibers relative to the weight of the non-dried fiber weight. Attention should be paid to identify the difference between regain and moisture content. If the absorbed water weight is W and the dry fiber weight is F , we have $R = 100 W / F$ and $M = 100 W / (F + W) = (100 W / F) / (1 + W/F) = R / (1 + R/100)$.

Usually in commercial productions, appropriate temperatures and times are necessary to heat the fibers to obtain a dry weight. For a more precise dry

Table 2
Structure parameter and related properties

Structure	Related properties
Chemical structure	Almost every properties
Molecular weight	Mechanical properties, process features
Molecular conformation	Mechanical properties
Crystallinity and crystal size	Mechanical properties, process, dyeing, density, thermal, vapor permeable, fatigue
Degree of orientation	Mechanical properties
Fibril	Mechanical properties, fatigue, optical
Surface feature	Handle, optical, adhesive,
Cross-section	Handle, optics, thermal insulation, fiber crimp

weight, a strong water-absorbing reagent and vacuum environment are necessary.

2. FIBER STRUCTURE AND ITS DETERMINATION

Fiber structure and morphology are on a nano to micrometer length scale. In morphological scale, skin-core distribution, cross-section shape, hollow, twist and helical, conjugate, fibril, macro-fibril, *etc.* are involved. In micro-structure level, it involves crystal unit cells and dimensions, amorphous domains, crystallinity, chain orientation, *etc.* Generally speaking, the synthetic fibers' structure is simpler than that of natural fibers. Well-known relationships between fiber structure and properties are listed in Table 2. There are two models that explain the structure-property relationship: a two-phase model and two phases with an intermediate region.

2.1. Two-phase model

The idea of a two-phase model of polymer materials has generally been accepted since the 1960s. The two phases consist of a crystalline phase, in which the chains are regularly and tightly packed and an amorphous phase, in which the chains are more on less randomly arranged. These two phases are assumed to be in series arrangement in polymer fiber forms. Based on this model, several structural parameters need to be determined such as crystallinity, crystallite sizes, the degree of the orientation of crystallites, the degree of the molecule orientation in amorphous phase, *etc.* Comparing with small molecules, polymer crystal unit cell parameters of the same polymer are not necessary to be constant. Poly(ethylene terephthalate) (PET) is a good example in which the one-dimensional (1D) unit cell dimensions can change up to 10%, corresponding to the crystal density changes from 1.455 to 1.515 g/cm³ (see Table 3, the density of PET oligomer single crystal can reach as high as 1.559 g/cm³). The amorphous density is also varying [7]. This is because the unit cell parameters were determined via fiber samples. The preparations of these fiber samples were different, and lead to substantial variation of the unit cell parameters. Although the two-phase model implies that only single amorphous phase exists without regarding to molecular orientation, many reports have shown that two amorphous regions do exist.

2.2. Intermediate state model

An intermediate region between amorphous and crystalline phases was reported in Nylon fibers [16]. Its existence was confirmed using nuclear magnetic resonance (NMR) narrow and broad line analysis [17], and also in isotactic polypropylene (*i*-PP) [18,19] and PET fibers using WAXD method [20]. Lindner reported that the WAXD pattern in non-crystalline PET could be

Table 3
The Published Unit Cell Parameters of PET

Author	a(Å)	b(Å)	c(Å)	α (°)	β (°)	γ (°)	Density (g/cm ³)
Bunn (1954) [8]	4.56	5.94	10.75	98.5	118	112	1.455
Asbury (1946) [9]	5.54	4.14	10.86	107.5	112.2	92.23	1.471
Tomasholskii (1964) [10]	$d = 4.52$	5.98	10.77	101	118	111	1.479
Kilian (1960) [11]	$d_{(100)} = 3.40$ $d_{(010)} = 5.02$						1.495
Kinoshita (1979) [12]	4.50	5.90	10.76	100.3	118.6	110.8	1.501
Zahn (1957) [13]	$d_{(100)} = 3.40$ $d_{(010)} = 5.02$						1.501
Fakirov (1975) [14]	4.48	5.85	10.75	99.5	118.4	111.3	1.515
Liu and Geil (1997) [15]	4.675	5.836	10.831	96.26	128.30	106.62	1.559

deconvoluted into isotropic and oriented diffraction [21]. On the other hand, an anisotropy of the diffuse scattering of non-crystalline fraction in PET fibers was found using solid NMR technique [22]. In many semi-crystalline polymers, the co-existence of non-crystalline phase (mobile at T_g) and rigid amorphous fraction (mobile at the temperature, $T_g < T < T_m$) was proved [23].

All the above research analyses support the model of two phases with the intermediate region. In that model the oriented polymer materials include a liquid-like amorphous region, in which the chains are arranged randomly, and an oriented (or rigid) amorphous region, where the chains are oriented, but not crystallized, in addition to a crystalline phases. In WAXD patterns, a liquid-like amorphous region corresponds to a diffuse halo, evenly distributing along the whole azimuthal range. The oriented amorphous region corresponds to diffused arcs. The crystalline phase corresponds to a group of sharp diffraction spots or arcs. Takayanagi assumed in oriented polymer materials, tie molecules run parallel to stacks of alternating crystalline and amorphous phases (parallel series model) [24]. Here, the tie molecules construct the oriented amorphous region; the stacks of alternating crystalline and amorphous phases construct fibrils, in which the amorphous phase is random coils. The fraction of tie molecules ($tm\%$) can be calculated as follows

$$tm\% = \frac{\nu_a E_{fib} (E_c - E_a) - E_a (E_c - E_{fib})}{\nu_a E_c (E_c - E_a) - E_a (E_c - E_{fib})} \quad (1)$$

where E_{fib} is the fiber modulus along the fiber axis, E_c is the crystal modulus along the fiber axis (856 g/d or 110 GPa for PET), E_a is the modulus of the amorphous phase without taut tie molecules (17.8 g/d or 2.1 GPa for PET) and ν_a represents the amorphous fraction, which is equal to $(1 - \nu_c)$, based on density calculations.

2.3. Crystallinity

There are several methods for measuring crystallinity, which are summarized in Table 4.

2.3.1. Wide angle X-ray diffraction (WAXD)

Qualitative measurements of crystallinity in polymers are difficult to obtain. The main assumption for the WAXD method to determine crystallinity is that this method is based on the two-phase model, *i.e.* crystalline-amorphous

Table 4.
Primary methods of measuring crystallinity

Methods	Description	Comments
WAXD	1. Modified classic method 2. Mathematical simulation peak separation method	Different method and treatment (normalization, 2θ ranges) offer different results
SAXS	Invariant power method Correlation function	
DSC	$X_{cr} = (H_a - H) / \Delta H_c$ X_{cr} : Crystallinity ΔH_c : 100% crystalline specimen enthalpy H_a : enthalpy of amorphous material H : enthalpy of specimen	To obtain reproducible results, specific considerations are needed (see 3.1)
Density	$1/D = X_{cr}/D_c + (1-X_{cr})/D_a$ X_{cr} : Crystallinity D : Specimen density D_c, D_a : Density of crystalline and amorphous regions	D_c, D_a are different from different fiber treatments.
IR	$X_{cr} / (1 - X_{cr}) = (E_c / E_a) \times K$ X_{cr} : Crystallinity E_c, E_a : Absorances of crystalline and amorphous regions	Not easy to have repeatable results
NMR	Width of shape of the adsorbed curve Ratios of quantities adsorbed by specimen to reference specimen	Not easy to have repeatable results

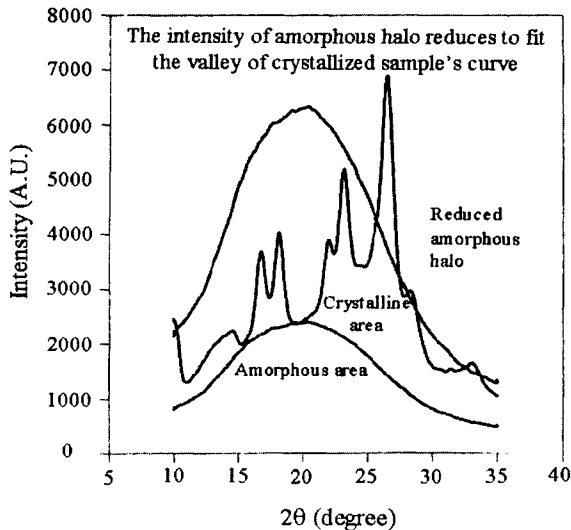


Fig. 6. The schematic graph of crystallinity calculation. Reduce PET amorphous halo to fit the valley of WAXD curve of crystalline PET sample [26]

model of the fiber structure. Here, two important WAXD methods to determined crystallinity are introduced.

2.3.1.1. Modified classic method

The classic method provides crystallinity measurements in terms of the ratio of the integrated intensities under crystalline diffraction peaks to the sum of the crystal peaks and the amorphous halo [25]. This method was originally established for cellulose fiber crystallinity measurements. It uses ground cellulose as a pure amorphous cellulose specimen, giving a linear relationship between the diffraction intensity and the 2θ angle. The separation of amorphous and air scattering areas is somewhat arbitrary.

The modified the classic method (for PET) used the intensity trace of an amorphous polymer which could be deduced proportionally until it met the observed trace of a partly crystalline sample at the special points [26] (see Fig. 6).

First, it should be noted that the amorphous halo curve can be obtained from quenched polymers, polymer melts or precipitated polymers. Second, the tested specimen should be unoriented, by cutting the fiber into powder or rotating the sample holder in order to obtain a powder or powder-like pattern.

Crystallinity X_{cr} = crystalline peak area / (crystalline area + amorphous area)

2.3.1.2. Mathematical simulation peak separation method

It was supposed that the intensity distribution Q_i along 2θ for a crystalline diffraction peak could be summed by the Gaussian and the Cauchy functions [27]. The whole diffraction curve (after normalization) for a polymer specimen can be expressed as

$$Y = \sum_{i=1}^B Q_i + R \quad (2)$$

$$X_{cr} = \sum_{i=1}^B Q_i / Y \quad (3)$$

where, Y is the integral intensity under whole diffraction curve, X_{cr} is the crystallinity (%); $Q_i = f_i G_i + (1 - f_i) C_i$ is the integral intensity under one crystal peak, B is the number of peaks in this diffraction curve, G_i is Gaussian function ($G_i = A_i \exp\{-\ln 2 [2(x - P_i)/W_i]^2\}$), C_i is Cauchy (or Lorentz) function ($C_i = A_i / \{1 + [2(x - P_i)/W_i]^2\}$).

Here, each peak is represented by 4 parameters: f_i is the profile function parameter, the content percentage of Gaussian function in a whole peak area; A_i is the peak height; W_i is the half height peak width, P_i is the peak position, and x is the 2θ angle.

Amorphous halo R can be represented by the equation

$$R = a + bx + cx^2 + dx^3 \quad (4)$$

where a , b , c , and d are parameters calculated from the simulation curve for an amorphous halo of non-crystalline polymer.

Assuming S is the summation of the differences between experimental d -spacing and calculated d -spacing, the S value could be minimized, and the most probable solution could be obtained by using the commercial software (PEAKFIT) or software written by researchers.

2.3.2. Small angle X-ray scattering (SAXS)

There are two ways to estimate the crystallinity of polymers based on SAXS experiments, one is based on the invariant power, and the other is based on the correlation length by means of correlation function analysis.

2.3.2.1. Invariant power

Integrate the SAXS intensity over the entire scattering angle range is denoted as the invariant power (or invariant value) Q [28],

$$Q = \int s^2 I(s) \cdot ds \quad (5)$$

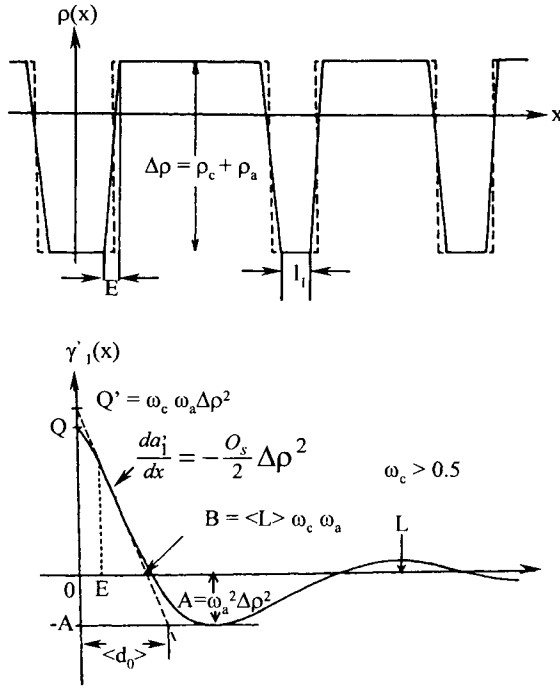


Fig. 7. Upper: schematic diagram of electron density distribution normal to the crystal lamellar surface; bottom: Corresponding correlation function [29]

where s is scattering factor of $2\sin\theta/\lambda$, $I(s)$ is the scattering intensity distribution along the s coordinate.

The scattering invariant power of a partially crystalline polymer forming a two-phase system is given by

$$Q = cV_s X_{cs} (1 - X_{cs}) (\Delta\rho)^2 \tag{6}$$

where c is a constant, which involves incident X-ray intensity, cross-sectional area, sample thickness and area, absorption ratio, instrumental factor, etc., V_s is the volume fraction of entities (spherulites, packed lamellae or fibril), X_{cs} is the degree of crystallinity with those entities, $\Delta\rho$ is the density difference between the crystalline and non-crystalline regions. X_c is equal to $V_s X_{cs}$

2.3.2.2. Correlation functional length [29]

This can be expressed by

$$\gamma'_1(x) = \int_0^\infty 4\pi s^2 I(s) \cos(2\pi s x) ds \tag{7}$$

$$X_{cs} = (L - d_a) / L \quad (8)$$

where L is the correlation functional length (crystal plus amorphous) and d_a is the correlation functional length of the amorphous phase. Fig. 7 shows the L and d_a lengths on the curve separately.

2.4. Orientation and molecular chain conformation

2.4.1. Birefringence

Usually, birefringence of a fiber is defined as the difference between the refractive index parallel to the fiber (n_{\parallel}) and the perpendicular to the fiber (n_{\perp}). There are two ways of obtaining birefringence measurements: the immersion method and retardation method. Here, we are going to focus on the convenient retardation method for fibers with a diameter D . In order to minimize the error in the measurement of D , the method is normally restricted to the fiber of regular cross-section (circle or elliptical) or microtome sections. Otherwise, n_{\parallel} and n_{\perp} need to be measured separately.

Most drawn fibers show a uniaxial positive birefringence (PET 0.16, nylon 0.06, rayon 0.04). However, some of man-made fibers, cellulose acetate and polyacrylnitrile fiber also show negative birefringence in addition to this positive birefringence.

The retardation can be expressed as

$$R = (N + dN) = D(n_{\parallel} - n_{\perp}) \quad (9)$$

where N is the integer of wave period number and dN is the fraction of wave period.

If a fiber is placed between two crossed polarizers with its axis at an arbitrary angle relative to the vibration direction of the polarizer, the light emerging from the fiber can be split into two components, where one vibrates parallel to the fiber axis with lower speed, called the slow light (e light); the other vibrates perpendicular to fiber axis with a higher speed, called the fast light (o light). Their light speeds are V_{\parallel} and V_{\perp} , respectively. If the times for these two lights passing through a distance in the fiber are t_{\parallel} and t_{\perp} , respectively, and the light speed in air (or vacuum) is V , while slow light merges on the surface of fiber, fast light has passed a distance, R , in the air:

$$R = V(t_{\parallel} - t_{\perp}) = V(D/V_{\parallel} - D/V_{\perp}) = D(V/V_{\parallel} - V/V_{\perp}) \quad (10)$$

Due to the Law of Refraction, we obtain

$$n_{\parallel} = V/V_{\parallel}, \quad n_{\perp} = V/V_{\perp} \quad (11)$$

$$R = D(n_{\parallel} - n_{\perp}) = D \Delta n \quad (12)$$

Experimentally, if the angle between the polarizer and fiber axis is 45° , the two amplitudes of e and o light are equal. By using of a simple wedge, the Babinet or Berek compensator enables superimposition of a known variable retardation upon that of the fiber. Both compensator and fiber placed with their vibration directions at 45° to those of the crossed polarizers, and in such a case, their retardations have opposite signs. When white light is used, the fringe of zero retardation ($N = 0$) is usually the true black one. The compensator is then adjusted until the black fringe within the fiber is brought back to the same position in the field as originally occupied by the black fringe when the fiber was absent, and the compensator retardation was set to zero. The fiber retardation is then equal and opposite to the known retardation introduced by the compensator.

2.4.2. Sound speed method for orientation measurement

The sound speed estimates the degree of orientation involved in both the crystalline and the amorphous regions. The principle is that sound waves propagate anisotropically if the fiber structure is anisotropic. The propagation speed reaches a maximum when the propagation direction is parallel to molecular chains (along the primary bond), and reaches a minimum, when the propagation direction is perpendicular to molecular chains.

As the parameter to describe the degree of orientation of molecules, sound speed orientation factor, f_s , can be defined as

$$f_s = 1 - \frac{C_u^2}{C^2} \quad (13)$$

where C_u is the sound speed in non-oriented fibers, and C is the sound speed in oriented fiber sample.

2.4.3. Dichroism

An oriented polymer sample shows different absorbance for light with plan polarization in two perpendicular directions. The dichromic ratio is the ratio of light absorbance measured in two mutually perpendicular directions. For a sample of uniaxially oriented fibers, there would be two absorbance terms, A_{\parallel} and A_{\perp} , corresponding to polarization of light parallel to and perpendicular to the fiber axis, respectively, and the dichromic ratio D is defined as

$$D = A_{\parallel} / A_{\perp} \quad (14)$$

The dichroism orientation factor can also be deduced from Hermans orientation factor:

$$f_D = \frac{3 \langle \cos^2 \phi \rangle - 1}{2} = (D-1)(D+2) \quad (15)$$

This formula fits the condition that the dipoles in the samples are parallel to molecular chains. If there is a tilt dipole with an angle α between chain molecules and dipoles, the formula should be modified to be:

$$f_D = \frac{3 \langle \cos^2 \phi \rangle - 1}{2} \cdot \frac{3 \langle \cos^2 \alpha \rangle - 1}{2} = (D-1)(D+2) \quad (16)$$

2.4.4. WAXD measurement of the degree of orientation in crystalline region

Fibers are uniaxially oriented materials. For the calculation of the degree of orientation, the diffraction intensity distribution of crystal plane (00*l*) along the azimuthal ring can be adopted. For oriented crystals, the molecular direction (which lies along the *c* axis) superimposes on the crystal plane (00*l*) direction (except for a triclinic unit cell). For triclinic unit cell, the diffraction spot (*hkl*), which is close to the meridian, is adopted for the orientation measurement. The angle between this (*hkl*) vector and the fiber axis is used for correction.

As a parameter to describe the orientation, an average orientation angle is defined as:

$$\langle \cos^2 \phi' \rangle = \frac{\int_0^{90} I(\Psi) \cos^2 \Psi \sin \Psi d\Psi}{\int_0^{90} I(\Psi) \sin \Psi d\Psi} \quad (17)$$

where ψ is the azimuthal angle, and ψ is equal to zero at peak position.

If there is an angle ρ between the fiber axis and (*hkl*) vector, the following correction must be made

$$\langle \cos^2 \phi \rangle = \frac{\langle \cos^2 \phi' \rangle}{\cos^2 \rho} \quad (18)$$

The Hermans orientation factor is also used to characterize the orientation of molecules. That factor is defined as follows:

$$f_x = \frac{3 \langle \cos^2 \phi \rangle - 1}{2} \quad (19)$$

2.4.5. Orientation of amorphous region

The relationship between the total birefringence and the Hermans orientation factor, *f*, can be expressed as

$$\Delta n = v_c \cdot \Delta n_c^0 \cdot f_c + (1 - v_c) \Delta n_a^0 \cdot f_a + \Delta n_f \quad (20)$$

where Δn is the total birefringence, v_c is the volumetric crystallinity (%) from density method, Δn_c^0 is the birefringence of a perfectly oriented pure crystalline material, Δn_a^0 is the birefringence of a perfectly oriented pure amorphous material, f_c is the degree of orientation in crystalline region, f_a is the degree of orientation in amorphous region, and Δn_f is the birefringence caused by the deformation of electrical field around phase borders. For polymers, this is negligible. If all parameters are known in Eq. (20), the orientation of amorphous region f_a can be calculated

3. THERMAL ANALYSIS OF FIBER

Wunderlich presented an extensive discussion of the theoretical basis of thermal analysis (TA) of fibers [30]. Recently, a completely summarized the research works on thermal characterization of fibers was provided [31]. Fibers are different from bulk polymers. They are distinct in anisotropy and flexibility, *i.e.* fibers possess high molecular orientations. TA can probe physical, chemical and mechanical property changes of fibers as a function of temperature, stress and in certain cases, specific environments. However, TA of fibers possesses both anisotropic microscopic and macroscopic properties. This creates a high internal stress and a dimensional instability. Therefore, sample preparations, experimental conditions and testing procedures, and the explanations of results require specific care. In experiments, for example, the fiber orientation provides an entropy driving force for fiber shrinkage upon heating, which is called thermal shrinkage. The relationship between driving force and the change of entropy can be simplified based only on equilibrium thermodynamics:

$$f = \left(\frac{dU}{dl} \right)_{T,V} - T \left(\frac{dS}{dl} \right)_{T,V} \quad (21)$$

where f is the stretching or shrinkage force resulting from an incremental change in fiber length dl . Generally speaking, higher molecular orientation usually leads to an early crystallization. This is because the orientation decreases the entropy in the melt prior to crystallization, and this reduces the barriers of crystallization by increasing the undercooling. Note that crystal melting is a first-order phase transition, and based on equilibrium thermodynamics:

$$\Delta G_m^0 = \Delta H_m^0 - T_m^0 \Delta S_m^0 = 0 \quad (22)$$

$$\text{Thus, } T_m^0 = \frac{\Delta H_m^0}{\Delta S_m^0} \quad (23)$$

where ΔG_m^0 , ΔH_m^0 , ΔS_m^0 are the Gibbs free energy, enthalpy and entropy changes upon melting for equilibrium polymeric crystals. T_m^0 is the equilibrium melting temperature. The orientational order in fibers reduces the entropy change upon crystallization and leads to the increased melting temperature; thus, the undercooling increases. Keep in mind that the two processes, *i.e.* thermal shrinkage, which leads to an increase of entropy and decrease of chain orientation, and the crystallization, which solidifies highly oriented chains and forms orientated crystals, occur at almost the same time and they are competing with one another to construct fiber micro-structure and form distinguishable properties.

Enormous developments of TA have been achieved in the past three decades. Even though all analysis methods associated with the temperature change may be called TA methods, only differential thermal analysis (DTA), differential scanning calorimeter (DSC), swelling differential scanning calorimeter (SDSC), thermo-mechanical analysis (TMA), dynamic mechanical analysis (DMA), thermogravimetry (TGA), thermal wide angle X-ray diffraction (TWAXD), and thermal small angle X-ray scattering (TSAXS) are typically considered traditional thermal characterizations. With these TA facilities, researchers can obtain information about chemical, physical, structural, morphological and mechanical behaviors of polymer fibers as functions of temperature (see Table 5).

Table 5
Properties which can be studied by TA

Class	Properties
Chemical properties	Decomposition Degradation
Structural properties	Crystal and polymorphism Crystallinity Crystallization kinetics Liquid crystal structure and its transition
Morphological properties	Size of crystal and amorphous domains
Physical properties	Melting point Crystallization process Polymorphism transition
Mechanical properties	Thermal modulus Thermal shrinkage and shrinkage stress Thermal expansion Internal stress

3.1. Differential scanning calorimetry (DSC)

In fiber science and technology, DSC is the most commonly applied thermal characterization method utilized to provide the thermodynamic and kinetic information, including heat capacity, crystallization, melting and phase transition temperatures, heats of transitions, crystallinity, decomposition and the kinetics of phase transitions and chemical reaction processes, *etc.*

3.1.1. Fiber sample preparation

Because of the lengthiness of the fiber and the tendency to shrink upon heating, sample preparation for DSC experiments becomes important to achieve reproducible results. There are two ways to pack samples with free ends: cutting fibers into short fibers or powders, or making fiber coils. Be cautious when cutting fibers in order to keep an even length distribution and arrange sample packing to achieve a high heat conductivity in the sample pan during measurements. To produce a small fiber coil, a simple method is carefully winding the fiber with necessary length around a form (such as a tweezers' tip). It is much easier than the tedious fiber cutting work. In this method, the lids of the aluminum pan should always be crimped to prevent spurious effects due to sample movement during heating. Although both methods generally produce reproducible results, the cutting fiber method is generally recommended. If a

Table 6
Some Considerations for DSC Characterization of Fibers

Factors	Effects	Mechanism
<i>Sample preparation</i>		
Free to shrink (cutting fiber or coil)	Double melting peak	Melt-recrystallize-melt
Constrained	Single melting peak	Reducing entropy change upon heating
<i>Fiber processing</i>		
As-spun fiber (amorphous)	Crystallize when melting	Kinetic control
Oriented	T_g shifts to higher temperature	Segment mobility
Oriented & annealed	T_g shifts to higher temperature	Segment mobility
Unconstrained	T_m decreases when increasing heating rate	Heating rate dependent reorganization
Constrained	T_m increases when increasing heating rate	Superheating due to entropy decreasing
Annealed	T_m increases when increasing heating rate	Superheating due to entropy decreasing
Fiber with extended chain	Superheating in the melting	Entropy reduction

special atmosphere is employed, holes should be punched on the lids. Some considerations for DSC operations are listed in Table 6.

With the internal stress, fibers shrink upon heating. This shrinkage causes a contact obstacle with the inner surface of the pan. For this kind of free-to-shrink nylon 6 fibers, the double melting peaks were observed, which was attributed to the superposition of three processes [32,33]. These three processes are: first, the perfection of the original crystals, and then, the melting of the perfected crystals simultaneously with the recrystallization and finally, the melting of the recrystallized crystals. They also observed a single melting peak for drawn nylon 6 fibers under constrained condition, *i.e.*, with the fixed fiber length. The melting peak appeared at a higher temperature range than those of

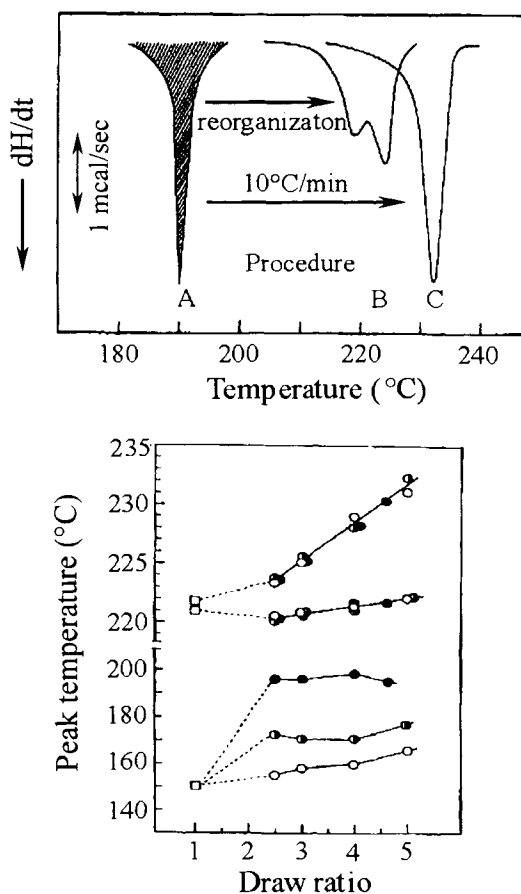


Fig. 8. (a) The DSC melting curves of 5x nylon 6 fibers as a function of sample preparation procedure. (b) the melting point of the nylon 6 fiber as a function of the draw ratio and sample preparation procedure [33]

the double peaks observed in the free-to-shrink samples and increased linearly with the draw ratio. Mead and Porter also studied this kind of constrained fiber samples and concluded that the constrained condition retarded the relaxation of chain molecules during the melting and slows recrystallization and crystal perfection process [34].

To illustrate the sample, an obvious evidence was provided to verify the samples preparation effects on the melting behavior of the drawn nylon 6 fiber [35]. Three preparation procedures were carried out. In procedure A, the sample is irradiated with X-rays in acetylene gas in order to cross-link the amorphous parts of the fibers. Thus, the crystals melted without the reorganization of imperfect crystals during heating. In procedure B, no special treatment was used for the fibers *i.e.* they are free-to-shrink. Therefore, double melting peaks were observed. In procedure C, the fibers are constrained. Only a single melting peak was found at a higher temperature. These observations are illustrated in Fig. 8.

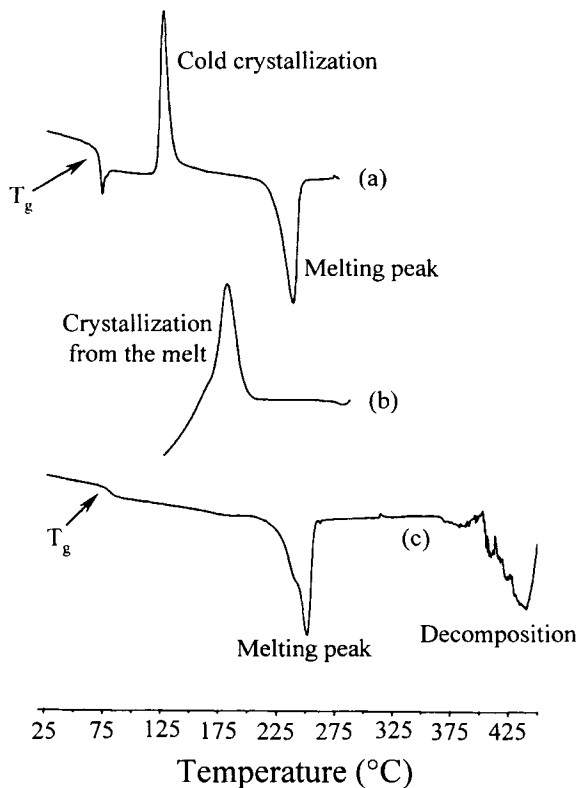


Fig. 9. DSC diagrams of as-spun PET fibers: (a) first heating, (b) first cooling, (c) second heating (Ben Morris, Hoechst Celanese Advanced Materials Group, unpublished results)

3.1.2. Sample processing history

The effects of fiber processing history on thermal characterization was confirmed [36,37]. T_g marks the starting temperature at which a sufficient mobility is imparted to molecular chain segments for processing, such as thermal shrinkage and crystallization, to occur. The chain orientation and processing history of the fibers significantly affects the T_g . Fig. 9 shows a set of typical DSC curves for as-spun PET fibers at 10°C/min. Curve (a) records the first heating process. From low to high temperatures, a glass transition, an exotherm associated with a cold crystallization (crystallization upon heating from the glass), and a melting endotherm is observed. On cooling (curve b), a crystallization-from-melt process is observed. On the second heating trace (curve c), the cold crystallization is no longer present. Philip (1972) developed a simple scheme for the identification of synthetic fibers. In order to erase the processing history effect on the fibers, his identification method depends on the second heating parameters though still using the first heating to remove processing history [38].

3.1.3. Heating rate effects on oriented fibers

Miyagi and Wunderlich investigated the effects of the heating rate on crystal melting of PET fibers [39]. T_m drops with increasing heating rate for unconstrained fibers because of the heating-rate dependent reorganization. T_m rises with increasing heating rate for constrained fibers because of the superheating with a smaller entropy change. This heating rate dependence was suggested to associate with the pre-melt endotherm in PET textile fibers [40].

3.2. Swelling differential scanning calorimetry (SDSC) [41]

Upon replacing the surrounding gaseous medium by a suitable swelling solvent, several advantages are gained. First, the heat conduction is enhanced, creating a faster and more sensitive responses of fibers to heat. Secondly, the temperature of transition is lowered by the swelling solvent in avoiding chemical reactions, such as cyclizations. This makes the thermal analysis of swollen fibers particularly suitable in studying the different structures and textures of the fibers stepwise in the swell process without modification by heating. Finally, detrimental effects of oxygen are avoided due to the immersing from the swelling solvent.

In the case of SDSC, the test can be conducted in a sealed liquid pan. Thus, it is possible to raise the temperature to a point above the boiling point of the swelling solvent without vaporization. On the other hand, the depression of melting point can be described by the Flory's equation:

$$\frac{1}{T_m} - \frac{1}{T_m^0} = \frac{R}{\Delta H_u} \frac{V_u}{V_1} (1 - \chi_1 v_1) v_1 \quad (24)$$

where T_m is the melting point of the polymer with a swelling solvent, T_m° is the melting point of the polymer without a swelling solvent, v_1 is the mol fraction of solvent, H_u is the heat of fusion, V_u is the molar volume of solvent in the swelling agent, V_l is the molar volume of polymer, χ_1 is the interaction parameter and R is the gas constant.

Fig. 10 shows a typical SDSC diagram of polyacrylic fiber in 80% DMF aqueous as a swelling solvent. The four endothermic peaks represent the disassociation energies of different structures and texture regions in the fiber. The peak at the lowest temperature represents the disassociation energy of mesomorphous structures of the fibers, which is a structure between the crystalline and amorphous phases. The second endothermic peak originates from the swelling of crystalline structure, which reveals to be sharp, and this is strongly supported by the WAXD results. The third broad endothermic peak represents gel-sol transitions. And the highest temperature endothermic peak is tentatively attributed to the disentanglement process of the macromolecular chains in the sol.

3.3. Thermo-mechanical analysis (TMA)

TMA is a measurement of dimensionally related changes as a function of temperature. It offers various quantitative thermo-mechanical information, such as coefficients of thermal expansion, onset of thermal transitions or dimensional changes, thermal shrinkage (at zero tension) as a function of temperature, thermal shrinkage stress (at zero dimensional change) as a function of temperature, mechanical modulus as a function of temperature, and TMA 'fingerprint' of the fiber processing history, *etc.* All these results can help to identify fiber spinning processes and characterize fiber properties for different applications.

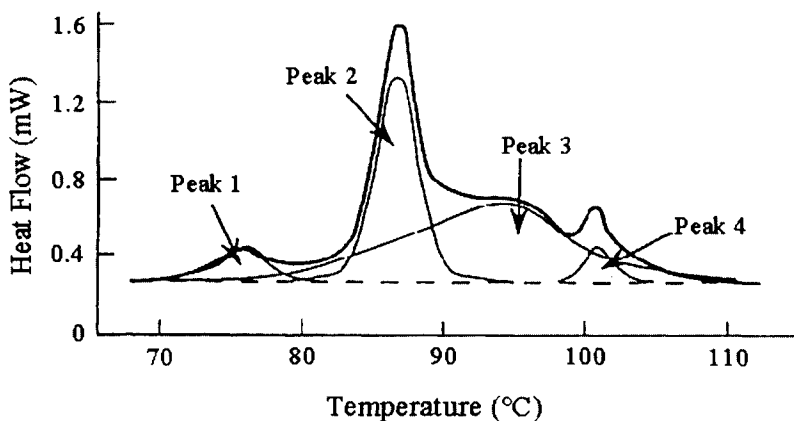


Fig. 10. Typical swelling DSC thermogram of polyacrylic fiber in 80% DMF [41]

Because the parameters monitored by TMA are identical to the major variables of the fiber spinning process, and therefore, once an understanding of the responses on the TMA is achieved, the fiber formation conditions and histories can also be deduced [42]. A typical shrinkage thermal behavior at zero-load for a drawn semi-crystalline fiber involves four regions [31]. These four regions are illustrated in Fig. 11. Region 1 is between room temperature and T_g , reversible thermal expansion can be observed, and the dS_T/dT value remains constant. In region 2 (in the T_g range), irreversible shrinkage occurs due to the relaxation of orientated amorphous chains, except for tie molecules in crystalline regions and the value of dS_T/dT which appears at a maximum corresponding to the temperature on the maximum rate of relaxation. Region 3, which is between T_g and T_m , is the structurally perfect region. Irreversible shrinkage occurs due to reorganization, chain folding, recrystallization and other structure changes. In region 4 (in the T_m region), rapid shrinkage takes place until fiber failure. All the molecules are driven to return to their original random coil state.

TMA is also the most efficient method in measuring the coefficient of linear thermal expansion (CTE). In bulk polymers, CTEs are always positive with increasing temperature. However, for oriented polymeric fibers, CTE is negative in most cases above T_g , even though the coefficient of volume thermal expansion (CVTE) is always positive. The anisotropy of bond energies along and between chain molecules have a difference of about one to two order of magnitude. The relaxation of this anisotropic bond orientation causes the CTE in the chain direction to be negative above T_g . Hence the CTE above T_g is irreversible until structural equilibrium is achieved. The maximum value of CTE

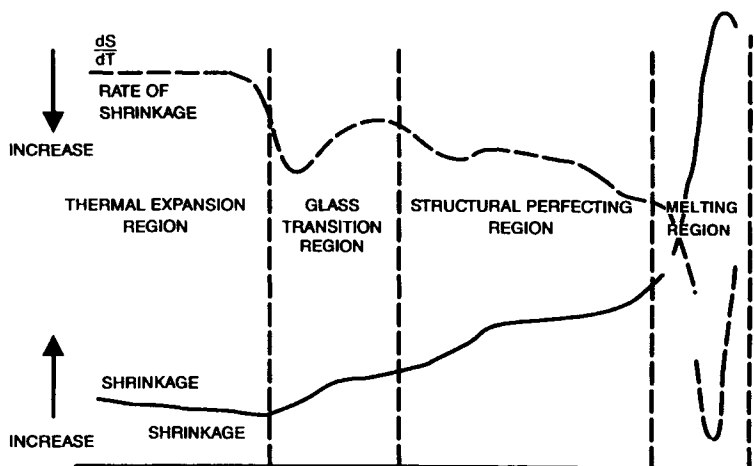


Fig. 11. Diagrammatic representation of a shrinkage and a differential shrinkage (dS_T/dT) TMA curve of a drawn, partially crystalline fiber [31]

indicates the complete disorientation state, while the minimum value gives rise to the perfect oriented state. Since CTE depends more strongly on the chain orientation than on crystallinity, TMA becomes the preferred method in monitoring the orientation in fibers.

3.4. Dynamic mechanical analysis (DMA)

In fiber science, DMA is also the most important thermal characterization technique, which is helpful to establish fiber structure and property relationships.

In most cases, the DMA instrument supplies a sinusoidal tensile strain to one end of the fiber sample, and measure the stress response at the other end. With such a design, DMA can determine two parameters, E' and E'' . E' is the storage modulus, which is the real part of the complex modulus, and E'' , the loss modulus, is the imaginary part of the complex modulus.

Generally speaking, E' decreases with increasing temperature except for the cases during cold crystallization of as-spun fibers or cross-linking. The maximum peak on E'' (or $\tan\delta$) versus temperatures indicates energy dissipation and thus, reveals the occurrence of transitions, which are associated with relaxation processes of certain structures. Typically, there are four transition types could be determined by DMA. First, glass transition, which is generally assigned as an α transition in amorphous polymers (in crystalline polymers, they may not be necessary as α transitions. This relaxation corresponds to the onset of the cooperative motion of the segments. Because of the frequency dependence, the T_g values measured by DMA are different from those obtained in DSC experiments.

For the α_c or α' transition, which occurs at higher temperatures than the α transition for crystalline polymers, which lies between T_g and T_m , and is attributed to molecular relaxation related to crystals. This transition should be at least at or above the minimum temperature of the fiber drawing process, at which sufficient segment mobility of the crystals may be initiated. A cold crystallization may occur during initial heating of as-spun fibers. It happens at the temperature higher than T_g and accompanied by a considerable increase of the E' .

Finally, several secondary transitions that are associated with sub-molecular relaxation of chain molecules may also occur. Those transitions are usually assigned β , γ , δ by decreasing temperature. Their magnitude is generally smaller and more frequency dependent (lower activation energy) than that of the α -transition.

The origins of these relaxation processes are generally attributed to side-group relaxation, end-group motion or backbone "crank-shift" type of motions. Specific assignment of those processes need to be further assisted by other

experimental methods, such as nuclear magnetic resonance (NMR). Generally speaking, these sub- T_g relaxation processes are largely non-cooperative in nature.

Differing from DMA experiments for thick rods or bars, DMA tests for fibers require a static tension because the smaller fiber diameters cannot support significant tensile and compressive stresses. Furthermore, the magnitude of the static tensile stress will affect the DMA results, especially in the case of the fibers with a storage modulus [43]. Not enough tensile stress could lead to sample buckling so that a truncated stress signal will be obtained. But too much static stress would cause fiber deformation and changes in micro-structure. Usually, DMA measurements are carried out in a wide-range of temperatures. The thermal expansion, creep and shrinkage could change the initial static stress. Therefore, autotension is necessary for DMA experiments to adjust the sample tension as temperature changes. Several types of autotensions are used in modern DMA instruments to keep the static force constant. This is done by predicting static force from measured sample moduli and tracking the dynamic force.

The transition temperatures measured by DMA are strongly dependent on frequency. For example, in E' versus temperature diagrams, the relaxation temperatures shift toward higher temperatures as the frequency increases, in accordance with kinetic considerations (time-temperature superposition). If the transitions can be described by a single relaxation process of the Arrhenius type, a plot between logarithmic frequency and the reciprocal transition temperature generates the activation energy which reveals the energy which is necessary to achieve this specific type of relaxation. This energy can also be used to judge the type of relaxation processes.

3.5. Thermogravimetric analyzer (TGA)

TGA analysis offers a tremendous potential for characterizing thermal stability of polymers and fibers. It provides qualitative and quantitative data for kinetics of thermal weight losses of the samples (generally degradation), the influence of additives and chemical modification on fibers and textile materials, the behavior of copolymer or polymer blends, and finally, the influence of fiber sizing treatments and compatible coatings on fabrics. Combined with other analytical instrumentations, such as mass spectroscopy or vapor-phase chromatography, to identify the chemical species released from the fiber sample during heating, TGA is made much more beneficial.

Nevertheless, TGA results obtained from different operators or laboratories are harder to reproduce. In addition to a number of other factors, the major reason for this is an extreme sensitivity of TGA results to the surface-to-volume ratio, which is particularly difficult to control in fiber samples. Therefore, in a report of TGA results, details of sample weight and preparation, heating rate, and atmosphere should always be included.

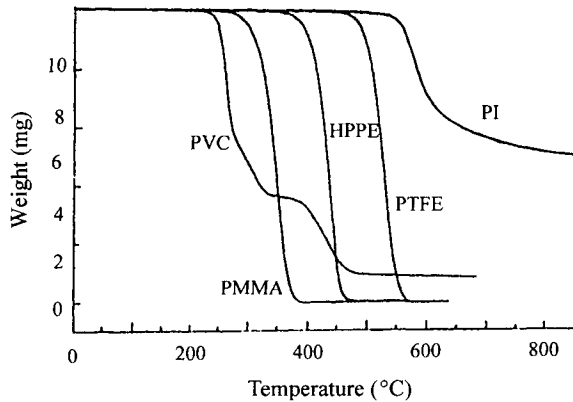


Fig. 12. TGA diagrams and relative thermal stability of polymers [44]

For *i*-PP fibers, the measured degradation rate constant changed from -0.001 to 0.065 corresponding to surface/volume ratio from 2 to 50. For a better reproducibility, a simple solution for this problem is to carefully grind the samples to obtain optimal and reproducible packing, keeping in mind that grinding may substantially change the thermal stability due to generating a number of chemical radicals due to the chemical bond breaking.

Fig. 12 shows several typical TGA thermal diagrams of some polymers [44]. Poly(vinyl chloride) fibers have two degradation steps which means that two materials are co-existing. The first step may be attributed to the degradation of plasticizer. Others have only one step of weight loss due to their degradation.

3.6. Thermal wide angle X-ray diffraction (TWAXD)

TWAXD has been widely and successfully used, for crystallization polymorphism of polymer, polymer liquid crystal structure analysis and other phase transition thermodynamics and kinetics. TWAXD needs a precisely controlled sample temperature and a rapid response time during temperature changes. For fiber applications, a transmission X-ray method is necessary and the fiber samples have to be under temperature control in a hot stage. The direct X-ray passes through the small hole of the hot stage onto the fiber samples. Generally, a period of about 10 min is needed to achieve temperature balance. For the reflection method, sticking aligned fiber on Aluminum or Berilium sheet with a thickness of about 0.2 mm is a quick and easy way to obtain temperature balance.

One example of this method is shown in Fig. 13, in which polymorphism of a polyester can be identified by heating the sample to different temperatures. The K_O is an orthorhombic crystalline phase; the K_{T1} and K_{T2} are two triclinic crystalline phases with different unit cell dimensions [45].

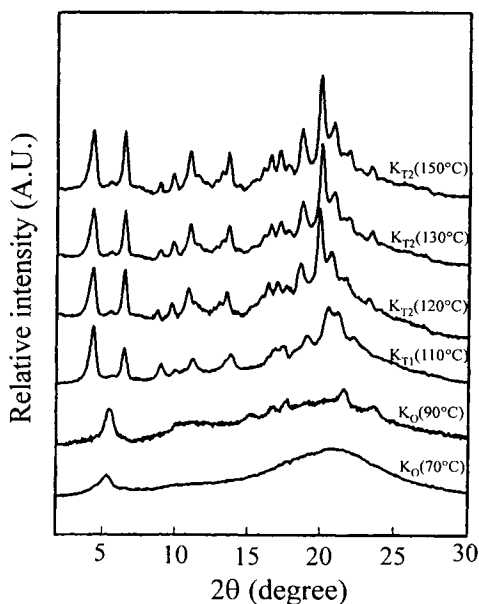


Fig. 13. A set of TWAXD powder patterns of a polyester fiber, shows three different crystalline phases at different temperatures [45]

3.7. Thermal small angle X-ray scattering (TSAXS)

TSAXS has been used to offer changes of crystal lamellae and long spacing as a function of temperature, crystallization time, and/or sample preparation procedure. An excellent sample for temperature control facility was specially designed which can quickly shift a sample from one hot stage to another. It works with the quick measure on synchrotron X-ray source.

Fig. 14 provides an example to used SAXS to measure the crystal thickness and amorphous thickness in isotactic polypropylene fibers as a function of draw ratio and draw temperature [46].

The long period was found to increase slowly with increasing draw temperature. Meanwhile, the crystal thickness increased rapidly, and the amorphous thickness decreased, implying that more chains in the amorphous phase were crystallized with increasing draw temperature. This observation indicates that the recrystallization process makes the existing lamellae more perfect and allows them to be thickened. The long period and the crystal thickness were found to increase before the draw ratio reached the value of 2.0. The corresponding amorphous thickness remained unchanged with draw ratio. This result indicates that drawing at high temperatures also creates more perfect crystals. The long period, the crystal, and amorphous thickness did not change

when the draw ratio became larger than 2.0. At high draw ratios, the transition from the amorphous phase to the mesophase became dominant and thereby did not affect the overall lamellar structure.

3.8. Summary of TA methods

The anisotropy and flexibility of fibers lead to a series of specific considerations in applying TA experiments to characterize fibers' structures and properties. The functions of TA techniques for fiber characterization are summarized in Table 7.

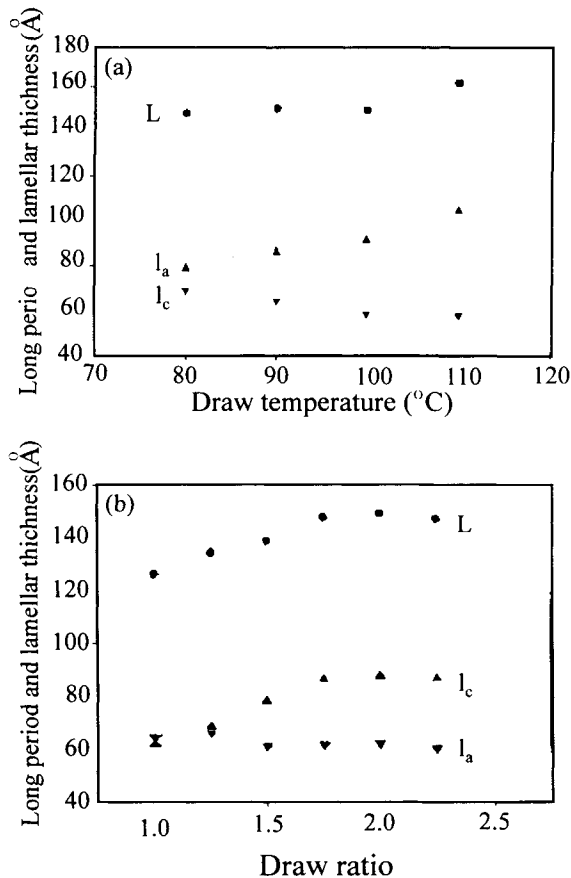


Fig. 14. Change of long distance, crystal thickness, amorphous thickness of *i*-PP fibers drawing (a) at a draw ratio of 2 at different temperatures and (b) at a temperature of 100°C with different draw ratios (L , l_c and l_a represent the long distance, crystal thickness and amorphous thickness, respectively) [46]

Table 7

The functions of ta instruments for quantitative fiber characterization

Functions	DSC	SDSC	TMA	DMA	TGA	TWAXD	TSAXS
T_g	+	+	+	+	-	-	-
T_m	+	+	+	-	-	+	-
Degradation Temp.	+	-	-	-	+	-	-
Thermal stability	+	+	+	+	-	-	-
Thermal expansion	-	-	+	-	-	+	-
Thermal shrinkage	-	-	+	-	-	+	-
Shrinkage stress	-	-	+	-	-	+	-
Internal stress	-	-	+	-	-	+	-
Modulus	-	-	+	+	-	-	-
Processing history	+	+	+	-	-	-	-
Motion of molecules, segments & side group	-	-	-	+	-	-	-
Polymorphism	+	+	-	-	-	+	-
Crystallization kinetics	+	+	-	-	-	+	+
Crystallinity	+	+	-	-	-	+	+
Orientation	-	-	-	-	-	+	+

4. CONVENTIONAL FIBERS AND THEIR MODIFICATIONS

Conventional fibers are raw materials for apparel productions in the traditional textile industry. In the past two decades, this area has matured. New fibers are being developed mainly for specific application, so-called “high-performance fibers”. In the conventional fiber area, a few noticeable developments, for example, the Carilon[®] fiber, are produced by the melt spinning of newly synthesized aliphatic polyketone copolymer. Its raw materials (ethylene and carbon monoxide) are inexpensive and easy to obtain. Other examples are a new variation of Rayon[®], poly(trimethylene teraphthalate) fibers and ultrathin *i*-PP fibers.

4.1. Conventional fibers

The process and main features of conventional fibers are listed in Table 8. The mechanical properties of some conventional fibers are summarized in Table 9.

4.1.1. Nylon fibers

Because of the tradition of industry, all linear polyamides are called Nylon. Nylon has good mechanical properties and is widely used in fiber products of apparel, carpets, and tire cords. Nylon is also used in the production of upholstery fabrics, seat belts, ropes, parachutes, fishing lines and nets, *etc.*,

Table 8
The process and main features of conventional fibers

Fibers	Processing	Features
Polyester	Melt spin	Good strength, modulus, excellent recovery, low moisture regain
Nylon	Melt spin	Good strength, recovery, low moisture regain
Polyacrylonitrile	Solution spin (melt & semi-melt spin is developing)	Wool-like handle, comfortable
Polyolefin	Melt spin	Dye ability still need improve
Polyvinyl alcohol	Wet spin	Dye ability need improve
Cellulose	Solution spin	Comfortable, high cost
Cellulose acetate	Solution spin	Soluble in water

Table 9
The mechanical properties of conventional fibers (65% r.h.; 20°C) [30,31,32]

Fibers		Relative strength (N/tex)	Extension to break (%)	Work rupture (mN/tex)	Initial modulus (N/tex)
Polyester	medium	0.47	15	53	10.6
	high	0.56	7	22	13.2
	staple	0.47	37	119	8.8
Nylon 66	Medium	0.48	20	63	3.0
	High	0.66	16	58	4.4
	staple	0.37	43	101	1.0
Nylon 6		0.29	46	77	0.6
Polyacrylonitrile	Orlon staple	0.27	25	47	6.2
	modacrylic	0.34	34	63	8.8
Polypropylene		0.65	17	71	7.1
polyethylene	High density	0.34	10	19	4.4
	Low density	0.08	20-40	11-26	0.9
Viscose rayon	High strength	0.41	12	28	8.8
	polynosic	0.26	7	11	13.2
Triacetate		0.12	30	18	3.1
Polyvinyl alcohol		0.17	26	24	2.2

because the abrasion resistance of nylon is high. Nylon 66 and nylon 6 are by far the most important commercially produced fibers. They are melt spun and then drawn, and finally heat-treated to prevent the shrinkage. The moisture regain of nylons is several percent, depending on the chemical structure of nylon and the

relative humidity. Acting as a plasticizer, moisture can lower T_g , and thus influence measured properties. The more important properties of nylons include high flexibility and resilience coupled with high strength (3.6 - 7.2 cN/dtex) and temperature stability. The nylons are available as a monofilament, continuous-filament fiber, and staple.

The glass transitions of nylon homopolymers and copolymers as a function of the molecular structure and the moisture content have been investigated [47]. Using DSC and DMA, they showed that the T_g lowering due to moisture is only dependent on the average spacing between amide groups along the chain, and they derived a procedure for accurately predicting dry and wet glass-transition behavior. The thermal analysis results of nylon fibers are usually difficult to explain due to the fact that these polymers exist in different crystal forms [48,49].

4.1.1.1. Nylon 6

The T_g of nylon 6 is $\sim 40^\circ\text{C}$ [50], the T_m^0 of the α -crystal form is 270°C , and the heat of fusion of 100% crystalline nylon 6 is 230 J/g [51].

DSC was employed as a sample characterization method in a study of the "crystalline memory" effect on the crystallization kinetics of nylon 6 [52]. Precursor crystallinity was found to profoundly influence both the rate and the nature of further crystallization [53,32,33].

The melting behavior of nylon 6 fibers as a function of drawing and annealing history has received considerable attention in the thermal analysis literature. The effects of draw ratio, annealing time and temperature, measurement atmosphere, and heating rate on nylon fiber thermal behavior have been studied in detail with DTA [54,55]. The conclusion was that a increasing heating rate leads to a increasing T_g , ($47 - 58.5^\circ\text{C}$, at $2 - 50^\circ\text{C}/\text{min}$) and broaden the dehydration peak. Stretching increases the T_m (a draw ratio of ~ 3 increases T_m from 221 to 225°C), free-to-shrink annealing of drawn fibers tends to lower the T_m , and the atmosphere employed (air, nitrogen, vacuum) can cause significant T_m shifts. The heats of fusion and crystallinities of variously drawn nylon 6 fibers were determined by DSC, and define the overall crystalline perfection of the fiber structures [56]. The specific heat of drawn nylon 6 has been measured by using DTA to monitor the effects on fiber texturing structures and dyeing [57]. An exothermic peak at $142 - 150^\circ\text{C}$ was controlled with the processes and structural parameters. Several research groups have monitored nylon 6 fiber shrinkage as a function of their processing conditions [58,59]. DSC measurements were utilized to determine the nature and amount of elastomer present on coated nylon fabrics [60]. Nylon fiber thermal stability was also investigated using DTA [61].

The effect of molecular weight and moisture on high-speed melt spinning of nylon 6 fibers was reported [62]. It was found that the heat of fusion for both

the dried and undried fibers decreased with increasing molecular weight. In contrast to density, surprisingly enough, the crystallinity of the fibers increased with increasing molecular weight. This phenomenon was explained by an increased amount of the α -form crystal as the molecular-weight of the fibers increase. It is known that the density of the α - form crystal (monoclinic) is considerably higher than that of the γ - form crystal (pseudo-hexagonal). A γ to α crystal transition was suggested to take place on the running threadline. On the other hand, WAXD and DSC were used to investigate the effect of drawing nylon 6 fibers under elevated pressures using [63]. The presence of two crystal forms (α and γ) was observed in the filaments drawn at atmospheric pressure, and a structural conversion from the γ form to the α monoclinic form was recorded with increasing pressures. The heats of fusion also increased linearly with the applied pressure.

TMA was employed to study tension effects during a commercial annealing process of nylon 6 carpet fibers [64]. DSC and thermal stress analysis were also employed to characterize the changes in the fiber structure and morphology. Annealing decreases the shrinkage of nylon 6 fibers due to a development of the crystallites during heat setting [65]. This leads to an overall disorientation of the amorphous chains

A DMA study on nylon 6 monofilaments was carried out [66]. The dynamic mechanical behavior was found to depend on the water content of the fiber. The highest-temperature transition of the dry filament was observed at 90°C (α transition). As the relative humidity increased, a shoulder appeared first on the lower temperature side of the α relaxation peak that shifted to lower-temperatures (as low as $\sim 6^\circ\text{C}$) and finally, it became a separate peak. The splitting of the α relaxation peak was explained by the presence of water. The α relaxation was attributed to motions of two parts of amorphous phases. The regular amorphous part was affected by the presence of water and thus shifts its relaxation peak to lower temperatures. However, a more ordered amorphous part was unaffected by the presence of water, and thus, no shift of the α relaxation was found. A β relaxation peak for the dry fibers was recorded at -27°C which shifted to lower temperatures with increasing water content. This transition could be observed in nylons only when moisture or low molecular weight components are present. Therefore, it should be attributed to the water-carbonyl group motion. It was suggested that even trace amounts of water can be responsible for this relaxation peak to appear in dry nylon fiber samples. A γ relaxation was observed at -107°C , and is ascribed to motions of the methylene units in the nylon backbones.

Khanna described the evaluation of thermal histories of nylon 6 unoriented and biaxially oriented fibers by DSC, TMA, and DMA [67]. It was suggested that the correlation between the annealing conditions and the thermal properties,

was caused by formation of small crystals in the amorphous phase during the heat treatment.

4.1.1.2. Nylon 66

The T_g of nylon 66 is 50°C [50]. The T_m^0 of the α -form crystal (triclinic) is estimated to be 280°C. The heat of fusion of the 100% crystalline α form is around 300 J/g [51].

The method of polymerization, either the melting or interfacial method, of nylon 66 and also in nylon 610 was investigated [68]. Results of DSC and other techniques showed that different molecular weight distributions might cause differing fiber properties. DSC was used to study the grafting of polyacrylic acid onto nylon 66 [69], while T_g and cold-crystallization behaviors of a series of nylon 66 copolymers were also investigated [70-72].

The effects of drawing and annealing on the dynamic mechanical properties of nylon 66 fibers were studied [73]. The dynamic storage modulus increased with increasing draw ratio. The position of the α relaxation taking place at 80 - 90°C was affected minimally by annealing processes, but the transition moved to higher temperatures with increasing draw ratio (and thus, increasing the degree of orientation).

The α relaxation of nylon 66 fibers was also found shifted to higher temperatures as a result of molecular-weight increase [74]. Bell studied the relationship between the dynamic mechanical properties of nylon 66 fibers and its dye diffusion behavior [75]. A linear relationship between the diffusion coefficient and the loss modulus was observed. The nylon 66 crimped fibers were characterized by DMA using the usual tensile mode [76]. The dynamic compression mechanical properties were also measured. The experiments performed in the compression mode led to an understanding of the crimp parameters (crimps per inch, crimp amplitude) in affecting the properties. A high fiber-to-fiber friction was deduced from these experiments for the highly crimped fibers.

4.1.2. Polyolefin fibers

Polyolefin fibers possess many advantages, such as low cost, good tensile properties, chemical resistance, and durability. Disadvantages are low T_m and poor aesthetics restricting. The most important polyolefin fibers are polyethylene (PE) and *i*-PP. They are usually used in apparel; furniture, carpet and rug productions, carpet backing, carpet face fibers; rope, cordage and twine. The relatively new gel-spun ultra-high molecular weight PE fibers are used in cordage and braided rope, cut-resistant gloves, and sporting goods (such as helmets, skis, fishing equipment, and ballistic protection).

4.1.2.1. Polyethylene (PE) fibers

The T_m^0 of PE was measured directly on macroscopic extended-chain crystals [77]. It is at 145°C, and the heat of fusion of 100% crystalline PE is 293 J/g. The T_g is within a very broad temperature range and still in argument, -36°C [78], and -128°C [79] were accepted by different researcher as the T_g of PE.

Ultra-oriented high-density PE (HDPE) fibers were prepared by solid-state extrusion [80]. The crystallinity, density, T_m , and negative CTE (shrinkage) parallel to the fiber axis increased with increasing draw ratio and reached limiting values at draw ratios of 20-30. The T_m of the fibers also increased with increasing extrusion temperatures. The optimum temperatures for obtaining fibers with maximum orientation of the amorphous phase in the semi-crystalline PE fibers were determined to be 80 - 100°C, *i.e.*, near the temperature of the α relaxation.

The thermal properties of ultrahigh-strength gel-spun HDPE fibers were reported [81]. High draw ratios were achieved between 90°C and 135°C, and their Young's modulus increase linearly with the draw ratio (up to 32). The heats of fusion increased rapidly with the draw ratio, and reached 260 J/g (*i.e.*, ~ 90% crystallinity) for the fiber with the highest draw ratio. Smook and Pennings studied the influence of the draw ratio on fiber structure and morphology at 148°C of gel-spun PE fibers using DSC [82]. Some typical DSC diagrams recorded in unconstrained and constrained conditions are shown in Fig. 15. The formation of shish-kebab morphologies at a draw ratio of 6 was observed and it

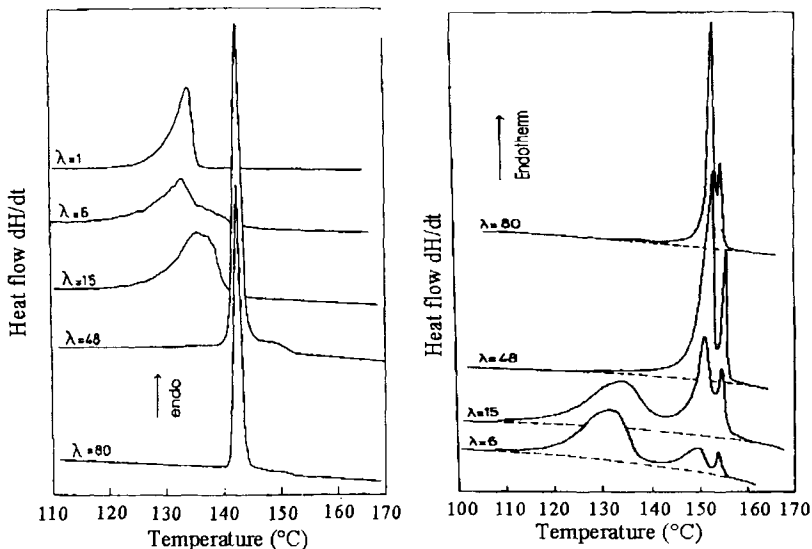


Fig. 15. (a) Melting curves of ultrahigh-molecular weight linear polyethylene fibers in unconstrained state; (b) melting of the same sample in constrained state [82]

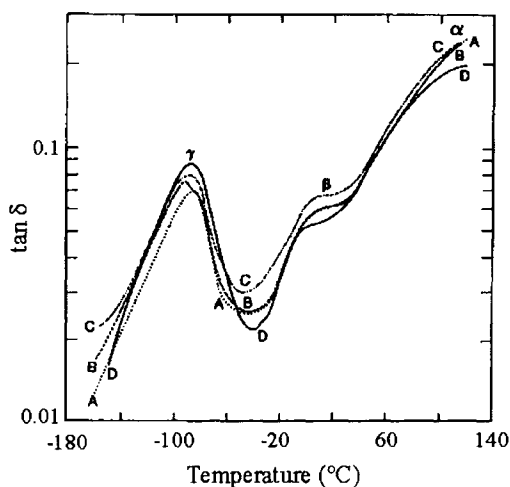


Fig. 16. Loss tangent versus temperature curves for a low density PE fiber at different draw ratios: A. 1.4, B. 2.0, C. 2.7, D.3.5 [66]

changed to a smooth fibrillar structure for the fully drawn fibers with a draw ratio of 80. The crystallinity increased during drawing from 53 to 94% for the fully drawn fibers. The latter displayed a very narrow melting endothermic peak (the width of the peak was $\sim 5^\circ\text{C}$) in unconstrained heating experiments, while a T_m at 150°C was observed in the constrained condition. The T_m continuously increased with increasing draw ratio, reaching its final value at $\lambda = 48$. The as-spun fiber had a single melting peak at 136°C . Three melting endothermic peaks were recorded for the hot-drawn fibers. The lowest melting peak was attributed to melting of folded chain lamellae in the shish-kebabs. The intermediate endotherm was ascribed possibly to an orthorhombic-to-hexagonal lattice transformation, while the highest endotherm might correspond to the melting of the hexagonal phase. The heat of fusion of the hexagonal lattice was estimated to be 81 J/g . In addition, there was a large difference in the heats of fusion of the fibers when measured in unconstrained and constrained conditions at any different draw ratio. These differences were attributed to the retaining of a partially ordered melt in the constrained experiments.

DSC and WAXD were combined to study on highly oriented PE fibers [83]. Utilizing constrained experiments, they confirmed the orthorhombic to hexagonal transformation prior to melting. The highest T_m was recorded at $160 - 162^\circ\text{C}$. It is noteworthy that the degree of crystalline orientation remained unchanged even at 150°C , just prior to the melting of the fiber. The extended chain crystal structure was found beyond a draw ratio of 20, while the orthorhombic and monoclinic crystal forms were found in WAXD experiments

[84]. It was also found that the fraction of the monoclinic crystal form increased with increasing draw ratio.

Dynamic mechanical behavior of low- and high-density PE monofilaments (LDPE and HDPE, respectively) with different draw ratios was studied [66]. Three major relaxations were recorded in LDPE fibers (Fig. 16). The α relaxation occurred at 110°C; this process was found earlier to depend mainly on the crystalline thickness [85]. The β relaxation was observed at 10°C. The origin of this peak is still in being debated to see whether this corresponds to the T_g of PE, or is attributed to motions associated with the branched structure in PE. Popli and co-workers (1984) also considered that this relaxation results from the relaxation of chain units in the interfacial region. Finally, the γ relaxation occurred at -91°C. This peak was explained by the concerted motion of three or four methylene units in the chains. Similar transitions were observed for HDPE monofilaments, but the intensity of the β relaxation was considerably smaller.

4.1.2.2. Polypropylene (*i*-PP)

Several techniques have been developed to produce high-modulus, high strength *i*-PP fibers. First, quenching of the as-spun fiber could yield a pseudo-hexagonal or smectic ordered structure. If these fibers were then drawn at slow rates to high draw ratios at 130 - 135°C, the fibers with very high modulus could be obtained [86,87]. Second, a special two-stage drawing process at controlled temperatures was invented [88]. In addition, zone annealing was also proposed to be an effective processing method [89].

i-PP is a semi-crystalline material, with a T_g of -14°C [90]. The T_m^0 of *i*-PP was reported in the range of 187.5 to 220°C depending on different extrapolations methods using various metastable crystals [91-95,51]. The heat of fusion of 100% crystalline *i*-PP, was estimated to be 165 J/g.

Samuels reported several detailed structural investigations of *i*-PP fibers [93,94,96,97]. He compared the melting behavior of the as-spun *i*-PP fibers to that of drawn and annealed fibers (draw ratios between 1.4 and 4.5), shown in Fig. 17. Three parameters were used to describe the structural changes of the fibers: crystallinity (X), the average orientation of the chains in the crystalline phase (f_x), and the average orientation of the chain in the amorphous phase (f_{AM}). The melting diagrams were recorded in constrained measurements, and two melting peaks were obtained for the most drawn and annealed fibers. The temperature of the higher-melting peak (T_{2m}) exhibited a linear dependence on amorphous orientation in the fiber, but did not depend on the crystalline orientation. The minimum amorphous orientation for the T_{2m} to appear was $f_{AM} = 0.4$. When T_{2m} was extrapolated to $f_{AM} = 1.0$ (in this case, all the non-crystalline chains would be aligned parallel to the fiber axis), a value of 220°C was obtained, which is the T_m^0 of the α -crystal form of *i*-PP according to some

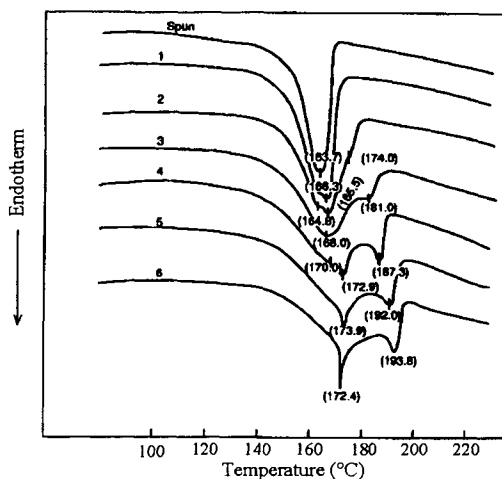


Fig. 17. Melting curves of polypropylene fibers drawn to different ratios at 90°C
 Draw ratio: (1)1.39, (2)1.84, (3)2.29, (4)2.7, (5)3.21, (6)3.58 [93]

reports [91]. The temperature of the lower-temperature melting peak (T_{lm}) also only dependent on the amorphous orientation, and this peak could be extrapolated to generate a T_m^0 of 185°C in the case of fully oriented non-crystalline chains ($f_{AM} = 1.0$). No explanation was provided with regard to the origin of the T_{lm} . It was suggested that the multiple melting peaks of the fiber samples were related to similar crystal-melting phenomena in isothermally crystallized samples, but extended to higher melt temperatures by the restrained amorphous chains. Also, 170°C was obtained in these experiments as the T_m^0 of the β crystal form (pseudo-hexagonal) of *i*-PP.

Jaffe studied the melting and crystallization behaviors of as-spun *i*-PP fibers [98]. Rate-dependent melting experiments indicated that the T_m of fibers increased with decreasing heating rate, implying recrystallization during melting. From the time dependency of the melting of *i*-PP fibers spun at various stress levels, it was concluded that high-stress spun fibers contained two crystalline morphologies, fibrillar and lamellar morphologies. However, no truly extended-chain crystal structure was present in the fibers. The melted fibers were crystallized again isothermally to provide insight into the structure of possible nucleating fibrils. The as-spun fibers were heated to a temperature (T_i) between 170 and 230°C, and cooled to the fixed crystallization temperature of 130°C. The sample with high-stress extrusion crystallized considerably faster than the sample without this history, meaning that the row and the spherulitic morphologies of the starting samples were retained. The crystallization process slowed down with increasing the T_i , implying that with increasing T_i the crystal nuclei were being continuously destroyed. Polarization optical microscopy

indicated that as T_i was increased, the morphology observed on crystallization varied from row to mixed spherulite morphology.

A DMA curve of hard elastic *i*-PP fibers was reported [99]. The E' decreased gradually from -130 to -40°C, and no dissipation was observed on the E'' in this temperature region. In the temperature range of -40 to ~ 0°C, there was a sudden drop in the E' of the fiber, and a clear absorption peak in the E'' could also be found, corresponding to the T_g of *i*-PP (the β transition). The high-temperature α relaxation of *i*-PP fiber was observed at 50 - 100°C, and it was attributed to lamellar surface or interlamellar interaction [100]. However, this was not described in the work of Zhu *et al.* The γ transition of *i*-PP fiber was extremely broad with a maximum at ~ -60°C.

Dynamic mechanical behavior of zone-annealed *i*-PP fibers was studied [89]. The E' was increased three-fold as a result of multi-step zone drawing and zone annealing. These authors could not observe any low-temperature dissipation peak. The T_g was recorded at 8°C, and a high-temperature relaxation at 80°C was also found. The multi-step zone-drawn and zone-annealed *i*-PP fibers had the highest-intensity α -relaxation peak. The peak temperature of the α relaxation also possesses the highest temperature for this sample. No clear explanation was given of the origin of the α relaxation.

The effect of heat treatment on the degradation kinetics of *i*-PP was investigated [101], and showed that those treatments caused the observed activation energy of degradation to increase (precursor, 221 kJ/mol; steam treated at 125°C for 30 min, 308 kJ/mol; dry heated at 160°C for 40 s, 229 kJ/mol). The shrinkage force behavior of as-spun *i*-PP fiber as a function of spinning speed was reviewed [102]. A special TMA instrument, the "flexible thermo-mechanical analyzer" (FTMA), was used to measure the absolute bonding strength of *i*-PP and copolyester fibers [103]. These measurements confirmed that *i*-PP fiber normally bonds better than copolyester fibers.

DTA results also showed that wear causes structural degradation of *i*-PP fabrics, as evidenced by loss of crystallinity and reduction of melting point [104].

4.1.3. Polyacrylonitrile (PAN)

Because PAN fibers feel wool-like, the largest application is in knitted textiles. The tensile properties of acrylic fibers are low (2.7 - 3.6 cN/dtex tenacity) and, like nylon, they are quite sensitive to moisture content. Acrylics have excellent resistance to sunlight and good resistance to various chemicals. Their flame retardancy is reasonably good and is improved significantly by incorporating vinyl halogens as comonomers into the polymer chains. PAN fiber is one of the most important precursors for graphite fiber production. It is also used as asbestos replacement and as moisture-absorbent synthetic paper. PAN fiber is generally prepared by wet spinning (most often from solutions in

dimethylformamide, dimethylacetamide, or dimethyl sulfoxide, both wet and dry spinning), followed by drawing and usually, texturing. Commercial PAN fibers are almost always made of copolymers of acrylonitrile (AN) with 5-10% methyl acrylate or vinyl acetate in order to improve dyeing properties and increase solubility. These copolymers may also contain vinyl halogen comonomers (vinyl bromide, vinyl chloride, or vinylidene chloride) to make the fibers flame-retardant [105]. The addition of these comonomers results in a decrease in the T_m and crystallinity.

The T_m^0 of PAN cannot be directly determined because the polymer degrades at temperatures below its T_m . The extrapolation of the T_m of PAN gels to the inciting point of pure PAN gave $T_m^0 = 317^\circ\text{C}$ [106]. Slade obtained $T_m^0 = 322^\circ\text{C}$ [107] using extrapolations of T_m of copolymers of acrylonitrile with vinyl acetate, and other authors obtained similar values. However, the heat of fusion of 100% crystalline PAN could not be determined with these extrapolations because the calculated values seem to depend on the comonomer used. The value ranges from 45 to 100 J/g. The copolymer extrapolation method for determining ΔH_f^0 of polymers assumes that the comonomer units are excluded from the crystals of the polymers of the primary monomer. However, the different copolymers reported were vastly different in chemical structures and this leads to partial incorporations of some comonomers into the crystals.

A peculiar DSC technique was developed to use water to achieve a maximum depression of the T_m of PAN and its copolymers [108-110]. The reciprocal T_m of the copolymer systems used (AN with vinyl acetate, ethyl vinyl ether and vinyl chloride) depends linearly on the comonomer molar fraction. Furthermore, the slopes of the curves for the wet and dry copolymers were found to be identical; the absolute value of the slope increased with increasing size of the comonomer. This phenomenon made it possible to calculate T_m of the dry polymer on the basis of T_m of the wet polymer. Using this technique, Frushour

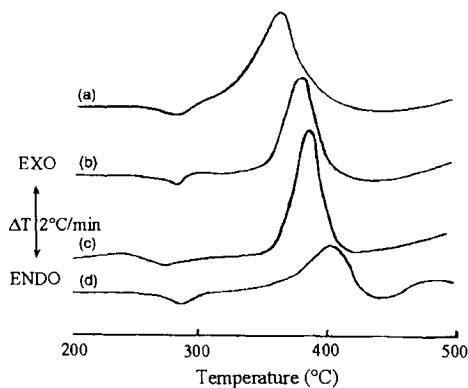


Fig. 18. DSC diagram of various acrylic fibers showing the melting region: (a) Orlon, (b) Cashmilion, (c) Creelan 61B, (d) Acrilan 16 [111]

calculated the T_m of different terpolymers and tetrapolymers with a high degree of accuracy (Fig. 18). He determined a value of 344°C as T_m^0 of the PAN homopolymer. Fast-heating-rate DTA experiments could be directly used to characterize commercial acrylic fibers [111].

The T_g of PAN was identified to be between 85 and 140°C, depending on the thermal analysis techniques used, but a great deal of confusion still exists in literature concerning the T_g of PAN. DSC and TMA measurements usually yield T_g in the region of 85 - 95°C, although dilatometry method provided the evidence of T_g to be equal to 104°C [106]. On the other hand, DMA and DEA give higher T_g values (105 - 140°C). Bohn *et al.* (1961) found a break in the slope of the thermal expansion versus temperature plot at 85°C, but they also recorded a change in the slope of the WAXD d -spacing versus temperature plot at ~ 90°C [112]. It is quite difficult to explain this phenomenon on the basis of the traditional two-phase model of semi-crystalline polymers, in which the T_g in the amorphous phase should not be affected by the crystalline phase. Also, the WAXD pattern of this polymer lacked a definite amorphous halo. It was suggested that this polymer might be a 100% laterally ordered material. Therefore, the transition at 85 - 90°C was interpreted as a pseudo-glass transition of the laterally bonded ordered structure. A "doubly bonded single phase" was proposed in the solid-state structure of PAN, and this phase as glassy, possessed some degree of orientation and molecular packing might be present [113].

It is particularly important to understand how the T_g of PAN is influenced by different comonomers and water content. Howard measured the T_g of a series of copolymers of AN with vinyl acetate (VAc) [114]. When the VAc content was varied between 0 and 27%, T_g was constant at 87°C (this is the T_g of pure PAN). At higher VAc levels (beyond 27%), the reciprocal of the T_g changed linearly with the VAc content, and extrapolation to 0% VAc content using the Fox and Lashaek equation gave 110°C as a T_g of the PAN homopolymer. This observation was attributed to the effect of the crystalline phase on the amorphous phase. It was suggested that the crystallinity of PAN decreases drastically with increasing VAc content. In agreement with this suggestion, Frushour and Knorr found that the heat capacity jump at the T_g , and thus, the amorphous content, increases sharply with increasing VAc content [105]. Since water strongly plasticizes PAN, the T_g of a copolymer with 7% VAc content drops 36°C under the influence of water. There is extensive literature on the dynamic mechanical properties of PAN fibers, but the data are often controversial. Even the designation of relaxation processes is inconsistent [115-120]. Two transitions were generally known at that time: the β transition at 70°C, and the α_a transition at 110°C (the subscript "a" stands for amorphous; thus, this is the glass transition), with activation energies of 84 and 209 kJ/mol, respectively.

A special PAN fiber sample was prepared by wet spinning and drawing in water to the ratio of 4 - 16 at various temperatures [117]. This sample was then air-dried and steam treated at 90 - 180°C at a constant length. The steam-treated filament exhibited a new relaxation at 160°C with $E_a = 398$ kJ/mol. The changes in the intensity of this new relaxation peak were parallel to changes in the WAXD pattern intensity. This new relaxation (designated as α_x) was thus assigned to some unidentified motion in the crystalline phase. Minami found three relaxation processes [118] (measurements performed at 110Hz): two α peaks (α_a at 160°C and α_x at 110°C) and a third peak at 280°C (see Fig. 19). The highest-temperature peak was attributed to chemical reactions (cyclization, cross-linking or degradation). On the basis of the change of the intensity of this peak with the draw ratio, Minami attributed the lower-temperature α transition to molecular motion in the para-crystalline region, and the higher-temperature α relaxation to the glass transition. Fig. 20 shows the dependence of the mechanical loss factor $\tan\delta$ on temperature for PAN fibers of different draw ratios. As can be seen, the intensity of the higher-temperature α relaxation decreases with increasing the draw ratio, and thus with increasing the degree of orientation. This seems to support the assignment that this relaxation is attributed to the glass transition of PAN. He also investigated amorphous PAN, and the sample had only one transition at $\sim 165^\circ\text{C}$ (glass transition). The α_I and α_{II} relaxations were also reported at 110 and 165°C [121]. To increase the complexity regarding the relaxations in PAN, two relaxation peaks for the homopolymer PAN at 110 and 280°C (measurements at 110 Hz) was identified by DMA [119]. It is clear that the 280°C peak originates from some kind of

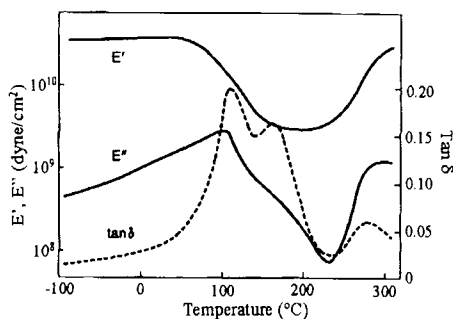


Fig. 19. Dynamic tensile storage and loss moduli as well as loss tangent for undrawn PAN fiber [118]

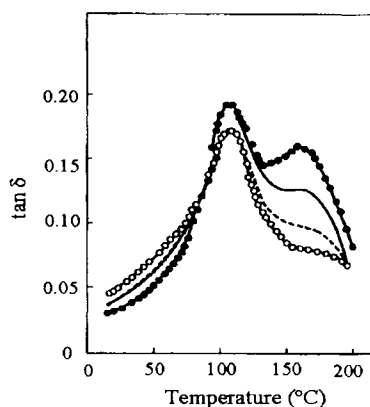


Fig. 20. Loss tangent as a function of temperature for drawn PAN fibers [118]

chemical reactions (e.g., cyclization). When AN was copolymerized with acrylic acid and vinyl pyrrolidone and the comonomer content was increased, the 110°C relaxation peak diminished and another relaxation peak appeared at 160°C with increased intensity. Therefore, the question of the T_g of PAN has not been resolved. Ko and coworkers also recorded two relaxation peaks on the $\tan\delta$ versus temperature plots, and they were at 125°C and 254°C [120].

Applied tension would affect on shrinkage and the shrinkage stress of acrylonitrile copolymer fibers a lot, this was verified by a specially designed TMA method [122,123]. This technique provided the thermal relaxation of the stress and strain, and calculated the activation energy of the entropic retraction. SDSC was also used to investigate different structures existing in PAN fibers. The results obtained were useful for improving the annealing processes of acrylic fibers. The concept of the shrinkage modulus was in the first time introduced in those works.

Two glass transitions for PAN fibers were found [124]. It was also noted that the fibers behave differently in the presence of solvents. A linear relationship between the E'' and the dye diffusion constant was established in PAN copolymers system (the comonomer was VAc) [116]. Since a similar relationship was found for nylon 66 [75], this indicates that the dependence of the dye diffusion on the chain mobility of polymers may be a general phenomenon.

Mathur *et al.* studied the shrinkage behavior and weight loss of PAN precursors used for preparing carbon fibers and discussed the implication of PAN fiber shrinkage on carbon fiber formation [125]. The TGA method was get used to identify the commercial acrylic fibers based on their differing weight loss patterns [126], this method was really efficient. TGA, DTA, and thermal volatilization analysis were used to investigate the thermal degradation of PAN [127]. A sharp exothermic peak recorded at 300°C was attributed to the cyclization process of nitrile groups. During air pyrolysis, this exotherm shifted to higher temperatures. It could be removed by isothermal aging below 200°C. It was noticed that the aforementioned exotherm shifted to higher temperatures with increasing comonomer (methyl acrylate) content because of the inhibiting the cyclization by the presence of comonomer [128]. DTA and TGA were employed by several authors in studying the mechanism and kinetics of acrylic degradation [129-131]. Factors such as comonomer content, spinning method, and additives as well as fiber spinning conditions such as heating rate, atmosphere, and sample size, were investigated. The results indicated that the fibers are extremely sensitive to the oxygen concentration, the surface-to-mass ratio, and additives or other chemical species present in the fibers.

The oxidative stabilization process (pre-oxidation), which transforms PAN fiber into a structure capable of maintaining its integrity at high temperatures

(1000 - 3000°C) necessary for carbon fiber production, is exceedingly complex. Concurrent phenomena taking place include, as mentioned earlier, cyclization of the PAN structure, a decrease in the number of nitrile groups, and increased conjugation due to the CN bond formation (manifest in the fiber changing color from white to black). While heating the fiber, oxidative cross-linking, dehydrogenation of the cyclized structure, melting of the PAN crystalline domains and shrinkage of fiber length up to 30% were all observed. The rate and order at which these reaction took place was a function of atmosphere, comonomer content, temperature, applied stress, and original fiber structure. Among these studies, DTA, TGA, and TMA were applied to understand the stabilization mechanism [132-134]. The high-temperature shrinkage was considered to result from the compaction of PAN during cyclization to a ladder-like type structure. As oriented semi-crystalline polymers, the PAN chain molecules simultaneously undergo shrinkage with the crystals [135-137], and the correlation of high-temperature shrinkage rate maximum with melting temperature was shown [138]. It was speculated that, although chemical rearrangements are very important physical structure changes play a role.

4.1.4. Polyesters

4.1.4.1. Poly(ethylene terephthalate) (PET)

Commercial PET fibers are melt spun and can be drawn and heat-treated to generate a broad property range suitable for diverse end-use applications. In practice, fibers with draw ratios of 3:1 to 6:1 are generally used, depending on the purposes of the application. The drawing is carried out above the T_g (usually at 90 - 100°C) and often in two or three stages. The amount of moisture regained in PET is quite low (< 1%), rendering fiber properties essentially unaffected by moisture absorption except for at high temperatures, where hydrolytic degradation can be detrimental. The low moisture regain leads to comfort problems in apparel applications, and this deficiency could be overcome by blending textured staple with cotton. Other key properties of PET are high tensile (especially modulus) and shape permanence in textiles through annealing. Other applications of PET involve the carpet, curtain and upholstery industry, ropes, the paper industry, production of tents, and sutures and synthetic arterial replacements. One of the most important applications involves the tire cord fabrication.

The T_g of PET is at 79°C; its heat capacity increase at T_g is 77.8 J/(°Cmol) [50,95], and its T_m^0 has been determined by extrapolation to be 280°C [139-141]. The heat of fusion of the 100% crystalline polymer is ~ 140 J/g [51]. The non-equilibrium T_m of PET is usually at around 250 - 260°C. Several reviews on TA dedicated to PET fibers have been published [142-145]. The glass transition behavior of PET has been investigated [36]. Annealing below T_g leads to a

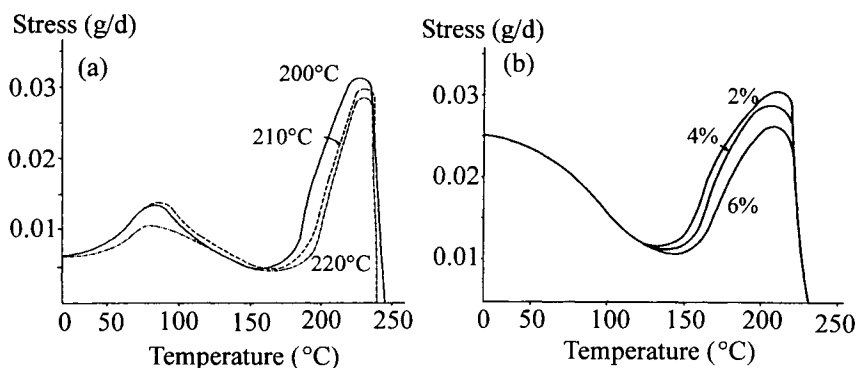


Fig. 21. TMA diagrams showing the effects of false-twist texturing variables on the resultant traces for polyester feed fiber: (a) effect of the first heater temperature; (b) effect of overfeed (relaxation) [102]

material that, upon annealing at elevated temperatures, PET was able to crystallize to generate a higher degree of crystallinity. Hagege, Halip and Vanicek studied T_g of partially oriented (PO) fibers [37], the effect of drawing on T_g [146], and the effect of comonomer content [147], respectively. They all agreed that T_g could be affected by fiber structure, morphology and fiber processing conditions.

Jeziorny compared crystallinity values of PET fibers as determined by DSC and WAXD methods and found a reasonable agreement between these two techniques [148]. The kinetics of cold crystallization of undrawn, unoriented fibers was investigated [149], and it was found that the process to be first-order between 100 and 115°C with an activation energy of 184 kJ/mol. Melt crystallization kinetics were studied, and double crystallization exotherms under a wide crystallization temperature region were observed [150,151]. It was ascribed that this observation was the formation of separate morphologies (folded chain and fringed micelles).

The effect of spinning conditions on the properties of PET PO fibers has been investigated by both DSC and TMA [152-155]. Spinning speed, melt drawdown and throughput, and molecular weight could affect on the structure, crystallinity, and chain orientation of PET PO fibers. A similar study of high-speed PET spinning utilizing DSC and TMA data was presented [155]. Warwick and Vevers investigated the shrinkage behavior of PET PO fibers [156], and Ikeda studied the crystallization kinetics of PET PO fibers [157]. The latter study concluded that shrinkage measurements are more sensitive than DSC for detecting the early stages of such rapid crystallization events. It was showed that increasing spun fiber orientation (birefringence) leads to a decrease in the observed peak temperature of cold crystallization (increased crystallization rate)

[158]. In a follow-up note, the cold crystallization peak temperature is dependent on heating rate for a specific PET fiber sample [159]. Fig. 21 showed the influence of spinning speed (orientation) on the shrinkage force of as-spun PET fibers. Fig. 21a was explained that the lower-temperature peak was attributed to molecular orientation and fiber age, and the higher-temperature peak was associated with increasing fiber crystallinity [102].

Smith and Stewart were the first to study the cold crystallization rate of isotropic and oriented PET fibers [160]. The fibers were kept at a constant length during heating; the crystallization was followed by density measurements. Shrinkage measurements were also made in boiling water. The crystallinity of the starting fibers was $\sim 8\%$. The cold crystallization peak of the samples moved to lower temperatures with increasing birefringence of the fibers, *i.e.*, with increasing take-up speed during filament spinning. The Avrami presentation of isothermal cold crystallization data showed a definite decrease of the Avrami exponent as birefringence increased, indicating the nucleating effect of orientation. Heuvel and Huisman provided an example of the change cold crystallization in the as-spun PET fibers detected in DSC as a function of spinning conditions, as show in Fig. 22 [161]. Increasing spinning speeds lead to an increase of molecular orientation in the spun fiber prior to solidification, which in turn, causes an increase of crystallization rates and crystallinity during the fiber spinning. The shift in cold crystallization temperature to lower

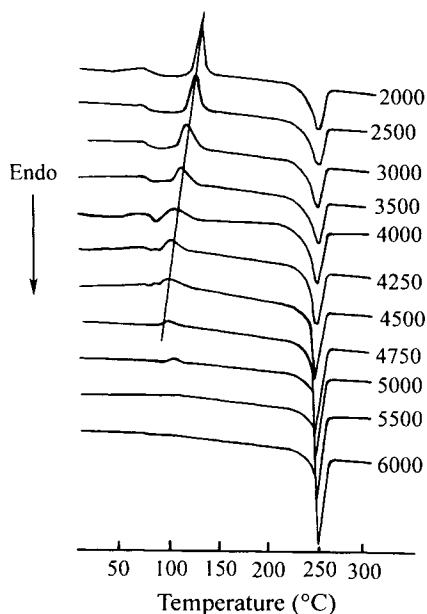


Fig. 22. DSC melting curves of as-spun PET fibers as a function of fiber wind-up speed [161]

temperatures was close to linear with increasing the orientation and could be used as a measure of spun-fiber orientation by correlating the cold crystallization peak temperature with an orientation parameter such as birefringence or sonic modulus.

A drop was observed in the CTE measured in the stretching direction as a function of increasing raw ratio of PET samples drawn at 7.5%/min at 75°C. These data, reported in 1961, were the earliest to show the CTE-orientation correlation in polymers [162]. During uniaxial drawing, the heat effects and structural changes occurred in amorphous PET [163], which could be monitored by calorimetry. A multiplicity of the structure-monitoring techniques such as density, birefringence, and infrared spectroscopy were used to follow the structural changes taking place during polyester drawing [164]. It was concluded that DTA was the most sensitive technique to small changes in chain orientation. With increasing draw ratios and draw temperatures up to 80°C, the exothermic peak temperature and the heat of the observed cold crystallization decreased, and the sum of the heats of fusion increased. The total analysis showed that increasing draw ratio reduced molecular motions, which drastically reduced chain mobility as stretches greater than 150%. The reduction of the temperature and that heat of cold crystallization as a function of increasing draw ratio (similar to the observations made on oriented spun fibers) was also reported [165,166]. Huh and Choi found multiple melting peaks in drawn PET fibers by DTA [167]. Different heating rate results illustrated that these peaks were originated by the rearrangements of unstable crystals. Shrinkage force spectra were used to evaluate the effect of draw texturing variables on the performance of the resulting crimped PET fibers [168]. TMA data was employed to elucidate the controlling factors of PET thread line stability during drawing [169]. The effects of increasing draw ratios and draw temperatures on the shrinkage force of PET fibers were also investigated [102,170]. Increasing amounts of stretch and decreasing draw temperature increased the shrinkage force levels observed. Higher draw temperatures shifted the shrinkage force peak maxima to higher temperature values, implying that a more thermally stable, oriented structure was being produced. Hassel used shrinkage force measurements to differentiate orientation and crystallinity of PET fibers [171]. Khanna and co-workers discussed the extension/shrinkage behavior of heat-treated PET fibers in morphological changes [67]. They found a linear relationship between the shrinkage onset temperatures of the fibers and the annealing temperatures, and they proposed a method to estimate the fiber orientation factor using DMA measurements. Rodriguez-Cabello and coworkers studied the shrinkage behavior of PET fibers during thermal annealing in an unconstrained condition [172].

The effects of molecular weight, extrusion temperature, wind-up speed, and annealing conditions on the T_g of undrawn PET fibers, and the effect of draw

ratios of hot-drawn PET fibers on their density, crystallinity, and T_g , were studied using mainly crystallinity measurements and DSC [173]. Changes in molecular weight, extrusion temperature, and cooling rate changed the T_g within 3°C, but it was raised from 75 to 114°C as a result of drawing and subsequent annealing. They noted a small change in the slope of the volume-temperature curve at 40 - 60°C and attributed this to a secondary transition of PET.

After the drawn crystalline PET fibers are produced, annealing processes are important to generate different end-use products. Thermal analysis techniques can be used to establish the effects of annealing and deformation with fiber structure, morphology and end-use performance. Annealing has been shown by many authors to result in pre-melt endotherms in the DSC observations [174-178,144,42]. The exact position of the endothermic peak depends on annealing time, temperature, stress, and media, as well as fiber spinning parameters. All these variables have been combined in the Krefeld group concept of T_{eff} [40,42,175]. It has similarly been shown that the temperature, deformation rate, and extent experienced by a fiber define the dimensional and structural stability of the resultant fibers as monitored by TMA [42,142,179-188]. These results have been utilized as a process diagnostic, to define aspects of fiber structures such as orientation and crystallinity, and to predict end-use performance characteristics as diverse as textile dyeing behavior [42,183], annealing effectiveness [42], and the fatigue behavior of tire cords [184].

Kunugi and coworkers compared the effectiveness of the zone-annealing method on PET with annealing under release, at fixed length, and under tension [185,186]. The zone-annealing method produced fibers with high modulus and strength. The T_m of 258°C was associated with melting of metastable crystals. DSC, DMA, optical microscopy, and IR measurements suggested that the superstructure of the zone-annealed fiber was mainly a fringed micelle structure made up of highly oriented crystals and extended amorphous chains.

It was studied that highly crystalline PET fibers could be prepared at low spinning speeds by altering the temperature profile of the fiber while it was still beyond T_g [187]. The effect of processing conditions and cold drawing on the cold crystallization and melting properties, as well as on the fiber structure and morphology, were investigated [188].

Warner compared the melting of PET in constrained and unconstrained conditions [189,190]. A smaller heat of fusion was observed when the fiber was constrained, while the cold crystallization temperature reached a minimum at some relatively low overall orientation. The effects of orientation on the crystallization of pre-oriented PET fibers were studied [191]. Comparison of DSC and IR results of PO fibers obtained at different wind-up speed and thus, having different levels of *trans*-conformation in the segments, indicated that

macromolecular segments in the trans conformation started to crystallize below T_g , (for crystallization of two metastable phases in PET [194]).

Thompson and Woods were the first to report measurements of dynamic E' and E'' on PET fibers of different degree of orientation and crystallinities [195]. The temperature of the primary relaxation was found to increase from 80 to 125°C with increasing crystallinity. At the same time, the apparent activation energy decreased from 762 kJ/mol to 406 kJ/mol. A second relaxation process was found at $\sim -40^\circ\text{C}$ with an activation energy of 71 kJ/mol. Kawaguchi reported results of DMA measurements on PET fibers of different crystallinities and draw ratios using a cantilever vibration method [196]. He found two relaxation processes: the α transition at $\sim 100^\circ\text{C}$, which was attributed to the glass transition of PET, and a β -relaxation process at $\sim -40^\circ\text{C}$ (local-mode relaxation). The temperature of the α transition increased with increasing crystallinity up to the crystallinity value of $\sim 30\%$ and then, decreased again. This phenomenon was attributed to crystal size changes with changing crystallinity [197], or due to changes in the number of crystallites [198]. The temperature of the α relaxation is always dependent on the draw ratio of the fiber, but the detailed analytical dependence is much more complex because the crystallinity dependence is superimposed with this [199]. The β relaxation in PET is a superposition of two (or three) processes, the hindered rotation of the methylene groups and the motion of the carbonyl groups associated with the *gauche*- and *trans*- conformations of the polymer chains [24,197,200,201]. Miller and Murayama investigated the effect of spinning speed on dynamic mechanical properties of PO and drawn PET fibers [202]. The E' of the PO fibers increased with increasing spinning speeds, and the crystallinity of these fibers also increased from 5 - 6% to $\sim 35\%$ with high amorphous orientation. The dynamic E' of the PET fibers increased with increasing draw ratios, as expected (Fig. 23a). The height of the $\tan\delta$ peak at the α relaxation correlated well with the amorphous orientation of the fibers, as can be seen in Fig. 23b. Samuels studied the shrinkage, tenacity, long spacing, and SAXS intensities of drawn and annealed PET fibers as a function of annealing temperature [203], using literature data [199,204,205] of other authors. He established a linear relationship between the peak temperature of the E'' and the orientation of the amorphous regions in the fibers. He stated that the structural property correlations of a polymer could only be achieved within one set of fair fabrication parameters. Dumbleton *et al.* demonstrated the usefulness of the DMA method for practical purposes, and they found that the E'' measured under dyeing conditions can be related to the dye diffusion constant D . They concluded that diffusion is controlled by segmental mobility [206]. Lawton and Murayama measured dynamic mechanical properties of PET fibers in the dry state and in dyeing liquid media (water and tetrachloroethylene) [207]. T_g of

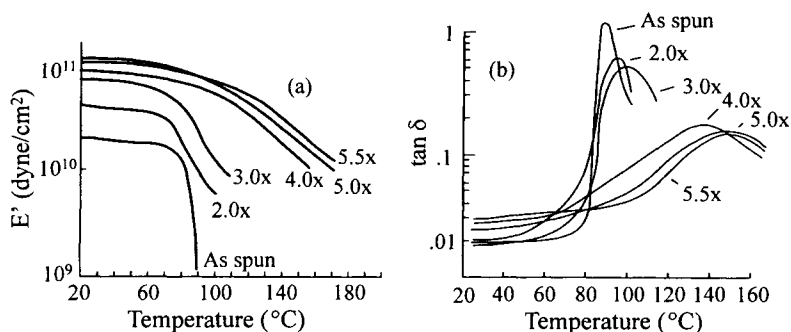


Fig. 23. (a) Dynamic storage modulus (E') and (b) loss tangent for PET flat fiber drawn to different ratios [202]

PET was significantly depressed in those dyeing media. A relationship was proposed between the viscoelastic properties of PET above T_g and the rate of disperse dyeing. De Araujo and Simal reported a DSC and DMA investigation of annealed PET fibers post-treated in benzoic acid solutions (benzoic acid is a carrier used to accelerate the dyeing process) [208]. It was suggested that a new (α_c) transition appeared at 140 - 160°C, indicating a new crystal relaxation process taking place due to the plasticizing effect of benzoic acid.

It is verified that annealing of PET fibers produces a small endothermic peak corresponding to that temperature [40]. As known today, an endotherm of this kind is not limited to fibers and can always be seen in the DSC melting diagram of semi-crystalline polymers in any physical form, *i.e.*, film, granules, *etc.*, and this phenomenon is often called the “double melting peak” [209].

TGA was employed to study the flame retardation of PET fabrics [210]. They investigated pyrolysis and gaseous combustion of PET fabrics containing

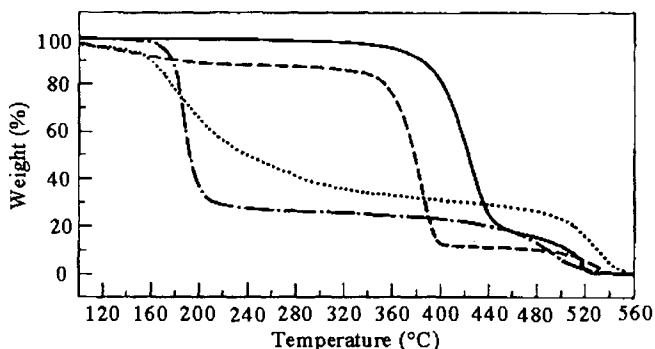


Fig. 24. TGA traces of PET fabric (—) compared to brominated polymers for flame retardation studies (---) poly(4-bromostyrene); (-·-·-) poly(vinyl bromide); and (.....) poly(vinylidene bromide) [210]

poly(4-bromostyrene), poly(vinyl bromide), and poly(vinylidene bromide). Thermal stability of the flame retardants is important when the interaction between them and the material being flame retarded is considered. Therefore, TGA diagrams of PET fibers and the other three bromo-containing polymers were recorded and are shown in Fig. 24. All the organic bromides used were found to release HBr during pyrolysis. In fact, some of them released HBr at temperatures too low for their potential applications as flame retardants.

Water vapor diffusion and absorption in textured polyester were studied by DSC and TGA [211]. By comparison of the observed behavior with that of the precursor fiber, a temporary surface modification occurred in the texturing process. TGA and DTA techniques were used to investigate the thermo-oxidative stability of polyester under conditions similar to that of fiber spinning [61,212]. The effects of copolymerization on the thermal stability of chemically modified PET fibers have been studied [213,214]. Using TGA and DSC techniques, it was found that the fiber melting and decomposition temperatures decreased as the comonomer content increased. The crimpability of poly(ethylene terephthalate-isophthalate) copolymers was investigated using both shrinkage and shrinkage-force measurements [215,216]. Selivansky and Lewin used several methods to characterize straining phenomena in PET PO fibers when the fibers were deformed above and below T_g (thermal retraction, density, DSC, and WAXD) [217]. They observed that strain-induced crystallization occurred both above and below T_g .

4.1.4.2. Poly(butylene terephthalate) (PBT)

PBT is an important engineering polymer. It crystallizes much more rapidly than PET, and this determines that the application as a molding resin is more expensive. Its crystallization can be easily controlled during processing. The advantages of PBT fibers lie in their resiliency and easy dyeability.

Illers determined 140 J/g as the heat of fusion of 100% crystalline PBT [218]. However, thermal analysis of PBT may sometimes be complicated by the known stress-induced crystal-to-crystal (α to β form) transition [219-221]. Cheng and co-workers (1988) estimated the T_m^0 of PBT to be 245°C and determined the T_g of efficiently quenched samples of amorphous PBT to be -25°C [222]. This is much lower than T_g of the semi-crystalline polymer (40 - 50°C).

Lu and Spruiell prepared melt-spun PBT fibers and studied the influence of the drawing and annealing conditions on the structural and mechanical properties [223]. Both α and β form crystals have triclinic unit cells, but different crystallographic dimensions along the chain axis directions, since the β form crystal possesses extended conformation of the four methylene unites. The amount of the β form crystal was found to increase with the draw ratio and was

directly proportional to the drawing stress at any given draw ratio. This strain-induced, reversible α - β crystal transition of PBT fibers was also studied using DSC under tension [224], WAXD, and IR spectroscopy. They found the zero heating rate T_m for the α (unstrained) crystals to be 225°C and 219°C for the β (strained) crystals. Melt-spun PBT fibers from polymers of different molecular weights were prepared [225]. Amorphous (glassy) fibers were produced at low spinning speeds and high cooling rates. The T_m increased with increasing take-up speed and the reduction of mass throughput during extrusion, indicating a change in the crystal size. The shrinkage of the fibers also increased with increasing take-up speed. The presence of the β form crystals in the fibers increased the shrinkage, as might have been expected. The online structural development during the melt-spinning of PBT was studied by IR microscopy and optical microscopy [226].

Ward and coworkers carried out a thorough investigation comparing mechanical properties and structures of PET, poly(trimethylene terephthalate), and PBT fibers and determined that the T_g of these fibers decreased with increasing numbers of methylene groups [221]. Schultze-Gebhardt studied the influence of different structures of PBT fibers on stress-strain characteristics of the fibers and recorded by the DMA [227]. Rong and Williams measured the dynamic mechanical properties of PBT monofilaments drawn at ratios of 3.9 and 4.2 [66] (Fig. 25). Two relaxations were recorded on the E'' and $\tan\delta$ versus

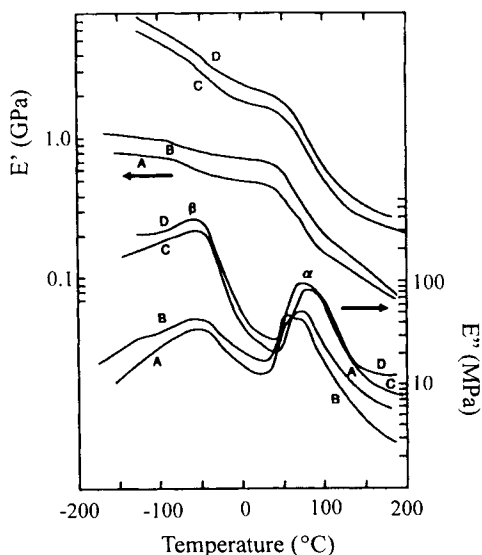


Fig. 25. Dynamic storage and dynamic loss moduli of PBT films and fibers as a function of temperature: A. quenched film control; B. slowly cooled film control; C. monofilament with draw ratio of 3.9; D. monofilament with draw ratio of 4.2 [66]

temperature diagram. The lower temperature relaxation peak, recorded at -50°C , increases in magnitude with increasing draw ratio but stays at a constant temperature after heat treatment or drawing. This relaxation was attributed to either restrictions in motion of the ester and/or methylene units or to a cooperative wagging and rocking motion of the phenylene rings. The higher-temperature relaxation is the glass transition. As expected, the peak magnitude decreases with decreasing cooling rate or with drawing, and it shifts to higher temperatures.

4.1.5. Poly(vinyl alcohol) (PVA)

PVA fiber is wet spun from concentrated aqueous solutions. The solution of PVA is coagulated in an aqueous solution of sodium sulfate or in an alkaline coagulating bath (sodium hydroxide). The resulting as-spun fiber cannot be washed with water, since it is water-soluble. It becomes insoluble in water after drawing because the fiber becomes partially crystalline. When the drawn PVA fiber is relaxed, it again becomes water-soluble. A dry spinning method can also be used to produce PVA fibers [228,229].

PVA fiber offers flame protection, resulting in many useful applications. PVA fibers are used in the textile industry as a general apparel fiber, making ropes, fishery materials, fire hoses, industrial heavy fabrics, reinforcing fibers, radial tire cords, *etc.*

The T_g of PVA in the literature is scattered around two values, 70°C and 85°C , respectively, which are probably dependent on the thermal history and water content of the samples. The T_m of PVA is $\sim 267^{\circ}\text{C}$, while isotactic PVA was reported to be 212°C [229]. No T_m^0 has been reported. When the T_m of PVA fibers is measured, it increases for constrained fibers from 237°C without tension to 245°C for the measurement at fixed length [229].

Gel spinning is a relative new spinning technique applicable to PVA. Stocks and Berghmans proposed a mechanism for thermo-reversible gelation of PVA [230], Cebe and Grubb were the first to describe gel drawing of PVA fibers, and the maximum draw ratio obtained was 20 [231]. They noticed that after the drawing, the melting peaks of the fibers became considerably narrower, and the T_m exhibited an increase of about 6.5°C when compared to the T_m of the gel. This was an indication of the more perfect crystals that were formed during the drawing. The crystallinity of the fibers was increased with the draw ratio and the drawing temperature. However, Gel-spun PVA fibers were more difficult to draw. This difficulty is ascribable to the existing hydrogen bonds between the main chains (this is why the T_m of PVA is much higher than that of PE). Ultra-high molecular weight PVA fibers are also gel spun [232]. Despite the low draw ratios (10 - 20), relatively high-modulus and high-strength fibers were obtained (75 GPa and 2.3 GPa, respectively). Garrett and Grubb demonstrated gel

drawing of PVA fibers at draw ratios up to 38, but these draw ratios could be achieved only at drawing temperatures close to the T_m of the gel (228°C) [233]. The relaxation of the polymer chains at such high temperatures resulted in insufficient chain extension, and therefore, the modulus was lower than that for PE and PP at similar draw ratios.

Dynamic mechanical properties of drawn, gel-spun PVA fibers were studied [234]. The T_g was dependent on the crystallinity of the fiber samples (T_g was between 45 and 85°C). A strong crystalline relaxation (α relaxation) was found, above which the segments in the crystalline phase possesses some mobility despite the hydrogen bonding. The authors attributed the cause of this α relaxation to the possibility that gel drawing of PVA. They suggested that other polymers with strong hydrogen bonding couldn't be gel drawn to high ratios because they lack the crystalline relaxation. The temperature of this α relaxation increased with the draw ratio. For the isotropic gel, the $T_\alpha = 160^\circ\text{C}$, while at $\lambda = 19$, $T_\alpha = 120^\circ\text{C}$. At draw ratios higher than 19, this relaxation could not be identified. Although no simple model could be developed to explain this relaxation phenomenon, it was evident that the disappearance of the α relaxation with increasing draw ratio must have had drastic influences on the gel drawing of PVA fibers. The T_m of the crystals also increases with the draw ratio, but this increase was much slower than that of T_α , thus narrowing the temperature range where this mobility was in effect. Other methods for fiber spinning (such as solution spinning) and annealing process (such as zone-drawing) had also been reported to improve fibers' mechanical properties [235,236].

5. HIGH PERFORMANCE FIBERS

With rapid development of advanced materials, fiber material scientists have projected a steady increase in the demand for high performance fibers. Since the 1970s, many new aromatic polymer fibers have been developed based on several technological discoveries. These include the inventions of lyotropic and thermotropic liquid crystal polymers and ultra-high molecular weight polymer. Most of the fibers are produced via dry-jet wet or gel spinning methods. All of these fibers are specialty products aimed in certain areas of industrial, military and aerospace applications, which require specific high performance characteristics. Compared with conventional textile fibers, high-performance fibers have excellent mechanical properties, thermal stability, and other features, such as chemical resistance, electrical properties, or unique biological response behaviors. They can be divided into the inorganic fibers and organic polymer fibers. The representatives of the inorganic fibers are carbon, boron, silicon carbide (SiC), high strength glass, alumina (Al_2O_3), aluminum-titanium alloy fibers, which are not further discussed here. The high performance organic

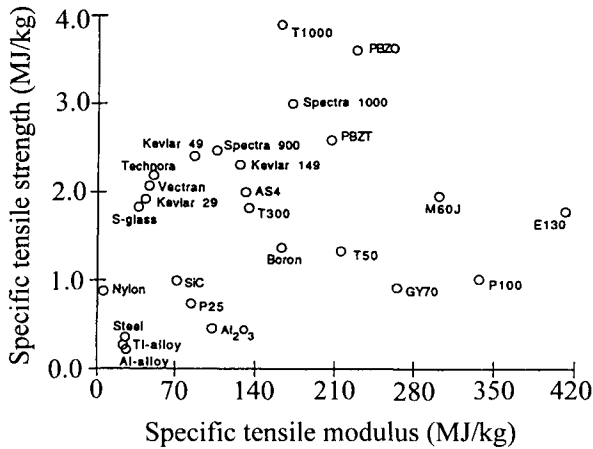


Fig. 26. Specific tensile strength and specific tensile modulus of various fibers

polymer fibers include aromatic polyamide fibers such as poly(*p*-phenylene terephthalamide) (PPTA), aromatic polyesters such as polyester-polyacrylate fiber, aromatic heterocyclic polymer fibers, such as poly(*p*-phenylene benzobisthiazole) (PBZT) and poly(*p*-phenylene benzobisoxazole) (PBZO), aromatic polyimide polymer fibers, and ultra-high molecular weight fibers. High-performance organic fibers possess lower densities than those of inorganic fibers. However, the high-performance inorganic fibers have higher compressive strengths and a higher maximum use temperature.

The mechanical properties of high-performance fibers significantly exceed those of conventional textile fibers, such as nylon and PET, especially when comparison is based on the specific properties, such as specific strength and specific modulus as shown in Fig. 26. A summary of mechanical performance of those fibers is shown in Table 12. Table 13 provides the information of the high-performance fibers produced in the United States [237,238].

5.1. Aromatic polyamide fibers

As a class of aromatic polymer, to distinguish them from aliphatic polymers, examples are poly(*m*-phenylene isophthalamide), known as Nomex[®] from DuPont, poly(*p*-benzamide), called Fiber B (DuPont), polyamide hydrazide, X-500 studied by Monsanto in the early 1970s, and poly(*p*-phenylene terephthalamide) (PPTA), and DuPont's Kevlar[®] fibers. We focus on the first commercial and the most successful aramid fiber Kevlar[®] (PPTA) fibers.

PPTA is synthesized by the condensation polymerization of terephthaloyl chloride ($\text{ClCO-C}_6\text{H}_4\text{-COCl}$) and *p*-phenylene diamine ($\text{H}_2\text{N-C}_6\text{H}_4\text{-NH}_2$). *N*-methyl pyrrolidone (NMP) and dimethylacetamide (DMAc) are used as solvents. They are used often in the presence of an inorganic salt such as lithium chloride or calcium chloride. The chemical reaction is normally carried out at a low

temperature (preferably at 10 - 20°C) to avoid degradation and side reactions. The degree of polymerization (DP) of PPTA is relatively low, with a MW in the range of 17,000 – 63,000 g/mol.

Table 12
Properties of Fibers

Materials (fibers)	Density (g/cm ³)	Tensile strength (GPa)	Tensile modulus (GPa)	Compressive strength (GPa)	Maximum use temperature (°C)
Steel	7.8	2.8	200	–	500
Al alloy	2.7	0.6	71	–	–
Ti alloy	4.5	1.2	106	–	–
Alumina	3.7	1.7	350-380	6.9	1200
Boron	2.5-2.6	3.5	415	5.9	2000
SiC	2.8	2.8	200	3.1	1300
S-glass	2.46	4.5	90	>1.1	300
E-glass	2.58	3.4	76	4.2	350
Pitch-based					
carbon P100	2.15	2.2	725	0.48	600
PAN-based					
M60J	1.94	3.8	585	1.67	600
Kevlar 49	1.45	3.5	125	0.39-0.48	250
Kevlar 149	1.47	3.4	185	0.32-0.46	250
PBZT	1.58	4.1	325	0.26-0.41	350
PBZO	1.56-1.58	6.0	360	0.2-0.4	350
Spectra 1000	1.0	3	172	0.17	100
Vectra	1.4	2.9	65	–	150
Technora	1.39	3.04	70	–	250
PIF	1.45	3	110	0.6	350
Nylon	1.14	1.0	6	0.1	150
PET	1.39	1.16	12.2	0.09	150

Table 13
High-performance fibers produced in the United States [3]

Fiber type	Producer	trademark	End uses
Aramid	DuPont	Nomex [®]	Thermal protective apparel, electrical insulation, filter
Aramid	DuPont	Kevlar [®]	Protective apparel, armor, composites, rubber goods, ropes and cables, asbestos replacement
Polyester	Hoechst Celanese	Vectra [®]	Thermoplastic composites
Polybenzimidazole	Hoechst Celanese	PBI	Protective apparel
Heterocyclic	Toyobo	PBO, ABPBO	Composites, military
Polyethylene	Honiwell	Spectra [®]	Armor, ropes, composites
Bicomponent	Avtex	ES	Nonwoven fabrics
PAN based carbon fibers	Hysol-Grafil BASF	Mananite [®] Celilon [®]	Composites Composites
Pitch based carbon fibers	BP/Amoco Ashland	Thornel [®] Carboflex [®]	Composites Composites
Boron	Avco		Aerospace structures
SiC	Avco		Metal matrices
Al ₂ O ₃ -B ₂ O ₃ -SiO ₂	3M	Nextel [®]	Ceramic reinforcement
Glass	Owens-Corning	Fiberglass [®]	Composites, armor
PPS*	Phillips	Ryton [®]	Chemical-resistant filtration

* PPS = Poly(phenylene sulfide)

The PPTA polymer is soluble in strong acids such as concentrated sulfuric acid, chloro- and fluorosulfonic acid, nitric acid and hydrogen chloride. Kwolek discovered that PPTA/H₂SO₄ solution is isotropic at polymer concentrations below 12%. When the polymer concentration is increased above 12%, PPTA molecules pack closer together and the polymer molecules are oriented the form liquid crystal polydomain. The solution becomes liquid crystalline at about 20%. This is called lyotropic liquid crystal, *i.e.* the liquid crystal behavior appears in more than one component system [239,240]. Fig. 27 shows the schematic structure of the molecules at different concentrations.

Fig. 28 presents a correlation of bulk viscosity of PPTA/H₂SO₄ solution versus PPTA concentration [241]. In dilute concentration region (< 12%), the

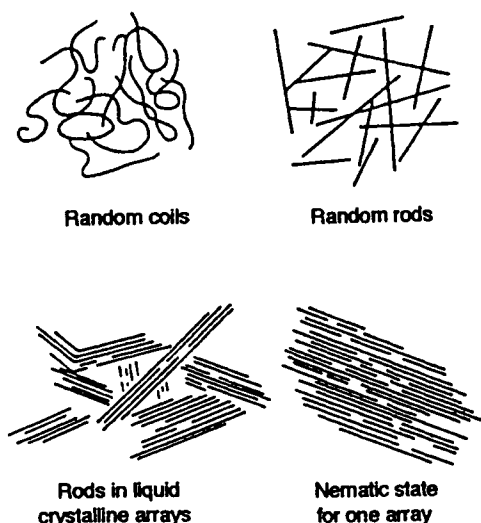


Fig. 27. Schematic diagram different molecular packing of PPTA/H₂SO₄ solution [239]

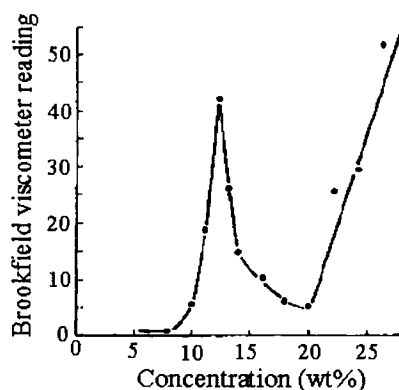


Fig. 28. Viscosity changes of lyotropic liquid crystal (PPTA/H₂SO₄ solution) as a function of concentration [241]

solution viscosity increases sharply with increasing polymer concentration. Above 12%, the solution viscosity decreases with increasing concentration due to the onset of solution anisotropy. Above 19%, the solution viscosity increases again because of increasingly tighter polymer packing. As conventional polymers, the solution viscosity is also affected by the polymer molecular weight and temperature.

Blades invented an ingenious dry-jet wet spinning process for spinning an anisotropic solution of aramid polymers to produce fibers by coagulating the fiber in water [242,243]. The as-spun fiber is heat treated at temperatures above 300°C under tension to substantially increase its tensile strength and modulus. When an anisotropic solution is extruded through a spinneret capillary, the capillary shear causes the liquid crystalline domains near the wall to align along the direction of flow. At the capillary exit, some disorientation of liquid crystalline domains occurs because of solution viscoelasticity. However, the disorientation is quickly overcome under spinning tension in the air gap. This gives rise to a highly crystalline, highly oriented fiber structure.

Thermal behavior of PPTA fibers was studied by DTA, TGA, and TMA [244,245]. In the TGA experiments, the polymer was stable up to 460°C (2°C/min heating rate in a nitrogen atmosphere). DSC measurements confirmed the thermal and thermo-oxidative stability of the fiber. The effect of absorbed water was observed in both DSC and TGA measurements. TMA measurements revealed a change in the slope of the dimensions versus temperature curves at

115°C that disappeared upon reheating. This was attributed to water release. More pronounced slope change was recorded between 325°C and 425°C, which was linked to a relaxation associated with the hot drawing of the fibers. Chaudhuri and co-workers compared the basic thermal properties of wholly aromatic polyamides, including PPTA [246]. Poulaert and coworkers studied the temperature variation of thermal conductivity of Kevlar® and compared it to that of PE and trans-polyacetylene [247]. Jaffe and Jones characterized PPTA fibers using a variety of thermal techniques (Fig. 29) [248].

Haraguchi reported their dynamic mechanical analysis of PPTA fibers [249]. Two major relaxation regions were distinguished on the $\tan\delta$ versus temperature DMA diagram (labeled by β and β^* , having peak temperatures at 0°C and 250°C). The β -dissipation region was resolved into three relaxations processes. The authors suggested that the β relaxation be attributed to molecular motion in the amorphous regions, whereas the β^* relaxation was attributed to motion in the crystalline regions. Kunugi and coworkers studied dynamic mechanical properties of low-crystallinity and low-orientation PPTA fibers

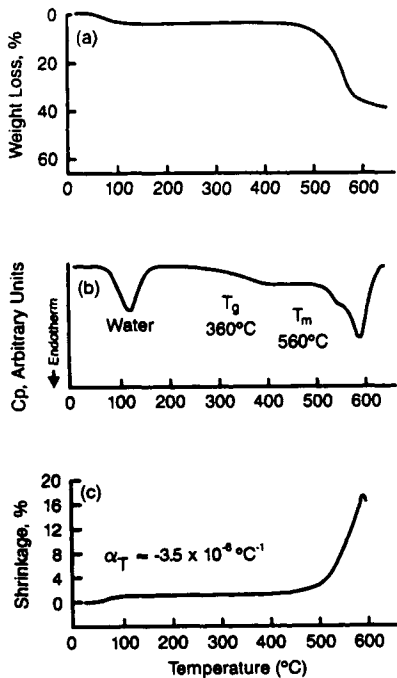


Fig. 29. Different thermal analysis methods of PPTA fibers: (a) TGA diagram, (b) DSC diagram, (c) TMA diagram [248]

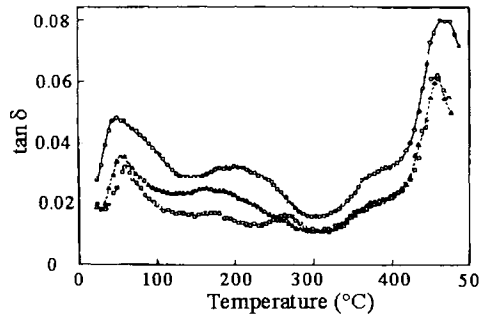


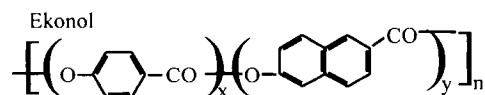
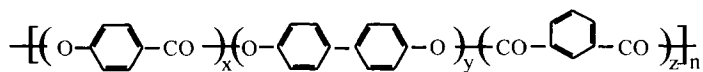
Fig. 30. Loss tangent of PPTA fibers as a function of temperature: (open circles) as spun fiber with low crystallinity and low orientation spun from an isotropic dope; (open triangles) fiber annealed at 200°C; (open square) fibers annealed at 300°C [250]

[250]. These fibers were spun from an isotropic dope (DuPont's PPTA fiber is spun from an anisotropic dope) to increase the effect of the amorphous regions of the transitions. Five relaxation processes were observed at 460°C (α), 270°C and 170°C (observed in annealed samples), 60°C (β) and -30°C (γ). The E' modulus increased with increasing annealing temperature. For a given sample, the E' drastically decreased at high temperature ($\sim 400^\circ\text{C}$). Two major dispersions were recorded, a relaxation at 460°C and the β relaxation at 60°C (Fig. 30). The activation energy of the α relaxation was 766 kJ/mol, considerably higher than that for relaxations of other crystalline polymers. The authors concluded that the high activation energy of the relaxation was a consequence of the difficulty of moving the rigid chains. The origins of the 170°C and 270°C peaks were not clear. The 60°C dissipation peak (β) was assigned to the motion of amide groups in the amorphous regions, since its intensity drastically decreases when the moisture content of the fibers is removed. The -30°C dissipation peak (γ) was assigned as a local-mode relaxation due to some internal rotations.

Typically, PPTA (Kevlar[®]) fibers show high melting temperatures higher than 530°C, zero strength temperature at about 640°C, high T_g s higher than 375°C, which ensure the relatively high thermal stability. They also possess low combustibility, low density (1.44 - 1.45 g/cm³).

5.2. Aromatic Polyester Fibers

Since the late 1970s, many aromatic copolyesters have been synthesized, incorporating *para*-oriented mesogenic aromatic dioxy, oxycarboxyl and dicarboxyl segments. One attractive feature of these polymers is that they can form liquid crystalline phases over a wide temperature range without solvents (thermotropic liquid crystalline behavior). As a result, they can be spun using conventional melt-spinning techniques to achieve high performance properties, resulting in a more cost-effective solution than solution spinning. The polymeric chains of the thermotropic liquid crystalline polymers become oriented during melt spinning, and the long relaxation times characteristic of these polymers prevent chain disorientation during cooling. Two of them have been commercialized in the past few years: Ekonol[®] and Vectra[®]



Vectra

The spinning and annealing conditions are very critical to the fiber formation and ultimate fiber properties. The temperature of melt spinning must be above the crystal-to-liquid crystal (usually nematic) transition temperature to guarantee formation of the liquid crystalline phase. The higher the processing temperature, the faster the melt degrades; the lower the temperature, the higher the melt viscosity and the poorer the processing. Because of the viscosity problem, the upper limit of the molecular weight for the melt spinning of the thermotropic liquid crystal polymers is relatively low, resulting in lower fiber tensile strength. However, the possibility of these fibers undergoing a solid state polymerization during the annealing can lead to a significant increase in the molecular weight, and thus the tensile properties. This process thus requires much longer heat-treatment times than conventional fibers.

Compared with the solution spinning of lyotropic liquid crystal polymers, melt spinning of thermotropic liquid crystal polymers do not need solvent disposal and thus, no recycling problems exist. It is easy to obtain small diameter fibers, and less problems caused by the outer layer of the fibers, the "skin", and the center or the "core".

Kuhfuss and Jackson recognized that copolymers of *p*-oxybenzoate and ethylene terephthalate (POB/PET) are liquid crystalline beyond 35 (mol)% POB content [251,252]. Copolyesters containing 60 and 80 (mol)% POB became the first commercially available thermotropic liquid crystal polymers because the POB/PET copolymers of these compositions exhibited the maximum flexural modulus, tensile strength, and notched Izod impact strength on the properties versus composition relationships.

A series of high molecular weight main-chain liquid crystalline copolyesters were investigated in detail [219,253-255] in the whole compositions of PET and *p*-hydroxybenzoic acid (HBA). The mechanical properties of injection-molded pieces of these copolyesters with 40 - 90% oxybenzoate unit content were anisotropic. It is noteworthy that at lower shear rates the polymer became shear sensitive as the HBA content increased. A minimum was observed in the melt viscosity versus composition dependence at ~ 60 - 80 (mol)% of HBA. Menczel and Wunderlich studied the 60/40 mole ratio (POB/PET) by DSC, observing two T_g s for this copolymer [256]. In accordance with the DSC results, polarization optical microscopy observations indicated the presence of two separate birefringent phases, indicating a microphase separation. A minor amount of three-dimensional oxybenzoate-type crystallinity was also found (T_m at ~ 250°C). This phase separation was verified later [257,258,259,260]. The phase diagrams of the POB/PET copolymer system were studied [261]. Two glass transitions were found for the POB concentration range in which the copolyesters exhibited a nematic phase, and the glass transition temperatures were practically independent of the composition of a given copolymer. The T_g of the PET-rich phase was close to the T_g of PET, while the glass transition

temperature of the POB-rich phase was $\sim 180^\circ\text{C}$. The three-dimensional crystallinity in most samples was about 30%, and, in contrast to the glass transition temperatures, the temperature of the crystal-to-nematic transition was found to be strongly dependent on the composition.

The reorganization reaction proceeding in the liquid crystalline state was studied [262]. Dynamic mechanical properties of the 50/50, 40/60, 30/70 and 20/80 POB/PET copolyesters were studied [263,264]. Four relaxation processes were identified. The broad α process is orientation dependent and is similar to the high-temperature relaxation observed in stretched PET. For highly oriented samples, this relaxation was recorded at temperatures as high as 158°C . The α relaxation at 88°C was assigned to the main-chain motion of PET segments found in the PET-rich phase in an environment that is similar to the homopolymer PET. This transition is essentially the glass transition of the PET-rich phase. A β relaxation peak at 62°C was attributed to motion of PET segments located in the PET-rich phase that interact with the POB segments. Finally, a γ relaxation observed at 45°C was attributed to local motions of PET segments found in the POB-rich phase.

Fiber spinning from the nematic melt of the copolyester containing 60 (mol)% POB units was performed by several research groups. Sugiyama *and coworkers* found a yield stress value for this copolymer in shear flow [265]. Their results indicated that the crystalline orientation in the melt-spun fibers did not change dramatically with the draw-down ratio, probably because the crystalline orientation was increased to its limiting value during the flow through the die. Muramatsu and Krigbaum found during fiber spinning from the nematic melt of the copolymer containing 60 (mol)% POB that some draw-down was always necessary to optimize the fiber properties [266,267]. However, they observed that the necessary spin draw ratio decreased as the length-to-diameter ratio of the capillary is increased. They also indicated that preheating the melt to temperatures higher than the spinning temperature increased the fiber modulus, because the reduction of the viscosity of the melt due to the melting of POB type crystals produced better chain orientation, and thus, higher moduli.

In the 1970s, a class of liquid crystalline copolyesters of HBA and 2-hydroxy-6-naphthoic acid (HNA) were studied [268-274]. They suggested that at low shear stresses, uneven stress distributions on the three-dimensional network of HNA-rich crystallites might cause flow instability and melt fracture. When the applied stress was raised to a critical value, the melt fracture disappeared. Since yield stress is often associated with unmolten crystals, it should disappear at higher temperatures. However, the yield stresses in these experiments approached an asymptote as the melt temperature increased. Therefore, the yield stresses were suggested to relate to a network of three-dimensional crystallites formed at higher temperatures by HNA blocks. In

addition, it was shown that the mechanical properties of the fibers decrease as the spinning temperatures approached the crystal-to-nematic transition temperature. This was attributed to the existence of incompletely melted crystallites, which have a strong effect on the rheological and mechanical properties of fibers. The optimum melt temperature was found to be $\sim 20^\circ\text{C}$ higher than that of the crystal-to-nematic transition. The authors found that the viscosity of the melt is strongly decreased when the polymer melt is preheated at 335°C and spun at 325°C . Mechanical properties of thermotropic copolyester fibers can be improved by annealing (at $\sim 10^\circ\text{C}$ below the crystal-to-nematic transition temperature). Yang and Krigbaum found that well-oriented fibers (produced with high spinning draw ratio) could be more easily improved as a result of annealing [274].

DSC data on the HBA/HNA fibers are reported [274,275]. Detailed DSC measurements on the 73/27 (mol)% HBA/HNA copolymer are reported [276]. The T_m of the as-spun HBA/HNA fiber was 282°C but increased to 316°C after annealed at 230 and 260°C . The sample degraded during annealing at 305°C , also verified by WAXD method.

The thermo-mechanical behavior of these fibers under both static and dynamic conditions are of interest since they are both associated with the internal molecular and supermolecular structures, as well as on the nature of the polymer chain dynamics in the solid state. The first report on the dynamic mechanical spectrum of HBA/HNA fibers was provided [277]. Three mechanical relaxations were observed, an α relaxation was in the temperature range $110\text{--}125^\circ\text{C}$ (corresponding to the glass transition), a β relaxation did not have temperature specified shift with composition, this relaxation probably corresponds to the onset of naphthalene ring rotation, and a γ relaxation was at about -60°C .

Menczel and coworkers studied as-spun and heat-treated HBA/HNA monofilaments using DSC, DMA, and TMA [278]. In the DMA experiments, the α relaxation was observed at $\sim 100^\circ\text{C}$. A new dissipation peak was found at 65°C . This relaxation had not been previously reported. It appeared as a shoulder of the α relaxation peak, and the origin of this process is not clear because it was not seen during reheating. It was also observed in TMA experiments in the vicinity of 50°C . The β relaxation was recorded at $20\text{--}30^\circ\text{C}$. DSC measurements gave 100°C as the T_g of HBA/HNA, and melting was observed in the temperature range of $200\text{--}280^\circ\text{C}$. The melting diagram of HBA/HNA often consists of two peaks. This was interpreted by several authors as proof that this polymer has two crystal forms. However, WAXD patterns did not provide conclusive evidence. The crystal structure was reported to be ordered, two-dimensional structure along the equator and an aperiodic structure along the meridian. The concept "paracrystalline" was introduced to describe

this ordered structure [279]. It was also reported that a hexagonal and a rectangular two-dimensional lattice exist in HBA/HNA fibers depending upon annealing conditions [280]. However, a precise melting behavior of HBA/HNA fiber still remains to be clarified.

5.3. Poly(phenylene sulfide) (PPS)

PPS is emerging as an important high performance polymer possessing good chemical-resistance, thermal, and textile properties. It is insoluble in almost all organic solvents at room temperature. Only strong oxidizing agents can attack the polymer, such as concentrated sulfuric or nitric acid. The potential applications of PPS fibers include industrial flue gas filters, dryer felts for the paper industry, specialty papers for the electrical and electronic industry, and specialty filter media for hot, corrosive chemicals. The PPS fibers for commercial applications is melt spun and subsequently, drawn at elevated temperatures. Its boiling water shrinkage can be as low as 0 - 5% or as high as 15 - 25%, depending on the spinning conditions. The moisture regain of PPS fibers is very low. The polymer is thermally stable and it may be classified as a low-flammability fiber because its limiting oxygen index is 34 - 35%. The T_g and the T_m of this polymer are dependent somewhat on the method of synthesis [281].

Extensive literature exists on thermal properties of PPS. The heat of fusion of 100% crystalline PPS was estimated as $\Delta H_f^0 = 80$ J/g[282]. The difference of specific heat capacities of the solid and melt PPS was determined to be 29.9 J/°Cmol for the heat capacity increase at the T_g . Menczel and Collins performed a thermal analysis study on PPS of different molecular weights [283]. As expected, the T_g increased with molecular weight, and T_g of the highest-molecular-weight quenched amorphous sample was found to be 92.5°C. T_g was somewhat dependent on crystallinity. The T_m^0 was determined by the Hoffman-Weeks method to be 348.5°C [284]. In DMA measurements of PPS flex bars (1 Hz), the glass transition at 110°C and a secondary transition (likely to be the onset of rotation of the phenylene rings) at -92°C were obtained. A similar secondary transition was determined using dielectric measurements [285].

Song and coworkers reported detailed DSC results on PPS fibers [286,287]. They prepared fibers by melt spinning three previously dried PPS samples of different molecular weights. The as-spun fibers were largely amorphous, cold crystallization was recorded on the DSC traces. The crystallinity of the fiber did not change with draw-down ratio. The as-spun fiber was subsequently drawn at 90°C, 100°C and 150°C to different solid draw ratios. The fibers drawn at 90 and 100°C were still largely amorphous, but the fibers drawn at 150°C (*i.e.*, much beyond T_g) exhibited a reasonable amount of crystallinity and orientation (Fig. 31). The crystallinity values were given as a

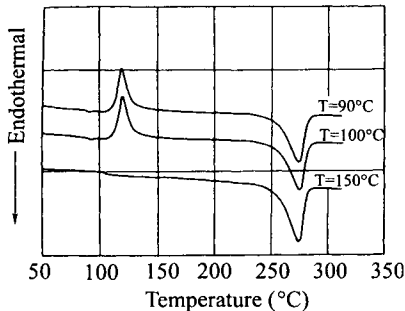


Fig. 31. DSC diagrams of medium-molecular-weight PPS fibers, melt-spun and then drawn at different temperature [289]

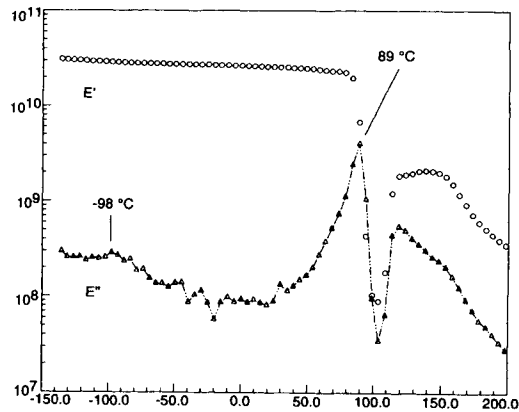


Fig. 32. Dynamic tensile storage modulus and loss modulus of as-spun PPS fibers

function of draw-down ratio and solid draw ratio. Young's modulus and the tensile strength of the drawn fibers increases with both the draw-down ratio and the solid draw ratio. As expected, the elongation to break, decreased with increasing solid draw ratio.

Menzel studied melting and dynamic mechanical behavior of PPS fibers including as-spun and hot-drawn fibers. The T_g was found to be between 87°C and 99°C, depending on the applied frequency. The temperature dependence of the tensile storage and loss moduli, as well as of $\tan\delta$ for as-spun (*i.e.*, largely amorphous) PPS fiber is shown in Fig. 32.

5.4. Poly[2,2'-(*m*-phenylene)-5,5'-bibenzimidazole] (PBI)

PBI is a thermally stable polymer synthesized from tetra-aminobiphenyl-(3,3'-diaminobenzidine) and diphenyl isophthalate. It is used in different forms, such as fibers, composites, and neat resin, primarily for high-temperature applications, but it has application in other fields. For example, during spacewalks, the lifeline that connects the astronauts to the spacecraft has been made of PBI. PBI has excellent dimensional stability at high temperatures stability, and it emits very little smoke when it is exposed to extremely high temperatures. It is resistant to chemicals, and it retains its integrity even when charred. It has high moisture regain. PBI fibers can be blended with other fibers (cotton, glass, aramids), or can be used neat, since its comfort in garments is close to that of cotton. An additional application of PBI fiber is production of graphite fibers.

PBI fiber was generally produced by dry-spinning at ~ 25 (wt)% solution in dimethylacetamide [288]. After the solvent was evaporated, the residual

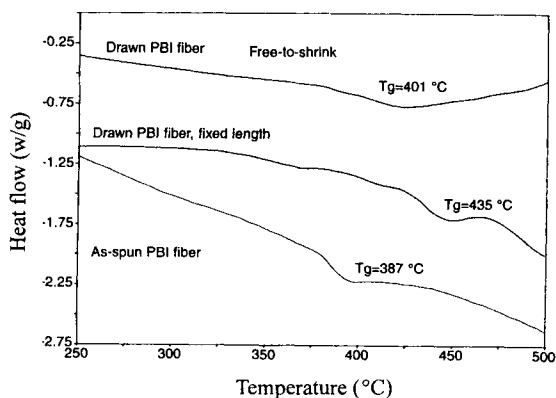


Fig. 33. DSC diagrams of as-spun and drawn PBI fibers [293]

solvent and lithium chloride, which was used to lengthen the shelf lifetime of the dope, were removed by washing with water. Finally, the fiber was drawn and submitted to a two-stage sulfonation process to reduce the thermal shrinkage [289]. The PBI fiber had a high equilibrium moisture content ($\sim 15\%$). Its limiting oxygen index (the concentration of oxygen required to sustain steady-state burning) was 41%. Therefore, it would not support burning in air.

PBI is an amorphous polymer, but can crystallize in the presence of phenol at 290 - 350°C or on pressure treatment with, a phenol/water mixture. Crystallization may also occur when the polymer is treated with formic acid at room temperature, but no advantage crystallization was noticed in the fiber properties [290-292]. The DSC thermal diagrams of the as-spun and drawn PBI

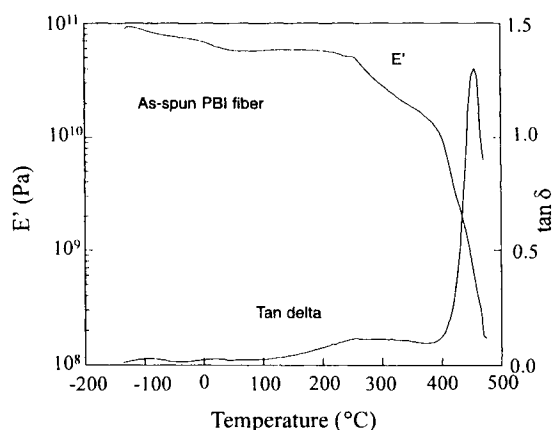


Fig. 34. Dynamic tensile storage modulus and loss tangent of as-spun PBI fiber, showing three relaxation processes in addition to the primary relaxation (glass transition) at 445°C [293]

fibers recorded in unconstrained and constrained conditions are shown in Fig. 33 [293]. As expected, the as-spun fiber showed the lowest T_g of 387°C. T_g of the drawn fiber was much higher even in the unconstrained condition, of which it was at 401°C. Finally, the T_g of the drawn fiber when it is in the constrained condition is considerably higher, and it was at 435°C. The DMA diagram (E' and $\tan\delta$) of the as-spun and drawn fiber are shown in Fig. 34 of the as-spun fiber (peak temperature of $\tan\delta$) was at 437 - 465°C, depending on the frequency. The apparent activation energy of this process was 460 kJ/mol. Three other transitions below the T_g could also be observed: a β transition at 240 - 330°C with an activation energy of 106 kJ/mol, and two other relaxation processes at -20°C and -90°C.

5.5. Aromatic polyimides

Aromatic polyimides have excellent thermal stability, and chemical resistance. These polyimides are under development for composites, micro-electronic applications, electrical insulation, *etc.* They also show low moisture absorbance, flame retardancy, and produce very little smoke in flame. Disadvantages from the point of view of fibers are that polyimides are difficult to process them due to their insolubility in conventional solvents. They do not melt below their degradation temperature. Therefore, fiber developments from these polyimides have not been very successful so far. The polyimide fiber was made by solution spinning (dry spinning) using organic polar solvents, such as N, N-dimethylformamide. The spinning is followed by draw ratios between 4 and 7. This fiber is available as crimped staple fiber and monofilament fiber.

Most work on thermal analysis of polyimide fibers was carried out by scientists of the former USSR. Kabilov and coworkers carried out a mass-spectrometric study of decomposition of a polyimide fiber prepared from pyromellitic anhydride and benzidine [294]. They showed that the decomposition products were observed beyond 400°C. At the temperature interval between 400 and 520°C, decomposition products of the polyamic acid (remaining in the polymer as a result of incomplete imidization) were seen. The decomposition of the polyimide itself started beyond 520°C, and the products of decomposition were water, CO, CO₂, benzonitrile, benzene dicyanide, and biphenyl. At 720°C, atomic and molecular nitrogen was observed, which was suggested to result from the development of a graphite-like system. The dependence of the thermo-oxidative stability of polypyromellitimide fibers on the paramagnetic centers formed in the fiber during hot drawing was demonstrated [295]. The concentration of free radicals increased suddenly at $DR > 2$, and this concentration increased with increasing drawing temperature between 400 and 550°C (the drawing was carried out in air). The thermo-oxidative stability was shown to decrease with increasing drawing temperature

and draw ratio. It was suggested that the free radicals formed during hot drawing play an active role in oxidation of the fiber. Kalashnik observed exothermic peaks in the DTA traces of poly(pyromellitimide) fibers prepared from 4,4'-diaminodiphenyl ether and pyromellitic anhydride [296]. The position and intensity of these peaks depended on the thermal history of the fiber. Three exotherms were found for the as-received fiber, with maxima at 365, 435, and 530°C. The first of these exotherms was assigned to a phase transition to a mesomorphic state, while the second one was suggested to be caused by crystallization. These were recorded only for fibers that had not been hot drawn.

A series of poly(arylene pyromellitimide)s were tested on the mechanical and thermal properties [297]. Fibers were wet spun from a DMF solution of the poly(amic acid), and the poly(amic acid) fibers were imidized chemically. Two weight loss steps were observed in the TGA diagram of these polyimides. The first at around 100°C, which was assigned to water loss, and the second one above 200°C, associated with loss of residual DMF. A significant weight loss in air starts beyond 500°C for these polymers. Jinda studied the influence of the imidization method of 4,4'-oxydiphenylene pyromellitimide fiber (thermal or chemical) on the long-term thermal stability [298]. Fibers of higher crystallinity, drawn beyond 400°C, had poor long-term thermal stability at 290°C. The thermal stability of these fibers deteriorated regardless of the imidization method. The fibers having lower crystallinity could be drawn at 290°C. The tenacity and the elongation of these fibers were fully retained during 65 h at 290°C.

Cheng and coworkers made detailed studies on the thermal mechanical and dynamic properties of a series of aromatic polyimides, which is synthesized from 3,3',4,4'-biphenyltetracarboxylic dianhydride (BPDA) and 2,2'-bis(trifluoromethyl)-4,4'-diaminobiphenyle (PFMB) [299-300]. The mechanical properties of these BPDA-PFMB fibers can be improved remarkably by drawing due to drastic increases in overall orientation, crystal orientation and crystallinity. These three structural parameters, however, do not show parallel changes with increasing draw ratio. It was observed that the CTE of BPTA-PFMB fibers after drawing generally showed negative values in the solid state when low stresses were applied during measurement. For as-spun fibers, the CTEs were constant over a certain applied stress region, which was on the same order of magnitude as CTEs of in-plan oriented BPTA-PFMB films along the film surface. This might indicate that within this region the stress applied is at the same level as the internal stress frozen into the fibers during spinning and drawing. T_g of as-spun fibers showed a linear decrease at low applied stress region, then level off when the applied stress becomes high. Dynamic mechanical data indicated two relaxation processes in as-spun fibers above room

temperature: and α relaxation corresponding to the glass transition and a β relaxation process which was a sub-glass transition. In the fibers with a draw ratio of above three times, the α relaxation was totally suppressed. This revealed a rigid fraction (above T_g) dependence of this relaxation in the fibers. The β relaxation was crystallinity dependent. The activation energy (about 160 kJ/mol) of the β relaxation in as-spun fibers is about 50 kJ/mol lower than that of drawn fibers, indicating that the cooperativity of molecular motion in the fiber changed with orientation and crystallinity.

5.6. Poly(ether ether ketone) (PEEK)

PEEK emerged as an important crystalline high-performance engineering polymer during the past decade, and a relatively large number of publications deal with thermal analysis and structure of this polymer.

The T_m^0 was determined to be 382 - 395°C and the heat of fusion of 100% crystalline PEEK is $\Delta H_f^0 = 130$ J/g [301,302]. The T_g is 146 - 157°C, depending on the crystallization conditions [303].

Zhen *et al.* was the first to prepare fibers from PEEK by melt spinning and subsequent hot drawing [304]. The spinning and drawing temperatures were estimated from thermal parameters of a PEEK film specimen. The T_g was 160°C, the peak temperature of cold crystallization was 173°C, T_g was 337°C, and the peak temperature of crystallization on cooling was 280°C. TGA measurements indicated that the material started degrading at $\sim 400^\circ\text{C}$. Thus the spinning was conducted at a T_m of 380°C. As expected, the maximum draw ratio increased with increasing drawing temperatures; the maximum draw ratio in these experiments was 3.5 (at 270°C).

Shimizu and coworkers prepared PEEK fibers at different take-up speeds, subsequently hot drawing to draw ratios of 1 to 4. They also annealed the fibers at temperatures of 200°C to 325°C. The authors studied the molecular, amorphous, and crystalline orientations. The crystallinity and the crystallite sizes were determined from WAXD, density, and birefringence measurements. The as-spun fibers were largely amorphous and exhibited cold crystallization on DSC thermal diagram. This cold crystallization disappeared naturally on the heat-treated and drawn fibers. Nevertheless, the as-spun fibers did have some crystallinity. It is believed that the crystallization proceeds mainly in the highly oriented regions of the fibers, since the birefringence of the amorphous regions of the as-spun fibers is more than 10 times as strong as that of the crystalline regions. When the as-spun fibers were heat treated at constant length, the amorphous orientation increased continuously up to the heat-treatment temperature of 325°C. The T_g was shown to be a linear function of the amorphous birefringence in the region of birefringence of 0 to 0.12. The temperature dependence of Young's modulus, tensile strength, and elongation at

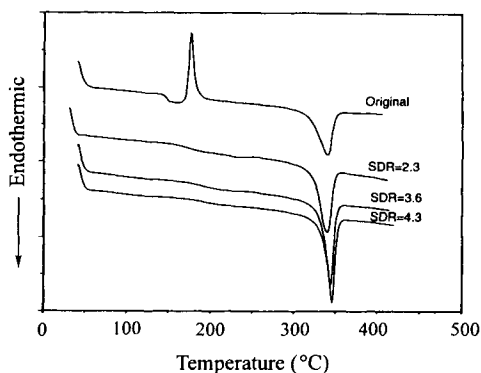


Fig. 35. DSC diagram of PEEK fibers; melt spun and drawn to different ratios in the unconstrained state [286]

break were presented for as-spun and heat-treated fibers. The initial modulus of the fibers at different crystallinity depended on the orientation of the amorphous regions [305].

A detailed study of crystallization and orientation during melt spinning and drawing of PEEK fibers was made [286]. They indicated that draw-down ratios and spin-line stresses could significantly induce crystallization in the spinline. The solid draw ratios during the subsequent drawing were between 2.3 and 4.3. At low draw-down ratios, the fibers were largely amorphous, and a strong cold crystallization was observed on the DSC diagram (Fig. 35). When the draw-down ratio increased, the crystallinity of the fibers increased from 9% to 21%. The T_m in these experiments was constant. However, the T_g increased because of the increase in crystallinity, as was shown [303]. The cold crystallization temperature decreased with increasing draw-down ratio. When the as-spun fibers were subjected to drawing in the solid state, the more and more crystallization took place during drawing and the crystallinity reached 30–37%. As expected, the melting peak sharpened with increasing solid-state draw ratio. The mechanical properties of these fibers showed their Young's modulus and the tensile strength increased with increasing draw-down ratio or spinline stress; the elongation to break decreased with increasing draw-down ratio. Increasing the draw ratio led to an increase in Young's modulus and tensile strength.

5.7. Aromatic heterocyclic fibers [306]

Among the aromatic heterocyclic polymers, the most attractive for potential use as high performance fibers at present are PBZT and PBZO. These two polymers offer excellent fiber tensile and thermal properties unsurpassed by other aromatic fibers. Polymer chemists at the U.S. Air Force's Materials

Laboratory, working along directions parallel to the DuPont workers, were exploring aromatic heterocyclic polymers for high-temperature applications in the 1960s. These polymers have higher thermal stability than the polyesters or the aramides. Recently, Dow Chemical Company and the Toyoto Company commercialized PBZO fibers, because of their excellent mechanical properties and cheaper synthetic route compared to PBZT.

PBZT and PBZO are soluble only in strong proton acids such as polyphosphoric acid (PPA), methanesulfonic acid (MSA), chloro-sulfonic acid (CSA), trifuric acid. By dissolving isolated trans-PBZT in MSA (about 10%) or using PBZT/PPA solution (5 - 6%), a nematic spinning dope was made for dry-jet wet spinning. The superior mechanical properties of PBZT and PBZO fibers were achieved with an optimized combination of high molecular weight polymers, liquid crystal spinning dope, spinning process and finally, tensioned annealing at high temperature.

The thermal mechanical properties and degradation behaviors were studied on these two fibers [307]. Their long-term mechanical tensile performance at high temperatures was critically associated with the stability of the C-O or C-S linkage at the heterocyclic rings on these polymers' backbones. PBZO fibers with the C-O linkages displayed substantially higher thermal stability compared to PBZT containing C-S linkages. It was found that the thermal degradation mechanisms for both of these heterocyclic polymers were identical.

5.8. Carbon fiber [308]

Carbon fiber is produced from a precursor fiber such as rayon, polyacrylonitrile (PAN), or mesophase pitch. The precursor is thermally decomposed, followed by heat treatment at high temperature to convert it to carbon. For example, PAN precursor fiber is first oxidized at 250°C, then carbonized at 800°C, and finally graphitized by heating to 1400 - 2500°C. The PAN-based carbon fiber, which generally gives higher mechanical properties than the pitch-based fiber, is often referred to as graphite fiber to reflect its purer crystal form. Both types of fibers give outstanding tensile moduli, and high tensile and compressive strengths. They are also thermally stable at temperatures up to 500°C. These good properties have made carbon fiber attractive for use in advanced composites. The major benefit of carbon fiber in composite is the savings of up to 30 - 40% in structural weight, which is a critical design factor in many weight-sensitive applications. The business outlook for carbon fiber in the 1990s, according to one estimate, will reach \$3 billion. Many fiber producers are therefore pursuing the carbon fiber market. Hercules, Hysol-Grafil, BASF, Amoco and Ashland are the US producers.

Table 14
Comparison of Selected High Performance Fibers

	Kevlar fiber	Carbon fiber	High strength PE fiber	S-2 fiber	glass
Physical properties					
Density, g/cm ³	1.44	1.8	0.97	2.48	
Melt temperature, °C	550	4000	147	1200	
Tenacity					
GPa	2.3-3.4	4.0	2.6-3.0	4.8	
g/d	18-26.5	25	30-35	21.9	
Modulus					
GPa	55-143	400	120-171	85	
g/d	430-1100	1800	1400-2000	390	
Specific strength, 10 ⁶ in	6.9-10.1	9.6	11.5-13.4	8.4	
Specific modulus, 10 ⁸ in	1.6-4.2	6.9	5.3-7.6	1.5	
Performance parameters					
Tensile strength	+	++	++	-	
Tensile modulus	+	++	++	-	
Toughness	+	-	+	-	
Compressive properties	-	++	+	+	
Shear properties	-	+	+	+	
Thermo properties	+	++	--	++	
Hydrolytic stability	-	+	+	++	
Solvent resistance	+	++	-	++	
Impact resistance	++	-	+	-	
Adhesion	-	+	--	-	
Vibration damping	++	-	+	-	
Light stability	-	+	+	+	
Creep	+	+	--	+	
Dimensional stability	+	+	-	+	
Flame resistance	+	++	--	++	
Moisture regain	-	+	+	+	
Nonabrasiveness	+	-	+	-	
Light weight	+	-	++	-	

+ = good, ++ = very good, - = poor, -- = very poor.

6. CONCLUDING REMARKS

By a summary of major physical properties and performances of Kevlar[®] aramid, carbon, high strength polyethylene, and glass fibers in Table 14, a trend of fiber thermal and mechanical properties can be understood. Carbon fiber shows the best thermal stability with a T_m of about 4000°C, but has a moderate specific strength and modulus because of its high density. High strength PE fiber has excellent specific strength and modulus, but a low melt temperature, ~ 145°C. Kevlar[®] aramid fiber provides good thermal stability and specific properties, which are in between carbon and PE fibers. The costs of these fibers are fairly competitive. For maximum cost effectiveness, a recent trend in advanced composites is to use the hybrid structures of two or several different fibers such as Kevlar[®]/carbon or Kevlar[®]/glass.

Clearly, Kevlar[®] aramid fiber has a much broader range of applications than other high performance fibers. It is employed for reinforcement, wear, friction, ballistic resistance in both rigid and flexible structures, and even as a thixotrope. Carbon and glass fibers are largely limited to the reinforcement of rigid composites. High strength PE fiber is found to have applications in rigid and flexible structures. Although there are some processing difficulties in molding and laminating, it can be used as a reinforcing fiber for composite materials in low temperature applications. It is predictable that future technological developments will probably dictate further increases in fiber mechanical, thermal, electrical and optical properties. TA methods are going to be continuously playing an important role in characterizing and determining thermal and mechanical properties of polymer fibers as a part of developing new generation of products in high technology applications.

REFERENCES

1. J. L. Riley, in *Polymer Processes; Chemical Technology of Plastics, Resins, Rubbers, Adhesives and Fibers*, C. E. Schildknecht (Ed.), Wiley-Interscience, New York, NY, 1956, Chapter XVIII.
2. E. M. Hicks, E. A. Tippetts, J. V. Hewett, and R. H. Brand, in *Man-Made Fibers, Science and Technology*, H. F. Mark, S. M. Atlas, and E., Cernia, (Ed.), Wiley-Interscience, New York, 1967, Vol. 1, p. 375.
3. R. Meredith, *J. Textile Inst.*, T107 (1945) 36.
4. M. J. Coplan, C. S. Grove, Jr., R. S. Casey, and J. L. Vodonik, *Ind. Eng. Chem.*, 54 (1962) 55.
5. G. Dong, H. Ruo, Q. Wang, and Z. Cao, *Man-made Fiber Technology*, Textil Publisher, Beijing, China, 1981, 71.
6. W. E. Morton, and J. W. S. Hearles, in *Physical Properties of Textile Fibers*, The Textile Inst., Manchester, UK, 1993, p. 215.
7. N. S. Murthy, *Polym. News*, 16 (1991) 358.

8. R. de P. Daubeny, C. W. Bunn, C. J. Brown, *Proc. Roy. Soc. (London)*, A226 (1954) 531.
9. W. T. Arstbury and C. J. Brown, *Nature*, 158 (1946) 871.
10. Y. Y. Tomashpol'skii and A. S. Markova, *Vysoko-molekul Soedin.*, 6 (1964) 27.
11. H. G. Kilian, H. Halboth, and E. Jenckel, *Kolloid-Z.*, 172 (1960) 166.
12. Y. Kinoshita, R. Nakamura, Y. Kitano, and T. Ashida, *Polym. Prepr., Am. Chem. Soc., Div. Polym. Chem.*, 20 (1979) 454.
13. H. Zahn and R. Krizikalla, *Macromol. Chem.*, 23 (1957) 3.
14. S. Fakirov, E. W. Fischer, and G. F. Schmidt, *Makromol. Chem.*, 176 (1975) 2459.
15. J. Liu, P. H. Geil, *Journal of Macromolecular Science, Physics*, B36 (1997) 61.
16. I. Sandeman, A. Keller, *J. Polymer Sci.*, 19 (1956) 401.
17. D. Hyndman, G. F. Origlio, *J. Polymer Sci.*, 39 (1959) 556.
18. H. Sobue, and Y. Tabata, *J. Appl. Polymer Sci.*, 2 (1959) 62.
19. H. Sobue, and Y. Tabata, *J. Polymer Sci.*, 39 (1959) 427.
20. A. Zhang, H. Jiang, C. Wu, L. Zhou, L. Xuan, B. Qian, *Text. Res. J.*, 55 (1985) 387.
21. W. L. Lindner, *Polymer*, 14 (1973) 9.
22. L. W. Jelinski, J. J. Dumais, P. I. Watnick, M. D. Sefcik, A. Engel, and M. D. Sefcik, *Macromolecules*, 16 (1983) 409.
23. B. Wunderlich, *Progress in Colloid & Polymer Science*, 96 (1994) 22.
24. M. Takayanagi, M. Yoshino, and S. Minami, *J. Polym. Sci.*, 61 (1962) S7.
25. P. H. Hermans, and A. Weidinger, *Makromol. Chem.*, 44-46, (1961) 24.
26. G. Farrow, D. Preston, *Brit. Appl. Phys.*, 11 (1960) 353.
27. A. M. Hindeleh, and D. J. Johnson, *Polymer*, 19 (1978) 27.
28. P. Schouterden, M. Vandermarliere, C. Riekel, M. H. J. Koch, G. Groeninckx, and H. Reynaers, *Macromolecules*, 22 (1989) 237.
29. C. G. Vonk, and G. Kortleve, *Kolloid-Z.*, 220 (1967) 19-24.
30. B. Wunderlich (Ed), *Thermal analysis*, Academic Press INC, San Diego, CA, 1990.
31. M. Jaffe, J. D. Menczel, and W. E. Bessey, in *Thermal Characterization of Polymeric Materials*, 2nd Edition E. A. Turi (Ed.), Academic Press Inc., San Diego, CA, 1997, Chapter 7.
32. M. Todoki, and T. Kawaguchi, *J. Polym. Sci., Polym. Phys. Ed.*, 15 (1977) 1067.
33. M. Todoki, and T. Kawaguchi, *J. Polym. Sci., Polym. Phys. Ed.*, 15 (1977) 1507.
34. W. T. Mead, and R. S. Porter, *J. Appl. Phys.*, 47 (1976) 4278.
35. M. Todoki, *Thermochim. Acta*, 93 (1985) 147.
36. A. Siegmann, and E. Turi, *J. Macromol. Sci., Phys.*, B10 (1974) 689.
37. R. Hagege, *Text. Res. J.*, 47 (1977) 229.
38. W. M. S. Philip, *J. Forensic Sci.*, 17 (1972) 132.
39. A. Miyagi, and B. Wunderlich, *J. Polym. Sci. Polym. Phys. Ed.*, 10 (1972) 1401.
40. H.-J. Berndt, and A. Bossmann, *Polymer*, 17 (1976) 241.
41. J. Zhao, P. Hu, C. Wu, and B. Qian, *Journal of China Textile University*, 17 (2000) 1.
42. G. Valk, *Lenzinger Ber.*, 33 (1972) 1.
43. Y. P. Khanna, W. M. Wenner, R. Kumar, and S. Kavesh, *J. Appl. Polym. Sci.*, 38 (1989) 571.
44. J. Chiu, *Appl. Polym. Symp.*, 2 (1966) 25.
45. J. Ge, A. Zhang, K. W. McCreight, R.-M. Ho, S.-Y. Wang, F. W. Harris, and S. Z. D. Cheng, *Macromolecules*, 30 (1997) 6498.
46. S. Ran, X. Zong, D. Fang, B. S. Hsiao and B. Chu, *Macromolecules*, 34 (2001) 2569.
47. D. R. Buchanan, and J. P. Walters, *Text. Res. J.*, 47 (1977) 398.
48. J. P. Parker, and P. H. Lindenmeyer, *J. Appl. Phys.*, 21 (1977) 821.

49. J. L. White, and J. E. Spruiell, *Appl. Polym. Symp.*, 33 (1978) 91.
50. U. Gaur, S.-F. Lau, and B. Wunderlich, *J. Phys. Chem. Ref. Data*, 12 (1983) 29.
51. B. Wunderlich, *Macromolecular Physics*, Academic Press, New York, 1980, Vol. 3.
52. E. Turska, and S. Gogolweski, *J. Appl. Polym. Sci.*, 19 (1975) 637.
53. M. Todoki, and T. Kawaguchi, *Kobunshi Ronbunshu*, 32 (1975) 112.
54. H. Artunc, *Lenzinger Ber.* 40 (1976) 10.
55. H. Artunc, and G. Egbers, *Chemiefasern/Text.-ind.*, 26 (1976) 510.
56. W. Wishiewska, *Polymer*, 17 (1972) 517.
57. K. Gyori, G. Bialo, and I. Rusznak, *Magy. Textiltech.*, 29 (1976) 457.
58. F. Fujimoto, and M. Yamashita, *J. Text. Match. Soc. Jpn.*, 17 (1971) 124.
59. R. Hirschler, B. Mihalik, and G. Mikesi, *Kolor. Ert.*, 13 (1971) 223.
60. F. W. Hampson, and T. R. Manley, *Chem. Ind. (London)*, 16 (1974) 660.
61. K. Dimov, I. Aleksandrova, R. Lazarova, and K. Bechev, *Tekst. Prom-st (Sofia)*, 19 (1970) 24.
62. K. Koyama, J. Suryadevara, and J. E. Spruiell, *J. Appl. Polym. Sci.*, 31 (1986) 2203.
63. S. Miyata, and I. Balakov, *J. Macromol. Sci., Chem.*, A16 (1981) 1233.
64. L. A. Dennis, and D. R. Buchanan, *Text. Res. J.*, 57 (1987) 625.
65. E. A. Turi, and Y. P. Khanna, *Polym. Prepr., Am. Chem. Soc., Div. Polym. Chem.*, 26 (1985) 8.
66. S.-D. Rong, and L. H. Williams, *J. Appl. Polym. Sci.*, 30 (1985) 2575.
67. Y. P. Khanna, T. J. Taylor, and R. Kumar, *J. Appl. Polym. Sci.*, 42 (1991) 693.
68. B. Jasse, and A. Moutte, *Bull. Soc. Chim. Fr.*, 6 (1972) 2251.
69. G. N. Arons, and R. W. Macnair, *U.S. Army Natick Lab. Rep.*, No. 71-17-CE (TS-174) (1970).
70. T. Kiyotsukuri, and Y. Nagasawa, *Sen'i Gakkaishi*, 32 (1976) T-187.
71. F. J. Hybart, and J. D. Platt, *J. Appl. Polym. Sci.*, 11 (1967) 1449.
72. G. E. Sweet, and J. P. Bell, *J. Polym. Sci., Part A-2*, 10 (1972) 1273.
73. J. H. Dumbleton, and T. Murayama, *Kolloid-Z. Z. Polym.*, 238 (1970) 410.
74. T. Murayama, and B. Silverman, *J. Polym. Sci. Polym. Phys. Ed.*, 11 (1973) 1873.
75. J. P. Bell, *J. Appl. Polym. Sci.*, 12 (1968) 627.
76. D. C. Felty, and T. Murayama, *J. Appl. Polym. Sci.*, 26 (1981) 987.
77. B. Wunderlich, and G. Czornyj, *Macromolecules*, 10 (1977) 906.
78. U. Gaur, and B. Wunderlich, *Macromolecules*, 13 (1980) 445.
79. C. L. Beatty, and F. E. Karasz, *J. Macromol. Sci., Rev. Macromol. Chem.*, C17 (1979) 37.
80. W. T. Mead, C. R. Desper, and R. S. Porter, *J. Polymer Sci., Polym. Phys. Ed.*, 17 (1979) 859.
81. P. Smith, and P. J. Lemstra, *J. Mater. Sci.*, 15 (1980) 505.
82. J. Smook, and J. Pennings, *Colloid Polym. Sci.*, 262 (1984) 712.
83. N. S. Murthy, S. T. Correals, and S. Kavesh, *Polym. Commun.*, 31 (1990) 50.
84. C. Xiao, Y. Zhang, S. An, and G. Jia, *J. Appl. Polym. Sci.*, 59 (1996) 931.
85. R. Poli, M. Glotin, and L. Mandelkern, *J. Polym. Sci., Polym. Phys. Ed.*, 22 (1984) 407.
86. W. C. Sheehan, and T. B. Cole, *J. Appl. Polym. Sci.*, 8 (1964) 2359.
87. H. P. Nadella, H. M. Henson, J. E. Spruiell, and J. L. White, *J. Appl. Polym. Sci.*, 21 (1977) 3003.
88. E. S. Clark, and L. S. Scott, *Poly. Eng. Sci.*, 14 (1974) 682.
89. T. Kunugi, T. Ito, M. Hashimoto, and M. Ooishi, *J. Appl. Polym. Sci.*, 28 (1983) 179.
90. E. Passaglia, and H. K. Kevorkian, *J. Appl. Sci.*, 34 (1963) 90.

91. W. W. Cox, and A. A. Duswalt, *Polym. Eng. Sci.*, 7 (1967) 309.
92. J. G. Fatou, *Eur. Polym. J.*, 7 (1971) 1057.
93. R. J. Samuels, *J. Polym. Sci., Polym. Phys. Ed.*, 13 (1975) 1417.
94. R. J. Samuels, *Appl. Polym. Symp.*, 27 (1975) 205.
95. U. Gaur, and B. Wunderlich, *J. Phys. Chem. Ref. Data*, 10 (1981) 1051.
96. R. J. Samuels, *J. Macromol. Sci., Phys.*, B4 (1970) 701.
97. R. J. Samuels, *J. Polym. Sci., Polym. Phys. Ed.*, 17 (1979) 535.
98. M. Jaffe, *Thermal Methods in Polymer Analysis*, S. W. Shalaby, (Ed.), Franklin Institute Press, Philadelphia, PA, 1978, p. 93.
99. Y. Zhu, N. Okui, T. Tanaka, S. Umemoto, and T. Sakai, *Polymer*, 32 (1991) 2588.
100. E. Passaglia, and G. M. Martin, *J. Res. Natl. Bur. Stand., Sect. A*, 68 (1964) 519.
101. R. Baltenas, G. Monkeviciute, and V. Paskevicius, *Tr. Litov. Nauchno-Issled. Inst. Tekst. Prom-sti.*, 1 (1971) 237.
102. D. R. Buchanan, and G. I. Hardegree, *Text. Res. J.*, 47 (1977) 732.
103. S. K. Mukhopadhyay, J. W. S. Hearle, and P. W. Foster, *J. Text. Inst.*, 79 (1988) 235.
104. P. P. Andrienko, T. S. Shastuk, and A. L. Pavlov, *Izv. Vyssh. Uchebn. Zaved., Tekhnol. Legk. Prom-sti.*, 6 (1976) 15.
105. B. B. Frushour, and R. S. Knorr, in *Handbook of Fiber Science and Technology*, M. Lwein and E. M. Pearce (Ed.), Dekker, New York and Basel, 1985, Vol. 4, p. 171.
106. W. R. Krigbaum, and N. Tokita, *J. Polym. Sci.*, 43 (1960) 467.
107. P. S. Slade, *Thermochim. Acta*, 1 (1970) 5459.
108. B. G. Frushour, *Polym. Bull.*, 4 (1981) 305.
109. B. G. Frushour, *Polym. Bull.*, 7 (1982) 1.
110. B. G. Frushour, *Polym. Bull.*, 11 (1984) 375.
111. P. Dunn, and B. C. Ennis, *Thermochim. Acta*, 3 (1971) 81.
112. C. R. Bohn, J. R. Schaeffgen, and W. O. Statton, *J. Polym. Sci.*, 55 (1961) 531.
113. R. D. Andrews, and R. M. Kimmel, *Polym. Lett.*, 3 (1965) 167.
114. W. H. Howard, *J. Appl. Polym. Sci.*, 5 (1961) 303.
115. G. R. Cotton, and W. C. Schneider, *Kolloid-Z. Z. Polym.*, 192 (1963) 16.
116. J. P. Bell, and T. Murayama, *J. Appl. Polym. Sci.*, 12 (1968) 1795.
117. S. Okajima, M. Ikeda, and A. Takeuchi, *J. Polym. Sci., Part A-1*, 6 (1968) 1925.
118. S. Minami, *Appl. Polym. Symp.*, 25 (1974) 145.
119. J. Ferguson, and N. G. Ray, *Fibre Sci. Technol.*, 15 (1981) 99.
120. T.-H. Ko, P. Chiranairadul, H.-Y. Ting, and C.-H. Lin, *Proc. Natl. SAMPE Symp.*, 32nd, (1987) 219.
121. P. Rizzo, G. Guerra, and F. Auriemma, *Macromolecules*, 29 (1996) 1830.
122. B. Qian, P. Yang, H. Tian, and P. Hu, *J. Polym. Eng.*, 5 (1985) 65.
123. B. Qian, Z. Sun, C. Wu, and H. Tian, *J. Polym. Eng.*, 7 (1987) 87.
124. M. R. Padhye, and A. V. Karandikar, *J. Appl. Polym. Sci.*, 33 (1987) 1675.
125. R. B. Mathur, T. L. Dhami, and O. P. Bahl, *Polym. Degradation. Stab.*, 14 (1986) 179.
126. R. E. Andrey, L. R. Mulling, and K. W. Smalldon, *Thermochim. Acta*, 32 (1979) 91.
127. N. Grassie, and R. McGuchan, *Eur. Polym. J.*, 6 (1970) 1277.
128. A. K. Kulshreshtha, V. N. Garg, and Y. N. Sharma, *J. Appl. Polym. Sci.*, 31 (1986) 1413.
129. V. O. Gorbacheva, T. K. Mikhailova, S. G. Fedorkina, N. F. Konnova, M. T. Azarova, and A. F. Konkin, *Khim. Volokna*, 15 (1973) 16.
130. N. Grassie, and R. MaGuchan, *Eur. Polym. J.*, 8 (1972) 865.
131. M. Minagawa, *Nippon Kagaku Kaishi*, 2 (1974) 387.

132. E. Fitzer, and D. J. Mueller, *Makromol. Chem.*, A4 (1971) 117.
133. E. Fitzer, and D. J. Mueller, *Polym. Prepr., Am. Chem. Soc., Div. Polym. Chem.*, 14 (1973) 386.
134. D. J. Mueller, E. Fitzer, and A. K. Fieldler, *Int. Fonf. Carbon Fibers, Their Compos. Appl. Pap.*, 1971, Vol. 2, p. 1.
135. P. Dunn, and B. C. Ennis, *J. Appl. Polym. Sci.*, 14 (1970) 1795.
136. G. Hinrichsen, *Angew Makromol. Chem.*, 20 (1971) 121.
137. G. K. Layden, *J. Appl. Polym. Sci.*, 15 (1971) 1283.
138. R. M. Kimmel, *Fiber Society Lecture*, (1971).
139. M. Ikeda, *Kobunshi Kagaku*, 24 (1967) 378.
140. A. Wlochowicz, and W. Przygocki, *J. Appl. Polym. Sci.*, 17 (1973) 1197.
141. M. Droescher, and G. Wegner, *Polymer*, 19 (1978) 43.
142. H.-J. Berndt, and G. Heidemann, *Dtsch. Faerber-Kal.*, 76 (1972) 408.
143. K. Dimov, K. Bechev, R. Lazarova, and I. Aleksandrova, *Faserforsch. Textil- tech.*, 21 (1970) 492.
144. G. Heidemann, and H. J. Berndt, *Melliand Textilber.*, 6 (1976) 485.
145. Y. Yamazaki, *Sen'i Kako*, 23 (1971) 628.
146. V. Halip, *Mater. Plast. (Bucharest)*, 8 (1971) 80.
147. J. Vanicek, *Chem. Prum.*, 25 (1975) 423.
148. A. Jeziomy, *Polymery (Warsaw)*, 15 (1970) 71.
149. B. Miller, *J. Appl. Polym. Sci.*, 11 (1967) 2343.
150. Y. Mitsuishi, and M. Ikeda, *J. Polym. Sci. Polym. Phys. Ed.*, 4 (1966) 283.
151. Y. Mitsuishi, H. Domae, *Sen-i Gakkaishi*, 21 (1965) 528.
152. J. Shimizu, K. Toriumi, and K. Tumai, *Sen'i Gakkaishi*, 33 (1977) 208.
153. J. Shimizu, N. Okui, A. Kaneko, and K. Toriumi, *Sen'i Gakkaishi*, 34 (1978) 64.
154. J. Shimizu, N. Okui, T. Kikutani, and K. Toriumi, *Sen'i Gakkaishi*, 34 (1978) 35.
155. G. Perez, and C. Lecluse, *Proc. Int. Chem. Fiber. Conf.*, 18 (1979) 1.
156. J. O. Warwicker, and B. Vevers, *J. Appl. Polym. Sci.*, 25 (1980) 977.
157. R. M. Ikeda, *J. Polym. Sci., Polym. Lett. Ed.*, 18 (1980) 325.
158. R. G. Quynn, *J. Appl. Polym. Sci.*, 16 (1972) 3393.
159. D. L. MacLean, *J. Appl. Polym. Sci.*, 18 (1974) 625.
160. F. S. Smith, and R. D. Stewart, *Polymer*, 15 (1974) 283.
161. M. Heuvel, and R. Huisman, *J. Appl. Polym. Sci.*, 22 (1978) 2219.
162. A. V. Sidorovich, and E. V. Kuvshinskii, *Vysokomol. Soedin.*, 3 (1961) 161.
163. G. P. Andrianova, G. A. Arutyunov, and Y. V. Popov, *J. Polym. Sci., Polym. Phys. Ed.*, 16 (1978) 1139.
164. H. E. Seyfurth, H. Henkel, K. Langner, F. Schonherr, and E. Wiesener, *Faserforsch. Textiltech.*, 23 (1972) 235.
165. G. Coppola, and P. Frediani, *Nuova Chim.*, 49 (1973) 37.
166. W. Schauler, and E. Liska, *Faserforsch. Textiltech.*, 26 (1975) 225.
167. Y. W. Huh, and Y. Y. Choi, *Sumyu Konghakhoe Chi.*, 14 (1977) 49.
168. T. Kitakawa, *Fiber Prod.*, 8 (1980) 50.
169. S. Backer, and W. Yang, *Text. Res. J.*, 46 (1976) 599.
170. S. Hoffrichter, *Faserforsch. Textiltech.*, 24 (1973) 289.
171. R. L. Hassel, *Am. Lab. (Fairfield, Conn.)*, 9 (1977) 35.
172. J. C. Rodriguez-Cagello, J. Santos, J. C. Merino, and J. M. Pastor, *J. Polym. Sci. Polym. Phys. Ed.*, 34 (1996) 1243.
173. N. P. C. Chao, J. A. Cucolo, and T. W. George, *Appl. Polym. Symp.*, 27 (1975) 175.
174. H.-J. Berndt, H. Schultz, and G. Heidemann, *Melliand Textiler. Int.*, 54 (1973) 773.

175. K. Maeda, and H. Kanetsuna, *Kogyo Kagaku Zasshi*, 69 (1966) 1784.
176. H. J. Oswald, E. A. Turi, P. J. Harget, and Y. P. Khanna, *J. Macromol. Sci., Phys.*, B13 (1977) 231.
177. G. Prati, and A. Seves, *Tinctoria*, 70 (1973) 267.
178. E. Wiesner, *Faserforsch. Textiltech.*, 19 (1968) 301.
179. H.-J. Berndt, and G. Heidemann, *Melliand Textilber. Int.*, 55 (1974) 548.
180. H.-J. Berndt, and G. Heidemann, *Melliand Textilber*, 1 (1977) 83.
181. G. Heidemann, and H. J. Berndt, *Melliand Textilber*, 54 (1973) 546.
182. G. Heidemann, and H. J. Berndt, *Chemiefasern Text.-Anwendungstech./Text.-Ind.*, 24 (1974) 46.
183. R. McGregor, P. L. Grady, T. Montgomery, and J. Adeimy, *Text. Res. J.*, 47 (1977) 598.
184. N. V. Mikhailov, L. G. Tokareva, V. O. Gorbacheva, E. Z. Fainberg, G. M. Terekhova, N. S. Khokhlova, and N. G. Karkova, *Khim. Volokna*, 5 (1970) 9.
185. T. Kunugi, A. Suzuki, and M. Hashimoto, *J. Appl. Polym. Sci.*, 26 (1981) 213.
186. T. Kunugi, A. Suzuki, and M. Hashimoto, *J. Appl. Polym. Sci.*, 26 (1981) 1951.
187. R. K. Gupta, and K. F. Auyeung, *J. Appl. Polym. Sci.*, 34 (1987) 2469.
188. M. J. Napolitano, and A. Moet, *J. Appl. Polym. Sci.*, 32 (1986) 4989.
189. S. B. Warner, *J. Therm. Anal.*, 28 (1983) 17.
190. S. B. Warner, *J. Therm. Anal.*, 28 (1983) 23.
191. M. Todoki, T. Kawaguchi, *Therm. Anal.*, [Proc. Int. Conf.], 5th (1977) 205.
192. R. Galli, M. Canetti, P. Sadocco, A. Seves, and L. Vicini, *J. Polym. Sci., Polym. Phys. Ed.*, 21 (1983) 717.
193. A. K. Jain, V. B. Gupta, *J. Macromol. Sci., Phys.*, B29 (1990) 49.
194. V. Busico, P. Corradini, F. Riva, A. Seves, and L. Vicini, *Macromol. Chem., Rapid Commun.*, 7 (1980) 423.
195. A. B. Thompson, and D. W. Woods, *Trans. Faraday Soc.*, 52 (1956) 1383.
196. T. Kawaguchi, *J. Polym. Sci.*, 32 (1958) 417.
197. K.-H. Illers, and H. Breuer, *J. Colloid. Sci.*, 18 (1963) 1.
198. J. H. Dumbleton, and T. Murayama, *Kolloid-Z. Z. Polym.*, 220 (1967) 41.
199. J. H. Dumbleton, T. Murayama, and J. P. Bell, *Kolloid-Z. Z. Polym.*, 228 (1968) 54.
200. G. Armeniades, and E. Baer, *J. Polym. Sci., Polym. Phys. Ed.*, 9 (1971) 1345.
201. H. K. Yip, and L. H. Williams, *J. Appl. Polym. Sci.*, 20 (1976) 1217.
202. R. W. Miller, and T. Murayama, *J. Appl. Polym. Sci.*, 29 (1984) 933.
203. R. J. Samuels, *J. Polym. Sci., Part A-2*, 10 (1972) 781.
204. J. H. Dumbleton, *J. Polym. Sci., Part A-2*, 7 (1969) 667.
205. J. H. Dumbleton, *Polymer*, 10 (1969) 539.
206. J. H. Dumbleton, J. P. Bell, and T. Murayama, *J. Appl. Polym. Sci.*, 12 (1968) 2491.
207. E. L. Lawton, and T. Murayama, *J. Appl. Polym. Sci.*, 20 (1976) 3033.
208. M. S. De Araugo, and A. L. Simal, *J. Appl. Polym. Sci.*, 60 (1996) 2437.
209. W. Zhou, J. Rodriguez-Arnold, Z. Bu, A. Zhang, S. Z. D. Cheng, A. J. Lovinger, E. T. Hsieh, T. W. Johnson, R. G. Geerts, G. R. Hawley, M. B. Welch, *Proceedings of the Conference of the North American Thermal Analysis Society*, 26th, Cleveland, Sept. 13-15, 1998, 175.
210. M. Day, T. Suprunchuk, J. D. Cooney, and D. M. Wiles, *J. Appl. Polym. Sci.*, 33 (1987) 2041.
211. J. F. Quinson, B. Chabert, J. Chauchard, J. P. Soulier, and G. Edel, *Bull. Sci. Inst. Text. Fr.*, 2 (1973) 1.

212. K. Dimov, I. Aleksandrova, R. Lazarova, and K. Bechev, *God. Nauchnoissled. Inst. Khim. Prom-st.*, 8 (1971) 297.
213. J. Budin, and J. Vanicek, *Chem. Vlakna*, 27 (1977) 14.
214. D. S. Varma, K. V. A. R. Kumar, and A. Veena, *Man-made Text. Indis*, 22 (1979) 73.
215. L. P. Repina, R. V. Vorobeva, and E. M. Aizenshtein, *Khim. Volokna*, 15 (1973) 53.
216. V. P. Krapotkin, G. I. Fantina, V. E. Geller, and E. M. Aizenshtein, *Khim. Volokna*, 15 (1973) 12.
217. D. Selivansky, and M. Lewin, *J. Appl. Polym. Sci.*, 27 (1982) 2337.
218. K.-H. Illers, *Colloid Polym.Sci.*, 258 (1980) 117.
219. W. J. Jackson, Jr. and H. F. Kuhfuss, *J. Polym. Sci., Polym. Chem. Ed.*, 14 (1976) 2043.
220. M. G. Breerton, G. R. Davies, R. Jakeways, T. Smith, and I. M. Ward, *Polymer*, 19 (1978) 17.
221. I. M. Ward, M. Wilding, and H. Brody, *J. Polym. Sci., Polym. Phys. Ed.*, 14 (1976) 263.
222. S. Z. D. Cheng, R. Pan, and B. Wunderlich, *Makromol. Chem.*, 189 (1988) 2443.
223. F.-M. Lu, and J. E. Spruiell, *J. Appl. Polym. Sci.*, 31 (1986) 1595.
224. K. Tashiro, Y. Naki, M. Kobayashi, and H. Tadokoro, *Macromolecules*, 13 (1980) 137.
225. S. Chen, and J. E. Spruiell, *J. Appl. Polym. Sci.*, 33 (1987) 1427.
226. S. Chen, W. Yu, and J. E. Spruiell, *J. Appl. Polym. Sci.*, 34 (1987) 1477.
227. F. Schultze-Gebhardt, *Acta Polym.*, 30 (1979) 652.
228. I. Sakurada, in *Handbook of Fiber Science and Technology*, M. Lewin and E. M. (Ed.), M. Dekker, New York, NY, 1985.
229. I. Sakurada, (Ed.) *Polyvinyl Alcohol Fibers*, M. Dekker, New York, NY, 1985.
230. W. Stocks, and H. Berghmans, *J. Appl. Polym. Sci.*, 29 (1991) 609.
231. P. Cebe, and D. Grubb, *J. Mater. Sci.*, 20 (1985) 4465.
232. Y. D. Kwon, S. Kavesh, and D. C. Prevorsek, *U.S. Pat.* 4, 440 (1984) 711.
233. P. D. Garrett, and D. T. Grubb, *J. Mater. Res.*, 1 (1986) 861.
234. P. D. Garrett, and D. T. Grubb, *J. Polym. Sci. Part B. Polym. Phys.*, 26 (1988) 2509.
235. T. Kunugi, T. Kawasumi, and T. Ito, *J. Appl. Polym. Sci.*, 40 (1990) 2101.
236. R. Schellekens, and C. Bastiaansen, *J. Appl. Polym. Sci.*, 43 (1991) 2311.
237. H. H. Yang, *Aromatic High Strength Fibers*, Wiley-Interscience, New York, NY, 1989.
238. H. Jiang, W. W. Adams, R. K. Eby, *Mater. Sci. Technol.*, 12 (1993) 597.
239. S. L. Kwolek, *U. S. Pat.* 3,671,542 (1972).
240. S. L. Kwolek, *U. S. Pat.* 3,819,587 (1974).
241. T. I. Bair, and P. W. Morgan, *U. S. Pat.* 3,673,143 (1972).
242. H. Blades, *U. S. Pat.* 3,869,429. (1975).
243. B. Huang, Q. Wu, J. Zhu, Z. Wu, *Zhongguo Fangzhi Daxue Xuebao*, 16 (1990) 23.
244. J. R. Brown, and B. C. Ennis, *Text. Res. J.*, 47 (1977) 62.
245. L. Penn, and F. Larsen, *J. Appl. Polym. Sci.*, 23 (1979) 59.
246. A. K. Chaudhuri, B. Y. Min, and E. M. Pearce, *J. Polym. Sci., Polym. Chem. Ed.*, 18 (1980) 2949.
247. B. Poulaert, J.-C. Chielens, C. Vandenhende, and R. Legras, *Polym. Comun.*, 26 (1985) 132.
248. M. Jaffe, and S. Jones, in *High Technology Fibers*, M. Lewin, and J. Preston (Ed.), Part A, M. Dekker, New York, NY, 1985, Vol. III, p. 349
249. K. Haraguchi, T. Kajiyama, and M. Takayanagi, *Sen'i Gakkaishi*, 33 (1977) T535.

250. T. Kunugi, H. Watanabe, and M. Hashimoto, *J. Appl. Polym. Sci.*, 24 (1979) 1039.
251. H. F. Kuhfuss, and W. J. Jackson Jr., U.S. Pat. 3,778,410 (1973).
252. H. F. Kuhfuss, and W. J. Jackson Jr., U.S. Pat. 3,804,805 (1974).
253. W. J. Jackson Jr., and H. F. Kuhfuss, U.S. Pat. 4,140,846 (1979).
254. W. J. Jackson Jr., G. G. Gebeau, and H. F. Kuhfuss, U.S. Pat. 4,153,779 (1979).
255. W. J. Jackson Jr. and J. G. Morris, U.S. Pat. 4,181,792 (1980).
256. J. Menczel, and B. Wunderlich, *J. Polym. Sci., Polym. Phys. Ed.*, 18 (1980) 1433.
257. V. A. Nicely, J. T. Dougherty, and L. W. Renfro, *Macromolecules*, 20 (1987) 573.
258. A. E. Zachariades, E. J. Economy, and J. A. Logan, *J. Appl. Polym. Sci.*, 27 (1982) 2009.
259. E. Joseph, G. L. Wilkes, and D. G. Baird, *Polymer*, 26 (1985) 689.
260. J. Blackwell, G. A. Gutierrez, and R. A. Chivers, in *Polymer Liquid Crystals*, A. Blumstein, (Ed.), Plenum, New York, NY, 1983, p. 167.
261. W. Meesiri, J. Menczel, U. Gaur, and B. Wunderlich, *J. Polym. Sci., Polym. Phys. Ed.*, 20 (1982) 719.
262. R. W. Lenz, J.-I. Jin, and K. A. Feichtinger, *Polymer*, 24 (1983) 327.
263. R. S. Benson, and D. N. Lewis, and L. J. Effler, 30 (1989) 2188.
264. R. S. Benson, and D. N. Lewis, *Polym. Commun.*, 28 (1987) 289.
265. H. Sugiyama, D. N. Lewis, J. L. White, and J. F. Fellers, *J. Appl. Polym. Sci.*, 30 (1985) 2329.
266. H. Muramatsu, and W. R. Krigbaum, *J. Polym. Sci. Polym. Phys. Ed.*, 24 (1986) 1695.
267. H. Muramatsu, and W. R. Krigbaum, *J. Polym. Sci. Polym. Phys. Ed.*, 25 (1987) 803.
268. G. W. Calundann, *Ger. Offen.* 2,721,738 (1977).
269. G. W. Calundann, U.S. Pat. 4,067,852 (1978).
270. G. W. Calundann, U.S. Pat. 4,130,545 (1978).
271. G. W. Calundann, U.S. Pat. 4,161,470 (1979).
272. G. W. Calundann, U.S. Pat. 4,184,996 (1980).
273. G. W. Calundann, H. L. Davis, F. J. Gorman, and R. M. Mininni, *Ger. Offen.* 2,721,787 (1977).
274. D.-K. Yang, and W. R. Drigbaum, *J. Polym. Sci. Polym. Phys. Ed.*, 27 (1989) 1837.
275. H. Muramatsu, and W. R. Krigbaum, *Macromolecules*, 19 (1986) 2850.
276. Y. C. Kim, and J. Economy, *Macromolecules*, 32 (1999) 2855.
277. H. N. Yoon, and M. Jaffe, *Abstr. Pap., Am. Chem. Soc. Natl. Meet.*, 185th Seattle, (1983).
278. J. Menczel, and G. L. Collins, and C. K. Saw, *J. Therm. Anal.*, 46 (1996) 753.
279. A. B. Erdemir, D. Johnson, I. Karacan, and J. G. Tomka, *Polymer*, 29 (1988) 597.
280. J. Blackwell, A.-I. Schneider, C. M. McCullagh, *Materials Research Society Symposium Proceedings*, 321 (Crystallization and Related Phenomena in Amorphous Materials), 1994, p. 71.
281. J. G. Scruggs, and J. O. Reed, in *Handbook of Fiber Science and Technology*, M. Lewin and J. Preston (Ed.), M. Dekker, New York, NY, 1985, Vol. 3, p. 335.
282. D. G. Brady, *J. Appl. Polym. Sci.*, 20 (1976) 2541.
283. J. Menczel, and G. L. Collins, *Polym. Eng. Sci.*, 32 (1992) 1264.
284. J. D. Hoffman, and J. J. Weeks, *J. Res. Natl. Bur. Std.*, 66A (1962) 13.
285. S. J. Rigby, and D. Dew-Hughes, *Polymer*, 15 (1974) 639.
286. S. S. Song, J. L. White and M. Cakmak, *Sen'i Gakkaishi*, 45 (1989) 243.
287. S. S. Song, J. L. White and M. Cakmak, *Int. Polym. Process.*, 4 (1989) 96.

288. A. B. Conciatori, E. C. Chenevey, T. C. Bohrer, and A. E. Prince, Jr., *J. Polym. Sci.*, C19 (1967) 49.
289. R. B. Sandor, *High Perform. Polym.*, 2 (1990) 25.
290. R. W. Singleton, *Appl. Polym. Symp.*, 9 (1969) 133.
291. R. W. Singleton, H. D. Noether, and J. F. Tracy, *J. Polym. Sci.*, Part C, 19 (1967) 65.
292. B. A. Conciatori, A. Buckley, and D. Stuetz, in *Handbook of Fiber Science and Technology*, M. Lwein, and J. Preston (Ed.), Dekker, New York and Basel, NY, 1985, Vol. 3, Part A, p. 221.
293. J. Menczel, *Journal of Thermal Analysis and Calorimetry*, 59 (2000) 1023.
294. Z. A. Kabilov, T. M. Muinov, Yu. N. Szazanov, L. A. Shibaev, L. N. Korzhavin, N. R. Prokopchuk, and F. S. Florinskii, *Izv. Akad. Nauk Tadzh. SSR, Otd. Fiz.-Mat. Geol.-Khim. Nauk.*, 1 (1976) 34.
295. E. V. Dovbii, A. T. Kalashnik, G. V. Kozhina, A. M. Shchetinin, G. G. Frenkel, S. P. Papkov, G. I. Kudryavtsev, and Z. G. Oprits, *Vysokomol. Soedin. Ser., B* 23 (1981) 871.
296. A. T. Klashnik, O. I. Romanko, A. M. Shchetinin, G. G. Frenkel, Z. G. Oprits, V. Y. Efremov, and S. P. Papkov, *Khim. Volokna*, 3 (1982) 37.
297. B. S. Rao, and I. K. Varma, *Indian J. Text. Res.*, 10 (1985) 171.
298. T. Jinda, *Sen'i Gakkaishi*, 46 (1990) 163.
299. S. Z. D. Cheng, Z. Wu, M. Eashoo, S. L. C. Hsu, F. W. Harris, *Polymer*, 32 (1991) 1803.
300. M. Eashoo, D. Shen, Z. Wu, C. J. Lee, F. W. Harris, and S. Z. D. Cheng, *Polymer*, 34 (1993) 3209.
301. D. J. Blundell, and B. N. Osborn, *Polymer*, 24 (1983) 953.
302. J. M. Barton, J. R. Lloyd, A. A. Goodwin, and J. N. Hay, *Br. Polym. J.*, 23 (1990) 101.
303. S. Z. D. Cheng, M. Y. Cao, and B. Wunderlich, *Macromolecules*, 19 (1986) 1868.
304. X. J. Zhen, T. Kitao, and I. Taniguchi, *Sen'i Gakkaishi*, 41 (1985) T1.
305. J. Shimizu, T. Kikutani, Y. Ookoshi, and A. Takaku, *Gakkaishi*, 43 (1987) 507.
306. M. Jaffe, G. Calundann, and H. Yoon, in *Handbook of Fiber Science and Technology*, M. Lewis and J. Preston (Ed.), Dekker, New York, NY, 1996, Vol. III, p. 83.
307. Z. Wu, F. Li, L. Huang, Y. Shi, X. Jin, S. Fang, K. Chuang, R. E. Lyon, F. W. Harris, and S. Z. D. Cheng, *Journal of Thermal Analysis and Calorimetry*, 59 (2000) 361.
308. P. Ehrburger, J. J. Herque, and J. B. Donnet, in *Recent developments in carbon fiber treatments*, ACS Symp. Ser. 21 (Pet. Deriv. Carbons, Symp.), 1976, p. 324.

Chapter 12

Thermal properties of high temperature polymer matrix fibrous composites

Roger J. Morgan^a, E. Eugene Shin^b and Jason E. Lincoln^c

^aDepartment of Engineering, Texas A&M University, College Station, TX 77843-3123

^bNASA Glenn Research Center at Lewis Field, Mail Stop 49-1, 21000 Brookpark Rd., Cleveland, OH 44135

^cPolymer Matrix Composites Research Team, Material and Manufacturing Directorate, Air Force Research Laboratory/MLBC, 2941 P Street, Room 136, Wright-Patterson Air Force Base, OH 45433-7750

1. INTRODUCTION

Thermal characterization techniques have been widely used to identify the physical, chemical and mechanical phenomena that control fabrication, structure and service performance of polymer matrix fibrous composites from the molecular level through the microscopic and macroscopic dimensional levels. We recently reviewed the thermal characterization of composites and their constituents in terms of composite fabrication processes, structure and service environment degradation mechanisms [1].

The utilization of polymer matrix fibrous composites falls into the following principal genetic areas, namely:

- Aerospace/military;
- Automotive;
- Civil infrastructure;
- Industrial; and
- Recreational.

Applications of composites in the aerospace/military arena include commercial and military aircraft, helicopters, missiles, ground vehicles, personnel protection, submarines, ships, and space vehicles. These composites provide weight savings, lower manufacturing costs, impact resistance, radar

transparency, ballistic resistance, dimensional stability, low thermal expansion, and noise suppression [1].

In the automotive industry, composites compete with steel, aluminum and magnesium for future light weight structures for a whole range of composites, such as cam covers, oil pans and seals under the hood, drive shafts, bumpers, leaf springs to exterior all-composite car bodies. The key to their increased utilization relative to metals is the development of a cheap carbon fiber in the \$2 - 3 per pound range. The advantages of composites utilization in the automotive industry include weight savings, corrosion resistance, and economics of manufacturing, such as a decrease in the number of fabrication steps and the ease of formation of aerodynamic shapes.

Future materials utilization in the automotive industry has to satisfy “the whole-life criteria” for materials utilization, illustrated in Fig. 1. These criteria are:

- The component application functional requirements, such as impact resistance, acoustic signature for noise suppression and fluid containment;
- Materials selection and type;
- Recyclability;
- Low cost, fast processing-fabrication procedures;
- Performance criteria in terms of structural characterization of damage state and associated reliability and durability;
- Design optimization; and
- Economic competitiveness.

As indicated in Fig. 1, all these whole-life cycle criteria are interrelated and modification of one criteria changes all the others.

In the civil infrastructure arena the deteriorating state of the world’s infrastructure [2] has led the Civil Engineering Research Foundation to recommend the use of alternative materials that have attributes of lower cost, lighter weight, reduced maintenance and enhanced durability [3]. Polymeric composites and coatings have seen a significant utilization increase as structures in bridges, decks, columns, roads, pipes and high rise buildings. The principle materials used in these applications are chopped glass fiber-polyester matrix and polymeric (epoxy filled) concrete composites and epoxy coatings.

These polymers and composites will be exposed to complex infrastructure service environment conditions of a range of combinations of stress, time, temperature, moisture, radiation, chemical and gaseous environments and are expected to perform for 50 years or more. These materials should be required to pass a series of specifications based on (i) inherent and (ii) residual mechanical, physical and thermal properties after accelerated service environment exposure conditions. The lack of understanding of the fundamental parameters controlling

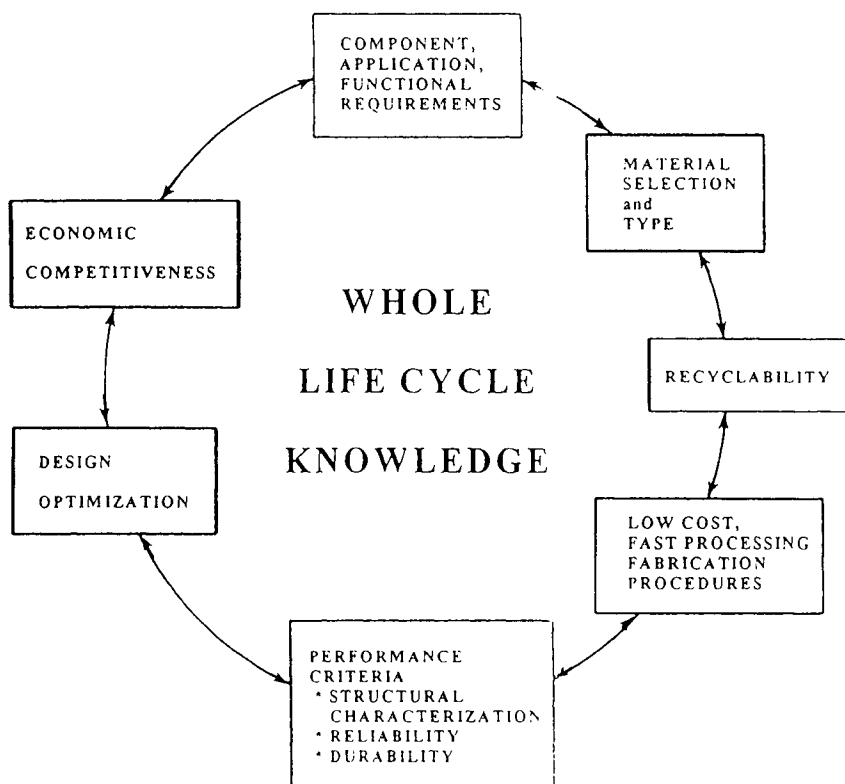


Fig. 1. Whole life cycle knowledge

long-term materials performance, necessarily leads to over design and in-service prototype evaluations and, furthermore, inhibits greater utilization.

Composite industrial use is wide-ranging, such as in appliances, business equipment, construction materials, oil drill pipes, engines, electronic circuit board bases, machine tools, and rapidly growing prosthetics applications in the medical field.

Recreational applications are in bicycles, fishing rods, golf shafts, racing cars, boats, skis, and tennis rackets.

The key to enhanced utilization of polymer matrix fibrous composites, PMFC's is their low cost, efficient processing and confidence in their long-term performance. In this chapter we will address the performance of PMFC's, as determined by processing conditions and service environment exposure, and illustrate the utilization of thermal characterization techniques for PMFC performance characterization in conjunction with other physical, chemical and mechanical characterization techniques. We will specifically address the durability and aging mechanisms of high temperature PMFC's in aerospace

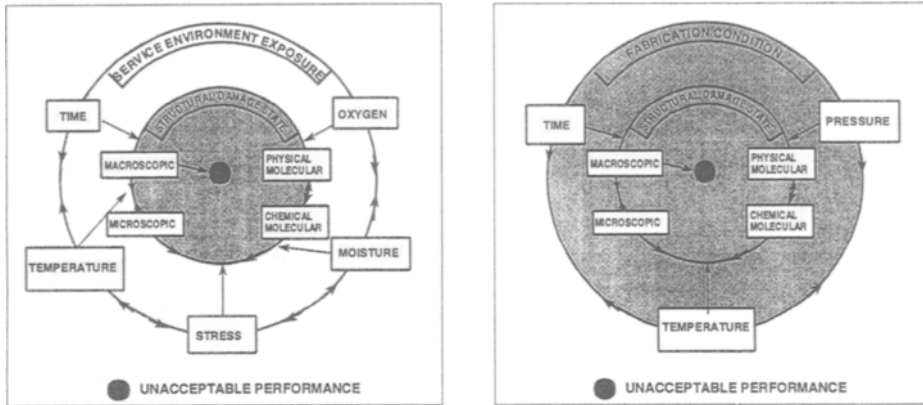
SERVICE ENVIRONMENT EXPOSUREFABRICATION CONDITIONS

Fig. 2. Critical performance failure sequence path diagrams

service environments, as these are one of the most extreme exposure environments for PMFC's.

Based on our previous durability studies [1] we have developed a systematic durability methodology to evaluate the long-term performance of polymers and their composites. This methodology involves initially studying the effects of individual and combined core test service environments upon polymer and composite performance in order to identify the most likely synergistic service environments and controlling physical, chemical and mechanical parameters of the ultimate critical failure path. This methodology requires knowledge of the effects of (i) fabrication and (ii) service environment exposure conditions upon physical and chemical molecular, microscopic and macroscopic structural damage states and how the individual kinetics and synergistic growth of the damage states leads to an unacceptable performance criteria, as illustrated in the critical performance failure sequence path diagrams in Fig. 2. From this methodology, specific failure path threshold 3-D structural performance phase diagrams are developed that plot three critical parameters that control damage state development, for example, moisture concentration, temperature, molecular physical structural damage state. The information contained in these specific critical phase diagrams can be utilized for:

- Lifetime modeling;
- Structural analyses design optimization;
- Development of meaningful accelerated test procedures; and
- Evaluation of the health of deployed structures.

The structural threshold phase diagrams are generic in nature and allow evaluation of the development of structural damage states in components of different geometries and service environment exposure conditions.

The two types of high temperature polymer matrix-carbon fiber composites utilized in aerospace applications are (i) cross linked bismaleimide, BMI, thermoset and (ii) predominantly thermo-plastic polyimide, PI, - carbon, C, fiber composites. Based on our previous studies [1-13] we have identified the critical aging mechanisms that involve (i) further cure of BMI-carbon fiber composites with associated T_g increases, mechanical property decreases and enhanced microcrack development in service environment exposure conditions, and (ii) hygrothermal induced thermal and mechanical property deterioration as a result of physical and chemical structural changes in BMI- and PI- carbon fiber composites.

The role of thermal characterization procedures in studying these BMI and PI performance deterioration mechanisms will now be addressed.

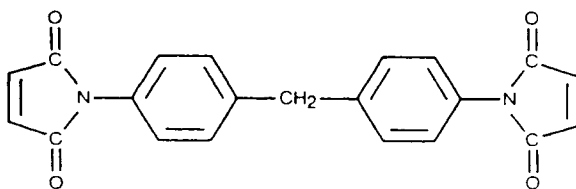
2. RESULTS AND DISCUSSION

2.1. Bismaleimide composite matrices

2.1.1. Background and cure characterization

Over the past fifteen years, high temperature thermoset bismaleimides (BMI's) have been developed that have T_g 's in the 250 - 350°C range and that exhibit superior hot-wet mechanical properties than epoxies. The predominant BMI resin system that is used as a composite matrix is based on 4, 4' -

Matrimid 5292 Component A:
4,4'-Bismaleimidodiphenylmethane



Matrimid 5292 Component B:
0,0'-Diallyl Bisphenol A

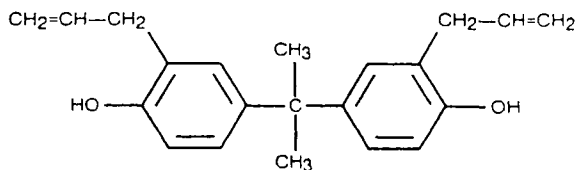


Fig. 3. The chemical structures of BMPM and DABPA monomers

bismaleimidodiphenyl methane (BMPM) – 0, 0' - diallyl bisphenol A (DABPA) BMI resin system (Matrimid 5292, Ciba-Geigy). The chemical structures of the BMPM and DABPA monomers are illustrated in Fig. 3. The cure-structure-property relations of BMPM – DABPA BMI resins have been extensively studied utilizing thermal techniques such as differential scanning calorimetry (DSC) and dynamic mechanical analyses (DMA) together with Fourier transform infrared spectroscopy (FTIR).

Systematic studies of the cure characteristic as a function of time-temperature and monomers ratio [4,11,14,15] revealed three principal temperature regimes for the cure reactions namely: (i) 100 - 200°C, (ii) 200 - 300°C and (iii) 300 - 350°C. DSC plots for the BMI resin and it's composites revealed cure exotherm peaks in each of the three temperature regions as illustrated in Fig. 4.

Below 150°C, the BMPM and DABPA manomers react to form the “ene” molecule, Digure [5], which contains three active C=C bonds capable of polymerization. Above 200°C the ally L(A), propenyl (B), and maleimide (C), carbon double bonds of the “ene” molecule illustrated in Fig. 5 undergo fast, free radical sequential polymerization producing the principal cure exotherm centered at 250°C in Fig. 4. FTIR studies show all the maleimide and allyl C=C bonds are consumed under standard cure conditions at 250°C after 3 hours. However, it is

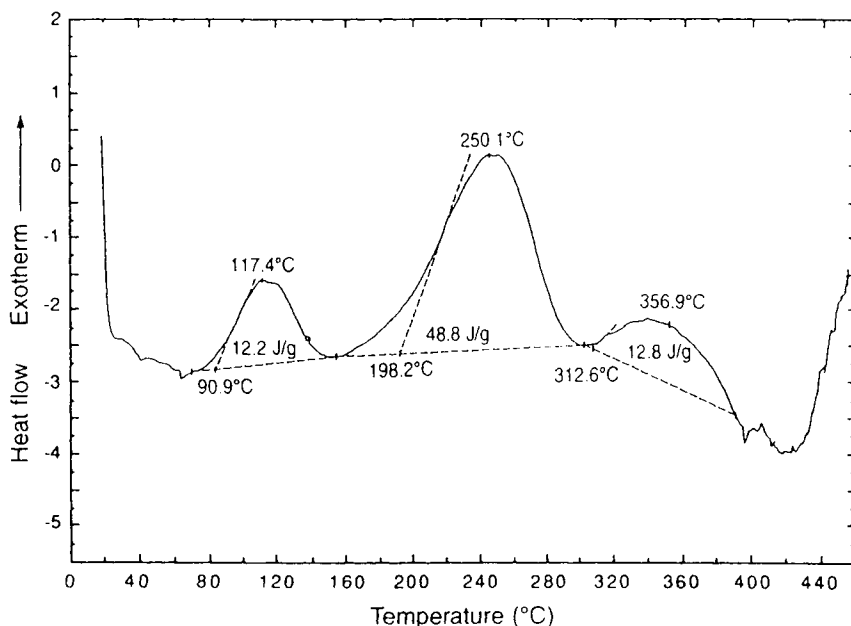


Fig. 4. DSC curve of BMPM-DABPA (1:1 molar) – AS4 carbon fiber composite after prepregging [4]

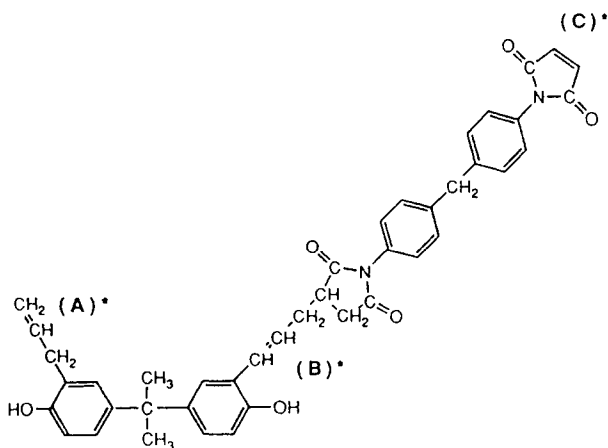


Fig. 5. The chemical structure of the BMPM-DABPA "Ene" adduct prepolymer that contains (A), (B) and (C) active carbon double bonds capable of polymerization

uncertain if all the more sterically restricted propenyl C=C bonds are consumed under these standard cure conditions, as it is difficult to detect such groups by FTIR. In the same temperature region the hydroxyl groups undergo slow dehydration to form ether linkages, Reaction (1), resulting in a complex crosslinked network.



The ether crosslink reaction is only ~ 50% complete after 9 hours at 250°C. Mass spectroscopy studies revealed H₂O evolution concentrations consistent with this dehydration reaction.

Above 250°C, further cure occurs that can be diffusion controlled, principally by further dehydration followed by complex dissociation of the resultant ether linkages to form stiffer carbon linkages. These reactions are responsible for the exotherm exhibited near 350°C in Fig. 4. This further cure of the BMI resin results in a ~ 0.2% density decrease; 0.3 wt% loss; 10% modulus and 25 - 40% ductility loss in the 25 - 177°C service environment temperature range and ~ 100°C increase in *T_g* resulting in an ultimate *T_g* at near 350°C. These dissociation and recombination network changes results in a stiffer, more molecularly open crosslinked network. Little heat is evolved for these reactions, as compared to the free radical C=C cure reactions. In Fig. 6 the *T_g*s, as determined from DSC measurements, versus isothermal cure time for temperatures in the 130 to 300°C for the BMI resin are plotted. The ratio of the additional heat evolved in a DSC run for a "cured" matrix (ΔH_2) compared to the total heat evolved in a DSC run of an initially uncured matrix (ΔH_1), $\Delta H_C/\Delta H_T$ is

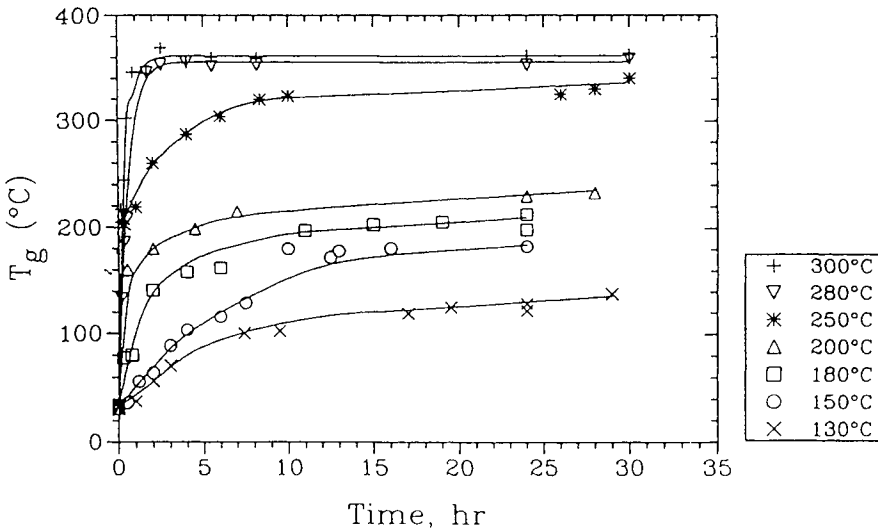


Fig. 6. T_g versus isothermal cure time for BMPM – DABPA (1:1 molar) BMI system in the 130°C to 300°C temperature range

commonly utilized to determine the degree of conversion, α , by the expression $(1 - \Delta_C/\Delta_T)$. In Fig. 7 the degree of cure, α , determined from the DSC plots for the BMI resin versus T_g for isothermal cure temperatures of constant cure time of 10

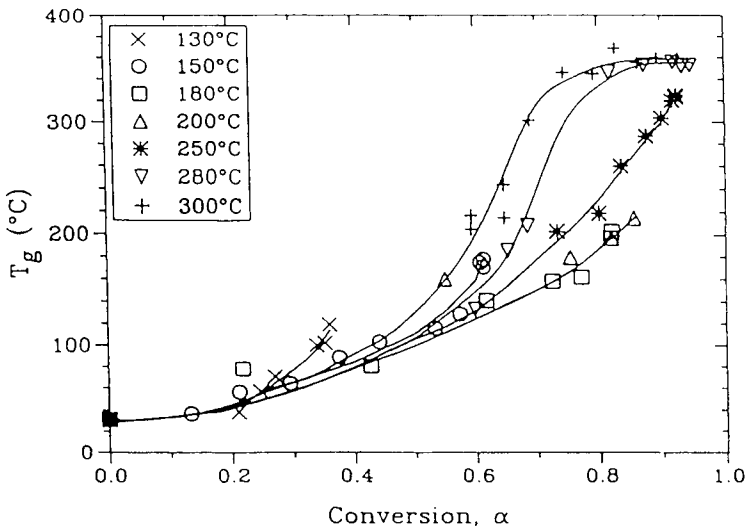


Fig. 7. T_g versus degree of cure, α , for isothermal cure temperatures in the 130°C to 300°C range for a constant cure time of 10 hours for the BMPM-DABPA (1:1 molar) BMI system

hours is illustrated. This plot clearly indicates the T_g for a specific degree of cure, α , is cure history path dependent, as the isothermal $T_g - \alpha$ plots do not fall on one common plot. For example, for a 90% degree of cure at isothermal cure temperature 250°C the T_g is 280°C; however, for the same degree of cure at isothermal cure temperatures of 280°C and 300°C, the T_g is 70°C higher at 350°C. The lack of sensitivity of the degree of cure, α , to the T_g , at the higher cure temperatures is a result of the dehydration reaction and the subsequent ether bond dissociation and rearrangement evolving little heat of evolution compared to the free radical principal cure reactions of the C=C bond. Hence, DSC exotherms can not be utilized to monitor the degree of cure of resins that form from more than one chemical reaction which exhibit considerably different heats of reaction. Hence, the primary performance issue for BMI-C fiber composites is that they are not fully cured under standard 250°C cure conditions and could continue to cure over prolonged periods of time in service environment at 177°C resulting in matrix embrittlement. Extrapolation of all available high temperature reaction rate data to the 175 - 200°C temperature range indicates insignificant further cure and associated BMI embrittlement occurs in the dry, 175 - 200°C temperature range service environment because of glassy-state diffusion restrictions and decreases in reaction rates of unreacted species at these lower temperatures. Our analyses reveals no change in toughness after 120,000 hours exposure at 175°C and only a 20% decrease at 200°C for the same time period [18].

2.1.2. Composite microcracking formation and prevention

In addition to the further curing and embrittlement of BMI's, their carbon, C, Fiber composites in the form of $[0^\circ/90^\circ]_s$ laminates always microcrack under standard cure conditions (1.5 hr 177°C, 2hr 200°C and 6 hr 250°C). By modifying the composite cure cycle from 1.5 hr at 177°C to 8 hr at 177°C, followed by the standard higher temperature cure microcracking was eliminated [19]. Characterization of the microcrack formation and the mechanism responsible for their elimination was determined by a combination of monitoring in-situ microcrack formation directly in the environmental scanning electron microscope, ESEM, together with dynamic mechanical analyses, DMA and DSC studies on the thermomechanical properties between microcracked composites and those fabricated without microcracks.

In Fig. 8 we plot transverse microcrack density of the BMI-C fibers composites as a function of cure conditions. For the composites precured for 8 hr at 177°C no microcrack formation in ESEM was observed upon cool-down until a post-cure of 6 hr at 300°C was used.

DSC results provide insight to the mechanisms associated with microcracking in the BMI-C fiber composites. Dynamic DSC scans are shown in Fig. 9, where represents the principle crosslinking reaction peak and ψ is the

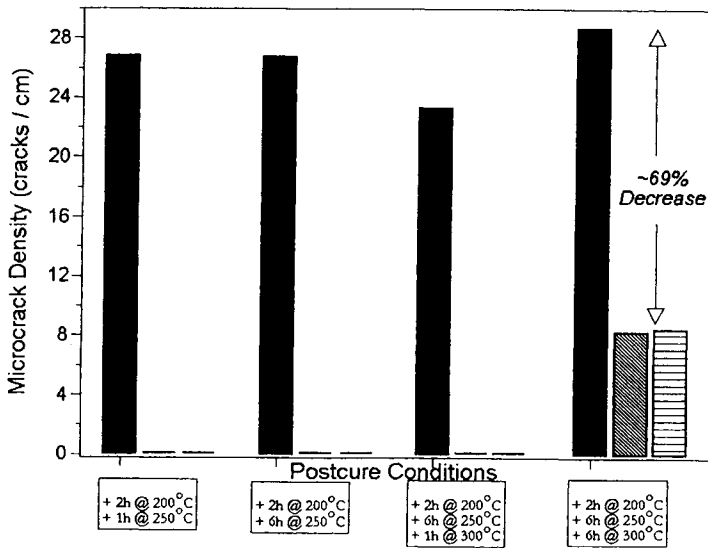


Fig. 8. Transverse microcrack density as a function of cure conditions. Initial cure cycle of:

■ 1.5 h at 177°C (1:1 molar), ▨ 8.0 h at 177°C (1:1 molar), and ▤ 8.0 h at 177°C (1:0.87 molar) for BMI-C fiber [0°/90°], composite laminates

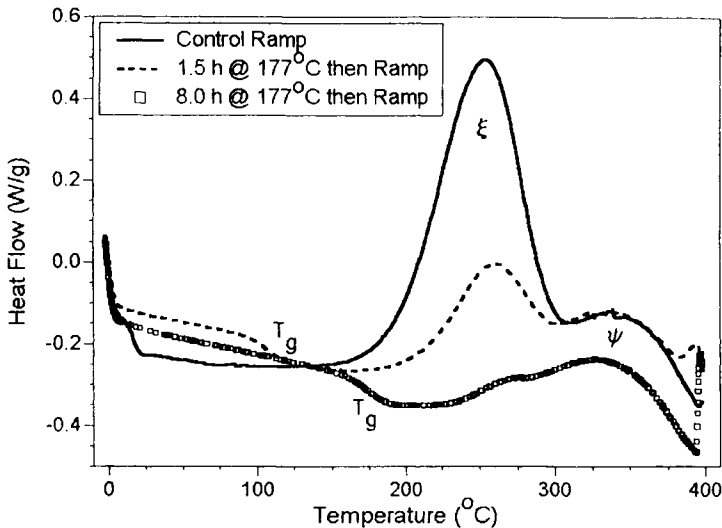


Fig. 9. Dynamic DSC scans of BMPM-DABPA (1:1 molar) BMI resin for (i) uncured (ii) 1.5 hr at 177°C and (iii) 8 hr at 177°C cures prior to DSC run diffusion-controlled portion of the reaction. Exposure to 177°C prior to the DSC run decreases the exotherm of the main cure ξ peak, that ultimately completely disappears after 8 hr at 177°C. Fig. 10 displays the degree of conversion as a

function of time at 177°C from the total exotherms associated with both the ξ and ψ peaks, and demonstrates that the degree of cure is 23% larger for 8 hr at 177°C versus 1.5 hr. The heat of reaction of both the ξ and ψ peaks as a function of initial cure time-temperature treatment are illustrated in Fig. 11.

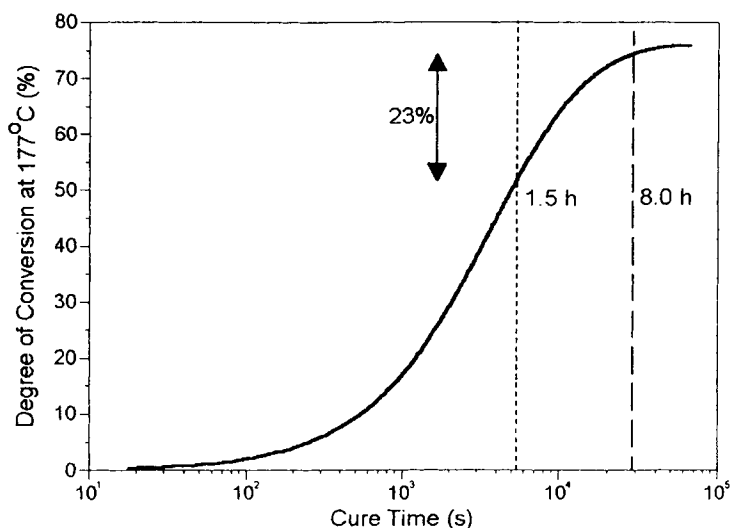


Fig. 10. Degree of conversion of BMPM-DABPA (1:1 molar) BMI resin as a function of time at 177°C prior to DSC run

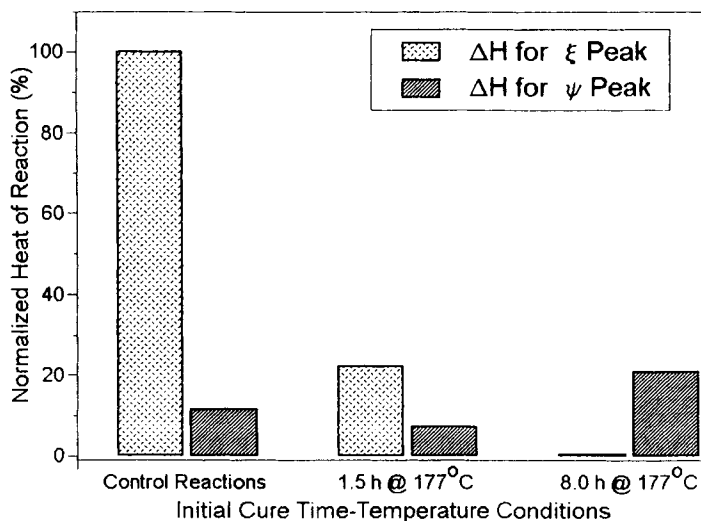


Fig. 11. The heat of reaction of the DSC and ψ peaks as a function of initial cure time-temperature treatment

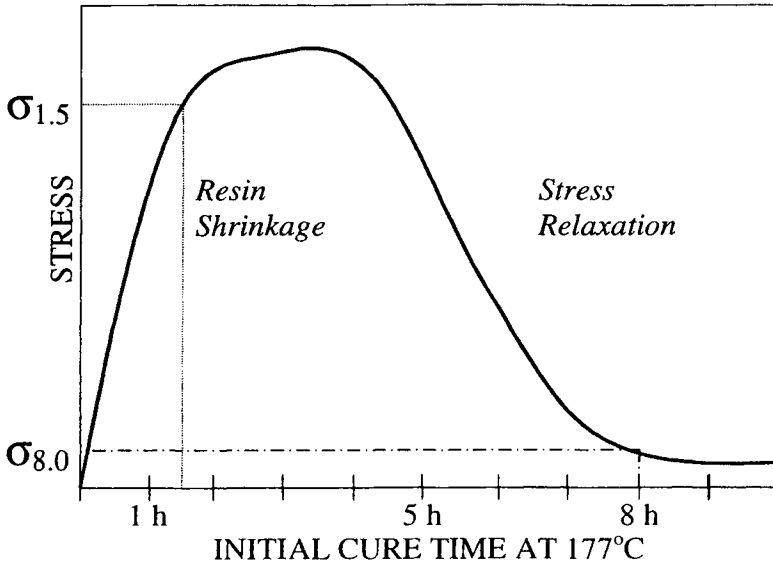


Fig. 12. Qualitative depiction of resin shrinkage stress development during the initial cure regime at 177°C for composite laminates

The longer 8 hr 177°C precure allows for slow further cure together with time for relaxation of the cure induced shrinkage stresses, as illustrated in Fig. 12. The elimination of these shrinkage stresses at 177°C, together with less cure and associate shrinkage stresses upon post-curing produces a stronger fiber-matrix interface band prior to cooling thus reducing the chances of fiber-matrix interfacial failure upon cooling. Note the in-situ ESEM studies indicated microcracks always initiated from fiber matrix interfacial failure during cooling as a result of two sources of stresses, namely (i) resin shrinkage stresses and (ii) mismatch in the coefficient of thermal expansion of the fiber and matrix, which is proportional to $(\alpha_M - \alpha_F) \Delta T$ where $\alpha_M - \alpha_F$ are the thermal expansion coefficients of the matrix and fibers and ΔT is the temperature difference from the temperature for the onset stress buildup (generally near the polymer matrix T_g or the highest composite fabrication temperature). For carbon fibers the thermal coefficient of expansion in the fiber longitudinal direction ($\alpha_{F,||}$) is approximately $-0.4 \mu\text{m}/\text{m}^\circ\text{C}$, whereas in the fiber transverse direction ($\alpha_{F,\perp}$) is closer to that of the polymer matrix with reported values of $+18 \mu\text{m}/\text{m}^\circ\text{C}$ [20]. Hence, any transverse stresses generated by $(\alpha_M - \alpha_{F,\perp})$ thermal mismatches are small compared to $(\alpha_M - \alpha_{F,||})$ - generated composite longitudinal stresses. As a result of these thermal mismatches the polymer is in compression transverse to the fiber direction with stress magnitudes in the 5 MPa range, and in tension

parallel to the fiber direction with stress magnitudes in the 15 – 25 MPa range [20].

While the fibers in unidirectional composites are generally subjected to compression, this is not the case in multidirectional laminates [21]. Hahn [21] has shown that transverse average stress in each ply of a laminate is tensile after cool-down. The transverse ply stress can be high enough to cause ply cracking, especially at low temperatures under dry environments. The residual ply stresses in a laminate can be determined by using laminate plate theory. For example, the transverse stress σ^R in 90° ply of a (0,90) symmetric laminate is given by

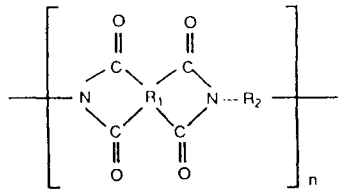
$$\bar{\sigma}_{90}^R = \frac{E_T}{1 + (1 + 2\nu)E} (e_L - e_T) \quad (1)$$

where e_L and e_T are the thermally induced lamina strains parallel and normal to the fibers, respectively, ν is the major Poisson ratio, and E is the modulus ratio E_T/E_L .

2.2. Polyimide composites

2.2.1. Background

Polyimides, PI, have found considerably application as high temperature composite matrices with T_g 's in the 200 to 450°C range. The structure of polyimides is represented by the general formula



where R_1 and R_2 are aromatic moieties.

PI – C fiber composites are, however, susceptible to hygrothermal induced degradation in present and future aerospace service environments. The hygrothermal degradation mechanisms are (i) composites blistering upon rapid heating as a result of moisture evolution from physically entrapped moisture and, also, repolymerization of hydrolytically degraded PI that chemically produces water molecules, and (ii) direct mechanical and thermal property deterioration caused by hydrolytic chemical depolymerization (Fig. 13) [22]. Over the last five years these degradation mechanisms have been characterized, which involved considerable utilization of thermal analyses techniques.

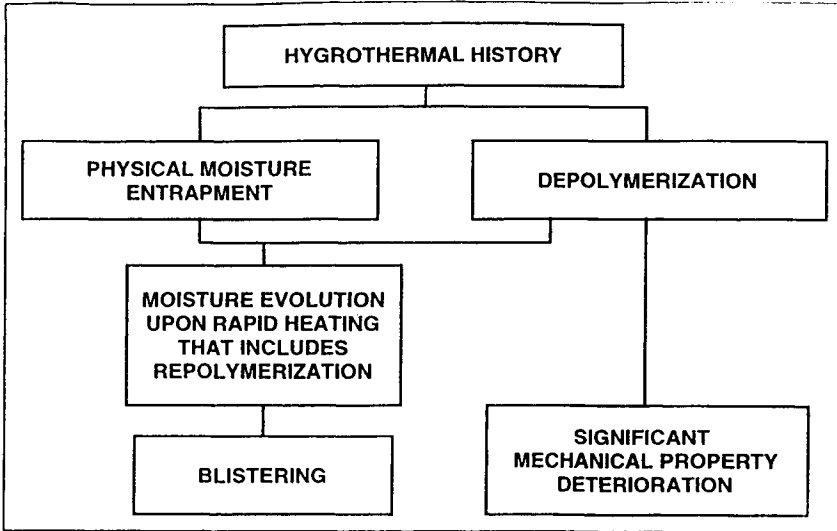


Fig. 13. Critical hygrothermal induced degradation mechanisms of polyimides

2.2.2. *Hygrothermal spike damage*

PI – C fiber composites absorb up to 2 wt% moisture. Upon exposure to a rapid thermal spike moist composites can blister. Blisters initiate within the

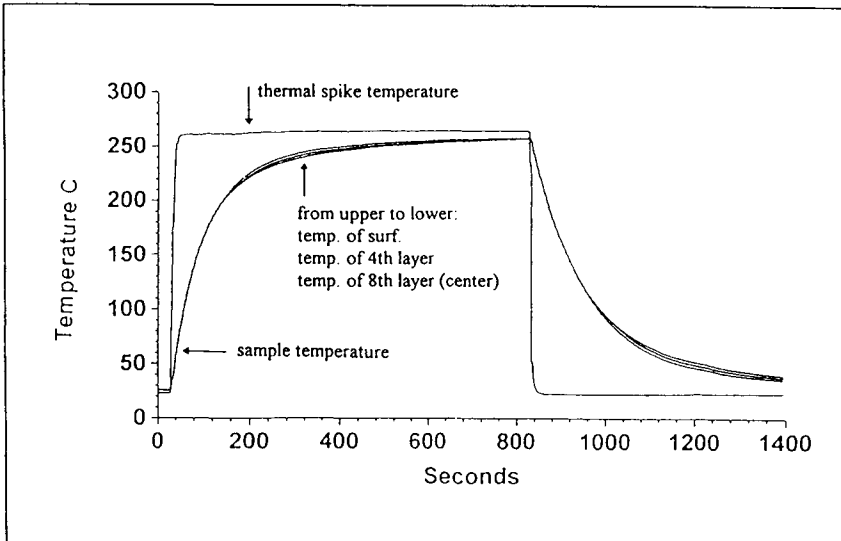


Fig. 14. Thermal spike temperature-time profile and actual composite temperature through 16 ply composite

resin and/or at the fiber matrix interface when the water vapor pressure exceeds the moisture, plasticized resin yield stress [23]. In Fig. 14 we illustrate a typical simulated thermal spike that composites can be exposed to in aerospace environments.

We have monitored the effects of hygrothermal spiking from 30°C to 250°C for up to 12 cycles on both wet and dry BMI's and PI's and their composites [14]. The PI in these studies was Avimid K3B (DuPont) formed from an aromatic diethyl esterdiacid and an aromatic diamine in N-methyl-2-pyrrolidone (NMP) with a dry T_g near 250°C. The most dramatic result observed was severe blistering of moisture saturated K3B-carbon fiber composites at 229°C at the first spike. Similar type of blistering was also observed in K3B neat resin after several more thermal spikes. However, all other specimens including dry K3B and all BMI resins and composites, wet or dry, showed no damage or structural morphological changes. Matrix cavitation and associated delamination depends on a series of variables such as (i) previous humidity-time-temperature exposure and associated moisture concentration profiles; (ii) component thickness; and (iii) rapid heat-time service environment exposures, such as thermal spikes. However, BMI-carbon fiber composites exhibit no evidence of blistering for a similar thermal spike. A thermoset is more resistant to cavitation and associated macro blistering for a similar thermal spike. A thermoset is more resistant to cavitation and associated macro blistering than a thermoplastic because

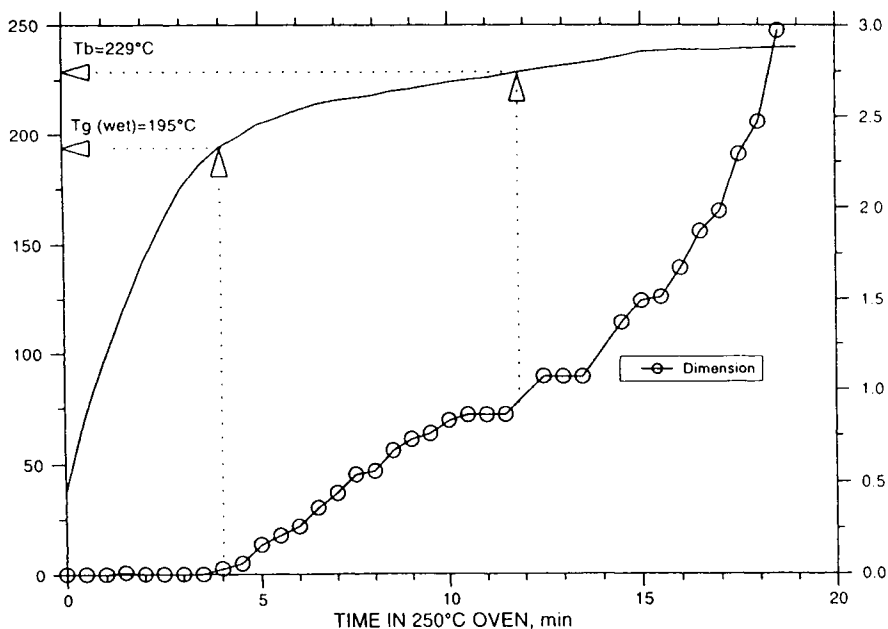


Fig. 15. Dimensional change of a wet K3B-PI-C fiber composite during thermal spiking

thermoset cavitation requires rupture of covalent crosslinked molecular segments. The onset of blistering was determined by monitoring a dimensional thickness change of the specimen using a high temperature precision dial indicator with 0.01 mm resolution. In Fig. 15 we show the dimensional of a wet K3B-C fiber composite during a thermal spiking. The composite blisters at 229°C and the wet T_g was detected to be 195°C.

Moisture weight gain behavior was monitored during the entire thermal spike exposure, illustrated in Fig. 16. The exposure cycle consisted of three steps, *i.e.*, (i) initial saturation at 30°C, 90% RH, (ii) absorption and desorption during thermal spiking, and (iii) desorption during dry conditioning at 80°C in vacuum. Both [0/90] and [0] BMI composite laminates were used to identify the effects of microcracks on moisture absorption behavior. The crossply laminate always contained cure-induced microcracks while the unidirectional laminate was completely microcrack-free. At the initial wet conditioning the BMI composite and K3B resin reached the equilibrium moisture saturation in a relatively short exposure time per thickness while K3B composite and BMI resin were still absorbing moisture even after the extended exposure time. During thermal spiking, BMI resin, BMI unidirectional composite, and K3B composite behaved similar, *i.e.*, (i) the moisture content decreased gradually at the early

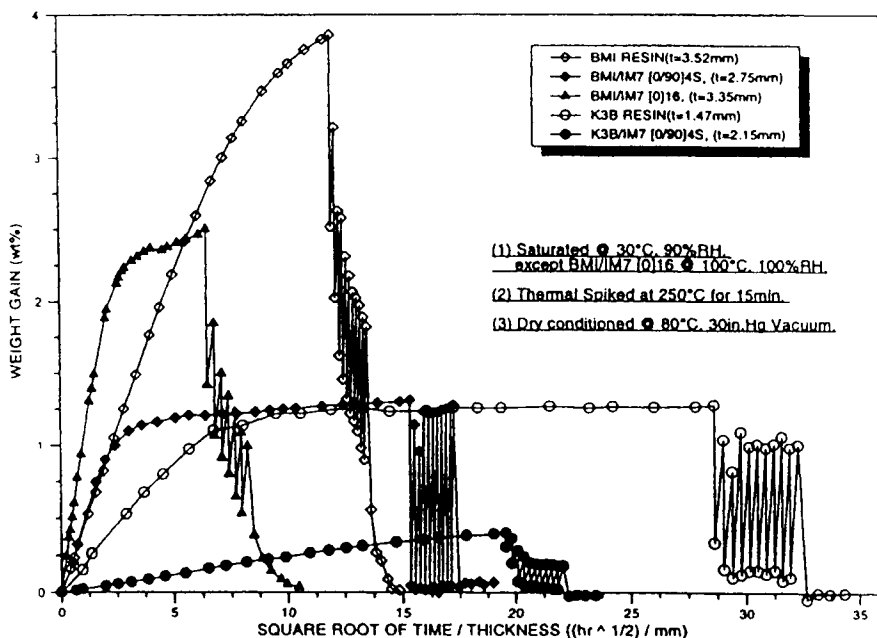


Fig. 16. Moisture absorption-desorption behavior for BMI and PI resins and their composites as a function of thermal spike exposure cycles

spikes until leveling off at about 50 w% loss and (ii) the amount of water in and out during thermal spiking was about 30 - 40% of maximum moisture content. On the other hand, both cross-ply BMI composites and K3B resin always maintained a high moisture content and almost 80 to 90w% gain and loss during spiking which implies high diffusion rate of the systems. In the cross-ply BMI composites the microcracks are the main cause of the high diffusion rate of the systems. In the cross-ply BMI composites the microcracks are the main cause of

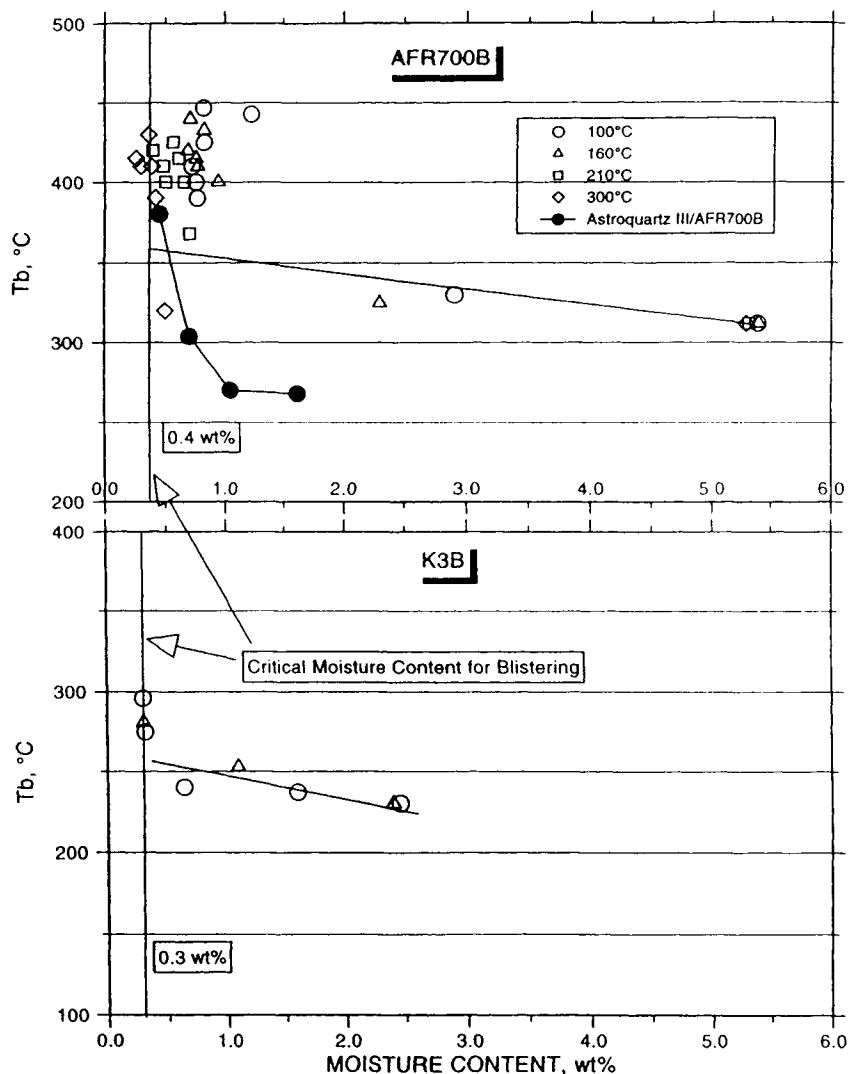


Fig. 17. Blister initiation temperature T_g as a function of initial moisture content for K3B and AFR-700B PI's

the high diffusivity while the intergranular boundary effect is suspected for K3B resin since the resin plaque was fabricated by compression molding of a fully imidized K3B powder. It was also observed that the diffusivity of the K3B composites was almost doubled after the spiking exposures because of the hygrothermal-induced damage; micro-cavitation, blistering and delamination. Interestingly enough, there are always some residual moisture left in all BMI/IM7 composites regardless of drying time while BMI resin, K3B resin and composites came back to the original dry weight. This is most likely due to that the wet T_g of the BMI composites is higher than the spiking temperature so that some lock-in moisture can not diffuse out at lower drying temperature.

The amount of absorbed moisture to cause blistering in the neat PI's such as K3B and AFR-700B is quite low. (AFR-700B is a fluorinated PI with norbornene crosslinks and a T_g in the 325 - 350°C range). In Fig. 17 we show plots of blister temperature T_g versus initial moisture content for these polyimides and the critical moisture content for blistering is only 0.3 wt% for K3B and 0.4 wt% for AFR-700B PI's. These small amounts of moisture can originate for absorbed, mobile moisture that can't diffuse quickly enough out of the composite during thermal spike exposure or from repolymerization of hydrolytically degraded polyamic acid with subsequent water generation (see following section on chemical hydrolytic degradation of PI's) or from molecularly "locked-in" moisture. In the latter case at higher temperatures new matrix H-bonding sites become available to moisture as the molecular structure of the matrix expands with temperature. Upon relatively rapid cool-down water molecules can become locked into molecular cages and can only diffuse out upon subsequent exposure to high temperatures. Such water molecules can not be released at low temperatures but upon release at higher temperatures act as plasticizers and blistering agents. In controlled isothermal drying experiments we observed in the 130°C to 180°C temperature range ≥ 0.2 wt% moisture can not be removed from K3B and AFR-700B PI's after 200 hrs under vacuum [24].

Hence, small quantities of absorbed moisture can cause blistering of thermoplastic PI's upon exposure to hygrothermal spikes.

2.2.3. Hydrolytic degradation

PI's are susceptible to hydrolytic polymer chain scission as a result of (i) scission of any inherent amide group defects present as a result of non-ring closure to the imide ring and (ii) imide ring opening to amide formation followed by scission of the amide group. Hydrolytic attack of the imide ring reverses the polymerization reaction, Fig. 18, resulting in the formation of the polymamic acid, followed by chain scission and associated molecular weight and strength decreases resulting ultimately in regeneration of the monomers [18,22,25-26, 28]. The geometric position of the hydrolytic induced scission in a thermoplastic polymer chain or in a thermoset crosslinked network can significantly effect the

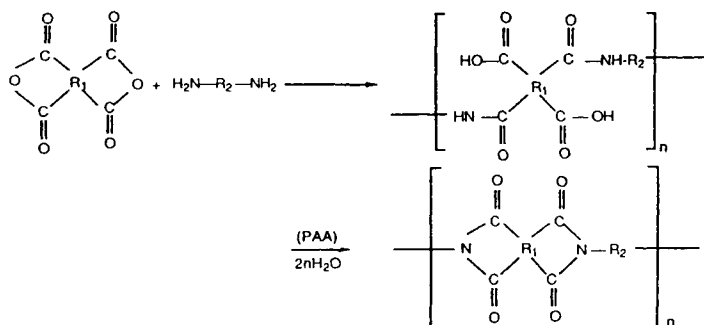


Fig. 18. Polyimide polymerization reaction

resulting mechanical strength decrease [18]. For the thermoplastics, one random scission per macromolecule, which is a scission of <1% of the total inherent initial imide rings causes the strength to decrease by ~ 50% [18]. However, if hydrolytic attack preferentially occurs at the ends of the macromolecules, as we have observed for Kevlar, polyphenylene terephthalamide, macromolecules that results in acid or amine monomer formation [27] there is no direct initial strength decrease. The acid monomer can, however, catalyze hydrolytic random chain scission because acids can accelerate imide and amide hydrolyses by upto ~ 10^5 times faster [1]. For thermosets, hydrolytic scission at a crosslink rather than in an inter-crosslink network segment would cause more serious mechanical property deterioration because crosslink scission generates 1.5 to 2 times greater

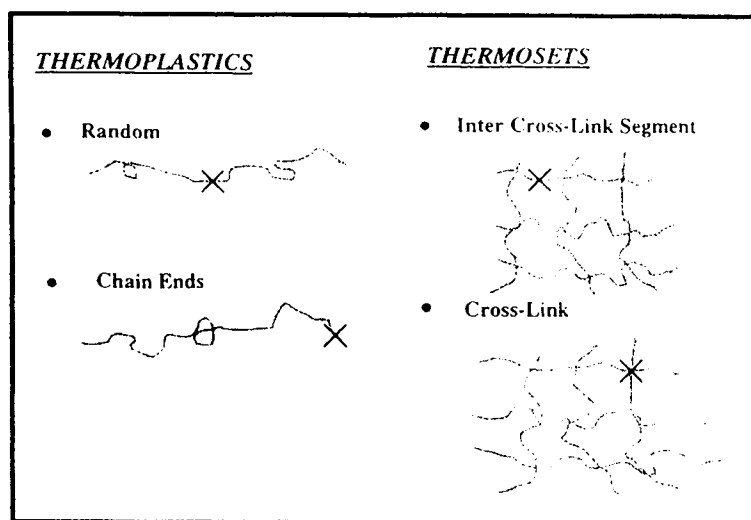


Fig. 19. Schematic presentation of PI hydrolytic molecular scission degradation mechanisms

number of disconnected network defects, depending if the crosslink has 3 to 4 network interconnections. In Fig. 19 we schematically represent the PI hydrolytic molecular scission degradation mechanisms.

In order to ascertain the characteristic and kinetics of hydrolytic degradation of PI's where $< 1\%$ scissions can cause a $\sim 50\%$ decrease in strength requires:

- Accelerated high temperature (177 - 250°C hygrothermal exposures that can cause measurable thermal property changes in terms of days exposure rather than year time frames at lower temperatures ($\leq 100^\circ\text{C}$).
- The utilization of DSC to monitor T_g shifts (reversible and irreversible), polyamic acid and monomer formation and the irreversible decomposition of the monomers themselves, together with TGA for weight loss.

Other characterization techniques, such as, FTIR to monitor imide group disappearance and sensitive gel permeation chromatography, GPC, to monitor molecular weight changes can be utilized to compliment DSC observations.

A conventional pressure bomb method was used to simulate a high temperature steam environment at temperatures ranging from 177°C to 250°C, which were based on actual in-service temperature range, and times from 30 minutes up to 64 days [26]. The PI's studied were K3B, AFR-700B and PETI-5 PI's. (PETI-5 is a fully imidized oligomer with phenylethyl terminated ends that form crosslinks in the 350–375°C temperature range).

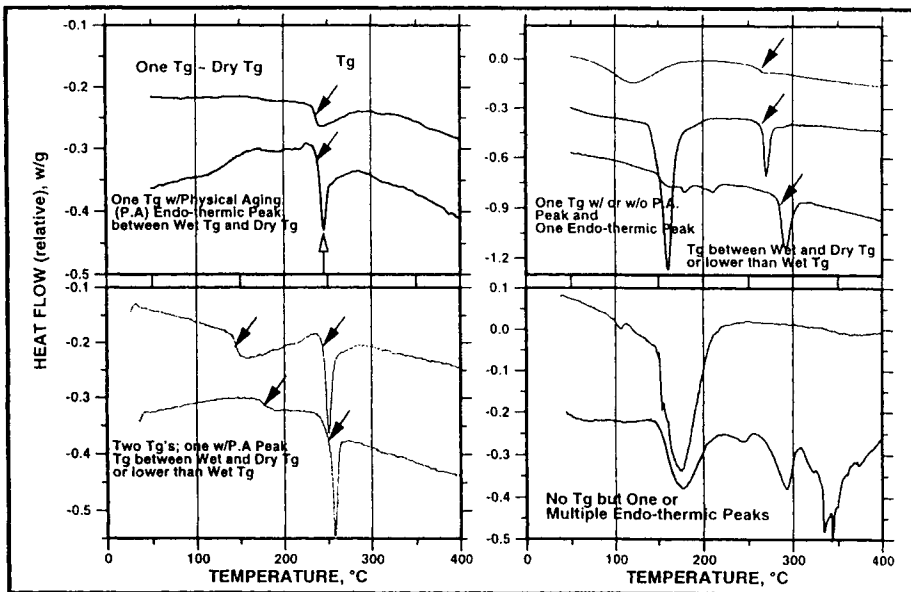


Fig. 20. Typical DSC curves from first scan of PI's after exposure

Fig. 20 shows the typical DSC curves from the first scan after various hydrothermal aging exposure for the three PI systems studied. In the figure, the curves are in the order of longer exposure time and/or higher exposure temperature from top to bottom and from left to right. Lower exposure temperatures and/or shorter exposure times normally did not alter the type of DSC curve significantly, *i.e.*, a clear glass transition at the temperatures near or lower to the original dry T_g , but in some cases, the glass transition was mixed with a sharp endothermic peak that was known as a typical enthalpic relaxation peak due to physical aging effects. In those cases, calculating an actual T_g that can be comparable to others without the physical aging effects was not straightforward as will be discussed later. With increasing exposure time and/or higher exposure temperature, the curves appeared with either an additional glass transition at the lower temperature region that could be considered as a T_g of polyamic acid or low Mw polymer chains by the hydrolytic induced scission, or an endothermic peak at temperatures much lower than the polyimide T_g that could be from melting of crystalline monomer species. Eventually, when the exposure temperature was very high and/or the exposure time was much longer, the glass transition disappeared from the DSC curve and was replaced by one or multiple endothermic peaks. Thus, from either the characteristic shape of DSC

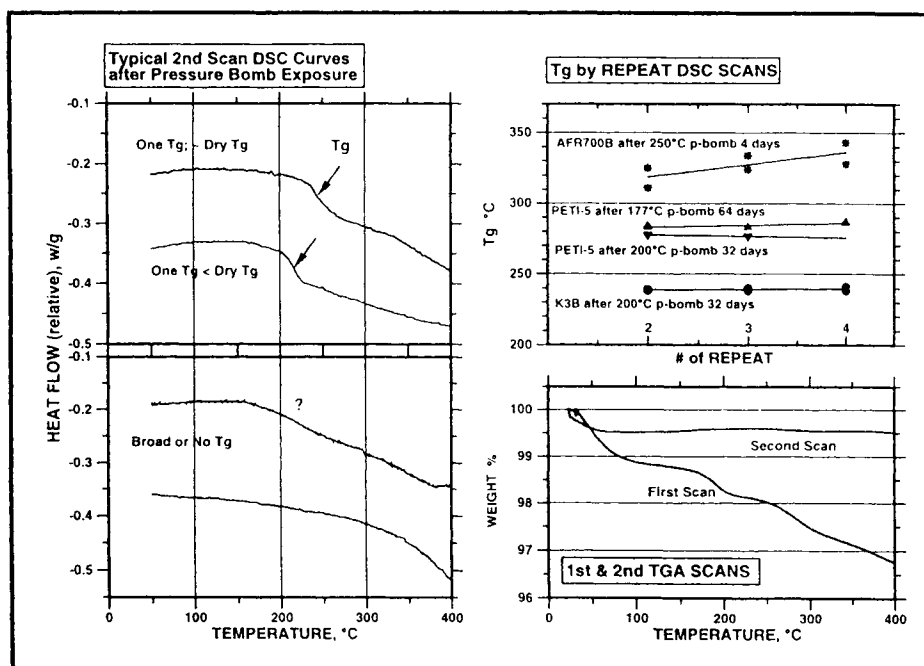


Fig. 21. Typical DSC curves from second scan after exposure and their stability

curve or T_g changes one can easily estimate the mode or stage of the degradation process and the degree of degradation, respectively.

The typical DSC curves from the second scan are plotted in Fig. 21, and this information was used to determine whether the degradation process was reversible or irreversible and then how much if irreversible, especially by the T_g shift. The degraded polymer was assumed to be re-polymerized during the first scan to 400°C since it was higher than the original imidization and/or cure reactions in the case of the thermosetting systems. Therefore, the recovery of T_g values compared to the original dry T_g can be used as a quantitative indicator of permanent irreversible degradation whilst the 100% irreversible degradation was indicated by no T_g appearance. In order to further justify this assumption, it was necessary to evaluate the stability of the second scan T_g . Even though AFR700B showed a slight increase of T_g with the number of further repeat scans, they can be considered as a stable quantity of material status. TGA weight loss results were also supportive of the consideration (Fig. 21).

As indicated in Fig. 20 because of the physical aging induced endothermic peak, especially in K3B and PETI-5 the actual T_g calculation was somewhat cumbersome. However, based on the assumption that the degree of physical aging effect is linearly proportional to the endothermic peak area, and thus the peak temperature, a conversion factor to calculate actual T_g from the endothermic peak temperature versus endothermic peak area correlation, as

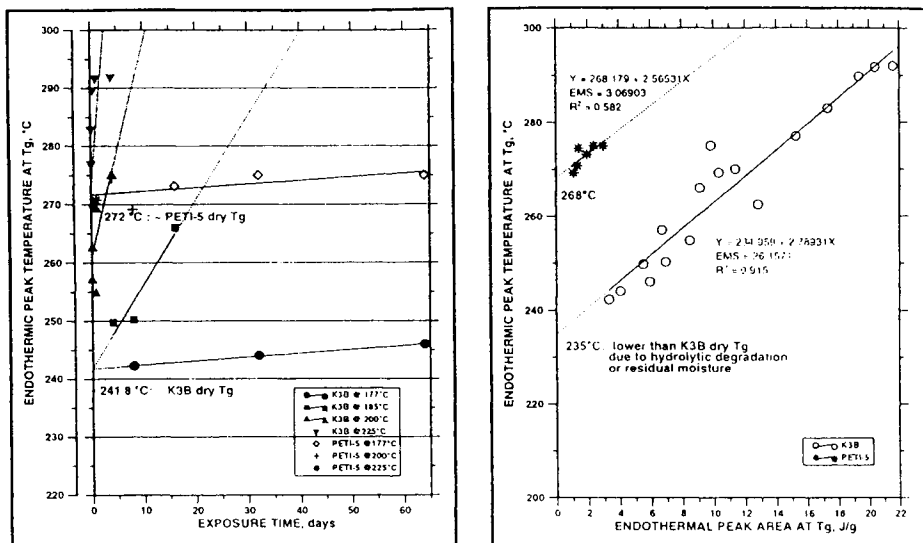


Fig. 22. Calculation of actual T_g from physical aging induced endothermic peak temperature

shown in Fig. 22. It is also of interest to note that K3B showed a linear correlation between the endothermic peak temperature and exposure time and the physical aging was strongly dependent on exposure temperatures and time. In the case of PETI-5 the relation was temperature independent and the effects of physical aging were much less because of its partially cross-linked network structure. In the case of AFR-700B which is a highly cross-linked thermoset system, the physical aging effect was not noticeable.

The hydrolytic degradation of imide group has been characterized by FT-IR analyses in detail [26]. The typical IR spectra from the starting materials and the exposed materials at 250°C pressure-bomb for various intervals are shown in Figs. 23 through 25 for K3B, PETI-5 and AFR-700B, respectively. In the cases of K3B and AFR-700B, the spectra basically showed peaks from imide ring structures disappearing with the hygrothermal exposure (dashed lines in Figs. 23 and 25 and new peaks related to the monomer structure appearing with the exposure time (solid lines in Figs. 23 and 25). This simply indicates that those polyimides were depolymerized by imide ring opening resulting in the formation of the polyamic acid, followed by further chain scission and thus regeneration of the monomers or even de-monomerization processes. However, in the case of PETI-5, there were no significant changes in peak positions but considerable changes in peak intensities, which was indicative of possible changes in network structure due to the hygrothermal aging, provided that the IR intensity was partly

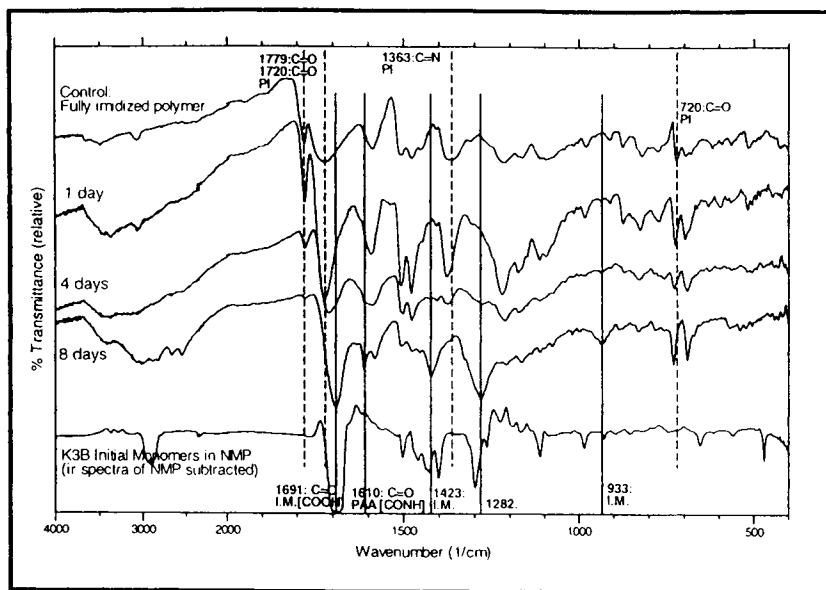


Fig. 23. FTIR spectra of K3B PI after 250°C hydrothermal exposure

dependent on mobility/flexibility of the polymer chains. Similar results but at different intensities were also observed from the exposed samples at other

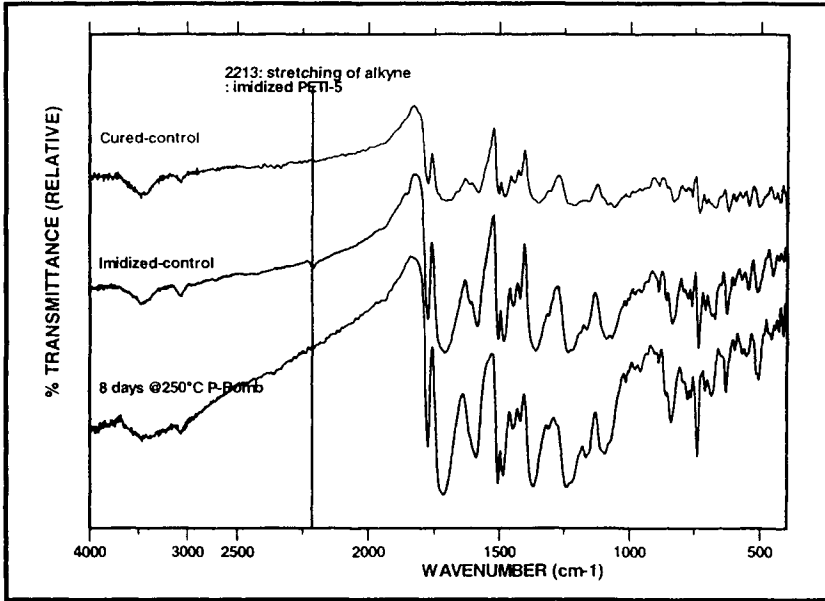


Fig. 24. FTIR spectra of PETI-5 PI before and after 250°C hydrothermal exposure

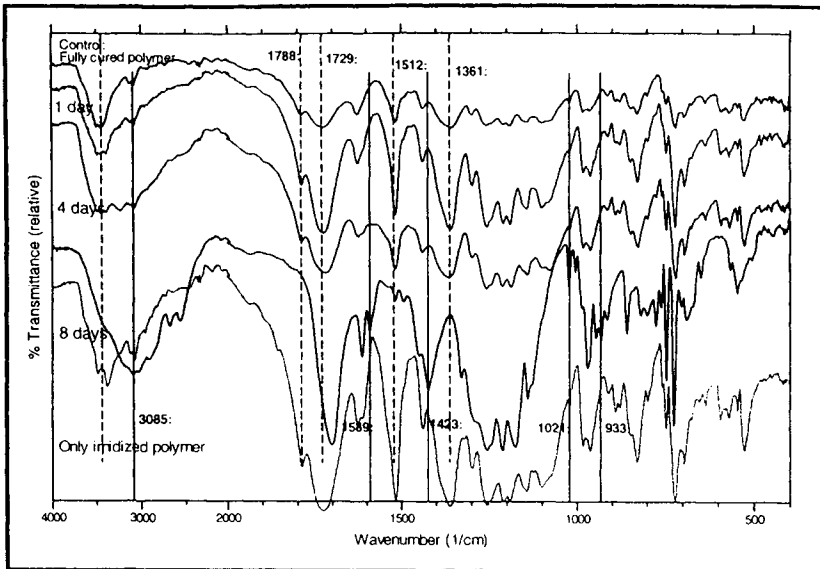


Fig. 25. FTIR spectra of AFR-700B PI after 250°C hydrothermal exposure

exposure temperatures.

This hydrolytic induced chain scission was also confirmed by a significant residual mechanical property deterioration in K3B [15,26] and AFR-700B [15,22]. After 1,000 hours hydrothermal exposure at 160°C, AFR-700B had lost ~ 70% strength and 85% strain-to-failure while K3B lost about 18% strength and 21% strain-to-failure, but after 24 hrs exposure at 200°C, the strength of K3B deteriorated by ~ 95%. AFR-700B strength deteriorated much more rapidly than K3B.

Based on primarily the DSC results a hydrothermal degradation phase diagram was developed for the PI's in terms of actual exposure time and temperature for the onset of various degradation modes [28]. These modes were (i) depolymerization of the PI to polyamic acid (ii) further depolymerization to the monomers and (iii) irreversible degradation by decarboxylation of the diacid monomer, and their threshold temperature-time characteristics for the PI's are shown in Fig. 26. From Fig. 26, it can be concluded that the order of PI hydrolytic degradation susceptibility is AFR-700B > K3B > PETI-5. AFR-700B is the most susceptible as a result of hydrolytic scission of norbornene derived

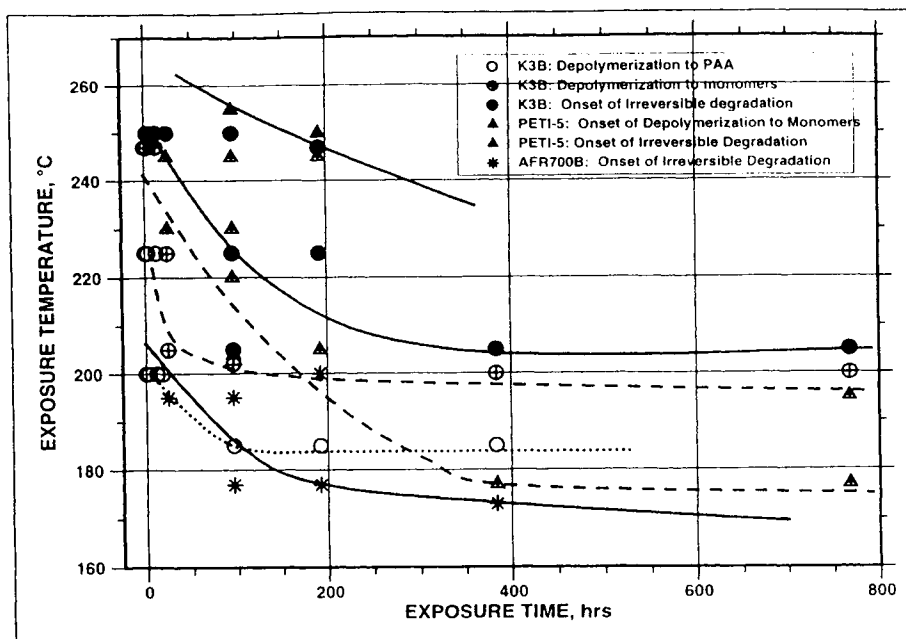


Fig. 26. Hydrothermal degradation phase diagram of PI's for exposure temperature versus exposure time for onset conditions for (i) depolymerization to polyamic acid, (ii) depolymerization to monomers and (iii) irreversible degradation

crosslinks formed by the Michael addition reaction. Nuclear magnetic resonance, NMR, studies show the susceptibility of these norbornene crosslinks to hydrolytic chain scission [29-31]. The K3B PI higher rate of hydrolytic degradation relative to that of PETI-5 PI is most likely a result of preferential hydrolytic attack of the ends of the macromolecules that results in acid and arrive monomer formation, as has been observed for Kevlar, polyphenylene terephthamide [27]. As mentioned earlier in this section, the acid monomer can catalyze hydrolytic random chain scission of the imide and amide groups of the K3B by upto $\sim 10^5$ times faster [1]. PETI-5 PI contains no macromolecular ends and the phenyl ethynyl derived crosslinks are paraffinic in nature and thus are hydrolytically resistant.

As a result of these findings the norbornene PI oligomer end groups of AFR-700B have been replaced with phenyl ethynyl groups, as shown in Fig. 27. Initial characterization of the structure-property relations of the AFR-PEPA-N resins show good hydrolytic resistance, processibility and thermomechanical properties with T_g 's upto 450°C [32].

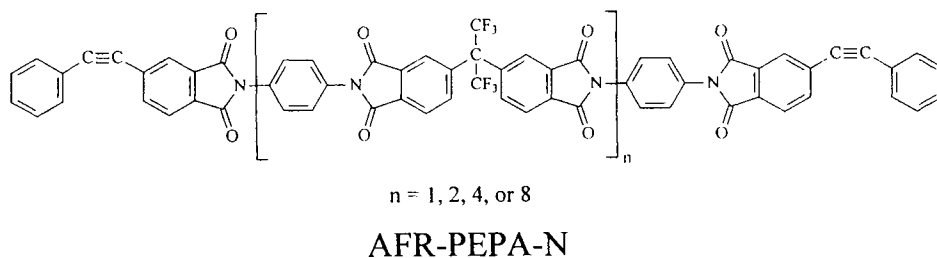


Fig. 27. The structure of the 4 - (phenylethynyl) phthalic anhydride (PEPA) end capped AFR-N imide oligomer

3. CONCLUDING REMARKS

In this chapter we have addressed the utilization of thermal characterization procedures, supplemented by other characterization techniques, to study the performance deterioration mechanisms of high temperature PMFC's. For bismaleimide matrices and their composites (i) the characterization of further cure and structure-property modifications and (ii) composite microcrack formation and prevention by modification of the cure cycle were addressed. In the case of polyimide matrices and their composites hygrothermal induced degradation in terms of (i) water vapor physical, induced blistering and (ii) chemical, hydrolytic chain scission characteristics and mechanisms were addressed.

REFERENCES

1. R. J. Morgan, "Thermal Characterization of Composites", Chapter 9 in *Thermal Characterization of Polymeric Materials* (2nd Edition), Ed. E.A. Turi, Academic Press, Inc., 1997, pp. 2091-2261.
2. AASHTO, (1996), "The Bottom Line: Transportation Investment Needs 1998-2002", American Association of State Highway and Transportation Officials (AASHTO).
3. Civil Engineering Research Foundation, (1993), "High Performance Construction Materials and Systems: An Essential Program for American and Its Infrastructure", Executive Report 93-5011.
4. R. J. Morgan, E. E. Shin, C. Dunn, R. J. Jurek and A. Jurek, Proc. of 39th SAMPE Conf., 39 (1994) 1564.
5. H. H. Man and R. J. Morgan, Proc. of 7th ASM/ESD Advanced Composites Conf., Detroit, MI, 555, (1991).
6. R. J. Morgan, R. J. Jurek, A. Yen and T. Donnellan, *Polymer*, 34 (1993) 835.
7. E. E. Shin, R. J. Morgan, Proc. of ANTEC 93 on Plastic Engineering, SPE, II, 1357, (1993).
8. E. E. Shin, Q. Zheng and R. J. Morgan, Proc. of SEM 50th Ann. Spring Conf. On Experimental Mechanics, SEM Inc., 366, (1993).
9. E. E. Shin, R. J. Jurek, L. T. Drzal, R. J. Morgan, J. K. Choi and A. Lee, Proc. of ASME Meeting, San Francisco, 183, (1995).
10. E. E. Shin, C. Dunn, E. Fouch, R. J. Morgan, M. Wilenski and L.T. Drzal, Proc. of ASME Meeting, San Francisco, 191, (1995).
11. R. J. Morgan, E. E. Shin, J. E. Lincoln, J. Choi and A. Lee, Proc. of 28th National SAMPE Tech. Conf., Seattle, WA, Nov., 1996, pp. 213-224.
12. E. E. Shin, R. J. Morgan, M. Wilenski, J. Zhou, J. E. Lincoln and L.T. Drzal, Proc. of 28th Nat'l SAMPE Tech. Conf., Seattle, WA, Nov., 1996, pp. 225-235.
13. R. J. Morgan, E. E. Shin, B. Rozenberg, and A. Jurek, *Polymer*, 38 (1997) 639.
14. E. E. Shin, R. J. Morgan, J. Zhou, J. Lincoln, R. Jurek and D. B. Curliss, Proc. of American Soc. For Composites, 12th Technical Conf., Technomic Co., Dearborn, MI, October 1997, pp. 1113-1122.
15. R. J. Morgan, E. E. Shin, J. Lincoln, J. Zhou, L. T. Drzal, A. Lee and D. B. Curliss, Proc. of High Temple Workshop XVIII, Hilton Head, SC, January, 1998, Paper Q.
16. B. A. Rozenber, G. N. Boiko, R. J. Morgan and E. E. Shin, *Polymer Sci. Ser. A*, 43 (2001) 386.
17. B. A. Rozenber, E. A. Dzhavadyan, R. J. Morgan and E. E. Shin, *Polymer Sci. Ser. A*, 43 (2001) 400.
18. R. J. Morgan, E. E. Shin and J. Zhou, Proc. of 44th International SAMPE Symposium, Long Beach, CA, May, 1999, pp. 1098-1110.
19. J. E. Lincoln, R. J. Morgan and E. E. Shin, "Fundamental Investigation of Cure-Induced Microcracking in Carbon Fiber/Bismaleimide Cross-Ply Laminates", *Polymer Composites* (In Press).
20. J. A. Nairn and P. Zoller, *J. Mater. Sci.*, 20 (1985) 355.
21. H. T. Hahn, *J. Astronaut. Sci.*, 32 (1984) 253.
22. R. J. Morgan, E. E. Shin, J. E. Lincoln, J. Zhou, L. T. Drzal, M. S. Wilenski and A. Lee, Proc. of 43rd International SAMPE Symposium, Anaheim, CA, May/June, 1998, pp. 106-119.

23. Z. Zheng and R. J. Morgan, *J. Comp. Mater.*, 27 (1993) 1427.
24. E. E. Shin, R. J. Morgan, J. Zhou, J. Lincoln and R. Jurek, *J. of Thermoplastic Composite Materials*, 13 (2000) 40.
25. C. J. Wolf and R. S. Solomon, *Proceedings of National SAMPE 15th Technical Conference*, Cincinnati, OH, pp. 504-510, (1983).
26. E. E. Shin, R. J. Morgan, J. Zhou, J. K. Sutter and M. A. Meador, *Proceedings of 44th International SAMPE Symposium*, Long Beach, CA, 2382-2396, May, (1999).
27. R. J. Morgan and N. L. Butler, *Polymer Bulletin*, 27 (1992) 689.
28. E. E. Shin, R. J. Morgan and J. Zhou, *Proc. of 45th International SAMPE Symposium*, Long Beach, CA, (2000).
29. D. B. Curliss, *Proc. of the 28th Int'l SAMPE Tech. Conf.*, pp 790-796, (1996).
30. K. E. G. Thorp, D. Curliss and W. A. Price, *Proceedings of High Temple Workshop XX, Paper W*, San Diego, CA, (2000).
31. W. A. Price and D. Curliss, *Proceedings of High Temple Workshop XX, Paper V* Sand Diego, CA, (2000).
32. J. E. Lincoln, W. A. Price, D. B. Curliss and R. J. Morgan, *Proc. of High Temple Workshop XXI, Clearwater Beach, FL, February 2001, Paper I*.

Chapter 13

Thermal analysis and calorimetry of elastomers

Donald J. Burlett and Mark B. Altman

Goodyear Tire & Rubber Company, 142 Goodyear Blvd., Akron, Ohio, 44305

1. INTRODUCTION

Elastomers are a unique and industrially important class of polymers. The wide variety of polymers that are included in this class possess a range of physical properties that provide a large variety of potential applications. Their properties make them useful for applications ranging from tires and conveyor belts to medical tubing and erasers.

The unique physical properties of elastomers are due to the chemical composition of the polymers. The very nature of the viscoelastic behavior of elastomers is due to the chemical structures of the monomer units used to build them. Additionally, their low glass-to-rubber transition temperatures, their ability to form networks and their interaction with fillers result from these chemical structures. At the same time, these chemical structures make the polymers vulnerable to thermal and oxidative degradation. To achieve the desirable physical properties and to retain them, it is important to understand the structure of the polymers themselves, their interaction with other polymers, the multitude of additives used with them and the stability of these sometimes fragile polymers.

Many analytical techniques have proven useful in the characterization of elastomers. Among the most commonly used are nuclear magnetic resonance (NMR), infrared (IR) and Fourier Transform infrared spectroscopy (FTIR), mass spectrometry (MS), gel permeation chromatography (GPC) and a host of rheology-based techniques. However, one class of analytical techniques that has proven extremely important to the characterization of elastomers is that of thermal analysis and calorimetry. There are a large number of thermal-based techniques that are routinely used to characterize both the chemical and physical aspects of elastomers.

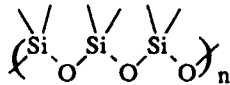
Because each elastomer possesses a unique set of properties, the applicability of different calorimetric and thermal analysis techniques to the elastomers varies. To fully understand which of the techniques is most useful for

examining each of the elastomers, it is important to first understand the fundamental differences between the structure and properties of the various elastomers. Then, the choice of application of the different techniques to the characterization of the elastomer and its uses will become clearer.

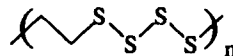
1.1. Viscoelasticity

The most important characteristic of this class of polymers is elasticity - the ability to undergo large elastic deformations. In simple terms, this means the ability to stretch and reversibly return to its original shape. The key requirement for this ability (being “rubbery”) is that the polymer consist of long, flexible chainlike molecules. From a chemical standpoint, the backbone should be made up of many non-collinear single valence bonds capable of rapid rotation about the backbone possibly as a result of thermal agitation. Many of the monomer repeat units of common elastomers fit this description, as shown in Fig. 1. Thermoplastic elastomers also contain these flexible, long chain segments and expectedly show the same “rubbery” behavior.

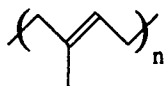
These viscoelastic properties are controlled by both the chemical nature of the structural units shown in Fig. 1 and other factors including, but not limited to the sequence of the monomer units, the molecular weight and molecular weight distribution, the presence or absence of branching from the main chain and gelling and/or crosslinking. The memory (elasticity) and the dissipative (viscous) properties of the polymer depend on the time scale of the experiment (or application) as it relates to the relaxation times which are characteristic of the elastomer structure. These relaxation times are influenced by the factors mentioned above and by time and temperature. It is this relationship between the relaxations to time and temperature that make them ideally suited to characterization by calorimetric and thermal analysis methods.



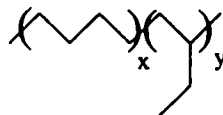
Polydimethylsiloxane (PDMS)



Polysulfide rubber (T)



Polyisoprene (IR)



Polybutadiene (BR)

Fig. 1. Examples of elastomer repeat units (PI, PBd, PDMS, T)

1.2. Glass-to-rubber transition

Simply, the glass-to-rubber transition temperature (T_g) or glass transition temperature is the temperature at which the polymer undergoes a change from a glassy, organized structure to a rubbery, amorphous structure. A unique characteristic of many elastomers is that their T_g is typically below room temperature, in many cases significantly below room temperature. When different polymers are compared to each other at equal temperature differentials from their T_g , they often behave similarly. Since elastomers have such low T_g 's, at room temperature they are far enough above T_g , to have relaxation times short enough to allow them to deform under relatively low stresses in reasonably short periods of time. This indicates that the lower temperature T_g 's contribute to the "rubbery" character of the polymers.

The T_g is characterized not by a change in volume with respect to temperature but rather by a change in the rate of change of the volume with respect to temperature. With respect to thermal analytical characterization, the determination of this transition must be performed with knowledge and careful control of experimental conditions because the position of this transition is a function of the rate of the measurement. Of course, the exact temperature determined for the T_g will depend on the thermal history of the material, rate of temperature change during the measurement and the characteristic time scale of the measuring probe.

The temperature of this glass-to-rubber transition has an effect on the physical properties of the elastomer. As will be shown later, the temperature of this transition varies widely among elastomers and can be used to predict various physical properties.

1.3. Crystallinity

There are many elastomers that have small to moderate amounts of crystallinity within their matrix. These crystallites can act as reinforcing domains within the matrix and can be considered as physical crosslinks which permit the unvulcanized semi-crystalline rubber to support stress for indefinite periods of time. Even more important is the ability of some elastomers to crystallize upon being stressed, producing a state in which this stress-induced crystallization raises the strength of the polymer. The rapid melting of these stress-induced crystallites permits rapid strain and stress recovery. This type of crystallinity is unique to elastomers and is differentiated from the crystallinity observed in other classes of polymers. This difference in crystalline nature may well give rise to the most advantageous properties of an elastomer.

Polybutadiene (BR), some ethylene-propylene (EP) rubbers and many Thermoplastic elastomers (TPE's) have a significant amount of crystallinity at room temperature. Other rubbers, such as natural rubber (NR) and butyl rubber

(IIR) crystallize significantly when stressed. These differences are important factors in determining the physical character of the elastomer.

1.4. Chemical composition

The chemical composition of an elastomer plays an important role in its physical and chemical properties. Many aspects of the incorporation of different monomers are important to these characteristics. Among the controlling factors are:

- a) number of monomers incorporated (homopolymers versus copolymers – polybutadiene versus styrene-butadiene rubbers) and ratio of monomers (trace amounts to equal amounts of co-monomers - high versus low styrene content in SBR)
- b) microstructure (incorporation of monomers in variety of ways; vinyl-1,2- versus *trans*-1,4- versus *cis*-1,4- incorporation of butadiene monomer)
- c) distribution of monomers in a copolymer (random versus block)
- d) degree of branching (for example, linear versus star-branched)
- e) molecular weight (high versus low molecular weight)
- f) gel (highly gelled to totally gel-free)

Each of these characteristics of the chemical structure of an elastomer has a bearing on the physical and chemical nature of the resulting elastomer.

1.5. Additives

Elastomers by themselves are somewhat limited in their utility. It is by the addition of numerous different types of materials (additives) that elastomers provide the widest variety of uses. The following is a list of various additives that are commonly used to enhance and expand the properties of elastomers. Each class has a specific purpose for addition.

- I. Reinforcing Agents and Inert Fillers (to increase modulus and improve strength)
 - a. Carbon blacks
 - b. Silicas
 - c. Others (talc, clays, inorganics, short fibers, etc.)
- II. Oils (to improve extensibility or act as a simple extender)
 - a. Aromatic oils
 - b. Paraffinic oils
 - c. Others
- III. Curing agents (to form networks with the elastomer molecules)
 - a. Vulcanizing agents (actual crosslink forming materials)
 1. Sulfur
 2. Peroxides

- 3. Others (bis-maleimides, zinc oxides, etc.)
 - b. Accelerators (materials to improve the action of the vulcanizing agent)
 - c. Activators or retarders (materials to increase or decrease the cure rate)
- IV. Antidegradants (to improve the useful lifetime of the elastomeric material)
 - a. Antioxidants (to protect against oxygen attack)
 - b. Antiozonants (to protect against ozone attack)
 - c. Miscellaneous (to protect against thermal, acid, base, ultraviolet, etc.)
- V. Processing Aids (to improve processing of the elastomer)
 - a. Plasticizer (to assist in breakdown or softening during processing)
 - b. Tackifier (for enhanced post-processing properties)
 - c. Softeners, etc.
- VI. Miscellaneous
 - a. Colorants
 - b. Blowing Agents
 - c. Reodorants
 - d. Abrasives

Although this list of additives is not complete, it does provide some idea of the range of materials that may be added to elastomer to improve or expand their utility. The addition of materials to elastomers is more often the rule rather than the exception.

1.6. Stability

The chemical structures that impart the useful physical properties of elastomers are extremely vulnerable to degradation. Degradation can be caused by exposure to high temperatures, oxygen, ozone, acids, and/or many other chemicals. Antidegradants are commonly used to protect the elastomer from attack by these chemicals. This aspect of elastomer utilization is very important and a great deal of attention has been paid to preparation and evaluation of protective systems for elastomers.

1.7. Calorimetry and thermal analysis techniques

Analysis of elastomers to determine their physical and chemical characteristics is a very important area of study. A number of calorimetry and thermal analysis techniques are routinely utilized for elastomer analysis. The number of such techniques continues to expand as the nature of elastomer research changes. A brief description is given here of some of the major techniques used for elastomer analysis.

Differential Scanning Calorimetry (DSC) - A technique in which the heat flow rate (power) to the sample is monitored against time or temperature while the temperature of the sample, in a specified atmosphere, is programmed. In practice, the difference in heat flow rate to a pan containing the sample and to a reference pan (empty or not) is monitored. This technique is typically used to characterize temperatures and heats associated with glass transitions, melts, endotherms and exotherms associated with curing and degradation and other processes that involve heat flow. Derivative techniques include: dynamic differential calorimetry, temperature modulated differential scanning calorimetry, high pressure DSC, photo-DSC, thermoluminescence, thermal conductivity, and thermal diffusivity [1].

Differential Thermal Analysis (DTA) - A technique in which the difference in temperature between a sample and a reference material is monitored against time or temperature while the temperature of the sample, in a specified atmosphere, is programmed. This technique is used for much the same types of thermal events as DSC where determination of characteristic temperatures alone is sufficient [1].

Accelerated Rate Calorimetry (ARC) - A technique that provides time (t), temperature (T) and pressure (P) data for a thermally initiated chemical reaction under adiabatic conditions. This technique is typically used for thermal hazards evaluation because of its unique capability to mimic the conditions in a reaction vessel. This technique can provide: 1) adiabatic rate of self-heating, 2) adiabatic time to explosion, 3) rate of pressure rise, 4) maximum rate of reaction, 5) kinetic data such as E , n and preexponential terms and 6) heat of reaction ΔH_r . These results are applicable to the design and performance evaluation of batch reactors and storage vessels where agitation does not affect behavior.

Adiabatic Calorimetry - A technique in which the temperature of the sample is monitored while raising the temperature of its surroundings internal to the calorimeter. Heat exchange between the calorimeter and its environment is virtually eliminated. This technique has yielded measurements of heat capacities and heats of fusion to better than $\pm 0.1\%$.

Differential Calorimetry (DC) - A technique where the heat flow of a sample is measured relative to a reference. This is commonly performed under isothermal conditions. This technique is applied to the same evaluations as DSC.

Thermogravimetric Analysis (TGA) - A technique in which the mass of the sample is monitored against time or temperature while the temperature of the sample, in a specified atmosphere, is programmed. A variety of thermal programs can be used (isothermal, increasing, etc.) and the mass or weight changes can be associated with a variety of processes including loss of volatile components, degradation, absorption of chemicals, etc. This technique is used extensively for compositional analysis of elastomeric compounds. This

equipment is used for a variety of techniques including evolved gas analysis (EGA) and derivative thermogravimetry (DTG) [1].

Thermomechanical Analysis (TMA) - A technique in which the deformation of the sample under non-oscillating stress is monitored against time or temperature, while the temperature of the sample, in a specified atmosphere, is programmed. The stress may be compression, tension, flexure or torsion. Expansion, penetration and extension are just three modes used to evaluate these changes. Typical phenomenon measured include glass transitions, melting, swelling, strain crystallization, and others [1].

Dynamic Mechanical Analysis (DMA, DMTA) - A technique in which the storage modulus (elastic response) and loss modulus (viscous response) of the sample, under oscillatory load, are monitored against time, temperature, or frequency of oscillation while the temperature of the sample, in a specified atmosphere, is programmed. Variables in the technique include: the mode of load application, amplitude and frequency of load. This method is used to characterize glass transitions and other subtle transitions, melting and physical properties [1].

Dielectric Thermal Analysis (DETA) - A technique in which the dielectric constant (permittivity, relative permittivity) and dielectric loss factor of the sample, in an oscillatory electric field, are monitored against time or temperature while the temperature of the sample, in a specified atmosphere, is programmed. Ion mobility in the matrix and dipole moments of structural units play a role in the dielectric response of the elastomer. Typical phenomenon characterized are melts, glass transitions, etc. [1]

Thermally Stimulated Current/Relaxation Map Analysis (TSC/RMA) - A technique which monitors, against time or temperature, the current which is generated when dipoles change their alignment in the sample, while the temperature of the sample, in a specified atmosphere, is programmed. The technique is applied in various ways, for example, the sample may be pre-treated by heating and cooling in an (non-oscillatory) electric field to create aligned frozen dipoles. The sample can then generate a thermally stimulated current during subsequent heating with no field applied. This technique can be used to characterize glass transitions and similar relaxation process [1].

Simultaneous Techniques - This refers to the application of two or more techniques to a (single) sample at the same time. A hyphen is used to separate the abbreviations, e.g. simultaneous thermogravimetric analysis and differential scanning calorimetry (TGA-DSC) [1].

Combined Techniques - These refers to the application of a thermal analysis technique coupled with another analytical technique. Examples include thermogravimetric analysis with mass spectroscopy (TGA-MS), thermogravimetric analysis with infrared analysis (TGA-IR), DTA-thermo-microscopy, etc. These techniques are used to provide more information than is strictly

available from the thermal technique. By coupling the techniques, the events seen by thermal analysis can be characterized from a chemical standpoint, providing more information that thermal analysis alone could provide [1].

Many other specialized techniques exist within this field. Our intention here was to point out the most commonly used techniques that will be described in the discussion of analysis of elastomers of various kinds.

2. CLASSES OF ELASTOMER

The classes of elastomers have been broken down into categories based on general chemical characteristics. Within each category, individual elastomers will be described along with some of the key chemical and physical attributes and a few examples of the more common applications.

2.1. Diene rubber (homopolymers)

These elastomers consist of chains made up of a single monomer. Variations in microstructure are possible, especially for synthetic elastomers.

<u>Polymer</u>	<u>Key Physical Properties</u>	<u>Uses</u>
1. Natural Rubber (NR)	high molecular weight, structural integrity, strain crystallizable, hot strength, high tensile	tires, hoses, belts, anti-vibration mounts
2. Polyisoprene (IR)	resilience, hot tensile, tack, hot tear resistance	tires, belts, gum rubber products
3. Polybutadiene (BR)	low abrasion, crack growth resistant, low heat buildup, good resilience, control of microstructure	tires, hoses, belts, shoe soles
4. Chloroprene (CR)	oil and abrasion resistant, some crystallinity present, heat and weather resistant, modifiers used (S, AO, etc.)	adhesives, belts, molded and extruded products, gaskets

2.2. Diene rubbers (copolymers)

These elastomers contain various combinations of monomers that include isoprene or butadiene. Again, microstructural variations are possible and often used for their beneficial properties.

<u>Polymer</u>	<u>Key Physical Properties</u>	<u>Uses</u>
1. Styrene-Butadiene-Isoprene (SBR),	good wear and aging, abrasion resistant, good filler interaction, control of	tires, adhesives, chewing gum, industrial products

IBR, SIR, SIBR)	microstructure and chemical composition	
2. Acrylonitrile Rubber (NBR, NIR)	control ACN level, can be modified with COOH, gel content control, abrasion resistant, water, oil and chemical resistant	hose, seals, injection and compression molded products
3. Butyl Rubber (IIR)	abrasion resistant, low gas permeability, high hysteresis, control of unsaturation level	inner liners, electrical insulation, seals, footwear, engine mounts
4. Ethylene-Propylene- Diene Rubber (EPDM)	heat, ozone and oxygen resistant, saturated chain, control crystallinity	tires, automotive hoses, plastics additive

2.3. Halogenated rubbers

These are elastomers that either contain halogenated monomers or are post-polymerization halogenated.

<u>Polymer</u>	<u>Key Physical Properties</u>	<u>Uses</u>
1. Bromo-Butyl (BIIR)	low gas permeability, oxid./ozon. resistant, cure compatible	inner liners, white sidewalls, belts, hoses
2. Chlor-Butyl (CIIR)	low gas permeability, heat and flex resistant, controlled chlorination	inner liners, pharmaceutical stoppers
3. Chlorinated-Polyethylene (CM)	controlled chlorination, ozone, heat, weather resistant, good flex, abrasion resistant	hoses, belts, molded products
4. Chlorosulfonated-(CSM)	flame, heat, oil and ozone resistant	hose, belts, electrical products
5. Fluorocarbon Rubbers (CFM, FKM)	compression set resistant, low temp. flex, flexible, chemical resistant	aircraft applications, automotive seals, o-rings, hoses
6. Fluorosilicone Rubber (FMQ)	heat, ozone, oxidation resistant	molded products
7. Epichlorohydrin Rubber (CO)	low gas permeability, ozone resistant	belts, hoses
8. Ethylene oxide-epichlorohydrin (ECO)	solvent and ozone resistant, low temperature flexibility	wire coatings, hoses, belts, adhesives

2.4. Vinyl rubber

These elastomers are based on vinyl monomers. Many have saturated backbones.

<u>Polymer</u>	<u>Key Physical Properties</u>	<u>Uses</u>
1. Acrylate - Copolymer (ACM)	heat and oil resistant, saturated backbone	seals, hoses, tubing, rollers
2. Ethyl-vinyl acetate copolymer (EAM)	heat, oil and weather resistant, low compression set, control of composition	o-rings, seals, adhesives, hoses, impact modifiers
3. Vinyl pyridine Rubber	functional group interaction	latex adhesives
4. Ethylene-acrylic Rubber	heat and oil resistance	hoses, tubing
5. Ethylene-propylene Rubber (EPM)	oxygen, ozone and heat resistance	tires, electrical, molded products

2.5. Miscellaneous rubber

The remainder of the various elastomers that don't fit into any of the categories listed above.

<u>Polymer</u>	<u>Key Physical Properties</u>	<u>Uses</u>
1. Silicone Rubber (MQ)	inorganic backbone, good flex, heat resistant, insulator, damping	automotive parts, hoses, seals, gaskets
2. Polysulfide Rubber (T)	solvent resistant, low permeability to gases	rollers, putties, solvent hoses
3. Thermoplastic Elastomers		
a. Polyurethanes (YAU, YEU)	thermoplastic handling, control of hard and soft segments, control the crystallinity and properties	medical applications, automotive parts, footwear
b. Polyolefins (YEPM)	good weatherability	non-tire automotive applications
c. Styrene-butadiene block copolymers (YSBR, YSIR)	hot strength, high tensile control of properties range	footwear, adhesives, plastics additive
d. Copolyesters (Y)	flex fatigue resistant, abrasion resistant	non-tire automotive applications

It is obvious that a great variety of physical and chemical properties are possible with the multitude of possible elastomer structures. This diversity makes elastomers such a versatile class of polymers. These key physical and chemical properties are the main reason that thermal analysis and calorimetry techniques are important for the examination and identification of elastomers. Evaluating these properties and their retention are the primary applications of the techniques which will be discussed in this chapter.

3. SINGLE ELASTOMERS

At the core of the analysis of elastomers and products containing elastomers is the characterization of the chemical and physical attributes of the individual elastomers. Knowing the attributes of the individual elastomers provides the framework for many of the standard analyses used to determine compositions of products and the nature of material problems. Thermal analytical and calorimetric techniques provide tools for the characterization of key chemical and physical properties of elastomers.

3.1. Glass transition temperature

The glass transition temperature (T_g) of an elastomer can be described as the temperature at which the polymer undergoes a transition between the amorphous state and the glassy state. This physical transformation is important in determining the physical properties that the elastomer will exhibit. Polymer scientists have, for years, used the T_g as an indicator of the stiffness or modulus of the elastomer and to help determine the microstructure of elastomers. The T_g has also been used to describe the brittle point of an elastomer.

The T_g can be determined by several techniques which utilize the various aspects of the glass-to-amorphous transition. DSC can be utilized to detect the heat flow associated with the change in heat capacity of the elastomer as it moves through the transition. This is a very common approach to determining this transition [2,3]. It should be noted that these determinations have more often been performed in the heating mode (proceeding from the glassy state to the amorphous state). This technique has the advantage that it is easy to perform but has the disadvantage that it does not result in an equilibrium measurement. If the measurement were taken moving from the amorphous state to the glassy state by cooling, the measurement would represent an equilibrium measurement. It should also be noted that the value obtained from determinations performed using DSC is often reported as a single number, often the extrapolated onset, inflection points or the half-height of the transition [4]. To be totally accurate and consistent, the inclusion of an onset point, an indication of the width of the transition, often a midpoint (half-height or inflection point) and the change in

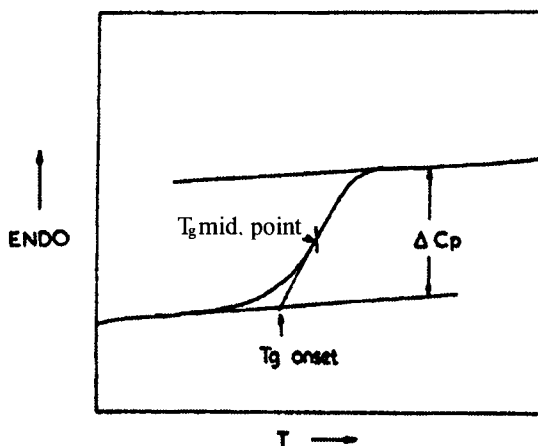


Fig. 2. Glass transition - definition of parameters

heat capacity across the transition (ΔC_p) should be provided (Fig. 2) along with the experimental conditions used for the determination.

The technique of DSC has been used to determine the effect of epoxidation on the T_g of synthetic polyisoprene [5] and natural rubber [6,7] where the T_g increases linearly with epoxidation level of the elastomer. Many standard elastomers have been evaluated to determine T_g [8]. In these examples, both onset (departure from the baseline), extrapolated onset (using the intercept of the baseline and tangent at the inflection point) are provided for several heating rates, demonstrating the time/temperature dependence of the transition. DSC has also been used to characterize lattices of natural rubber [9].

Determination of T_g by DSC has been successfully used in studying the chlorination of *cis*-1,4-polybutadiene. It was demonstrated that as the degree of chlorination increases, the T_g of the *cis*-1,4-PB remains essentially constant, indicating that the chlorinated BR actually exists in two domains, a BR phase and a chlorinated phase (Fig. 3) [10].

A DSC study to determine the dependence of T_g on the total molecular weight at constant isoprene content for a series of styrene-isoprene-styrene block copolymers showed the presence of one, two or three T_g 's. The third T_g was thought to show the presence of an interphase [11].

Another approach to determining the T_g is via thermomechanical analysis (TMA). This approach depends on the change in the rate of thermal expansion associated with the transition. The results of an evaluation of a polyurethane elastomer, where T_g is determined using a penetration probe, is shown in Fig. 4 [12]. Several different probe types (free expansion, expansion with load and tension) can also be used to determine the T_g of elastomers [8]. This technique is

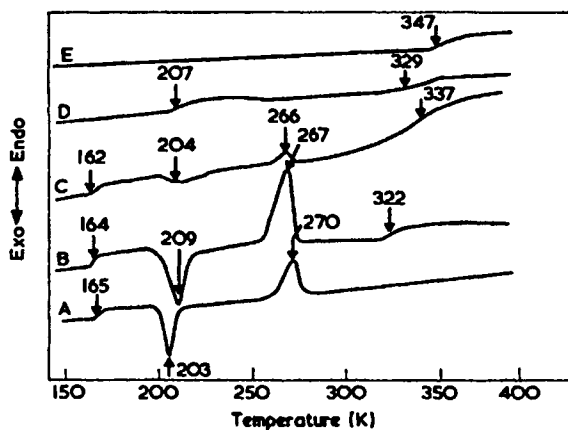


Fig. 3. DSC scans of partially chlorinated *cis*-1,4-polybutadiene: A, *cis*-1,4-polybutadiene; B, 42% chlorination; C, 65% chlorination; D, 81% chlorination; E, 100% chlorination

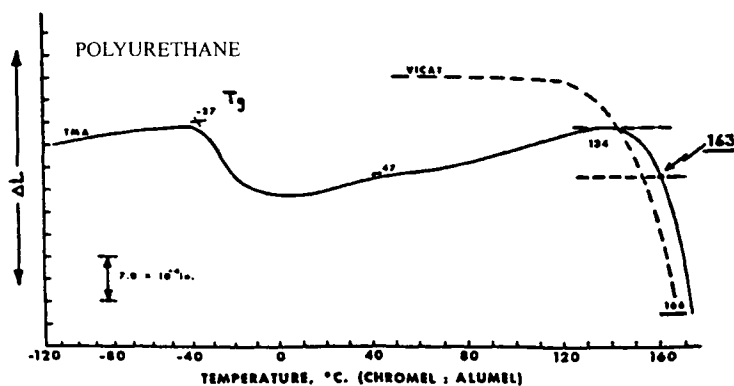


Fig. 4. Comparison of TMA and VICAT test on a polyurethane elastomer

considered more sensitive than DSC for the determination of this class of transitions. Experiments are usually performed in the heating mode and this again indicates the transition is not determined from an equilibrium measurement.

Determination of T_g by TMA has been promoted to characterize and monitor changes in ethylene-propylene-diene terpolymer (EPDM) due to aging conditions [13]. Other techniques (DMA and DSC) have been used for similar investigations [14].

Dynamic load thermomechanical analysis (DLTA) is an approach related to TMA which is reported to determine not only T_g but also give a picture of the

overall elastic behavior of a sample, in a single experiment. A number of polysulfides, polyacrylates, polyurethanes and a silicon rubber have been examined by this technique. The silicon rubber has a relaxation at -50°C and then up to 200°C behaves as an ideal rubber-elastic. The polysulfides and polyurethanes showed viscous flow at 150°C and the polyacrylates soften above 50°C indicating a pseudoplastic behavior [15].

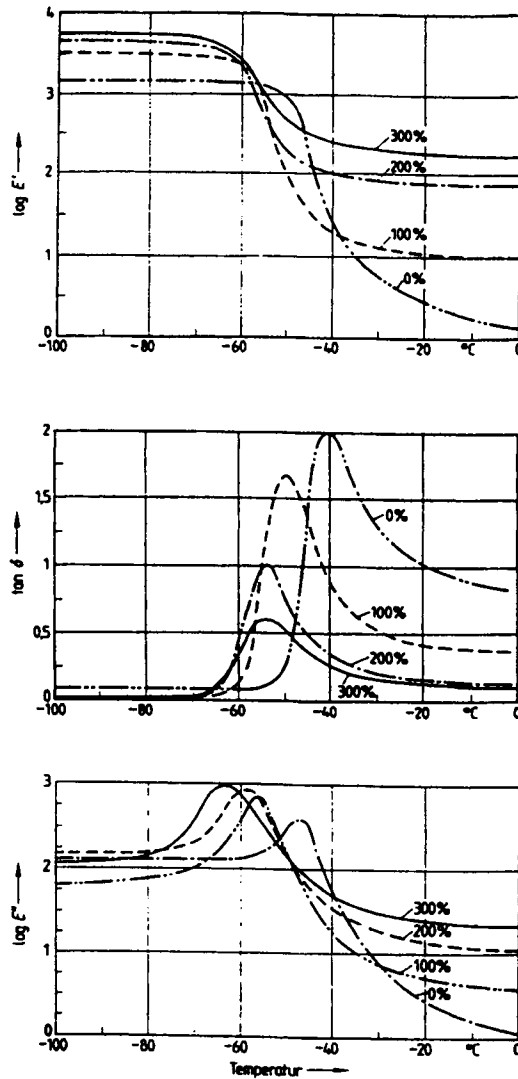


Fig. 5. DMTA curves (E' , E'' and $\tan \delta$) for NR at various extensions

The use of dynamic mechanical thermal analysis (DMTA) provides another avenue for determination of the glass transition temperature [16,17]. In this technique, several different sets of data can be used to characterize the T_g . A plot of the storage modulus (E') versus temperature reveals a change in slope associated with the softening of the elastomer as it becomes amorphous. The onset of this drop in modulus can be used to designate the T_g . Additionally, the peaks of the E'' (loss modulus) and tangent δ curves can be used to denote the temperature of the transition. The technique of DMTA has been used to determine the effect of epoxidation on the T_g of polybutadiene [18] where the T_g increases with epoxidation level of the elastomer. This technique has also been utilized to show the sensitivity of the T_g to orientation of an elastomer [16,17]. Natural rubber is known to crystallize upon extension and this can affect the glass transition temperature. As shown in Fig. 5, the T_g shifts to lower temperatures upon being oriented by extension.

A technique related to DMTA is Fourier Transform Mechanical Analysis (FTMA), where a shear sandwich type sample configuration is excited by a random signal (band limited white noise) and a simple transfer function analysis is performed to yield a complex modulus for the sample. This technique permits the determination of T_g at different frequencies in a single experiment, as compared to a number of single frequency experiments performed sequentially during a single run. In this example, master curves constructed from data for neoprene and NBR are shown [19].

Dielectric spectroscopy (DEA), along with DSC, have been used in a study of nine segmented polyetherurethanes synthesized with poly(tetrahydrofuran)glycol. The dielectric loss properties, including T_g , were shown to be strong functions of the soft segment molecular weights [20].

Electrothermal analysis can also be used to detect the glass transition [21]. The resistivity of the polymer shows a sharp drop at the transition temperature indicating an increase in dipole mobility. Other transitions not detected by DSC have been detected by this method but the nature of these transitions is not clearly understood.

Radiothermoluminescence, a technique where the sample is irradiated and the resulting luminescence is measured as a function of temperature, has been used to determine a relaxation (T_g) in the T_g region, as determined by other techniques, for a doped block SBR and the corresponding BR [22].

The thermally stimulated current (TSC) technique has been used to detect relaxations, including the T_g , of a polyether-block amide copolymer undergoing various thermal histories. The copolymer has a poly(tetramethylene glycol) (PTMG) soft segment and a polyamide hard segment [23].

3.2. Crystalline melts

Many elastomers have crystalline domains within their matrix which are important to their properties. The presence of these domains in an elastomer can lead to substantial self-reinforcement and these elastomers can possess a high value of modulus in the cured state. Among the elastomers that are capable of forming crystalline domains are polybutadiene (BR) and chloroprene (CR). DSC is commonly the technique of choice to characterize the endotherms associated with the melting of these crystalline domains [8,24-27]. The shapes and locations of these melt endotherms is usually determined by the heat history of the elastomer during formation of the crystals. This can apply to both crystallization in the solid state [25-27], where the heat history or annealing can lead to significant differences in the nature of the melt endotherm, and growth of crystalline polymers such as trans-1,4-polyisoprene from solution [24], where the heat history and solvent can cause variations in the crystalline form derived and, consequently, in the melt profile. DSC has also been used to characterize the chlorination level of a polybutadiene by following the decrease in the size of the crystalline melt endotherm and change in T_g as chlorination levels are increased [28].

Crystalline domains can also be created by low temperature treatment of elastomers like natural rubber and synthetic polyisoprene. The generation of these domains is controlled by several factors including average cis sequence, presence of nucleating agents such as stearic acid and the time and temperature of the annealing [26]. The size of the melt endotherm (ΔH_f) can be related to the annealing temperature and there appears to be a specific temperature where optimum crystallization occurs. Again, this temperature is affected by the factors mentioned above.

As previously stated, DSC has been used to follow the melting of crystalline domains in polymers, in following this melting a second melting process is sometimes observed. This has been ascribed to melting of secondary crystals often formed by the reorganization of primary crystals into different chain folding regimes. Such second melting has been observed in certain polyurethanes, poly(ethylene terephthalate), poly(dimethylvinylsiloxanes), polyethylene, polypropylene and stereospecific polybutadienes [29].

Analysis of the melting and crystallization behavior by DSC of segmented polyurethanes of varying composition suggests that the hard segments form crystalline domains whose size and therefore melting temperatures are dependent on factors of heating rate, annealing temperature, and hard segment length. At lower heating rates, melting and subsequent reorganization of crystals have been observed [30-34]. Aging of segmented polyurethanes has shown an upward shift in endothermic peak temperatures upon high humidity aging indicating a change in hard segment crystallinity due to an increase in ordering and phase separation [35].

Similar studies of segment segregation and crystallinity were carried out on a series of polyether(ester)urethanes and -urethaneureas utilizing a TMA in the so called impulse mode, where the load is periodically varied [36]. A similar study was conducted on a series of polyether-urethanes using dielectric spectroscopy with complimentary DSC [20]. Segmental mobility, crystallinity of the soft segments and the nature of the interphase region play a significant role in determining the phase structure of the polymer and its consequent physical properties. Since these transitions occur at temperatures that coincide with application temperatures, these phenomenon are significant for material design.

DSC studies of a tetramethyl-p-silphenylenesiloxane/dimethyl siloxane (TMPS/DMS) block copolymers, which act like a thermoplastic elastomer, found that the copolymer melting temperature increases as the crystalline (hard) TMPS constituent was increased [37].

3.3. Stretching and deformation calorimetry

When an elastomer is stretched, both heat and work are exchanged. Using a highly sensitive stretching calorimeter [38,39], measurements have been made on both SBR and NR to determine the thermoelastic behavior of the elastomers. As seen in Fig. 6, both NR and SBR show similar behavior at each of the temperatures used for the analysis. At increasing analysis temperatures, the heat of elongation becomes negative at much shorter elongations. These effects may

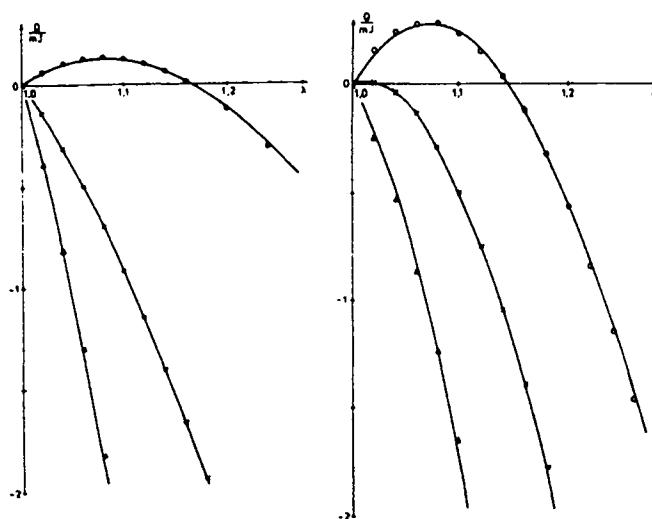


Fig. 6. Heat of elongation for NR (left) and SBR (right) at various temperatures. Measuring points: 0 = 22°C, x = 61°C, $\Delta = 90^\circ\text{C}$, -- = calculated

be related to some “rotational freedom” which is not available at temperatures below the freezing temperature. This behavior was modeled assuming that the elastomers were behaving globally like Van-der-Waals conformational gases but locally showing the behavior of an elastic fluid.

Using a similar calorimeter, stress-induced crystallization was observed in cis-1,4-polybutadiene. In this two stage process, initially the polymer is crystallized with the crystal nuclei formed parallel to the direction of the applied stress and then at a critical strain the crystals begin to grow normal to this direction giving rise to a shish-kebob morphology [40].

DSC and the closely related technique, deformation calorimetry where the sample is deformed and the resulting heat flow is measured, have been extensively utilized in measuring the change of T_g with microstructure in a class of materials known as segmented polyurethanes. Segmented polyurethanes contain two incompatible segments which form blocks or segments, one hard and one soft. The soft segment possess a T_g which varies with chemical composition and thermal history [30,41]. T_g increases with annealing and quenching but returns with time [33]. T_g of the soft segment have also been studied in hydroxy terminated BR containing PURs and has been shown to be an excellent indicator of degree of phase separation [42]. The effect of hard segment composition and concentration on the deformation has also been studied by DSC [34,43].

3.4. Thermal and oxidative stability

The thermal and oxidative stability of single elastomers is very important for both their utility in varied applications and the characterization of blends of elastomers and their applications. Techniques that are capable of identifying a

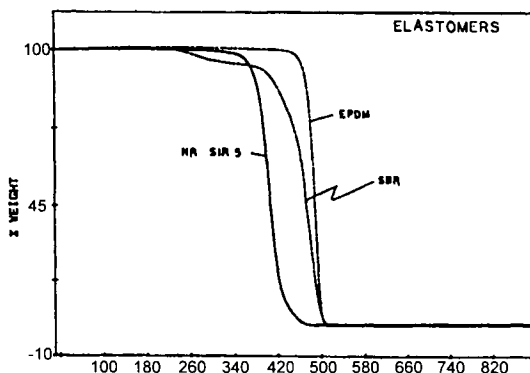


Fig. 7. TGA curves for NR, EPDM and SBR - comparative

single elastomer from its degradation can be used to characterize and/or identify the composition of a blend. The most commonly used technique to characterize the stability of an elastomer is thermogravimetry (TGA). The degradation temperature and the nature of the degradation curves are characteristic of each elastomer and can often be used to characterize the components of a blend [2,4,44-48]. As shown in Fig. 7, NR, EPDM and SBR each have a different degradation temperature and their degradation profiles are different. Another approach to these analyses is to utilize derivative thermogravimetry (DTG), where derivative curves are used to characterize the degradations, represented as peaks. As shown in Fig. 8, the location and shape of the curves are characteristic of the elastomer. Distinct differences are reported in the peak temperatures for NR (365°C), SBR (447°C) and BR (465°C), as well as their shapes which vary from sharp peaks to peaks with significant shoulders.

Chlorine containing elastomers can often be identified by an additional step in their degradation process in a nitrogen atmosphere. The first step involves a weight loss due to elimination of HCl plus partial chain decomposition with the second step being associated with decomposition of the main chain structure. For example, polyethylene degrades in a one step process while chlorinated polyethylene will degrade in a two-step process, under the same conditions [49,50]. Other elastomers, and classes of elastomers, have their own characteristic degradation schemes which can be characterized by means of kinetic analyses such as PU foams [51], silicone elastomers [52-55], fluorocarbon elastomers [56-58]. Often mathematical methods, such as factor analysis, can be used to enhance the identification of elastomers and their blends as shown with chloroprene rubber (CR) and butadiene-acrylonitrile rubber (NBR) where the blending of NBR with small amounts of CR causes the loss of some of its distinctive degradation characteristics [59].

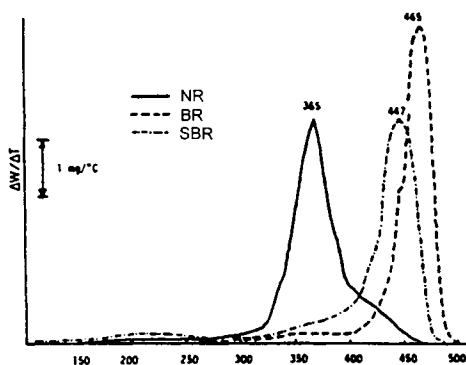


Fig. 8. DTG curves for NR, EPDM and SBR - comparative

TGA curves can also help determine the chemical composition of elastomer. One example is the shift in the decomposition temperature for natural rubber that is epoxidized [60,61]. As the level of epoxidation is increased, the degradation temperature of the elastomer is increased. Characterization of the styrene content of SBR has been accomplished by studying the profiles of DTG curves for various SBR's [62]. Also, the relative acrylamide/acrylate ratio in a copolymer can be determined with very good accuracy (relative standard deviation of only 2.4%) [63].

A related technique is evolved gas analysis (EGA), where the degradation products produced by a TGA-like technique are characterized by other analytical techniques such as Fourier Transform Infrared (FTIR) or mass spectrometry (MS). The use of ion ratio-temperature profiles can provide structural information on the elastomer being evaluated, which can be used as fingerprints for the identification of the elastomer [64-67].

The use of DSC to characterize the degradation of elastomers as a means of identification has been discussed [68]. Different elastomers are shown to have exothermic and endothermic peaks at various temperatures, representing either microstructural differences or different chemical composition. The technique described here was applied to BR primarily and all scans were conducted in a nitrogen atmosphere. The exothermic peaks observed were ascribed to cyclization of BR and endothermic peaks were attributed to thermal degradation.

4. BLENDS

Most elastomers have one or more properties that merit their use in a manufactured product. However, more often than not, each elastomer has a deficiency in another property which would tend to decrease its utility in the given application. For instance, natural rubber is an elastomer that provides very good modulus in a cured compound and has very good tear properties due to its ability to strain crystallize. However, it does not possess good abrasion resistance. The use of natural rubber for a tire tread would be acceptable except for the lack of abrasion resistance. As many elastomer-based product manufacturers have known for many years, a carefully conceived and produced blend of elastomers can provide only the best properties from both of the elastomers for the final product. Therefore, it would seem sensible to blend natural rubber with polybutadiene to produce a compound with better abrasion resistance and good tear strength.

This approach to developing new compounds with improved physical properties has become even more important today, considering the difficulty and expense involved in introducing and producing new elastomers. The ability to utilize known elastomers in blends with controlled morphologies and distribution

of additives has become one of the most fertile areas of research in the elastomer using industries.

The physical properties of blends of elastomers depend, in part, on the nature of the resulting mixture of the elastomers. The miscibility of the two (or more) elastomers, their blend ratio and the morphology that is developed during mixing and curing will dictate the resulting physical properties. Because these various factors play such a large role in determining the resulting physical properties, it is very important to be able to characterize these properties with respect to the two elastomers used. Thermal analysis and calorimetry techniques provide very useful tools in the characterization of elastomer blends.

4.1. Glass transition temperature

The T_g of an elastomer is a characteristic property, as described previously, which can be used to characterize the components of a blend and, when the two or more elastomers are immiscible, the composition of the blend. As shown in Fig. 9, NR and SBR are immiscible when blended and, when examined using DSC, continue to show characteristic step changes associated with the T_g of each polymer [69]. The T_g of each elastomer remains essentially unchanged at all compositional variations. This has also been noted for other incompatible combinations of elastomers [70,71], blends of NR and ENR [72] and even for SBR's that have different styrene contents [73]. The fact that the two elastomers are immiscible allows each elastomer to respond separately to the thermal conditions.

When two elastomers are totally miscible in each other, the picture changes radically. The T_g 's are not separated and usually cannot be easily identified. The two elastomers are mixed intimately enough that the response of the individual elastomers cannot be separated and they appear to respond as one polymer. The step transition characteristic of T_g can become a single broad

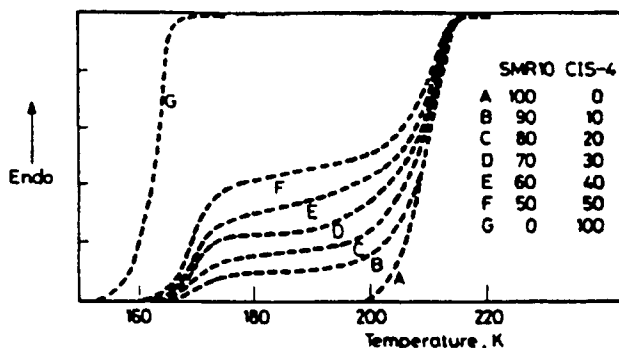


Fig. 9. T_g of NR/BR vulcanizates normalized to the same total displacement as the reference samples

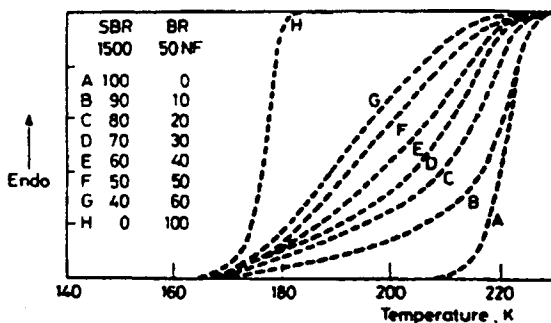


Fig. 10. T_g of SBR/BR vulcanizates normalized to the same total displacement as the reference samples

transition, two broadened transitions that are moved toward each other or some hybrid of these possibilities, depending on the degree to which the two elastomers are miscible [74]. As shown in Fig. 10, when two miscible elastomers are mixed, the glass transitions can become indistinct, showing a single very broad transition through the two individual glass transition temperatures. Identification of the component elastomers can be extremely difficult under these circumstances. Because of these differences, DSC has long been used to determine the miscibility of the components of polymer blends.

Another technique which has become more commonly used in the characterization of blends is dynamic mechanical analysis (DMA or DMTA) [17,75,76]. As noted earlier, this technique relies on the response of the elastomer to a sinusoidal stress. T_g can be detected by both a drop in the E' (storage modulus) curve and a peak in the E'' (loss modulus) or tangent curves.

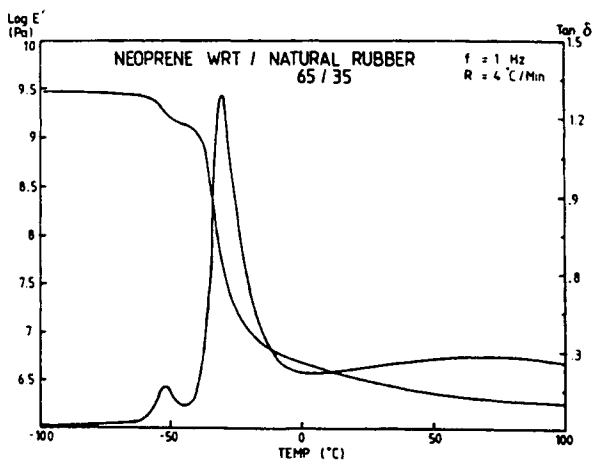


Fig. 11. DMTA thermogram of 65/35 Neoprene WRT/natural rubber blend

When an immiscible elastomer pair is examined, the individual transitions are still present for each elastomer. As shown in Fig. 11, the loss peaks associated with both Neoprene WRT and natural rubber are still present in this blend.

When a miscible blend is examined, the result is usually a single loss peak or step change in the storage modulus curve. The two elastomers are acting as one material and a single response to the temperature scan is noted. The position of the loss peak depends primarily on the composition of the blend, typically falling somewhere between the loss peaks of the two original elastomers.

Quantitative or semi-quantitative analysis of elastomer blends based on the T_g 's of the component elastomers can usually be performed for partially miscible [18] or immiscible blends. For DSC scans, the change in heat capacity (ΔC_p) across the glass transition is a constant for each elastomer. When immiscible blends are examined, the ΔC_p for each component will often reflect its portion of the blend. Referring to Fig. 8, the size of the heat capacity changes in each step should roughly reflect the composition of the blend. Plots of the ΔC_p versus the weight % of a component typically produce a linear relationship. When this technique is applied to miscible blends, quantitative (or semi-quantitative) relationships become more complicated. An evaluation of the total change in heat capacity across the entire transition zone would allow for a semi-quantitative analysis of the composition if both elastomers did not have the same ΔC_p in this region. (If both elastomers had the same ΔC_p , then it would be impossible to differentiate between various compositions using this approach.)

Quantitative analysis of DMTA data is a little less straight forward. Two possibilities exist for semi-quantitative analysis of this data. Each one depends on the type of blend that is being evaluated. For immiscible blends, one might be able to ascertain the composition on the basis of the heights of the loss peaks for each elastomer. As the level of one component increases, its loss peak would increase accordingly. This may or may not be completely accurate and must be determined for each case. For miscible blends, it is sometimes possible to correlate the position of the loss peak (between the positions of the two original elastomers) to the composition. Again, this is an approach that must be verified for each case.

4.2. Composition analysis

Composition analysis is a traditional approach to analyzing elastomers in a blend [25,27,44,71,77-82]. Each elastomer has its own characteristic decomposition temperature that can often be used to differentiate the components of a blend. Using thermogravimetry (TGA), the blend in question is heated in either a vacuum, or in a nitrogen or air atmosphere to degrade the elastomers in the blend. As each component is degraded, it produces a step loss in weight. The temperature of the loss should correspond to the elastomeric component. The derivative curve of a thermogram (DTG) shows these weight

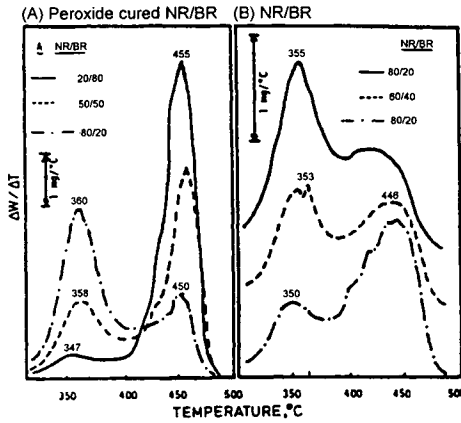


Fig. 12. DTG curves of (A) peroxide cured NR/BR, (B) NR/BR blends from tire sidewalls

losses as peaks which are much easier to use for characterizing the components of the blend. The decomposition temperatures of several elastomers, as determined by TGA and DTG, have already been shown in Fig. 7 and 8. The appropriate temperatures for each elastomer can be used to determine the components of a blend. As shown in Fig. 12, the composition of a blend can only be roughly estimated from the DTG curves. Various blend ratios of NR and BR are shown and it is obvious that the size of the DTG peak is not the same for each elastomer [44].

The TGA curve provides direct data on the composition of the blend. The actual weight losses associated with each component can be calculated from the TGA curve and usually, but not always, can be used to accurately determine the composition of the blend. Quantitative analysis of blends using TGA requires that the elastomers in question do not affect each other during the degradation process. Also, care must be taken during analyses, especially with cured compounds, to assure that the degradation of additives and other components does not interfere with the degradation of the elastomers being analyzed. As stated in the section on single elastomers, often mathematical methods, such as factor analysis, can be used to enhance the identification of elastomers and their as shown with chloroprene rubber (CR) and butadiene-acrylonitrile rubber (NBR) [59]. When the decomposition of two elastomers overlap because of the type of degradation steps involved, quantitative analysis of the blend composition can be very difficult. An example is this is the evaluation of SBR/BR blends. These two elastomers have similar degradation curves because both contain common monomeric units from butadiene. Each polymer degrades in a two step process, the first step (h1) associated with volatile depolymerization

and the second (h_2) attributed to degradation of residue resulting from the cyclization and crosslinking. An investigation of these degradations has been conducted using TGA/DTG and it has been shown that under controlled conditions, the height of the first DTG degradation peak (h_1) can be correlated to the BR content in a blend [83]. However, several factors must be controlled for this analysis: 1) amount of carbon black in the compound, 2) uniformity of the compound and 3) oil content of the compound. Although the nature of each elastomer involved in this study was noted, there was no mention of potential effects related to microstructure of the elastomers.

Another approach to analyzing blends is to evaluate the peak temperature (T_p) and the ΔH_{ox} of a blend by DSC and to correlate these values to the composition of the blend. This has been done for a very difficult blend to analyze, NR/IR [84]. It has been shown that a relationship between the peak temperature or the heat of oxidation and the composition of a blend of NR and IR exists. By evaluating known compositions, it is possible to characterize blends of unknown composition. In this case, an increase in the NR content of the blend results in an increase in both T_p and ΔH_{ox} with neither relationship being strictly linear. Similar results can be obtained for the activation energy (E_a) and the isothermal induction time (t_i) for these oxidations.

Beyond the simple extraction of compositional information for a blend or the determination of the components based on the decomposition temperatures of

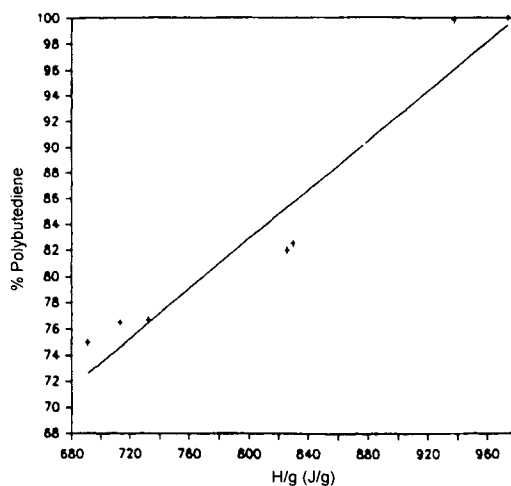


Fig. 13. Correlation of cyclization exotherm (J/g) versus polybutadiene content in a blend

the components (both typically done via TGA/DTG curves), it is possible to characterize the compatibility of two components of a blend using similar data [85]. Epoxidized natural rubber (ENR) and poly(ethylene co-acrylic acid) (PEA) are known to have a strong chemical interaction that can lead to miscibility at certain compositions. This interaction, and the formation of a single phase, can be detected by the changes in the decompositional pattern of the blend. Each of these polymers shows a multiple peak decomposition pattern. In blends with high levels of ENR (50-70%), a multistage decomposition is observed indicating separate phases. However, when the ENR level is much smaller (10-30%), a two stage decomposition pattern emerges with the temperature of the first weight loss, T_{1max} (determined from the DTG curves), appearing at higher temperatures than observed for blends with higher ENR levels. This increase in the peak temperature is indicative of the strong interaction of the phases.

A method to determine the amount of polybutadiene in a mixture was suggested using the cyclization exotherm noted for polybutadiene [68]. In this technique, the enthalpy/g of the blend was calculated by integration of the peak between 250°C and 450°C. As shown in Fig. 13, there is reasonably linear relationship between the polybutadiene content of the mixture and the enthalpy. Of course, the example provided covers a very limited polybutadiene content range and there was only one example offered. A broader application of this technique would require further investigation of the applicability to blends with other elastomers and wider ranges of polybutadiene contents. This reference did provide exothermic peak data for polymers other than polybutadiene but it is unclear if the linear relationship holds for other elastomers

5. ADDITIVES

As important as the properties of elastomers are, equally important are the additives which are combined with them to enhance their properties. The addition of fillers or reinforcing agents to increase modulus or stiffness, plasticizers and oils to extend the elastomer or reduce its stiffness, antidegradants to preserve the nature, and therefore the properties, of the elastomers and other additives are all to improve upon the chemical and physical properties of an elastomer. It would be hard to think of an application that uses an elastomer alone without any additives.

The amounts and characteristics of the additives determine the ultimate performance of the elastomer. It is for that reason that a great deal of attention has been paid to analyzing additives in elastomer systems. This discussion will be broken down to a few broad classes of additives. The curatives and antidegradants will be deferred until later sections on curing and stability, respectively.

5.1. Fillers and reinforcing agents

Fillers and reinforcing agents are two types of additives that can be distinguished from each other by the manner in which they contribute to the elastomer's properties. They will be defined in the following way: fillers simply take up space and the resulting increase in modulus can be calculated on the basis of the volumes of the components whereas reinforcing agents interact with the elastomer and produce modulus increases that are greater than calculated from volume contributions alone. An example of a filler would be silica and a reinforcing agent would be carbon black. The characteristics and quantity of these materials are key for many properties including modulus, tear properties, hysteresis, etc. For this reason, techniques have long been used to analyze filled elastomer systems. For the balance of this discussion, we will refer to both of these types of additives as "fillers".

The most widely used techniques for quantifying filler levels are thermogravimetry (TGA) and derivative thermogravimetry (DTG). Numerous examples of this traditional technique exist, where pyrolysis up to 500 - 600°C is followed by a combustion step. Organic fillers degrade during the combustion or oxidative step whereas inorganic fillers usually remain as ash [25,55,77-79,81,86-92]. Recording the weight loss of the components allows determination of the filler content. Of course, as well established as this technique is, the details associated with determining the weight loss for individual components is not always straight forward because the weight loss steps have a tendency to run together and a sharp transition between weight losses is the exception rather than the rule. Also, some elastomers produce a

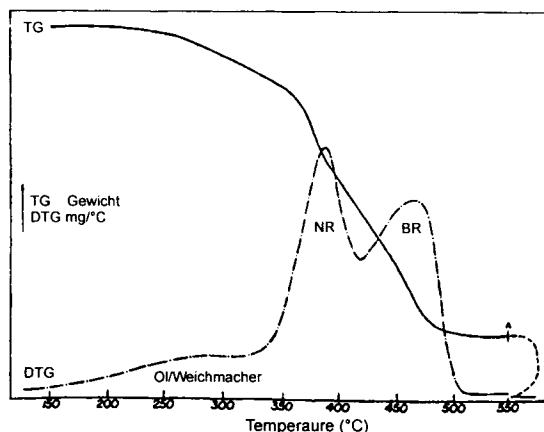


Fig. 14. TGA/DTG curves of a NR/BR blend

“char” upon degradation, which can complicate the analysis. The use of the derivative of the weight loss curve does provide some assistance in determining where to assign the endpoints for weight losses, but this is not a foolproof technique. As shown in Fig. 14, the minimum points in the DTG curve can be used to assign the cutoff between weight loss steps. Of course, there are many pitfalls in using this technique and these are discussed in greater detail elsewhere [93,94].

By coupling thermogravimetry and Fourier transform infrared spectroscopy (TGA-FTIR) or thermogravimetry and mass spectroscopy (TGA-MS) the weight loss and the nature of the evolved components are obtained simultaneously. TGA-FTIR has been used to identify and quantify carbon black and inorganic fillers in SBR [65].

The determination of “fillers” in elastomer systems via thermogravimetry is not limited to solid elastomers. The determination of calcium carbonate in filled latex carpet backing has been accomplished using standard TGA techniques [86]. In this method, the water, polymer and carbon dioxide from the calcium carbonate can be accurately determined.

Recently, efforts have been made to improve the differentiation between degradation steps to provide clearer breaks in the weight loss processes. Several methods are now offered where the temperature program is altered to allow each degradation process to proceed closer to completion before the temperature is allowed to proceed [87,95-98]. One involves switching from a constant heating rate to an isothermal stage when the rate of weight loss exceeds a predetermined value. Once the rate of weight loss tapers off, the original heating rate is resumed until another weight loss process occurs. In a second technique, the same constant heating rate is used and when a weight loss starts to take place, the scanning rate is decreased. As the rate of weight loss increases, the scanning rate is further decreased. Again, as the rate of weight loss tapers off, the scanning rate returns to the original rate. These methods offer interesting approaches and much discussion has been generated concerning the validity of the various techniques. These approaches often offer improvements in resolution of weight loss steps and should be considered for difficult cases.

Resolution of the interference provided by elastomer that contain a heteroatom involves dealing with the “char” produced upon elastomer degradation [74]. The char produced has been shown to interfere with the correct determination of carbon black content. The level of char produced has been related to both the heteroatom content of the elastomer and the ratio of heteroatom to hydrogen atoms [49]. Either way, knowing the heteroatom level in the elastomer is important to compensating for the char in carbon black determination. A preliminary analysis of heteroatom by some other technique can help establish this level. Also, being able to identify the elastomer by other thermal techniques can often solve this problem. Once known, the char level

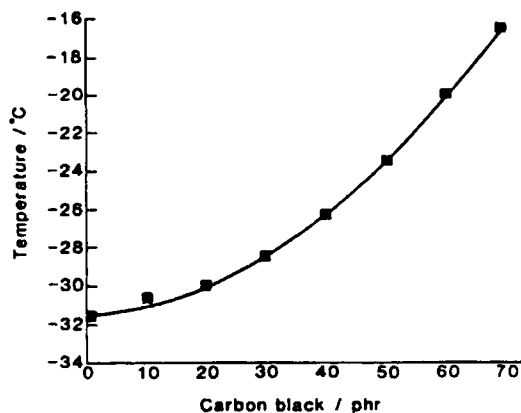


Fig. 15. Change in BR crystallization temperature with increased carbon black loading

expected can be determined using either literature values for char or by separately determining this with the raw polymer. This char level can then be subtracted from the carbon black level determined in the standard TGA-DTG experiment. Additionally, it has been suggested that by using a leaner oxygen content in the oxidative gas used for carbon black degradation, lowering the heating rate or using isothermal steps or reducing the pressure while using a lean oxygen feed, the separation of char from carbon black might be possible.

Another approach to quantifying the carbon black content of a polymer is by measuring its affect on the crystallinity. Fig. 15 shows that during a cooling experiment, the temperature of the onset of polybutadiene (BR) crystallization was related to the carbon black loading of the compounded elastomer. This technique can also be used to characterize the phase distribution of a filler in a blend. Combining the examination of crystallization temperature by DSC with electron microscopy it was shown that carbon black transfers between phases of BR-IR and BR-EPDM blends during [99].

Another increasingly important area that thermal analysis and calorimetry can be used for is the characterization of the fillers themselves. It is important to know the content of filler in the elastomer but being able to identify the filler at the same time can be extremely useful. Several different approaches have been taken using TGA (and DTG) to identify fillers. In one approach, after the polymers and oils have been pyrolyzed, the oxidative degradation of the carbon black can be used to characterize the specific surface area of the carbon black [81,88,89]. By determining the temperature at which 15% of the carbon black has been combusted (T_{15}), the specific surface area can be approximated. As shown in Fig. 16, when free carbon black is combusted, there is a nearly linear

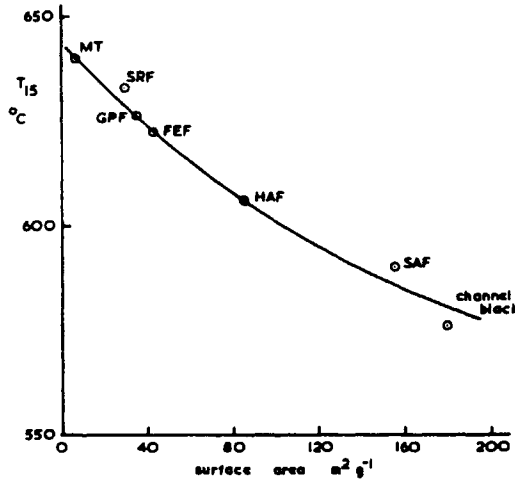


Fig. 16. T_{15} values for free carbon blacks of different surface areas

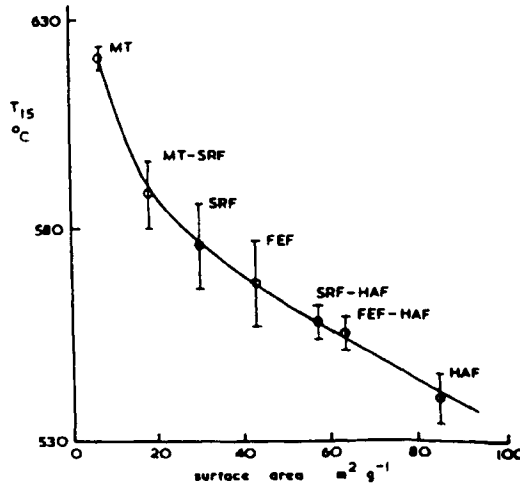


Fig. 17. T_{15} values for carbon blacks in NR formulations

relationship with specific surface area. When the carbon black is in an elastomer, the linearity of the relationship is not perfect but still quite useful for calculations. As seen in Fig.17, the T_{15} of carbon black in natural rubber approximates a linear correlation except at very low surface area. This technique does require attention to variables that effect the relationship. These include maximum temperature during the pyrolysis step, flow rate and heating rate during the combustion step, cure method of the rubber and manufacturing source

of the carbon black. Within the framework of a quality control laboratory, with proper calibrations standards and consistent technique, this approach is quite reasonable. Otherwise, caution must be used in drawing conclusions from a T_{15} determination.

The average mean diameter (AMD) of a carbon black has been described as an effective way of characterizing the physical-chemical nature of a carbon black. This AMD, which can be measured microscopically, can also be calculated using the Smith formula based on the determined tint and DBP (amount of dibutyl phthalate absorbed) values for the carbon black. The determination of the AMD via thermal methods has been suggested using TGA to determine the temperature at which 50% of the carbon black has been combusted (T_{50}) [79]. A relationship between the T_{50} and the AMD may exist but is not linear across the entire range of particle sizes, as shown in Fig. 18. This analysis is complicated by the need to avoid milling of the sample, which can change the effective particle size of the carbon black. Also, differences in the pyrolysis temperature of certain elastomers were noted when comparing this technique (for using unmilled) versus standard milled samples. Natural rubber causes the carbon black to combust at higher temperatures in milled samples, in spite of the fact that natural rubber pyrolyzes at lower temperature than SBR. This difference was postulated to relate to bound rubber that remains on the surface after the standard pyrolysis step and delays the combustion step. The non-linearity appears to take place at the AMD of N330 HAF carbon black and it was suggested that this provides a division between the carcass and tread blacks. Again, caution should be exercised in using this technique because of the number of variables that remain unresolved or unexplored at this time.

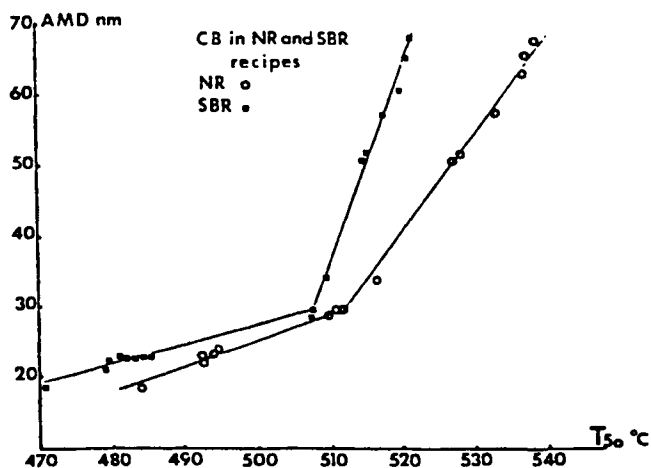


Fig. 18. Identification of carbon black type via T_{50} values in NR and SBR

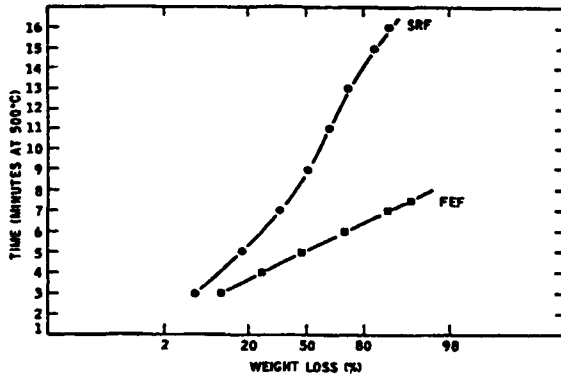


Fig. 19. Carbon black weight loss versus time at 500°C

Another method for characterizing the carbon black in compounds is the isothermal oxidation of the carbon black at 500°C [81]. When different carbon blacks are oxidized by this method, they produce different weight loss curves that are attributed to different oxidation processes. As shown in Fig. 19, one carbon black (FEF) gives a nearly linear plot of weight loss versus time while another carbon black (SRF) gives a non-linear curve with a significantly different weight loss rate. It is suggested that these curves can be used to fingerprint the carbon black for characterization purposes. The number of variables unexplored in this work suggest the need for establishing strict procedures for analysis.

Thermogravimetry has also been used to characterize the reinforcing nature of carbon blacks [100]. By determining the specific reaction rate of the combustion of the carbon black and comparing it to the surface area of the carbon black, results indicate that higher surface area carbon blacks are both less reactive to oxidation and provide significant interaction with rubber, which has been attributed to the presence of exposed basal planes, thereby acting as reinforcing materials instead of acting as simple fillers. This method of characterizing the carbon black can help in the selection of reinforcing blacks for carbon black-elastomer composites.

The interaction of carbon black or other fillers with elastomers can also be characterized using dynamic mechanical analysis. In fact, this approach can provide significant information concerning the properties that result from addition of fillers and reinforcing materials. At low strains, unfilled single elastomer systems usually display linear viscoelastic behavior between T_g and T_m but carbon black filled elastomers often do not. This phenomena has been ascribed to reversible filler-filler structures [101]. Similar results have been seen in polyethylacrylate filled with carbon black and with silica and were attributed to "cross-linking" type filler-rubber interactions [102].

In one study, evaluation of the dynamic modulus and hysteresis of carbon black-filled elastomers was carried out using a variety of experimental conditions [103]. The results showed that for carbon blacks with equal surface areas, higher structure provided higher dynamic modulus and comparable hysteresis. When equivalent structure carbon blacks are used, higher surface area blacks gave higher modulus and higher hysteresis. From these results, two primary means of reinforcement were concluded. At large strains, hydrodynamic interaction dominates the dynamic and tensile properties. Here, the strain field is modified in the region of the carbon black aggregates controlling the effective volume of the carbon black. At low strains, increases in the modulus beyond those predicted by the hydrodynamic interaction are the result of the entanglement network formed between the carbon black and the elastomer. This is essentially an increase in the effective crosslink density of the network. This is the result of rubber tightly bound to the carbon black and is directly attributed to the surface area and surface chemistry of the carbon black. This type of characterization provides significant information for the design of filled elastomer systems.

Another DMA study involved evaluation of carbon black filled elastomers under both normal and solvent swollen conditions [104,105]. Storage modulus, loss modulus and loss tangent were evaluated at various temperatures, carbon black loadings and for various surface area carbon blacks. Increasing the carbon black content increases hysteresis even under swollen conditions. Swelling in a solvent (or oil) also can reverse trends in loss modulus at low and high amplitudes. In fact, the storage modulus of vulcanizates with various carbon black loadings show no regular trend when swollen. Overall, the results point to specific interaction between the carbon black and the elastomer (loose network entanglement, weak elastomer filler attachment and weak inter-aggregate interaction) that can be disrupted by solvent swelling.

Comparison of the interaction of several “fillers” with an elastomer (ENR) was conducted using DMA to characterize the differences in mechanical response [106]. With increasing interaction between the elastomer and the “filler”, the loss tangent peak height is reduced and the peak spreads over a wider temperature range. The storage modulus curve also increases its spread with the same increase in interaction. The fact that a clay-filled sample had similar properties to a gum sample supports the non-reinforcing nature of clay.

Fillers also affect other properties of elastomer composites. The heat transfer properties of elastomers have become very important to the rubber industry. The rate at which heat gets into and out of an elastomer (thermal conductivity) affects the processing steps involved in preparation and processing. These properties have continued to increase in importance with consideration of the thermal properties of cured elastomeric products. The thermal conductivity of a filled elastomer is affected by both the carbon black level of the sample and

the structure of the carbon black. However, there is some conflict in the literature with regard to the effect of carbon black content on the thermal conductivity, k , of a cured elastomeric compound. One report showed an increase in thermal conductivity with increasing carbon black content which reversed at high contents (exceeding 20 volume % in the compound) [107]. This work appeared to confirm previous indications that the thermal conductivity was an additive function of the volume fraction of the constituents. However, recent work disputes this claim and shows a reverse trend, where thermal conductivity decreases with increased carbon black content up to about 80 phr where the conductivity begins to increase [108]. Accompanying this decrease in thermal conductivity are decreases in the thermal capacity, a , and increases in the thermal diffusivity, c . The structure of the carbon black also affects the thermal conductivity. Increasing structure has the same apparent effect as does a tighter bond and increases the thermal conductivity. Comparing the thermal conductivity of carbon blacks to silica and zinc oxide shows that zinc oxide increases the conductivity more than carbon black which increases it more than silica. These results are useful for the design of the compounds where thermal conductivity is an important consideration. There is also a conflict in these references concerning the effect of temperature on the thermal conductivity. A resolution of these differences will be necessary. The importance of this aspect of elastomer characterization will increase in the future.

The electrical properties of elastomers have been both a key property in their use and a convenient method of characterizing polymer structure. Among the variables that can affect the electrical properties are time, temperature and mechanical strain. This link between the electrical and mechanical properties offers a new means of characterizing the viscoelastic response of elastomers.

One example of a technique that utilizes this link is DC conductivity measurements which have been performed on filled elastomers to characterize the effect of fillers at various loadings, temperatures and under various cyclic strains [109,110]. It has been shown that electrical conductivity, S , decreases with increased numbers of strain cycles and amplitude of a cyclic deformation. Also, there is a distinct temperature dependence for the conductivity, with increasing temperature resulting in decreased conductivity. The decrease in conductivity is attributed initially to the breakdown of the carbon black structure. This is followed by a tendency for the carbon black to align during the application of the cyclic strain. Finally, a balance between these two mechanisms results in an almost temperature independent behavior. Therefore, only at high deformations (>30% strain) and large numbers of cycles (>106) does the conductivity become temperature independent. Natural rubber was also shown to have better conductivity than SBR, possibly attributable to the additional materials that are inherently part of this rubber.

Above, we have discussed traditional fillers and reinforcing agents. Another class of reinforcing materials that have appeared in recent years are thermoplastic polymers [111-114]. The use of thermoplastics as reinforcing agents is dependent on the proper dispersion of the thermoplastic in the elastomer. One approach to assuring the proper dispersion of the thermoplastic is to utilize a copolymer containing segments of both polymers involved in the blend. DSC can be used to characterize the compatibilization process by monitoring the crystallization of the thermoplastic phase and the effect the copolymer has on that crystallization. Additionally, DMTA can be used to monitor changes in T_g of the elastomer and the a transition of the thermoplastic. In the case of a polyethylene/polyisoprene blend being compatibilized by a polyethylene/polyisoprene copolymer, DSC was used to show broadening of the polyethylene crystallization peak and DMTA was used to show lowering of both T_g and a transition [115]. This data points towards better compatibilization of the pair and enhanced interpenetration of the two components.

5.2. Oils, plasticizers

The other primary additives used in elastomer systems are oils and plasticizers, both used to decrease the modulus of the elastomer composite. Characterizing the nature and level of these components can be as important as understanding the effect of fillers. Again, a variety of thermal techniques can be used to characterize these materials.

Thermogravimetry is one of the more traditional techniques used to quantify the amounts of this class of materials in a compound. The standard approach of pyrolyzing a sample and estimating the oil level from the scan has been used to quantify the oil content [2,25,74,116-118]. The primary problem encountered with the analysis of oils and plasticizers is the overlap with the elastomer degradation peaks. Several approaches are offered in the literature to overcome these difficulties. The interpretation of the curves can be improved by use of one of three techniques: 1) overlay the TG curve of the unextended elastomer (under the same experimental conditions) to determine the onset temperature and separate the oil from the elastomer, 2) use a graphical extrapolation of the linear regions of the oil weight loss and plateau before the elastomer degradation and 3) use the minimum of the DTG curve to determine the changeover from oil to elastomer. In the latter technique, the proportionality of the segments of the loss curves from the oil and elastomer are not exact in this overlap region and care must be taken to avoid assuming equality of components in this area. Additionally, it has been suggested that extraction of oil from the sample prior to analysis might improve the determination. Recent advances in the capabilities of temperature programming for TGA runs have also improved the quality of the separations of the different components and, in turn, improved quantification of oil and plasticizer levels [87,95-98]. Additionally, the use of

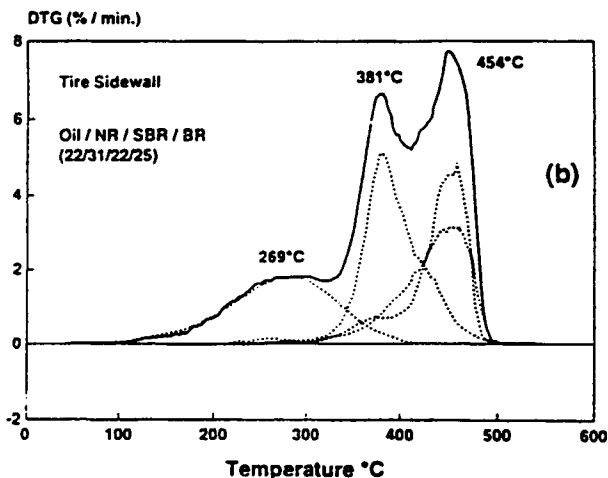


Fig. 20. Identification of tire rubber from passenger tire sidewalls: (a) tested and simulated DTG curves of samples; (b) curve simulation based on 22% oil + 31% SBR + 25% BR

vacuum instead of passive gas during the initial pyrolysis steps has improved the separation of the peaks associated with oil volatilization and polymer degradation [119].

Further improvements in the analysis of the TGA/DTG curves has been accomplished by the use of kinetic simulation [120]. In this technique, a series of DTG curves are generated from pure components of the compound, allowing generation of kinetic parameters of the degradation of each material. Once the components of a compound have been identified qualitatively, the kinetic data can be used to generate model curves to fit the curves generated for the entire compound. Relatively accurate analyses of the curves can be conducted using the kinetically derived curves, as shown in Fig. 20. This technique has been applied to both the elastomer and oil portion of a number of compounds containing various rubbers.

DSC can be used to characterize both the approximate level of a plasticizer and the interactions between the plasticizer and the elastomer. In an example, dimethylterephthalate (DMT) was used as a plasticizer at various concentrations for both *cis*- and *trans*-polyisoprene [121]. The T_m of the plasticizer was shown to decrease monotonically with the concentration of the plasticizer in the elastomer. The *trans*-polyisoprene affects the DMT melt point more than the *cis* elastomer, suggesting a stronger interaction between DMT and the *trans*-polyisoprene. However, when either the plasticizer or elastomer are in a crystalline state, any interaction vanishes due to phase separation.

DSC can also be used to determine the compatibility/solubility of a plasticizer-type material [122,123]. Here, an endotherm appears in the DSC curve when the solubility of the plasticizer in the elastomer has been exceeded. The temperature dependence of this solubility can also be determined by the same method.

Both DSC and DMTA can be used to characterize the effect of adding oil or plasticizer [124]. Increasing the paraffinic plasticizer level in bromobutyl rubber was shown to decrease T_g of the elastomer and to decrease the E' values. The effectiveness of the plasticizer decreases with increasing level in the rubber. Also, the energy absorption intensity ($\tan \delta$ peak height) increases with increasing plasticizer content. These results cannot be used for quantitative analyses but do provide information on the interaction of the plasticizer with the elastomer. DMTA was used to determine the effective character of epoxidized rubber added to an epoxy resin. In this series of partially miscible blends, it was used to distinguish between rubber: 1) dissolved in the matrix, acting as a plasticizer, 2) incorporated into the matrix, acting as a flexibilizer and 3) rubber phase separated from the resin, the rubber acting as a toughner [18].

5.3. Other additives and components

Solvents are one class of material that can be used in the manufacture of polymers (chlorination, etc.) or be part of the final product (glues, etc.). The determination of their presence can be vital to both the utility of the product and environmental concerns. This might be accomplished by TGA using an isothermal step at a low temperature or by using a low pressure preliminary step, again at low temperature, to remove these volatiles [74].

During the chlorination of polymers, tetrachloromethane is used to dissolve the polymer and act as a solvent during the reaction. At the end of the process, the solvent must be removed. TGA has been used successfully to determine the quantity of residual solvent left in these polymers [125]. This material is detected as an early weight loss in the scan. It was also noted that if a plasticizer is added to the chlorinated elastomer during the manufacturing process, essentially no chlorinated solvent is detected after the drying step.

Solvents are often used as bases or carriers in glues or adhesive film-forming materials. TGA has been used to characterize the rate of evaporation of the solvent from the cement [126]. First, the evaporative rates were established for the appropriate solvents at the desired temperatures and these were compared to the rates of evaporation during adhesive film-forming. It was noted that the evaporation rate tails off due to formation of a film. The severity of the tailing is due to the hardness of the film being formed, which restricts the permeability of the solvent. The temperature dependence of these evaporations was also studied.

The use of resins and oils to modify an adhesive's performance has been studied by DMTA [127]. The loss tangent and storage modulus of elastomers

used in pressure sensitive adhesives were evaluated and compared to a set of operating parameters for an adhesive system proven to be successful for this application. Modification of the properties by these additives was shown to enhance certain polymers, making them viable materials for use in adhesive systems. Additionally, the compatibility of the resins used can also be ascertained by these techniques.

Monitoring the dimensional changes by thermomechanical analysis (TMA) can be used to accurately quantify effects of fillers, plasticizers, blowing agents etc. in thermoplastic elastomer systems, such as cellular thermoset foams [128].

Compatibilizers are another class of additive that are sometimes included in elastomer systems. The compatibilizer, sometimes called interfacial agents, are used to improve properties of blends of two or more elastomers by preventing gross segregation of phases and by improving interfacial adhesion, thus yielding improved dispersion during mixing. The efficiency of these compatibilizer, often block or graft copolymers of the elastomers to be compatibilized, can be determined by a DSC examination of the glass transition or crystalline melt properties.

5.4. Compositional analysis/formula reconstruction

The overall process of analyzing the additives in an elastomeric compound is a major part of process control and trouble shooting in the rubber industry. The primary technique used is TGA using many of the approaches discussed above. But the use of other techniques such as DSC, DMTA, etc. to complement the TGA analysis is common. There are many examples of compositional analysis of a variety of elastomeric compounds both cured and uncured [4,27,71,78-81,86,87,129,130] and further refinements in the technique to improve accuracy and increase the ability to identify the additives, such as varying TGA pyrolysis atmospheres to maximize component separations [131], can be expected in the future.

6. CURING

Once elastomers and additives have been mixed together to give the desired compound, vulcanization (or curing) must occur to reach the final, semi-permanent physical state of the product. The vulcanization, or curing, process involves the establishment of bonds between the polymer chains in the matrix, which reduces the viscous nature of the matrix. These bonds can be generated by a variety of chemical means including peroxides, sulfur-based curatives, ionic crosslinkers, resin systems, *etc.* Each curing system differs in some aspects and should be considered separately. There are many ways to characterize curing processes by thermal or calorimetry techniques: by examining the energy

associated with the cure process, the rate of curing and the state of cure of the elastomer network. The following will include brief examinations of each of these types of curing systems.

6.1. Peroxide cures

Peroxide cures can be described as free radical cures initiated by the thermal decomposition of a peroxide. Upon generation of a free radical oxygen species, a hydrogen is abstracted from the polymer chain. The resulting carbon radical species then reacts with another free radical (possibly on another polymer chain), reacts with another double bond to produce a new free radical species (and possibly a crosslink) or begins a degradation process of polymer chain breaking. (The extent to which each of these different reactions occurs is dependent on the chemical structure of the elastomer.) The net result of this process is to generate carbon-carbon bonds between polymer chains. The temperature at which the peroxide decomposes and the rate of the generation of the free radical species are dependent on the structure of the peroxide used. DSC can be used to determine the ΔH , E and k_d associated with the decomposition of the peroxide [132] as well as the exotherm associated with curing

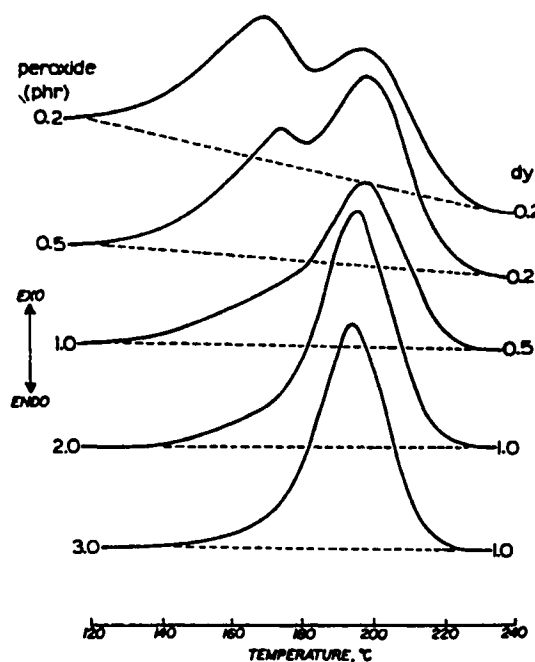


Fig. 21. Effect of dicumyl peroxide level on the enthalpy profile of nitrile rubber

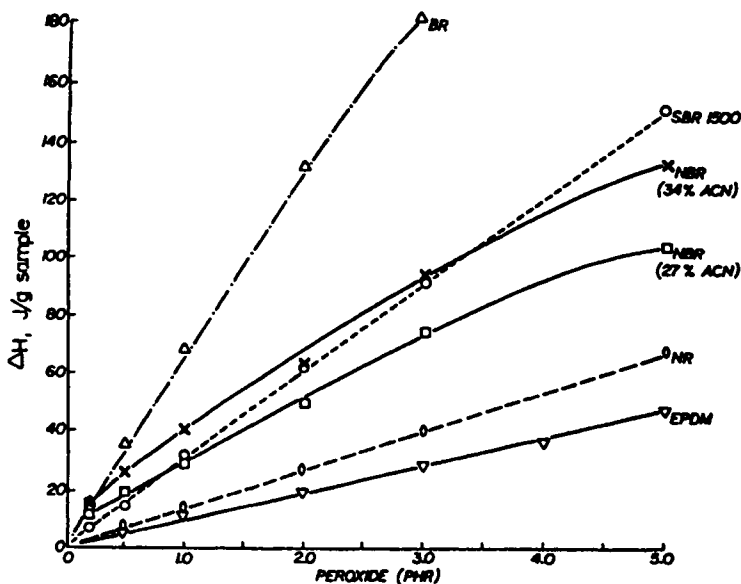


Fig. 22. Enthalpy of cure of various elastomers versus dicumyl peroxide level

[8,62,132,133]. As shown in Fig. 21, the peroxide cure of an elastomer typically shows two peaks, the lower temperature peak diminishing in size at higher peroxide levels. The first peak is usually associated with the reaction of the peroxide with antioxidant or some other additive or impurity. All synthetic elastomers have antioxidants added to prevent degradation and natural rubber has a reasonable level of protein and other organic material to react with the peroxide during the cure. The exotherm resulting from a peroxide cure (ΔH_v) can be correlated to the level of peroxide used and the elastomer being cured [62,132,134]. Fig. 22 shows a nearly linear relationship between the cure exotherm and the peroxide level used for a variety of elastomers. Of the elastomers evaluated, only NBR does not intercept the origin at 0 parts of peroxide, having a not very reproducible enthalpic event of about 8 J/g that is not associated with the peroxide cure. It should also be noted that this evaluation extended only to 5 parts of peroxide. These results could be used to determine the level of peroxide used for curing, assuming that other additives do not interfere with the exotherm.

Thermomechanical analysis has also been used to characterize the cure of a peroxide cured system [2]. The degree of cure can be determined by measuring the dimensional changes as a function of temperature. As the degree of cure increases, the magnitude of dimensional change is increased. This

analysis also provides coefficient of thermal expansion data, which is quite useful in designing elastomer systems for specific applications. TMA has been used to characterize the state of cure of a chlorosulphanated polyethylene compound [4]. The state of cure, uncured through fully cured, can be determined by measuring the dimensional changes as the temperature is increased. State of cure can also be measured by DSC T_g determinations [135,136].

6.2. Sulfur-based

Sulfur-based cure systems remain the most common type of cure package used with elastomers. The distinctive nature of sulfur-based crosslinks makes them especially useful in demanding applications. Unlike the carbon-carbon bonds formed by peroxide cure systems, the sulfur-sulfur bonds that are part of the mixture of crosslinks formed by sulfur-based curative systems can be broken and reformed under high strain, allowing the elastomeric network to relieve some of the stress developed during processing or in-use. This “give” provides some unique characteristics that make sulfur-based curing of elastomers desirable.

The characterization of these curative systems is usually performed by DSC. Many examples exist for the characterization of the cure exotherm using standard dynamic scans [8,62,68,80,81,137-142]. These scans can be used to

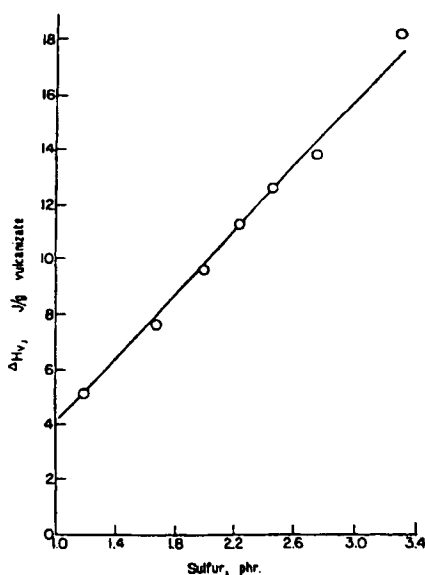


Fig. 23. Dependence of enthalpy of vulcanization on sulfur level. Calibration curve for 80:20 NR:BR blend

characterize both the magnitude and the temperatures of the exotherm. The size of the exotherm can be related to the level of sulfur in the cure system [62,81]. A simple plot, like that shown in Fig. 23, can be used to correlate the sulfur level with the size of the exotherm. However, more sophisticated approaches can be taken. By determining the ΔH_v and the peak temperature, T_p , of a series of samples, a series of equations were derived to describe the sulfur and accelerator in the cure system. It was found that the ΔH_v was related to the sulfur level and the peak temperature was related to the amount of accelerator. This approach works well for a specific rubber compound but is not universally applicable.

DSC can provide information concerning the nature of the cure system. As shown in Fig. 24, the ratio of sulfur to accelerator can be ascertained by the shape of the curve. Unaccelerated sulfur curing shows a single peak at a substantially higher temperature than for a sulfur-accelerator combination. During the transition from sulfur-only to the low sulfur-to-accelerator ratios,

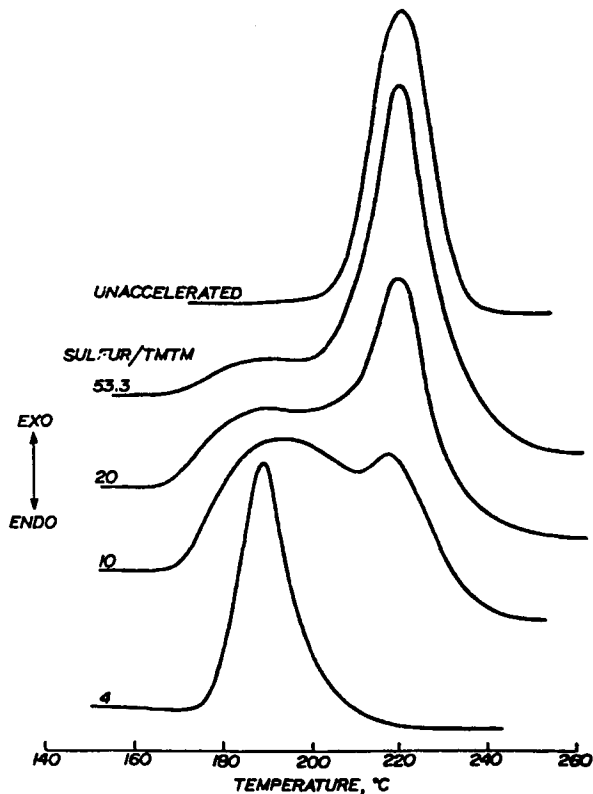


Fig. 24. DSC scans of NR compounds with various ratios of sulfur/accelerator

there are two peaks associated with the cure. Only at the low sulfur-to-accelerator ratio of about 4:1 does the cure return to a single peak. DSC can also detect the influence of impurities in the elastomer, such as the proteins, etc., in natural rubber that cause the cure rate to be faster and the cure exotherm to appear at lower temperatures.

DSC curves have also been used to characterize the state of crosslinking in a material. The residual exotherm for a sample can be empirically related to the state of cure. The higher the state of cure, the smaller the residual cure exotherm that can be observed. (This applies to samples with the same cure system.) This technique has been used to characterize the state of cure as a function of the cross section of the sample, as shown in Fig. 25 [62,142]. Here the center of the sample is not cured completely and shows a larger residual exotherm than the sections from the outside of the sample.

Differential calorimetry (DC) can be used to characterize the state of cure of tire rubbers (SBR/NR) containing a sulfur-based cure package [143,144-146]. The purpose of this approach was to characterize the kinetics of the cure reaction in terms of the effects of cure enthalpy, thermal conductivity and mold temperature. Using this information, one can calculate the state of cure of samples with various cure enthalpies, various cross-sectional diameters and at various temperatures. This information is very important for assuring that

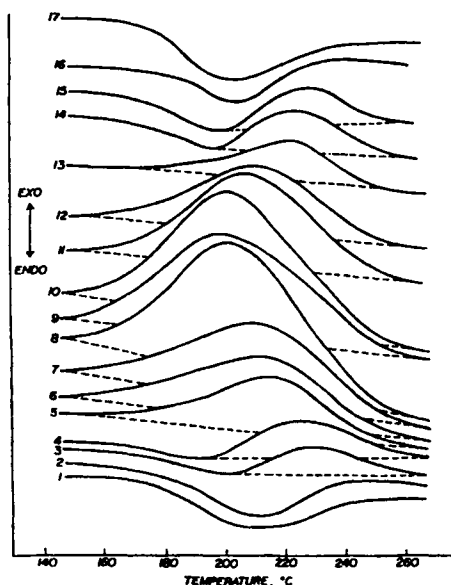


Fig. 25. DSC curves of sections through a thick block of rubber

samples are cured properly and for knowing the cross-sectional cure state of various products.

The potential for utilizing DSC scans to characterize the kinetics of curing has always been appealing. Several attempts to correlate cure exotherm data from DSC curves with rheological data for curing have been made [137,142,147]. These were made in the hopes of providing kinetic data for the establishment of crosslinks directly from DSC or DC data. Unfortunately, there is not a direct relationship between the DSC curves and the curves derived from rheometers and other rheological instruments. As seen in Figs. 26 and 27, the curve derived from DSC data for a standard sulfur cure appears to resemble the derivative (rate of change) of a rheometer curve while the curve for an efficient cure system did not show any apparent relationship.

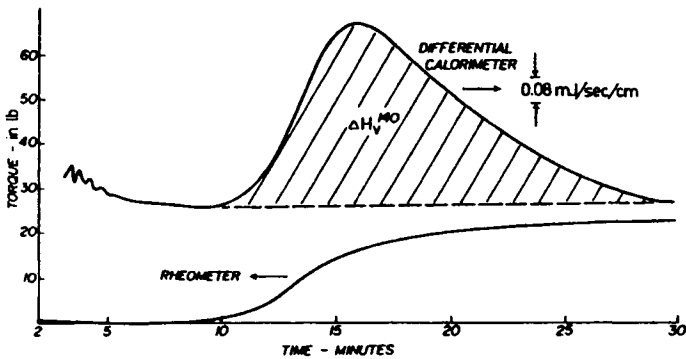


Fig. 26. Comparison of DC and rheometer curves for standard sulfur cure

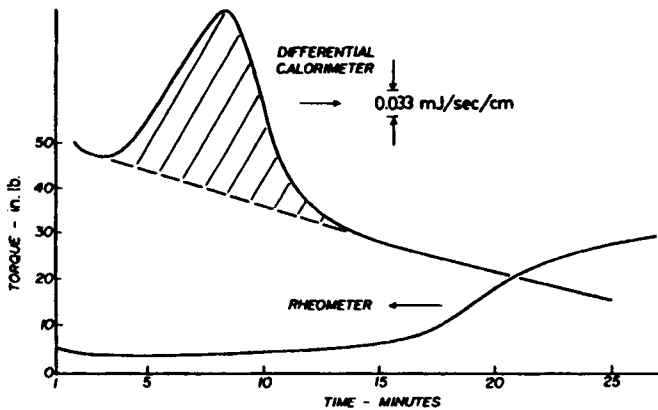


Fig. 27. Comparison of DC and rheometer curves for efficient vulcanization cure

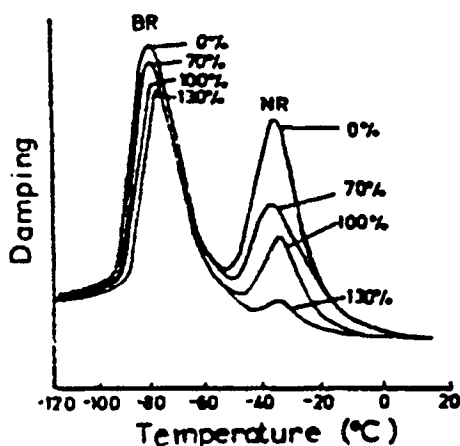


Fig. 28. DMTA damping curves for NR/BR blends at various percentages of optimum cure time

Dynamic mechanical analysis has been used to characterize the nature of curing of blends of polymers [140]. In this technique, the damping peaks of the elastomers in a blend were monitored as a function of cure time. The assumption made in this study is that the size of the damping peak will decrease as the state of cure increases. Since each elastomer has its own characteristic damping peak, it is possible to follow the curing of each elastomer as a function of time. As seen in Fig. 28, at various percentages of the optimum cure time the damping peak for natural rubber is decreasing much faster than the peak for polybutadiene. This is ascribed to the natural rubber phase curing faster than the polybutadiene phase. This differential in curing rate can affect the ultimate physical properties of the compound. The quantitative use of these damping peak decreases is intriguing but require further evaluation before the state of cure of each phase of a blend can be ascertained from these types of curves.

The interaction of the various components of a standard sulfur cure system have been studied to more fully understand the curing mechanism [138,139, 148,149]. By evaluating the nature of the endotherms and exotherms generated from various combinations of the curative system components, details of their role in the curing process can be established. Here, a systematic evaluation was made of the interaction of the individual components, their binary pairs and other in combinations. In this way, various parts of the curing scheme were assembled. The interaction of zinc oxide and stearic acid, zinc oxide with various accelerators and sulfur with accelerators was noted.

Another example of curative interaction study was performed on an elastomer compounded for controlled release of an additive [150]. In this

example, sodium lauryl sulphate was added to either natural rubber or synthetic polyisoprene for controlled time release. Unfortunately, the additive interferes with the cure as observed by the reduced ΔH_v . As the level of additive is increased, the size of the ΔH_v decreases. The threshold at which the cure exotherm was effected was also determined by examining various levels of additive.

6.3. Miscellaneous

Other crosslinking reactions can be used to cure elastomers. Among them are the use of resin cure systems, the generation of ionic crosslinks and self-vulcanizing systems utilizing other chemical reactions. The resin cures usually consist of a resorcinol or resorcinol-derivative that reacts with another chemical to form a network with the elastomer. Typical of the chemicals that form resins with resorcinol are hexamethylenetetramine or hexamethoxymethylmelamine. The cure associated with these systems can be detected by DSC as separate cure peaks, typically occurring at lower temperatures than the sulfur-based cure, [62] as seen in Fig. 29.

Resin cures are also used in resorcinol-formaldehyde-latex (RFL) adhesive systems, commonly used for adhesion of fabric to elastomers. DSC can be used to follow the cure of the resin system [151]. The cure reaction for these resin systems are claimed to be endothermic and are difficult to follow in some cases.

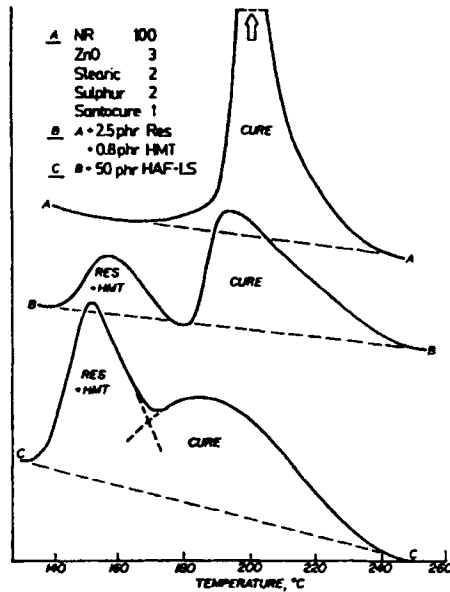


Fig. 29. DSC curves for resin and sulfur curing of NR

However, the T_g of the RFL system reflects the heat history and state of cure. The T_g of the rubber in the latex can also be observed in these systems.

Analysis of a bis-maleimide/piperazine (BMI) cure of amino terminated polydimethyl-siloxane elastomer (PDMS) showed that the incorporation of flexible PDMS blocks into a rigid BMI network significantly influences the cure process [152]. Using a torsion braid analyzer (TBA) at isothermal conditions to monitor the curing reaction, some correlation was found between the heat of the reaction for crosslinking (DSC) and G' behavior during crosslink formation, as obtained from TBA.

The crosslinking of a two part elastomeric liquid silicone resin system, consisting of PDMS with vinyl methyl silanol and a low temperature catalyst, H_2PtCl , was monitored by DMA technique at 100kHz [54]. This high frequency method allows the crosslinking, and the polymerization in this system, to be monitored throughout the transition of the liquid to the solid state.

Ionic crosslinks provide another means of chemically increasing stiffness in elastomers systems. A number of chemical approaches are available to generate these crosslinks, including grafting acid functions to elastomers. Phosphonylation of EPDM has been used to functionalize an elastomer for ionic crosslinking [153]. Although the formation of the ionic crosslinks in such a system is not reported, the effect of the ionic crosslinks has been studied by thermomechanical analysis. TMA (via measuring probe deflection) has shown

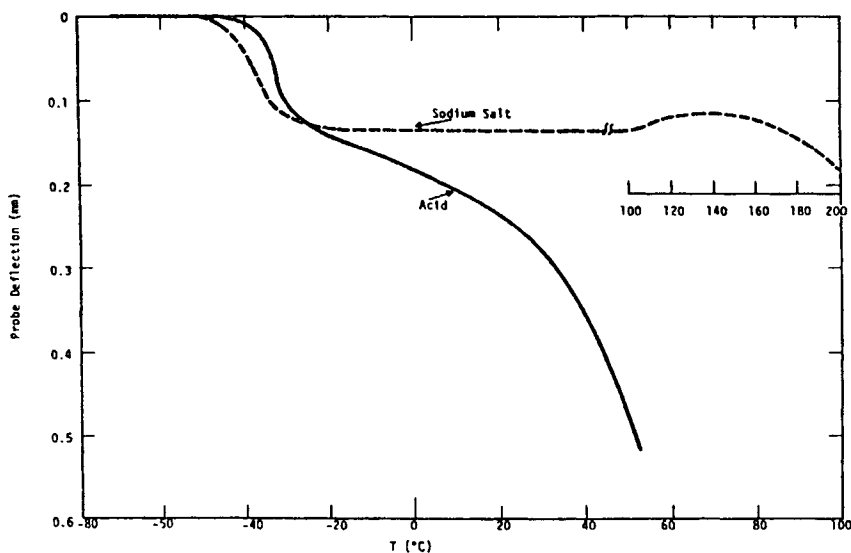


Fig. 30. TMA curves for phosphonylated EPDM - acid and salt forms

that at low phosphorylation levels, the T_g of the elastomer is hardly affected and a typical plateau region is observed. However, at higher phosphorylation levels, the T_g moves to higher temperatures and there is a larger plateau region. When the phosphonic acid groups are titrated to the sodium salt, the T_g is lowered and the plateau region is prolonged, as shown in Fig. 30. Although not quantitative, this approach does provide some characterization of the effect of this class of crosslinks.

Self-vulcanizable blends of elastomers exist where each elastomer has a functional group that allows the formation of crosslinks. An example of such a system is the crosslinking of carboxylated nitrile rubber and epoxidized natural rubber [154]. DSC has been used to show the cure exotherm associated with the self-vulcanization process. The temperature of onset of the crosslinking depends on the ration of the two elastomers in the blend. At high epoxy-to-acid ratios, the cure exotherm occurs at higher temperatures. This reflects the nucleophilic nature of the acid functionality. The ΔH_v of this crosslinking also depends on the ratio. Again, at high epoxy-to-acid ratios, the size of the exotherm is much reduced. DTA has been used to study the thermal behavior of epoxidized butadiene crosslinked with hydroxy containing compounds [155]. The efficiencies of the various cure systems for producing more flexible rubbers was compared and evaluated.

The cure kinetics of a rubber-toughened thermoset, diglycidyl ether of bisphenol-A, with a series of amines, and 60% amine-terminated butadiene acrylonitrile (ATBN) has been studied by DSC under isothermal and dynamic conditions [156]. The phase behavior of the system was undetectable by DSC but was shown to have a significant effect on both the rate of curing and the extent of cure.

7. STABILITY

The ultimate utility of elastomeric compounds in products depends on the maintenance of the physical properties that were built in to them during compounding and established during crosslinking. Unfortunately, the very reason that elastomers have their distinctive properties makes them vulnerable to both thermal and oxidative degradation. The unsaturation in the main chain of most elastomers is the functionality that is susceptible to attack by oxygen, ozone, numerous other chemicals and heat. The evaluation of the stability of elastomers and the success of various stabilizers in protecting them has become an important task for thermal analysis and calorimetry. Aside from the use of "degradation processes" in compositional analysis, a number of thermal techniques have been used to characterize the stability of elastomers and elastomer containing products.

7.1. Oxidative stability

The effect that oxygen, ozone and other oxidizing materials have on elastomers directly affects their physical properties and thus product performance. Oxygen attack causes free radical species to be generated that often cause either crosslinking or breakdown of elastomer chains. Examples of this reaction are the oxidative gelling of polybutadiene or the oxidative breakdown of natural rubber. Each elastomer's physical properties are affected by oxidation but the chemical structure of the elastomer dictates the mode by which this degradation takes place. Ozone reacts with the unsaturation in an elastomer causing a double bond to be cleaved. When the unsaturation is in the main chain, the chain is cleaved. If the unsaturation is pendent to the main chain, the chain is functionalized and smaller molecules may be volatilized. For both oxygen and ozone, these reactions are exothermic and are easily detected using differential scanning calorimetry or other heat flow detecting techniques. The fact that these oxidation processes may also lead to the generation of volatile materials lends these processes to evaluation by thermogravimetry.

There are many examples in the literature of the use of DSC to characterize oxidation processes [84,157-162]. Typically, these evaluations are conducted in one of two ways: either a dynamic scan is performed with an increasing temperature program or the experiment is performed isothermally. In the dynamic scan technique, the characteristic temperature of the exothermic peak is used to characterize the difference in oxidation resistance between elastomers. As shown in Fig. 31, the stability of the natural rubber is better than that of synthetic polyisoprene. This is ascribed to both the natural antioxidants in the natural rubber and the pro-oxidative catalyst residues left in the synthetic

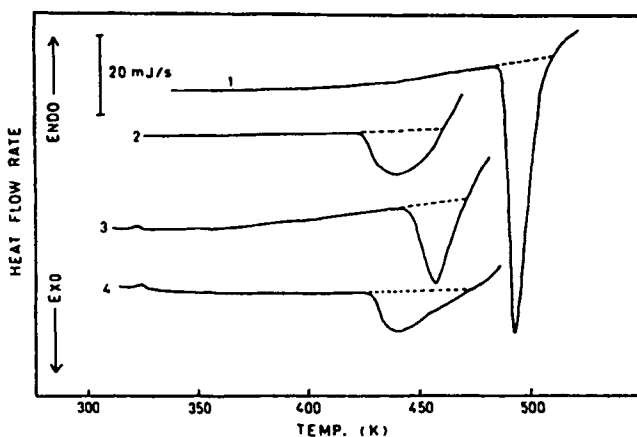


Fig. 31. Comparison of various polyisoprenes in air by DSC

polymer. The same situation occurs between gutta percha and its synthetic analog. These differences in the stability of natural rubber and synthetic polyisoprene has been used as a tool to differentiate between them in blends [84]. The ΔH_{ox} for these same blends also correlates with composition. This points out the opportunity to utilize the heat of oxidation as a characteristic of the material.

Differences in scan rate will result in different peak temperatures which can be utilized to further characterize the oxidation process [158]. Equations by Kissinger and Doyle-Ozawa have been derived to calculate the activation energy of the oxidation process, which in turn can be used to calculate the isothermal oxidative induction time. Comparison of the activation energies of various elastomers can be used to describe the elastomer's relative oxidative stability.

These techniques can also be used to characterize the effectiveness of various antioxidants that are added to the elastomer to preserve its physical properties. Again, comparing the peak temperature of the oxidation process will provide a qualitative measure of the effectiveness of the antioxidant [118,160]. A plot of the activation energies that result for the elastomer due to the addition of an antioxidant can also be used to characterize its effectiveness [158,159]. Typically, addition of an antioxidant to an elastomer will result in an increase in the activation energy. However, the level of antioxidant used must be optimized because the presence of too much antioxidant can have the same effect as too little.

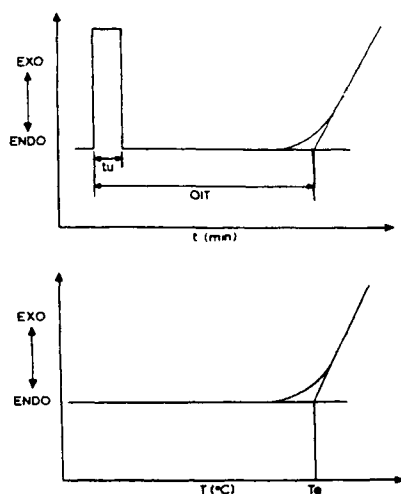


Fig. 32. DSC scans showing the calculation of OIT (1) and T_e (2)

The oxidative stability of elastomers, and the effectiveness of antioxidants, can be also evaluated by DSC using either the change in heat during oxidation, the activation energy of oxidation, the isothermal oxidative induction time (OIT), the onset temperature of oxidation (T_e) or the oxidation peak temperature (Fig. 32 shows the determination of OIT and T_e) [163,164].

The isothermal OIT technique is useful for comparison but usually requires the use of an elevated temperature. Isothermal or oxidation induction times, calculated from the activation energy of the oxidation, can be confirmed by this method. Since estimates of the lifetime of an elastomeric compound are often difficult to do at the temperature of use, elevated temperatures are used to bring the experiment into a reasonable time frame.

A series of dynamic DSC experiments was performed on polybutadiene rubber samples with a number of different antioxidants to test the applicability of performing the dynamic method for predicting isothermal oxidation induction time [164]. Arrhenius plots of the samples were superimposed to form a single plot using a shift factor dependent on the oxidation peak temperature (T_p) obtained for the different samples in dynamic experiments. The superimposed plot was then used to predict the OIT of other butadiene samples. A DSC study of the effect of two antioxidants on the stabilization of hydroxyl terminated polybutadienes was performed by both the isothermal and the dynamic methods with similar results [163].

DSC or DTA has also been used to study the oxidation induction times (OIT) as a function of the depth of the rubber from the surface [117,162]. As expected, the exterior portions of a sample show a faster decrease in OIT than does the interior. Also, shown in this example was the effect of binding the antioxidant to the elastomer. Here, the bound material did not migrate to the surface and maintained greater oxidation resistance over time.

TGA has been used to characterize the oxidative stability of natural rubber as a function of the level of epoxidation [60]. As the epoxidation level is increased, the oxidative stability is also increased. This is a result of the decreased in unsaturation in the elastomer. However, at the same time the oxidative stability is increased, the thermal stability is decreased.

The stability of a cured elastomer network evaluated as a function of crosslinking system utilized can be evaluated by dynamic mechanical analysis [141]. Examining the changes in both the storage modulus, E' , and loss tangent, $\tan \delta$, changes in the network can be observed. As shown in Fig. 33, significant changes in both curves are noted for an epoxidized natural rubber compound cured with a standard sulfur cure, with as little as 2 days aging. The poor aging observed is tied to the acid catalyzed ring-opening reaction of the epoxide groups. These reactions lead to ether crosslinks which significantly alter the elastomer's physical properties. Other cure systems were compared, including semi-efficient vulcanizations, peroxide cures, dibasic acids and the effect of

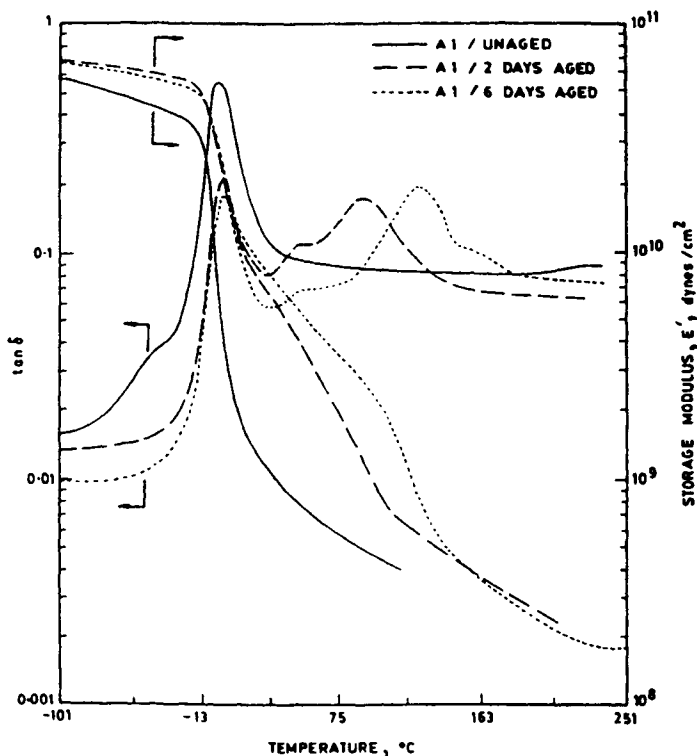


Fig. 33. Storage modulus, E' , and loss tangent, $\tan\delta$, versus temperature for cured, epoxidized NR

added sodium carbonate. The peroxide and dibasic acid cures were found to show the least effect upon aging.

As mentioned previously, dynamic mechanical analysis has also been used to characterize the aging of cure elastomers using various cure systems [141]. Dramatic effects are observed upon aging of epoxidized natural rubber for several sulfur-based curative systems. For standard sulfur cure systems, an increase in E' is observed and new peaks are observed, presumably associated with the generation of a second phase consisting of furanized NR. Addition of sodium carbonate does not stop this from taking place, as noted from the curves for that cure system.

The effect of resins (unsaturated acids) on the high temperature degradation of guayule rubber has been evaluated by TGA [165]. The presence of these acids leads to an additional peak in the DTG curve and lowers the degradation temperature, primarily due to the lower decomposition temperature of the acids. The activation energy of the oxidation of guayule rubber in air is

lower than that in nitrogen when the first 10% of the weight loss is determined. However, when the weight loss greater than 10% is used for the comparison (utilizing the method of Freeman and Carroll), the activation energies are the same. The same method of Freeman and Carroll was used to analyze data from dynamic TGA studies of the thermal degradation of fluorocarbon elastomers and compounds of the elastomers and silicate fillers, carbon black and cross-linker systems [56,57].

The thermal oxidative degradation of a dimethylsiloxane rubber containing ferric oxide was investigated by DMA and TGA [166]. The major weight loss event obtained from TGA was found to correspond to the major stiffening event as determined by DMA, both possessing a temperature maximum at 40% ferric oxide content, denoting maximum thermal oxidative protection.

TGA has been proven to be a valuable tool for the determination of the stability of silicone polymers [55]. Weight loss as a function of temperature reveals crucial information regarding the thermal stability, decomposition volatiles and the kinetic properties of silicone elastomers, base silicone resins, fillers, and their interactions with each other.

Isothermal TGA analyses were shown to be suitable for the characterization of silicone rubbers and silicone rubber containing products [52,53,167]. At a given temperature, the overall reaction rate constant calculated from the experimental results was shown to be related to the thermal stability of the rubber, with and without thermal stabilizers or antioxidants.

Flammability data for rubber compounds has been obtained by TGA [168]. Although this is an extreme form of oxidative stability, the TGA data correlated reasonably well with micro-scale flammability tests such as critical oxygen index and the ignition temperature. Comparison of TGA curves in air and in nitrogen provides a temperature at which combustion could occur. This temperature compares reasonably with the results of other flammability testing.

Another technique that can be used to characterize the degradation of an elastomer is electrothermal analysis [21]. It appears that the resistivity of an elastomer drops upon degrading and the temperature of the degradation can be determined. Although this technique does not appear to be as sensitive as TGA, it does have possible application as a confirmational technique when used with TGA.

Ozone also can attack the unsaturation in an elastomer and produce significant damage. DSC can be used to characterize the exotherms associated with ozonation but these are more difficult to detect since this is primarily a surface phenomenon. TGA has been used to follow the weight gain and subsequent weight loss associated with the reaction [169]. The effect of ozone on the oxidative stability of an elastomer has been characterized [161]. As expected, exposure to ozone decreases the stability of the elastomer up to the

point at which the unsaturation available has decreased significantly. At that point, oxidative stability will increase due to an overall decrease in unsaturation but the damage done to the elastomer makes this an unimportant fact. A DSC study of the thermal decomposition of ozonides prepared from two polybutadiene rubbers of differing microstructures suggested that the cis-ozonide species exhibited higher thermal stability than the trans by comparing the activation energies and enthalpies of thermal decomposition [170].

7.2. Thermal

Thermal aging without oxidative attack is a less common occurrence but can become the predominant factor at high temperatures. These processes are endothermic and reflect an internal degradation of the elastomer. Thermal cyclization, rearrangement of functional groups and main chain degradation are all possible routes to the breakdown of the elastomer. DSC has been used to characterize the thermal cyclization of polybutadiene [68], the ΔH value of this process can be used to characterize the BR content of a blend.

The thermally induced rearrangement of the epoxide group is a degradation that has been characterized by TGA [60,61]. As the level of epoxidation of natural rubber is increased, the oxidative stability increased, based on the increase in the T_{max} of the DTG curve, however, at the same time, the thermal stability is decreased. The addition of dinitrophenyl hydrazine to these elastomers resulted in an increase in the thermal stability of the elastomer presumably from a chemical stabilization of the epoxides.

TGA can be used to model the pyrolytic degradation of rubber from scrap tires [171]. The degradation is conducted to mimic the pyrolysis of scrap rubber to generate gases, liquids and carbon, which can be used as resources. The modeling done here was to evaluate the thermal degradation of the rubber and the effect of added potassium carbonate as a potential catalyst for the pyrolysis. The carbonate demonstrated no significant effect on the degradation, as measured by TGA, specifically not decreasing the degradation temperature. However, pyrolysis GC results showed some catalytic activity and a change of the product mix in the presence of the carbonate.

The thermal degradation of an elastomer used as a binder in a pyrotechnic system was characterized by TGA [172,173]. TGA coupled with mass spectroscopy and DSC has been used to monitor the degradation of alloprene to produce hydrogen chloride. The hydrogen chloride is used to react with nitrates present to produce the desired pyrotechnics. It was also shown that the exothermic reaction produced in this system was decreased with increasing binder levels. The atmosphere produced in these reactions is necessary for the overall reaction. This was confirmed by DSC where larger exotherms were observed in samples with lids.

The influence of metal oxides on the thermal degradation of chlorine containing polymers [174] was studied by TGA. Chlorine containing elastomers were shown to undergo degradation and decomposition, with the evolution of hydrogen chloride in a stage prior to destruction of polymer chains. Polychloroprene (CR), chlorinated polyethylene (CP) and epichlorhydrin homopolymer (CO) were compounded with various metal oxides and heated in a nitrogen atmosphere. Zinc oxide was found to accelerate the dechlorination step in all polymers, magnesium oxide was found to improve thermal stability while antimony and aluminum trioxides were found to lower the thermal stability and change the character of the degradation processes. Similar TGA experiments were performed on chlorine containing polymers and their vulcanizates to study the influence of other compounding ingredients [49,50,175]. It was found that in polymers with similar chain structure the carbon residue formed in pyrolysis increased with increase in the chlorine ratio. The same type of TGA studies were performed on non-chlorine containing elastomers, IR, BR, SBR and EPDM. It was found that the fillers had little effect on the temperature of maximum rate of degradation (T_{max}) and the rate of degradation but, in most cases, an increase in activation energy was observed [175].

Evolved gas analysis (EGA) is another technique that can be used to characterize the thermal degradation of an elastomer [64]. The sample is heated under vacuum until degradation takes place. In this example, a mass spectrometer is used to characterize the degradation products. The fragments from the elastomer can be used to follow the degradation of the elastomer as a function of temperature. By following the generation of a particular ion that is characteristic of the elastomer in the mass spectrogram, various elastomers can be analyzed and their degradations compared. The onset of degradation can be determined from the onset of appearance of a particular ion.

A technique related to evolved gas analysis is pyrolysis-gas chromatography. In this technique, a sample is pyrolyzed at a specified temperature and the by-products are analyzed by either gas chromatography or gas chromatography coupled with another technique, such as mass spectrometry. This approach has been used to characterize the thermal decomposition of polysulfide rubber [176,177,178]. Analysis of the decomposition products, coupled with TGA data showed that the decomposition involves a radical mechanism. The mechanism of decomposition was found to be the same for both liquid polysulfide and cured polysulfide rubber.

Electrothermal analysis can be used to determine the upper limits of thermal stability of an elastomer [21]. A non-reversible change takes place in many elastomer at about 200°C, potentially representing the initial stages of the carbonization of the elastomer. This is monitored by the decreases in resistivity of the elastomer. As seen in Fig. 34, for both NR and BR and NR/BR blends compounded with 60 phr carbon black, a drop in resistivity is observed in the

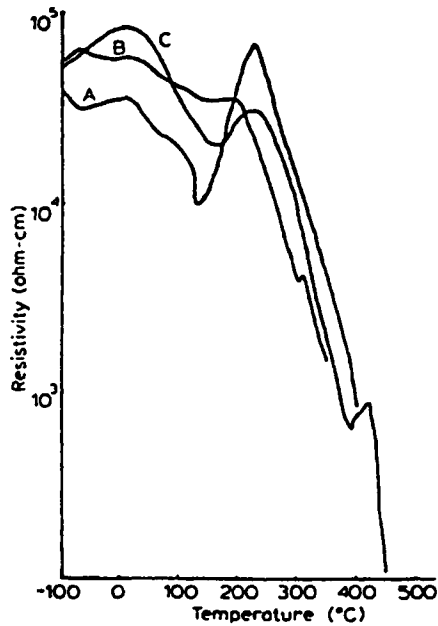


Fig. 34. ETA curve of (A) NR, (B) BR and (C) 40:60 NR:BR (60 phr N375)

area of 200°C. A transition is not observed in TGA or DSC curves for these materials in this temperature range, perhaps demonstrating that electrothermal analysis may be uniquely capable of determining some aspects of the thermal stability of elastomers.

7.3. Other

Photo-oxidation can be evaluated by characterizing the oxidative stability of an elastomer after exposure to light [161]. It was observed that exposure of butyl rubber to UV light decreases the isothermal induction time of the elastomer.

The thermal stability of an elastomer can be studied by flowing-afterglow technique (FLAG) which uses the energy-transfer reactions of rare gas, metastable atoms from a fast-flowing, rare-gas plasma with the elastomer. This technique is reported to give information about the kinetics and mechanisms of degradation under service conditions; 25-35°C in air [179]. The volatile thermal decomposition products from an elastomer can be monitored to yield qualitative and quantitative information. Results from a polyester based thermoplastic polyurethane showed that between 35 and 234°C, only CO₂ was released as a

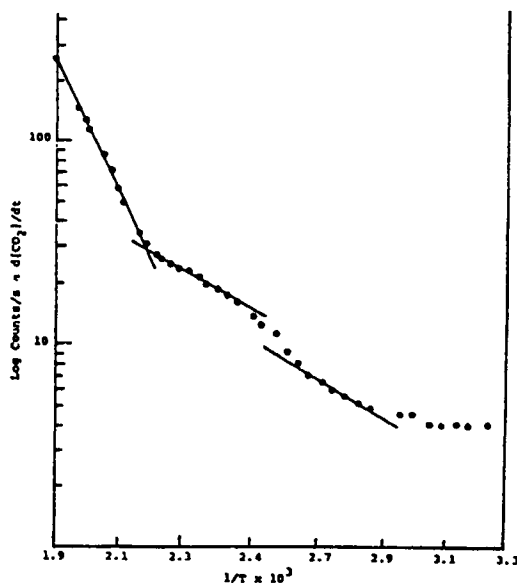


Fig. 35. Arrhenius plot of Estane 5703 thermal degradation

decomposition product but above 65°C three distinct processes can be discerned by analyzing the data by the use of an Arrhenius Plot (Fig. 35).

Exposure of an elastomer to fuels can result in significant changes in the physical properties. Dynamic mechanical analysis (DMA) can be used to characterize both the nature of these changes and the severity of the changes based on the fuel involved [180]. It has been shown that different fuels interact differently with EPDM, CSM and NBR depending on the compounding and cure state. Typically, the T_g of the elastomer is lowered upon exposure to fuels and the extent of this lowering depends on the nature of the elastomer and the fuel involved. It was shown that EPDM is significantly affected by fuel exposure whereas NBR shows a smaller change in T_g for the same fuels. These results were compared to weight gains associated with fuel exposure and hardness measurements. Hardness of the elastomers did not change significantly and could not be used for this evaluation. Weight gain and loss tangent peak temperatures compared favorably in estimating the effect of fuel exposure.

Another example of DMA analysis of elastomers exposed to liquids is the evaluation of creep and recovery of hydrogel elastomers [181]. Hydrogel elastomers are elastomers that have very high levels of water associated with them and their properties depend on the water level. The creep and recovery as well as stress-strain characteristics of a set of hydrogel elastomers (polyvinyl

alcohol) was evaluated using a DMA unit with a special cell where the sample could be immersed in water or subjected to moist air.

8. QUALITY CONTROL

The use of thermal analysis and calorimetry for quality control or quality assurance applications has become commonplace due to a combination of ease of sample preparation and test set-up and of the vast amount of information available from “simple” test results. This non-glamorous area utilizes the many thermal analysis and calorimetry techniques available to routinely characterize the nature and composition of elastomer compounds both before, during and after processing. The combination of results from thermal techniques and the application of statistical process control (SPC) provides a means of monitoring quality.

DSC and DTA curves essentially provide the fingerprint of a compound, any variations in compound mixture, raw materials or often even process conditions can be visually established. Establishing a baseline curve permits visual comparison with subsequent batches [4]. DSC and DTA are routinely used to monitor the degree of cure in samples and to assure that the correct cure system is being used [8,117]. The nature of the cure exotherm can be used to fingerprint the curative system for easy confirmation of compounding correctness, also the placement and shape of the T_g can sometimes be used to indicate the state of cure of an elastomer [135,136]. The cure exotherm has also been used to monitor the quantity of curatives present for mixing in production situations [81]. DSC and DTA have also been used to provide routine checks on the elastomers being used for both incoming quality assurance and for confirmation of formulations [8,117,182]. Monitoring of the positions of the T_g 's of the polymers in a compound can often be used to confirm that the correct elastomers, and correct grades of elastomer, were included in that compound [8,116], while monitoring of the shape, and of the position, of the T_g event also gives information about the quantity of any plasticizers present in the compound [4].

TGA has been used to confirm the composition of a complex compound [4,8,116,149,182,183], including the confirmation of the chemical nature of the elastomer in the compound. A standard compositional analysis using TGA provides a wealth of information on oils, low molecular weight organic components, on polymers, high molecular weight components, on carbon black levels as well as allowing characterization of the ash content. The advantage of the use of factor analytical methods to analyze the results of TGA experiments has been shown to greatly enhance to separation of elastomers in blends [59], this technique has the potential to be used to discover differences in nominally identical materials from different batches. TGA has also been reported as a tool

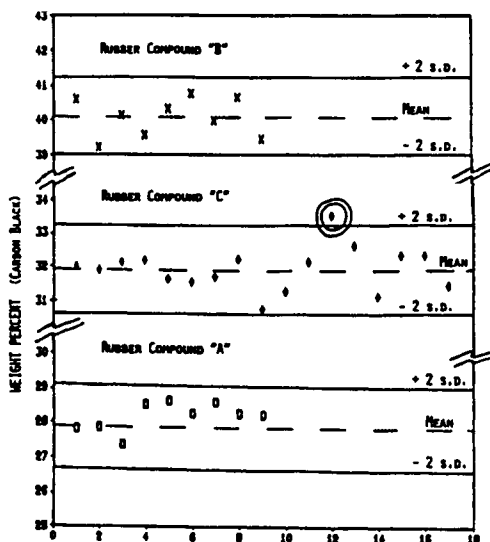


Fig. 36. Statistical scatter plot - three typical production rubber compounds

to measure filler levels, degree of incorporation and thermal stability of RTV silicone materials [55,91], all quantities valuable to any QA testing of RTV versus

TGA has also been used to check the stability of both starting elastomers and final products [4,8,117]. Coupling statistical process control with TGA data has also been reported [149]. As seen in Fig. 36, it is possible to track the consistency of compounding by plotting the determined value for the rubber or carbon black versus the number of production batches or time to track the consistency of the weighing/mixing of ingredients. This approach to quality control should become more common place as thermal analysis equipment becomes more common in production situations.

TMA measurements result in curves which show dimension changes of a compound which can be used to monitor a variety of properties, under a variety of conditions which can be related to specific applications. This versatility makes this technique potentially valuable for quality control applications. Applications of TMA include measuring softening to monitor the state of cure and expansion of foam to monitor the blowing agents and cure systems [4]. Dynamic load TMA has been used to detect differences in crosslinking in commercial sealant systems which lead to poor product properties and higher than desired creep flow [15].

The variety of quality control applications is virtually limited only by the imagination of the user and the limitations of the equipment on hand or of available techniques. Many applications have been previously discussed through

out this chapter and almost all of the techniques can be used in the quality control laboratory to solve problems or to monitor the quality of incoming raw materials or products being manufactured.

9. FUTURE OPPORTUNITIES

9.1. Instrumentation

The last 15 to 20 years has seen a dramatic change in the nature of thermal analysis and calorimetry. It has moved from individually constructed and relatively primitive instrumentation to highly sophisticated, mass produced instruments and the variety of commercially available instruments has increased. Most recently, we have seen these instruments contain new sophisticated computer systems that permit the use of complex temperature control programs and vastly increased capabilities for data acquisition and analysis.

One of the emerging techniques that utilizes these new capabilities is temperature modulated DSC, in which the temperature program consists of a linear heating rate with a superimposed sinusoidal component. The data acquired from such a complex heating program can be separated into a kinetic component and a heat capacity component. This separation of the conventional, total heat flow, DSC signal into two independent signals permits unprecedented separation and identification of heat flow events. This is especially true for the analysis of elastomers where, for the first time, the glass transition event can be cleanly separated from the "enthalpic relaxation" which often causes problems with the identification and quantification of T_g . In elastomers it is not uncommon to see crystallization and melt events which are overlapping, as in the case where small and/or imperfect crystals are formed and then undergo melting followed by reorganization into larger and/or more perfect crystals, often temperature modulated DSC can separate these two events. As additional investigations into the underlying theoretical basis of temperature modulated DSC are conducted, new sets of experimental conditions and data interpretations which result in improved separations should be possible.

There is an emerging class of TGA techniques which makes use of this greatly improved computer control of the temperature program. This class includes stepwise isothermal and so-called "controlled rate" TGA. The former technique employs a series of isothermal temperature "soaks" and the later entail complex manipulations of the heating program in the detected region of weight change events to maximize separation of these events. These techniques involve control of the programmed heating employed to provide more detailed information about transitions, resulting in greatly improved compositional analyses. This can be especially useful for the quantification of components of elastomer and rubber containing compounds where separation is especially difficult do to the common inclusion of oils and resins in compounds.

Coupled techniques, continue to show promise for providing more information about elastomer systems. This is in part due to the use of computers which allow for improved temperature control and for better capabilities to handle the incredible amount of information resulting from these multiple techniques. This, coupled with continuing improvements in interfacing techniques which should do away with problems such as “cold spots” in combined TGA techniques, will result in greatly improved analyses. Additionally, the coupling of even more analytical techniques with thermal and calorimetric techniques, including DTA-AFM (combined DTA and Atomic Force Microscopy) should take place and result in opportunities for elastomer analyses.

The availability of commercially prepared units has slowly increased and their use should increase steadily. Since most of these techniques are still relatively early in their development, further refinements will continue and new applications and information will undoubtedly be forthcoming.

An additional facet of future opportunities in instrumentation must include the ever increasing area of data analysis techniques. Due to the improvements in computer capabilities data from newly emerging and more traditional techniques can be interpreted by statistical and data modeling to yield information about the elastomers and elastomer systems under study. Some of the data analysis techniques which are currently being developed and being utilized to extract meaningful information from thermal data include partial least squares (PLS), principle component analysis, factor analysis and all methods of material property modeling.

There are a number of areas within the elastomer field that have shown increased importance and will likely be involved in future applications of thermal and calorimetric techniques.

Blends have increased in importance in recent years because of regulatory problems associated with producing new materials. The use of blends to achieve unique physical characteristics will continue to grow and the application of current and new techniques to characterize both the composition and nature of the blends will be very important. As has been noted in the previous sections, the ability of thermal techniques to characterize the nature of the interfacial regions of blends is important and will continue to be a major area of development. Interfacial engineering will be a prominent part of this effort and techniques that address these issues will grow in importance.

Functionalization and reactive processing represent two major areas associated with new material development that complements blend technology. Characterization of both the compositional changes in the elastomers and the processes that are used to accomplish these changes have shown continued interest and have grown significantly in the past 10 years. The kinetics of

functionalization and structure formation in elastomer systems will have increasing value.

Tailoring of the microstructure of traditional elastomers to achieve specific properties is virtually in its infancy. As characterization techniques improve, more information linking elastomer microstructure to properties will be forthcoming. This data will then be used as input for computer modeling of structure-property relationships which will be used to guide the polymer chemist to "build" polymers with specified structures to achieve desired properties.

Polymer/filler interaction will continue to be a significant area of technology development. The design of these interactions for continued improvement in physical properties will require an even greater understanding of all aspects of the interactions. Thermal and calorimetric techniques have already shown utility in this respect and should continue to be very useful in characterizing these systems.

Thermoplastic elastomers have increased in utility over the past ten years and a great deal of research has gone into their development and use. The development of new materials in this category should continue and their uses will continue to expand. Thermal techniques will be necessary to fully understand the nature of these multi-domain materials.

The application of elastomer in the fields of medical devices, recyclable industrial materials and bio-degradable materials will also spur further research involving this class of analytical techniques. Certainly, the application of thermal analysis and calorimetry to elastomer systems is a well established area but the future holds a great many opportunities for further development of current techniques and new techniques to answer the questions of the future.

REFERENCES

1. J. O. Hill, For Better Thermal Analysis and Calorimetry, Ed. III, International Confederation For Thermal Analysis, (1991).
2. J. L. Laird and G. Liolios, *Am. Lab.*, 22(1) (1990) 46.
3. D. R. Burfield and K. L. Lim, *Macromolecules*, 16 (1983) 1170.
4. J. L. Laird and G. Liolios, *Rubber World*, 201(4) (1990) 13.
5. C. K. L. Davies, S. V. Wolfe, I. R. Gelling and A. G. Thomas, *Polymer*, 24 (1983) 107.
6. D. R. Burfield, K.-L. Lim, K.-S. Law and S. Ng, *Polymer*, 25 (1984) 993.
7. C. S. L. Baker, I. R. Gelling and R. Newell, *Rubb. Chem. Tech.*, 58 (1985) 67.
8. D. W. Brazier, *Rubb. Chem. Tech.*, 53 (1980) 437.
9. D. R. Burfield, *Polym. Comm.*, 24 (1983) 178.
10. H. Kawaguchi, Y. Sumida, J. Muggee and O. Vogl, *Polymer*, 23(12) (1982) 1805.
11. G. C. Meyer and J. M. Widmaier, *J. Polym. Sci., Polym. Phys. Ed.*, 20(3) (1982) 389.
12. P. Burroughs, *Proc. Int. Rubb. Conf., Milan, Italy, 1979*, p. 484.
13. G. D. Gaddy, W. J. Rossiter, Jr. and R. K. Eby, *ASTM Spec. Tech. Publ. 1136 (Mater. Charact. Thermomech. Anal.)* (1991), 168.

14. G. D. Gaddy, W. J. Rossiter, Jr. and R. K. Eby, ASTM Spec. Tech. Publ. 1088 (Roofing Res. Stand. Dev., 2nd Vol.) (1990) 37.
15. R. Riesen, W. Bartels, Therm. Anal., Proc. Int. Conf., 7th, Volume 2, 1982 p.1050.
16. R. E. Wetton and R. DeBlok, Kunststoffe, 79(1) (1991) 60.
17. R. E. Wetton, R. D. L. Marsh and J. G. Van de Velde, Therm. Acta, 75(1) (1991) 1.
18. P. Bussi and H. Ishida, Polymer, 35(5) (1994) 956.
19. S. N. Ganeriwala and H.A. Hartung, Polym. Mater. Sci. Eng., 60 (1989) 600.
20. M. A. Vallance, A. S. Yeung and S. L. Cooper, Colloid Polym. Sci., 261(7) (1983) 541.
21. A. K. Sircar, T. G. Lamond and J. L. Wells, Therm. Acta, 37 (1980) 315.
22. L. Y. Zlatkevich, L. F. Nichols and N. T. Crabb, J. Appl. Polym. Sci., 25(5) (1980) 963.
23. H. S. Faruque and C. Lacabanne, J. Mater. Sci., 22(2) (1987) 675.
24. P. Boochathum, Y. Tanaka, and K. Okuyama, Polymer, 34(17) (1993) 3694.
25. F. Staub, Am. Lab., 18(1) (1986) 56.
26. D. R. Burfiled and Y. Tanaka, Proc. Int. Rubber Conf. (1986) Mtg. Date 1985, Vol. 2, p. 140.
27. K. Baker and J. Leckenby, Kaut. Gummi Kunstst., 40(3) (1987) 223.
28. H. Kawaguchi, Y. Sumida, J. Muggee and O. Vogl, Polymer, 23(12) (1982) 1805.
29. M. Yagpharov, J. Therm. Anal., 31(5) (1986) 1073.
30. C. M. Brunette and W. J. MacKnight, Rubb. Chem. Tech., 55(5) (1982) 1413.
31. J. Blackwell and C. D. Lee, Polym. Mater. Sci. Eng., 49 (1983) 49.
32. C. S. Schollenberger and L. E. Hewitt, Polym. Prepr., Am. Chem. Soc., Div. Polym. Chem. 19(1) (1978) 17.
33. T. R. Hesketh, J. W. C. Van Bogart and S. L. Cooper, Polym. Eng. Sci., 20(3) (1980) 190.
34. C. S. Wang and D.J. Kenney, J. Elastomers Plast., 27(7) (1995) 182.
35. D. M. Crawford, A.R. Teets and D. Flanagan, D., Report (1988), BRDEC-2463, Order No. AD-A197673, 28 pp. Avail.: NTIS From: Gov. Rep. Announce. Index (U. S.) 1988, 88(24), Abstr. No. 861,807.
36. B. Ya. Teitel'baum and T.A. Yagfarova, J. Therm. Anal., 22(1) (1981) 67.
37. Y. Nagase, T. Fukatsu, K. Ikeda and Y. Sekine, Polymer, 24(4) (1983) 463.
38. G. W. H. Hohne, H. G. Kilian, and P. Trogele, Therm. Anal., Proc. Int. Conf. 7th Ed. Miller, B., (Wiley), Vol. 2, 1982, p. 955.
39. H. G. Kilian, G. W. H. Hohne, P. Trogele and H. Ambacher, J. Polym. Sci., Poly., Symp., 71 (1984) 221.
40. F. De Candia, G. Romano and R. Russo, Makromol. Chem., Rapid Commun., 6(1) (1985) 15.
41. Yu. K. Godovskii and N.P. Bessonova, Colloid Polym. Sci., 261(8) (1983) 645.
42. N.S. Schneider and R.W. Matton, Polym. Eng. Sci., 19(15) (1979) 1122.
43. Yu. K. Godovsky and N.P. Bessonova, Thermochim. Acta, 247(1) (1994) 19.
44. A. K. Sircar, J. Sci. and Ind. Res., 41 (1982) 536.
45. T. R. Manley, Prog. Rubb. Plast. Tech., 5(4) (1989) 253.
46. R. L. Zeyen, Rubber World, 199(4) (1989) 14.
47. R. L. Zeyen, Kaut. Gummi Kunstst., 41(10) (1988) 974.
48. M. S. Farlling, Rubber World, 197(4) (1988) 20.
49. D. Jaroszynske and T. Kleps, Rubbercon 81 [Eighty-One], Int. Rubber Conf., Volume 1, Plast. Rubber Inst., London, (1981), p. C5.1.
50. D. Jaroszynska, T. Kleps and D.J. Gdowska-Tutak, Therm. Anal., 19(1) (1980) 69.
51. F. E. Rogers and T. J. Ohlemiller, J. Macromol. Sci., Chem., A15(1) (1981) 169.

52. G. Liptay, J. Nagy, A. Borbely-Kuszmán and J. Ch. Weis, *J. Therm. Anal.*, 32(6) (1987) 1683.
53. G. Liptay, J. Nagy, A. Borbely-Kuszmán and J. Ch. Weis, in Blazek, Antonin (Ed.), *Therm. Anal., Proc. ICTA, 8th Volume 2, Alfa, Bratislava, (1985) p. 225.*
54. H. L. W. Chan and J. Unsworth, *Eur. Polym. J.*, 21(4) (1985) 377.
55. C. P. Wong, *ACS Symp. Ser.*, 242(Polym. Electron.) (1984) 285.
56. D. Jaroszynska and T. Kleps, in Blazek, Antonin (Ed.), *Therm. Anal., Proc. ICTA, 8th, Volume 2, Alfa, Bratislava, Czech, 1985, p. 191.*
57. D. Jaroszynska and T. Kleps, *J. Therm. Anal.*, 31(4) (1986) 955.
58. D. Jaroszynska and T. Kleps, *Thermochim. Acta*, 93 (1985) 191.
59. C. H. Lochmuller, S. J. Breiner, M. N. Koel, and M. A. Elomaa, *Anal. Chem.*, 63(17) (1991) 1685.
60. S. Roy, T. K. Chaki, B. R. Gupta and B. R. Maiti, *Proc. Nat'l. Symp. Therm. Anal.*, 8th, (Bombay, India), 1991, p. 346
61. T. K. Chaki, S. Roy and B. R. Gupta, *Ind. J. Nat. Rubb. Res.*, 5 (1&2) (1992) 217.
62. J. J. Maurer and D. W. Brazier, *Kaut. Gummi Kunstst.*, 36(1) (1983) 37.
63. N. L. Dassanayake and R. W. Phillips, *Anal. Chem.*, 56 (1984) 1753.
64. M. Erdogan, T. Yalcin, T. Tincer and S. Suzer, *Eur. Polym. J.*, 27(4/5) (1991) 413.
65. J. A. J. Jansen, J. H. Van der Maas, A. Posthuma De Boer, *Appl. Spectrosc.*, 46(1) (1992) 88.
66. S. M. Dyszel, *Anal. Calorim.*, 5 (1984) 277.
67. R. B. Prime and B. Shushan, *Anal. Chem.*, 61(11) (1989) 1195.
68. G. Rugo, M. Urbani, D. Barbattini, C. Nastasi, M. Orsi and M. Poponessi, *Kaut. Gummi Kunstst.*, 39(3) (1986) 216.
69. M. J. R. Loadman, *J. Therm. Anal.*, 31 (1986) 1183.
70. N. B. Milestone, *Chem in New Zealand*, June 1988, p. 55.
71. D. P. Macaione, R. E. Sacher and R. E. Singler, *Sagamore Army Mater. Res. Conf. Proc.*, Vol. Date 1985, 32nd (Elast. Rubb. Tech.), 1987, p. 317.
72. S. C. Ng and K. K. Chee, *Rubb. Chem. Tech.*, 62 (4) (1989) 585.
73. V. Weuster, *Gummi Fasern Kunststoffe*, 44(10) (1991) 534.
74. S. Mohanty, S. Roy, R. N. Santra and G. B. Nando, *J. Appl. Polym. Sci.*, 58(11) (1995) 1947.
75. R. E. Wetton and P. J. Corish, *Polym. Test.*, 8 (1989) 303.
76. K. A. Mazich, M. A. Samus, P. C. Killgoar, Jr. and H. K. Plummer, *Rubb. Chem. Tech.*, 59(4) (1986) 623.
77. A. K. Sircar, *Sagamore Army Mater. Res. Conf. Proc. (1987), Vol. Date 1985, 32nd (Elast. Rubb. Tech.)*, p. 73.
78. N. V. Schwartz, *Gummi Fasern Kunststoffe*, 37(6) (1984) 274.
79. G. Rugo, D. Barbattini, G. Cappellazzo and M. Poponessi, *Proc. Int. Rubb. Conf. (Venice)*, 1979 p. 472.
80. J. A. Foreman and S. R. Sauerbrunn, *Annual Tech. Conf. Soc. Plast. Eng.*, 50th (Vol. 1), 1992, p. 707.
81. P. Burroughs, *Proc. Int. Rubber Conf.*, 1979 (Venice), p.484.
82. R. N. Santra, P. G. Mukunda, G. B. Nando and T. K. Chaki, *Thermochim. Acta*, 219(1-2) (1993) 283.
83. I. Amri Amraee, A. A. Katbab and S. Aghafarajollah, *Rubb. Chem. Tech.*, 69 (1996) 130.
84. S. H. Goh, *Therm. Acta*, 41 (1980) 261.
85. S. Mohanty, P. G. Mukunda and G. B. Nando, *Polym. Degrad. Stab.*, 50 (1995) 21.

86. N. R. Loadman, *Nat. Rubb. Tech.*, 19(2) (1988) 21.
87. W. J. Sichina, *Am. Lab.*, 25(7) (1993) 45.
88. E. L. Charsley and J. G. Dunn, *Plast. Rubb. Proc. Appl.*, 1 (1981) 3.
89. E. L. Charsley and J. G. Dunn, *Rubb. Chem. Tech.*, 55 (1982) 382.
90. E. L. Charsley and J. G. Dunn, *Plast Rubb. Proc. Appl.*, 1 (1981) 3.
91. C. P. Wong, *Org. Coat. Appl. Polym. Sci. Proc.*, 48 (1983) 300.
92. D. P. Macaione, R. E. Sacher and R. E. Singler, *ASTM STP 997 C M Ernest, Ed.*, 1988, p. 59.
93. A. K. Sircar and T. G. Lamond, *Rubb. Chem. Tech.*, 48 (1975) 301.
94. A. K. Sircar, *Rubb. Chem. Tech.*, 65 (3) (1992) 503.
95. W. J. Sichina, *Proc. North Am. Therm. Anal. Soc.*, 21st, Sept. 13-16, 1992, Atlanta, GA, pp. 206.
96. W. J. Sichina, *Proc. North Am. Therm. Anal. Soc.*, 21st, Sept. 13-16, 1992, Atlanta, GA, pp. 214.
97. S. R. Sauerbrunn and P. S. Gill, *Proc. North Am. Therm. Anal. Soc.*, 21st, Sept. 13-16, 1992, Atlanta, GA, pp. 220.
98. R. L. Blaine and F. J. Leek, *Proc. North Am. Therm. Anal. Soc.*, 24th, Sept. 10-13, 1995, San Francisco, CA, pp. 338.
99. P.M. Fouche and W.J. McGill, *Plast. Rubber Process. Appl.*, 12(4) (1989) 227.
100. J. A. Azizi, D. Dollimore, P. J. Dollimore, G. R. Heal, P. Manley, W. A. Kellner and W. J. Yong, *J. Therm. Anal.*, 40 (1993) 831.
101. J. W. E. Gearing and M. R. Stone, *Polym. Compos.* 5(4) (1984) 312.
102. N. Nakajima, M.H. Chu and Z. G. Wang, *J. Elastomers Plast.*, 22(3) (1990) 174.
103. J. M. Funt, *Rubb. Chem. Tech.*, 61 (1988) 842.
104. C. Neogi, A. K. Bhattacharya and A. K. Bhowmick, *Rubb. Chem. Tech.*, 63 (5) (1990) 651.
105. C. Neogi, A. K. Bhowmick and S. P. Basu, *J. Elast. Plast.*, 23 (1991) 152.
106. S. Varughese and D. K. Tripathy, *Plast. Rubb. Compos. Proc. Appl.*, 17 (1992) 219.
107. A. K. Sircar and J. L. Wells, *Rubb. Che. Tech.*, 55(1) (1982) 191.
108. G. M. Nasr, M. M. Badawy, S. E. Gwaily and G. Attia, *Polym. Int.*, 38 (1995) 249.
109. G. M. Nasr, K. A. Darwish, S. A. Khairy, H. H. Hassan and E. Ateia, *Polym. Int.*, 38 (1995) 257.
110. M. Amin, G. M. Nasr, H. H. Hassan, S. El-Guiziri and M. Abu-Abdeen, *Polym. Bull.*, 22 (9189) 413.
111. The Goodyear Tire & Rubber Company, US 5,023,301, 11 June 1991.
112. The Goodyear Tire & Rubber Company, US 4,996,262, 26 February 1991.
113. The Goodyear Tire & Rubber Company, US 5,202,384, 13 April 1993.
114. The Goodyear Tire & Rubber Company, us 4,996,263, 26 February 1991.
115. X. Zhang, H. Chen, T. Tang and B. Huang, *Macromol. Chem. Phys.*, 196 (1995) 3585.
116. H. Mohler and E. Kaiserberger, *J. Therm Anal.*, 37 (1991) 1805.
117. B. L. Treherne, *Elastomerics*, May 1982, p. 25.
118. T. R. Manley, *Dev. Rubb. Rubb. Compos.*, 1 (1980) 131.
119. I. Groves and L. C. Thomas, *Research and Development*, Feb., 1988, p. 133.
120. J. Yang, S. Kaliaguine and C. Roy, *Rubb. Chem. Tech.*, 66(2) (1993) 213.
121. S. C. Ng and K. K. Chee, *J. Appl. Polym. Sci.*, 37 (1989) 3227.
122. E. Immelman and R. D. Sanderson, *Therm. Acta*, 207 (1992) 161.
123. D.P. Fang, C.C. Riccardi and R.J.J. Williams, *Polymer*, 34(18) (1993) 3960.
124. N. K. Dutta and D. K. Tripathy, *Kaut. Gummi Kunstst.*, 43(6) (1990) 488.
125. H. D. Otto and H. Lotze, *Polym. Paint. Colour J.*, 180 (4268) (1990) 613.

126. M. Popescu, V. Matei, A. Simion and A. Danet, *J. Therm. Anal.*, 26 (1983) 65.
127. D. W. Bamborough and P. M. Dunkley, *Materiaux et Techniques*, Mar-Apr., 78(3-4) (1990) 87.
128. W. R. Randall and J. A. Riedel, *Rubber World*, 207(4) (1993) 23.
129. J. J. Gibbons, *Am. Lab.*, 19(1) (1987) 33.
130. M. A. Riad, D. E. Packham, G. A. Kelany, S. A. Hussain and K.Y., *Al-Khalaf, J. Oil Colour Chem. Assoc.*, 73(2) (1990) 74.
131. J. Gillmor and R.J. Seyler, *ASTM Spec. Tech. Publ. 997(Compos. Anal. Thermogravim.)* (1988) 38.
132. D. W. Brazier and N. V. Schwartz, *Therm. Acta*, 39 (1980) 7.
133. G. Liptay, L. Ligethy and J. Nagy, in H.G. Wiedemann (Ed.), *Therm. Anal.*, [Proc. Int. Conf. Therm. Anal.], 6th Volume 1, Birkhaeuser, Basel, Switz., 1980, p. 477.
134. D. Devanathan and R. Carr, *Tech. Pap., Reg. Tech. Conf. - Soc. Plast. Eng.*, (Plast. Prog. Process., May 5-8) 1980 p. 613.
135. L. Little, *Elastomerics*, 121(2) (1989) 22.
136. B. N. Ranganathan, *SAMPE Q.*, 15(2) (1984) 38.
137. D. W. Brazier, G. H. Nickel and Z. Szentgyorgyi, *Rubb. Chem. Tech.*, 53 (1) (1980) 160.
138. C. M. Kok, *Eur. Polym. J.*, 21(6) (1985) 579.
139. C. M. Kok, *Eur. Polym. J.*, 22(13) (1986) 1015.
140. M. G. Huson, W. J. McGill and P. J. Swart, *J. Polym. Sci., Polym. Lett. Ed.*, 22(3) (1984) 143.
141. S. Varughese and D. K. Tripathy, *Polym. Degrad. Stab.*, 38 (1992) 7.
142. D. W. Brazier, *Dev. Polym. Degrad.*, 3 (1981) 27.
143. A. Sadr-Bazaz, M. Hivert and J. M. Vergnaud, *Therm. Acta*, 71 (1983) 237.
144. A. Khouider, J. B. Rochette and J. M. Vergnaud, *Therm. Acta*, 89 (1985) 93.
145. J. Y. Armand, J. Bourgois, M. Touchard and J. M. Vergnaud, *Therm. Acta*, 108 (1986) 345.
146. J. Y. Armand and J. M. Vergnaud, *Therm. Acta*, 116 (1987) 111.
147. R. Ding, A. I. Leonov and A. Y. Coran, *Rubb. Chem. Tech.*, 69 (1996) 81.
148. M. H. S. Gradwell and W. J. McGill, *J. Appl. Polym. Sci.*, 58(12) (1995) 2185.
149. M. H. S. Gradwell and W. J. McGill, *J. Appl. Polym. Sci.*, 58(12) (1995) 2193.
150. E. Immelman and R. D. Sanderson, *Therm. Acta.*, 207 (1992) 177.
151. D. B. Rahrig, *J. Adhesion*, 16 (1984) 179.
152. R. Greco, P. Laurienzo, M. Malinconico, E. Martuscelli, N. Perenze and A. Sorrentino, *Adv. Polym. Technol.*, 13(2) (1994) 141.
153. R. A. Weiss, *J. Polym. Sci., Polym. Chem. Ed.*, 18(9) (1980) 2887.
154. R. Alex and P. P. De, *Kaut. Gummi Kunstst.*, 43(11) (1990) 1002.
155. A. A. Z. El Fayoumi, *Egypt. J. Chem.*, 24(6) (1981) 413.
156. S. Wasserman and G. P. Johari, *J. Appl. Polym. Sci.*, 48(5) (1993) 905.
157. S. H. Goh, *Therm. Acta*, 39 (1980) 353.
158. P. H. Lye and H. K. Toh, *J. Appl. Polym. Sci.*, 29 (1984) 2627.
159. V. Gonzalez, *Rubb. Chem. Tech.*, 54(1) (1981) 134.
160. A. Adhikary, A. S. Deuri and R. Mukhopdhyay, *Proc. Nat'l. Symp. Therm. Anal.*, 9th (India), 1993, p. 254
161. G. Balazs, S. Doszlop, O. Biro and L. Palotas, *J. Therm. Anal.*, 36 (1990) 1861.
162. B. Stenberg and F. Bjork, *J. Appl. Polym. Sci.*, 31 (1986) 487.
163. H. Berg, B. Stenberg and R. Sanden, *Plast. Rubber Process. Appl.*, 12(4) (1989) 235.
164. S. H. Goh, *Thermochim. Acta*, 80(1) (1984) 75.

165. A. K. Bhowmick, S. Rampalli, K. Gallagher, R. Seeger and D. McIntyre, *J. Appl. Polym. Sci.*, 33 (1987) 1125.
166. W. H. Dickstein, R. L. Siemens and E. Hadziioannou, *Thermochim. Acta*, 166 (1990) 137.
167. G. Liptay, J. Nagy, J. Ch. Weis and A. Borbely-Kuszmán, *Thermochim. Acta*, 85 (1985) 399.
168. Y. Nakagawa and T. Komai, *J. Fire Sci.*, 8 (1990) 455.
169. D. J. Burlett, *Proc. North Am. Therm. Anal. Soc.*, 17th, Oct. 9-12, 1988, Lake Buena Vista, FL, pp. 654.
170. M. Anachkov, S. Rakovski and A. Stoyanov, *Int. J. Polym. Mater.*, 16(1-4) (1992) 307.
171. M. M. Barbooti, E. B. Hassan and N. A. Issa, *J. Petroleum Res.*, 8(2) (1989) 229.
172. E. L. Charsley, S. B. Warrington, P. Emmott, T. T. Griffiths and J. Queay, *J. Therm. Anal.*, 38 (1992) 641.
173. P. Emmott, T. T. Griffiths, J. Queay, E. L. Charsley and S. B. Warrington, *Proc. Int. Pyrotech. Semin.*, 16th, 1991, p. 937.
174. T. Kleps and M. Piaskiewicz, *J. Therm. Anal.*, 32(6) (1987) 1785.
175. T. Kleps, D. Jaroszynska and M. Piaskiewicz, *Therm. Anal.*, 36(6) (1990) 2257.
176. T. S. Radhakrishnan and M. Rama Rao, *J. Appl. Polym. Sci.*, 34(5) (1987) 1985.
177. T. S. Radhakrishnan and M. Rama Rao, *J. Anal. Appl. Pyrolysis*, 9(4) (1986) 309.
178. M. Rama Rao and T. S. Radhakrishnan, *J. Appl. Polym. Sci.*, 30(2) (1985) 855.
179. M. L. Matuszak and G. W. Taylor, *J. Appl. Polym. Sci.*, 27(2) (1982) 461.
180. J. A. Hiltz, R. M. Morchat and I. A. Keough, *Therm. Acta.*, 226 (1993) 143.
181. Q. B. Bao and C. S. Bagga, *Therm. Acta*, 226 (1993) 107.
182. H. Mohler, *Kaut. Gummi Kunstst.*, 44(4) (1991) 369.
183. R. H. Schuster, *Kaut. Gummi Kunstst.*, 40(7) (1987) 642.

This Page Intentionally Left Blank

Chapter 14

Polymer degradation

Joseph H. Flynn

Scientific Thermal Research & Data Analysis (STRDA), 5309 Iroquois Road,
Bethesda, MD 20816, USA, FAX: +011 301 229 4752,
e-mail:rflynn@capaccess.org

1. INTRODUCTION

The purpose of this chapter is to present a brief review of the thermal and oxidative degradation of polymeric materials. This will include some of the recent developments in these areas. Its main thrust will be toward setting forth the present understanding of the chemical and physical aspects of thermal, oxidative and hydrolytic reactions and the present speculations as to their kinetics and mechanisms. This review should serve as a useful background for those who are using thermal analysis methods to study these thermal reactions in polymeric materials.

The methods of thermal analysis employed in the investigation of polymer degradation reactions include all of those which are used to study the reactions of other materials. However, the techniques most widely used are Thermogravimetric Analysis (TGA) and Evolved Gas Analysis (EGA). The latter includes pyrolysis gas chromatography and mass spectroscopy (MS). All the techniques may employ isothermal, constant heating rate, oscillating, jumping, and constant reaction rate, types of temperature control. Infrared spectroscopy (IR) is another valuable tool used in the investigation of polymer degradation reactions and it is often combined with these other techniques. Differential Scanning Calorimetry (DSC), Thermal Mechanical Analysis (TMA), Dynamic Mechanical Analysis (DMA), Dielectric Thermal Analysis (DETA), and Modulated DSC are also employed, but much less frequently in polymer degradation studies. Discussion of, and concrete examples of the applications of the various thermal analytical methods to the investigation of polymer reactions, are found in other chapters of this volume and in "Thermal Analysis" in the "Encyclopedia of Polymer Science and Engineering" [1].

Also this Chapter may be considered, partly, as a sequel to a review, "Degradation and Pyrolysis Mechanisms" in "Pyrolysis and GC in Polymer

Analysis" published in 1985 [2] and coauthored by the present author and Dr. Roland E Florin. (Therefore, this author wishes to acknowledge a considerable input by Dr. Florin, especially in many of the theoretical discussions which are included in this chapter). Since this review can cover only a small portion of the vast amount of material on polymer degradation and stabilization, the reader is referred to the many other books, reviews and test methods. Many of these are listed in the bibliography at the end of this chapter.

As a matter of expediency, this chapter will limit itself to "degradation" and ignore most of the vast amount of work on "stabilization", that is, the effects of additives, catalysts, stabilizers, destabilizers, *etc.*, on the degradation kinetics. These complicating factors will be introduced only peripherally where discussion of them assists the understanding of the effects of traces of them, as contaminants, upon the chemistry and kinetics of the "pure" degradation reaction, especially upon its initiation step.

Only "slow" oxidation and thermally induced oxidation of polymers will be discussed in this chapter and some discussion of "lifetime prediction methods" will be included. Thus, only the "primary process" of the burning of polymers – thermal degradation to form combustible gases – is addressed in this review.

Fortunately the bulk of the applications of the methods of thermal analysis to the degradation of polymers in literature are directed toward the thermal and oxidative reactions rather than degradation by other factors. Therefore, books and reviews on other forms of degradation (radiative, biological, mechanical, *etc.*) which often can occur in conjunction with thermal, oxidative and hydrolytic degradation reactions of polymers are only listed in the bibliography at the end of this chapter for the reader's convenience.

As Professor Norman Grassie, one of the surviving "pioneers" of the golden era (circa 1945 - 1975) for the development of polymer degradation theory and science, has pointed out recently [3], "The rapid diversification in the application of polymers which has taken place in recent years has in turn resulted in the increasing complexity of studies of polymer degradation in order to understand the deterioration reactions which occur, as well as in complex studies of polymer stabilization in order to try to overcome the natural shortcomings of these materials." This "rapid diversification" has led in the past ten years to an explosion of papers on the various aspects of the degradation of polymeric materials. Therefore, even with the above limitations to the scope of this chapter, it is foolhardy to try to write a comprehensive review of the degradation of anything more than a single polymeric species. At one point in the 1970's, with such a goal in mind, this author had collected over three hundred articles on the thermal degradation of polystyrene. Since it is impossible to cover even a majority of pertinent articles found in the various journals, or even all of those found in the "Journal of Polymer Degradation and Stability", only the main features of the degradation of some representative polymers are described herein.

These considerations are a further reason for the lengthy bibliography at the end of this chapter.

2. GENERAL PHYSICAL, STRUCTURAL AND THERMODYNAMIC CONSIDERATIONS

2.1. Effect of physical state on degradation

Commercial polymers and plastics, with the exception, of course, of elastomers, are glassy or semicrystalline materials at the temperatures at which they are used. Even at the higher temperatures at which degradation occurs, most polymers are, at best, highly viscous liquids. Thus most of the chemical reactions taking place during the thermal degradation and oxidation of polymers involve the movement of reactant, intermediate (*e.g.*, free radicals), and product species through a rigid (or at least highly viscous) matrix. Therefore, diffusion or even in some cases, segmental motion, are critical and often rate-limiting factors in the kinetics of polymer degradation. These diffusional and “cage” effects and other such phenomena are discussed later during the description of the degradation of specific polymeric materials.

It is well known that cure (polymerization) reactions take place extremely slowly when the temperature of polymerization is below the glass transition temperature, T_g , of the substrate. This is well illustrated during isothermal cure of resins where the glass transition temperature increases with degree of cure. When the increasing glass transition temperature reaches the experimental (isothermal) temperature, the rate of cure decreases orders of magnitude as it then depends upon the slow diffusion of radical species through the glassy polymer matrix. There is mounting evidence that the reverse depolymerization (degradation) reactions of polymers show a similar break in rate of degradation at T_g (or at T_m), the melting temperature, for crystalline polymers). Examples of this phenomenon are given subsequently for cases of thermal or oxidative degradation of many different polymers, for example, poly(methyl methacrylate), polystyrene, poly(vinylchloride), and polyurethanes, where onset of weight-loss or an acceleration of the rate of oxidative degradation occurs at the glass transition, melting, and softening temperatures. These features will be noted in the discussions of the individual polymers.

Thus, more rapid thermal decomposition of uncrosslinked (vinyl) polymers occurs above the melting temperatures for crystalline polymers and above the glass transition and/or softening temperatures for amorphous polymers, and such reactions are often a bulk phase phenomenon (homogeneous). On the other hand, for the cases of crosslinked polymers and some high melting polymers, the degradation reaction is from the outset or later becomes diffusion or surface limited. This reaction rate dependence on the ability of radicals and molecules to diffuse through the polymer matrix is even more widely observed for oxidative

and hydrolytic degradation of polymers. For example, the initial step in the oxidation of polyethylene at low temperatures – the formation of hydroperoxide groups – occurs only in the noncrystalline regions. Polyurethanes are another example of this dependence. Their degradation rate accelerates at temperatures where the hard segment crystallites which act as cross links begin to melt. Large diisocyanate moieties diffuse out with great difficulty and therefore polyurethanes containing them degrade at higher temperatures than those containing less bulky diisocyanate groups. Thus it appears that most polymer degradation (and oxidation) reactions have a spurt in their rate above their melting or glass transition (or softening) temperatures where increased segmental and molecular motion allow greater movement of “reacting species” through the medium so that they may come in contact with one another.

From the above facts, one wonders if many of the polymers which do not exhibit a distinct glass, melting, or softening transition below their degradation temperature are, in actuality, “melting with decomposition” in their degradation temperature range. Thus polymers “stable at higher temperatures” may owe their stability not just to stronger chemical bonds (and absence of weak links) but to the fact that they are condensed ring and/or dense crosslinked substances in which the movement of attacking agents and chain propagating radicals have very low rates of diffusion into their rigid inflexible interior structure.

An obvious corollary to the above facts is that Arrhenius parameters for polymer degradation and oxidation reactions obtained from high temperature experiments of thermal analysis can not be extrapolated through a phase change to make lifetime predictions at lower service temperatures [4]. Such extrapolations through a phase change and/or a ceiling temperature (see below) invalidate the lifetime predictions made from many of the “accelerated aging” experiments found in thermal analysis literature [5].

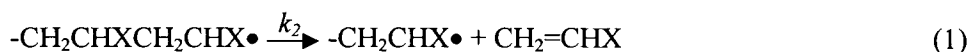
2.2. Energetics – bond energies

The strengths of the bond between the atoms which make up the polymer chain are obviously important factors in the determination of the overall stability of polymeric materials. A table of bond dissociation energies will be presented later, and the effects of the strength of bonds and particularly “weak links” on the kinetics and mechanism of the degradation reactions of vinyl polymers will be illustrated in subsequent sections.

2.3. Thermodynamics – ceiling temperatures

When polymers are thermally degraded, they are in a high temperature region where they are thermodynamically unstable. On the other hand, when polymers are utilized, they are in a lower temperature region where they are thermodynamically stable. This stability-instability reversibility with respect to temperature for polymers has been formalized by the concept of ceiling

temperature (T_c) which was developed by Dainton and Ivin [6] and was reviewed extensively by Bushfield [7]. The equations defining the ceiling temperature were developed from the thermodynamic equilibrium between the propagation and depropagation reactions for a free radical chain vinyl polymer degradation mechanism. For this case the depropagation step is



and the propagation step is



so when the two opposing rates are equal, the resulting equilibrium is

$$k_2[R\bullet] = k_{-2}[R\bullet][M]$$

where $[R\bullet]$ and $[M]$ are the radical and CH_2CHX (monomer) concentrations, respectively. For this equilibrium,

$$[M] = k_2[R\bullet]/k_{-2}[R\bullet] = k_2/k_{-2} = K \quad (3)$$

where K has the character of an equilibrium constant for the polymerization/depolymerization reaction and can be described in terms of the change in free energy ΔF° , enthalpy ΔH° , and entropy ΔS° during the polymerization reaction, that is,

$$K = \exp(-\Delta F^\circ/RT) = \exp(\Delta S^\circ/R) \exp(-\Delta H^\circ/RT) \quad (4)$$

If we add the condition that $[M]$ is unity in some convenient units, for example, one torr pressure, then, when $K = [M] = 1$,

$$\ln K = 0 = \Delta S^\circ/R - \Delta H^\circ/RT_c$$

and this temperature, T_c , is defined as the ceiling temperature and is given by

$$T_c = \Delta H^\circ/\Delta S^\circ \quad (5)$$

The ceiling temperature, being a thermodynamic quantity, will depend only on initial and final states, monomer and polymer, respectively, and not on the reaction mechanism. Therefore the ceiling temperature applies equally well to a polymerization-depolymerization equilibrium brought about by anionic or

cationic initiators [2]. Obviously similar thermodynamic developments can be applied to any reversible association dissociation degradation reaction. For example, in the oxidation of polymers [8], ceiling temperatures for the vinyl radical – peroxy radical equilibrium:



have been calculated for various partial pressures of oxygen.

Also, as the ceiling temperature is a thermodynamic quantity, it will tell us only whether a polymerization or depolymerization reaction is favored under specified conditions, not whether it will actually take place in finite time. Therefore nothing can be learned from the ceiling temperature, itself, about the rates of the polymerization or depolymerization reactions. Monomers may exist indefinitely in a metastable state at temperatures below their T_c , and many polymers do not degrade at an appreciable rate at temperatures well above their T_c in the absence of proper catalysts or when under physical restraints to molecular movement. On the other hand, for some systems, this monomer-polymer equilibrium is almost instantaneously reversible (such a rapid reversibility appears to apply to the polyurethane link in many polyurethanes [9]). The ceiling temperature is an important limiting factor in the use of thermoanalytical methods to predict service lifetimes of polymers from kinetics constants obtained at elevated temperatures. That is, temperature extrapolations of experimental Arrhenius constants can not be extended through the ceiling temperature range.

Vinyl (addition type) polymerizations need to be strongly exothermic in order to overcome the unfavorable entropy term in the free energy equation which results from the decrease in the numbers of molecular species. This exothermic character is always present since the difference between the formation of two single C-C bonds (2×83 kcal/mol) and the breaking of one C=C bond (143 kcal/mol) is 23 kcal/mol. The reverse depolymerization reactions are endothermic in inert atmospheres. However, oxidative degradations are always exothermic. On the other hand, for condensation type polymerizations, the splitting out of water may result in a favorable entropy of polymerization so that these polymerizations can take place in spite of their endothermicity. In these cases, the overall degradation (hydrolysis) may be exothermic. Obviously purely thermal degradation of condensation polymers will take place by paths other than the reverse of the polymerization reaction. This is, of course, also the case for the majority of polymers whose pyrolyses take paths not resulting solely in monomer formation and involve many other species.

The ceiling temperature is defined by the concentrations (activities) of the reactants and products, and the forward and reverse rates constants also depend

on volatility and diffusivity (cage effects) of these species. The effect of monomer concentration on the polymerization/depolymerization reaction equilibrium can be seen for the case of polystyrene whose T_c is calculated to be 230°C [10]. Staudinger [11] polymerized liquid styrene (high monomer concentration) at 260°C to obtain an average DP of 33. On the other hand, high molecular weight polystyrene, when heated in a vacuum (where obviously the partial pressure of styrene was maintained at a low value) at a rate of nine degrees/day, loses over two percent of its weight by the time it attains the ceiling temperature of 230°C [12]. Ceiling temperatures are often calculated at one torr partial pressure of monomer. It is a long known fact that many polymers begin to degrade in a vacuum at a measurable rate at a temperature about fifty degrees below that required to bring about a comparable rate of degradation in nitrogen at one atmosphere.

Reviews of the general mechanisms for the thermal, oxidative and hydrolytic degradations of polymers are next presented, preceding the descriptions of the degradative reactions for specific polymeric materials.

3. GENERAL THERMAL DEGRADATION MECHANISMS

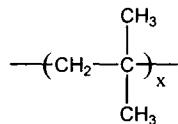
3.1. Types of degradation reactions

The many possible types of thermal degradation reactions can be discussed more coherently by separating them under the four imperfect headings given by Mita [13]. They include random main-chain scission, depolymerization, carbonization, and side group reactions.

Random chain scission is the breaking of the main polymer chain to produce smaller molecules of all sizes. The molecular weight falls rapidly from the start, but only after the process has continued for a long time are there many molecules small enough to be volatile. There are no preferences for monomer formation. Depolymerization is the successive removal of monomer units from an end of the chain, sometimes compared to the opening of a zipper, after an occasional initial break. In the ideal case, monomer is the only product. The carbonization reaction is more difficult to define, although it occurs often. It may include, as component processes, cross-linking, polyene formation by elimination of side chains, cyclization, and aromatization by dehydrogenation. The details of these mechanisms are often obscure, and the intermediate products often defy identification. Usually some random scission occurs concurrently. The side group reactions include the splitting off of a side group to leave the polymer backbone intact. Examples are the elimination of hydrogen chloride from polyvinyl chloride (PVC) to leave a polyene structure and the elimination of isobutylene from poly(*t*-butyl methacrylate) to leave polyacrylic acid.

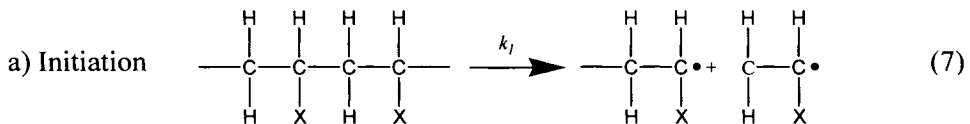
3.2. Free radical chain reaction theory

The first two classes listed above, random chain scission and depolymerization, and a combination of them, have been explained in a comprehensive way by the free radical chain reaction theory, developed by several groups along slightly different lines. (Thermooxidative degradation, discussed subsequently, has also been explained by free radical mechanisms.) This unified mechanism and its simpler special cases seem to account well for the main features of pyrolysis of a wide variety of vinyl polymers and their near relatives. The theory not only applies to vinyl polymers, strictly $(\text{CH}_2\text{CH}_2)_x$, but also more broadly to linear polymers having aliphatic carbon main chain, such as poly(isobutylene)

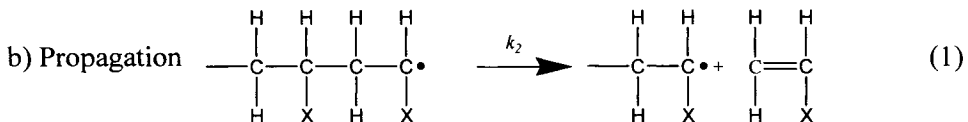


and poly(tetrafluoroethylene) $(\text{CF}_2\text{-CF}_2)_x$. Where adequate reviews of these model mechanisms exist, reference will be made to them [14-17] rather than to the original papers. The names associated with the mathematical development are Wall and Simha, Jellinek, Gordon and Boyd. Unfortunately, the terminology differs among authors and sometimes it shifts in successive papers by the same authors. Many important elements of these models for degradation kinetics were drawn from the concept of F. O. Rice that thermal decomposition of hydrocarbons was a chain reaction with free radical intermediates [18,19], from the free radical theory of vinyl polymerization of Staudinger [20], and the theory of condensation polymerization of Flory [21].

The four essential reactions, a), b), c), and d), (some of which have been subdivided) are:

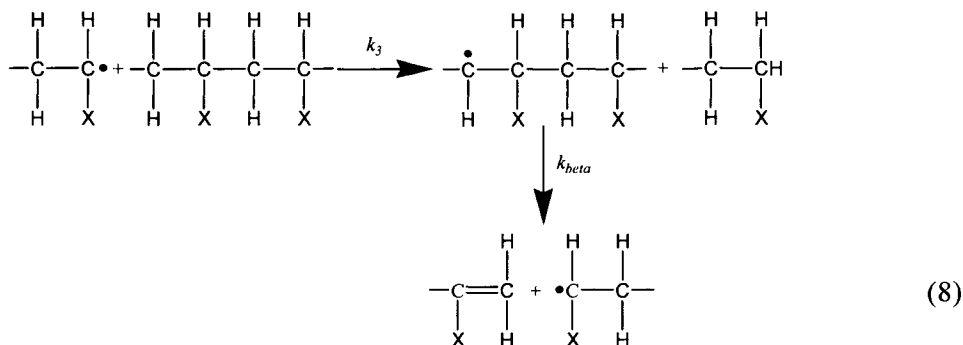


(The initiation reaction may be subdivided into special cases, *e.g.*, random, end and weak link.)

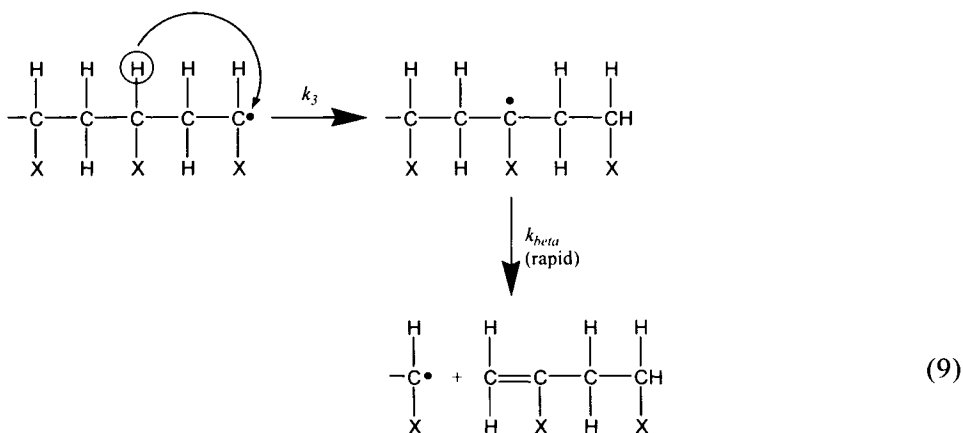


c) Transfer, followed by β -scission. Two sub-types with different kinetics consequences have to be considered.

Intermolecular:

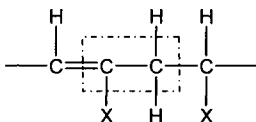


Intramolecular:



The symbols used are those of Wall and coworkers. Thus radical species are formed by the initiation process, the radicals bring about further scission by a kinetics chain reaction represented by the depropagation and transfer steps, and the kinetics chain is ended as radicals are removed from the system by the termination reaction.

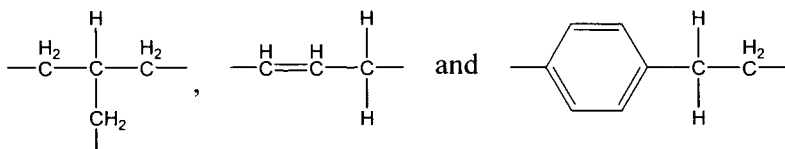
A few comments are in order. The initiation process shown is the dissociation of a main chain bond. This may occur at random along the main chain. However, there is evidence that, in some polymers, scission at chain ends is preferred. The C-C and C-H bonds in beta position to the allylic carbon,



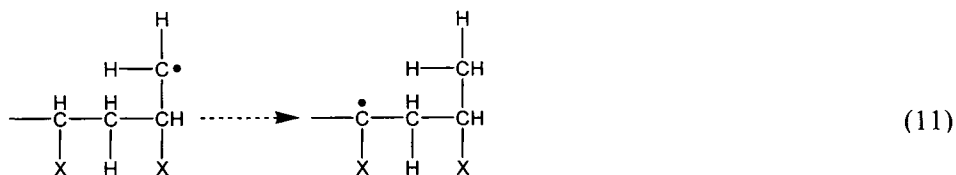
are calculated to be weaker than the bonds in a pure saturated chain. (Since unsaturated structures are labile and will initiate new radical chains, termination by disproportionation will only temporarily destroy chain-propagating species. Similarly, chain transfer reactions may bring an eventual branching of the kinetics chain through the production of labile terminal double bonds. These complications are not usually included in kinetics models.) The same inherent weakness would occur in the neighborhood of a double bond anywhere else in the chain. Some of the relevant bond dissociation energies are given in Table 1.

Trace oxygen-containing groups, hydroperoxide side groups, and residual peroxide catalyst in the polymer are other obvious sites for initiation, and, in practice, it is very difficult to exclude them completely from the polymer structure. As will be seen later, the kinetics for weak-point initiation differs somewhat, and end-initiation kinetics differ considerably, from the random initiation case.

The activation energy for the depropagation reaction is computed with some confidence from vinyl polymerization data, that is, from the heat of polymerization plus the relatively small activation energy for propagation in polymerization, and it is usually around 20 or 30 kcal/mol. Its estimation is simplified by the fact that in radical polymerization the termination reaction - either combination or disproportionation - occurs with near zero activation energy and does not contribute to the overall activation energy for the degradation. For chain transfer the estimated activation energies depend upon the type of hydrogen which is abstracted, being more or less parallel to the C-H bond dissociation energies, and are the lowest for tertiary, allylic and benzylic hydrogens,



respectively. Some of these quantities are given in Table 1, where the values are chiefly taken from data on small molecules. The activation energies are probably nearly equal for the inter- and intra-molecular varieties of transfer, but at certain positions on the radical chain, especially when the transition state is a five- or six-membered ring, the probability of intramolecular reaction should be much higher, for example,



These reactions may be compared with the well-known condensation reactions of organic molecules. Careful identification and quantification of products from poly(ethylene) and poly(propylene) degradations [22-24] seem to show that the radical product shown above can, in turn, attack new hydrogens at comparable distances down the carbon chain before the intermediate undergoes β -scission to give the final volatile product. These successive intramolecular transfer steps are often called a "back-biting" mechanism.

Results similar to the above are obtained from pyrolysis gas chromatography integrated with hydrogenation and mass spectrometry [25-27]. The mechanistic ideas they have used have been extended and applied to various analytical problems such as determination of olefin copolymer composition and the nature and number of branches, not only in polyethylene but also in PVC, first by reducing the latter with lithium aluminum hydride [28,29]. It is important to realize that intramolecular transfer offers a way of producing molecules in the dimer and trimer size range much earlier and in much greater proportions than would be expected from random scission alone. Sometimes it is convenient mathematically to treat intermolecular transfer as a type of propagation. It should be pointed out that although the weaker C-H bonds are preferred sites for transfer, the differences in energy are not so great as to make them exclusive sites, especially at higher temperatures. These preferences may be overcome if weaker bonds are shielded or the stronger ones are overwhelmingly numerous. Thus there is plausible evidence that in poly(isobutene) even primary hydrogens on methyl groups are attacked [30].

Termination was modeled in Eq. (10) by a bimolecular disproportionation reaction. This is mathematically convenient and is also the most probable mechanism at the high temperatures involved. If the kinetic chain length is large, especially if there is much chain transfer, termination by combination rather than by disproportionation should not alter the kinetics very much. On the other hand, small radicals may evaporate so as to give rise to an apparent unimolecular termination. This will lead to greater differences in the kinetics. The plausible alternatives have led to controversies in which mechanisms that differ considerably in detail are defended in order to explain very similar overall results, as in references [31,32], for example.

As was pointed out in the introduction, the rates of all the reactions involving two large polymer molecules are affected to an uncertain degree by the

Table 1. Bond Dissociation Energies of C—C and C—H Bonds (kcal/mol)^a: $R_1 - R_2 + R_1 + R_2$

R ₁	R ₂													
	n-Alkyl				Branched alkyl		Radical		sp ² Radical					
	CH ₃	C ₂ H ₅	n-C ₃ H ₇	n-C ₄ H ₉	i-C ₃ H ₇	t-C ₄ H ₉	CH ₂ =CHCH ₂	PhCH ₂	CH ₂ =CH	Ph	CH ₂ =CHCH(CH ₃)	PhCH(CH ₃)	PhC(CH ₃) ₂	CF ₃
H	104	98	97.6	98	94.5	91.1	86.8	85.1	104	104	85.7	81.6	76.5	—
CH ₃	88.4	84.5	84.9	84.7	83.8	80.5	73.6	71.9	93.7	94	72.3	68.7	65.7	90
C ₂ H ₅		81.6	81.4	81.4	80.2	76.9	70.3	68.8	90.0	90.6	67.8	66.5	—	—
n-C ₃ H ₇			81.4	81.2	80.0	76.8	70.3	69.0	98.7	90.8				
i-C ₃ H ₇					77.7	73.4	67.7	67.8	88.5	87.7				
t-C ₄ H ₉						67.6	—	—	81.1	82.2				
CH ₂ =CHCH ₂							60	58	78.4	—				
PhCH ₃									56	—	72.7			
CH ₂ =CH ₂										101.7	100.8			
Ph											100.5			
CF ₃													—	97

^aCalculated from the heats of formation of radicals and molecules.
Source: Ref. 13

hindrance to motion due to surrounding molecules. When a molecule in a liquid dissociates, the surrounding molecules can keep the fragments in one another's proximity for up to a hundred collisions, with opportunity to recombine, before they escape. This "cage effect" could be even more important in a viscous polymer melt than in ordinary thin liquids. Likewise, when two free radicals come together, there is no real energy barrier preventing reaction at every collision, but their diffusion through a viscous medium before they collide will be governed by an effective activation energy for diffusion. Thus the termination rate constant, k_4 , may be much smaller for large polymeric radicals than for small ones. Although there has been much discussion in reviews [33,34], the tendency has been not to include these effects explicitly. This neglect is justified only if the governing mobility is related, not to the high bulk viscosity of the medium, but to some sort of much lower viscosity related to chain segment motion. These cage diffusional effects are undoubtedly important in solid reactions (for example, low temperature radiation and oxidation), however, they would be less significant in a rubber or a melt. In the case of poly(methyl methacrylate), however, a k_4 much smaller than that typical of small molecules has been deduced from experimental data [35,36].

Two general approaches have been made to the treatment of the general set of equations for initiation, propagation, transfer and termination reactions: (1) starting with a monodisperse sample, that is, a single molecular weight, and enumerating all reactions which form all species of intermediates and products [15,37] and (2) starting with a polydisperse sample and operating on moments of molecular weight distributions [16,17]. The latter method is relatively easy if the starting sample has the "most probable" or Gaussian molecular weight distribution - a distribution that is the natural result of condensation and some related polymerizations, and which tends to be approached in any event after a few random scissions even in a monodisperse polymer.

Whichever method is used for the numerical treatment and discussion, it is convenient to use three parameters in the description of the kinetics: the reduced time, $\tau = k_1 t$; the zip length, $(1/\varepsilon) - 1$; and the transfer constant, σ . They are defined as follows and illustrated explicitly for random initiation:

$$\begin{aligned} (1/\varepsilon) - 1 &= (\text{probability of propagation})/(\text{probability of termination} + \text{transfer}) \\ &= \frac{k_2}{k_4 R + k_3 k_4 R^2 / k_1} = \frac{k_2}{k_4 R [1 + \sigma / 2]} \end{aligned} \quad (12)$$

$$\sigma = (\text{probability of transfer})/(\text{probability of initiation}) = k_3 R / 2 k_1 \quad (13)$$

where k_1 , k_2 , k_3 , and k_4 are the rate constants for initiation, propagation, transfer and termination in Eqs. (7), (1), (8), (9) and (10) and the R 's above refer to the

concentration (not number) of radical species. It can be noted in passing that when there is no transfer reaction ($\sigma = 0$), the product $\varepsilon[1 - \varepsilon]^i$ represents the probability of “zipping” down the chain i monomer units after a polymer radical has been initiated. In contrast to these depolymerization equations, a simple vinyl polymerization produces no intermediate products analogous to the shortened chain in depolymerization. Although the treatment of the general equations does not produce analytical results except for special cases, some qualitative idea of what to expect can be gained from graphs of a few asymptotic cases, Figs. 1, 2 and 3, where N is the initial (monodisperse) degree of polymerization and L is the DP of the smallest fragment which will not distill from the system. The kinetics expressions contain several rate constants, each with its own activation energy, and these rates are not simply multiplied together. A consequence, not always appreciated, is that the “product mix” can vary with pyrolysis temperature, as also can the shape of the rate curves. Madorsky [38] found an approximate constancy of volatile product ratio over a temperature range of

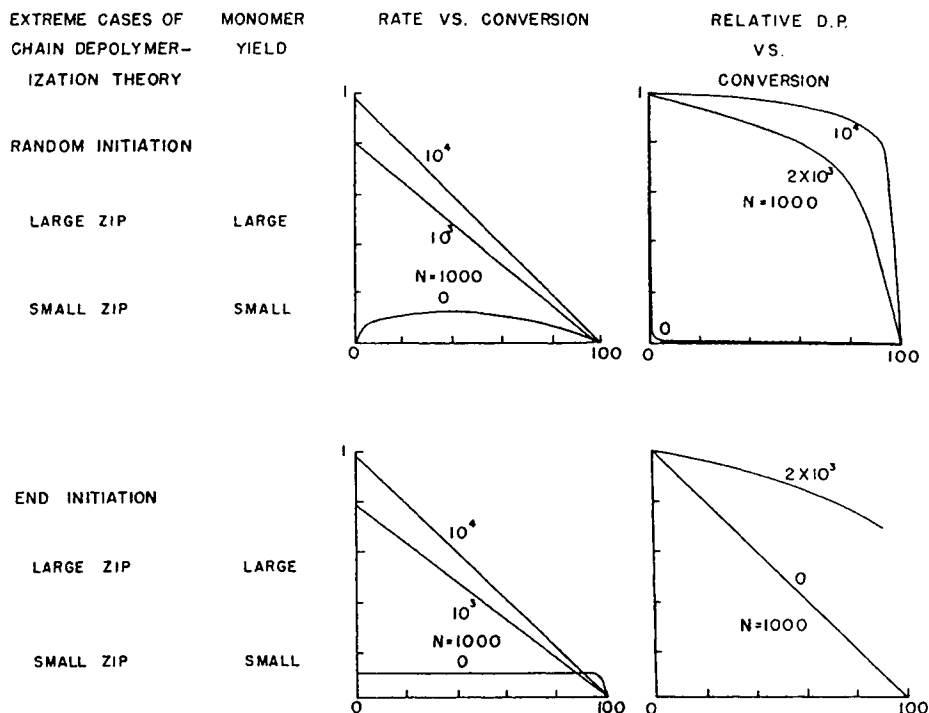


Fig. 1. Comparison of theoretical results for extreme cases of the depolymerization theory. Values of zip $[(1/\varepsilon) - 1]$ are shown above the curves. All curves are for $N=1000$, $\alpha = 0$, and $L = 4$. The rate scale for rate curves with zip = 0 are multiplied by factors of 100 for random initiation and 50 for end initiation (from ref. 243).

100°C or so, but, for example, experiments with polystyrene over a wider temperature range show a shift toward mostly monomer by 700°C and some molecules even smaller than monomer above 800°C [39,40]. Some of the increase in monomers at high temperatures may result merely from cracking of oligomers before they can escape from the hot zone. On the other hand, as the cited references suggest, and contrary to the usual picture, the oligomers may be secondary products from originally formed monomers.

In any event, volatile fragments from flash pyrolysis techniques may differ both in stoichiometry and kind from volatiles obtained from degradation experiments under more mild conditions. For example, the pyrolysis of poly(vinyl chloride) (PVC) in the 200°C to 400°C range produces more than six times as much hydrogen chloride as benzene [41] while, on the other hand, pyrolysis at above 600°C results in a two to one HCl to benzene ratio [42].

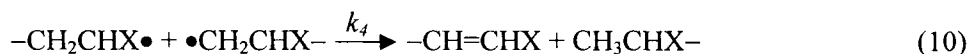
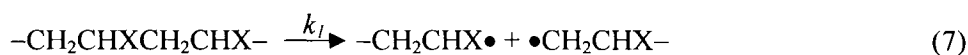
In Fig. 1, where no transfer occurs, one can compare the monomer yield, rate and relative *DP* for various relations of initial molecular weight and zip length. Large zip results in a linearly decreasing rate curve, while the molecular weight plotted against conversion is initially horizontal and above the diagonal. Random initiation and zero zip are equivalent to simple random decomposition which is discussed later. End initiation and zero zip produce a horizontal rate curve and a diagonal *DP* curve. Transfer, however, will push all curves toward that for random scission. The random scission case and a few other asymptotic cases can be expressed in a closed form and will be discussed later in some detail.

3.3. Random scission

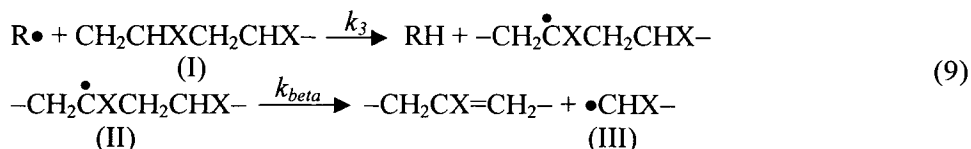
3.3.1. General theory

In the general free radical chain theory of pyrolytic degradation, an important asymptotic case is that in which any bond along the main chain of a linear polymer can be broken with equal probability. The mathematical treatment has been available for many years [14,15,43-45]. It is simpler to consider bonds only between monomer units, although in a polymer such as polyethylene -CH₂CH₂CH₂CH₂- there is no real distinction between bonds between the original CH₂=CH₂ units and those within them, and even for polymers where the bonds differ, both types might be vulnerable.

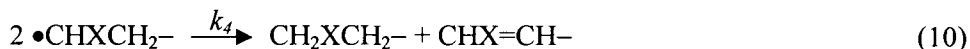
There are two sequences in the free radical scheme which can result in random scission. First, initiation followed by immediate termination by disproportionation:



Here the effective rate in a steady state where the initiation step is rate limiting can be represented by k_1 times the number of chain units. Second, attack by a free radical I at any point along the chain, followed by scission of the intermediate radical II (that is, intermolecular transfer) with termination of all radicals by disproportionation:



The radical (III), $\bullet\text{CHX}-$, reacts as $\text{R}\bullet$ above or else via



In this case, as in the general scheme, beta-scission is assumed to be more rapid than any possible competing reaction for radical II. The effective rate in a steady-state radical chain reaction will be k_3 times the radical concentration times the number of chain units. For a long kinetic chain length, this rate may be much larger than in the first case. Parts of the following discussion apply also to situations much more general than pyrolysis, such as the acid-catalyzed hydrolysis of polyesters, polyamides, and many natural polymers. The theory is closely related to Flory's classical account of condensation polymerization, but applied in reverse. However, it is more complicated, especially when applied to the situation most often considered, that is, when pyrolysis takes place in an open system from which monomer and other small molecules are free to evaporate and leave. However we will consider a simpler closed system first.

3.3.1.1. Closed system

The statistical development of this case has been presented many times, more recently in reference [2]. This treatment gives a useful kinetic equation for large initial degree of polymerization, $DP_{no} = N$, and where α is the fraction of bonds broken,

$$1/DP_n - 1/DP_{no} = [1 + \alpha(N-1)]/N - 1/N = [\alpha(N-1)]/N = \alpha \tag{14}$$

If the bond breaking is first order then $(1 - \alpha) = \exp(-kt)$; for small α , $\alpha = kt$, and so

$$1/DP_n - 1/DP_{no} = kt \tag{15}$$

Thus for an appreciable initial proportion of the random degradation, a plot of $1/DP_n$ against time will be almost linear as found in many cases, e.g., refs. 46,47.

3.3.1.2. *Open systems*

One may consider degradation in an open system from which monomer and other molecules up to $L - 1$ monomer units long can evaporate while L and higher can not. To make the computation relatively simple, the artificial assumption of a sharp cutoff is made: all molecules up to $L - 1$ and none of $DP \geq L$ evaporate. This idea was based on arguments given by Frenkel [48] that above a certain size L the sum of van der Waals attractions to all nearest neighbors will be greater than the bond dissociation energy between two chain units, and therefore a molecule of size greater than L should dissociate rather than evaporate, even in a perfect vacuum. The value of L will depend on the nature of the monomer units, being smaller for large or highly polar units. In samples of appreciable thickness, or in contact with the gas phase at appreciable pressure, molecules of a size approaching L may evaporate only slowly, and the effective L may vary with surface to volume ratio, pressure and flow rate of purge gas [49]. Flynn [50] measured the vaporization of $C_{94}H_{190}$ in vacuum without finding evidence of degradation.

The solution for the open system, which includes rather involved summations gives [51]:

$$1 - C = [(1 - \alpha)^{L-1}/L][N + \alpha(N - L)(L - 1)] \quad (16)$$

Assuming first order scission, that is, $(1 - \alpha) = \exp(-kt)$, then changing variables and differentiating, one obtains for the rate of volatilization

$$dC/d(kt) = (L - 1)(1 - C) - [(1 - \alpha)^L(N - L)(L - 1)]/N \quad (17)$$

and the number average DP is

$$DP = [N + \alpha(N - L)(L - 1)]/[1 + \alpha(N - L)] \quad (18)$$

The rate dC/dkt rises at first, goes through a maximum, and then falls. This is reasonable from qualitative arguments as, at first, most fragments are too big to evaporate, while later on, when many molecules are only a little larger than L , each new cut has a good chance of producing volatile material.

Ozawa [52,53] has adapted these equations for random degradation of polymers to the case of constant heating rate kinetics to obtain values for L and

the Arrhenius parameters from data for the TGA of polymer degradation reactions.

The location of the maximum, found by differentiating the rate with respect to alpha, is

$$(\alpha)_{max} = (N - 2L + 1)/[L(N - L)]$$

or

$$(\alpha)_{max} = 1/L \quad \text{for } N \gg L \tag{19}$$

The conversion and rate of conversion at the maximum (for $N \gg L$) reduce to

$$C_{max} = 1 - [(L - 1)/L]^{L-1} [(2L - 1)/L] \tag{20}$$

and

$$(dC/dkt)_{max} = (L - 1)[(L - 1)/L]^{L-1} \tag{21}$$

Numerically the location of C_{max} is not very sensitive to L for low L and is

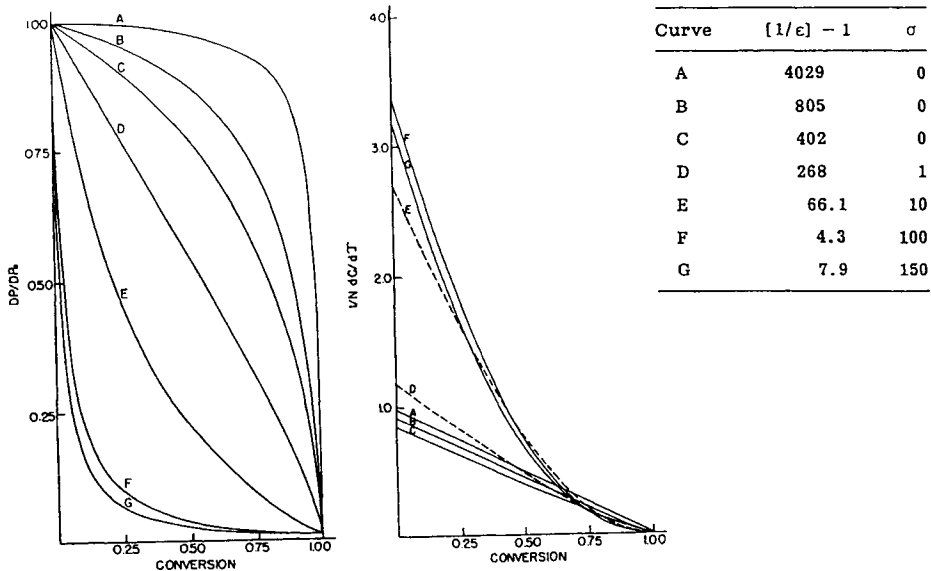


Fig. 2. Effect of the zip, $(1/\epsilon) - 1$, and transfer constant, σ , at constant N and L on the relative number average DP and rate of volatilization for depolymerization with random initiation, N 403, L 4 (from ref. 243)

about 26% conversion.

Figs. 2 and 3 give calculated curves for the course of molecular weight and rate of conversion with degree of conversion for several initial conditions. Comparison with curves for the pyrolysis of linear polyethylene [54] in Fig. 4 shows fair agreement. However, low density polyethylene does not show such a maximum rate phenomenon.

Jellinek has developed a theory for random scission modified by randomly distributed weak bonds [15]. Since weak bonds tend to break first, one simple result is that a plot of $1/DP - 1/DP_0$ against time will rise rapidly at first and more slowly later. These theories were reviewed in 1978 [55]. It is plausible that the many branch points in low density polyethylene function as weak links and these may furnish abundant volatile material early in the degradation, thus preventing the appearance of a maximum rate. It must be added that even with high density linear polyethylene, although the rate curve conforms to the shape predicted by the theory of random scission, the molecular weight distribution of the volatiles deviates from that calculated from random scission theory [14,22-24]. The general concept of weak links has very wide application, and specific forms of it have been invoked in many researches, including some in which weak links of specific structures have been deliberately incorporated in the polymer chain.

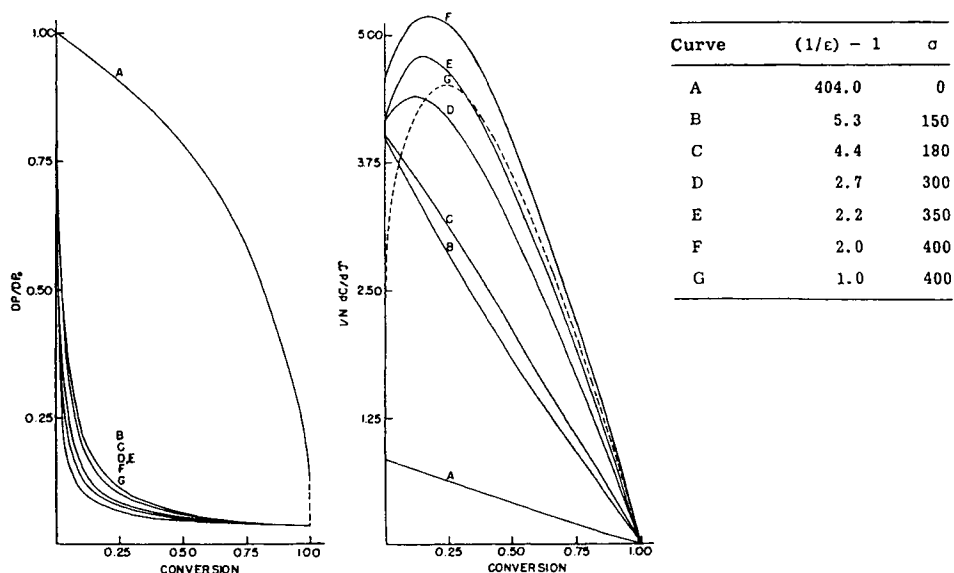
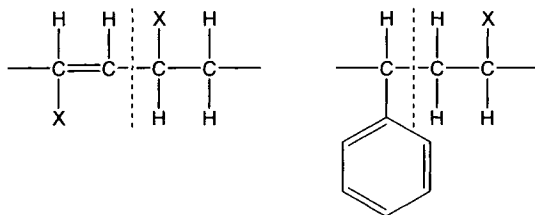


Fig. 3. Effect of zip and transfer constant on the relative number average DP and the rate of volatilization, for depolymerization with random initiation, $N = 403$, $L = 12$ (from ref. 243)

The allylic carbon-carbon bond next to an unsaturated end group or a benzene ring is one special case, that is



It is also very difficult to exclude the presence of a few peroxide or hydroperoxide groups in almost any polymer sample; therefore, one can expect almost any polymer decomposition to be at least somewhat complicated by the participation of weak links in the degradation reaction.

In summary, although random scission seldom occurs in polymer pyrolysis uncomplicated by weak links or other special reactions, it is nevertheless peculiar to polymers and not easily fitted into the framework of knowledge of

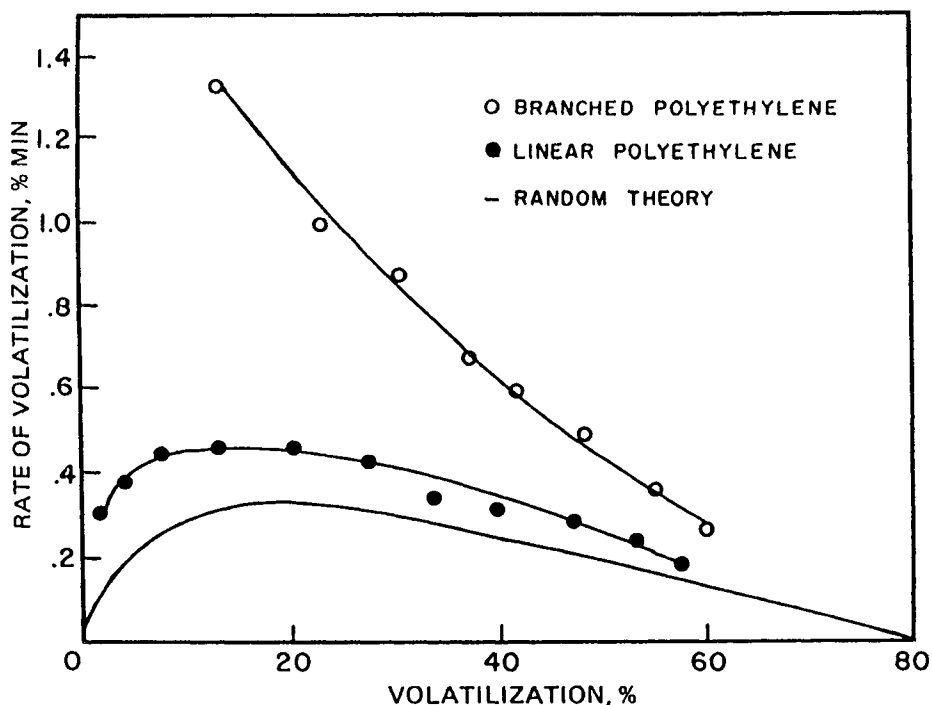


Fig. 4. Pyrolysis of linear and branched polyethylene, compared with random depolymerization theory (from ref. 244) (o: branched polyethylene; •: linear polyethylene; -: random theory)

Table 2. Special Cases of Depolymerization Behavior

Zip	Termination	Initial molecular weight distribution	Weight loss rate	Order	Dependence of initial rate of molecular weight	Molecular weight versus time	Molecular weight versus conversion
Random initiation							
Short $1/\epsilon - 1 \ll DP_{n0}$	1st order	Insensitive to distr.	$dC/dt = Zk_1(1/\epsilon - 1)(1 - C)$ early stages only	1st in early stages	Independent	$(1/DP_n) - (1/DP_{n0}) = k_1 t$	Drops rapidly until $DP_n \approx 1/\epsilon - 1$
	Disproportionation	Insensitive	$dC/dt = Zk_1(1/\epsilon - 1)(1 - C)$ early stages only	1st in early stages	Independent	$(1/DP_n) - (1/DP_{n0}) = k_1 t$	Drops rapidly until $DP_n \approx 1/\epsilon - 1$
	Recombination	Most probable	$dC/dt = 4k_1(1/\epsilon - 1)(1 - C)$ fairly wide range	1st, wider range	Independent	$\ln(DP_n/DP_{n0}) = -Zk_1(1/\epsilon - 1)t$	$(DP_n/DP_{n0})^2 = w/m\epsilon Q$
Long $1/\epsilon - 1 \gg DP_{n0}$	Mono		$dC/dt = k_1 DP_{n0}(1 - C)$	1st	Proportional to DP_{n0}	$DP_n = DP_{n0}$	Stays constant
	Most probable		$dC/dt = Zk_1 DP_n(1 - C)$	Not quite 1st	Proportional to DP_{n0}	$(1/DP_n) - (1/DP_{n0}) = k_1 t$	Falls slowly
End initiation							
Short	1st order	Mono	$dC/dt = (k_1/DP_n)(1/\epsilon - 1)(1 - C)$	Zero until $DP_n \gg 1/\epsilon - 1$	Inversely proportional to DP_{n0}	$DP_n - DP_{n0} = -k_1(1/\epsilon - 1)t$	$DP_n/DP_{n0} = 1 - C$ while $(1/\epsilon - 1) \ll DP_n$
		Most probable	$dC/dt = (k_1/DP_{n0})(1/\epsilon - 1)(1 - C)$	1st	Inversely proportional	$DP_n = DP_{n0}$	Stays constant
	Disproportionation	Mono	$dC/dt = (k_1/DP_n)(1/\epsilon - 1)(1 - C)$	Not 1st	Inversely proportional to $(DP_{n0})^{1/2}$	Complicated in $(DP_n)^{1/2}$	$DP_n/DP_{n0} = 1 - C$ while $(1/\epsilon - 1) \ll DP_n$
		Most probable	$dC/dt = (k_1/DP_{n0})(1/\epsilon - 1)(1 - C)$	1st	Inversely proportional to $(DP_{n0})^{1/2}$	$DP_n = DP_{n0}$	Stays constant
	Recombination	Most probable	$dC/dt = k_1(1 - C)/2$	1st	Independent	$\ln(DP_n/DP_{n0}) = k_1 t/4$	$DP_n/DP_{n0} = (1 - C)^{-4}$ rapid increase
Long $1/\epsilon - 1 \gg DP_{n0}$		Insensitive to distr.	$dC/dt \approx k_1(1 - C)$	1st	Independent	$DP_n = DP_{n0}$	Stays constant

small-molecule reactions. Many of its features, such as a maximum in the rate of weight loss curve, are approximated in more complicated polymer degradation reactions.

It should be emphasized that the “autocatalytic” increase in rate of weight loss resulting from the random scission kinetics should never be represented by n th order reaction kinetics. This has been frequently done in TGA studies found in literature and it results in the calculation of energies of activation that are in great error. When first order kinetics are erroneously used in place of random scission kinetics, calculated activation energies may be twice their correct values [4].

However polymer degradations which fit “autocatalytic” mass loss kinetics may well yield a first order kinetics fit when the degradation is measured by change in degree of polymerization (DP) (*e.g.*, light scattering, osmotic pressure, viscosity, *etc.*) or by changes in functional group concentration (*e.g.*, infra red analysis). These methods measure chain scission as shown in Eq. (15). (As pointed out above, a brief spurt in the rate may occur initially due to the weak links). Such first order bond breaking occurs for the degradation of many polymers as will be observed in Table 2. DSC, in that it measures the heat evolved by the degradation reaction, might be included in these latter methods. However, here, the measured enthalpy change is usually a complex function of not only the enthalpy change from the degradation reaction and release of strained configurations, but also, heats of vaporization of products and phase changes in the bulk. Further complications result from gross base line shifts due to changes in physical state and especially to losses of mass which lower the heat capacity of the substrate.

4. GENERAL THERMO-OXIDATIVE MECHANISMS

4.1. Introduction and scope

This discussion is limited to the oxidation of polymeric materials by a gaseous oxygen atmosphere (diluted with inert gases, such as in air). Oxidation by other gaseous or liquid oxidizing agents is not included; nor is the broad area covering the effects on the oxidative degradation of polymers containing interactive additives and impurities such as stabilizers, “biodegraders”, flame retardants, antioxidants, residual initiators, *etc.* However citations of books and review articles on these scientifically and commercially important aspects of polymer oxidation are included in the bibliography at the end of the chapter.

As stated in the introduction, only slow, “low temperature” oxidation is discussed here. Combustion and burning reactions of polymeric materials usually take place in the gas phase and not in the polymer substrate. The heat generated from these gaseous exothermic oxidation reactions cause the polymer to degrade, and the gaseous products emitted from these degradation reactions fuel the

continuing combustion. Thus flame retardants which increase the amount of char (thus lessening the amount of volatiles) or cause the burning in the gas phase to take place at a lower temperature are often effective. This, of course, does not give a complete picture for burning and combustion. For this the reader is referred to the bibliography at the end.

Most of the techniques of thermal analysis have been utilized in the study of thermal oxidation of polymers, both in the investigations of mechanisms of oxidation, and in the development of test methods for the measurement of property deterioration as a result of oxidation.

In this section, the discussions of the oxidative degradation of specific polymers are not presented separately. These discussions are included along with those of the thermal degradations of specific polymers later on in this article. Although the addition of oxygen into the thermal degradation equations does introduce the possibility of many more molecular and radical species entering into the sequence of equations describing the kinetics, thermal oxidation also has an overall simplifying effect on the kinetics. This is because nearly all thermal oxidations at moderate temperatures of vinyl polymers (and also many other types of organic polymers) are postulated to involve the hydroperoxide radical in the propagation step of the degradation. Conversely, this is also the case for oxygen catalyzed polymerizations. No doubt related to the above facts, we find that most oxygen initiated polymerization and depolymerization reactions have energies of activation in the 20 - 25 kcal/mol (or about 100 kJ/mol) range (the activation energies for purely thermal degradation reactions are usually even higher.) The activation energy for the diffusion of oxygen in polymers is about 10 kcal/mol (or about 40 kJ/mol). Thus, energy of activation measurement is a way to distinguish between "diffusion limited" and "chemical reaction limited" oxidation processes. This "universal" activation energy for oxygen induced polymerizations and depolymerizations certainly does not prove that all of these reactions have the same rate limiting step (such as hydroperoxide group dissociation or reaction). However, it does suggest that there is some sort of a close relationship in the mechanisms for almost all of these oxygen catalyzed polymerizations and depolymerizations described in scientific literature. A generalized free radical mechanism has been developed to model these oxidative degradation reactions for polymers.

4.2. Oxidation mechanisms

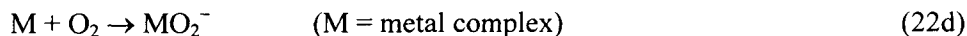
It has been a basic postulate of many years standing that the mechanism for the direct oxidation by air at moderate temperatures of almost all organic compounds involves, as an early oxidation product, the hydroperoxide group, R-O-O-H. The hydroperoxide group can be present initially in a polymer specimen (as a result of its preparation, storage, processing, *etc.*). At temperatures from ambient to over 100°C these hydroperoxide groups will be slowly generated in

the presence of oxygen at labile groups and linkages on the polymer chain. For example, tertiary carbon atoms are more susceptible to autooxidation than secondary, which are, in turn, more easily attacked than CH₃ groups. Unsaturated linkages and ether groups are easily attacked and aldehydes are more susceptible than ketones. Residual metals and other catalysts present in the polymeric material also may initiate hydroperoxide group formation.

Some typical chemical equations for polymer oxidation [56], involving free radical chain mechanisms, whose essentials were first proposed by Bolland [57] and Bateman [58] fifty years ago, are:



The initiation reactions for the case of hydrocarbons include:



Hydroperoxide builds up as the reaction proceeds and, after a while, thermal decomposition of hydroperoxide groups becomes the main source of free radical formation by branching reactions such as:





The hydroperoxides can also react to form labile carbonyls [59].

In all known oxidations, it has been found that k_2 is 10^4 to 10^6 times k_2' , so Eq. (26) with a rate constant k_3 is usually assumed to be the chain termination process.

The oxidation mechanism has been discussed in general and for specific polymeric materials in many papers and reviews [60-62]. In a recent series of papers, Gugumus has reinvestigated the low temperature thermooxidation of polyethylenes and polypropylenes in great detail and the kinetics and mechanisms developed by him are summarized next [59,63-68]. We review this work here as a model for the oxidative degradation of polyolefins and other polymeric systems.

Previous studies of the kinetics for the buildup of hydroperoxides in polyolefins had indicated a parabolic [69] or a quartic [70] rate dependence. This confusion had resulted in part because only a portion of the reaction was measured and the induction times were taken into account improperly. Gugumus investigated the thermal oxidation of low density polyethylene (LDPE), high density polyethylenes (HDPE) (Ziegler and Phillips types), linear low density polyethylene (LLDPE), and polypropylene (PP), in air at temperatures from 40 to 100°C, measuring free and associated hydroperoxides and carbonyl groups by IR. When the total curves and induction times are properly evaluated, the logarithm of the carbonyl group concentration was initially linearly proportional to time, but, as the oxidation progressed, a linear concentration-time dependence for carbonyl and free hydroperoxide groups was found. Eventually the hydroperoxide concentrations reached a steady state value as their rate of production was matched by their rate of decomposition. The reaction takes place initially at the surfaces and spreads into the interior of the polymers through their amorphous regions. It is thought that the diffusion of chain carrying radicals rather than diffusion of oxygen may be rate limiting at the lower temperatures [66]. As the oxidation proceeds, the main source of hydroperoxide decomposition (the chain branching reaction) is from the associated hydroperoxide groups.

The oxidation kinetics are well fitted by a heterogeneous model. The main differences among the polyethylenes in their rate of oxidation results from differences in polymer density, crystallinity, and manufacturing processes [68].

The diffusion limited reaction observed during low temperature oxidations of many polymers may well result from the slow diffusion of chain-propagating radicals into the polymer rather than the diffusion of molecular oxygen. The

alkyl radicals are presumed to diffuse much more rapidly than more bulky oxygen-containing ones.

The effect of the physical state of the substrate upon the kinetics of the oxidation reaction can be seen in Fig. 5 where results from the TGA for polystyrene in air heated at rates of 0.0001, 0.001, 0.01 and 0.1°C/sec are represented by a plot of rate of weight-loss with respect to temperature versus fraction conversion [71]. If the kinetics remained unchanged, then the curves would have a similar shape with maximum rate decreasing with increasing heating rate. However, the rate in the experiment at 0.01°C/sec shows an acceleration at 70% conversion and the rate at 0.1°C/sec shows a radical autocatalytic change at 15% conversion. These two changes in the kinetics both occur at 270°C. The viscosity of molten polystyrene decreases dramatically at about 250°C so this greater mobility of the interacting species drastically alters the reaction kinetics. Examples of this type of behavior are found throughout polymer degradation literature where a surge in rate takes place when the temperature surpasses the temperature of a glass transition, melting transition, or a physical property change.

Descriptions of the oxidative degradation of specific polymers, copolymers

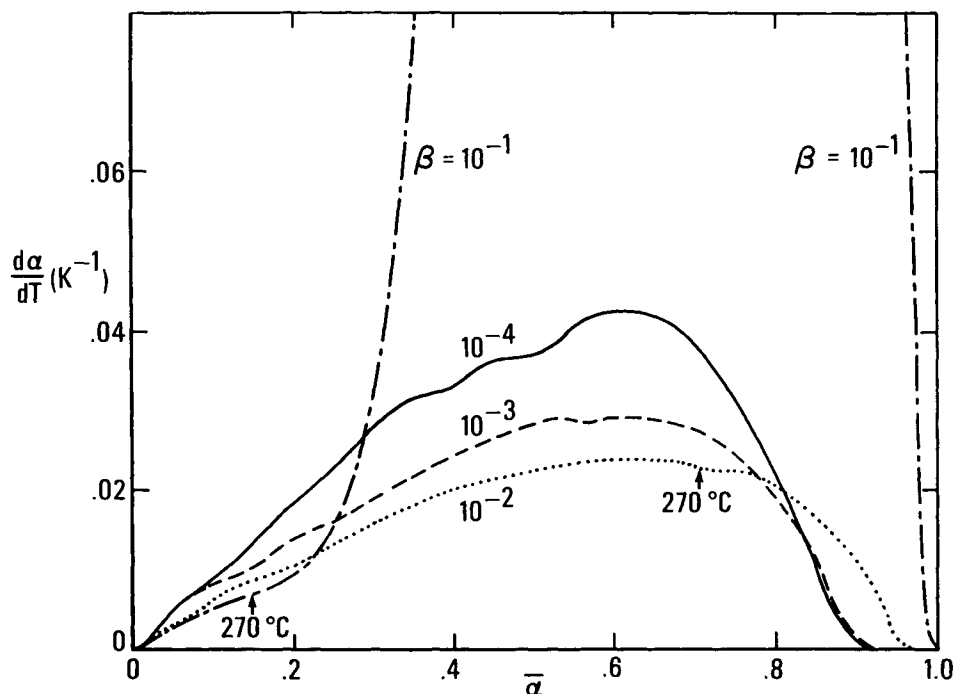


Fig. 5. Rate versus conversion for polystyrene in air at heating rates of 10^{-1} , 10^{-2} , 10^{-3} , and 10^{-4} °C/sec

and blends are included in subsequent sections where these polymeric materials are discussed.

5. GENERAL HYDROLYSIS MECHANISMS

5.1. Introduction

The hydrolysis of polymers may be investigated in water solution, in contact with liquid water or in contact with water vapor. The latter case, the degradation (usually hydrolysis) of polymers in the presence of water vapor, is reviewed in this chapter. Obviously, solid polymers do not react with atmospheric water vapor. The water must be adsorbed on the surface or be within the solid polymer. In fact, many polymers containing polar groups adsorb water avidly and will retain it, especially if it is "bound water", quite tenaciously, even at temperatures well above water's boiling point of 100°C at one atmosphere pressure and in a vacuum.

The usual methods of thermal analysis, TGA, DSC, TMA, TVA, *etc.*, are used to investigate hydrolytic degradation. However, more often, changes in physical and mechanical properties are measured. The increase in carboxyl and other functional groups formed by the saponification reaction are measured by IR spectroscopy or by wet chemical methods such as acid number determination.

All polymers that are formed by condensation reactions with the elimination of water are, of course, susceptible to the reverse reaction, degradation by hydrolysis. Such reactions most often result in random scission along the backbone chain. Some examples of polymers susceptible to hydrolysis are: polymethylmethacrylate (PMMA), polyacrylonitrile (PAN), polyoxymethylene (POM), polysulfones, poly-amides (Nylon), polycarbonates (bisphenyl A polycarbonate), poly-ethylene-terephthalate (PET), polyurethanes (PU), phenolformaldehyde resins, polydimethyl siloxanes, polynucleic acids (DNA, *etc.*) and polysaccharides (cellulose, amylose, *etc.*). Main chain hydrolysis usually results in scission while side group hydrolysis may only alter the chemical properties of the polymer chains; for example, poly(methyl methacrylate) will hydrolyze without chain scission.

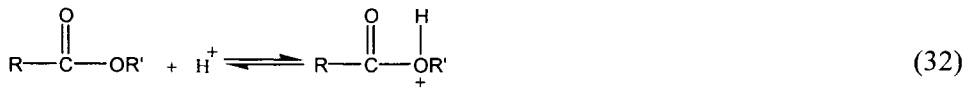
All of the above polymers also may degrade thermally or oxidatively, and, for many of them, these are the primary modes of their degradation. At very high temperatures, for example, in combustion or burning situations, the degradation will be purely thermal or oxidative and hydrolysis will not be involved. However, hydrolysis, or at least water-catalyzed degradation, is often involved in the slow degradation and deterioration of these polymers at use conditions, and the determination of the kinetics of hydrolysis is important in their lifetime prediction.

The hydrolysis mechanisms in solid polymers are heterogeneous and often diffusion limited but they follow the same chemical reactions as found for

acid-base catalysis in homogeneous solution [72]. Acidic carboxyl end groups formed during the hydrolysis reaction often catalyze further hydrolysis, and the reaction kinetics may be autocatalytic in nature. The hydrolytic degradation of polymers has been reviewed by Reich and Stivala [73].

5.2. Hydrolysis mechanisms

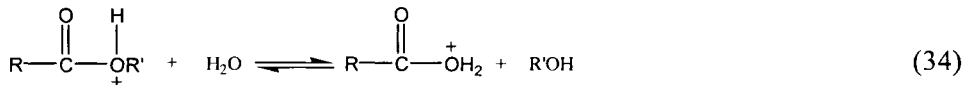
As was found to be the case for low temperature oxidative degradation, hydrolytic degradation takes place much more rapidly and often exclusively in the amorphous regions of semicrystalline polymers. Thus crystalline or highly cross-linked polymers are much more hydrolysis resistant than are their amorphous counterparts. Chapman [74] found that tactic poly-N,N-dimethylacrylamide hydrolyzes six or seven times more rapidly than the atactic polymer. The degree of crystallinity in cellulose has, for many years, been measured by removal of the amorphous regions by hydrolysis. A simple mechanism [75] has been suggested for the hydrolysis of polyesters:



The equilibrium is rapidly established after which one of the two following reactions may occur:



or



A study of the hydrolysis of a polyester soft segment polyurethane is given as an example in the following section on Lifetime Prediction Methods. The hydrolytic degradation reactions for individual polymers are included along with the discussions of their thermal and oxidative degradations in the sections on Examples of Degradation of various polymers.

6. LIFETIME PREDICTION OF POLYMERS BY THERMAL ANALYSIS

The application of the methods of thermal analysis to the prediction of long term properties of polymeric materials is particularly tempting as these techniques are

rapid and instruments with “Lifetime Prediction” programs are readily available. In a typical lifetime prediction routine, an activation energy is calculated from the polymer degradation kinetics by utilizing a form of the Arrhenius equation:

$$\ln k(t) = \ln A - E/RT \quad (35)$$

where k is the rate constant, t , the time, A , the preexponential factor, E , the energy of activation, R , the gas constant, and T , the absolute temperature. A failure criterion is posited such as, for example, a 5% weight-loss from a TGA experiment. Then the logarithms of the times to reach failure are calculated for temperatures of interest. Thus a plot of logarithm of time versus reciprocal temperature is used to predict times to failure at service temperatures that are outside the time range of experimental temperature measurement. Such predictions clearly depend on the reaction mechanism and the kinetics constants remaining unchanged over the range of extrapolation. However, many predictions from these artificial “aging experiments” are found to be inaccurate.

It is abundantly demonstrated in the Introduction and the body of this chapter that no extrapolation of kinetic parameters for degradation should be attempted over a temperature range within which a viscosity (softening point) change or a melting or glass transition takes place in the substrate. Moreover, such extrapolations are invalid if they pass through a ceiling temperature where the equilibrium shifts its direction. Satisfactory lifetime prediction methods can be developed but only after a thorough analysis of the causes of service failure [76]. The changes in the polymer which bring about its failure may be oxidative, hydrolytic or photochemical reactions, or, in other cases, physical and mechanical effects such as crazing, stress fracture, crystallization, *etc.* Guide lines for and an example of a properly developed lifetime prediction method were recently published by Flynn [76].

Thus thermal analysis methods alone are seldom sufficient to develop a reliable lifetime prediction method. A lifetime prediction method for magnetic recording tapes by Brown, Lowery and Smith [77] is a good example of how such a method may be properly developed. After an analysis of the hydrolytic stability of the PET tape base and its cross-linked polyester polyurethane (PEPU) coating, these authors concluded that hydrolysis of the PEPUs caused its detachment from the tape and failure. Therefore their final approach to estimate lifetimes was to write on the tapes, age them at temperatures below 100°C at high relative humidity, read the data on the tapes after aging and continue the aging reading attempts until they became unreadable. Extrapolation of these times of failure to ambient conditions gave useful tape lifetimes of at least 20 years [77]. A more complete description of the development of this test method is given in reference [76].

7. SOME SPECIFIC EXAMPLES OF DEGRADATION

From the discussion on ceiling temperature, it might be expected that high temperature would simply reverse the polymerization process. However, this does not generally happen, and monomer is seldom the major product of a polymer thermal degradation. In the few instances where this is the case, the mechanism can be interpreted without resorting to complex numerical analysis. A few examples of polymer degradations which follow these simpler cases are given in the following section.

7.1. Special cases for the degradation of vinyl type polymers

7.1.1. End initiation, complete zip: [poly(methylmethacrylate)]

If initiation occurs at the chain ends and the zip length of the propagation step is much larger than the length of the polymer chains, the rate of initiation is proportional to the number of molecules $1/DP_n$, but each end initiation converts the whole polymer molecule to monomer – an amount proportional to DP_n . Thus the rate of monomer production changes proportionally to $(1/DP_n)(DP_n)$ which makes it independent of polymer molecular weight.

Also, since each polymer molecule, regardless of its size, has the same chance to be initiated at its end, and once initiated it is destroyed completely, the average molecular weight does not change as the pyrolysis proceeds. Grassie and Melville's classic studies of a series of poly(methyl methacrylate) samples showed that this actually took place over a long interval of conversion [78]. At high conversion, these relations fail to describe the kinetics as refractory residue appears. Polymer samples of much higher molecular weight and less active end groups show a more complicated but still readily explainable behavior. As in the previous case the product is always overwhelmingly monomer [79,80]. It is curious that the only other polymethacrylate polymer which yields monomer is poly(phenylmethacrylate). In most of the others, the ester group splits off as an olefin leaving a polymethylacrylic acid residue. The degradations of many of these will be discussed subsequently.

7.1.2. Random initiation, complete zip: [poly(alpha-methylstyrene)]

If initiation occurs randomly and the zip length is much greater than the length of the molecule, the rate should be proportional to the number of monomer units in the sample, which is independent of the molecular weight of the polymer. The initiation rate will be proportional to the number of monomer units in the sample, which is independent of molecular weight, while the monomer produced per initiation will be equal to the number of units which the molecule contained before initiation and, therefore, proportional to molecular weight. Again the molecular weight will not change. On the other hand, if initiation is random but zip length is considerably shorter than the molecular

size, the rate will be independent of molecular weight, and the molecular weight will decrease as time goes on. For this case the steady state radical concentration is

$$[R\bullet] = (k_1[m]/k_4)^{0.5} \quad (36)$$

and the rate of monomer production, m , is given by

$$dm/dt = k_2R\bullet = k_2[R\bullet]V \quad (37)$$

where $[R\bullet]$ is the steady state concentration of radicals, V is the volume of the sample, $R\bullet$ the steady state number of radicals, $[m]$ the monomer production rate, and k_1 , k_2 and k_4 the rate constants for initiation, propagation and termination, respectively. Here, the rate expression does not contain molecular weight as a variable. It is qualitatively evident that scission, monomer loss to the extent given by the zip length, $(1/\varepsilon - 1)$, and termination by disproportionation will operate to create smaller polymer molecules and reduce the average molecular weight. The mathematical theory can be developed to cover the whole intermediate ranges of behavior between the above extremes. Poly(α -methylstyrene) has been investigated over a wide range of molecular weights and is found to be represented by these above cases rather well although it is still uncertain whether the high molecular weight ideal is ever attained [81].

7.1.3. Poly(tetrafluoroethylene)

When poly(tetrafluoroethylene) is pyrolyzed at low pressure, monomer is the only product of importance, and the rate of volatilization is independent of molecular weight, thus following the high-molecular weight model discussed in connection with poly(α -methylstyrene). The molecular weight of polytetrafluoroethylene is extraordinarily difficult to monitor experimentally but seems to decrease slowly [82]. At higher pressures of more than a few torr, the yield of monomer is replaced gradually by other products.

7.1.4. Polystyrene

Polystyrene has been studied for many years [2]. The monomer yield is moderately high. The rate of volatilization nevertheless begins low, goes through a maximum, and then drops off, as with random scission. This variation of rate and molecular weight as functions of initial molecular weight and conversion fit the model of mainly end initiation and bimolecular or unimolecular termination, and weak bonds may be involved. Wall and coworkers [83] have matched experimental results with theoretical calculations based on end initiation plus intermolecular transfer. Although the data of differing investigators are in fair

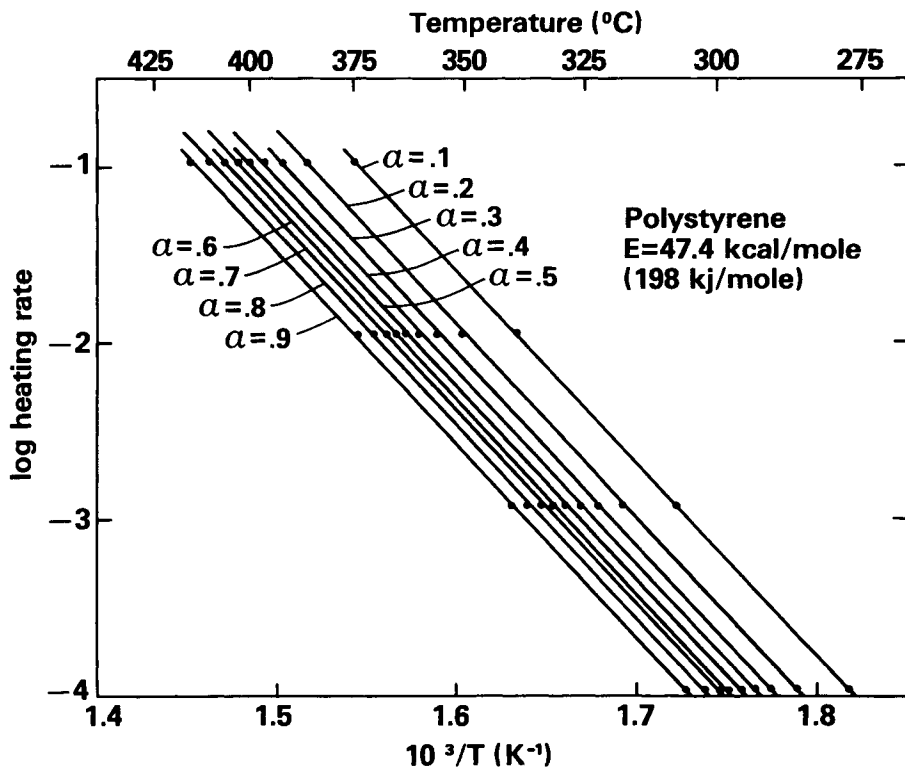


Fig. 6. Logarithm heating rate versus reciprocal absolute temperature for polystyrene in vacuum: Curves for $\alpha = 0.1, 0.2, 0.3, 0.4, 0.5, 0.6, 0.7, 0.8,$ and 0.9

agreement, the interpretation has continued to remain ambiguous [31]. McNeill [84] has reviewed the decomposition mechanism and finds that it involves random backbone scission, followed by depolymerization of the secondary radical end and intra- and inter-molecular transfer of the primary radical end. The energy of activation remains constant throughout the reaction over a temperature range from 280 to 420°C as demonstrated in the logarithm heating rate versus $1/T$ isoconversional TGA plots in Fig. 6 [85].

The value of its energy of activation for the thermal decomposition of polystyrene was established by the temperature jump method to be 45 kcal/mol in both vacuum and nitrogen by Dickens [86].

The thermo-oxidative degradation of polystyrene has begun to receive serious attention [87]. Gol'dburg *et al.* [88] have suggested that the mechanism included the accumulation of hydroperoxide in the first step of the reaction in the temperature region around 200°C. The rate depends upon sample thickness above this temperature. However hydroperoxides are not observed at

temperatures of 300°C and higher where they are no longer stable. TGA experiments performed at heating rates from 9°C/day to 6°C/min in oxygen, shown in Fig. 5, indicate an acceleration in weight loss rate above 270°C [89].

The viscosity of molten polystyrene decreases dramatically above about 250°C which permits much more rapid diffusion of reacting species. The main products of the thermoxidative degradation at 300°C are styrene, carbon dioxide, water, benzaldehyde, alpha-methylstyrene, phenol, phenylacetaldehyde and acetophenone [87]. Hydroperoxides can not accumulate at these temperatures so it is probable that alkyl radicals are involved in the oxidation [90-91].

7.1.5. Other special cases

A number of other special cases have been deduced theoretically and are listed or tabulated by various authors [9,92,93]. Some of these are displayed in Table 2.

7.2. Degradation of some other vinyl-type polymers

Many vinyl-type polymers follow diverse and often more complex patterns of degradation reactions. The degradation of some of these are described in this section.

7.2.1. Poly(vinyl chloride) (PVC)

PVC is a vinyl-type polymer whose initial degradation can be classified mainly as a side group reaction, the splitting off of HCl. This is followed by cyclization and chain scission at higher temperatures.

The thermal dehydrochlorination of Poly(vinylchloride) (PVC) has been extensively studied both in inert and oxidative atmospheres. This reaction has considerable industrial importance because processing temperatures may induce instability, requiring careful control of impurities and the addition of stabilizers. The degradation of PVC has been reviewed by Stivala [94,95], Hjertberg [96], Wypych [97], Ivan [98], Bacaloglu [99] and McNeill [100].

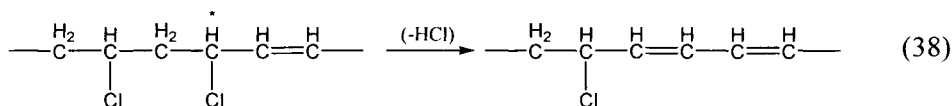
The thermal degradation of PVC begins at a relatively low temperature, just above its T_g (80 - 100°C) [101]. Although the rate of degradation has been clearly correlated with the concentration of allylic and tertiary Cl, there is no definite evidence on the nature of the initiation act at low temperatures. When heated above 200°C, PVC loses weight rapidly and autocatalytically, mostly by evolution of HCl, and the polymer becomes dark [102].

PVC shows two degradation stages. During the first one (200 - 350°C), HCl and benzene are evolved but only small amounts of alkyl aromatic hydrocarbons (toluene, xylene, etc.) are formed. At 360 - 500°C, aromatization of the rings takes place for which reaction scission is a prerequisite, and benzene becomes a major product [103].

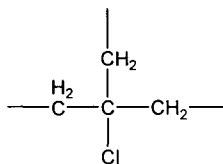
The mechanism of benzene formation throughout the temperature range has been considered to begin with scission at the tertiary Cl and to continue with the formation of benzene through the cyclization of chain ends, of which the unsaturation of the penultimate bond is the structure most labile to dehydrochlorination.

The initiation of the dehydrochlorination has correlated with the labile sites or "defects" of the chemical structure such as: the allylic chlorine atom of the internal saturation, the tertiary chlorine atom of the butyl branches and the head-to-head units formed in the course of synthesis. The head-to-head structures have an increased tendency to split off Cl but, as shown by studies on model compounds prepared by chlorinating *cis*-1,4-polybutadiene, they do not propagate the dehydrochlorination reaction more readily than regular PVC [104].

The evolution of HCl often follows an S-shaped curve with an apparent induction period followed by more rapid HCl loss. As the weight-loss proceeds, the visible and UV spectra shift in a way consistent with the appearance of short polyene sequences at first. This is followed by longer and longer conjugated polyene units. This suggests that an initial unsaturation makes the adjacent part of the chain unstable toward HCl elimination.



and so forth. Tests of model compounds suggest that not only are units adjacent to an unsaturation less stable, but many structures such as tertiary chlorine



which can be introduced by side reactions during polymerization also are. Polymers with deliberately introduced irregularities of this sort were found to be much less stable [105].

At the same time, it is possible that physical "defects" contribute to the dehydrochlorination [100]. A certain conformation of syndiotactic segments of chains in which the Cl atoms are trans relative to a double bond makes the dehydrochlorination very easy, while the presence of a Cl atom gauche to the unsaturation favors the termination of polyene growth [106]. Syndiotactic chains of up to 13 vinylchloride units are present in commercial suspension PVC samples, as part of very small imperfect crystallites dispersed in the polymer matrix. Overall, the conformation responsible has a concentration of the same

order of magnitude as the defects of the chemical structure and it is likewise dispersed.

Benzene formation begins at low temperatures (a little above T_g) [107] as soon as polyenes of suitable length are formed through dehydrochlorination. Polyenes are very active in crosslinking, and molecular enlargement has been observed at a very low degree of dehydrochlorination, (0.5% at 180°C) [108]. Several mechanisms for benzene formation in the early stages of thermal degradation have been advanced: the cyclization of a triene radical situated at a chain end [109] and formed through dehydrochlorination followed by the scission of the macromolecular chain, the thermal condensation of a triene [110] within the chain, or the reaction of a triene in the triplet state easily achievable by thermal excitation [111]. The last hypothesis is still very appealing though it did not gain experimental support with the passing of years.

At intermediate temperatures, chain ends can make an important contribution to dehydrochlorination if found to have labile structure. It is largely accepted in the literature that chain ends contribute to the formation of mononuclear hydrocarbons.

At high temperatures, the initiation of dehydrochlorination takes place in the whole mass of the polymer by random scission of the secondary chlorine atoms, and it becomes an important volatile product presumably formed as a result of cyclization of the intermediate polyene structure.

It is considered that at higher temperatures benzene and alkyl benzenes are formed by an intramolecular process (cyclization) which starts at the chain ends of the macromolecules, while the inner part of the macromolecules is bound into a crosslinked network. The network is formed through (1) Diels-Alder condensation of double bonds belonging to different chains [112] generating cyclohexane rings and within the chain generating cyclohexadiene rings, which then become aromatic, and (2) crosslinking through free radical attack on unsaturation. The extent to which either of these processes takes place is not known, but both crosslinked and conjugated structures have been identified [113]. The Diels-Alder condensation, however, is considered a major process, for the use of a dienophile strongly reduces PVC crosslinking [114]. The present picture of PVC as it degrades at temperatures above 250°C is that of a crosslinked internal "core" to which "loose" branches are attached. The branches or chain ends produce benzene and other aromatic hydrocarbons by the cyclization of the free ends.

When PVC is degraded in vacuum up to 500°C [100], HCl is the major fraction (53% of the polymer), followed by tar (24%), char (9.5%), liquid fraction (7%) and gas (6.6%). 10% of the Cl atoms remain in the polymer after HCl evolution ceases. Benzene accounts for 80% of the liquid and 5.6% of the polymer.

The thermooxidative dehydrochlorination of PVC has been extensively studied. It has been found that the process is autocatalytic [115,116]. It appears to be much more complex than the thermal reaction. The thermal dehydrochlorination is accelerated, main chain scission can occur, and coloration is less. The polyenes are susceptible to oxidation, and peroxy radicals initiate further HCl loss. Aromatics are no longer a major product.

Poly(vinylidene chloride) (and fluoride) do not form alkyl aromatics, only unsubstituted aromatics are evolved, and the thermal degradation occurs in a single stage [117].

7.2.2. Poly(methylacrylic acid) (PMAA)

The thermal degradation of PMAA has been examined by Grant and Grassie [118] and Jamieson and McNeill [119]. PMAA begins to dehydrate at 200°C with the formation of anhydride groups. These are intramolecular at the beginning, but become intermolecular at 250°C. The intramolecular structures are six-membered anhydride rings of the glutaric anhydride type [120].

The anhydride formation is complete at 250°C. Over the temperature interval 300 - 400°C, the anhydride decomposes with massive scission and weight-loss and the formation of a little unsaturation in the remaining polymer. Aromatic rings are not formed until 400 - 420°C when the decomposition of the anhydride accelerates.

7.2.3. Polyvinyl acetate (PVA)

In PVA, unsaturation begins to appear in the chain at 160°C [121]. Grassie [122] degraded PVA at temperatures above 190°C in a vacuum and suggested that deacetylation occurred intramolecularly with the intermediate formation of a six-member cyclic product. PVA exhibits a two-stage decomposition when heated in vacuum at 10°C/min [123]. The first stage, between 260 and 380°C produces a large amount of acetic acid and is endothermic. The unzipping of acetic acid is thought to involve a free radical process and $\text{CH}_3\text{COO}\cdot$ chain carriers. The second stage, between 380 and 500°C, is related to the degradation of the unsaturated backbone formed in the first stage. Aromatics are formed and a significant amount of char remains. Likewise, in the combustion of polyvinylacetate, acetic acid is abstracted from a saturated polyhydrocarbon chain, and a considerable amount of benzene and other aromatic hydrocarbons are formed together with a porous carbon residue [124].

7.2.4. Polyvinyl(isopropenylacetate) (PVIPA)

The degradation of PVIPA shows many features in common with that of PVA [120]. Both show a two stage decomposition under programmed heating,

the first involving elimination of acetic acid in a zipper deacetylation of short zip length.

7.2.5. Polyvinyl alcohol (PVAL)

Polyvinyl alcohol melts at 230°C, just below the onset of its degradation (as is often the case). However, it no longer melts after being heated in air at 200°C and its degree of carbonization in inert atmosphere is 32% [125]. On heating in air at 200°C, a PVAL fiber undergoes dehydration and oxidation, ultimately leading to formation of conjugate double bonds and carbonyl groups serving as intramolecular bridges. Cleavage of the main chain occurs which results in formation of acetaldehyde, crotonic aldehyde and other compounds.

7.3. Degradation of some heterochain polymers

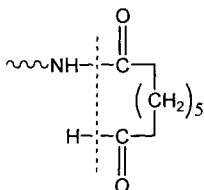
In addition to the carbon chain vinyl polymers, many polymers whose main chain contains the heteroatoms O, N, or S also decompose to yield volatile products. The free radical chain reaction mechanism appears to apply to these decompositions but others are affected by water and acidic and basic catalysts, so therefore they may proceed by ionic pathways. The thermal, oxidative and hydrolytic degradations of a selection of these polymers are discussed next.

7.3.1. Polyacetal and related polyethers

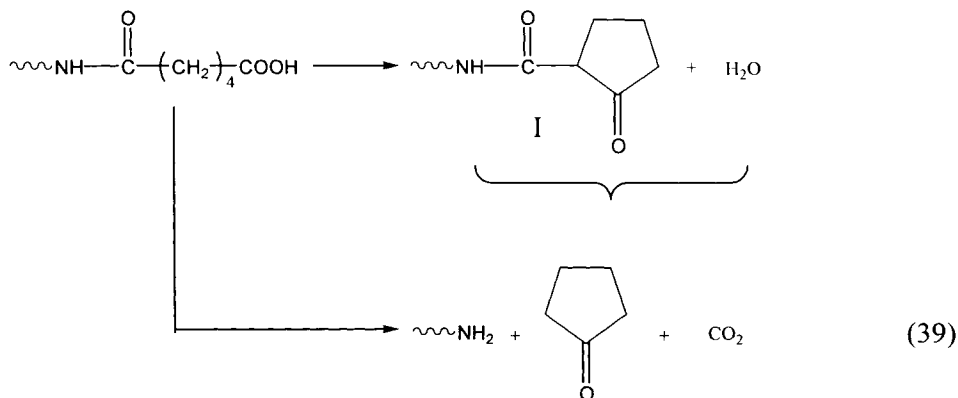
The industrially important polyacetal which is polymerized from formaldehyde, $(-\text{CH}_2\text{-O-})_x$ decomposes to yield its monomer. If the end groups are $-\text{CH}_2\text{OH}$ or CHO , as in the long-known polyformaldehyde, the material decomposes thermally at above 90°C, and decomposes hydrolytically as well. The discovery of endcapping with acetyl groups [126] made possible the production of a useful material that decomposes at much higher temperatures, 160°C in air and at 250°C in inert atmosphere. Also it is unaffected by mild hydrolytic agents. The heat of polymerization of formaldehyde is low, 7.4 kcal/mol, and those of its higher homologs are still lower [13]. These polymers have quite low ceiling temperatures (see 2.3). Polyethylene oxide $(-\text{CH}_2\text{CH}_2\text{O-})_x$, polypropylene oxide $(-\text{CH}_2\text{CH}(\text{CH}_3)\text{-O-})_x$ and polytetramethylethylene oxide $(-\text{CH}_2\text{CH}_2\text{CH}_2\text{CH}_2\text{-O-})_x$ decompose by random scission to give oligomers of high average molecular weight plus a little aldehyde monomer. Their degradation temperatures are lower than those of the carbon-carbon polymers, for example, 350°C for polyethylene oxide versus 390°C for polyethylene under comparable conditions. As in polyolefins, branched chains are destabilizing [127,128]. However, polyethylene oxide yields mainly the cyclic dimer, dioxane, in the presence of cationic catalysts and polytetramethylene oxide yields the monomer, tetrahydrofuran, under these conditions [129,130].

7.3.2. Nylon 6

Nylon 6 regenerates epsilon-caprolactam upon heating at 250°C [131,132]. An appreciable retardation of the degradation is achieved by acetylation of the amino end groups. This suggests that a back-biting attack by the amino end group is somewhat more important than the other possible reactions, that is,

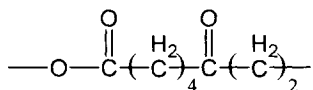


This reaction has a favorable cyclic intermediate and product. Nylons polymerized from dibasic acids and amines behave less simply, especially when, as is inevitably the case, a little moisture is present. A great variety of products including cyclopentanone, hydrocarbons and carbon dioxide have been recorded [133,134]. A possible intermediate for cyclopentanone formation has been suggested [135].



7.3.3. Poly(ethylene adipate)

The thermal degradation of poly(ethylene adipate),



was investigated by Hashimoto [136] who reported cyclic dimer as the main product, accompanied by cyclic monomer and cyclic 3-oxopentamethylene ester. McNeill [137] found the main fraction of products to consist of cyclic oligomers. Therefore its degradation is similar to that of other aliphatic polyester polymers

such as poly(tetramethylene sebacate) [138], polyacetide [139,140], and polyglycolide [141]. At the start of the decomposition (below 300°C), carbon dioxide, acetaldehyde and 2-ethylacrolein are evolved.

7.3.4. Polyurethanes

Polyurethanes heated above 200°C form a volatile yellow smoke containing practically all the nitrogen content of the polymer and leaving much of the polyol component as a residue. The loss is slow at 200°C but is virtually complete in 15 minutes at 300°C [142]. At rapid heating, ether and ester soft segment polyurethanes behave much alike in this respect.

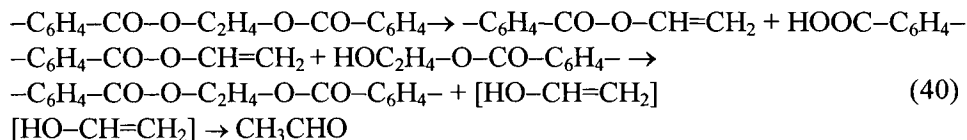
Polyurethanes have low ceiling temperatures and they depolycondense into comonomers [143-145]. This reaction is reversible below 200°C [146]. The diisocyanate linkage disappears about 210°C in a MDI (methylene bis-(4-phenyl diisocyanate), 1,4-butanediol polyurethane without soft segments [147]. Explosive loss of mass just above the hard segment melting temperature suggests that the diffusion of the dissociated diisocyanate moiety from the polymer is hindered at lower temperatures [9]. At higher temperatures, carbodiimide and urea structures form. TDI polymers begin to decompose at a lower temperature and with a lower activation energy than do similar MDI polyurethanes, probably due to the higher mobility of the TDI fragment [148]. Both oxidation and methoxymethylation of the surface of MDI and TDI polyether and polyester soft segment 1-4 butanediols result in increased thermal stability [9]. Thus suppression of the depolycondensation reaction by chemical blockage of the surface may result in a material with an increased service life as thermal stability of a polyurethane may depend upon the low diffusivity of its diisocyanate comonomer.

At very high pyrolysis temperatures, pyrograms resembling those of the parent polyether or polyester components are formed while temperatures above 800°C yield simpler compounds, for example, acetonitrile, benzonitrile, pyridine, benzene and hydrogen cyanide. Pyrolysis at 1000°C yields a total nitrogen recovery of 70 - 80%, much of it as hydrogen cyanide [142].

Polyether soft segment polyurethanes are susceptible to oxidative degradation while polyester ones are easily hydrolyzed. An ether based PU showed no loss of tensile strength after 18 months at 25°C and 100% RH. A similar ester based one, on the other hand, lost 90% of its tensile strength under the same conditions [149]. A study on the hydrolysis of a polyester soft segment PU was used as an illustration in the section on Lifetime Prediction.

7.3.5. Polyethylene Terephthalate (PET)

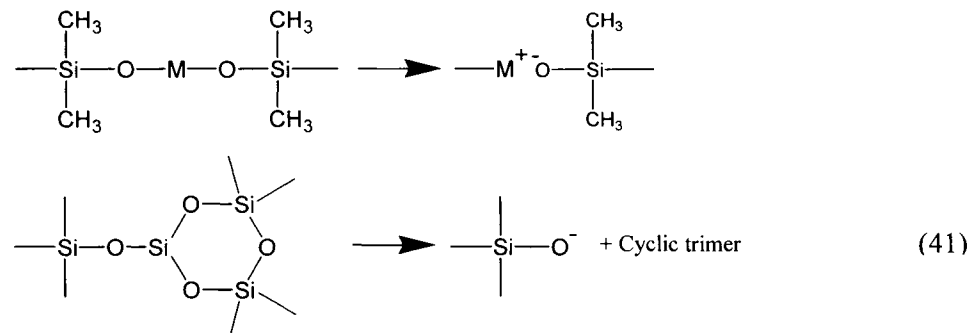
PET decomposes at 0.5%/minute at 340°C. The mechanism appears to be unimolecular β -elimination at random sites [150-152].



Thus, as long as glycol hydroxyl end groups exist, the chain is broken only temporarily and then reformed, producing acetaldehyde and carboxyl end groups. The purely aliphatic polyesters decompose at considerably lower temperatures by a more complicated mechanism.

7.3.6. Polysiloxanes

Polysiloxanes are sensitive to the presence of basic and acidic contaminants, and reproducible behavior is hard to obtain [153]. A pure poly(dimethylsiloxane) oil of estimated molecular weight 10^5 showed less than 10% weight loss in eight hours at 363°C in vacuum. Most of the weight loss curves showed a maximum, which suggests random scission; nevertheless, the above author favored instead an ionic mechanism activated in all cases by minute traces of metallic ions (for example, 0.05% or less of barium). Tetramer and trimer are the main products of degradation in vacuum. Oxygen has a profound effect on the reactions [154].



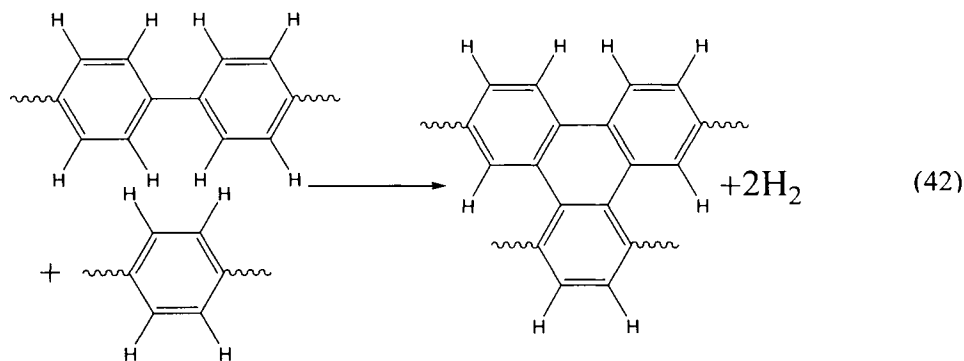
7.3.7. Cellulose

The thermal decomposition of cellulose is important in the combustion of wood, paper and textiles. It has been known for a long time that the thermal decomposition of pure cellulose in vacuum produces levoglucosan, (1,6-anhydro- β -D-glucopyranose), in proportions sometimes as high as 44% [155,156]. Mechanisms have been written involving radical scission of the 1-4 glucosidic linkage and displacement of the oxygen atom attached to the C-1 carbon atom of a glucosyl unit [157,158].

The total mechanism of decomposition must be extremely complex. A review is given in Conley's book [159]. Many other products are observed in smaller amounts. At higher pressure, and especially when acid or base catalysts such as zinc chloride, antimony trichloride, or borax are added, charring reaction is promoted at the expense of levoglucosan formation [160,161], and water and carbon dioxide become important products. One stage of the charring reaction is exothermic. This change of mechanism underlies the use of fire retardant additives to cotton, paper and wood since the products from charring are much less combustible. Other wood components (lignin and xylan) have been investigated [162,163].

7.4. Pyrolytic reactions and aromatic and temperature-resistant thermo-setting polymers

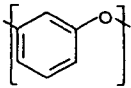
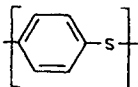
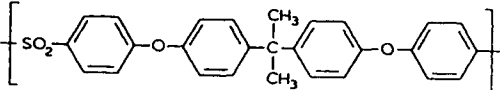
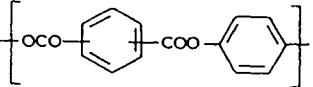
Aromatic rings are relatively more stable to heat than are aliphatic chains. When they do react, they show a tendency toward condensation reactions with the elimination of hydrogen. The end result of a series of condensations of this sort is graphitic carbon. It may be noticed in this case that weight loss is a misleading guide to extent of reaction. In the ideal case shown in Eq. (42), polyphenylene could condense completely to graphite and hydrogen with a weight loss of only 5%. Although Table 1 indicates that the aromatic C-H bond, 104 kcal/mol, is a little stronger than the C-C bond between rings, 100.5 kcal/mol, the difference is not great, and the product H₂ can easily escape from the system.



7.4.1. Poly(phenylenes)

Polyphenylenes, Y(-C₆H₄)_xY, are quite resistant to decomposition but cannot be processed into useful objects. The loss of weight up to 400°C levels off after an initial mild change and is accompanied by little change in elemental analysis. Above 400°C, the proportion of carbon atoms in the residue increases. Unsubstituted poly(phenylenes) are somewhat more stable than substituted ones

Table 3. Thermal Degradation of Aromatic Polymers

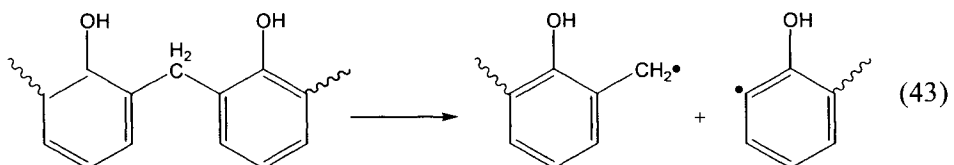
Polymer and formula	Wt.-Loss by 450°C	Principal products
m-polyphenylene oxide 	55.5%	H ₂ , H ₂ O, CO
p-polyphenylene sulfide 	56.0%	H ₂ , H ₂ S
Ether—sulfone 	61.0%	H ₂ , SO ₂ , CO, CH ₄
Polycarbonate (p,m) 	52.3%	H ₂ , CO, CO ₂

Source: Ref. 165

[164]. Table 3 [165] shows the behavior of a few polymers having phenylene rings linked by other groups. Many of these products have tractable and useful physical properties which they may retain to higher temperatures than do aliphatic chain polymers.

7.4.2. Phenolformaldehyde resin

Phenol-formaldehyde thermosetting resin was one of the early commercially produced polymers. Phenol-formaldehyde polymers are heat-resistant and do not begin to decompose at an appreciable rate until near 300°C. In the absence of oxygen the first break is likely to be α to the CH₂ group



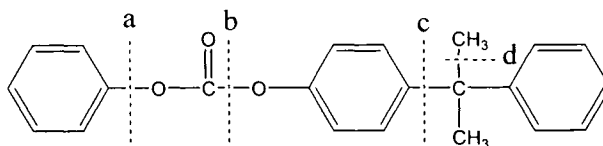
The oxidative degradation in the 100°C to 200°C range has been investigated by Conley [166,167] and at temperatures from 350°C to 400°C by Berlin [168]. In the presence of oxygen, the CH₂ group is first oxidized to carbonyl. The rate of carbonyl group formation increases at 180°C, at which temperature the hydroperoxy groups are no longer stable. The volatile products include cresols. In the higher temperature oxidation, during which thermal chain scission occurs, the rate of weight-loss is initially inhibited by oxidized structural groups in the surface layers. This is followed by more rapid oxidation. An appreciable char is left.

7.4.3. Epoxy resins

The degradation of some epoxy resins was studied, and these materials were found to be less stable than polycarbonate or polyphenylene sulfide [169]. At a programmed heating rate of 10 degrees/minute, the maximum rates of weight loss came near 380°C to 400°C compared with 500°C to 520°C for commercial polycarbonate and 550°C for phenylene polysulfide. Phenols are important volatile products.

7.4.4. Polycarbonates

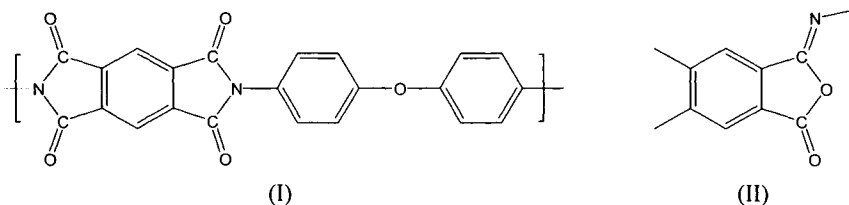
Tsuge [170] and coworkers pyrolyzed aromatic polycarbonates and detected products such as carbon dioxide, phenols, diphenylcarbonate, and C₁-C₃ hydrocarbons. These products can be explained by assuming chain scission as shown below. Solvent polymerized bisphenol A polycarbonate, which has tert-butyl end groups, also contains *p*-tert butyl and other *p*-substituted phenols.



In a more recent investigation of the thermal degradation of polycarbonate in the absence of air and moisture, McNeill and Rincon [171] concluded that although ester interchange reactions may be involved, many features and products are best explained by homolytic process. The mechanism of the degradation has been further discussed by Montaudo [172] and Rincon [173].

7.4.5. Poly(pyromellitimide) *H film*

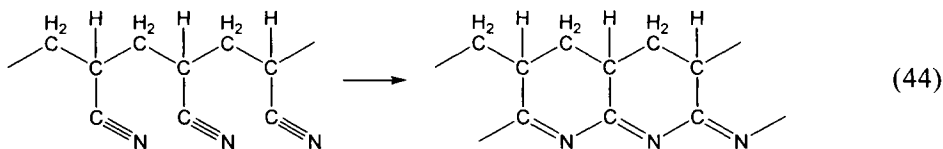
Many heterocyclic polymers have been synthesized for high temperature use. The well-known commercial poly(pyromellitimide), H-film,



has a lifetime of six days in air and one year in helium at 380°C during which the ultimate elongation at break deteriorates from 70% to 1%. The activation energy for tensile and elongation loss is 39 kcal/mol in air and 55 kcal/mol in vacuum. Weight loss is negligible in air up to 420°C and in vacuum to 500°C; corresponding activation energies are 33 and 74 kcal/mol [174-177]. In vacuum, a 46% char is left. Although the primary break is probably at the amide group, the volatiles are mainly CO and CO₂. These tell little as to the mechanism of the reaction or structure of the polymer. On further heating, the char tends to hold nitrogen more tenaciously than oxygen. A number of other similar polymers, notably certain poly(benzimidazoles), show roughly similar thermal behavior [178]. Recent literature on the degradation and stability of polyimides has been reviewed by Cella [179].

7.4.6. Polyacrylonitrile (PAN)

Polyacrylonitrile is a vinyl-type polymer which undergoes side group cyclization to form a condensed ring, thermally stable polymer as in Eq. (44) [180]. An exotherm accompanies the cyclization reaction.



The details of the cyclization mechanism are still not clear [181,182]. Since the inhibitor (DPPH) reduces the cyclization exotherm, it appears that the reaction proceeds by a free radical mechanism. However some acidic and basic additives, for example, KCN, can make cyclization proceed, although slowly, at lower temperatures, suggesting that these additives can induce an ionic mechanism of cyclization.

The first stage in the industrial production of graphite fibers from PAN involves "oxidative stabilization" by heating them in air at 200 - 300°C. The main steps of this reaction are proposed to be cyclization of the CN groups, initiated by OH radicals, and the oxidation of the resulting hydronaphthridine ladder through a stepwise formation of hydroperoxides and acridones [183].

At higher temperatures, above 700°C, hydrogen is evolved and the rings become aromatic. Above 900°C, the rings break down evolving nitrogen and leaving pure carbon. If PAN fibers are pyrolyzed initially at 1000°C, and subsequently heat-treated at about 2700°C, graphite fibers of a rather orderly lattice structure are obtained.

In contrast polymethacrylonitrile decomposes mainly by depolymerization (although nitrile cyclization to give a ladder polymer structure, may occur under certain conditions [184]).

8. COPOLYMERS, BLENDS, MIXTURES

8.1. Introduction

The thermal degradation reactions of large numbers of copolymers, polymer blends, and polymer mixtures have been investigated over the years by the usual thermal analytical methods to elucidate their degradation mechanisms. A great portion of the early work on their thermal degradation was carried out by Norman Grassie [185]. His work has been continued by Ian McNeill and his students and associates over the past twenty five years, and with even much greater intensity, over the past five years. This continued interest has been spurred, in part, by practical considerations such as improving the stability of commercially important polymers, for example, PVC, by incorporating in them other polymeric materials which will suppress their deterioration. These polymer mixtures result in materials with different and often improved physical properties when compared to the individual homopolymers. Also the increased recycling of polymer wastes has drawn attention toward the properties of polymer mixtures. Many copolymers have been studied also by pyrolysis gas chromatography/mass spectrometry to obtain clues as to their structure [186].

The results of many of the investigations of copolymer degradation, especially those of alternating polymers and of blends, are summarized below. As was the case for homopolymers in the earlier days of the investigation of their degradation reactions, most of the work thus far has been directed toward thermal degradation in inert atmospheres and much less toward oxidative or radiative degradation. Also there is less published research devoted to the effects of retardants, *etc.*, on these systems. (Of course, investigation of the retardation or enhancement of the degradation of one component mono/polymer by the degradation products of its co-mono/ polymer has been one of the chief purposes of many of these studies.) The degradation reactions reviewed and singled out for more discussion here are mainly for those systems where interaction between the components affects the kinetics and product composition. Some of the other copolymer, mixture and blend systems whose thermal degradation reactions have been studied are only briefly mentioned and, undeniably, other studies have been completely omitted.

Copolymers may be random, alternating or block. Block copolymers, -AAAAABBBBB-, *etc.*, usually degrade as do a mixture of their homopolymer units. Alternating copolymers, -ABABABAB-, are actually homopolymers, made up of the unit, AB. However their scission may produce new monomer-sized units, as is demonstrated subsequently. Random polymers, -ABBABAAABBBBAAB-, *etc.*, lie intermediate between block and alternating copolymers, but their degradation behavior is usually more like the latter. Examples of thermal degradation studies for these three cases are presented below. (Polyurethanes, which should be classified as copolymers, are discussed under homopolymers.)

In defining the degradation reactions of (compatible) blends and (incompatible) mixtures of polymers, this distinction is muddled since their phase diagrams may change with temperature (and pressure) in the same way as those for low molecular weight systems do. That is, a binary system of polymers may be a composite mixture at low temperatures and become a homogeneous blend at higher (degradation) temperatures, and the phase diagrams of tertiary and larger systems may contain regions of miscibility of any two or even all of the component polymers.

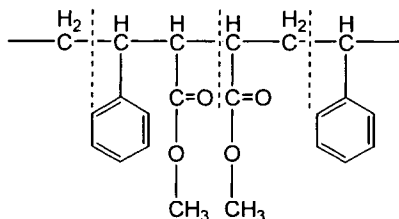
8.2. Simple degradation theory and early investigations

The simplest assumption for the degradation of a copolymer is that the products are additive - that the yield of monomer A is equal to the yield of monomer A in pure A polymer multiplied by the fraction of A existing in the A-B copolymer. That is, each component polymer will degrade as if the others were present only as inert dilutants. The yield of A relative to monomer content of A in the copolymer is called the normalized yield. This additive behavior occurs for many block copolymers and some polymer blends although many exceptions are recorded in the case of blends, and this behavior is seldom the case for alternating or random copolymers. Thus, although a more thermally unstable component will not necessarily affect the degradation of another component in copolymers, blends and mixtures, in many cases, one of the monomeric or polymeric components will exercise a "catalytic" effect on the degradation of its copolymers. This effect can be inhibitive, where, for example, a random or alternating copolymer unit will interrupt the process by which the other copolymer's radicals "zip" down to monomer size. This appears to be the case for the methyl methacrylate-acrylonitrile copolymer described below. On the other hand, radicals formed by a more unstable component polymer may trigger the degradation of another component polymer at a temperature lower than its normal degradation temperature or promote its crosslinking, thus delaying its weight loss until higher temperatures.

A classic example of the former case occurs with blends of polystyrene and poly- α -methylstyrene. In 1967 Richards and Salter [187] found that the latter

Many of the copolymers and polymer mixtures included in the descriptions below were studied by Ian McNeill and associates using thermal volatilization analysis, TGA and IR techniques. McNeill found in 1971 [197], for example, that poly- α -methylstyrene retards the dehydrochlorination of polyvinylchloride. Pyrolytic behavior can be expected to be more complicated for random and alternating copolymers. In a series of styrene copolymers examined by Pyrolysis Gas Chromatography (PGC) by Jones in 1969 [198], only the methyl methacrylate copolymer yielded styrene proportional to its content in the copolymer. Most of the other copolymers gave less than half the expected amount of styrene and one gave less than 10%.

In many of these cases new "monomers" may result from degradation, for example, for the copolymer of styrene and dimethyl fumarate, cutting along the dotted lines can produce two new monomers.



Schemes have been proposed to take account of boundary effects of this sort, using the distribution of A-A and A-B linkages which is readily calculated from composition and copolymerization parameters [14,199]. However, actual experiments usually result in a much more complex mixture of products which do not follow these ideal relationships. More complex theories have been developed taking into account bond dissociation energies and the stability of the resultant chain radical [200], and boundary effects which change as a function of monomer distribution [201]. These theories have been reviewed by Ahlstrom [202] and have been found to be applicable in some cases.

Some polymers such as poly(methylmethacrylate) (PMMA) depolymerize with a long zip length. Methyl methacrylate units in PMMA may be interrupted by other units so that they can zip for only short sequences. When acrylonitrile is a comonomer with methyl methacrylate, an induction period occurs at 220°C during which very little monomer is produced. Meanwhile the molecular weight drops rapidly (it hardly does at all in pure PMMA) to a level about equal to the average MMA sequence length in the copolymer [78,185].

In styrene-acrylonitrile copolymers, the "normalized yield" of acrylonitrile monomer increases as the styrene content increases. Presumably the shorter sequence of acrylonitrile units is less prone to undergo the competing charring reaction which occurs in the acrylonitrile homopolymer [203].

Poly(tetrafluoroethylene) is known to yield monomer almost exclusively in a vacuum and cyclic dimer at higher pressures. However, its copolymers with a series of hydrogen-bearing monomers, although volatilizing almost completely, yielded instead a variety of molecules up to approximately the C₁₆ range, even from polymers containing 90% tetrafluoroethylene. The failure to yield monomer was ascribed to an abstraction reaction by radicals, -CF₂CF₂• [204],



The sequence distribution in more tractable copolymers can be determined from correlations between hybrid and trimer content if these species are identifiable [205]. A more indirect knowledge of sequences has been obtained in some vinyl chloride copolymers. Polyvinylchloride (PVC) produces benzene by cyclization of an initially formed polyene, which was discussed under side group reactions. The corresponding product with polyvinylidene chloride is 1,3,5-trichlorobenzene while the copolymers of the two produce chlorobenzene and *m*-dichlorobenzene as well [206].

8.3. More recent investigations

Some of more recent investigations on the thermal decomposition of alternating copolymers and blends are catalogued and briefly described below.

8.3.1. Thermal degradation of some alternating copolymers

Interest has been evinced in the thermal degradation of alternating copolymers in the past few years. Recent studies using the TVA technique on TGA experiments heated at 10°C/min have been reviewed recently by McNeill [207]. In vinyl acetate-maleic anhydride alternating copolymer, the vinyl acetate units are thermally less stable than maleic anhydride units so deacetylation occurs at a lower temperature than backbone scission. However, rearrangement occurs, leading to backbone conjugation. Above 260°C, the modified chain breaks down and OH groups formed may participate in intermolecular dehydration. The hydrophilic nature of the polymer decreases as the ester units are converted to hydrocarbon units. This controlled low temperature breakdown of this alternating copolymer into a new macromolecular structure whose degree of breakdown may be tailored to obtain intermediate water sorption properties is the first example of controlled degradation of an alternating copolymer being applied to develop a polymeric material with useful end properties (such as for controlled-drug release) [208].

Isopropenyl acetate-maleic anhydride alternating copolymer degrades quite differently than the previous vinyl acetate one. When heated at 10°C/min in vacuum, at temperatures below 200°C, CO₂ is eliminated to form backbone

ketonic structures. At higher temperatures acetic acid and CO are eliminated to form cyclic lactones in the chain. The modified polymer chain thermally degrades in the 350 - 500°C range [209].

Allyl acetate-maleic anhydride alternating copolymer is isomeric with the isopropenyl one above, however its degradation appears to be more complex. Nevertheless, the dominant low temperature process generates CO₂ and forms ketone structures in the backbone. At a higher temperature acetic acid and CO are evolved and cyclic lactones are formed in the chain. Chain scission in the modified polymer occurs in the 350 - 500°C range [209].

In *trans*-stilbene-maleic anhydride alternating copolymer, unsaturated hydrocarbon copolymers with maleic anhydride are quite stable with an onset of degradation above 300°C. The major volatile product at 400°C is CO₂ plus some CO. Stilbene, plus small amounts of toluene, styrene, maleic anhydride and many other higher molecular weight products are formed. The decomposition is complex, involving a series of concurrent reactions [210].

The initial decomposition of the thermally stable acenaphthylene-maleic anhydride alternating copolymer appears to be anhydride breakdown to form conjugated double bonds in the backbone. Some backbone scission occurs from 300°C on, and a second stage of degradation occurs above 500°C [209].

Vinyl acetate-crotonic acid alternating copolymer is less stable than PVA and degrades in two stages. The first stage of degradation is cyclization of adjacent acetate and acid side groups with the elimination of acetic acid to form γ -lactones which decarboxylate with the elimination of CO₂. In the second stage there is lactone decomposition leading to extensive chain scission and only 3% residue at 500°C [211]. On the other hand, vinyl acetate-diethyl maleate alternating copolymer degrades between 250 and 500°C in two overlapping stages. Acetic acid is the predominant product at low temperatures (250°C). A large amount of ethyl acetate among the products suggests the occurrence of direct interaction between acetic acid and maleate groups, while the evolution of ethylene and CO₂ suggest that decomposition of the ester group is taking place [209].

For the isopropenyl acetate-diethyl maleate alternating copolymer, the change from vinyl to isopropenyl acetate as comonomer has a similar effect on this system as was the case described previously in isopropenyl acetate-maleic anhydride. The tendency for isopropenyl acetate copolymers to undergo chain scission results in more higher molecular weight products. Acetic acid is the main volatile product plus some ethyl acetate, isopropenyl acetate and other esters. A lower amount of CO₂ and ethylene suggests that the maleate groups have reacted before their decomposition temperature is reached [209].

Ethylene-carbon monoxide alternating copolymer, -CH₂CH₂-CO-, is stable up to 325°C. Its degradation has been investigated by TGA and flash photolysis

at 500°C. Main chain scission produces 4 to 10 times as much $\text{---CH}_2\text{CH}_2\text{---}\overset{\text{O}}{\parallel}{\text{C}}\cdot$ as $\text{---}\overset{\text{O}}{\parallel}{\text{C}}\text{---}\dot{\text{C}}\text{HCH}_2\text{---}\overset{\text{O}}{\parallel}{\text{C}}\text{---}$ radicals. The activation energy increases with extent of degradation due to crosslinking and aromatization. Carbonaceous residues may be as high as 30% [212].

Methylvinylidene cyanide-vinyl acetate alternating copolymer degrades in dry helium starting at about 265°C with a maximum rate at 340°C at a heating rate of 2.3°C/min. Products like acetic acid, acetonitrile, hydrogen cyanide and acetamide indicate elimination reactions along the main chain. It is proposed that two parallel consecutive reactions take place. The first is random elimination creating double bonds, and the second is an autocatalytic zipper mechanism forming a conjugated system [213].

In vinyl acetate-methacrylic acid copolymer (65% alternating units), the cross-linking mechanisms of both homopolymers are perturbed due to their reduced sequences. Thus less anhydride is formed. Instead, a large proportion of lactone rings between alternating vinyl acetate and methacrylic acid units is formed. These induce early decomposition so that the copolymer has a lower thermal stability than either of the homopolymers [214-216].

This summary on alternating polymers gives a sense of the vast new field that is opening up in the tailoring of new specialized polymeric materials with unique properties. Obviously thermal analysis will play a very important part in their characterization.

8.3.2. Thermal degradation of block copolymers

As stated previously, a block copolymer usually degrades as if the homopolymers of the component blocks were present as a mixture. Therefore, the two blocks may degrade independently as is the case for a poly(tert-butyl aziridine)/poly (methyl methacrylate) ABA type block copolymer [217], or, for example, radicals from one block may catalyze degradation of the other block. Only a few studies have been made on the thermal degradation of block copolymers.

8.3.3. Thermal degradation of some random copolymers

Random copolymers often degrade somewhat similarly to alternating copolymers but a greater assortment of products are possible due to the uneven and uncertain sequences of the comonomer units. Random copolymers are not in general completely random in a statistical sense and many might be described as either imperfect block or imperfect alternating copolymers. The thermal degradation of some random type copolymers were described earlier in this section. Some other cases follow:

Phenyl methacrylate (PMA)/styrene (ST) copolymer degrades in nitrogen by a single step weight loss process for 10 - 90% compositions. Both monomers are found among the degradation products indicating that a depolymerization (unzipping) reaction occurs. Carbon monoxide, propene and dimethyl ketene which are not found in the homopyrolyses are also found. It was concluded that the constituent chain units degrade in an essentially independent fashion in this system [218].

In glycidyl methacrylate (GMA)/methymethacrylate (MMA), monomers are the main degradation products from a single step weight loss in the 300°C range. However, anhydride rings, along with many other minor products, form, especially at high GMA content [219].

The degradation of glycidyl methacrylate (GMA)/styrene (ST) copolymers (10 - 86% GMA) in nitrogen indicated degradation behavior intermediate between the two homopolymers and it has been concluded that the constituent chain units behave independently. However ST had a stabilizing effect on the GMA in that its presence reduces the number of labile unsaturated chain ends [220].

The thermal degradation of polychlorotrifluoroethylene (CTFE)/vinylidene fluoride (VDF) copolymer in nitrogen yielded products that are the same as those obtained from the homopolymers except for the presence of some HCl [221].

Thermal degradation of poly(methylmethacrylate) (PMMA) / polychlorotrifluoro-ethylene (CTFE) copolymer in nitrogen produced predominantly monomer units and there was little evidence of interaction. It was suggested that the copolymer might have a more or less block structure [222].

The degradation of glycidyl methacrylate (GMA)/vinyl acetate (VAc) copolymer having 90 to 6% GMA in nitrogen was investigated by TGA, DTA, TVA and MS. Lactones are formed between adjacent GMA and VAc units, and glycidyl acetate is one of the major products. The copolymers were slightly more stable than might be expected from their homopolymer constituents [223].

The degradation of styrene rich chlorotrifluoroethylene (CTFE)/styrene (ST) copolymers was investigated in nitrogen atmosphere by TGA, TVA, MS and FTIR. The two homopolymers have remarkably similar weight loss curves with a maximum rate slightly above 400°C when heated at 10°C/min in a stream of nitrogen. The degradation of the copolymers shows a very slight destabilization effect [224].

The thermal degradation of three compositions of styrene (ST)/methylacrylic acid (MAA) copolymer was performed in nitrogen both isothermally and at a heating rate of 10°C/min. TGA and TVA (MS and IR) analyses were performed. The copolymers were intermediate in stability between the homopolymers. However more methylacrylic acid and fewer anhydride rings were formed as a result of the interdispersion of the styrene units. The rings and MAA units decreased the possibilities for transfer by polystyryl radicals [225].

An ethylene/ethylene-ethyl acrylate (EEA) copolymer was thermally degraded in nitrogen and in air at 10°C/min in TGA and DSC instruments. TVA (GC, MS, IR) were performed on the products. The copolymer is more stable than PEEK and less stable than LDPE. It is more stable in nitrogen than in air, as expected. The degradation products, which consist of ethanol, chain fragments, carbon dioxide, and ethylene, indicate that although the degradation is initiated by random chain scission, some process other than depolymerization is occurring. The ethanol probably results from cyclization of the ester groups which changes the chemical nature of the repeat units along the chain [226].

Methacrylonitrile/styrene (MANS) copolymers of 10/1, 1/1 and 1/10 MAN/styrene compositions, thermally degraded in nitrogen atmosphere, were found to yield products similar to the homopolymer degradations. The two monomers were the chief volatile products but short chain fragments arising from parts of the chain with adjoining dissimilar units were found. The 10/1 copolymer yielded a large amount of tars which probably arose from the depropagating PMAN radicals undergoing transfer by tertiary hydrogen abstraction occurring at styrene units [227].

Grafting butadiene onto an acrylonitrile/butadiene/styrene (ABS) terpolymer stabilizes the butadiene structure but renders the SAN less stable. Grafting methylacrylic acid onto ABS and especially its sodium salt increases its thermal stability [228].

The degradation of 2-sulfoethyl methacrylate (2-SEM)/methyl methacrylate (MMA) copolymer gives more residue than is expected based upon the amount of 2-SEM in the copolymer, indicating that MMA is also incorporated in the residue [229].

Poly(ethylene glycol allenyl-methyl ether)s (PEGA)/styrene copolymer exhibited low thermal stability. Greater stability was attained from copolymerizing PEGA oligomers with styrene [230].

8.3.4. Thermal degradation of some blends and mixtures

A publication in 1991 by McNeill, [231] includes a bibliography of previous studies on the thermal degradation of polymer blends by the Glasgow group (Grassie, McNeill, *et al*) from 1968 to 1990 and briefly summarizes the types of behavior which have been found to occur. Some even more recent studies of the degradation of polymer blend systems are summarized below.

PVC/polydimethylsiloxane (PDMS) is a heterogeneous system, and it shows no change in the nature of the products of degradation. However, destabilization of the PVC occurred at low percentages PDMS. Enhanced stability of both polymers was found at greater than 50% PDMS and much slower weight loss than expected occurred at 10% PVC. It is presumed that crosslinking of the PDMS results from abstraction of hydrogen by chlorine radicals diffusing from the PVC which begins to degrade at a lower temperature

[232].

The PVC/bisphenol A polycarbonate (PC) system appears to be another example of the destabilization of the PC by HCl or chlorine radicals migrating from the less stable PVC. Degradation products were the same as obtained from the homopolymers [233].

PDMS was stabilized in mixtures with low density polyethylene (LDPE), polyethyl acrylate (PEA), and ethylene ethyl acrylate copolymer (EEA) (which contain polar groups). Cross-linking occurs in the PDMS from the reactions of diffusing radicals from the other components [234].

The PC component in polystyrene (PS) and bisphenol A polycarbonate (PC) blends is destabilized, probably by small radicals migrating from the PS phase [235], while in polymethoxystyrene (PMeS) and bisphenol A polycarbonate (PC) blends the PC component is destabilized, probably by small radicals migrating from the PMeS phase [236]. Furthermore, interaction occurs during the degradation of poly(methylmethacrylate) (PMMA) and poly-4-bromostyrene (PBrS) blends resulting in some stabilization of the PBrS. The copolymer of MMA and BrS behaved on degradation like PBrS which has been found to behave closely analogously to polystyrene [236].

Powder mixtures of PVC and poly(tetramethylene sebacate) (PTMS) blend showed no evidence of interaction during degradation, but, in cast film specimens, the PVC was stabilized at low to moderate PTMS content. Increase in residue was explained by chlorine chain carriers causing crosslinking in the PTMS [231]. While in PVC and poly(ethylene adipate) (PEAR) blends, it appears to be that interaction occurs in both the powder mixture and in the cast film specimens [237]. In PVC and poly alpha methylstyrene-acrylonitrile copolymer (PMSAN) blend, the thermal degradation in a nitrogen atmosphere of the PVC component is accelerated by the copolymer while the PVC retards degradation of its copolymer. Blends with more than 50% PMSAN are more stable than PVC [238]. However, in PVC and poly- α -methylstyrene/acrylonitrile/methyl-methacrylate copolymer (PMSANMMA) blends, the thermal degradation in a nitrogen atmosphere of the PVC component is accelerated by products from the degradation of its copolymer while PVC retards the latter's degradation. It appears that the blends were miscible at the temperatures of the thermal degradation [239].

Thermal degradation in a nitrogen atmosphere of poly(ethylene-co-acrylic acid) (PEA)-epoxidized natural rubber (ENR) blends exhibited greater thermal stability than its components alone. The 20% ENR blend was the most stable [240], and thermal degradation in nitrogen of PVC-*cis*-polybutadiene (PBR) blend indicated that the stability of the blends increased with PBR content [241].

In poly(1,4-phenylene sulfide) (PPS) mixed with and in the presence of polystyrene (PS), vacuum pyrolysis studies were made with a 1:1 mixture of the two polymers and also with the two homopolymers degrading in proximity to

each other so that product gases of the one passed over the other. These results were compared with the separate degradations of the homopolymers. The PS in the mixture was destabilized by the PPS but the latter was unaffected by the PS degradation which is almost complete prior to significant degradation of PPS. Homopolymers degrading in proximity to one another showed no synergism [242].

9. CONCLUDING REMARKS

This Chapter has attempted to present, under spatial restrictions, a review of many of the basic concepts and theories pertaining to the thermal, oxidative and hydrolytic degradation of polymeric materials. Also the degradation reactions and postulated mechanisms for them are described for a representative spectrum of specific polymers, copolymers and blends.

When thermal analysis methods are applied to polymer degradation studies, most of the techniques and resulting graphs and figures are not distinguishable in form from those for similar experiments involving lower molecular weight organic and even inorganic compounds. However, the interpretation of the kinetics and the development of mechanisms for the complex reactions taking place in these cases require a broad knowledge of general polymer degradation theory and practice.

Therefore, it is hoped that this review of the basics will serve a useful purpose as a source of background for those engaged in the thermal analytical studies involving polymer degradation. (Note: the four years following the preparation of this Chapter have seen the publication of many significant new papers, particularly in the areas of polyolefin oxidation and copolymer thermal degradation. A major portion of these papers are to be found in the journal, *Polymer Degradation and Stability* published by Elsevier Science Limited [JHF]).

10. BIBLIOGRAPHY

(This section lists many books, monographs, reviews, related to polymer degradation, stabilization, oxidation, irradiation, *etc.*, in chronological order of publication.)

- Die Hochmolekularen Organischen Verbindungen, H. Staudinger, Springer, Berlin, 1932.
- The Aliphatic Free Radicals, F. O. and K. K. Rice, The Johns Hopkins Press, Baltimore, 1935.
- Principles of Polymer Chemistry, P. J. Flory, Cornell Press, Ithaca, 1952, pp 69-105, 317-346.

- Polymer Degradation Mechanisms, Proceedings of the NBS Semicentennial Symposium on Polymer Degradation Mechanisms, National Bureau of Standards Circular 525, 1953, 280 pp.
- Degradation of Vinyl Polymers by H. H. G. Jellinek, Academic Press, New York, 1955.
- Analytical Chemistry of Polymers, Part II, ed G. M. Kline, Chapt 5, Pyrolysis, by L. A. Wall, Academic Press, New York, 1955.
- Chemistry of Vinyl Polymer Degradation and Decomposition, by N. Grassie, Butterworths, London 1956.
- Catalysis, ed P. H. Emmett, Chapt 3, R. Simha and L. A. Wall, Mechanism of Polymer Formation and Decomposition, Reinhold, New York, 1958. .
- Recent Advances in the Theory of Thermal Degradation of Hetrodisperse Polymers, SCI Monograph No. 13, Society of Chemical Industry, London, 1961.
- Degradation of Polymers by L. A. Wall and J. H. Flynn, in Rubber Chemistry and Technology, Vol 35, No 5, December, 1962.
- Analytical Chemistry of Polymers, ed G. M. Kline, Chapter 5 by L. A. Wall, Academic Press, New York, 1962, pp 1181-248.
- Thermal Degradation of Organic Polymers by S. L. Madorsky, Interscience, New York, 1964.
- Mechanisms of Oxidation of Organic Compounds, W. A. Waters, John Wiley, New York, 1965.
- Aging and Stabilization of Polymers, M. B. Neiman, Consultants Bureau, New York, 1965.
- Encyclopedia of Polymer Science and Technology, Vol 4, H. H. G. Jellinek, John Wiley & Sons, 1966, pp 740-793.
- Polymer Handbook, Eds J. Brandrup and E. H. Immergut, V.1 Energies of Activation for the Thermal Degradation of Polymers, V.2 Products of Degradation of Polymers, by N. Grassie, John Wiley & Sons, New York, 1966.
- High Temperature Resistant Polymers, A. H. Frazer, Interscience-Wiley, New York, 1968.
- Autooxidation of Hydrocarbons and Polyolefins, by L. Reich and S. S. Stivala, Marcel Dekker, New York, 1969.
- Thermal Stability of Polymers, Vol I, ed R. T. Conley, Marcel Dekker, New York 1970.
- Elements of Polymer Degradation, by L. Reich and S. S. Stivala, McGraw Hill, New York, 1971.
- The Chemical Structure and Thermal Characteristics of Polymers, V. V. Korphak, Israel Program for Scientific Translation, Jerusalem, 1971.

- The Mechanisms of Pyrolysis, Oxidation and Burning of Organic Molecules, Nat. Bur. Standards, Spec. Pub., 357, 1972.
- Polymer Stabilization, ed. W. L. Hawkins, Wiley-Interscience, New York, 1972.
- Reactivity, Mechanism and Structure in Polymer Chemistry, Eds, A. D. Jenkins and A. Ledwith, John Wiley, New York, 1974.
- Comprehensive Chemical Kinetics, Eds, C. F. Bamford and C. F. H. Tipper, Vol 14, Degradation of Polymers, by C. David, J. F. Rabek, *etc.*, Elsevier, Amsterdam, 1975.
- Degradation and Stabilization of Polymers, ed. G. Geuskens, John Wiley-Applied Science, London, 1975.
- Photodegradation, Photo-oxidation and Photostabilization of Polymers, B. Ranby and J. F. Rabek, Wiley, London, 1975.
- Ultraviolet Light Induced Reactions in Polymers, ACS Symposium Series #25, ed S. S. Lahana, ACS Washington DC, 1976.
- Developments in Polymer Degradation, ed, N. Grassie, Elsevier, London, Vol 1-7 (1977-).
- Aspects of Degradation and Stabilization of Polymers, H. H. G. Jellinek, ed.; Elsevier, Amsterdam, 1978.
- Stabilization and Degradation of Polymers, Eds., D. L. Allara and W. L. Hawkins, Advances in Chemistry Series No.169, Am. Chem. Soc., Washington, 1978, 411 pp.
- Polymer Degradation and Stability (an international journal since 1979) ed N. Grassie, Elsevier, Amsterdam.
- Durability of Macromolecular Materials, ed., R. B. Eby, ACS Symposium Ser., No.95, Am Chem Soc, Washington, 1979, 476 pp.
- Developments in Polymer Stabilization, ed G. Scott, (Vols 1), Applied Science, London (1979).
- Thermally Stable Polymers, Synthesis and Properties, P. E. Cassidy, Marcel Dekker, New York 1980.
- Polymer Degradation, Principles and Practical Applications, W. Schnabel, Hanser International, Macmillan, New York, 1981.
- Photodegradation and Photostabilization of Coatings, Eds, S. P. Pappas and F. H. Winslow, ACS Symposium Ser., No.151, Am. Chem. Soc., Washington, 1981.
- Degradation and Stabilization of Polymers, Eds, H. H. G. Jellinek and H. Kachi, Elsevier, Amsterdam, Vol. 1 (1983), Vol. 2 (1989).
- Degradation and Stabilization of Polyolefins, ed N. S. Allen, Applied Science Publishers, London, 1983.
- Chromatographic Science Series, Vol. 20, Pyrolysis and GC in Polymer Analysis, Eds, S. A. Liebman and E. J. Levy, Marcel Dekker, NY, 1984.

- (Chapter 4, Degradation and Pyrolysis Mechanisms, J. H. Flynn and R. F. Florin) (Chapter 5, Microstructure of Synthetic Polymers, D. H. Ahlstrom)
- Degradation and Stabilization of PVC, ed E. D. Owen, Elsevier, London, 1984.
 - Polymer Degradation and Stability, W. L. Hawkins, Springer-Verlag, Berlin, 1984.
 - Photochemical Conversion and Stabilization of Polymers, V. Ya Shlyapintokh. Hanser Publishers, Macmillin, New York, 1984.
 - Degradation and Stabilization of PVC, ed E. D. Owen, Chapt 2, Thermal Degradation of PVC by T. Hjertberg and E. M. Sorvek, Elsevier, London (1984) pp 21-80.
 - Polymer Degradation and Stabilization, N. Grassie and G. Scott, Cambridge Press, Cambridge, 1985.
 - Polyvinyl Chloride Degradation, J. Wypych, Elsevier, Amsterdam, 1985.
 - New Trends in the Photochemistry of Polymers, Ed. N. S. Allen and J. F. Rabek, Elsevier, London 1985.
 - Encyclopedia of Polymer Science and Engineering, Eds Mark-Bikkales-Overburger-Menges, 2nd edition, Suppl. Vol., Thermal Analysis by J. H. Flynn, John Wiley, New York, 1989, pp 690-723.
 - Chemical Reactions of Natural and Synthetic Polymers, M. Lazar, T. Bleha and J. Rychly, Ellis Horwood, Chichester, 1989.
 - Mechanisms of Polymer Degradation and Stabilization, ed., G. Scott, Elsevier, London, 1990, 329pp.
 - Oxidation Inhibition in Organic Materials, ed P. P. Klemchuk and J. Pospisil, CRC Press, Boca Raton FLA, 1990, Vol 1.
 - Degradation Of Filled Polymers, High Temperature and Thermal Oxidation Processes, M. T. Byrk, Ellis Horwood, Chichester, 1991, 199 pp.
 - Irradiation Effects of Polymers, ed., D. W. Clegg & A. A. Colyer, Elsevier, London, 1991, 450 pp.
 - Polymers in Conservation, ed., N. S. Allen, M. Edge and C. V. Horie, Royal Society of Chemistry, 1992, 216 pp.
 - Handbook of Polymer Degradation, ed., S. Halim Hamid, Mohamed E. Amin & A. G. Maadhah, Marcel Dekker, New York, 1992, 649 pp.
 - Polymer Durability, Degradation, Stabilization, and Lifetime Prediction, Eds., R. L. Clough, N. C. Billingham, and K. T. Gillen, Advances in Chemistry Serries No.249, Am. Chem. Soc., Washington, 1993, 712 pp.
 - Atmospheric Oxidation and Antioxidants, Vols I-III, ed., G. Scott, Elsevier, Amsterdam, 1993.
 - Polymer Photodegradation, J. F. Rabek, Chapman and Hall, London 1995.

REFERENCES

1. J. H. Flynn, Thermal Analysis, in Encyclopedia of Polymer Science and Engineering, Eds, Mark-Bikales-Overburger-Menges, Supplement Volume, Second Edition, John Wiley, New York, 1989, pp 690-723.
2. J. H. Flynn and R. E. Florin, Chapt 4 Degradation and Pyrolysis Mechanisms, in Pyrolysis and GC in Polymer Analysis, Eds S. A. Liebman and E. J. Levy, Marcel Dekker, New York, 1985, pp 149-208.
3. N. Grassie, Polymer Degradation and Stability, 40 (1993) 137.
4. J. H. Flynn, Thermochim. Acta, 131 (1988) 115.
5. J. H. Flynn, J. Therm. Anal., 44 (1995) 499.
6. F. S. Dainton and K. J. Ivin, Quart Rev, 12 (1958) 61.
7. W. K. Busfield, Ceiling Temperatures, in Aspects of Degradation and Stabilization of Polymers, ed H. H. G. Jellinek, Elsevier, Amsterdam, 1978, pp 39-78.
8. Y. Kamiya and E. Niki, The Role of Temperature in the Oxidative Degradation of Polymers, in Degradation and Stabilization of Polymers, Vol. 1, ed H. H. G. Jellinek, Elsevier, Amsterdam, 1983, pp. 337-357.
9. J. H. Flynn and Z. Petrovic, J. Therm. Anal., 41 (1994) 549.
10. L. A. Wall, in The Mechanism of Pyrolysis, Oxidation and Burning of Organic Molecules, Natl Bur Standards, Spec Pub 357 (1972).
11. H. Staudinger, M. Brunner, K. Frey, P. Garbach, R. Signer and S. Wehrli, Ber., 62B:241, (1929) 2921.
12. J. H. Flynn and B. Dickens, in Durability of Macromolecular Materials, ed, R. B. Eby, ACS Symp. Ser., 95 (1979) 97.
13. I. Mita, in Aspects of Degradation and Stabilization of Polymers, ed H. H. G. Jellinek, Elsevier Amsterdam 1978 p 248.
14. L. A. Wall and J. H. Flynn, Rubber Chem. Technol., 35 (1962) 1157.
15. H. G. G. Jellinek, Degradation of Vinyl Polymers, Academic Press, New York, 1955.
16. R. H. Boyd, in Thermal Stability of Polymers, Vol I, ed R. T. Conley, Marcel Dekker, New York 1970, Chapt 3.
17. M. Gordon, in Recent Advances in the Theory of Thermal Degradation of Heterodisperse Polymers, SCI Monograph 13, Society of Chemical Industry, London, 1961, pp. 163-180.
18. F. O. Rice and K. F. Herzfeld, J. Am. Chem. Soc., 56 (1934) 284.
19. F. O. Rice and K. K. Rice, The Aliphatic Free Radicals, Johns Hopkins Press, Baltimore, 1935.
20. H. Staudinger, Die Hochmolekularen Organischen Verbindungen, Springer, Berlin, 1932, p. 151.
21. P. J. Flory, Principles of Polymer Chemistry, Cornell Press, Ithaca, 1953, pp. 69-105, 317-346.
22. Y. Tsuchiya and K. Sumi, Polym. Lett., 6 (1968) 357.
23. Y. Tsuchiya and K. Sumi, J. Polym. Sci., A1 6 (1968) 415.
24. Y. Tsuchiya and K. Sumi, J. Polym. Sci., A1 7 (1969) 1599.
25. M. Seeger and E. M. Barrall II, J. Polym. Sci., Polym. Chem. Ed., 113 (1975) 1515.
26. J Evner, M. Seeger and H. J. Cantow, Angew. Chem. (Internat Ed), 10 (1971) 346.
27. B. R. Northmore, Brit. Polym. J., 4 (1972) 511.
28. D. H. Ahlstrom, S. A. Liebman and K. B. Abbas, J. Polym. Sci., Polym. Chem. Ed., 14 (1976) 2479.
29. Y. Sugimura and S. Tsuge, Macromolecules, 12 (1979) 512.

30. Y. Tsuchiya and K. Sumi, *J. Polym. Sci.* A17, (1969) 813.
31. G. G. Cameron, J. M. Meyer and I. T. McWalter, *Macromolecules*, 11 (1978) 696.
32. L. A. Wall, S. Straus, R. E. Florin and L. J. Fetters, *J. Res. Nat. Bur. Standards*, 77A (1973) 157.
33. C. R. Patrick, in *The Mechanism of Pyrolysis, Oxidation and Burning of Organic Molecules*, Natl Bur Standards, Spec Pub 357 (1972) pp 35-41.
34. A. N. North, in *Reactivity, Mechanism and Structure in Polymer Chemistry*, Eds, A. D. Jenkins and A. Ledwith, John Wiley, New York, 1974, p 142.
35. P. R. E. J. Cowley and H. W. Melville, *Proc. Roy. Soc. (London)*, A210 (1952) 461.
36. P. R. E. J. Cowley and H. W. Melville, *Proc. Roy. Soc. (London)*, A211 (1952) 320.
37. L. A. Wall, in *Analytical Chemistry of Polymers, Part II*, ed G. M. Kline, Academic Press, New York, 1962 Chapt 5, pp. 181-248.
38. S. Straus and S. Madorsky, *J. Res. Nat. Bur. Standards*, 66A (1962) 250.
39. G. J. Knight, *Polym. Lett.*, 5 (1967) 855.
40. S. Tsuge, T. Okumoto and T. Takeuchi, *J. Chromatogr. Sci.*, 7 (1969) 250.
41. R. M. Lum, *Proc 11th No Am Therm Anal Conf.*, Vol II, (1981) pp. 459-465.
42. M. M. O'Mera, *J. Polym. Sci.*, A1 8 (1970) 1887.
43. W. Kuhn, *Ber.*, 63 (1930) 1303.
44. N. Grassie, *Chemistry of Vinyl Polymer Degradation and Decomposition*, Butterworths, London, 1956.
45. R. Simha and L. A. Wall, in *Catalysis, Vol VI*, ed P. H. Emmett, Chapt 3 Mechanisms of Polymer Formation and Decomposition, Reinhold, New York 1958.
46. N. Grassie and S. M. Grant, *Europ. Polym. J.*, 2 (1970) 255.
47. I. S. Gur and H. L. Batnagear, *Indian. J. Chem.*, 7 (1969) 495.
48. J. Frenkel, *Theory of Liquids*, Oxford University Press, London. (1946) p. 451.
49. B. Dickens, in *Proc 2nd Europ Symp on Therm Anal*, ed D. Dollimore, Heyden, London 1981, p 219.
50. L. A. Wall, J. H. Flynn and S. Straus, *J. Phys. Chem.*, 74 (1970) 3237.
51. R. Simha and L. A. Wall, *J. Phys. Chem.*, 56 (1952) 707.
52. T. Ozawa, *Bul. Chem. Soc. Japan.*, 38 (1965) 1881.
53. T. Ozawa, *J. Therm. Anal.*, 2 (1970) 301.
54. L. A. Wall, *Society of Chemical Industry London Monograph*, 13 (1961) 145.
55. H. H. G. Jellinek, *Degradation and Depolymerization Kinetics in Aspects of Degradation and Stabilization of Polymers*, ed H. H. G. Jellinek, Elsevier, Amsterdam, 1978, pp. 6-9.
56. F. R. Mayo, *Acc. Chem. Res.*, 1 (1968) 193.
57. J. L. Bowland, *Proc. Roy. Soc.*, A186 (1946) 218.
58. L. Bateman, *Quart. Rev. (London)*, 8 (1947) 147.
59. F. Gugumus, *Polym. Deg. and Stab.*, 53 (1996) 161.
60. Y. Kamiya and E. Niki, Chapt 3 *Oxidative Degradation in Aspects of Degradation and Stabilization of Polymers*, ed H. H. G. Jellinek, Elsevier, Amsterdam, 1978, pp. 90-147.
61. Y. Kamiya and E. Niki, Chapt 7 *The Role of Hydroperoxides in the Oxidative Degradation of Polymers in Degradation and Stabilization of Polymers Volume 1*, ed H. H. G. Jellinek, Elsevier, Amsterdam, 1983, pp. 337-357.
62. H. H. G. Jellinek, Chapt 4 in *The Oxidative Degradation of Polymers in Degradation and Stabilization of Polymers Volume 2*, ed H. H. G. Jellinek and H. Kachi, Elsevier, Amsterdam, 1989, pp. 297-310.
63. F. Gugumus, *Polym. Deg. and Stab.*, 46 (1994) 123.
64. F. Gugumus, *Polym. Deg. and Stab.*, 49 (1995) 29.
65. F. Gugumus, *Polym. Deg. and Stab.*, 52 (1996) 131.

66. F. Gugumus, *Polym. Deg. and Stab.*, 52 (1996) 145.
67. F. Gugumus, *Polym. Deg. and Stab.*, 52 (1996) 159.
68. F. Gugumus, *Polym. Deg. and Stab.*, 55 (1997) 21.
69. N. N. Emanuel, *Polym. Sci. USSR.*, 27 (1985) 1505.
70. J. Petroj and J. Marchal, *J. Radiat. Phys. Chem.*, 16 (1980) 27.
71. J. H. Flynn, *Proc 2nd Europ Symp on Thermal Analysis*, ed D. Dollimore, Hayden, London (1981) pp. 115-120.
72. R. P. Bell, *Acid-Base Catalysis*, Oxford U Press, London, 1941.
73. L. Reich and S. S. Stivala, *Elements of Polymer Degradation*, McGraw-Hill, New York, 1971, pp. 68-74.
74. C. B. Chapman, *J. Polym. Sci.*, 45 (1960) 547.
75. D. A. S. Ravens, *Polymer*, 1 (1960) 237.
76. J. H. Flynn, *J. Therm. Anal.*, 44 (1995) 499.
77. D. W. Brown, R. E. Lowery and L. E. Smith, *Macromolecules*, 13 (1980) 248; *Prediction of the Long Term Stability of Polyester Recording Media*, NBSIR (Natl Bur Standards Reports) 82-2530, June 1982; 83-2750, August 1983; 84-2988, December 1984; 86-3474, June 1986.
78. N. Grassie and H. W. Melville, *Proc. Roy. Soc. (London)*, A199 (1949) 1.
79. H. H. G. Jellinek and M. D. Leh, *Macromol. Chem.*, 115 (1968) 89.
80. C. D. David, in *Comprehensive Chemical Kinetics*, Vol 14, Eds, C. H. Bamford and C. F. H. Tipper, Elsevier, Amsterdam, 1975.
81. Roestamsjah, L. A. Wall, R. E. Florin, M. Aldridge and L. J. Fetters, *J. Res. Nat. Bur. Standards*, 83 (1978) 371.
82. J. C. Siegle, L. T. Muus and T-P. Lin and H. A. Larson, *J. Polym. Sci.*, A2 (1964) 391.
83. L. A. Wall, S. Straus, J. H. Flynn, D. McIntyre and R. Simha, *J. Phys. Chem.*, 70 (1966) 53.
84. I. C. McNeill, M. Zulfiqar and T. Kousar, *Polym. Deg. and Stab.*, 28 (1990) 131.
85. J. H. Flynn, *J. Thermal. Anal.*, 34 (1988) 367.
86. B. Dickens, *Polym. Deg. and Stab.*, 2 (1980) 249.
87. I. C. McNeill, L. P. Razumovskii, V. M. Gol'dberg and G. E. Zaikov, *Polym. Deg. and Stab.*, 45 (1994) 47.
88. V. M. Gol'berg, V. N. Yesenin and G. E. Zaikov, *Polym. Sci. USSR*, 28 (1976) 1819.
89. J. H. Flynn, *The Role of Thermal Analysis in the Lifetime Prediction of Polymers*, in *Proc 2nd European Symp on Therm Anal*, ed D. Dollimore, Hayden, London (1981) p. 223.
90. E. T. Denisov and Yu B. Shilov, *Vysokomolek Soed*, 25A (1983) 1196.
91. V. N. Tesenin, I. A. Krasotkina and G. I. Zaikov, *Vysokomolek Soed*, 25B (1983) 48.
92. H. H. G. Jellinek in *Aspects of Degradation and Stabilization of Polymers*, ed *ibid.*, Elsevier Amsterdam 1978 Chapter 1.
93. C. David in *Comprehensive Chemical Kinetics*, Vol 14, Eds., C. H. Bamford and C. F. H. Tipper, Elsevier, Amsterdam 1975, p55.
94. L. Reich and S. S. Stivala, *Elements of Polymer Degradation*, McGraw-Hill, New York, 1971.
95. S. S. Stivala, J. Kimura and L. Reich, Chapt 1 in *Degradation and Stabilization of Polymers*, Vol 1, ed H. H. G. Jellinek, Elsevier, London, 1983, p. 1.
96. T. Hjeertberg and E. M. Sorvik, in *Degradation and Stabilization of PVC*, ed E. D. Owen, Elsevier, London, 1984, p 21 and references therein.
97. J. Wypych, *Polyvinyl Chloride Degradation*, Elsevier, Amsterdam, 1985.

98. B. Ivan, T. Kelen and F. Tudos, Chapt 8 in *Degradation and Stabilization of Polymers*, Vol 2, ed H. H. G. Jellinek, Elsevier, London, 1989, pp. 483-714.
99. R. Bacaloglu and M. Fisch, *Polym. Deg. and Stab.*, 53 (1996) 301, 315, 325.
100. I. A. McNeill, I. Memetea and W. J. Cole, *Polym. Deg. and Stab.*, 49 (1995) 181.
101. G. Palma and M. J. Carezza, *J. Appl. Polym. Sci.*, 14 (1970) 1737.
102. C. David in *Comprehensive Chemical Kinetics*, Vol 14, Eds., C. H. Bamford and C. F. H. Tipper, Elsevier, Amsterdam, 1975, p78.
103. S. A. Liebman, D. H. Ahlstrom and C. R. Foltz, *J. Polym. Sci., Polym Chem*, 16 (1978) 3139.
104. S. Crawley and I. A. McNeill, *J. Polym. Sci.*, 16 (1978) 2593.
105. V. P. Gupta and L. E. St Pierre, *J. Polym. Sci.*, A1 8 (1970) 37.
106. J. Behnish and H. Zimmermann, *Makromol. Chem.*, 190 (1989) 2347.
107. M. M. O'Mera, *J. Polym. Sci.*, A1 8 (1970) 1887.
108. T. Hjeertberg, E. Martinsson and E. Sorvik, *Macromolecules*, 21 (1988) 603 and references therein.
109. M. M. O'Mara, *Pure. Appl. Chem.*, 49 (1977) 649.
110. W. H. Starns Jr and D. Edelson, *Macromolecules*, 12 (1979) 797.
111. G. A. Rasuvaev, L. S. Troitskaya and B. B. Troitskeii, *J. Polym. Sci.*, 9 (1971) 2673.
112. F. H. Winslow, W. O. Baker and W. A. Yager, *Proc. Conf. Carbon*, (1956) p. 93.
113. N. Grassie and G. Scott, *Polymer Degradation and Stability*, Cambridge U Press, Cambridge (1985) and references therein.
114. T. Kelen, I. Bela, T. T. Nagy, B. Turcsanyi, F. Tudos and J. P. Kennedy, *Polym. Bull. (Berlin)*, 1 (1978) 79.
115. G. Talimini and G. Pezzin, *Makromol. Chem.*, 39 (1960) 26.
116. A. Guyot, J. P. Benevise, and Y. Trambouse, *J. Appl. Polym. Sci.*, 6 (1962) 103.
117. G. Montaudo and C. Puglisi, *Polym. Deg. and Stab.*, 33 (1991) 229.
118. D. H. Grant and N. Grassie, *Polymer*, 1 (1960) 445.
119. A. Jamieson and I. C. McNeill, *Eur. Polym. J.*, 10 (1974) 217.
120. I. C. McNeill and J. J. Liggat, *J. Polym. Deg. and Stab.*, 36 (1992) 291.
121. D. L. Gardner and I. C. McNeill *J. Therm. Anal.*, 1 (1969) 389.
122. N. Grassie, *Trans. Farad. Soc.*, 48 (1952) 379; 49 (1953) 835.
123. I. C. McNeill in *Comprehensive Polymer Science*, Vol 6, ed G. Eastmond, A. Ledwith, S. Rosso and P. Sigwalt, Pergamon Press, Oxford, 1989 p480.
124. N. A. Khalturinsky and A. A. Berlin in *Degradation and Stabilization of Polymers 2*, ed H. H. G. Jellinek, Elsevier, Amsterdam, 1989 p. 220.
125. N. A. Khalturinsky and A. A. Berlin in *Degradation and Stabilization of Polymers 2*, ed H. H. G. Jellinek, Elsevier, Amsterdam, 1989 p. 224.
126. W. Kean and J. H. Cherdron, *Makromol. Chem.*, 40 (1960) 101.
127. A. Davis and H. H. Golden, *Makromol. Chem.*, 81 (1965) 38.
128. S. L. Madorsky and S. Straus, *J. Polym. Sci.*, 36 (1959) 183.
129. H. Meerwein, D. Delfs and H. Morshel, *Angew. Chem.*, 72 (1960) 927.
130. D. J. Worsfield and A. M. Eastham, *J. Am. Chem. Soc.*, 79 (1957) 877, 900.
131. S. Smith, *J. Polym. Sci.*, 30 (1958) 459.
132. N. Ogata, *Bul. Chem. Soc. Japan*, 34 (1961) 1201.
133. B. G. Achhammer, F. W. Reinhart and G. M. Kline, *J. Res. Nat. Bur. Standards*, 46 (1953) 391.
134. L. H. Peebles and F. W. Huffman, *J. Polym. Sci.*, A-19 (1971) 1807.
135. F. Wiloth, *Makromol. Chem.*, 144 (1971) 283.

136. S. Hashimoto and T. Yamashita, *Dodhidha Daigaku Rikogaku Kenkyu Hokoku*, 17 (1976) 102.
137. I. C. McNeil and S. Basan, *Polym. Deg. and Stab.*, 41 (1993) 311.
138. I. C. McNeil and S. Basan, *Polym. Deg. and Stab.*, 33 (1991) 263.
139. I. C. McNeill and H. A. Leper, *Polym. Deg. and Stab.*, 11 (1995) 267.
140. I. C. McNeill and H. A. Leper, *Polym. Deg. and Stab.*, 11 (1985) 309.
141. I. C. McNeill and H. A. Leper, *Polym. Deg. and Stab.*, 12 (1985) 373.
142. W. D. Wooley, *Brit. Polym. J.*, 4 (1972) 27.
143. J. Chambers and C. B. Reese, *Brit. Polym. J.*, 8(2) (1976) 48.
144. A. Ballistreri, S. Foti, P. Moarsvigna, G. Montuado and E. Scamparrino, *J. Polym. Sci. (Chem)*, 18 (1980) 1923.
145. F. Gauboraud and J. P. Vantelon, *J. Polym. Sci.*, 19 (1981) 139; *ibid* 20 (1982) 2063.
146. N. Grassie, M. Zulfiquar and M. J. Guy, *J. Polym. Sci. (Chem)*, 18 (1980) 265.
147. N. Grassie and M. Zulfiquar, *Proc 2nd Internat Conf on Degradation and Stabilization of Polym*, Dubrovnik Yugoslavia (1978); *J. Polym. Sci. (Chem)*, 16 (1978) 1563.
148. J. H. Flynn, W. J. Pummer and L. E. Smith, *Am. Chem. Soc. Polym. Prepr.*, 18 (1977) 757.
149. W. M. Athey, *Rubber Age*, 96 (1960) 705.
150. S. Straus and L. A. Wall, *J. Res. Natl. Bur. Standards*, C6 (1958) 30.
151. E. P. Goodings, *Soc. Chem. Ind. Monograph*, No 13 (1961) p 211.
152. R. J. P. Allan, R. L. Foreman and P. D. Ritchie, *J. Chem. Soc.*, (1955) 2711.
153. C. W. Lewis, *J. Polym. Sci.*, 33 (1958) 153.
154. N. Grassie, R. Jenkins, J. Cunningham and I. G. MacFarlane, *Degradation Reactions in Polymers*, Air Force Materials Lab Report TR-73-273 (1973),
155. A. Pictet and J. Sarsin, *Helv. Chim. Acta.*, 1 (1918) 78.
156. O. P. Goldova and R. H. Krylova, *Dokl. Akad. Nauk. SSSR*, 116 (1957) 419.
157. M. H. Tsang and R. Bacon, *Carbon*, 2 (1964) 211.
158. F. K. Kilzer and A. Broido, *Pyrodynamics*, 2 (1963) 151.
159. R. T. Conley, in *Thermal Stability of Polymers* (ed R. T. Conley) Marcel Dekker, New York, 1970, p 523.
160. F. Shafizadeh and L. Y. Fu, *Carbohydrate Research*, 29 (1973) 113.
161. Y. Tsuchiya and K. Sumi, *J. Appl. Polym. Sci.*, 14 (1970) 2003.
162. F. Shafizadeh, G. D. McGinnis and C. W. Philpot, *Carbohydrate Research*, 25 (1972) 23.
163. F. Shafizadeh and G. D. McGinnis, *Carbohydrate Research*, 16 (1971) 273.
164. W. W. Wright, *SCI Monograph No 13*, Soc. Chem. Ind., London, 1961, p 248.
165. G. F. Ehler, K. R. Fisch and W. R. Powell, *J. Polym. Sci.*, A-17 (1965) 2931, 2955, 2969.
166. R. T. Conley and J. F. Bieron, *J. Appl. Polym. Sci.*, 7 (1963) 103, 177.
167. R. T. Conley, *J. Appl. Polym. Sci.*, 9 (1965) 1117.
168. A. A. Berlin, V. V. Yarkina and A. P. Firsov, *Vysok Soedin*, A10 (1968) 2157.
169. L. H. Lee, *J. Polym. Sci.*, A3 (1965) 8559.
170. S. Tsuge, T. Okumoto, Y. Sugimura and T. Takeuchi, *J. Chromatogr.*, 7 (1969) 253.
171. I. C. McNeill and A. Rincon, *Polym. Deg. and Stab.*, 31 (1991) 163.
172. G. Montaudo and C. Puglisi, *Polym. Deg. and Stab.*, 37 (1992) 91.
173. A. Rincon and I. C. McNeill, *Polym. Deg. and Stab.*, 40 (1993) 343.
174. J. F. Heacock and C. E. Berr, *SPE. Trans.*, 5 (1965) 102.
175. C. E. Sroog, in *Encyclopedia of Polymer Science and Technology*, vol 11, ed N. M. Bikales, Interscience, New York 1969, pp. 261-267.
176. S. D. Bruck, *Polymer*, 5 (1964) 435.

177. S. D. Bruck, *Polymer*, 6 (1965) 49.
178. G. P. Shulman, in *Thermal Stability of Polymers*, Vol 1, ed, R. T. Conley, Marcel Dekker, New York, 1970, p. 563.
179. J. A. Cella, *Polym. Deg. and Stab.*, 37 (1992) 99.
180. N. Grassie and I. C. McNeill, *J. Polym. Sci.*, 27 (1958) 207.
181. C. D. David, in *Comprehensive Chemical Kinetics*, Vol 14, Eds, C. H. Bamford and C. F. H. Tipper, Elsevier, Amsterdam, 1975, p. 55.
182. N. Grassie and G. Scott, *Polymer Degradation and Stability*, Cambridge U Press, Cambridge (1985).
183. L. T. Menetea, N. C. Billingham and E. T. H. Then, *Polym. Deg. and Stab.*, 47 (1995) 189.
184. I. C. McNeill and T. Mahmood, *Polym. Deg. and Stab.*, 45 (1994) 285.
185. N. Grassie, IUPAC Internat Symp on Macromol Chem, Budapest 1969. Pp. 725-745.
186. *Pyrolysis and GC in Polymer Analysis*, ed S. A. Liebman and E. J. Levy, Chaps 3-5, Marcel Dekker, New York 1985.
187. S. H. R. Richards, D. A. Salter, *Polymer*, 8 (1967) 127, 139.
188. L. M. Robeson, M. Matzner, L. J. Fetters and J. E. McGrath, in *Recent Advances in Polymer Blends, Grafts and Blocks*, ed, L. H. Sperling, Plenum, New York, 1974 p 281.
189. N. Grassie and I. C. McNeill, *J. Chem. Soc.*, (1956) 3929; *J. Polym. Sci.*, 27 (1958) 207.
190. N. Grassie and J. N. Hay, *J. Polym. Sci.*, 56 (1962) 189; *Soc. Chem. Ind. Monograph*, 13 (1961) 184.
191. N. Grassie and J. N. Hay, *Makromol. Chem.*, 64 (1963) 82.
192. N. Grassie and E. M. Grant, *Europ. Polym. J.*, 2 (1966) 255.
193. N. Grassie and E. Farish, *Europ. Polym. J.*, 3 (1967) 619.
194. N. Grassie and B. J. D. Torrance, *J. Polym. Sci.*, A-16 (1968) 3303, 3315.
195. I. C. McNeill, *Europ. Polym. J.*, 4 (1968) 21.
196. N. Grassie and E. Farish, *Europ. Polym. J.*, 1 (1969) 305.
197. I. C. McNeill, D. Neil, A. Guyot, M. Bert and A. Michel, *Europ. Polym. J.*, 7 (1971) 453.
198. C. E. R. Jones and G. E. J. Reynolds, *Brit. Polym. J.*, 1 (1969) 197.
199. L. A. Wall, *Natl. Bur. Standards, Circ No 525* (1953) 239.
200. Y. Shibazki and H. Kambe, *Kobunshi Kagaku*, 21 (1964) 71.
201. S. Tsuge, T. Kobasyaski, Y. Sugimura, T. Nagaya and T. Takeuchi, *Macromolecules*, 7 (1979) 988.
202. D. H. Ahlstron, *Pyrolysis and GC in Polymer Analysis*, ed S. A. Liebman and E. J. Levy, Chapt. 5, *Microstructure of Synthetic Polymers*, Marcel Dekker, New York 1985.
203. S. Igarashi and H. Kambe, *Makromol. Chem.*, 79 (1964) 180.
204. C. N. Cascaval and R. E. Florin, *J. Fluorine Chem.*, 13 (1979) 65.
205. M. Blaszo and G. Varhegyi, *Europ. Polym. J.*, 14 (1978) 625.
206. T. Shin, T. Okumoto and T. Takeuchi, *Macromolecules*, 2 (1969) 200.
207. I. C. McNeill, S. Ahmed, L. Memetea, M. H. Mohammed, G. E. Zaikov and A. Ya Polishchuk, *Polym. Deg. and Stab.*, 52 (1996) 171.
208. I. C. McNeill, A. Ya Polishchuk and M. H. Zaikov, *Polym. Deg. and Stab.*, 37 (1992) 223.
209. I. C. McNeill, S. Ahmed, L. Memetes, M. H. Mohammed, G. E. Zaikov and A. Ya Polishchuk, *Polym. Deg. and Stab.*, 47 (1995) 319.
210. I. C. McNeill, A. Ya Polishchuk and M. H. Zaikov, *Polym. Deg. and Stab.*, 52 (1996) 171.
211. I. C. McNeill, S. Ahmed and L. Memetea, *Polym. Deg. and Stab.*, 46 (1994) 303.
212. J. C. Chien and A. X. Zhao, *Polym. Deg. and Stab.*, 40 (1993) 257.

213. B. Boinon, M. Raihane and J. P. Montheard, *Polym. Deg. and Stab.*, 43 (1994) 27.
214. I. C. McNeill, S. Ahmed and L. Memetea, *Polym. Deg. and Stab.*, 47 (1995) 33.
215. I. C. McNeill, S. Ahmed and L. Memetea, *Polym. Deg. and Stab.*, 48 (1995) 89.
216. I. C. McNeill, L. Memetea, S. Ahmed and W. J. Cole, *Polym. Deg. and Stab.*, 48 (1995) 395.
217. S. Zulfiqar, M. Zafar-ur-Zaman, A. Munir and I. C. McNeill, *Polym. Deg. and Stab.*, 50 (1995) 33.
218. S. Zulfiqar, K. Masud, B. Siddique and A. Piracha, *Polym. Deg. and Stab.*, 52 (1996) 293.
219. A. Piracha and S. Zulfiqar, *Polym. Deg. and Stab.*, 51 (1996) 27.
220. M. Zulfiqar, A. Piracha and S. Zulfiqar, *Polym. Deg. and Stab.*, 43 (1994) 403.
221. S. Zulfiqar, M. Zulfiqar, M. Rizvi, A. Munir and I. C. McNeill, *Polym. Deg. and Stab.*, 43 (1994) 423.
222. S. Zulfiqar, M. Zulfiqar, M. Rizvi and A. Munir, *Polym. Deg. and Stab.*, 43 (1994) 341.
223. A. Piracha, S. Zulfiqar and I. C. McNeill, *Polym. Deg. and Stab.*, 51 (1996) 319.
224. S. Zulfiqar, M. Rizvi and A. Munir, *Polym. Deg. and Stab.*, 44 (1994) 21.
225. I. C. McNeill and J. J. Liggat, *Polym. Deg. and Stab.*, 36 (1992) 291.
226. I. C. McNeill and M. H. Mohammed, *Poly Deg and Stab* 48 (1995) 175.
227. I. C. McNeill and T. Mahmood, *Polym. Deg. and Stab.*, 46 (1994) 195.
228. M. Suzuki and C. A. Wilkie, *Polym. Deg. and Stab.*, 47 (1995) 217, 223.
229. S. L. Hurley, M. L. Mittleman and C. A. Wilkie, *Polym. Deg. and Stab.*, 39 (1993) 345.
230. Y. A. Aggour, *Polym. Deg. and Stab.*, 51 (1996) 265.
231. I. C. McNeill, J. G. Gorman and S. Besan, *Polym. Deg. and Stab.*, 33 (1991) 263.
232. I. C. McNeill and S. Besan, *Polym. Deg. and Stab.*, 39 (1993) 139.
233. I. C. McNeill and S. Besan, *Polym. Deg. and Stab.*, 39 (1993) 145.
234. I. C. McNeill and M. H. Mohammed, *Polym. Deg. and Stab.*, 50 (1995) 285.
235. A. Rincon and I. C. McNeill, *Polym. Deg. and Stab.*, 40 (1993) 125.
236. A. Rincon and I. C. McNeill, *Polym. Deg. and Stab.*, 40 (1993) 343.
237. I. C. McNeill and S. Besan, *Polym. Deg. and Stab.*, 41 (1993) 311.
238. T. Kovacic, I. Klaric, A. Nardelli and B. Baric, *Polym. Deg. and Stab.*, 40 (1993) 91.
239. T. Kovacic, B. Baric and I. Klaric, *Polym. Deg. and Stab.*, 49 (1995) 365.
240. S. Mohanty, P. G. Mukunda and G. B. Nando, *Polym. Deg. and Stab.*, 52 (1996) 235.
241. M. K. Naqvi and A. R. Sen, *Polym. Deg. and Stab.*, 33 (1991) 362.
242. O. A. Peters and R. H. Still, *Polym. Deg. and Stab.*, 42 (1993) 41, 49; 44 (1994) 107, 113.
243. L. A. Wall and R. E. Florin, *J. Res. Nat. Bur. Standards*, 60 (1958) 451.
244. L. A. Wall and S. Straus, *J. Polym. Sci.*, 44 (1960) 313.

This Page Intentionally Left Blank

Chapter 15

Thermally stimulated currents: recent developments in characterization and analysis of polymers

Bryan B. Sauer

E. I. DuPont de Nemours and Company, Inc., Central Research and Development, Experimental Station, Wilmington, Delaware 19880-0356

This review emphasizes the application of thermally stimulated currents (TSC) and thermally stimulated currents-thermal sampling (TSC-TS) techniques to amorphous and more complicated semi-crystalline and liquid crystalline polymers. Semi-crystalline and related polymer systems are used to illustrate the analysis and interpretation of the TSC techniques. The unique contribution of TSC-TS is in many cases its ability to resolve cooperative transitions, especially in the case of broad or overlapping transitions. Examples are given which reflect the accuracy, reproducibility, and sensitivity of TSC and TSC-TS. Advantages of TSC include its speed of measurement and programmable polarization and depolarization sequences. The flexibility of sample size and geometry are also important for studies of polymers. Comparison with other thermal and relaxation techniques is emphasized and has been shown to be crucial in resolving any controversy concerning interpretation.

1. INTRODUCTION

Thermal and relaxation techniques are widely used for characterization of amorphous polymers, blends, semi-crystalline materials, and other multi-phase materials. Standard methods include NMR, dilatometry, DSC, dynamic mechanical (DMA), rheology, and a.c. dielectric [1-3]. Thermal properties, morphology, and degree of crystallinity can be related to final properties such as strength, toughness, and thermal and environmental resistance. Thermally stimulated currents (TSC), also known as thermally stimulated discharge currents [4,5] or thermally stimulated dielectric depolarization, is a less conventional relaxation technique with a sensitivity comparable to DMA and a.c. dielectric [4,5]. For example TSC results have been quantitatively related to low frequency a.c. dielectric loss measurements for dipolar relaxations, *e.g.*, those associated with chain segmental motions [4-7]. The low equivalent frequency (~

10^{-3} Hz) [4], high data acquisition rate, and high sensitivity make TSC quite useful for the study of relaxations in a variety of materials.

A TSC measurement entails releasing stored charge in an electret by raising the temperature of the sample [4-8]. The typical electret, referred to as a thermal electret [4], is made by cooling a sample under an electric field from elevated temperatures. The drop in temperature freezes in dipolar orientation or charges, which can then relaxed or released later by heating. Because of its relationship to areas such as electrical, technological, device, and characterization, there is renewed interest in thermally stimulated processes in polymers and other materials as is evidenced by the high level of academic and technological activity in the field.

The history of electrets has been summarized in several earlier reviews [4-14]. Electrets were studied by Gray in 1732 [15], where he cooled molten waxes, rosins, sulfur and other materials under an electric field. Electret properties of waxes and related materials were investigated systematically for the first time in 1919 by Eguchi [16]. Many different methods for formation of electrets have been developed since then starting with the standard thermal electret, photoelectret, thermo-photo electret, and magnetoelectret [4-9,12,13]. Electrets have also been formed by a variety of other irradiation techniques including corona and other energetic (γ -ray, β -ray, X-ray, electron beam, ion) irradiations. Details of these electret formation techniques has been given in recent reviews [4,8,13]. Further progress in understanding electrets was made with the advent of thermal depolarization methods first developed by Randall and Wilkins [17] and Frei and Groetzinger [18]. This method was adopted in 1964 for dipolar relaxation studies by Bucci and co-workers [19] who coined the term Ionic Thermal Conductivity, ITC. Relaxation spectra were obtained with the standard method, and activation energies were derived from a method coined ITC-fractional polarizations, which is now widely applied to polymers and materials relaxation studies. Various results for non-polymeric systems have been reviewed previously [7,19,20].

In the 1960's, interest developed in understanding polymer electrets and other electrical device related systems because of technological advances. The high stability of the "permanent" charge in polymers showed that polymer films were an ideal choice for the polymer electret microphone invented by Sessler and West [21]. Electrets formed at high temperatures from films of high temperature-high melting polymers, were found to be the most stable for this application [22]. The same stability, on the order of 1 to 1000 years or more, [22] makes isothermal relaxation studies at the use temperatures unrealistically long. The practical lifetime of polymer electrets was found to be many years and the first "foil-electret" based microphone was commercialized by SONY in the late sixties. The thermally stimulated techniques were shown to accelerate the tests of these materials so evaluation of stability of the electret was almost

routine, leading to a large rise in the number of investigations of polymer electrets in the early 1970's [4,5].

By 1970 the analysis and interpretation were already quite advanced, culminating in the systematic use of TSC (and other thermally stimulated techniques) for molecular interpretation of polymer relaxations [4,5,7]. Extensive comparison with other relaxation techniques such as dynamic mechanical analysis [4,5] and a.c. dielectric [4,5] verified the accuracy of the TSC technique and illustrated some of the advantages of TSC including flexible sample geometry, speed of measurement, and low equivalent frequency for enhanced resolution of relaxations. Controlled temperature-polarization sequences over narrow temperature regions were applied to resolve broad transitions into "narrow distributions of relaxations" [23,24]. Polymer structural series (*e.g.*, methacrylate series with different vinyl groups) were examined by TSC and detailed comparisons were made with other loss techniques such as a.c. dielectric [4,5]. Sophisticated analysis of fully polarized broad TSC transitions, analogous to dielectric loss transitions, gave comparable results to those obtained by other techniques in terms of fitting relaxation distribution functions [25]. In the late 1980's the first commercial-computer controlled TSC instrument became available, further enhancing interest in the materials characterization capabilities of the TSC and related thermally stimulated techniques, and it is the new developments in materials characterization and thermal analysis that will be mainly addressed in this review.

Several reviews of TSC are available [4-14] with some very recent ones [11-14] indicating the sustained high interest in the field. The present review will emphasize the new developments with this technique showing both the unique resolving power for weak relaxations, and also simple experimental methods for verifying the accuracy and improving precision of the technique. For confirmation of the accuracy and interpretation of TSC results, comparison with other techniques is necessary. It will be shown in various examples that differential scanning calorimetry (DSC) can be useful in interpreting the TSC results for complicated systems such as crystalline polymers or blends.

Unlike conventional a.c. dielectric techniques, TSC has the capability of varying the temperature-time-polarization sequence in order to partially excite or de-excite various transitions. In particular, the TSC thermal sampling (TSC-TS) technique (also known as thermal windowing [32] and fractional polarizations [12,19] has become more popular in recent years partly because of the advent of the commercial TSC instrument supplied by Solomat, Inc. (name of Company has changed to TherMold Partners, Stamford CT). In TSC-TS, the sample is polarized over a very narrow temperature range. TSC-TS should not be confused with "thermal cleaning" [25,27] (also referred to as multi-stage TSC) which consists of "full" polarization over wide temperature ranges, with subsequent thermal cycling to partially erase the polarization at certain temperatures.

TSC-TS has been applied to polymers showing the capability of resolving complex dielectric transitions into narrow distributions. These studies have illustrated the advantages of the programmable nature of the polarization sequence which allows one to excite relaxations over narrow temperature regions. In general, explanations for the TSC-TS results and the relationship of the activated parameters to glass transition phenomena are somewhat controversial. The data indicate that the TSC-TS method is uniquely sensitive in the case of weak or overlapping relaxations, where one can resolve “cooperative relaxations”, *e.g.* those corresponding to high values of the apparent activation energy E_a , even if the species are a minor fraction of the overall relaxing species [24,28]. Extensive comparison with other techniques has been useful at arriving at this conclusion, although the theoretical basis for this high sensitivity to the fraction of cooperatively relaxing species is not well understood. Qualitative discussion of this high sensitivity is given in section 4. Briefly, the high sensitivity to the cooperative relaxations is related mainly to the polarization and depolarization sequences used, and from the method used for calculating the apparent activation energy (E_a) from the low temperature side of the TSC-TS peaks. It will be shown with many experimental examples that one of the most interesting applications is to use the TSC-TS values of E_a to characterize broad and weak glass transition regions. The method involves comparing the values of E_a with a recently developed semi-empirical prediction [28,29], to characterize the cooperative nature of the relaxations.

The literature is growing at a rapid pace because of the important capabilities of TSC to the study of electrical, relaxation, and thermal properties of polymers and other materials. Reviews of TSC applied to polymers are available, as are reviews of TSC applied to many other areas of material science and physics [12,13]. The literature survey by Lavergne and Lacabanne in 1993 contains 500 references [12]. Van Turnhout emphasizes the analysis of relaxation distributions, structure property determinations, interpretation of transitions using many clever control experiments, mathematical analysis of relaxation distributions, and comparison with different relaxation and thermal analysis techniques [4,5]. He also gives a very complete summary of the many sample and instrument geometries used for TSC and related studies. Although he discusses thermal windowing where samples are “fully” polarized and then partially relaxed by heating to incrementally higher temperatures, he does not talk about TSC-TS (also known as fractional polarizations) technique originally developed by Bucci *et al.* [19], and applied to polymers by Chatain *et al.* [23], and Zeilinski and Kryszewski [24]. The TSC-TS technique and its interpretation will be reviewed below, with some emphasis on the reproducibility of data from various laboratories.

We now present a partial list of selected TSC-TS references by polymer type. Some recent references for TSC-TS studies are given, although the list is

far from complete. "Global" TSC references will not be given here, nor will thermal windowing or other related techniques. Such results for amorphous polymers such as poly(methyl methacrylate) (PMMA), polystyrene, and many others have been presented in the book by Van Turnhout [4]. He also studied many other semi-crystalline polymers and oriented films. Many other references to global TSC studies of polymers can be found [7-14,28].

Possibly the most widely studied amorphous polymers by TSC-TS are bisphenol-A polycarbonate (Lexan[®], PC) [28,30,31] and poly(methyl methacrylate) [26,28,32,33], Poly (vinyl chloride) (PVC) [34,35] has been widely studied, and the results have been compared to those obtained by thermally stimulated creep [34]. Crystallizable polymers include semi-crystalline polyethylene [36-39], poly(propylene) [40,41], PPS [42], PEO [43,44], PBT [45], nylon 6,6 [23], poly(ethylene terephthalate) (PET) [46,47], poly(oxymethylene) (POM) [48], and poly(*trans*-1-octenylene) [49]. Also, poly(aryl ether ketones) including PEEK [50,51] and PEKK [50,52]. Thermally stimulated creep studies of polyethylene [53], poly(propylene) [40,53], and PVC [34,54] also show much promise in resolving complex transitions. The TSC and TSC-TS literature for liquid crystalline polymers and liquid crystals has increased rapidly starting only a few years ago, and will be reviewed in section 6. Studies of fluorinated polymers will also be reviewed in section 6. Composites [55] and "nano-composites" [44] have also been studied by TSC-TS, and crazed polymers have been studied by TSC [56]. Blends of PVC [57], semi-crystalline polyesters [45], and PEEK [50] have been studied by TSC-TS, and PVC blends have also been studied by TS-creep [54]. Polypropylene copolymers have been extensively studied by TSC-TS [58-60].

2. EXPERIMENTAL SECTION

2.1. TSC Instrument

The TSC instrument used in our laboratory was a Solomat model 41000 (Name of company has changed to TherMold Partners, Stamford, CT. The TSC instrument is now TherMold TSC-RMA 9000 or 3000). The instrument typically is used over the temperature range of about -180°C to 300°C. A Faraday cage shields the sample and a cold finger and a heating coil are used for the temperature control [4,7,61]. Before the experiment is started the sample cell is evacuated to $\sim 10^{-4}$ mbar and then flushed with 1.1 bar of high purity He (Grade 5.5, 99.9995%, Keen compressed gas). Most TSC instruments have the same common feature where the main component is a very sensitive electrometer for detection of the depolarization currents. Modern instruments allow one to routinely measure currents down to the 10^{-16} amps.

Temperature is recorded using a PT-100 thermocouple positioned in the cell near the sample. The temperature calibration for our instrument was routinely

checked with different polymers with known glass transitions such as bisphenol-A polycarbonate (Lexan[®] $T_g = 147^\circ\text{C}$ at heating rates of $7^\circ\text{C}/\text{min}$).

2.2. Sample preparation and geometry

Thermally stimulated polarization and depolarization can be performed using a variety of sample geometries and electrode arrangements. These have been reviewed by Van Turnhout [4,5]. A common method for the formation of electrets for device applications is to charge the polymeric film using an air gap, in part motivating many studies of thermally stimulated processes using this arrangement for polarization.

For all of the results reviewed here, both sides of the sample are in “contact” with electrodes, somewhat like the standard arrangement for a.c. dielectric. Parallel plate electrodes were used in the majority of the experiments with the upper plate spring-loaded to maintain electrical contact during thermal cycling. Films for TSC were between 0.05 and 0.3 mm thick with areas of 2 to 100 mm^2 for TSC. Films were pre-dried typically by heating to close to T_g under vacuum, and then stored if necessary under dry conditions to avoid water vapor sorption. Film thickness also did not affect the results to a first approximation. For most of the samples, 0.1 - 0.4 mm thick unmetallized films were sandwiched between spring loaded steel disks used as electrodes.

In some cases the “parallel plate” geometry was not used. One alternative was to use colloidal silver by painting it onto the polymer sample. It also served as glue for small wires which were then fixed to the instrument electrodes and served to suspend the sample in the Faraday cage near the thermocouple. The silver painted electrodes could not be used above ca. 180°C because of decomposition. One must also be aware of the possibility of plasticization by the solvent (xylenes) used in the silver suspension.

To improve electrical contact for some studies, both sides of the polymer film were sputter coated with gold/paladium as is quite standard in the literature. In certain cases, mainly with high T_g polymers, the sputter coating lead to irreproducible and spurious results, mainly in terms of a modified shape of the global TSC curve just below T_g [50]. The TSC-TS results did not seem to be affected but typically we avoided the use of sputter coated electrodes on our polymer films for experiments above 100°C . This may be specific to the instrument used and not necessarily a general phenomenon for all TSC experiments. Cracking of the gold/paladium coating on the films during thermal cycling was observed for high temperature polymers and this could possibly be a factor contributing the irreproducible data which generally consisted of spurious signals sometimes an order of magnitude larger than expected. Experiments with different sample areas showed some advantages of smaller sample areas, at least with the high temperature polymers [50]. We found that rather small

sample areas of about 5-25 mm² were optimum, unless working with very low loss materials where larger sample areas were sometimes needed.

2.3. Polarization/Depolarization Sequences

A schematic for the polarization sequence used for the standard global TSC experiment is shown in the left hand side of Fig. 1. The sample is heated and then polarized by a static electric field (~ 1000 kV/m) over a temperature range from the polarization temperature T_p down to the "freezing temperature" T_o , with cooling during polarization at $30^\circ\text{C}/\text{min}$ to freeze in polarization. With the sample short circuited and $E = 0$, the depolarization current is then measured as the sample is heated at $7^\circ\text{C}/\text{min}$ from T_o to the final temperature $T_f (\geq T_p)$ resulting in a global TSC spectrum. The spectrum is due to a convolution of all dielectrically and electrically active relaxations over the temperature and frequency range probed. Van Turnhout [4] has presented many examples of various polarization sequences and experimental geometries. He has also considered the effect of full or partial polarization in the study of broad loss transitions.

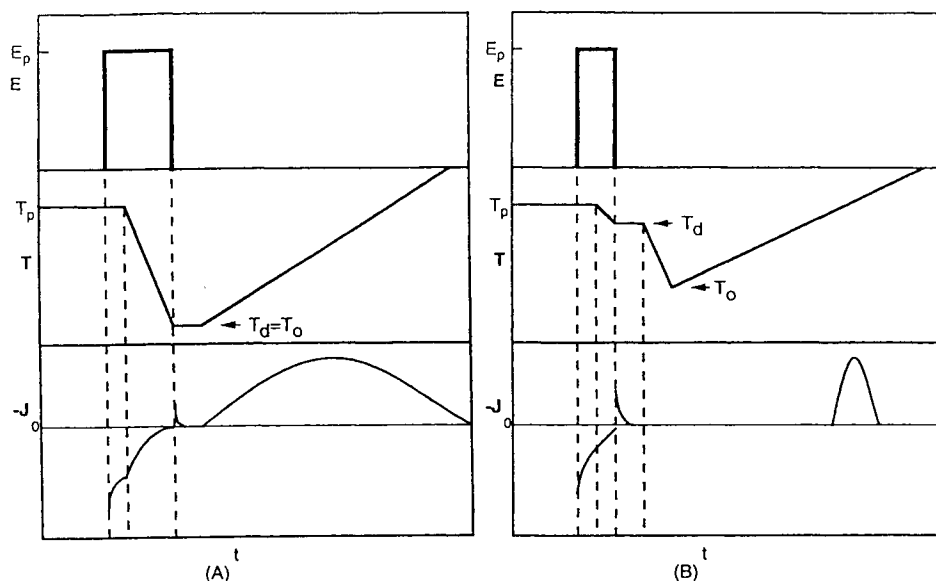


Fig. 1. A schematic of the polarization sequence taken from reference 42 for: (A) "Global" TSC polarized over a wide temperature range, and (B) TSC thermal sampling (TSC-TS) for narrow polarization temperature windows. The ordinates are from top to bottom, respectively, polarization field strength (E), temperature, and depolarization current (J). The x-axis is time. See methods section for details of polarization times, polarization temperatures (T_p), depolarization temperatures (T_d), and quench temperatures (T_o).

Spectra in the TSC-TS mode were obtained using the standard procedure indicated in Fig. 1b [23,28,42]. The important aspect of the TSC-TS experiment is the very narrow temperature window over which the sample is polarized relative to the global TSC (Fig. 1a). First, the polarizing field is applied for 2 min. at T_p . With the field left on, the sample is cooled at $5^\circ\text{C}/\text{min}$ to $T_p - 5^\circ\text{C}$. At this point the field is removed to depolarize for 2 min. at $T_p - 5^\circ\text{C}$. The sample is then quenched at $30^\circ\text{C}/\text{min}$ with the field off to about 40°C below T_p . The TSC-TS depolarization current is then measured upon reheating at $7^\circ\text{C}/\text{min}$ to values about 40°C above T_p . This same polarization sequence has been used in all of the results from this laboratory, although we have found that the resulting activated parameters are remarkably insensitive to small differences in the exact details of polarization sequence. In other words, the polarization parameters can be modified slightly but the TSC-TS technique will still do an effective job of exciting only a narrow distribution of relaxations.

3. ANALYSIS OF TSC-TS DATA

3.1. Bucci-Fieschi-Guidi and related analysis methods

For an ideal Debye relaxation with a single relaxation frequency, relaxation times $\tau(T)$ can be obtained from the experimental TSC-TS spectra using the standard Bucci-Fieschi-Guidi [19] or “BFG” method. A slightly modified version of this method applied to nearly single Debye relaxation spectra will be described below. Relaxation times (T) for a single Debye relaxation are defined by the BFG equation [4,19]:

$$\tau(T) = P(T)/J(T) \quad (1)$$

where $P(T)$ is the remaining polarization as is illustrated schematically in Fig. 2 at an arbitrary temperature. The TSC-TS current spectra are integrated numerically to obtain $P(T)$ [19]

$$\tau(T) = \frac{1}{\beta} \left\{ \int_{T'}^T J(T') dT' \right\} / J(T) \quad (2)$$

where β is the heating rate, T_u is an upper temperature where all current has been released, and $J(T)$ is the depolarization current. $\tau(T)$ is thus calculated and can be plotted as a “BFG” Arrhenius curve as a function of $1/T$. The Solomat analysis uses a slightly modified form of the BFG method contrary to what is stated in our previous publications. Furthermore, the limits of the integral in the “BFG equation” given in some of our previous reports are incorrect [28,50,52], although the calculations were done correctly.

For distributed relaxations it is known that the BFG method gives low values of E_a [4], although for properly cleaned peaks this can be a minor factor in obtaining accurate values of E_a because the distribution of relaxations is forced to be narrow by the narrow polarization windows used in the TSC-TS polarization sequence. For thermally sampled TSC peaks with a narrow distribution of relaxations, one can apply an empirical correction [62]. This will remove or reduce the curvature found in $\tau(T)$ vs. $1/T$ BFG plots. The standard definition of P is:

$$\beta P(T) = \int_T^{\tau_c} J(T') dT' = \int_0^{\tau_c} J(T') dT' - \int_0^T J(T') dT' = \beta P_0 - \int_0^T J(T') dT' \quad (3)$$

Remember that P_0 is readily determined by numerically integrating the area of the entire experimental TSC-TS spectrum, as is indicated by Eq. (2). The modified method consists of dividing the total polarization (P_0) by a factor of about 1.3 as is shown in Eq. (4) to correct for the fact that the total polarization is larger than it would be for a single Debye relaxation [62].

$$\beta P(T) = \beta P_0 / 1.3 - \int_0^T J(T') dT' \quad (4)$$

The modified value of $P(T)$ is then used in the BFG equation (Eq. (1)). The value of 1.3 is empirically determined and the method allows one to only obtain accurate values of $\tau(T)$ up to the peak maximum in the TSC-TS spectra. With the BFG method, curvature in the Arrhenius plot is generally seen well before the peak maximum, unless the peak is due to a single Debye relaxation [4].

Using a depolarization heating rate of about $7^\circ\text{C}/\text{min.}$, the values of $\tau(T)$ determined from each TSC-TS spectrum fall in a range of about $10^1 \text{ s} < \tau < 10^4 \text{ s}$. They are plotted versus reciprocal temperature in the BFG Arrhenius or related plots. The Arrhenius equation is typically used analyze the temperature dependence of the relaxation data:

$$\tau(T) = \tau_0 \exp(E_a/RT) \quad (5)$$

where τ_0 is the pre-exponential factor, E_a is the apparent activation energy, and R is the ideal gas constant. One TSC-TS spectrum typically gives one value of E_a . For a linear dependence of $\ln(\tau)$ on $1/T$, the slope is equal to $E_a/R = E_a/1.987$ if E_a is in cal/mol. The magnitude of the Arrhenius prefactor (τ_0) is in many cases unrealistic for high E_a relaxations such as glass transitions, and often reaches values smaller than 10^{-60} s. Unfortunately, the corresponding Eyring intercept (related to ΔS^\ddagger discussed below) also becomes physically unrealistic in the vicinity of glass transition like relaxations, so it offers no improvement.

The other method of empirical analysis that is commonly used and may give more physically realistic parameters, at least in the case of low temperature non-cooperative relaxations, is based on Eyring's activated states equation.

$$\tau = 1/2\pi f = h (kT)^{-1} \exp(\Delta H^\ddagger/RT) \exp(-\Delta S^\ddagger/R) = h (kT)^{-1} \exp(\Delta G^\ddagger/RT)$$

$$\Delta G^\ddagger = \Delta H^\ddagger - T\Delta S^\ddagger \quad (6)$$

Here f is frequency, k is Boltzmann's constant, h Plank's constant, and ΔH^\ddagger , ΔS^\ddagger , and ΔG^\ddagger are the activated states enthalpy, entropy, and free energy, respectively. If one considers the frequency plot, then the intercept of the Eyring plot of f/T_{max} vs. $1/T_{max}$ is $k/(2\pi h)\exp(\Delta S^\ddagger/R)$ from which ΔS^\ddagger can be calculated. Alternatively, one can calculate ΔS^\ddagger using

$$\Delta S^\ddagger(\tau, T) = R[\ln(h/\tau kT)] + \Delta H^\ddagger/T \quad (7)$$

As with the analysis of relaxation times determined by other techniques [1], the two different ways of representing the data, the Eyring $\ln(\tau T)$ vs. $1/T$ analysis, or the Arrhenius $\ln(\tau)$ vs. $1/T$ analysis, are essentially equivalent ways of looking at the same data. There is no way to distinguish any difference in quality of fit between the two equations, even for data covering almost 8 decades in frequency and spanning more than 100°C, as will be discussed later in the context of Fig. 16 (see below).

3.2. TSC-TS curve fitting methods

An alternative method for obtaining relaxation parameters from TSC-TS data is to fit the curve directly using the standard equation derived by Bucci, *et al.* for a single Debye relaxation [19]:

$$J(T) = P_0 / \tau_0 \exp\{-E_a / RT - s / \tau_0 \int_{T_0}^T \exp(-E_a / RT') dT'\} \quad (8)$$

Here P_0 is a constant related to the polarization. The integral in Eq. (8) can be approximated as [43]:

$$\int_{T_0}^T \exp(-\frac{E_a}{RT'}) dT' = \frac{T' \exp(-x)(x + 3.0396)}{x^2 + 5.0364x + 4.1916} \Big|_{T'=T_0}^{T'=T} \quad (9)$$

where x equals E_a/RT . Eq. (8) is a rapidly changing function which, unlike experiment, predicts a spectrum which is quite asymmetric as a function of temperature. One can generate symmetric spectra by assuming a Gaussian distribution of relaxations as in [36,37,43]:

$$J(T) = \int_0^{\infty} \exp[-(E_a - E_{a,0})^2 / 2\sigma^2] J(T, E_a) dE_a \quad (10)$$

where $E_{a,0}$ is the mean activation energy and σ is the width of the Gaussian distribution. Surprisingly, one can also generate symmetric TSC spectra by assuming discrete values of E_a [28,52]:

$$J(T) = \sum_{i=1}^3 a_i J(T, E_{a,i}) \quad (11)$$

where a_i is the amplitude corresponding to the i th activation energy $E_{a,i}$, and J is calculated using Eq. (8). We have found that in general, assuming two or three discrete values of E_a with a distribution less than $\pm 0.03E_a$ results in a relatively symmetric peak which fits the data.

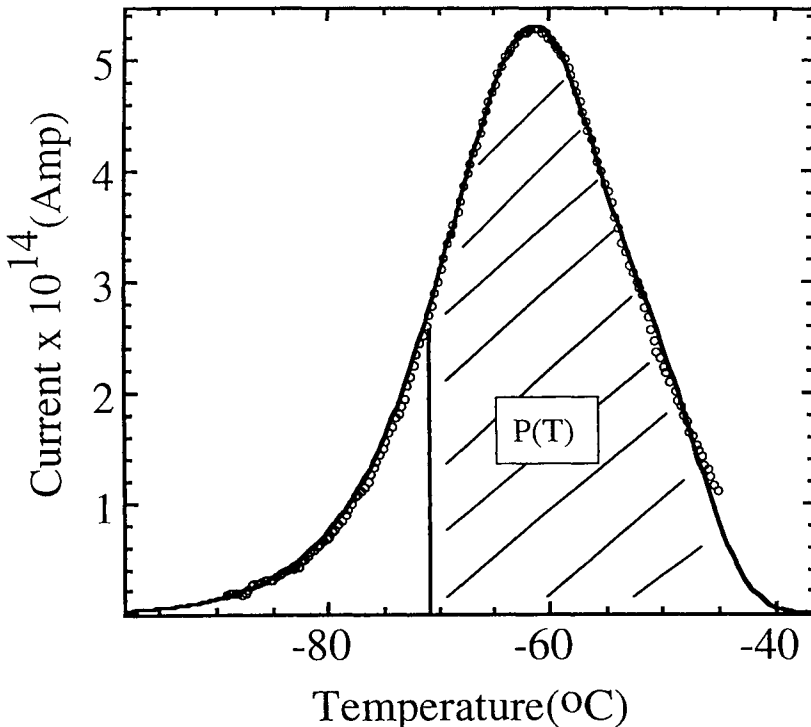


Fig. 2. Representative TSC-TS spectrum for poly(aryletherketoneketone) PEKK [52]. The remaining polarization for a temperature of -71°C is indicated by the shaded region. The solid line is a fit using Eq. (11).

It has been suggested that there is more than an order of magnitude discrepancy [37] between the full peak fitting method (Eq. (10)) and the Bucci (Eq. (1)) methods of analysis. Others have shown that the mean values of E_a determined by the two methods agree within a few percent [28,52]. Several more examples will be given later and the various analysis procedures for fitting the data will be compared in Section 5.1.

3.3. Compensation

In the discussion of TSC-TS data, one must address the issue of compensation because of its prevalence in the literature. This is still a controversial area regarding interpretation of the TSC-TS relaxation curves. Since the results are accurate and reproducible, regardless of the analysis scheme chosen, the data hopefully will lead to the same conclusions. The compensation equation (Eq. (12)) suggests that at the compensation point T_c , all relaxations occur at a single relaxation time τ_c . Read [63] has obtained experimental evidence with low frequency mechanical measurements at the compensation point in polypropylene [40], proving that there is no unique relaxation at T_c as would be expected considering the heterogeneous local environments in polymer glasses and related materials which generally contribute to broad transitions.

Compensation, also called the "isokinetic" effect [64], has been controversial for more than thirty years in its application to chemical kinetics [64-66]. Compensation is the linear relationship or "correlation" between the apparent activation energy, E_a , and the prefactor, $\log \tau_o$ (or equivalently a correlation between ΔH^\ddagger and ΔS^\ddagger from the Eyring analysis) [28,64]. The controversy in chemical kinetics is apparently similar to that in polymer relaxations. Exner [64] has discussed the danger of attempting to correlate E_a and $\log \tau_o$ because they are not independent of each other. Garn [65] also discusses the same issues in detail. Although significant effort over thirty years has been devoted to dismissing the validity of compensation [64-66], it is still prevalent in the materials relaxation literature.

At this point we discuss the mathematical details of using the compensation equation to fit the data. Compensation is defined in terms of the linear dependence of E_a with $\ln \tau_o$, or in an algebraically similar form in terms of the ΔH^\ddagger and ΔS^\ddagger [28,67]. The compensation point is defined in frequency-temperature space by two phenomenological parameters; the compensation temperature T_c and the compensation frequency or relaxation time, $[f_c = 1/(2\pi\tau_c)]$:

$$\tau_o = \tau_c \exp(-E_a/RT_c) \quad (12)$$

Substituting Eq. (12) into the Arrhenius equation (Eq. (5)) gives the compensation equation:

$$\tau(T) = \tau_c \exp[E_a(1/T - 1/T_c)/R] \quad (13)$$

Eq. (12) shows that the slope of a plot of $\ln \tau_o$ vs. E_a/R gives the reciprocal compensation temperature ($1/T_c$), and the intercept is the compensation frequency τ_c . An analogous expression can be derived starting with the Eyring equation instead of the Arrhenius equation [28,67].

To illustrate compensation, a typical plot of Arrhenius curves of BFG relaxation times is shown in Fig. 3 for PEMA. Each experimental curve, covering the range $10 \text{ s} < \tau < 1000 \text{ s}$, was obtained from a single TSC-TS

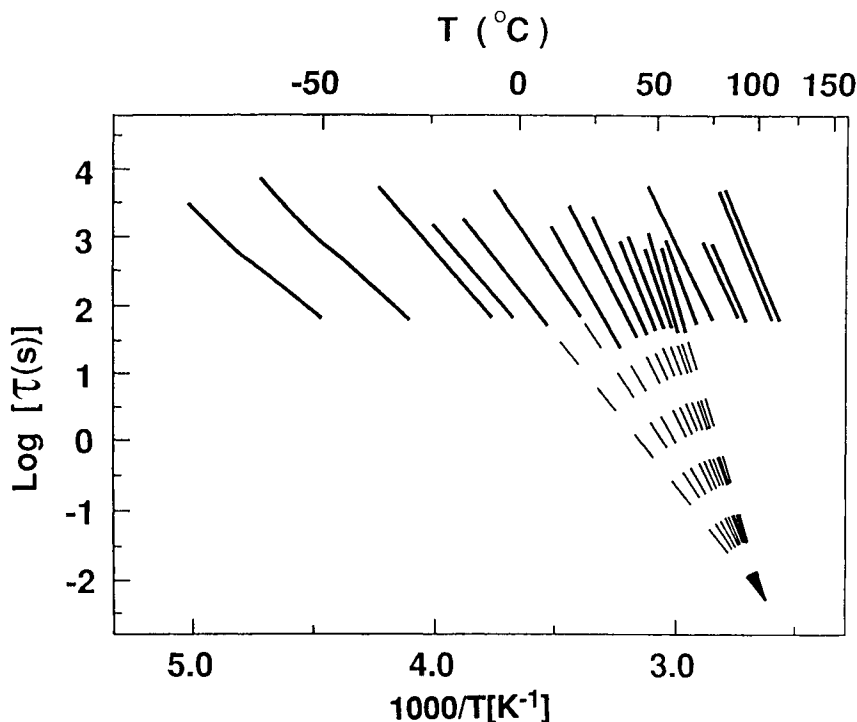


Fig. 3. Arrhenius plots of BuCCI curves for poly(ethyl methacrylate) PEMA of the calculated relaxation times (τ) versus $1/T$ obtained by fractional integration of the TSC-TS spectra. The polarization temperatures are approximately the center point of each line and the peak maxima occur near the high temperature end of each Arrhenius line. The extrapolated compensation point is indicated by the dashed lines coming to a focus [28].

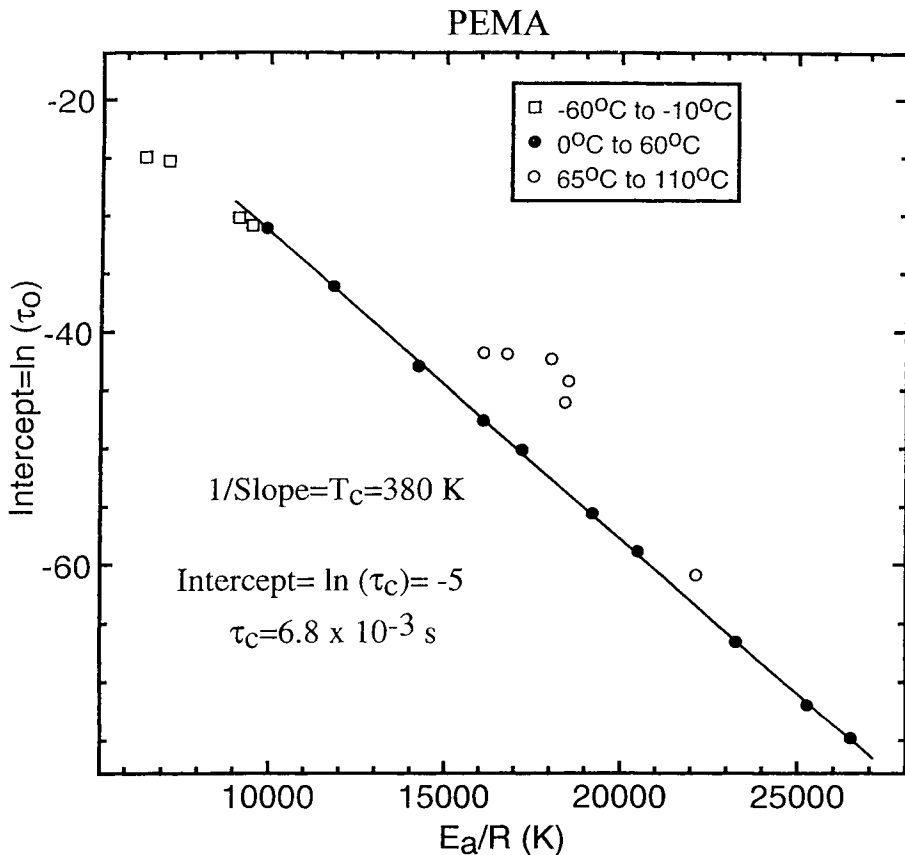


Fig. 4. Arrhenius parameters for PEMA plotted as intercept ($\log \tau_0$) versus slope (E_a/R) to indicate the region of compensation. The linear points indicate the region of compensation. Ranges of T_p (°C): \square : -60 to -10; \bullet : 0-60; \circ : 65-110 [28].

spectrum taken at a given polarization temperatures (T_p) using the modified BFG method of obtaining $\tau(T)$ as a function of T (Eq. (4)). Qualitatively, it can be seen that the slope (E_a/R) increases substantially near T_g ($T_g \sim 55^\circ\text{C}$), which causes the extrapolated lines to come to a focus point in frequency-temperature space. The focus point is defined mathematically by the two compensation parameters, τ_c and T_c . One can examine the quality of fit to the compensation equation (equation 3.12) by the linearity of the plot of E_a vs. $\ln \tau_0$. The linear fit is quite good for PEMA (Fig. 4) for the points corresponding to T_p between 0°C up to $T_p = T_g \sim 60^\circ\text{C}$, e.g., those data points corresponding to the compensating lines. From the slope of the linear data in Fig. 4, we extract values of $T_c = 108 \pm 5^\circ\text{C}$ and $\tau_c = 6.8 \times 10^{-3}$ sec. Recent work has reiterated the idea that compensation

is due to the covariance of E_a and $\ln\tau_o$ [68], so these parameters probably have little or no physical significance.

4. INTERPRETATION OF GLOBAL TSC RESULTS

4.1. Comparison of global TSC with a.c. dielectric and other techniques

Significant effort has been devoted to the comparison of TSC results with those obtained using a.c. dielectric, DSC, dynamic mechanical, and other methods. Van Turnhout [4] has shown quantitative similarities between experimentally obtained "global" TSC spectra and low frequency isochronal dielectric loss spectra. He derived relationships which illustrate the quantitative relationship between a.c. dielectric loss(ϵ'') and the depolarization current ($J[t]$):

$$\epsilon''(f) = J(t)/(A2\pi \epsilon_o f E) \quad (14)$$

where A is the area of the sample, E the TSC polarizing field strength in V/m, $\epsilon_o = 8.854 \times 10^{12}$ F/m is the vacuum permittivity, and f is the equivalent frequency of the TSC experiment defined by:

$$f = E_o/(2\pi sRT^2) \quad (15)$$

where s is the inverse heating rate(eg., $7^\circ\text{C}/\text{min} = 8.57^\circ\text{C}/\text{sec}$), and $R = 1.987$ cal $\text{K}^{-1}\text{mol}^{-1}$ is the ideal gas constant. The equivalent frequency of TSC is on the order of 10^{-3} Hz or 10^{-4} Hz for typical heating rates.

Each global TSC scan represents a convoluted spectrum of the dielectrically active relaxations excited between T_p and T_o . It has been shown that the integrated peak area of a given transition is related to the strength of the transition defined by the dielectric increment [4]

$$\Delta\epsilon = \frac{1}{E\epsilon_o} \int_{t_o}^{\infty} \frac{J}{A} dt \quad (16)$$

where t_o to infinity is the time-span which covers the entire transition measured upon reheating at constant rate, and the dielectric increment is defined as [1]

$$\Delta\epsilon = \epsilon'_\infty - \epsilon'_o \quad (17)$$

where ϵ'_∞ is the dielectric constant at high frequency(or low temperature), and ϵ'_o is the dielectric constant at low frequency(or high temperature). Since the TSC experiment is obtained at constant heating rate, temperature was converted to

time in Eq. (16). Thus, the strength of the transitions measured by TSC can be quantitatively compared with those measured by a.c. dielectric, and this is a very important tool in verifying the accuracy of TSC [4,56].

4.2. Global TSC studies of glass transitions and $T > T_g$ transitions, comparisons with other techniques

We start with a discussion of glass transitions and higher temperature ($T > T_g$) transitions in amorphous and low to moderate crystallinity polymers and related materials, because these are the most widely studied and are also somewhat controversial. Relaxation studies of glass transitions are also of interest because the glass transition is the dominant relaxation and is important in understanding mechanical and thermal properties, even in semi-crystalline

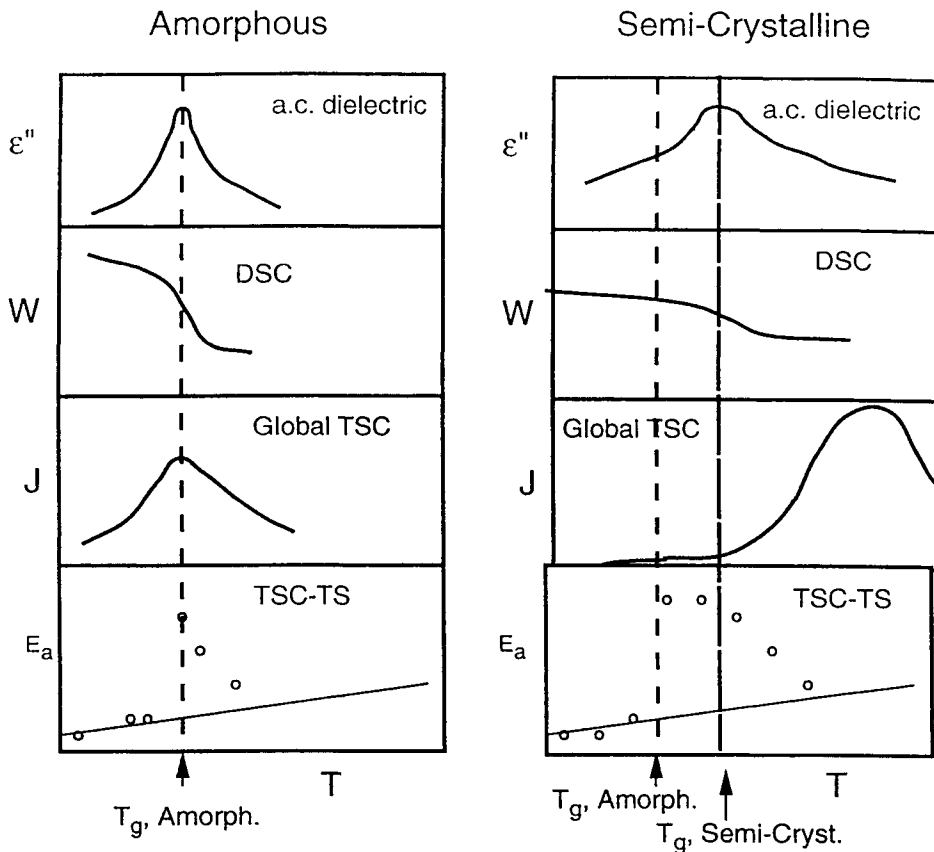


Fig. 5. Schematic of the sensitivity of different thermal analysis techniques for the study of glass transitions in a model amorphous polymer (left) versus the same material in its semi-crystalline form (right). All are corrected to the same equivalent frequency of about 10^3 Hz for comparison purposes.

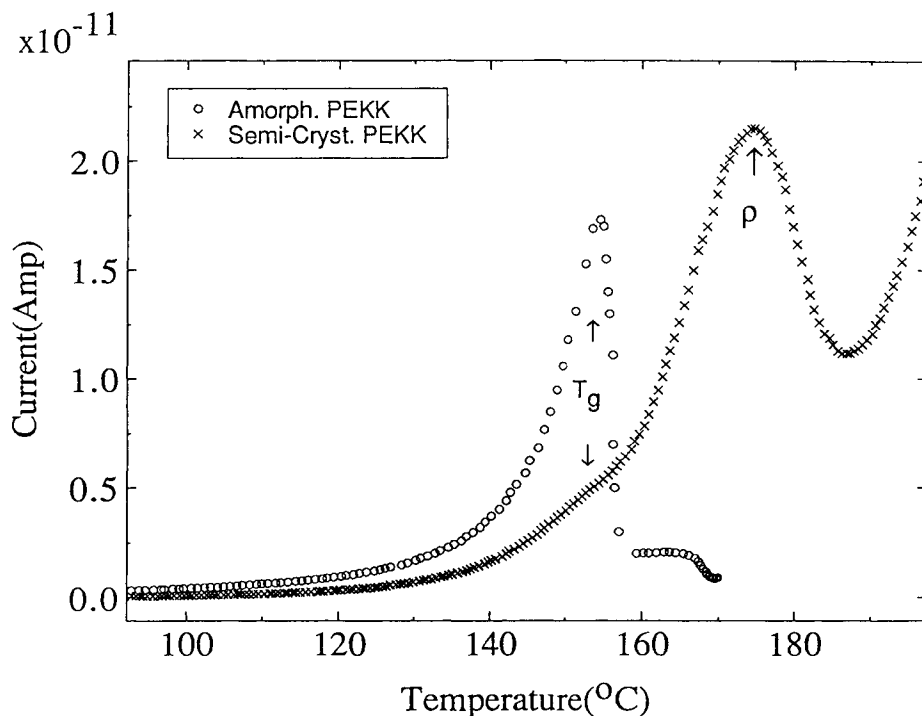


Fig. 6. Global TSC for PEKK [52]. The glass transition does not shift substantially with crystallinity, but becomes broader and weaker. Heating rate was $7^{\circ}\text{C}/\text{min}$, $T_p = 160^{\circ}\text{C}$ for amorphous, and $T_p = 260^{\circ}\text{C}$ for the crystalline sample.

amorphous material, it is shown that all techniques detect the same T_g , with TSC typically detecting a slightly broader transition due to the integral relationship between the strength of the transitions (related to each other by Eq. (16)). Regarding the general sensitivity of the various methods, DSC typically detects only cooperative relaxations which tend to occur over a relatively narrow range of about 15°C for amorphous polymers [69]. Relaxation techniques like a.c. dielectric, DMA, NMR, and global TSC detect a broader spectrum of motions, where a mixture of both cooperative and more localized non-cooperative motions contribute to a “total” transition width which is sometimes 50°C wide or more, depending on the measurement frequency, even if the DSC transition is ca. 15°C wide.

For the semi-crystalline form of the same hypothetical moderate crystallinity polymer, the transitions are typically broader, weaker, and sometimes shifted to slightly higher temperatures [69] as can be seen directly in a.c. dielectric and DSC data in the right hand side of Fig. 5. The situation should not be confused with the flexible high crystallinity materials such as

polyethylene or poly(tetrafluoroethylene). The vertical dashed line indicates the T_g for the original amorphous state, and the vertical solid line indicates the slightly shifted semi-crystalline T_g . Although the glass transition is relatively easily detected by DSC and a.c. dielectric, a clear maximum is generally not seen in the global TSC spectrum, because the transition becomes too weak and broad to detect directly. We are only concerned with complete polarization in this example. With partial polarization, a TSC maximum can be introduced at any desired temperature by limiting the maximum polarization [4]. The broadened transition is not detected because of the integral relationship of the strengths of the glass transitions in term of $\Delta\epsilon'$ and J defined by Eq. (16), which lead to an exaggerated broadening in global TSC. Furthermore, with global TSC the $T > T_g$ peak (ρ transition) is very strong and overlaps strongly with the very weak and broad glass transition, as is illustrated schematically in Fig. 5 and by experimental data in Figs. 6 and 8. This can cause confusion because one is tempted to associate the ρ transition with the semi-crystalline glass transition because it is approximately where one would expect it to be, e.g., somewhat above T_g . A strong indication that it is not a dipolar transition like the glass transition, is that it is usually at least as intense as the amorphous glass transition (e.g., Fig. 6), which we already know from other techniques is not true.

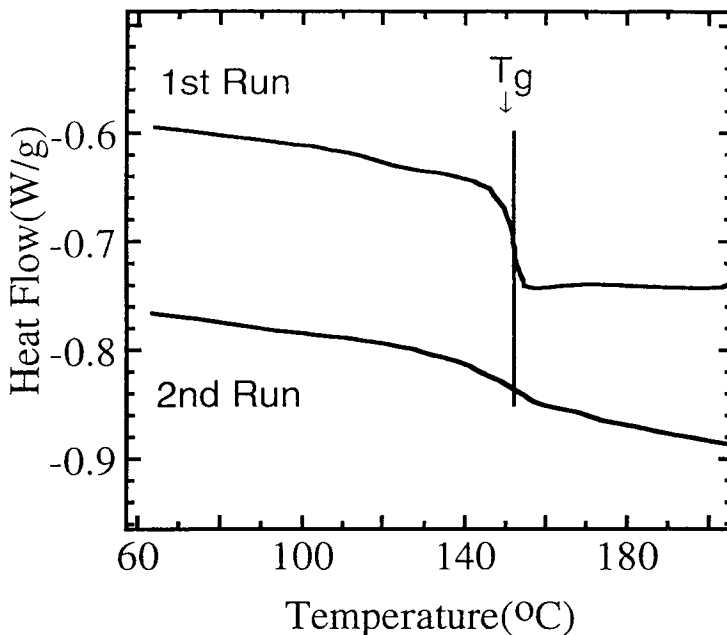


Fig. 7. DSC at 10°C/min for amorphous and semi-crystalline PEKK showing the weakening of the glass transition. The samples were the same as those studied in Fig. 6.

In many cases it is much more intense, and Eq. (16) shows that this cannot be the case. Furthermore, on closer examination with the results from other techniques at the same frequency such as DSC, it is generally found that the ρ peak does not really occur at the correct temperature. Either or both of these features are strong evidence that the ρ transition is not the glass transition.

Let us now turn to actual experimental data on some moderate crystallinity, "rigid" high T_g polymers. The importance of this class of polymers [including PET and poly(aryl ether ketones), and many others], which are utilized in a variety of relaxation and crystallization studies, is that they can be quenched into their purely amorphous forms unlike more rapidly crystallizing, lower T_g polymers like polyethylene and poly(butylene terephthalate), where the purely amorphous form is very difficult to obtain and/or study. As was discussed above, in many cases the semi-crystalline glass transition "peak" is difficult to detect directly in semi-crystalline polymers by global TSC. In some experimental examples, the broadened glass transition can be detected as a low temperature shoulder on the ρ transition [50,52], while in other examples it is so weak that no hint of it remains [42,50,51] in the global TSC spectrum, as was the

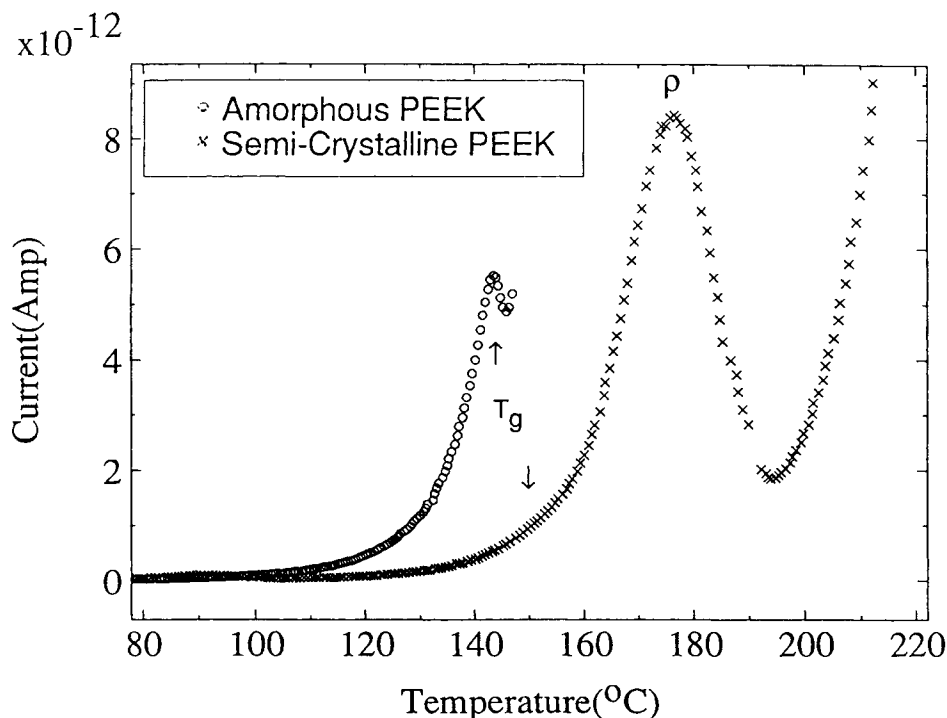


Fig. 8. Global TSC for PEEK (150G, ICI). $T_p = 150^\circ\text{C}$ for amorphous PEEK, and $T_p = 200^\circ\text{C}$ for semicrystalline PEEK [50]

case for our hypothetical semi-crystalline material in Fig. 5. For example, global TSC spectra for typical polymers in their amorphous vs. semi-crystalline state are given in Fig. 6 and Fig. 8. For the lower crystallinity PEKK, where DSC clearly shows that the glass transition is not shifted to higher temperatures (Fig. 7), one can see a weak shoulder on the TSC corresponding to the semi-crystalline polymer at the approximate temperature where the original amorphous glass transition was detected. This is indicated by the arrow in Fig. 6. The DSC data for PEKK in Fig. 7 for the same systems, show that the transition is only a factor of two weaker in terms of the total step in heat capacity, yet because it becomes broader and overlaps with the strong ρ transition, it becomes significantly less intense in the semi-crystalline global TSC, and cannot be detected as a clear peak.

For the slightly higher crystallinity PEEK material in Fig. 8, no hint of the glass transition is detected in the global TSC after crystallization because the transition becomes so weak and broad due to crystallinity, leading to some controversy [50,51]. The amorphous glass transition is seen by TSC (Fig. 8) and DSC (Fig. 9) to be sharp and relatively strong, while the semi-crystalline glass transition is seen to be weaker and shifted from the nominal $T_{g,\text{amorph}} = 143^\circ\text{C}$ to about $T_{g,\text{cryst.}} = 153^\circ\text{C}$ in the DSC results (Fig. 9) for the particular crystallization conditions chosen [69,70]. Without the DSC data, one may be tempted to assign the ρ transition at about 177°C in Fig. 8 as the semi-crystalline glass transition, which is incorrect because it occurs at the wrong temperature according to DSC

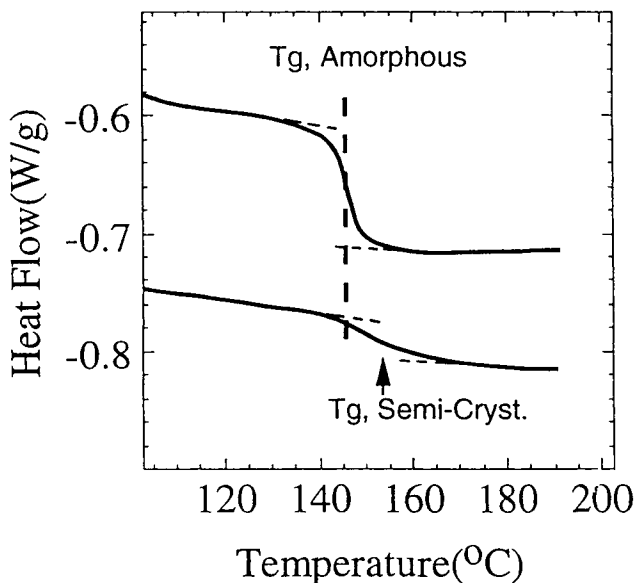


Fig. 9. DSC at $10^\circ\text{C}/\text{min}$ heating rates for amorphous and semi-crystalline PEEK

(and other methods such as DMA), and is also too intense relative to that expected based on the DSC results (Fig. 9). This reinforces the need for comparison with other techniques where it is seen by DSC and dielectric that the real semi-crystalline glass transition occurs at a temperature well below the ρ transition (Fig. 6). Unlike global TSC, using the values of the activation energies (E_a) determined by the TSC-TS method, the glass transition region is defined as the region where cooperative high activation energy relaxations are detected. Thus, the TSC-TS technique shows the same trend as DSC in terms of the position of T_g as we have emphasized in Fig. 6. Other features of the TSC-TS technique and its corresponding values of E_a for PEKK and other semi-crystalline materials, will be used as examples in later sections.

4.3. Interpretation of the $T > T_g$ or ρ transition at higher temperatures

As was discussed above, the ρ transition occurs above T_g although the exact physical basis of the transition could vary depending on the system. The ρ transition has been shown in many studies to be due to injected space charges and/or other electrode effects, although this is still controversial. For semi-crystalline polymers and for other materials with multi-phase morphologies such as composites, Maxwell-Wagner interface polarization [4] also contributes to the measured signal. Space charges must also contribute above T_g because they are almost always associated with mobile charged impurities such as ions, and these are invariably released above T_g . The presence of water almost always enhances the ρ transition [4,28].

Further confirmation of the space charge mechanism is seen in Van Turnhout's original experiments. Van Turnhout [4] performed an "interrupted" global TSC experiment where the PMMA film was first polarized in the normal way during cooling to the quench temperature, and then removed from the cell and sectioned into three layers. Next, each layer was studied separately in a standard depolarization heating experiment. For the outer sections, which were originally adjacent to the original polarizing electrodes, previously injected space charges contributed to a strong ρ peak in the global TSC. The ρ peak was absent from the spectra taken using the inner section. These results proved that the ρ transition was due to free charge carriers injected near the electrode surface, and is also why vacuum treatment well below T_g to remove water from the surface but not necessarily the bulk, is sometimes effective in suppressing some of the electrode space charge effects in the cases where water plays a role [28]. It is estimated that the space charge penetration is a few micrometers into the outer surface of the polymer film [4].

An alternative explanation for the high temperature ρ transition regards the idea that it is due to a viscoelastic relaxation such as the so-called the liquid-liquid transition (T_{ll}). For many polymers it generally occurs at $T_g + 0.2T_g$ [71]

with T_g in degrees Kelvin. Thermal annealing of the polymer in the vicinity of T_H is necessary to detect T_H in many cases, using standard thermal analysis methods [71,72]. Bernes *et al.* [11] have interpreted the ρ transition in polystyrene and other polymers as T_H . There is much evidence against this assignment, especially in the case of the TSC in these high temperature regions where the data are complicated by space charge contributions. Plazek and coworkers have used viscoelastic measurements to investigate the liquid-liquid transition regions by a variety of techniques, and have failed to detect T_H in their measurements [73]. This suggests that the ρ transitions are not true viscoelastic transitions.

Other routine experiments designed to facilitate interpretation of TSC transitions, include the determination of the dependence of the current maxima on the magnitude of the polarization electrical field strength (E) [4]. For transitions above T_g , the current does not always scale linearly with E [4,52], while for transitions at T_g and below, the majority of the literature suggest that scaling with E holds. This linear dependence is one indication that the processes are dipolar although it is not always a definitive test because Maxwell-Wagner charging at buried interfaces is sometimes 100% efficient and can look like a dipolar process [4,5].

Sample drying can be another experimental tool to check the effects of impurities such as water, on the ρ transition. The ρ transition in PEMA at ca. 115°C is well separated from the glass transition peak at 57°C, and annealing at T_g or slightly higher under 10^{-4} mbar gave rise to a strong decrease in the ρ peak, while the β and α transitions are not influenced [28]. Results for PEMA and PMMA show that the ρ transition is almost impossible to remove completely by drying [4,28].

5. INTERPRETATION OF TSC-THERMAL SAMPLING (TSC-TS) RESULTS

TSC-thermal sampling [23,24] (also known as thermal windowing, fractional polarizations [12,19] or thermal slicing [74]) is one of the important aspects of depolarization techniques which distinguishes TSC from conventional techniques such as a.c. dielectric and DMA. The TSC thermal sampling method using narrow polarization windows (*i.e.*, small $T_p - T_d$) should not be confused with thermal cleaning [25,27] which is also referred to as fractional cleaning [10] and multi-stage TSC [4]. Thermal cleaning refers to a sample polarized over a wide temperature range, and then thermally relaxed by heating, cooling, and then heating up to successively higher temperatures. Thermal cleaning has been reviewed previously [4,7] and will not be discussed further here. We will present TSC-TS data obtained by essentially one method. It is also closely

related to the TSC-TS data acquisition method recommended by TherMold, Co., manufacturers of the commercial TSC instruments.

5.1. Comparison of fitting routines for TSC-TS spectra applied to experimental data

To analyze experimental spectra taken with the standard TSC-TS method [23,28], we now describe the available fitting methods. Values of E_a are recorded in Table 1 for two representative TSC-TS experimental spectra using the various fitting methods. The TSC-TS spectrum for PEKK ($T_g = 156^\circ\text{C}$) taken with $T_p = -70^\circ\text{C}$ is shown in Fig. 10. This spectrum is typical of almost all spectra taken well below T_g ; in fact we will show below that the value of E_a determined for many materials well below T_g depends only on temperature, and in many cases is independent of the material.

Using Eq. (8) to fit the peak with a single value of E_a , gives only

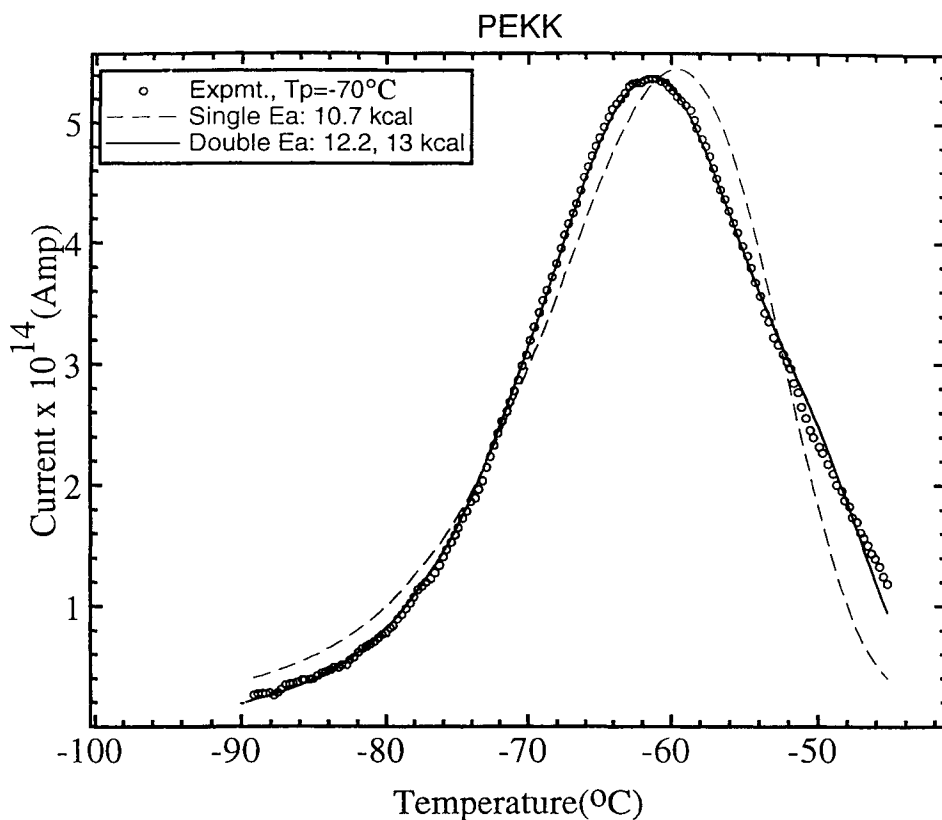


Fig. 10. TSC-TS spectra for amorphous PEKK with $T_p = -70^\circ\text{C}$ and a $7^\circ\text{C}/\text{min}$ heating rate. The fits are described in the text [52].

approximate agreement (dashed curve in Fig. 10). Experiment is always more symmetric than theory if a single value of E_a chosen for simulation using Eq. (8). The three parameters in the "single E_a fit" are $P_o = 123 \times 10^{-14}$, $\tau_o = 1.57 \times 10^{-10}$ s, and $E_a = 10.7$ kcal/mol. If one uses Eq. (11) with a narrow distribution in E_a , which we will refer to as a "double E_a fit", one can easily generate symmetric peaks which agree well with experiment (Fig. 10). For example, the solid curve shown in Fig. 10 was generated with two values of E_a , e.g., a total of 4 parameters ($P_o = 68.8 \times 10^{-14}$, $\tau_o = 1.8 \times 10^{-12}$ s, and $E_{a,1} = 12.2$ kcal/mol, and $E_{a,2} = 13$ kcal/mol). Very good agreement with the experimental data is seen, even though discrete values of E_a were chosen, as opposed to a continuous distribution [31,37,43]. It should be noted, that equally good fits can be obtained using a distribution in τ_o . For example, a fit using two values of τ_o with fixed E_a , gives equally good agreement for these spectra characterized by a narrow distribution in relaxation times. For spectra which are too broad to be fitted to a narrow distribution of E_a , one finds that for each different widely spaced value of E_a , corresponding distinct values of τ_o also must be used to give a good fit. This is because E_a and τ_o are not independent, and must vary simultaneously because of the Arrhenius equation and the fixed measurement frequency [68]. This has been discussed in detail in the context of compensation analysis [68].

The Arrhenius plots of BFG relaxation times were obtained by using the BFG (Eq. (2)) and modified BFG (Eq. (4)) methods, and integrating a TSC peak such as that in Fig. 10 up to the maximum in current. The calculated relaxation times are given in Fig. 11. The two methods are roughly consistent, depending on the region chosen for analysis of the BFG data, since some curvature is seen at the higher temperatures.

Table 1

Apparent activation energies in kcal/mol determined for two representative TSC-TS spectra

	PEKK, $T_p = -70^\circ\text{C}$ (Fig. 10)	Lexan®, $T_p = 140^\circ\text{C}$ (Fig. 13)
TSC initial rise method	9.9	46*,**
BFG method, Eq. (1)	13.5	85**
Modified Bucci Method	14	90**
Single E_a curve fit method	10.7	94**
Distributed E_a curve fit method	12.7±0.4	99**

*For the low temperature "tail", the initial rise analysis gave a value of about $E_a = 26$ kcal/mol.

**For the analysis of the TSC-TS peak, we ignored the low temperature tail corresponding to the low activation energy part.

The standard TSC initial slope method [4] for analysis of single Debye relaxations is:

$$E_a = -R \partial(\ln J)/\partial(1/T) \quad (18)$$

Applying this method to the PEKK data taken at $T_p = -70^\circ\text{C}$, we extract a somewhat lower value of E_a , as has been seen in many other cases (Table 1) [4].

It is important to make a distinction between the TSC-TS results and the "global" results of Van Turnhout and others, who showed that for fully polarized transitions such as the very broad γ transition in poly(cyclohexyl methacrylate), that BFG or related analyses give very low values of E_a . This is because the

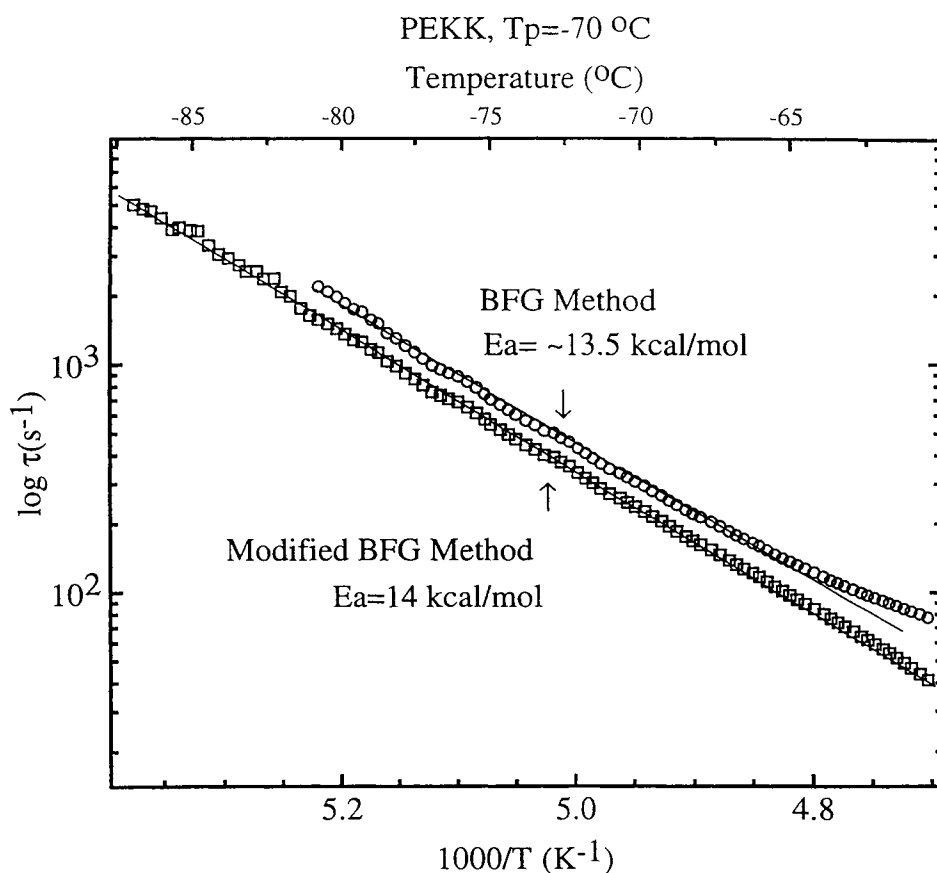


Fig. 11. BFG or Arrhenius plot of relaxation time (τ) vs. $1/T$. The data were obtained by numerical integration of the TSC-TS spectrum (see text).

BFG equation was derived for a single Debye relaxation, and the very broad global relaxations in polymers are highly distributed so the method is obviously not applicable. Let us consider an example where the TSC-TS method is applied to separate a broad global transition into its individual components. For example, like poly(cyclohexyl methacrylate) [4] a very broad β transition in polycarbonate is detected at -130°C (10^{-3} Hz) in the global TSC (or by other relaxation techniques). The separation into narrow peaks by the TSC-TS technique is illustrated in Fig. 12 for the broad β relaxation in Lexan[®] (polycarbonate) [28]. These individual TSC-TS spectra begin to approximate single Debye peaks, which is the heart of the TSC-TS method, and explains the success of the BFG and other methods in fitting the TSC-TS peaks to a narrow distribution of relaxations. We will return to this issue later, in terms of an examination of the literature and the effectiveness and reproducibility of the TSC-TS method over the years.

A typical TSC-TS spectrum is shown in Fig. 13 for Lexan[®] polarized at $T_p = 140^\circ\text{C}$. For this spectrum taken close to T_g ($\sim 147^\circ\text{C}$, 10^{-3} Hz), the single E_a fit

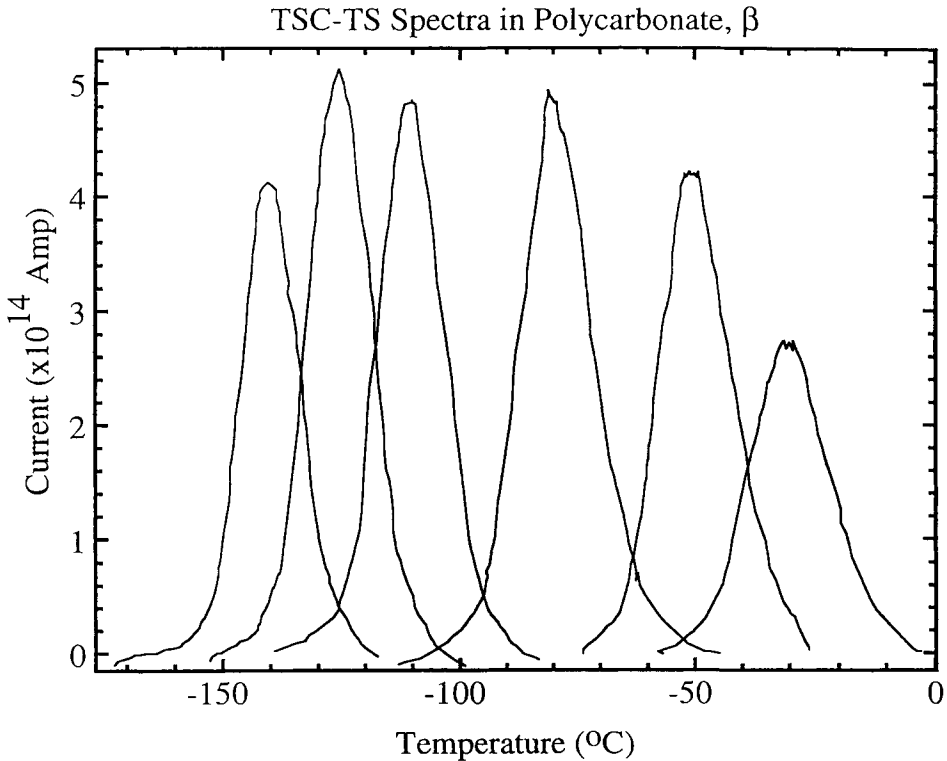


Fig. 12. TSC-TS spectra taken in the β transition region of Lexan[®] PC. The β transition for PC is very broad.

does not agree with experiment, nor does the distributed E_a fit agree at low temperatures if a narrow distribution is assumed, which was shown earlier to effectively fit spectra taken well below T_g (Fig. 10). The peak region approximately agrees with the single E_a fit, but the fit deviates significantly on the low temperature side (Fig. 13). The modified BFG analysis was applied and the data are shown in Fig. 14. A significant change in slope can be seen at about 140°C . A better perspective can be seen from the modified BFG data for several Lexan[®] spectra taken near T_g (Fig. 15). Approximately independent of T_p , one can see remarkable changes in slope (E_a) at about the low frequency glass transition of about 147°C . The reason for this is that, independent of initial polarization temperature, as one scans across a second order transition such as a

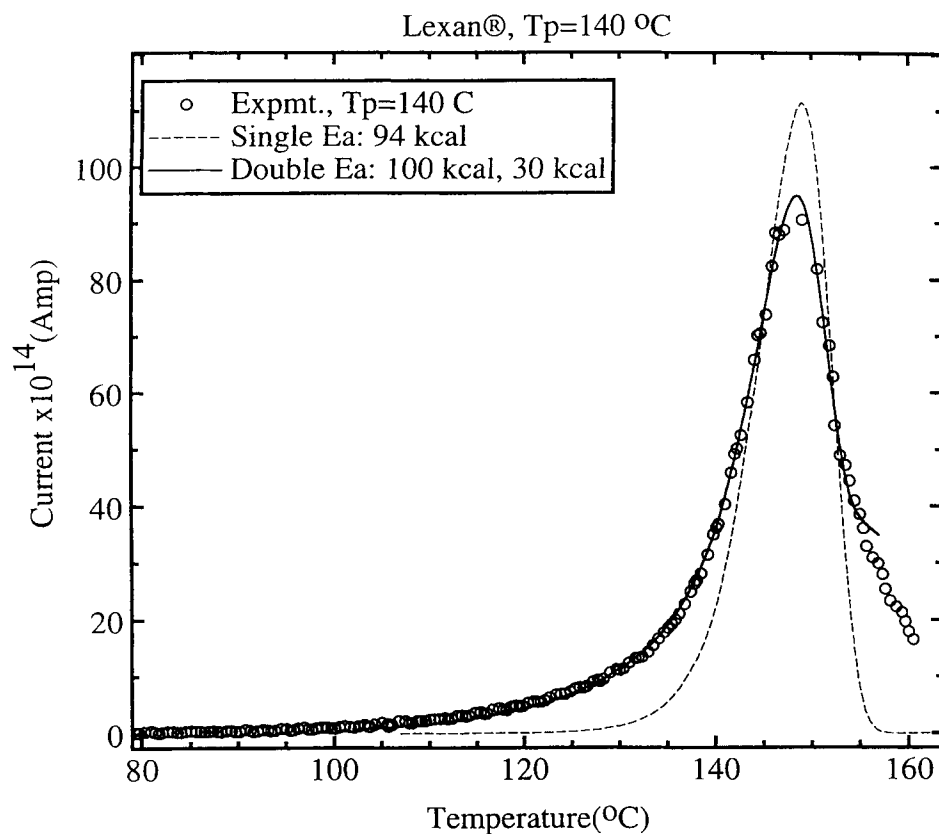


Fig. 13. TSC-TS spectrum for PC illustrating the low temperature tail in the vicinity of T_g (147°C). The spectrum was taken at $E = 2000 \text{ kV m}^{-1}$ and $T_p = 140^\circ\text{C}$. The deviation of the experimental data from the dashed curve fit shows that the low temperature tail corresponds to a non-cooperative relaxation region. Around the low frequency T_g , the activation energy increases significantly [28].

glass transition in the depolarization step, the amplitude and freedom for cooperative motions increases significantly. To a first approximation, the highly cooperative motions are seen above 147°C in the BFG plots, regardless of whether the sample was initially polarized above or below “ T_g ” as long as one is close enough to T_g .

The results of the various fits are given in Table 1 for Lexan[®] showing that the initial rise method gives the lowest values. The value for E_a of 99 kcal/mol from the distributed E_a fit is in good agreement with that determined by the Bucci plot which gave $E_a = 94$ kcal/mol (Table 1). For the “distributed” E_a fit, two widely separated values were chosen, with the lower value of $E_a = 30$ kcal/mol set to a fixed value since the fit is not extremely sensitive to this value and cannot extract it uniquely. The 6 parameters were: $P_{o,1} = 509 \times 10^{-14}$, $\tau_{o1} = 5.5 \times 10^{-52}$ s, and $E_{a,1} = 99$ kcal/mol, and $P_{o,2} = 1043 \times 10^{-14}$, $\tau_{o,2} = 6.35 \times 10^{-15}$ s, and $E_{a,2} = 30$ kcal/mol (Fig. 13). The quality of the single E_a fit (Eq. (8)) is so poor, that the value is not entirely meaningful. The initial rise method (Table 1) gives low values for obvious reasons related to the broad low temperature tail in Fig. 14.

Although the peak fitting routines are very sensitive to small variations in

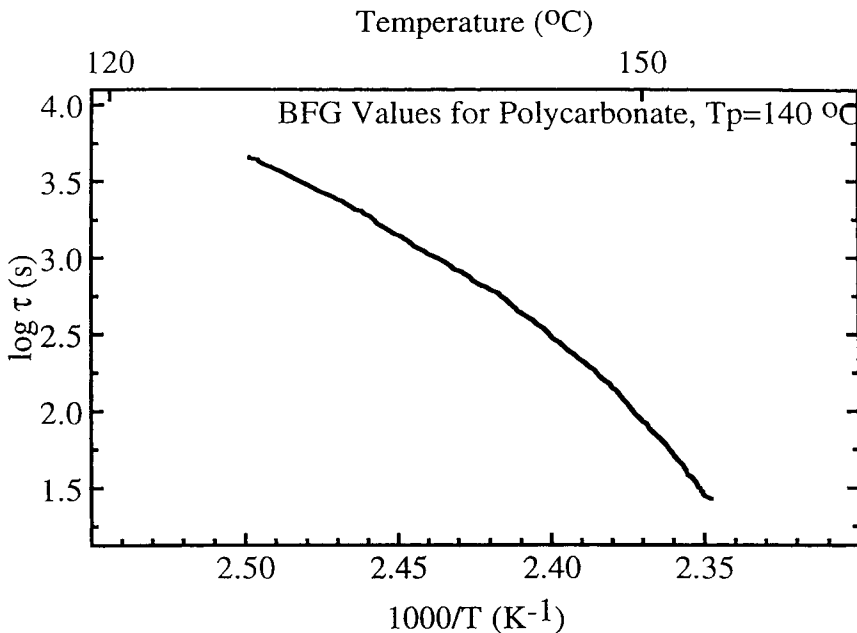


Fig. 14. BFG values of the time constants obtained by integrating the TSC-TS curve in Fig. 13 for PC, the non-Arrhenius behavior is seen at about the low frequency T_g (= 147°C).

E_a , in general, we feel that there is not enough information to determine the type of distribution of E_a (or τ_0). Thus, in most cases we will mainly concentrate of the mean value of E_a , and how it is influenced by temperature and other material properties and morphologies. In the case of Lexan[®] near T_g in Fig. 13, it is evident that to fit the data, one must consider separate values of E_a to describe both the low temperature tail and the main peak. Since one is crossing a second order transition (glass transition) in the depolarization step, it may not be entirely useful to dwell on this part of the analysis, since it is somewhat related to the technique and the finite broadness of the depolarization curves.

5.2. Comparison of TSC-TS apparent activation energies with standard relaxation methods

Although the determination of E_a described above is precise, it is not entirely conventional relative to other relaxation techniques and there is some confusion and controversy in the literature. Because of the large body of

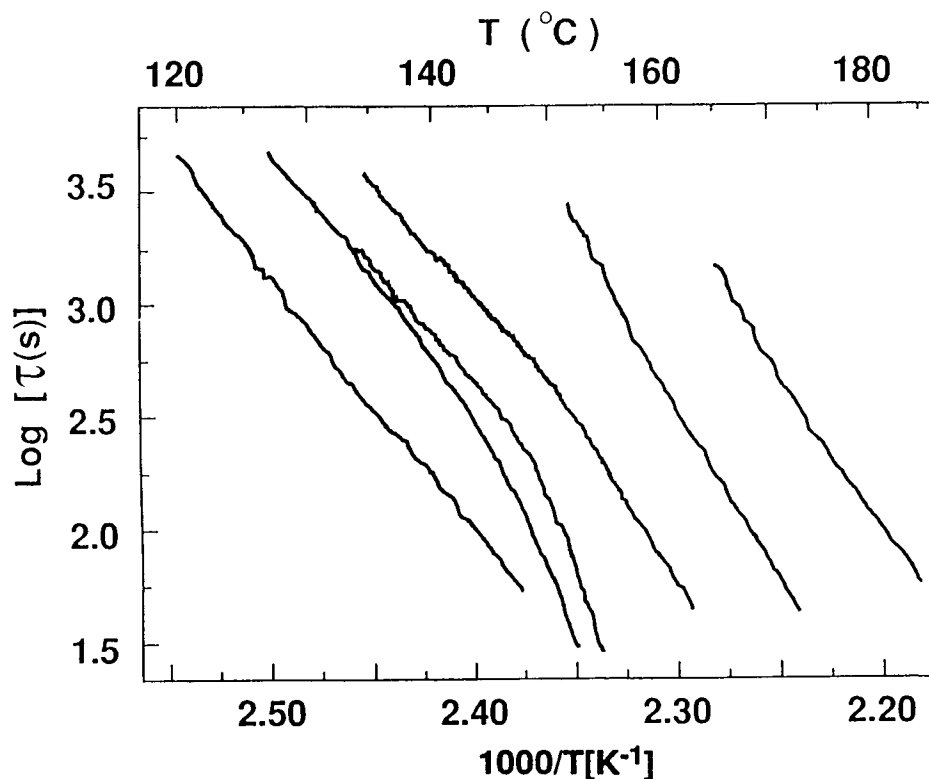


Fig. 15. Arrhenius plots of integrated TSC-TS spectra showing non-Arrhenius behavior in the vicinity of T_g for PC. T_p ($^{\circ}\text{C}$) (from left to right): 130: 140: 150: 155: 165: 180. The inflection is due to the presence of a lower E_a process below T_g [28].

literature on obtaining activation energies by a.c. dielectric, dynamic mechanical, NMR, and DSC, it is important to verify the of the accuracy of the TSC-TS technique. We choose the activated parameter E_a for our comparisons, but the conclusions would be essentially the same for a different choice of an activated parameter, as will be discussed below. In some cases it is also important to remember that one must correct for the different measurement frequency for comparisons with other techniques.

Because low temperature relaxations generally follow an Arrhenius relationship as studied by TSC-TS, verification by other techniques is generally much less complicated than for higher temperature transitions, such as glass transitions. In several cases in the literature, including that of low temperature relaxations in oxidized polyethylene [36,37], it was shown that E_a determined from TSC-TS data deviate from other techniques [1]. In many cases activation energies are quite accurate for secondary and glass transitions [28]. In other

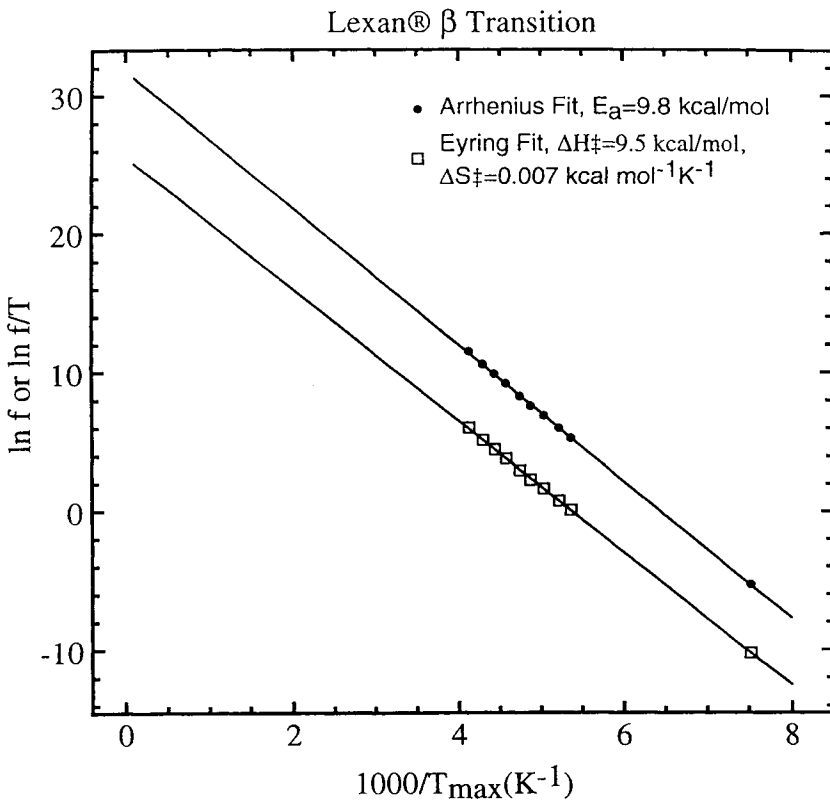


Fig. 16. Arrhenius plot of $\log(f)$ versus the reciprocal peak temperature $1/T_{max}$ for the β relaxation in PC for both TSC (0.005 Hz) and a.c. dielectric data. The Eyring plot of f/T vs. $1/T$ is also shown.

cases the values of E_a determined by the TSC-TS method for the glass transition are a factor of 1.5 to 4 times lower than those obtained by other relaxation methods, but this depends on the experimental method used and/or the analysis routine applied. For example, rather broad polarization windows ($T_p - T_d = 30^\circ\text{C}$ versus the normal narrow window of $T_p - T_d = 5^\circ\text{C}$), were sometimes chosen in the work of Vanderschueren [75] resulting in "broad TSC-TS" spectra. Because these were much broader than a single Debye relaxation, analysis of these with the standard BFG method gave a much lower values of E_a than one would obtain for a TSC-TS spectrum obtained with the narrower polarization windows. Van Turnhout has extensively discussed the application of the BFG method to broad TSC peaks [4]. In many cases it was desired to fully polarize broad transitions for analysis of the entire distribution of relaxations and comparison with the analysis of the broad transitions measured by a.c. dielectric. We will only consider the spectra taken with narrow polarization temperature windows.

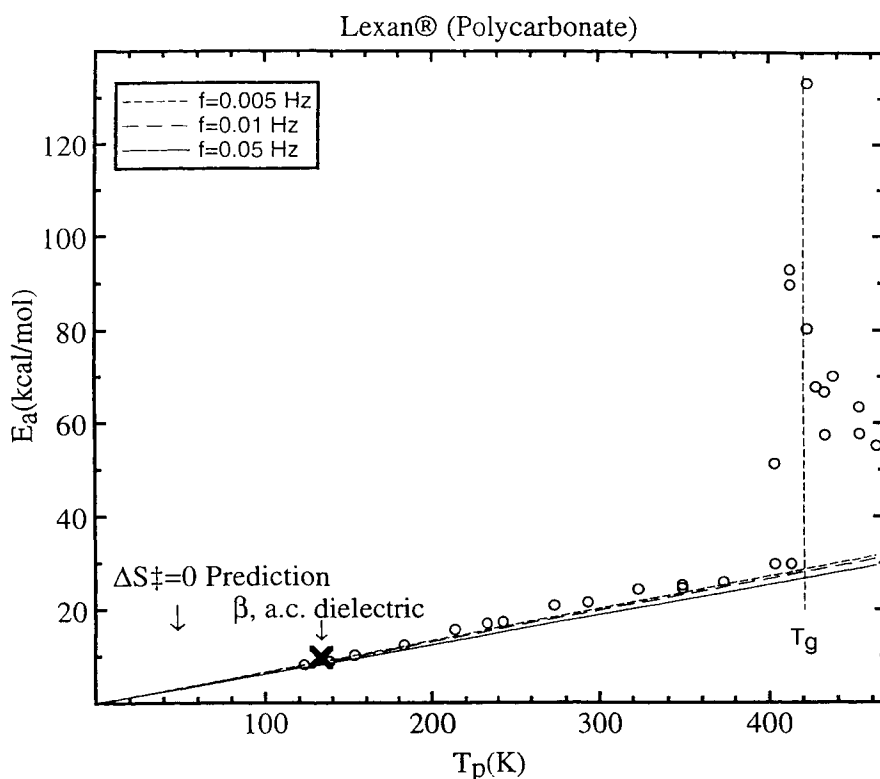


Fig. 17. Apparent activation energies E_a versus T_p for PC. The dark cross at 133 K is from the Arrhenius relaxation map of the a.c. dielectric data. The solid curves were calculated using the activated states equation with no adjustable parameters and $\Delta S^\ddagger = 0$ and the indicated frequencies (f).

In general, the examples shown below suggest that the accuracy of the TSC-TS method is comparable to the other relaxation techniques, giving some confidence that the TS data can be used to quantify the nature of cooperative and non-cooperative relaxations. To compare with TSC-TS values of E_a , a.c. dielectric data were collected for the low temperature β transition in Lexan[®] [28]. The Arrhenius relaxation map of measurement frequency (f) versus the a.c. dielectric loss (ϵ'') peak maximum temperature ($1/T_{max}$) is shown in Fig. 16. The points corresponding to the maximum of the global TSC current peak are at an equivalent frequency of $f = 0.005$ Hz ($\ln f = -5.3$), and are also included in Fig. 16 and the data are found to be linear over almost 8 orders of magnitude in frequency, giving a slope of $E_a = 9.8$ kcal/mol.

The data are also plotted in Fig. 16 in the Eyring representation of f/T_{max} vs. $1/T_{max}$.

$$f = 1/(2\pi\tau) = kT/(2\pi h)\exp(-\Delta H^\ddagger/RT) \exp(\Delta S^\ddagger/R) \tag{19}$$

Here k is Boltzmann's constant (1.38×10^{-23} J K⁻¹), temperature is in degrees Kelvin, h is Plank's constant (6.6262×10^{-34} J s), and ΔH^\ddagger and ΔS^\ddagger are the activated states enthalpy and entropy, respectively.

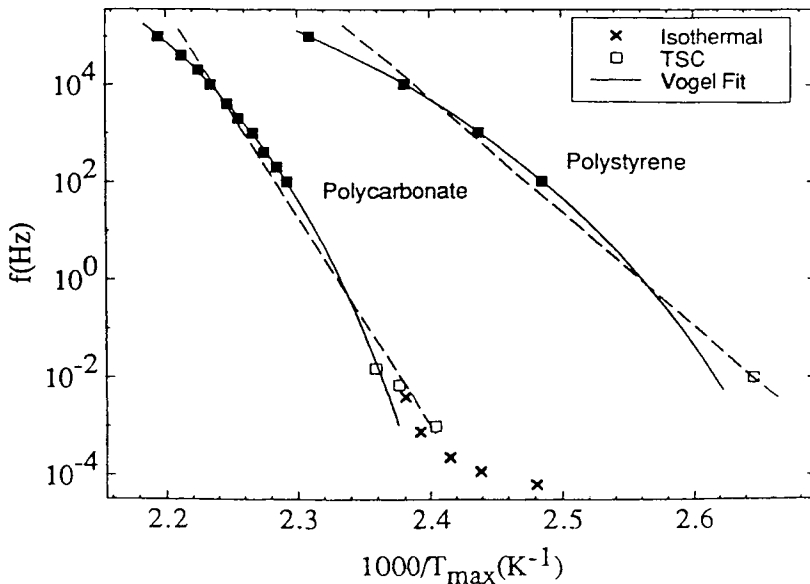


Fig. 18. Arrhenius plot of $\log(f)$ versus the reciprocal peak temperature $1/T_{max}$ for the (T_g) relaxation in PC and PS [28]. The points between 10^2 and 10^5 Hz are a.c. dielectric data. T_g s obtained from global TSC maxima at different heating rates: \square , data from isothermal depolarization measurements (x).

Although not always recognized, this type of plot is also linear, even over the wide frequency range covered, because the temperature range is still too narrow to distinguish between the Arrhenius and Eyring representations. The Eyring activated states enthalpy determined from the slope in Fig. 16 is $\Delta H^\ddagger = 9.5$ kcal/mol. The slightly lower value for the Eyring activation enthalpy (ΔH^\ddagger) is expected because ΔH^\ddagger and E_a are related by [29]:

$$E_a = \Delta H^\ddagger + RT \quad (20)$$

We will return to a detailed discussion of the Eyring and related analyses below. If one takes $E_a = 9.8$ kcal/mol at -140°C (133 K) from Fig. 16 (this temperature corresponds to correcting the a.c. dielectric data to the TSC frequency), one can then compare this value with the TSC-TS determined values of E_a in Fig. 17. The values are seen to agree within experimental error. The $\Delta S^\ddagger = 0$ prediction in the figure and interpretation of the various parameters will be discussed in the next section.

Arrhenius relaxation maps of the glass transition region for a.c. dielectric and TSC are shown in Fig. 18 for Lexan[®] polycarbonate and PS [28]. The data from 10^2 Hz to 10^5 Hz exhibit significant curvature as is the usual case for the glass transition. Three low frequency points for polycarbonate are from TSC spectra taken at different scan rates and are roughly consistent with the extrapolated Vogel curve. Points derived from isothermal depolarization data taken using the Solomat TSC instrument are also included [28]. The data indicate the difficulties in making an one-to-one comparison between different techniques.

The curvature at high frequencies is typically analyzed using an empirical analysis such as the Vogel equation:

$$-\ln f = a_1 + a_2 / (T - T_\infty) \quad (21)$$

where $f = 1/(2\pi\tau)$ is the measurement frequency, and a_1 , a_2 , and T_∞ are parameters to be obtained from the fit. T_∞ is the critical temperature where the relaxation becomes infinitely slow.

The Vogel equation is equivalent mathematically to the WLF equation [1]:

$$\log(\tau/\tau_0) = \log(f_0/f) = -C_1(T-T_0)/[C_2+(T-T_0)] \quad (22)$$

where C_1 and C_2 are material constants, and T_0 is a fitting parameter somehow related to T_g .

Non-linear regression using the Vogel equation gives the solid curve for polycarbonate with the fitted parameters $a_1 = -28.6$, $a_2 = 1136$, and $T_\infty = 389$ K.

For PS the fitted parameters are $a_1 = -27.0$, $a_2 = 1541$, and $T_\infty = 333.5$ K. Even though the values of E_a are frequency dependent, an average value is indicated by the dashed lines, resulting in $E_a = 195 \pm 20$ kcal/mol for PC and $E_a = 107 \pm 15$ kcal/mol for PS. Three lower frequency points for PC were obtained from TSC spectra taken at different scan rates including $15^\circ\text{C}/\text{min}$ ($f = 0.015$ Hz), $7^\circ\text{C}/\text{min}$ ($f = 0.007$ Hz), and $1^\circ\text{C}/\text{min}$ ($f = 0.001$ Hz) giving the three open squares. The Vogel curve which was fitted to the high frequency data, does not extrapolate well through the low frequency data (Fig. 18) because of non-equilibrium volume relaxation effects below T_g .

5.3. The zero entropy prediction and a description of methods for distinguishing cooperative and non-cooperative relaxations

We start with a rearranged form of Eyring's activated states equation (Eq. (19)) applied previously to relaxation data from many techniques [29,76]:

$$E_a = \Delta H^\ddagger + RT = RT[1 + \ln(k/2\pi h) + \ln(T/f)] + T\Delta S^\ddagger \quad (23)$$

inserting in the values for the constants, k and h :

$$E_a = RT[22.92 + \ln(T/f)] + T\Delta S^\ddagger = RT[24.76 + \ln(T\tau)] + T\Delta S^\ddagger \quad (24)$$

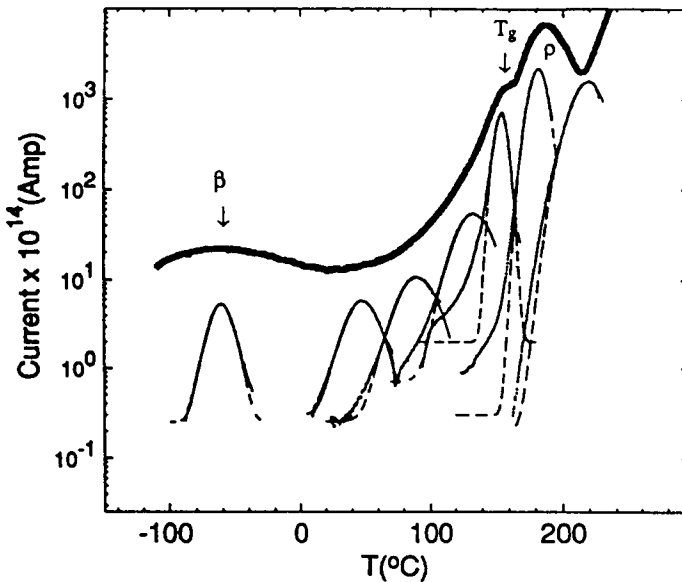


Fig. 19. Global TSC spectrum and TSC-TS spectra for semi-crystalline PEKK. The polarization temperatures, T_p , for the thermally cleaned spectra from left to right are -70 , 40 , 80 , 120 , 150 , 180 , and 210°C [52].

where temperature is in Kelvin. It is evident that for $\Delta S^{\ddagger} = 0$ (or very small values), Eq. (24) is almost linearly related to temperature in degrees Kelvin, as can be seen in Fig. 17. For TSC, equivalent frequency, f ($= 1/2\pi\tau$), is about 5×10^{-3} Hz (f is defined by Eq. (15)) [4]. Starkweather [29,76] has compared relaxation data derived mainly from a.c. dielectric and DMA for a variety of materials with Eq. (24) with $\Delta S^{\ddagger} = 0$, and has found some surprising correlations for many materials in the case of non-cooperative low temperature relaxations. For TSC, we can also see remarkable trends by comparing with Eq. (24) with ΔS^{\ddagger} equal to zero. We refer to this as so-called $\Delta S^{\ddagger} = 0$ prediction in future discussions. Fig. 17 shows the comparison with the values of E_a measured by TSC-TS for a typical amorphous polymer, polycarbonate. The experimental points agree well with the $\Delta S^{\ddagger} = 0$ prediction at lower temperatures. The prominent maximum in E_a at the low frequency T_g , is one striking feature of the results, and is not unexpected based on the discussion above of the very high activation energies associated with the glass transition determined by a variety of techniques.

Sample calculations of the $\Delta S^{\ddagger} = 0$ line are given for three different values of f in Fig. 17, indicating the rather weak dependence of the E_a on f as is expected because of the logarithmic term (Eq. (24)). Because almost every material has at least one cooperative relaxation such as a glass transition, the measured values of E_a for essentially all materials depart from the zero activation entropy curve at least once, and exhibit a prominent maximum at T_g .

In a practical sense, Eq. (24) is also very useful to confirm the accuracy of the TSC-TS technique and analysis, because measured values of E_a for low temperature, non-cooperative relaxations should agree exactly with the $\Delta S^{\ddagger} = 0$ prediction, allowing one to minimize the number of experiments needed to characterize these low temperature regions. How does one know if a low temperature transition is non-cooperative? One can determine this experimentally by TSC-TS or other relaxation methods as we have done in Fig. 17 for polycarbonate. This begins to consume considerable effort if a wide temperature range must be examined. One can also consider the evidence that indicates the cooperative low-temperature relaxations are only found in certain polymers, typically those without vinyl substitution or with methylene sequences at least four units long. For example, well studied low temperature γ transitions in PE at about -120°C (1 Hz), PTFE at -100°C (1Hz), poly-[oxymethylene] at -80°C (1Hz), are classic examples of transitions exhibiting relatively "high" activation energies [1], even though they are not glass transitions. These transitions are attributed to localized kink motions of a few main chain carbons and will be discussed in more detail later.

To summarize, we reiterate the important conclusion that E_a is not a material property for certain relaxations, typically non-cooperative ones, and systematic TSC-TS experiments are sometimes not needed since the results are already known by the $\Delta S^\ddagger = 0$ prediction. Many examples exist where the low temperature non-cooperative transition regions are well described by the $\Delta S^\ddagger = 0$ prediction. These include Lexan[®], poly(acrylates), poly(methyl acrylates), polystyrene, aromatic polyesters, PEEK, *etc.* For these one can be relatively confident that E_a will agree with the $\Delta S^\ddagger = 0$ prediction, at temperatures well below T_g .

Since this semi-empirical analysis seems promising in providing experimental guidance, and allows one to use TSC-TS in a rather sensitive and unique manner for the analysis of weak and complicated cooperative transitions, other examples of such characterization will be provided later.

5.4. Explanation of high sensitivity of TSC-TS for cooperative motions

Possibly the most important question in understanding the unique aspect of the TSC-TS method which sets it apart from other techniques in the characterization of cooperative transitions, is the origin of its very high sensitivity to cooperative relaxations. Most spectra contain contributions from both cooperative and non-cooperative relaxations. Since the question is difficult to answer from first principles, we attempt to answer it by providing some experimental examples and reiterating the important features of the BFG and related analyses, which contribute to the sensitivity. We expect in the future that more detailed analysis of the results from a mathematical and physical standpoint will become clearer [10,77].

The modified BFG method of obtaining $\tau(T)$ (Eq. (4)), and the TSC-TS curve fitting method (equations 8 and 11) will be used in our examples. Since both methods give about the same median value of E_a (see Section 5.1), the discussion of the sensitivity of the analysis applies to both methods.

Let us first consider the example of the relatively weak glass transition in semi-crystalline PEKK. The glass transition is barely visible as a shoulder in the global TSC (Figs. 6 and 19), yet for a TSC-TS spectra taken at the temperature region of the DSC (Fig. 7) glass transition, high values of E_a are extracted from the data (Fig. 20) even though the ρ peak has a stronger contribution to the TSC-TS spectrum, than the cooperative dipolar relaxations. Fig. 20 shows a strong maximum at the low frequency glass transition of both amorphous and semi-crystalline states. Well below T_g the motions are highly non-cooperative because of their localized nature giving rise to values of E_a which agree well with the empirical $\Delta S^\ddagger = 0$ prediction. In the glassy state just below T_g one can also make predictions of the cooperativity [78]. The theory of Adam and Gibbs [78] suggests that there should be an Arrhenius dependence of relaxation times with

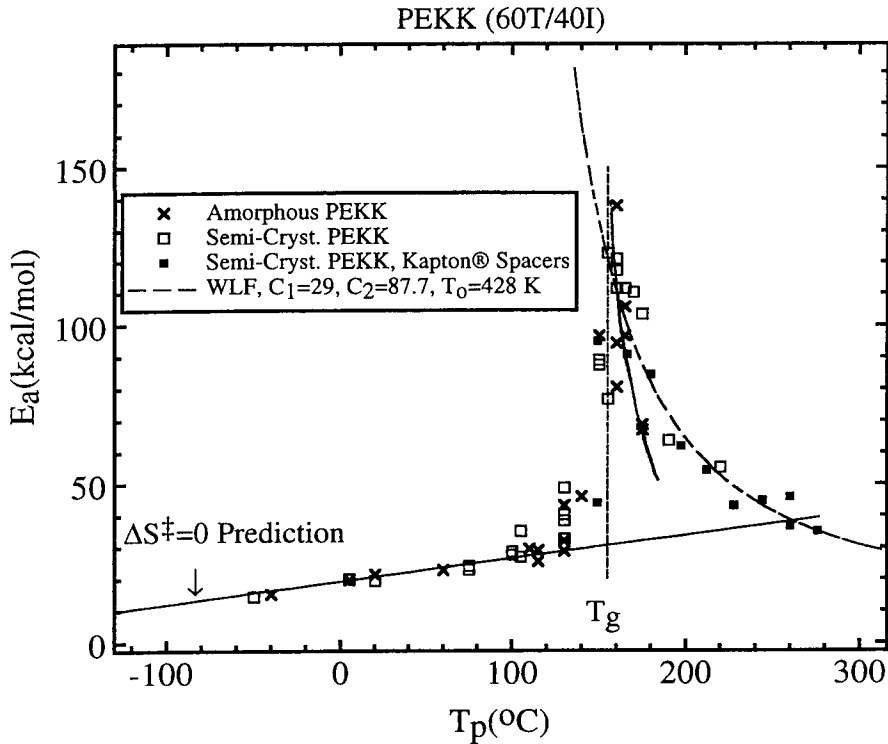


Fig. 20. Activation energies(E_a) vs. polarization temperature(T_p) for PEKK before and after crystallization [50]. The maxima in the values of E_a around the glass transition for both amorphous and semi-crystalline states are quite similar. At lower temperatures the values for both samples fall on the $\Delta S^{\ddagger} = 0$ prediction (solid line) indicating the non-cooperative nature of the relaxations. The method for generating the WLF curve was described earlier.

the values of E_a increasing with temperature as the glassy structure approaches equilibrium at T_g , where the maximum value of E_a is obtained. Fig. 20 also shows the expected decrease in E_a above T_g , also predicted by the Adam-Gibbs theory. The rate of decrease of E_a above T_g is qualitatively more rapid for the amorphous samples, showing that the glass transition is sharper. In this preliminary data, we used thin films of a very high T_g polymer (Kapton[®]) to sandwich the semi-crystalline PEKK sample and act as blocking layers to reduce the space charge contributions. These preliminary data show that above T_g the values of E_a return approximately to the $\Delta S^{\ddagger} = 0$ prediction, but do not fall below it.

Recall that with the BFG or modified BFG method (Eq. (4)), the analysis is only applied to the low temperature side up to the TSC-TS peak maximum, and this analysis gives relatively high values of E_a ($= 140$ kcal/mol, Fig. 20) near the

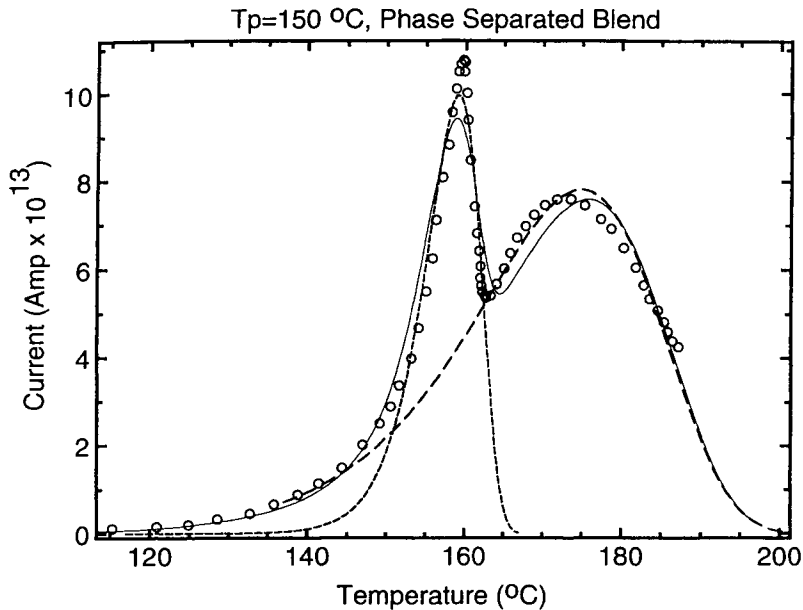


Fig. 21. Experimental TSC-TS spectra taken with $T_p = 150^\circ\text{C}$ using a phase separated blend (see text). In this temperature region, one phase is above its T_g giving rise to the narrow peak, and the other phase is well below its T_g [79].

semi-crystalline PEKK glass transition at $T_p = 160^\circ\text{C}$. Why then is the low temperature side of the TSC-TS spectra so sensitive to the high E_a cooperative relaxations?

The answer becomes clearer after looking at an actual TSC-TS spectrum for a model phase separated blend polarized ($T_p = 150^\circ\text{C}$) near the lower T_g component ($T_g = 155^\circ\text{C}$) [79]. This sample contains 30% by volume of the lower T_g ($= 155^\circ\text{C}$) component, and 70% of the higher T_g ($= 205^\circ\text{C}$) component. The dipole strengths of the two phases are about the same. At $T_p = 150^\circ\text{C}$ we expect cooperative relaxations from one phase, and at the same time overlapping non-cooperative, sub- T_g , contributions from the other phase. This is clearly seen in the experimental data in Fig. 21 with a sharp peak at the lower temperatures due to the cooperative high E_a relaxations, and a broader peak at higher temperatures due to non-cooperative low E_a relaxations. The important feature of these results is that if one did not know anything about the sample, and blindly applied the BFG or related analysis to the double “peak” TSC-TS spectrum, one would only extract contributions from the lower T_g material, giving a high value of E_a . For the data shown, we determined a value of 105 kcal/mol (and $\tau_o = 10^{-56}$ s). This value of E_a is not significantly affected by the presence of the broad second peak, corresponding to the contribution of the other 70% of the sample.

One can see in the deconvoluted peaks in Fig. 21 that the contributions to the low temperature side of the sharper peak, from the broad peak is small. One can numerically subtract the first narrow peak and apply the BFG analysis to the second broad peak, or equivalently one can use equation 11 to fit both peaks simultaneously. Such a fitted curve is shown in Fig. 21 using two pairs of values of E_a and τ_o ; those for the broader peak are 30 kcal/mol, $\tau_o = 10^{-16}$ s, and for the sharper peak are 105 kcal/mol, $\tau_o = 10^{-56}$ s, respectively. This example is an exaggerated case where we have a clear separation of peaks, and gives an example where the low activation energy component has essentially no contribution to the high value of E_a when the BFG or related analysis are applied to the data on the low temperature side of the first peak. This is the qualitative basis for the high sensitivity of TSC-TS to high E_a relaxations and holds for polymers such as PMMA polarized below the glass transition, although the situation is not always this simple because two separate peaks are almost never resolved.

To summarize, the examples given above indicate qualitatively why the TSC-TS method weights the cooperatively relaxing fraction so heavily. This is important because one of the most interesting applications of the technique is the study of broad and weak relaxations, and these are invariably overlapped strongly with other types of non-cooperative relaxations in a single TSC-TS spectrum.

5.5. Selections from TSC-TS literature and comparison with the zero entropy prediction

The literature is becoming extensive in this field, in part due to the recent availability of a commercial TSC instrument from Solomat with computer control, which is especially important for TSC-TS data acquisition because of the large number of separate experiments needed to characterize a material. We present some of the available data, mainly for polymer systems that can be compared because they have been studied independently in different laboratories. We also conclude this section with a recently reported analysis method to detect low frequency cooperative relaxations in terms of activated parameters, from mathematical analysis of a.c. dielectric data.

We start with a comparison of a relatively well studied system, Vectra[®] A950 liquid crystalline polymer (LCP). The glass transition in this aromatic copolyester is broadened because of crystallinity and chemical heterogeneity. It can be seen in Fig. 22 that the results of Collins and Long [80] agree quite well with those of Sauer *et al.* [81] even the very broad low temperature tail extending about 100°C below the peak glass transition which is about 80°C at TSC frequencies. This is an interesting new observation. The results are also consistent with those TSC-TS results obtained by Saffell *et al.* [82]. Recall that

for typical homopolymers such as PC (Fig. 16) or PEKK (Fig. 20) have very sharp increases in E_a at the DSC T_g . The main glass transition is rather weak dielectrically and mechanically, but is verified by other relaxation techniques [83,84] to be at about 80°C at TSC frequencies. The broadened glass transitions in Vectra® and related amorphous and semi-crystalline LCPs have been studied by many other relaxation methods, as will be discussed later.

Another well studied polymer is poly(ethylene terephthalate) (PET). This polymer can be studied in many forms including oriented Mylar® films, *etc.* Amorphous unoriented PET has a low frequency T_g of about 70°C [85-87]. Although values of E_a versus T_p taken using the TSC-TS method were not available, the TSC-TS results [47] show that PET has a rather sharp glass transition like polystyrene. Some of the original thermal cleaning studies [27] were on Mylar® film and the results are shown in Fig. 23. The rather sharp increase in E_a at T_g is similar to that shown for polystyrene [28]. Because Creswell and Perlman [27] used the thermal cleaning technique, the peaks are broader than those obtained by the standard TSC-TS method. Since the BFG method is only accurate when applied to single Debye relaxations, their use of the BFG method for analysis of these “broad” peaks gave the expected low

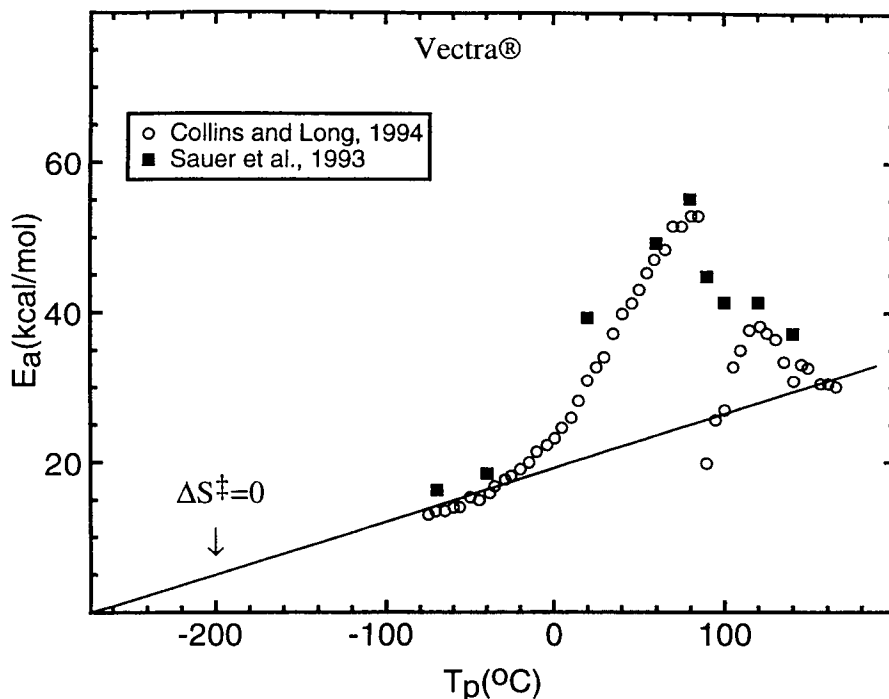


Fig. 22. Values of E_a from the TSC-TS technique for Vectra® A950 LCP. Data were taken from references [80,81].

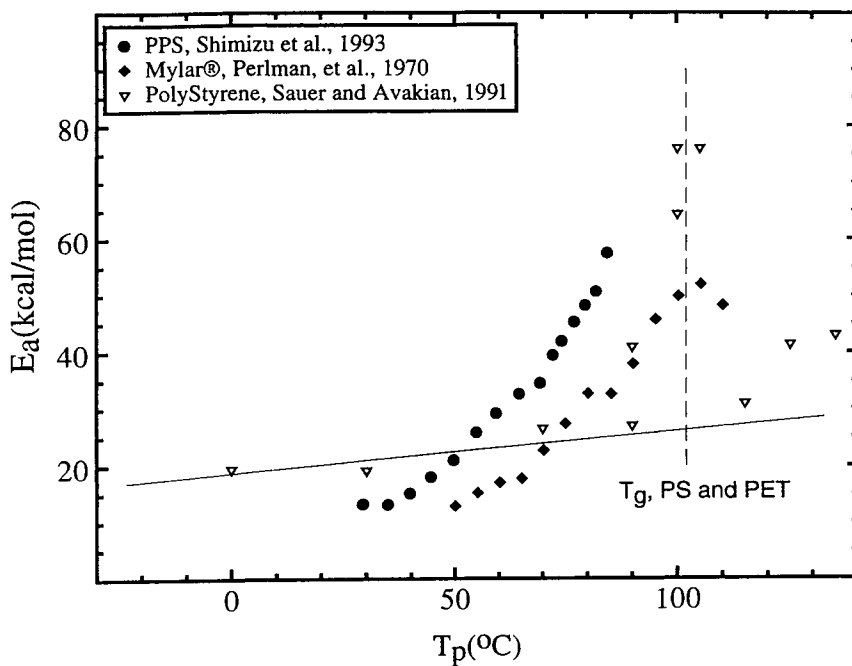


Fig. 23. Values of E_a for three different polymers, poly(phenylene sulfide) [42] has a T_g of $\sim 80^\circ\text{C}$, while polystyrene [28] and oriented PET (Mylar[®]) [27] have glass transitions of about 100°C . PPS and PET are semi-crystalline.

values of E_a , as can be seen in Fig. 23. Experience tells us that the values cannot fall below the $\Delta S^{\ddagger} = 0$ prediction. The trend for the onset of cooperative motions is still roughly correct showing that these types of conclusions can be made using a variety of related methods. Although PET film is one of the most widely studied materials by TSC [4,47,86-88], there is still much to learn about the application of TSC-TS to the study of oriented and semi-crystalline oriented polymer films. For example, it is known by DMA that T_g is increased substantially by orientation induced crystallization in PET film, but characterization by TSC-TS on the low temperature side of the glass transition shows very similar cooperative motions compared to amorphous PET. The intensity of the global TSC relaxation in semi-crystalline or oriented PET is reduced significantly [47], as is known by other techniques [1,85].

Bisphenol-A polycarbonate (Lexan[®] film) is another widely studied polymer. TSC-TS results from two laboratories are shown in Fig. 24 showing a similar maximum in E_a at about the low frequency T_g ($= 147^\circ\text{C}$) for this polymer. Small differences in the data are likely due to slightly different polarization sequences or averaging schemes when fitting the Arrhenius curves.

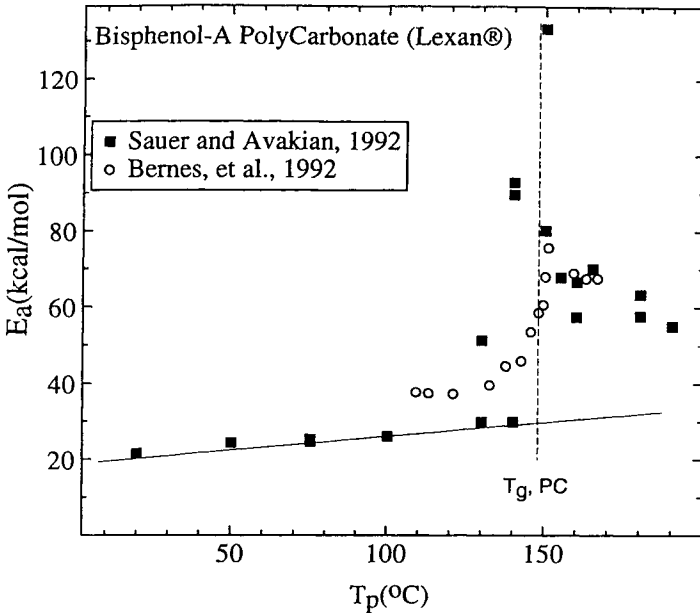


Fig. 24. Comparison of literature values of E_a from the TSC-TS technique for bisphenol-A polycarbonate (PC), the DSC glass transition is 147°C [28,30].

Possibly the most widely studied amorphous polymer by TSC-TS is PMMA [24,26,28,32,33]. Results are shown in Fig. 25 indicating that the broad cooperative relaxations around the glass transition can be consistently reproduced between two independent laboratories [28,32]. The data suggest that the cooperative glass transition like relaxations extend down to almost 100°C below the main T_g which is about 106°C. The results can be contrasted with those for other amorphous (*e.g.*, Lexan[®], polystyrene), semi-crystalline homopolymers (PEEK, PEKK), and even blends (PEEK/PEI), where the onset of the cooperative relaxations is very sharp in terms of the sharp increase in E_a just before the main glass transition. This shows one of the unique contributions of TSC-TS in suggesting that the properties of one of the most widely studied “model” glassy systems such as PMMA and related methacrylates, are not nearly as simple as would be expected. The broad low temperature cooperative relaxations have been attributed to chemical heterogeneity due to tacticity variations in PMMA [28,33].

5.6. Comparison with new analysis of derivatives of a. c. dielectric data to obtain activated parameters

It is clear from many examples that TSC-TS detects a maximum in E_a at glass transitions or related cooperative relaxations. It was emphasized above that

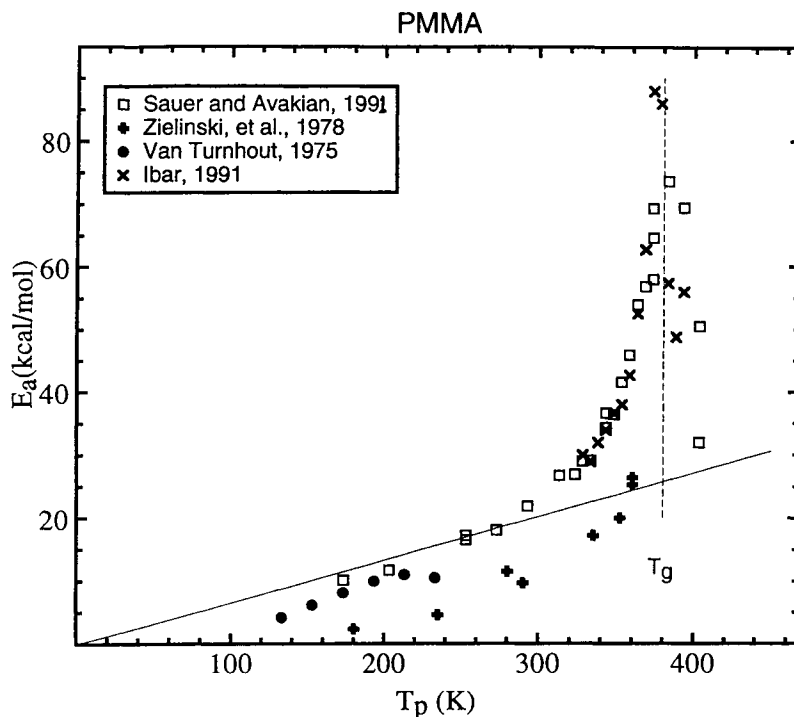


Fig. 25. Comparison of literature values of E_a for atactic PMMA ($T_g = 103^\circ\text{C}$) [28,32]

an advantage of TSC-TS is that one does not need a “peak” in the global spectrum for resolution of weak or overlapping cooperative relaxations. One can choose a T_p in any region, say in between transitions such as was the case for Lexan[®]. Furthermore, to detect cooperative relaxations leading to a maximum in E_a , the transition does not need to be visible in the global TSC spectrum, as was shown in Fig. 19 and Fig. 20 and related discussion. It would be interesting to analyze a.c. dielectric data in the same way and obtain activated parameters at any given temperature away from a given transition. Such analysis has recently become available [89,90], where E_a is calculated from derivatives of the dielectric constant, ϵ' :

$$E_a(f,T)/R = \partial\epsilon'/\partial(1/T)/[\partial\epsilon'/\partial\ln(2\pi f)] \quad (25)$$

Multiple frequency data are needed for these calculations. For one experimental example, Steeman *et al.* [90] chose PVC. There are also experimental TSC-TS data available [34,91]. Calculated values obtained using Eq. (25) are represented by the curves shown in Fig. 26, at the frequencies indicated on the plot. It is seen that a maximum occurs at a value equal to the

low frequency (ca. 10^{-3} Hz) glass transition of about 80°C , approximately independent of the measurement frequency (1 Hz or 128 Hz). It is interesting that the maximum in E_a from the analysis occurs at 80°C for these frequencies, while the a.c. dielectric ϵ'' maximum (loss peak) occurs well above this temperature for PVC [90] because of the higher frequencies. Apparently the method is detecting the region of maximum cooperativity which occurs closer to the low frequency T_g , as would be predicted by the theory of Adam and Gibbs [78]. The magnitude of their calculated values of E_a at the peak in E_a , also decreases significantly for the analysis at higher frequencies. They have suggested that this is due to overlapping transitions [90]. The glass transition in PVC looks quite broad by the method of Steeman *et al.*, somewhat like the glass transition for PMMA studied by TSC-TS (Fig. 25). The values of ΔS^\ddagger are also calculated by standard equations by Steeman *et al.* [90]. The values of ΔS^\ddagger show the same trend and contribute no additional information because they are mathematically related to E_a .

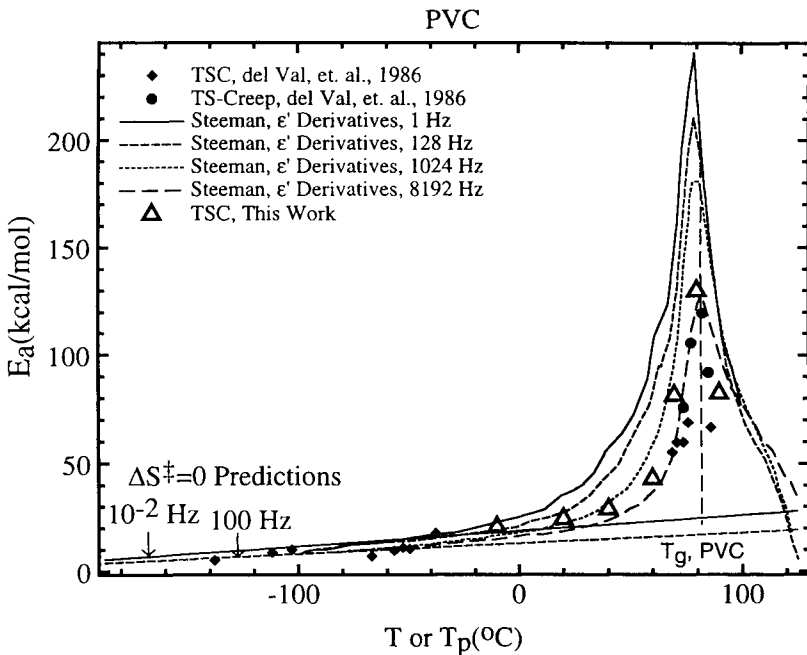


Fig. 26. Apparent activation energies versus temperature for PVC obtained from TSC-TS and Steeman *et al.*'s [90] derivative analysis method of a.c. dielectric data showing a prominent maximum at T_g . Broad cooperative relaxations extending down to ca. 20°C are indicated by the departure of the values from the $\Delta S^\ddagger = 0$ prediction. The variation of Steeman *et al.*'s values with measurement frequency is discussed in the text. Some literature TSC-TS and TSC-creep values were taken from references [34,91], and for all the thermally stimulated data, the temperature axis is the polarization temperature.

6. TSC APPLICATIONS

6.1. Examples of TSC and TSC-TS studies of amorphous polymers

Global TSC spectra are characterized by a broad spectrum of relaxations similar to low frequency dielectric loss experiments. Other differences arise because TSC is a direct current measurement and accumulation of charges at buried interfaces (Maxwell-Wagner) or injection of space charges near the electrode surfaces leads to detection of current by transient techniques such as TSC. These are not typically detected as peaks by “transient” techniques like a.c. dielectric. The TSC results above T_g for PEMA and PMMA are quite sensitive to impurities such as adsorbed water. These impurities lead to space charge injection near electrode surfaces giving rise to transitions above T_g referred to as ρ transitions (Fig. 27). TSC spectra for PEMA and PMMA are given in Fig. 27 and are generally consistent with earlier data [4]. The films were dried close to T_g under vacuum (10^{-4} mbar) for ~ 1 day.

The peak temperatures for the β and α transitions for PEMA, PMMA, and other related polymers discussed below are summarized in Table 2, where β refers to a secondary low temperature relaxation occurring below the glass

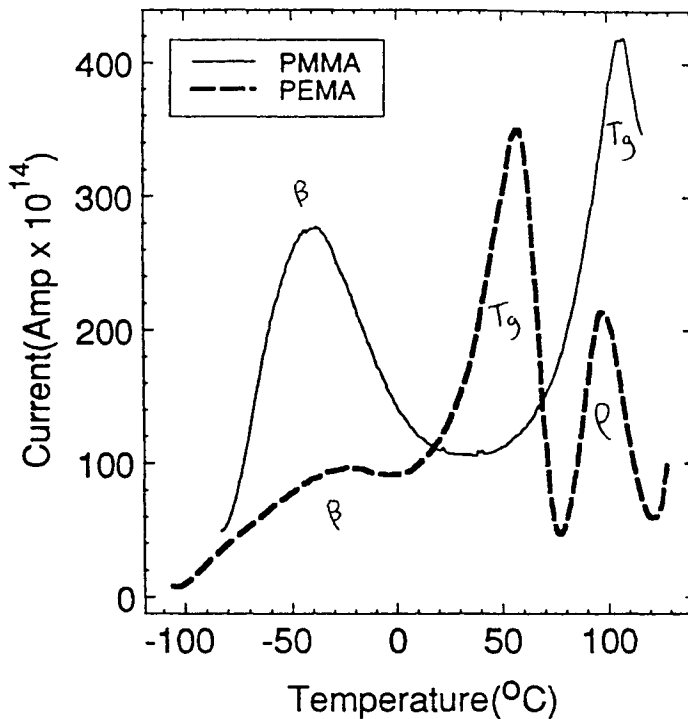


Fig. 27. Global TSC spectra from PMMA and PEMA [28]

transition (α). The values of T_g (α) measured by TSC are comparable to those measured by DSC at the same scan rate as is indicated in Table 2. Van Turnhout [4] has previously shown a similar agreement with DSC.

Representative TSC-TS spectra for a standard polymer were given in Fig. 19 along with the global TSC spectrum. Recall that for each choice of T_p , a single TSC-TS spectrum can be obtained, so the only limitation on the number of spectra is the choice of T_p . Typically, the results indicate that the relaxations are a continuum, and one should not be deceived into thinking that the discrete spectra are unique. In some cases in the literature, spectra were taken every few degrees. In Fig. 19 we only present representative spectra for clarity purposes, and the complete set of T_p 's can be judged by the plots of E_a versus T_p presented elsewhere. Many examples [24] show that the intensity of the TSC-TS peaks generally follows that of the global TSC curve, as is roughly indicated in Fig. 19. At temperatures well below T_g , each TS-TSC spectra for PEKK is characterized by a narrow distribution of relaxations characterized by a narrow range of values of E_a . For all polymers far enough below T_g , the activation energies agree with the zero entropy prediction. The zero activation entropy line in Fig. 20 indicates the non-cooperative relaxation region. We emphasize that unlike other techniques such as a.c. dielectric or DMA, the relaxation dynamics are determined at any temperature by the TSC-TS method characterizing E_a over the complete temperature range. The effect of overlapping relaxations and the sensitivity of TSC-TS to cooperative relaxations was discussed above.

6.2. Amorphous and semi-crystalline liquid crystalline polymers

In glass transition and related TSC-TS studies, liquid crystalline polymers (LCPs) are some of the most intensely studied systems in the literature. DSC is the standard technique where in addition to glass and secondary transitions, DSC can clearly detect nematic to isotropic or crystalline to nematic transitions [81,92] in nematic LCPs. The crystal to nematic transition is a primary melting transition analogous to crystal melting in an isotropic polymer. The complex thermal behavior has been investigated in several TSC and TSC-TS studies [93-96] and in other TSC-TS studies the semi-crystalline and random (or not so random) copolymer nature of the LCPs has been emphasized [81,97].

6.2.1. Side-chain LCPs

Data from Simon [93] for a side chain LCP for the glass transition ($= 3^\circ\text{C}$) and space charge regions (higher temperature rising signal) are shown in Fig. 28. The LCP alignment is in two different directions relative to the polarization direction. Homeotropic refers to the parallel alignment of the LC groups to the electric field, and planar refers to the LC groups aligned perpendicular to the field. TSC results for this and other LCPs show that the position of the glass transition is almost unchanged while significant changes in dipolar intensity for

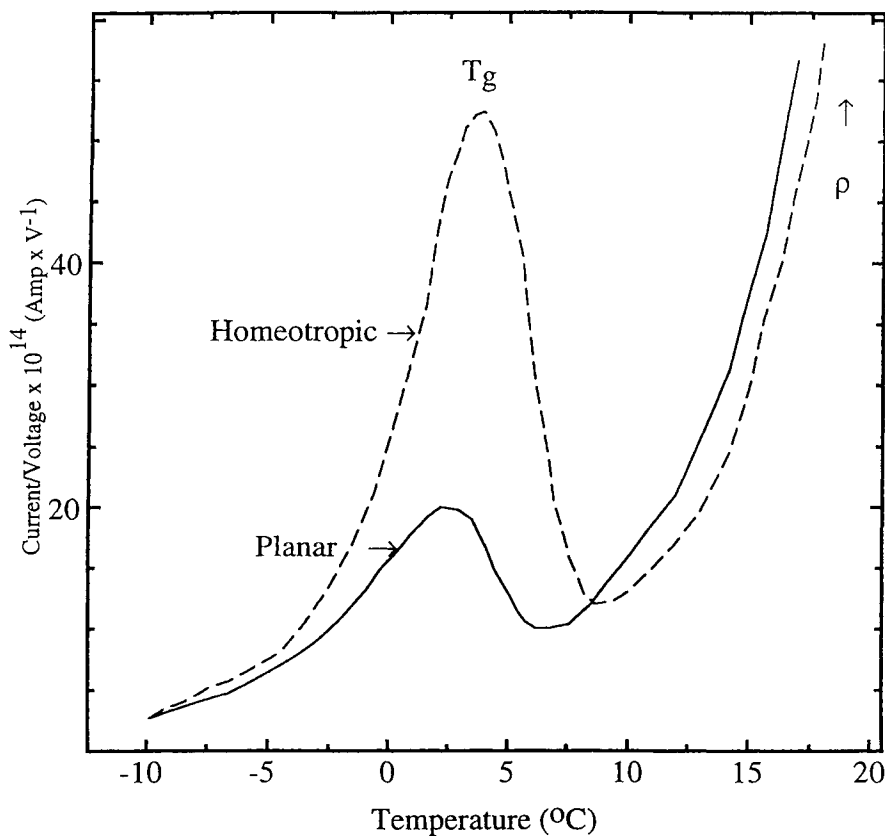


Fig. 28. Global TSC for side-chain LCPs [93]

the two alignments are detected. These compared favorably to the dielectric strengths measured by a.c. dielectric. Activation energies were also obtained [93] using the TSC initial rise method [4], and were consistent with those obtained by other dielectric techniques.

Moura-Ramos and coworkers [95,96,98] have studied side-chain LCPs using global TSC and TS-TSC from low temperatures to well above the glass transition. The results have been systematically compared to those from DSC and a.c. dielectric. Using the modified BFG analysis on TSC-TS spectra from a side-chain LCP with a siloxane backbone and polar mesogens, values of E_a were calculated (Fig. 29) showing a sharp increase in the values of E_a at the low frequency T_g , which indicates the abrupt nature of the onset of the glass transition. This trend is consistent with studies of several isotropic polymer glasses reviewed previously. At low temperatures, the values approximately

agree with the $\Delta S^\ddagger = 0$ prediction indicating that TSC-TS is detecting non-cooperative secondary motions. The molecular basis of the higher temperature transitions including the ρ transition (Fig. 29) in a variety of side-chain LCPs [95], and their relationship to the nematic to isotropic transition and space charge transitions, are discussed.

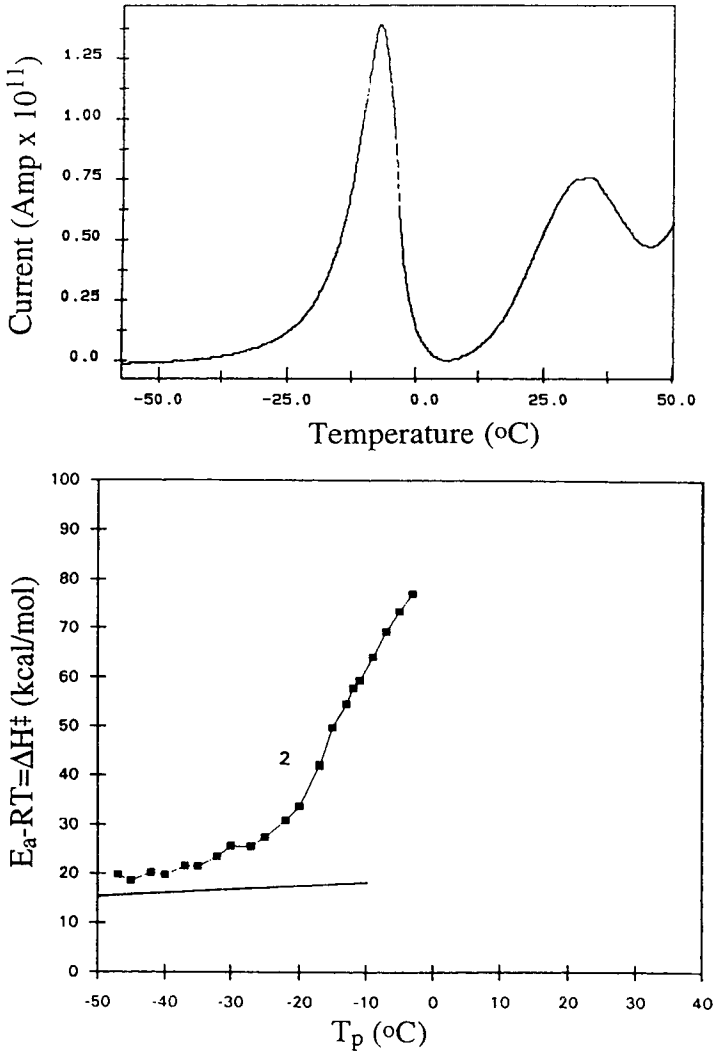


Fig. 29. Global TSC (top) and TSC-TS values of E_a for a side-chain LCP (bottom) [95], the cooperative relaxations in the glass transition region are characterized by the TSC-TS values of E_a .

6.2.2. Copolyester main-chain LCPs with broad glass transitions

Few TSC studies concerning thermotropic main-chain LCPs have been reported [80-82,94,97]. Aromatic copolyesters such as Vectra® A950 [semi-crystalline random copolyester of 1,4-hydroxy benzoic acid, HBA, 0.73 mole fraction, and hydroxy naphtholic acid (0.27)] have been studied in this and other

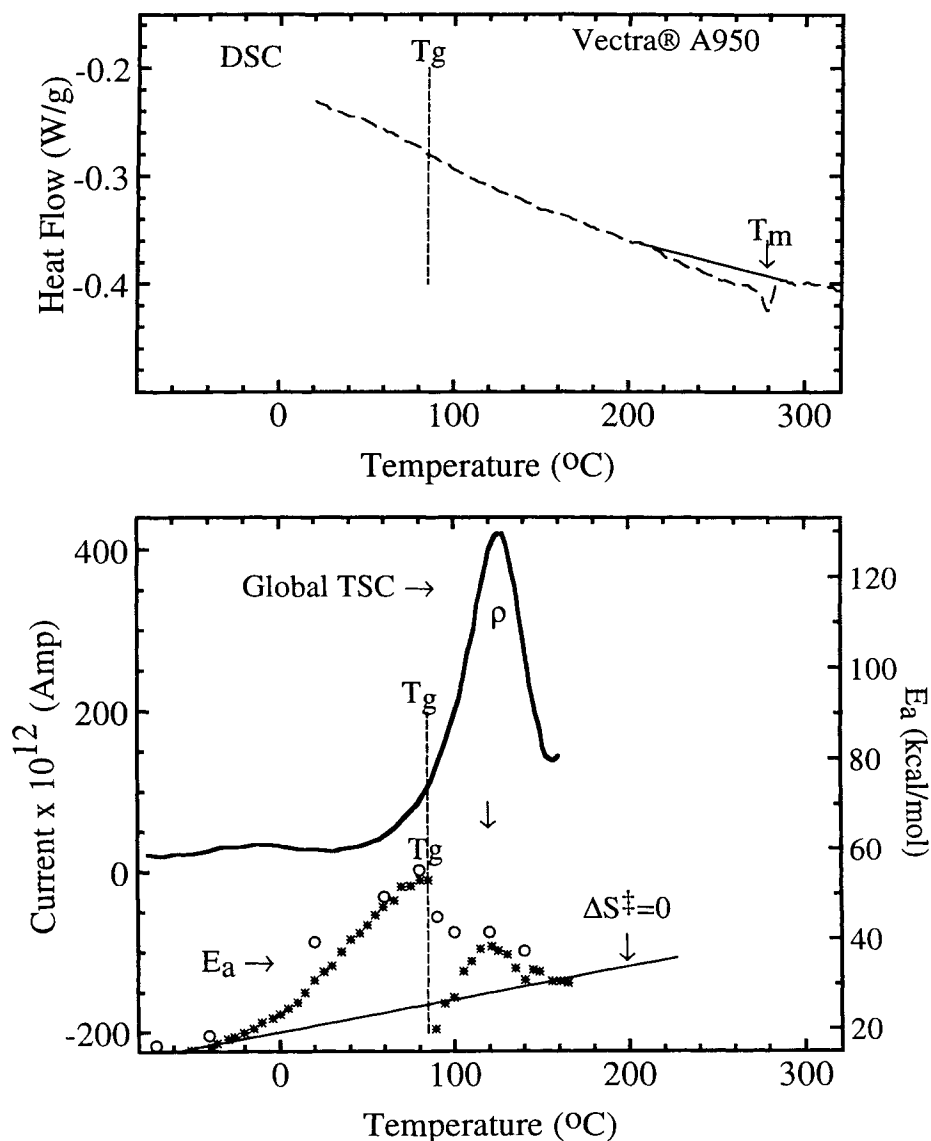


Fig. 30. DSC (top), global TSC, and TSC-TS values of E_a for Vectra® LCP (bottom), the broad glass transition is characterized by the different techniques (see Fig. 22 caption).

laboratories. The micro-phase separated blocky copolyesters have also been studied by Brostow [94]. These LCPs contain ethylene terephthalate and 1,4-hydroxy benzoic acid (HBA). The possible contributions of chemical heterogeneity to the broadened transitions in the “single phase” copolyesters will be discussed below. These and related wholly aromatic LCPs are technologically important because of their high thermal resistance and good melt processability [99].

Here we present TSC-TS and related thermal analysis data for a typical copolyester main-chain wholly aromatic LCPs which shows that TSC-TS provides a unique characterization of the broadened glass transitions in both non-crystalline and semi-crystalline LCPs. The broad transitions are not due to liquid crystalline character, but are due to chemical heterogeneity or blockiness of the LCP chains. The semi-crystalline Vectra[®] LCP data are from a variety of

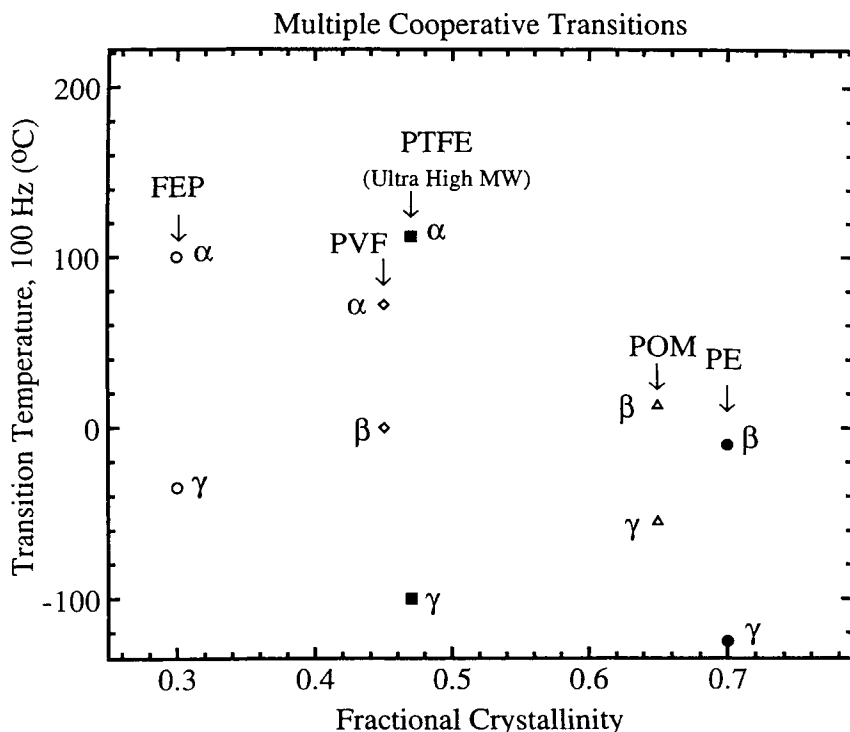


Fig. 31. Measured transition temperatures for polymers as a function of percent crystallinity. Upper transitions are glass transitions (see text). FEP 100 is an 88% tetrafluoroethylene (TFE) copolymer with ca. 12 wt% (or 8 mole %) hexafluoropropylene (HFP)[1]. FEP 100 has a $T_m = 270^\circ\text{C}$, PTFE has a $T_m = 333^\circ\text{C}$, linear polyethylene has a $T_m = 134^\circ\text{C}$, PVF has a $T_m = 210^\circ\text{C}$, and poly(oxy methylene) (POM, $-\text{CH}_2\text{CH}_2\text{O}-$) has a T_m of 180°C [108].

sources [80-82].

All LCPs were typically dried at their glass transitions in a vacuum oven for 24 hours. Films were pressed by hand in the melt between sheets of Kapton[®], cooled, and the Kapton[®] subsequently removed. DSC data for the glass transition region of Vectra[®] A950 are shown in Fig. 30 (top). A slight change in the DSC slope is seen in the vicinity of T_g , but the normal step in heat capacity seen for lower crystallinity LCPs is absent. The glass transition is weak and broad because of crystallinity. The high surface area of the defective crystallites in this class of copolymers apparently leads to a large constraining effect on the amorphous motions. Calorimetry data have been presented previously for HBA/HNA copolymers (Vectra[®] family of LCPs) and other related materials also showing a very broad glass transition [100]. Our Vectra[®] LCPs were quenched from the melt ($\sim 380^\circ\text{C}$) and are of moderate crystallinity. Vectra[®] in this form has a broad and weak crystal to nematic endotherm starting at 215°C with a shallow endothermic peak at 266°C (Fig. 30). The global TSC shows part of a low temperature secondary relaxation at $\sim -10^\circ\text{C}$, and a strong ρ transition at 130°C . DMA [83,84] and low frequency a.c. dielectric show that the glass transition peak is at 90°C , so the ρ transition at 130°C is clearly too high in temperature to be the glass transition. It is also much too intense. Further proof is seen in the TS-TSC determination of E_a which clearly shows that the maximum cooperative high- E_a relaxations are occurring well below the ρ transition. This is also a case where DSC is not sensitive enough, but TSC-TS clearly is. In the global TSC spectra, the ρ transition is attributed to space charge migration [4], and seems reasonable since this type of transition is usually seen 30 - 50°C above T_g . The situation is very similar to that for semi-crystalline PEEK discussed earlier, where DSC and TSC-TS show directly that the ρ transition in global TSC is too intense and too high above T_g to be the glass transition (see Figs. 30 and 31).

6.3. High crystallinity flexible polymers and fluoropolymers

Relaxation studies using a.c. dielectric, DMA, and other methods have been summarized for a variety of fluorinated and non-fluorinated polymers [1]. The relaxation and thermal properties of this technologically important class of polymers are very complicated because of high crystallinity and high chain flexibility. Two of the most extensively characterized fluoropolymers are PVF and poly(vinylidene fluoride) (PVF₂ or PVDF), and the review of by Enns and Simha [101] summarizes the complicated thermal transitions for these and also give references to TSC and a.c. dielectric studies. Elegant TSC results for a variety of fluoropolymers has also been reported by van Turnhout [4,5]. Other TSC reports include studies of PTFE [102,103], PVF [102,104], and PVF₂ [102,105]. Recent TSC-TS experiments on PVF₂ [106,107] and PVF₂

copolymers [62,107] have emphasized the low and high temperature “cooperative” transitions, which compliment the characterization by dielectric [101] and DMA. TSC-TS was applied to investigate piezoelectric state in PVF₂ [62]. Another lower crystallinity (< 5%) halogenated polymer, PVC, was discussed earlier.

Similar to the TSC-TS studies of high crystallinity fluorinated polymers by Lacabanne and coworkers [62,106,107], we have also studied PTFE, PVF, PTFE copolymers, and related polymers using TSC-TS. Here we review some of the results for the polymers in Fig. 31, where their crystallinities were determined by DSC as was described previously. These provide examples of the unique contributions of TSC-TS (Fig. 31), including the detection of two “cooperative” high- E_a transitions [108]. The origin of these multiple cooperative transitions will be discussed.

We use poly(vinyl fluoride) [PVF, -(CH₂CHF)-] as an example because the results illustrate many of the important features of the TSC-TS technique applied

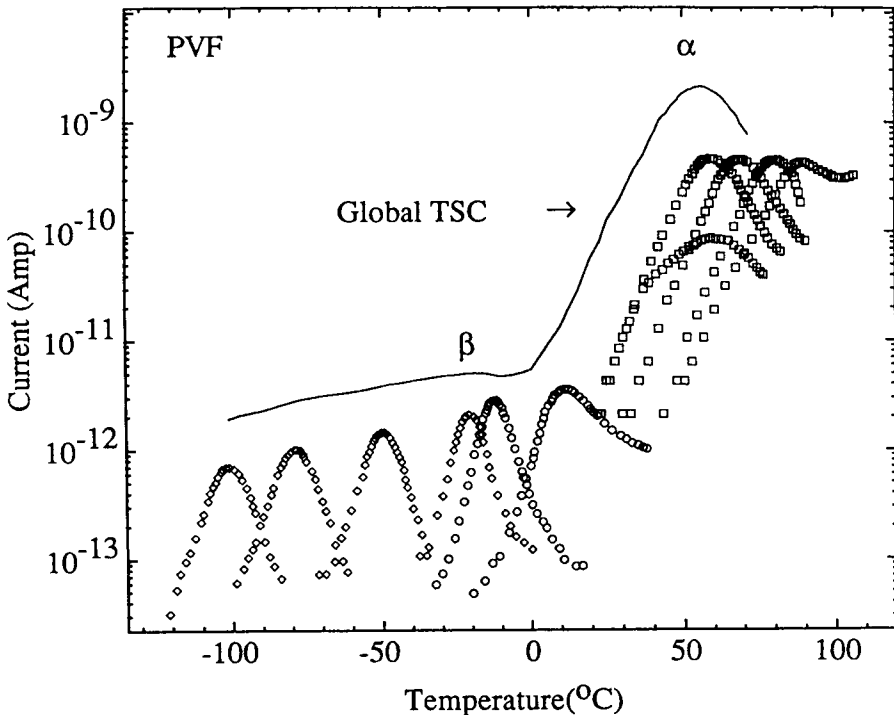


Fig. 32. Global TSC for PVF (solid curve) and typical examples of individual spectra obtained using the TSC-TS method. The current increases by several orders of magnitude from the β relaxation region to the α region. The β relaxation seems very weak and broad on this log scale [108].

to high crystallinity polymers [108]. The electrical signal of PVF is also significantly stronger than that for PTFE and FEP because of the stronger dipoles. The global TSC curve and the raw TSC-TS spectra for PVF are plotted in Fig. 32. A weak β relaxation is detected at -17°C , and a broad but stronger α or glass transition is determined at about 50°C which is verified by DSC. The values of E_a from BFG analysis of the TSC-TS spectra are shown in Fig. 33 and indicate that both the α and β are cooperative relaxations. Such double peaks in E_a in homopolymers are unique to flexible semicrystalline polymers including PTFE, poly(oxymethylene), copolymers, and maybe polyethylene. One can also examine such data in order to determine the temperature region over which cooperative motions are detected. Note that α , β , γ etc., do not refer to a specific molecular mechanism, they are just part of the scheme to categorize relaxations [1]. The frequency corrected values of the α and β transitions for PVF are plotted in Fig. 31, and the molecular origin of the β relaxation will be discussed below. The accuracy of TSC-TS was verified by comparing the results with those from higher frequency a.c. dielectric [108].

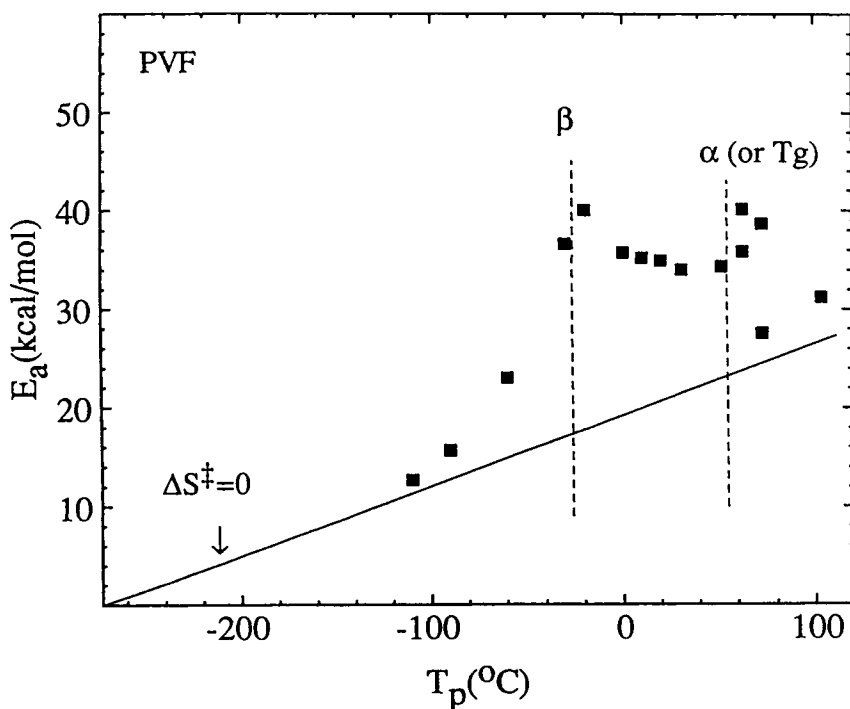


Fig. 33. E_a vs. temperature obtained by analyzing the TSC-TS spectra. Two cooperative transitions for PVF are detected. The cooperative relaxations are indicated by the departure from the $\Delta S^\ddagger = 0$ curve. The vertical dashed lines are the peak positions from the global TSC peaks [108].

TSC-TS studies were carried out for the polymers in Fig. 31 (except polyethylene, PE), and the results also showed two peaks in E_a like PVF in Fig. 33. For some of the polymers in Fig. 31, the glass transitions are very weak due to high crystallinity. This has caused substantial controversy over the years. Additional confusion arises from the lower temperature cooperative transitions detected in these materials. The TSC-TS results are consistent with the assignment of the upper transitions in Fig. 31 as the glass transitions. The lower cooperative transitions have also been often assigned to glass transitions, but McCrum *et al.* [1], Boyer [109], Boyd [110], and others have shown that this is wrong.

The similarities of the low temperature cooperative relaxations (β for PVF, and γ for the others) in Fig. 31, suggest that they can be all attributed to a concerted local mode motion, like the γ transition in PE [111]. Typically, they are not cooperative unless crystal/amorphous interfaces are present [48,112]. The dependence of the lower transition temperatures on the polymer structure in Fig. 31, can be rationalized based on local frictional differences, *e.g.*, the low temperature transition is a little higher in temperature for POM because of hydrogen bonding, and a little higher in PVF because of stronger dipolar interactions plus more bulky F atoms relative to polyethylene. PVF is the least reliable in this context because of possibilities of chemical heterogeneity due to the well known tacticity variability and contributions from head-to-head, versus head-to-tail placement of monomers. This could lead to multiple phases or modified crystal morphologies, both of which could contribute to complications.

7. CONCLUDING REMARKS

Examples have been given here which reflect the accuracy, reproducibility, and sensitivity of TSC and TSC-TS. Advantages of TSC include its speed of measurement and programmable polarization and depolarization sequences. The flexibility of sample size and geometry are also advantages for studies of polymers. The sample requirements are a few milligrams or less, and polymers can be studied in the liquid, fiber, or powder states. In general, explanations for the TSC-TS results and the relationship of the activated parameters to glass transition phenomena are somewhat controversial [28,62]. In most cases of TSC and relaxation data from other techniques [1], activated parameters are extracted. As is well known, the absolute values of E_a are not physically realistic, but do show that a cooperative relaxation is detected in a certain temperature region. The values of E_a are in many cases larger than a primary chemical bond strength (ca. 50 kcal/mol) which immediately shows that the process is complex. The situation is no better if one considers the corresponding activated states entropy or related parameters. It has been concluded that the values of the activated parameters are unrealistically high simply because the distributions of

relaxations are changing very fast with each small increment in temperature [29], and the Arrhenius or related analyses are far too crude to make physical sense of this. Related interpretations include inter-molecular coupling models [112,113].

This review in part emphasizes the application of TSC and TSC-TS to the study of semi-crystalline and related systems where the unique contribution of TSC-TS is in many cases its ability to resolve cooperative transitions. Applications of TSC-TS have been discussed showing the resolution of complex dielectric transitions into narrow distributions. In most cases overlapping relaxations are present, and the resolution of these overlapping relaxations is explained by using experimental examples. We have emphasized here that in the case of weak or overlapping relaxations, that one can resolve “cooperative relaxations”, *e.g.* those corresponding to high values of the apparent activation energy E_a , even if the species are a minor fraction of the overall relaxing species [28,33]. Comparison with other techniques has been useful at arriving at this conclusion, and this usually resolves any controversy concerning the interpretation. The detailed theoretical basis for this high sensitivity to the fraction of cooperatively relaxing species is not well understood, although qualitative discussion of this high sensitivity is given.

With these deficiencies in mind, we have presented many examples of a semi-empirical method of comparing the values of E_a with a $\Delta S^\ddagger = 0$ prediction. This allows the full sensitivity of the TS-TSC method to be applied in a simple fashion, and also makes contact with more conventional thermal and relaxation analysis techniques. The magnitude of the apparent activation energy obtained by the TS method allows one to assign the relaxations as either cooperative (glass transition like) or non-cooperative ones. One can also define the position and breadth of the glass transition with a higher degree of precision than other techniques. The physical basis for the maximum in the apparent activation energy at T_g is well understood. The explanation is related to the cooperative nature of the relaxations at T_g . In the equilibrium melt well above T_g the segmental motions are relatively uncorrelated and are characterized by a small value for the configurational entropy [78]. As one reduces the temperature and approaches the glass transition the nature of the motions change because of the restrictions due to reduced free volume. Thus, the cooperative unit necessary for motion becomes larger and larger as one approaches the glass transition. According to Adam and Gibbs [78] this leads to an increase in the configurational entropy and gives a quantitative description of the increase in the apparent activation energy at T_g . The functional dependence of the configurational entropy theory for the equilibrium melt in the region above T_g gives rise to an equation mathematically equivalent to the WLF equation [78].

In the future we should expect many more applications of TSC, TSC-TS, and other techniques to the field of material science and physics. Recently, many new reports of work on semi-crystalline materials including fluoro-

polymers have appeared [62,107,108]. The same is true for liquid crystal polymers and liquid crystals. Other experimental work on polymers will continue in an effort to understand the influence of composition, orientation, and crystallinity on relaxations and thermal properties. Eventually, for a more complete understanding of thermally stimulated techniques, a better theoretical understanding is needed [77,114,115]. A quantitative theory for the nature of the "narrow distributions" obtained by TSC-TS is not yet available. One must also compare with the results of isothermal techniques, and the experimental acquisition of such isothermal depolarization data can be made with only slight experimental modification of conventional TSC equipment. Literature shows substantial progress in this area [10].

ACKNOWLEDGMENT

I would like to thank Drs. Howard Starkweather, Jr., Peter Avakian, Mimi Keating, Benjamin Hsiao, Mr. William Kampert, Mr. Nicholas DiPaolo, and Mr. John Dowell of DuPont for their many contributions over the past ten years.

REFERENCES

1. N. G. McCrum, B. E. Read, G. Williams, "Anelastic and Dielectric Effects in Polymeric Solids", Dover, NY, 1991. Original Issue, John Wiley, London, 1967.
2. B. Wunderlich, "Thermal Analysis", Academic Press, New York, 1990.
3. "Thermal Characterization of Polymeric Materials", E.A.Turi, Ed., Academic Press, San Diego, 1997.
4. J. van Turnhout, *Polymer J.*, 2 (1971) 173. J. van Turnhout, "Thermally Stimulated Discharge of Polymer Electrets", Elsevier: Amsterdam, 1975.
5. J. van Turnhout, in "Topics in Applied Physics: Electrets", Vol. 33, G. M. Sessler, Ed., Springer-Verlag, 1980, p. 81.
6. P. Hedvig, "Dielectric Spectroscopy of Polymers", Adam. Hilger, Bristol (1977).
7. J. Vanderschuren, J. Gasiot, "Thermally Stimulated Relaxations in Solids", P. Bräunlich, Ed.; Springer-Verlag, Berlin, 1979.
8. G. M. Sessler, in "Topics in Applied Physics: Electrets", Vol. 33, G. M. Sessler, Ed., Springer-Verlag, 1980, p. 1.
9. R. Chen, Y. Kirsh, *Analysis of Thermally Stimulated Processes*: Pergamon Press: Oxford; International Series on the Science of the Solid State; 1981.
10. K. Jonscher, in "Dielectric Relaxation in Solids"; Chelsea Dielectrics Press: London, 1983, pp. 263-265.
11. Bernes, R. F. Boyer, D. Chatain, C. Lacabanne, J. P. Ibar, in "Order in the Amorphous State of Polymers"; S. E. Keinath, Ed.; Plenum Press: 1987, p. 305.
12. Lavergne, C. Lacabanne, *IEEE Elec. Insul. Mag.*, 9 (1993) 5.
13. P. K. C. Pillai, in "Ferroelectric Polymers", H. S. Nalwa, Ed.; Marcel Dekker, New York, 1995, p. 1.
14. R. K. Chartoff, in "Thermal Characterization of Polymeric Materials", E. A.Turi, Ed., Academic Press, San Diego, 1997.
15. S. Gray, *Philos. Trans. R. Soc. London, Ser. A*, 37(1732) 285.

16. M. Eguchi, *Proc. Phys. Math. Soc. Jpn.*, 1(1919) 326.
17. T. J. Randall, M. H. F. Wilkins, *Proc. R. Soc. London*, A184(1945) 347, 366, 390.
18. H. Frei, Groetzinger, *Phys. Z.*, 37 (1936) 720.
19. Bucci, R. Fieschi, G. Guidi, *Phys. Rev.*, 148 (1966) 816.
20. B. Z. Gross, "Charge Storage in Solid Dielectrics", Elsevier, Amsterdam, 1964.
21. G. M. Sessler, J. E. West, *J. Acoust. Soc.*, 40 (1966) 1433.
22. G. M. Sessler, J. E. West, in "Electrets and Related Electrostatic Charge Storage Phenomena", L. M. Baxt, M. M. Perlman, Eds.; Electrochemical Society, New York, 1968.
23. Chatain, P. Gautier, C. Lacabanne, *J. Polym. Sci, Polym. Phys.*, 11 (1973) 1631.
24. M. Zielinski, T. Swiderski, M. Kryszewski, *Polymer*, 19 (1978), 883.
25. M. Kryszewski, M. Zielinski, S. Sapieha, *Polymer*, 17 (1976), 212.
26. Gourari, M. Bendaoud, C. Lacabanne, R. F. Boyer, *J. Polym. Sci, Polym. Phys. Ed.*, 23 (1985), 889.
27. R. A. Creswell, M. M. Perlman, *J. Appl. Phys.*, 41 (1970), 2365.
28. B.B. Sauer, P. Avakian, *Polymer*, 33 (1992) 5128.
29. H.W. Starkweather, Jr., *Macromolecules*, 14 (1981) 1277.
30. Bernés, D. Chatain, C. Lacabanne, *Polymer*, 33 (1992) 4682.
31. M. Aldana, E. Laredo, A. Bello, N. Suarez, *J. Polym. Sci., Polym. Phys. Ed.*, 32 (1994) 2197.
32. J. P. Ibar, *Polym. Eng. Sci.*, 31 (1991) 1467.
33. B. B. Sauer, Y. Kim, *Macromolecules*, 30 (1997) 3323.
34. J.J. del Val, A. Alegria, J. Colmenero, *J. Appl. Phys.*, 59 (1986) 3829.
35. J. M. Barandiaran, J.J. del Val, J. Colmenero, C. Lacabanne, D. Chatain, J. Millan, G. Martinez, *J. Macromol. Sci. -Phys.*, B22 (1983-1984) 645.
36. P. Fischer, P. Röhl, *J. Polym. Sci, Polym. Phys. Ed.*, 14 (1976) 531.
37. P. Fischer, P. Röhl, *J. Polym. Sci, Polym. Phys. Ed.*, 14 (1976) 543.
38. J. M. Meseguer, J. L. Duenas, Gomes Ribelles, R. Diaz Calleja, *J. Appl. Polym. Sci.*, 37 (1989) 1645.
39. Chatain, c. Lacabanne, J.-C. Monpagens, *Makromol. Chem.*, 178 (1977) 583.
40. N. G. McCrum, *Polymer*, 25 (1984) 299.
41. M. Jarrigeon, B. Chabert, D. Chatain, C. Lacabanne, G. Nemoz, *J. Macromol. Sci.-Phys.*, B17 (1980) 1.
42. H. Shimizu, K. Nakayama, *J. Appl. Phys.*, 74 (1993) 1597.
43. D. R. Figueroa, J. J. Fontanella, M. C. Wintersgill, J. P. Calame, C. G. Andeen, *Solid State Ionics*, 28 (1988) 1023.
44. R. Vaia, B. B. Sauer, O. Tse, E.P. Giannelis, V. Mehrotra, *J. Polym. Sci., Polym. Phys. Ed.*, 35 (1997) 59.
45. B. B. Sauer, P. Avakian, G. M. Cohen, *Polymer*, 33 (1992) 2666.
46. C. Lacabanne, D. Chatain, Monpagens, Berticat, *Ph. J. Appl. Phys.*, 50 (1979) 2723.
47. C. Lacabanne, A. Lamure, G. Teyssedre, A. Bernes, M. Mourgues, *J. Non-Cryst. Solids*, 172 (1994) 884.
48. B. B. Sauer, P. Avakian, E. A. Flexman, M. Keating, B. S. Hsiao, R. K. Verma, *J. Polym. Sci., Polym. Phys. Ed.*, 35, (1997) 2121.
49. J. Fraile, A. Torres, J. Jiménez, J. A. Saja, *Polymer*, 30 (1989) 1977.
50. B. B. Sauer, B. S. Hsiao, *J. Poly. Sci.: Poly. Phys Ed.*, 31 (1993) 917.
51. M. Mourgues-Martin, A. Bernes, C. Lacabanne, *J. Therm. Anal.*, 40 (1993) 697.
52. B. B. Sauer, P. Avakian, H. W. Starkweather, B. S. Hsiao, *Macromolecules*, 23 (1990) 5119.

53. P. Demont, D. Chatain, C. Lacabanne, D. Ronarc'h, J.-L. Moura, *Polymer Eng. Sci.*, 24 (1984) 127.
54. J. J. del Val, C. Lacabanne, A. Hiltner, *J. Appl. Phys.*, 63 (1988) 5312.
55. Dufresne, C. Lacabanne, *Polymer*, 34 (1993) 3173.
56. L. L. Berger, B. B. Sauer, *Macromolecules*, 24 (1991) 2096.
57. M. D. Migahed, A. El-Khodary, M. Hammam, A. Shaban, H. R. J. Hafiz, *J. Mat. Sci.*, 25 (1990) 2795, and M. D. Migahed, T. Fahmy, *Polymer*, 35 (1994) 1688.
58. D. Ronarc'h, P. Audren, J.-L. Moura, *J. Appl. Phys.*, 58 (1985) 466.
59. D. Ronarc'h, P. Audren, J.-L. Moura, *J. Appl. Phys.*, 58(1985) 474.
60. S.-I. Chen, *J. Mat. Sci.*, 28 (1993) 3823.
61. J. P. Ibar, "Fundamentals of Thermal Stimulated Current and Relaxation Map Analysis"; SLP Press: New Canaan, CT, 1993.
62. Teyssedre, C. Lacabanne, *J. Phys. D: Appl. Phys.*, 28 (1995) 1478.
63. B. E. Read, *Polymer*, 30 (1989) 1439.
64. O. Exner, *Nature*, 201 (1964) 488.
65. P. D. Garn, *J. Thermal Anal.*, 10 (1976) 99.
66. R. R. Krug, W. G. Hunter, R. A. Grieger, *J. Phys. Chem.*, 80 (1976) 2335.
67. J.-P. Crine, *J. Appl. Phys.*, 66 (1989) 1308.
68. B. B. Sauer, J. J. Moura Ramos, *Polymer*, 38 (1997) 4065.
69. S. Z. D. Cheng, M.-Y. Cao, B. Wunderlich, *Macromolecules*, 19 (1986) 1868.
70. P. Huo, P. Cebe, *Macromolecules*, 25 (1992) 902.
71. R. F. Boyer, *J. Macromol. Sci.-Phys.*, B18 (1980) 461.
72. P. L. Kumler, G. A. Machajewski, J. J. Fitzgerald, L. R. Denny, S.E. Keinath, R.F. Boyer, *Macromolecules*, 20 (1987) 1060.
73. D. J. Plazek, *J. Polymer Sci., Polymer Phys. Ed.*, 20 (1982) 1533, and J. Chen, C. Kow, L. J. Fetters, D. J. Plazek, *J. Polymer Sci., Polymer Phys. Ed.*, 20 (1982) 1565, and S. J. Orborn, D. J. Plazek, *J. Polymer Sci., Polymer Phys. Ed.*, 23 (1985) 41, and J. Chen, C. Kow, L. J. Fetters, D. J. Plazek, *J. Polymer Sci., Polymer Phys. Ed.*, 23 (1985) 13.
74. V. Halpern, *J. Phys. D: Appl. Phys.*, 1997, to be published.
75. J. Vanderschueren, *J. Polymer Sci., Polymer Phys. Ed.*, 15 (1977) 873.
76. W. Starkweather, Jr., *Macromolecules*, 21 (1988) 1798.
77. V. Halpern, to be published.
78. Adam, J. H. Gibbs, *J. Chem. Phys.*, 43 (1965) 139.
79. B. B. Sauer, unpublished data.
80. G. Collins, B. Long, *J. Appl. Polym. Sci.*, 53 (1994) 587.
81. B. B. Sauer, R. Beckerbauer, L. Wang, *J. Poly. Sci., Poly. Phys Ed.*, 31 (1993) 1861.
82. R. Saffell, A. Mattheiesen, R. McIntyre, J. P. Ibar, *Thermochemica Acta*, 192 (1991) 243.
83. M. H. Alhaj-Mohammed, G. R. Davies, S. Abdul Jawad, I. M. Ward, *J. Polym. Sci., Polym. Phys. Ed.*, 26 (1988) 1751.
84. D. J. Blundell, K. A. Buckingham, *Polymer*, 26 (1985) 1623.
85. C. Coburn, R. H. Boyd, *Macromolecules*, 19 (1986) 2238.
86. Belana, M. Pujal, P. Colomer, S. Montserrat, *Polymer*, 29 (1988) 1738.
87. J. Belana, P. Colomer Vilanova, *J. Mat. Sci.*, 26 (1991) 4823.
88. J. Belana, P. Colomer, M. Pujal, S. Montserrat, *J. Macromol. Sci., Phys.*, B23 (1984-85) 467.
89. R. Díaz-Calleja, E. Riande, J. San Román, *J. Polym. Sci., Polym. Phys. Ed.*, 30 (1992) 1239.
90. P. A. M. Steeman, J. van Turnhout, *Macromolecules*, 27 (1994) 5421.

91. Nogales, B. B. Sauer, *J. Polym. Sci., Polym. Phys. Ed.*, 36, (1998) 913.
92. D. J. Blundell, *Polymer*, 23 (1982) 363.
93. G. P. Simon, *Polymer*, 30 (1989) 2227.
94. W. Brostow, B. K. Kaushik, S. B. Mall, I. M. Talwar, *Polymer*, 33 (1992) 4687.
95. J. F. Mano, N. T. Correia, J. J. Moura Ramos, A. C. Fernandes, *J. Polym. Sci., Polym. Phys. Ed.*, 33 (1995) 269.
96. J. F. Mano, N. T. Correia, J. J. Moura Ramos, *Polymer*, 35 (1994) 3561.
97. B. B. Sauer, N. V. DiPaolo, P. Avakian, W. G. Kampert, H. W. Starkweather, Jr., *J. Polym. Sci., Polym. Phys. Ed.*, 31 (1993) 1851.
98. J. J. Moura-Ramos, J. F. Mano, D. Coates, *Mol. Cryst. Liq. Cryst.*, 281 (1996) 267.
99. C. Sawyer, M. Jaffe in "High Performance Polymers", E. Baier, A. Moet, Eds., Hanser, New York, 1991, p. 56.
100. M.-Y. Cao, B. Wunderlich, *J. Polym. Sci., Polym. Phys. Ed.*, 23 (1985) 521.
101. J. B. Enns, R. Simha, *J. Macromol. Sci., Phys.*, B13 (1977) 11.
102. T. Takamatsu, E. Fukada, *Polym. J.*, 1 (1970) 101.
103. R. L. Remke, H. von Seggern, *J. Appl. Phys.*, 54 (1983) 5262.
104. R. McGhie, G. McGibbon, A. Sharples, E. J. Stanley, *Polymer*, 13 (1972) 371.
105. T. Mizutani, T. Yamada, M. Ieda, *J. Phys. D: Appl Phys.*, 14 (1981) 1139.
106. C. Lacabanne, D. Chatain, T. ElSayed, D. Broussoux, F. Micheron, *Ferroelectrics*, 30 (1980) 307.
107. G. Teyssedre, A. Bernés, C. Lacabanne, *J. Polym. Sci., Polym. Phys. Ed.*, 33 (1995) 2419.
108. B. B. Sauer, P. Avakian, and H. W. Starkweather, Jr., *J. Polym. Sci.: Polym. Phys.*, 34 (1996) 517.
109. R. F. Boyer, *J. Polym. Sci., Symp. No. 50*, 189 (1975) and R. F. Boyer, *Plastics Polym.*, 41 (1973) 15, and R. F. Boyer, *Plastics Polym.*, 41 (1973) 71.
110. R. H. Boyd, *Polymer*, 26 (1985) 323.
111. R. H. Boyd, *Polymer*, 26 (1985) 1123.
112. B. B. Sauer in "Performance of Plastics", W. Brostow, Ed., Hanser, New York, 2000, p. 208.
113. K. L. Ngai, C. M. Roland, *Macromolecules*, 26 (1993) 6824.
114. E. Marchal, *J. Chem. Phys.* 105 (1996) 6068.
115. E. Marchal, *Makromol. Chem., Rapid Commun.* 14 (1993) 597.

This Page Intentionally Left Blank

Chapter 16

Temperature modulated differential scanning calorimetry (TMDSC) – basics and applications to polymers

C. Schick

Department of Physics, University of Rostock, Universitätsplatz 3, 18051 Rostock, Germany
E-mail: christoph.schick@physik.uni-rostock.de

1. INTRODUCTION

Differential Scanning Calorimetry (DSC) is one of the most effective analytical techniques to characterize the physical properties of polymers. DSC allows determining heat capacities in both solid and liquid states and phase transition temperatures and the corresponding enthalpy and entropy changes as well as heat capacity changes. On the other hand it is well known from dynamic measurements, like dielectric spectroscopy or dynamic mechanical analysis, that the signal to noise ratio can be significantly improved if only the response of the sample at the specific frequency of the perturbation is analyzed. The data treatment is then often based on Fourier analysis of periodic signals. From mechanical and dielectric measurements, it is known that the information available from periodic measurements at different frequencies, frequency domain measurements, is also available from single pulses or sharp steps in the perturbation, time domain measurements. Both of frequency and time domain measurements now can also be performed in calorimetry. The general concepts have already been well described [1-7]. In this chapter a personal view on these techniques is going to be presented. It is not the aim to give a comprehensive overview about all possible applications to polymers. A literature search in March 2002 yields ca. 700 references regarding dynamic (periodic and step) calorimetry. Among them are approximately 350 dealing with temperature modulated DSC (TMDSC) and ca. 170 are related to polymers.

Periodic perturbations are in use in calorimetry since 1910 when Corbino [8,9] used the nowadays so-called 3ω -method [10,11] to determine the heat capacity of electrically conducting wires. In the 1960's the AC-calorimetry was developed by Kraftmakher [12] and Sullivan and Seidel [13]. All these authors considered heat capacity as a real valued quantity. It was known from

ultrasound propagation in gases that, in general, heat capacity should be considered as a frequency dependent complex quantity [14]. The first direct measurement of the frequency dependent complex heat capacity was performed in 1971 by Hamann, *et al.* [15] at the glass transition of an inorganic polymer, namely, amorphous selenium. Interestingly, they used for their experiments a differential scanning calorimeter. Therefore, they did not only perform the first direct measurements of complex heat capacity but also, for the first time, a temperature modulated DSC (TMDSC). This idea, the combination of DSC and periodic temperature perturbations was reconsidered in 1993 by Reading *et al.* [16,17] and Salvetti *et al.* [18]. At that time it was possible to overcome the limitations of the setup proposed by Gobrecht *et al.* [15] because of the dramatic improvements of computer technology. Consequently, TMDSC became available as a standard tool in thermal analysis and is since then widely used in polymer characterization. TMDSC is commercially available from different instrument manufacturers which use their own trade names. TA Instruments – MDSC™, PerkinElmer Instruments – DDSC™, StepScan™ DSC, Mettler Toledo – ADSC™, Seiko – ODSC™. On the other hand most of the manufacturers offer tools to generate temperature-time profiles which can be used to perform TMDSC measurements. Then, the data treatment must be performed outside the commercially available software. Actually software can be found on different locations at the World Wide Web (see *e.g.* [19-21]). Before discussing details of TMDSC, however, let us consider the basics of the technique.

In Fig. 1 the schemes of the different types of temperature modulated calorimeters (TMC) are shown. Basically two cases must be considered: (i) The perturbation is the heat-flow and the resulting temperature oscillations are measured (AC, 3ω). (ii) The perturbation is the temperature and the heat-flow rate necessary to realize the programmed temperature time profile at a position close to the sample is measured (TMDSC). Depending on the actual design the

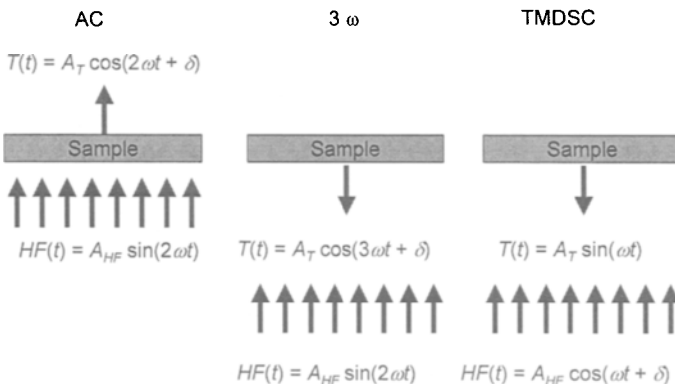


Fig. 1. Schemes of different types of temperature modulated calorimeters. For explanation of the different symbols, see text.

periodic power may be applied to one surface of the sample and the resulting temperature oscillations are measured on the opposite surface like in some types of AC calorimeters. In the cases of the 3ω -method, TMDSC and some other AC calorimeters the temperature oscillations are measured on the same side where the power is applied.

Let us first consider the simplest possible case: Constant time independent static thermodynamic heat capacity, no losses (adiabatic conditions) and no time delay due to heat transfer limitations. Under these conditions the phase angle δ equals zero in any case. According to basic thermodynamics we can write

$$\delta Q = C_p \cdot \Delta T = c_p \cdot m_s \cdot \Delta T \quad (1)$$

where δQ is the applied heat, ΔT is the resulting temperature increase, C_p is heat capacity, c_p is specific heat capacity, and m_s is sample mass. In case of DSC a linear heating or cooling profile is applied to determine heat capacity. Assuming constant heat capacity and sample mass for each infinitesimally small temperature step differentiation according to time yields

$$\frac{\delta Q}{dt} = C_p \frac{dT}{dt} \text{ or } HF = C_p \cdot q_o \quad (2)$$

HF is heat-flow rate and q_o is heating or cooling rate. Introducing periodic temperature, $T(t) = A_T \sin(\omega t)$, and heat-flow rate, $HF(t) = A_{HF} \cos(\omega t)$ profiles as indicated in Fig. 1 we obtain in the simplest possible case, $\delta = 0$,

$$A_{HF} \cos(\omega t) = C_p \frac{dT(t)}{dt} = C_p \omega A_T \cos(\omega t) = C_p A_q \cos(\omega t) \quad (3)$$

where A_{HF} is amplitude of the periodic heat-flow rate, A_T is amplitude of the temperature oscillations, $A_q = \omega A_T$ is amplitude of the heating rate oscillations and $\omega = 2\pi/t_p$ is angular frequency with t_p the period of the oscillations. For the heat capacity we get

$$C_p = \frac{A_{HF} \cos(\omega t)}{A_q \cos(\omega t)} = \frac{A_{HF}}{A_q} \quad (4)$$

Here one advantage of the periodic temperature and heat-flow rate profiles becomes obvious for the first time – heat capacity can be obtained from the amplitudes of the corresponding signals. It is not necessary to measure each point of the heat-flow rate or temperature signal with the final accuracy. It is enough to determine the amplitudes with high accuracy. This can be easily done by means of Fourier analysis of periodic signals, by rectification techniques (lock-in amplifiers) or by non-linear least square fitting of a cosine function at

the given frequency ω . Generally speaking, the signal to noise ratio can be significantly improved because only contributions just at the predefined frequency ω will be considered. High frequency noise or long term drifts will not disturb the heat capacity determination.

But in practice, the situation is much more complicated and more promising. In most cases heat-flow rate and heating rate are not in phase and a phase angle δ between them must be introduced. Then, the ratio of the amplitudes yields an effective complex heat capacity $C_{p\text{eff}}^*$.

$$C_{p\text{eff}}^*(T, t, \chi, \omega, \dots) = \frac{A_{HF}^*}{A_q^*} \quad (5)$$

The modulus (magnitude) of this quantity is often called reversing heat capacity or modulus of complex heat capacity. The details of the data treatment in TMDSC and the different strategies to interpret them will be given in section 3.

As indicated in Eq. (5) temperature modulated calorimetry and thus also TMDSC allows the measurement of an effective complex heat capacity as a function of temperature, T , time, t , conversion, χ , frequency, ω , and other variables. Here we always assume isobaric conditions. Especially frequency, ω , and time, t , are independent variables not used in classical equilibrium thermodynamics, which opens up new possibilities to study the dynamics of the sample. For comparison, in DSC the dynamics of the sample under investigation may be studied by changing the heating or cooling rate. A dynamic range between 0.001 K/min and 500 K/min [23] can be realized with commercially available instruments, with no general limitation to lower rates, except the time needed for the measurement. For extremely small samples heating rates up to 60,000,000 K/min can be achieved [24]. In temperature modulated calorimetry the variation of the modulation frequency allows for testing the dynamics of the sample. Therefore, it is an important aim to broaden the frequency range accessible by the different instruments as much as possible. Eight orders of magnitude in frequency are actually available for heat capacity spectroscopy by combining the results from different types of calorimeters [25]. As for the heating rate there is no general limitation at lower frequencies, except the time needed for the measurement. At high frequencies a fundamental problem of calorimetry related to the temperature gradient that is necessary to transfer heat from one body to another comes into play. Because heat does not propagate but flows, there is always a time needed to transfer a certain amount of heat from one body to another. This time significantly limits the frequency range available in calorimetry and especially in TMDSC [1]. Recent developments to use unconventional detection techniques by Toen *et al.* [26,27] will probably significantly extend the frequency range to higher frequencies.

As mentioned before, information about the dynamics of a system can also be obtained from step or pulse response measurements instead of applying periodic perturbations. Such step response measurements were first performed at the glass transition using adiabatic calorimeters in the 1970's (for a review see [27]). Here, the temperature drift of the sample under close to perfect adiabatic conditions was measured after applying a certain amount of heat. Because of the large time constant the adiabatic calorimeters are limited to frequencies below 10^{-2} Hz. In DSC increasing the temperature stepwise and measuring the heat-flow rate as a response is known since the 1970's [29]. Originally this technique was applied to purity determination based on the van't Hoff equation. Claudy [30] proposed that the deconvolution of the signals obtained from such step heating measurements could be used to evaluate the thermodynamic (reversible) and a kinetic components of a thermodynamically controlled event. Recently, in 1999, PerkinElmer Instruments reconsidered [31] this step technique which is nowadays available as StepScan™ DSC (SSDSC) for heat capacity measurements [32]. The equivalence of the results obtained from frequency dependent measurements (TMDSC) with that from step response measurements (SSDSC) will be shown in section 3.3.

In the following a short description of the different types of DSC used for temperature modulated measurements (heat-flow (disc and Calvet type) and power compensation) and the data treatment algorithms (Fourier analysis, linear and stationary response) will be given. Next, the main strategies for the interpretation of the data will be discussed (reversing and non-reversing heat capacity; complex heat capacity). Finally, some applications and the benefits and limitations of the method will be shown.

2. DIFFERENTIAL SCANNING CALORIMETRY (DSC) – BASIC CONSIDERATIONS

Two types of DSC are commonly in use, *i.e.*, heat-flow DSC and power compensation DSC. Both have their advantages and disadvantages which will be discussed in respect to application for TMDSC. A more detailed description of these instruments can be found in several handbooks of thermal analysis (see *e.g.* [31-42]).

2.1. Heat-flux DSC

A heat-flow DSC consists of two sample positions which are connected to the furnace via a thermal resistor. This resistor can be designed as a plate of known thermal properties. The most important properties of the plate material are heat capacity and thermal conductivity. These instruments then belong to the class of “quantitative differential thermal analysis” (DTA), see Fig. 2.

As in conventional differential thermal analysis (DTA), the information about the difference in the thermal properties of the sample in comparison to the reference is obtained from the temperature at the sample thermometer in respect to the temperature at the reference thermometer. Often thermocouples are used to detect these temperatures or, as in most cases, only the difference between both. The general equation describing such systems can be derived from application of Fourier's law of heat conduction for the different parts of the equipment, see *e.g.* [32,33]. The heat-flow rate difference, HF , between the heat-flow rates to the sample and the reference pan is given by

$$HF = \frac{\Delta T}{R_r} + \Delta T_o \left(\frac{1}{R_s} - \frac{1}{R_r} \right) + (C_r - C_s) \frac{dT_s}{dt} - C_r \frac{d\Delta T}{dt} \quad (6)$$

with ΔT the temperature difference between sample and reference thermometer, ΔT_o the temperature difference between sample and some reference temperature near the furnace temperature, T_s is the sample thermometer reading, R_s , C_s and R_r , C_r are the thermal resistors between the thermometer and the reference position near the furnace and the relevant heat capacities of these parts of the plate for the sample and the reference side, respectively.

For most heat-flow DSCs only the first term in Eq. (6) is considered and R_r is obtained from calibration runs. Recently, TA Instruments introduced the T-Zero™ technology [45,46] which considers all terms in Eq. (6). In the advanced version the thermal contacts between the heat-flow sensor and the sample as well as the reference pan are taken into account. The parameters of Eq. (6) are determined from calibration scans. Generally speaking, Eq. (6) yields some kind of online desmearing of the measured heat-flow rate. This works reasonably well because of the high reproducibility of the parameters of Eq. (6) as it is generally the case for heat-flow DSCs. Application of Eq. (6) to TMDSC and the correction for the thermal contacts yield some dynamic calibration for the instrumental influences. A similar approach, starting from a more general point of view, is already available in the literature [47]. The advantages of the T-

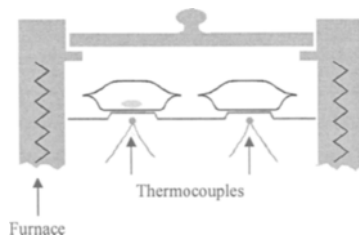


Fig. 2. Schematic drawing of a heat-flow differential scanning calorimeter (disk type)

Zero™ approach over conventional heat-flow DSCs using other algorithms for desmearing is currently not visible, because the main problem of all two-dimensional heat-flow sensors is not solved. For two dimensional heat-flow sensors, there is always a heat exchange between the sample (and reference) and the furnace which is not considered by the sensor and consequently not by Eq. (6). This is because of the unavoidable temperature difference between sample (and reference) and the furnace. The heat exchange occurs via the purge gas by heat conduction and convection as well as by radiation and changes as soon as the temperature difference between sample (reference) and furnace changes due to changing sample properties or changing thermal contacts for successive measurements. This problem limits the accuracy of two dimensional heat-flow sensors for heat capacity measurements to about 5% [48-51]. Also; the baseline curvature and reproducibility are not significant issues for this type of instruments. Non reproducible heat-flow from the furnace to the sample is the reason for insufficient accuracy for the measurement of absolute thermodynamic quantities like heat capacity and latent heats.

2.2. Tian-Calvet type DSC

To overcome the limitation of the two dimensional heat-flow sensors in respect to accuracy three dimensional sensors can be used. A nearly perfect solution of this problem was given by Tian and Calvet in 1940s [52]. Instead of using a two-dimensional sensor a three-dimensional cylindrical geometry was proposed, see Fig. 3.

These sensors measure all heats exchanged across the radial thermocouples, each consisting of several junctions. Only the heat exchanged in axial direction is not recorded. Because the sample is shorter than the sensor length, 10 mm versus 40 mm at 5 mm diameter in the case of the Setaram DSC

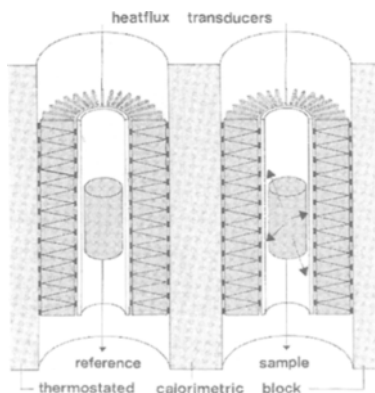


Fig. 3. Schematic drawing of a Calvet type heat-flux differential scanning calorimeter

121, the axial losses can be neglected. These Calve calorimeters yield an accuracy of about 1% for heat capacity and latent heats [53]. But there is one essential disadvantage of this calorimeters – the large time constant of the measuring system. For the fastest Calvet type DSC commercially available, the Setaram DSC 121, it is in the order of several minutes. Therefore, these calorimeters are limited to slow heating and cooling rates as well as low frequencies when used in temperature modulated mode. As shown later, the frequency range for TMDSC measurements can be significantly extended to lower frequencies using such instruments. With a Setaram DSC 121 it is possible to measure at frequencies as low as 10^{-5} Hz, corresponding to 28 hours period. Such measurements are extremely time consuming but sometimes of great scientific value.

2.3. Power compensation DSC

Another solution to prevent an unrecorded heat exchange with the surrounding and keeping the time constant of the measuring system small was introduced by O'Neill in 1964 [54]. The basic idea of the power compensation DSC is as follows: The sample and reference are located in a light cup, mass *ca.* 1 g, made of a high thermal conducting material, platinum iridium alloy in the case of the PerkinElmer Instrument DSCs. The temperature of both cups is controlled such way that their heating rate is always the same*, also during phase transitions or other heat adsorbing or releasing events. The measured signal, *HF*, is the difference between the powers necessary to realize the same heating rate for the two cups†.

For an ideal symmetric system the heat capacity of the sample can be obtained from Eq. (2). Unfortunately, the symmetry of such systems is not as perfect as for most of the heat-flow DSCs. Therefore, it is always recommended to subtract the heat-flow rate from a measurement under identical conditions (the same temperature-time-program and the same external conditions) without the sample in place (empty pan measurement). This procedure gives highly accurate C_p values under the condition that the heating rate profile is not perturbed by the transitions under investigation and the external conditions (losses) are reproduced in both runs.

The always existing thermal lag between the cup and the sample due to the thermal contacts between the cup and the sample and the thermal conductivity of the sample itself is beneficial to fulfill these prerequisites during an ideal first-order phase transition. As for any calorimeter the heat-flow to the sample

Due to some asymmetry in the losses to the surrounding a constant temperature difference, up to several K, between the cups may be introduced to correct for the asymmetry.

† The actual signal is the residual temperature difference between both cups because a proportional amplifier is used for the control circuit. But this temperature difference is proportional to the power difference.

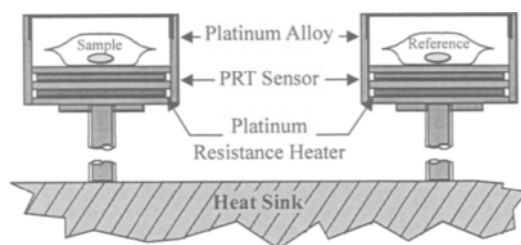


Fig. 4. Schematic drawing of a power compensation differential scanning calorimeter (PerkinElmer Instruments)

becomes not infinite at the phase transition temperature because of these thermal resistors. This allows the control circuits to react properly and to keep the heating rate of the cups constant. Since the sample lags behind the cup temperature, all heat is exchanged with the cup. Due to the high thermal conductivity of the cup material, all heat is recognized by the control circuits independent of when and where it is exchanged. As shown by Wunderlich [51], Richardson [55] and Hoehne [56,57], the accuracy of such power compensation DSCs may reach 0.5% under perfect experimental conditions. In everyday use uncertainties around 1.5% can be reached depending on the temperature range and the external conditions (ambient – sub-ambient operation, temperature range, *etc.*) [58].

The signal of a power compensation DSC is very sensitive to changes of the surrounding of the cups, *e.g.* temperature of the heat sink, color of the surface (deposition of decomposition products or water) *etc.* This is a significant disadvantage of the power compensation DSC, especially, if it is used in a non-ideal environment. Recently, the stability at sub ambient operation of the most popular power compensation DSC was significantly improved by introducing a rotating cover to the heat sink resulting in dramatically reduced ice formation at the surface (Pyris Diamond DSC, PerkinElmer Instruments).

In temperature modulated mode the power compensation DSC has the advantage of high accuracy and a short time constant which allows frequencies in the range 8×10^{-4} Hz (20 minutes period) up to 0.1 Hz (10 s period and shorter for high thermal conducting materials).

2.4. Combination of heat-flow DSC and power compensation

A combination of the more robust two dimensional disk type heat-flow DSC with the concept of power compensation seems to be promising because it may be possible to keep the advantages of the heat-flow DSC like good symmetry, no ice formation, *etc.* and to reduce the time constant as well as the unrecorded heat exchange with the furnace. The scheme of such an instrument is shown in Fig. 5.

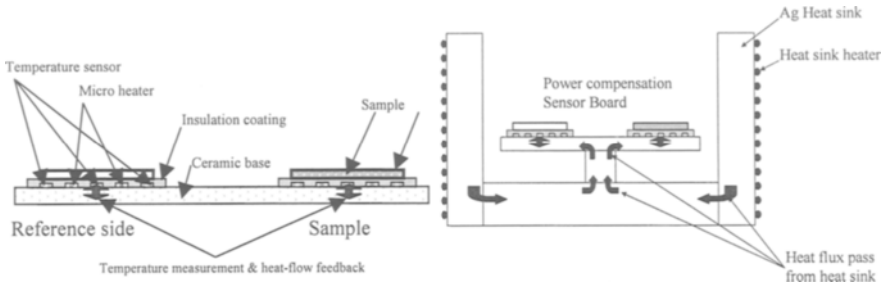


Fig. 5. Scheme of a heat-flow DSC with power compensation (Seiko SieTA™ DSC sensor [59])

However not all advantages of the power compensation DSCs, as described in 2.3, can be benefited. The power compensation yields a significant reduction of the time constant in respect to sample induced changes, for example, as seen in the width of a melting transition. But one essential problem remains, the sample lags behind the temperature of the sample support which is temperature controlled by the power compensation control circuit. This thermal lag is due to the thermal contact between the support and the sample pan which is often in the order of 20 mW/K. At first-order transitions, the sample lags additionally behind the temperature of the support also the temperature of the support is controlled. This is the same as for the PerkinElmer Instruments power compensation DSCs. But in the case of the combined instrument this change in the thermal lag yields, as in the case of the normal two-dimensional plate-like heat-flow instruments, an unrecognized heat exchange with the furnace. Also the sample dependent lag is smaller compared to the normal heat-flow DSC. Again, it limits the accuracy of the instrument. The application of such combined instruments for TMDSC measurements is possible and was checked for the Setaram DSC 141. The limitation of using higher frequencies as for common heat-flow DSCs remains as long as a large furnace must be temperature modulated. The modulation of the power compensation sensor alone overcomes this limitation and may yield higher frequencies as in common power compensation DSCs because of the even lighter design of the sample support.

3. TEMPERATURE MODULATED DIFFERENTIAL SCANNING CALORIMETRY (TMDSC)

Temperature modulated DSC (TMDSC) can be considered as an extension to DSC. The linear heating, cooling or isothermal operation of the DSC is extended by the addition of a periodic temperature (heating rate) profile to one of the basic modes. The periodic part can be generated by the furnace of the DSC (Ohm heating) or by irradiation with an intensity-modulated (chopped) light beam [60-

62]. With the help of this periodic perturbation quantities like complex heat capacity consisting of a real and an imaginary part or the reversing and non-reversing heat capacity (heat-flow rate[†]) can be obtained often in addition to the “common” DSC signal (total heat capacity). Strictly speaking, there is no need for periodic temperature modulation to obtain the commonly used signals. Similar experiments can be performed by applying temperature steps (spikes in heating rate) in time domain as will be discussed later.

3.1. Complex heat capacity and reversing and non-reversing heat capacity

Let us first make some basic considerations: Under constant pressure heat capacity C_p is defined as

$$C_p = \frac{dH}{dT} \quad (7)$$

and specific heat capacity c_p as

$$c_p = \frac{C_p}{m_s} = \frac{1}{m_s} \frac{dH}{dT} \quad (8)$$

where H is enthalpy, T temperature and m_s sample mass. Under linear heating or cooling with rate q_o

$$T(t) = T_o + q_o t \quad (9)$$

as usually applied in DSC, C_p can be obtained from

$$C_p = \frac{HF}{q_o} \quad (10)$$

where HF is the heat-flow rate necessary to heat the sample with the rate q_o . As mentioned before it is necessary to correct for the asymmetry of the measuring system by either subtracting an empty scan in time domain or by using measured and stored values to describe the asymmetry as in T-Zero™ DSC.

In the simplest case of TMDSC, a periodic temperature perturbation at a single frequency ω is superimposed to a linear temperature time profile

$$T(t) = T_o + q_o t + A_T \sin \omega t \quad (11)$$

[†] Because heat capacity is the quantity characterizing the sample [32 Wunderlich Buch] we will mostly discuss heat capacities also often the results from TMDSC are given as heat-flow rates. In this case the total heat-flow rate results from Eq. (15) and the reversing heat-flow rate, $HF_{reversing}$, equals $C_{p,reversing} \cdot q_o$.

and consequently

$$q(t) = \frac{dT(t)}{dt} = q_o + \omega A_T \cos \omega t = q_o + A_q \cos \omega t \quad (12)$$

where t is time, ω is angular frequency ($\omega = 2\pi/t_p$) with t_p the period, A_T is amplitude of temperature perturbation, A_q is amplitude of heating rate oscillation. The heat-flow rate response to such a heating rate perturbation which consist of a constant, q_o , and a periodic, $A_q \cos \omega t$, part can be deconvoluted in the two corresponding responses.

$$HF(t) = HF_{total} + HF_{periodic} \quad (13)$$

Assuming a pure thermodynamic heat capacity (no excess contributions, no time dependence, *etc.*) we obtain

$$HF(t) = C_p \cdot q(t) = C_p \cdot q_o + C_p \cdot A_q \cos(\omega t) \quad (14)$$

$C_p q_o$ equals the normal DSC response and can be obtained from averaging the oscillating heat-flow rate over one period of the modulation

$$HF_{total} = \frac{1}{t_p} \int_{t-t_p/2}^{t+t_p/2} HF(t) dt \quad (15)$$

Often, the abbreviation $HF_{total} = \langle HF(t) \rangle$ is used. $C_p A_q$ equals the amplitude of the oscillating part of the heat-flow rate A_{HF} . According to the assumptions made here the ratio of HF_{total}/q_o and A_{HF}/A_q equals the heat capacity C_p . In real experiments this is not always the case and additionally, a phase angle, δ , between heating rate and heat-flow rate appears. The phase angle may be due to several reasons and needs to be carefully calibrated before it can be used to obtain information about the samples dynamics [47,63-74]. In case the two terms do not yield the same magnitude of heat capacity the difference is called non-reversing heat capacity as will be discussed next.

3.1.1. Determination of reversing and non-reversing heat capacity

3.1.1.1. Temperature modulated DSC (TMDSC)

Next it is assumed that the Boltzmann superposition principle also holds in case of more complex situations. The response on the two independent perturbations can be written as the sum of the two separate responses, see Eq. (13). Then, in a TMDSC experiment with underlying rate q_o two basically independent measurements are performed – a constant rate DSC and a periodic one. If this deconvolution is valid three heat capacities can be obtained, *i.e.*, the

total heat capacity from the response to the underlying linear heating or cooling according to

$$C_{p\ total} = \frac{HF_{total}}{q_o} \quad (16)$$

and from the oscillating part of the heat-flow rate the magnitude or modulus of the effective complex heat capacity which is often named reversing heat capacity

$$|C_{p\ eff}^*| = C_{p\ reversin\ g} = \frac{A_{HF}}{A_q} \quad (17)$$

The total heat capacity is considered to represent contributions from base-line heat capacity (phonons) as well as latent heats. Assuming that the reversing heat capacity corresponds to events only which are reversing in the time scale of the modulation the difference between both can be considered as the non-reversing heat capacity as discussed by Reading *et al.* [16,17,75-79], Claudy [30] and Salvetti *et al.* [80].

$$C_{p\ non-reversin\ g} = C_{p\ total} - C_{p\ reversin\ g} \quad (18)$$

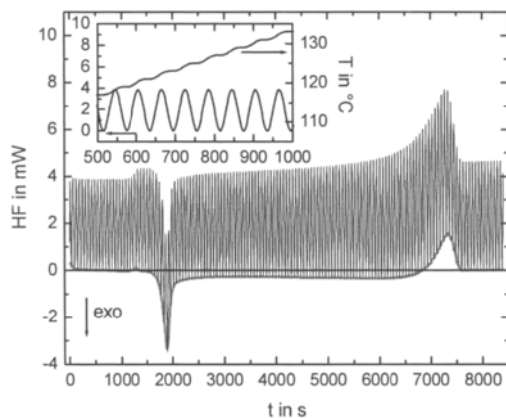


Fig. 6. TMDSC measurement of initially amorphous PEEK from 100°C to 380°C. The inset shows a part of the temperature profile, $t_p = 60$ s, $A_T = 0.3141$ K, $q_o = 2$ K/min, heat only condition, and the resulting heat-flow rate. In the empty pan corrected heat-flow rate at about 1500 s glass transition, at about 2000 s cold crystallization and around 7000 s melting can be seen. The thick line in the bottom part of the heat-flow rate is the non-reversing heat-flow rate, see Fig. 7 (Mettler Toledo DSC 821).

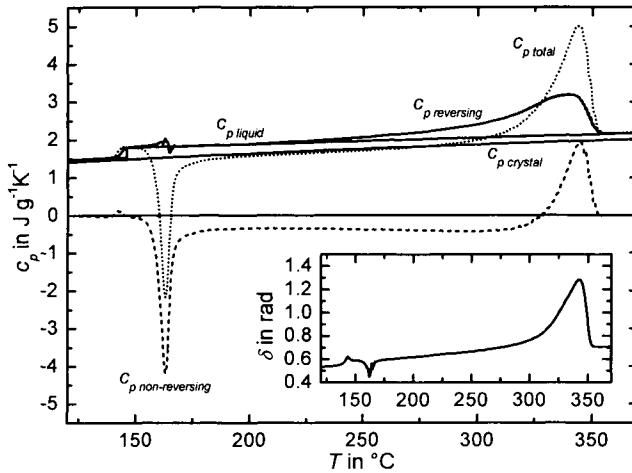


Fig. 7. Total (dotted, Eq.(16)), reversing (line, Eq.(17)) and non-reversing (dashed, Eq.(18)) specific heat capacities from the measurement shown in Fig. 6. For comparison the expected heat capacities for the crystal and the melt are added [81]. The inset shows the measured phase angle between heating rate and heat-flow rate.

To illustrate such a TMDSC measurement and the resulting curves a typical temperature-time profile, the measured heat-flow rate and the different heat capacities for an initially amorphous PEEK are shown in Figs. 6 and 7.

To distinguish between reversing and non-reversing contributions requires first of all a correct determination of the so-called reversing contribution according to Eq. (17). The key issue is which processes contribute to the reversing heat capacity? This depends strongly on the measuring conditions. Truly non-reversing latent heats on melting, as an example, contribute to the so-called reversing heat capacity depending on the ratio of heating rate amplitude and underlying heating rate. The applicability and the limitations of this approach will be discussed in sections 3.2 and 4.2.4.1.

Another way of evaluating data from a TMDSC measurement is offered by Mettler Toledo in the ADSC software [82]. The data are evaluated in time domain. Because the non-reversing heat-flow rate under a condition of heating (cannot be during cooling) equals the enveloping curve of the heat-flow rate, see Fig. 6, there is no need for Fourier analysis to deconvolute the measured heat-flow rate. The total signal is obtained by gliding integration according to Eq. (15) and the reversing component from the difference between total and non-reversing signal. Here the signal stands for heat-flow rate or heat capacity. The idea of treating data from non-continuous heating rate DSC experiments in time domain was further developed by PerkinElmer Instruments. With the StepScan™ DSC approach, a rate-controlled thermal analysis technique is offered which

allows in shorter time the deconvolution of the measured signals into reversing and non-reversing contributions (5500 s compared to 8500 s for TMDSC on the example of the PEEK measurements).

3.1.1.2. StepScan™ DSC (SSDSC)

From a combination of short heating (or cooling) steps with isotherms similar information like in TMDSC is available. A typical temperature-time profile, the heat-flow rate and specific heat capacities are shown in Figs. 8 and 10 for an initially amorphous PEEK sample. In Fig. 9 the details of data treatments are given.

In SSDSC heat capacity can be determined in several ways. As in common DSC for each heating period the heat-flow rate displacement in a steady state is measured and heat capacity is obtained from Eq. (10). This evaluation requires the steady state for each heating step. Therefore, the heating and the isothermal segment should not be too short (at least 20 s for a power compensated PerkinElmer Instruments DSC). If the isothermal period is small enough, it may happen that heat-flow rate does not go back to zero as expected. In Fig. 8 this can be seen during cold crystallization. The reason is that the exothermic excess heat-flow rate from the crystallization process is not sensitive to the temperature

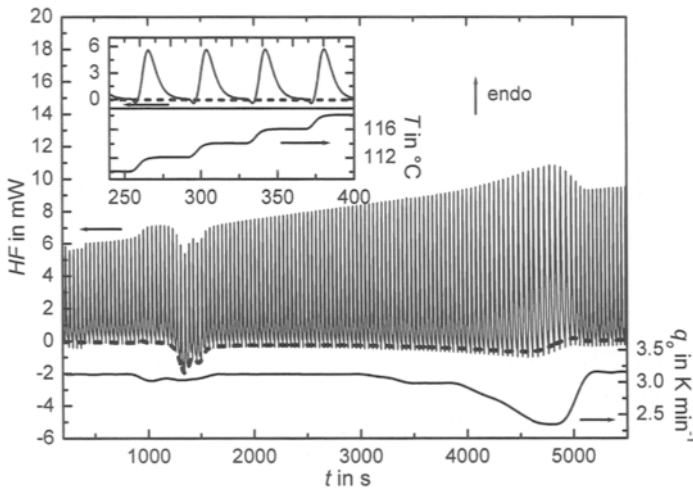


Fig. 8. StepScan™ DSC measurement of initially amorphous PEEK from 100°C to 380°C. The inset shows a part of the temperature profile (step height $\delta T = 2$ K, heating rate $q = 20$ K/min, $t_{iso-max} = 1$ min, absolute criterion = 0.02 mW) and the resulting heat-flow rate. The bottom part shows the mean underlying heating rate which varies according to the length of the isotherms. In the empty pan corrected heat-flow rate at about 1,000 s glass transition, at about 1,500 s cold crystallization and around 4,500 s melting can be seen (PerkinElmer Pyris Diamond DSC).

steps. Connecting the heat-flow rate values at the end of each isotherm yield the so-called iso-K base-line (see Fig. 9 for details). The iso-K base-line becomes unequal zero if processes contribute to the heat-flow rate which are not sensitive to the temperature profile (non-reversing). During cold crystallization, for example, the heat-flow rate does not come back to zero during the isotherm because crystallization proceeds independently on actual heating rates. That the non-reversing heat-flow rate and the heat-flow rate at isothermal parts of a TMDSC measurement are the same can be seen in Fig. 6. Because in SSDSC heat (cool) only conditions are always realized the non-reversing heat-flow rate and consequently the non-reversing heat capacity can directly be obtained from the isoK-base-line without any further data treatments. The only condition to be fulfilled is that the isotherm is not too long to avoid equilibration during each step (isoK-base-line then equals to zero). Isotherms of 20 s to 60 s are appropriate for a reasonable deconvolution into reversing and non-reversing heat capacity or heat-flow rates. The heat-flow rate sensitive to the temperature profile results in the reversing heat capacity as in TMDSC because it contains all contributions faster than the step time, this will be discussed in section 4.3.1.2. According to Eq. (1), heat capacity can be obtained from the ratio of the applied heat and the resulting temperature step. In SSDSC the temperature step, δT , is predefined and the heat-flow rate response, $HF(t)$, is measured. Heat capacity can be obtained from the area under the heat-flow rate peaks according

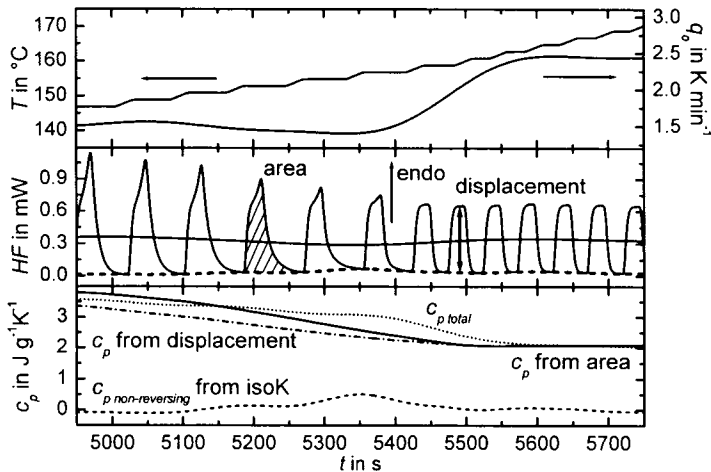


Fig. 9. StepScan™ DSC measurement of a PHB/PCL 50/50 blend in the temperature region of PHB melting. $\delta T = 1$ K, $q = 5$ K/min, $t_{iso-max} = 1$ min, absolute criterion 0.001 mW (PerkinElmer Pyris Diamond DSC).

$$C_p = \frac{1}{\delta T} \int_0^{t_s} HF(t) dt \quad (19)$$

where t_s is step time consisting of heating and isothermal time for each individual step. By varying the step time the relevant time scale of a SSDSC experiment can be varied. As in TMDSC the total heat capacity can be obtained from the average heat-flow rate over each step divided by the average heating rate during the step. The details of data treatments of a SSDSC measurement are shown in Fig. 9 and the results from the measurement shown in Fig. 8 are presented in Fig. 10.

For SSDSC as for TMDSC a total heat-flow rate and an underlying heating rate can be obtained by smoothing both signals appropriately. In Eq. (15), t_p has to be replaced by the maximum length of the steps $t_{iso\ max}$ and from Eq. (16) total heat capacity is available. In SSDSC information about processes which are non-reversing within the time scale of the experiment, $t_{iso\ max}$, are available from the isoK-base-line. The isoK-base-line connects the endpoints of the isothermal segments. As long as all processes are completed within $t_{iso\ max}$ the isoK-base-line equals zero. If $t_{iso\ max}$ is too short or reorganization occurs the heat-flow rate does not return to zero and the isoK-base-line contains the same information as the non-reversing heat-flow rate in a heat only TMDSC experiment. Dividing the isoK-base-line by the underlying heating rate yields the

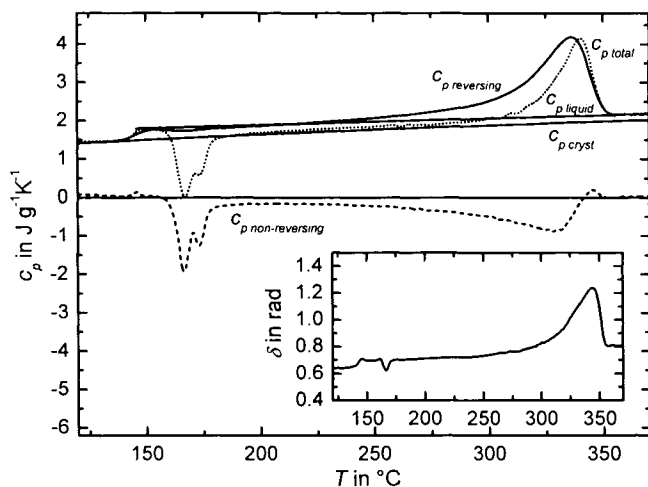


Fig. 10. Total (Eq. (16)), reversing (Eq. (19)) and non-reversing (from isoK-base-line) specific heat capacities from the measurement shown in Fig. 8. For comparison the expected heat capacities for the crystal and the melt are added [81]. The inset shows the measured phase angle between heating rate and heat-flow rate, see 3.3.2.

non-reversing heat capacity. The important point here is that all data treatments are done in time domain. No Fourier analyses is applied and consequently there are no limitations because of linearity or stationarity. Following the concept of deconvolution of the signals into reversing and non-reversing contributions, SSDSC offers three independent ways to determine reversing signals. Because total and non-reversing heat capacity are available straight forward (see above), the reversing heat capacity can be computed as the difference between the total and the non-reversing components (see Fig. 9 and Fig. 53). The non-reversing component is not well defined during melting. It may be seriously influenced by heat transfer limitations. Therefore, it seems to be much better to calculate the reversing heat capacity straight forward from the measured heat-flow rate. In SSDSC two possibilities are available. According to Eq. (19) reversing heat capacity is given by the ratio of the area under the heat-flow peak and the height of the temperature step (c_p from area). If the heating rate is sufficiently slow and a steady state is reached during the heating segment heat capacity can be obtained, as in standard DSC, from the displacement of the heat-flow rate in respect to the isoK-base-line according to Eq. (10) (see Fig. 9, c_p from displacement). While for the c_p determination from the displacement steady state during the heating segment is a prerequisite, this is not the case for the c_p determination from the area. Because the steady state during the heating segment is not reached in the measurement presented in Fig. 8, c_p from displacement was not available. The difference between the reversing heat capacities shown in Fig. 9 and Fig. 53 below is due to the fact that in the melting region a steady state is not reached during the heating segment. Because a steady state during the heating segment is not a prerequisite for the c_p determination from area, much faster heating rates can be used which generate some peak in heating rate which can be used to determine the frequency spectrum of complex heat capacity as discussed in 3.3.2. The fast heating and short equilibrium times at the isotherms result in much shorter measuring times as can be seen from a comparison of Figs. 6 and 8. For both measurements the relevant time scale (period) is 1 minute. Because the isothermal time can be shortened if the heat-flow rate fulfills a certain criterion SSDSC allows for rate controlled TMDSC.

In SSDSC the length of the isotherms is not always predefined. Depending on the setting of the equilibration criteria the next step in temperature occurs as soon as the criterion is fulfilled. Consequently, the underlying heating rate may change depending on sample response. This can be seen in Figs. 8, 9 and 53 below at melting. This allows a dramatic reduction of measuring time in case of long equilibration times. As long as no time dependent processes occur in the sample the instrument will only stay at the isotherm for the time needed to reach steady state after the temperature step. For the power compensation DSC this time is in the order of 0.5 minutes. If a time dependent process yield an increasing heat-flow rate at longer times the length of the isotherm will be

adapted accordingly. This way rate-controlled DSC experiments can be performed [33,83-84]. In Figs. 8 and 9 the maximum time for the isotherms was set to 1 minute. Therefore, the results corresponds to a time scale of 1 minute also most of the steps were actually much shorter.

Because data treatment in SSDSC is straight forward and not based on Fourier analysis there is no need for linearity or steady state neither during the heating nor the isothermal step. Therefore, this method is very attractive for reasonable precise heat capacity determination, separation of the non-reversing contribution and all are in relatively short times. Looking for heat capacity from the integral or the displacement and for the non-reversing isoK-base-line does not require linear response because no Fourier analysis is applied as in TMDSC. But as in TMDSC the results depend someway on the experimental conditions, enlarging the isotherms, as an example, will reduce the effects in the isoK-base-line because zero may be reached at the end of each isotherm after sufficient long waiting time. Since all data treatments are done in time domain in SSDSC, it is easy to understand the influence of the different experimental parameters (see 3.2 and 4.2.4.1). A more sophisticated analysis of SSDSC data based on Laplace transformation allows under linear response a complete deconvolution into frequency dependent complex heat capacity as shown in section 3.3.2.

3.1.2. Determination of complex heat capacity

Another approach to treat data from calorimetric measurements under periodic perturbation was used by Gobrecht *et al.* [15], Birge *et al.* [10], Schawe [85] and others. It only considers the periodic part of the response only and describes the measured heat capacity as a complex value.

$$C_p^* = C_p' - iC_p'' \quad (20)$$

with C_p' the real and C_p'' the imaginary part of the complex heat capacity, respectively.

$$C_p' = |C_p^*| \cos \delta_s \quad \text{and} \quad C_p'' = |C_p^*| \sin \delta_s \quad (21)$$

where δ equals the phase angle due to time dependent processes in the sample excluding heat transfer. In real measurements the measured phase angle (argument of $C_{p,eff}^*$) is mainly due to limitations in heat transfer. Therefore, C_p^* ; C_p' ; C_p'' and δ_s , characterizing the sample properties, must be replaced by $C_{p,eff}^*$; $C_{p,eff}'$; $C_{p,eff}''$ and δ when measured values are discussed. To obtain C_p^* ; C_p' ; C_p'' and δ_s carefully calibration of $C_{p,eff}^*$ is needed (see section 3.4).

The description of heat capacity as a complex value is directly based on the linear response approach. The occurrence of a frequency (time) dependent

heat capacity can be discussed as a result of the heat exchange between different degrees of freedom of the system under consideration. This was discussed for the first time in 1940 by Schaefer [14] in order to describe the heat capacity of gas molecules consisting of two or more atoms. Differences in the time constant for the heat transfer to translational and rotational degrees of freedom yield the complex heat capacity. The imaginary part of the complex heat capacity results in an increase of the entropy of the bath coupled to the calorimeter what can be considered as a loss (see [5,6,10,85-87]). Generally speaking, the heat capacity can be considered as entropy compliance in the framework of the fluctuation dissipation theorem (FDT) (see [88]). This way the frequency dependent complex heat capacity establishes a direct link to the dynamics of the processes under investigation. In case of glass transition this is generally accepted while for other processes like melting of polymers the situation is more complex mainly because of calibration problems. It is often difficult to distinguish between sample related phase shifts and heat transfer influences.

The linear response approach allows a precise description of the measured quantities as long as its prerequisites, linearity and stationarity, are fulfilled. In the case of calorimetry this is often not the case and therefore, interpretations of the results become problematic. It should be mentioned that both approaches, complex heat capacity and reversing, non-reversing heat capacity, are based on the determination of the modulus of complex heat capacity. But there is no further similarity and one should be carefully to not mix the different heat capacities.

3.2. Data treatment algorithms

The data treatment in TMDSC is based on the determination of the modulus of the effective complex heat capacity (see Eq. (15)). For that reason first of all, the amplitudes of the heat-flow rate and of the temperature (heating rate) perturbation must be determined or known. Commonly, this is done by means of Fourier analysis of the measured signals. In this section, we will give some details of the algorithms used and the prerequisites for applying them. A more detailed description can be found in references [47,77,85,89-90].

First, the measured heat-flow rate is often averaged over one period by gliding integration in order to obtain the total heat-flow rate and according to Eq. (12) the total heat capacity. Strictly speaking, this is only correct as long as the amplitude of the periodic component does not change during one single period as will be shown below. Next, the total heat-flow is subtracted in order to derive the periodic part of the heat-flow rate. The procedure and some of the inherent problems are shown in the next figures. Because we are very often interested in effects that yield changes in heat capacity and consequently changes in the heat-flow rate amplitude with time or temperature, we will first discuss the separation

procedure for a simulated heat-flow rate profile of such type. Let us assume a peak in heat capacity that can be described by a Gauss-function versus time

$$C_p = C_{p,o} + \frac{A}{w \cdot \sqrt{\pi/2}} e^{-\frac{2(t-t_c)^2}{w^2}} \quad (22)$$

with offset $C_{p,o} = 1 \text{ J K}^{-1}$, centre $t_c = 600 \text{ s}$, width $w = 150 \text{ s}$ and area $A = 10,000 \text{ J K}^{-1} \text{ s}$.

Multiplying this heat capacity with a periodic heating rate profile according to Eq. (12), $q(t) = q_o + A_q \cdot \cos(\omega \cdot t)$, with $\omega = 2\pi/60 \text{ s}$, $q_o = A_q = 3 \text{ K/min}^{-1} = 0.05 \text{ K/s}$ (heat only, corresponding to a temperature amplitude of 0.47 K) yields the periodic heat-flow rate shown in Fig. 12.

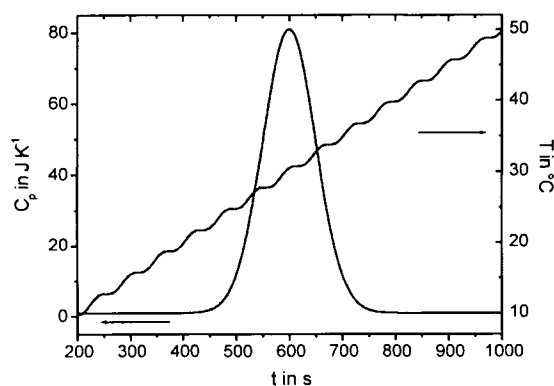


Fig. 11. Input functions for heat capacity and temperature for the calculations (see text)

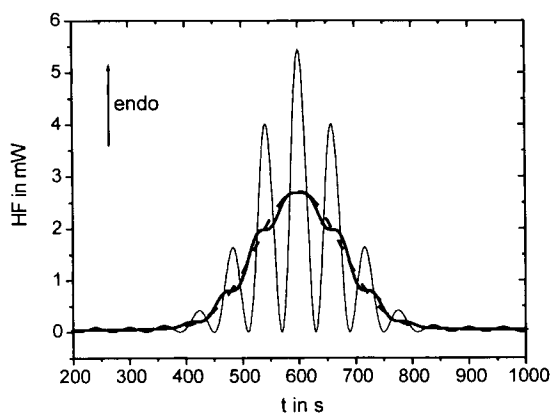


Fig. 12. Simulated heat-flow rate, thin line, total heat-flow rate obtained from averaging, $HF_{total\ average}$, thick line, and true total heat-flow rate, dashed line.

Commonly, the average of this periodic function is obtained by gliding integration according to Eq. (15). Since the amplitude changes with time the different parts of a single period contribute differently to the average. This yields the oscillations in the average which result in differences compared to the true total heat-flow rate (input function $C_p q_o$) up to 10%. It should be mentioned that the often recommended condition to have at least 5 periods within the peak is fulfilled in this example, see Fig. 12.

Next, the amplitude and phase of the periodic part of the heat-flow rate are obtained by means of Fourier analysis. Again gliding integration as described in [77,85,89] is commonly used. A more illustrative way of determining the amplitude and phase of the signals is the fit of a sine function to the measured values in a certain time window (at least one period). This can be done by least square fits of a sine function with given frequency (the same as used for the perturbation) and variable amplitude and phase.

In the time interval 436 s to 496 s a sine function, $HF(t) = A_{HF}\sin(\omega t)$, is fitted to the periodic part of the heat-flow rate. It results in an amplitude of 0.61 mW. At 466 s, the center of the time interval, the amplitude of the original signal equals 0.55 mW. Again a 10% deviation appears. Deviations of the fit from the input heat-flow rate can be seen at the minimum and maximum due to the amplitude increases with time. These deviations between the fit and the measured heat-flow rate can be reduced by introducing higher harmonics in the fit. Here, the response is non-linear because of non-stationarity, for details see [91-94]. Since such effects appear very often they must be considered and a critical analysis of the data obtained from each measurement is recommended.

Commonly, the complex amplitudes are obtained by means of Fourier analysis of gliding integration over one period according to

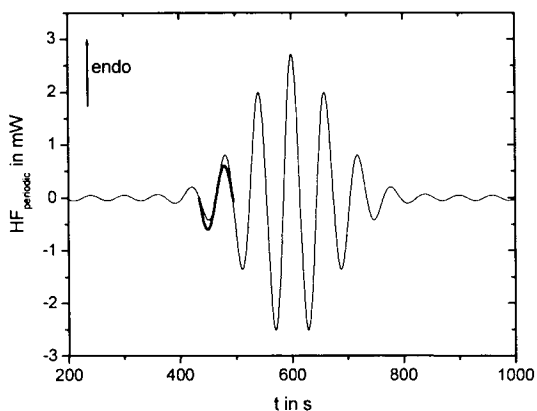


Fig. 13. Periodic part of the simulated heat-flow rate, thin line, and fit of a sine function to one period, thick line

$$F[f(t)](\omega) \equiv A_f^*(\omega) = \frac{2}{t_p - t_p/2} \int_{t_p - t_p/2}^{t_p/2} f(t) \cos(\omega t) dt - i \frac{2}{t_p - t_p/2} \int_{t_p - t_p/2}^{t_p/2} f(t) \sin(\omega t) dt \quad (23)$$

where $f(t)$ stands for heat-flow rate, $HF(t)$, heating rate, $q(t)$, or temperature, $T(t)$, respectively. The magnitude or modulus of these complex functions can be obtained from

$$|A_f^*| = \sqrt{(\operatorname{Re}(A_f^*))^2 + (\operatorname{Im}(A_f^*))^2} \quad (24)$$

and the argument or phase angle from

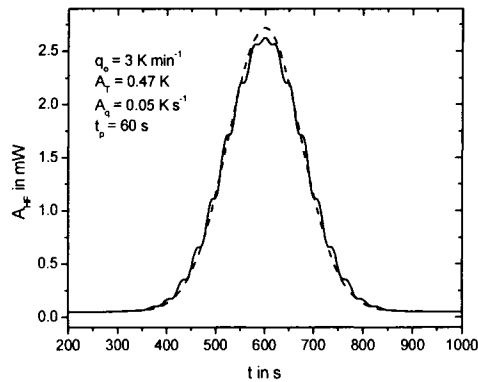


Fig. 14. Amplitude of the periodic part of the simulated heat-flow rate, Fig. 12, obtained from Eq. (20), line, and the input function itself, dashed line

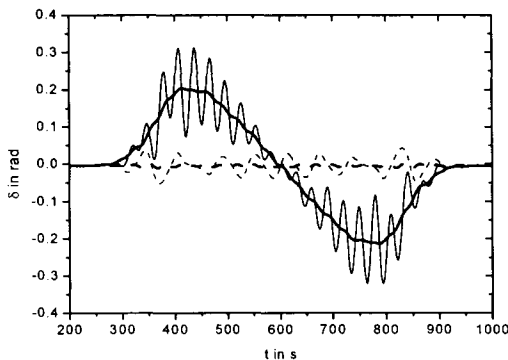


Fig. 15. Argument of $HF(t)$ after subtraction of the true HF_{total} , dashed lines, and $HF_{total\ average}$ from Eq. (19), solid lines. The thick lines result from an additional smoothing over one period

$$\delta = \arctan\left(\frac{\text{Im}(A_f^*)}{\text{Re}(A_f^*)}\right) \quad (25)$$

Also, deviations in the order of a few percent can be seen between the input function and the heat-flow rate amplitude according to Eq. (20). In our simple model no time dependence is assumed. Consequently, the phase angle between heat-flow rate and heating rate should be zero at all times. In Fig. 15 the argument (phase angle) of the heat-flow rate according to Eq. (20) is shown.

The positive and negative peaks in the phase angle are due to the increasing and decreasing heat capacity, respectively. Snyder and Mopsik [95] used the term dynamically induced loss for this phenomenon which is also observed at glass transitions [96,97] and must be considered if the phase angle or the imaginary part of heat capacity is quantitatively discussed. It should be mentioned that the phase angle due to a time-dependent processes in the sample (relaxations) is often very small. At glass transitions, as an example, the peak maximum equals to 0.04 rad (see below in Fig. 20).

This example, peak in heat capacity, was chosen to demonstrate the inherent problems of the data treatment by means of Fourier analysis in case of changing heat capacity. The values obtained deviate for several percent from the expected input values. These problems occur if heat capacity is changing significantly with time or temperature within a single period of the perturbation, non-stationarity, as it is often the case in measurements [91-94,98,99]. Another problem appears if the response depends on the amplitude of the perturbation, non-linearity, what often occurs at phase transitions. To avoid falsification and to allow for a quantitative discussion appropriate measuring conditions must be chosen [47,93,100-108]. How to choose correct experimental parameters was discussed for TMDSC in detail in [94] and only the main conclusions will be repeated here. Assuming a linear operating DSC (all non-linearity is caused by sample properties) the reason for non-linearity is the temperature, time or heating rate amplitude dependence of heat capacity. Accepting a certain uncertainty, η , from non-linearity (say $\eta = 2\%$), conditions can be formulated to stay within this arbitrary chosen limit. In most cases heat capacity is temperature dependent (see example given above). Then, a temperature amplitude, A_T , must be chosen according to Eq. (26) to have an uncertainty smaller than η .

$$\frac{\Delta c_p(\omega)}{c_p(\omega)} \approx \frac{1}{c_p(\omega)} \frac{dc_p(\omega)}{dT(\omega)} A_T \leq \eta \quad (26)$$

If heat capacity is heating-rate dependent, as often observed in the melting or crystallization region of polymers, A_q must fulfill Eq. (27).

$$\frac{\Delta c_p(\omega)}{c_p(\omega)} \approx \frac{1}{c_p(\omega)} \frac{dc_p(\omega)}{dq(\omega)} A_q \leq \eta \quad (27)$$

Beside non-linear response due to too large amplitudes evolution of heat capacity with time yields also non-linearity which is called non-stationarity. If heat capacity depends on time, *e.g.* during quasi-isothermal crystallization the period of the perturbation must be small enough to prevent significant changes of heat capacity during a single period, see Eq. (28).

$$\frac{\Delta c_p(\omega)}{c_p(\omega)} \approx t_p \frac{1}{c_p(\omega)} \frac{dc_p(\omega)}{dt} \leq \eta \quad (28)$$

In case of scanning and temperature dependent heat capacity underlying heating rate and period must be chosen to fulfill Eq. (29).

$$\frac{\Delta c_p(\omega)}{c_p(\omega)} \approx q_0 \cdot t_p \frac{1}{c_p(\omega)} \frac{dc_p(\omega)}{d\langle T \rangle} \leq \eta \quad (29)$$

For the example discussed above for a period of 60 s the underlying heating rate should be less than 0.05 K/min to meet an accuracy of 2% for the complex heat capacity. It must be mentioned that the phase is mainly influenced (see Fig. 15) and the modulus of complex heat capacity is less sensitive to non-stationarity (see Fig. 14). Nevertheless, if a certain accuracy is required for a quantitative heat capacity determination then one should simultaneously meet conditions of linearity and stationarity, Eq. (26-29). For a more detailed description see [94].

3.3. Frequency dependent heat capacity

In temperature modulated DSC a new independent variable, namely frequency, becomes a parameter. The dynamic study of a certain process by means of heat capacity spectroscopy requires the measurement of the frequency dependence of the effective heat capacity. There may be several reasons why effective heat capacity becomes frequency dependent. For example, the heat capacity of the sample may be complex and therefore, frequency dependent as in the case of glass transition. Also, there may be heat transfer problems which yield a complex effective heat capacity. In real measurements the combinations of complex sample heat capacity and heat transfer effects are commonly observed.

There are basically two ways to generate the spectrum of the effective heat capacity beside all problems of calibration which will be discussed later. The one is the measurement at different modulation frequencies – frequency domain –, and the other one uses the broad spectrum covered by sharp single peaks or steps

– time domain. Here, we will discuss these different ways to generate the spectrum of the effective heat capacity. In TMDSC the frequency range available is limited by heat transfer processes. This may be either due to the instrument or the sample itself. For common TMDSC equipment the possible frequency range is somewhere between 0.1 Hz and 0.001 Hz. The upper limit is defined by the sample – sample-pan combination including different thermal contacts and the thermal conductivity of the sample. This, as an example allows for the determination of the thermal conductivity of the sample as will be discussed in section 3.5. The lower limit is given by the sensitivity of the instrument or some software limitations as in the case of the TAI DSC 2920. Using high sensitive instruments like the Setaram DSC 121, lower frequencies down to 10^{-5} Hz are accessible.

3.3.1. Periodic perturbations – frequency domain

3.3.1.1. Single frequency measurements

One way to generate the spectrum of the effective heat capacity is to perform measurements at several single frequencies. This can either be done successively at frequency scans at several constant temperatures, as commonly done in dielectric or shear spectroscopy, or during several temperature scans at several constant frequencies. Because it is often difficult to reproduce the sample properties of complex materials, like polymers, or these properties are changing with time, it may be impossible to measure under isothermal conditions. To obtain the frequency dependence often single frequency measurements are performed and the cooling or heating scans were repeated several times applying perturbations at different frequencies [60,61,70,100,109-129]. This procedure is very time consuming and requires stable samples which do not change their properties during the different scans. To overcome this limitations it is important to perform simultaneous multi-frequency measurements.

3.3.1.2. Multi frequency measurements

It is well known from Fourier analysis of periodic signals of arbitrary shape that these signals, $f(t)$, can always be described as a sum of Fourier components including those at higher harmonics.

$$f(t) = \sum_{n=1}^{\infty} (a_n \sin(n\omega_0 t) + b_n \cos(n\omega_0 t)) \quad (30)$$

This can be used to apply a variable frequency temperature perturbation in TMDSC experiments. However, from the theory nothing is said about the shape of the input signal. It can be any periodic function with the only limitation, that $A_q(\omega)$ could not equal zero (see Eq. (18)). Therefore, we can add some higher harmonics to the sinusoidal heating rate and measure them simultaneously at the

same time. One can add any frequency $\omega = n\omega_0$ as long as n is integer without changing the basic period of the resulting signal. In fact, it is not necessary to program all higher harmonics of interest, some inharmonic periodic heating rate profiles are enough to analyze the higher harmonics. Inharmonic perturbations, for example, can be programmed as common saw-tooth. The application of this temperature profile to multi-frequency measurements is analyzed in reference [130]. Since the temperature amplitude of higher harmonics of a saw-tooth is inversely proportional to the square of the harmonic number, the heat-flow rate decreases very fast at higher harmonics resulting in a low signal-to-noise ratio. Wunderlich and co-workers [131] suggested a complex saw-tooth, which has first four even harmonics with the same temperature amplitude and consist of 14 linear heating/cooling segments per period. In that case the heating rate amplitude increases linearly with the harmonic number. We proposed a multi-frequency TMDSC method where the experimental parameters are selected in an optimal way for the simultaneous dynamic heat capacity measurement at different frequencies [132,133].

Real measurements are always accompanied by noise. If it is mainly white noise, it has equal contribution at all frequencies. If the measured heat-flow rate has the same amplitude at all harmonics then, the heat capacity spectrum is determined with about the same uncertainties due to the noise at different frequencies. Since the amplitude of the heat-flow rate is proportional to the heating rate amplitude (not temperature amplitude) an optimal heating rate signal would be one with all higher harmonics of the same amplitude. Such heating rate profile can be generated with one delta function, $\delta(t-t_i)$, in heating rate per period (see Fig. 16). Therefore we propose to use a temperature profile consisting of temperature steps [132,133].

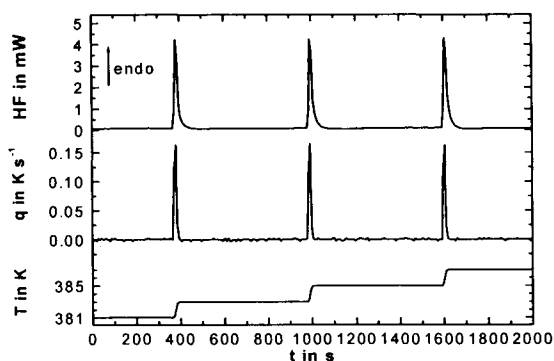


Fig. 16. Part of the measured temperature-time profile, bottom, the heating rate profile, middle, and the heat-flow rate profile, top, of a StepScan™ DSC measurement, The programmed step was 2 K, heating rate 10 K/min and $t_{iso\ max} = 10$ min, absolute criterion = 0.001 mW (PerkinElmer Instruments Pyris 1 DSC).

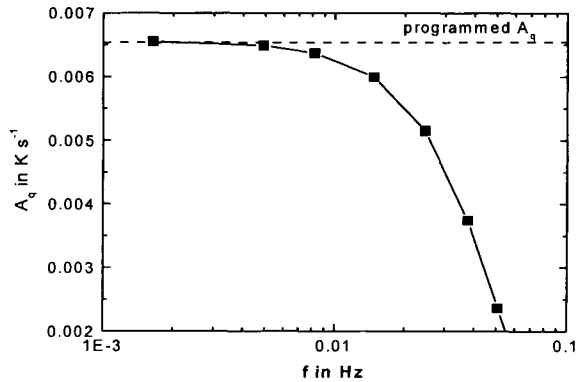


Fig. 17. Amplitude of programmed, dashed line, and measured, points, heating rate amplitude for the data from Fig. 16.

Whether one has isotherm or slow heating or cooling between the temperature steps depends on underlying heating or cooling rate, which can be easily added to the temperature-time program (see [132] for details).

In real measurements, however, measured (real) temperature is smeared by the instrumental lag, which leads to a damping of higher harmonics of the heating rate. In addition, heat transfer and possible time-dependent processes in the sample damp the heat-flow rate spectrum [73].

The measured heating rate spectrum coincides with the programmed up to about 0.01 Hz. At higher frequencies the measured heating rate amplitude decreases because of the instrumental time constant. It is worth to mention that the apparatus damps not only the heating rate and heat-flow rate spectrum but also the noise spectrum. Therefore, under certain conditions, the uncertainty for heat capacity measurements due to signal to noise ratio remains below 1.5% until a frequency of 0.15 Hz [132]. Choosing an appropriate low basic frequency it is possible to obtain heat capacity up to the 256th harmonic. This corresponds to approximately two and a half orders of magnitude in frequency.

We have analyzed two limiting factors in regard to the experimental determination of dynamic heat capacity: noise level and non-linear response [132]. Larger temperature amplitudes guarantee better signal-to-noise ratio but result in non-linear response of the instrument and the sample. Therefore it is important to find out the optimal experimental conditions for heat capacity measurements for each instrument and each sample (sample pan, thermal conductivity, heat capacity, *etc.*).

Assuming measuring conditions for which falsification due to non-linear or non-stationary response can be neglected the ratio of complex heat-flow rate and heating rate amplitudes yield the effective complex heat capacity

$$C_{p\text{ eff}}^*(\omega) = \frac{A_{HF}^*(\omega)}{A_q^*(\omega)} = \frac{A_{HF}^*(\omega)}{\omega A_T^*(\omega)} \quad (31)$$

which can also be expressed in terms of real and imaginary part of complex heat capacity according to Eq. (20). Let us assume further that for some periodic heating rate $q(t)$ our instrument has such sampling rate, that we get n points per period for $HF(t)$ and $q(t)$. If one is interested only in the value of $C_{p\text{ eff}}^*(\omega)$ then it is not necessary to determine separately $A_{HF}^*(\omega)$ and $A_q^*(\omega)$. One can directly calculate $C_{p\text{ eff}}^*(\omega)$ omitting all normalization factors[§] [132]:

$$C_{p\text{ eff}}^*(\omega) = \frac{A_{HF}^*(\omega)}{A_q^*(\omega)} = \frac{\sum_{i=1}^n HF_i \cos(\omega t_i) - i \sum_{i=1}^n HF_i \sin(\omega t_i)}{\sum_{i=1}^n q_i \cos(\omega t_i) - i \sum_{i=1}^n q_i \sin(\omega t_i)} \quad (32)$$

The points HF_i and q_i should be taken with the same sampling rate (number of points per unit time) and equidistant. This way of calculating complex $C_{p\text{ eff}}^*(\omega)$ is preferable because there is no need to take care for the initial phase of $A_{HF}^*(\omega)$ and $A_q^*(\omega)$.

3.3.2. Non-periodic perturbations – step response in time domain

In differential scanning calorimetry (DSC) one commonly measures heat-flow rate into the sample under non-zero heating/cooling rates, *i.e.* under scanning of temperatures. In general case the relation between the heating rate and the heat-flow rate can be very complicated. Under linear and stationary thermal response this relation is described by a convolution product. There are two ways to resolve the convolution product: whether to use Fourier transformation or Laplace transformation. Temperature Modulated DSC (TMDSC) applies periodic temperature oscillations to the system and analyzes the amplitude and phase of the corresponding periodic heat-flow rate. The measured signals are Fourier-transformed to obtain the dynamic heat capacity c_p^* (see above). Another way to resolve the complicated relation between the heat-flow rate and the heating rate is the analysis in time domain of the heat-flow rate in response on a step perturbation [133]. To best of our knowledge the first stepwise method for differential thermal analysis (DTA) was introduced by Staub and Perron [29]. In their method the temperature is increased stepwise; the heat effects being determined by an analysis of the transient thermoelectric

[§] Because of causality the imaginary part of complex heat capacity must be positive. Therefore we use, as common, the negative sign in front of the imaginary part of the complex amplitudes.

effects after each step; between the steps temperature is kept constant until equilibrium is attained. At that time, the end of 1970's, the data were collected by a chart recorder and a quantitative analysis of the results was very difficult. But one was able to determine the area under the curves and to make a rough estimation of a time constant.

Schawe *et al.* [134,135] proposed a method to measure the dynamic behavior of DSC instruments by steps in heating rate (switching from isotherm to heating with constant heating rate and switching from heating to isotherm, respectively). The apparatus function, which is calculated by Laplace transformation of the heat-flow rate just after switching, describes the dynamic behavior of the instrument and how the measured signal is smeared. This apparatus function is used to desmear the whole measured heat-flow signal.

Agarwal and Farris [136,137] proposed the pulsed DSC method, where an input pulse of temperature is applied to the system and the output heat-flow rate is collected. Essential point of the method is that both the input and the output must return to their initial unperturbed state at the end of the experiment. A simple Laplace analysis of the input and output data yields the equilibrium specific heat and a mean relaxation time, whereas the frequency dependent quantities are calculated by Fourier transform [137].

We proposed another method of generating frequency dependent quantities by DSC, where the programmed temperature consists of a sharp single step followed by an isothermal segment [133].

As shown above and in [132] the periodic heating rate $q(t)$ should contain a delta function to generate a uniform heat-flow rate spectrum (*i.e.* constant $A_q(\omega_n)$ at different frequencies $\omega_n = n\omega_0$, $\omega_0 = 2\pi/t_p$, t_p is the basic period of $q(t)$, n is integer). Then the temperature-time profile should have infinite sharp stepwise changes. Let us consider a single period of such a heating rate function together with the respective heat-flow rate as shown in Fig. 16. If the period is long enough then the heat-flow rate reaches the steady state value before the next temperature step. Since the signals are periodic the peak in the heat-flow rate starts from the same steady state value. We can set the steady state value of the heat-flow rate to zero without influencing the amplitudes of all harmonics. The same we can do with the heating rate [132].

Since we have a steady state part of the heat-flow rate before the peak, the peak itself does not "feel" the previous peaks. Consequently the shape of the peak is exactly identical as that of a single peak measured with only one heating rate pulse (see Fig. 17). We can treat this peak as a single period of some fictitious periodic function with basic period t_p (see [132] for details), and calculate $C_p^* \text{ eff}(\omega)$ at a set of frequencies $\omega'_n = n2\pi/t_p$. The shortest possible basic period $t_{p \text{ min}}$ of such function is the time the heat-flow rate returns back to the steady state value after the perturbation. The longest basic period $t_{p \text{ max}}$ is the time interval the heat-flow rate has been actually measured after the temperature

step. Since we can vary the basic period in a certain range for this single step at temperatures we generate a continuous spectrum of heating rate instead of a discrete spectrum in case of the periodic $q(t)$. Then, $C_{peff}^*(\omega)$ can be calculated for a continuous frequency range $\omega \geq 2\pi/t_{p\ max}$. Finally, the data treatment becomes nothing else as an operational calculus. Effective heat capacity we can determine as:

$$C_{peff}^*(\omega) = \frac{\int_0^{t_p'} HF(t)e^{-i\omega t} dt}{\int_0^{t_p'} q(t)e^{-i\omega t} dt} \quad (33)$$

We fix the integration limits and vary only the frequency ω to obtain the heat capacity spectrum. If we measure n points of heat-flow rate and of heating rate during the time interval $(0, t_p')$ the integrals can be changed to sums and Eq. (33) equals exactly to Eq. (32), since $e^{-i\omega t} = \cos(\omega t) - i\sin(\omega t)$. The data treatment can be performed by a software available for download from our website [22].

The area under the heat-flow rate peak is the total amount of heat absorbed by the sample due to the stepwise increase of temperatures. This heat equals to the numerator in Eq. (33) at $\omega = 0$ and the height of the temperature step equals the denominator. Therefore, $C_{peff}^*(0)$ calculated by Eq. (33) or Eq. (32) for $\omega = 0$, corresponds to the total heat capacity as long as a steady state value is reached at the end of the isotherm. If this is not the case the area under the peak corresponds to the heat capacity due to the degrees of freedom relaxing within the time of the isotherm. Then, the pieces of information obtained are basically the same as from reversing heat capacity. The value of the heat-flow rate at the end of the isotherms is due to degrees of freedom not relaxed within the isotherm. It is the so-called isoK base-line in StepScan™ DSC which yield information about the non-reversing changes in respect to the time scale of the isotherms, see section 3.1.1.2.

Summarizing this part of the data treatment we can conclude that

- the frequency selective algorithm significantly increases the signal to noise ratio as well known also from rectification algorithms (lock-in amplifiers) as long as the conditions of linearity and stationarity are fulfilled;
- under certain conditions, which will be specified next, a deconvolution in a reversing and a non-reversing heat capacity or heat-flow rate is possible. This allows for the separation of overlapping effects;
- the complex heat capacity establishes a direct link to the dynamics of the sample under investigation.

3.4. Calibration

Modern TMDSC and DSC apparatuses are highly precise measurement devices. Nevertheless, they are often used to obtain qualitative information only. To overcome this unsatisfactory situation there is great demand for accurate and easy to handle calibration routines for heat capacity (heat-flow rate) as well as temperature. For DSC these calibration routines are available. A metrological based procedure was recently suggested [138]. Often these procedures developed for DSC are also applied for TMDSC. This yields sometimes large uncertainties because in DSC steady state is assumed what is often not the case in TMDSC especially at shorter periods (higher frequencies). We have been dealing with the basics of heat capacity calibration algorithms for TMDSC and showing some practical applications [73,74]. Because of the importance of calibration for TMDSC in general, we are going to briefly repeat in part here.

3.4.1. Heat Capacity Calibration

The periodic perturbations in temperature (heating rate) or single steps allow for the investigation of time dependent processes. This is done by calculating the interesting quantities from magnitude and phase angle (relative to that of the modulated heating rate function) of the measured heat-flow rate. Unfortunately, the measured quantities contain effects from the apparatus (the DSC) too and careful "calibration" should be done to separate these influences from the measured signal and come to reliable results of the properties of the sample itself. Calibration means the quantitative determination of all apparatus parameters and the proper correction on the measured raw data. The calibration procedures for temperature, heat-flow rate and heat are well established for commercial DSCs [138]. For TMDSC there is an additional calibration procedure needed which corrects for the huge effect of the frequency on the magnitude and phase angle of the measured complex heat capacity. Several attempts to correct for this effect can be found in literature [47,65,68-74,89,101,102,104,139-167].

To be able to correct these effects and to minimize them by choosing optimum experimental conditions, what is always preferable against correction, one should be aware about the physics behind. Therefore, at first, we present the TMDSC and the pathway of heat transfer by means of simple model considerations leading to some formulas describing this behavior approximately. These considerations form the basis for different calibration procedures for the magnitude as well as the phase angle of the complex heat capacity of the sample and can be found in the literature [73,74,150]. Finally we will discuss some of these calibration procedures in details.

A DSC is built by different parts, and each part in principal has a certain heat conductivity and a certain heat capacity. Any contact area between different

parts acts as an additional heat resistance. In addition, it often includes some sophisticated electronics that amplifies the voltages from the sensors to the measured signal transferred to the computer. No matter how complicated a DSC is, can be dissected into a network of simple mechanical elements and, hopefully, linear electronics. There is no limit for the number of elements in such a network. In order to obtain these properties, a set of linear differential equations must be solved. The number of equations is the same as the number of elements in question, this number can be high for a complex modern equipment. Nevertheless, we shall, in what follows, restrict ourselves to very simple models, which are absolutely sufficient to learn about the principle behind heat transfer in the DSC and to the sample and its influence on TMDSC signals.

In Fig. 18 the different elements influencing the heat transfer from the DSC measuring system to the sample are schematically shown. The heat-flow is limited by a thermal resistance between the oven (base plate in case of a heat-flow DSC) and the sample pan. The effective time constant is determined not only by the sample heat capacity but also by the sample pan heat capacity which has to be considered [47]. Another thermal contact, which may change during the measurement, exists between the sample pan and the sample. And last but not least, the thermal conductivity of the sample itself limits the heat transfer and will influence the dynamic behavior of the DSC – sample arrangement. This influence can be used to obtain thermal conductivity from the dynamic behavior of a DSC [168] as discussed in the next section. This dynamic behavior is rather complex, and therefore, a simple model is needed to discuss the basics of the

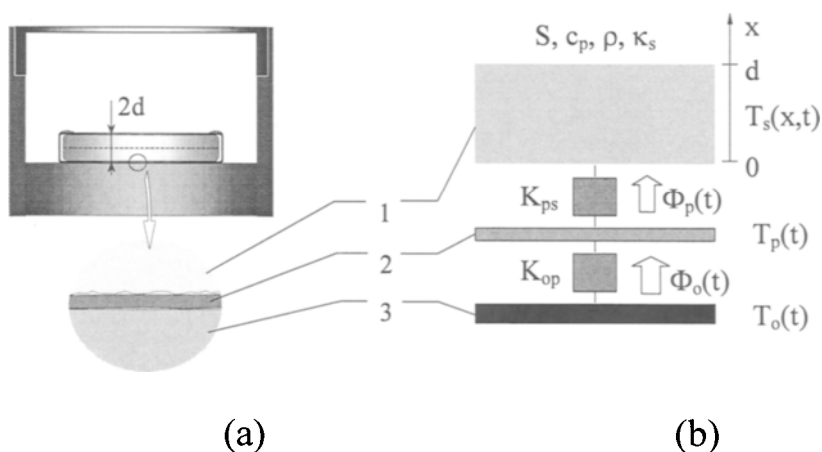


Fig. 18. The schematic view of a single DSC oven in case of the power compensation PerkinElmer Instruments DSC (a) and its block diagram (b). 1 – sample, 2 – pan, 3 – oven.

heat transfer in a DSC under periodic perturbation.

The model of choice to evaluate a heat-transfer network is often that of electrical analogy, which has proved its worth in DTA and DSC analysis since decades ago [169]. From the physical point of view, the transport of energy (heat-flow) is based on the same type of equations, as is the transport of charge (current), the knowledge from theory of electricity (in particular alternating-current (ac) theory) can thus easily be applied to heat transport problems. The advantage of looking on electrical networks rather than on often complex heat conducting solid objects is that there are a lot of powerful tools from electrical line network and the transfer theory available for that purpose.

The total network describing a DSC (the “box”) has one “input” (the temperature-time program) and one “output” (the heat-flow rate into the sample, which is calculated from the differential temperature or directly measured as differential heat-flow rate). To evaluate the behavior of an apparatus it is often sufficient to look at the so-called “transfer function” $P(\omega)$ of the “box”, a complex function in frequency domain [134,170], which is defined as the quotient of the output function $Out(\omega)$ over the input function $In(\omega)$. The transfer function (in frequency domain) is mathematically connected with the “step response” or “pulse response” functions (in time domain) via Fourier transform. It will go beyond the scope of this paper to derive all details of the features of these functions; the interested reader is referred to textbooks of transfer theory. However, the transfer function of the apparatus is in principle the “calibration” function we need to correct the measured quantities for apparatus influences.

From the transfer theory of linear systems it is known that the overall transfer function of a network can be calculated from the transfer functions of the individual components [134,170]. In particular, it holds that for transfer elements connected *in series* the total transfer function is the *product* of those from the elements. In other words, the magnitudes of the complex functions have to be multiplied, whereas the phase angles connect additively. On the other hand, for the transfer elements connected *in parallel*, the total transfer function is the *sum* of those of the components.

These facts enable to breakdown the complicated heat-transfer network of a DSC into simple components with rather easy transfer functions (for reasons of understanding the principle behind). These transfer functions can then be assembled properly and give rise to the transfer behavior of the total TMDSC (both with and without the sample included). We shall proceed this way and look at the single components first and connect the results later. Knowing the transfer function enables the determination of the correction function and thus a proper calibration.

The simplest component of heat conducting networks is an object having a certain thermal resistance R_{th} and a certain heat capacity C_p . The respective electrical analogy element is the low-pass filter with a resistor R and a capacitor

C in series. The complex transfer function, taking ac-voltage as input and output functions, can easily be calculated (see textbooks of physics), it is:

$$P^*(\omega) = \frac{1}{1 - i\omega RC} = \frac{1}{1 + (\omega RC)^2} + \frac{\omega RC}{1 + (\omega RC)^2} i \quad (34)$$

with the angular frequency $\omega = 2\pi f$ (f frequency). Changing R to R_{th} , C to C_p and voltage to temperature generates the respective transfer function for the thermal behavior of such an element. Therefore we can calculate the magnitude (absolute value, modulus):

$$Abs(P^*(\omega)) = \sqrt{\text{Re}^2(P^*(\omega)) + \text{Im}^2(P^*(\omega))} = \frac{1}{\sqrt{1 + (\omega R_{th} C_p)^2}} \quad (35)$$

and the phase angle (argument):

$$Arg(P^*(\omega)) = \tan^{-1} \left(\frac{\text{Im}(P^*(\omega))}{\text{Re}(P^*(\omega))} \right) = \tan^{-1}(\omega R_{th} C_p) \quad (36)$$

of the complex transfer function in the case of thermal quantities. These equations indicate that the magnitude of the (modulated) temperature on the output side (compared to the input side) drops with increasing frequency, and there is a phase shift between both signals. In other words, the measured quantities (output) are not constant for a constant input function but depend on the frequency applied. The larger the frequency of temperature modulation and the heat capacity and the thermal resistance of the considered RC -element, the larger the change (falsification) of the output quantities will be.

For a given heat conducting element with a given R_{th} and C_p (the product is a characteristic time τ), the frequency dependence of the complex transfer function can be presented graphically.

To calculate the (complex) heat-flow rate into a RC -element from the transfer function of Eq. (34), for a given modulated temperature function (with frequency ω), we have to multiply with C_p and ω . The magnitude of that function is easily to be represented in the Bode plot via a simple shift in y-direction of the magnitude of the transfer function (Fig. 19), which leaves the shape of the curve unchanged. To obtain the phase angle of the heat-flow rate, we have to take a phase jump of $\pi/2$ between temperature and heat-flow into consideration, where we have to subtract from the argument of the transfer function. Again, this is a simple shift in y-direction in the Bode-plot (Fig. 19), leaving the shape of the curve unchanged. To get the proper heat-flow (or c_p) curve of a certain RC -element, we only have to shift the transfer function properly in the Bode plot.

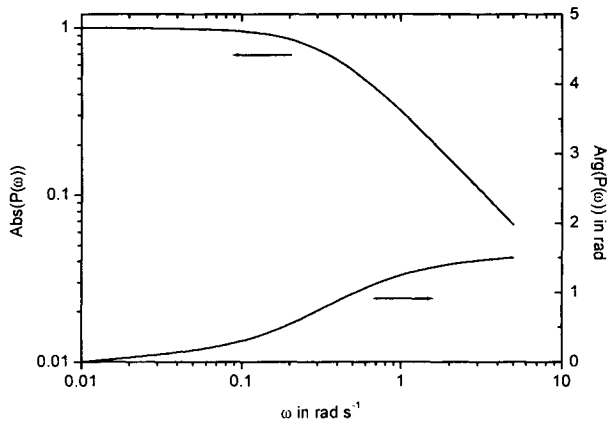


Fig. 19. Bode plot: magnitude (upper) and phase angle (lower) of transfer function of an RC-element ($R_{th} = 0.03 \text{ K m/W}$, $C_p = 100 \text{ mJ/K}$, $\tau = 3 \text{ s}$)

3.4.2. Temperature calibration

Well-developed calibration algorithms are available for standard DSC. These calibration routines take care for the calibrations of the thermometer itself and the thermal lags between the thermometer and the sample pan by studying the melting of a pure substance, *e.g.* indium or other metals with well-known transition temperatures. To exclude the thermal lag inside the sample, which may be in the order of a Kelvin for low thermal conducting materials like polymers [151-154], it is necessary either to correct for the thermal lag by means of desmearing algorithms [134,135,170-174] or to extrapolate to zero heating rate as recommended [138]. In everyday practice the DSC's are often calibrated at a heating rate of interest, *e.g.* 20 K/min. According to Fig. 19 this means that calibration only considers the bottom thermal resistor and taking into account the heat capacity of the calibration sample. This heat capacity is often much smaller than sample heat capacities used in measurements. The upper thermal resistor, describing the thermal contact between sample pan and sample may be much better for a metal than for a polymer. Nevertheless, such single rate calibration is often insufficiently applied also for TMDSC measurements. Because of the problems related to non-linear and non-stationary response TMDSC measurements have to be carried out at slow heating rates (often at 1 K/min or slower). Therefore, temperature calibration in TMDSC should take care for heating-rate dependencies of the indicated temperature. Very often it is not known what data treatment algorithms or smoothing procedures are applied inside commercially softwares. It seems to be necessary to perform a

simultaneous temperature calibration of the TMDSC apparatus and data treatment algorithms. For this reason, a well-defined transition is needed which can be measured in the TMDSC mode. Then, the final result, complex heat capacity or reversing heat capacity, can be used for calibration. It was shown that the smectic A to nematic transition of 4,4'-n-octyloxycyanobiphenyl (8OCB) is suitable for calibration of TMDSC [175] and other temperature modulated calorimeters [176]. It is recommended to check the temperature calibration of the TMDSC under the experimental conditions normally applied (sample mass, heating rate, temperature amplitude, *etc.*) to assure that temperature calibration from standard DSC can be applied to TMDSC or to determine possible deviations.

3.4.3. Heat capacity calibration examples

Most of the problems of the calibration are related to the heat-transfer. The resulting changes of measured amplitude and phase angle of the heat-flow

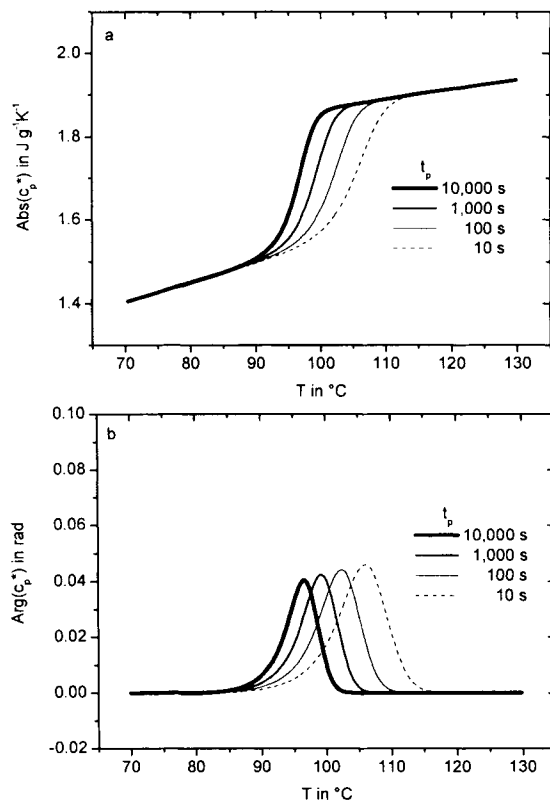


Fig. 20. Calculated magnitude (a) and argument (phase angle, b) of the complex heat capacity $c_p^*(T)$ of PS for different modulation periods t_p (see [96])

rate appear most noticeably when large amounts of heat have to be exchanged and the thermal conductivity of the sample is low. A good example is polymer melting because of a large latent heat involved and a low thermal conductivity of polymers. Therefore, obtaining the different calibration algorithms in the melting region of polymers is difficult. Note there is no reference material available with well-known frequency dependent (complex) heat capacity in the melting region. We simply do not know which correct values one should expect there. For this reason, we chose the glass transition of a low thermal conducting polymer as an example for which the complex frequency dependent heat capacity is known [74]. According to model calculations in the case of polystyrene (PS) [96] one expects a frequency dependence of the complex heat capacity as shown in Fig. 20.

Note that outside the glass transition region c_p^* s are real values (*i.e.* $\text{Arg}(c_p^*) = 0$) and should be frequency independent. In the transition region the shape of c_p^* curves is step-like and the step height is more or less independent on modulation frequency, but with frequency increase by one decade the glass transition temperature T_g shifts about 3.5 K towards higher temperatures.

For the measurements we took a rather large PS sample (25 mg) to force a larger influence of heat transfer to the sample. We used a PerkinElmer Instruments Pyris 1 DSC with a block temperature of 5 K, nitrogen purge, and standard aluminum pans of about 25 mg mass. We chose the multi-frequency approach, see 3.3.1.2 [132], to generate the complex heat capacity spectrum of this material as a set of functions at discrete frequencies. Of course, it is also possible to get the results in the common way, but in this case we have to perform a lot of single measurements at different frequencies which need much more time. More importantly, there would be an increased scattering in heat capacity values from the varying measurements.

The uncorrected results (raw data) of $C_{p,eff}^*$ (from the sample plus pan) for the glass transition region of PS are shown in Fig. 21. Taking a criterion, which defines the accepted uncertainties for magnitude, 2%, and phase angle, 0.02 rad, into account one could in this case (and with this DSC) measure the amplitude with an uncertainty at modulation periods down to 2.5 minutes, but for this period $C_{p,eff}^*$ is already systematically somewhat too low. For the phase angle, on the other hand, one only obtains acceptable results at modulation periods of 20 minutes. In other words, modulation periods should be longer than 20 minutes to obtain the correct phase angle without any calibration. This is nearly one order of magnitude more than for the magnitude measurement. For shorter periods a calibration method must be applied.

3.4.3.1. Results from "first-order" calibration

If we want to perform the simple calibration procedure presented in section 3.1 in [73], we have to compare the measured heat capacity outside the

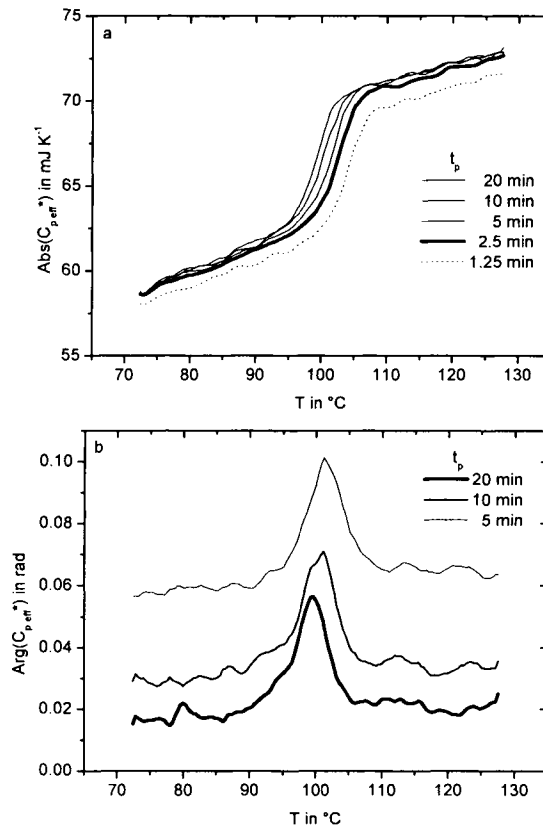


Fig. 21. Measured raw data of magnitude (a) and phase angle (b) of the effective complex heat capacity C_{peff}^* of PS (25 mg) in an Al pan (25 mg) versus temperature for different modulation periods t_p . PerkinElmer Instruments Pyris 1 DSC

transition region with the true value and to determine some complex calibration factor, which depends on frequency and corresponds to the transfer function of the apparatus and the sample system for the temperature in practice. The simple calibration procedure assumes this factor to be the same even for other temperatures and the region of transition as well as meaning the multiplication of the total measured C_{peff}^* with this factor.

Multiplication of a complex function with a complex factor performs the multiplication of the magnitude with the absolute value of the calibration factor and the addition of the argument of that factor to the phase angle. Actually, we have to multiply the $\text{Abs}(C_{peff}^*)$ curve at each frequency with a proper factor to give the right value at some temperatures outside the transition (in our example at 130 $^{\circ}\text{C}$) and to shift the $\text{Arg}(C_{peff}^*)$ curve vertically. It thus becomes zero at the reference temperature outside the transition (e.g. at 130 $^{\circ}\text{C}$), because the heat

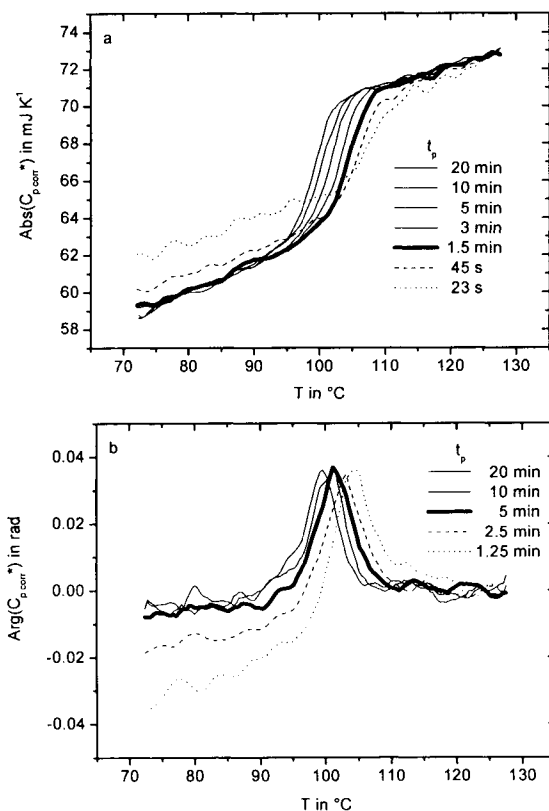


Fig. 22. “First-order” corrected magnitude (a) and phase angle (b) of effective complex heat capacity C_{peff}^* (data from Fig. 21) versus temperature for different modulation periods t_p

capacity is real valued there (no phase shift). The results of such a calibration algorithm are shown in Fig 22.

With our quality criterion in mind we find from these results that the value of the $Abs(C_{peff}^*)$ curve with 45 s modulation period does not satisfy our requirements below the glass transition region. Consequently, this calibration algorithm works well for $Abs(C_{peff}^*)$ down to a modulation period of 1.5 minutes. The phase angle $Arg(C_{peff}^*)$ does not satisfy our criterion at the modulation period of 2.5 minutes for lower temperatures, whereas the phase angle calibration works well down to a period of 5 minutes in this case.

3.4.3.2. Results from “second-order” calibration

This improved calibration procedure cannot use only one calibration factor for all temperatures, but starts from the fact that this factor must change with

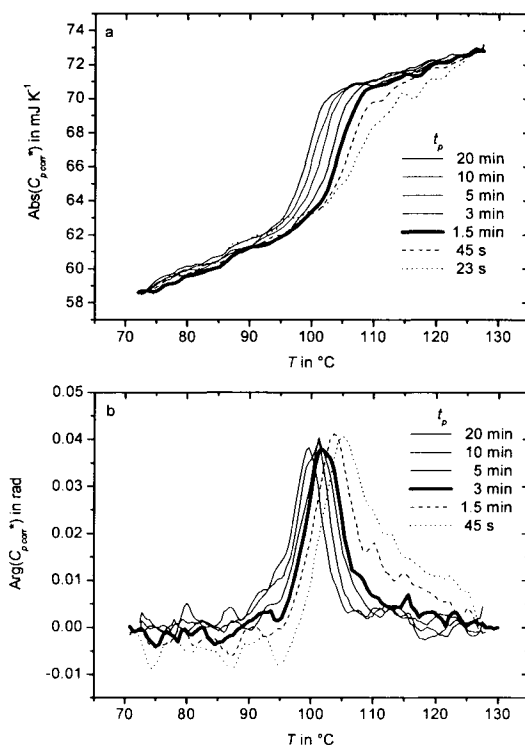


Fig. 23. “Second-order” corrected magnitude (a) and phase angle (b) of effective complex heat capacity C_{peff}^* (data from Fig. 21) versus temperature for different modulation periods t_p

temperatures. One way is to determine the transfer function on both temperatures above and below the transition. In our example, we determined the transfer functions at about 70°C and at about 130°C. They turned out to be different and we get two different complex calibration factors at 70°C and at 130°C. If one assume a linear temperature dependence of the calibration factor in the temperature range 70 - 130°C one has (i) to multiply the $Abs(C_{peff}^*)$ curve of each frequency by a factor which changes linearly (*i.e.* a straight line) so that all curves coincide at the two reference temperatures below and above the transition region (in our example at 70°C and 130°C) and (ii) to subtract from $Arg(C_{peff}^*)$ curve of each frequency a straight line so that the resulting curves are zero at those temperatures (*i.e.* at 70°C and 130°C) because C_p is real valued there. This type of phase angle calibration is used in the PerkinElmer Instruments DDSC™ software. The results of such a calibration are shown in Fig. 23.

As can be seen, the value of $Abs(C_{peff}^*)$ below the glass transition region at 45 s modulation period is now in good agreement with the values at longer

periods, but deviations remain just above the glass transition. In the temperature region 110 - 115°C the $Abs(C_{peff}^*)$ curve at 45 s does not satisfy our criterion. Therefore the “second-order” calibration algorithm applied to the magnitude (using two reference temperatures above and below the transition) yields only a minor improvement in comparison to the “first-order” calibration. The respective phase angle calibration works well down to a modulation period of 3 minutes. At 1.5 minutes and shorter periods a tendency of the measured phase angle ($Arg(C_{peff}^*)$ curves) to be much above the expected value is clearly visible for temperatures above the glass transition.

So far the methods presented in sections 3.1 and 3.3 in [73] can be used to determine the calibration function (*i.e.* the reciprocal transfer function) for the “first” or the “second-order” calibration. Wunderlich *et al.* [130,177] introduced an effective time constant to describe the frequency dependence of the measured apparent heat capacity in a temperature region where the sample heat capacity is frequency independent [73]. By extrapolation of $1/c_p^2$ over ω^2 against $\omega \rightarrow 0$, in other words, using this time constant approach, they corrected the measured c_p values outside as well as inside the transition region. This calibration procedure is essential identical to that in determining the total transfer function of the apparatus and sample system with the restriction that in (see [177]) only the magnitude (absolute value) calibration is discussed. This is due to the authors limit themselves to static heat capacity determinations. However, the calibration algorithm they recommend works similar to both for the “first-order” and the “second-order” calibrations, depending on whether one uses only one or both temperature regions outside the transition in question.

To improve the “second-order” calibration algorithm presented above, one has to make further assumptions how the transfer function may depend on temperature and/or on sample properties. Weyer *et al.* [70], for example, discussed in details the wrong phase angle calibration (the overestimated values above the glass transition at 1.5 minutes and 45 s periods of Fig. 23). They assumed that the phase lag φ due to heat transfer can be described as $\varphi = \omega Abs(C_{peff}^*)/K$, with ω being the angular frequency of temperature modulation and K , the thermal contact between the sample and the aluminum pan. They presented an improved “second-order” phase angle calibration algorithm by subtracting a non-straight line but somewhat curved which is proportional to the measured heat capacity, *i.e.* $Abs(C_{peff}^*)$, from the measured phase angle in that region. Provided the thermal contact between sample and pan is kept constant (*e.g.* by using silicon oil as contact medium) such a correction works well down to a modulation period of 1 minute. A similar algorithm was suggested by Hutchinson [71]. It should be emphasized that the thermal contact changes with temperature (in particular during transitions!) in a generally unknown manner.

3.4.3.3. "Third-order" calibration

As stated before the total transfer function (apparatus and sample system) is a product of the transfer functions of its elements. In other words the (complex) total calibration factor, the reciprocal of the transfer function, can also be taken as a product of the calibration factors of its separate parts. Here we consider the total calibration factor $B^*(\omega, C_p^*(\omega), K, \dots)$ (depending on frequency ω and all sample parameters including heat capacity $C_p^*(\omega)$, thermal contacts K etc.) as a product of two factors: one factor $B_1^*(C_p^*(\omega), K, \dots)$ depending on sample parameters stands for the sample influence, and another factor $B_2^*(\omega)$, which relies only on frequency (and of course on temperature) describing the influence of the apparatus on the measured quantity:

$$B^*(\omega, C_p^*(\omega), K, \dots) = B_1^*(C_p^*(\omega), K, \dots) \cdot B_2^*(\omega) \quad (37)$$

In section 3.4 (as described in [73]) it is described how to determine $B_2^*(\omega)$, the apparatus calibration function. It includes the dynamic response of the instrument (and software filtering, sampling rate etc.). It can be determined in advance and can be used for all further measurements provided that the instrumental settings are kept the same.

The first step of the calibration algorithm is to correct the measured (non-calibrated) effective heat capacity $C_{p\text{eff}}^*(\omega)$ for the instrument dynamic response: $C_{p\text{eff}}^*(\omega) \cdot B_2^*(\omega) = C_\beta^*(\omega)$. This results in $C_\beta^*(\omega)$, the actual apparent heat capacity of the sample as seen by the instrument from the furnace. The sample itself behaves like a simple RC-element [73]. This means that

$$C_\beta^*(\omega) = \frac{C_p^*(\omega)}{1 - \frac{i\omega C_p^*(\omega)}{K}} \quad (38)$$

For those temperatures where the sample heat capacity is frequency independent the magnitude should read:

$$|C_\beta^*(\omega)| = \frac{C_p^*}{\sqrt{1 + \left(\frac{\omega C_p^*}{K}\right)^2}} \quad (39)$$

K is the effective thermal contact and $C_p^*(\omega)$ is the net heat capacity of the sample and the aluminum pan. If we plot $1/|C_\beta^*(\omega)|^2$ for different frequencies versus ω^2 the points should lie on a straight line and the slope of the curve should

equal $1/K^2$. When the unit of $|C_{\beta}^*(\omega)|$ is J/K and that of ω is rad/s then the effective thermal contact K reads in W/K. From Fig. 24, it is evident that for our sample the approach with one effective thermal contact holds up to $\omega^2 = 0.08 \text{ rad}^2 \text{ s}^{-2}$ (which equals a period $t_p = 23 \text{ s}$). At higher frequencies the measured values deviate downward from the straight line showing the increasing influence of the thermal conductivity of the sample itself.

Calculating these curves in dependence on temperatures we are able to determine the effective thermal contact K between the sample and the instruments from the respective slopes as a function of temperature (see Fig. 25).

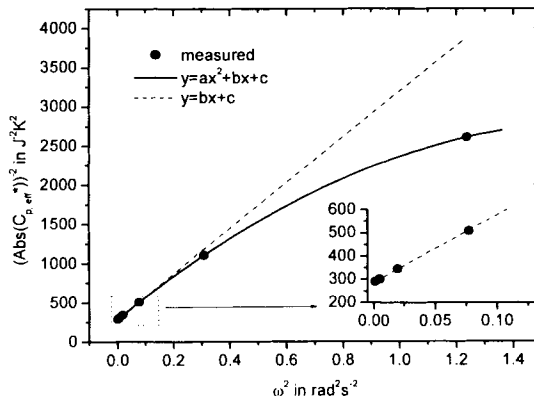


Fig. 24. Squared reciprocal magnitude of $C_{\beta}^*(\omega)$ versus squared angular frequency (inset: linear behavior in the low frequency region)

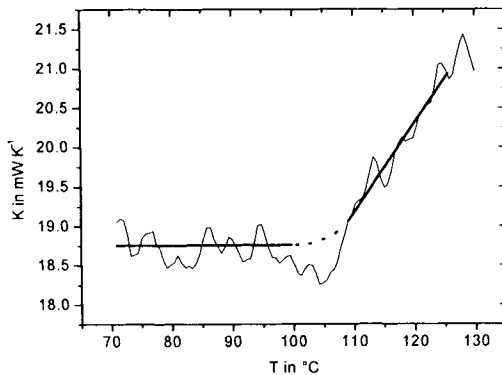


Fig. 25. Effective thermal contact K versus temperature. The thin line gives the measured values from the slope of curves (like in Fig. 24) determined at all temperatures. The thick line is the fit function used for calibration. In the glass transition region this function has to be interpolated (dotted line)

In the glass transition region, the sample heat capacity depends on frequency, K is not determined correctly there and we have to interpolate the correct K value in the glass transition region from the values in both solid and liquid (dotted line in Fig. 25). It is obvious that the thermal contact is not a constant but increases with temperature above the glass transition region.

The second step of the calibration algorithm is to correct for the sample dynamic response, but it is not necessary to determine $B_1^*(\omega, C_p^*(\omega), K, \dots)$ explicitly. Since Eq. (2) is valid for complex $C_p^*(\omega)$ we can rearrange it to get $C_p^*(\omega)$:

$$C_p^*(\omega) = \frac{C_\beta^*(\omega)}{1 + \frac{i\omega C_\beta^*(\omega)}{K}} \quad (40)$$

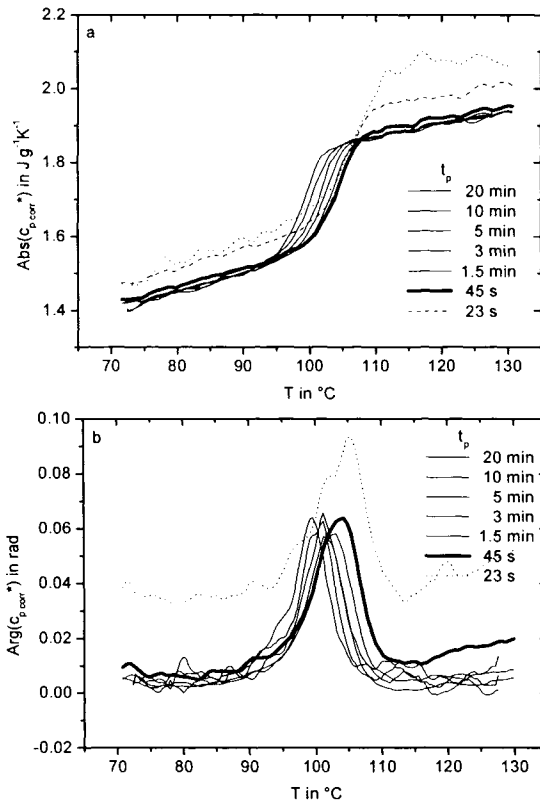


Fig. 26. "Third-order" corrected magnitude (a) and phase angle (b) of complex sample heat capacity c_p^* (data from Fig. 21) versus temperature for different periods t_p

With the (known) heat capacity of the sample pan one can calculate the corrected complex specific heat capacity of the PS sample:

$$c_p^*(\omega) = \frac{C_p^*(\omega) - C_{p,pan}}{m_s} \quad (41)$$

where $C_{p,pan}$ is the heat capacity of the (aluminum) pan and m_s is the sample mass. The results of these calculations are shown in Fig. 26. Obviously, the calibration algorithm works both for the magnitude and the phase angle for modulation periods down to 45 s. If we want to correct results for higher frequencies (smaller periods) we have to take the thermal conductivity of the sample into account. An interesting point to note is that the curves with 23 s and 12 s periods do not change the shape compared to the curves at longer periods.

As this example shows, the period range resulting in correct values is not much larger for the “third-order” calibration than for the simpler methods. It is, however, the only method which allows to determine the change of the transfer function during the measurements, in particular, even in the transition region. Of course, the modulation form should be obtained from a multi-frequency response: the temperature-step (periodic or non-periodic) method or any periodic non-sinusoidal temperature modulation method.

3.4.3.4. Remark concerning small samples

The problems resulting from the heat transfer can be minimized by using very small samples (very small sample pans as well) for the measurements [23]. We performed such a measurement with a 2 mg PS sample wrapped in an aluminum foil of 2 mg. The sample was very thin and flat with the same diameter as the standard aluminum pans. The results from the measurements using a “second-order” calibration algorithm are shown in Fig. 27.

In this case the curves coincide, within the limits of experimental uncertainties, down to modulation periods of 7.5 s. Nevertheless, it is difficult to make a quantitative analysis with these data due to the poor quality. Larger samples will, of course, result in a better signal-to-noise ratio at the expense of falsified heat capacity curves because of the heat transfer issue. It is a matter of experience to find the right balance between the uncertainties caused by a low signal-to-noise ratio and those from a faulty correction due to the sample heat transfer problem.

3.4.4. Conclusions regarding calibration

It has been shown that there are different possibilities to calibrate the TMDSC regarding the heat transfer. Particularly if it is sufficient to correct the magnitude of the (complex) apparent heat capacity and disregard the phase angle, one can for practical purposes use the known heat capacity of the sample

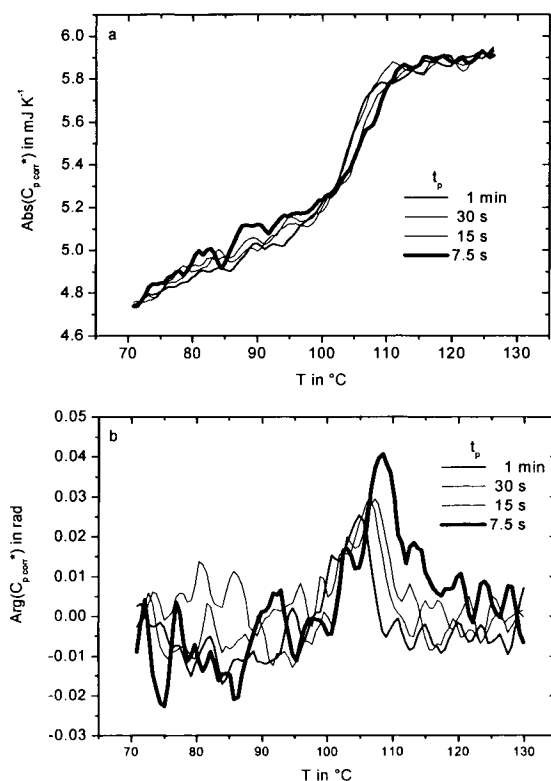


Fig. 27. “Second-order” corrected magnitude (a) and phase angle (b) of effective complex heat capacity C_{peff}^* of a small PS sample ($m_s = 2$ mg) in Al foil ($m_{Al} = 2$ mg) versus temperature for different modulation periods t_p

(in temperature regions outside of reactions or transitions) as an internal reference and correct the measured values correspondingly.

A single multiple frequency measurement offers a possibility to obtain a frequency dependence of the measured heat capacity. This allows, in temperature regions where the sample heat capacity is frequency independent, to extrapolate the measured quantity to zero frequency to get the correct heat capacity value.

In cases where the complex heat capacity is of interest (e.g. at transitions), both the magnitude and the phase angle must be corrected. To obtain a detailed insight into the heat transfer behavior of the DSC as well as the sample itself, the advanced calibration procedure is recommended which allows separating between the influences of the apparatus and the sample as well as to determine the change of the transfer function during the measurement. The example has shown that the more simple calibration procedures lead to nearly the same

uncertainties of the results in everyday measurements as the more sophisticated “third-order” calibration procedure does. We recommend, however, the “third-order” calibration procedure in all cases where the heat transfer conditions could change during the measurement.

3.5. Thermal conductivity

For the determination of accurate heat capacity values from TMDSC, a precise calibration, which takes the falsification due to heat transfer problems into account, is needed. On the other hand if we know the influence of the heat transfer on the heat capacity data it allows obtaining information about thermal conductivity of our sample and thermal contacts between sample and the measuring system [178]. Thermal conductivity data are important in industry for modeling and control of processes such as, polymer injection molding, encapsulation of electronic devices *etc.* Therefore, it seems to be an attractive task to use TMDSC as a tool for thermal conductivity measurements of low thermal conducting materials like polymers.

As reported first by Marcus *et al.* [179-181], thermal conductivity can be measured without modification of the commercially available DSC cell. They calculated the thermal conductivity from the ratio of apparent and true heat capacities measured for a thick (about 3 mm) and a thin (about 0.5 mm) sample, respectively, in a temperature modulated mode. They used one additional calibration step to take into account the heat losses through the surrounding purge gas. The method is based on the assumption that “the face of the specimen at the heat source follows the applied temperature modulation” [179], which means no thermal resistance between the sample and the furnace.

Simon and McKenna [182] pointed out two problems in the method proposed by Marcus and Blaine. First, the equation relating the apparent heat capacity to the thermal conductivity is limited in range due to an approximation made in their derivation (see reference [183]). Second, a thermal resistance between the sample and the furnace can have a significant effect on the measured apparent heat capacity. They, as well as Marcus and Reading [181], also mention that thermal conductivity could be easily obtained from a single sample run at several frequencies, *i.e.*, it is not necessary to measure two samples. But what is necessary in any case is to know the heat transfer coefficient. “If the heat transfer coefficient is not known, an accurate value of thermal conductivity cannot be obtained” [182].

We based on our method [168], which is briefly explained here, as presented in [47]. With this model one can thoroughly describe the dynamic behavior of DSC and TMDSC systems under conditions of an appreciable temperature gradient inside the sample. A question about how to get all the parameters of the model, arises. On the example of one measurement, we present an algorithm to determine the most important parameters: sample heat

capacity, effective thermal contact between the sample and the furnace and finally sample thermal conductivity for the case of real valued heat capacity and thermal conductivity. Furthermore we present experimental results with different solid samples and various experimental conditions. Measured thermal conductivity data are compared with expected values. Finally, we discuss possible reasons for some systematic bias between measured and expected thermal conductivity values. We analyze the validity of the model used and how it can be monitored by the measured results, and make some suggestions regarding how to improve the method.

3.5.1. Data treatment

3.5.1.1. The idea

It is important to know how good the temperature waves propagate through the sample under investigation. Low frequency temperature waves go through the whole sample without damping, the whole sample is modulated and therefore a large apparent heat capacity is measured. Higher frequency temperature waves are damped and the sample is partly modulated – the measured apparent heat capacity is smaller. The damping is stronger for poor thermal conducting materials. This is also the basic idea of the methods proposed by Marcus and Blaine [179] and Simon and McKenna [182]. However, the same damping effect appears by finite thermal contact (heat transfer coefficient) between the sample surface and the furnace – a poor thermal contact damps the temperature waves stronger than a good one. Note that the thermal contact and thermal conductivity lead to different frequency dependences of apparent heat capacity [47]. This difference allows to separate the damping effects due to the thermal contact and the thermal conductivity. This approach overcomes the limitations discussed by Simon and McKenna [182]. Moreover, it is not necessary to measure apparent heat capacity at different frequencies with TMDSC. The spectrum of temperature waves can be easily generated by a single step in the temperature program [133].

3.5.1.2. The algorithm

The DSC set-up, as shown in Fig. 18 and described in [47], is simplified to the case when a solid sample is measured directly in the DSC furnace (see Fig. 28). Three parameters need to be determined: specific heat capacity c_p , effective thermal contact between the sample and the furnace K and thermal conductivity κ .

Effective heat capacity C_{peff}^* at different frequencies can be calculated from step response analysis [133] as the ratio of heat-flow rate amplitude A_{HF}^* and heating rate amplitude A_q^* (according Eq. (33), see section 3.3.2.), where points of heat-flow rate, HF_{is} , and heating rate, q_{is} , should be taken both with the same sampling rate (number of points per unit time). We collect the points from

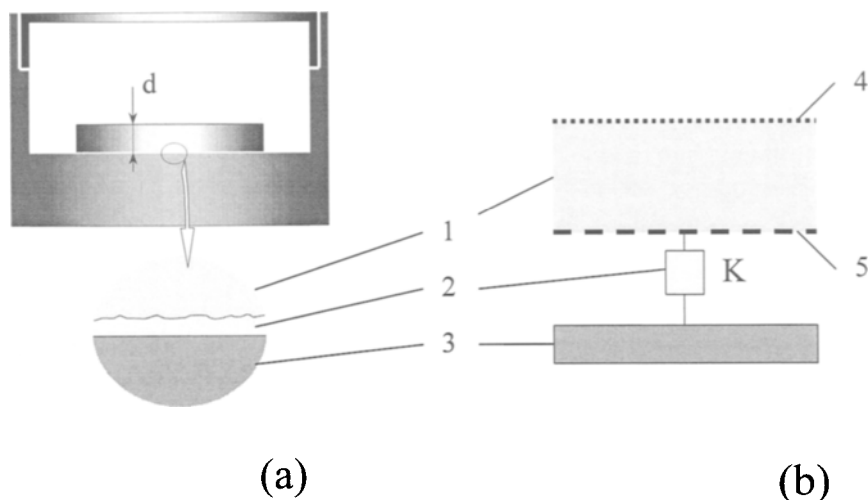


Fig. 28. The schematic view of the furnace (a) and its block diagram (b). 1 - sample, 2 – grease layer, which produces an effective thermal contact K, 3 - DSC furnace, 4 – adiabatic layer at upper surface of the sample, 5 – bottom surface of the sample

the beginning of the temperature step until the heat-flow reaches the steady state value at the isotherm [133], having in total n points. After that the $C_{peff}^*(\omega)$ values should be corrected for apparatus influence (instrumental delay) [47,73,74] according to the procedure described in section 3.4.3.3:

$$C_{papp}^*(\omega) = C_{peff}^*(\omega) \cdot B_2^*(\omega) \quad (42)$$

where $C_{papp}^*(\omega)$ is an apparent heat capacity at frequency ω , $B_2^*(\omega)$ is the dynamic calibration factor of the instrument [47,73,74].

The first parameter of the system, the specific heat capacity c_p , can be easily determined as:

$$c_p = C_{peff}(0)/m_s \quad (43)$$

where m_s is the sample mass and $C_{peff}(0)$ is calculated from Eq. (33) for $\omega = 0$.

The two other parameters are determined as described below. As an example we took the apparent heat capacity data of a poly(ϵ -caprolactone) (PCL) disk with thickness $d = 1.42$ mm and diameter of about 6 mm. Apparent heat capacity is given as [168]:

$$C_{papp}^*(\omega) = \frac{C_\alpha^*(\omega)}{1 - \frac{i\omega}{K} C_\alpha^*(\omega)} \quad (44)$$

where $C_{\alpha}^*(\omega)$ is the apparent heat capacity in case of ideal thermal contact between the sample and the furnace. In other words, it is the apparent heat capacity one would measure directly on the bottom surface of the sample, see Fig. 28. We rewrite Eq. (44) as:

$$C_{\alpha}^*(\omega) = \frac{C_{p\text{ app}}^*(\omega)}{1 + \frac{i\omega}{K} C_{p\text{ app}}^*(\omega)} \quad (45)$$

The only unknown parameter in Eq. (45) is K because $C_{p\text{ app}}^*(\omega)$ is measured. Values of $C_{p\text{ app}}^*(\omega_k)$ for a set of different frequencies ω_k and $C_{\alpha}(\omega_k)$ for three different values of K are shown on Fig. 29. The lower the frequency ω_k , the larger the modulus of $C_{p\text{ app}}^*(\omega_k)$ and $C_{\alpha}^*(\omega_k)$.

On the other hand $C_{\alpha}^*(\omega)$ should be described by the solid curve in Fig. 29 (see [168] for details). The theoretical $C_{\alpha}^*(\omega)$ curve in a polar plot representation depends only on the value $C_{\alpha}(\omega = 0)$, the true heat capacity $c_p \times m_s$ of the sample. The correct value for K is then the value at which all $C_{\alpha}^*(\omega_k)$ points, calculated by Eq. (45), lie on the theoretical curve. The value of K follows from an iterative procedure. For the example shown in Fig. 29 the iteration yields $K = 0.029 \text{ W/K}$. In this way the second parameter of the system is determined.

The next step is to determine sample thermal conductivity κ .

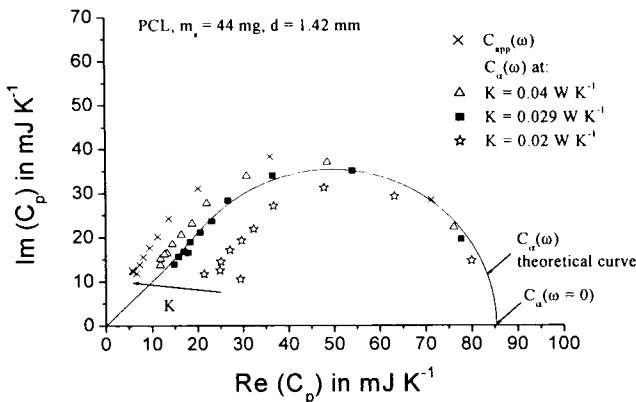


Fig. 29. Polar plot of $C_{app}(\omega_k)$ and $C_{\alpha}(\omega_k)$ for different effective thermal contacts K . The horizontal and vertical axes show the real and the imaginary parts, respectively. The solid curve represents the theoretical values of $C_{\alpha}(\omega)$ for the given $C_{\alpha}(\omega = 0)$ (see [168] for details).

$$C_{\alpha}^*(\omega) = -\frac{1}{i\omega} \kappa \cdot S \cdot \alpha \tanh(\alpha \cdot d) \tag{46}$$

denotes the apparent heat capacity which would be measured directly at the surface of the sample (see [168] for details), $\alpha = \sqrt{\frac{\omega}{|\chi|}} \exp\left\{\frac{i}{2} \arg\left(-i \frac{\omega}{\chi}\right)\right\}$, $\chi = \frac{\kappa}{\rho \cdot c_p}$ is the thermal diffusivity [47]. All parameters in Eq. (46), except thermal conductivity κ , are known (density ρ can be calculated from the sample mass

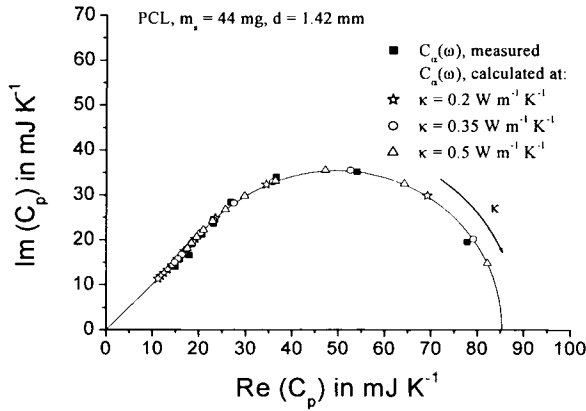


Fig. 30. Polar plot of $C_{\alpha}(\omega\kappa)$, measured and calculated for different values of thermal conductivity κ . The horizontal and vertical axes show the real and the imaginary parts, respectively.

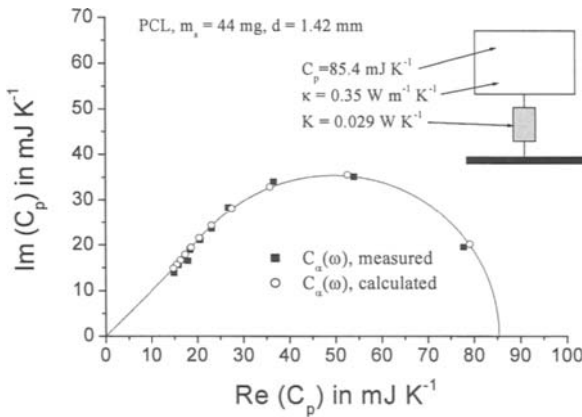


Fig. 31. Polar plot of $C_{\alpha}(\omega\kappa)$, calculated with the optimal parameter κ and measured values. The horizontal and vertical axes show the real and the imaginary parts, respectively.

and sample volume, which are set before measurement). At any given frequency $\omega_k \neq 0$ increasing of κ leads to shifting the position of the $C_{\alpha}^*(\omega_k)$ point on the theoretical curve towards $C_{\alpha}(\omega = 0)$ (see Fig. 30).

By varying κ in Eq. (46) in an iterative way, the condition is reached where the same set of ω_k calculated $C_{\alpha}(\omega_k)$ points coincide with measured points $C_{\alpha}(\omega_k)$, determined by Eq. (5). In the example discussed here the iteration yields $\kappa = 0.35 \text{ W m}^{-1} \text{ K}^{-1}$. Thus, the third parameter of the system has been determined. As one can see from Fig. 31 the measured points for $C_{\alpha}(\omega_k)$ coincide not exactly with the theoretical ones, but this scatter corresponds to only 1 to 2 percent uncertainties in determination of thermal conductivity κ and effective thermal contact K .

The algorithm to determine thermal conductivity and effective thermal contact from the spectrum of $C_{app}(\omega_k)$ is realized on MS-Excel™ spreadsheet with Visual Basic™ macros and available for download at [22].

3.5.2. Experimental results

Four samples with known thermal conductivity were measured: PS and poly(methyl methacrylate) (PMMA) (ASTM interlaboratory test for thermal conductivity by MTDSC) and epoxy resins 160 and 4173 (provided by Mathis Instruments). Samples were prepared in disk shape with diameter $D = 6 \text{ mm}$ (epoxy resins) and $D = 6.4 \text{ mm}$ (PS and PMMA) and thickness d of about 0.5 and 1 mm. The measurements were performed by PerkinElmer Pyris-1 DSC with Lauda RC6 cooling system. DSC block temperature was set to $+5^{\circ}\text{C}$. Purge gas

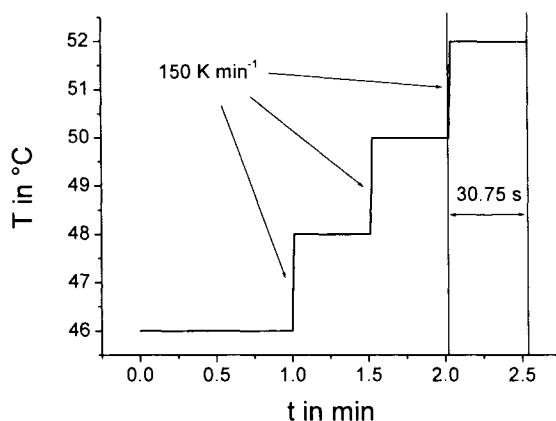


Fig. 32. Temperature-time program, consisting of 2 K steps in temperature and 30 s isotherms. Temperature steps were programmed as short heating segments with 150 K/min heating rate.

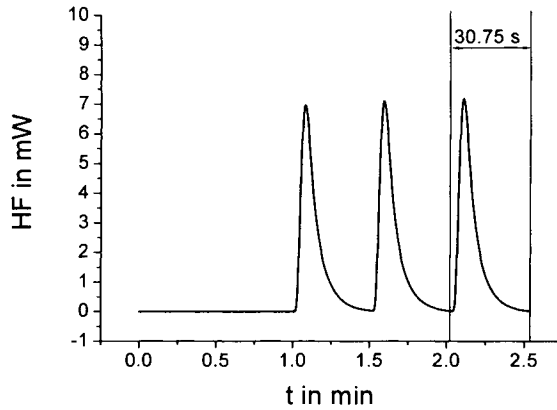


Fig. 33. Example of the measured heat-flow rate, HF , versus time which corresponds to the temperature-time program, shown in Fig. 32. The last peak was taken for further data evaluation.

was nitrogen with gas flow of 20 ml/min. Since the furnace floor is slightly curved [184] and the disks are not flexible we used ApiezonTM grease to get homogeneous thermal contact over the whole contact area between the bottom of the sample and the furnace. It is more important to homogenize the contact rather than to minimize its resistance. The temperature-time program shown in Fig. 32 was used to generate the spectrum of apparent heat capacity.

The initial isotherm of 1 min was added to check whether heat-flow drift at steady state is remarkable. The corresponding heat-flow rate after empty furnace correction is shown in Fig. 33. (Since we did not use a pan we subtracted the heat-flow measured with an empty furnace.)

In this example the last step was evaluated. Interesting point is that heat-flow in the last step did not really start from steady state neither reach steady state at the end. However it is still possible to evaluate the data correctly. This fact allows shortening the duration of the measurement, as discussed in [133].

We took into consideration up to 7 frequencies $\omega_k = k \times \omega_0$, $k = \{1, 2, \dots, 7\}$, $\omega_0 = 2\pi/t_p$ and period $t_p = 30.75$ s. The results of thermal conductivity determination are shown in Table 1.

There could be two reasons for this disagreement: inhomogeneous thermal contact in the case of the thin disk or a too thick disk. In both cases, the one dimensional model used for the calculation could not give exact values of thermal conductivity. However one can get some range of possible values of the thermal conductivity. One gets an impression about the validity of the model to describe the given experimental conditions from the width of the range or how faulty were the experimental conditions.

Table 1

Comparative thermal conductivities measured at 51°C for four different samples

material	measured κ in $\text{W m}^{-1} \text{K}^{-1}$	expected κ in $\text{W m}^{-1} \text{K}^{-1}$
PS	0.168-0.172	0.1562 [185]
PMMA	0.212-0.215	0.197 [186]
epoxy resin 160	0.63	0.61 [187]
epoxy resin 4173	1.70-1.85	1.83 [187]

3.5.3. Discussion of thermal conductivity determination

The one-dimensional model we used in this method assumes a negligible heat-flow through the upper surface of the sample disk. However it is true to some extent. There is some heat-flow through the purge gas to the sample inside the measuring cup. This heat-flow would shift the adiabatic layer from the upper surface downwards into the sample. This would lead to a shortening of the effective sample thickness d resulting in overestimated thermal conductivity values, which were calculated for a larger actual thickness. The overestimation of the thermal conductivity values for low thermal conducting samples (PS and PMMA, see Table 1) can be accounted for with this explanation. This effect is minor for higher thermal conducting materials because the heat-flow through the sample is larger.

The one-dimensional model also assumes no radial heat-flow inside the sample, and a homogeneous thermal contact between the bottom surface of the disk and the furnace. If the model fails to describe the actual, more complicated sample setup (e.g., inhomogeneous thermal contact), the measured $C^*_\alpha(\omega_k)$ would not agree with the calculated $C^*_\alpha(\omega_k)$ as shown in [168]. This can be used as an internal test of the validity of the model since the model is not designed to describe a case of complex frequency dependent heat capacity. Therefore the method results in uncertain thermal conductivity values.

There are three possible directions for further improvement of this method of thermal conductivity measurement. First, the heat-flow through the purge gas may be considered to improve the accuracy of thermal conductivity determination. Second, the sample pan effect, presented in [47], may be considered. Using a pan will allow measuring liquid samples and samples that undergo liquid-to-solid transitions in a broad temperature range. Third, heat capacity and thermal conductivity may be considered as being complex and frequency dependent values and measured within transition (like glass transition or melting). However, it would be possible to separate the influence of heat

transfer (thermal conductivity and thermal contact) and frequency dependence of heat capacity only by performing at least two measurements of two samples with different thickness.

3.5.4. Conclusion regarding thermal conductivity

The proposed method permits thermal conductivity and heat capacity of low thermal conducting materials to be determined in a single run using standard power-compensated DSC. Accuracy of the thermal conductivity determination is within about 10% of true values (Marcus and Blaine reported the precision of their approach of 3% [179-181], what is questionable [182]). No modifications of the instrument are needed. In addition to thermal conductivity and heat capacity, the effective thermal contact between the sample and DSC furnace is determined. The method has an internal check of the accuracy of the measured results which helps to select "correct" measurements. In the case of a faulty measurement it reports a possible range of thermal conductivity and thermal contact.

4. APPLICATIONS

4.1. Precise heat capacity

The knowledge of heat capacity from zero Kelvin up to the temperature of interest from thermodynamics allows for a total description of the material properties.

$$\text{Enthalpy} \quad H - H_o = \int_0^T C_p dT \quad (47)$$

$$\text{Energy} \quad U = \int_0^T C_v dT \quad (48)$$

$$\text{Entropy} \quad S = \int_0^T \frac{C_p}{T} dT \quad \text{or} \quad S = \int_0^T \frac{C_v}{T} dT \quad (49)$$

$$\text{Gibbs Energy} \quad G = H - TS \quad (50)$$

$$\text{Free Energy} \quad F = U - TS \quad (51)$$

With a known heat capacity (and known heat of transitions) the thermodynamic properties of a material are known (see e.g. [34]):

U, H total thermal motion and energy
 S disorder
 G, F stability

Therefore, the detailed knowledge of heat capacity in a broad temperature range is of general interest. Precise measurements of heat capacity at low temperatures are commonly performed by adiabatic calorimeters. Uncertainties below 1% are reached at temperatures below room temperature. In the case of higher temperatures and low thermal conducting materials like polymers, some additional problems arise which significantly limit the uncertainty of heat capacity measurements. Therefore it is a difficult task to perform accurate (uncertainty below 1%) heat capacity measurements at higher temperatures for low thermal conducting materials.

In case of quasi-isothermal measurements, as well as true values of heat capacity and thermal conductivity (no time or frequency dependence of sample heat capacity and sample thermal conductivity), all frequency dependence observed in the apparent heat capacity is due to the heat transfer. As shown in section 3.4, this allows for a correction for the influence of heat transfer and other instrumental variables on the measured heat capacity. In this way, the advantages of frequency selective data treatments as commonly applied in TMDSC, see section 3, become visible. The obtained heat capacities are essentially independent of long-term drifts and high frequency noise in comparison to the length and frequency of the temperature modulation. In

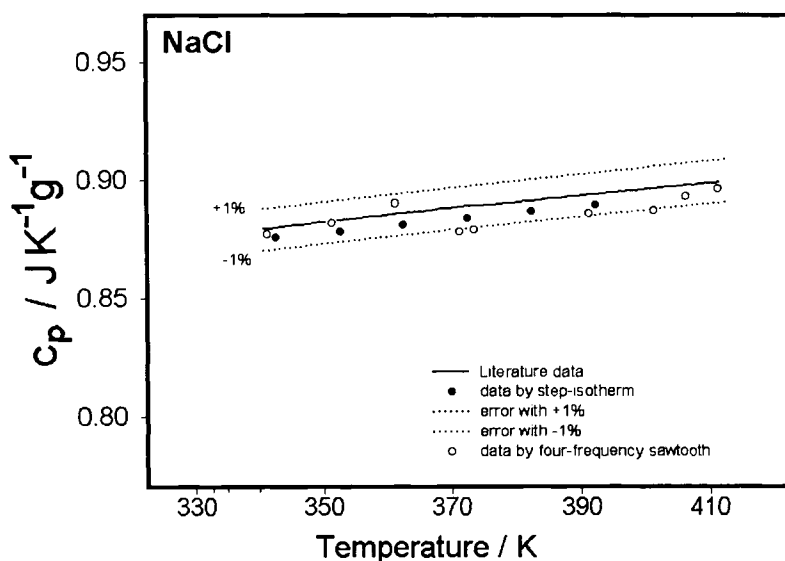


Fig. 34. Heat Capacity of NaCl. Comparison of literature data (—) [192] with the step-isotherm temperature profile (●) (PerkinElmer Instruments Pyris 1 DSC), see 3.3.1.2 for details, and four-frequency sawtooth temperature profile (○) (TA Instruments DSC 2920) (for details, see Ref. 131, reproduced from Ref. 191)

common DSC, using PerkinElmer Instruments power compensation design, an accuracy of 1.5% at temperatures above ambient are possible, see Wunderlich [51,188,189], Hoehne [56,57] and Richardson [55,190]. Also a very detailed study recently published [58] for a two dimensional heat-flow systems demonstrated accuracies better than 5% are difficult to realize or even impossible. Applying the “Third-order” calibration, section 3.4.3.3, yields an uncertainty of heat capacity below 1% as shown in [191].

The highly accurate measured heat capacity for NaCl is shown in Fig. 34. In this figure the low scatter of the data from the step-isotherm method is especially impressive [191]. In this case the instruments were calibrated by sapphire standards and the measured powder sample had a significantly lower thermal conductivity. It is important to note that the thermal conductivities for polymers in general are higher than NaCl. However, this example shows that highly accurate heat capacity measurements polymers at temperatures above room temperature are possible.

4.2. Glass transition

The study of the glass transition by TMDSC is one of the most successful applications of TMDSC to polymers due to several reasons:

- Variation of the modulation frequency allows for an independent study of the dynamics of glass transition
- Because of the high sensitivity and high quality of the heat capacity data weak glass transitions can be studied which are difficult to observe in normal DSC scans
- In some cases, glass transitions superimposed with truly non-reversing events like evaporation, cold crystallization, or curing can be detected in the complex heat capacity

4.2.1. Vitrification and dynamic glass transition

At the glass transition, a TMDSC measurement with underlying scanning represents the superposition of two independent experiments. Namely, the periodic one and the common linear scan DSC experiment. The corresponding time scale is given by the modulation period and the scan rate, respectively. The raw data of a cooling experiment through the glass transition region of polystyrene are shown in Fig. 35.

After appropriate calibration of the data, see section 3.4, the different heat capacities can be obtained. The glass transition temperature** from the total heat

** For the determination of the glass transition temperature several procedures are in use, see e.g. [Assessment of glass transition Riga]. Here we use the fictive temperature [Tool, Richardson] as T_g from the total heat capacity and the maximum of the imaginary part of complex heat capacity which corresponds to the temperature of the half step of the real part of complex heat capacity.

capacity (vitrification) depends, as in common DSC scan measurements, on the cooling rate. The glass transition temperature from the complex heat capacity (dynamic glass transition, α -relaxation) depends on the modulation frequency

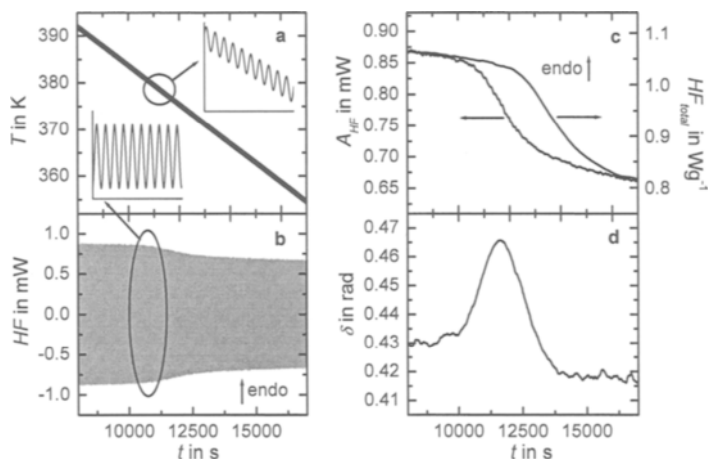


Fig. 35. TMDSC scan measurement on cooling through the glass transition region of PS. **a** - temperature-time-profile, **b** - measured heat-flow rate, **c** - amplitude of heat-flow oscillations, left curve, and total heat-flow rate, right curve, **d** - measured phase angle between heat-flow rate and heating rate. $t_p = 60$ s, $T_A = 0.5$ K, $q_o = -0.25$ K/min (PerkinElmer Instruments DSC 2, $m_s = 14$ mg and Setaram DSC 121, HF_{total} , $m_s = 230$ mg)

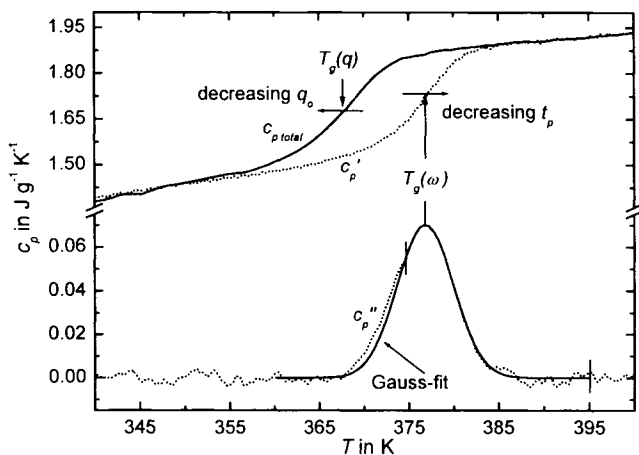


Fig. 36. Glass transition of PS from the data of Fig. 35, total heat capacity from Eq. (16) and real and imaginary part of complex heat capacity from Eqs. (17) and (21)

employed [10,11,15,196-198]. Both the cooling rate and the frequency can be varied independently in this setup. This allows for a direct comparison of the corresponding time scales of cooling rate and frequency [109-111,126,199].

A most probable relaxation time, τ , at a given temperature can be determined from the maximum of the imaginary part of complex heat capacity,

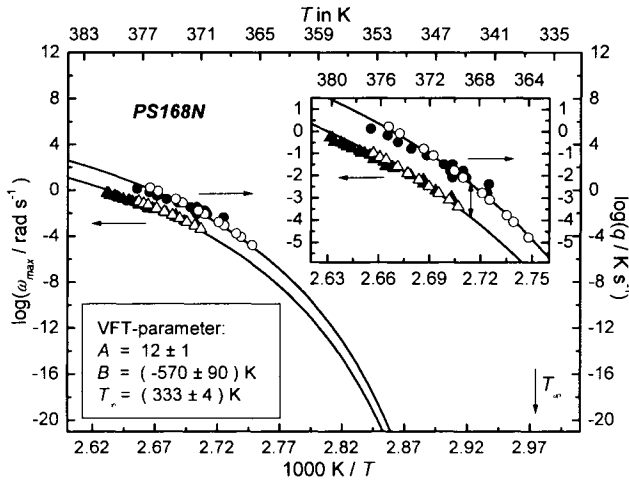


Fig. 37. Frequency dependence (left curve) and cooling rate dependence (right curve) of the glass transition temperature of PS (for details, see Ref. 110)

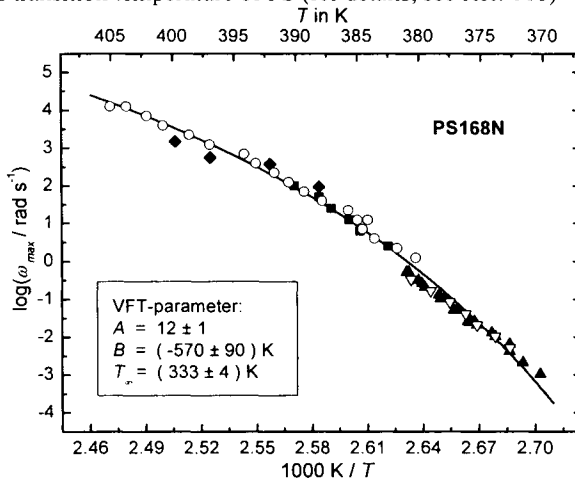


Fig. 38. Activation diagram for polystyrene obtained from different calorimetric methods, \blacklozenge - Photo-acoustic [202], \circ - 3ω [25,126], \blacksquare - AC-calorimetry [203], ∇ - TMDSC multi frequency analysis [133], \blacktriangle - TMDSC [25,126]. The solid line represents data from dielectric spectroscopy.

which corresponds at the glass transition to the maximum of the measured phase angle, according to

$$\omega \cdot \tau = 1 \text{ or } \tau = \frac{t_p}{2\pi} \quad (52)$$

From a comparison of the cooling rate and frequency dependence of the glass transition at cooling rate 10 K/min as shown in Fig. 37 the mean relaxation time is on the order of a few hundred seconds depending on the material under investigation [110]. Therefore, it is reasonable to include glass transition temperatures from DSC cooling experiments at 10 K/min in Arrhenius representations at $\log(\omega/\text{rad s}^{-1}) = -2$ [110]. For details about glass transition see *e.g.* [88].

With TMDSC it is possible to obtain information about molecular dynamics ($\tau = 1/\omega = f(T)$) at the glass transition in a temperature range of about 10 K, see Fig. 37. To broaden the temperature range, it is necessary to broaden the frequency range. This can be done by combining different methods to measure complex heat capacity or effusivity. The result of such a combined study of the dynamic glass transition for 7 orders of magnitude in frequency is shown in Fig. 38: TMDSC was used at low frequencies, 3ω -method at high frequencies and AC and photo-acoustic methods were used in the medium range.

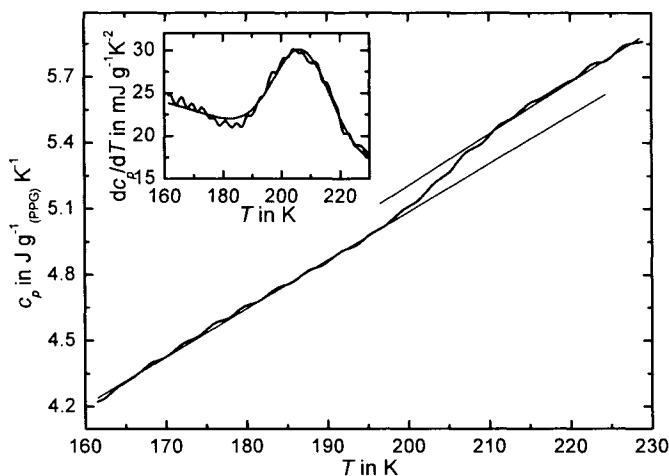


Fig. 39. TMDSC scan measurement in the glass transition region of polypropyleneglycole PPG 2000 in porous sol gel glass, pore size 2.5 nm. The inset shows the temperature derivative of heat capacity. Sample mass 1.09 mg, glass matrix 26 mg, $t_p = 200$ s, $A_T = 0.5$ K, $q_o = 2.5$ K/min (PerkinElmer Instruments DSC 2)

For comparison, the data from dielectric spectroscopy are included. Both data sets coincide very well for PS [110] and polypropylene glycol [200], but there were other examples, *e.g.* PVAc [110], propanol [201] or polycarbonate [97], where this was not the case.

As an example of the high quality of heat capacity data from TMDSC scan measurements, the results from a polypropyleneglycole sample confined in a porous sol gel glass [204] with pore size of about 2.5 nm are shown in Fig. 39. The increase in heat capacity was mainly due to the heat capacity of the sol gel glass, 25 mg, while the step in heat capacity is due to the glass transition of the PPG, 6 mg, in confined geometry. For the determination of the glass transition temperature, it is often helpful to evaluate the temperature derivative of the measured heat capacity, see inset in Fig. 39.

Often, a Gaussian type function can be fitted to the derivative curve. Here we used a Gaussian curve and a linear term because of the slope of the data

$$\frac{dc_p}{dT} = y_0 + s \cdot x + \frac{A}{w \cdot \sqrt{\pi/2}} e^{-\frac{2(T-T_g)^2}{w^2}} \quad (53)$$

From the fit we get T_g as the centre and a measure of the width of the transition, w that can be used for further calculations (see *e.g.* [88,110,205,206]). The derivative often allows for a separation of overlapping weak glass transitions as shown by Hourston *et al.* [207-214].

4.2.2. Non-reversing heat capacity at glass transition

4.2.2.1. General criticism

Fig. 36 shows that there is a difference between the total and complex heat capacities due to different and independently chosen time scales. Following the concept of reversing and non-reversing heat capacity, specifically heat-flow rates, a significant non-reversing heat capacity appear as in Fig. 40.

The different heat capacities available from the TMDSC scan measurements (see section 3.1) in the glass transition region of PS are shown for different underlying cooling rates in Fig. 40 [96]. With an increase in cooling rate, the step in the total heat capacity is shifted toward higher temperatures as is expected from DSC measurements. The real as well as the imaginary part of the complex heat capacity are only slightly affected by the different underlying cooling rates. Only at 1 K/min can changes due to the violation of the condition of stationarity (see section 3.2) can be observed. Consequently the non-reversing heat capacity shows significant changes with changing underlying cooling rate. Strictly speaking, the difference between total heat capacity and reversing heat capacity is a result of the different time scales of both measurements, and has basically nothing to do with reversing and non-reversing contributions to the heat capacity. In this case, the non-reversing heat capacity (heat-flow rate) has

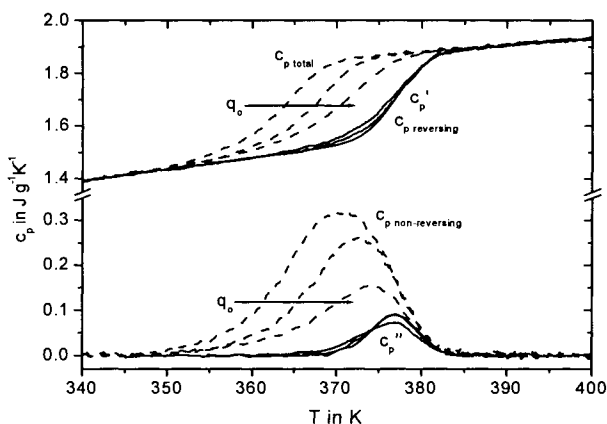


Fig. 40. TMDSC scan measurements at different underlying cooling rates (0.001 K/min – 1 K/min), for details see [96]. Real (reversing heat capacity) and imaginary part of complex heat capacity – solid lines, total and non-reversing heat capacity – dashed lines (PerkinElmer Instruments DSC 2 and Setaram DSC 121)

no physical meaning. It should be mentioned that the imaginary part of the complex heat capacity and the formally determined non-reversing heat capacity both show a peak in the glass transition region (see Fig. 40). However, while the imaginary part of the complex heat capacity is a physically well defined and useful quantity, the non-reversing heat capacity is not. Therefore, one should be aware that these quantities are not interrelated.

4.2.2.2. Enthalpy retardation

Unfortunately, there is another problem involving non-reversing heat capacity. It was mentioned in several papers [16,17,75-77,215-223] that the non-reversing heat capacity could be used to study enthalpy retardation due to annealing below the glass transition. As is well known from DSC measurements, the annealing peak will show up in the total heat capacity and with increasing annealing, the integral of the non-reversing heat capacity may increase. However, as shown above, the non-reversing heat capacity depends on the difference between the timescales due to linear heating and modulation frequency. Consequently, the area under the peak in the non-reversing heat capacity becomes an arbitrary number [140,224-226]. The same qualitative information about the enthalpy retardation can be obtained by extrapolating the liquid heat capacity to lower temperatures and integrating the remaining peak above this line, dashed line in Fig. 41. Such measurements can be performed in DSC mode at heating rates of 20 K/min instead of the necessary low scanning rates in TMDSC.

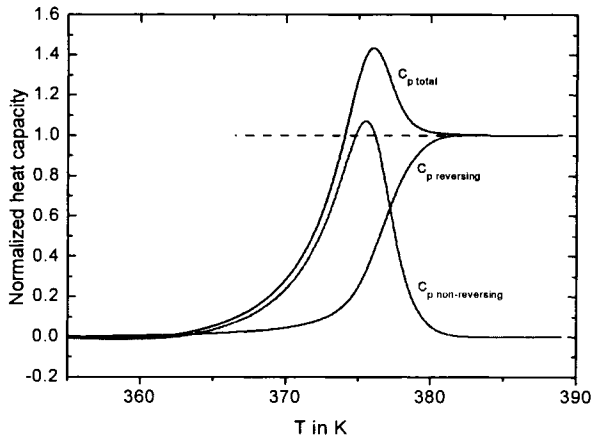


Fig. 41. Normalized heat capacities at glass transition

To overcome the problems of the somewhat arbitrarily chosen baseline for the integration in the case of the evaluation of the non-reversing heat capacity, it was suggested [215-217,223,227,228] two measurements be performed: The first without any annealing resulting in a non-reversing signal due to the difference in the time scales and the second after annealing. The correct enthalpy change is then given by the difference between the area under the peaks of the second and first measurements of the non-reversing heat capacity. This is correct only as long as the reversing heat-capacity is not influenced by the annealing, which what is not the case for long annealing times [96,125,140,215]. Eq. (54) represents nothing more than the difference between the total heat capacities of the annealed and the unannealed sample commonly done in DSC.

$$\begin{aligned}
 \Delta H_{\text{annealing}} &= \int_{T_0}^{T_i} C_{p \text{ non-reversing annealed}} dT - \int_{T_0}^{T_i} C_{p \text{ non-reversing unannealed}} dT \\
 &= \int_{T_0}^{T_i} (C_{p \text{ total annealed}} - C_{p \text{ reversing}}) dT - \int_{T_0}^{T_i} (C_{p \text{ total unannealed}} - C_{p \text{ reversing}}) dT \\
 &= \int_{T_0}^{T_i} (C_{p \text{ total annealed}} - C_{p \text{ total unannealed}}) dT
 \end{aligned} \tag{54}$$

Again, it is much easier, faster, and gives a higher accuracy if one performs the measurements of the total heat capacities or heat-flow rates of the annealed and the unannealed samples by common DSC at or around heating rates of 20 K/min.

4.2.3. Modeling the results from TMDSC at glass transition

Several approaches are available to model the measured signals and heat capacities from TMDSC measurements at glass transition [20,87,91,96,97,102, 158,229-240]. Most of them are based on the Tool-Narayanaswamy-Moynihan (TNM) model which affords a reasonable description of the features of the measured curves if a non-Arrhenius dependency of the relaxation time on temperature is included [96,97]. As long as vitrification (step in c_p total) is well separated from the dynamic glass transition (step in c_p reversing), the dynamic glass transition can be described as an equilibrium relaxation process [97]. Under these conditions, the non-linearity parameters of the TNM model as stated by Simon are not needed [234]. Fig. 42 shows measured and calculated heat capacities for PS in the glass transition range (for details see [96]).

Because glass transition has been studied in detail by TMDSC and precise heat capacity data are available, the “higher order” effects were investigated such as higher harmonics because of the violation of the condition of linearity and stationarity [92-94,97,158,232,233,239-247]. A large number of publications on glass transition studies by TMDSC can be found for a wide variety of different glass formers such as polymers, low molecular mass compounds, metals, inorganic glasses, bio-polymers, *etc.*

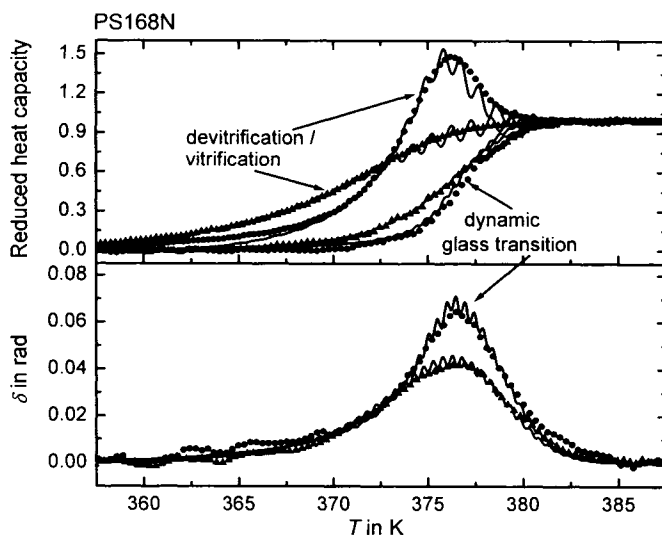


Fig. 42. Reduced heat capacity and phase angle from TMDSC measurements, $t_p = 60$ s, $A_T = 0.5$ K, $q_o = \pm 1$ K/min. (PerkinElmer Instruments DSC2 and Setaram DSC121) Δ - TMDSC on cooling, \circ - TMDSC on heating, solid line - TNM-model; TNM-parameters: $\ln(\tau_o / \text{s}) = -28.02$, $\Delta h^* / R = 1305$ K, $T_\infty = 333$ K, $x = 0.22$, $\beta = 0.56$ [96,97]

4.2.4. Glass transitions superimposed by latent heats

While the concept of reversing and non-reversing heat capacity is questionable for the glass transition itself, there are several applications where a deconvolution into these two components is possible. In the following examples we will discuss the superposition of a glass transition with truly non-reversing latent heats. Under these conditions, it is often very difficult to detect a glass transition in DSC and the advantages of TMDSC become evident. Again, it is not the aim of this paper to give a comprehensive overview about all possible situations and applications. A few selected cases will be discussed to show the basic ideas, and to help the reader to draw his own conclusions. We will start with some simple model calculations to illustrate the deconvolution process under ideal conditions. Much more sophisticated approaches can be found in the literature, see *e.g.* Toda [68,114-116], Schawe [142,248-253], Salvetti [80,254,255], van Mele [256-258].

4.2.4.1. Basic considerations

In section 3.2, a truly reversing process was assumed for the model calculations. Let us now assume a superposition of a sigmoidal, increasing reversing heat capacity and a truly non-reversing latent heat. This may represent a glass transition superimposed with a non-reversing melting. For the model calculation, we assume that all contributions to the heat-flow rate are temperature or heating rate controlled and no time dependent processes occur [259]. Under such conditions, the reversing base-line heat capacity (sigmoidal increasing) contributes to the heat-flow rate signal while the non-reversing latent heat (Gauss peak) contributes at only temperatures that are higher than the previously reached highest temperature.

For the calculation, a superposition of a sigmoidal reversing base-line heat capacity, $C_{p \text{ baseline}}$, Eq. (55), with a non-reversing time independent excess heat capacity, $C_{p \text{ excess}}$ Eq. (56), was used.

$$C_{p \text{ baseline}} = C_{p2} + \frac{C_{p1} - C_{p2}}{1 + e^{(T-T_c)/dx}} \quad (55)$$

with $C_{p1} = 0.8 \text{ J K}^{-1}$, $C_{p2} = 1.4 \text{ J K}^{-1}$, $T_c = 500 \text{ K}$ and $dx = 5 \text{ K}$.

$$C_{p \text{ excess}} = \frac{A}{w\sqrt{\pi/2}} e^{-\frac{2(T-T_c)^2}{w^2}} \quad (56)$$

with $A = 100 \text{ J}$, $w = 10 \text{ K}$ and $T_c = 500 \text{ K}$

For the resulting $C_{p \text{ total}}$, which corresponds to the reversing heat capacity under heating only conditions the heat-flow rate was calculated for the conditions given in Fig. 43. The heat-flow rate was evaluated in the common

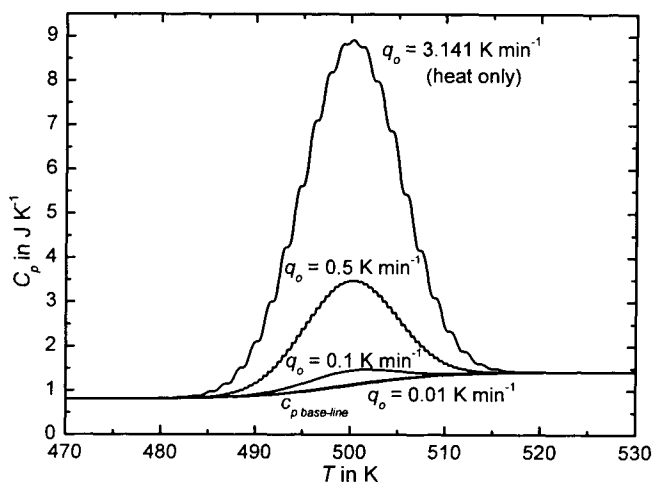


Fig. 43. Reversing heat capacity from model calculations, see text, for different heating conditions. $t_p = 60$ s, $A_T = 0.5$ K

way (see section 3.2). The resulting moduli of complex heat capacity (reversing heat capacity) for different underlying heating rates are shown in Fig. 43. At the highest underlying heating rate of 3.141 K/min, temperature always increased (heating only condition). For this and all higher heating rates, the reversing heat capacity equals $c_{p, total}$, the input function. For lower heating rates, the contribution of the non-reversing excess heat capacity to the reversing heat capacity decreased to a value at $q_o = 0.01$ equal to $c_{p, baseline}$, the reversing part of the input function. This example shows that there is not a prior deconvolution to a reversing and a non-reversing component in TMDSC. As soon as the non-reversing component is temperature dependent, it contributes to the reversing component [260]. Nevertheless, there are other cases where the non-reversing component is mainly time and not temperature dependent make deconvolution possible. The description of the corresponding heat-flow rates then needs more sophisticated models that go beyond the scope of this paper. Further information is available from the studies by Toda [114-116,120,149,261-265], Schawe [112,113,266-268], Höhne [269,270], Lacey [157,217,271], and others [127,272-281].

Therefore, the study of glass transitions superimposed by non-reversing events requires a carefully study of the non-reversing component and selection of appropriate measuring conditions. In the example given above, it is possible to study the underlying glass transition if the contributions from the non-reversing excess heat capacity to the heat-flow rate during a single modulation period are minimized. This is possible by decreasing the heating rate (preferable quasi-

isothermal), decreasing the period, or increasing the temperature amplitude [259].

4.2.4.2. Glass transition superimposed by melting

Because of the large contribution of excess heat capacities to the reversing heat capacity as discussed above, only a few examples are available for the

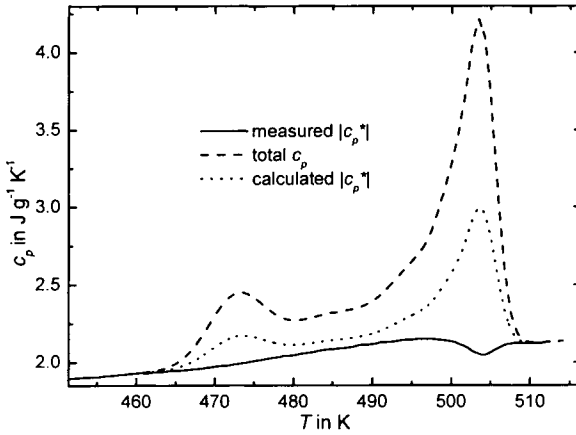


Fig. 44. TMDSC measurement in the melting region of PC, $A_T = 0.5$ K, $t_p = 100$ s, $q_0 = 0.5$ K/min and the result of a model calculation assuming non-reversing melting and no time dependence (TA Instruments DSC 2920)

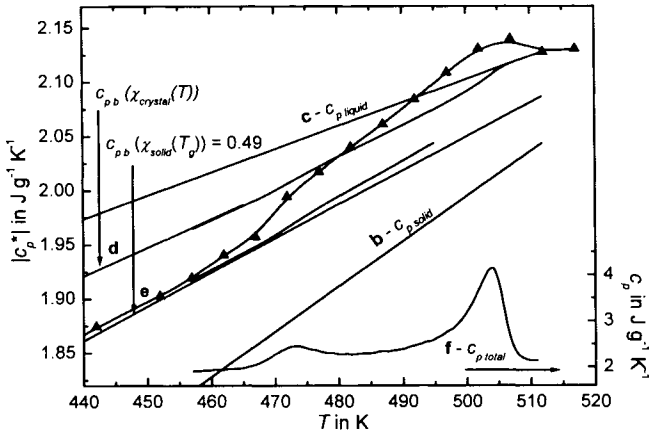


Fig. 45. DSC and quasi-isothermal TMDSC measurement of semicrystalline PC ($A_T = 0.5$ K, $t_p = 100$ s), curve **a**. Curve **b** and **c** correspond to heat capacities from ATHAS databank for crystalline and liquid PC, respectively. Curve **d** was estimated from a two-phase model and curve **e** from a three phase model using $\chi_{solid}(T_g)$. Curve **f** shows the total heat capacity in the melting region ($q_0 = 0.5$ K/min) [283] (TA Instruments DSC 2920)

separation of a glass transition from melting (e.g. [282]). Such a study requires a sample with very slow melting kinetics. However, there is a chance that melting proceeds independent of the actual temperature and does not contribute to the periodic part of the heat-flow rate. Semicrystalline polycarbonate is an example of such a behavior.

From the measured $c_{p\ total}$, the expected reversing heat capacity was estimated under the assumption of total non-reversing excess heat capacity (see section 4.2.4.1 and [259]). The measured reversing heat capacity was significantly smaller. In this case melting proceeded mostly independent of the temperature oscillations. By further reducing the underlying heating rate, we should be able to study the changes in base-line heat capacity underneath the double melting peak. In Fig. 45, quasi-isothermal measurements are shown that clearly show the significant increase of heat capacity in the temperature range of the lowest endotherm. This can be attributed to the devitrification of the rigid amorphous fraction [283].

At the lowest endotherm the increase in base-line heat capacity can be measured because no other contribution to the reversing heat capacity appears. However, the measured heat capacity becomes larger than liquid heat capacity at the main melting peak also under quasi-isothermal conditions. This is not possible without contributions from latent heats and consequently, base-line heat capacity is no longer measured. The effect was first studied by Wunderlich *et al.* [284] and is called reversing melting. It will be discussed in more detail in section 4.4 below.

4.2.4.3. Glass transition superimposed by crystallization

Polymer crystallization generally requires a sufficient super-cooling on the order of 10 K. Therefore, small temperature oscillations commonly applied in TMDSC should not significantly influence the rate of crystallization. Nevertheless, in cold crystallization, where crystallization is controlled by mobility of the polymer melt, the modulation of the crystallization rate can be used to measure growth rate as shown by Toda for several polymers [115,117,149,263-265]. Also reversing melting can be observed on crystallization (see section 4.4 below). If we want to study glass transition superimposed by crystallization these effects have to be prevented.

The glass transition of PC superimposed by crystallization of PET in a bilayer film [16] is one classic example that demonstrates the possibilities of the deconvolution into reversing and non-reversing signals [17,76,285]. Here we will discuss a homo polymer, poly hydroxybuterate (PHB), undergoing cold crystallization that does not show reversible melting at these low temperatures.

The initially amorphous PHB sample shows a glass transition at about 2 K that is seen in the reversing and the total heat capacity. On further heating, cold crystallization starts around 300 K. The exothermic peak in the total and

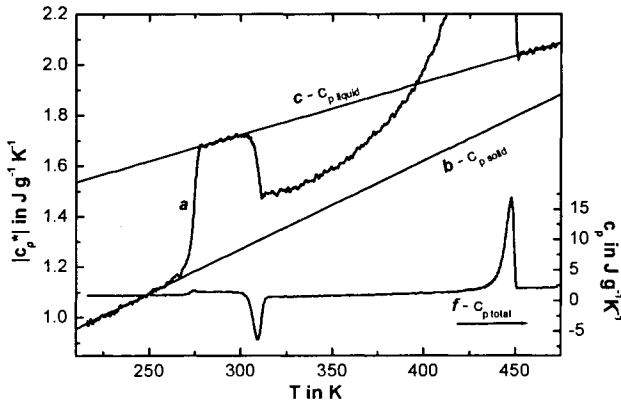


Fig. 46. TMDSC scan measurement of initially amorphous PHB at underlying heating rate 1 K min^{-1} , temperature amplitude 0.4 K and period 60 s , curve **a**. Curve **b** and **c** correspond to heat capacities for solid and liquid PHB, respectively. Curve **f** shows the total heat capacity (PerkinElmer Instruments Pyris 1 DSC) [283]

downward step in the reversing heat capacity is attributed to this crystallization event. The decrease in the reversing heat capacity is due to the transformation of liquid material into crystalline and rigid amorphous material. The melt transformed into the rigid amorphous fraction of the semicrystalline polymer undergoes a structural induced vitrification process on heating [283]. Because there is no reversible melting during crystallization for PHB, the processes can be quantified as shown below. At higher temperatures above 350 K , even though reversing heat capacity as well as the total heat capacity increases, crystallization can still be detected. This is due to the reorganization of the imperfect crystals formed during cold crystallization. This will be discussed in more detail in section 4.3.1.2 below. However, we are able to study vitrification of PHB by TMDSC independently on the superimposed latent heat during crystallization. Although these effects can be separated from DSC measurements, iterative procedures are necessary and assumptions regarding the coupling of the rigid amorphous fraction to the crystalline fraction must be made [286]. Because there is no reversing melting and no contribution from the latent heat to the reversing heat capacity, we are able to study vitrification in more detail by quasi-isothermal experiments [283,287-290].

Base-line heat capacity was measured as a function of time and compared with the predictions of a two and three phase model (for details see [289]). The rigid amorphous fraction in PHB was established during the quasi-isothermal crystallization as could be seen from the agreement of line **e** with the measured

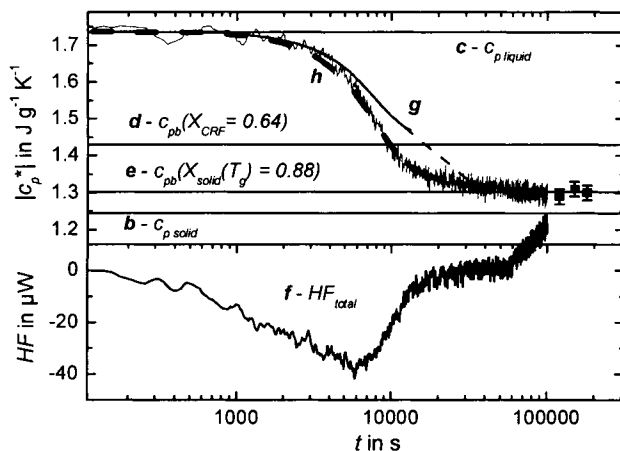


Fig. 47. Time evolution of heat capacity during quasi-isothermal crystallization of PHB at 296 K, temperature amplitude 0.4 K and period 100 s, curve **a**. Curve **b** and **c** correspond to solid and liquid heat capacities, respectively. Curve **d** was estimated from a two-phase model and curve **e** from a three-phase model, using $\chi_{solid}(T_g)$ from Δc_p . The squares represent measurements at modulation periods ranging from 240 s to 1,200 s. Curve **f** shows the exothermic effect in the total heat-flow and curves **g** and **h** the expected values from model calculations, see text and [289] (PerkinElmer Instruments Pyris1 DSC)

heat capacity at the end of the crystallization process. For PHB, we were able to measure the exothermic effect due to the crystallization process. The Pyris 1 DSC allows for a quantitative measurement over 17 hours and the maximum of the heat-flow rate was less than 40 μW . From the integral, we obtained the enthalpy change, $h(t)$, and the crystalline fraction as a function of time. The time dependence of base-line heat capacity could be determined from

$$c_{p,b}(t) = c_{p,liquid} - \frac{\chi_{CRF}(t)}{\chi_{CRF}(\infty)} (c_{p,liquid} - c_{p,b}(\infty)) \quad (57)$$

The calculation can be performed for two cases. (i) the RAF was formed during the whole crystallization process or (ii) the crystalline morphology was first build up during main crystallization and in a second step, e.g. during secondary crystallization at longer times, the RAF was formed. Therefore during main crystallization, very little if any RAF should be present. This situation (ii) should be described by Eq. (57) where $c_{p,b}(\infty)$ equals the value from a two-phase model, line **d**, taking into account liquid and crystalline material only. Curve **g** in Fig. 47 shows the result. Although the behavior at longer times ($>10,000$ s) was not known, the result during main crystallization was not in agreement with

the measured curve. To calculate $c_p(t)$ according to the assumption (i), $c_{p,b}(\infty)$ equals the value from a three-phase model, line *e*. Here it is assumed that the rigid amorphous fraction was formed during or just after the formation of the lamella. Curve *h* in Fig. 47 shows the result. This result is in agreement within the scatter of the experimental points. This example was given here because it displays the possibility of studying structural induced (isothermal) vitrification superimposed by latent heats by means of TMDSC. Furthermore, because of the quantitative heat capacity data, we were able to compare the measured data with predictions from model calculations. In this method we are able to make more substantial contributions to science compared to only previous qualitative results from DSC and TMDSC.

4.2.4.4. Glass transition superimposed by chemical reactions

Another area where it is possible to study vitrification superimposed by latent heats is conversion induced vitrification. Such processes appear during polymerization reactions such as curing [18,80,122,248,252,253,255,256,291-299]. A typical example is shown in the Fig. 48.

During the process of often exothermic network formation, molecular mobility decreases and the initial liquid compounds vitrify. Information about this vitrification process is essential because the chemical reaction goes from a chemical to a diffusion controlled regime. If the chemical reaction rate is not significantly changed by the temperature oscillations of a TMDSC measurement, the latent heat will not contribute to the reversing heat capacity. Then the vitrification of the reacting system could be studied. Again the advantage of quantitative calorimetric data becomes visible when the data are compared with predictions from model calculations or the data can be used to adjust parameters of the model [255,258,294].

As discussed in section 4.2 vitrification is a dynamic phenomenon and generally heat capacity becomes frequency (time) dependent. Including this and possible contributions from the chemical reaction to the complex heat capacity again needs sophisticated models which are currently under construction, e.g. by Schawe *et al.* [248].

4.2.4.5. Glass transition superimposed by evaporation

Evaporation of a solvent is another non-reversing event that is sometimes coupled with a glass transition of the drying material. As for crystallization and chemical reactions, the process of evaporation may induce the vitrification of the material because of the decreasing plasticizing effect of the evaporating solvent. On the other hand, it may be possible that the glass transition of the material is not altered by the evaporation but the endothermic evaporation may dominate the DSC signal. TMDSC allows for a study of base-line heat capacity and therefore, the glass transition if there are no contributions from the endothermic

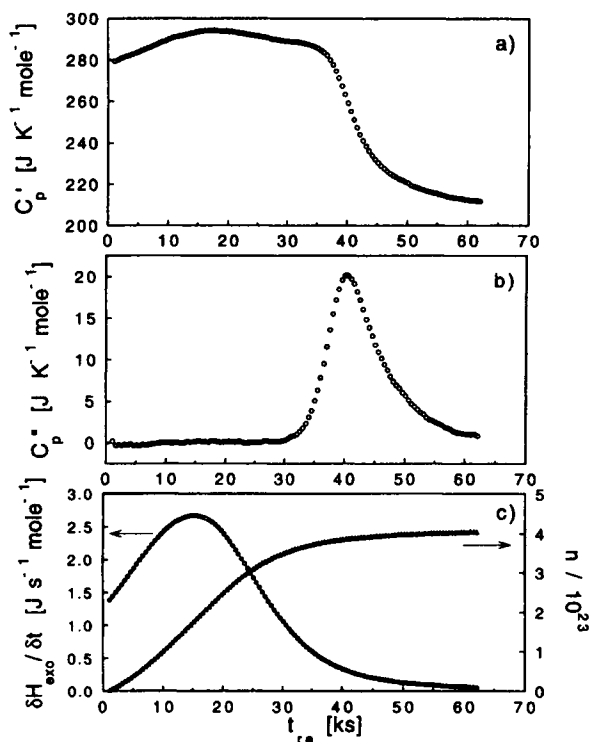


Fig. 48. The real (a) and imaginary (b) components of specific heat capacity at 0.01 Hz measured during the linear chain growth, *i.e.*, —A—B—A—B— structure, with A being *n*-hexylamine and B, diglycidyl ether of bisphenol A at 300.1 K. In this process, the nitrogen atom of then-hexylamine covalently bonds with one terminal carbon atom of the epoxy groups of two B molecules. Part (c) contains a plot of the heat release $(\partial H / \partial t)_r$ and a plot of the number of covalent bonds formed as the reaction occurred. The plots are against time during the course of the macromolecule's growth (Reproduced from [255]).

evaporation to the reversing heat capacity. This is often the case because evaporation in polymers is diffusion controlled and evaporation rate is not significantly influenced by the temperature modulation. Fig. 49 shows a typical example [251].

4.2.5. Conclusions regarding glass transition

Although there is no generally accepted theory for glass transition, TMDSC seems to be a powerful technique to gain information about this interesting phenomenon of condensed matter physics. The main points are:

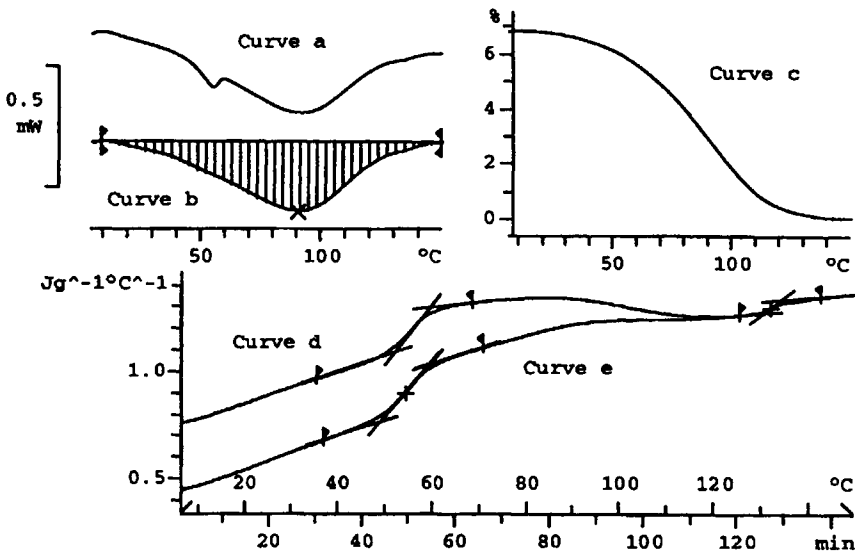


Fig. 49. Evolution of the specific heat capacity of a pharmaceutical sample in a pan with a pierced lid. Curve a: original total heat-flow rate (endothermic downwards); curve b: base-line corrected heat-flow rate; curve c: remnant water content in the sample; curve d: apparent specific heat capacity; curve e: specific heat capacity of the dry sample (Reproduced from [251])

- Due to the high signal to noise ratio, detailed information about the step in heat capacity at glass transitions is available. This is also true for very weak glass transitions.
- Frequency dependent complex heat capacity allows for a study of the dynamics of the underlying relaxation process. The imaginary part of complex heat capacity (phase angle) is very sensitive to violations of linearity and stationarity of the response and to small changes in the system under investigation.
- Glass transitions superimposed by non-reversing events may be separated if the experimental conditions are carefully selected.

4.3. Phase transitions

From the very beginning, the concept of reversing and non-reversing heat capacity was developed to allow for a separation of reversing and non-reversing contributions to phase transitions especially polymer melting. Unfortunately, the deconvolution does not always give correct and meaningful results at phase transitions. However, the application of periodic or step-like temperature profiles often allows for a detection of re-organization and re-crystallization in polymers upon heating through the melting range. Finally, for most

semicrystalline polymers, a frequency dependent excess heat capacity can be observed in the temperature range between the glass transition and final melting. The process behind that phenomenon is called reversing melting, and it seems to be related to the molecular processes at the crystal surfaces in semicrystalline polymers. Interestingly, it is also observed during and after isothermal crystallization. Under certain conditions, the frequency dependence of the apparent complex heat capacity can be linked to the kinetics of crystallization and melting.

4.3.1. First-order phase transitions

Polymer crystallization and melting are considered first-order phase transitions with broad transition intervals due to a broad distribution of crystallite sizes. Therefore, an understanding of the results available from TMDSC in a first-order phase transition region is essential for a correct interpretation. To the best of my knowledge, there is not yet a description available that takes into account all influences on the measured signals. Therefore, we will restrict ourselves to a discussion of the major problems appearing in TMDSC experiments in first-order transitions.

4.3.1.1. Calibration related problems

The basic ideas of calibration are described in section 3.4. Here we will highlight some of the problems at phase transitions to avoid meaningless measurements. The first problem when studying an ideal first-order phase transition is the unavoidable difference between the measured and sample temperature due to the infinite heat capacity at the transition temperature. During melting of a pure metal, indium for example, the sample temperature stays fixed at the transition temperature until the heat of fusion is transferred to the sample. The time needed for that depends on the effective thermal contact as discussed in section 3.4.1 and the temperature difference across the thermal contact. In analogy to electrical circuits we can write:

$$HF = \frac{\Delta T}{R_{th}} \quad (58)$$

The heat-flow rate, HF , and consequently, the time needed to transfer the heat of fusion depends on the effective thermal resistance, R_{th} , as well as on the temperature difference, $\Delta T = T_F - T_S$. Because T_S stays constant during the time needed to transfer the heat of fusion, ΔT depends only on the temperature time profile, T_F , of the furnace. Here it becomes obvious that the measured heat-flow rate depends only on the parameters of the measuring system and the temperature profile, and it does not depend on sample properties. Such a situation is shown in Fig. 50.

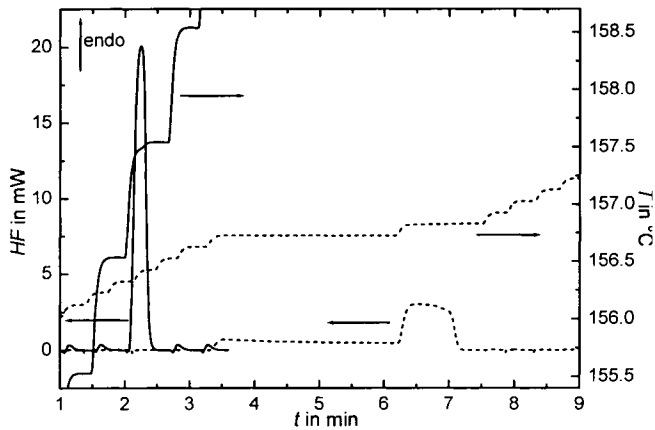


Fig. 50. SSDSC measurement in the melting range of indium. Heat-flow rate and temperature measured close to the sample position (often incorrectly named "sample temperature") versus time for two different temperature-time-profiles. a - $\delta T = 1$ K; b - $\delta T = 0.1$ K; $q = 10$ K/min; $t_{iso-max} = 5$ min; absolute criterion = 0.001 mW (PerkinElmer Instruments Pyris Diamond DSC)

For the measurement with a step height of 1°C , melting occurs during the step from 156.5°C to 157.5°C . There is only a slightly longer time needed to come back to a constant heat-flow rate compared with the other steps. This is due to the large temperature difference $\Delta T = 0.9^\circ\text{C}$ between the furnace temperature, which is measured, and the actual sample temperature, 156.6°C in the case of melting indium. For the 0.1°C steps, the picture changes dramatically. At 156.7°C the temperature difference becomes small, $\Delta T \approx 0.1^\circ\text{C}$, and according to Eq. (58), the heat-flow rate becomes small as can be seen in Fig. 50 between 3.5 and 6 minutes. Then in the next step between 6 and 7 minutes $\Delta T \approx 0.2^\circ\text{C}$ and the heat-flow rate increased. In both steps the heat-flow rate stayed at a constant value because of the constant temperature difference and a constant thermal resistor R_{th} , see Eq. (58). After transferring the total heat of fusion at about 7 minutes, the heat-flow rate decreased rapidly because sample temperature increased and the temperature difference ΔT decreased. The time needed for transferring the total heat of fusion depends on the chosen step temperature and will yield meaningless phase information in a TMDSC measurement, see also [300].

Limiting the equilibration time to 10 s yields a quasi continuously increasing heat-flow rate until the total heat of fusion is transferred. As expected from Eq. (58) the heat-flow increased for approximately the same amount for each step in temperature except the first where the starting temperature was

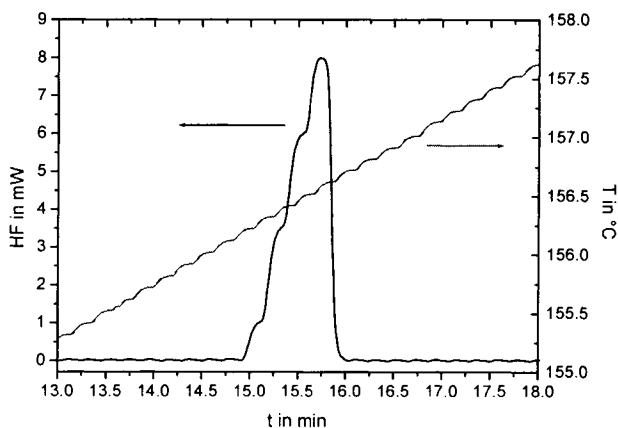


Fig. 51. SSDSC measurement in the melting range of indium. Heat-flow rate and temperature measured close to the sample position (named “sample temperature” in the case of the PerkinElmer Pyris 1 DSC) versus time. $\delta T = 0.1^\circ\text{C}$; heating rate $10^\circ\text{C}/\text{min}$; $t_{\text{max isotherm}} = 10$ s, absolute criterion = 0.001 mW (PerkinElmer Diamond DSC)

below melting temperature and increased until it reached melting temperature. Under such conditions, the SSDSC approach does not give meaningful heat capacities. With a further decrease in isothermal time, the SSDSC converges to a DSC scan measurement, which is preferable, in case of sharp first-order phase transitions.

Beside all of the problems violating the conditions of linearity and stationarity under such conditions, see section 3.2, the heat capacities obtained from TMDSC measurements are meaningless because they are mainly independent of sample properties. The only way to examine such data is an analysis in time domain as shown by Wunderlich [301,302], O’Reily [281], and Hatta [67,303]. In general, calibration of the measured signals according to section 3.4.1 seems to be difficult [271] because of unknown and changing parameters of the system when going through a first-order phase transition.

4.3.1.2. Reorganization - The influence of the temperature time profile

For polymers melting in a broad temperature range the problem of heat transfer may be reduced so that calibration is possible. However, one should have in mind that for a single crystal that melts at a well defined temperature, the situation may be similar to the case discussed above. As shown by Lacey and Nikolopoulos [271], under certain, partly unrealistic assumptions, a qualitative description of the TMDSC signals in the melting range of polymers is possible. Because of the tendency of polymers to reorganize and to recrystallize on

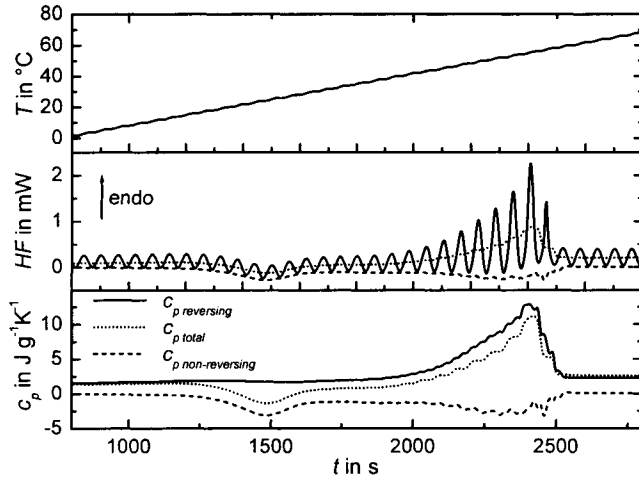


Fig. 52. TMDSC measurement of a quenched PHB/PCL 50/50 blend in the temperature region of PHB crystallization and PCL melting. $A_T = 0.318$ K; $t_p = 1$ min; $q_o = 2$ K/min (Mettler Toledo DSC 821)

heating, the temperature profile used may have a significant influence on these processes.

Obtaining information about reorganization by TMDSC is one of the most important applications to polymer melting [79,304-311]. Let us start with the very simplified model used for the calculation of the curves in Fig. 43. It is assumed that the excess heat capacity is truly non-reversing and no time dependency occurs. Then melting proceeds only if the actual temperature becomes higher than the previously reached highest temperature. Under the condition that the sample is always heated (never cooled), the reversing heat capacity equals the total heat capacity. If a heating rate profile is chosen where the heating rate varies between zero and a maximum value ($q_o = 3.141$ K/min in Fig. 43), the heat-flow rate should go to zero as soon as the actual heating rate equals zero. In case of crystallization or reorganization an exothermic heat-flow rate may also appear during isothermal conditions. The signals obtained during such processes are shown in Fig. 52 for a PHB/PCL 50/50 blend. Here crystallization, melting, and reorganization can be seen in a very narrow temperature range.

During the crystallization of PHB, the heat-flow rate and the total heat capacity became exothermic. The amplitude of the heat-flow rate oscillations did not change much and therefore, reversing heat capacity was not influenced much during cold crystallization. A more detailed picture for pure PHB is shown in Fig. 46. The non-reversing heat capacity, the difference between total and reversing heat capacity, see 3.1.1 for details, covers all information from cold

crystallization. During the melting of PCL, the situation was more complex. While the total heat capacity became clearly endothermic during the isothermal segments, an exothermic heat-flow rate could be observed. This exothermic heat-flow rate was evidence for a reorganization during the melting of PCL. Because of the additional exothermic contribution to the heat-flow rate, the amplitude of the oscillating part increased and the reversing heat capacity became larger than the total heat capacity. The difference, which became exothermic, clearly indicated the occurrence of reorganization or recrystallization during the TMDSC scan. Heat only conditions are preferable for these studies of reorganization, but it is often difficult to meet the conditions of linearity, stationarity, and heat only. Therefore, the reversing heat capacity may be falsified. Lowering the underlying heating rate improves the situation in respect to stationarity. It yields a lower reversing heat capacity and consequently, does not allow the separation of the contribution due to the exothermic heat-flow. The situation becomes even more complex if melting shows significant time dependence as shown on the example of PC in Fig. 44. Again, the reversing heat capacity becomes smaller than expected from the total heat capacity and the exothermic contribution can not be separated. Therefore, it seems to be better to study reorganization or recrystallization in a time domain to avoid Fourier transformation. This can be done by looking for the exothermic heat-flow rate at these times when the heating rate equals zero, see Fig. 52. This approach is used by Mettler Toledo in the ADSC™ version of TMDSC, and

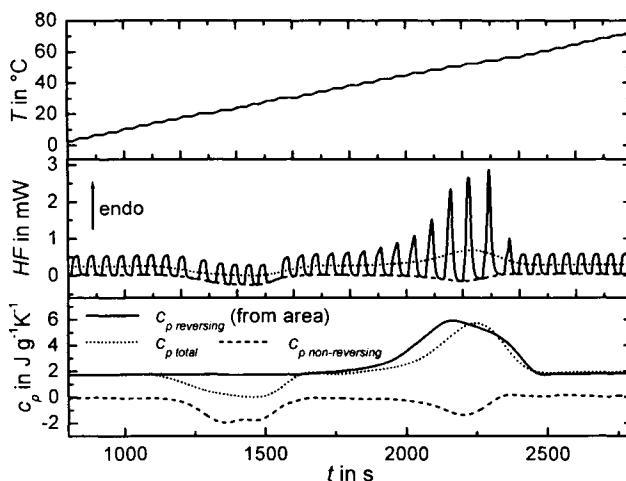


Fig. 53. StepScan™ DSC measurement of a quenched PHB/PCL 50/50 blend in the temperature region of PHB crystallization and PCL melting. $\delta T = 1$ K, $q = 5$ K/min, $t_{iso-max} = 1$ min, absolute criteria = 0.001 mW (PerkinElmer Instruments Pyris Diamond DSC)

even more directly during the isotherms of a StepScan™ Temperature profile, see Fig. 53.

The exothermic heat-flow can be observed in the isotherms during the cold crystallization of PHB (around 1400 s) and during the melting of PCL (around 2200 s). The different heat capacities were determined as described in 3.1.1.2. Generally speaking, TMDSC and StepScan DSC allow for the investigation of reorganization and recrystallization on heating of semicrystalline polymers. A quantitative evaluation of the peak regions is still questionable because of limitations in calibration. The evaluation of the isothermal segments of StepScan DSC or ADSC type measurements seems to be preferable because no Fourier analysis is involved. However, this is sometimes limited because of the very complex behavior of the polymers. In PEEK, at higher temperatures (around 50 minutes) during the isotherms (Fig. 8), recrystallization was still expected to occur, the heat-flow remains endothermic indicating a serious time dependence of heat transfer, as in Fig. 50, or of the melting process. To separate this measurements with different sample sizes can be performed in order to study the influence of the heat transfer.

4.3.1.3. Crystallization and melting kinetics

A study of crystallization and melting kinetics requires knowledge of the origin of the measured apparent complex heat capacity during these events. Several approaches can be found in literature. Schawe *et al.* [112,113,266,267, 312] and Toda *et al.* [114,116,120,261] extracted the melting kinetics, especially the superheating, from TMDSC scan measurements. Toda *et al.* [149,262-265] found a good correlation of polymer crystal growth rates from quasi-isothermal TMDSC measurements with direct observation of the growing crystals by light microscopy. Salvetti *et al.* [254] drew some conclusions about the time scale of a protein unfolding transition from complex heat capacity. Toda *et al.* [68] developed a calibration method to correct for the apparatus influence and to extract information about melting kinetics from apparent complex heat capacity. Lacey *et al.* [271] tried to describe melting and recrystallization in TMDSC measurements. Höhne *et al.* [313] used a deconvolution of the measured signal in a Taylor series to describe the recrystallization of nascent high molecular mass polyethylene. All these approaches are in need of certain models to describe the melting process. Because this topic goes beyond the scope of this paper it will not be discussed in detail here. However, careful calibration of the measured signals is necessary [68], see section 3.4. Calibration in the melting range is not simple because of possible changes in heat transfer properties of the sample itself or the thermal contacts. To illustrate the complexity of the situation, one can again look at the results for complex heat capacity from such a simple model as used in section 4.2.4.1. In Fig. 54 the result is shown for two different

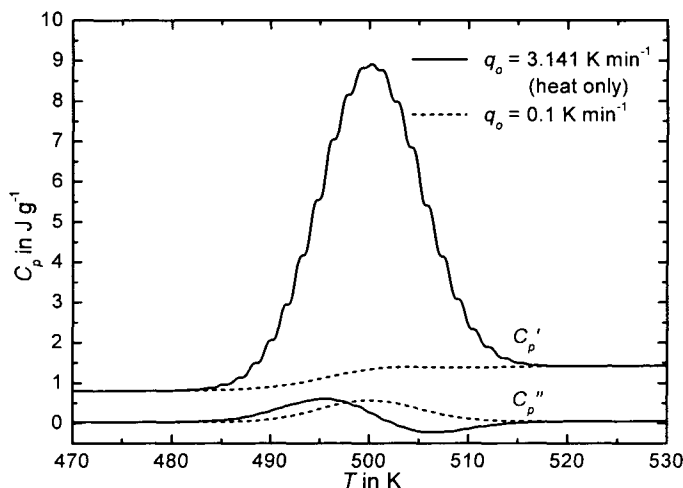


Fig. 54. Complex apparent heat capacity from model calculations, see 4.2.4.1 for details, for different heating conditions, $t_p = 60$ s, $A_T = 0.5$ K

underlying heating rates with no time dependence of any of the signals (neither sample itself nor caused by heat transfer).

This example was used here to demonstrate, at least, part of the problems of data treatment in TMDSC. There is also no time dependence in the model an imaginary part of the apparent heat capacity appears. It is about 7% of the real part and can not be neglected. The reason for this is the temperature dependence of the heat capacity (input function) and the scan conditions (dynamic induced loss [95]). This was discussed in detail for the case of glass transition [97] but must be considered and, if possible, corrected for if one wants to draw any conclusion from the imaginary part of heat capacity on melting. While melting always contributes to the periodic part of the heat-flow rate and consequently to complex heat capacity, this is often not the case during crystallization at large super-cooling. Then the growth rate is only slightly dependent on temperature modulation, and the contribution to the periodic part of the heat-flow rate becomes small [149].

4.4. Reversing melting and crystallization

The melting temperature of polymer crystals shows a broad distribution. Melting ranges of 100 K and more can be found. Therefore, the determination of crystallinity from the heats of fusion is often difficult. Base-line heat capacity^{††}, which is needed as base-line for the peak integration, is not known over the

^{††} Base-line heat capacity corresponds to the heat necessary to increase the temperature of the sample without changing crystallinity. In other words, it is the heat capacity without any contribution from latent heats [Mathot].

whole broad melting range. Mathot [37,314,315] proposed a method based on a two-phase model neglecting the rigid amorphous fraction. The melt heat capacity is extrapolated to lower temperatures as base-line for the integration, and the temperature dependence of the heat of fusion of the infinite crystal is taken into account. This method yields crystallinity as function of temperature for polymers with a broad melting range.

In general, base-line heat capacity is the superposition of the heat capacity of the crystalline, the rigid amorphous, and the mobile amorphous fraction of a semicrystalline polymer [37,283]. The influence of the rigid amorphous fraction on base-line heat capacity becomes significant at lower temperatures, close to the glass transition [286]. For a correct determination of the heat of fusion in that temperature range, knowledge about base-line heat capacity is needed.

In common DSC, measured heat capacity is the superposition of base-line and excess heat capacities. For measurements through phase transitions, it is not possible to distinguish them. In some cases, base-line heat capacity can be obtained from model calculations. For low molecular mass compounds where base-line heat capacities can be measured outside the transition region, the change in the transition region can be estimated from the progress of the phase transition (sigmoidal base-line for peak integration). However, this is only possible for two-phase systems. As soon as a third fraction is present, the information available from a single heat capacity curve is not enough to distinguish the three fractions. Assuming a certain coupling between the RAF and the CRF allows us to solve the problem in an iterative way [286]. However, the validity of the assumption must be independently checked, and the experimental data must be of high accuracy. Therefore, a direct measurement of base-line heat capacity is favorable.

To avoid latent heat contributions, it would be nice to measure at constant temperature. However, changes in temperature are a prerequisite for the measurement of heat capacity. On the other hand, high molecular mass polymers need a super-cooling on the order of 10 K for crystallization. Therefore quasi-isothermal experiments with small temperature amplitudes should enable us to measure base-line heat capacity. On stepwise heating after a certain time, when all crystallization, re-organization, and re-crystallization has finished, no contributions from the latent heat to the measured heat capacity are expected. Base-line heat capacity should be available from such measurements. This is basically the same idea already discussed in section 4.2.4.1 for the study of glass transitions superimposed by latent heats. It was shown by Wunderlich *et al.* [284] that this does not work for most polymers.

In Fig. 55 the results from DSC (thin line) and quasi-isothermal TMDSC measurements (single points resulting in a thick line) on semicrystalline PET are shown. Above the glass transition at about 350 K, heat capacity is below the value expected from a two-phase model (dashed line). This is predicted by the

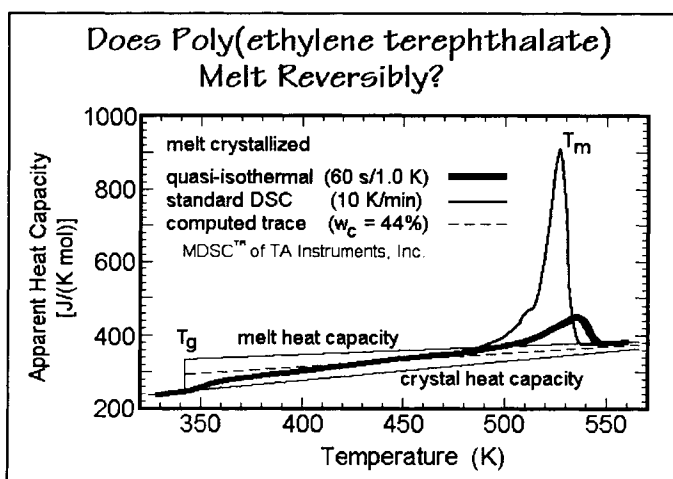


Fig. 55. Heat capacity by standard DSC (medium thick line) and reversing heat capacity by quasi-isothermal TMDSC (single points yielding a thick line). Both on the same melt-crystallized PET. The thin lines indicate the Data Bank data for the amorphous and crystalline PET; the broken line indicates the computed heat capacity for 44% crystalline PET [284] (reproduced from [300]).

corresponding three-phase model. However, above 420 K, heat capacity crosses the dashed line, and around 510 K, it even goes above the heat capacity of the melt. The heat capacity values above the liquid heat capacity in Fig. 55 can not all be explained without contributions from latent heats. Consequently, these quasi-isothermal measurements do not allow the measurement of the base-line heat capacity in the melting region of PET. Also, high molecular mass polymers need a super-cooling of about 10 K for crystallization. Here, contributions from the melting and crystallization to the measured heat capacity are observed at temperature changes of 1 K. For PCL it was shown [127] that even at 0.005 K, amplitude latent heats contribute to heat capacity, see Fig. 56. A review by B. Wunderlich concerning reversing melting can be found in [300].

A more detailed study of the excess heat capacity under quasi-isothermal conditions yields a frequency dependence of the excess heat capacity [119,124, 127,273]. The origin of the excess heat capacity during quasi-isothermal measurements and its frequency dependence is not well understood. It is probable that the molecular processes involved are related to the surface of the polymer crystallites, and according to Wunderlich [284], the term reversing melting is used. For polymers showing a sliding diffusion in the crystallites (α relaxation in case of polyethylene or polyethylene oxide), large contributions to reversing melting are due to surface melting [273]. For other semi-crystalline polymers, processes at the lateral surfaces may be responsible for reversing melting and the corresponding excess heat capacity [316-318].

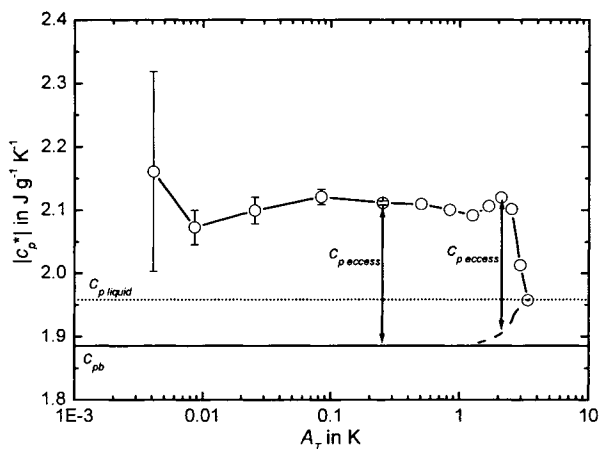


Fig. 56. Quasi-isothermal TMDSC in the melting region of PCL, heat capacity as a function of temperature modulation amplitude A_T , the arrows indicate the excess heat capacity. $m_s = 142$ mg, $t_p = 20$ min, $T_\theta = 334$ K (Setaram DSC 121) [127]

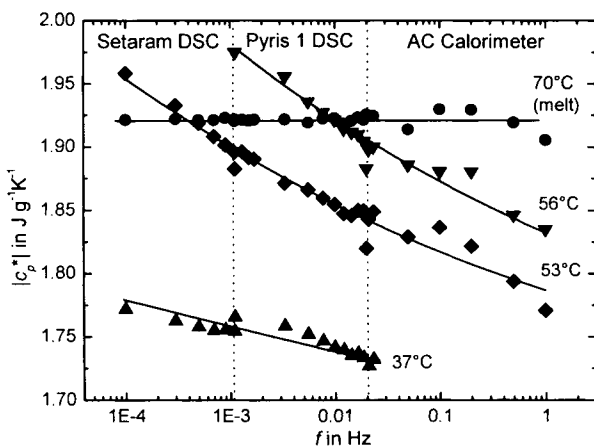


Fig. 57. Frequency dependence of the reversing specific heat capacity in the melting range of PCL, quasi-isothermal measurements, $T_A = 0.5$ K, at the temperatures and with the instruments indicated.

The frequency dependence and the missing amplitude dependence of the excess heat capacity strongly support the view that the reversing melting is not caused by temperature changes during the measurement (the perturbation). The reversing melting is intrinsically present as fluctuations of chain segments at the crystal surfaces. This view is supported by the presence of a mechanical relaxation process in the same frequency range that can be seen under truly

isothermal conditions at the same temperatures [127,319]. Reversible melting can be observed for most polymers in a broad temperature range between the glass transition and final melting. To avoid contributions from irreversible changes in polymer morphology, quasi-isothermal experiments are preferable. Nevertheless, scanning contributions due to reversible melting can be seen and must be considered for interpretation of heat capacity data. Therefore, crystallinity determination by TMDSC [79] can not be recommended. In the very least, it must be checked if the reversing heat capacity represent base-line heat capacity. We recommend the method proposed by Mathot *et al.* [37,314, 315] for crystallinity determination by DSC. This method is preferable because it is firmly based on physical principles, and the time needed for the scan measurements at high heating rates is much shorter compared to TMDSC measurements.

Interestingly, for most polymers studied [320], the heat capacity on heating and cooling coincides in the temperature region where the polymer is semicrystalline. In Fig. 58 on cooling below 400 K, as soon as the sample crystallized, a large excess heat capacity appeared. The spikes observed at crystallization were caused by violation of stationarity (see section 3.2). It was shown by Toda *et al.* [265] and Scherrenberg *et al.* [275] that it is possible to follow the development of the excess heat capacity during isothermal crystallization. This effect can not only be observed for PE where surface melting [272,273] may largely contribute to the excess heat capacity, but

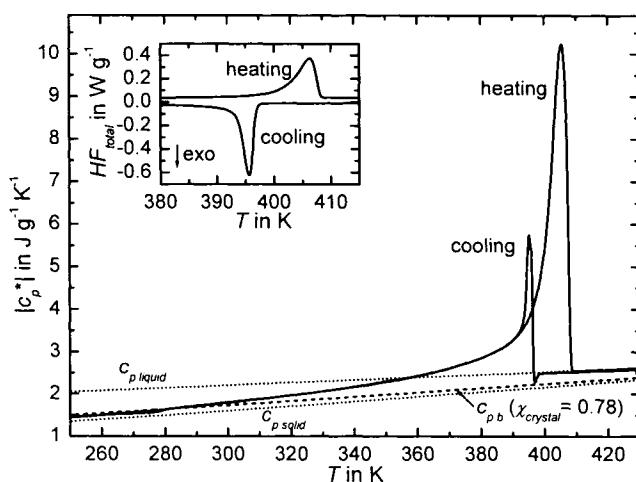


Fig. 58. Reversing heat capacity and total heat-flow rate, inset, for polyethylene (HDPE 6011H, BASF) on heating and cooling. The dotted lines represent the data from ATHAS databank [81] for liquid, solid and the 78% crystalline PE. $q_0 = 0.5 \text{ K/min}$, $A_T = 0.5$, $t_p = 100 \text{ s}$ [320] (TA Instruments DSC 2920)

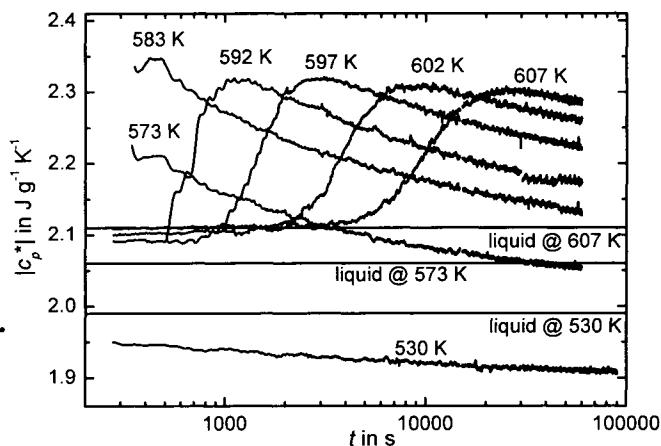


Fig. 59. Modulus of complex heat capacity at quasi-isothermal crystallization of PEEK at different temperatures, $A_T = 1$ K, $t_p = 200$ s (PerkinElmer Instruments Pyris Diamond DSC)

reversible melting can also be observed for semi-rigid polymers [300].

At high temperatures after some induction period the increase of heat capacity because of the formation of the polymer crystals can be seen. During secondary crystallization, heat capacity decreases. This indicates a stabilization process of the already present crystals (decreasing fluctuations at the surface). For long times heat capacity is higher than expected from a two-phase model indicating reversible melting.

As for the excess heat capacity in the melting range and for the excess heat capacity at the end of quasi-isothermal crystallization a frequency dependence can be observed.

From glass transition (see section 4.2), it is a generally accepted practice to describe heat capacity by complex numbers. The typical frequency dependence, as known from other dynamic measurements, is observed: a sigmoid step in the real and a peak in the imaginary part of heat capacity [10,15,126]. A similar frequency dependence of heat capacity of semi-crystalline polymers was observed outside the glass transition range [124,127,273]. These observations were related to the occurrence of the excess heat capacity that can be observed in a rather wide temperature range between glass transition and melting temperatures.

The frequency dependence of complex heat capacity under quasi-isothermal conditions yields information about the characteristic time scale of the molecular processes related to the excess heat capacity. This was discussed in detail for PE by Strobl *et al.* [273,323] and Saruyama [121] applying other calorimetric techniques [60,324] than TMDSC. We have studied the frequency

dependence of heat capacity for PCL, sPP, PHB, PC, and an ethylene octene copolymer (EOM) [127], see Fig. 61. To extend the frequency range available with TMDSC (10^{-5} Hz - 10^{-1} Hz), an AC calorimeter was used (see [325]). For Polycaprolactone (PCL), a mean relaxation time on the order of a few seconds

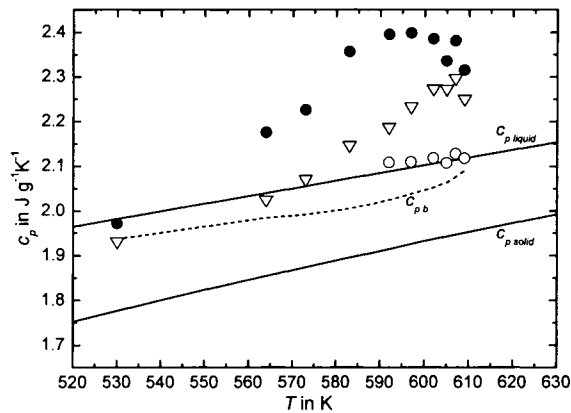


Fig. 60. Heat capacity of PEEK during isothermal crystallization. Maximum of heat capacity – solid circle, heat capacity after 60,000 s – open triangles, heat capacity during induction time open circles. The straight dotted lines represent data from ATHAS databank for crystalline and liquid PEEK, respectively. The curved dashed line for base-line heat capacity was obtained from heat of fusion data and a two-phase model. $A_T = 0.5$ K, $t_p = 100$ s (PerkinElmer Instruments Pyris 1 DSC) [321].

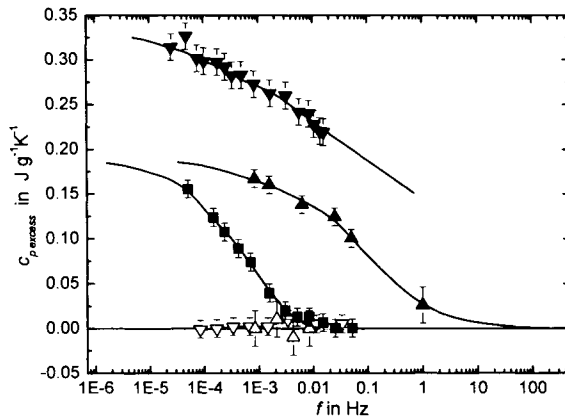


Fig. 61. Frequency dependence of excess heat capacity during isothermal crystallization of PCL (▲) after 120,000 s at 328 K, of sPP (■) after 10,000 s at 363 K, of PC (▽) after 900,000 s at 457 K, EOM [322] (▼) after 80,000 s at 393 K and of PHB (△) after 100,000 s at 296 K as a function of modulation frequency. (PerkinElmer Instruments Pyris 1 DSC, Setaram DSC 121 and AC calorimeter) [318]

can be estimated for the process at 328 K, while for sPP at 363 K, it is on the order of 500 s. For EOM at ambient temperatures, the relaxation time is below one second: far outside the frequency range available [127]. For PC and PHB, we did not observe any frequency dependence after isothermal crystallization at 457 K and 296 K, respectively. For these polymers, a frequency dependent excess heat capacity was only observed at higher temperatures in the melting range [283].

The frequency range available is still not broad enough for a detailed discussion of the curve shape (see Fig. 61). But from the curves, one expects to measure base-line heat capacity without contributions from reversing melting at high frequencies. For PCL high means greater than about 100 Hz, which is outside the accessible frequency range for our experimental techniques. But for sPP, PHB, and PC, measurements at frequencies of about 0.01 Hz, which is inside the frequency range of TMDSC, allow for the measurement of the high frequency asymptotic value. For these semi-crystalline polymers, base-line heat capacity is experimentally accessible in the temperature range between conventional glass transition and melting. Therefore, it is possible to study the formation and the disappearance of the rigid amorphous fraction (RAF) [283], see also section 4.2.4.3.

In general, the frequency dependence of the excess heat capacity, as shown in Fig. 61, allows for the measurement of the base-line heat capacity at sufficiently high frequencies. Whether or not the high frequency limit can be reached for a particular polymer by the calorimeters available and whether or not the curve is shifted along the frequency axis with temperature has to be determined for each single experiment. An open question remains if a time-temperature-superposition is possible for the frequency dependent excess heat capacity. An understanding of the origin of the excess heat capacity as well as its frequency dependence will result in a better overall understanding of the molecular processes responsible for the attachment and detachment steps during polymer crystallization. Therefore, this may be one of the most important fields for the application of TMDSC in polymer science in future.

4.5. Other processes

Beside glass transition, melting, crystallization, mesophase transitions and chemical reactions in polymers, TMDSC can yield additional information leading to a better understanding and description of other processes. Although this is not a complete list, a few examples including relevant references are given.

- Phase separation in polymer blends [326]
- Interphase formation and compatibility in polymer blends [207,209,212-214,218,327-329]
- Denaturation of proteins [254]

Gelatinization and retrogradation of starch and other food science related problems [330-332]

5. CONCLUDING REMARKS

Polymers are often, from the view point of thermodynamics, in a non-equilibrium state. Typical examples including: the glass transition where the polymer goes from an super-cooled melt to a non-equilibrium glassy state; and the formation of a semicrystalline morphology where the amorphous phase is far from the thermodynamic equilibrium of the melt, but the often imperfect crystals, having dimensions in the order of nanometers, are far from the equilibrium state of the infinite perfect crystal. In such non-equilibrium states, enthalpy and consequently heat capacity become time dependent. To learn about these non-equilibrium states, one needs non-equilibrium thermodynamics as a theoretical basis on one hand and on the other hand, experimental techniques to probe the time dependencies. Heat capacity spectroscopy, including TMDSC, is one of the most valuable tools to do this. It allows the measurement of time and, via Fourier transformation the frequency dependence of the heat capacity in a wide range of experimental conditions. From the frequency dependence of heat capacity, new information can be gained for a better understanding of the molecular dynamics at the glass transition as well as during melting and crystallization.

Comparing simultaneous experiments at two different time scales, defined by modulation frequency and heating rate, respectively, allows under certain restrictions, the separation of reversing and non-reversing processes in complex polymer systems. Among the wide variety of experimental techniques to measure frequency and time dependent heat capacity, temperature modulated differential scanning calorimetry (TMDSC) is the most widely used. Sample preparation and the experiment itself can be easily performed as in standard DSC, the choice of proper experimental conditions and correct data treatment are often difficult. Therefore, correct calibration of the measured signals is an essential prerequisite for quantitative data analysis, which is always preferable to qualitative discussions.

Among all the possibilities in studying the dynamics of polymers, TMDSC is a valuable tool for precise heat capacity measurements in a wide temperature range for low thermal conducting materials where other calorimetric techniques are often very limited regarding accuracy.

Applying TMDSC to polymers will help in gaining insight into the complex processes in polymeric materials. Knowing the basics of the method and the principles behind it will help in avoiding faulty measurements and misinterpretation of the experimental results. This contribution is intended to support people to reach this goal.

ACKNOWLEDGMENTS

I acknowledge the valuable contributions of all my coworkers, especially M. Merzlyakov, A. Hensel, A. Wurm and S. Weyer, which made this paper possible. B. Wunderlich, G.W.H. Höhne, E. Donth, V.B.F. Mathot, G. Strobl and H. Marand gave me substantial support when entering the field of TMDSC and polymer crystallization.

REFERENCES

1. E. Gmelin, *Thermochim. Acta*, 305 (1997) 1.
2. H. Suga, *Thermochim. Acta*, 355 (2000) 69.
3. Y. H. Jeong, *Thermochim. Acta*, 377 (2001) 1.
4. I. K. Moon, D. H. Jung, K. B. Lee, Y. H. Jeong, *Appl. Phys. Lett.*, 76 (2000) 2451.
5. Y. H. Jeong, *Thermochim. Acta*, 305 (1997) 67.
6. N. O. Birge, P. K. Dixon, N. Menon, *Thermochim. Acta*, 305 (1997) 51.
7. Y.A. Kraftmakher, *Modulation Calorimetry* (Plenum Press, New York, 1984)
8. O. M. Corbino, *Physik. Zeitschr.*, Xii (1911) 292.
9. O. M. Corbino, *Physik. Zeitschr.*, Xi (1910) 413.
10. N. O. Birge, S. R. Nagel, *Phys. Rev. Lett.*, 54 (1985) 2674.
11. T. Christensen, *J. Phys.*, 46 (1985) C8.
12. Y. A. Kraftmakher, *Zurnal Prikladnoj Mehaniki I Tehniyeceskoj Fiziki*, 5 (1962) 176.
13. P. Sullivan, G. Seidel, *Ann. Acad. Sci. Fennicae A*, VI (1966) 58.
14. K. Schäfer, *Zeitschrift Für Physikalische Chemie*, 46 (1940) 212.
15. H. Gobrecht, K. Hamann, G. Willers, *J. Phys. E: Sci. Instrum.*, 4 (1971) 21.
16. S. Sauerbrunn, B. Crowe, M. Reading, *Am. Lab.*, 24 (1992) 44.
17. M. Reading, *Trends Polym. Sci.*, 8 (1993) 248.
18. M. Cassettari, F. Papucci, G. Salvetti, E. Tombari, S. Veronesi, G. P. Johari, *Rev. Sci. Instrum.*, 64 (1993) 1076.
19. B. Wunderlich et al., See On WWW URL: <http://web.utk.edu/~athas/databank/intro.html>.
20. B. Wunderlich, *J. Therm. Anal.*, 48 (1997) 207.
21. D. Price, see on WWW URL: <http://www.sump4.com/mmta/>.
22. C. Schick et al., See On WWW URL: <http://www.uni-rostock.de/fakult/manafak/physik/poly/downloads>.
23. M. F. J. Pijpers, V. B. F. Mathot, B. Goderis, R. Scherrenberg, E. van Der Vegte, *Macromolecules*, 35 (2002) 3601.
24. L. H. Allen, G. Ramanath, S. L. Lai, Z. Ma, S. Lee, D. D. J. Allman, K. P. Fuchs, *Appl. Phys. Lett.*, 64 (1994) 417.
25. H. Huth, M. Beiner, S. Weyer, M. Merzlyakov, C. Schick, E. Donth, *Thermochim. Acta*, 377 (2001) 113.
26. C. Glorieux, K.A. Nelson, G. Hinze, M.D. Fayer, *J. Chem. Phys.*, 116 (2002) 3384.
27. M. Chirtoc, E. H. Bentefour, C. Glorieux, J. Thoen, *Thermochim. Acta*, 377 (2001) 105.
28. H. Suga, *Thermochim. Acta*, 377 (2001) 35.
29. H. Staub, W. Perron, *Anal. Chem.*, 46 (1974) 128.

30. P. Claudy, J. C. Commercon, J. M. Letoffe, *Thermochim. Acta*, 128 (1988) 251.
31. B. Cassel, *Am. Lab.*, 7 (1975) 9.
32. B. Cassel, *Am. Lab.*, 32 (2000) 23.
33. M. E. Brown (ed.), *Handbook of Thermal Analysis and Calorimetry: Principles and Practice*, Elsevier Science, Amsterdam, 1998.
34. B. Wunderlich, *Thermal Analysis*, Academic Press, New York, 1990.
35. W. Hemminger, G.W.H. Höhne, *Calorimetry - Fundamentals and Practice*, VCH, Weinheim, 1984.
36. G. W. H. Höhne, W. Hemminger, H.-J. Flammersheim, *Differential Scanning Calorimetry - An Introduction For Practitioners*, Springer, Berlin, 1996.
37. V. B. F. Mathot, *Calorimetry and Thermal Analysis of Polymers*, Hanser Publishers, München, 1994.
38. E. Turi, *Thermal Characterization of Polymeric Materials*, Academic Press, 1997.
39. T. Hatakeyama, Z. Liu, *The Handbook of Thermal Analysis*, John Wiley & Sons, 1998.
40. M. E. Brown, *Introduction To Thermal Analysis*, Kluwer Academic Publishers, Dordrecht, 1998.
41. P. Haines, *Principles of Thermal Analysis and Calorimetry*, Royal Society of Chemistry, London, 2002.
42. M. E. Brown, *Introduction To Thermal Analysis: Techniques and Applications (Hot Topics In Thermal Analysis and Calorimetry)*, Kluwer Academic Publishers, Dordrecht, 2002.
43. J. Ford, G. Buckton, P. Timmins, *Pharmaceutical Thermal Analysis*, Taylor & Francis, London, 2001.
44. W. M. Groenewoud, *Characterisation of Polymers By Thermal Analysis*, Elsevier Science, Amsterdam, 2001.
45. R. L. Danley and P. A. Caulfield, DSC Baseline Improvements Obtained by a New Heat-flow Measurement Technique, *Proc. 29th NATAS Conference (2001)* 667.
46. R. L. Danley and P. A. Caulfield, DSC Resolution and Dynamic Response Improvements Obtained by a New Heat-flow Measurement Technique, *Proc. 29th NATAS Conference (2001)* 673.
47. M. Merzlyakov, C. Schick, *TCA*, 330 (1999) 65.
48. V. M. Glazov, A. S. Pashinkin, M. S. Mikhailova, *Scan. J. Metall.*, 30 (2001) 388.
49. Y. Jin and B. Wunderlich, *J. Therm. Anal.*, 36 (1990) 1519.
50. K. L. Ramakumar, M. K. Saxena and S. B. Deb, *J. Therm. Anal. Calorim.*, 66 (2001) 387.
51. B. Wunderlich, *J. Therm. Anal.*, 5 (1973) 117.
52. E. Calvet, H. Prat and H. A. Skinner, *Recent progress in microcalorimetry*, Pergamon Press, Oxford, London, New York, Paris, 1963.
53. T. M. V. R. de Barros, R. C. Santos, A. C. Fernandes, M. E. M. Da Piedade, *Thermochim. Acta*, 269/270 (1995) 51.
54. M. J. O'neill, *Anal. Chem.*, 36 (1964) 1238.
55. M. J. Richardson, Quantitative aspects of differential scanning calorimetry, *Thermochim. Acta*, 300 (1997) 15.
56. G. W. H. Höhne, E. Glöggler, *Thermochim. Acta*, 151 (1989) 295.
57. G. W. H. Höhne, *J. Therm. Anal.*, 37 (1991) 1987.
58. S. Rudtsch, *Thermochim. Acta*, 382 (2002) 17.
59. Seiko Instruments Inc., application notes.
60. M. Nishikawa, Y. Saruyama, *Thermochim. Acta*, 267 (1995) 75.

61. Y. Saruyama, *J. Therm. Anal.*, 49 (1997) 139.
62. P. Kamasa, A. Buzin, M. Pyda and B. Wunderlich, *Thermochim. Acta*, 381 (2002) 139.
63. I. Hatta, *Int. J. Pharm.*, 192 (1999) 33.
64. I. Hatta, A. A. Minakov, *Thermochim. Acta*, 330 (1999) 39.
65. I. Hatta, N. Katayama, *J. Therm. Anal., Cal.*, 54 (1998) 577.
66. I. Hatta, S. Muramatsu, *Jpn. J. Appl. Phys. Lett.*, 35 (1996) L 858.
67. I. Hatta, H. Ichikawa, M. Todoki, *Thermochim. Acta*, 267 (1995) 83.
68. A. Toda, T. Arita, C. Tomita, M. Hikosaka, *Polymer*, 41 (2000) 8941.
69. Y. Saruyama, *Thermochim. Acta*, 282/283 (1996) 157.
70. S. Weyer, A. Hensel, C. Schick, *Thermochim. Acta*, 305 (1997) 267.
71. Z. Jiang, C. T. Imrie and J. M. Hutchinson, *Thermochim. Acta*, 315 (1998) 1.
72. Z. Jiang, C. T. Imrie and J. M. Hutchinson, *Thermochim. Acta*, 336 (1999) 27.
73. G. W. H. Hoehne, M. Merzlyakov, C. Schick, *Thermochim. Acta*, in press.
74. M. Merzlyakov, G. W. H. Hoehne, C. Schick, *Thermochim. Acta*, in press.
75. P. S. Gill, S. R. Saurbrunn, M. Reading, *J. Thermal. Anal.*, 40 (1993) 931.
76. M. Reading, A. Luget, R. Wilson, *Thermochim. Acta*, 238 (1994) 295.
77. M. Reading, D. Elliot, V. L. Hill, *J. Thermal. Anal.*, 40 (1993) 949.
78. M. Reading, *J. Therm. Anal. Cal.*, 64 (2001) 7.
79. E. Verdonck, K. Schaap, L. C. Thomas, *Int. J. Pharm.*, 192 (1999) 3.
80. M. Cassettari, G. Salvetti, E. Tombari, S. Veronesi, G. P. Johari, *Physica A*, 201 (1993) 95.
81. B. Wunderlich, *Pure Appl. Chem.*, 67 (1995) 1019, see on WWW URL: <http://web.utk.edu/~athas/databank/intro.html>.
82. Mettler Toledo, Instrument manual for DSC 822.
83. J. Rouquerol, *Bull. Soc. Chim. Fr.*, (1964) 31.
84. F. Paulik and J. Paulik, *Anal. Chim. Acta*, 56 (1971) 328.
85. J. E. K. Schawe, *Thermochim. Acta*, 261 (1995) 183.
86. J. Korus, M. Beiner, K. Busse, S. Kahle, R. Unger and E. donth, *Thermochim. Acta*, 305 (1997) 99.
87. E. Flikkema, G. A. vanekenstein, G. Ten Brinke, *Macromolecules*, 31 (1998) 892.
88. E. Donth, *Glass Transition*, Springer, Berlin, 2001.
89. A. Boller, Y. Jin, B. Wunderlich, *J. Therm. Anal.*, 42 (1994) 307.
90. Z. Jiang, C. T. Imrie and J. M. Hutchinson, *Thermochim. Acta*, 387 (2002) 75.
91. Y. H. Jeong, I. K. Moon, *Phys. Rev. B-Condens. Matter*, 52 (1995) 6381.
92. C. Schick, M. Merzlyakov, A. Hensel, *J. Chem. Phys.*, 111 (1999) 2695.
93. M. Merzlyakov, C. Schick, *Thermochim. Acta*, 330 (1999) 55.
94. M. Merzlyakov, C. Schick, *J. Thermal. Anal. Cal.*, 61 (2000) 649.
95. C. R. Snyder, F. I. Mopsik, *J. Chem. Phys.*, 110 (1999) 1106.
96. S. Weyer, M. Merzlyakov, C. Schick, *Thermochim. Acta*, 377 (2001) 85.
97. S. Weyer, M. Merzlyakov, A. Wurm, C. Schick, *Coll. Polym. Sci.*, Submitted.
98. J. Wang, G. P. Johari, *J. Non-Cryst. Solids*, 281 (2001) 91.
99. G. W. H. et al. Hoehne, *Thermochim. Acta*, accepted.
100. J. E. K. Schawe, *Thermochim. Acta*, 271 (1996) 127.
101. Z. Jiang, C. T. Imrie, J. M. Hutchinson, *J. Therm. Anal., Cal.*, 64 (2001) 85.
102. S. L. Simon, *Thermochim. Acta*, 374 (2001) 55.
103. S. Guinot, F. Leveiller, *Int. J. Pharm.*, 192 (1999) 63.
104. A. Marini, V. Berbenni, G. Bruni, A. Maggioni, M. Villa, *J. Therm. Anal.*, 56 (1999) 699.

105. J. N. Cao, Y. Long, R. A. Shanks, *J. Therm. Anal.*, 50 (1997) 365.
106. I. Hatta, *Jpn. Appl. Phys. Lett.*, 33 (1994) L 686.
107. S. A. Knopp, S. L. Nail, *J. Therm. Anal. Cal.*, 60 (2000) 319.
108. F. Cser, F. Rasoul, E. Kosior, *J. Therm. Anal.*, 50 (1997) 727.
109. A. Hensel, J. Dobbertin, J. E. K. Schawe, A. Boller, C. Schick, *J. Therm. Anal.*, 46 (1996) 935.
110. A. Schick, C. Hensel, *J. Non-Cryst. Solids*, 235-237 (1998) 510.
111. J. E. K. Schawe, *J. Therm. Anal.*, 47 (1996) 475.
112. J. E. K. Schawe, E. Bergmann, *Thermochim. Acta*, 305 (1997) 179.
113. J. E. K. Schawe, G. R. Strobl, *Polymer*, 39 (1998) 3745.
114. A. Toda, M. Hikosaka, K. Yamada, *Polymer*, 43 (2002) 1667.
115. A. Toda, Y. Takahashi, T. Arita, M. Hikosaka, T. Furukawa, *J. Chem. Phys.*, 114 (2001) 6896.
116. A. Toda, Y. B. Saruyama, *Polymer*, 42 (2001) 4727.
117. A. Toda, C. Tomita, T. Arita, M. Hikosaka, *J. Therm. Anal. Cal.*, 64 (2001) 775.
118. A. Toda, T. Arita, M. Hikosaka, *J. Mater. Sci.*, 35 (2000) 5085.
119. A. Toda, C. Tomita, M. Hikosaka, Y. Saruyama, *Thermochim. Acta*, 324 (1998) 95.
120. A. Toda, C. Tomita, M. Hikosaka, Y. Saruyama, *Polymer*, 39 (1998) 5093.
121. Y. Saruyama, *Thermochim. Acta*, 377 (2001) 151.
122. G. van Assche, B. van Mele, Y. Saruyama, *Thermochim. Acta*, 377 (2001) 125.
123. Y. Saruyama, *TCA*, 330 (1999) 101.
124. Y. Saruyama, *Thermochim. Acta*, 305 (1997) 171.
125. A. Boller, C. Schick, B. Wunderlich, *Thermochim. Acta*, 266 (1995) 97.
126. S. Weyer, A. Hensel, J. Korus, E. Donth, C. Schick, *Thermochim. Acta*, 305 (1997) 251.
127. M. Merzlyakov, A. Wurm, M. Zorzut, C. Schick, *J. Macromol. Sci.-Phys.*, B38 (1999) 1045.
128. G. Salvetti, C. Ferrari, E. Tombari, *Thermochim. Acta*, 316 (1998) 47.
129. C. Ferrari, G. Salvetti, E. Tognoni, E. Tombari, *J. Therm. Anal.*, 47 (1996) 75.
130. R. androsch, B. Wunderlich, *Thermochim. Acta*, 333 (1999) 27.
131. B. Wunderlich, R. androsch, M. Pyda, Y. K. Kwon, *Thermochim. Acta*, 348 (2000) 181.
132. M. Merzlyakov, C. Schick, *Thermochim. Acta*, 377 (2001) 193.
133. M. Merzlyakov, C. Schick, *Thermochim. Acta*, 380 (2001) 5.
134. J. E. K. Schawe, C. Schick, G. W. H. Hohne, *Thermochim. Acta*, 229 (1993) 37.
135. J. E. K. Schawe, C. Schick, G. W. H. Hohne, *Thermochim. Acta*, 244 (1994) 49.
136. N. Agarwal, R. J. Farris, *Thermochim. Acta*, 334 (1999) 39.
137. N. Agarwal, R. J. Farris, *Proc. 27th Natas Conference* (1999) 15.
138. S. M. Sarge, W. Hemminger, E. Gmelin, G. W. H. Höhne, H. K. Cammenga, W. Eysel, *J. Therm. Anal.*, 49 (1997) 1125.
139. S. Montserrat, *J. Therm. Anal. Cal.*, 59 (2000) 289.
140. J. M. Hutchinson, A. B. Tong, Z. Jiang, *Thermochim. Acta*, 335 (1999) 27.
141. Z. Jiang, C. T. Imrie, J. M. Hutchinson, *Thermochim. Acta*, 336 (1999) 27.
142. J. E. K. Schawe, *Thermochim. Acta*, 361 (2000) 97.
143. U. Jorimann, G. Widmann, R. Riesen, *J. Therm. Anal.*, 56 (1999) 639.
144. J. E. K. Schawe, E. Bergmann, W. Winter, *J. Therm. Anal.*, 54 (1998) 565.
145. T. Ozawa, K. Kanari, *Thermochim. Acta*, 338 (1999) 7.
146. T. Ozawa, K. Kanari, *J. Therm. Anal.*, 56 (1999) 691.
147. T. Ozawa, K. Kanari, *J. Therm. Anal. Cal.*, In Press.

148. T. Ozawa, K. Kanari, *J. Therm. Anal.*, 54 (1998) 521.
149. A. Toda, T. Arita, C. Tomita, M. Hikosaka, *Polym. J.*, 31 (1999) 790.
150. G. W. H. Hohne, N. B. Shenogina, *Thermochim. Acta*, 310 (1998) 47.
151. F. U. Buehler, J. C. Seferis, *J. Therm. Anal. Cal.*, 63 (2001) 21.
152. F. U. Buehler, J. C. Seferis, *Thermochim. Acta*, 348 (2000) 161.
153. F. U. Buehler, C. J. Martin, J. C. Seferis, *J. Therm. Anal.*, 54 (1998) 501 .
154. F. U. Buehler, J. C. Seferis, *Thermochim. Acta*, 334 (1999) 49.
155. B. Schenker, F. Stager, *Thermochim. Acta*, 305 (1997) 219.
156. M. Reading, K. Jones, R. Wilson, *Netsu Sokutei*, 22 (1995) 83.
157. A. A. Lacey, C. Nikolopoulos, M. Reading, *J. Therm. Anal.*, 50 (1997) 279.
158. S. L. Simon, G. B. Mckenna, *Thermochim. Acta*, 307 (1997) 1.
159. K. Ishikiriyama, B. Wunderlich, *J. Therm. Anal.*, 50 (1997) 337.
160. I. Moon, R. Androsch and B. Wunderlich, *Thermochim. Acta*, 357-358 (2000) 285.
161. A. Boller, I. Okazaki, K. Ishikiriyama, G. Zhang and B. Wunderlich, *J. Therm. Anal.*, 49 (1997) 1081.
162. B. Wunderlich, A. Boller, I. Okazaki and K. Ishikiriyama, *Thermochim. Acta*, 305 (1997) 125.
163. B. Wunderlich, Y. M. Jin and A. Boller, *Thermochim. Acta*, 238 (1994) 277.
164. S. X. Xu, Y. Li and Y. P. Feng, *Thermochim. Acta*, 360 (2000) 157.
165. S. X. Xu, Y. Li and Y. P. Feng, *Thermochim. Acta*, 359 (2000) 43.
166. S. X. Xu, Y. Li and Y. P. Feng, *Thermochim. Acta*, 343 (2000) 81.
167. S. X. Xu, Y. Li and Y. P. Feng, *Thermochim. Acta*, 360 (2000) 131.
168. M. Merzlyakov, C. Schick, *Thermochim. Acta*, 377 (2001) 183.
169. F. W. Wilburn, J.R. Hesford, J.R. Flower, *Anal. Chem.* 40 (1968) 777.
170. G. W. H. Höhne, J. E. K. Schawe, *Thermochim. Acta*, 229 (1993) 27.
171. J. Schawe, C. Schick, *Thermochim. Acta*, 187 (1991) 335.
172. J. E. K. Schawe, G. W. H. Hohne, C. Schick, *Thermochim. Acta*, 244 (1994) 33.
173. H. J. Flammersheim, N. Eckardt, W. Kunze, *Thermochim. Acta*, 187 (1991) 269.
174. A. T. W. Kempen, F. Sommer, E. J. Mittemeijer, *Thermochim. Acta*, 383 (2002) 21.
175. A. Hensel, C. Schick, *Thermochim. Acta*, 305 (1997) 229.
176. C. Schick, U. Jonsson, T. Vassilev, A. Minakov, J. Schawe, R. Scherrenberg, D. Lőrinczy, *Thermochim. Acta*, 347 (2000) 53.
177. R. Androsch, I. Moon, S. Kreitmeyer, B. Wunderlich, *Thermochim. Acta*, 357-358 (2000) 267.
178. D. Bertolini, M. Cassettari, G. Salvetti, E. Tombari, S. Veronesi, *Rev. Sci. Instrum.*, 61 (1990) 2416.
179. S. M. Marcus, R. L. Blaine, *Thermochim. Acta*, 243 (1994) 231.
180. S. M. Marcus, R. L. Blaine, *Therm. Conduct.*, 22 (1994) 826.
181. S. M. Marcus and M. Reading, United States Patent No. 5 335 993 (1994).
182. S. L. Simon, G. B. Mckenna, *J. Reinf. Plast. Compos.*, 18 (1999) 559.
183. R. L. Blaine, S. M. Marcus, *J. Therm. Anal.*, 54 (1998) 467.
184. S. M. Sarge, W. Poßnecker, *Thermochim. Acta*, 329 (1999) 17.
185. C. Y. Ho, P. D. Desai, K. T. Wu, T. N. Havill, T. Y. Lee, NBS Publication Gcr-77-83 (1977).
186. D. R. Salmon, National Physical Laboratory, Teddington, Middlesex, TW11 OLW, England (1993).
187. The value from Hot Disk measurements was kindly provided by Mathis Instruments, Canada.
188. B. Wunderlich, *J. Therm. Anal.*, 30 (1985) 1217.

189. M. J. Richardson, *Thermochim. Acta*, 300 (1997) 15.
190. M. J. Richardson, *The Application of Differential Scanning Calorimetry To The Measurement of Specific Heat*, Plenum Press, New York, 1992.
191. P. Kamasa, M. Merzlyakov, M. Pyda, J. Pak, C. Schick, B. Wunderlich, *Thermochim. Acta*, in press (2002).
192. M. W. Chase Jr., *NIST-JANAF Thermochemical Tables*, 4th Ed., *J. Phys. Chem. Ref. Data*, Monograph 9, 1998.
193. R. J. Seyler, ASTM, Philadelphia, PA, 1994.
194. A. Q. Tool, *J. Am. Ceram. Soc.*, 29 (1946) 240.
195. C. M. Roland and K. L. Ngai, *J. Rheol.*, 36 (1992) 1691.
196. Ts. Vassilev, Ts. Velinov, I. Avramov and S. Surnev, *Appl. Phys. A*, 60 (1995) 1.
197. X. Hu, Y. Li, S. C. Ng and Y. P. Feng, *Metastable Mech. Alloy. Nanocryst. Mater.*, 10 (2001) 123.
198. X. Hu, Y. Li, S. C. Ng and Y. P. Feng, *Phys. Rev. B*, 62 (2000) 3169.
199. E. Donth, J. Korus, E. Hempel, M. Beiner, *Thermochim. Acta*, 305 (1997) 239.
200. I. K. Moon, Y. H. Jeong, T. Furukawa, *Thermochim. Acta*, 377 (2001) 97.
201. A. Yatsu, S. Kojima, T. Suzuki, *Japanese Journal of Applied Physics Part 1-Regular Papers Short Notes & Review Papers* 33 (1994) 3230.
202. T. Vassiliev, Unpublished Data.
203. A. A. Minakov, Unpublished Data.
204. A. Schonhals, H. Goering, K. W. Brzezinka, C. Schick, *J. Phys. IV France*, 10 (2000) 271.
205. E. Hempel, G. Hempel, A. Hensel, C. Schick, E. Donth, *J. Phys. Chem. B*, 104 (2000) 2460.
206. E. Donth, E. Hempel, C. Schick, *J. Phys. Condens. Matter*, 12 (2000) L281.
207. G. G. Silva, J. C. Machado, M. Song, D. J. Hourston, *J. Appl. Polym. Sci.*, 77 (2000) 2034.
208. D. J. Hourston, M. Song, F. U. Schafer, H. M. Pollock, A. Hammiche, *Polymer*, 40 (1999) 4769.
209. M. Song, D. J. Hourston, F. U. Schafer, H. M. Pollock, A. Hammiche, *Thermochim. Acta*, 315 (1998) 25.
210. M. Song, D. J. Hourston, H. M. Pollock, F. U. Schafer, A. Hammiche, *Thermochim. Acta*, 305 (1997) 335.
211. D. J. Hourston, M. Song, H. M. Pollock, A. Hammiche, *J. Therm. Anal.*, 49 (1997) 209.
212. M. Song, A. Hammiche, H. M. Pollock, D. J. Hourston, M. Reading, *Polymer*, 37 (1996) 5661.
213. D. J. Hourston, M. Song, A. Hammiche, H. M. Pollock, M. Reading, *Polymer*, 38 (1997) 1.
214. M. Song, A. Hammiche, H. M. Pollock, D. J. Hourston, M. Reading, *Polymer*, 36 (1995) 3313.
215. M. Reading, R. Luyt, *J. Therm. Anal.*, 54 (1998) 535.
216. M. Reading, *J. Therm. Anal.*, 54 (1998) 411.
217. K. J. Jones, I. Kinshott, M. Reading, A. A. Lacey, C. Nikolopoulos, H. M. Pollock, *Thermochim. Acta*, 305 (1997) 187.
218. D. J. Hourston, M. Song, A. Hammiche, H. M. Pollock, M. Reading, *Polymer*, 37 (1996) 243.
219. A. M. Lammert, R. M. Lammert and S. J. Schmidt, *J. Therm. Anal.*, 55 (1999) 949.
220. Y. Wang, R. Song, D. Y. Shen, *J. Macromol. Sci.-Phys.*, B37 (1998) 709.

221. G. O. R. A. van Ekenstein, G. Ten Brinke, T. S. Ellis, *Polym. Mater. Sci. Eng.*, 76 (1997) 219.
222. M. Bonnet, M. Buhk, G. Trogner, K. D. Rogausch, J. Petermann, *Acta Polym.*, 49 (1998) 177.
223. K. Six, G. Verreck, J. Peeters, P. Augustijns, R. Kinget and G. van den Mooter, *Int. J. Pharm.*, 213 (2001) 163.
224. S. Montserrat, *J. Polym. Sci. Polym. Phys.*, 38 (2000) 2272.
225. N. A. Bailey, J. N. Hay, D. M. Price, *Thermochim. Acta*, 367-368 (2001) 425.
226. J. M. Hutchinson, *Thermochim. Acta*, 324 (1998) 165.
227. M. Song, *J. Therm. Anal. Calorim.*, 63 (2001) 699.
228. D. Q. M. Craig, M. Barsnes, P. G. Royall and V. L. Kett, *Pharm. Res.*, 17 (2000) 696.
229. J. M. Hutchinson, S. Montserrat, *Thermochim. Acta*, 286 (1996) 263.
230. J. M. Hutchinson, S. Montserrat, *Thermochim. Acta*, 305 (1997) 257.
231. J. E. K. Schawe, *Colloid Polym. Sci.*, 276 (1998) 565 .
232. J. E. K. Schawe, *J. Polym. Sci. Polym. Phys.*, 36 (1998) 2165.
233. J. E. K. Schawe, S. Theobald, *J. Non-Cryst. Solids*, 235 (1998) 496 .
234. S. L. Simon, G. B. Mckenna, *J. Chem. Phys.*, 107 (1997) 8678.
235. S. L. Simon, G. B. Mckenna, *Thermochim. Acta*, 348 (2000) 77.
236. I. Okazaki, B. Wunderlich, *J. Polym. Sci. Polym. Phys.*, 34 (1996) 2941.
237. B. Wunderlich, I. Okazaki, *J. Therm. Anal.*, 49 (1997) 57.
238. I. K. Moon, Y. H. Jeong, *Pure Appl. Chem.*, 69 (1997) 2321.
239. I. K. Moon, Y. H. Jeong, *Thermochim. Acta*, 377 (2001) 51.
240. K. Kanari, T. Ozawa, *Thermochim. Acta*, 305 (1997) 201.
241. T. Ozawa, K. Kanari, *Thermochim. Acta*, 253 (1995) 183.
242. K. Kanari, T. Ozawa, *J. Therm. Anal.*, 49 (1997) 979.
243. T. Ozawa, *Pure Appl. Chem.*, 69 (1997) 2315.
244. T. Ozawa, K. Kanari, *Netsu Sokutei*, 22 (1995) 98.
245. G. P. Johari, C. Ferrari, E. Tombari, G. Salvetti, *J. Chem. Phys.*, 110 (1999) 11592.
246. H. Hoff, *Can. J. Phys.*, 68 (1990) 198.
247. I. Hatta, *Thermochim. Acta*, 272 (1996) 49.
248. J. E. K. Schawe, I. Alig, *Colloid Polym. Sci.*, 279 (2001) 1169.
249. J. E. K. Schawe, *Thermochim. Acta*, submitted.
250. J. E. K. Schawe, *J. Therm. Anal. Cal.*, 64 (2001) 599.
251. M. Schubnell, J. E. K. Schawe, *Int. J. Pharm.*, 217 (2001) 173.
252. I. Alig, W. Jenninger, J. E. K. Schawe, *Thermochim. Acta*, 330 (1999) 167.
253. W. Jenninger, J. E. K. Schawe, I. Alig, *Polymer*, 41 (2000) 1577 .
254. G. Salvetti, E. Tombari, L. Mikheeva, *J. Phys. Chem*, in press.
255. C. Ferrari, G. Salvetti, E. Tombari and G. P. Johari, *Soft Matt. Phys.*, 54 (1996) R0158.
256. G. van Assche, A. van Hemelrijck, H. Rahier, B. van Mele, *Thermochim. Acta*, 305 (1997) 317.
257. G. van Assche, A. van Hemelrijck, B. van Mele, *J. Therm. Anal.*, 49 (1997) 443.
258. A. van Hemelrijck, B. van Mele, *J. Therm. Anal.*, 49 (1997) 437.
259. A. Wurm, C. Schick, *Colloid Polym. Sci.*, submitted.
260. S. R. Aubuchon, L. C. Thomas, *TA Instruments Applications Note* (1999).
261. A. Toda, T. Arita, C. Tomita, M. Hikosaka, *Thermochim. Acta*, 330 (1999) 75.
262. A. Toda, T. Oda, M. Hikosaka, Y. Saruyama, *Thermochim. Acta*, 293 (1997) 47.
263. A. Toda, C. Tomita, M. Hikosaka, Y. Saruyama, *Polymer*, 39 (1998) 1439.

264. A. Toda, C. Tomita, H. Masamichi, Y. Saruyama, *Polymer*, 38 (1997) 2849.
265. A. Toda, T. Oda, M. Hikosaka, Y. Saruyama, *Polymer*, 38 (1997) 231.
266. J. E. K. Schawe, W. Winter, *Thermochim. Acta*, 330 (1999) 85.
267. J. E. K. Schawe, *Thermochim. Acta*, 305 (1997) 111.
268. J. E. K. Schawe, G. W. H. Hohne, *J. Therm. Anal.*, 46 (1996) 893.
269. G. W. H. Hohne, *Thermochim. Acta*, 330 (1999) 45.
270. G. W. H. Hohne, *Thermochim. Acta*, 330 (1999) 93.
271. A. A. Lacey, C. Nikolopoulos, *Ima J. Appl. Math.*, 66 (2001) 449.
272. B. Goderis, H. Reynaers, R. Scherrenberg, V. B. F. Mathot, M. H. J. Koch, *Macromolecules*, 34 (2001) 1779.
273. T. Albrecht, S. Armbruster, S. Keller, G. Strobl, *Macromolecules*, 34 (2001) 8456.
274. R. Scherrenberg, V. Mathot, P. Steeman, *J. Therm. Anal.*, 54 (1998) 477.
275. R. Scherrenberg, V. Mathot, A. van Hemelrijck, *Thermochim. Acta*, 330 (1999) 3.
276. B. B. Sauer, W. G. Kampert, E. N. Blanchard, S. A. Threefoot, B. S. Hsiao, *Polymer*, 41 (2000) 1099.
277. W. B. Hu, T. Albrecht, G. Strobl, *Macromolecules*, 32 (1999) 7548.
278. K. Ishikiriyama, B. Wunderlich, *Macromolecules*, 30 (1997) 4126.
279. L. C. Thomas, *TA Instrument Applications Note*, (1999).
280. J. Cao, *Thermochim. Acta*, 329 (1999) 89.
281. K. A. Q. Oreilly, B. Cantor, *Proc. Roy. Soc. London A-Math. Phys. Sci.*, 452 (1996) 2141.
282. G. Pompe, U. Schulze, J. Hu, J. Piontek, G. W. H. Hohne, *Thermochim. Acta*, 337 (1999) 179.
283. C. Schick, A. Wurm, A. Mohamed, *Colloid Polym. Sci.*, 279 (2001) 800.
284. I. Okazaki, B. Wunderlich, *Macromolecules*, 30 (1997) 1758.
285. Y. Li, S. C. Ng, Z. P. Lu, Y. P. Feng, K. Lu, *Phil. Mag. Lett.*, 78 (1998) 213.
286. M. Alsleben, C. Schick, *Thermochim. Acta*, 238 (1994) 203.
287. C. Schick, A. Wurm, M. Merzlyakov, A. Minakov, H. Marand, *Macromol. Symp.*, 165 (2001) 83.
288. C. Schick, A. Wurm, M. Merzlyakov, *ASTM STP 1402*, ASTM, Philadelphia, 2001.
289. C. Schick, A. Wurm, Natas 2000 Mohamed, *Thermochim. Acta*, Accepted.
290. C. Schick, A. Wurm, M. Merzlyakov, A. Minakov, H. Marand, *J. Therm. Anal. Cal.*, 64 (2001) 549.
291. E. Tombari, C. Ferrari, G. Salvetti, G. P. Johari, *J. Phys.-Condens. Matter*, 11 (1999) A317.
292. M. Cassettari, G. Salvetti, E. Tombari, S. Veronesi, P.G. Johari, *J. Non-Cryst. Solids*, 172 (1994) 554.
293. G. van Assche, E. Verdonck, B. van Mele, *J. Therm. Anal. Cal.*, 59 (2000) 305.
294. G. van Assche, E. Verdonck, B. van Mele, *Polymer*, 42 (2001) 2959.
295. B. van Mele, G. van Assche, A. van Hemelrijck, *J. Reinf. Plast. Compos.*, 18 (1999) 885.
296. G. van Assche, A. van Hemelrijck, H. Rahier, B. van Mele, *Thermochim. Acta*, 268 (1995) 121.
297. J. E. K. Schawe, I. Alig, *Colloid Polym. Sci.*, 279 (2001) 1169.
298. I. Alig, W. Jenniger, J. E. K. Schawe, *J. Non-Cryst. Solids*, 235-237 (1998) 504.
299. S. Montserrat, I. Cima, *TCA*, 330 (1999) 189.
300. B. Wunderlich, *Prog. Polym. Sci.*, submitted.
301. R. Androsch, B. Wunderlich, *Thermochim. Acta*, 364 (2000) 181.
302. A. Boller, M. Ribeiro, B. Wunderlich, *25th Natas Conference (1997)* 706.

303. I. Hatta, S. Nakayama, *Thermochim. Acta*, 318 (1998) 21.
304. W. G. Kampert, B. B. Sauer, *Polymer*, 42 (2001) 8703.
305. Y. Wang, J. Lu, D. Y. Shen, *Polym. J.*, 32 (2000) 560.
306. R. Androsch, B. Wunderlich, *Macromolecules*, 32 (1999) 7238.
307. L. Judovits, J. D. Menczel, A. G. Leray, *J. Therm. Anal.*, 54 (1998) 605.
308. M. Pyda, B. Wunderlich, *J. Polym. Sci. Polym. Phys.*, 38 (2000) 622.
309. J. D. Menczel, L. H. Judovits, *PMSE*, 78 (1998) 210.
310. A. G. Leray, L. Judovits, 25th Natas Conference (1997) 72.
311. S. X. Lu, P. Cebe, M. Capel, *Macromolecules*, 30 (1997) 6243.
312. F. Cser, F. Rasoul and E. Kosior, *J. Therm. Anal.*, 52 (1998) 293.
313. B. Borde, H. Bizot, G. Vigier and A. Buleon, *Carbonhyd. Polym.*, 48 (2002) 83.
314. V. B. F. Mathot, M. F. J. Pijpers, *J. Therm. Anal.*, 28 (1983) 349.
315. V. B. F. Mathot, M. F. J. Pijpers, *Thermochim. Acta*, 151 (1989) 241.
316. C. Schick, M. Merzlyakov, A. Minakov, A. Wurm, *J. Therm. Anal. Cal.*, 59 (2000) 279.
317. R. Androsch, B. Wunderlich, *Macromolecules*, 34 (2001) 5950.
318. C. Schick, A. Wurm, A. Natas 2001 Mohammed, *Thermochim. Acta*, submitted.
319. Y. Men, G. Strobl, *Polymer*, 43 (2002) 2761.
320. A. Wurm, Ph. D. Thesis, Rostock, 2001.
321. A. Mohammed, Ph. D. Thesis, Mansoura, 2002.
322. S. vanden Eynde, V. B. F. Mathot, G. W. H. Hohne, J. W. K. Schawe, H. Reynaers, *Polymer*, 41 (2000) 3411.
323. T. Albrecht, S. Armbruster, S. Keller, G. Strobl, *Eur. Phys. J.*, E6 (2001) 237.
324. T. Albrecht, S. Armbruster, B. Stuhn, K. Vogel, G. Strobl, *Thermochim. Acta*, 377 (2001) 159.
325. A. A. Minakov, Y. V. Bugoslavsky, C. Schick, *Thermochim. Acta*, 317 (1998) 117.
326. G. Dreezen, G. Groeninckx, S. Swier, B. van Mele, *Polymer*, 42 (2001) 1449.
327. M. Song, D. J. Hourston, H. M. Pollock, A. Hammiche, *Polymer*, 40 (1999) 4763.
328. M. Song, H. M. Pollock, A. Hammiche, D. J. Hourston, M. Reading, *Polymer*, 38 (1997) 503.
329. D. J. Hourston, F. U. Schafer, J. S. Bates, *J. Appl. Polym. Sci.*, 60 (1996) 2409.
330. P. de Meuter, J. Amelrijckx, H. Rahier, B. van Mele, *J. Polym. Sci.*, 37 (1999) 2881.
331. P. de Meuter, H. Rahier, B. van Mele, *Int. J. Pharm.*, 192 (1999) 77.
332. V. M. F. Lai, C. Y. Lii, *Cereal Chem.*, 76 (1999) 519.

INDEX

- 1,2-poly(butadiene) 125
1,4-poly(butadiene) 125
2-hydroxy-6-naphthoic acid (HNA) 471, 472, 473, 703
 α -transition 278, 434
 β -transition 280
A
absolute extent of reaction 312
accelerated rate calorimetry (ARC) 524
accuracy 4, 27, 82–85, 91, 209, 233, 310, 450, 538, 556, 653, 655, 668, 682, 684, 687, 705, 706, 715, 719–722, 737, 767, 768, 770, 776, 794, 801
acrylate copolymer (ACM) 528, 634, 640
acrylonitrile rubber 537, 542
activation energy 38, 64, 73, 116, 119, 121, 127, 129, 149, 150, 152, 159, 163, 176, 182, 289, 331, 332, 334, 336, 340, 372, 374, 378, 385, 393, 394, 398, 434, 435, 448, 452, 454, 458, 469, 476, 478, 543, 568, 569, 570, 573, 596, 599, 600, 609, 615, 625, 630, 637, 656, 661, 663, 664, 673, 676, 679, 691, 707
activation step 181
activity 129, 130
activity coefficient 129, 130
additive 27, 33, 115, 159, 207, 286, 309, 435, 452, 519, 522, 523, 527, 528, 539, 542, 544, 545, 552, 553, 555, 556, 558, 563, 564, 588, 608, 627, 630, 632, 746
adhesive 295, 301, 303, 304, 305, 308, 314
adiabatic calorimeter 1, 2, 717, 769
adiabatic condition 2, 524, 715, 717
adsorption 172
aliphatic amine 304
alloy 292, 463, 465, 720, 721, 807
alternating copolymer 159, 273, 632, 634–637
American Society for Testing and Materials (see also ASTM) 107, 352
amorphous 16–18, 23, 32, 36, 37, 45, 99, 105, 115, 117, 123, 127, 149, 150, 155, 159, 161, 167, 175, 187, 189–191, 200, 203, 205–207, 212, 213, 217, 224, 245, 253, 274, 276, 279–281, 286, 288, 289, 326, 338, 352, 355, 364–367, 380, 381, 383, 384, 386, 388–390, 393–398, 400, 402, 403, 405, 417–421, 423–428, 430, 432–434, 437, 438, 442, 443, 446, 447, 450, 451, 456–458, 460, 461, 468, 469, 473–475, 478, 479, 489, 521, 529, 533, 589, 611, 614, 653, 657, 668, 669–672, 675, 687–689, 692–694, 697, 698, 703, 706, 708, 714, 725–727, 781, 782, 784, 794, 795, 800, 801
amplitude of relaxation 113
anisotropy 23, 247, 362, 366, 369, 374, 375, 385, 396, 397, 409, 418, 426, 433, 438, 467
annealing 61, 66, 86, 87, 88, 89, 92, 93, 179, 182, 184, 185, 187, 192, 204, 210, 228, 240, 270, 327, 328, 329, 330, 350, 356, 358, 359, 386, 387, 388, 389, 392, 393, 394, 402, 403, 441, 442, 443, 446, 448, 452, 453, 454, 456, 457, 458, 459, 460, 463, 469, 470, 472, 473, 480, 534, 536, 674, 775, 776
apparent activation energy 119, 127, 378, 458, 476, 656, 661, 664, 707
aromatic amine 304
aromatic heterocyclic fiber 479
Arrhenius 38, 73, 75, 76, 78, 116, 119, 149, 150, 163, 331, 435, 569, 575, 590, 592, 604, 615, 660, 661, 662, 665, 666, 676, 677, 680, 681, 682, 683, 684, 685, 688, 693, 707, 773, 777
Arrhenius equation 119, 163, 331, 615, 661, 665, 676
Arrhenius parameter 590, 604, 666
ASTM 84, 104, 313, 765
autocatalytic mechanism 332
B
baseline 41, 45, 89–91, 93, 204, 205, 209, 210, 231, 310, 311, 323, 329, 330, 335, 343, 345, 530, 576, 719, 731, 776
benzoic acid 459, 470, 701, 702
benzoxazine resin 307, 308
biaxial orientation 358, 404
birefringence 291, 371, 384, 394, 423, 425, 426, 454, 455, 456, 478
bismaleimide 305, 306, 495, 516
block copolymer 171, 273, 274, 275, 282, 530, 535, 632, 637
body implant 295

- Boltzmann constant 118, 163
 bond dissociation energies 590, 596, 603, 634
 bond rotation 119, 133
 branches 126, 200, 296, 597, 620, 621
 brittleness 59, 102
 bromo-butyl 527
 butyl rubber 521, 527, 555, 574
C
 calcium carbonate 546
 calibration 3, 4, 5, 36, 41, 88, 90, 91, 93, 204, 324, 333, 549, 657, 718, 731, 732, 737, 744, 746, 748, 749, 750, 751, 752, 753, 754, 755, 756, 757, 758, 759, 760, 762, 770, 787, 789, 792, 801
 calorimeter 1, 2, 59, 204, 342, 347, 349, 427, 524, 535, 536, 714, 715, 716, 717, 718, 719, 720, 732, 749, 769, 796, 799, 800
 calorimetry 1, 2, 10, 13, 14, 34, 36, 45, 59, 66, 85, 86, 92, 94, 178, 224, 249, 251, 295, 308, 330, 342, 343, 345, 348–350, 360, 431, 456, 496, 519, 523–525, 529, 535, 536, 539, 547, 556, 561, 566, 567, 576, 578, 580, 587, 655, 703, 713, 716, 717, 722, 732, 741, 801
 carbon fiber 452, 453, 480–482, 492, 495, 496, 502, 505
 cationic photo-polymerization 342
 cationic polymerization 304, 342
 ceiling temperature 590, 591, 592, 593, 615, 616, 623, 625
 cellulose 411, 412, 420, 423, 440, 613, 614, 626
 cement 555
 ceramic 466, 722
 chain microstructure 198, 200
 chain-folding 175, 176
 chemical composition 6, 26, 27, 323, 519, 522, 527, 536, 538
 chemical equilibrium 33
 chemical reaction 33, 40, 86, 88, 213, 296, 299, 309, 310, 321, 330, 337, 348, 350, 415, 428, 431, 451, 452, 464, 499, 524, 564, 589, 609, 613, 615, 644, 784, 800
 chemical resistance 305, 443, 463, 473, 476
 chiral liquid crystalline polyester 257
 chloro-butyl 527
 chlorinated polyethylene 537, 573
 chloroprene 526, 534, 537, 542, 573
 chlorosulfonated 527
 clay 522, 551
 closed system 602
 coating 295, 303, 305–307, 339, 344, 355, 357, 359, 435, 492, 527, 615, 643, 658, 722
 combined technique 525
 combustion 459, 545, 548, 549, 550, 571, 608, 609, 613, 622, 626
 comonomer 197–200, 202, 203, 208, 213, 218, 219, 221, 224, 225, 231, 233, 239, 240, 251, 252, 448–450, 452–454, 460, 625, 633, 634, 636, 637
 compensation 664–666, 676, 717, 720–722, 730, 745, 770
 complex compliance 114
 complex dielectric permittivity 147
 complex heat capacity 14, 15, 40, 45, 714, 716, 717, 723, 725, 730–732, 737, 740, 741, 743, 744, 749–753, 759, 770, 771, 773, 774, 775, 779, 784, 786, 787, 792, 793, 798
 complex reaction 641
 composites 99, 113, 295, 302–304, 306, 466, 474, 476, 480, 482, 491–496, 499, 503–508, 516, 550, 551, 657, 673
 composition 1, 6, 26, 27, 33, 34, 76, 81, 160, 161, 171, 192, 198, 276, 280–282, 295, 314, 323, 470–472, 519, 522, 527, 528, 534, 536–538, 539, 541–544, 556, 566, 568, 576, 579, 597, 631, 634, 658, 708
 compressibility 5, 51, 56, 169
 compression 20, 101, 103, 117, 219, 227, 228, 229, 231, 236, 239, 302, 356, 443, 502, 503, 508, 525, 527, 528
 computer modeling 117, 580
 concurrent reactions 636,
 condensation 171, 298, 301, 302, 303, 305, 310, 369, 464, 592, 594, 597, 599, 602, 613, 621, 627, 633
 configurational entropy 50, 68, 70, 76, 78–81, 124, 125, 318, 325, 394, 707
 conformational change 117, 119, 126
 conformer 117–120, 122–127, 132, 133, 137, 138, 140, 142
 consecutive reactions 637
 conversion 217, 296–299, 311–315, 319–323, 325, 330–335, 341, 345–349, 412,

- 413, 442, 498, 500, 501, 512, 601, 604, 605, 612, 616–618, 644, 716, 784
conversion factor 217, 512
cooling 3, 36–39, 41, 53, 54, 56, 59, 77, 81, 84, 86–88, 91, 92, 96, 103, 104, 161, 181, 182, 187, 199–208, 210, 212, 213, 215–217, 219–222, 225–228, 231, 232, 235–237, 245, 251, 254–261, 268, 280, 282–284, 286, 290, 310, 318, 325–328, 335, 348, 356–358, 361, 369, 386, 391, 412, 430, 431, 457, 461, 462, 469, 478, 502, 525, 529, 547, 654, 659, 673, 674, 715, 716, 720, 722, 723, 725–727, 738–741, 765, 770–775, 777, 781, 793–795, 797
cooling curve 203, 206, 207, 217, 221, 231, 257, 258, 431
cooperative relaxation 120, 127, 163, 656, 662, 669, 679, 684, 686, 687, 688, 690, 691, 694, 695, 696, 698, 700, 705, 706, 707
copolyester 180, 448, 469, 470, 471, 472, 528, 691, 701, 702
copolymer 16, 26, 27, 29, 30, 33, 34, 102, 113, 158, 159, 161, 167, 171, 187, 197–201, 203–206, 208, 213, 216, 218–222, 224–233, 235–237, 239, 240, 273–276, 278, 281, 282, 284–286, 290, 435, 439, 441, 443, 449, 450, 452, 460, 470–472, 522, 526, 528, 530, 533, 535, 538, 553, 556, 597, 612, 631–641, 657, 698, 702–705, 799
copper 397
corrosion 303, 492
coupled techniques 579
craze 102
critical point 168, 171, 174, 296
critical temperature 685
crosslink density 316, 318, 319, 320, 325, 328, 340, 551
cross-linking 187, 434, 451, 453, 593, 637, 640
crucibles 310
crystal defects 184, 390, 402
crystal growth rate 177, 178, 180, 181, 792
crystal imperfections 399
crystal melting 167, 183, 184, 187, 245, 253, 259, 260, 367, 392, 426, 431, 447, 698
crystal unit cell 182, 183, 281, 417
crystalline morphology 182, 215, 783, 801
crystalline phase 78, 159, 183, 203, 217, 224, 364, 365, 383, 384, 389, 397, 399, 417, 418, 436, 446, 450, 451, 463
crystallinity 16, 17, 19, 26, 32, 167, 175, 178–180, 183, 184, 186, 187, 189, 190, 199, 200, 204, 206–210, 212, 213, 215, 217–219, 224, 226–228, 233, 236, 239, 255, 275, 289, 357, 366, 382, 386, 387, 390, 391, 393–399, 416, 417, 419–422, 426–428, 434, 439, 441, 442, 444–446, 449, 450, 454–458, 462, 463, 468, 470, 471, 473, 477–479, 521, 526–528, 534, 535, 547, 611, 614, 653, 668, 669, 671, 672, 691, 703–706, 708, 793, 794, 797
crystallite size distribution 198, 202
crystallization 3, 16, 37, 40, 41, 44, 45, 86, 161–163, 167, 171, 175–184, 186–188, 191, 197–206, 208–210, 213, 216–220, 224, 227–233, 236, 239, 254–256, 259–263, 268, 273, 279, 281–287, 290, 318, 349, 359, 360, 364, 371, 380–383, 386, 389–391, 393, 394, 396, 402, 426–428, 431, 434, 436, 437, 439, 441, 443, 447, 448, 454–458, 460, 473, 475, 477–479, 521, 525, 534, 536, 547, 553, 578, 615, 671, 672, 689, 693, 727, 728, 736, 737, 770, 781–784, 786, 787, 790–795, 797–802
cyanate ester resin 306
- D**
data acquisition 578, 654, 675, 691
deconvolution 349, 717, 724, 727, 728, 730, 731, 743, 778, 779, 781, 786, 792
definitions 50, 95, 167, 169, 412
deformation dilatometers 84
degradation 89, 250, 253, 306, 311, 415, 427, 435, 436, 439, 448, 451–453, 465, 476, 480, 491, 503, 504, 508–510, 512, 513, 515, 516, 519, 523, 524, 537, 538, 542, 543, 546, 547, 553, 554, 557, 558, 566, 567, 570–575, 587–594, 596, 597, 601, 603–606, 608, 609, 611–616, 618, 619, 621–626, 629–644
dehydration 306, 415, 441, 497, 499, 623, 635
demixing 277
density 16, 17, 56, 69, 74, 94, 118, 120, 121, 126, 128, 132, 136, 138, 140, 159, 168, 177, 178, 184, 187, 190, 203, 208, 209, 216–219, 228, 233, 239, 275, 282,

- 343, 362, 363, 373, 374, 376–380, 383–385, 394, 409, 412, 415–419, 422, 426, 440, 442, 444–446, 455–457, 460, 465, 469, 478, 481, 482, 497, 499, 500, 551, 605, 611, 640, 764
- dental material 205
- depolarization current 367, 368, 657, 659, 660, 667
- depolymerization 503, 515, 542, 589, 591–594, 600, 604–606, 609, 618, 631, 633, 638, 639
- derivative 67, 68, 82, 85, 87, 169, 171, 172, 330, 331, 363, 368, 524, 525, 537, 541, 545, 546, 562, 564, 773, 774
- derivative thermogravimetry (see also DTG) 525, 537, 545
- diamond 10–12, 17, 117, 721
- dichroism 424
- dichromic ratio 424
- dielectric analysis 147, 149, 160, 277, 366, 367
- dielectric constant 115, 147, 366, 369, 395, 396, 525, 667, 695
- dielectric loss 128, 135, 140, 147, 155, 157, 159, 280, 306, 366, 384, 395, 396, 404, 525, 533, 653, 655, 667, 684, 697
- dielectric loss factor 147, 155, 280, 525
- dielectric permittivity 115, 147
- dielectric relaxation 115, 120, 133, 134, 158, 278, 279, 366
- dielectric response 525
- dielectric techniques 655, 699
- dielectric thermal analysis (DETA) 525, 587
- diene rubber 160, 522, 526, 569, 572
- differential scanning calorimetry (see also DSC) 13, 14, 34, 59, 66, 85, 86, 92, 178, 251, 308, 348, 349, 360, 431, 496, 524, 525, 567, 587, 655, 713, 717, 722, 741, 801
- differential thermal analysis (see also DTA) 427, 524, 717, 718, 741
- diffusion 45, 94, 176, 181, 199, 221, 279, 322, 328, 329, 337, 338, 340, 341, 347, 350, 412, 443, 452, 458, 460, 497, 499, 500, 507, 589, 590, 599, 609, 611, 613, 619, 625, 784, 785, 795
- diffusion coefficient 279, 443
- diffusion-controlled 322, 328, 329, 337, 500
- diffusivity 508, 524, 552, 593, 625, 764
- dilatometry 59, 82–85, 178, 450, 653
- dipole moment 157–159, 278, 366, 525
- direct extraction 199
- dispersion 99, 364, 365, 381, 388, 390, 397, 399, 403, 553, 556
- dissolution 199
- DMA 38, 122, 147, 157, 277, 364–367, 372, 373, 375, 376, 384, 389, 391, 396, 397, 404, 427, 434, 435, 439, 441–443, 450, 451, 456–459, 461, 468, 472, 473, 476, 496, 499, 525, 531, 540, 551, 565, 571, 575, 576, 587, 653, 669, 673, 674, 687, 693, 698, 703, 704
- DMTA 525, 532, 533, 540, 541, 553, 555, 556, 563
- draw ratio 357, 360, 382, 385–387, 389–391, 393, 394, 399, 400, 403, 411, 429, 430, 437, 438, 441, 443–447, 451, 453, 456, 458, 460–463, 471–474, 476–479
- dry spinning 410, 449, 462, 474, 476
- DSC 2, 3, 14, 34–46, 59, 66, 67, 86–93, 95, 126, 160, 161, 163, 178, 179, 180, 184, 186, 187, 189, 190, 198–202, 204, 205, 208, 209, 212, 213, 215, 217–222, 224–226, 228, 231, 233, 236, 237, 239–241, 251, 254, 256–258, 260, 261, 265, 275–277, 281–283, 286–288, 290, 291, 301, 308–315, 317–319, 320, 323, 324, 327–336, 338, 342–351, 360, 364, 365, 373, 380–383, 389, 391, 399, 400, 404, 419, 427–432, 434, 439, 441–445, 449, 450, 452, 454, 455, 457, 459–461, 467, 468, 470, 472–475, 478, 479, 496–501, 510–512, 515, 524, 525, 529–531, 533–536, 538–541, 543, 547, 553–557, 559–562, 564–569, 571, 572, 574, 576, 578, 587, 608, 613, 639, 653, 655, 667–673, 682, 688, 692, 694, 698, 699, 701, 703–705, 713–732, 736–739, 741–746, 748–751, 753, 758–762, 765, 768–785, 787–801
- DSC, calibration 3, 4, 5, 36, 4, 88, 90, 91, 93, 204, 324, 333, 718, 731, 732, 737, 744, 746, 748, 749–760, 762, 770, 787, 789, 792, 801
- DSC, Calvet principle
- DSC, derivative 85, 87, 169, 331, 363, 524, 562, 564, 773, 774

- DSC, disk 343, 344, 718, 721, 762, 765–767
- DSC, heat flux 717, 719, 722
- DSC, high pressure 301, 310, 524
- DSC, high sensitivity 654, 656, 688, 691, 707, 770
- DSC, interpretation 14, 33, 46, 50, 63, 82, 222, 227, 233, 391, 578, 618, 641, 653, 655, 656, 664, 667, 668, 673, 674, 685, 707, 717, 732, 787, 797
- DSC, modulated temperature 14, 301, 342, 351, 747
- DSC, photo 342–345, 524, 773
- DSC, power compensation 770
- DTA 427, 441, 448, 450, 452, 453, 456, 460, 467, 477, 524, 525, 566, 569, 576, 579, 638, 717, 718, 741, 746
- DTA, calibration
- DTA, interpretation 553
- DTA, qualitative 554
- DTA, quantitative
- DTG 525, 537, 538, 541–548, 553, 570, 572
- durability 101, 102, 104, 249, 443, 492–494
- dynamic glass transition 79, 770, 773, 777
- dynamic heat spectroscopy 86, 94, 95
- dynamic mechanical analysis 147, 157, 160, 364, 365, 388, 427, 434, 468, 525, 540, 550, 563, 569, 570, 575, 587, 655, 715
- dynamic mechanical thermal analysis (DMTA) 533
- dynamic methods 569
- E**
- EGA (evolved/exchanged gas analysis) 525, 538, 573, 587
- elastomer 274, 441, 519–522, 523–531, 533–559, 561, 563–580, 589
- electrical conductivity 552
- ellipsometry 85, 362, 363
- enantiotropic 245, 246, 259–261, 264, 265, 268
- endothermic 44, 88, 180, 227, 276, 317, 318, 326, 328–330, 380, 382, 432, 445, 457, 459, 511–513, 534, 538, 564, 572, 592, 622, 703, 784, 786, 791, 792
- energy 5–9, 32, 38, 46, 50, 51, 64, 68, 73, 79, 80, 82, 85, 103, 111, 112, 115–123, 127, 129, 132, 133, 136, 143, 148–150, 152, 159, 163, 164, 169–171, 173, 176, 177, 182, 185, 204, 251, 253, 254, 259, 260, 288, 289, 299, 300, 305, 315, 317, 319, 331, 332, 334, 336, 340, 343, 344, 372, 374, 378, 383, 385, 393, 394, 398, 427, 432, 434, 435, 448, 452, 454, 458, 469, 476, 478, 543, 555, 556, 568–570, 573, 574, 591, 592, 596, 597, 599, 600, 603, 609, 615, 618, 625, 630, 637, 656, 661–664, 673, 676, 679, 691, 707, 746, 768
- entanglement 117, 128, 134, 136, 138–140, 142, 199, 202, 432, 551
- enthalpy 1, 5, 28, 37, 50, 58–60, 62–68, 70, 85, 86, 87, 89–94, 96, 121–123, 163, 169, 176, 177, 201, 204, 206–208, 210, 212, 213, 226, 232, 236, 250, 263–268, 276, 299, 310, 313, 317, 326–328, 330, 419, 427, 544, 557, 558, 559, 561, 591, 608, 662, 684, 685, 713, 723, 768, 775, 776, 783, 801
- enthalpy of reaction 313, 330
- enthalpy of vaporization 310
- enthalpy retardation 775
- entropy 5, 15, 29, 32, 50, 68–70, 76, 78–81, 94, 111, 117, 121, 122, 123–126, 132, 136, 163, 169, 251, 257, 259, 263–268, 274, 287, 299, 318, 325, 328, 374, 383, 386, 394, 426–428, 431, 591, 592, 662, 684, 686, 687, 691, 698, 706, 707, 713, 732, 768
- entropy of mixing 122, 274, 287
- EPDM 197, 527, 531, 536, 537, 547, 565, 573, 575
- epoxy resin 302, 303, 329, 332, 347, 350, 555, 629, 765, 767
- epoxy-amine reaction 298
- equilibrium 5, 8, 14–16, 18, 27, 28, 33, 34, 39–41, 44, 53–55, 58–66, 68, 69, 71, 73, 76, 79, 87, 88, 94, 96, 111, 112, 121, 126, 128, 129, 131, 172–174, 179, 183–187, 189, 207, 245, 246, 251, 253, 255, 259, 261, 287–291, 297, 325–327, 335, 367, 381, 386, 392, 426, 427, 433, 453, 475, 506, 529, 531, 591–593, 614, 615, 686, 689, 707, 716, 730, 742, 777, 801
- equilibrium 5, 8, 14–16, 18, 27–28, 33–34, 39–41, 44, 53–55, 58–66, 68–71, 76, 79, 87–88, 94, 96, 111, 121, 126, 128–129, 131, 172–174, 179, 183–187, 189, 207,

- 245–246, 251, 253–255, 259, 261, 287–291, 297, 325–327, 335, 367, 381, 386, 392, 426–327, 433, 453, 469, 475, 506, 529, 531, 591–593, 615, 686, 689, 707, 716, 730, 742, 777, 801
- equilibrium constants 591
- equilibrium melting temperature 5, 41, 184, 207, 253, 290, 386
- equilibrium, thermal 367
- etching 21, 22, 25, 32, 187
- ethylene sequence length distribution 202, 203, 216, 220, 228
- ethylene-1-butene copolymer 219, 220
- ethylene-1-octene copolymer 200, 218, 225, 226, 228–231, 233, 235, 237, 239
- ethylene-propylene (EP) copolymers 200, 219, 236
- ethylene-propylene-diene rubber 527, 531
- ethyl-vinyl acetate copolymer (EAM) 528
- evaporation 40, 310, 343, 348, 355, 410, 412, 555, 770, 784, 785
- evolved gas analysis 525, 538, 573, 587
- excess entropy 123, 126
- exothermic 40, 88, 179, 181, 227, 254, 256, 258, 309, 313, 318, 328–330, 347, 441, 452, 456, 477, 538, 544, 567, 572, 592, 608, 627, 727, 781, 783, 784, 790–792
- expansion coefficient 85, 116, 121, 317, 338, 362, 502
- expansivity 5, 169
- explosive 625
- extent of reaction (see also fractional) 298, 299, 311–313, 320, 321, 329, 330, 345, 348, 627
- extrapolated onset 42, 529, 530
- extrusion draw ratio (EDR) 393
- Eyring's activated states 662, 686
- F**
- factor 6, 7, 5563, 64, 70, 73, 85, 97–102, 115, 116, 118, 122, 124, 127, 128, 134, 135, 139, 142, 144, 147, 149–151, 153, 155–158, 161, 162, 174–176, 204, 217, 236, 280, 284, 285, 288, 289, 291, 305, 317–319, 330, 332, 334, 337, 338, 340, 350, 377, 397, 402, 409, 416, 422, 424, 425, 428, 435, 451, 452, 456, 480, 512, 520, 522, 525, 534, 537, 539, 542, 543, 569, 572, 576, 579, 588, 589, 590, 592, 600, 615, 658, 661, 664, 672, 683, 740, 741, 744, 751–753, 755, 762
- fast heating 187, 335, 450, 730
- fiber structure and morphology 417, 442, 444, 457
- fibril 184, 279, 382, 399, 416–418, 422, 445, 447
- fictive temperature 58, 61, 63–65, 81, 88–90, 94, 129, 317, 770
- filament winding 302, 303
- fillers and reinforcing agents 545, 553
- film 85, 94, 174, 188, 307, 309, 344, 355–367, 369, 371–383, 385–390, 393–404, 459, 461, 477, 478, 555, 629, 640, 654, 657, 658, 673, 689, 692, 693, 697, 703, 781
- first-order phase transition 50, 426, 787, 789
- flexibility 137, 175, 180, 302, 316, 426, 438, 441, 514, 527, 653, 703, 706
- flow rates 35, 40, 41, 111, 137, 144, 524, 548, 603, 714–718, 720, 723–730, 732–736, 739–744, 746, 747, 761, 766, 771, 774, 776, 778, 779, 781, 783, 786–791, 793, 797
- fluctuation dissipation theorem (FDT) 732
- Fluid confinement dilatometry 82
- fluoropolymers 158, 344, 703
- foam 305, 537, 556, 577
- food 359, 801
- Fourier transform 92, 161, 168, 348, 496, 519, 533, 538, 546, 741, 742, 746, 791, 801
- Fourier transform infrared spectroscopy (see also FTIR) 496, 519, 546
- fractionation 198, 199, 202, 233, 257, 282
- free energy 5, 50, 51, 68, 82, 85, 111, 118–120, 132, 136, 143, 163, 164, 169, 170, 173, 176, 177, 185, 253, 254, 259, 260, 288, 299, 427, 591, 592, 662, 768
- free radical chain reaction 594, 623
- free radical photo-polymerization 339, 342, 346
- free volume 50, 76–78, 80, 81, 115, 116, 121, 122, 124–126, 128, 317, 318, 326, 328, 338, 395, 707
- frequency 3, 5, 9–14, 16, 17, 19–23, 35–37, 39, 40, 92–95, 113–115, 118–120, 128, 130, 131, 135, 139–144, 147–150, 152, 154, 155, 158–161, 163, 277, 280, 332, 364, 366, 367, 372, 374–376, 384, 390,

- 397, 402, 434, 435, 474, 476, 525, 533, 565, 653, 655, 659, 660, 662, 664–669, 671, 676, 679, 680, 682, 684–688, 691–693, 695–697, 699, 703, 705, 713–717, 720, 723, 724, 730–732, 734, 737–740, 742–744, 746, 747, 750, 751, 753–759, 761–763, 765, 767–773, 775, 784, 786, 787, 795, 796, 798–901
- frequency dependent 37, 94, 366, 434, 686, 714, 717, 731, 732, 737, 742, 750, 767, 786, 787, 800
- frequency dependent heat capacity 37, 737, 750, 767
- frequency domain 713, 737, 738, 746
- frequency factor 332
- frequency spectrum 10, 12, 16, 17, 19, 20, 730
- FTIR 496, 497, 510, 513, 514, 519, 538, 546, 638
- fusion (see also melting) 29, 36, 72, 44, 45, 50, 94, 120, 176, 177, 179, 181, 184–187, 189, 190, 199, 221, 279, 288, 289, 322, 328, 329, 337, 338, 340, 341, 347, 350, 381, 386, 387, 392, 399, 403, 412, 432, 441–446, 449, 450, 452, 453, 456–460, 473, 478, 497, 499, 500, 507, 524, 589, 590, 599, 609, 611, 613, 619, 625, 668, 670, 681, 784, 785, 787, 788, 793–795, 799
- G**
- gas chromatography (GC) 363, 573, 587, 597, 631, 634
- GC-MS 222
- gel point 296–299
- gelation 298–300, 386, 389–391, 462
- gel-spun PE fiber 444
- Gibbs energy 5, 768
- glass formation 50, 54–58, 71,
- glass transition 3, 14, 16–18, 25, 29–32, 34, 36–40, 46, 49–56, 59, 61, 62, 66–68, 72, 73, 75–88, 92–97, 104, 118, 120, 121, 137, 149, 150, 152, 154, 156, 159, 161–164, 171, 176, 190, 200, 207, 213, 228, 236, 239, 254, 256, 274–276, 290, 305, 309, 310, 315–329, 336, 337, 345, 347, 348–351, 360, 364, 365, 367, 371, 380, 381, 384, 390–392, 396–399, 403, 431, 434, 441, 450–453, 458, 462, 470–473, 475, 478, 511, 521, 524, 525, 529, 530, 533, 539, 540, 541, 556, 578, 589, 590, 612, 615, 656, 658, 661, 668–674, 679–685, 687–696, 698–707, 714, 717, 725, 727, 732, 736, 737, 750, 752–757, 767–781, 784–787, 793, 794, 797, 798, 800, 801
- glass transition temperature 16, 32, 34, 36, 40, 49, 52–55, 59, 72, 73, 77, 78, 80–84, 88, 94, 95, 104, 137, 176, 207, 236, 254, 256, 274–276, 290, 305, 309, 310, 315–329, 336, 337, 345, 347, 348–351, 365, 470, 471, 521, 529, 533, 539, 589, 750, 770, 771–774
- glass-reinforced composite 302
- glass-transition temperature 32, 34
- glassy state 54–57, 75, 77, 84, 89, 91, 116, 121, 122, 129, 325, 326, 338, 499, 529, 688, 801
- graft copolymer 273, 274, 556
- group vibration 21–28, 32, 36
- gutta percha 125, 568
- H**
- halogenated rubber 527
- heat capacity 1–5, 7–24, 27–46, 51, 68–70, 75, 81, 85–87, 89, 91, 94, 95, 169, 190, 200, 204–207, 209–213, 218, 225–228, 231–233, 275, 276, 348, 349, 363, 392, 428, 450, 453, 473, 529, 530, 549, 578, 608, 672, 703, 713–720, 723–733, 736–787, 790–801
- heat capacity calibration 744, 749
- heat capacity, constant pressure 5, 16, 19, 37, 55, 56, 85, 170, 723
- heat capacity, constant volume 5, 7, 19, 55, 56, 69, 81
- heat capacity, non-reversing 92, 93, 348–350, 717, 723–732, 743, 770, 774–781, 784, 786, 790, 791, 801
- heat capacity, reversing 3, 35–40, 42–45, 92, 93, 348–350, 716, 717, 723–732, 743, 749, 770, 774–787, 790, 791, 795–797, 800, 801
- heat capacity, specific 2, 8, 74, 15, 40, 205, 206, 231, 715, 723, 761, 762, 786, 796
- heat exchange 524, 719–722, 732
- heat flow 35, 37, 39–42, 45, 86, 92, 93, 213, 348, 349, 362, 524, 529, 536, 567, 578, 668, 714–736, 739–749, 761, 762, 766, 767, 770, 771, 774, 776, 778, 779, 781, 773, 786–793, 797
- heat flux 2, 86, 717, 719, 722

- heat flux DSC (see DSC, heat flux) 86, 717
 heat of fusion 32, 44, 120, 179, 184–189, 288, 289, 381, 387, 392, 399, 403, 432, 441, 443–446, 449, 453, 457460, 473, 478, 787, 788, 794, 799
 heat of reaction 33, 299, 309–315, 321, 329, 330, 335, 347, 501, 524
 heat of transition 29, 43, 204, 382, 768
 heat of vaporization 120
 heat sink 721, 722
 heat transfer 290, 357, 412, 551, 715, 730–732, 737, 738, 740, 744–746, 749, 750, 754, 758–760, 769, 792, 793
 heat transfer coefficient 760, 761
 heating curve 87, 180, 200, 202–207, 210, 213, 218, 221, 227, 228, 231
 heating rate 2, 4, 35, 36, 39, 45, 53, 86, 87, 90, 91, 163, 187, 188, 222, 227, 245, 251, 256, 283, 286, 287, 290291, 310, 311, 324, 325, 334, 336, 348, 381, 382, 384, 389, 392, 394, 400, 428, 431, 435, 441, 447, 450, 452, 455, 456, 461, 467, 530, 534, 546–548, 578, 587, 603, 612, 618, 61, 629, 637, 638, 658, 660, 661, 667, 669, 672, 675, 684, 715, 716, 720–730, 732–744, 748, 749, 761, 765, 771, 775, 776, 778, 779, 781, 782, 789–791, 793, 797, 801
 heats of transition 1, 45, 256, 360, 428
 Hermans orientation factor 424, 425
 heterogeneity 198, 691, 694, 702, 706
 heterogeneous 117, 173, 176, 178, 197–198, 204, 239–240, 396, 611, 613, 639, 664
 heterogeneous nucleation 176, 177, 204, 396
 hexatic 248
 high performance fiber 412, 414, 439, 463, 464, 479, 481, 482
 high resolution 367
 homogeneous 168–169, 173, 176, 186, 197–201, 203–204, 218–220, 225–226, 229–231, 235, 237, 239–241, 359, 614, 632, 766–767
 hot stage 291, 380, 391, 436, 437
 hot-stage microscopy 380
 humidity (see moisture content) 156, 157, 366, 399, 441, 442, 505, 534, 615
 hydrocarbon polymers 157
 hydrolysis mechanism 613, 164
 hydrolytic degradation 453, 508, 510, 513, 515, 516, 588, 590, 593, 613, 614, 623, 641
 hydrosilylation 298, 308
- I**
 ignition temperature 571
 inclusion 60, 203, 216, 230, 529, 573, 578
 indium 41, 42, 204, 333, 334, 748, 787–789
 induction period 620, 634, 798
 infrared and Raman spectroscopy 184
 infrared spectroscopy (see also FTIR) 16, 345, 456, 496, 519, 546, 587
 injection 302, 305, 470, 527, 697, 760
 inorganic fiber 463–464
 in-phase 94, 113–114
 insulator 295, 303, 343, 369, 528
 integrated circuit 303, 307
 interface 180, 189–190, 203, 279, 289, 356, 362, 502, 505, 673–674, 697, 706
 internal energy 79, 169
 internal stress 189, 323, 426–427, 429, 439, 477
 intrinsic viscosity 131–137
 ion mobility 525
 irreversible 3, 37–38, 40, 43, 45, 192, 296, 350, 365, 433, 510, 512, 515, 797
 irreversible melting 43
 irreversible thermodynamics 38
 isobaric glass formation 54–55, 57
 isochoric 55–57
 isoK-base-line 728–731
 isokinetic effect 664
 isolated 21, 133, 134, 136, 140–141, 171–172, 239, 480
 isotactic polymethyl methacrylate (PMMA) 66
 isotactic polypropylene 180, 387, 417, 437
 isothermal conditions 285, 333, 524, 565, 738, 781, 790, 795, 797–798
 isothermal mode 43, 395–396
 isotropization 41, 42, 245, 257, 259
- K**
 Kevlar[®] 125, 464–466, 468–469, 481–482, 509, 516
 kinetic model 289, 341
 kinetics 37, 39–40, 51–53, 57–59, 67, 76, 79, 163, 171, 174, 176, 178–180, 191, 202, 206, 222, 245, 247, 254–255, 261, 268, 290, 299–300, 315, 321, 328, 330, 332,

336–337, 340–341, 343, 345–346, 350–351, 380, 427–428, 435–436, 439, 441, 448, 452, 454, 494, 510, 561–562, 566, 574, 579, 587–590, 592, 594–597, 599–600, 603, 608, 609, 611–616, 631, 641, 664, 781, 787, 792

L

lamellar crystals 174, 176, 183, 185, 187, 239, 268, 281, 288, 359, 382, 391, 392, 399
laminated film 359

Langmuir-Blodgett 355, 356

length change dilatometry 84

lifetime prediction 588, 590, 613–615, 625, 644

light and electron microscopes 183

limit of metastability 174

linear variable differential transformer 85

linear viscoelastic 62, 68, 70, 72–73, 94–97, 99, 112, 119, 127, 139, 143–144, 550

linearity 60–61, 63, 93, 161, 260, 369, 548–549, 666, 730–732, 736–737, 743, 777, 786, 789, 791

liquid crystal 3, 32, 42, 88, 171, 180, 245–268, 369, 427, 436, 463, 466, 467, 469–471, 480, 653, 657, 691, 698, 702, 708

liquid crystalline polymer 42, 245–247, 249, 250–251, 253, 255, 262–263, 265, 268, 469, 653, 657, 691, 698

liquid-liquid phase separation 175

liquids 16, 18, 19, 27, 28, 32, 67, 73, 75–77, 94, 118–121, 168, 174, 246, 344, 572, 575, 589, 599

liquidus 325

local thermal analysis 362–363

loss tangent (see phase angle and also 147, 445, 451, 459, 468, 475, 551, 555, 569–570, 575

low temperature 7, 9, 11, 17–19, 23, 35, 45, 82, 123, 152, 154, 157, 169, 171, 205, 207, 213, 217, 371, 384, 386, 389, 397, 399, 401–402, 448, 482, 503, 508, 527, 534, 555, 565, 590, 599, 608, 611, 614, 619, 621, 632–633, 635–636, 656, 662, 667, 671, 676, 679–682, 684, 687–691, 693–694, 697, 699, 703, 706, 769, 781
LVDT 85

lyotropic 246, 249, 463, 466–467, 470

M

macro-fibril 417

macromolecule 1, 5, 16, 23–24, 27, 29, 31–33, 42–43, 45, 66, 78, 171, 273, 380, 399, 509, 516, 621, 785

macroscopic 491, 493–494

macroscopic 6–7, 18, 23, 45, 168–169, 171, 174, 178, 182, 189, 191, 281, 296–298, 381, 426, 444, 491, 494

macroscopic system 6

magnetic field 171

mass spectrometry (MS) 519, 538, 573, 597, 631

MDSC 349, 714

measured curve 209, 210, 777, 784

melt spinning 410, 439, 441, 461, 469–470, 473, 478–479

melt viscosity 138, 470

melting 5, 16–18, 22, 25, 30, 37, 40–41, 43–46, 83, 161, 167, 171, 176–177, 183–185, 187–190, 197–200, 202–204, 206–210, 213, 217–219, 221–222, 224, 227, 229–233, 236, 239, 245, 251, 253–254, 257, 259–260, 273–274, 279, 282–283, 286–291, 309, 318, 328, 333–334, 348, 350, 360, 364, 367, 380–384, 386–387, 389, 391–392, 399–400, 402, 410–411, 416, 426–432, 441, 443–449, 453, 455–457, 459–460, 462, 469, 471–474, 479, 511, 521, 525, 534–535, 578, 589–590, 612, 615, 625, 654, 698, 722, 725–728, 730, 732, 736, 748, 750, 767, 778, 780–782, 786–798, 800–801

mesogenic groups 245–247, 249, 259–260, 263–268

metal 86, 94, 103, 111, 167, 197, 228, 231–233, 235, 357, 360, 466, 492, 573, 610, 626, 748, 777, 787

metastable 16–17, 78, 167, 173–175, 184–187, 245, 253, 259, 262, 386, 446, 457–458, 574, 592

metastable phase 175, 253, 262, 458

metastable state 173–175, 592

methods 36, 45, 49, 82, 84–86, 89, 97, 118, 167–169, 179, 184, 186–187, 189–191, 199, 209, 245, 248, 251, 259, 273, 277, 281, 287–288, 355, 358, 360–362, 386, 409–410, 419–420, 427–428, 435, 438, 446, 454, 460, 463, 468, 482, 520, 537, 542, 546, 549, 569, 576, 579, 587–588, 592, 608–609, 613–615, 631, 641, 653–

- 655, 659–660, 662, 664, 667, 669, 673–676, 678, 681, 683, 686–688, 692–693, 703, 754, 758, 761, 772–773
 Mettler Toledo 714, 725–726, 790–791
 micro 5–7, 18, 23, 45, 50, 73, 76, 85, 168–169, 174–175, 177–178, 180, 183–184, 191–192, 198, 200, 213, 215, 222, 228, 233, 239, 249, 253, 273, 275, 278, 280–281, 288, 290–291, 304, 306, 355, 362–363, 380–381, 395, 409, 417, 423, 426–427, 435, 447, 457, 461, 470, 476, 491, 494–495, 499–500, 502, 506–508, 516, 522, 525–527, 529, 536, 538, 543, 547, 549, 571–572, 579–580, 644, 654, 673, 702, 722, 792
 microcracking 499
 microscopy 180, 183–184, 192, 222, 239, 249, 253, 275, 278, 288, 290–291, 380–381, 447, 457, 461, 470, 525, 547, 579, 792
 miscibility 159–161, 275, 281, 285, 539–540, 544, 632–633
 miscible mixtures 274–276, 288
 mixture 43, 141, 156, 171, 175, 274–276, 279, 281–282, 284–286, 288, 297–298, 312, 475, 539, 544, 559, 576, 631–632, 634, 637, 639–641, 669
 mixtures, binary 274–275
 mobility 60, 62, 73, 78, 174, 200, 203, 210, 221, 255–256, 276, 281, 299, 314, 316, 319, 322–323, 325–326, 328, 337–338, 340–341, 350, 364, 367–368, 384, 428, 431, 434, 452, 456, 458, 463, 514, 525, 533, 535, 599, 612, 625, 781, 784
 mode, isothermal 43, 395–396
 modulated temperature DSC (MTDSC) 301, 348, 351
 modulation 3–4, 34–37, 39, 41–42, 44–45, 224, 348–349, 716, 722–725, 737, 747, 749–754, 758–760, 769–771, 775, 779, 781, 783, 785, 793, 796, 799, 801
 modulation amplitude 35, 42, 44, 796
 modulation frequency 3, 35, 37, 39, 716, 750, 770, 775, 799, 801
 modulus, bulk 55, 69
 modulus, complex 144, 434, 533
 modulus, loss 113–114, 140, 364, 366, 390, 403, 434, 443, 525, 533, 540, 551
 modulus, shear 69, 118, 136, 277–278
 modulus, storage 113, 140, 277, 347, 364–365, 386–387, 389–391, 403, 434–435, 443, 459, 474–475, 525, 533, 540–541, 551, 555, 569–570
 modulus, tensile 118, 364, 401, 464, 481
 modulus, Young's 444, 474, 478–479
 moisture 308, 356, 360, 399–401, 416, 440–442, 448, 453, 469, 473–476, 481, 492, 494, 503–508, 624, 629
 molar volume 288, 432
 mole fraction 701
 molecular mobility 60, 62, 73, 78, 174, 255–256, 337, 340, 350, 784
 molecular orientation 246–247, 357, 362, 411, 417, 426, 455
 molecular weight 76, 81, 113, 116, 118–119, 123, 131–142, 184, 191, 249, 253, 256–258, 273, 287, 299, 307, 373, 391, 404, 416, 441–443, 454, 456–457, 461–464, 467, 470, 473, 480, 508, 510, 520, 522, 526, 530, 533, 576, 593, 599, 601, 605, 616–617, 623, 626, 632–634, 636, 641
 monotropic 245–246, 259–262, 264, 268
 morphology 46, 147, 167, 175–178, 181–185, 188, 197–198, 213, 215–216, 222, 233, 236, 239, 273, 279, 366, 399, 417, 442, 444, 448, 454, 457, 536, 539, 653, 783, 797, 801
 multilayer 359–360, 363, 380
 multiple relaxation modes 113
N
 naphthalene 251, 472
 natural rubber 160, 295, 521, 526, 530, 533–534, 538, 540–541, 544, 548–549, 552, 558, 561, 563–564, 566–570, 572, 640
 nematic 247–249, 253, 265, 267, 369, 470–472, 480, 698, 700, 703, 749
 network 139, 142, 296–299, 312, 314, 318–319, 325, 340, 347, 471, 497, 508–510, 513, 519, 522, 551, 557, 559, 564–565, 569, 621, 745–746, 784
 NIST (US National Institute of Standards) 85
 noise 492, 533, 713, 716, 739–740, 743, 758, 769, 786
 non-Arrhenius 73, 76, 78, 680–681, 777
 non-cooperative relaxation 679, 684, 686–688, 691, 698

- non-equilibrium 15, 34, 59, 68, 94, 686, 801
 non-equilibrium 15, 34, 59, 68, 94, 686, 801
 non-equilibrium thermodynamics 68, 801
 non-isothermal crystallization 181–182, 255
 non-linear regression 685
 Nonlinear viscoelastic 73, 95, 99
 nonlinearity 63
 non-periodic perturbation 741
 nonreversing heat capacity 3, 723–724, 775
 non-reversing heat capacity 717, 723–725, 728, 730, 732, 743, 774–776, 778, 786, 790
 nuclear magnetic resonance (NMR) 119, 157, 190, 198, 222, 228, 231, 233, 253, 312, 417–419, 435, 516, 519, 653, 669, 682
 nucleation 173, 175–178, 181, 198, 200, 202–204, 222, 224, 233, 254–255, 259, 261, 281, 285–287, 289, 381, 396
 nucleation barrier 176–177, 200, 202–203, 254
 nylon 28, 155–157, 167, 399–404, 411, 417, 423, 429–430, 439–443, 448, 452, 464–465, 613, 624, 657
O
 onset temperature 42, 456, 553, 569
 open systems 602–603
 oscillation 15, 21, 39, 94, 120, 348, 366, 394, 525, 714–715, 724, 734, 741, 771, 781, 784, 790
 out-of-phase 94
 overall crystallization rates 178, 262–263
 oxidation 40, 158, 303, 366, 415, 452, 477, 527, 530, 533, 538, 543, 550, 567–570, 572, 574, 588–590, 592, 599, 608–612, 619, 622–623, 625, 629–630, 641–644
 oxidative degradation 519, 547, 566, 571, 587, 589, 592, 594, 608–609, 611–612, 614, 618–619, 625, 629
 oxidative stability 306, 369, 460, 467, 476, 536, 567–569, 571–572, 574
P
 packing density 373–374, 376–380
 parallel measurements 380
 parallel plate capacitor 148
 peak area 420, 512, 667
 peak height 44, 152, 159, 162, 421, 551, 555
 peak temperature 87, 181–182, 221, 230, 233, 255, 384, 393, 397–398, 401, 448, 454–456, 458, 468, 476, 478, 512–513, 534, 537, 543–544, 560, 568–569, 575, 682, 684, 697
 performance characteristics 457, 463
 Perkin-Elmer 205, 347, 381–382, 400
 permeability 527–528, 555
 permittivity 115, 147–149, 152–153, 155, 161, 279, 525, 667
 permittivity, relative 525
 permittivity, unrelaxed 152
 peroxide cure 542, 557–559, 569
 pharmaceuticals 527, 786
 phase 16, 35, 45, 50–51, 78, 93–94, 113–114, 148, 159, 167–176, 180, 183, 189–192, 200, 203, 205–207, 209, 212, 217, 224, 228, 245–249, 251–253, 255–262, 264–266, 268, 273–281, 285–286, 305, 310, 355, 361, 364–365, 383–384, 389–390, 395–397, 399–400, 402–403, 417–419, 422–423, 426, 428, 432, 435–438, 442–446, 450–451, 458, 463, 469–471, 477, 480, 494–495, 515, 530, 534–536, 544, 547, 553–556, 563, 566, 570, 589–590, 603, 608–609, 632–633, 640, 653, 673, 690, 702, 706, 713, 715–716, 720–721, 724, 726, 729, 731–732, 734–737, 741, 744, 746–754, 757–759, 771, 773, 777, 780, 782–784, 786–789, 794–795, 798–801
 phase angle 113, 148, 715–716, 724, 726, 729, 731, 735–736, 744, 746–754, 757–759, 773, 777, 786
 phase diagram 171, 173, 255–256, 470, 494–495, 515, 632
 phase stability 172, 174, 245, 260
 phase transitions 50–51, 167, 169–171, 173–174, 191–192, 245–246, 253–257, 259–262, 268, 426, 428, 436, 477, 713, 720–721, 736, 786–787, 789, 794, 800
 phenolformaldehyde 295, 613, 628
 phenol-formaldehyde condensation 298
 photo 302, 304, 315, 338–348, 411, 524, 574, 615, 636, 643–644, 654, 772–773
 photo-calorimetry 342–343, 345
 photo-DSC 342, 343, 344, 345, 524, 688
 photo-initiated polymerization 338, 339, 342,

- p-hydroxybenzoic acid (HBA) 470, 471, 472, 473, 701, 702, 703,
 physical aging 49, 50, 59, 73, 95, 96, 99, 100, 101, 102, 103, 104, 105, 120, 325, 326, 327, 328, 329, 330, 350, 352, 511, 512, 513,
 physical crosslink 274, 521,
 plastic deformation 30, 144, 415
 plasticizer 161, 399, 436, 441, 508, 523, 544, 553, 554, 555, 556, 576
 plateau 20, 112, 553, 566
 polarization 57, 147, 148, 279, 367, 368, 380, 381, 383, 424, 447, 470, 653, 654, 655, 656, 657, 658, 659, 660, 661, 662, 663, 665, 666, 667, 670, 673, 674, 679, 680, 681, 683, 684, 685, 686, 689, 693, 696, 698, 706, 708
 polarization sequence 653, 655, 656, 659, 660, 661, 693, 706
 polarized light microscopy 183, 249
 poly(2,6-dimethyl-1,4-phenylene oxide) 160
 poly(4-methyl pentene) 125
 poly(α -methyl styrene) 125, 302
 poly(acrylates) 688
 poly(amino acid) 24, 25, 31
 poly(azomethine ether) 263
 poly(butylene terephthalite) (PBT) 191, 282, 283, 284, 285, 286, 291, 460, 461, 657
 poly(ester imide) 256
 poly(ether ether ketone) (PEEK) 161, 180, 181, 182, 185, 191, 478–480, 639, 657, 671, 672, 688, 694, 703, 725, 726, 727, 792, 798, 799
 poly(ether ether ketone) 161, 255, 478
 poly(ethyl methacrylate) 125, 665
 poly(ethylene terephthalate) 37, 44, 180, 187, 188, 356, 392, 453, 534, 657, 692
cis-polyisoprene 125
 poly(L-lactide) 290
 poly(methyl acrylates) 688
 poly(methyl methacrylate) 66, 99, 101, 280, 589, 599, 613, 616, 657, 765
 poly(methylacrylic acid) (PMAA) 622
 poly(oxybenzoate-co-oxynaphthoate) 29
 poly(oxyethylene) 26, 43
 poly(oxymethylene) 25, 26, 657, 705
 poly(oxymethyleneoxyethylene) 26
 poly(oxymethyleneoxytetramethylene) 26
 poly(oxyoctamethylene) 26
 poly(oxytetramethylene) 26
 poly(oxytrimethylene) 26
 poly(p-benzamide) 249, 464
 poly(phenylene sulfide) (PPS) 466, 473, 693
 poly(pivalolactone) 290
 poly(p-phenylene benzobisoxazole) (PBZO) 464, 479, 480
 poly(p-phenylene benzobisthiazole) (PBZT) 464
 poly(p-phenylene terephthalamide) (PPTA) 464
 poly(propylene oxide) 365
 poly(pyromellitimide) 477, 629
 poly(styrene-co-butadiene) 33
 poly(*t*-butyl acrylate) 125
 poly(tetrafluoroethylene) 28, 286, 594, 617, 635, 670
 poly(thio-1,4-phenylene) 180
 poly(trifluoro-chloroethylene) 125
 poly(trimethylene terephthalate) 461
 poly(vinyl acetate) 54, 58, 59, 70, 82, 327
 poly(vinyl alcohol) 462
 poly(vinyl chloride) 99, 436, 601, 619
 poly(vinyl fluoride) 704
 poly[2,2'-(*m*-phenylene)-5,5'-bibenzimidazole] (PBI) 466, 474
 polyacrylonitrile (PAN) 411, 412, 440, 448, 480, 613, 630, 633
 polyamic acid 306, 476, 508, 510, 511, 513, 515
 polyamides 154–157, 251, 304, 365, 399, 439, 468, 602
 polybutadiene 34, 160, 521, 522, 526, 530, 533, 534, 536, 538, 544, 547, 563, 567, 569, 572, 620, 640
 polycarbonate 56, 65, 98, 124, 126, 129, 152, 154, 348, 610, 613, 629, 640, 658, 678, 685, 687, 693, 774, 781
 polydioxanone 36
 polyether 32, 251, 255, 264, 533, 535, 623, 625
 polyether imide 125
 polyether sulfone 125
 polyethylene (branch) 125, 197, 198
 polyethylene (linear) 125, 203, 204, 221, 222, 444, 605, 702

- polyethylene 16–27, 29–32, 125, 138, 158, 159, 167, 180, 197, 198, 202, 203, 204, 206, 207, 209, 212, 221, 222, 348, 381–387, 440, 443, 444–446, 484534, 537, 553, 559, 573, 590, 597, 601, 605, 611, 623, 640, 657, 670, 671, 682, 705, 706, 792, 795
- polyethylene terephthalate 37, 44, 125, 180, 187, 348, 356, 392–399, 453–460, 534, 657, 692
- polyimide (PNMA) 125
- polyimide 125, 180, 182, 191, 306, 311, 362, 369–381, 404, 464, 476–478, 503, 508, 511, 513, 516, 630
- polyimide composites 503–516
- polyimide fiber 476–478
- polyisobutylene 114, 125, 128, 694
- polyisoprene 125, 135, 141, 526, 530, 534, 553, 554, 564, 567, 568
- polymer blends 159–161, 175, 273, 274–291, 328, 435, 540, 631, 632, 639, 640, 800
- polymer crystal growth 176, 181, 792
- polymer crystal unit cell 417
- polymer degradation 89, 250, 253, 306, 311, 415, 427, 435, 436, 439, 448, 451, 452, 453, 465, 476, 480, 491, 503, 508, 510, 512, 513, 515, 516, 519, 523, 524, 537, 542, 543, 546, 547, 553, 554, 557, 558, 566, 567, 570–580, 587–641
- polymer fiber 409–482
- polymer matrix fibrous composite 491–517
- polymer thin film 355, 362, 404
- polymeric composites and coatings 492
- polymerization 24, 79, 197, 201, 216, 220, 228, 231, 239, 250, 251, 296, 297, 298, 299, 304, 305, 307, 308, 312, 315, 337, 338, 339–348, 369, 443, 460, 464, 465, 470, 496, 503, 508, 515, 527, 542, 565, 589, 591, 592, 593, 594, 596, 600, 602, 604, 609, 616, 618, 620, 623, 631, 633, 784
- polymethyl acrylate 125
- polymethyl methacrylate 66, 99, 101, 125, 280, 589, 599, 613, 616, 657, 765
- polymorphism 427, 436, 439
- polyolefin fiber 443
- polyolefins 158, 381, 528, 611, 623, 642, 643
- polyoxides 25, 26, 28, 33
- polyoxybutylene 125
- polyoxyethylene 125
- polyoxymethyl ether 125
- polyoxypropylene 125
- polyphenylene oxide 125
- polyphenylene sulfide 125, 629, 466, 473–474, 693
- polypropylene 125, 158, 167, 180, 303, 383, 387–392, 417, 437, 440, 446–448, 534, 611, 623, 657, 664, 774
- polysaccharides 613
- polystyrene 34, 37, 65, 101, 102, 117, 118, 125, 141, 145, 160, 274, 278, 362, 588, 589, 593, 612, 617, 618, 619, 633, 640, 657, 674, 688, 692, 693, 694, 750, 770
- polysulfide rubber 528, 573
- polysulfone 125, 613
- polyurethane 251, 274, 305, 315, 528, 530, 532, 534, 536, 574, 589, 590, 592, 613, 614, 625, 632
- polyvinyl acetate 120, 125, 622
- polyvinyl alcohol (PVAL) 440, 462–463, 623
- polyvinyl chloride 65, 99, 125, 161, 277, 436, 593, 601, 619–622
- polyvinyl methylether 125
- polyvinylbutyl ether 125
- polyvinylhexyl ether 125
- polyvinylisopropyl ether 125
- potassium permanganate
- powders 343, 453, 454, 458, 459, 624
- power compensation DSC 717, 720–721, 722, 730
- power law 98
- precision 1, 2, 4, 27, 35, 40, 83, 363, 395, 506, 655, 707, 768
- pre-exponential factor (see also frequency factor) 332, 334, 661
- pressure 1, 5, 16, 19, 37, 50, 54, 55, 56, 57, 67, 69, 76, 78, 79, 81, 82, 84, 85, 117, 169, 170, 253, 274, 301, 302, 310, 356, 358, 359, 362, 380, 395, 409, 410, 442, 475, 505, 510, 513, 524, 547, 555, 556, 591, 592, 593, 603, 608, 613, 617, 627, 632, 635, 723
- pressure DSC (see DSC, high pressure)
- pressure vessel 302
- primary amine 304
- proportional integral derivative (see PID)
- protein 24, 25, 31, 558, 561, 792, 800
- pultrusion 302

purge gas 603, 719, 760, 765, 767
 purity 558, 657, 717
 pyrolysis gas chromatography 573, 587,
 597, 631, 634
 pyrolysis mechanism 587, 644
 pyrotechnics 572

Q

quality assurance 576, 810
 quasi-isothermal mode 43
 quasi-isothermal TMDSC 34, 35, 36, 41,
 43, 44, 780, 792, 794, 795, 796
 quenched 36, 61, 88, 96, 97, 101, 102, 116,
 122, 179, 320, 322, 327, 329, 380, 396,
 420, 460, 461, 473, 660, 671, 703, 790, 791

R

random chain scission 509, 516, 593, 594,
 639
 random conformations 117, 127
 random copolymer 29, 275, 276, 278, 286,
 632, 637, 698
 random equilibrium 172
 random errors 91
 rate controlled thermal analysis 726
 rate controlling step 412
 reaction vessel 524
 recrystallization 185, 187, 188, 198, 200,
 204, 206, 227, 282, 392, 429, 430, 433,
 437, 447, 791, 792
 reduced temperature 8, 75
 reduced time 62, 63, 68, 69, 70, 96, 97, 98,
 599
 reference material 524, 750
 refractive index 362, 423
 relative permittivity 525
 relaxation 14, 37, 38, 39, 59, 63, 63, 64, 66,
 69, 71, 73, 87, 96, 97, 99, 111–145, 147–
 164, 173, 276, 277, 278, 279, 280, 281,
 286, 322, 328, 329, 337, 348, 350, 364,
 365–367, 371–377, 381, 384, 385, 386,
 388–404, 415, 430, 433, 434, 435, 442,
 443, 446, 448, 450, 451, 452, 454, 458,
 459, 461, 462, 463, 468, 469, 471, 472,
 475, 476, 477, 478, 502, 511, 520, 521,
 525, 532, 533, 578, 653, 654, 655, 656,
 659, 660, 661, 662, 664, 665, 668, 669,
 671, 673, 676, 677, 678, 681, 682, 683–
 700, 703–708, 736, 742, 771, 772, 777,
 786, 795, 796, 799, 800
 relaxation map analysis (RMA) 367, 525

relaxation modulus 59, 97, 112, 113, 114,
 116, 127, 128, 140, 143
 relaxation process 111–145, 173, 371, 373,
 374, 375, 384, 399, 434, 435, 450, 451,
 458, 659, 469, 471, 475, 476, 477, 478,
 525, 777, 786, 796
 relaxation spectrum 113, 114, 115, 129,
 140,
 relaxation time 14, 38, 39, 63, 64, 87, 97,
 100, 111–145, 155, 173, 328, 415, 469,
 520, 521, 660, 662, 664, 665, 676, 677, 688,
 742, 772, 773, 777, 799, 810
 relaxation-controlled 322
 reorganization 3, 187, 188, 198, 199, 200,
 202, 204, 221, 222, 224, 227, 233, 282,
 290, 291, 384, 428, 430, 431, 433, 471,
 534, 578, 729, 782, 789, 790, 791, 792
 repeatability 90, 91, 93
 reproducibility 343, 436, 653, 656, 678,
 706, 718, 719
 residence time 311
 resin transfer molding 302
 resolution 76, 85, 92, 104, 276, 290, 303,
 363, 367, 396, 506, 546, 552, 655, 695, 707
 reversible crystallization 3, 45, 224
 reversing 3, 35, 36, 37, 38, 39, 40, 42, 43,
 44, 45, 92, 93, 348, 349, 350, 716–732,
 743, 749, 770, 774–801
 reversing and non-reversing heat capacity
 717
 reversing heat capacity 3, 36, 37, 39, 40,
 42, 44, 716, 717, 723–728, 730, 732, 743,
 749, 774, 775, 776, 778, 779, 781, 782,
 784, 785, 786, 790, 791, 795, 797
 reversing melting and crystallization 793
 rigid amorphous 32, 45, 179, 189, 190,
 191, 206, 418, 781, 782, 784, 794, 800
 rigid amorphous fraction 32, 190, 191, 418,
 781, 782, 784, 794, 800
 rigidity 123, 136, 138, 183, 253, 257, 260,
 301, 302, 318, 369
 rigid-rod polymer 249
 rubber (see also elastomer) 57, 117–119,
 127, 128, 160, 274, 295, 305, 349, 466,
 519–522, 526–528, 530, 532–534, 537, 538,
 540–542, 544, 548–552, 554–558, 560,
 561, 563–574, 577, 578, 580, 599, 640, 642

rubbery 57, 127, 128, 305, 316, 317, 318, 322, 323, 325, 326, 327, 328, 346, 363, 520, 521

S

sample holder 343, 345, 420

sample mass 4, 5, 35, 36, 45, 330, 715, 723, 749, 758, 762, 764, 773

sample pans 758

sample preparation 275, 309, 343, 345, 360, 426, 428, 437, 576, 658, 801

sample size 35, 81, 276, 452, 653, 706, 792

sample temperature 3, 41, 85, 94, 328, 387, 436, 722, 787, 788, 789

sampling 367, 653, 655, 659, 674, 741, 755, 761

sapphire 3, 4, 204, 770

sealant 305, 308, 577

secondary amine 304

secondary relaxations 149, 152, 161, 163, 703

second-order phase transition 51

selenium 32, 714

self-heating 524

semicrystalline 16, 27, 36, 37, 44, 45, 155, 167, 175, 185–191, 360, 364, 365, 367, 589, 614, 657, 672, 673, 688, 701, 705, 781, 782, 787, 792, 794, 797, 798, 801

semicrystalline polymers 155, 167, 175, 185, 187, 189, 190, 365, 614, 673, 705, 787, 792, 798

sensitivity 92, 310, 311, 324, 325, 382, 435, 499, 533, 653, 654, 656, 668, 669, 688, 691, 698, 706, 707, 738, 770

sensors 40, 358, 718, 719, 721, 745

shrinkage 308, 326, 360, 365, 387, 388, 426, 427, 429, 431, 432, 433, 435, 439, 440, 441, 442, 444, 448, 452, 453, 454, 455, 456, 458, 460, 461, 473, 475, 502

shrinking 326

side chain LCP 698–700

silica 324, 522, 545, 550, 552, 571

silicone rubber 528, 571

simulation 72, 80, 217, 222, 229, 419, 421, 554, 676

simultaneous technique 525

simultaneous TG-DSC 389

single crystal 181, 283, 285, 286, 385, 391, 392, 417, 789

size exclusion chromatography 199, 363

skeletal vibration 20, 21, 22, 23, 25, 27, 28
skin-core 417

small angle X-ray scattering (SAXS) 183, 184, 190, 216, 217, 218, 219, 224, 236, 239, 285, 288, 289, 290, 385, 421, 427, 437, 458

smectic 247, 248, 249, 252, 255, 256, 258, 260, 268, 446, 749

smectic crystal 248, 255, 256

soft order 246

software 39, 89, 90, 212, 227, 324, 334, 336, 421, 714, 726, 738, 743, 748, 753, 755

solid-solid transition 171

solubility 369, 371, 449, 555

solution spinning 410, 463, 469, 470, 476

solution-casting 355

sound speed orientation 424

specific heat capacity (see heat capacity, specific) 2, 4, 15, 40, 205, 206, 231, 715, 723, 758, 761, 762, 786, 796

spherulites 181, 183, 239, 279, 380, 396, 422

spin-coating 355

spinodal mechanisms 175

stability 5, 45, 83, 90, 91, 93, 167, 172, 173, 174, 175, 183, 185, 187, 188, 189, 202, 204, 221, 224, 245, 247, 254, 260, 263, 264, 268, 288, 295, 301, 304, 306, 306, 368, 369, 383, 415, 416, 426, 435, 436, 439, 441, 456, 457, 460, 463, 467, 469, 471, 474, 476, 477, 480, 481, 482, 492, 511, 6512, 519, 523, 536, 537, 544, 566, 567, 568, 569, 571, 572, 573, 574, 577, 588, 590, 615, 619, 625, 630, 631, 633, 634, 637, 638, 639, 640, 641, 642, 643, 644, 654, 721, 748

stable equilibrium 172

standard 10, 34–37, 40–41, 43–45, 76, 79, 84, 88, 91, 104, 107, 227, 333–334, 343, 348, 356–357, 362, 496–497, 499, 529–530, 538, 546–547, 549, 553, 559, 562–563, 569–570, 576, 642–643, 645–651, 653–654, 658–662, 668, 673–675, 677, 681, 683, 692, 696, 698, 714, 730, 748–750, 758, 768, 770, 795, 801

standard method 653, 654

steady state 3–4, 35–36, 40, 43, 45, 112–113, 143–145, 343, 346, 602, 611, 617, 727, 730, 731, 742–744, 762, 766

- step 2, 7, 16, 19, 22, 36, 45, 52, 53, 61, 62,
 65, 86–87, 92–93, 132, 167, 199–200, 204–
 206, 212, 225, 228, 251, 262, 266, 296,
 298–299, 303–305, 309, 313, 317–318,
 323–324, 337, 340, 342, 349–351, 356,
 358–359, 368, 382–384, 391, 395, 412,
 431, 436, 448, 477, 492, 506, 537, 539,
 541–542, 545–549, 551, 554–555, 573,
 578, 588, 590–591, 595, 597, 602, 609,
 616, 618, 630, 638, 672, 680–681, 703,
 713–715, 717, 726–731, 737, 739–744,
 746, 750, 755, 757–758, 760–763, 765–
 766, 769–770, 774, 777, 782, 783, 786,
 788, 791–792, 794, 798, 800
 storage vessel 524
 stress relaxation 96, 97, 111, 119, 365
 stretching and deformation calorimetry 535
 structural recovery 49, 58–63, 66–67, 72–
 73, 76, 81, 84–87, 93–96, 99–104
 styrene butadiene rubber 160, 522
 sublimation 40
 sulfur-based cure 559, 561, 564
 supercooling 41, 88, 200, 202, 203, 288–
 289
 surface area 177, 361, 547–548, 550–551,
 703
 surface tension effects 412
 surroundings 524
 swelling differential scanning calorimetry
 (SDSC) 431
 symbols 71, 100, 321, 595, 714
 systematic error 91
T
 TA Instruments DSC 769, 780, 797
 techniques 798, 800, 801, 803
 technology 2, 47, 104, 108, 192–194, 241–
 242, 246, 270, 349, 352–353, 428, 482,
 485, 488–490, 579–580, 642, 649, 714, 718
 temperature calibration 3, 88, 91, 93, 324,
 657, 748–749
 temperature control 39, 83, 192, 436–437,
 578–579, 587, 657, 722
 temperature correction 333–334
 temperature measurement 45, 441, 615,
 722
 temperature modulated differential
 scanning calorimetry (TMDSC) 34, 86, 92,
 524, 713, 722, 801
 temperature resistance 305–307
 temperature scale 8
 temperature-jump 60
 temperature-modulated DSC 2
 tensile strength 307, 413, 464, 467, 470,
 474, 478–479, 481, 625
 terminal relaxation zone 114
 TGA 363, 427, 435–436, 439, 452–453,
 459–460, 467–468, 477–478, 510, 512,
 524–525, 536–538, 541–547, 549, 553–
 556, 569–574, 576–579, 587, 604, 608,
 612–613, 615, 618–619, 634–636, 638–639
 thermal analysis 1, 16, 32, 34, 36, 46–47,
 49, 92, 105, 108, 170, 173, 178–179, 181,
 184, 188, 190–193, 195, 222, 240–243,
 245–246, 269, 273–275, 286, 314, 334,
 351, 355, 360, 362–363, 365, 404, 409,
 426–427, 431, 441, 450, 457, 460, 468,
 473, 476, 478, 483, 487, 490, 519–520,
 523–526, 529, 533, 539, 547, 566, 571,
 573–574, 576–578, 580, 587, 588, 590,
 609, 613–615, 637, 641, 644–645, 647,
 655–656, 668, 674, 702, 708, 714, 717–
 718, 726, 741, 803
 thermal and oxidative stability 536
 thermal conductivity 14, 83, 90, 94, 282,
 290, 310, 363, 468, 524, 551–552, 561,
 654, 717, 720–721, 738, 740, 745, 750,
 758, 760–761, 763–770
 thermal constant 176, 587
 thermal decomposition 311, 557, 572–574,
 589, 594, 610, 618, 626, 635
 thermal degradation 306, 311, 415, 452,
 480, 503, 515, 538, 571–573, 575, 588–
 589, 592–593, 609, 616, 619, 621–622,
 624, 629, 631–633, 635, 637–642, 644–645
 thermal equilibrium 367
 thermal events 524
 thermal gradients 90–91, 93
 thermal lag 81, 91, 208, 720, 722, 748
 thermal motion 5, 18, 340, 768
 thermal oxidation 415, 550, 569, 609, 611,
 644
 thermal reaction 335, 587, 622
 thermal resistance 702, 745–747, 760, 787
 thermal shrinkage 426–427, 431–432, 439,
 475
 thermal small angle X-ray scattering
 (TSAXS) 427, 437, 439

- thermal wide angle X-ray diffraction (TWAXD) 427, 436–437, 439
 thermally stimulated current (TSC) 367–369, 381, 383–384, 402, 405, 486, 525, 533, 653–665, 667–708
 thermally stimulated currents-thermal sampling (TSC-TS) 653, 655–666, 668, 673–708
 thermistor (or thermoresistors) 363
 thermocouples 361, 657–658, 718–719
 thermodynamic 1, 5, 13, 15–16, 28, 38, 49–52, 56–57, 59–60, 67–68, 70–71, 75–76, 79–82, 95, 104–105, 111, 119, 122, 124, 132, 138, 167–174, 176–177, 183–184, 189, 191, 202, 222, 245, 246, 251, 253–254, 257, 259–260, 264–266, 268, 287, 288, 292, 299, 318, 319, 325–326, 392, 426, 428, 436, 589–592, 715–717, 719, 724, 768, 801
 thermodynamic equilibrium 111, 172, 259, 325–326, 591, 801
 thermodynamic state 59–60, 79, 95, 325
 thermodynamics 1, 5, 13, 15–16, 38, 50, 68, 71, 81, 105, 122, 167, 169, 171–172, 174, 183, 191, 253, 268, 287, 292, 426, 436, 590, 715–716, 768, 801
 thermogravimetric analysis 363, 524–525, 587
 thermogravimetry 427, 525, 537, 541, 545–546, 550, 553, 567
 thermoluminescence 524, 533
 thermomechanical analysis (TMA) 360–361, 371, 373, 380, 404, 427, 432–434, 439, 442, 448, 450, 452–454, 456–457, 467–468, 472, 525, 530–531, 533, 535, 556, 558–559, 565, 572–573, 577, 587, 613, 662, 682, 684, 713, 789, 802
 thermoplastic elastomer 274, 292, 520–521, 528, 535, 556, 580
 thermoset 40, 101, 295–310, 312, 315–316, 318–321, 323, 330, 332, 337, 339, 340, 343, 345, 349–352, 495, 505–506, 508–509, 512–513, 556, 566, 627–628
 thermotropic 245–246, 249, 251, 253, 263, 268, 463, 469–470, 472, 701
 thermotropic main-chain liquid crystalline polymer 246, 249, 253, 263, 268
 thermoviscoelastic 67, 68, 70–72
 thin films 85, 174, 309, 355, 359–360, 362–363, 365–366, 404, 689
 tie molecules 202, 383, 386, 418–419, 433
 time-aging time superposition 96–97, 99
 time-dependent properties 100
 time-structure superposition 96
 time-temperature superposition 336, 366, 435
 toughness 102, 302, 305, 415, 481, 499, 653
 transients 310, 335, 343, 697, 741
 transition temperature 16, 32, 34, 36, 40, 49, 52–55, 59, 72–73, 77–78, 80–82, 84, 88, 94–95, 104, 137, 169–171, 176, 207, 236, 245, 250, 253–254, 256–260, 264–267, 274–276, 290, 305, 309–310, 315–318, 320–323, 326–328, 337, 345, 347–351, 365–367, 369, 380, 428, 435, 470–472, 519, 521, 529, 533, 539, 589, 702, 706, 713, 721, 748, 750, 770–774, 787
 transition temperatures 16, 32, 34, 36, 40, 49, 52–55, 59, 72–73, 77–78, 80–82, 84, 88, 94–95, 104, 137, 169–171, 176, 207, 236, 245, 250, 253–254, 256–260, 264–267, 274–276, 290, 305, 309, 310, 315–318, 320–323, 326–328, 337, 345, 347–351, 365–367, 369, 380, 428, 435, 470–472, 519, 521, 529, 533, 536, 539, 589, 702, 706, 713, 721, 748, 750, 770–774, 787
 transmission electron microscopy 184, 253, 275
 TSC 367, 381, 383, 402, 525, 533, 653–665, 667–708
 twines 443
 two-phase model 167, 189–190, 206–207, 228, 417, 419, 450, 780, 783, 794, 798
U
 uniaxial negative birefringence 371
 uniaxial positive birefringence 423
 Unsaturated polyester 302
 unstable equilibrium 172
V
 vacuum 310, 356, 400, 415, 417, 423, 441, 506, 508, 541, 554, 573, 593, 603, 613, 618, 621, 622, 626, 630, 635, 640, 658, 667, 673, 697, 703
 vibration 9–10, 12–13, 17, 19, 20–25, 27–28, 30, 32, 33, 36, 45–46, 120, 122, 135, 317, 396, 423–424, 458, 481, 526

vinyl rubber 528

viscoelastic 49, 62–63, 67–68, 70–73, 94–97, 99–101, 105–106, 111–114, 116–119, 127, 131, 133, 139, 142–143, 147, 152, 163, 375, 385, 390, 402, 413, 459, 467, 519–520, 550, 552, 673–674

viscosity 73–78, 84, 111, 112, 117, 131, 132–134, 136–139, 142–145, 176, 199, 296–297, 305, 344, 466–467, 470–472, 599, 608, 612, 615, 619

vitrication 40, 174–175, 201, 206, 210, 232, 236, 299–301, 345, 349–351, 770–771, 777, 781–782, 784

volatility 593

volume recovery 58, 60–62, 64, 70, 72, 96, 100

W

waxes 654

weight-loss 435–436, 452, 477, 510, 512, 537, 542, 544–546, 550, 553, 555, 571, 589, 608, 612, 615, 619, 620, 622, 626–627, 629–630, 632, 638–639

wet spinning 410, 412, 448, 451, 467, 480

wide angle X-ray diffraction (WAXD) 184, 190, 207–208, 215, 217–219, 224, 228, 235–236, 239, 249, 252, 256, 258, 265, 382–383, 417–420, 425, 427, 432, 436–437, 439, 442, 445, 450–451, 454, 460–461, 472, 478

Williams, Landel and Ferry (WLF)

equation 74, 77–78, 122, 127, 164, 685, 707

worm-like 136–137, 142

X

X-ray diffraction 16, 178, 184, 190, 249, 282, 382, 384, 403, 419, 427, 436

X-ray reflectivity 362

Y

yield point 117, 414

yield strain 117, 144–145

yield strength 59, 101

Z

zero entropy prediction 686, 691, 698

zinc 523, 552, 563, 573, 627